Lecture Notes in Civil Engineering

Amit Prashant
Ajanta Sachan
Chandrakant S. Desai *Editors*

Advances in Computer Methods and Geomechanics

IACMAG Symposium 2019 Volume 1

Springer

Lecture Notes in Civil Engineering

Volume 55

Lecture Notes in Civil Engineering (LNCE) publishes the latest developments in Civil Engineering - quickly, informally and in top quality. Though original research reported in proceedings and post-proceedings represents the core of LNCE, edited volumes of exceptionally high quality and interest may also be considered for publication. Volumes published in LNCE embrace all aspects and subfields of, as well as new challenges in, Civil Engineering. Topics in the series include:

- Construction and Structural Mechanics
- Building Materials
- Concrete, Steel and Timber Structures
- Geotechnical Engineering
- Earthquake Engineering
- Coastal Engineering
- Ocean and Offshore Engineering; Ships and Floating Structures
- Hydraulics, Hydrology and Water Resources Engineering
- Environmental Engineering and Sustainability
- Structural Health and Monitoring
- Surveying and Geographical Information Systems
- Indoor Environments
- Transportation and Traffic
- Risk Analysis
- Safety and Security

To submit a proposal or request further information, please contact the appropriate Springer Editor:

– Mr. Pierpaolo Riva at pierpaolo.riva@springer.com (Europe and Americas);
– Ms. Swati Meherishi at swati.meherishi@springer.com (Asia - except China - and Australia/NZ);
– Ms. Li Shen at li.shen@springer.com (China).

Indexed by Scopus

More information about this series at http://www.springer.com/series/15087

Amit Prashant · Ajanta Sachan ·
Chandrakant S. Desai
Editors

Advances in Computer Methods and Geomechanics

IACMAG Symposium 2019 Volume 1

Springer

Editors
Amit Prashant
Indian Institute of Technology Gandhinagar
Gujarat, India

Ajanta Sachan
Indian Institute of Technology Gandhinagar
Gujarat, India

Chandrakant S. Desai
University of Arizona
Tucson, AZ, USA

ISSN 2366-2557 ISSN 2366-2565 (electronic)
Lecture Notes in Civil Engineering
ISBN 978-981-15-0885-1 ISBN 978-981-15-0886-8 (eBook)
https://doi.org/10.1007/978-981-15-0886-8

This Springer imprint is published by the registered company Springer Nature Singapore Pte Ltd.
The registered company address is: 152 Beach Road, #21-01/04 Gateway East, Singapore 189721, Singapore

Preface

The Symposium of the International Association for Computer Methods and Advances in Geomechanics (IACMAG) was held at the Indian Institute of Technology Gandhinagar, Gujarat, India, during the period 5–7 March 2019. Computer applications of geomechanics have been gaining much popularity from the early days of the International Conference on Numerical Methods in Geomechanics at Vicksburg in 1972, Blacksburg in 1976 and Innsbruck, Austria, in 1988. It was in that very context the IACMAG was established and it has been growing ever since with various stakeholders contributing significantly from different nations across the world. IACMAG aims at fostering multidisciplinary research and ideas pertaining to geomechanics with particular emphasis on integrating both the practical and the fundamental aspects. The field of geomechanics has evolved with time, and in this regard, IACMAG takes into account the need for judicious simplification of fundamental aspects of geomechanics with a proper amalgamation of theory and experimentation in order that they find their use in practical problems and challenges faced in the industry today.

IACMAG has grown steadfastly in its scope and size encompassing various aspects of constitutive modelling of geomaterials, computational methods and emerging fields of bio-cementation as well as treatment of geomaterials. The Symposium at IIT Gandhinagar aimed at providing a platform for exchanging ideas and recent developments as well as for discussing future visions related to the field of geomechanics and geotechnical engineering. A Pre-Symposium Workshop on "Behaviour of Civil Engineering Materials" was also held in this regard on 4 March 2019 with its focus on the material models commonly used in analysis and design of structures. It also included a hands-on session for implementing simple computer applications of geotechnical engineering for industry and academia. The IACMAG Symposium 2019 included 11 keynote/invited speakers of repute from different backgrounds of the geotechnical engineering community. It involved four parallel sessions with main themes of the symposium being primarily focussed on (i) Geomaterial Behaviour and Material Modelling—including multi-scale modelling, micro-structural instabilities, liquefaction, chemical and bio-effects in geomaterials and field/laboratory testing; (ii) Earthquake Engineering—including

dynamics of geomaterials, earth embankments and dams; (iii) Geosynthetics and Ground Improvement with thrust areas on bio-treatment, soft and expansive clays; and (iv) Analysis and Design of Structures—including bridges and foundations as well as soil–structure interaction problems.

We thank all the authors for their contribution to the IACMAG Symposium 2019 that has resulted in the proceedings which is being published in two volumes. IACMAG follows its long-standing tradition in selecting and reviewing these papers with great rigour, and we hope that the proceedings will provide a glimpse of the state-of-the-art practices followed in different fields related to geomechanics and its allied branches. We would also like to express our sincerest of appreciation to the reviewers of the papers and to various technical and financial sponsors for making this event a grand success.

Gandhinagar, India — Ajanta Sachan
Gandhinagar, India — Amit Prashant
Tucson, AZ, USA — Chandrakant S. Desai

Contents

About the Editors

Amit Prashant is a Professor in Indian Institute of Technology Gandhinagar, India. After his PhD and post-doctoral work in the University of Tennessee at Knoxville (USA), he went on to work as an Assistant Professor in IIT Kanpur from 2005 to 2010, before joining IIT Gandhinagar in 2010. His research interests include constitutive modeling for granular materials, numerical modeling of geotechnical structures, and earthquake geotechnical engineering. In 2005, he received the Young Researcher Fellowship Award from Massachusetts Institute of Technology, Cambridge (USA) during the 3rd M.I.T. Conference on Computational Fluid and Solid Mechanics. He has also been awarded the Excellence Award in Institution Building and Outreach in 2013 and 2015 respectively. Prof Prashant has published more than 60 research articles in reputed journals and conferences, and organizes activities to encourage student initiatives and increase industry-academia interaction.

Ajanta Sachan is an Associate Professor in Indian Institute of Technology Gandhinagar, India. After her B.E in Civil Engineering, she worked in WAPCOS Limited and IIT Kanpur, India before pursuing her PhD in University of Tennessee at Knoxville, USA. Her research interests include material characterization, studying shear strength and compressibility behavior in soils, etc. Dr Sachan serves as a reviewer in 7 journals and is a member of American Society of Civil Engineers (ASCE), USA, Earthquake Engineering Research Institute (EERI), USA and the National Information Centre for Earthquake Engineering (NICEE), India. She has published more than 50 research papers, and has served in various administrative capacities.

Chandrakant S. Desai is a Regents' Professor (Emeritus) in the Department of Civil and Architectural Engineering and Mechanics at the University of Arizona, Tucson, USA. After completing his MS and PhD from Rice University Houston and University of Texas, Austin in 1966 and 1968 respectively, he joined the U.S. Army Corps of Engineers' Waterways Experiment Station, where he worked till 1974. Subsequently, he joined The University of Arizona, where he has served on

various capacities. Prof Desai has authored or edited 23 books and over 345 research papers over the course of his career, which has involved the development and application of constitutive laws with design and fabrication of new and innovative test devices, and of computer methods for solution of a wide range of problems in civil, mechanical and electronics engineering. He has been the founding president of the IACMAG and founding Editor-in-Chief for two international journals in Geomechanics. He has received many awards and distinctions, and is a member of a number of technical societies including an elected Distinguished Member of the American Society of Civil Engineers, USA.

Dynamic Soil–Foundation–Structure Interaction for Bunds in Goa

Leonardo Souza and P. Savoikar

Abstract This paper provides a concise review of Dynamic (Seismic) Soil–Foundation–Structure Interaction (DSFSI) presenting the main methods of DSFSI which are an important and integral part of such studies. The paper spotlights the areas which can use DSFSI including traditional structures like bunds and new structures like pile, pile raft, and mat foundations. Traditional Goan Saraswat Bunds are ancient coconut tree-lined road and flood control embankments found all over Goa which have lasted for thousands of years through storms and earthquakes. Today, as the concept of sustainable construction practices gains growing recognition, they deserved to be studied. The behavior of the tree on top of a bund during earthquakes can be studied using Single-Degree-of-Freedom and vibration damping by pendulum. This paper also presents an equation for the interaction of coconut tree roots as soil springs for their role in damping of the Seismic waves in the bunds. Modeling the bund in MIDAS-GTS-NX showed marginal reduction in acceleration and displacement by the presence of coconut trees.

Keywords Dynamic soil–foundation–structure interaction · DSSI · DSFSI · Soil–structure interaction · DSSI of bunds · Traditional Goan Saraswat Bunds

1 Introduction

Due to increased construction activities along the earthquake-prone zones, Soil–Structure Interaction in its various avatars (Soil–Structure Interaction—SSI, Structure–Soil–Structure Interaction—SSSI, Dynamic Soil–Structure Interaction—DSSI, Dynamic (Seismic) Soil–Foundation–Structure Interaction—DSFSI) has come to prominence. It has been applied to modern structures like High-Rises, Bridges, Harbors, and Nuclear Power Plants and also to traditional historic structures. This paper

L. Souza (✉) · P. Savoikar
Department of Civil Engineering, Goa Engineering College, Farmagudi 403401, Goa, India
e-mail: lrdcs@rediffmail.com

P. Savoikar
e-mail: psavoikar@gmail.com

A. Prashant et al. (eds.), *Advances in Computer Methods and Geomechanics*, Lecture Notes in Civil Engineering 55,
https://doi.org/10.1007/978-981-15-0886-8_1

will attempt to analyze if and how it can be applied to Traditional Goan Saraswat Bunds (TGSB), which are historic embankments found in Goa. They are different from other embankments due to the pair of rows of coconut trees planted on top of them.

1.1 Dynamic Soil–Foundation–Structure Interaction (DSFSI)

Dynamic Soil–Foundation–Structure Interaction (DSFSI) studies the interactive relationship between building structures and foundation during earthquakes where the vibrations in one (soil or structure or foundation) cause and/or affect the vibrations in the other.

In analysis of structure, it is erroneously assumed that all structural elements are fixed at the foundation, resisting translation ($F_X = 0$, $F_Y = 0$), settlement ($F_Z = 0$), and rotation ($M_\theta = 0$ or $M_X = 0$, $M_Y = 0$, $M_Z = 0$) (Fig. 1). However in seismic zones, structures get excited by ground shaking caused by earthquake and develop inertial forces. These introduce bending moments and base shears at the interface of structure and foundation. Ignoring these effects can lead to catastrophic response under earthquake loadings. These effects depend on type of structure, foundation, and soil (Fig. 2).

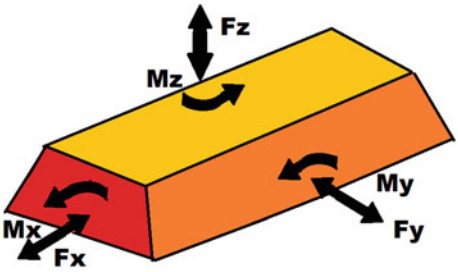

Fig. 1 Forces acting on the foundation during earthquake

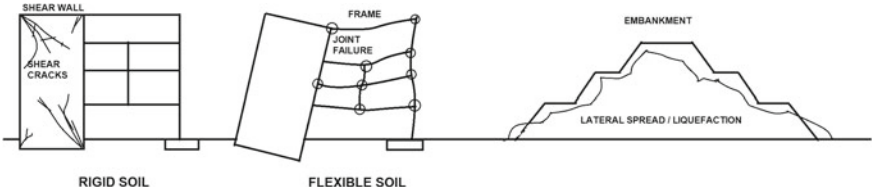

Fig. 2 A structural systems (on rigid soils and flexible soils) and bunds

Hence DSFSI is coupled with problems which links the mathematical relationship between the active and reactive forces along the surface of contact. Both can only be jointly determined. Winkler model, though often used for idealization of soil response due to its simplicity, has the disadvantage of treating soil as a uniform continuum.

2 Literature Review

Sharma et al. [16] conducted a detailed review of the seismic SSI studies associated with building structures by reviewing 110 papers and they concluded that researchers studying SSI articulated diverse views while dealing with the effects of SSI. It describes at length, the origin and developments in the subject of soil–structure interaction. However, from the literature, contradictory opinions were observed about its need, benefits, and demerits. They concluded that Codes provide insufficient procedure on SSI for buildings and their need for improvement. They felt a necessity to examine SSI in detail in order to identify the possible scenarios in seismic SSI by including nonlinearity and ground motion characteristics for both building and soil while evaluating the seismic response of the structure. In current SSI studies, identification of proper parameters to modify ground motion is often ignored. Hence innovative methods that take these into account are needed.

The earliest attempt to analyze DSFSI was initiated in Japan in 1935 by Sezawa and Kanai [15]. They modeled the structure as a thin cylindrical rod with the base as a hemispherical tip fully embedded in a homogeneous half-space. The theory of Dynamic Soil–Structure Interaction (DSSI) was first formulated by Reissner in 1936 [13] through an article. He applied time-harmonic vertical loads to test the behavior of circular disks lying over elastic half-spaces by assuming uniform stress distribution underneath the plates and that the central displacement of the load equals the plate displacement. Hadjian et al. [6] reported the earliest work on Dynamic Soil–Structure Interaction (DSSI). They used the continuum approach in combination with the finite element approach to solve DSSI problems. Kausel [10], Lou et al. [12], Roesset [14] have also documented and extensively reviewed the development of DSSI. They obtained the fundamental analytical solutions for foundations at the surface of an elastic half-space. The conflicting aspects of DSSI were critically appraised, highlighting the existing contradictions. The advantages and disadvantages of the existing standard methods of DSSI analysis, viz., the direct method and sub-structuring method were discussed. Lai and Martineli [11] have beautifully explained the concept and importance of Dynamic Soil–Foundation–Superstructure Interaction analysis when assessing the structural response of shallow and deep foundation typologies in reaction to earthquake loading. Various codes from different countries have given diverse methods of dealing with DSFSI. Eurocode 8, EN 1998-1 [2], states the conditions to consider SSI, however, avoids specific procedures for the technical computation of DSFSI. ASCE 7-05 [1] accommodates DSFSI effects by either adjusting the results obtained from fixed base analysis or by including soil flexibility. IS 1983 [8], the Indian standard for earthquake resistant design, exempts structures supported on rock

and rock-like material from the consideration of SSI while avoiding the mention of DSFSI in the procedure for analysis and design of foundations in soils. Both ASCE 7-05 [1] and FEMA (356-2000 [3], 440-2005 [4], 450-2003 [5]), permit reduction of base shear force by taking into consideration damping with a suitably modified time period. The DSSI modeling using various constitutive models and interface nonlinearity is suggested by Japanese code JSCE [9].

There is however inadequate information on DSFSI as applied to trees and their role in vibration damping of dynamic loading. Modeling by conventional software is also not possible as there is no provision to consider the damping effects of tree mass and tree roots.

3 Applications of DSFSI

DSFSI can be widely used for any type of structure combined with any type of foundation. The nature of the ground motion and the surrounding soil cause amplification and de-amplification of the seismic waves governing the unique structural response in DSFSI.

3.1 Modern Structures

Pile Foundation: The nonlinear soil behavior and liquefaction during earthquakes cause an extremely complex seismic response of structures supported on a pile foundation [7, 17, 19]. The DSFSI of soil–pile–structure interaction has been studied widely and is extremely important for its seismic analysis and design.

Bridge Foundation: When a bridge traverses a basin or a valley, it usually needs columns with different lengths. Bridges with varying column lengths have detrimental seismic behavior during earthquake events [19]. A sizeable concentration of seismic forces in the shorter columns (the stiffer parts of the lateral resisting system) causes stiffness irregularities in these type of bridges. Very high shear and moment forces arise in these columns. Eurocode uses a force-based bridge design methodology.

Shallow Foundation: DSFSI has significantly improved the performance of buildings on shallow foundations like mat foundations [7, 17] during many Earthquakes. Comparison of traditional fixed base response, with numerical analyses of buildings on beds of nonlinear springs, has shown a reduction in the forces transferred to structures due to DSSI.

Combined Pile Raft Foundation: The effect of axial load along with seismic forces on combined piled raft foundation system showed appreciable improvement as compared to other foundation systems [17] in layered soil.

Jetty Design: The conventional engineering assumption representing seismic input as vertically polarized shear waves is usually adopted as a starting point in jetty design

as these waves are often assumed to be critical. It is an oversimplification, where Rayleigh waves and vertical motions may also affect the jetty's seismic response. Their effect of using DSFSI is a matter for future research.

Nuclear reactors: Nuclear reactors [7, 19] are vital structures that need to properly designed for both earthquake loads and blast loads. DSFSI is critically needed for the design of such structures.

3.2 Historic Structures

There are scarce studies done on DSFSI for historic structures and this is a promising field of research. Many such important structures (Gopurams, minarets, Clock towers, religious structures, palaces, etc.) have survived thousands of years and an attempt must be made to understand why some remained while others fell during earthquake events.

3.3 Traditional Goan Saraswat Bunds

Traditional Goan Saraswat Bunds (TGSB) are long-established road and flood control embankments found all over Goa. They have lasted for thousands of years through storms and earthquakes and even cannon fire [18] with minor annual maintenance. Their heights vary from 1 to 3 m (with few touching 6–9 m). Today, as the concept of sustainable construction practices gains growing recognition, they deserved to be studied. Their behavior during earthquakes can be studied using SDOF and DSFSI as discussed below. This is a subject worthy of further research as it has wide applicability in rural India. The coconut tree can be taken as a structural element causing damping due to inverted pendulum SDOF system, while the roots can be considered as foundation elements with spring damping systems.

4 Kinematic and Inertial Effects of Seismic Waves

Due to the presence of a dynamically excited structure at a soil site, two phenomena known as kinematic and inertial effects occur. Kinematic Interaction represents the seismic input in the absence of the structure sitting at the site. The second phenomenon Inertial Interaction results from the dynamic coupling between a structure and its supporting ground.

The magnitude of kinematic interaction depends on the structural geometry, foundation size, foundation embedment, free-field motion kinematics, and the angle of incidence of the seismic waves (Fig. 3). However, there is no kinematic interaction when a foundation located at ground surface (i.e., a shallow foundation) is hit by a

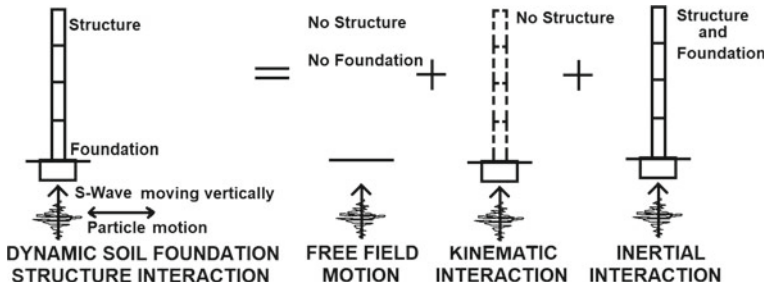

Fig. 3 Kinematic and inertia interaction

vertically propagating S wave. The dynamic response of the foundation is frequency-dependent due to the inertial and dissipative properties of the soil–foundation system. Consider a Single-Degree-Of-Freedom (SDOF) system with a mass M and a spring with flexural stiffness K, which is fixed at the base and subjected to horizontal displacement. It is controlled by M and K (Fig. 4a).

The following relation gives the fundamental period T_{fix} of the system (Eq. 1):

$$T_{fix} = 2\pi/\sqrt{K/M} \tag{1}$$

When a rotational spring indicating soil compliance, where the base can rotate, is connected at the base for the above SDOF system, (Fig. 4b) the following pair of equations give the global response of the system (Eqs. 2, 3):

$$F = K_{eq}u = K_{rot}u_{rot} = Ku_{flex} \tag{2}$$

$$u = u_{rot} + u_{flex} \tag{3}$$

where u denotes displacement along x-axis, u_{rot} denotes rotational displacement, u_{flex} is the displacement due to bending, and K_{rot} is the rotational stiffness of the spring,

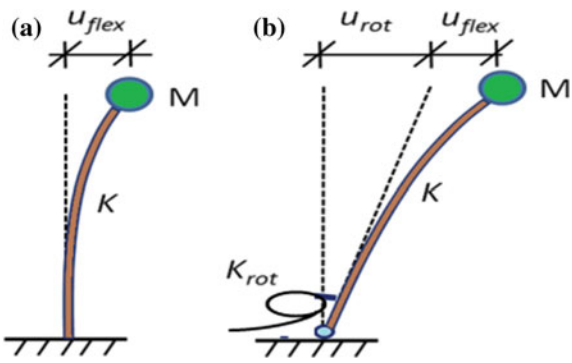

Fig. 4 SDOF system with **a** fixed base and **b** rotation spring base

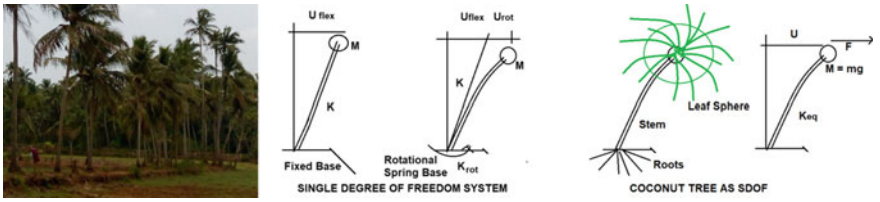

Fig. 5 Coconut tree as a structural element with root foundation—inverted pendulum damping system

the following relations give the equivalent stiffness (K_{eq}) and the fundamental period (T_{eq}) of the system (Eqs. 4, 5):

$$K_{eq} = 1/\left(\frac{1}{K} + \frac{1}{K_{rot}}\right) \tag{4}$$

$$T_{eq} = 2\pi/\sqrt{K_{eq}/M} \tag{5}$$

Thus, it can be seen that the SSI effect augments the natural period of the structure. This concept is easily applicable to Coconut trees placed on bunds (Fig. 5).

5 Methods of Analyses

The traditional DSFSI analysis methods are direct and indirect (substructure) approaches. The macroelement concept is a comparatively new and innovative approach in geotechnical engineering to solve DSFSI problems that combines the merits of the direct and indirect approaches without their shortcomings.

5.1 Direct Approach

This approach is conceptually easy but computationally difficult. The structure and the soil volume are both a part of the same model (Fig. 6). Using one of several numerical discretization techniques (e.g., Finite Element Method, Spectral Element Method, and Finite Difference Method), this can be analyzed in a single step. Soil nearer the foundation can be discretized into smaller elements for greater accuracy. The zone of fine discretization may extend to twice base width at discretion of designer and the nodes in figure represent the points where the interaction takes place. The Eq. (6) of motion is given by

$$\ddot{u}_{total} M_{total} + u_{total} K \quad = -M_{total} \ddot{u}_{base} \tag{6}$$

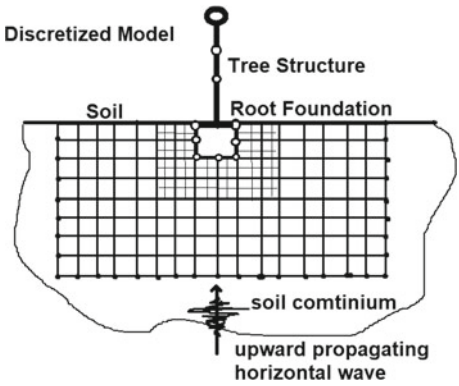

Fig. 6 Model for direct approach for coconut tree

where $\ddot{u}_{base}$ represents the input motion applied at the base of the model, M_{total}, K $\ddot{u}_{total}$, and u_{total} are the mass and stiffness matrix of the global system and the acceleration and displacement vectors of the system, respectively.

5.2 Substructure Approach

This approach is conceptually difficult but computationally easier (Fig. 7). By splitting the superstructure–foundation–soil system into two subsystems (kinematic interaction and inertial interaction) whose response is determined independently, the DSFSI problem is solved.

The seismic response of the superstructure–foundation–soil system is computed using the following three steps:

1. Solve the Kinematic Interaction (KI) problem. Evaluate the change with respect to the free-field ground motion of the seismic wave-field induced by the presence of the foundation. Thus, compute the Foundation Input Motion (FIM)
2. Calculate the frequency-dependent, Dynamic Impedance Matrix (DIM) which represents the dynamic response of the soil–foundation subsystem detached from

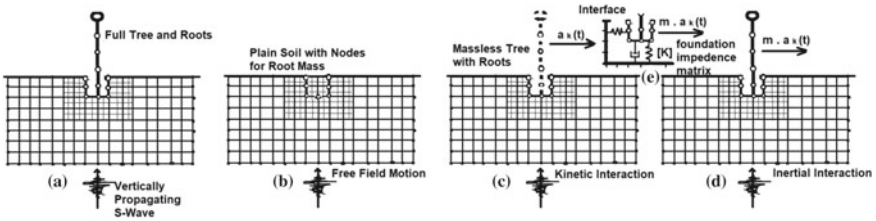

Fig. 7 DSSI using the substructure approach. **a** Geometry of SSI problem; Splitting of the problem into **b** free-field motion, **c** kinematic response, and **d** inertial response; **e** spring dashpot connection of soil and foundation for the transfer of waves

the superstructure. The DIM is complex-valued and generally fully populated due to the coupling between the three translational and three rotational (six) degrees-of-freedom of the foundation.

3. Calculate the dynamic response of the whole system (superstructure, foundation, and surrounding soil) subjected to the FIM (step 1 above) by connecting the finite element model of the superstructure with the foundation–soil subsystem through DIM (step 2 above). Consider Inertial Interaction in this step. Response Spectrum Method (RSM) or the Time-History Method (THM) can be used for the dynamic analysis of the whole system.

The equation of motion (Eq. 7) is given by

$$\ddot{u}_{kin} M_{soil} + u_{kin} K = -M_{soil} \ddot{u}_{base} \tag{7}$$

where $\ddot{u}_{base}$ represents the input motion applied at the base of the model, M_{soil} and K are the mass and stiffness matrix of the global system, u_{kinl} is the kinematic displacement vector that gives the FIM. This is then substituted in the equation for the global system.

5.3 Macroelements Approach

The assumption of linearity of the overall soil-structural system is a severe limitation of the substructure approach. These nonlinearities in DSFSI may arise in different ways, (nonlinear constitutive behavior of structural materials, geometrical nonlinearity along the soil–structure interfaces, and soil nonlinearity in hydromechanical response). These effects can considerably impact the overall structural response under both static and dynamic loadings. The macroelement gives proper foundation response under any loading (horizontal, vertical, and rotational) (Fig. 8). In the macroelement approach for strip foundations, a set of generalized force and displacement vectors $\bar{Q}$ and $\bar{q}$ is usually written in dimensionless form (Eqs. 8, 9, 10) as follows:

$$\bar{Q} = \begin{bmatrix} \xi \\ h \\ m \end{bmatrix} = \frac{1}{v_{\max}} \begin{bmatrix} V \\ H \\ M/B \end{bmatrix} \tag{8}$$

$$\bar{q} = \begin{bmatrix} \eta \\ \varepsilon \\ \zeta \end{bmatrix} = \frac{1}{B} \begin{bmatrix} v \\ u \\ \theta \end{bmatrix} \tag{9}$$

$$\bar{Q} = C_{ep} \bar{q} \tag{10}$$

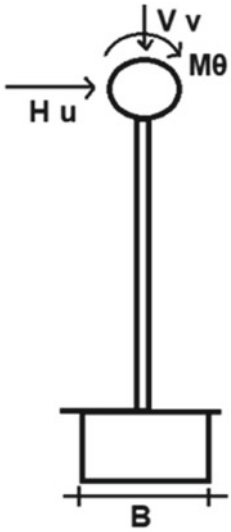

Fig. 8 DSSI using macroelements approach

A generalized non dimensional stiffness matrix C_{ep} is used to relate $\overline{Q}$ and $\overline{\varrho}$

Where V_{max}, V, H, and M is the maximum normal force, vertical force, the horizontal force, and the moment, respectively, and v, u, and θ is the vertical, horizontal, and rotation displacement, respectively.

5.4 Computer Aided Design

The main feature of DSFSI is the calculation of the force–displacement relationship at the nodes along the soil–structure interface. For DSFSI, the vastness of the complexities involved mandates a computerized analysis. Many commercially available software like ADINA, DYNA4, MIDAS, GEOSTUDIO, OPTUM G2, PLAXIS, etc., are available for such analysis. By using these software, the displacement of each node of the soil–structure interface can be easily computed by assuming a linear soil response with rigid and massless foundation.

6 DSFSI of Bunds

6.1 Damping from Coconut Tree

Coconut trees are placed in uniformly spaced rows on the top of TGSB's. They have a narrow stem of uniform diameter of 250 mm and a height of 5–15 m. The whole mass of leaves and nuts is modeled as a spherical mass 3 m diameter (the actual leaf

length is 3–5 m, but the mass is taken as concentrated in middle third) placed on weightless rod and acts as a synchronized inverted pendulum damper. The equations of damped motion (Eqs. 11, 12, 13) for oscillation of tree are given below.

$$\ddot{\theta} + \frac{c}{ml}\dot{\mathrm{O}} + \frac{g}{l}\sin\theta = \frac{\tau_c}{ml^2} \tag{11}$$

It can also be written as

$$\ddot{\theta} + \frac{c}{ml}\dot{\mathrm{O}} + \frac{g}{l}\sin\theta = F\sin(2\pi f\, T_o) \tag{12}$$

$$T_o = 2\pi\sqrt{\frac{l}{g}} \tag{13}$$

where θ is the angular position of the pendulum mass, l is length of massless rod (arm), m is the mass of pendulum, c is the linear damping coefficient, τ_c is the input torque causing motion, g is acceleration due to gravity, F is the forcing amplitude, f is the frequency of motion, and T_o is the period.

6.2 Damping from Coconut Roots

On excavation around coconut trees fibrous root system, it was found that every root has average diameter of 7 to ±3 mm and a length of 5–10 m. Coconut roots have reasonably high elasticity and frictional resistance with soil. They can hence be modeled as a collective spring-damper system (Fig. 9).

The equations of damped motion (Eqs. 14, 15, 16) of roots are given below.

$$\ddot{u} + 2\zeta\omega_o\dot{u} + \omega_o^2 u - 2f_r\dot{u} = 0 \tag{14}$$

$$\textit{natural frequency in radians} = \omega_o = \sqrt{\frac{k}{m}} \tag{15}$$

$$\textit{damping ratio} = \zeta = \frac{c}{2\sqrt{mk}} \tag{16}$$

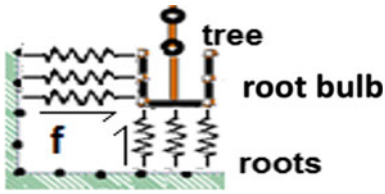

Fig. 9 Coconut tree roots as spring dampers

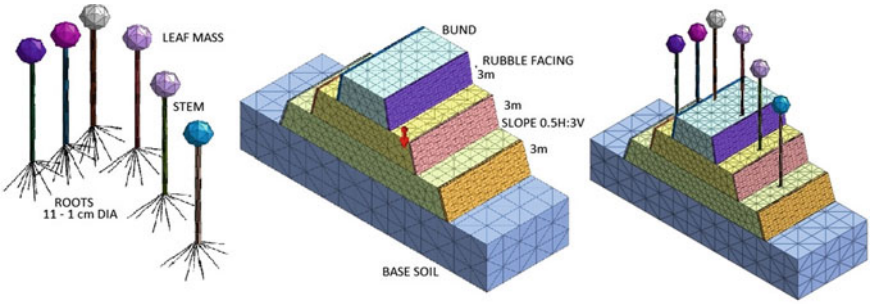

Fig. 10 3D model of bunds Unreinforced/Reinforced by Coconut tree using MIDAS-GTS-NX

where u is the displacement vector, f_r is friction between soil and roots, k is root spring stiffness, m is the mass of roots, and c is the linear damping coefficient.

6.2.1 Computerized SSI of Bunds Using MIDAS

Coconut trees were modeled as lumped masses with 11 single mesh embedded beam element (fibrous root system) 5 m long and treetop as sphere 3 m dia on 10 m 30 cm diameter stem (Fig. 10), with bunds of 3 benching layers of side-slope 0.5 H: 3 V using MIDAS-GTS-NX software. The small size of roots makes it impossible for finer modeling. (Larger number of roots refused to mesh.) The bund was modeled with 1 m mesh and the subsoil 2 m mesh. MIDAS offers auto connect to connect all mesh elements. Releasing M_z at the base of stem allows for rotational spring effect. An earthquake load was taken from MIDAS library of Type III as it closely represents Goa Region and the acceleration and horizontal displacement for reinforced and unreinforced bunds were calculated for linear dynamic loading considering only self-weight. It was not possible to effectively model the roots as springs and trees as pendulum damping masses, as most software are primarily designed for soil and structures.

The tree was modeled as Isotropic Elastic material as it only carried tensile and bending stresses, while the soils were modeled as Isotropic Mohr–Coulomb material as dynamic loading was used. Soil and roots were tested at Goa Engineering college labs and results are given in Table 1.

Table 1 Properties of materials used in MIDAS for computation

Materials	E kN/m^2	1/m	e_o	γ kN/m^3	c kN/m^2	ϕ °	K_o	Damping factor	Type
TREE	8000	0.3	0.65	20			1	0.2	Elastic
RUBBLE	4E4	0.3	0.65	22	150	40	0.30	0.3	Mohr–Coulomb
BUND	1.2E4	0.3	0.5	16.8	18	30	0.52	0.25	Mohr–Coulomb
BASE SOIL	1.2E4	0.33	0.55	19.5	12	38	0.38	0.25	MC

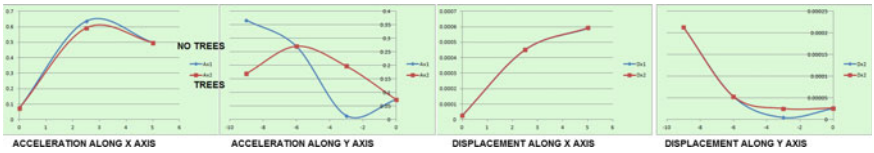

Fig. 11 Acceleration and displacement on bunds with coconut trees (red) and without (blue)—at 0, 2.5, 5 m along width and 0, −3, −6, −9 along depth of bund in Global x-direction

6.3 Results and Discussions

The results (Fig. 11 and Table 2) showed marginal improvement of acceleration 0.0039 m/s^2 and displacement of 0.000001 m near tree offset by diminishing effect away from the tree.

It is also seen that the modeling of fibrous roots as individual elements did not give expected results so there is a need to model them differently (perhaps as a separate soil layer with increased shear strength and damping constant).

7 Conclusions

It is vital to evaluate the effects of DSFSI on structures in a modern development scenario. DSFSI can be used to study new and traditional structures like TGSB's of Goa. As the DSFSI analytical calculations are complex, computer software is preferred. On using MIDAS-GTX-NX software, the presence of single coconut trees has shown marginal reduction in earthquake damage of acceleration 0.0039 m/s^2 and displacement of 0.000001 m near tree, especially in Goa. This is because the present computer-based analysis programs don't model trees and root elements. There is a need to develop software programs to model trees for DSFSI as they provide good damping in case of earthquakes. Modeling a tree as a pendulum and roots as spring dampers is an effective way to deal with the situation. There is scope for further refinement in the modeling process as fibrous roots can't be effectively modeled as individual elements but may need to be modeled as a modified soil layer. An extended model study with rows of coconut trees needs to be done.

Table 2 Variation of acceleration and displacement away from the center (tree)

X Fig no	Without trees		With coconut trees		Y	Without trees		With coconut trees	
	Ax(11c)	Dx(11d)	Ax(11a)	Dx(11b)		Ax(11c)	Dx(11d)	Ax(11a)	Dx(11b)
0	0.07429	0.000027	0.0739	0.000026	0	0.074291	0.000026	0.07397	0.000026
2.5	0.63474	0.000451	0.5928	0.000451	−3	0.014979	0.000005	0.19779	0.000025
5	0.49751	0.000590	0.4991	0.000593	−6	0.27091	0.000053	0.27091	0.000053
					−9	0.36704	0.000213	0.1703	0.000213
Acceleration in x-direction = Ax m/sec^2				Displacement in x-direction = Dx m					

References

1. ASCE 7-05 (2006) Minimum design loads for buildings and other structures (ASCE Standard ASCE/SEI 7-05). American Society of Civil Engineers, Virginia
2. Eurocode 8 (2004) Design of structures for earthquake resistance part 1: general rules, seismic actions and rules for buildings (EN 1998-1: 2004). European Committee for Normalization (CEN), Belgium
3. FEMA 356 (2000) Prestandard and commentary for the seismic rehabilitation of buildings. Federal Emergency Management Agency, Washington, DC
4. FEMA 440 (2005) Improvement of nonlinear static seismic analysis procedures. Applied Technical Council, Redwood City
5. FEMA 450 (2003) NEHRP recommended provisions for seismic regulations for new buildings and other structures part 1: provisions. Building Seismic Safety Council BSSC, Washington, DC
6. Hadjian AH, Luco JE, Tsai NC (1974) Soil–structure interaction: continuum or finite element? Nucl Eng Des 31(2):151–167
7. Heintz JA (2012) Soil-structure interaction for building structures. NNational Institute of Standards and Technology, NEHRP Consultants Joint Venture, NIST GCR 12-917-21, US dept of Commerce
8. IS 1893 (2002) Indian Standard Criteria for earthquake resistant design of structures, part 1: general provisions and buildings. Bureau of Indian Standards BIS, New Delhi
9. JSCE (2007) Guidelines for concrete no. 15: standard specifications for concrete structures. Japan Society of Civil Engineers JSCE, Tokyo
10. Kausel E (2010) Early history of soil–structure interaction. Soil Dyn Earthq Eng 30(9):822–832
11. Lai CG, Martinelli M (2013) Soil-structure interaction under earthquake loading: theoretical framework, ALERT Doctoral School. The Alliance of Laboratories in Europe for Research and Technology, Technische Universit¨at Dresden, Germany
12. Lou M, Wang H, Chen X, Zhai Y (2011) Structure–soil–structure interaction: literature review. Soil Dyn Earthq Eng 31(12):1724–1731. https://doi.org/10.1016/j.soildyn.2011.07.008
13. Reissner E (1936) *Stationäre, axialsymmetrische, durch eine schüttelnde Masse erregte Schwingung eines homogenen elastischen* Halbraum. Ingenieur-Archiv VII(6):381–396
14. Roesset JM (2013) Soil structure interaction the early stages. J Appl Sci Eng 16(1):1–8
15. Sezawa K, Kanai K (1935) Decay in the seismic vibration of a simple or tall structure by dissipation of their energy into the ground. Bull Earthq Res Inst, Jpn 13(681–696):1935
16. Sharma N, Dasgupta K, Dey A (2018) A state-of-the-art review on seismic SSI studies on building structures. Innov Infrastruct Solut 3:22. https://doi.org/10.1007/s41062-017-0118-z
17. Shetgaonkar SS, Savoikar P (2017) Seismic response of multistoried building with different foundations considering interaction effects. In: Proceedings of conference ICRAMMCE2K17. Hyderabad
18. Souza L, Naik N, Chanekar T, Savoikar P (2016) Stability of traditional 'Bundhs'—Earthen Levees—From Goa. In: Indian geotechnical conference IGC2016, 15–17 December 2016, IIT Madras, Chennai, India
19. Wolf JP (1985) Dynamic soil-structure interaction. Prentice-Hall International, Englewood Cliffs, NJ

Bearing Capacity of Inclined Reinforced Sand Bed on Clay

P. Rajashekar Reddy, G. V. Narsimha Reddy and E. Saibaba Reddy

Abstract Reinforcement is arranged (placed) usually horizontal underneath the footings, to restrain developed tensile strains in soil, which in turn increases the reinforced sand bed shearing resistance by means of interfacial bond resistance and limited by tensile strength of its own. Present work analyzes geosynthetic reinforced foundation bed with reinforcement placed inclined downward from center toward edges at an inclination varying from 0 to 10° and evaluated the normalized bearing capacity values. Sand bed reinforced with inclined reinforcement overlying clay is studied by computing enhancement in normalized bearing capacity against reinforced foundation bed with reinforcement placed horizontally. The variation of normalized bearing capacity with angle of shearing resistance of sand bed, length of reinforcement, interface angle of shearing resistance, and intensity of surcharge is studied. This paper quantifies the increase in bearing capacity of sand bed reinforced with inclined reinforcement over the conventional method of placing reinforcement horizontally.

Keywords Normalized bearing capacity · Inclined reinforcement · Reinforced foundation bed · Foundation on soft clay

1 Introduction

Traditionally for reinforced foundation beds, placement of reinforcement is in the horizontal direction but transverse to the gravity stress application. Tensile force mobilized in the reinforcement due to interfacial friction between reinforcement and soil results in an increase in bond resistance. Meyerhof [3] developed bearing capacity solution for strip footing resting on dense sand bed overlying homogeneous clay using punching mode of shear failure. Quast [5] considered the force in the reinforcement to act tangential to the slip surface. Bonaparte and Christopher [1] considered force in the reinforcement to act along a direction between tangent to the slip surface in

P. Rajashekar Reddy (✉) · G. V. Narsimha Reddy · E. Saibaba Reddy
JNTUHCEH, Hyderabad, India
e-mail: raj2002.shekar@gmail.com

A. Prashant et al. (eds.), *Advances in Computer Methods and Geomechanics*, Lecture Notes in Civil Engineering 55,
https://doi.org/10.1007/978-981-15-0886-8_2

the reinforcement and alignment of reinforcement. Kumar and Madhav [2] analyzed reinforced earth wall with sheet reinforcement inclined downward with inclination varying between 0 to 10° and found increase in the factor of safety against pullout. It is proposed to study the increase in bond resistance of inclined reinforcement due to increase in normal stress on the reinforcement to pull out of reinforcement. Hence, parametric study has been carried out to study the effect of inclination of reinforcement in sand bed in improving bearing capacity.

2 Problem Definition and Formulation

Consider a strip footing having width, B resting on top of a sand bed overlying soft homogeneous clay. Depth of the sand bed is taken as H. The unit weight and angle of internal friction of sand bed is taken as γ and ϕ, respectively. Undrained shear strength of clay is taken as c. A single layer of geosynthetic reinforcement is placed in the sand bed at a distance u from the bottom of the footing center of which inclined at an angle α with bottom of footing (Fig. 1). The interface shear resistance and tension developed in the reinforcement are Φr and $T_{r,}$ respectively. A uniform surcharge pressure of w (load due to soil above the base of the footing) will be acting on reinforced foundation bed. Reinforcement is subjected to overburden pressure increasing from γu at the center of footing to γH at the free end. The bottom of the footing is assumed as rough and reinforcement does not fail by rupture, i.e., strength of reinforcement is strong enough and fails due to pullout only. Failure is initiated by the punching mode in the top sand layer.

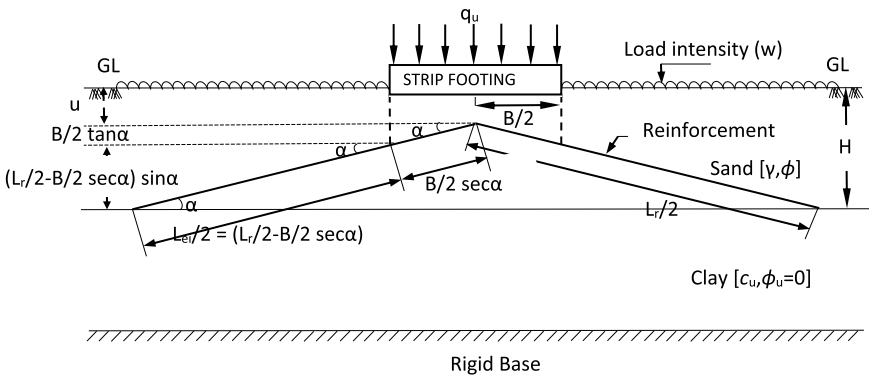

Fig. 1 Definition sketch

3 Method of Analysis

3.1 Ultimate Bearing Capacity of Sand Bed on Soft Clay

Meyerhof [3] presented bearing capacity solution for embedded strip footing at depth, D resting in dense sand bed overlying soft homogeneous clay having undrained shear strength, c. Width of strip footing is B, γ and ϕ are unit weight and angle of shearing resistance of the sand. Total passive earth pressure, p_p acts on the punching surface created by the strip footing in dense sand at an angle δ with the horizontal. Punching shear failure in thin sand bed and general shear failure with thick bed are shown in Fig. 2.

Shearing stresses are developed on both sides of the sand column, as the footing punches into the soft clay. Bearing capacity, q_{us}, of a strip footing embedded at depth D from the bottom of footing in dense sand bed resting over homogeneous soft clay is

$$q_{us} = cN_c + \frac{\gamma H^2}{B}\left(1 + \frac{2D}{H}\right)K_s \tan\phi + \gamma D \tag{1}$$

For a strip footing supporting on surface of sand bed, the above equation becomes

$$q_{us} = cN_c + \frac{\gamma H^2}{B}K_s \tan\phi \tag{2}$$

Bearing capacity of a footing on double-layered system is limited to the bearing capacity of a sand layer of infinite extent

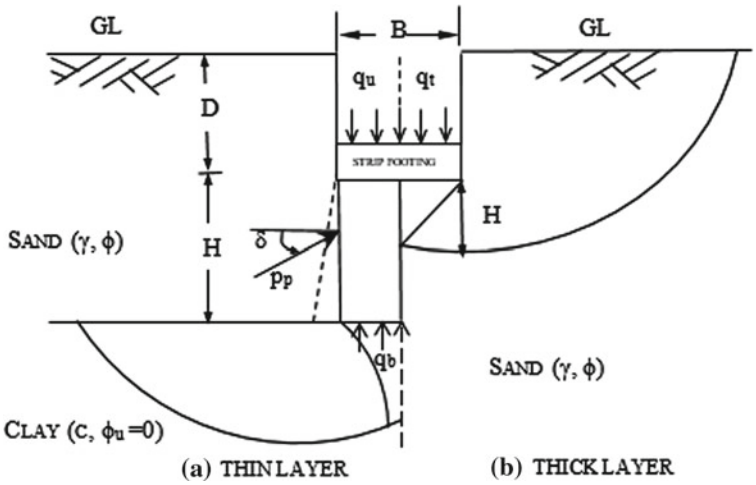

Fig. 2 Bearing capacity of sand bed overlying clay [3]

$$q_{us} = \gamma D N_q + 0.5\gamma B N_\gamma \tag{3}$$

where K_s = Punching shear coefficient and is obtained from the chart given by Meyerhof and Hanna [4], which depends on angle of shearing resistance of sand, ϕ, undrained cohesion of clay, and bearing capacity ratio q_2/q_1, where q_1, q_2 are ultimate bearing capacities of footing on surface of sand bed and soft homogeneous clay, respectively. N_c, N_q, N_γ are bearing capacity factors and for $\phi_u = 0, N_c = 5.14$.

Normalizing Eq. (3) with undrained cohesion of clay,

$$q^*_{us} = N_c + \left(\frac{\gamma B}{c}\right)\left(\frac{H}{B}\right)^2 K_s \tan\phi \tag{4}$$

q_{us}* is the combination of strength contribution of the upper sand layer and lower homogeneous clay layer to the bearing capacity of footing, where $\gamma B/c$ = Ratio of density of sand bed times width of footing to cohesion of clay, H/B = Normalized sand bed thickness.

3.2 Bond Resistance of Inclined Downward Reinforcement

As the surface strip footing pushes through the sand bed into the underlying homogeneous clay, the inclined downward geotextile reinforcement of length, L_r placed at an angle of α with horizontal with center of reinforcement at center of footing is intersected by the punching shear failure surface which consists of two vertical planes at the edges of the footing as shown in Fig. 3. Shear stresses are developed on both sides of sand column. Geosynthetic reinforcement is subjected to overburden pressure increasing from $\gamma\left(u + \frac{B}{2}\tan\alpha\right)$ at point of intersection with punching shear failure plane to $\gamma\left[u + \frac{B}{2}\tan\alpha + \left(\frac{L_r}{2} - \frac{B}{2}\sec\alpha\right)\sin\alpha\right]$ at the farthest end (i.e., tip of inclined reinforcement). Vertical stress and tension developed in the reinforcement are obtained for an average depth of reinforcement,

$$u_{avg} = \frac{\left[u + \frac{B}{2}\tan\alpha\right] + \left[u + \frac{B}{2}\tan\alpha + \left(\frac{L_r}{2} - \frac{B}{2}\sec\alpha\right)\sin\alpha\right]}{2} \tag{5}$$

The vertical stress acting on the reinforcement from punching shear failure intersection plane to the tip of reinforcement is q.

q = overburden pressure above reinforcement = $\gamma\ u_{avg} + w$

$$q = \frac{\gamma\left(u + \frac{B}{2}\tan\alpha + \frac{1}{2}\left[\left(\frac{L_r}{2} - \frac{B}{2}\sec\alpha\right)\sin\alpha\right]\right)}{2} + w \tag{6}$$

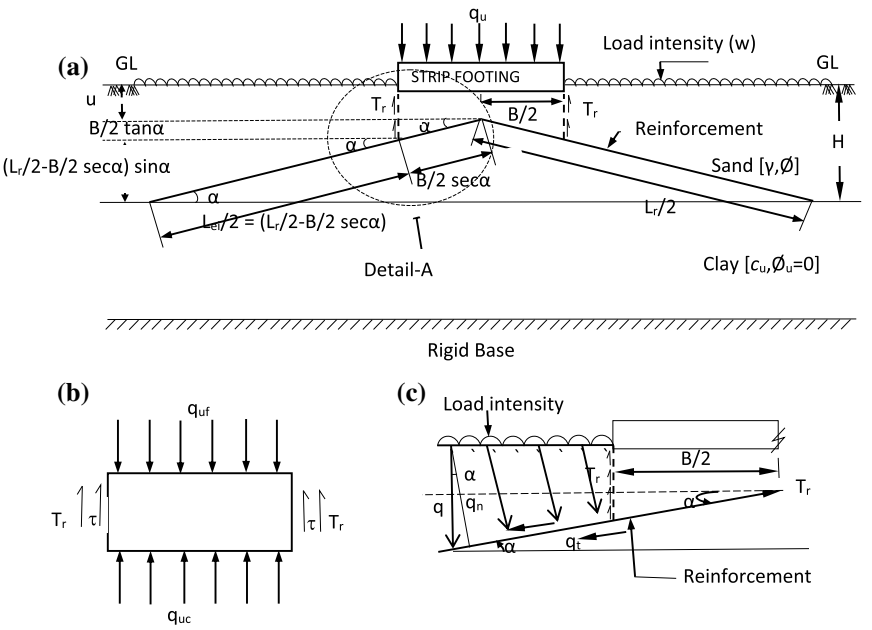

Fig. 3 **a** Punching shear failure of footing, **b** stresses on sand column, and **c** reinforcement alignment

Stresses tangential, q_t and normal, q_n to the alignment of geotextile reinforcement are

$$q_t = \left\{ \frac{\gamma}{2}\left(u + \frac{B}{2}\tan\alpha + \frac{1}{2}\left[\left(\frac{L_r}{2} - \frac{B}{2}\sec\alpha \right)\sin\alpha \right] \right) + w \right\} \sin\alpha \tag{7}$$

$$q_n = \left\{ \frac{\gamma}{2}\left(u + \frac{B}{2}\tan\alpha + \frac{1}{2}\left[\left(\frac{L_r}{2} - \frac{B}{2}\sec\alpha \right)\sin\alpha \right] \right) + w \right\} \cos\alpha \tag{8}$$

Direct resistance against pullout of reinforcement is offered by tangential stress q_t and due to an increase in normal stress component (q_n), additional frictional resistance will be mobilized.

$$\text{Total mobilized resistance to pull out, } T_r = (q_n L_{ei} \tan \emptyset_r) + (q_t L_{ei}) \tag{9}$$

where L_{ei} = effective length of inclined reinforcement, beyond the edge of the footing.

For the reinforcement layer placed in the sand bed, the axial tensile force is developed in the reinforcement layer for an effective length of L_{ei} beyond the edge of the footing, due to mobilization of interface shear resistance.

Taking into consideration the effective length of geotextile reinforcement L_{ei} on either side of the footing, axial stresses will be developed in geosynthetic reinforcement layer due to development of shear stress on either side of the sand-reinforcement interface, T_r is

$$T_r = \left\{ \frac{\gamma}{2}\left(\frac{u}{B} + \frac{1}{2}\tan\alpha + \frac{1}{2}\left[\left(\frac{Lr}{2B} - \frac{1}{2}\sec\alpha \right) \sin\alpha \right] \right) + \frac{w}{B} \right\} (L_r - B\sec\alpha)(\tan\phi_r \cos\alpha + \sin\alpha) \tag{10}$$

Bearing capacity of reinforced sand bed on soft homogeneous clay with inclined reinforcement is given by

$$q_{uir} = cN_c + \frac{\gamma H^2}{B} K_s \tan\phi + \left\{ \frac{\gamma}{2}\left(\frac{u}{B} + \frac{1}{2}\tan\alpha + \frac{1}{2}\left[\left(\frac{Lr}{2B} - \frac{1}{2}\sec\alpha \right) \sin\alpha \right] \right) + \frac{w}{B} \right\} (L_r - B\sec\alpha)(\tan\phi_r \cos\alpha + \sin\alpha) \tag{11}$$

Normalizing the above Eq. (12) with undrained cohesion of clay c gives

$$q^*_{uir} = N_c + \left(\frac{\gamma B}{c} \right) \left(\frac{H}{B} \right)^2 K_s \tan\phi + \left\{ \frac{\gamma B}{2c}\left(\frac{u}{B} + \frac{1}{2}\tan\alpha + \frac{1}{2}\left[\left(\frac{Lr}{2B} - \frac{1}{2}\sec\alpha \right) \sin\alpha \right] \right) + \frac{w}{c} \right\} \left(\frac{L_r}{B} - \sec\alpha \right) (\tan\phi_r \cos\alpha + \sin\alpha) \tag{12}$$

The beneficial effect of geotextile reinforcement for increasing the ultimate bearing capacity is quantified through a nondimensional parameter, the normalized bearing capacity ratio.

The normalized bearing capacity ratio q_{uc}* is the ratio of bearing capacity of footing on homogeneous clay layer to the undrained shear strength of clay. Similarly, q_{us}* is the ratio of bearing capacity of sand bed overlying homogeneous clay layer to the undrained shear strength of clay.

q_{uir}* is the ratio of bearing capacity of geosynthetic reinforced sand bed with reinforcement placed inclinedly considering axial tension in reinforcement overlying clay to that of undrained shear strength of clay. This ratio quantifies the contributions of reinforced sand bed considering axial pullout of the inclined reinforcement to the overall bearing capacity of the footing. Even though the strength of subsoil clay layer is less, it is taken into account to avoid conservatism.

3.3 Modified Width of Excavation for Reinforced Sand Bed Due to Downward Inclination of Reinforcement

Let L_r be the length of the geosynthetic reinforcement placed inclined downward with its center below the center of the footing and placed at an angle α with the horizontal at a depth u from the bottom of the footing in a sand bed of thickness H. L_{ip} is the length of reinforcement in plan (Fig. 4). ΔL_{ip} is the difference in actual length of reinforcement and length of reinforcement in plan. Width of excavation is reduced marginally when reinforcement is placed inclined downward and the same can be calculated as below

In the triangle "*mno*".

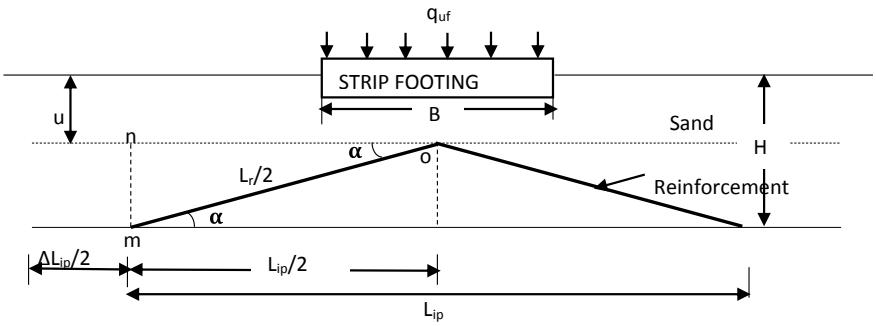

Fig. 4 Modified width of excavation for reinforced sand bed

$$\cos\alpha = \frac{\frac{L_{ip}}{2}}{\frac{L_r}{2}};\ L_{ip} = L_r \cos\alpha$$

$$\Delta L_{ip} = L_r - L_r \cos\alpha = L_r(1 - \cos\alpha)$$

4 Results and Discussions

Bearing strength of strip footing resting on the reinforced sand bed on soft homogeneous clay with inclined reinforcement depends on α, the angle of inclination of geosynthetic reinforcement with horizontal. It also depends on *u/B*, ϕ, *H/B* related to sand bed, $\gamma B/c$ ratio of sand bed density times width of strip footing and c undrained shear of homogeneous clay, ϕ_r interface shearing resistance between geotextile layer and sand, $(L_r - B)$ length of reinforcement beyond edge of footing. It is assumed that reinforcement will not fail in rupture and pullout of reinforcement is the only possible mode of failure. It is assumed that reinforcement placed inclined does not affect the failure zones that are usually considered in bearing capacity. This effect will be considered in future research. To generalize the effect of parameters for a wider area, they are presented in a dimensionless form. In addition to the above parameters, saving of width of excavation for inclinedly placed reinforcement is studied for inclination of reinforcement, α varying from 0 to 10°. Results are illustrated in graphical form for the following range of nondimensional parameters, α (0 to 10°), *H/B* (0 to 0.5), and $\gamma B/c$ (1.6 to 2.0). Calculations are made for L_r/B (2.5 to 4.0), ϕ_r/ϕ of 0.67, 0.75, and 1.0. The effect of these parameters on bearing capacity is quantified in this paper for different α values and compared normalized bearing capacity factors of inclined reinforcement with horizontally placed reinforcement in the sand bed.

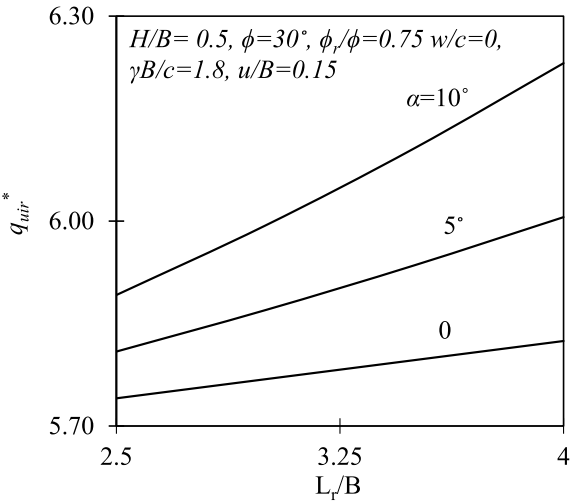

Fig. 5 Variation of q_{uir}* with L_r/B—Effect of α

4.1 q_{uir}* *Versus* L_r/B: *Effect of* α

Normalized bearing capacity of reinforced sand bed on clay with inclined reinforcement, q_{uir}* with L_r/B for different angles of inclination of reinforcement, α is depicted in Fig. 5 for $H/B = 0.5$, $u/B = 0.15$, w/c = 0, $\phi_r/\phi = 0.75$, $\gamma B/c = 1.8$.

For angle of inclination of reinforcement, $\alpha = 5°$, q_{uir}* increases from 5.81 to 6.01 with an increase in L_r/B from 2.5 to 4.0, due to development of higher anchorage against pullout of reinforcement in the resistant zone. q_{uir}* increases from 5.8 to 6.11 a 5.34% increase with increase in α from 0 to 10° for $L_r/B = 3.25$. The increase in q_{uir}* is due to combination of increase in normal stress applied on the reinforcement and additional shear resistance mobilized in the resistant zone, as the reinforcement is placed inclined with certain angle.

4.2 *Effect of* γB/c

Variation of inclination of reinforcement, α with the normalized bearing capacity of reinforced sand bed with inclined reinforcement on clay, q_{uir}*, for different values of $\gamma B/c$ are depicted in Fig. 6, for $\phi = 30°$, $H/B = 0.5$, $u/B = 0.15$, $\phi_r/\phi = 0.75$, w/c = 0. With increase in α, q_{uir}* increases nonlinearly, due to overburden pressure and this significantly with increase in $\gamma B/c$. q_{uir}* increases from 5.79 to 5.95 a 3.81% increase with increase in $\gamma B/c$ from 1.6 to 2.00 for an inclination of reinforcement of 5°, due to increase in density of sand bed and/or wider footing.

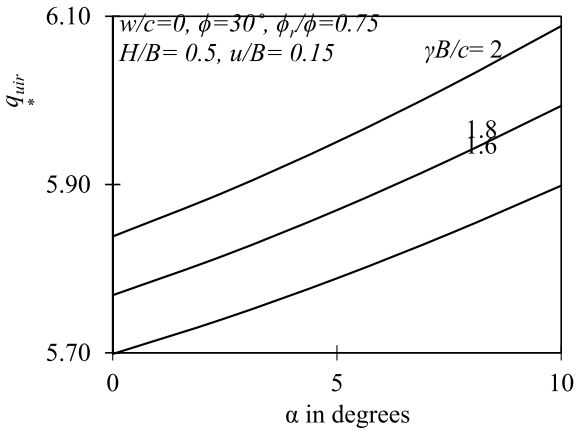

Fig. 6 q_{uir}* versus α—Effect of $\gamma B/c$

4.3 q_{uir}* Verses α—Effect of ϕ

Figure 7 illustrates the variation of inclination of reinforcement, α with normalized bearing capacity of sand bed with inclined reinforcement overlying homogeneous clay for different values of ϕ, for $H/B = 0.5$, $u/B = 0.15$, $w/c = 0$, $\phi_r/\phi = 0.75$, and $\gamma B/c = 1.8$. With increase in α from 0 to 10° for $\phi = 30°$, q_{uir}* increases from 5.77 to 5.99 an increase of 3.81%, due to additional normal stress acting on the reinforcement in the resisting zone. For an inclination of reinforcement of 5°, there is a 12.63% increase in q_{uir}* from 5.70 to 6.42 with increase of ϕ from 25° to 40° due to mobilization of frictional component.

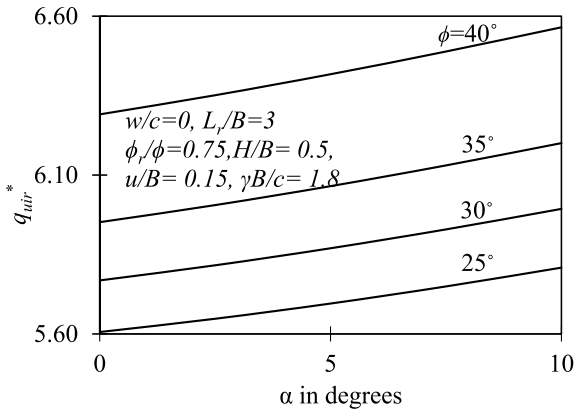

Fig. 7 q_{uir}* versus α—Effect of ϕ

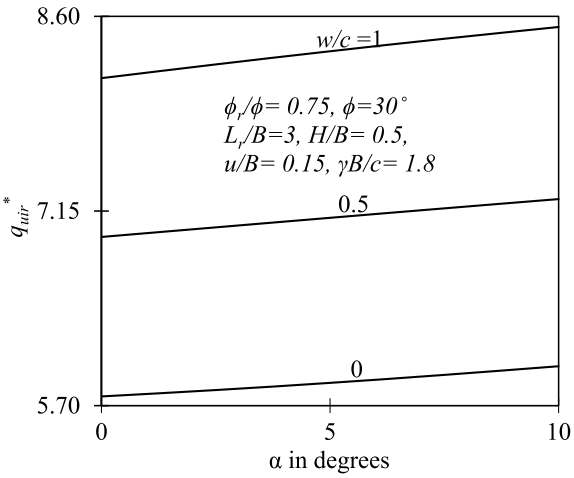

Fig. 8 q_{uir}* versus α—Effect of w

4.4 *Variation of* $\mathbf{q_{uir}}$* *with* α: *Effect of* w

Variation of angle of inclination of reinforcement, α with normalized bearing capacity of sand bed reinforced with inclined reinforcement resting on homogeneous clay [q_{uir}*] for various values of normalized surcharge w/c are presented in Fig. 8 for $L_r/B = 3$, $H/B = 0.5$, $u/B = 0.15$, $\phi r/\phi = 0.75$, $\phi = 30°$, and $\gamma B/c = 1.8$.

q_{uir}* increases from 6.96 to 7.24, a 4.02% increase within inclination of reinforcement from 0 to 10° at a normalized surcharge of 0.5. Due to the increase in surcharge, normal force on the reinforcement increases thereby bearing capacity q_{uir}* increases from 5.87 to 8.34, a 42.07% increase due to combined effect of increase in normal stresses resulting mobilization of additional shear resistance at $\alpha = 5°$.

5 Conclusions

- Use of inclined reinforcement reduces the width of excavation marginally.
- For parameters considered in the analysis, normalized bearing capacity of sand bed reinforced with inclined reinforcement, q_{uir}* compared with that for horizontally reinforced sand bed on clay increases linearly by 3.4%, 7.6% for inclination of reinforcement of 5°, 10°, respectively. This increment is due to the consideration of additional bond resistance due to increase in normal stress on the reinforcement due to pullout of reinforcement.
- q_{uir}* for a particular angle of inclination of reinforcement, (α) increases with $\gamma B/c$ due to increase in density of sand bed and or wider footing.

- Bearing capacity of inclined reinforced sand bed on homogeneous clay layer q_{uir}* for a given inclination of reinforcement increases with angle of shearing resistance due to mobilization of frictional component, additional normal stress exerted on the reinforcement in resistance zone.
- q_{uir}* increases with an increase in surcharge, development of tensile force due to increase in normal stress in the reinforcement contributes to the enhancement of bearing capacity. For higher surcharge pressures, inclined reinforcement is advantages over horizontal reinforced system.

References

1. Bonaparte R, Christopher BR (1987) Design and construction of reinforced embankments over weak foundation. Transp Res Rec 1153:26–39
2. Kumar, Madhav (2011) Pullout of inclined reinforcement in reinforced earth wall. Indian Geotech J 41(2):95–99
3. Meyerhof CG (1974) Ultimate bearing capacity of footings on sand layer overlying clay. Can Geotech J 223–229
4. Meyerhof CG, Hanna, AM (1978) Ultimate bearing capacity of foundations on layered soils under inclined load. Can Geotech J 565–572
5. Quast P (1983) Polyester reinforcing fabric mats for the improvement of embankment stability. In: Proceedings of 8th international conference on soil mechanics and foundation engineering, pp 531–534

Deaggregation of Seismic Hazards for Two Different Sites in Indore Region

Deepshikha Shukla and C. H. Solanki

Abstract Education as well as health centers with advanced facilities play an important role in the growth and infrastructure development of any city. Past eight to nine decades have witnessed vast development in the infrastructure and these changes can be very clearly seen in Central Part of India namely Indore Region which has seen a lot many educational hubs like IIT and IIM. This region has also seen commercial development marking its importance in the economic development and growth of the region as a whole. To reduce the damage due to seismic activity, site-specific seismic hazarded analysis of these two institutes have been carried out using the probabilistic concepts. The study that has been carried out develops hazard curves and uniform hazards response spectra for three different probabilities of exceedance (50, 10, and 2%) in a span of 50 years. Seven different ground motion prediction equations have been used to estimate the uncertainty in the hazard estimation. To understand the seismic scenario of the earthquake sources, deaggregation of the seismic results has been done. Post deaggregation, it was observed that earthquakes with higher magnitude are contributing more significantly to the seismic activity for both the sites in Indore Region.

Keywords Deaggregation · Seismicity · Hazard estimation · Uniform hazard curves

1 Introduction

Natural hazards have always proved to have enough potential to cause damage to life and property. Any hazard related to ground motion is termed as seismic activity and the hazards that occur due to seismic activity are seismic hazards. It is very difficult to quantify the hazards but an attempt has always been made by the researchers globally to estimate the hazards from ground shaking, surface faulting, landsides, past data, and through various other methods. Indore is located in the central and Malwa–Nimar

D. Shukla (✉) · C. H. Solanki
Applied Mechanics Department, SVNIT, Surat, Gujarat, India
e-mail: deepshikhashukla@yahoo.com

A. Prashant et al. (eds.), *Advances in Computer Methods and Geomechanics*, Lecture Notes in Civil Engineering 55,
https://doi.org/10.1007/978-981-15-0886-8_3

region of India lying in Seismic Zone III as per the Seismic Zoning Map of India published by Geographical Survey of India (GSI) and is likely to be subjected to an intensity of VII as per MSK scale. This region has felt minor tremors in the past history. Studies have shown the presence of various major faults and lineaments in the study area. The study area selected is an area of 400 km with Indore city as center. The various faults and lineaments in and around Indore region are already picturized in the past. The occurrence of some earthquake events (Latur 1993 M 6.4; Jabalpur 1997 M 6.0 and Bhuj 2001 M 7.7) in this region has triggered the researchers to study the seismic activity in this region. Based on the research, it was found that the various regions can be divided into regions of low and high seismicity [1].

2 Methodology Adopted

In the present study, an attempt has been made to deaggregate the seismic hazards at two different important and critical sites at Indore Region namely Indian Institute of Technology (IIT) spreading over an area of 510 acres ranked ninth among all IITs in India and Indian Institute of Management (IIM) that extends up to 173 acres ranked seventh among all Business Schools in India. These two institutes are the leading education Institutes of India. The site-specific seismic hazard for both the sites have been carried out using the concepts of probability and taking the uncertainties into calculation. The seismic hazard curves and uniform hazard response spectra are developed for these port sites for three different probabilities of exceedance (50, 10, and 2%) in the span of 50 years. Deaggregation process has been carried out using [2]. In the deaggregation process, the different earthquake sources are identified and the contribution from each and every source is taken into account. The process of deaggregation was developed by [2] and is now used as an effective and an important tool to understand the scenario of seismic hazards. In this method, the total earthquake events are considered to get an insight at a given ground motion level, the total hazard is broken down into its contributions from different earthquake scenarios. The paper presents the results through deaggregation that explains the typical size and distance of earthquakes making largest contribution to the seismic hazard for 50%, 10%, and 2% probability in the span of 50 years. This methodology has been adopted for Mumbai port and JNPT sites (Table 1).

3 Seismicity of the Area

To quantify and estimate the seismic hazards, the various earthquake events are collected from different sources for the past 200 years. The concepts of probability are applied to the data for the estimation of the seismic hazards. The earthquake events higher than magnitude 3.0 are taken into the study. Narmada–Tapti region, Narmada Son fault, Burhanpur fault, and Gavilgadh fault are the major faults identified in

Table 1 Performance-based ground motion levels considered in the present study (modified after [3])

Designation	Probability of exceedance (%)	Earthquake return period (years)	Earthquake levels	Expected performance for structural facilities
Level 1	50	72	Operation level earthquake (OLE)	Minor damage with no interruption of services
Level 2	10	475	Contingency level earthquake (CLE)	Services interrupted over several months but possible to repair economically
Level 3	2	2475	Maximum considered earthquake (MCE)	No collapse but economically irreparable

the region. As per the earthquake data compiled for the region, it can be concluded that the region has experienced low to moderate earthquakes. The susceptible region in western MP lies on Burhanpur and Barwani-Sukta fault lines. The Peak Ground Acceleration for the region is 0.32. This region has experienced earthquakes 1868, (5.7 on the Richter scale) and 1938. The various faults and lineaments are shown in Fig. 1. The compiled earthquake data is further analyzed for the seismic analysis of the region. "Cumulative Visual Inspection" (CUVI) method formulated by Tinti and Mulargia [4] and Stepp's Method is applied to estimate the period of completeness of the catalog. The completeness analysis was performed for five different magnitude classes [5].

4 Seismic Sources

Seismotectonic map for the study region is prepared from Seismotectonic Atlas of India published by Geological Survey of India (2000) for the study area in and around the Indore Region. The study considers the different types of Gravity Faults, Minor and Major Lineaments, and Neo Tectonic Faults in the study area. Around 13 major faults are identified for the study area and about 225 earthquake events are identified for the study area. Figure 2 shows the location of the study area.

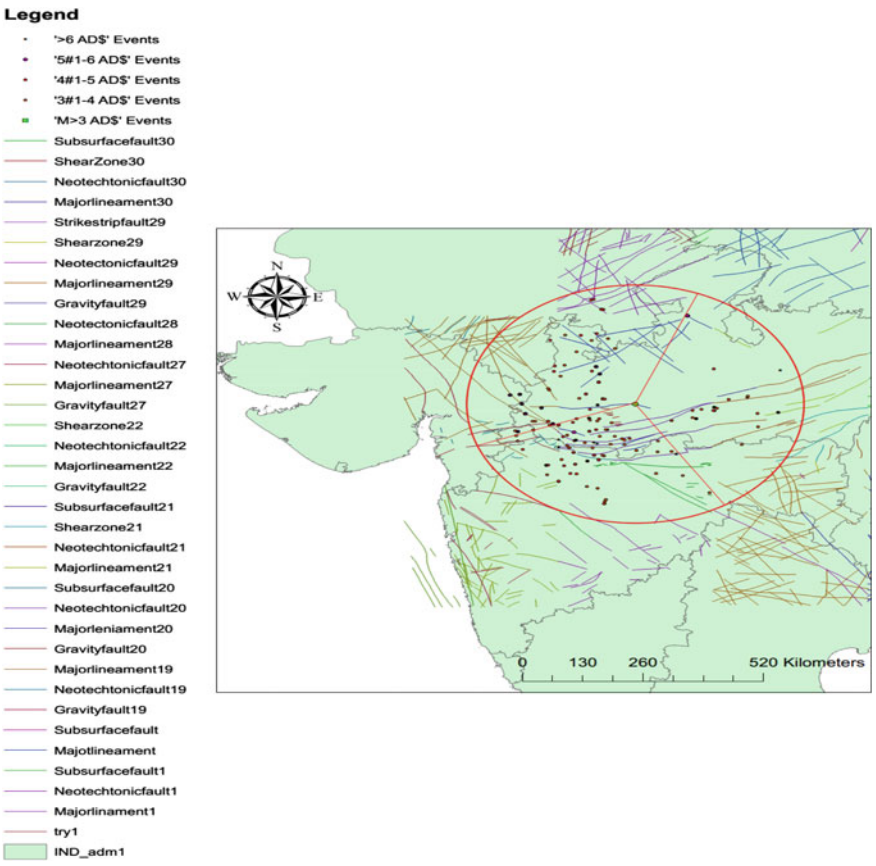

Fig. 1 Seismotectonic map of the study area showing various faults and lineaments underlying the study regions

5 Ground Motion Prediction Equations (GMPEs)

GMPEs are the equations that are used to express particular ground motion parameters as a function of maximum earthquake magnitude associated with each fault and respective distance from each target site represents attenuation characteristics of the region. The present study is based on GMPE proposed by Raghu Kanth and Iyengar [6] for Peninsular India and other GMPEs are proposed by Abrahamson and Silva [7], Boore et al. [8], Campbell [9] for motions in Western North America, Sadigh et al. [10] for motions in California, Toro et al. [11] and Atkinson and Boore [12].

Fig. 2 Location map of the study area

6 Probabilistic Seismic Hazard Analysis (PSHA)

Probabilistic Seismic Hazard Analysis for any region can be estimated manually by applying the methodology as proposed by the researchers. In this study, a computer program CRISIS 2007 [13] version 7.2 is used. First, the data was compiled from various sources and after the removal of the foreshocks and the aftershocks, the actual earthquake data for the region was prepared. Static and Dynamic window frame has been used for the declustering of the data. Guttenberg–Richter relation was used to develop an attenuation relation to calculate the mean probability of exceedance of the earthquake event due to any specific earthquake source of a certain magnitude. The data is computed for five different magnitude scales and then the hazard curves have been generated. The complete area of study of 400 km radius with Indore city as center was categorized in two different zones namely Single and Multi-Zone. In Multi-Zone, the area was again divided into three different zones randomly for the equal distribution of the earthquake events. The results obtained from the completeness period using CUVI Method and Stepp's Method are shown in Table 2. Earthquake exceedance was calculated for each fault and for different magnitudes. All GMPEs were used to predict ground motion. The seismic hazard at PGA and spectral acceleration at 1 s were generated for these two sites.

Table 2 Completeness data prepared for Indore Region

Completeness year	Interval (yrs)	Magnitude range	M_w	Number of events after completeness	Annual rate	Cumulative annual rate	log(n)
1992–2016	24	3–3.5	3.25	37	1.541667	3.744838	0.573433
1996–2016	20	3.5–4	3.75	14	0.7	2.203171	0.343048
1934–2016	82	4–4.5	4.25	48	0.585366	1.503171	0.177008
1987–2016	29	4.5–5	4.75	9	0.310345	0.917805	−0.03725
1934–2016	82	5–5.5	5.25	31	0.378049	0.607461	−0.21648
1926–2016	90	5.5–6	5.75	9	0.1	0.229412	−0.63938
1846–2016	170	>6	6.5	22	0.129412	0.129412	−0.88803

7 Results and Discussions

7.1 Seismicity Computation

Computation and analysis of the seismic data using the CRISIS computer program generated a hazard curve for the seismic sources selected for the region in terms of the ground motion parameter and Peak Ground Acceleration (PGA). The mean annual rate of exceedance for two different sites at Indore, i.e., IIT and IIM are drawn in Fig. 3. Higher hazard value can be seen for IIM as compared to that seen at IIT. The PGA is obtained at bedrock level for 5% damping for two different sites at Indore selected for the study and deaggregation of seismic hazards using PSHA. The PGA values for IIT Indore site for the return period of 2475, 475, and 72 years are 0.035 g, 0.085 g, and 0.152 g, respectively and for IIM site, the PGA values are 0.045 g, 0.092 g, and 0.175 g, respectively.

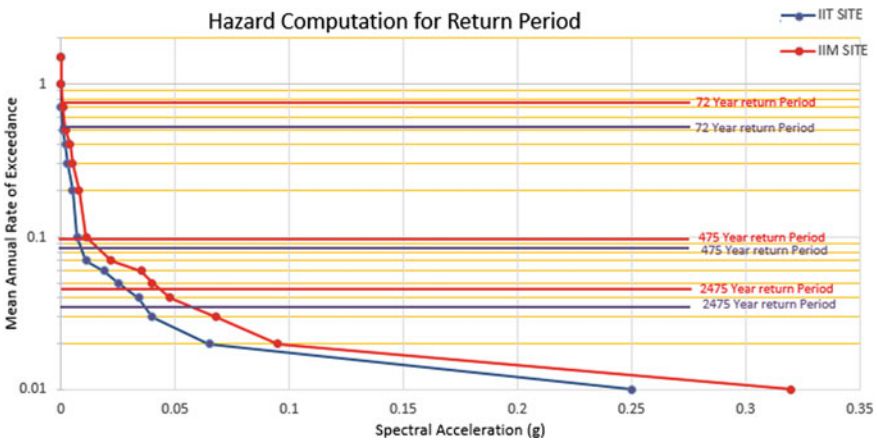

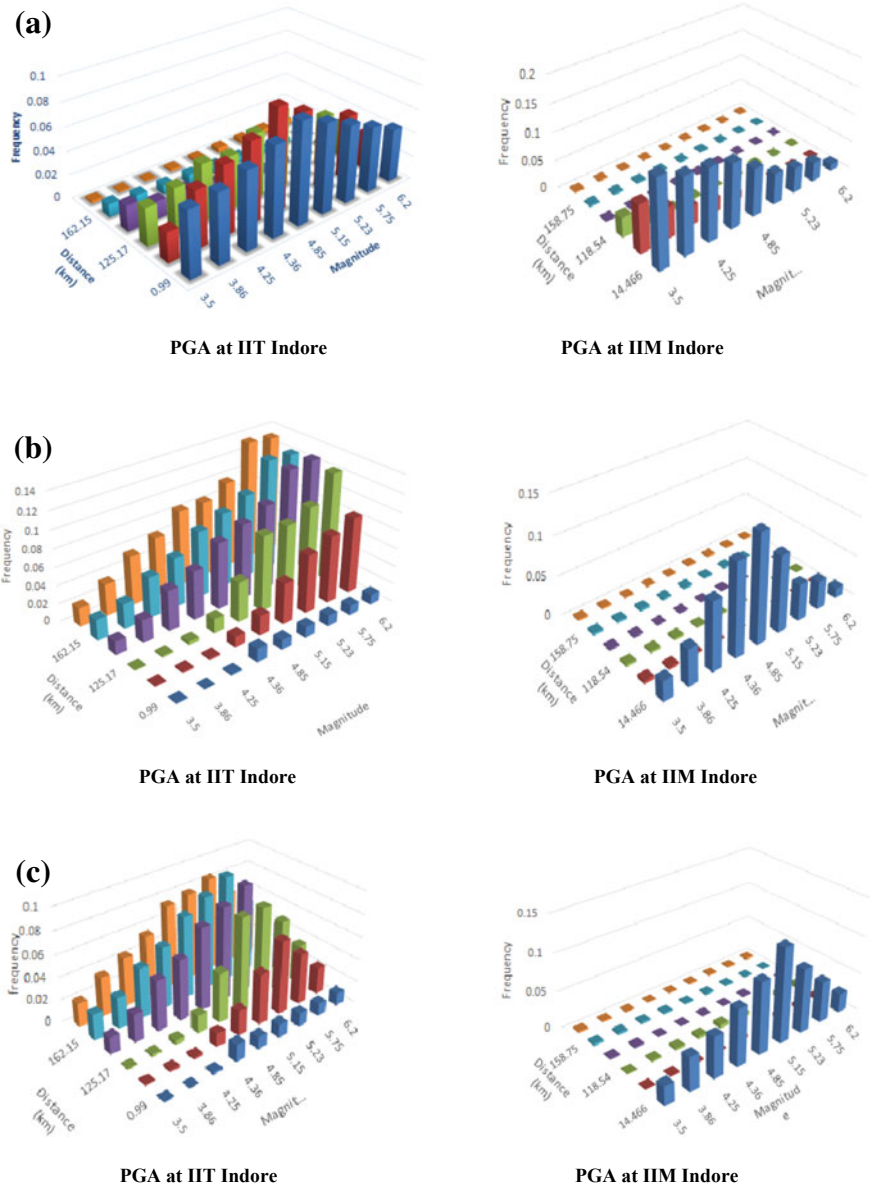

Fig. 3 Deaggregation for PGA for a return period of **a** 72 years, **b** 475 years, **c** 2475 years for two sites in Indore

7.2 Deaggregation of the Seismic Hazard

The PSHA results are represented in terms of mean annual rate of exceedance for a particular site taking into account the earthquake magnitudes and different source-to-site distances. In the deaggregation process, the source-to-site distance and earthquake magnitude has been calculated for each source. The deaggregation is computed based on two parameters namely magnitude and distance for all levels of spectral acceleration periods and for all attenuation relationships. The higher the return period and structural period, the earthquake events of higher magnitude contribute more to the ground motion at large. The deaggregated results thus obtained indicate that which magnitude and distance pair contributes more at a certain level for a particular site. The combination of Magnitude and Distance used for the deaggregation process are mentioned in Table 3. The spectral acceleration of 1 s is chosen to carry out the study. The return periods are taken as 72, 475, and 2475 years for the study area. It has been observed that as the number of return periods increases, the value of Peak Ground Acceleration (PGA) also increases and the earthquake magnitude becomes dominant for that particular site.

As seen from the above table, the deaggregation values as obtained for IIT Indore site is predominant than the values as obtained for IIM Indore Site. The earthquake magnitude M_w for IIT Indore site was taken as 4.59–6.21 and for IIM Indore site as 4.67–5.75. The value of S_a varies from 0.087 to 0.145 and for IIM site, it varies from 0.025 to 0.075 for S_a 1 s. As there are variations in PGA values, more earthquake scenarios are to be considered for the design basis.

Table 3 Magnitude–distance pair for two sites in Indore at different return periods

Site	Return period (years)	Hazard values		Magnitude–distance pair	
		PGA (g)	Sa (1 s)	At zero period	At 1 s period
IIT Indore	72	0.085	0.087	$M_w = 4.59$, D = 0.99 km	$M_w = 5.23$, D = 0.99 km
	475	0.168	0.121	$M_w = 5.38$, D = 0.99 km	$M_w = 5.63$, D = 0.99 km
	2475	0.315	0.145	$M_w = 6.21$, D = 0.99 km	$M_w = 6.37$, D = 0.99 km
IIM Indore	72	0.048	0.025	$M_w = 4.67$, D = 14.46 km	$M_w = 5.21$, D = 14.46 km
	475	0.115	0.042	$M_w = 5.58$, D = 14.46 km	$M_w = 5.89$, D = 14.46 km
	2475	0.205	0.075	$M_w = 5.75$, D = 14.46 km	$M_w = 6.02$, D = 14.46 km

8 Conclusion

In the present study, an attempt has been made to carry out the site-specific probabilistic seismic hazard and further deaggregation of the hazard curves at two different sites is done located at Indore. The results can be used to analyze the seismicity of the region that will give a better understanding of the seismicity of the area using the various attenuation relationships developed by researchers in the past. This approach gives a better understanding of the potential earthquake source and its effects as to the size and magnitude and which source contributes more to the seismic hazards. The hazard values thus obtained will be useful for planning hazard mitigation schemes and designing new earthquake-resistant structures. Deaggregation studies lead the design engineer to have a better choice to understand the earthquake scenario and the various characteristics.

Acknowledgements The authors would like to acknowledge the valuable inputs given by Prof (Dr.) DeepankarChoudhary, IIT Mumbai, M. ASCE. We also extend our sincere thanks to India Meteorological Department (IMD), New Delhi for sharing the valuable earthquake data for the study area.

References

1. Jaiswal K, Sinha R (2007) Spatial variation of maximum considered and design basis earthquakes in peninsular India. Curr Sci 92(5):639–645
2. Bazzurro P, Cornell CA (1999) Disaggregation of seismic hazard. Bull Seism Soc Am 89:501–520
3. Shukla J, Choudhury D (2012) Seismic hazard and site specific ground motion for typical ports of Gujarat. Nat Hazards 60(2):541–565
4. Tinti S, Mulargia F (1985) Completeness analysis of a seismic catalog. Ann Geophys 3:407–414
5. Desai S, Choudhury D (2014) Deterministic seismic hazards analysis for greater Mumbai, India. Geotechnical Special Publication No GSP 234, ASCE (ISBN 978-0-7844-1329-6), pp 389–398. https://doi.org/10.1061/978084413272.038
6. Raghu Kanth STG, Iyengar RN (2006) Seismic hazard estimation for Mumbai city. Curr Sci 91(11):1486–1494
7. Abrahamson NA, Silva WJ (1997) Empirical response spectral attenuation relations for shallow crustal earthquakes. Seismol Res Lett 68(1):94–127
8. Boore DM, Joyner WB, Fumal TE (1997) Equations from estimating horizontal response spectra and peak acceleration from Western North American earthquakes: a summary of recent work. Seismol Res Lett 68:128–153
9. Campbell KW (1997) Empirical near-source attenuation relationships for horizontal and vertical components of peak ground acceleration, peak ground velocity, and pseudo-absolute acceleration response spectra. Seismol Res Lett 68(1):154–179
10. Sadigh K, Chang CY, Egan JA, Makdisi F, Youngs RR (1997) Attenuation relations for shallow crustal earthquakes based on California strong motion data. Seismol Res Lett 68:180–189
11. Toro GR, Abrahamson NA, Schneider JF (1997) Model of strong ground motions from earthquakes in central and eastern North America: best estimates and uncertainties. Seismol Res Lett 68:41–58

12. Atkinson GM, Boore DM (1997) Some comparisons between recent ground motion relationships. Seismol Res Lett 68:24–40
13. CRISIS (2007) Version 7.2 Program for Computing Seismic Hazard developed by Ordaz M, Aguilar A, Arboleda. Instituto de Ingenieria, UNAM, Mexico

Uncertainties of Shear Forces and Bending Moments in Retaining Wall Due to Earthquake Loading

Vidhi Rasik Solanki, Prajakta Jadhav and Amit Prashant

Abstract The section design of a cantilever retaining wall stem requires factored shear forces and bending moments. Conventional design philosophies have adopted pseudostatic force based approach for the design of wall stem under seismic loading. This approach depends upon the selection of a suitable horizontal seismic coefficient (k_h). The primary aim of this study is to develop understanding of the uncertainties involved with respect to this seismic coefficient. A non-linear finite element model of cantilever retaining wall placed on medium dense sand has been developed in GiD and dynamic analysis has been performed in OpenSees. Four different earthquake motions with peaks concentrated over a certain time interval and peaks distributed for a larger duration of time have been selected for the analysis. These ground motion records have been scaled to 0.36 g PGA consistent with zone V. The forces and moments computed from dynamic analysis have been compared with those calculated using conventional pseudostatic force based methodologies to understand the influence of inappropriate selection of k_h value in design. Also, the uncertainty involved with respect to the location of the point of action of the dynamic increment has also been studied. The influence of this uncertainty has been reflected in the prediction of design moments. The study aims to evoke the need for modification in the current design philosophy which can efficiently capture these uncertainties with respect to seismic loading.

Keywords Cantilever retaining wall · Pseudostatic force based approach · Horizontal seismic coefficient · OpenSees · Uncertainties

V. R. Solanki · P. Jadhav · A. Prashant (✉)
Indian Institute of Technology Gandhinagar, Gandhinagar, India
e-mail: ap@iitgn.ac.in

V. R. Solanki
e-mail: solanki.vidhi@btech2014.iitgn.ac.in

A. Prashant et al. (eds.), *Advances in Computer Methods and Geomechanics*, Lecture Notes in Civil Engineering 55,
https://doi.org/10.1007/978-981-15-0886-8_4

1 Introduction

The conventional design methodology for seismic design of cantilever retaining wall approximates the complex and dynamic earthquake forces into a single pseudostatic force of $k_h W$ where k_h is the horizontal seismic coefficient and W is the weight of the triangular soil wedge behind the wall [1, 2]. Uncertainty in the value of k_h leads to unreliable calculation of shear forces which gets carry forwarded in the calculation of bending moment with an additional uncertainty in the location of the moment arm of the static and dynamic increment component of the seismic lateral earth pressure. Various studies in the literature have proposed values for k_h [3, 4] and also values for point of application of the seismic active thrust [5–7]. The primary aim of this paper is to make the readers aware of the uncertainties that need to be dealt with while designing for seismic forces and to evoke the need for modifying the current design philosophy to capture these uncertainties and incorporate them in the seismic design of cantilever retaining walls.

The accuracy with which the pseudostatic force is calculated depends on the accuracy in calculation of the variables involved such as soil density (γ) and k_h. Higher confidence in the value of soil density than in k_h is because of the ease with which numerous experiments could be carried out to determine the actual soil density. Unfortunately, carrying out numerous real-time tests on cantilever retaining walls to be able to predict the seismic forces and moments acting is tedious and impractical leading to higher uncertainty in the value of k_h. Bray et al. (2008) suggested that k_h lies between PGA/g and 0.5 PGA/g where PGA is the Peak Ground Acceleration. A study by Kolay et al. [4] has proposed that k_h equals PGA up to 0.45 g PGA and for PGA greater than 0.45 g, k_h assumes a constant value of 0.45. Atik and Sitar [8] have proposed a correlation between coefficient of dynamic increment earth pressure (ΔK_{AE}) and PGA. Other studies [9, 10] have also proposed equations for k_h which depend on PGA as well. Codal provisions by Australia [11] and New Zealand [12] suggest the use of k_h as a_{max} and 0.5 a_{max} depending on the deformation allowed. There is a need to identify and at the same time, mathematically quantify the uncertainties related to the value of k_h.

Several different recommendations for the point of application of the static (H_{st}) and dynamic increment component (H_{di}) of seismic active earth pressure in previous studies are an indication of the uncertainty in H_{st} and H_{di}. A study by Seed and Whitman [6] suggests that the static component acts at H/3 while the dynamic increment component acts between 0.6 and 2/3 H from the base of the stem-wall where H is the height of the stem-wall. Elms and Richard [7] suggest rectangular distribution of the total active seismic thrust and hence propose to use H/2 as the point of application of the total lateral seismic pressure. The present design approach, Allowable Strength Design (ASD) does not consider these specific uncertainties as it has only one Factor of Safety (FOS) to provide a reasonable safety margin against uncertainties in both load and resistance [13]. There is a need for an alternate design methodology which provides a quantitative safety margin rather than a factor that depends on experience and judgement [13] or a need for modification in ASD such that it can incorporate

the uncertainties and thereby improve its reliability for seismic design of cantilever retaining wall.

Four earthquakes with varying characteristics are scaled to 0.36 g PGA and used as input for dynamic analysis of a cantilever retaining wall. Shear forces and bending moment measured at the bottom of the stem-wall were obtained as the output results and were calculated using the Mononobe–Okabe method [1, 2] henceforth referred to as M-O method. The k_h values were back-calculated by comparing the measured and calculated shear forces and bending moments. Taking the values recommended by Kolay et al. [4] for k_h and by Seed and Whitman [6] for H_{st} and H_{di} as baseline, the variation in back-calculated k_h and in H_{st}, $H_{di,}$ respectively, has been analysed.

2 Model Description

A finite element model of cantilever retaining wall has been redeveloped in GiD and analysed in OpenSees in accordance with Kolay et al. [4]. The wall of height 12 m is retaining a horizontal soil mass of loose sand and is placed on medium dense sand. The domain simulated is 260 m long and 38 m deep. The details of the same are as shown in Fig. 1. The wall has been modelled using linear elastic beam-column elements of size 0.5 m. The soil mass has been modelled using quad elements and has been assigned properties corresponding to pressure-dependent multi-yield model. In

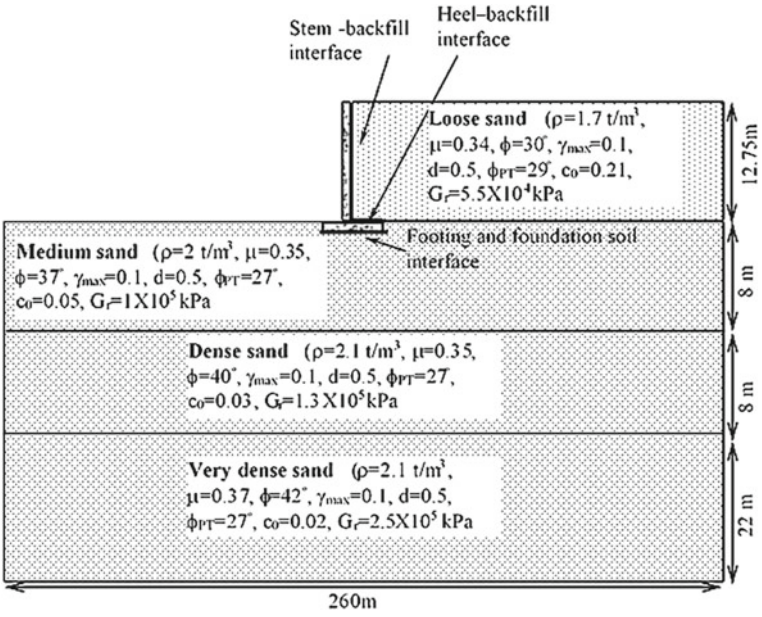

Fig. 1 Schematic diagram of computational model

order to consider slippage along the interfaces of wall with soil, three interfaces, viz, stem–backfill interface, SBI, heel–backfill interface, HBI, and footing–foundation–soil interface have been modelled in accordance with Kolay et al. [4].

3 Uncertainties Due to Earthquake Motion

Each earthquake characteristic has its own unique impact on the seismic behaviour of a structure. The values of k_h recommended in literature suggest that it is based only on the PGA of the earthquake, indirectly ignoring the effects of other earthquake characteristics such as duration of the earthquake, bracketed duration, frequency content and distribution of peak. The two earthquakes shown in Fig. 2, when scaled to the same PGA, will not cause similar forces and stresses in the retaining wall [14]. The earthquakes were scaled to the same PGA so that the effect due to this earthquake characteristic would remain the same for each case and the influence of the other characteristics on the design shear forces and bending moments is highlighted.

Four earthquakes were chosen from PEER database and their acceleration time histories were obtained. The selection was such that all the four earthquakes had varied characteristics as shown in Table 1. The acceleration time histories were scaled using SeismoSignal and the scaled velocity time histories were used as input

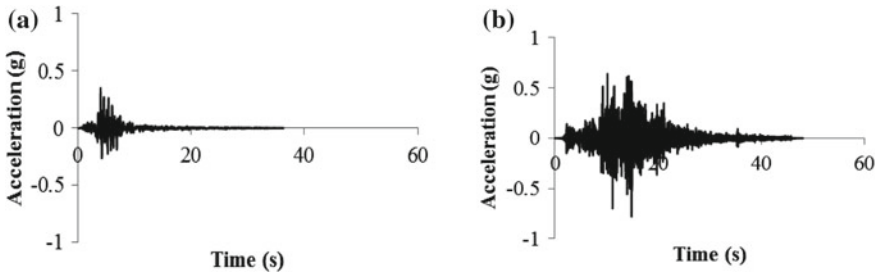

Fig. 2 Acceleration time histories of **a** Friuli and **b** Landers earthquakes (PEER)

Table 1 Characteristics of earthquakes chosen for dynamic analysis of cantilever retaining wall

Sr No	PGA (g)	Total duration (s)	Bracketed duration (s)	Peak distribution	Predominant period (s)
1	0.34	27	18.27	Distributed, wide peaks	0.28
2	0.78	85	33.33	Distributed	0.08
3	0.19	14	3.16	1 concentrated peak	0.28
4	0.40	15	14.21	5 concentrated peaks	0.38

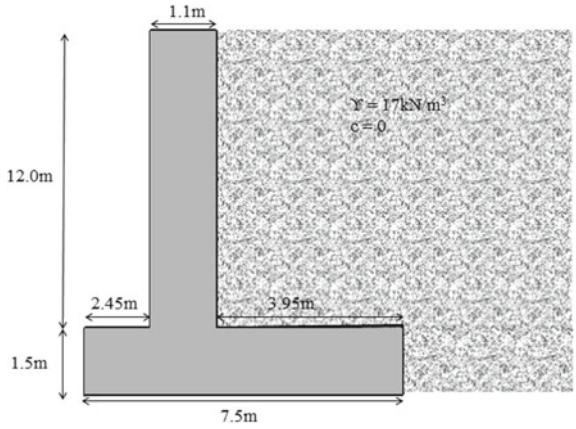

Fig. 3 Geometry of the cantilever retaining wall and soil parameters

to the dynamic analysis. The geometry of the cantilever retaining wall on which the dynamic analysis was performed is shown in Fig. 3. Shear force and bending moment at the base of the wall stem were obtained from analysis results.

The M-O method is one of the oldest methods in practice and provides a reasonable estimate of the seismic lateral earth thrust till date [1, 2]. Shear force is calculated by adding the seismic lateral earth pressure and $k_h W_{stem}$ where W_{stem} is the weight of the wall stem. Here, the seismic coefficient to be multiplied with W_{stem} is assumed to be k_h for the sake of simplicity and homogeneity [4]. Values for k_h as recommended by Kolay et al. [4] are used for shear force calculation. Bending moment is calculated by assuming that H_{st} is H/3, H_{di} is 0.6 H [6] and the wall seismic force acts at 0.5 H. The output shear force and bending moment values were located on their respective M-O curves in Fig. 4 and corresponding k_h values were noted. Henceforth, these k_h values will be referred as back-calculated k_h values. Also, values of H_{st} and H_{di} were calculated from static and dynamic increment stresses obtained from dynamic analysis, respectively. The M-O curves could be reproduced using the soil parameters mentioned in Fig. 3.

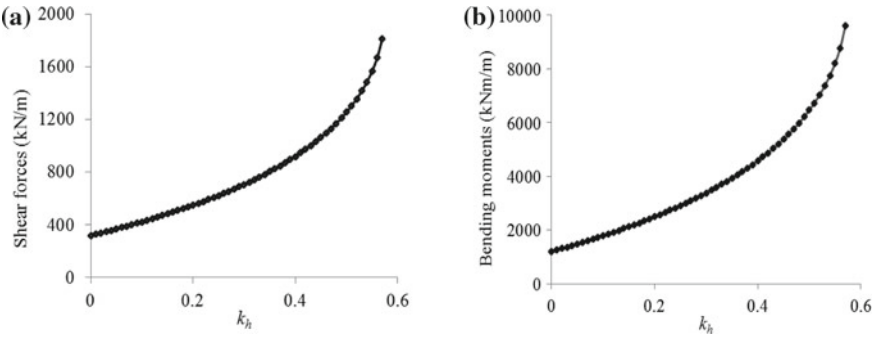

Fig. 4 M-O curves for **a** shear force and **b** bending moment for given wall geometry

4 Interpretations of the Uncertainties Observed

The calculated values of shear force and bending moments and those computed from dynamic analysis for the four earthquakes are shown in Table 2. As per Kolay et al. [4] recommendation, the value of k_h should be taken as 0.36 for all the four earthquakes and thus the design shear force would be 826 kN/m for each case. The design bending moment using Seed and Whitman [6] recommendation would be 4479 kNm/m. The computed values for both shear force and bending moment are significantly different from the calculated ones with computed shear forces ranging from 581 to 955 kN/m and computed bending moments ranging from 2341 to 4389 kNm/m. Similar conclusions can also be made about the back-calculated k_h values as shown in Table 3. The back-calculated k_h values for shear force range from 0.22 to 0.42 while those for bending moment range from 0.18 to 0.39. The recommendation by Kolay et al. [4] and that by Seed and Whitman [6] would sometimes underpredict and sometimes overpredict the actual shear forces and bending moments, respectively, leading to anything between unsafe to oversafe design using ASD. The use of a single value for k_h, H_{st}, and H_{di} as per previous studies will lead to unpredictable shear forces and bending moments unless over-conservative values are used leading to uneconomic designs. There is a need to account for this significant variation in the measured forces and moments in the design methodology used.

All the four analyses have shown that the static component acts at 0.28 H from the stem base which is lower than H/3 as per the assumption that the static stresses follow triangular distribution [6]. The value of H_{di} ranges from 0.41 to 0.57 H from the bottom which clearly signifies the uncertainty in the location of the dynamic

Table 2 Computed and predicted shear forces and bending moments

EQ No	Shear force computed from dynamic analysis (kN/m)	Calculated shear force (kN/m)	Bending moment computed from dynamic analysis (kNm/m)	Calculated bending moment (kNm/m)
1	787	826	3425	4479
2	581	826	2341	4479
3	683	826	3162	4479
4	955	826	4389	4479

Table 3 Obtained values of k_h for shear force, bending moment, H_{st} and H_{di} for four earthquakes

EQ No	k_h for shear force	k_h for bending moment	H_{st} (H)	H_{di} (H)
1	0.34	0.23	0.28	0.46
2	0.22	0.14	0.28	0.57
3	0.29	0.21	0.28	0.50
4	0.42	0.30	0.28	0.41

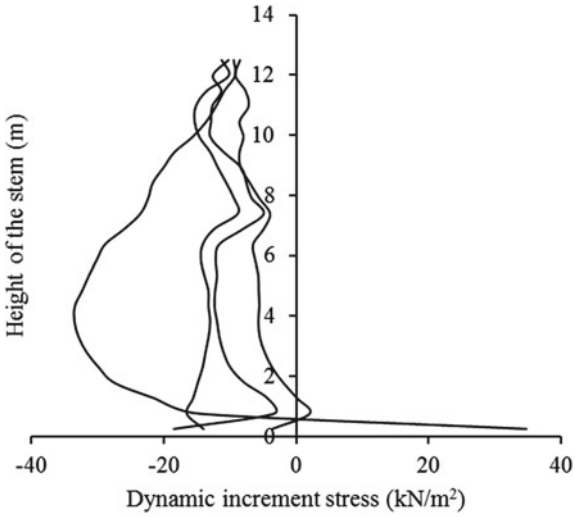

Fig. 5 Stresses in the stem-wall due to the dynamic increment component

increment component. The plot of the dynamic increment stress along the height of the stem-wall at the instant when the dynamic increment stress is the highest is shown in Fig. 5. The dynamic stress distribution obtained from analysis does not necessarily follow a linear or rectangular distribution as suggested by previous studies. Even if only four earthquakes are taken, the distribution is triangular for earthquake 4, rectangular for earthquake 2 and rectangular distribution with a kink in the mid-upper portion for earthquakes 1 and 3. The dynamic stress distribution varies depending on the earthquake characteristics. Figure 5 shows that the approximate location of the dynamic increment component lies somewhere around the wall mid-height. Higher variability in H_{st} and H_{di} can significantly affect the calculation of bending moments and thus need to be addressed in the design methodology used.

The calculation of unfactored shear forces and bending moments itself encompasses so many uncertainties that multiplying them with a factor of safety does not necessarily yield safe and reliable design. It is not feasible to comment how much safe or how much unsafe the design actually is. Since ASD has been in practice for years and its usage being simple, it would be extremely difficult to replace it with some other design philosophy which could identify and quantify the uncertainties. Therefore, there is a pressing need to modify certain parameters in ASD such that they capture the uncertainties and affect the design accordingly.

5 Conclusions

It is nearly impossible for two earthquakes to produce the same amount of impact on a structure. The variation in the back-calculated values of k_h and the calculated values of H_{st}, H_{di} clearly depict the complexity involved in determining the actual forces

and moments produced in the structure. Recommendations from previous studies such as that by Kolay et al. [4] for the value of k_h and Seed and Whitman [6] for H_{st} and H_{di} tend to sometimes produce safe while sometimes over-conservative design. The use of FOS in ASD does not provide the designers with a quantitative margin of safety. Since some of the sources of uncertainties are identified, it is necessary to figure out ways that can be used to capture these uncertainties. Despite its limitations, owing to the simplicity in the current approach, conventional design approach can still be adopted by engineers incorporating the aforementioned uncertainties.

Acknowledgements The authors would sincerely like to thank Prof. Dhiman Basu, IIT Gandhinagar and Prof. Durgesh C. Rai, IIT Kanpur for their valuable guidance in this study.

References

1. Okabe S (1926) General theory of earth pressure. J Jpn Soc Civ Eng, Tokyo, Jpn 12(1)
2. Mononobe N (1929) On determination of earth pressure during earthquake. In: Proceedings of World Engineering Congress, vol 9, pp 177–185
3. Bray JD, Travasarou T, Zupan J (2010) Seismic displacement design of earth retaining structures. In: Earth retention conference, vol 3, pp 638-655
4. Kolay C, Prashant A, Jain SK (2013) Nonlinear dynamic analysis and seismic coefficient for abutments and retaining walls. Earthq Spectra 29(2):427–451
5. Mononobe N, Matsuo M (1932) Experimental investigation of lateral earth pressure during earthquakes. Earthq Res Inst Res Off Public Work 884:902
6. Seed HB, Whitman RV (1970) Design of earth retaining structures for dynamic loads. In: ASCE specialty conference, lateral stresses in the ground and design of earth retaining structures. Cornell University, Ithaca, New York, pp 103–147
7. Elms DG, Richards R (1979) Seismic design of gravity retaining walls. University of Canterbury
8. Al Atik L, Sitar N (2010) Seismic earth pressures on cantilever retaining structures. J Geotech Geoenvironmental Eng 136(10):1324–1333
9. Noda S, Uwabe T, Chiba T (1975) Relation between seismic coefficient and ground acceleration for gravity quaywall. Rep Port Harb Res Inst 14(4)
10. Towhata I (2008) Geotechnical earthquake engineering. Springer Science & Business Media
11. Standards Australia AS 4678-2002 Earth retaining structures Standards
12. New Zealand NZS 1170.5:2004 Structural design actions. Part 5 Earthquake actions—New Zealand
13. Withiam JL, Voytko EP, Barker RM, Duncan JM, Kelly BC, Musser SC, Elias V (1998) Load and resistance factor design (LRFD) for highway bridge substructures. Report FHWA HI-98-032. Federal Highway Administration, Washington, DC

14. FEMA, No. 454 (2006) Designing for earthquakes. A manual for architects. FEMA (Federal Emergency Management Agency). Building seismic safety Council. Washington, DC
15. Pacific Earthquake Engineering Research Center (PEER), NGA database. http://peer.berkeley.edu/nga/search.html. Accessed March 2018
16. SeismoSoft (2017) SeismoSignal, v. 3.2.0, http://www.seismosoft.com/. Last accessed March 2018)

A Comparative Study on Shear Behavior of Pure Sand and Micaceous Sand Under Undrained Monotonic and Dynamic Loading Conditions

P. Seethalakshmi and Ajanta Sachan

Abstract Micaceous soils are considered undesirable for the construction of earthen structures due to low compatibility, high compressibility, and low shear strength. Mica particles are platy in nature with numerous foliated intact mica flakes. They tend to bend upon loading and rebound upon unloading caused by resilient nature. When mica particles are present with sand particles, it leads to intricate geometric assemblies such as bridging, ordering, and pore-filling phenomena. Such microstructure alters the shear behavior of micaceous sand under monotonic and dynamic loading conditions. This paper evaluates the shear behavior of micaceous sand in comparison to pure sand under monotonic and dynamic loading conditions. The results exhibited that the presence of mica deteriorated the stress–strain response of micaceous sand in comparison to pure sand during monotonic compression. It also altered the pore pressure characteristics from dilative to contractive nature. However, pure sand underwent liquefaction and the presence of mica increased the cyclic stability of micaceous sand during dynamic loading with repetitive stress reversal between compression and extension modes. The uniform sand–sand interparticle contacts might provide increased interparticle bonding in pure sand under monotonic compression, while it could be vulnerable due to loss of contacts under dynamic loading conditions. The sand–mica matrix with Bridging and Ordering effect deteriorated the monotonic shear behavior of micaceous sand, whereas it improved the dynamic behavior due to particle reorientation under repeated loading cycles.

Keywords Mica · Monotonic compression · Dynamic behavior · Bridging-ordering · Resilience

P. Seethalakshmi (✉) · A. Sachan
Indian Institute of Technology Gandhinagar, Gandhinagar, India
e-mail: seethalakshmi.p@iitgn.ac.in

A. Prashant et al. (eds.), *Advances in Computer Methods and Geomechanics*, Lecture Notes in Civil Engineering 55,
https://doi.org/10.1007/978-981-15-0886-8_5

1 Introduction

The shear strength behavior of soil majorly depends on the type of minerals, shape, and size of particles present in the soil mass. Mica particles (muscovite) are platy and elastic in nature, which tends to bend upon loading and rebound upon unloading due to its resilient nature [16]. The presence of weak and platy mica particles among hard and spherical sand particles causes complex geometric arrangements and also susceptible to break owing to fragile nature of mica [12]. The varying size and percentage of mica particles among sand would result in different microstructural distributions such as bridging, ordering, and pore-filling phenomena [10]. Bridging represents the irregular arrangements of sand below mica while ordering represents the regular arrangements of sand above mica resulting in increased nonuniform voids in the overall soil mass. Pore filling represents the filling of pores among larger sand particles by smaller mica particles which might improve the interparticle contacts with lesser void spaces. Such unique particle arrangements in micaceous sand resulted in high compressibility, low compactability, and low shear strength [5]. Hence, micaceous sand having mica content more than 10% is considered undesirable for any earthen structures [8]. The undrained monotonic shear behavior of micaceous sand at varying mica content was analyzed to considerable extent [6, 7]. Various researchers examined the effect of nonplastic fines on sand using DEM simulations and monotonic and dynamic triaxial experiments to depict the particle interactions during rearrangement leading to instability [1, 3, 11, 17]. However, the understanding behind the unconventional behavior of micaceous sand in comparison to pure sand with respect to the possible microstructure and their corresponding geometric rearrangements under monotonic and dynamic loading conditions remained unexplored. The current study aims at analyzing the shear behavior of pure sand verses micaceous sand pertaining to change in sand–mica and sand–sand configuration under dynamic loading in compression–extension modes and monotonic compression loading conditions.

2 Experimental Program

2.1 Material Properties and Specimen Preparation

The soil was collected from Sabarmati river basin in Gujarat, India. Silt content of 8% was removed by dry sieve analysis and pure sand with medium and fine grain size was used throughout the study. Commercially available mica powder of size varying from 0.3 μm to 0.5 mm was obtained from National Chemicals Pvt. Ltd. at Vadodara in Gujarat, India. Micaceous sand was prepared by admixing 80% pure sand and 20% mica powder by weight at dry state until the uniform condition was achieved. The grain size distribution curve of Sabarmati soil, pure mica, and prepared micaceous sand specimens are shown in Fig. 1.

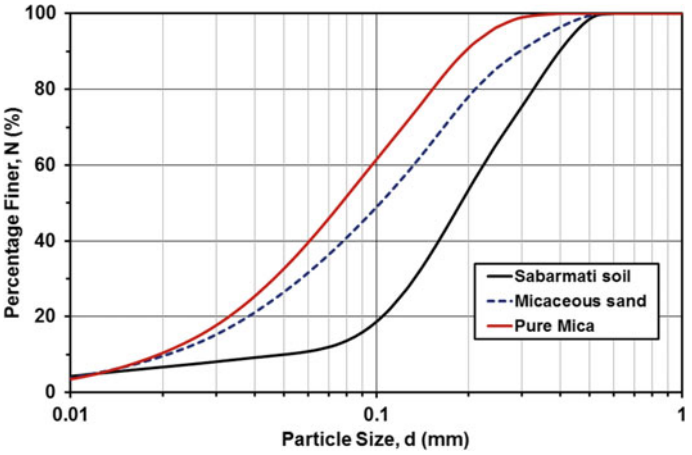

Fig. 1 Grain size distribution curves of Sabarmati sand, mica and micaceous sand

Addition of mica to sand increased the optimum moisture content and reduced the maximum dry density of micaceous sand as compared to pure sand as observed in standard proctor compaction test results. Even though several density indices such as global (constant) void ratio, skeleton void ratio, and equivalent skeleton void ratio were used in the past studies, shear behavior was observed to be contrastingly different due to complex intergranular matrix mechanisms. However, the global void ratio remained simple and useful state variable for critical state soil mechanics [20]. Hence, constant global void ratio ($e_g \approx 0.64$) was maintained in the current study for both micaceous sand and pure sand specimens irrespective of their maximum dry densities and relative densities (D_r). The natural water content of Sabarmati sand was being selected as the initial water content of all the specimens for sample preparation. Thus, solid cylindrical specimens of micaceous sand and pure sand were made using moist tamping technique at constant dry density of 1.64 g/cm^3 ($e_g = 0.64$) and water content of 10%, respectively. Moist tamping was chosen to prevent segregation of sand and mica particles in micaceous sand [13].

2.2 Testing Procedure

Soil specimens were subjected to saturation in three stages such as CO_2 saturation, water flushing, and forced saturation. CO_2 was passed from bottom to top of the specimen at constant cell pressure of 20 kPa for 1 hour in order to replace air with dissolvable CO_2. Water flushing was carried out from bottom to top surface of the specimen at constant cell and back pressure of 50 kPa and 30 kPa, respectively. It was continued until the discharge water was at least equal to the volume of voids (V_v) of the specimen. V_v was calculated from the known values of constant global void ratio

(e_g) at the time of sample preparation, mass of solids (M_s), specific gravity (G_s), and volume of solids (V_s) and the water discharged from top surface of the specimen was measured at regular intervals of time during water flushing. The process was terminated when the discharged quantity of water from the specimen was greater than or equal to (V_v) of the specimen. Forced saturation was done by gradually augmenting cell and back pressure with constant difference of 20 kPa. It was continued until the Skempton's pore pressure parameter (B-value) was obtained to be greater than or equal to 0.97. The fully saturated micaceous sand and pure sand specimens were further isotropically consolidated under constant confining pressure of 100 kPa and then subjected to various testing conditions such as undrained monotonic compression and undrained dynamic triaxial loading conditions in compression–extension modes. The Isotropically Consolidated Undrained Compression (CIUC) tests were conducted at a given strain rate of 0.1% per minute, which were continued until the specimens reached failure state. Failure is defined as the maximum deviatoric stress achieved or the deviatoric stress at 20% axial strain whichever occurs earlier during undrained monotonic compression. The strain-controlled cyclic triaxial tests were performed at a given frequency of 0.5 Hz and constant double amplitude axial strain of 1 mm magnitude per cycle in sinusoidal waveform with stress reversal (compression–extension). One complete cycle of compression–extension dynamic loading represents the loading of soil specimen in compression direction up to specified amplitude followed by unloading to the neutral position and then reloading in extension direction up to specified amplitude followed by unloading to the neutral position. A schematic representation of loading during strain-controlled monotonic compression and cyclic triaxial test is shown in Fig. 2.

The dynamic loading was continued until it reached 30 complete loading cycles. In order to obtain sufficient output data for determining the dynamic parameters and rate of stiffness degradation along with liquefaction susceptibility, the lower frequency of 0.5 Hz and a minimum of 30 cycles were selected. The magnitude of the double amplitude axial strain of 1 mm was decided such that it should be greater than threshold strain level of standard sands in order to ensure the continuous and uniform development of excess pore pressure under dynamic loading.

2.3 Evaluation of Monotonic and Dynamic Triaxial Testing Data

2.3.1 Monotonic Compression

The monotonic compression shear behavior of micaceous sand and pure sand was analyzed in terms of stress–strain, excess pore pressure response, secant young modulus variation, and strain energy dissipation. The secant young modulus was determined incrementally from 0.1 to 20% axial strain during undrained shear deformation using Eq. (1).

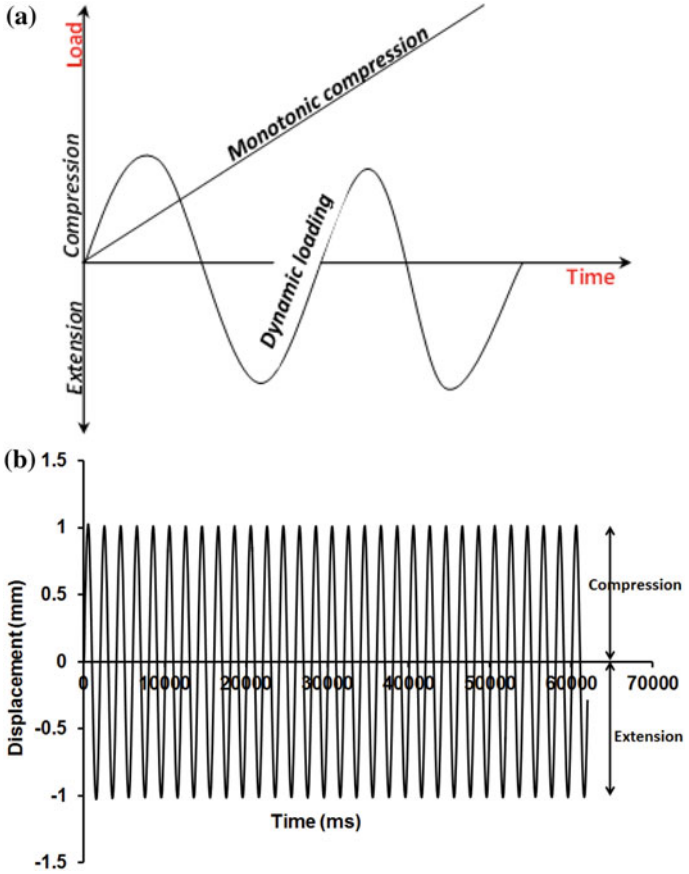

Fig. 2 Typical input response under different loading conditions. **a** Schematic representation of monotonic compression and dynamic loading, **b** input response during dynamic loading

$$E_{monotonic} = (\delta\sigma_{dm}/\delta\varepsilon_{am}) \tag{1}$$

The total dissipated strain energy/work done per unit volume comprised of volumetric and shear strain energy. It was also determined incrementally due to the highly nonlinear elastoplastic shear behavior of soil using Eqs. (2), (3), (4), (5), (6), and (7) as suggested by [17, 13].

$$\delta W_{monotonic} = \left(\delta W_p + \delta W_q\right) = (p' * \delta\varepsilon_p) + (q * \delta e_q) \tag{2}$$

$$\delta\varepsilon_p = (\delta\varepsilon_{am} + 2 * \delta\varepsilon_{rm}) \tag{3}$$

$$\delta\varepsilon_q = (2/3) * (\delta\varepsilon_{am} - \delta\varepsilon_{rm}) \tag{4}$$

$$p' = \left(\sigma'_1 + 2 * \sigma'_3\right)/3 \tag{5}$$

$$q = \left(\sigma'_1 - \sigma'_3\right) \tag{6}$$

$$W_m = \Sigma(\delta W_{monotonic}) = \Sigma(p' * \delta\varepsilon_p) + (q * \delta\varepsilon_q) \tag{7}$$

where δW_p is the volumetric strain energy; δW_q is the shear strain energy; $\delta\varepsilon_p$ is the incremental volumetric strain; and $\delta\varepsilon_q$ is the incremental shear strain [13]. The total volumetric strain was constant $\{\delta\varepsilon_p = (\delta\varepsilon_{am} + 2 * \delta\varepsilon_{rm}) = 0\}$ in undrained triaxial monotonic compression with the assumption that the change in axial strain was equivalent to twice the change in radial strain but in opposite direction [13].

2.3.2 Dynamic Compression–Extension Loading

Similarly, the cyclic shear strength parameters such as Damping ratio (D), and shear modulus (G) along with cyclic degradation index (δ) and the dissipated strain energy (ΔW_d) were computed. Energy dissipation (ΔW_d) demonstrates the quantity of energy dissipated due to application of cyclic loading on the soil specimen. Secant young modulus (E_{secdyn}) was computed as the gradient of highest deviatoric stress points in the hysteresis loop along both compression and extension direction with constant axial strain levels as suggested by [14] at a given cyclic loading (Fig. 3). The shear modulus (G) was evaluated using E_{secdyn} as per Eqs. (8) and (9) with the assumption of poisson's ratio as 0.5 for all saturated specimens under undrained conditions [2, 4]. The damping ratio (D), which is the ratio of dissipated energy and elastic energy, was determined using Eq. (10) by computing the area of hysteresis

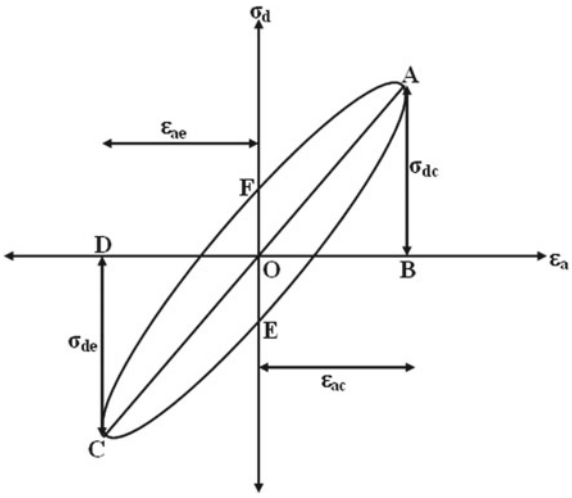

Fig. 3 Typical hysteresis response of cyclic triaxial test during compression–extension dynamic loading

loop as mentioned in Fig. 3 [14, 15].

$$E_{secdyn} = \frac{\sigma_{dc} + \sigma_{de}}{\varepsilon_{ac} + \varepsilon_{ae}} \tag{8}$$

$$G = \frac{E_{secdyn}}{2(1 + \upsilon)} \tag{9}$$

$$D(\%) = \left(\frac{\text{Area of hysterisis loop AECF}}{2\,\pi(\text{Area of } \Delta OAB + \text{Area of } \Delta OCD)} \right) \times 100 \tag{10}$$

where Area enclosed by hysteresis loop AECF = dissipated strain energy; Area enclosed by ΔOAB and ΔOCD = Elastic strain energy (Fig. 3) as per [14].

Cyclic degradation index (δ) is defined as the ratio of the shear modulus (G_N) at *N*th loading cycle to the shear modulus (G_0) in the first loading cycle [14]. The stiffness degradation of the soil specimens under repeated cycles of dynamic loading was evaluated using Eq. (11) [18]. The rate of stiffness degradation could be identified by comparing the value of δ at successive cycles of dynamic loading using δ versus number of cycles plot.

$$\delta = (G_N)/(G_0) \tag{11}$$

The work done per unit volume (ΔW_d) under cyclic loading conditions was determined using Eq. (12) as per [19].

$$\Delta W_d = \sum_{i=1}^{n-1} 0.5 * \left(\sigma_{d(i+1)} - \sigma_{d(i)}\right) * \left(\varepsilon_{a(i+1)} - \varepsilon_{a(i)}\right) \tag{12}$$

where σ_d = incremental cyclic deviatoric stress in both compression (σ_{dc}) and extension (σ_{de}), ε_a = incremental axial strain in both compression (ε_{ac}) and extension (ε_{ae}), n = number of points recorded at a given cycle as per [14]. The cumulative dissipated strain energy ($\Sigma\Delta W_d$) was also estimated for 30 cycles to understand the effect of mica on stiffness degradation, energy dissipation, and excess pore pressure variation of micaceous sand in comparison to pure sand.

3 Results and Discussion

3.1 Monotonic Shear Behavior

The undrained monotonic compression and dynamic loading test results showed significant variation in shear response of micaceous sand and pure sand due to the presence of mica. Table 1 shows the shear strength parameters of micaceous sand and pure sand under monotonic compression loading. The secant Young Modulus

Table 1 Shear strength parameters of micaceous sand and pure sand under monotonic compression

Parameters	Units	Pure sand	Micaceous sand
$(E_0)_{monotonic}$	(MPa)	39.4	8.8
$(E_f)_{monotonic}$	(MPa)	13.2	1.5
$(\sigma_{dm})_{peak}$ or $(\sigma_{dm})_f$	(kPa)	475.9	256.5
$(\varepsilon_{am})_f$	(%)	3.6	16.4
u_{max}	(kPa)	29.4	48.3
ε_{am} at u_{max}	(%)	0.18	0.61
u_{min}	(kPa)	−89.8	−21.0
ε_{am} at u_{min}	(%)	3.9	20.0
u_f	(kPa)	−88.5	−17.8
p′ at failure (using Eq. 5)	(kPa)	426.4	246.0
W_m (using Eq. 7)	(kJ/m^3)	12.3	35.2

($E_{monotonic}$) was determined using Eq. (1), variation in mean effective stress (p′) at failure was estimated at peak deviatoric stress using Eq. (5) and the cumulative work done (W_m) was evaluated as the sum of all incremental strain energies obtained at regular shear strain increments using Eq. (7) during shear deformation (Table 1). Pure sand was observed to have higher initial stiffness and larger peak deviatoric stress $(\sigma_{dm})_{peak}$ obtained at lower axial strain (4%) with a brittle response (Table 1).

Figure 4 shows stress–strain and pore pressure response of micaceous sand and pure sand under undrained monotonic compression loading. Micaceous sand showed lower initial stiffness and reduced peak deviatoric stress in comparison to pure sand which was obtained at much larger axial strain (16%) with ductile response (Fig. 4a). Phase transformation is the state at which the soil specimen undergoes transition from contractive to dilative nature [13]. The maximum positive excess pore pressure (u_{max}) at phase transformation was increased (from 29 to 48 kPa) and the minimum excess pore pressure (u_{min}) after phase transformation state was decreased (from −81 to −21 kPa) for micaceous sand (Table 1). The pore pressure response of micaceous sand was more contractive as compared to pure sand at larger strain levels (Fig. 4b). This depicted the higher contractive nature of micaceous sand in comparison to pure sand. The development of maximum and minimum pore pressures was observed to be prolonged for micaceous sand in comparison to pure sand due to the increased ductile nature.

The initial secant Young modulus $(E_0)_{monotonic}$ was higher for pure sand which was significantly smaller for micaceous sand. The degradation of $(E_0)_{monotonic}$ was greater and rapid for pure sand whereas it was noticed to be smaller and gradual for micaceous sand until achievement of peak stress (Fig. 5a). The extensive transformation in shear behavior of micaceous sand with reduced stiffness; minimized secant modulus, and lower peak deviatoric stress would appear due to the presence of platy mica particles among spherical sand particles. The stable closer sand–sand configuration of pure

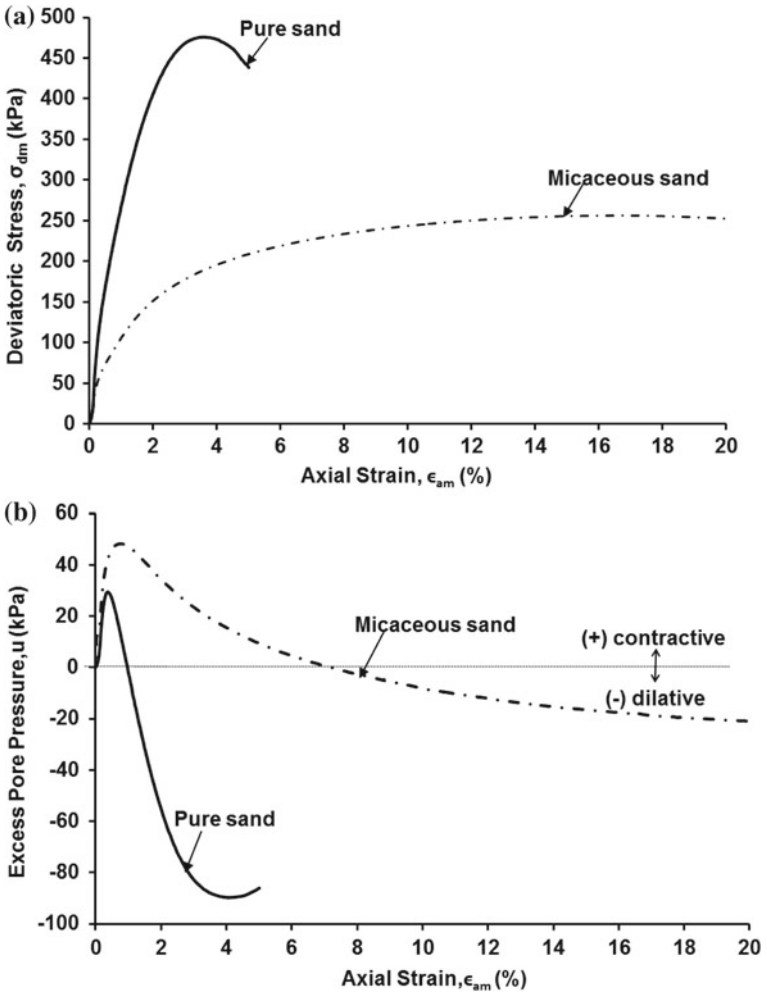

Fig. 4 Shear strength behavior of micaceous sand and pure sand under undrained monotonic compression. **a** Stress–strain response, **b** excess pore pressure evolution

sand would result in greater uniform interparticle contacts with less nonuniform void spaces among sand particles which would result into gain of higher stiffness and peak strength at lower strain levels. However, the critically metastable sand–mica matrix of micaceous sand could create larger nonuniform void spaces with reduced interparticle interactions due to increased bridging and ordering mechanisms among sand and mica particles which would be responsible for lower stiffness. The tendency to adsorb water among interflakes of mica at saturated state would result in holding higher water molecules which would result in larger water retention capacity of mica particles as compared to sand particles. The increased water retention capacity

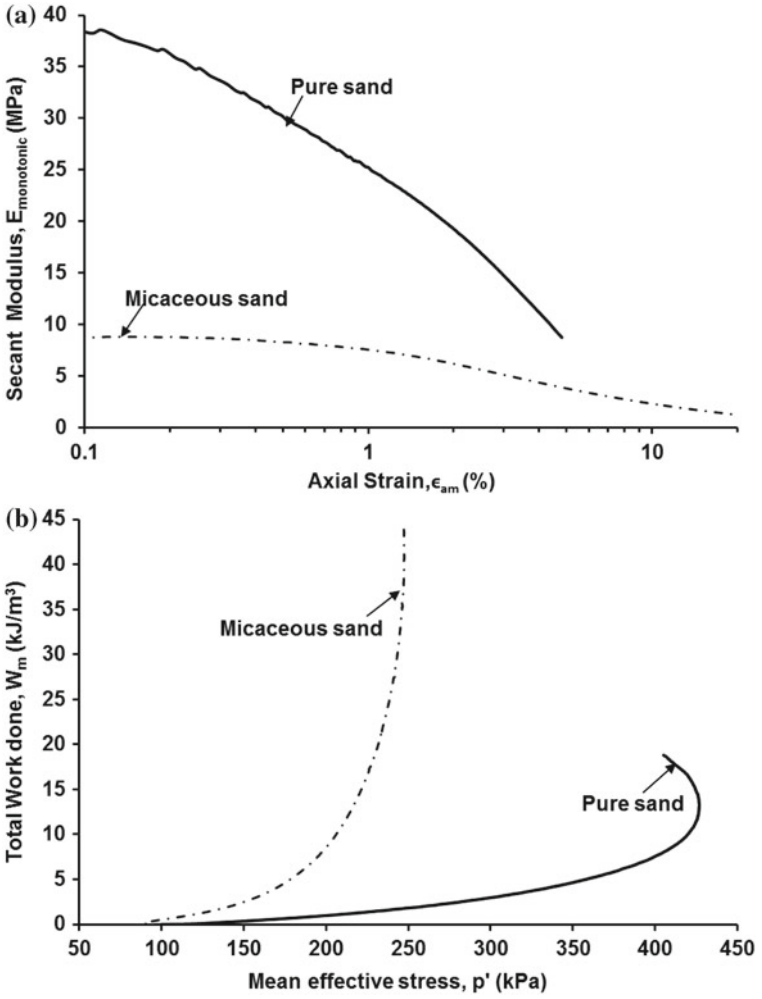

Fig. 5 Shear strength behavior of micaceous sand and pure sand under undrained monotonic compression. **a** Secant modulus degradation response, **b** dissipated strain energy response

of mica might induce high resilient nature which would be resulting in sustained stiffness and prolonged gain of peak strength of micaceous sand. The monotonic shear behavior of micaceous sand and pure sand specimens was further analyzed using energy dissipation criterion. Figure 5b shows the dissipated strain energy response of micaceous sand and pure sand with respect to volumetric stress (p') under undrained monotonic compression. The cumulative dissipated strain energy/total work done (W_m) was determined by summing up the incremental strain energy (δW_p and δW_q) at successive strain increments while the mean effective stress (p') was evaluated as per Eq. (5). As the change in volumetric strain is zero under undrained condition, the work

done per unit volume would be the representation of shear strain energy whereas the mean effective stress (p′) represents the volumetric stress variation (volumetric strain energy). Hence the work done was plotted against mean effective stress variation response in Fig. 5b.

The W_m versus p′ plot of pure sand showed flatter trend while the same was steeper for micaceous sand. Pure sand showed lesser work done per unit volume (W_m) achieved at much smaller shear strain (ε_q) with larger peak deviatoric stress and greater effective volumetric stress (p′). This indicated the greater influence of volumetric strain energy in comparison to shear strain energy in pure sand during shear deformation. The spherical sand particles would have consistent and strong sand–sand matrix interparticle interactions with uniform void spaces due to rolling over each other during shear deformation. Hence, the uniform distribution of contact force transfer mechanism among hard-hard sand particles might result in the increased influence of volumetric energy. However, micaceous sand showed higher dissipated strain energy (W_m) which was incremented steadily up to larger shear strains (ε_q) in spite of having lower peak deviatoric stress and reduced effective volumetric stress (p′). The critical strong sand and weak mica particle interactions in sand–mica matrix and the greater susceptibility of mica particles sliding among sand might develop stronger redistribution of force transfer among interparticle contacts. This might have resulted in the development of enhanced shear strain in micaceous sand responsible for the greater influence of shear strain energy than volumetric strain energy.

3.2 Dynamic Shear Behavior

The undrained cyclic behavior of micaceous sand and pure sand was observed up to 30 cycles with stress reversal along compression and extension direction (Fig. 6). Table 2 shows the variation in cyclic shear strength parameters of micaceous sand and pure sand under dynamic loading conditions.

The initial (0th cycle) loading cycle's peak deviatoric stress of pure sand was higher than that of micaceous sand depicting the reduction in stiffness of micaceous sand due to the addition of flaky mica particles among sand. Liquefaction could be defined as the rapid and complete loss of cyclic shear strength with negligible stiffness having excess pore pressure evolution equivalent to that of confining pressure making effective shear stress to be zero under dynamic loading [9, 14]. It was noticed that the cyclic stability of pure sand was degraded rapidly in the initial loading cycles leading to complete liquefaction at 5th loading cycle. However, the rate of degradation of cyclic shear strength was reduced for micaceous sand and showed cyclically stable response up to 30 loading cycles (Fig. 6a).

The development of pore pressure with successive cyclic loading in compression and extension direction was promptly increased in the case of pure sand. While the excess pore pressure of micaceous sand was developed along compression which was further decreased (dissipated) to the minimum level when the specimen was subjected

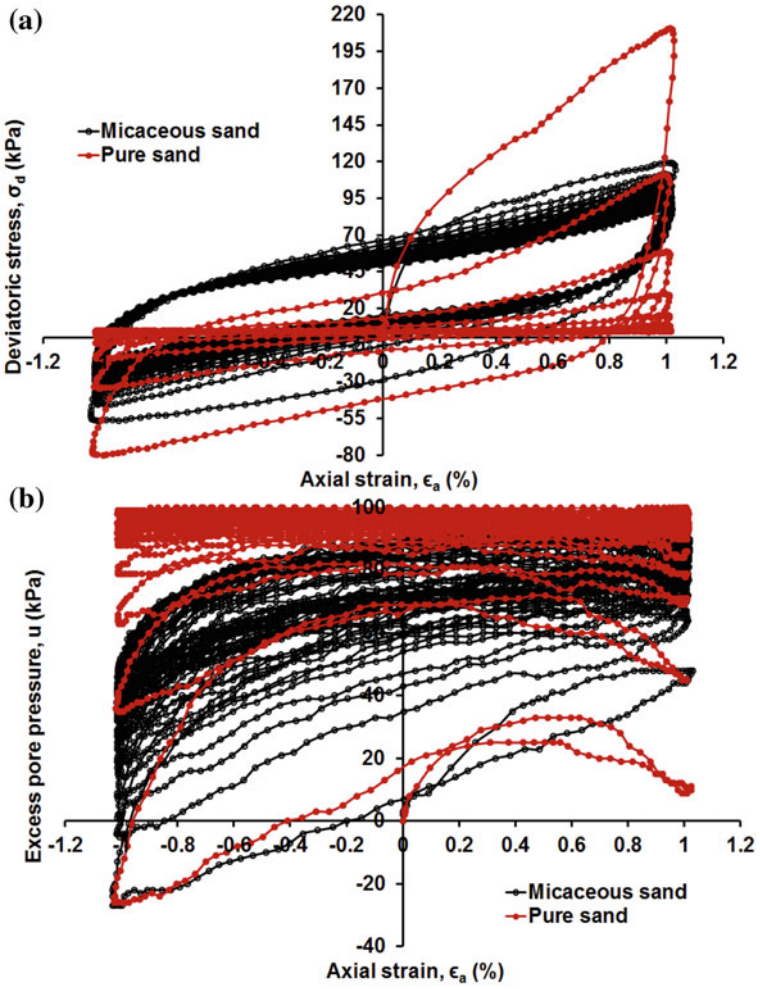

Fig. 6 Cyclic shear strength behavior of micaceous sand and pure sand under compression–extension dynamic loading. **a** Hysteresis response, **b** excess pore pressure evolution

to stress reversal along extension. The difference in excess pore pressure between compression and extension $(u_{max} - u_{min})_{EC}$ within the given loading cycle was thus increased and reached as (92–44) 48 kPa at the end of 30 cycles for micaceous sand. This resulted in reduced rate of increment in overall pore pressure with respect to confining pressure under compression–extension dynamic loading. Hence, excess pore pressure ratio ($r_u = \Delta u/\sigma_c'$) was obtained to be 1.0 for pure sand at 5th cycle whereas it was achieved to be 0.92 at the end of 30th cycle for micaceous sand. The dynamic parameters such as shear modulus (G) and damping ratio (D) of micaceous sand and pure sand underwent substantial variation owing to the presence of mica.

Table 2 Shear strength parameters of micaceous sand and pure sand under dynamic loading in compression–extension modes

Properties	Units	Pure sand	Micaceous sand
σ_{dc0} at 0th cycle	(kPa)	210.9	119.3
σ_{dc0} at 30th cycle	(kPa)	5.6	91.4
G_0	(GPa)	4.82	2.92
D_0	(%)	11.4	14.0
$*G_{average}$	(GPa)	1.58	2.53
$*D_{average}$	(%)	7.9	12.8
G_{30}	(GPa)	0.07	1.8
D_{30}	(%)	1.2	10.6
δ at 30th cycle	–	0.015	0.62
u_{maxEC} at 30th cycle	(kPa)	100	92
u_{minEC} at 30th cycle	(kPa)	94	44
$\Sigma\Delta W_d$	(kJ/m^3)	9.4	47.5

Figure 7a and b shows the variation in shear modulus and cyclic stiffness degradation under undrained compression–extension dynamic loading for micaceous sand and pure sand, respectively.

The initial shear modulus (G_0) at 0th cycle was significantly higher for pure sand while it was considerably low for micaceous sand. It could be attributed due to the interchange of strong and hard sand with weak and flexible mica resulting in the decrement of overall stiffness of micaceous sand specimens (Table 2). The shear modulus was degraded at a faster rate for pure sand which reached almost negligible value and the cyclic degradation index (δ) also reached the value of zero stating that the cyclic shear strength was completely lost at the end of six loading cycles. The rate of shear modulus degradation and the cyclic degradation index (δ) were observed to be much lower (0.62) for micaceous sand stating that there was very least amount of degradation in cyclic shear strength even at the end of 30 loading cycles. Hence, the average shear modulus (G_{avg}) was almost negligible for pure sand while it was nearly equivalent to the initial G_0 for micaceous sand (Table 2).

Figure 8a and b shows the variation in damping ratio (D) and strain energy dissipation (ΔW_d) response under undrained compression–extension dynamic loading for micaceous sand and pure sand, respectively. The initial damping ratio (D_0) was higher at the end of first cycle for micaceous sand as compared to pure sand (Table 2). This signified that the pure sand specimens were having higher rigidity and stiffness resulting in minimum dissipation of energy versus elastic strain energy while the resilient and flexible nature of mica particles were responsible for the higher damping ratio (D) of micaceous sand. The reduction in damping as well as work done per unit volume with increased number of cycles was due to the decreased stiffness caused by interparticle rearrangements. Total cumulative dissipated strain energy ($\Sigma\Delta W_d$), which was defined as the enclosed area of the hysteresis loop, was achieved to be

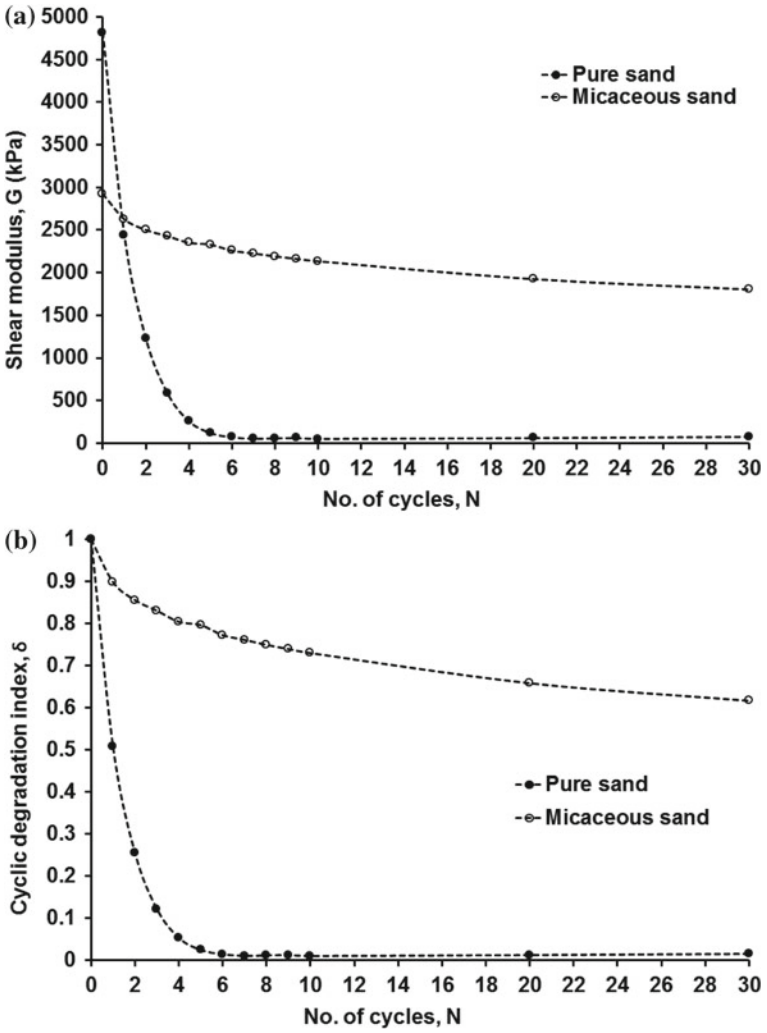

Fig. 7 Cyclic shear strength behavior of micaceous sand and pure sand under compression–extension dynamic loading. **a** Shear modulus degradation response, **b** cyclic stiffness degradation response

higher for micaceous sand as compared to pure sand due to sustained cyclic shear strength. This might be attributed due to the loss of sand–sand contacts in pure sand while the rearrangements of sand–mica particles might have increased contact area due to flaky mica particles in micaceous sand caused by the oscillatory movement (compression–extension) under dynamic loading.

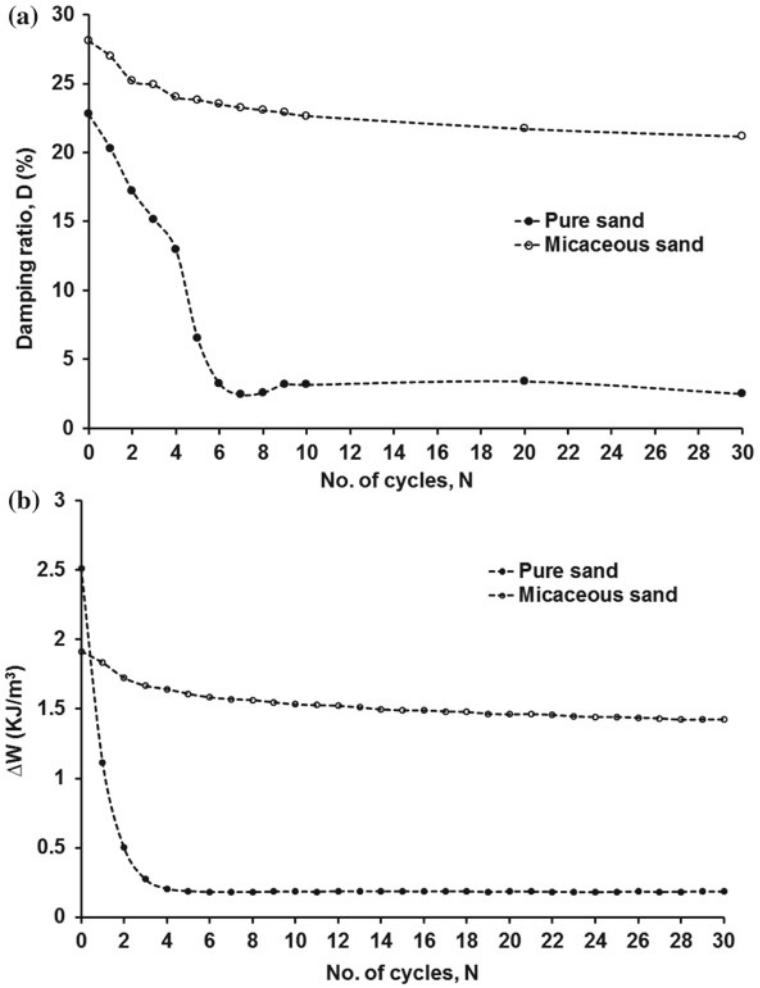

Fig. 8 Cyclic shear strength behavior of micaceous sand and pure sand under compression–extension dynamic loading. **a** Damping ratio degradation response, **b** dissipated strain energy response

4 Comparative Analysis of Micaceous Sand and Pure Sand

The continuous monotonic compression shearing might have improved the spherical sand–sand interparticle contacts resulting in greater shear strength of pure sand. The continuous dissembling of bridging-ordering mechanisms and higher susceptibility of slippage of mica among sand in sand–mica matrix during compression shearing might result in the achievement of deteriorated shear strength of micaceous sand. The compression–extension dynamic loading would reduce the spherical sand–sand

microstructural particle contacts due to rolling of particles over each other in back and forth motion with rapidly developed pore pressure making the pure sand vulnerable to liquefaction. However, the mica particles entrapped among sand particles might improve the interparticle interactions in sand–mica microstructure due to periodic repeated motion of dissembling bridging-ordering under compression and regaining of sand–mica contacts under extension due to the resilient and flexible nature of mica in micaceous sand. The cyclic regaining of sand–mica particle contacts under dynamic loading would result in making the micaceous sand to undergo the least stiffness degradation. Hence, it exhibited improved cyclic shear strength in comparison to pure sand.

Pure sand specimens showed desirable shear behavior under monotonic compression while micaceous sand specimens showed stable response under dynamic loading conditions. However, the initial stiffness was always lesser and the rate of stiffness degradation was slower for micaceous sand in comparison to pure sand under both monotonic compression and dynamic loading conditions. Such behavior could be observed due to the high water retention capacity of mica particle owing to the entrapped water molecules among mica flakes, which might enhance the resilient nature of mica leading to the sustaining of shear strengths until larger strain levels in monotonic compression and stable performance until higher number of cycles in dynamic loading conditions.

5 Conclusions

The current research examined the comparative study on shear behavior of micaceous sand and pure sand under undrained monotonic compression and dynamic (compression–extension) loading conditions and possible interpretations with respect to microstructural sand and mica particle rearrangements. Major observations are summarized as follows:

- In undrained monotonic compression, pure sand showed higher stiffness, larger peak stress, brittle stress–strain response, and dilative pore pressure response; while micaceous sand showed lower stiffness, reduced peak stress, ductile stress–strain response, and increased contractive pore pressure response.
- Higher influence of volumetric strain energy was witnessed by pure sand whereas increased influence of shear strain energy was observed by micaceous sand during monotonic compression.
- In undrained compression–extension dynamic loading, pure sand underwent liquefaction with zero effective shear stress whereas micaceous sand showed stronger cyclic stability with minimal stiffness degradation.
- The sand–sand matrix might be stronger and stable due to achievement of closely packed sand particles under monotonic compression which in turn became vulnerable due to rapid loss of contacts under compression–extension dynamic loading.

- The metastable sand–mica matrix with ordering and bridging might result in sliding during monotonic compression while the resilient and flexible nature of mica along with particle reorientation might have improved the interparticle contacts during to and fro motion under dynamic loading.

Acknowledgements Financial Support from IIT Gandhinagar is gratefully acknowledged. Any opinions, findings, and conclusions or recommendations expressed in this material are those of authors and do not necessarily reflect the views of IIT Gandhinagar.

References

1. Belkhatir M, Arab A, Della N, Missoum H, Schanz T (2010) Influence of inter-granular void ratio on monotonic and cyclic undrained shear response of sandy soils. CR Mec 338(5):290–303
2. Delfosse-Ribay E, Djeran-Maigre I, Cabrillac R, Gouvenot D (2004) Shear modulus and damping ratio of grouted sand. Soil Dyn Earthq Eng 24(6):461–471
3. El Shamy U, Denissen C (2012) Microscale energy dissipation mechanisms in cyclically-loaded granular soils. Geotech Geol Eng 30(2):343–361
4. Fahoum K, Aggour MS, Amini F (1996) Dynamic properties of cohesive soils treated with lime. J Geotech Eng 122(5):382–389
5. Frempong EM (1994) Geotechnical properties of some residual micaceous soils in the Kumasi Metropolitan Area (Ghana). Bull Eng Geol Env 49(1):47–54
6. Georgiannou VN (2006) The undrained response of sands with additions of particles of various shapes and sizes. Geotechnique 56(9):639–649
7. Georgiannou VN (2008) Unstable behaviour of model Jamuna micaceous sand. Geotechnique 58(10):825–829
8. Harris WG, Parker JC, Zelazny LW (1984) Effects of mica content on engineering properties of sand. Soil Sci Soc Am J 48(3):501–505
9. Hyodo M, Hyde AF, Aramaki N (1998) Liquefaction of crushable soils. Geotechnique 48(4):527–543
10. Lee JS, Guimaraes M, Santamarina JC (2007) Micaceous sands: microscale mechanisms and macroscale response. J Geotech Geoenviron Eng 133(9):1136–1143
11. Nemat-Nasser S, Shokooh A (1979) A unified approach to densification and liquefaction of cohesionless sand in cyclic shearing. Can Geotech J 16(4):659–678
12. Seethalakshmi P, Sachan A (2018a) Effect of successive impact loading on compactability, microstructure, and compressibility behavior of micaceous sand. Transp Infrastruct Geotechnol 5(2):114–128
13. Seethalakshmi P, Sachan A (2018b) Effect of mica content on pore pressure and stress-strain response of micaceous sand using energy dissipation and different failure mechanisms. Int J Geotech Eng
14. Seethalakshmi P, Sachan A (2019) Dynamic behaviour of micaceous sand with varying mica content and its association with compactability, compressibility and monotonic shear response. Int J Geotech Eng
15. Sitharam TG, Govindaraju L, Sridharan A (2004) Dynamic properties and liquefaction potential of soils. Curr Sci 87(10):1370–1378
16. Tate BD, Larew HG (1963) Effect of structure on resilient rebound characteristic of soils in the Piedmont Province of Virginia. Highway Res Rec 39:97–111
17. Tavenas F, Des Rosiers JP, Leroueil S, La Rochelle P, Roy M (1979) The use of strain energy as a yield and creep criterion for lightly overconsolidated clays. Geotechnique 29(3):285–303

18. Vucetic M, Dobry R (1988) Degradation of marine clays under cyclic loading. J Geotech Eng 114(2):133–149
19. Voznesensky EA, Nordal S (1999) Dynamic instability of clays: an energy approach. Soil Dyn Earthq Eng 18(2):125–133
20. Yang J, Wei LM, Dai BB (2015) State variables for silty sands: global void ratio or skeleton void ratio? Soils Found 55(1):99–111

Comparative Behavior of Mechanical Response of Earth Retaining Structures with Two Different Material Models

Smita S. Aldonkar and P. Savoikar

Abstract Retaining walls are the most commonly adopted solution to retain soils in hilly areas and in case of excavation involved structures like the railways, roadways prone to landslides. The failure of retaining structures and landslides is a major threat to human life and property. The study of soils and the failure criteria has to be understood before recommending a particular slope protection or retention technique. This paper illustrates the study of retaining wall with shelves in dry excavations. The established material models Mohr–Coulomb model (MC) and Hardening Soil (HS) are used. Midas GTS NX software is used for the analysis. The material model is used to analyze the soil behavior considering the parameters like the stiffness, loading, and unloading conditions. Model is studied creating different layers of soils. A comparative study is presented using the two models and using the MIDAS GTS NX Software. The study is basically carried out for the region of Goa and its soil conditions.

Keywords Lateritic soils · Mohr–Coulomb · Hardening soil · Constitutive modeling · MIDAS GTS NX

1 Introduction

Infrastructure is the key driver for the Indian economy. There is a major push in infrastructure development in the construction industry across the nation: buildings, roads, dams, bridges, jetties.

S. S. Aldonkar · P. Savoikar (✉)
Goa College of Engineering, Farmagudi, Ponda 403401, Goa, India
e-mail: psavoikar@gmail.com

A. Prashant et al. (eds.), *Advances in Computer Methods and Geomechanics*, Lecture Notes in Civil Engineering 55,
https://doi.org/10.1007/978-981-15-0886-8_6

1.1 Need of Retaining Structures in Goa

The Goa tourism industry demands better infrastructure and smoother roads connecting the States and within the State of Goa, which needs a lot of cutting and filling of earth. The protection of slopes can be done by gabion walls, soil nailing, reinforced earth, and different types of retaining walls. Due to scarcity of space, the construction of embankment needs to be carried out within the available space using retaining walls. Hence, the embankment requires retention of the backfill soils for the stability of slopes.

1.2 Types of Retaining Structures in Goa

Retaining walls used in Goa since 1960s were of gravity type, which are rigid in nature. In this type of structures, the stability of retaining wall against sliding is provided by the self-weight of the wall and therefore the retaining structures are bulky incurring more cost. The stability of such structures under dynamic conditions may be at risk.

The non-gravity type structures derive their stability by bending action. These are made up of reinforced cement concrete, viz., cantilever, and the counterfort type retaining walls. They can be designed for retaining the heights of different types of backfill and can be designed to make it economical. The sheet pile retaining walls are thin members, which derive their stability from the penetration depth into the soil and also can be anchored from the top end. These are mainly used in jetties and ships and dry docks along the rivers. The reinforced earth retaining structures are the flexible type of walls is now being implemented along the national highways in Goa. The gabion walls are the gravity types of structure for retaining the lateritic or gravely backfills and used along the Konkan railway tracks and near District Hospital in Ponda, Goa.

1.3 Retaining Walls with Relieving Shelves

Retaining walls with relieving shelves is an innovative method in retaining structure types. When cantilever retaining wall needs to be designed for height of more than 6 m, it can be designed efficiently and economically by providing relieving shelves. These shelves extend into the backfill and the earth pressure on the stem reduces, improving its stability. Various researches are carried out on the stability analysis of such walls. The variation in the shelf width and number of shelves along the height of the stem can be carried out for the optimization of the walls with the shelves.

2 Soils of Goa

2.1 Soil Profile of Goa

Goa experiences heavy seasonal rainfall. Lateritic soils undergo weathering and weathered profiles are of common occurrence in Goa. Laterite is the most widespread of all duricrust types. Laterite represents the uppermost levels of an extreme form of weathering profile, and typically forms 1–20 m thick surface layer or 'duricrust' that can extend over areas of a few, to hundreds, or even thousands of square kilometers [1]. Laterite profiles in Goa consist of a progression from unaltered protolith at the base, up through increasingly altered saprolite–parent rock, iron-enriched zones. The top layers are as an iron-rich laterite duricrust. The exposed lateritic section (25 m) reveals a weathering profile that progresses from the pinkish at the floor to red lateritic soil at the top (Fig. 1).

The sampled profile has been characterized using a combination of field observation and geotechnical analyses. Throughout the depth, the profile shows variation in colouration and composition. This colouration is due to increasing concentrations of Fe-rich oxyhydroxides. These laminations remain readily recognizable (Fig. 2).

2.2 Properties of Soil Used in the Model

Lateritic soils in Goa have properties varying with depth and color. The main soil is red lateritic soil and the underlying soil is of varied color and properties. The soil in the region of study was pinkish in color. They are silty sandy in nature with 15–30% clay content. The properties of soils like Young's modulus (E), Poisson's ratio (ν), friction angle (ϕ), cohesion (c), dilatancy angle (ψ), etc. used in the model are given below (Tables 1 and 2).

Fig. 1 Lateritic soil at Ponda, Goa

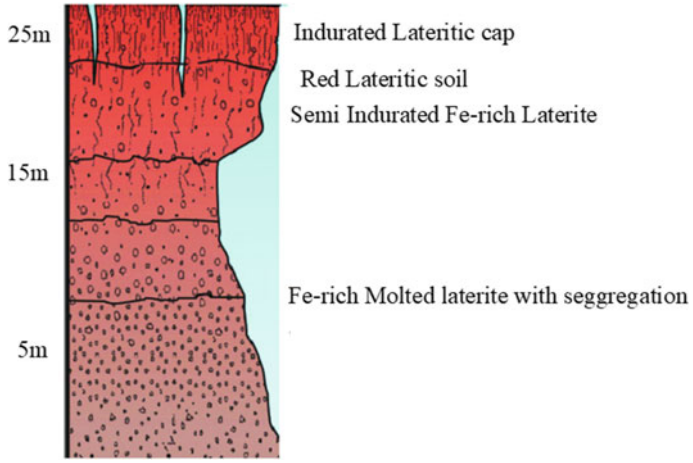

Fig. 2 Mineral content profile of lateritic soil at Ponda, Goa [2]

3 Constitutive Models

3.1 Types of Constitutive Models

There are different constitutive models provided for soils in MIDAS GTS NX. These can be broadly classified as Isotropic, Orthotropic, and Interface/Pile.

Some of the commonly used models in MIDAS GTS NX are

1. Elastic
2. Tresca
3. von Mises (Non linear)
4. Mohr–Coulomb
5. Drucker Prager
6. Hoek Brown
7. Generalized Hoek Brown
8. Hyperbolic (Duncan-Chang)
9. Strain Softening
10. Modified Cam Clay
11. Hardening Soil (small strain stiffness).

Isotropic materials have the same properties in every direction and are used to define material behavior properties of most linear elastic/nonlinear elastic/elasto-plastic materials. Orthotropic materials show directionally varying properties. Natural ground is generally layered and sloped, making it possible to have different strengths in each orthogonal direction. This option can also be used to define jointed rocks, which have different properties depending on the direction and behave differently according to the specific confinement conditions.

Table 1 Geotechnical properties of soils [2]

Soil type	E kN/m^2	ν –	γ kN/m^3	γ_{sat} kN/m^3	E_{50} kN/m^2	E_{oed} kN/m^2	E_{ur} kN/m^2	e_o –	K_o –	c kN/m^2	ϕ (°)	ψ (°)	P_{ref} kN/m^2
Red lateritic	1.2×10^4	0.33	19.5	22.2	4×10^4	4×10^4	12×10^4	0.5	0.38	12	38	7	80
Pink lateritic	1.2×10^4	0.3	16.8	17.6	15×10^4	15×10^4	45×10^4	0.45	0.52	17	33	3	70

Table 2 Properties of concrete [3]

Retaining wall Material	E kN/m^2	ν –	γ kN/m^3	γ_{sat} kN/m^3	K_o –
Concrete	2×10^7	0.18	25	25	1

3.2 Mohr–Coulomb Model (MC)

The first method of estimating stresses in soil was the Mohr–Coulomb (MC) method. Due to its constant stiffness, the analysis is simple and very fast. The model is ideally correct for stability test but the displacements and forces obtained do not give a realistic estimate of the failure. Parameters commonly used for MC model are given below:

1. Young's modulus (E, kN/m^2)
2. Poisson's ratio (ν)
3. Friction angle (ϕ, °)
4. Cohesion (c, kN/m^2)
5. Dilatancy angle (ψ, °)

3.3 Hardening Soil Model (HS)

Hardening Soil Model [4] is an advanced and latest model for modeling and simulation of soil behavior. In Mohr–Coulomb method, the limiting state of stress is calculated by these parameters: angle of friction friction (ϕ), cohesion (c) (sometimes for cohesionless soils the angle of dilatancy (Ψ) is also considered). But in HS model, soil stiffness is explained much more correctly using of extra three different input stiffnesses: triaxial stiffness (E_{50}), triaxial unloading stiffness (E_{ur}), oedometer loading stiffness (E_{oed}), and also used an extra cap. The primary load which creates both the elastic and plastic deformations has been explained in this model using the unloading–reloading moduli and also the compression modulus. The elastic deformation is recoverable upon unloading and plastic deformations are irrecoverable after unloading.

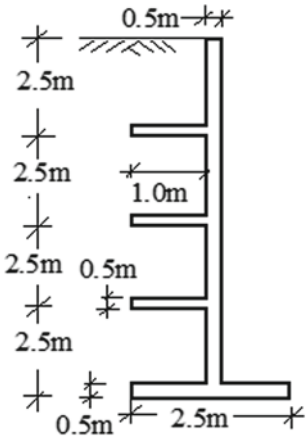

Fig. 3 Model used in the analysis

4 Constitutive Modeling Using MIDAS GTS NX

4.1 Model Geometry and Analysis Using MIDAS GTS NX

The material required for the model was defined first. A mesh size of 1 × 1 × 1 m is chosen for the model analysis. The base stratum, backfill, and the retaining wall with three relieving shelves were used. In the Mohr–Coulomb model, parameters used were Young's modulus, Poisson's ratio, friction angle, cohesion, and dilatancy angle (Table 1). In the Hardening Soil model, basic Mohr–Coulomb model parameters are used in addition to parameters (Table 1): Secant Modulus 50% strength, Oedometric Modulus, Unloading–Reloading Modulus, Unloading–Reloading Poisson's Ratio, Exponent of the stress-stiffness function, etc. The retaining wall of 10 m with the three relieving shelves at every of 2.5 m from the free end is considered for analysis and comparison using the MC and HS model. The geometry of model used in the analysis is shown in Fig. 3. Stem thickness is 0.5 m. Shelf thickness is 0.5 m and length is 1.0 m. The base slab is 2.5 m wide and 0.5 m thick. The retaining wall is modeled for retaining the Goan lateritic soil and with two layers of lateritic soils (red and pink laterite of 5 m thickness each, with properties as in Table 1).

4.2 Comparison of Displacements of Retaining Wall

Figure 4a and b shows horizontal displacement at different heights from top of the retaining wall using Mohr–Coulomb Model and Hardening soil model, respectively. Comparison of Mohr–Coulomb and Hardening Soil model displacement for retaining wall with three shelves is shown in Fig. 5. It can be seen that the high displacements

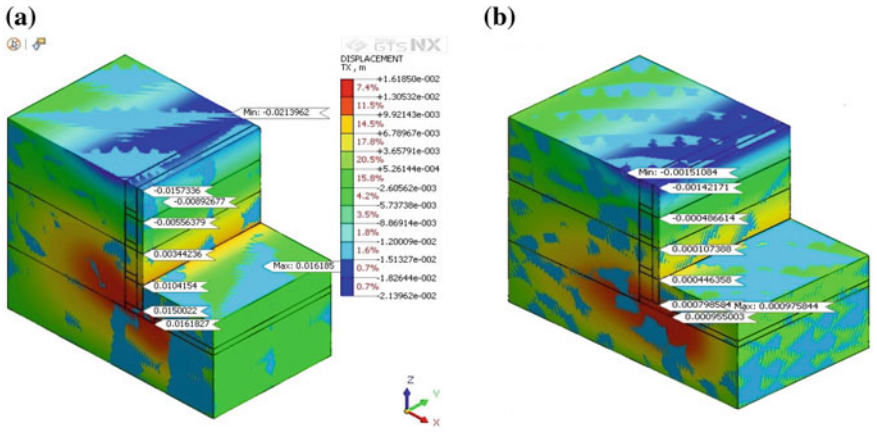

Fig. 4 Horizontal displacement (m) **a** Mohr–Coulomb Model and **b** Hardening Soil model

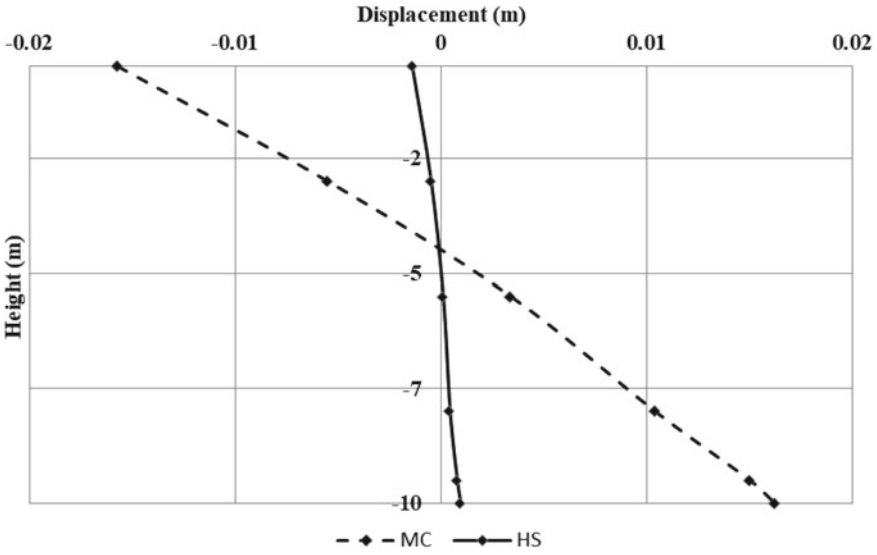

Fig. 5 Comparison of displacements at various depths of retaining wall using MC and HS model

were observed at the top for the MC model as compared to HS model. However, at the height of 0.42 H the displacements predicted by both models are the same.

4.3 Comparison of Stresses at Different Heights of Retaining Wall

Figure 6a and b shows stress variation at different heights from top of the retaining wall using Mohr–Coulomb and Hardening Soil model, respectively. Comparison of Mohr–Coulomb and Hardening Soil model stresses for retaining wall with three shelves is shown in Fig. 7. It can be seen that the higher stresses were observed at

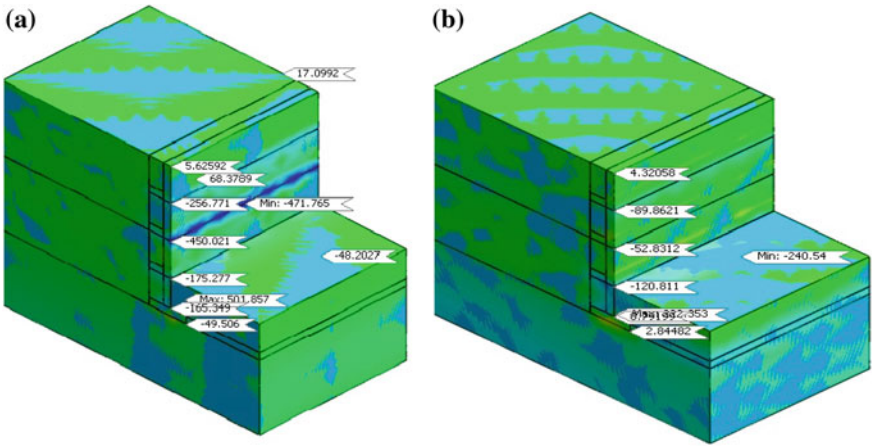

Fig. 6 Variation of stresses with height for **a** MC and **b** HS model

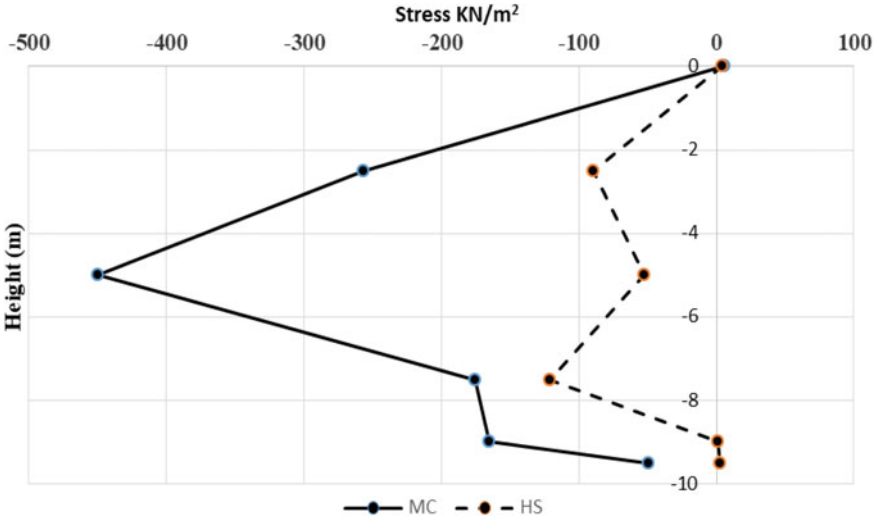

Fig. 7 Comparison of variation of stresses with height using MC and HS model

the mid height for the MC model whereas higher stresses were observed at 0.75 H for HS model. Also, the stresses observed in the case of MC model were higher than that of HS model.

5 Conclusions

It can be concluded from the comparative analysis of the cantilever retaining wall with three relieving shelves retaining wall in layered lateritic soils using Mohr–Coulomb and Hardening Soil model that

1. Higher displacements were observed at the top for the MC model as compared to HS model. However, at the height of 0.42 H the displacements predicted by both models are the same.
2. Higher stresses were observed at the mid height for the MC model whereas higher stresses were observed at 0.75 H for HS model.
3. MC model resulted in higher stresses than that of HS model.
4. The difference in behavior of the two models can be attributed to stiffness parameters used in the two models. Thus, HS model can be considered to give more realistic results than that given by the MC model.

References

1. Nash D, McLaren J (2007) Geochemical sediments and landscapes. Willey-Blackwell Publishers
2. Widdowson M (2009) Evolution of laterites in Goa. In: Mascarenhas A, Kalavampara G (eds) Proceedings of natural resources of Goa: a geological perspective, pp 35–68
3. Midas Manual MIDAS GTS NX
4. Schanz T, Vermeer PA, Bonnier PG (1999) The hardening soil model: formulation and verification. In: Beyond 2000 in Computational Geotechnics. Balkema, Rotterdam

Post-liquefaction Reconsolidation and Undrained Cyclic Behaviour of Chang Dam Soil

Majid Hussain and Ajanta Sachan

Abstract Understanding and determination of post-liquefaction stress–strain behavior of sandy soils under monotonic and cyclic loading is essential to estimate the deformations that might occur in liquefied deposits under further loading. The undrained response of reconsolidated specimens under multilevel cyclic loading simulates the post-liquefaction behavior of soils under earthquake aftershocks and other cyclic loading conditions. In the present study, post-liquefaction reconsolidation and undrained behavior of medium dense silty-sand of Chang dam under multilevel repeated cyclic loading is explored. The soil deposit underwent severe liquefaction during the 2001 Bhuj earthquake. During the first round of loading (C_0), the specimens were subjected to 50 cycles of cyclic loading at 0.4 mm amplitude (A) and 0.1 Hz frequency (f) and exhibited liquefaction. After C_0, developed excess pore water pressure was allowed to dissipate, and specimens were allowed to reconsolidate. Reconsolidated specimens were then subjected to second round of cyclic loading, C_1 ($A = 0.4$ mm, $f = 0.1$ Hz and $N = 35$), and this process was continued for C_2, C_3, and C_4 loading rounds. Significant reduction in void ratio (e) was observed each time when specimens were allowed to reconsolidate after each round of undrained cyclic loading, thereby increasing the liquefaction resistance. The increase in liquefaction resistance on repeated loading was reflected in the cyclic stress ratio (CSR) calculated for every cycle for each level of cyclic applied loading. The inclination of the peak deviatoric stress envelope (instability line) for each round of loading was observed to increase with repeated reconsolidation and cyclic loading.

Keywords Post-liquefaction · Cyclic loading · Reconsolidation · Stress path · Cyclic stress ratio (CSR)

M. Hussain (✉) · A. Sachan
Indian Institute of Technology Gandhinagar, Gandhinagar, India
e-mail: majid.hussain@iitgn.ac.in

A. Sachan
e-mail: ajanta@iitgn.ac.in

A. Prashant et al. (eds.), *Advances in Computer Methods and Geomechanics*, Lecture Notes in Civil Engineering 55,
https://doi.org/10.1007/978-981-15-0886-8_7

1 Introduction

When loose saturated sand deposits are subjected to shaking during an earthquake, there is reduction of mean effective stress (p') due to the buildup of excess pore water pressure (Δu) subsequently leading to liquefaction under undrained boundary conditions. Understanding the phenomenon of liquefaction and the methods to mitigate its effects has received considerable attention for the past few decades. The post-liquefaction mechanical behavior of soils is as important as liquefaction. Awareness about the post-liquefaction reconsolidation and stress–strain behavior of soils susceptible to liquefaction is necessary to estimate the earthquake-induced settlements and to evaluate the bearing capacity of the liquefied soil deposits [7, 27]. The effect of previous seismic stress–strain history (cyclic pre-shearing) is important in evaluating the undrained response of liquefied soil deposits. In addition to the induced shear strains (γ), pore pressure (Δu) and degree of post-liquefaction reconsolidation, undrained mechanical behavior of liquefied soils deposits is governed by the same factors that govern the liquefaction behavior of soils, viz, density, fines content, nature of fines, mode of loading, initial effective consolidation pressure (p'_c), and loading history. Initially, till early 1990s minimal work was carried out to understand the post-liquefaction behavior of sands [5, 24]. However, more recently various researchers [4, 10, 15, 17, 18, 23, 25] studied the post-liquefaction undrained shear behavior of sandy soils. Olson and Stark [12, 13] suggested a detailed procedure based on a well-documented large database of case histories to evaluate the liquefied strength and post-liquefaction stability of soil deposits susceptible to liquefaction.

Earthquake-induced ground settlements have two components: one resulting during the process of shear deformation of the soil (liquefaction) and the other due to reconsolidation of the liquefied deposits. Settlements resulting from post-liquefaction reconsolidation were reported to be directly related to the maximum induced γ and Δu; which developed during liquefaction [8]. A strong relationship between the post-liquefaction volumetric strains and the factor of safety against liquefaction was reported. Post-liquefaction reconsolidation behavior of the liquefied saturated sandy soils was explored by analyzing pore pressure dissipation curves using solidification and consolidation theory [20, 21]. The increased permeability after liquefaction (~5 times of the initial value) was also observed to facilitate larger settlements during reconsolidation stage of the liquefied deposits [3].

The post-liquefaction undrained monotonic shear behavior of liquefied soils was reported by many researchers [2, 4, 15, 17, 18, 24, 25]. If excess pore water pressure at the end of cyclic loading was allowed to dissipate, the post-liquefaction undrained monotonic stress–strain response was observed to be strongly dependent on relative density including the insignificant influence of amplitude of axial strain and initial confining pressure [18]. Amini and Trandafir [2] reported that the liquefied soil deposits would exhibit dilative post-liquefaction shear strength response, which would be strongly dependent on initial effective consolidation stress (p'_c). Wang et al. [26] observed that post-liquefaction shear strength and stiffness increased with the increase in the degree of reconsolidation both at small and large deformations. The

mentioned research also studied the post-liquefaction undrained monotonic behavior of soils considering the effect of degree of reconsolidation, relative density, initial effective confining pressure (p'_c), fines content, nature of fines, and shear strain amplitude. Robertson [16] presented cone penetration test (CPT)-based relationships to evaluate liquefied shear strength for a wide range of soils based on well-documented case histories. The case histories indicated that young, loose, nonplastic, or low-plastic soils would tend to be more susceptible to significant and rapid strength loss than older, denser and more plastic soils.

A number of investigators also explored liquefaction characteristics of previously liquefied soils under triaxial or simple shear testing conditions [5, 9]. The studies confirmed that liquefaction resistance of previously liquefied specimen could exhibit a marked increase or decrease in its response depending on the level of induced shear strain (γ), excess pore water pressure (Δu), and the initial relative density (D_r) of the specimens. It might be due to the elimination of local instabilities and creation of a nonuniform structure [5]. Oda et al. [14] provided microstructural interpretation of liquefaction mechanism of liquefied granular soils under cyclic loading. Influence of cyclic pre-shearing on undrained cyclic behavior of cohesionless soils was studied by Porcino et al. [15] and Sriskandakumar et al. [17]. The findings revealed that the cyclic response of pre-sheared specimens would depend on the degree of Δu and level of γ reached during the previous cyclic loading. Current study is focused on the evaluation of reconsolidation and liquefaction response of previously liquefied silty-sand specimens under multilevel undrained cyclic triaxial conditions. The research work was carried out to understand the reconsolidation and liquefaction response of already liquefied specimens to simulate the behavior under earthquake aftershocks and other cyclic loading conditions in high seismicity region. The response of reconsolidated specimens under four levels of cyclic loading after initial liquefaction was explored. The material studied consists of medium dense silty-sand collected from Chang dam of Kucth region Gujarat, India. The soil had experienced severe liquefaction during the 2001 Bhuj earthquake resulting in significant damage to the dam [19].

2 Experimental Program

2.1 Material Properties and Specimen Preparation

In the present study, the soil was collected from downstream toe of Chang dam at a depth of 0.5 m. The soil consists of 82% sand, 15% silt, and 1% clay and classified as medium dense silty-sand (SM). Basic geotechnical properties of the Chang dam soil are presented in Table 1. The grain size distribution (GSD) of the soil is illustrated in Fig. 1. Solid cylindrical specimens of 50 mm diameter and 100 mm height were prepared using moist tamping method at in situ dry density and water content of 1.6 g/cm^3 and 8%, respectively.

Table 1 Basic properties of test material

D_{10}	D_{50}	C_u	C_c	G_S	e_{max}	e_{min}	FC	*Soil class*
0.02	0.19	10	4.225	2.66	0.851	0.496	18	SM

where D_{10} and D_{50} are effective and mean particle diameters in mm, C_u and C_c are coefficients of uniformity and curvatures, respectively, G_S specific gravity, e_{max} and e_{min} are maximum and minimum void ratio and FC is fines content in %

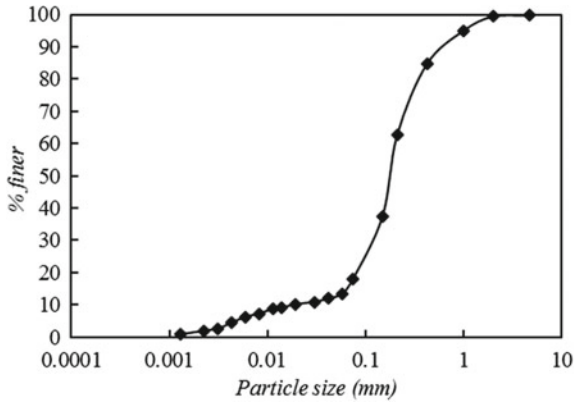

Fig. 1 Grain size distribution of Chang dam soil

2.2 Testing Procedure

The post-liquefaction reconsolidation and undrained cyclic behavior of medium dense silty-sand of Chang dam was investigated by conducting a series of isotropically consolidated undrained cyclic triaxial tests under strain-controlled conditions. In post cyclic loading, the liquefied specimens were subjects to four rounds of reconsolidation and undrained cyclic loading to evaluate the post-liquefaction cyclic behavior of the specimens. A schematic representation of the testing procedure along with drainage conditions is mentioned in Fig. 2. The prepared soil specimens were mounted on the loading frame of cyclic cum static triaxial testing machine and were saturated in three steps: CO_2 saturation, water flushing, and back pressure saturation. Specimens were flushed with CO_2 for 45 min at very low pressure (~5 kPa) while maintaining a cell pressure of 20 kPa [11]. After CO_2 flushing, water flushing was conducted by pushing water inside the specimen equal to 2–3 times the volume of the specimen. Back pressure was then applied in increments of 40 kPa (every 2 h) to acquire B (Skempton's pore pressure parameter) values greater than 0.98. During the saturation stage, the effective confining stress (p') was maintained at 20 kPa. After saturation, the specimens were isotropically consolidated to respective effective confining pressure (p'_c) of 100, 200, and 300 kPa. The consolidated specimens were further subjected to first round (C_0) of undrained (constant volume) harmonically varying cyclic axial loading of amplitude (A) 0.4 mm and frequency (f) 0.1 Hz

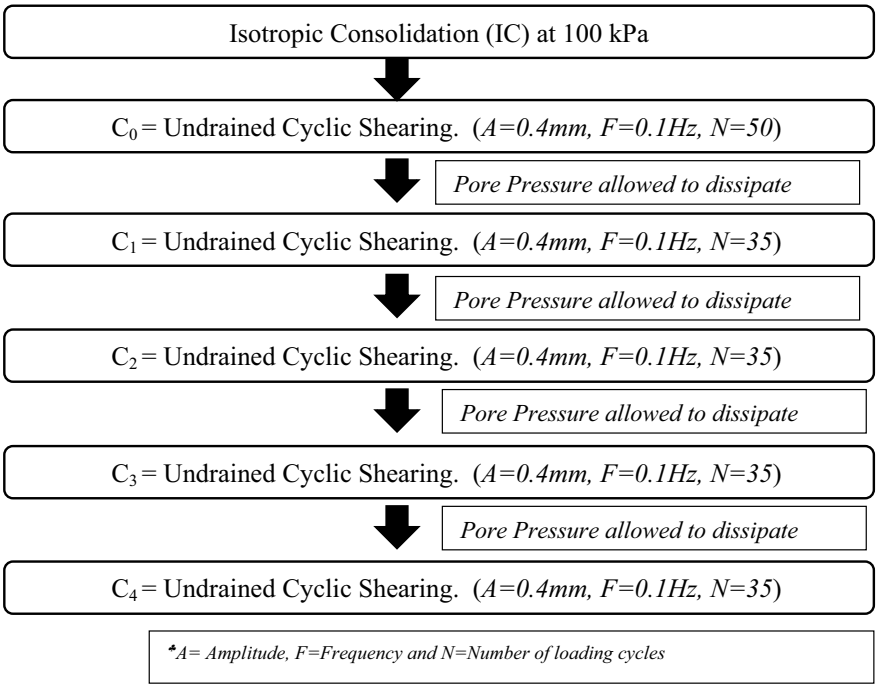

Fig. 2 Procedure adopted for repeated multilevel reconsolidation and cyclic loading

for 50 number of cycles (N). The liquefied specimens were then allowed to reconsolidate and further subjected to second round (C_1) of cyclic loading, ($A = 0.4$ mm, $f = 0.1$ Hz, and $N = 35$). The process was repeated three more times to arrive at the fourth round (C_4) of cyclic loading, as shown in Fig. 2. The number of cycles was restricted to 50 and 35 as the specimens exhibited liquefaction within 10 cycles during C_0.

3 Results and Discussion

Loose silty-sands are most susceptible to liquefaction owing to the large compressibility and small-undrained shear strength. These soils undersaturated and undrained conditions undergo liquefaction, even under moderate seismic/earthquake events. Due to their large susceptibility to liquefaction, the post-liquefaction cyclic behavior of such soils becomes essential to evaluate the settlements that will result from reconsolidation and further cyclic loading (aftershocks and other cyclic loads). The current study evaluates the cyclic, post-liquefaction reconsolidation, and undrained behavior of medium dense silty-sand of Chang dam under multilevel cyclic loading.

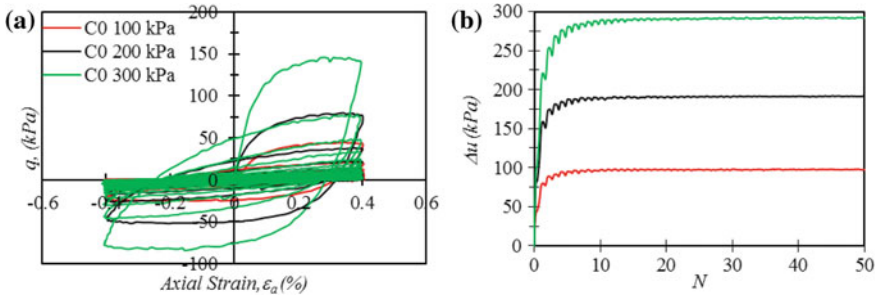

Fig. 3 Response of Chang dam soil during C_0. **a** Stress–strain, **b** excess pore water pressure

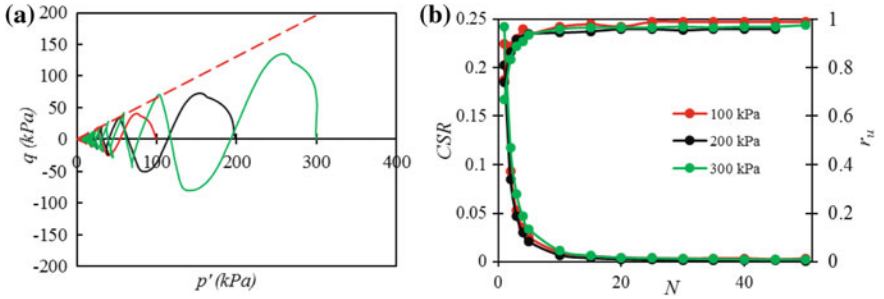

Fig. 4 Response of Chang dam soil during C_0. **a** Effective stress path, **b** evolution of *CSR* and r_u

Chang soil exhibited low liquefaction resistance under first round (C_0) of the applied strain control loading of amplitude (A) and frequency (f) to be 0.4 mm and 0.1 Hz, respectively. Figure 3 illustrates the stress–strain and excess pore water pressure (Δu) response of the soil at the three initial confining pressures (p'_c) of 100, 200, and 300 kPa. The specimens exhibited initial liquefaction within five cycles with Δu attaining values nearly equal to initial confining pressure (p'_c). Figure 4 shows the effective stress path and evolution of cyclic stress ratio (*CSR*) and excess pore water pressure ratio (r_u) with the number of loading cycles (N) for the specimens at the three p'_c. It was observed that *CSR* exhibited values as low as 0.003 at N equal to 10. The corresponding r_u values were evaluated to be higher than 0.97, indicating nearly initial liquefaction (Fig. 3b).

3.1 Post-Liquefaction Reconsolidation Behavior Under Repeated Multilevel Cyclic Loading

After C_0, the developed Δu was allowed to dissipate (reconsolidation) resulting in decreased void ratio. Subsequent cyclic loading after each level (round) is illustrated

Table 2 Reduction in void ratio during reconsolidation after each level of cyclic loading

p_c' kPa	Δe				
	IC	C_0	C_1	C_2	C_3
100	0.035	0.038	0.022	0.016	0.012
200	0.042	0.043	0.026	0.017	0.013
300	0.048	0.053	0.032	0.022	0.017

in Fig. 2. Reduction in void ratios due to reconsolidation at the end of four rounds of cyclic loading are presented in Table 2. The specimens exhibited significant decrease in void ratios with the increase in p'_c and with the subsequent levels of cyclic loading. The decrease in void ratio during reconsolidation after a particular round of loading was observed to increase with p'_c. At given p'_c, the reduction in void ratio decreased with the subsequent rounds of cyclic loading (Δe during reconsolidation decreased as the loading progressed from level C_0 to C_3), as mentioned in Table 2. The reduced void ratio led to lower compressibility, which resulted in suppressed contractive behavior and increased resistance to liquefaction on subsequent repeated cyclic loading. The reconsolidation volumetric strains could be directly transformed to the maximum shear strain amplitudes that might result during a seismic event [8].

3.2 Post-liquefaction Undrained Stress–Strain and Pore Pressure Behavior Under Repeated Multilevel Cyclic Loading

Specimens reconsolidated after C_0 was subjected to the second round (C_1) of cyclic loading (A = 0.4 mm and $f = 0.1$ Hz for N = 35). Figure 5a illustrates the response of specimens subjected to C_1. During C_1, q_{max} for each cycle was observed to be higher as compared to C_0 except for the first cycle. The lower value of q_{max} during first cycle might be due to the weakening of the soil fabric resulting from excessively high levels of r_u [17]. Although the immediate peak deviatoric stress was observed to be lower as compared to C_0, the reconsolidated specimens exhibited higher liquefaction resistance to further cyclic loading. This could be attributed due to the reduced void ratio resulting in more compact packing of the soil particles. Evolution of *CSR* and r_u with number of loading cycles (N) exhibited continuous decrease and increase, respectively for both C_0 and C_1. However, the respective values for C_1 were lower for r_u and higher for *CSR* as compared to C_0. Peak parameters evaluated at the end of loading cycles 1, 5, 10, and 35 are presented in Table 3.

After C_1, the specimens were allowed to reconsolidate and further subjected to C_2. Figure 5b illustrates the stress–strain and pore pressure response of the soil specimens subjected to C_2. Both *CSR* and r_u evolved at a slower rate during C_2 as compared to C_1 and C_0. The specimens exhibited significant improvement in liquefaction resistance

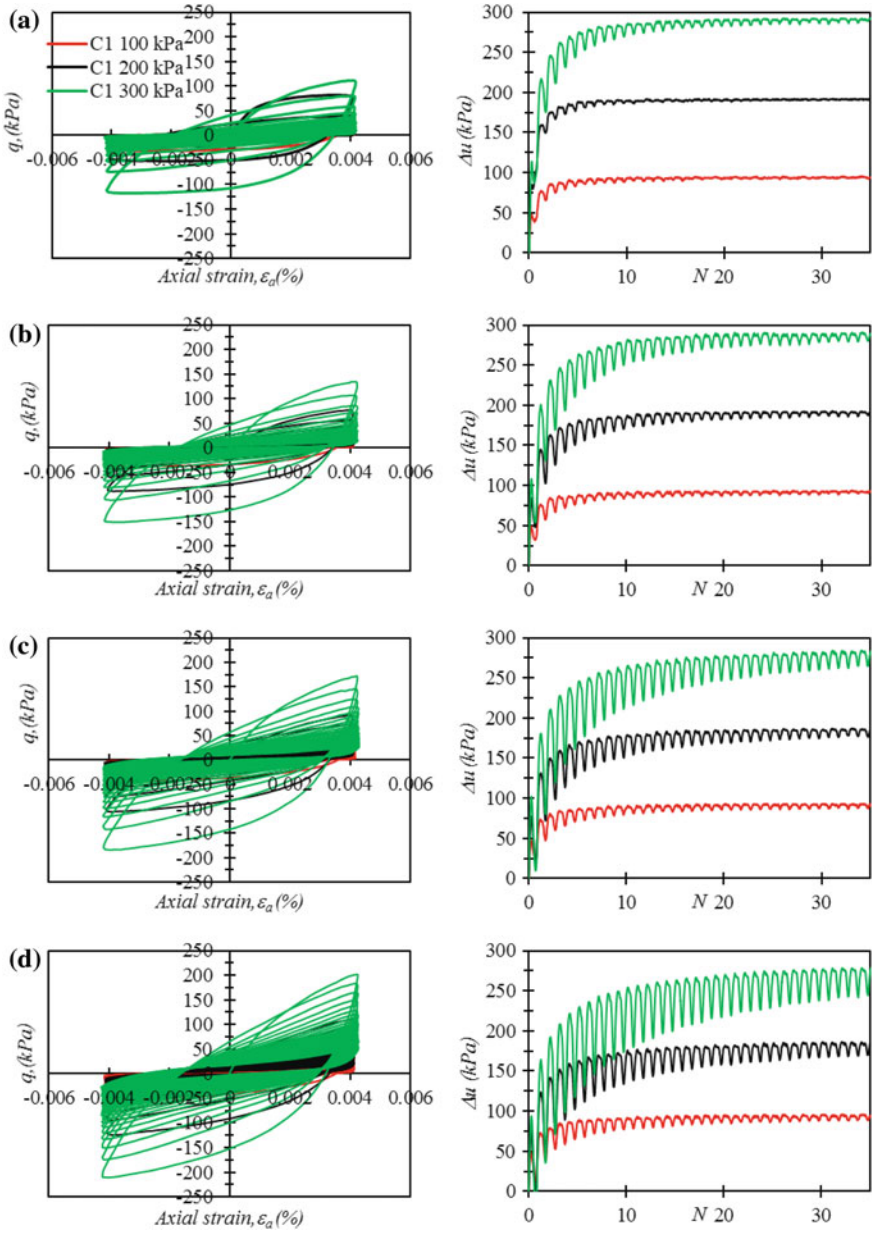

Fig. 5 Stress–strain behavior (**A**) and pore pressure response (**B**) of Chang dam soil subjected to repeated multilevel cyclic loading. **a** C_1, **b** C_2, **c** C_3, **d** C_4

Table 3 Summary of the test results of repeated multilevel reconsolidation and cyclic loading

p'_c	100 kPa				200 kPa				300 kPa			
N	1	5	10	35	1	5	10	35	1	5	10	35
C_0												
q_{max}	43.0	7.2	3.6	1.5	81.0	8.3	2.7	0.6	145.5	24.6	9.7	2.7
r_u	0.76	0.96	0.98	0.99	0.75	0.94	0.96	0.97	0.69	0.95	0.98	0.99
CSR	0.215	0.036	0.018	0.007	0.203	0.021	0.007	0.002	0.243	0.041	0.016	0.004
C_1												
q_{max}	31.2	7.4	4.7	2.1	81.7	11.5	4.5	1.5	111.4	37.2	19.0	5.7
r_u	0.71	0.96	0.96	0.97	0.74	0.94	0.95	0.96	0.62	0.90	0.95	0.97
CSR	0.156	0.037	0.024	0.011	0.204	0.029	0.011	0.004	0.186	0.062	0.032	0.009
C_2												
q_{max}	36.0	11.8	8.1	3.7	76.8	30.4	17.3	7.4	134.4	62.3	37.1	13.8
r_u	0.70	0.95	0.96	0.98	0.61	0.89	0.93	0.96	0.53	0.86	0.93	0.97
CSR	0.18	0.059	0.041	0.018	0.192	0.076	0.043	0.018	0.224	0.104	0.062	0.023
C_3												
q_{max}	41.2	15.2	11.4	5.4	91.8	44.2	27.8	11.1	172.1	98.2	66.1	27.8
r_u	0.64	0.92	0.92	0.94	0.52	0.84	0.89	0.93	0.43	0.79	0.88	0.95
CSR	0.21	0.076	0.057	0.027	0.229	0.111	0.070	0.028	0.287	0.164	0.110	0.046
C_4												
q_{max}	45.4	19.7	14.7	6.6	111.0	60.9	41.3	18.5	201.6	138.5	102.5	51.26
r_u	0.57	0.89	0.89	0.93	0.45	0.80	0.87	0.93	0.33	0.74	0.83	0.93
CSR	0.227	0.10	0.074	0.03	0.278	0.152	0.103	0.046	0.336	0.231	0.171	0.085

and were reflected in *CSR* and r_u evaluated at the end of cycles 1, 5, 10, and 35 (Table 3).

After C_2, specimens were subjected to two more rounds of reconsolidation and cyclic loading (C_3 and C_4). Figures 5c, d illustrate the stress–strain and pore pressure response of Chang dam soil subjected to C_3 and C_4. The results indicated further increase in liquefaction resistance as compared to previous round of cyclic loading. This was reflected in the increasing *CSR* and decreasing r_u for each cycle of subsequent loading rounds, as mentioned in Table 3. The r_u at the end of a particular cycle was found to be lower in subsequent levels of cyclic loading. A significant increase in deviatoric stress as compared to r_u was observed under repeated cyclic loading. This could be attributed due to the reduced void ratio thereby shifting the state of soil specimens lower and closer to the critical state line (*CSL*). The closeness of the state of specimen to the *CSL* increased upon subsequent levels of loading and hence the higher deviatoric stress was observed. This effect was found to increase with the increasing p'_c. For C_4 and p'_c equal to 300 kPa, q_{max} and p' at the end of 35 cycles were evaluated to be 51.3 kPa and 25 kPa, respectively, which indicated the strength degradation rather than initial liquefaction. Stress–strain response of specimens showed increased stiffness as compared to previous loading round (Fig. 5). During C_4, *CSR* at the end of 35 cycles was nearly 20 times as that of during C_0, however, the increase was a little lower during early stages of cyclic loading (Table 3). The increased resistance to liquefaction could be attributed due to the denser configuration of soil particles that resulted from reconsolidation after each round of cyclic loading. The difference in q_{max}, CSR and r_u at given number of cycles during subsequent loading levels increased with p'_c (Table 3) and could be attributed to the increased volumetric strains exhibited during the reconsolidation process (Table 2). The pore pressure response at the end of 35 cycles was found to exhibit r_u values of around 0.99 and 0.93 for C_0 and C_4, respectively, implying increased liquefaction resistance.

The excess pore pressure evolution (Δu) under four repeated rounds of cyclic loading is shown in Fig. 5. Excess pore water pressure evolution (Δu) during the subsequent levels of loading showed prominent maximum and minimum Δu within each cycle of loading. This was addressed as transient or oscillatory excess pore water pressure by Zen and Yamazaki [28]. The zone bounded by maximum and minimum Δu widened as the loading progressed from C_1 to C_4. This behavior exhibited the increased liquefaction resistance under the subsequent repeated multilevel cyclic loading. Anbazhagan [1] reported similar findings for soils with higher liquefaction resistance as they exhibited larger and wider oscillatory pore pressure response as compared to soils with lower liquefaction resistance. Seed and Rahman [22] reported that oscillatory response was most common in marine sediments except for non-cohesive sediments of loose to medium density. In the current study, the soil behavior shifted to more liquefaction resistant soil behavior on subsequent levels of cyclic loading.

3.3 *Effective Stress Path Behavior Under Repeated Multilevel Cyclic Loading*

The variations in deviatoric stress (q) and mean effective pressure (p') during the applied repeated cyclic loading were evaluated by following Cambridge soil mechanics group's definition of $p' - q$; where p' and q were evaluated to be $(\sigma'_1 + 2 * \sigma'_3)/3$ and $(\sigma_1 - \sigma_3)$, respectively. Figure 4a illustrates the cyclic effective stress path behavior of Chang dam soil subjected to C_0. The stress path at three initial confining pressures evolved with rapid reduction in p' due to large evolution of r_u subsequently leading to initial liquefaction within 10 cycles of the applied cyclic loading. The stress paths reached the instability line established from isotropically consolidated undrained triaxial compression tests [6] during the second cycle of loading at all the three p'_c.

Figure 6 illustrates the effective stress path response of Chang dam soil under repeated cyclic loading; C_1, C_2, C_3, and C_4. It could be observed that subsequent loading in soil mass exhibited higher mobilization of deviatoric stress, therefore, higher liquefaction resistance. On subsequent loading rounds, the slope of the q_{max} envelope, which coincided with the slope of the instability line during C_0, became steeper. The stress states $(p' - q)$ at the end of 35 cycles of loading were observed to move gradually away from the stress origin indicating significant presence of

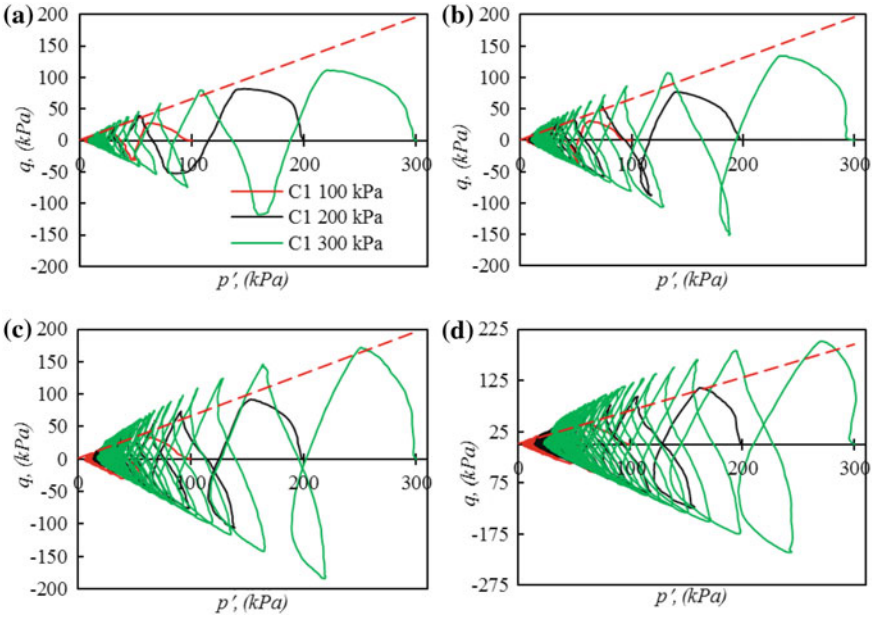

Fig. 6 Evolution of effective stress path under repeated multilevel cyclic loading. **a** C_1, **b** C_2, **c** C_3, **d** C_4

mean effective confining pressure (p') at the end of cyclic loading. Thus, the increase in liquefaction resistance increased with exposure to more levels of cyclic loading, which was further enhanced at higher initial confining pressures (p'_c). This supports the fact that the probability of liquefaction of a soil deposit during a future earthquake is greatly reduced for the soil, which has experienced liquefaction due to a similar magnitude earthquake.

The evolution of effective stress path under initial and repeated cyclic loading revealed strong impact of pre-shearing on the cyclic behavior of soil. The increase in the liquefaction resistance after cyclic pre-shearing was observed to be higher when level of pre-shearing was lower: low γ_{max} and lower r_u [15, 17]. With repeated cyclic shearing, the effective stress path moved away from the origin. The positive effect on the rate of excess pore water pressure development and effective stress path pattern could be helpful in mitigating the liquefaction, provided the initial pre-shear stress levels should remain below critical value and should not induce intolerable residual deformations. The effect of pre-shear repeated cyclic loading is effective only when the soil mass is allowed to reconsolidate after each level of loading.

4 Conclusions

This paper evaluated the reconsolidation and liquefaction behavior of previously liquefied medium dense silty-sand of Chang dam under multilevel cyclic loading. The experiments were conducted under cyclic triaxial conditions and the results were analyzed in the context of reconsolidation volumetric strains, cyclic stress–strain behavior, excess pore water evolution and effective stress path response. In summary, the post-liquefaction reconsolidation and liquefaction behavior under multilevel cyclic loading revealed the followings:

- Chang dam soil inherently has very low liquefaction resistance with excess pore water pressure (Δu) nearly reaching to initial effective confining pressure (p'_c) within 10 cycles of applied dynamic loading. Interestingly, the specimens consolidated to 300 kPa besides 100 kPa and 200 kPa also exhibited liquefaction within 10 cycles indicating very high susceptibility to liquefaction even at greater depths (~30 m).
- During reconsolidation, large volumetric strains as high as 6% were measured leading to reduction in void ratio by 0.052. The volumetric strains were found to increase with the increase in initial effective confining pressure (p'_c) but decreased with the subsequent levels of cyclic loading.
- The peak stress (q_{max}) during the first cycle of first level (C_1) of loading was observed to be lower as compared to the corresponding value of C_0 and could be attributed to the weakening of the soil fabric due to development of excessively high excess pore water pressure during C_0. During subsequent rounds of cyclic loading, the q_{max} was found to be higher than the previous level owing to the increased relative density due to the reconsolidation. The excess pore water pressure during

each cycle of subsequent level of loading was found to be lower as compared to the corresponding value during the previous level of loading.

- Effective stress path response exhibited significant increase in mean effective confining pressure (p') at the end of each level of cyclic loading as compared to previous level of loading. The value of p' was found to be strongly dependent on the initial effective confining pressure (p'_c).
- Cyclic stress ratio (*CSR*) at the end of 35 cycles of fourth repeated loading (C_4) was found to be nearly 20 times as compared to C_0. It showed large increase in liquefaction resistance of Chang dam soil after five levels of each cyclic loading and reconsolidation.

Acknowledgements Financial Support from IIT Gandhinagar is gratefully acknowledged. Any opinions, findings, and conclusions or recommendations expressed in this material are those of authors and do not necessarily reflect the views of IIT Gandhinagar.

References

1. Anbazhagan P (2009) Liquefaction hazard mapping of Bangalore, South India. Disaster Adv 2(2):26–35
2. Amini ZA, Trandafir A (2008) Post-liquefaction shear behavior of Bonneville Silty-Sand. In: Geotechnical Earthquake Engineering and Soil Dynamics, vol IV, pp 1–9
3. Arulanandan K, Sybico J (1992) Post-liquefaction settlement of sand-mechanism and in situ evaluation. Tech Rep NCEER 1(92):239–253
4. Dash HK (2008) Undrained cyclic and monotonic response of sand-silt mixtures. Doctoral dissertation, PhD thesis submitted to Indian Institute of Science, Bangalore in the Faculty of Engineering
5. Finn WD, Bransby PL, Pickering DJ (1970) Effect of strain history on liquefaction of sand. J Soil Mech Found Div 96(SM6)
6. Hussain M, Bhattacharya D, Sachan A (2019) Static liquefaction response of medium dense silty-sand of Chang dam. In: 8th international conference on case histories in geotechnical engineering. Geo-Congress, Philadelphia, USA, March, 24–27, 2019
7. Hamada M, Towhata I, Yasuda S, Isoyama R (1987) Study on permanent ground displacement induced by seismic liquefaction. Comput Geotech 4(4):197–220
8. Ishihara K, Yoshimine M (1992) Evaluation of settlements in sand deposits following liquefaction during earthquakes. Soils Found 32(1):173–188
9. Ishihara K, Okada S (1982) Effects of large preshearing on cyclic behavior of sand. Soils Found 22(3):109–125
10. Kokusho T, Kojima T (2002) Mechanism for postliquefaction water film generation in layered sand. J Geotech Geoenvironmental Eng 128(2):129–137
11. Lade PV (1972) The stress-strain and strength characteristics of cohesionless soils. Thesis Doctoral, University of California, Berkeley
12. Olson SM, Stark TD (2003) Yield strength ratio and liquefaction analysis of slopes and embankments. J Geotech Geoenvironmental Eng 129(8):727–737
13. Olson SM, Stark TD (2002) Liquefied strength ratio from liquefaction flow failure case histories. Can Geotech J 39(3):629–647
14. Oda M, Kawamoto K, Suzuki K, Fujimori H, Sato M (2001) Microstructural interpretation on reliquefaction of saturated granular soils under cyclic loading. J Geotech Geoenvironmental Eng 127(5):416–423

15. Porcino D, Marcianò V, Nicola Ghionna V (2009) Influence of cyclic pre-shearing on undrained behaviour of carbonate sand in simple shear tests. Geomech Geoengin: Int J 4(2):151–161
16. Robertson PK (2009) Evaluation of flow liquefaction and liquefied strength using the cone penetration test. J Geotech Geoenvironmental Eng 136(6):842–853
17. Sriskandakumar S, Wijewickreme D, Byrne PM (2012) Multiple cyclic loading response of loose air-pluviated Fraser River sand. In: Proceedings of the 15th world conference on earthquake engineering. Lisbon, September 24–28, 2012
18. Sitharam TG, Vinod JS, Ravishankar BV (2009) Post-liquefaction undrained monotonic behaviour of sands: experiments and DEM simulations. Géotechnique 59(9):739–749
19. Singh R, Roy D, Jain SK (2005) Analysis of earth dams affected by the 2001 Bhuj earthquake. Eng Geol 80(3–4):282–291
20. Soo Ha I, Ho Park Y, Mo Kim M (2003) Dissipation pattern of excess pore pressure after liquefaction in saturated sand deposits. Transp Res Rec: J Transp Res Board 1821:59–67
21. Scott RF (1986) Solidification and consolidation of a liquefied sand column. Soils Found 26(4):23–31
22. Seed HB, Rahman MS (1978) Wave-induced pore pressure in relation to ocean floor stability of cohesionless soils. Mar Georesour Geotechnol 3(2):123–150
23. Toyota N (1995) Post-cyclic triaxial behaviour of Toyoura sand. In: Proceedings of IS-TOKYO96, vol 1, pp 189–195
24. Vaid YP, Thomas J (1995) Liquefaction and postliquefaction behavior of sand. J Geotech Eng 121(2):163–173
25. Wang S, Luna R, Zhao H (2015) Cyclic and post-cyclic shear behavior of low-plasticity silt with varying clay content. Soil Dyn Earthq Eng 75:112–120
26. Wang S, Luna R, Onyejekwe S (2015) Postliquefaction behavior of low-plasticity silt at various degrees of reconsolidation. Soil Dyn Earthq Eng 75:259–264
27. Youd TL, Hansen CM, Bartlett SF (2002) Revised multilinear regression equations for prediction of lateral spread displacement. J Geotech Geoenvironmental Eng 128(12):1007–1017
28. Zen K, Yamazaki H (1990) Oscillatory pore pressure and liquefaction in seabed induced by ocean waves. Soils Found 30(4):147–161

Effect of Stress History on Stress–Strain and Volumetric Response of Laterite Soil Under Undrained and Drained Conditions

T. K. Abhijith, Majid Hussain and Ajanta Sachan

Abstract Laterite soils are tropically weathered residual soils containing significant iron content and are known for their highly dispersive nature. Laterite soils with high fines content dominated by silt fraction disperse easily in the presence of water due to weak binding forces. Thus, the soil particles get washed away with water creating local instabilities thereby triggering slope failures. Previous research on laterite soil has been limited to the basic geotechnical properties including grain size distribution (GSD), specific gravity (*Gs*), permeability, compaction, etc. The laterite soils are vulnerable to severe erosion, thereby inducing over consolidation in the soil and affecting its geotechnical behaviour. The effect of stress history on stress–strain and volumetric behaviour of laterite soil remains unexplored. In the current study, an experimental study was conducted on yellow laterite soil collected from Gosikhurd dam (Maharashtra, India) to evaluate its shear strength behaviour. A series of isotropically consolidated undrained and drained triaxial tests were performed under deformation-controlled triaxial testing conditions at different over consolidation ratio (OCR = 1, 2, 5, and 10). The results indicated significant increase in normalized shear strength, decrease in excess pore water pressure, and volumetric strain with increasing OCR.

Keywords Stress history · Over consolidation ratio · Laterite soil · Drained · Undrained

1 Introduction

Laterite soils are found in different forms in nature with variations in colour, grain size distribution (GSD), specific gravity (G_s), permeability, etc. [7]. Depending on the degree of weathering, laterite soils are found in the form of porous rock as well as highly weathered material. These soils are vulnerable to erosion and dispersion, resulting in catastrophic landslides [6]. Mineralogy of laterite soils, and its effects on

T. K. Abhijith · M. Hussain (✉) · A. Sachan
Indian Institute of Technology Gandhinagar, Gandhinagar, India
e-mail: majid.hussain@iitgn.ac.in

A. Prashant et al. (eds.), *Advances in Computer Methods and Geomechanics*, Lecture Notes in Civil Engineering 55,
https://doi.org/10.1007/978-981-15-0886-8_8

engineering properties has been explored to a great extent, [6, 7, 12, 13, 18]. Gidigasu [7] explored the geotechnical characteristics of Ghanaian laterite soils based on their mode of formation and the factors affecting their development. Kheoruenromne [12] investigated the mineralogical composition and formation of red and yellow laterite soils in the northeast plateau of Thailand. De Brito Galvao and Schulze [6] studied the mineralogical and chemical influences on the collapsible behaviour of laterite soil from the metallurgic zone of Minas Gerais, Brazil. Phanikumar et al. [15] conducted a series of one-dimensional oedometer tests on red laterite sample collected from Vellore, Tamil Nadu and evaluated its collapse potential.

The effect of stress history on volumetric response of various types of clayey soils has been investigated by few researchers [1, 8, 14, 16, 17]. Henkel [8] explored strength characteristics of over consolidated Weald and London clayey soils and compared their stress–strain and volumetric response. Parry [14] also investigated the stress–strain and volumetric characteristics of normally consolidated (NC) and over consolidated (OC) Weald clay by performing series of triaxial compression and extension tests. Sheahan et al. [16] evaluated the effect of rate sensitivity on NC and OC re-sedimented Boston Blue clay specimens performing a series of K_0 consolidated undrained compression tests. Abdulhadi et al. [1] studied undrained shear behaviour, compression and stiffness characteristics of re-sedimented Boston Blue clay at low and high pressures by performing K_0 consolidated undrained triaxial tests. Stróżyk and Tankiewicz [17] analysed the undrained shear behaviour of heavily over consolidated soils collected from deeper depths. However, the effect of stress history and drainage conditions on the mechanical behaviour of laterite soil is yet to be explored. These soils are vulnerable to severe erosion, which induces the states of over consolidation in the soil and thereby affects its engineering behaviour. The over consolidation and overburden effects in laterite soils have remained unexplored. In the current experimental study, effect of stress history on the undrained and drained mechanical behaviour of yellow laterite soil was explored. Stress–strain and pore pressure response of yellow laterite soil at over consolidation ratio (OCR) values of 1, 2, 5, and 10 were evaluated. Isotropically consolidated undrained compression (CIUC) triaxial tests were performed and the recorded response was analysed in the context of stress–strain, pore pressure evolution, effective stress path, effective stress ratio and obliquity behaviour of laterite soil at different OCR values under undrained boundary conditions, whereas isotropically consolidated drained compression (CIDC) triaxial tests were conducted to investigate the effect of stress history on stress–strain and volumetric response of laterite soil under drained boundary conditions during shear deformation of laterite soil.

2 Material Properties

Laterite soil used in the current study was collected from the Right Bank Canal of Gosikhurd dam in Nagpur at a chainage of 43,290 m away from the dam. Representative disturbed soil samples were obtained from the site and reconstituted in

the laboratory. The grain size distribution (GSD) indicated a high amount of fines content with silt and clay content of 65% and 18%, respectively. Liquid limit and plastic limit of the laterite soil were determined to be 45% and 25%, respectively. The soil used in the current study classified as clay of intermediate plasticity (*CI*). The dispersiveness of the laterite soil was determined by ASTM standards such as the crumb test [4], pinhole test [3], and double hydrometer test [5] and was categorized as intermediate dispersive soil with 46% dispersion value. The XRD pattern showed significant presence of Quartz, Illite, and Kaolinite. A very high percentage of iron (14%) was found to be present in the yellow laterite soil resulting in its higher specific gravity (G_s) of 2.82. 1-D oedometer test results indicated the compressibility of laterite soil to be very low with C_c equal to 0.18. Optimum moisture content (OMC) and maximum dry density (MDD) of the laterite soils were obtained to be 16.5% and 1.9 g/cc, respectively, as determined by performing Standard Proctor Test.

3 Specimen Preparation and Experimental Programme

The effect of stress history on stress–strain and volumetric response of laterite soil under undrained and drained boundary conditions were studied by conducting a series of CIUC and CIDC triaxial tests. The specimens were prepared using moist tamping method at in situ dry density and water content of 1.71 g/cc and 20%, respectively. Moist tamping was performed in a three-piece mould of 50 mm diameter and 100 mm height. The soil specimens were reconstituted by dividing the soil–water mixture in four equal parts. Each part was filled and tamped in the mould, which was held by the colon, base plate, and top plate. Same compactive effort was imparted to each layer to acquire uniformly dense specimen. After each layer, the surface was scratched with a knife to ensure the proper bonding of soil particles at the interface between two consecutive layers.

Undrained and drained shear strength parameters of yellow laterite soil were determined by performing a series of CIUC and CIDC triaxial tests on the soil specimens at different initial effective confining pressures (p'_c) of 100, 200, 300 and 400 kPa. The stress–strain, pore pressure and volumetric response of the soil specimens were studied for different over consolidation ratios (OCR = 1, 2, 5 and 10). OCR values 1, 2, 5, 10 were obtained by consolidating the specimen at an effective confining pressure (p') of 400 kPa and then reducing p' to 400 kPa, 200 kPa, 80 kPa and 40 kPa, respectively. During the creation of various over consolidated states, back pressure was kept constant while cell pressure was reduced ensuring specimens complete saturation of the specimens. The specimens were further sheared at constant strain rate using strain controlled triaxial system. Strain rates of 0.05% and 0.005% per minute were selected for the CIUC and CIDC tests, respectively.

4 Results and Discussions

Laterite soils are residual soils with dispersive nature. On submergence, they exhibit dispersion and show high susceptibility to erosion. Erosion induces varying degrees of over consolidation in the laterite soil deposits. The effect of stress history on shear strength response of laterite soils under undrained and drained boundary conditions was studied by performing two series of CIUC and CIDC triaxial tests. Specimens were subjected to isotropic consolidation prior to the deformation-controlled shearing. Figure 1 illustrates the time-dependent volumetric response of laterite soil specimen at OCR = 1, 2, 5 and 10. The consolidated specimens were further sheared and the mechanical response of yellow laterite soil was evaluated in the context of stress–strain behaviour, excess pore pressure/volumetric response. The evolution of parameters like β_{max}, *A parameter* and effective stress ratio at different over consolidation states and boundary conditions were analysed. Shear strength parameters under drained boundary conditions were obtained to be 38 kPa and 18° for cohesion (c') and friction angle (ϕ'), respectively. Under undrained boundary conditions, cohesion (c') and effective friction angle (ϕ') were determined to be 13 kPa and 22°, respectively (Fig. 2). The shear strength parameters were determined from CIUC and CIDC triaxial tests performed on normally consolidated specimens. The relatively higher cohesion value in the drained test could be due to the stress history effect induced during the specimen preparation by moist tamping technique

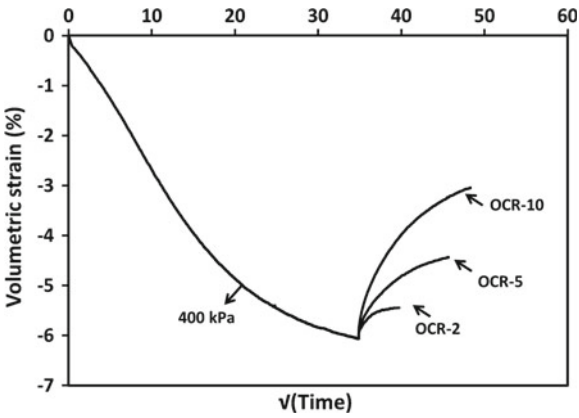

Fig. 1 Consolidation time history curve

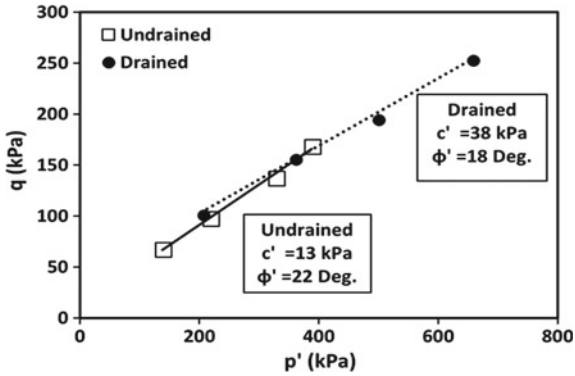

Fig. 2 Modified failure envelops of laterite soil under undrained and drained conditions

4.1 Effect of Stress History on Stress–Strain and Pore Pressure Response of Yellow Laterite Soil Under Undrained Triaxial (CIUC) Testing Conditions

The effect of stress history on stress–strain and excess pore water pressure response of laterite soil was explored under undrained conditions. This experimental research investigated heavily over consolidated (OCR = 10), lightly over consolidated (OCR = 2, 5) and normally consolidated (OCR = 1) specimens of laterite soil. The magnitude of mechanical parameters at failure for various OCR values is mentioned in Table 1. It was observed that increasing OCR value reduced the deviatoric stress (q_{max}) at failure due to the low effective confining pressure during shearing. The exhibited stress–strain response could be attributed to the combined effect of OCR and effective confining pressure (p'). The combined effect of p' and stress history was decoupled by normalizing the stress–strain curves by pre-shear p' to capture the independent effect of stress history. Figure 3a shows the relationship between normalized deviatoric stress and axial strain for soil specimens at different OCR values. The normalized stress–strain response showed increasing normalized q_{max} with the OCR (Fig. 3a). The variation in normalized q with OCR values exhibited the effect of stress history on the shear strength behaviour of yellow laterite soil. As the highly over consolidated isotropic states were created in the soil specimens, the pre-shear p' was shifted to a lower level with respect to the preconsolidation pressure (400 kPa). Thus, the compressibility was reduced, and hence, exhibited increasing load-carrying capacity of the soil. This can also be explained by over consolidation margin (OCM) which is a quantitative measure of how far the preconsolidation pressure (yield surface) is from the applied pressure. In the current study, OCM was calculated to be 360 kPa, 320 kPa, 200 kPa, and 0 kPa for OCR 10, 5, 2, and 1, respectively. Specimens with large OCM (higher OCR) exhibited higher normalized shear strength as compared to normally consolidated specimens (OCM = 0). By inducing higher OCR, the yield surface was pushed outwards which delayed and increased the normalized failure stress on further loading, as shown in Fig. 3a. The

Table 1 Effect of stress history on shear strength response of laterite soil under undrained and drained shearing

Loading condition	Shear strength parameters		OCR	σ_d (kPa)	σ_{nd}	Δu_f (kPa)	Δu_{nf}	β_{max}	σ_1'/σ_3'	A_f
Undrained	c' 13 kPa	φ' 22°	1	335	0.84	179	0.45	0.41	2.52	0.53
			2	275	1.37	20	0.1	0.41	2.53	0.07
			5	214	2.68	−35	−0.43	0.45	2.86	−0.16
			10	187	4.68	−46	−1.15	0.48	3.18	−0.25
						ε_{vf} (%)				
Drained	c' 38 kPa	φ' 18°	1	509	1.25	−2.69	–	0.37	–	–
			2	342	1.71	−0.48	–	0.43	–	–
			5	189	2.36	0.82	–	0.50	–	–
			10	155	3.88	0.75	–	0.58	–	–

where (σ_d) = Deviatoric stress at failure; (σ_{nd}) = Normalized deviatoric stress at failure; Δu_f = Excess pore water pressure at failure; Δu_{nf} = Normalized excess pore water pressure at failure; ε_{vf} = volumetric strain at failure; β_{max} = Maximum angle of obliquity, σ_1'/σ_3' = effective stress ratio and A_f = Skempton′s pore pressure parameter at failure

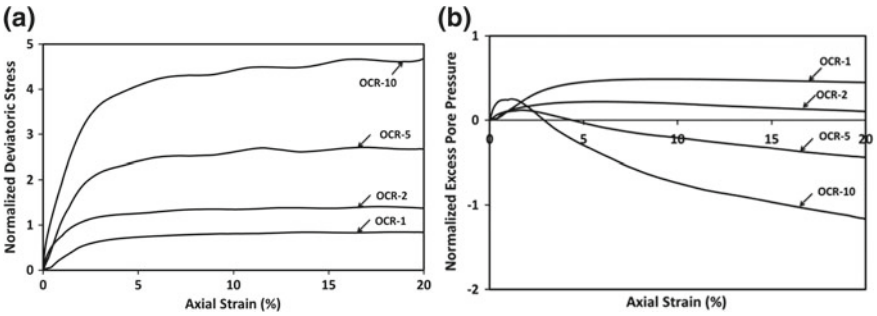

Fig. 3 Effect of stress history on response of laterite soil under undrained shearing conditions. **a** Normalized stress–strain, **b** normalized excess pore pressure

increase in OCM caused the growth of yield surface and possible particle rearrangement together could explain the effect of stress history on the undrained behaviour of laterite soil. Increased strength and stiffness could be clearly seen in Fig. 3a; however, the stress–strain response failed to capture this effect since confinement as well as stress history effect was coupled in it. Confining pressure effect dominated the response of soil in the coupled effect, and this could be attributed to the fact that soil being a pressure-dependent material.

The evolution of normalized excess pore water pressure (Δu_f) for specimens at failure with OCR values is shown in Table 1. It was found that the Δu_f reduced with increasing OCR values. The normalized Δu_f decreased from 0.45 to −1.15 as the OCR value increased from 1 to 10, respectively, (Fig. 3b). Normalized Δu_{nf} was calculated by dividing the Δu_f by the pre-shear p'. As the shearing induced excess pore water pressure (Δu) reduced with increasing OCR, the shear strength of the specimens increased. Δu_f decreased and became negative for OCR 10 and 5, as mentioned in Table 1. For OCR 10, the variations in Δu_f might not be captured due to low p' (40 kPa) as any fluctuation could significantly alter the relative magnitude. It was observed that the Δu started to become negative at a strain level of 2.89% and 4.38% for OCR values 5 and 10, respectively, thereby exhibiting dilative soil behaviour. However, at lower over consolidation levels such as OCR 1 and 2, the specimens showed contractive response throughout the shearing stage. The magnitude of Δu at the end of shearing was determined to be 179 kPa, 20 kPa, −35 kPa, and −46 kPa for specimens with OCR 1, 2, 5, and 10, respectively (Table 1). For highly and lightly over consolidated specimens (OCR 10 and 5), the pattern of Δu evolution exhibited dilative response at failure. However, laterite soil specimens at lower OCR values (OCR = 1 and 2) exhibited contractive response at failure. During undrained shearing, specimens at higher OCR values of 10 and 5 had lower void ratios as compared to the specimens with lower OCR values 1 and 2. This lead to the positive Δu throughout the shearing stage of specimens with OCR 1 and 2, and negative Δu for specimens with OCR 10 and 5 at their later stages of shearing.

Figure 4a shows the effective stress path for specimens with OCR values 1, 2, 5, and 10. Effective stress paths represented the relationship between deviatoric

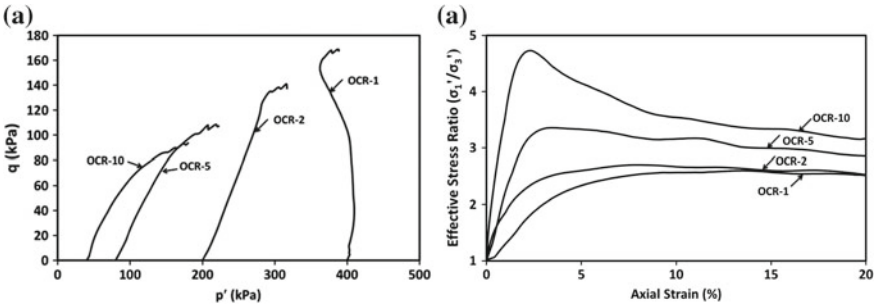

Fig. 4 Effect of stress history on response of laterite soil under undrained shearing conditions. **a** Effective stress path, **b** effective stress ratio

stress and mean effective pressure during the undrained shearing. The stress path for specimen with OCR 1 was found to be comparatively vertical during the initial stages of shearing; however, it further moved towards the origin. This could be attributed to the low compressibility of laterite soil specimens leading to low Δu. In the case of typical NC clays such as kaolinite and soft marine clays, the compressibility is higher as compared to laterite soil; therefore, leading to larger shearing induced Δu. In the present case of yellow laterite soil, the Δu was nearly half of deviatoric stress during shearing, and exhibited unique effective stress path response compared to typical normally consolidated clay behaviour. For specimens with OCR 5 and 10, the effective stress paths initially moved towards the origin, and then rapidly moved away from it due to the negative Δu indicating dilative nature at higher OCR values. The effective stress path of the specimens with high OCR values could be explained by their stress–strain and pore pressure response. Negative Δu during undrained shearing increased the p' resulting in higher deviatoric stress. However, stress path was observed to move towards the origin due to positive Δu during early stages of shear deformation.

The stress–strain relationship of laterite soil at different OCR values exhibited no distinct peak. As such a different failure criterion was used to analyse the response of laterite soil specimens; maximum effective stress ratio. Effective stress ratio (σ_1'/σ_3') was evaluated to define the failure with σ_1' and σ_3' being the effective major and minor principal stresses, respectively. Figure 4b shows the evolution of effective stress ratio with axial strain. A distinct peak was observed for the specimens with OCR 10 and 5 indicating dilative soil behaviour. The increased effective stress ratio subsequently resulted in the improved load carrying capacity of laterite soil. The distinct peak in the effective stress ratio could be attributed to higher mobilized friction angle in heavily and lightly over consolidated specimens. The mobilized friction angle being a function of effective stress ratio, the variation of the maximum effective stress ratio with OCR better captured the effect of stress history on shear strength behaviour of laterite soil, Fig. 4b. It was therefore evident that the effective stress ratio more efficiently captured the failure in laterite soils with different degrees of over consolidation as compared to peak deviatoric stress as failure criteria. The

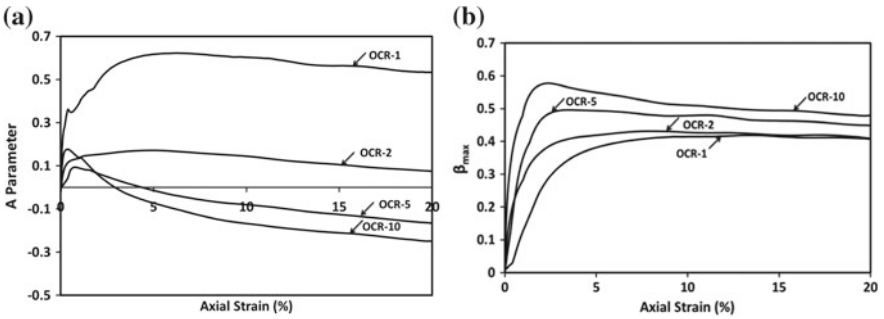

Fig. 5 Effect of stress history on response of laterite soil under undrained shearing conditions. **a** *A Parameter*, **b** angle of maximum obliquity (β_{max})

apparent stiffness was also found to increase with OCR in the adopted failure criteria of maximum effective stress ratio.

The evolution of the relative magnitude of Δu and shear strength of cohesive geomaterials is best explored by analysing the relationship of Skempton's pore pressure (A) *parameter* with axial strain. The relationship of *A parameter* with axial strain for laterite soil specimens is shown in Fig. 5a.

The response is the characteristic of a particular soil depending on several factors like the strain level, initial stress state along with the type of induced stress change and the stress history. A significant decrease in *A parameter* was observed with the increase in OCR values. At higher over consolidation levels OCR 10 and 5, the evolution of *A parameter* varied from positive to negative values indicating the effect of stress history on soil behaviour from contractive to dilative with the increase in OCR (Fig. 5a). The magnitude of *A parameter* in all the specimens was well below the values that caused the collapse of the soil structure. The values of *A parameter* were found to be similar to typical normally consolidated clays for OCR 1; however, the values were evaluated to be similar to that of lightly and heavily over consolidated clays for OCR 2, 5 and 10.

Failure of soil is a function of the critical combination of the applied normal and shear stress rather than maximum shear stress or maximum normal stress. This aspect of the failure of soils was explored by evaluating the angle of maximum obliquity (β_{max}). It is defined as a function of the maximum value of ratio of shear stress to the normal stress at a given strain level in Mohr space and is given by Eq. 1, where σ'_1 and σ'_3 are the major and minor effective principal stresses, respectively

$$\beta_{max} = \tan^{-1} \frac{\sigma'_1 - \sigma'_3}{\sigma'_1 + \sigma'_3} \tag{1}$$

This failure criterion captured the failure of laterite soil in a similar way as by the effective stress ratio (Fig. 5b). However, diminished distinct peaks were observed in the evolution of β_{max}. The effective stress ratio and angle of maximum obliquity response exhibited distinct peaks at higher over consolidation levels such as OCR

10 and 5. Both the parameters captured the combined response of stress–strain and excess pore pressure evolution. The changes in the pattern of Δu indicated soil response changing from contractive to dilative in OCR 10 and 5 at the corresponding stain levels of 2.5% and 4%, respectively. The peaks in the effective stress ratio and β_{max} evolution were also observed at around similar strain levels. In the effective stress path response, the transition from contractive to dilative occurred at around p' = 112 kPa, $q = 72$ kPa and $p' = 174$ kPa, $q = 94$ kPa for OCR 10 and 5 respectively.

4.2 Effect of Stress History on Stress–Strain and Volumetric Response of Laterite Soil Under Drained Triaxial (CIDC) Testing Conditions

The variation of deviatoric stress with axial strain did not show any distinct peak during drained shearing as observed in undrained shearing. Thus, instead of peak deviatoric stress, a particular axial strain level was taken to define the failure. A decreasing peak deviatoric stress with increasing OCR values was observed in the stress–strain behaviour of laterite soil due to the lower effective confining pressure at higher OCR levels. The magnitude of deviatoric stress at failure for various OCR is mentioned in Table 1. The shear strength behaviour demonstrated in the stress–strain response could be attributed to the combined effect of OCR and confining pressure. During the drained loading, specimens with different OCR were sheared at different confining pressure; therefore, the independent effect of stress history could be evaluated by normalizing the absolute stress–strain response. At higher OCR values, distinct peaks were observed in the normalized stress–strain response under drained conditions, a feature missing in undrained response. The effect of stress history on the drained shear strength behaviour of laterite soil conditions was reflected in the increased normalized q with OCR. Shearing of the specimens with high OCR required the pre-shear p' to be shifted to a lower level with respect to the preconsolidation pressure (400 kPa). This leads to the reduction in compressibility resulting in increased load-carrying capacity of laterite soil specimens under drained conditions. Higher normalized strength was mobilized in the specimens with large OCM (higher OCR) as compared to the normally consolidated specimens. This could be attributed to the fact that the heavily over consolidated specimens were being sheared (elastically) within the yield surface, which was pushed outwards relative to the pre-shear confining pressure. Therefore, specimens with higher large OCR mobilized higher normalized deviatoric stress at failure. Further at higher OCR, large OCM and associated particle rearrangement lead to a significant increase in the normalized deviatoric stress. Figure 6a shows the effect of OCR on the normalized strength and stiffness of laterite soil.

The evolution of volumetric strain (ε_v) with axial strain during drained shearing of the specimens at different OCR values is shown in Fig. 6b. The observations revealed the reduced ε_{vf} with increasing OCR, which was found to increase from −

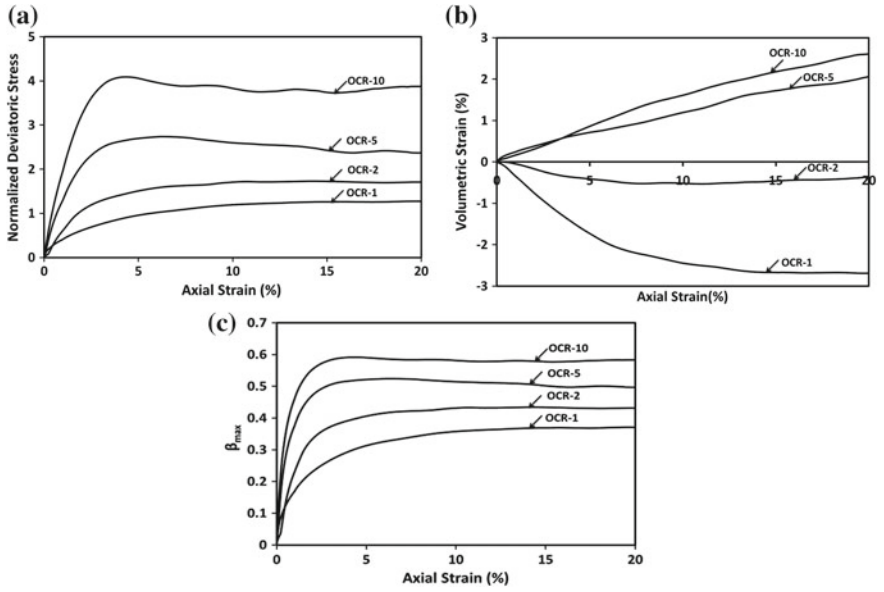

Fig. 6 Effect of stress history on response of laterite soil under drained shearing conditions. **a** Normalized stress–strain, **b** volumetric strain, **c** angle of maximum obliquity (β_{max})

2.69% to 0.75% as the OCR value increased from 1 to 10, respectively. Positive ε_{vf} was observed for OCR 10 and 5 from the starting of shear deformation to failure, thereby indicating dilative soil behaviour of laterite soil under drained conditions. At lower over consolidation levels such as OCR 1 and 2, ε_v showed negative values throughout the shearing stage indicating the contractive response of soil. The ε_v during the drained shearing captured the signature of Δu reflected under undrained boundary conditions. The magnitude of ε_v at the end of shearing was evaluated to be −2.69%, −0.48%, 0.82%, and 0.75% for OCR 1, 2, 5, and 10, respectively.

Under drained boundary conditions, the change in void ratio would also occur as the shearing proceeded. At the starting of the drained shearing, the void ratio of the specimens with higher OCR would be lower. As the shearing proceeded, particles would come closer to each other or roll over each other, thereby resulting in the expulsion or intrusion of the water. For OCR = 10, the specimen was already in a dense state at the end of consolidation. Hence, particles would roll over each other causing an increase in the void ratio during shearing stage. With continued shearing the specimen would suck the water, exhibiting dilative behaviour in the volumetric response of laterite soil. Due to the lower void ratio during drained shearing as compared to undrained shearing, the normalized deviatoric stress was found to be higher in the drained case at lower over consolidation levels. However, the reverse response was observed at higher OCR values, where the void ratio in undrained shearing was found to be lower than the drained shearing. Evolution of β_{max} did not

show any peak and evolved in a way similar to normalized stress–strain response under drained triaxial testing conditions, Fig. 6c.

5 Conclusions

The current experimental study examined the effect of stress history on stress–strain behaviour and volumetric response of yellow laterite soil under undrained (CIUC) and drained (CIDC) triaxial testing conditions. Key observations from this study are summarized as follows:

- Effect of OCR on the strength characteristics of laterite soils under drained and undrained boundary conditions as determined from the normalized stress–strain response, exhibited increased normalized deviatoric stress with increasing OCR.
- Normalized shear strength increased with increasing OCM.
- The relative excess pore water pressure under undrained conditions decreased with increasing OCR. Heavily over consolidated specimen exhibited dilative behaviour under undrained and drained boundary conditions.
- In undrained shearing of heavily over consolidated laterite soil specimens, effective stress ratio failure criterion was observed to capture the failure better as compared to peak stress failure criterion. Effective stress ratio failure criterion exhibited distinct peaks.
- Evolution of *A parameter* was found to be strongly dependent on OCR, heavily over consolidated soils exhibited negative values of *A parameter* except at lower axial strains.
- Under undrained conditions, the evolution of β_{max} in heavily over consolidated laterite specimens exhibited distinct peak, however, no such distinct peaks could be observed for lightly over consolidated specimens.
- Drained normalized shear strength increased with increasing OCR. However, peak shear strength was found to be lower as compared to undrained shear strength because of the increased volume due to the imposed drained boundary conditions for heavily over consolidated specimens.
- Due to the OCR effect, heavily over consolidated, and lightly over consolidated specimens exhibited opposite volumetric response under drained conditions. However, the magnitude of volumetric strain at failure decreased continuously with increasing OCR.

References

1. Abdulhadi NO, Germaine JT, Whittle AJ (2012) Stress-dependent behavior of saturated clay. Can Geotech J 49(8):907–916
2. ASTM International (2013) ASTM D5333-92 standard test methods for measurement of collapse potential of soils

3. ASTM International (2013) ASTM D4647/D4647M-13 standard test methods for identification and classification of dispersive clay soils by the pinhole test
4. ASTM International (2013) ASTM D6572-13e2 standard test methods for determining dispersive characteristics of clayey soils by the crumb test
5. ASTM International (2018) ASTM D4221-18 standard test method for dispersive characteristics of clay soil by double hydrometer
6. De Brito Galvao TC, Schulze DG (1996) Mineralogical properties of a collapsible lateritic soil from Minas Gerais, Brazil. Soil Sci Soc Am J 60(6):1969–1978
7. Gidigasu MD (1972) Mode of formation and geotechnical characteristics of laterite materials of Ghana in relation to soil forming factors. Eng Geol 6(2):79–150
8. Henkel DJ (1956) The effect of over-consolidation on the behaviour of clays during shear. Geotechnique 6(4):139–150
9. IS 2720 Part 5 (1985) Methods of test for soils; liquid and plastic limit analysis. Bureau of Indian Standards, New Delhi
10. IS: 2720 Part 4 (1994) Methods of test for soils; grain size analysis. Bureau of Indian Standards, New Delhi
11. IS: 2720, Part 15 (1986) Methods of test for soil; Determination of consolidation properties. Bureau of Indian Standards, New Delhi
12. Kheoruenromne I (1987) Red and yellow soils and laterite formation in the Northeast Plateau, Thailand. Chem Geol 60(1–4):319–326
13. Olufemi O (1988) Basic geotechnical properties, chemistry and mineralogy of some laterite soils from SW Nigeria. Bulletin of the International Association of Engineering Geology-Bulletin de l'Association Internationale de Géologie de l'Ingénieur 37(1):131–135
14. Parry RHG (1960) Triaxial compression and extension tests on remoulded saturated clay. Geotechnique 10(4):166–180
15. Phanikumar BR, Raghav R, Bhargav K (2016) Collapse behaviour of a lateritic soil. Geomech Geoengin 11(2):119–124
16. Sheahan TC, Ladd CC, Germaine JT (1996) Rate-dependent undrained shear behavior of saturated clay. J Geotech Eng 122(2):99–108
17. Stróżyk J, Tankiewicz M (2014) The undrained shear strength of over-consolidated clays. Procedia Eng 91:317–321
18. Townsend FC (1985) Geotechnical characteristics of residual soils. J Geotech Eng 111(1):77–94

Sensitivity Analysis of Pore Morphology Method and X-Ray CT Imaging in SWCC Predictions for Ottawa Sand

Mohmad Mohsin Thakur and Dayakar Penumadu

Abstract The hydromechanical response of partially saturated soils at macroscale is a manifestation of fundamental physics associated with pore scale. The Soil Water Characteristic Curve (SWCC) is an important state variable which affects mechanical as well as transport properties in a multiphase porous media. In present work, X-ray CT imaging and Pore Morphology Method (PMM) are leveraged to demonstrate robustness of a predictive approach in enhancing understanding of multiphase flow in sands from a pore scale perspective. The 3D microstructure of the Ottawa sand assembly is obtained from attenuation contrast-based X-ray Computed Tomography (CT) which serves as an input to PMM-based predictions. PMM relies on Young Laplace equation and mathematical morphology to simulate drainage and imbibition processes on an actual pore space. This approach is computationally efficient in comparison to computational fluid dynamics approach where highly nonlinear Navier Stokes equation is solved on a computational grid. In addition, the effect of X-ray CT resolution on SWCC predictions for drainage and imbibition is investigated. The effect of the surface roughness on wettability is demonstrated in numerical predictions by varying contact angle of the three-phase system. The spatial distribution of air and water corresponding to different capillary pressures is presented which can be helpful in developing improved multiscale modeling approaches in partially saturated sands.

Keywords SWCC · Ottawa sand · Pore morphology method · X-ray CT imaging

1 Introduction

In nature, soil agglomerate exists as a multiphase material with complex mechanical interaction between the solid, liquid, and the gas phase. The variation in degree of saturation results in the development of capillary suction which is captured in the

M. M. Thakur (✉) · D. Penumadu
Department of Civil & Environmental Engineering, The University of Tennessee, Knoxville, Tennessee, USA
e-mail: mthakur1@vols.utk.edu

A. Prashant et al. (eds.), *Advances in Computer Methods and Geomechanics*, Lecture Notes in Civil Engineering 55,
https://doi.org/10.1007/978-981-15-0886-8_9

form of Soil Water Characteristic Curve (SWCC). Generally, capillary suction in soils consists of matric suction which is the difference between the pore air pressure and pore water pressure. The matric suction is an important stress state variable in partially saturated soils which needs to be incorporated in the constitutive model framework. Several experimental studies have been carried out in the past to measure SWCC using different techniques [7, 13, 17, 22]. The choice of each technique depends upon the soil type and the range of suction required to describe the moisture retention behavior comprehensively. However, the experimental research in partially saturated soils is tedious due to the significant duration required to complete the tests. Therefore, there is a need to implement a numerical framework which can realistically predict multiphase properties in soils considering the pore and grain microstructure in 3D. In recent years, the advancements in nondestructive imaging techniques, specifically attenuation contrast-based X-ray Computed Tomography (CT) has made it possible to extract pore network of granular material like sands in a typical laboratory setting. It is, however, important to use high resolution X-ray CT to effectively capture the narrowest regions of the pores, typically referred to as pore throats. The maximum resistance to displacement of water by air during drainage is offered by pore throats. Therefore, in present work, X-ray CT imaging of Ottawa sand is performed at three different resolutions to investigate the effect of resolution on SWCC predictions. The 3D pore space data captured via CT scanning is used as an input in Pore Morphology Method (PMM), implemented in material library package, GeoDict. PMM is a direct pore scale modeling approach wherein Young Laplace equation is directly solved on the actual pore space. The detailed discussion on PMM is presented in next section. The effect of the variation in density, contact angle as well as the size of the structuring element used in PMM formulation on SWCC predictions is investigated. Furthermore, the spatial distribution of the pore water and pore air at different capillary suctions is obtained from numerical predictions.

The main objective of this work is to obtain SWCC of Ottawa sand from numerical predictions based on actual pore microstructure obtained from X-ray CT imaging. The spatial variation in pore water and pore air at different capillary pressures is obtained for both drainage and imbibition from numerical predictions which can provide better insights into the physics behind multiphase flow in partially saturated soils [9].

2 Materials and Methods

2.1 Materials

In this work, Ottawa sand was used to investigate the moisture retention behavior from PMM-based predictions. Ottawa sand has nearly round grains with a specific gravity equal to 2.65. The SEM image of the representative grains was presented in

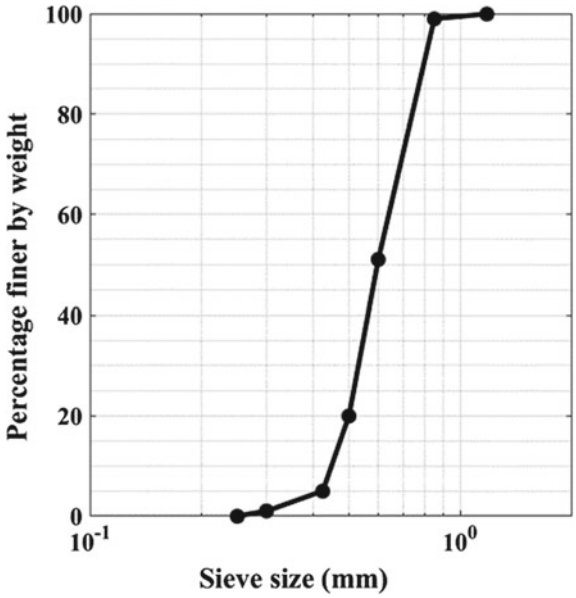

Fig. 1 Grain size distribution of Ottawa sand

a paper by one of the authors [10]. Ottawa sand consists of more than 99.5% SiO_2. The grain size distribution of Ottawa sand is shown in Fig. 1 which indicates Ottawa sand can be classified as poorly graded sand as per USCS classification system. The maximum void ratio and minimum void ratio for Ottawa sand are 0.746 and 0.512, respectively.

2.2 X-Ray CT Imaging

X-ray Computed Tomography is a powerful tool to capture the pore network of sands in 3D noninvasively. The use of X-ray CT imaging to characterize the geomaterials has increased rapidly with the improvements in computing power and the availability of the laboratory-based micro-CT scanners. The technique is based on the attenuation of the X-rays based on the Beer Lamberts law as shown in Eq. 1, where "I" is the intensity of radiation transmitted through the material, "I_o" is the intensity of the incident radiation, and $\mu(x)$ is the attenuation coefficient along the radiation path x. The rule of thumb is to target 20–30% transmission of the incident radiation through the thickness of the sample for successful microstructure imaging.

$$I = I_0 e^{\int -\mu(x)dx} \tag{1}$$

Computed Tomography in a laboratory micro-CT setup is performed by acquiring multiple radiographs of a sample by rotating it slowly in small increments between

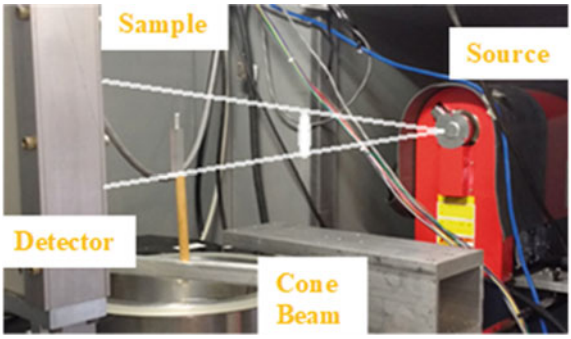

Fig. 2 Custom developed X-ray CT setup at the University of Tennessee, Knoxville

the source and the detector over a cumulative angular reach of 180° or 360°. The key step in acquiring a better-quality data for a specific X-ray resolution is to find an appropriate combination of X-ray energy and the current corresponding to a specific material of interest. One must be careful not to use too high energy as it can result in less contrast in the data. The detailed review of the application of X-ray Computed Tomography in geoscience can be found in in the literature [4, 25].

In present work, data acquired from X-ray CT imaging was used as an input for numerical predictions. The cylindrical mold of height and diameter equal to 0.35″ and 0.50″, respectively, was used to capture the pore network for numerical predictions. The idea was to preserve the boundary effects and use high resolution data in numerical predictions with the available computing resources. This approach is far superior compared to the one wherein a small volume is extracted from the center of a large specimen which does not capture inhomogeneities in pore network due to the boundary effects. The dry sand was deposited slowly from a funnel in five layers, each layer was tapped lightly with a steel rod of diameter and height equal to 2 cm and 12 cm, respectively. Each layer was tapped 24 times in total, 6 times on diametrically opposite ends to obtain a dense specimen corresponding to a minimum void ratio. Figure 2 shows custom developed CT setup used in this research at the University of Tennessee, Knoxville, which consists of a 160 kV micro focus X-ray source with a cone beam geometry and a flat panel detector of 50 μm detector pixel size. A total of 1525 projections (radiographs) were taken over an angular reach of 183° at 5-μ resolution. The X-ray energy and current were chosen as 130 keV and 120 μA after few initial iterations to obtain better contrast in the images.

2.3 Image Processing

The radiographs acquired at different angular orientations provide information only through the thickness of the sample. In present work, Filtered Back Projection method was used to reconstruct slices along the height of the sample in Octopus software to provide a 3D visualization of the pore and grain microstructure. The reconstructed

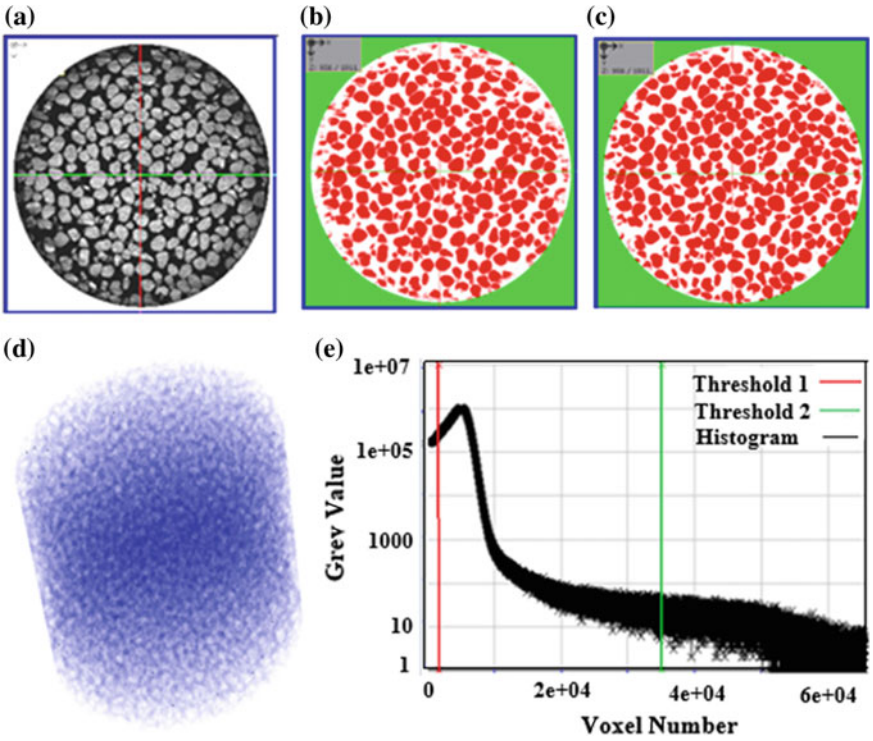

Fig. 3 Ottawa sand X-ray CT data, **a** raw slice; **b** OTSU segmented slice; **c** OTSU segmented + manually thresholding; **d** 3D visualization of pore space; **d** histogram

raw data from Octopus was then imported to GeoDict software (Math2Market GmbH, GeoDict 2018, https://www.geodict.com/) for image processing and numerical predictions. A series of image processing steps were followed to remove noise and segment CT data into grains and pores. Figure 3 shows segmentation of an agglomerate of Ottawa sand into grains and pores along with the histogram of the data. A median filter was applied to the reconstructed data set for smoothening and noise reduction. The data was segmented into grains and pores by OTSU segmentation followed by manual thresholding to adjust for local inhomogeneities. The detailed description of OTSU segmentation can be found in Refs. [15, 26]. 3D visualization of the pore space is shown in Fig. 3d.

2.4 Pore Morphology Method

The classical work by Hilpert and Miller [6] to simulate drainage in a completely wetting digital porous media based on the principles of mathematical morphology led

to the development of the Pore Morphology Method (PMM). The effect of variation in wettability was incorporated by including contact angle of the solid with the wetting and non-wetting phase interface in the governing equation [2, 19, 20, 24]. The pore space accessible to the non-wetting phase for the two-phase system with negligible gravity effects and well-defined contact angle for a spherical interface is given by the Young Laplace equation as presented in Eq. 2, where "r" is the minimum pore space accessible to non-wetting phase (air in sands), "σ" is the interfacial tension, "α" is the contact angle, and "P_c" is the capillary pressure. Therefore, for a given interfacial tension and contact angle, the problem becomes purely geometrical in nature. This reduces the computational requirements significantly and make it possible to make predictions on large CT data.

$$r = 2\sigma \cos\alpha / Pc \tag{2}$$

The implementation of PMM in GeoDict software includes several steps as summarized below

1. The location of the wetting and non-wetting phase reservoir needs to be specified. To replicate typical experimental boundary conditions in axis translation technique for the measurement of matric suction, the wetting phase/water reservoir and non-wetting phase/air reservoir location in present work was specified at the bottom and the top of the sample, respectively.
2. The spherical structuring element of radius "r" obtained from Eq. 2 is used to erode the pore space by non-wetting phase starting with the maximum radius for drainage and minimum radius for imbibition. The erosion of the set "X"/pore space by a structuring element B/sphere is given by the locus of the centers of "B" when "B" moves inside "X". This is equivalent to the Minkowski subtraction of the set X and reflected set of "B" with respect to the origin [6].
3. The pore space connectivity to the non-wetting phase is accessed and the disconnected regions of pore space are removed from the results of erosion. The rest of the pore space is subjected to morphological dilation followed by computation of degree of saturation based on the volume fractions of each component. The dilation of the set "X"/pore space by a structuring element B/sphere is given by the locus of the centers of "B" when the center of "B" moves inside "X". This is equivalent to the Minkowski addition of the set X and reflected set of "B" with respect to the origin [6].
4. The entire process is repeated from step 2 with decrease in radius of spherical structuring element for drainage and vice versa for imbibition.

3 Results and Discussion

3.1 SWCC Predictions Including the Impact of X-Ray Resolution

Most of the studies related to the prediction of multiphase flow properties from X-ray images did not consider the effect of resolution on predictions. The X-ray resolution used in past studies varies from as high as 7 μ to as low as 30 μ [9, 13]. In present work, X-ray CT data was acquired for dense Ottawa sand at 5-μ, 12-μ and 15-μ X-ray resolution. The specimen was prepared in a dry state according to the sample preparation technique described in Sect. 2.2 to achieve a target void ratio of 0.52 and dry density of 1.75 g/cm^3. The specific gravity of Ottawa sand is 2.65. Figure 4 shows SWCC predictions for dense Ottawa sand for both drainage and imbibition obtained from numerical predictions corresponding to the X-ray CT data captured at 5-μ, 12 μ, and 15-μ resolution. The general observations regarding SWCC are presented here first before discussing the impact of X-ray resolution on predictions. SWCC consists of three distinct parts: (a) the flat region in low suction range almost completely saturated called capillary regime, (b) large slope region in intermediate suction and intermediate saturation range called funicular regime, and

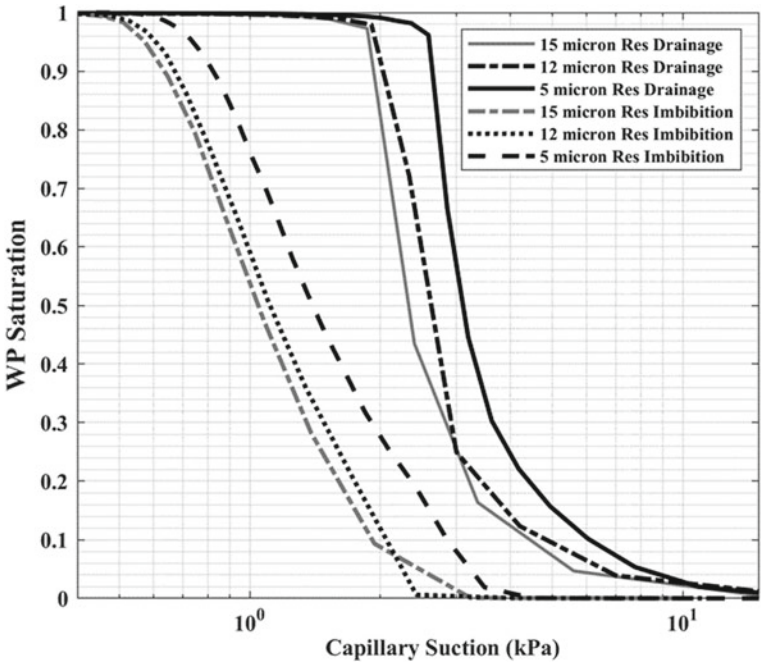

Fig. 4 SWCC predictions for dense Ottawa sand at different X-ray resolutions

(c) approximately flat region in high suction range with residual water content called pendular regime [12].

The behavior of partially saturated soils in funicular and pendular regime is complex due to the formation of liquid bridges and saturated pockets of water [13]. The value of the interfacial tension for water and air phase in numerical predictions was chosen as 72 mN/m [16]. The contact angle for Ottawa sand, air, and water interface corresponding to drainage and imbibition were chosen as 30° and 60° to account for the hysteresis in contact angle [8]. The onset of drainage is characterized by the air entry value which is the capillary pressure at which the widest pores begin to desaturate. The air entry value of coarse grained soils such as sands is low compared to the fine grained soils such as silts and clays [11]. The SWCC is not a unique relationship but depends upon the direction of flow, i.e., drying/wetting path as well as number of drying and wetting cycles [5]. This results in hysteretic behavior which is captured well in predictions for Ottawa sand as shown in Fig. 4. The hysteresis in SWCC can be attributed to number of reasons such as variation in wettability of sand grains during drying and wetting, local heterogeneity in chemical composition of sand grains, surface roughness which might result in trapping water in crevices during drainage, highly irregular nonuniform pore size distribution [3].

The spherical structuring element assumption in simulations results in over prediction of saturation in pendular regime which can be explained based on the shape of the air–water interface in the pendular regime. The interface between air and water can be curved with different values of curvature. The minimum and maximum values of radii of curvature of a surface are called principal radii of curvature (r_1, r_2) and can be used to represent an interface. In pendular regime, one of the principal radii of curvature can be negative (concave/inwards) and other positive (convex/bulging out). Therefore, a general form of Young Laplace equation (Eq. 3) without spherical structuring element assumption is expected to give better results [6].

$$Pc = \sigma \cos\alpha(1/r1 + 1/r2) \tag{3}$$

The impact of the X-ray resolution on SWCC predictions is shown in Fig. 4. It can be observed that with the increase in X-ray CT resolution, air entry value obtained from predictions also increases. The variation is noticeable corresponding to 5-μ resolution data in comparison to 12-μ and 15-μ resolution data. This suggests that 5-μ resolution data can capture pore throats better in comparison 12 μ and 15-μ resolution data. It is impertinent to mention here that the smallest pores offer maximum resistance to the displacement of pore water by pore air during drainage, therefore, are the most critical in predictions. The quantitative comparison is presented in Table 1 by fitting SWCC predictions to the Van Genuchten equation [23] as shown in Eq. 4, where "Se" is the effective degree of saturation, "Pc" is the capillary pressure, "α" and "n" are the Van Genuchten parameters. "α" is inversely related to the air entry pressure and "n" is related to the pore size distribution. The subscripts "d" and "w" in Table 1 denote drying and wetting.

Table 1 Van Genuchten parameters for different resolutions and density of Ottawa sand

Resolution (μm)	State	a_d	n_d	a_w	n_w	R_d^2	R_w^2
5	Dense	0.315	7.396	0.781	3.948	0.991	0.995
12	Dense	0.387	8.311	0.9715	4.316	0.995	0.997
15	Dense	0.427	8.954	1.033	4.405	0.992	0.999
5	Loose	0.458	7.419	1.099	3.898	0.979	0.994

$$Se = \frac{1}{(1 + (\alpha Pc)^n)^{1-\frac{1}{n}}} \tag{4}$$

3.2 *Effect of Variation in Contact Angle on SWCC Predictions*

The variation in contact angle of soil–water–air interface is expected due to several reasons. The surface of Ottawa sand is rough due to the various physical and chemical changes occurring over the years [1]. Furthermore, the curvature in the grains increases the complexity in contact angle estimation. Therefore, contact angle for a soil agglomerate is significantly different from the contact angle of a smooth plane solid surface of the same material. Furthermore, variation in rate of the flow results in the variation in the velocity of the contact line between sand, air, and water [21]. It is expected that the contact angle in sand grains will not be a single valued quantity, rather a range of contact angles is expected. The effect of the variation in contact angle was investigated in numerical predictions for dense Ottawa sand for both drainage and imbibition as shown in Fig. 5. It can be observed from Fig. 5 that with the increase in contact angle, there is a decrease in air entry value as well as capillary suction corresponding to different saturation levels. This is expected based on the Young Laplace equation (Eq. (2)) which is a manifestation of the energy balance.

3.3 *Effect of Variation in Density on SWCC Predictions*

The initial dry density of the specimen is expected to influence the moisture retention behavior of sands. The initial density affects the distribution of pores, pore throats, and grain contact coordination number. The influence of the initial density on SWCC predictions for loose and dense Ottawa sand is shown in Fig. 6. It can be observed that with the increase in density, capillary suction increases over the entire saturation regime. This is expected since the increase in relative density results in a compact configuration resulting in smaller size pores and pore throats. However, the increase in capillary suction with the increase in density is noticeable but not significant. The

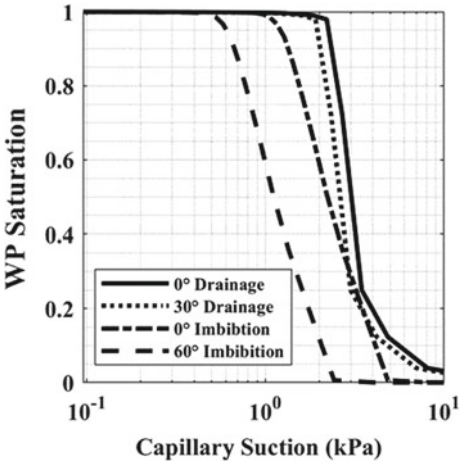

Fig. 5 Effect of contact angle on SWCC predictions of Ottawa sand

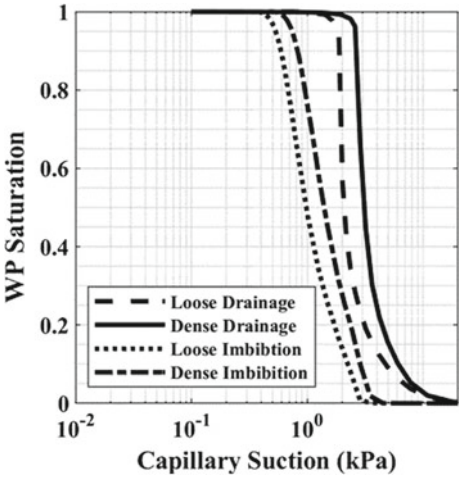

Fig. 6 SWCC predictions for dense and loose Ottawa sand

quantitative comparison is presented in Table 1 by fitting SWCC predictions to the Van Genuchten equation [23] as shown in Eq. 4.

3.4 Hysteresis Due to Nonuniform Pore Size Distribution

The effect of the nonuniform pore size distribution on hysteretic behavior is captured in PMM-based numerical predictions by considering different mechanisms for imbibition and drainage. For imbibition water invades the narrowest pores first before considering any other pore, however, for drainage air invades the pore space only

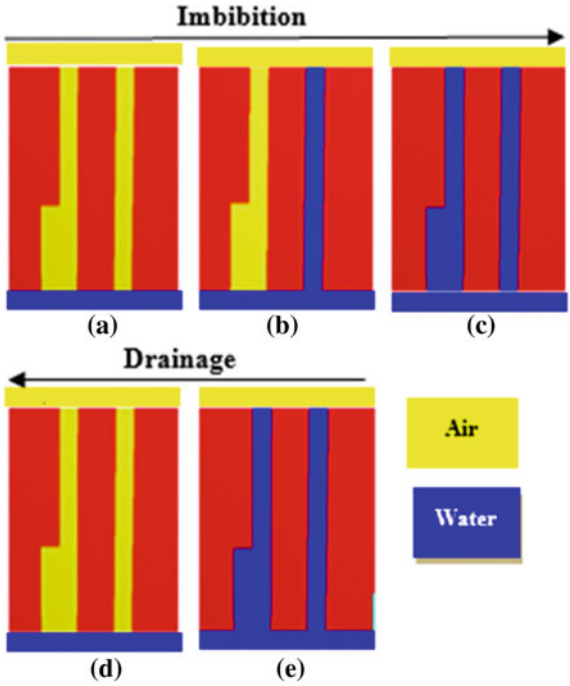

Fig. 7 Hysteresis effect on wettability due to nonuniform pore size distribution

when the capillary pressure is greater than the narrowest part of the pore. A simplified representation of nonuniform pore size distribution illustrating the hysteretic effect in predictions for the same contact angle is shown in Fig. 7. The air reservoir and water reservoir are located at the top and bottom, respectively. It can be observed that water invades the narrowest pore first before considering a large pore during imbibition as shown in Fig. 7a–c. For drainage, the size of the narrowest part of the pore is critical in determining pore fluid displacements, therefore, both the pores are invaded by air simultaneously during drainage as shown in Fig. 7e, f.

3.5 Experimental Validation

The predictions based on PMM were validated by measuring SWCC for Ottawa sand experimentally corresponding to drainage path using Hyprop 2 manufactured by METER group. The experimental setup includes two tensiometers placed at two locations along with the depth of the sample in a sampling ring placed on a weighing balance. The upper and lower tensiometers were positioned at 1.25 cm and 3.75 cm from the top, respectively. The air entry pressure value of tensiometers was 8 bars. Ottawa sand corresponding to void ratio of 0.52 and dry density of 1.75 g/cm^3 was used in the HYPROP test. The height of soil column and soil surface area was 5 cm

and 249 cm^2, respectively. The saturated sample was allowed to dry under the ambient pressure. The capillary suction is measured in terms of water tension by two tensiometers and variation in degree of saturation is monitored by weighing balance. The detailed description of experimental setup can be found in literature [18]. Figure 8 shows the SWCC obtained from experiments and PMM-based numerical predictions. It can be observed that the comparison between the experiment and prediction is promising. The receding contact angle in predictions was varied to match the experimental drainage results and it was found out that a receding contact angle equal to 55° results in a better match with the experimental results. The overprediction of degree of saturation in pendular regime by PMM predictions in comparison to experimental results is due to the spherical structuring element assumption as explained in Sect. 3.1. The use of general form of Young Laplace equation (Eq. (3)) is expected to give better results [6].

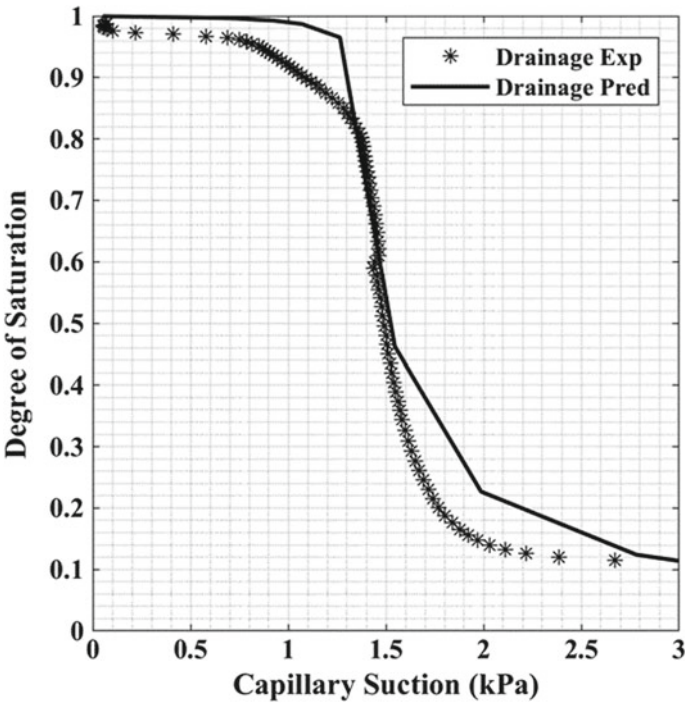

Fig. 8 Experimental and predicted SWCC for Ottawa sand corresponding to drainage path

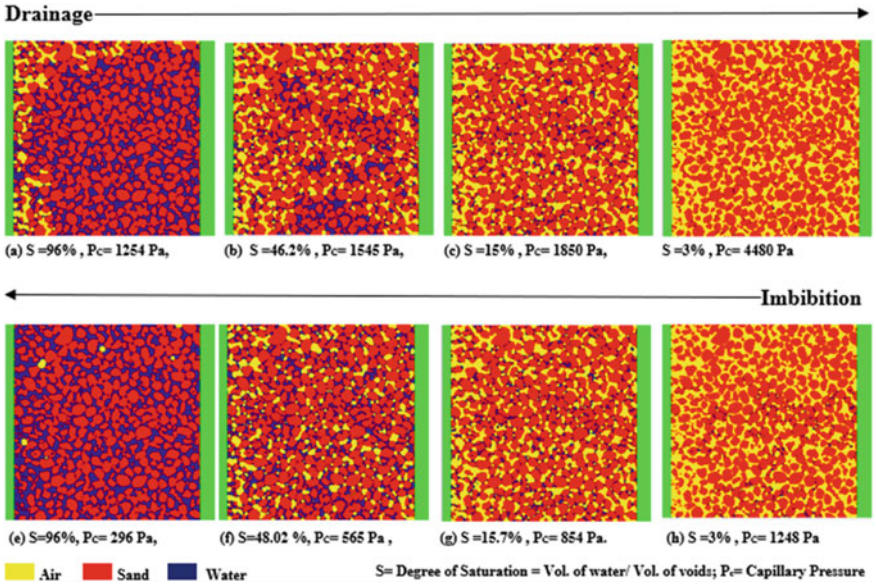

Fig. 9 Distribution of pore water and pore air at different saturations in Ottawa sand

3.6 Distribution of Pore Water and Pore Air

The displacement of pore water and pore air is controlled by local energy balance. The hydromechanical behavior of partially saturated soils is significantly affected by the distribution of pore water and pore air. Figure 9 shows the distribution of pore water and pore air in the central slice along vertical direction in dense Ottawa sand obtained from PMM-based numerical predictions. The distribution of water and air for drainage and imbibition is different with a significant variation in capillary pressure corresponding to same degree of saturation. The displacements at the pore scale lead to the formation of complex fluid front morphologies including formation of air/water pockets and entrapment of air/water in pore space. Figure 9e show air pockets in Ottawa sand during imbibition which is a result of the swelling of the water in corners and crevices leading to the snap-off. The spatial variation in degree of saturation along with void ratio necessitates questioning theoretical formulations based on macroscale parameters such as global porosity and global degree of saturation. The spatial distribution of pore water/pore air provides a link to answer complex hydromechanical interactions in sands which go beyond SWCC measurements. For instance, capillary pressures are large at lower degree saturation but most of water is concentrated near the particle contacts as shown in Fig. 9c, g. This results in lubrication near the particle contacts causing a decrease in friction angle, therefore, provides a contrasting effect to strength in comparison to capillary suction. Similarly, distribution of pore water/pore air can clarify the mechanics involved in impact-based loadings such as in split Hopkinson bar test [14]. The velocity of the

longitudinal compression wave is different in air and water, therefore, phase distributions at pore scale along with SWCC measurements can provide better understanding of correlating strength and partial saturation.

4 Conclusion

The response of the partially saturated sands can be highly intricate and requires proper understanding at the pore scale. In present work, X-ray computed tomography was used to capture pore network in 3D for Ottawa sand to predict drainage and imbibition directly on pore space based on pore morphology method. The following observations were concluded to facilitate multiphase understanding in partially saturated sands:

1. SWCC measurements from numerical predictions suggest low air entry value for Ottawa sand, which is a characteristic of granular materials like sands. The hysteresis due to contact angle and nonuniform pore size distribution in SWCC predictions is captured.
2. The comparison of SWCC measurements from experiments and PMM-based numerical predictions is demonstrated and the agreements with predictions are promising.
3. It is important to use high resolution X-ray Computed Tomography to capture pore networks effectively, specifically pore throats, which determine the displacement of pore water by pore air during drainage. X-ray CT data was acquired at 5-μ, 12-μ and 15-μ resolution for Ottawa sand and it was observed that some fraction of pore throats was not captured with the decrease in X-ray resolution.
4. The distribution of pore water and pore air was obtained for drainage and imbibition in numerical predictions. It was observed that at low saturations, pore water concentrates near the particle contacts which can clarify contrasting effect of particle lubrication and capillary suction to the strength of the grain assemblage.

Acknowledgements Dr. Penumadu would like to acknowledge DTRA support from Defense Threat Reduction Agency (DTRA) Grant HDTRA1-12-10045, managed by Dr. Douglas A. Dalton (Allen). The authors would also like to thank Dr. Sven Linden and Dr. Constantin Bauer from GeoDict for providing help with the GeoDict software.

References

1. Alshibli KA, Alsaleh MI (2004) Characterizing surface roughness and shape of sands using digital microscopy. J Comput Civ Eng 18(1):36–45
2. Becker J, Schulz V, Wiegmann A (2008) Numerical determination of two-phase material parameters of a gas diffusion layer using tomography images. J Fuel Cell Sci Technol 5(2):021006

3. Blunt MJ (2017) Multiphase flow in permeable media. Cambridge University Press
4. Cnudde V, Boone MN (2013) High-resolution X-ray computed tomography in geosciences: a review of the current technology and applications. Earth-Sci Rev Elsevier B.V. 123:1–17
5. Fredlund DG, Sheng D, Zhao J (2011) Estimation of soil suction from the soil-water characteristic curve. Can Geotech J 48(2):186–198
6. Hilpert M, Miller CT (2001) Pore-morphology-based simulation of drainage in totally wetting porous media. Adv Water Resour 24(3–4):243–255
7. Houston S, Houston W, Wagner A (1994) Laboratory filter paper suction measurements BT—laboratory filter paper suction measurements. Geotech Test J 17(2):185–194
8. Ishakoglu A, Baytas AF (2005) The influence of contact angle on capillary pressure-saturation relations in a porous medium including various liquids. Int J Eng Sci 43(8–9):744–755
9. Khaddour G, Riedel I, Andò E et al (2018) Grain-scale characterization of water retention behaviour of sand using X-ray CT. Acta Geotech 13(3):497–512
10. Kim FH, Penumadu D, Hussey DS (2012) Water distribution variation in partially saturated granular materials using neutron imaging. J Geotech Geoenvironmental Eng 138(2):147–154
11. Lu N, Kaya M, Godt JW (2014) Interrelations among the‘ soil-water retention, hydraulic conductivity, and suction-stress characteristic curves. J Geotech Geoenvironmental Eng 140(5):04014007
12. Manahiloh K (2013) Microstructural analysis of unsaturated granular soils using X-ray computed tomography. PhD Thesis, Washington State University, USA
13. Manahiloh KN, Meehan CL (2017) Determining the soil water characteristic curve and interfacial contact angle from microstructural analysis of X-ray CT images. J Geotech Geoenvironmental Eng 143(8):1–11
14. Martin BE, Chen W, Song B, Akers SA (2009) Mechanics of materials moisture effects on the high strain-rate behavior of sand. Mech Mater 41(6):786–798
15. Otsu N (1979) A threshold selection method from gray-level histograms. IEEE Trans Syst, Man, Cybern 9(1):62–66
16. Park J-Y, Ha M-Y, Choi H-J, Hong S-D, Yoon H-S (2011) A study on the contact angles of a water droplet on smooth and rough solid surfaces. J Mech Sci Technol 25(2):323–332
17. Sahin H, Gu F, Lytton RL (2014) Development of soil-water characteristic curve for flexible base materials using the methylene blue test. J Mater Civ Eng 7(1):1–7
18. Schindler U, Müller L, Eulenstein F (2016) Measurement and evaluation of the hydraulic properties of horticultural substrates. Arch Agron Soil Sci 62(6):806–818
19. Schulz VP, Becker J, Wiegmann A, Mukherjee PP, Wang C-Y (2007) Modeling of two-phase behavior in the gas diffusion medium of PEFCs via full morphology approach. J Electrochem Soc 154(4):B419
20. Schulz VP, Wargo EA, Kumbur EC (2015) Pore-morphology-based simulation of drainage contact angle. Transp Porous Media 107(1):13–25
21. Thompson PA, Robbins MO (1989) Simulations of contact-line motion: slip and the dynamic contact angle. Phys Rev Lett 63(7):766–769
22. Vanapalli SK, Nicotera MV, Sharma RS (2009) Axis translation and negative water column techniques for suction control. In: Laboratory and field testing of unsaturated soils, pp 33–48
23. Van Genuchten MT (1980) A closed-form equation for predicting the hydraulic conductivity. Soil Sci Soc Am J 44(5):892–898
24. Wargo EA, Schulz VP, Çeçen A, Kalidindi SR, Kumbur EC (2013) Resolving macro- and micro-porous layer interaction in polymer electrolyte fuel cells using focused ion beam and X-ray computed tomography. Electrochim Acta 87:201–212
25. Wildenschild D, Sheppard AP (2013) X-ray imaging and analysis techniques for quantifying pore-scale structure and processes in subsurface porous medium systems. Adv Water Resour 51:217–246
26. Zhang P, Lu S, Li J, Zhang P, Xie L, Xue H, Zhang J (2017) Multi-component segmentation of X-ray computed tomography (CT) image using multi-Otsu thresholding algorithm and scanning electron microscopy. Energy Explor Exploit 35(3):281–294

Safety Factor and Failure Mechanism in Geotechnical Engineering: A Numerical Study

H. C. Nguyen

Abstract Prediction of failure shapes and safety factors is the routine tasks for the geotechnical engineering profession. This paper presents an upper bound approach associated with the edge-based smoothed finite element method and second-order cone programming to estimate the ultimate load and its corresponding failure mechanism. The behavior of the whole domain is assumed to be rigid perfect plasticity and is governed by the Mohr–Coulomb failure criteria with the associated flow rule. The upper bound analysis turns to solve the optimization being casted as the second-ordered cone programming using a state-of-the-art code developed by mathematical researchers. Several simulations using the current numerical procedure have been carried out to investigate the dependency of safety factors and failure modes on soil parameters and geometry problems.

Keywords Safety factor · Failure mechanism · Geotechnical engineering

1 Introduction

Estimation of the limit state (i.e. the collapse load and the corresponding failure mechanism) has become a long-standing topic of interest. The limit analysis provides a powerful tool to estimate the ultimate load and its corresponding failure mechanism. For geomechanics, the upper bound that based on kinematic admissible fields [3, 6, 7] and the lower bound that bases upon stress fields [2, 6, 7] have been widely used to bracket the exact value of ultimate load. Prior studies show that most applications of limit analysis to soil mechanics studies lie with solving optimization problems rather than discretization techniques. Sloan [5–7], for example, forms the optimization problem with linear constraints; however, the drawback of optimization form is the large number constrains used in the optimization problem. It is, therefore, that Makrodimopoulos and Martin [2, 3] established the optimization problem subjected

H. C. Nguyen (✉)
Department of Civil and Environmental Engineering, Imperial College London, Skempton Building, London, UK
e-mail: h.nguyen15@imperial.ac.uk

A. Prashant et al. (eds.), *Advances in Computer Methods and Geomechanics*, Lecture Notes in Civil Engineering 55,
https://doi.org/10.1007/978-981-15-0886-8_10

to quadratic constraints, allowing large-scale problems in engineering practice to be solved efficiently.

Due to the fact that little attention has been paid to approximate either displacement or stress fields, Nguyen et al. [4] used edge-based smoothed finite element method (ES-FEM) to establish displacement fields and then formed optimization problems as second-order cone programming. The results obtained reveal that upper bound procedure using ES-FEM and SOCP can give stable results and fast convergence to determine ultimate loads than using the standard FEM. This study extends the work of Nguyen et al. [4] by exploring effects of soil parameters and geometry problems on the ultimate load and the plastic dissipation zones.

2 Upper Bound Procedure Using ES-FEM and SOCP

This section aims to provide a brief overview of how to form an upper bound procedure using ES-FEM and SOCP. Upper bound analysis is governed by the rate of work input and internal plastic dissipation, in which structure will collapse when the rate of input work, $W_{ext}(\dot{\boldsymbol{u}})$ exceeds the ability to observe energy of soil, $W_{int}(\dot{\boldsymbol{\varepsilon}})$, which can be expressed such that

$$W_{int}(\dot{\boldsymbol{\varepsilon}}) < W_{ext}(\dot{\boldsymbol{u}}) \tag{1}$$

where u and v are the velocity components in the x and y directions, respectively. The strain rates $\dot{\boldsymbol{\varepsilon}}$ can be expressed in the following form:

$$\dot{\boldsymbol{\varepsilon}} = \begin{bmatrix} \dot{\varepsilon}_{xx} \\ \dot{\varepsilon}_{yy} \\ \dot{\gamma}_{xy} \end{bmatrix} = \nabla \dot{\boldsymbol{u}} \tag{2}$$

It is convenient to separate $W_{ext}(\dot{\boldsymbol{u}})$ into two components $W^{\lambda}_{ext}(\dot{\boldsymbol{u}})$ *and* $W^{0}_{ext}(\dot{\boldsymbol{u}})$. The first term, $W^{\lambda}_{ext}(\dot{\boldsymbol{u}})$ relates to the external load which causes ground structures to collapse, while the second term, $W^{0}_{ext}(\dot{\boldsymbol{u}})$ is the additional external work which does not involve in making structure to fail It is, therefore, (1) can be rewritten as

$$W_{int}(\dot{\boldsymbol{\varepsilon}}) < W^{\lambda}_{ext}(\dot{\boldsymbol{u}}) + W^{0}_{ext}(\dot{\boldsymbol{u}}) \tag{3}$$

According to Makrodimopoulos and Martin [2, 3], the internal plastic dissipation, $D(\dot{\boldsymbol{\varepsilon}})$ can be calculated as

$$D_i(\dot{\boldsymbol{\varepsilon}}) = A_i c_i \cos\varphi_i \sqrt{\left(\varepsilon^i_{xx} - \varepsilon^i_{xx}\right)^2 + \left(\gamma^i_{xy}\right)^2} \tag{4}$$

where c is cohesion and φ is the internal friction angle of soil.

If $W_{ext}^{\lambda}(\dot{\boldsymbol{u}})$ is expressed in the form $\lambda^{+}W_{ext}^{\lambda}(\dot{\boldsymbol{u}})$ with the conditions $W_{ext}^{\lambda}(\dot{\boldsymbol{u}}) = 1$, λ^{+} is the collapse load multiplier. The failure condition can be then expressed as the following:

$$\lambda^{+} = \min \int_{\Omega} D_i(\dot{\boldsymbol{\varepsilon}}) - W_{ext}^{0}(\dot{\boldsymbol{u}})$$

Subject to

$$\begin{cases} W_{ext}^{\lambda}(\dot{\boldsymbol{u}}) = 1 \\ \dot{\boldsymbol{u}} = \dot{\boldsymbol{u}}_0 : u \in \Gamma_u \\ \varepsilon_{xx}^{i} + \varepsilon_{xx}^{i} = \varepsilon_{p}^{\Omega_i} \sin \emptyset \\ \boldsymbol{\varepsilon}_{p}^{\Omega_i} \geq \sqrt{\left(\varepsilon_{xx}^{\Omega_i} - \varepsilon_{xx}^{\Omega_i}\right)^2 + \left(\gamma_{xy}^{\Omega_i}\right)^2} \end{cases} \tag{5}$$

ES-FEM is then used to approximate the displacement fields. In ES-FEM (Fig. 1), basing on the mesh of elements, we further discretize the domain Ω into smoothing domains based on edges of the elements such that $\Omega = \bigcup_{i}^{N_{ed}} \Omega_k$ and $\Omega_i \cap \Omega_j = \emptyset$ for $i \neq j$, in which N_{ed} is the total number of edges of all elements in the entire problem domain. Moreover, ES-FEM shape functions are identical to those used in the standard FEM. However, instead of using compatible strains, the ES-FEM uses strains smoothed over local smoothing domains. Further details of ES-FEM can be referred to the work of Liu and Trung [1].

Upper bound procedure using ES-FEM and SOCP (see Nguyen et al. [4]) has become

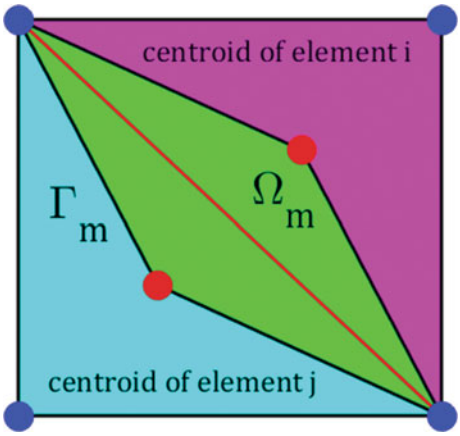

Fig. 1 Illustration of determination of smoothing domain

$$\lambda^{+} = \min \sum_{i=1}^{i=N_{edge}} d_p^{\Omega_i} - W_{ext}^{0}(\dot{\boldsymbol{u}})$$

Subject to

$$\begin{cases} W_{ext}^{\lambda}(\dot{\boldsymbol{u}}) = 1 \\ \dot{\boldsymbol{u}} = \dot{\boldsymbol{u}}_0 : u \in \Gamma_u \\ \varepsilon_{xx}^{i} + \varepsilon_{xx}^{i} = \varepsilon_p^{\Omega_i} \sin \emptyset \\ \boldsymbol{\varepsilon}_p^{\Omega_i} \geq \sqrt{\left(\varepsilon_{xx}^{\Omega_i} - \varepsilon_{xx}^{\Omega_i}\right)^2 + \left(\gamma_{xy}^{\Omega_i}\right)^2} \end{cases} \tag{6}$$

3 Stability and Failure Mechanism of Some Typical Problems in Geotechnical Engineering

3.1 Bearing Capacity of Footing Strips

One of the most fundamental problems in geotechnical engineering is to determine the capacity of shallow foundations. Terzaghi [8] gives the solutions of ultimate load of soil beneath the footing strip using assumption of failure mechanism. It is obvious that the results obtained would be dependent on the potential failure mechanism that can be happened under footing strip. Herein the dependency of failure mechanism on soil parameters is examined. Bearing in mind that Terzaghi [8] divides three bearing capacity factors (i.e., N_c, N_q and N_Y) that correspond to the ability to bear load of cohesion force, surcharge load, and unit weight. The bearing capacity of the footing strip q_{ult} can be expressed such that

$$q_{ult} = cN_c + qN_q + 0.5\gamma N_\gamma \tag{7}$$

Bearing capacity factor N_c is first considered. No failure assumption is made as Terzaghi [8] did; however, the behavior of the whole domain underneath footing is assumed to be rigid perfect plasticity. The corresponding failure mechanism is the solution to the optimization problem. Results reveal that these failure mechanisms vary with friction angles. Noting that, to receive the value of N_c, only cohesion force is considered while both surcharge load and soil weight are zero in the simulations (Fig. 2).

It is widely accepted that bearing capacity factor N_c is the largest factors among three bearing capacity factors proposed by Terzaghi [8]. Considering the special case of $\emptyset = 0°$ where the analytical solution is $2+\pi \approx 5.14$. The result obtained from the numerical procedure (i.e., $N_c = 5.1874$) agrees well with the theoretical solution. Herein the primary purpose is to investigate how failure mechanism evolves with

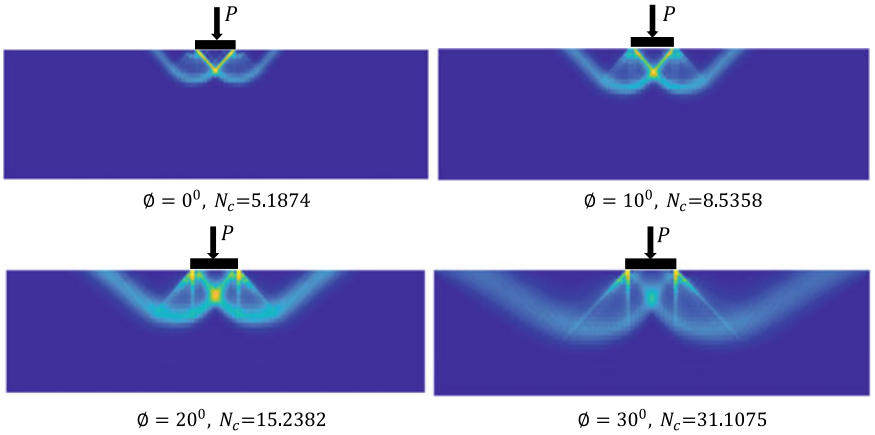

Fig. 2 The dependency of failure mechanisms on friction angle for bearing capacity N_c

friction angle rather than evaluating the efficiency of this numerical approach. Data obtained reveal that failure mechanisms largely depend on soil parameter and tend to expand with increasing friction angle of soil.

The influence of depth of shallow foundation on bearing capacity of soil represents as N_q in which soil weight and cohesion force are ignored in the simulations. This means that only q is equal to 1, while γ *and* c are 0. The failure mechanism for the case of $\emptyset = 30°$ is illustrated in Fig. 3. To determine the bearing capacity factor, N_γ which corresponds to the bearing capacity of sand under the footing strip resting on the ground surface. It is thus both q *and* c are set to be zero in the modeling; the ultimate load turns to $q_{ult} = 0.5\gamma N_\gamma$. When γ is equal to 1, it is obvious that N_γ can be calculated directly from the ultimate load, λ^+ that is obtained directly from solving the optimization problem.

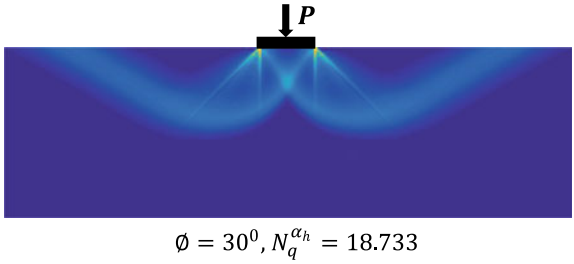

Fig. 3 Dependency of failure mechanisms on friction angle for bearing capacity N_q

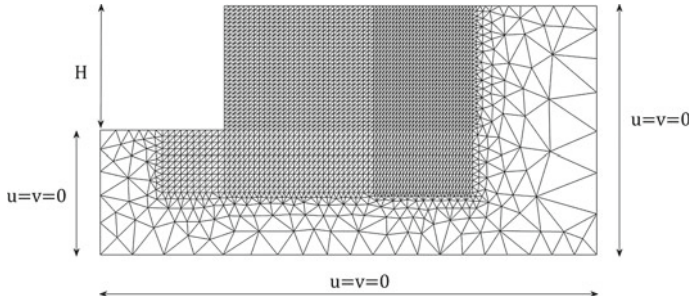

Fig. 4 Finite elements mesh and boundary conditions for cutting slope

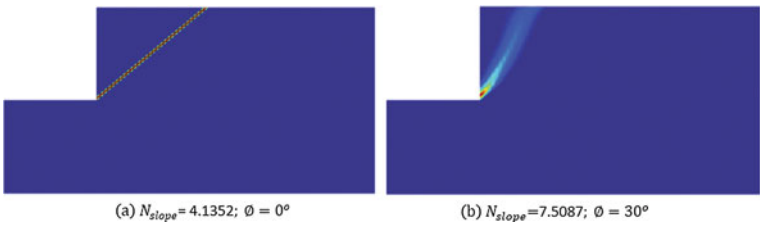

Fig. 5 Plastic dissipation distributions of cutting slope with friction angle Ø

3.2 The Stability of Slope

The stability of the slope is a long-standing subject of interest. Herein the factor that causes slope failure is only soil weight itself. The problem raised here is that, if we have a specific slope (i.e., shape and geometry determined), how to determine the unit weigh that leads to the failure of the slope. To answer this question, in simulation, the unit soil weight should be equal to 1, for which the ultimate load from optimization problem will be the maximum soil weight. It is widely known that the stability of slope represents as the factor, $N_{slope} = \gamma H/c$. For simplicity, we investigate the safety factor of the case of cutting slope that has geometry and boundary conditions as shown in Fig. 4. It is obvious that the safety factor increases with the increasing soil parameters, leading the changes in failure zones. Herein we only restrict to cases of friction angle (i.e., $\emptyset = 0° \; and \; \emptyset = 20°$), for which the failure zone can be revealed as illustrated in Fig. 5.

3.3 The Stability of Footing Strip Resting on Slope

Another problem that is widely investigated in geotechnical engineering is the stability of footing on the slope. It is worth noting that both soil weight and external

Fig. 6 Changes in plastic dissipation zones with friction angle $\emptyset$ varied ($L/B = 2$)

load on footing influence the stability of the slope. Moreover, the slope itself is stable without applying an external load to footing strip; however, this will add an extra load that reduces the stability of soil under the footing. To investigate this problem, it is imagined that there is a footing with the width of B; the distance between this footing and the edge of the slope is L. Factors that influence the stability of footing strip resting on the slope can be shortly expressed as

$$S_{slope}^{footing} = \frac{p'}{\gamma B} = f\left(\beta, \frac{L}{B}, \frac{H}{B}, \frac{c_u}{\gamma B}, \frac{q}{\gamma B}, \emptyset\right) \tag{8}$$

where p' is the average limit pressure beneath the footing; q is the surcharge load distribution. It should be noted that the ratio H/B should be chosen high enough so that failure zone is formed above the toe of the footing. Herein, this ratio $H/B = 3$ is adopted for all simulations. We shall restrict the initial conditions, for which just only effects of friction angle on the stability is investigated. The conditions are as follows: (i) $c_u/\gamma B = 1$, (ii) $q/\gamma B = 0$, and (iii) $B = 1$ and $L = 2$. It is obvious that safety factor is largely dependent on friction angle (Fig. 6).

3.4 Stability of Circular and Square Tunnels

The last problem considered in this study is the stability of tunnels, circular, and square tunnels. The purpose herein is to investigate how failure mechanism of two types of tunnels changes with soil parameters and their geometries. Definition of tunnels is illustrated in Figs. 7 and 8. It should be noted that tunnel length is assumed to be much larger than its diameter, so the ground deformation acts as in the plane strain condition. Noting also that the tunnel is formed in a general cohesive-frictional soil without any internal support. The dimensionless stability factors for a circular tunnel, $S_{tunnel}^{circular} = \gamma_{max} H/c$ and for a square tunnel, $S_{tunnel}^{square} = \gamma_{max} H/c$ are used as a reference quantity to assess the stability of the circular tunnel.

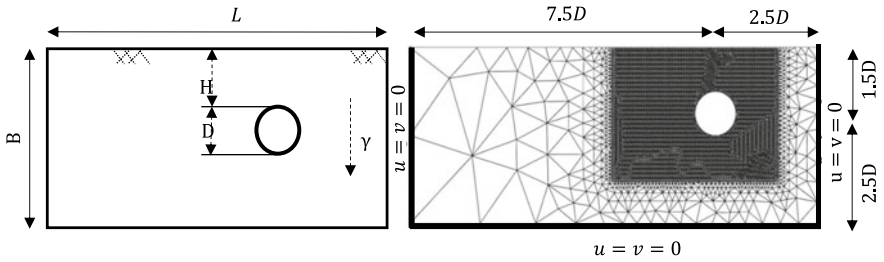

Fig. 7 Definition of the problem: finite elements mesh and boundary conditions for circular tunnel

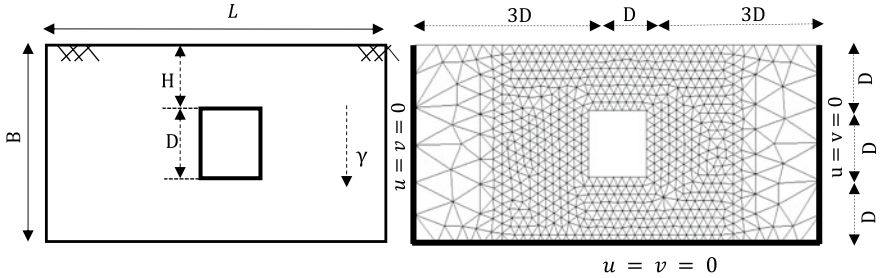

Fig. 8 Definition of the problem: finite elements mesh and boundary conditions for square tunnel

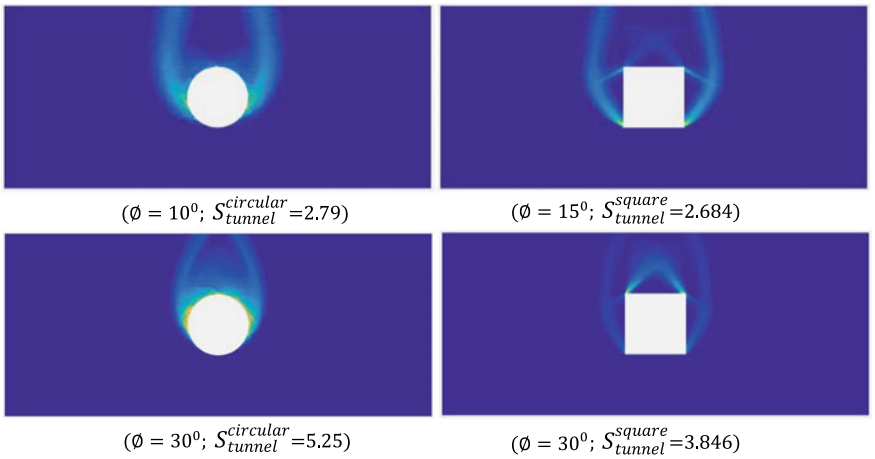

Fig. 9 Changes in plastic dissipation distributions ($H/D = 1$)

Figure 9 shows the dependency of plastic dissipation zones on friction angle. As expected, the safety factor increases with increasing friction angle; for both cases, the safety factor of the circular tunnel is much higher than that of the square tunnel.

4 Conclusions

An upper bound procedure using ES-FEM and SOCP has been presented to estimate the safety factor and the failure mechanism in geotechnical engineering. The plastic dissipation zone expands as the friction angle increases, leading to an increase in the safety factor. Various numerical examples were performed to show that the current method can provide accurate and stable solutions to the ultimate loads for all manner of plane strain geotechnical problems. However, energy dissipation associated with the sliding happened between adjacent smoothing domains should be further examined.

Acknowledgements The author wishes to thank Prof. C. V. Le for sharing his upper bound code for the Prandtl's problem using the Von Mises criterion. The author is very grateful to the financial support provided by Vied-Newton Ph.D. scholarship and Dixon Ph.D. scholarship for supporting the studies at Imperial College London.

References

1. Liu G-R, Trung NT (2016) Smoothed finite element methods. CRC press
2. Makrodimopoulos A, Martin CM (2006) Lower bound limit analysis of cohesive-frictional materials using second-order cone programming. Int J Numer Methods Eng 66(4):604–634. Wiley Online Library
3. Makrodimopoulos A, Martin CM 2007 Upper bound limit analysis using simplex strain elements and second-order cone programmingInternational. J Numer Anal Methods Geomech 31(6):835–865. Wiley Online Library
4. Nguyen HC et al (2012) Bearing capacity of footing strip resting on slope using upper bound limit analysis. J Eng Technol Educ
5. Sloan SW (1988) Lower bound limit analysis using finite elements and linear programming. Int J Numer Anal Methods Geomechanics 12(1):61–77. Wiley Online Library
6. Sloan SW (1989) Upper bound limit analysis using finite elements and linear programming. Int J Numer Anal Methods Geomechanics 13(3):263–282. Wiley Online Library
7. Sloan SW (2013) Geotechnical stability analysis. Géotechnique. ICE Publishing 63(7):531
8. Terzaghi K (1944) Theoretical soil mechanics. Chapman and Hali, Wiley, New York

Linear Static and Dynamic Analyses of Reinforced Concrete Spherical Dome Structure Under Seismic Loads

R. Pathak and R. K. Khare

Abstract Shells and spatial structures are adopted for construction of large span structures where large column-free area needs to be covered. The structures are expected to resist against various design loads mainly through their extremely strong capability which can be acquired through in-plane or membrane stress resultants and this is just the reason by which they themselves stand for external loads without columns as their structural components in the large span structures. Singly curved cylindrical shells and doubly curved spherical shells are commonly used as roofing units in civil engineering construction. The knowledge of their dynamic behaviour is important from the standpoint of analysis and design as they are subjected to dynamic loadings in their service life. In this study, the seismic behaviour of reinforced concrete spherical dome structures under static and dynamic loads is evaluated. IS: 2210-1988, Criteria for Design of RC Shell Structures and Folded plates, suggests to design shell structures for seismic loads in accordance with IS: 1893-2002, Criteria for earthquake resistant structure; however, lack in detail specifications for shell structures is to be adopted. Therefore, from this point of view, a methodology needs to be proposed for understanding the behaviour of shell structures under seismic loads. Linear static and dynamic analyses are performed on the basis of IS: 1893-2002 using SAP-2000 software. The Equivalent Static method is performed for 63 load combinations and the Response spectrum method is performed for 151 load combinations. The results shows that the spherical dome structure considered here with designed lateral force resisting system behaves well under seismic loading.

Keywords Dome structure · Double curved structure · Seismic behaviour · Linear static and linear dynamic analysis

R. Pathak (✉)
Civil Engineering Department, SVITS, SVVV, Indore, India
e-mail: raanapathak@gmail.com

R. K. Khare
Civil Engineering and Applied Mechanics Department, SGSITS, Indore, India

A. Prashant et al. (eds.), *Advances in Computer Methods and Geomechanics*, Lecture Notes in Civil Engineering 55,
https://doi.org/10.1007/978-981-15-0886-8_11

1 Introduction

Seismic behaviour of reinforced concrete spherical dome structures under static and dynamic loads is evaluated in this study. It is well-known that shells structures gain their strength by virtue of the three-dimensional development of their surfaces, with a resulting ability to carry external loads primarily through in-plane stresses rather bending. The internal force and stress distribution in shell structures are in general, spatial. Then a careful study must be performed to catch the real behaviour of such structures under lateral forces when bending will be a non-negligible effect [1, 2].

Linear static and dynamic analyses are performed for spherical dome structure. Linear static and dynamic analyses are performed on the basis of IS 1893 (Part 1): 2002, Criteria for earthquake resistant design of structures using SAP 2000 software [3]. The design spectrum used is of medium soil as per IS 1893 (Part 1): 2002, and the structure is analysed for lateral loads in Zone-V. The load combinations considered are as per IS 1893 (Part 1): 2002 for the structures. The equivalent static method is performed for 63 load combinations and the response spectrum method is performed for 151 load combinations.

2 Software Details (SAP 2000)

The structural analysis program SAP 2000 is a software package from Computers and Structures, which is based on the finite element method for modelling and analysis [4]. Among the features introduced by the analysis engine of SAP 2000 are modal analysis, static and dynamic analysis, linear and nonlinear analysis, and pushover analysis. The layered shell modelling can be possible in SAP 2000 which allows any number of layers to be defined in the thickness direction, each with an independent location, thickness, behaviour and material. Material behaviour maybe considered as linear and nonlinear both.

3 Modelling of Spherical Dome Structure

The domes are shells of revolution and can be of many types and shapes. These are the surfaces of revolution formed by a simple curve about its vertical axis. The curve can be a circle producing a spherical dome, an ellipse producing an elliptical dome and a hyperbola producing a hyperbolic dome. Conical domes are formed by an inclined straight line fixed at one point and moving over a circle at the other end. In this study, a simple spherical dome is considered.

A spherical dome to cover a circular area of 40 m diameter is considered in this study. The thickness of 150 mm with nominal reinforcement is provided and

supported on ring beam and columns. The height of columns is 12 m. Figure 1 shows the meshing view of dome structure. The details of parameters are given in Table 1.

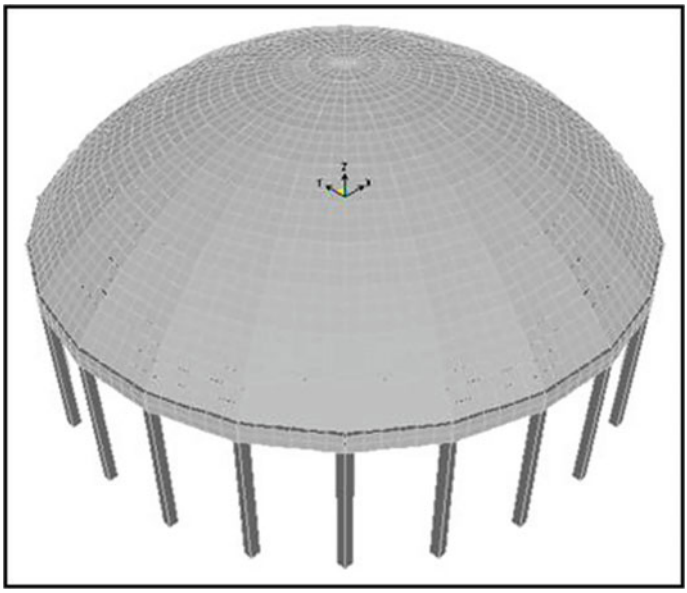

Fig. 1 Meshing view of spherical dome structure

Table 1 Details of parameters for spherical dome structure

Description	Parameter
Diameter of spherical dome	40 m
Live load	0.75 kN/m^2
Grade of concrete	M-25
Type of steel	HYSD bars
Column height	12.0 m
Column size	0.6 m × 0.6 m
Edge beam size	0.6 m × 1.22 m
Shell reinforcement	10d @ 200 c/c on both-faces
Radius of dome	25.45 m
Thickness of dome	0.15 m
Roll down angle	51.8°
Central rise	10.36
Centre to centre column spacing	15 m (radial)

Table 2 Modal characteristics of spherical dome structure

Mode	Period (S)	Frequency (Hz)	Modal participation mass ratio		
			X	Y	Z
1	0.0589	16.978	7.23E−16	2.196E−16	1.173E−15
2	0.0589	16.978	9.076E−18	4.245E−18	0
3	0.058465	17.104	4.1E−16	5.869E−16	2.05E−15
4	0.058465	17.104	4.141E−16	3.393E−16	7.317E−18
5	0.057511	17.388	2.188E−16	6.48E−19	2.72E−16
6	0.057511	17.388	1.499E−15	1.448E−15	2.016E−18
7	0.056063	17.837	1.444E−15	1.642E−15	7.459E−15
8	0.056063	17.837	1.213E−14	3.551E−15	1.543E−15
9	0.054739	18.269	1.717E−14	4.076E−16	**0.34199**
10	0.054662	18.294	2.095E−14	5.972E−15	2.905E−15
11	0.054662	18.294	4.607E−15	1.516E−14	5.804E−15
12	0.05403	18.508	**0.24072**	0.0172	6.362E−15
13	0.05403	18.508	0.0172	**0.24072**	1.865E−14

4 Modal Analysis

The modal analysis of spherical dome structure is performed for 50 modes to get a first important insight into structural dynamic properties [5–7]. The modal characteristics of the spherical dome structure are presented in the X-, Y- and Z-directions in Table 2 for first 13 modes. The prominent modes in the X-, Y- and Z-directions are Mode 12, 13 and 9, respectively. Figure 2 shows deformed shape of ninth mode. Figure 3 and Fig. 4 show deformed shape of twelfth mode and thirteenth mode for spherical dome structure, respectively [8, 9].

5 Linear Static Analysis of Shell and Spatial Structure

An effort has been made to apply the equivalent linear static methods permitted in IS 1893 (Part 1): 2002, Criteria for earthquake resistant design of structures, on Spherical Dome structure [10–12]. The design spectrum used is of medium soil as per IS 1893 (Part 1): 2002, and the Spherical Dome structure is analysed for lateral loads in Zone-V. The response due to earthquake force (EL) is the maximum of the following three cases if load is applied in x and y directions:

$$\pm EL_x \pm 0.3\,EL_y$$
$$\pm EL_y \pm 0.3\,EL_x$$
$$\pm\sqrt{(EL_x)^2 + (EL_y)^2}$$

x and y are two orthogonal directions.

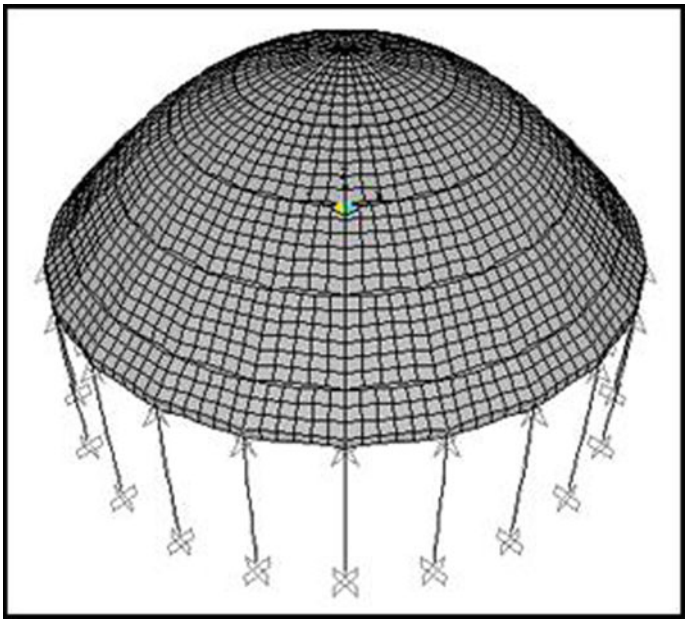

Fig. 2 Ninth mode shape of spherical dome structure

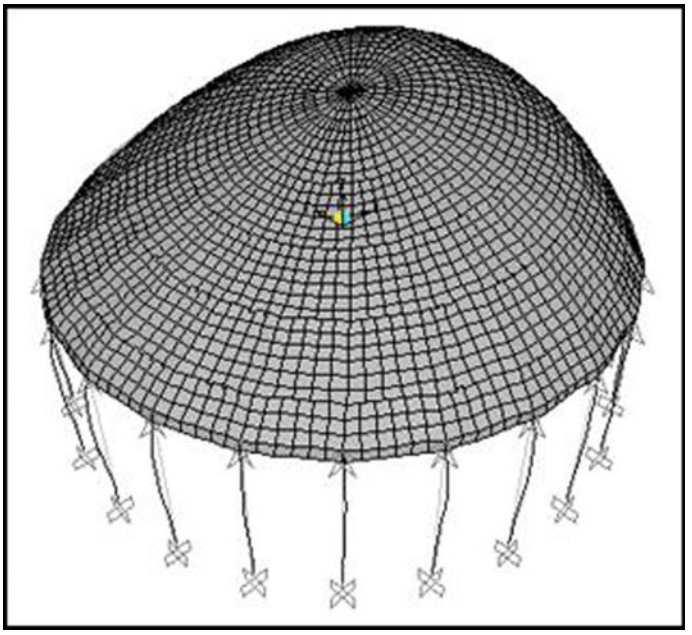

Fig. 3 Twelfth mode shape of spherical dome structure

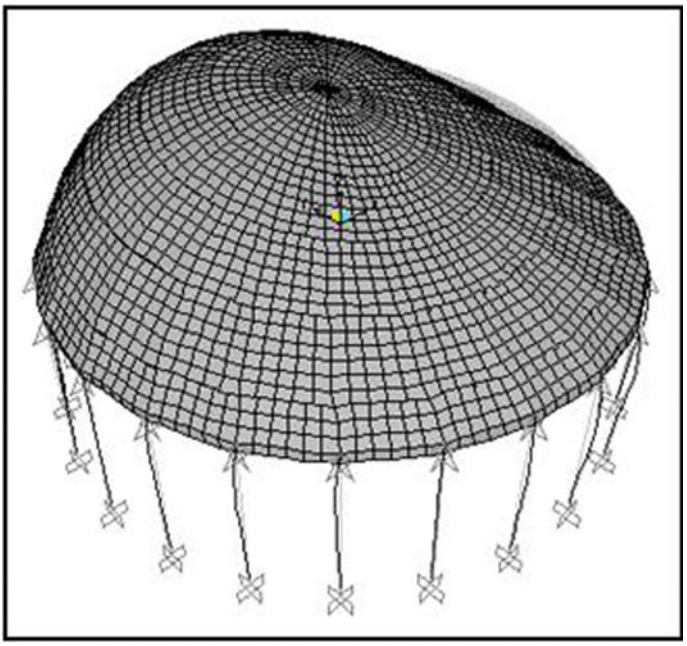

Fig. 4 Thirteenth mode shape of spherical dome structure

As per IS 1893 (Part 1): 2002, the following load combinations shall be accounted for:

$$1.5\,(\mathrm{DL} + \mathrm{IL})$$
$$1.2\,(\mathrm{DL} + \mathrm{IL} \pm \mathrm{EL})$$
$$1.5\,(\mathrm{DL} \pm \mathrm{EL})$$
$$0.9\,\mathrm{DL} \pm 1.5\,\mathrm{EL}$$

The Equivalent Static method is performed through 63 possible load cases.

6 Linear Dynamic Analysis of Shell and Spatial Structure

The type of linear dynamic analysis performed is the response spectrum analysis. This method is used for the prediction of displacements and element forces in structures. The analysis consists of a three-dimensional mode shapes and natural frequencies of vibration calculation. These are the undamped free vibration response of the structure. The structure has constant stiffness and mass effects. The mass is taken distributed along the structures by a density. Then, the structure is excited by a spectrum of known directions and frequency components. Modal analysis method

did not require a set of master degrees of freedom, and it gives more accurate answers with the comparison with reduced method for eigenvalues calculation. But, it takes somewhat longer to solve. In this method, a number of modes are considered for the structural response calculation. For each principal direction, the square-root-of-sum-of the- squares (SRSS) modes combination method is used for the purpose of structural design. This approach assumes that all the maximum modal values are statistically independent.

A well-designed structure should be capable of equally resisting earthquake motions from all possible directions. Three consecutive modal spectrum analyses were performed in the three principal directions x, y and z. As per IS 1893 (Part 1): 2002, when responses from the three earthquake components maybe combined using the assumption that when the maximum response from one component occurs, the responses from the other two components are 30 percent of their maximum. All possible combinations of the three components (EL_x, EL_y and EL_z) including variations in sign (plus or minus) shall be considered. Additionally, the response due to the combined effect of the three components can be obtained on the basis of 'square root of the sum of the square (SRSS)' [13, 14].

The analysis consists of a three-dimensional mode shapes and natural frequencies of vibration calculation. These are the undamped free vibration response of the structure. In this method, ten number of modes are considered for the structural response calculation. It is assumed that all the maximum modal values are statistically independent. The design spectrum used is of medium soil as per IS 1893 (Part 1): 2002, and the structure is analysed for lateral loads in Zone-V. Response spectrum analysis is performed for Spherical Dome structure for lateral loads in Zone-V as per IS 1893 (Part 1): 2002.

Three consecutive modal spectrum analyses are performed in the three principal directions x, y and z. As per IS 1893 (Part 1): 2002, when responses from the three earthquake components maybe combined using the assumption that when the maximum response from one component occurs, the responses from the other two components are 30 percent of their maximum. All possible combinations of the three components (EL_x, EL_y and EL_z) including variations in sign (plus or minus) are considered. Additionally, the response due to the combined effect of the three components is obtained on the basis of 'square root of the sum of the square (SRSS)'. Thus, the response due to earthquake force (EL) is the maximum of the following four cases:

$$\pm EL_x \pm 0.3\,EL_y \pm 0.3\,EL_z$$
$$\pm EL_y \pm 0.3\,EL_x \pm 0.3\,EL_z$$
$$\pm EL_z \pm 0.3\,EL_x \pm 0.3\,EL_y$$
$$\pm\sqrt{(EL_x)^2 + (EL_y)^2 + (EL_z)^2}$$

x and y are two orthogonal directions and z is vertical direction.

As per IS 1893 (Part 1): 2002, the following load combinations shall be accounted for:

Table 3 Absolute maximum displacement in shell elements of spherical dome structure

Parameters	Linear static analysis	Linear dynamic analysis
Horizontal displacement in X-direction, Ux (m)	0.00015	0.00014
Horizontal displacement in Y-direction, Uy (m)	0.00015	0.00014
Vertical displacement in Z-direction, Uz (m)	0.001	0.001

$$1.5\,(\mathrm{DL} + \mathrm{IL})$$
$$1.2\,(\mathrm{DL} + \mathrm{IL} \pm \mathrm{EL})$$
$$1.5\,(\mathrm{DL} \pm \mathrm{EL})$$
$$0.9\,\mathrm{DL} \pm 1.5\,\mathrm{EL}$$

The spectrum combination is performed through 151 possible load cases.

7 Results and Discussion

A comparative study has been performed to understand the behaviour of shell structure. Displacement, Membrane Forces, Membrane Stresses and Base reaction of Spherical dome structure are determined for dead load, live load and seismic loads. Absolute maximum values of all the parameters are tabulated. The contour plots for membrane stresses are helpful in understanding the distribution of stresses in shell elements and hence captured pictures are presented in this study.

7.1 Displacement

The absolute maximum values of nodal displacements for linear static and linear dynamic analysis cases for spherical dome structure are tabulated in Table 3. The maximum absolute horizontal displacements are equal to 0.002 m in X-direction and 0.008 m in Y-direction. The maximum absolute vertical displacement is equal to 0.008 m.

7.2 Membrane Forces

The internal membrane (in-plane) forces consist of two-membrane normal resultant forces F_{11}, F_{22} and a membrane in-plane shear force F_{12} per unit length. The bending forces field consists of two bending moments M_{11}, M_{22} per unit length, a twisting

Table 4 Absolute maximum membrane forces in shell elements of spherical dome structure

Parameters	Linear static analysis	Linear dynamic analysis
Membrane force in X-direction, F_{11} (kN/m)	87.32	87.32
Membrane force in Y-direction, F_{22} (kN/m)	104.24	104.24
In-plane shear force, F_{12} (kN/m)	3.01	0.67
Out of plane shear force in X-direction, V_{13} (kN/m)	0.1	0.0155
Out of plane shear force in Y-direction, V_{23} (kN/m)	1.08	1.08
Bending moment in X-direction, M_{11} (kN-m/m)	0.206	0.206
Bending moment in Y-direction, M_{22} (kN-m/m)	0.206	0.206
Twisting moment, M_{12} (kN-m/m)	0.0157	0.0157

moment M_{12} of the shell cross sections per unit length, and two transverse out of plane shear forces V_{13}, V_{23} per unit length. The X-, Y- and Z-directions are denoted as 1, 2 and 3 in element resultants as per SAP 2000. The absolute maximum membrane forces are tabulated to understand the behaviour of shell and spatial structures. The membrane forces are tabulated for spherical dome structure in Table 4 for linear static and linear dynamic analysis cases.

7.3 Membrane Stresses

The basic shell element stresses are identified as S_{11}, S_{22}, S_{12}, S_{13}, and S_{23}. S_{11} and S_{22} denote the membrane direct stress in X and Y direction, respectively. S_{12} denotes the membrane shear stress. S_{13} and S_{23} denote the plate transverse shear stress in X and Y direction, respectively. The absolute maximum membrane stresses are tabulated to understand the behaviour of shell and spatial structures. The absolute maximum membrane stresses for spherical dome structure are tabulated in Table 5.

7.4 Base Reaction

Absolute maximum values of base reaction in X-direction, Y-direction and Z-direction for Cylindrical Shell Structure, Spherical dome structure and V-type folded plate structure are tabulated. F_X, F_Y and F_Z are the base reaction in X-direction, Y-direction, and Z-direction, respectively. M_X, M_Y and M_Z are the base moment in X-direction, Y-direction and Z-direction, respectively. Absolute maximum values of horizontal base reaction and bending moment in X and Y-direction and vertical

Table 5 Absolute maximum membrane stresses in shell elements of spherical dome structure

Parameters	Linear static analysis	Linear dynamic analysis
Membrane direct stress in X-direction, S_{11} (kN/m^2)	615.82	615.82
Membrane direct stress in Y-direction, S_{22} (kN/m^2)	661.29	661.29
Membrane shear stress, S_{12} (kN/m^2)	51.00	13.42
Plate transverse shear stress in X-direction, S_{13} (kN/m^2)	2.18	0.44
Plate transverse shear stress in Y-direction, S_{23} (kN/m^2)	7.18	7.69

Table 6 Absolute Maximum Base reaction of spherical dome structure

Parameters	Linear static analysis	Linear dynamic analysis
Horizontal Force in X-direction, Fx (kN)	798.631	798.631
Horizontal Force in Y-direction, Fy (kN)	798.631	798.631
Vertical Force in Z-direction, Fz (kN)	15258.01	15258.01
Horizontal Bending Moment in X-direction, Mx (kN-m)	3980.809	3980.809
Horizontal Bending Moment in Y-direction, My (kN-m)	3980.809	3980.809
Vertical Bending Moment in Z-direction, Mz (kN-m)	3.336E−12	3.336E−12

base reaction and bending moment in Z-direction for spherical dome structure are tabulated in Table 6.

The contour plots for membrane stresses in spherical dome are presented in Figs. 5, 6, 7, 8 and 9. The contour plots are for the maximum values.

8 Conclusions

The linear static and dynamic analyses of Spherical Dome structure are done using finite element model in software SAP 2000. It is relatively a simpler way to explore the seismic behaviour of structures and an attempt has been made here for shell and spatial structures. A three-dimensional finite element analysis is performed to assess the seismic performance of the structure subjected to earthquake actions.

The prominent modes for Spherical Dome structure in the X-, Y-, and Z-direction are Mode 12, 13 and 9, respectively. The mass participation in X-direction is 24.07%, in Y-direction is 24.07% and in Z-direction is 34.20%.

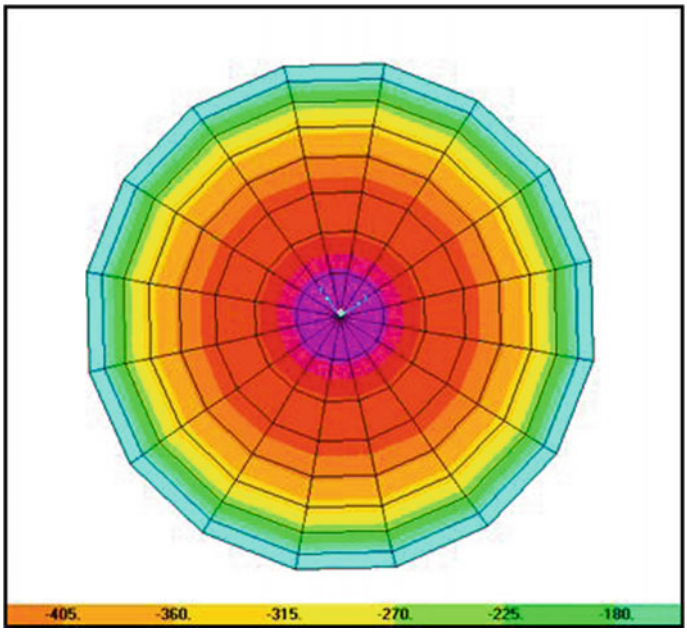

Fig. 5 Membrane direct stress in X-direction, S_{11}

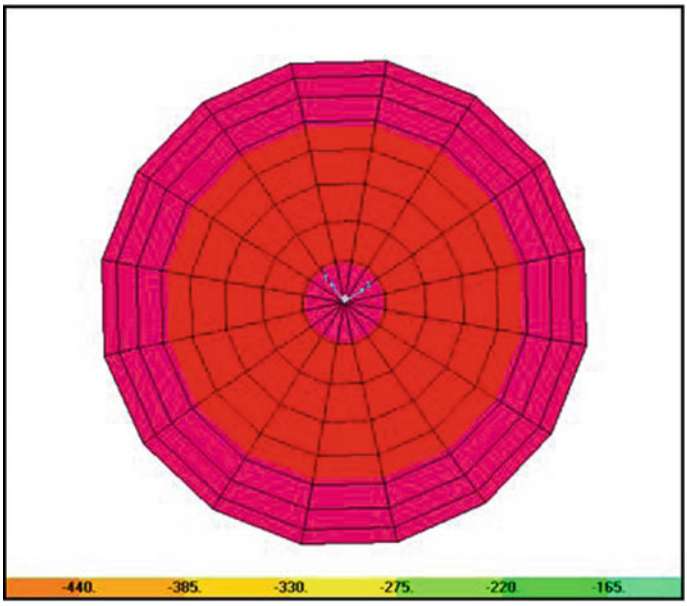

Fig. 6 Membrane direct stress in Y-direction, S_{22}

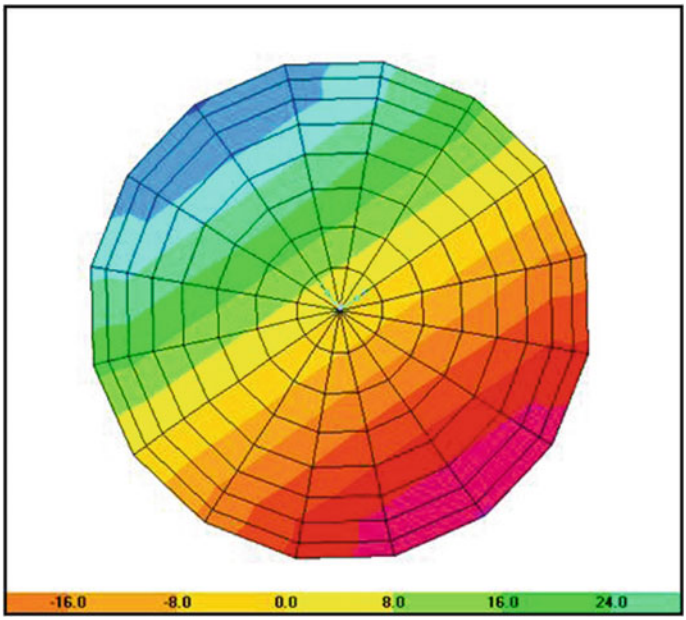

Fig. 7 Membrane shear stress in X-direction, S_{12}

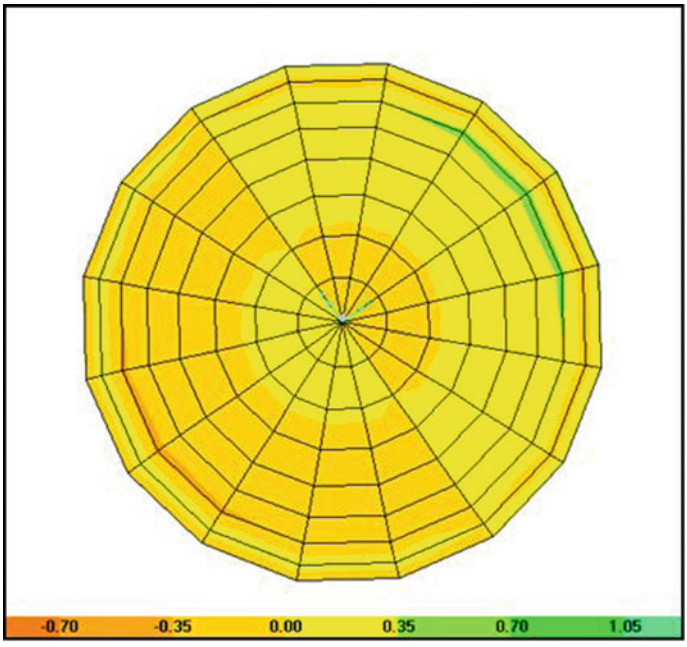

Fig. 8 Transverse shear stress in X-direction, S_{13}

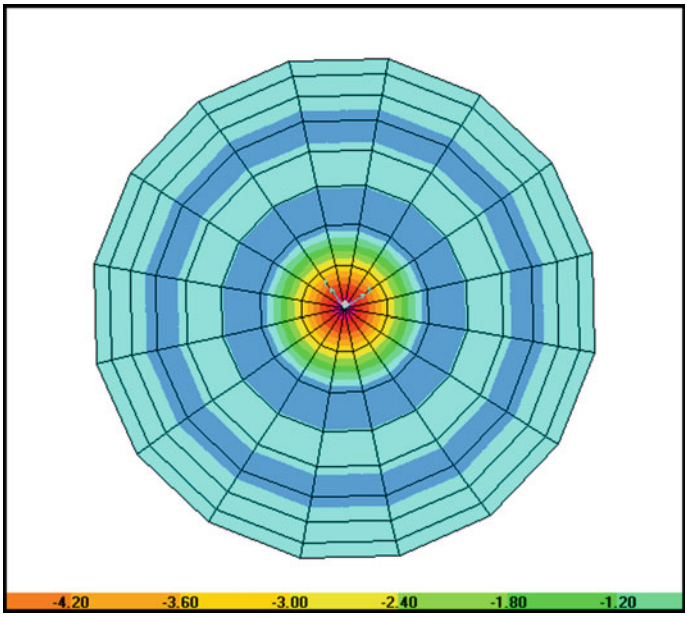

Fig. 9 Plate transverse shear stress in Y-direction, S_{23}

The mass participation of Spherical Dome structure in X and Y direction are same due to symmetry of structure.

Permissible storey drift as per IS 1893:2002 due to lateral force shall not exceed 0.004 times the storey height. The permissible storey drift is 0.048 m for 12 m storey height. The storey drift is within limit for all the cases. The maximum absolute horizontal displacements in X-direction and Y-direction and maximum absolute vertical displacement in Z-direction for Spherical Dome structure are within the permissible limit [15, 16].

The membrane stresses in Spherical Dome structure are within the permissible limit. The results show that the Spherical Dome structure considered here with designed lateral force resisting system behaves well under seismic loading. In general, it is observed that the Spherical Dome structure can carry the external seismic actions by membrane mechanism exclusively.

References

1. Belmouden Y, Lestuzzi P, Sellami S (2007) A modular shell system for housing. J Int Assoc Shell Spat Struct IASS 48(1):153–162
2. Boutagouga D, Djeghaba K (2013) Evaluation of linear and geometrically nonlinear static and dynamic analysis of thin shells by flat shell finite elements. Int J Civ Environ Struct Constr Arch Eng 7(2):168–174

3. Indian Standard Criteria of practice for Earthquake Resistant Design of Structures, IS 1893-2002, Bureau of Indian Standards, New Delhi, India
4. SAP 2000 Structural Analysis Program, Nonlinear Version 14.0.0, Computers and Structures, Inc. 2009. Berkeley, California
5. Hua LW, Shan YQ, Yu-Ji T (2005) Response analysis of national stadium under spatially varying earthquake ground motions. J Int Assoc Shell Spat Struct IASS
6. Luo YF, Yang MW (2008) Static elasto-plastic analysis of long-span rigid spatial structures under vertical earthquake. In: Proceedings of the 6th international conference on computation of shell and spatial structures, May 2008, NY, USA
7. Mander JB, Priestley MJN, Park R (1988) Theoretical stress-strain model for confined concrete. J Struct Eng ASCE 114(8):1804–1826
8. Meek JL, Wang Y (1998) Nonlinear static and dynamic analysis of shell structures with finite rotation. Comput Methods Appl Mech Eng 162:301–315
9. Samanta A, Mukhopadhyay M (2004) Free vibration analysis of stiffened shells by the finite element technique. Eur J Mech Solids 23:251–262
10. Song HW, Hyo S, Byun KJ, Maekawa K (2002) Failure analysis of reinforced concrete shell structures using layered shell element with pressure node. ASCE J
11. Varghese PC. Design of reinforced concrete shell and folded plates, Prentice Hall India Publication
12. Pathak R, Khare RK (2016) Seismic behaviour of concrete barrel shell structures under static & dynamic loads, ING-IABSE. J Bridges Struct 46(1):81–90
13. Pathak R et al (2011) Finite element modeling of 3-D shell structures. In: Proceeding of national seminar on design, construction and maintenance aspects of special structures, Rishiraj Institute of Technology, Indore, Oct 2011
14. Pathak R, Khare RK (2017) Seismic response prediction of reinforced concrete single barrel shell structures by nonlinear static analysis. Indian Concrete J 91(10):61–68
15. Indian Standard Criteria for Design of Reinforced Concrete Shell Structures and Folded plates, IS 2210-1988, Bureau of Indian Standards, New Delhi, India
16. Indian standard code of practice for plain and reinforced concrete for general building construction, IS 456: 1978. Bureau of Indian Standards, New Delhi, India

Shear Behavior of Geotextile-Reinforced Silty Sand Using Static Triaxial Testing

Akansha Srivastava and R. S. Dalvi

Abstract A total of 15 consolidated undrained triaxial tests were performed on samples with a size of 75 mm diameter and 150 mm height at three confining pressures of 50, 100 and 200 kPa for investigating the shear performance of nonwoven geotextile-reinforced silty sand and to study the excess pore water generation. The test comprises of zero, one, two, and three horizontal geotextile layers that were situated at regular vertical intervals inside the silty sand. Only one type of geotextile was utilized in all the tests. The results provide facts that as the confining pressure increases, the peak strength for the both case reinforced as well as in unreinforced samples increases. The results verified that the insertion of nonwoven geotextile reinforcement into sand-silt mixture enhanced peak deviator stress and shear strength parameters (c and ϕ), and reduce the loss of post-peak shear strength. Also, the usefulness of reinforcement on improving the net shear strength was evaluated using shear strength difference that is, the peak deviator stress difference between nonwoven geotextile-reinforced specimens and unreinforced specimens at a particular confining pressure. The results showed that strength difference decreased may reduce to zero at a certain reinforcement spacing (77–85 mm), which is equivalent to spacing diameter ratios of 1.02–1.13. For the geotextile-reinforced soil, as the number of geotextile layer increases, the strength improves due to the mobilization of larger tensile force at higher confining pressure. Also, the inclusion of geotextile layers restrained the horizontal displacement of soil. Failure patterns were visualized using Plaxis 2D finite element software for case of geotextile-reinforced silty sand specimen under axis symmetric triaxial loading.

Keywords Geotextile-reinforced silty sand · Triaxial test · Shearing strength · Excess pore water pressure · Finite element analysis

A. Srivastava (✉) · R. S. Dalvi
College of Engineering, Pune, India
e-mail: akansha309@gmail.com

R. S. Dalvi
e-mail: rsd.civil@coep.ac.in

A. Prashant et al. (eds.), *Advances in Computer Methods and Geomechanics*, Lecture Notes in Civil Engineering 55,
https://doi.org/10.1007/978-981-15-0886-8_12

1 Introduction

From many decades of construction material technology, it has been well known that soil is strong in compression as well as in shear while very weak in tension. Tension weakness of soil was overcome by the insertion of tensile material like geotextile within soil. Recently, the utilization of geotextile is broadly common in civil engineering especially, for the enhancement of soft soils, slope stabilization, and the construction of retaining walls and embankments for infrastructure amenities such as roads, highways, and railways. Several research works and theories were performed in many laboratories dealing with the reinforcement of granular and fine soils with geotextile.

Several papers have been studied to understand the beneficial effect of soil reinforcement [1–7]. Ingold and Miller [1] conducted triaxial tests on Kaolin clay reinforced using aluminum plates as well as permeable plastic layers under undrained conditions. Fabian and Fourie [2] presented the outcome of undrained tests that showed reinforcement material with high transmissivity could increase the undrained shear strength of clay by 40% while a material with low transmissivity can decrease the undrained shear strength by 40%. Ling and Tatsuoka [3] studied the behavior of saturated silty clay using plane strain device under drained condition; the results demonstrated that tensile stresses were mobilized by utilizing geotextile, ensuring a beneficial effect of reinforcement. Unnikrishnan et al. [4] performed static and cyclic loading undrained triaxial compression tests to evaluate the shear and deformation behavior of reinforced clay soils. Tafreshi et al. [5] performed triaxial tests on geotextile-reinforced silty sand to see the effects of a number of several geotextile layers and confining pressure at different imposed strain levels.

Noorzad and Mirmoradi [6] used to conduct unconfined and undrained triaxial tests to see the effects of confining pressure, soil type, relative compaction, and a number of reinforcement layers on the reinforced soil. Nguyen et al. [7] performed triaxial compression tests to investigate the shear behavior of sand and the mobilization of shear at the soil-geotextile interface.

The present study's aim is to understand the interaction between soil and nonwoven geotextile reinforcement under triaxial compression loading. Consolidated undrained triaxial tests are performed on sand-silt mixture reinforced with geotextile reinforcement. Failure patterns and horizontal displacement were visualized using Plaxis 2D finite element software for case of geotextile-reinforced silty sand specimen under axis-symmetric triaxial loading.

Three consolidated undrained tests were conducted on unreinforced sand specimens under different confining pressure whereas a total of twelve tests were performed on both unreinforced and reinforced silty sand specimens, in which silt content of 25% was maintained i.e., limiting fines content. It causes the increase in the voids between sand particles due to the adding up of silt content up to this point, loosen up the specimen causing an increase in excess pore pressure which in turn decreases the shear strength of soil.

2 Test Materials

2.1 Soil

Locally available uniform sand was used in this study and has been classified as SP. The non-plastic silt used in this study was collected from Katraj, Pune Maharashtra. Grain size distribution or the percentage of various sizes of soil grains present in a given dry sand soil sample is an important soil grain property (Fig. 1). The index properties of sand, silt, and sand-silt mixture are presented in Table 1.

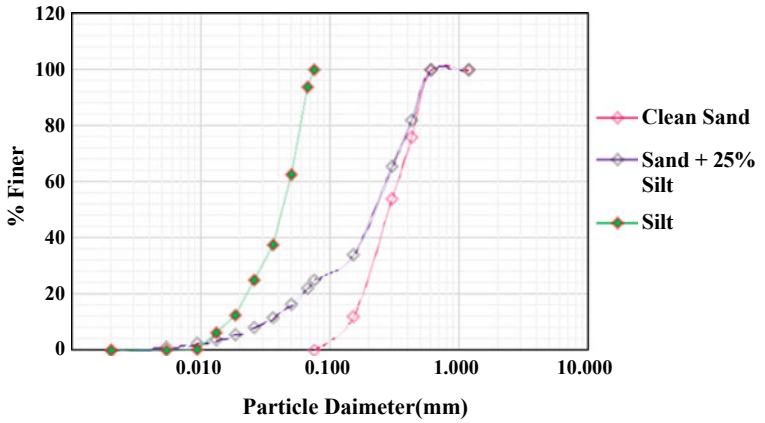

Fig. 1 Gradation curve for sand, silt, and sand-silt mixture

Table 1 Index properties of soils used in this study

Soil type	Sand	Silt	Sand + 25% Silt
D_{50} (mm)	0.280	0.061	0.225
C_u	2.240	3.671	8.660
C_c	0.850	1.163	1.620
G_S	2.416	2.751	2.484
γ_{min} (kN/m^3)	13.98	12.65	14.81
γ_{max} (kN/m^3)	15.16	15.70	17.13
e_{min}	0.609	0.753	0.450
e_{max}	0.745	1.175	0.677
W_L (%)	NP	NP	NP
Wc (%)	ND	ND	ND
P.I. (%)	NP	NP	NP

2.2 Reinforcement Material

A commercially available nonwoven geotextile reinforcement material provided by the manufacturers SKAPS was used in this study. This material was chosen because the deformation could be regained easily after load applied to the reinforcement was removed. The specifications for geotextile is summarized in Table 2.

3 Sample Preparation and Testing Procedure

A total of 15 consolidated undrained (CU) triaxial compression tests were carried out on the unreinforced clean sand, silty sand, and reinforced silty sand under different effective confining pressures (i.e., 50, 100, and 200 kPa) and comprises of zero to three geotextile layers alternatively placed at regular intervals. The size of sample was 75 mm diameter and 150 mm height. Experimental program is shown in Table 3. An automated acquisition system was used for obtaining experimental data. For sample preparation moist tamping method was used. In this method, pre-weighed quantity of soil mixed with 5% water and poured into a rubber membrane stretched inside a split mould and compacted carefully with tamper in five layers of calculated

Table 2 SKAPS GT-180 conforms to the minimum average roll values (MARV) listed below

Property	Test method	Metric (MARV)
Grab tensile strength	ASTM D 4632	0.911 kN
Grab elongation	ASTM D 4632	50%
Trapezoid tear strength	ASTM D 4633	0.378 kN
CBR puncture resistance	ASTM D 6241	2.370 kN
Permittivity	ASTM D 4491	1.35 s^{-1}
Water flow	ASTM D 4491	3657 l/min/m^2
Apparent opening size (AOS)	ASTM D 4751	0.180 mm
UV resistance	ASTM D 4355	70%/500 h

Table 3 Experimental program

Soil	Silt content	Confining pressure (kPa)	No. of geotextile layers	No. of tests
	0%	50, 100, 200	0	3
			0	3
Sand	25%	50, 100, 200	1	3
			2	3
			3	3
				Total tests = 15

height and weight. The unit weight and relative density of silty sand specimens were 15.14 kN/m^3 and 30%, respectively. After compaction and leveling of each silty sand layer, the geotextile was placed horizontally in the specimen as shown in Fig. 2 and geotextile arrangement is shown in Fig. 3. After the specimen was prepared, it was put into the triaxial cell for saturation. Cell was filled with water, and a effective confining pressure of 50 kPa was applied. To obtain a satisfactory degree of saturation, carbon dioxide gas was introduced into the soil sample at low pressure than confining pressure (50 kPa) for 15–20 min, letting air free. After that confining pressure and back pressure were applied to facilitate the saturation of the soil specimen. The Skempton pore pressure coefficient B, i.e., ($\Delta u/\Delta\sigma^3$), was checked during the saturation process. After saturation of the soil specimen it was isotropically consolidated under three confining pressures of 50, 100, and 200 kPa and then loaded axially at a 1.25 mm/min strain rate and tests were complete when axial strain reached 15% (Table 3).

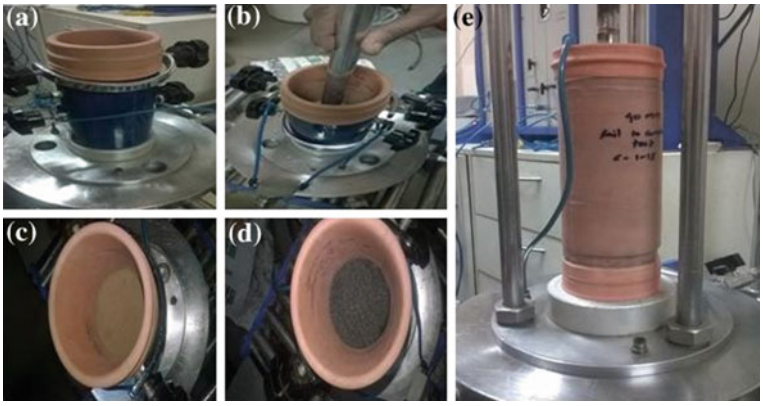

Fig. 2 **a** Stretching of membrane by applying vacuum; **b** compaction; **c** compacted silty sand; **d** geotextile placed horizontally; **e** complete reinforced specimen ready for test

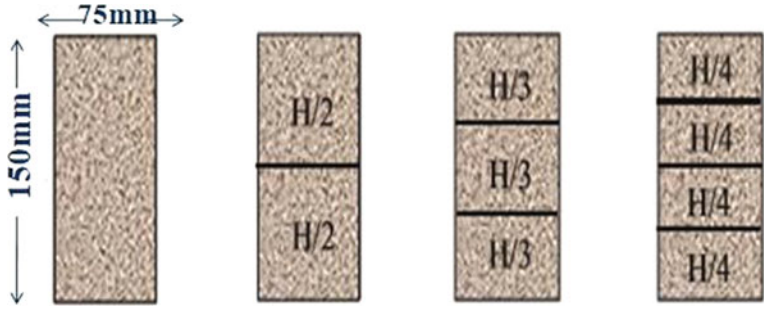

Fig. 3 Arrangement of geotextile layers for triaxial test

4 Results and Discussion

4.1 Deviator Stress–Axial Strain Behavior

Figure 4a shows the peak deviator stress–axial strain behavior of the specimen in unreinforced condition for different effective confining pressures. It was clearly seen that for the unreinforced specimen, stress reached its peak value at very low value of axial strain of 3%. Strength of the soil decreases and becomes steady until this test was stopped at an axial strain of 15%. Results show that as effective confining stress moves from 50 to 200 kPa and the peak deviator stress increases from 13 to 52 kPa and becomes steady. Figure 4b shows the variation of deviator stress with axial strain of three geotextile-reinforced specimens at different confining pressures. Results shows that as effective confining stress moves from 50 to 200 kPa the peak deviator stress increases from 95 to 207 kPa at larger axial strain.

Moreover, geotextile inclusion caused reduction in the loss of post-peak deviator stress, which shows that inclusion of permeable nonwoven geotextile proved effective in improving the shear strength of the sand-silt mixture. Fabian and Fourie [2] observed that the permeability of reinforcement affects water migration and moisture distribution within specimen and decreases the increase in pore water pressure due to dissipation through radial movement of water under undrained condition. It was observed that as effective confining stress and quantity of geotextile increased, peak deviator stress also increased. A similar trend is observed in case of one, and two geotextiles reinforced silty sand.

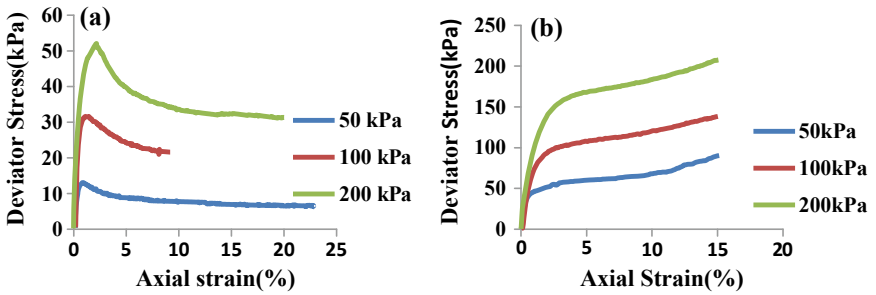

Fig. 4 Stress–strain behavior of: **a** unreinforced silty sand specimen; **b** three geotextile-reinforced silty sand specimen

4.2 *Effective Stress Path and Excess Pore Pressure Generation*

Figure 5a shows the effective stress path of the unreinforced specimen for different effective confining stresses. Results show that for the unreinforced specimen, deviator stress increases up to peak shear strength and then it starts to decrease. This happens due to an increase in excess pore pressure (Fig. 5b). The same trend is observed in a change of pore water pressure in case of unreinforced and reinforced specimen, i.e. excess pore pressure increases with an increase in axial strain and becomes steady, (Fig. 6b), however, peak shear strength is found to be increased after geotextile inclusion as shown in Fig. 6a.

Geotextile inclusion improved the interaction between the soil and the reinforcement by mobilizing the tensile force, which in turn increases the overall strength of the reinforced silty sand (Tensioned membrane reinforcement mechanism). The other mechanism involved is that the reinforcement is reversing the interface shear stress to act inward, thereby increasing the shear strength of a soil specimen (Lateral restraint reinforcement mechanism).

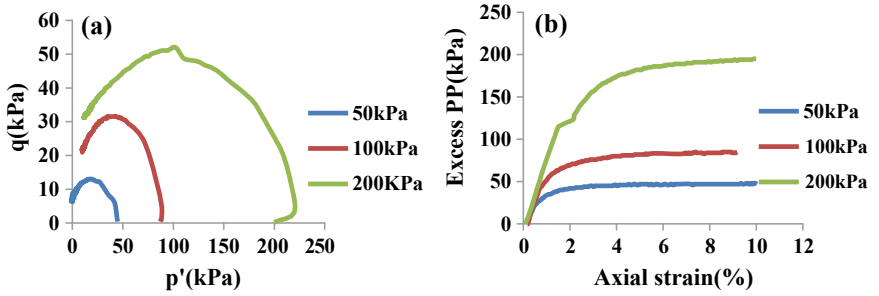

Fig. 5 **a** Effective stress path and; **b** excess pore water pressure responses of unreinforced silty sand specimen at a different confining pressure

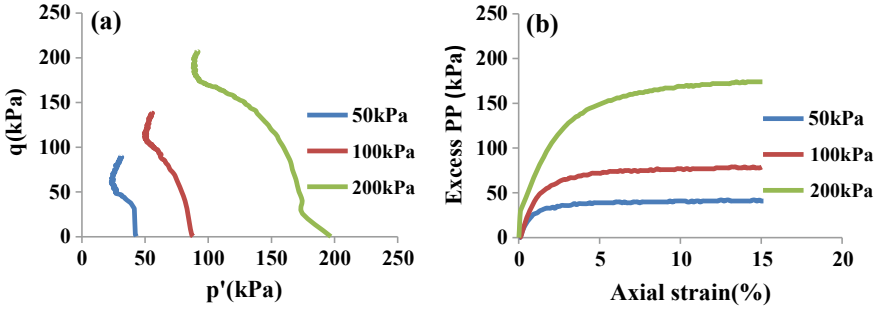

Fig. 6 **a** Effective stress path and; **b** excess pore pressure responses of three geotextile-reinforced silty sand specimen at a different confining pressure

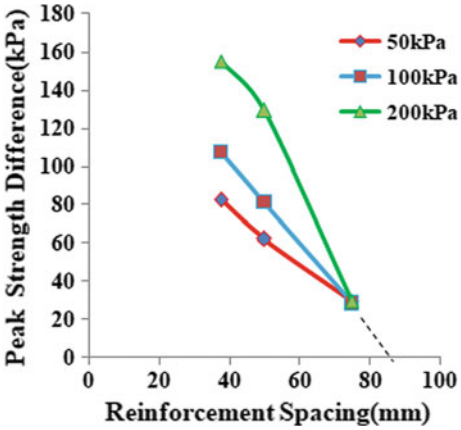

Fig. 7 Variation of shear difference with reinforcement spacing

4.3 Strength Difference

The beneficial effect of reinforcement on improving the net shear strength was evaluated using strength difference (S.D.), i.e., the peak deviator stress difference between nonwoven geotextile-reinforced specimens and unreinforced specimens at a particular confining pressure.

$$\text{S.D.} = \sigma_{d,max,re} - \sigma_{d,max,un} \tag{1}$$

Figure 7 shows that the strength difference decreased significantly as reinforcement spacing increased. The strength difference may reduce to zero (extrapolation of the curves in Fig. 6 to the horizontal axis) at certain reinforcement spacing. This work indicated that when the spacing of reinforcement was in the range of 77–85 mm, which is equivalent to spacing/diameter ratios of 1.02–1.13, the peak strength difference reduced from 29 kPa to 0. This observation corroborates triaxial compression test results on sand specimen reinforced with geotextile obtained by Gray and Al-Refeai [8]. They concluded that geotextile reinforcements placed at spacing/diameter ratios >1 had little or no effect on enhancing the peak deviator stress of reinforced soil.

4.4 Variation of Peak Deviator Stress with Confining Pressure

Figure 8 shows the effect of increase in effective confining pressure on peak deviator stress in both case of unreinforced as well as of reinforced sand-silt mixture with one, two, and three layers of geotextile. For both cases there is an increase in deviator stress with increase in effective confining pressure. There is more increase in value

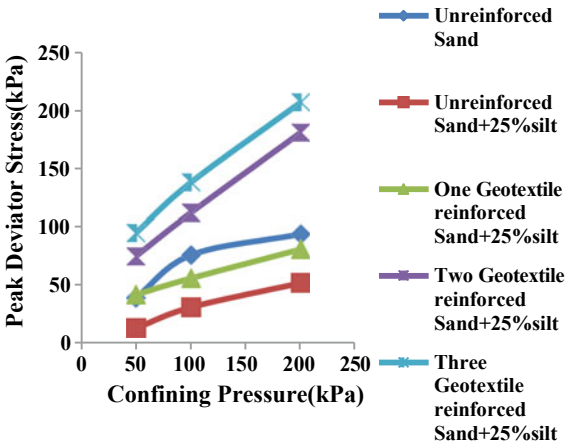

Fig. 8 Variation of peak deviator stress with confining pressure on unreinforced and reinforced specimen

of deviator stress from 39.07 to 93.98 kPa in case of unreinforced clean sand when compared with the deviator stress values that is from 13 to 52 kPa for unreinforced silty sand specimen, with increase in effective confining pressure from 50 to 200 kPa. Moreover, it was observed that for one geotextile layer reinforced silty sand specimen peak shear strength value increases from 42 to 81 kPa and for two geotextile layers reinforced silty sand specimen, it moves from 75 to 181 kPa, which is further less than the peak shear strength value for three geotextile-reinforced silty sand specimen, i.e., from 95 to 207 kPa by increasing effective confining pressure.

Actually, the mobilized reinforcement force increases as the quantity of reinforced layers and effective confining pressure increases. Moreover, peak value of shear strength was observed for three geotextile-reinforced silty sand specimen.

5 Failure Envelope

Shear strength parameters (c and ϕ) of unreinforced and reinforced silty sand specimen are calculated from peak $p' - q$ plot (Fig. 9). Where angle of internal friction (ϕ) has been calculated using equation proposed by Ishihara [9]:

$$M = (6 \sin \phi)/(3 - \sin \phi) \tag{2}$$

where, $M = q/p'$, q = peak deviator stress, p' = effective mean principal stress.

Where, q = peak deviator stress, p' = effective mean principal stress.

The calculated angle of internal friction and cohesion from peak $p' - q$ plot is shown in Fig. 10a and b, respectively. The result showed that the angle of internal friction and cohesion increased as the number of reinforcement layers increased, which ultimately increased the shear strength of soil.

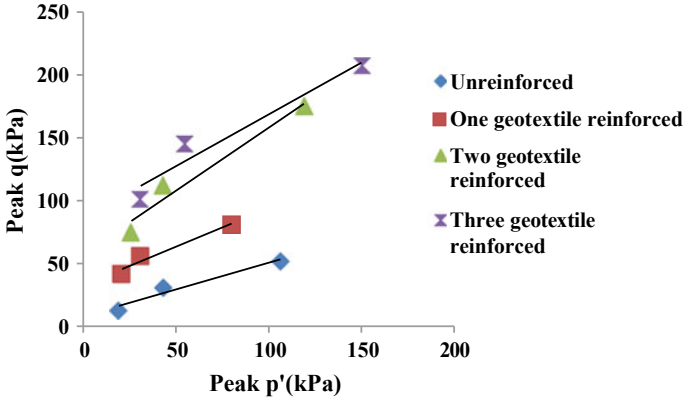

Fig. 9 Peak p′-q plot of unreinforced and reinforced specimen at different confining pressures

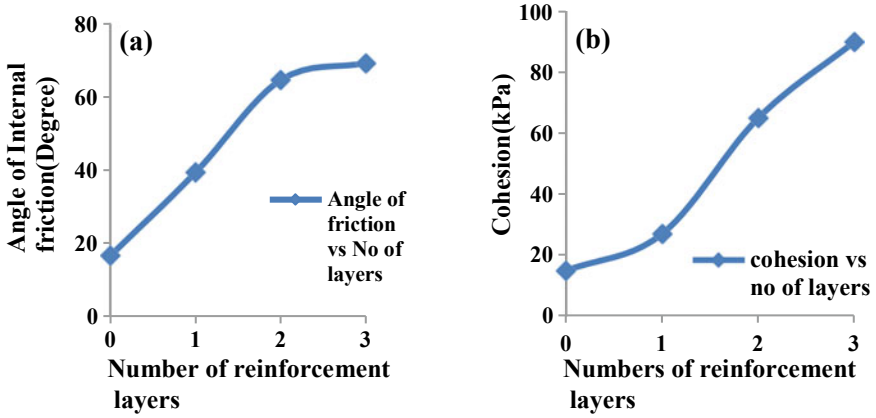

Fig. 10 **a** Friction angle and; **b** cohesion for unreinforced and reinforced silty sand specimen

6 Mode of Failure

Figure 11a–d shows photographs of unreinforced and reinforced specimens and the deformed geotextile after tests. The unreinforced specimen failed after bulging at its middle. The reinforced silty sand specimens (Fig. 11b–d) failure occurred due to bulging at the middle of two geotextile layers. The inclusion of reinforcement restrained the horizontal displacement of soil near the reinforced area, and consequently, larger horizontal displacement occurred in the middle of two geotextile layers. Moreover, comparatively less bulging (uniform) occurred as the number of reinforcement layers increased. The uniform deformation of a specimen suggested that the mobilized stresses were redistributed properly within the soil, thus improving the shear strength of the geotextile-reinforced soil. Similar behavior of the reinforced

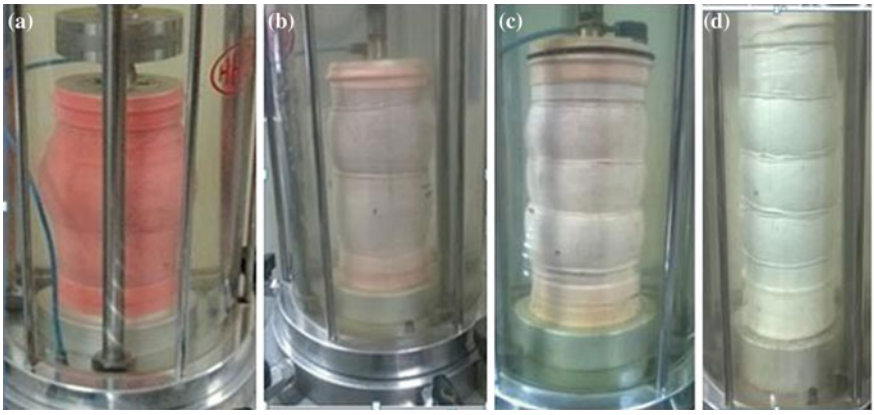

Fig. 11 Failure pattern of: **a** unreinforced; **b** one geotextile reinforced; **c** two geotextile; **d** three geotextile-reinforced specimen

specimens was reported by Nguyen et al. [7], Haeri et al. [10], and Khedkar and Mandal [11] for reinforced sand and Fabian and Fourie [2] for reinforced clay.

7 Finite Element Analysis

Finite element analysis was carried out using Plaxis 2D software for numerical simulation the case of unreinforced as well as for geotextile-reinforced silty sand specimen under axisymmetric triaxial loading conditions at only 50 kPa confining pressure. Axisymmetric Mohr–Coulomb model was considered for this problem as mentioned above. Figure 12a, b shows the geometry of unreinforced and one geotextile layer reinforced samples, respectively. Boundary conditions was applied as per Plaxis software standards. Confining pressure (σ_3), and prescribed displacement (15% = 0.0225 mm) applied to the sample as shown in Fig. 12. The properties of sand-silt mixture used in plaxis analysis are shown in Table 1. Failure behavior was visualized in finite element analysis for 15% prescribed displacement. Outcomes show that maximum horizontal displacement occurred at middle, in case of unreinforced specimen when compared to geotextile-reinforced specimen. The inclusion of reinforcement restrained the horizontal displacement of soil near the reinforced area, and consequently, larger horizontal displacement occurred in the middle of two geotextile layers. As the quantity of geotextile reinforcement layers increased (i.e., the shorter vertical reinforcement space), horizontal displacement decreased, as shown in Fig. 13.

The material properties obtained from experimental results, used for silty sand used in finite element methods are unit weight = 15.14 kN/m^3, poisons ratio = 0.25, cohesion = 15 kPa, angle of internal friction for unreinforced condition = 16.7°, Elasticity modulus = 3000 kN/m^2, and reinforcement properties from Table 2, used

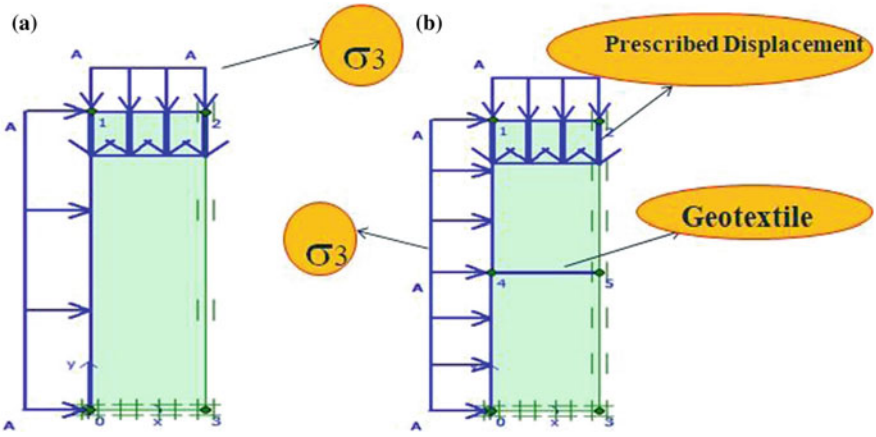

Fig. 12 **a** Geometry of unreinforced sample; **b** geometry of one geotextile-reinforced silty sand specimen

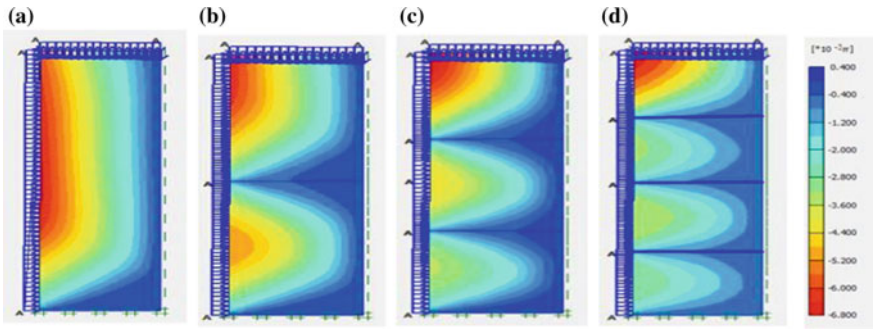

Fig. 13 Horizontal displacement at 50 kPa: **a** unreinforced sample; **b** one geotextile-reinforced sample; **c** two geotextile-reinforced sample; **d** three geotextile-reinforced sample

for geotextile are stiffness of reinforcement = 18.22 kN/m, thickness = 2 mm and flexural rigidity = 6.2 kNm^2/m.

8 Conclusions

- Test results obtained in this study show that the response of reinforced silty sand was influenced by confining pressure and reinforcement spacing.
- The increase in number of geotextile inclusion and effective confining pressure improved the interaction between the soil and the reinforcement by mobilizing the tensile force, which in turn increases the overall strength of the reinforced silty sand.

- There is increment in the evaluated values of cohesion and internal angle friction, i.e., (c and ϕ) with increase in the number of geotextile layers.
- The results verified that the insertion of nonwoven geotextile reinforcement into sand-silt mixture enhanced peak deviator stress and decreased the loss of post-peak shear strength.
- Bulging is more in case of unreinforced specimen as compared to geotextile-reinforced specimen because the lateral displacement restrained due to geotextile inclusion.

Finally, it should be reminded that the data obtained in this study relates to laboratory tests on saturated silty sand reinforced with flexible nonwoven geotextile under triaxial undrained conditions. The conducted tests simulate the worst conditions of reinforced soil, although these conditions deviate noticeably from those likely to prevail on-site, where the soil is probably partially saturated. Also, the reinforcement with higher stiffness and tensile strength is usually used for the GRS structures in the field. Despite these differences, the test data are expected to give useful information to interpret the behavior and failure mechanism of reinforced earth.

Acknowledgements All experiments were conducted in Geotechnical Engineering Laboratory (Civil Engineering Department) of College of Engineering Pune, Pune (C.O.E.P.). The authors are extremely grateful for this support.

References

1. Ingold TS, Miller KS (1983) Drained axisymmetric loading of reinforced clay. J Geotech Eng 109(7):883–898
2. Fabian K, Fourie A (1986) Performance of geotextile-reinforced clay samples in undrained triaxial tests. Geotext Geomembranes 4(1):53–63
3. Ling HI, Tatsuoka F (1993) Laboratory evaluation of a nonwoven geotextile for reinforcing on site soil. In: Proceeding of geosynthetics 93(2), 533-546
4. Unnikrishnan N, Rajagopal K, Krishnaswamy NR (2002) Behaviour of reinforced clay under monotonic and cyclic loading. Geotext Geomembr 20(2):117–133
5. Moghaddas Tafreshi SN, Asakereh A (2007) Strength evaluation of wet reinforced silty sand by triaxial test. Int J Civ Eng 5(4):274–283
6. Noorzad R, Mirmoradi SH (2010) Laboratory evaluation of the behavior of a geotextile reinforced clay. Geotext Geomem 28(4):386–392
7. Nguyen MD, Yang KH, Lee SH, Tsai MH, Wu CS (2013) Behavior of nonwoven-geotextile-reinforced sand and mobilization of reinforcement strain under triaxial compression. Geosynth Int 20(3):207–225
8. Gray DH, Al-Refeai T (1986) Behavior of fabric-versus fiber-reinforced sand. J Geotech Eng 112(8):804–820
9. Ishihara K (1993) Liquefaction and flow failure during earthquakes. Geotechnique 43(3):351–451
10. Haeri SM, Noorzad R, Oskoorouchi AM (2000) Effect of geotextile reinforcement on the mechanical behavior of sand. Geotext Geomembranes 18(6):385–402
11. Khedkar MS, Mandal JN (2009) Behaviour of cellular reinforced sand under triaxial loading conditions. Geotech Geol Eng 27(5):645–658

12. Ling HI, Tatsuoka F, Wu J T, Nishimura J (1993) Hydraulic conductivity of geotextiles under typical operational conditions. Geotext Geomembranes 12(6):509–542
13. Yang K-H, Yalew WM, Nguyen MD (2016) Behavior of geotextile-reinforced clay with a coarse material sandwich technique under unconsolidated-undrained triaxial compression. Int J Geomech 16(3):1–15

Pseudo-static Slope Stability Analysis for Cohesive-Frictional Soil by Using Variational Method

Sourav Sarkar and Manash Chakraborty

Abstract In this research work, the factor of safety of a rectilinear slope consisting of cohesive-frictional soil subjected to seismic load is determined on the basis of the calculus of variation theory and pseudo-static analysis. Unlike the conventional limit equilibrium method, variational calculus method neither requires kinematical assumption (i.e. the shape of the critical slip surface) nor any static assumption (i.e. distribution of normal stress along the slip surface). The factor of safety (F) is defined as a functional of normal stress and slip surface. The functional is minimized using Euler-Lagrangian equation. The critical slip surface and consequently critical factor of safety, F_s is being obtained by employing the (i) transversality conditions and the boundary conditions at the intersection of slip surface and the slope surface and (ii) continuity conditions and natural boundary conditions at the intermediate point of the slip surface. The value of F_s is obtained for different combinations of soil friction angle, and slope angle, β corresponding to varying horizontal (k_h) and vertical (k_v) seismic coefficients. The results suggest that the seismic coefficients, especially the value of k_h have significant impact on the stability of the slope. The design charts are prepared for different combinations of , β, k_h and k_v. For a certain , the factor of safety decreases with the increase of k_h, k_v and β. The available solutions compare quite well with the available solution for the pseudo-static slope stability analysis.

Keywords Variational calculus · Slope stability · Seismic coefficient · Limit equilibrium method

1 Introduction

Slope stability analysis is a classical problem in soil mechanics. Almost for the last eight decades, this problem was studied rigorously by several researchers [5, 7, 9,

S. Sarkar · M. Chakraborty (✉)
Indian Institute of Technology (Banaras Hindu University), Varanasi 221005, India
e-mail: manashchakra.civ@itbhu.ac.in

A. Prashant et al. (eds.), *Advances in Computer Methods and Geomechanics*, Lecture Notes in Civil Engineering 55,
https://doi.org/10.1007/978-981-15-0886-8_13

11, 18, 23, 26, 27]. Most of these studies were based on limit equilibrium approach. It is a well-known fact that the slope stability problem is an indeterminate problem and hence, the factor of safety cannot be obtained directly from the static equilibrium equations. In order to make these problems determinate, few assumptions are being considered for the analysis. These assumptions are related to the failure surfaces, interslice forces, and normal stress distribution along the slip surface. Due to the massive advancement in computational flexibility, in the recent few decades, different numerical schemes were employed for the slope stability analysis.

By using the available analytical and numerical technique, quite a number of works had been carried out for analyzing the stability of homogeneous c- slope subjected to seismic forces. Newmark [20] considered the plane sliding surface for homogeneous dams and embankments consisting of cohesionless soil and proposed sliding block theory for estimating permanent displacement of slope during earthquake. Goodman and Seed [10] assumed planar rupture surface for earthquake-induced slope stability consisting of cohesionless soil. Sarma [24] considered circular rupture surface for homogeneous dams and embankments influenced by seismic forces. Leshchinsky and San [14] used Baker and Garber's [4] variational approach in stability of slope with applied horizontal seismic acceleration. Ling and Leshchinsky [16] considered log-spiral failure surface for predicting the seismic performances of slopes. Kramer and Smith [13] introduced the permanent displacement effect of soil above the rupture surface and considered the dynamic response of soil above the slip surface. Sarma [25] calculated seismic bearing capacity of shallow foundation constructed near sloping surface. Rathje and Bray [21] analyzed earth structure considering nonlinear coupled seismic sliding. Loukidis et al. [17] used limit analysis to analyze the stability of slope under seismic loading condition. Wartman et al. [28] analytically studied dynamic response and deformation of the rigid inclined block due to shaking. Choudhury et al. [8] analyzed stability of slope under static and seismic conditions by using limit equilibrium approach. The failure surface of slope was considered to be circular.

It is clearly observed from the literature study that very few works had been done earlier for analyzing the soil slopes under seismic forces by using variational approach. The advantage of variational approach is that no prior assumptions regarding the critical slip surface and the normal stress distributions along the slip surface need to be considered. Kopacsy [12] was the first to introduce variational method in slope stability problem. Thereafter, few studies [2–4, 6, 19, 22] were carried out for the slope stability problems by using the calculus of variation.

In this present study, variational method is used to determine the critical slip surface and corresponding factor of safety for any slope subjected to seismic loading. The formulations proposed by Castillo and Revilla [22] for analyzing the homogenous cohesive soil slopes are extended here for any generalized c- soil and incorporating the pseudo-static seismic forces. The critical factor of safety (F_s) is obtained for different combinations of slope angle (β) and angle of friction (φ) of soil corresponding to varying horizontal (k_h) and vertical (k_v) seismic coefficients. The obtained critical slip surfaces are also presented for few cases.

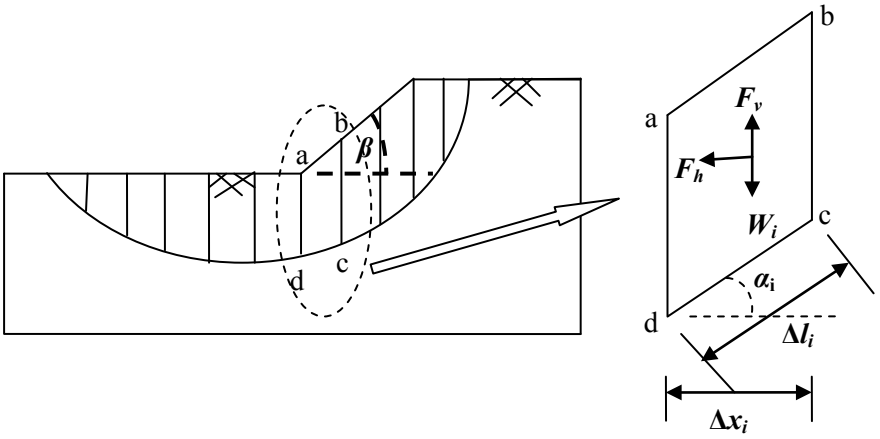

Fig. 1 Schematic diagram of a slope along with slip surface and considered slices

2 Problem Statement and Mathematical Background

A rectilinear slope of angle β with homogeneous $c - \varphi$ soil is subjected to vertical and horizontal seismic forces. It is intended to determine the critical failure surface and factor of safety for the given slope. Figure 1 shows the considered problem along with the chosen domain. The size of the domain is kept sufficiently high so that the failure surface is well contained within the domain. However, it is to be noted that the size of the domain has no influence on the computed solution.

The factor of safety is defined as the ratio of the available resisting moment to actual driving moment. Both these parameters are the function of the slip surface and the slope surface and hence they can be represented as functional. To determine the critical failure surface of a slope these functionals are required to optimize. To optimize the safety functional Euler-Lagrangian equation, as suggested in the calculus of variation, is being used. Pseudo-static analysis is being carried out for incorporating the seismic forces.

3 Analytical Formulation of the Problem

In this problem, the variational method is used in the framework of ordinary method of slice [9] under both vertical and horizontal seismic force. For any slice, i, as shown in Fig. 1, the equation of static equilibrium along x and y directions are satisfied. Hence, the factor of safety can be formulated as:

$$F = \frac{\sum_{i=1}^{n} [c\Delta l_i + \{(W_i - F_v)\cos\alpha_i - F_h \sin\alpha_i\}\tan\varphi]}{\sum_{i=1}^{n} (W_i \sin\alpha_i + F_h \cos\alpha_i - F_v \sin\alpha_i)} \tag{1}$$

where,

(i) c and are the cohesion and the internal friction angle of the soil.
(ii) W_i, Δx_i, Δl_i and α_i are the weight, width, length and the inclination angle of the ith slice, respectively; n represents the total number of slices.
(iii) $F_v (= k_v W_i)$ and $F_h = (k_h W_i)$ are the vertical and horizontal seismic forces, respectively.

By correlating Δl_i with Δx_i and plugging the expressions of F_v and F_h in Eq. (1) the factor of safety can be further expressed as:

$$F = \frac{\sum_{i=1}^{n} [c \Delta x_i \sec^2 \alpha_i + W_i \{(1 - k_v) - k_h \tan \alpha_i\} \tan \varphi]}{\sum_{i=1}^{n} W_i [(1 - k_v) \tan \alpha_i + k_h]} \tag{2}$$

This formulation is being expressed as the continuous slope surface by following the work of Revilla and Castillo [22], Baker and Garber [4]

$$F = \frac{\int_{x_0}^{x_3} [c\left(1 + y_i'^2\right) + \gamma (f_i - y_i)\left\{(1 - k_v) - k_h y_i'\right\} \tan \varphi] dx}{\int_{x_0}^{x_3} \gamma (f_i - y_i)\left[(1 - k_v) y_i' + k_h\right] dx} = \frac{\int_{x_0}^{x_3} P\left(x, y, y'\right) dx}{\int_{x_0}^{x_3} R(x, y, y') dx} \tag{3}$$

where,

(i) $\tan \alpha_i = y_i'$; $\sec^2 \alpha_i = 1 + y_i'^2$

(ii) $W_i = \gamma (f_i - y_i) \Delta x_i$; γ is unit weight of the soil, f_i and y_i represents the slope and the slip surfaces and
(iii) x_0 and x_3 are the abscissas of two end-points where slip surface cuts the slope profile.

The rectilinear slope shown in Fig. 1 can be mathematically expressed with the following three functions in the range of x_0 and x_3:

$$f_1(x) = 0 \quad x_0 \le x \le 0 \tag{4a}$$

$$f_2(x) = \frac{h}{h_1} x \quad 0 < x < h_1 \tag{4b}$$

$$f_3(x) = h \quad h_1 \le x \le x_3 \tag{4c}$$

Corresponding to each $f_i(x)$ there would be a distinct $y_i(x)$ in the interval of (x_{i-1}, x_i). The expression of factor of safety in Eq. (3) takes the following form:

$$F = \frac{\int_{x_0}^{x_1} P_1\left(x, y_1, y_1'\right) dx + \int_{x_1}^{x_2} P_2\left(x, y_2, y_2'\right) dx + \int_{x_2}^{x_3} P_3\left(x, y_3, y_3'\right) dx}{\int_{x_0}^{x_1} R_1\left(x, y_1, y_1'\right) dx + \int_{x_1}^{x_2} R_2\left(x, y_2, y_2'\right) dx + \int_{x_2}^{x_3} R_3\left(x, y_3, y_3'\right) dx} \tag{5}$$

The above functionals are required to be minimized to obtain critical slip surface and corresponding critical factor of safety, F_s. This is being performed by using Euler-Lagrangian equation as follows:

$$F_s = \frac{\frac{\partial P}{\partial y_i} - \frac{d}{dx}\left(\frac{\partial P}{\partial y_i'}\right)}{\frac{\partial R}{\partial y_i} - \frac{d}{dx}\left(\frac{\partial R}{\partial y_i'}\right)}; (i = 1, 2, 3) \tag{6}$$

After using Euler's equation the factor of safety can be written as:

$$F_s = \frac{2cy_i'' + \gamma \tan\varphi\left[(1 - k_v) - f_i' k_h\right]}{\gamma\left[(1 - k_v) f_i' + k_h\right]} (i = 1, 2, 3) \tag{7}$$

From Eq. 7, the slip surface in the three different ranges, as mentioned in Eqs. 4a, 4b and 4c, can be obtained. Figure 2 depicts all the three surfaces. These surfaces are constructed with the assumptions that the factor of safety remains to be the same along the slip surface. The three surfaces are:

$$y_1 = -\frac{\gamma \tan\varphi(1 - k_v)}{4c} x^2 + \frac{k_h}{4Nh} x^2 + B_1 x + D_1 \tag{8a}$$

$$y_2 = -\frac{\gamma \tan\varphi\left[(1 - k_v) - \frac{h}{h_1} k_h\right]}{4c} x^2 + \frac{\left[(1 - k_v)\frac{h}{h_1} + k_h\right]}{4Nh} x^2 + B_2 x + D_2 \tag{8b}$$

$$y_3 = -\frac{\gamma \tan\varphi(1 - k_v)}{4c} x^2 + \frac{k_h}{4Nh} x^2 + B_3 x + D_3 \tag{8c}$$

Here, $N(= c/(F_s \gamma h))$ indicates the stability number. The equation of all the surfaces consists of two integration constants. Therefore, the total number of unknown

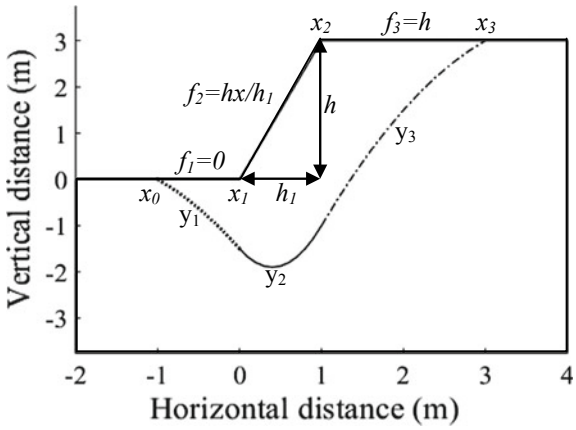

Fig. 2 Failure slip surface by variational method

parameters becomes nine—(i) x_0 and x_3, (ii) F_s and (iii) six integration constants (B_1, B_2, B_3, D_1, D_2 and D_3). These can be evaluated by the following nine equations.

(a) Two transversality conditions: Specified at two end-points (x_0 and x_3)

$$\left[P_{y'} - F_s R_{y'}\right]\left[f'(x) - y'(x)\right] + P - F_s R\,|_{x=x_i} = 0;\ \text{Where } (i = 0, 3) \quad (9)$$

(b) Two natural boundary conditions: Specified at two intermediate points x_1 and x_2 (i.e. the intersections of the slip surfaces)

$$y_i'(x_i) = y_{i+1}'(x_i)(i = 1, 2) \quad (10)$$

(c) Two continuity conditions: Specified at the intermediate points x_1 and x_2

$$y_i(x_i) = y_{i+1}(x_i)(i = 1, 2) \quad (11)$$

(d) Two boundary conditions: Specified at two end-points (x_0 and x_3)

$$y_1(x_0) = f_1(x_0) \quad (12)$$

$$y_3(x_3) = f_3(x_3) \quad (13)$$

(e) Equation for Factor of Safety, as provided in Eq. (5).

By using these nine equations nine unknown parameters can be evaluated. The expressions for the unknown parameters are as follows:

$$B_1 = B_2 = -1 + \frac{\gamma \tan\varphi(1 - k_v)}{2c}x_0 - \frac{k_h}{2Nh}x_0;$$

$$B_3 = 1 + \frac{\gamma \tan\varphi(1 - k_v)}{2c}x_3 - \frac{k_h}{2Nh}x_3$$

$$D_1 = D_2 = x_0 - \frac{\gamma \tan\varphi(1 - k_v)}{4c}x_0^2 + \frac{k_h}{4Nh}x_0^2$$

$$D_3 = \frac{\gamma h h_1 k_h \tan\varphi}{4c} + \frac{h_1(1 - k_v)}{4N} + \frac{\gamma h_1 \tan\varphi(1 - k_v)(x_0 - x_3)}{2c} - \frac{k_h h_1(x_0 - x_3)}{2Nh} + \frac{k_h x_0^2}{4Nh} - 2h_1 + x_0 - \frac{\gamma \tan\varphi(1 - k_v)x_0^2}{4c}$$

$$N = \frac{(1 - k_v) + \frac{k_h}{h}(x_3 - x_0)}{4 - \frac{\gamma h \tan\varphi k_h}{c} + \frac{\gamma \tan\varphi(1 - k_v)(x_3 - x_0)}{c}}$$

$$x_3 = \frac{-B + \sqrt{B^2 - 4AC}}{2A}$$

Most of the seismic failures in homogenous soil slopes are reported [14, 15, 1, 18] to fail by developing toe failure surface. Hence in the present analysis the value of x_0 is considered to be equal to zero.

For $x_0 = 0$,

$$A = \frac{\gamma h \tan\varphi(1-k_v)^2}{4c} + \frac{\gamma h \tan\varphi k_h^2}{4c}$$

$$B = h(1-k_v) - hk_h - \frac{\gamma h h_1 k_h^2 \tan\varphi}{4c} - \frac{\gamma h h_1 \tan\varphi(1-k_v)^2}{4c}$$

$$C = -hh_1(1-k_v) - h^2(1-k_v)$$

4 Results and Discussions

In the present article some typical slopes are analyzed using the formulation derived by using the calculus of variation. The cohesion ($c = 5\,\text{kN/m}^2$), the unit weight of soil ($\gamma = 20\,\text{kN/m}^3$) and the height of the slope ($h = 10\,\text{m}$) are maintained to be the same for all the cases. The factor of safety is calculated for different combinations of φ and β corresponding to varying k_h and k_v. The slope inclination angle (β) is varied within the range of 20° to 90° with a 5° interval. For each specific value of β, (i) three different internal friction angle, namely, 35°, 40° and 45° are chosen. The magnitude of k_h is kept equal to 0.1, 0.2 and 0.3 and corresponding to each k_h the vertical seismic coefficient k_v is varied as 0, $0.5k_h$ and k_h. As the slope is homogeneous, the failure is considered as toe failure ($x_0 = 0$).

Table 1 shows the typical results of critical factor of safety for slopes with different φ and β and subjected to different combinations of horizontal and vertical seismic forces. The results are presented for four different values of β, namely, 20°, 30°, 40° and 50°. Figure 3 shows the variation of critical factor of safety with k_h for different values of k_v/k_h. The graphs present the critical slip surface for different values of friction angle corresponding to four different value of β—25°, 35°, 55° and 65°. It is clearly observed from the obtained solutions that the critical factor of safety decreases with increase in horizontal and vertical seismic acceleration coefficient. For an example, for $\beta = 25°$ and =35°, when the value of k_h increases from 0 to 0.1 factor of safety reduces by 21% and for the same slope the factor of safety reduces by 34% when the value of k_h increases from 0 to 0.2. It is also noticed that the factor of safety reduces with (i) increase in β and (ii) decrease in φ. For $k_h = 0.2$, $k_v = 0.5k_h$ and $\beta = 25°$ the factor of safety improves by 18% with the increase in from 40° to 45°. Reduction of the slope angle further improves the stability of the slope. The critical factor of safety increases by 25% with the decrease of angle of slope from 35° to 25° for = 45° soil and $k_h = k_v = 0.2$.

Figure 4 shows the shape of the critical slip surface for $\beta = 60°$ and 80° with different combination of k_h and k_v. The volume of soil within the failure surface

Table 1 Critical factor of safety for different slopes corresponding to different seismic coefficients

k_h	φ	$\beta = 20°$			$\beta = 30°$			$\beta = 40°$			$\beta = 50°$		
	k_v	35°	40°	45°	35°	40°	45°	35°	40°	45°	35°	40°	45°
0	0	2.06	2.44	2.88	1.36	1.60	1.88	1.00	1.17	1.36	0.78	0.90	1.04
	0.00	1.57	1.86	2.20	1.11	1.31	1.53	0.84	0.98	1.14	0.66	0.76	0.87
0.10	0.05	1.55	1.84	2.17	1.10	1.30	1.52	0.83	0.97	1.13	0.65	0.75	0.86
	0.10	1.54	1.82	2.15	1.09	1.29	1.51	0.82	0.96	1.12	0.64	0.74	0.85
	0.00	1.26	1.50	1.77	0.93	1.09	1.28	0.71	0.83	0.96	0.56	0.64	0.73
0.20	0.10	1.22	1.44	1.70	0.91	1.07	1.25	0.70	0.82	0.95	0.55	0.63	0.72
	0.20	1.17	1.38	1.63	0.88	1.03	1.21	0.69	0.80	0.92	0.54	0.62	0.71
	0.00	1.06	1.25	1.48	0.80	0.94	1.10	0.62	0.72	0.83	0.48	0.55	0.62
0.30	0.15	0.98	1.16	1.37	0.75	0.88	1.04	0.60	0.68	0.79	0.46	0.53	0.60
	0.30	0.89	1.05	1.24	0.70	0.82	0.96	0.56	0.64	0.74	0.44	0.50	0.57

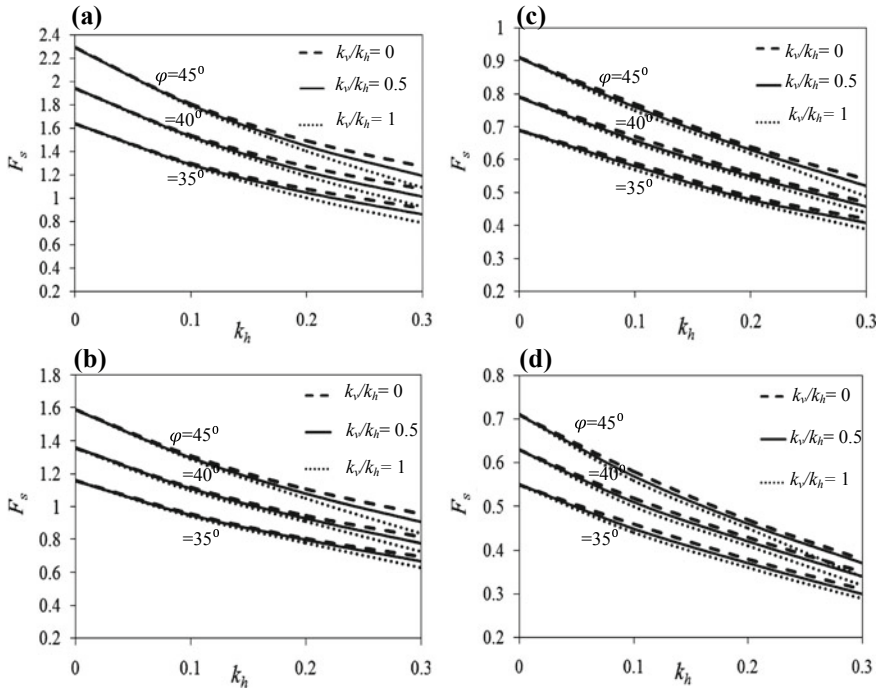

Fig. 3 Variation of critical factor of safety with k_h for: **a** $\beta = 25°$; **b** $\beta = 35°$; **c** $\beta = 55°$; **d** $\beta = 65°$

decreases as the strength of the soil (φ) increases. This feature is being observed irrespective of all slope angles. The shape of the slip surfaces changes significantly as the geometric profile of the slope changes. The figure also gives an impression that incorporation of the seismic forces increases the volume within the critical slip surface.

5 Comparison of Results

Table 2 shows the comparison of the present obtained solutions from the variational approach with the results provided by Newmark [20] and Choudhury et al. [8]. The comparisons are carried out for different values of and k_h correspond to three different β, namely, 20°, 25° and 30°. In this comparative study, the magnitude of k_v is kept equal to zero. The present analytical solutions are quite agreeable with the available solutions. It is to be noted that Newmark [20] assumed the failure surface to be planar and Choudhury et al. [8] considered the failure surface to be circular. However, in the present study there was no such approximation prior to the analysis.

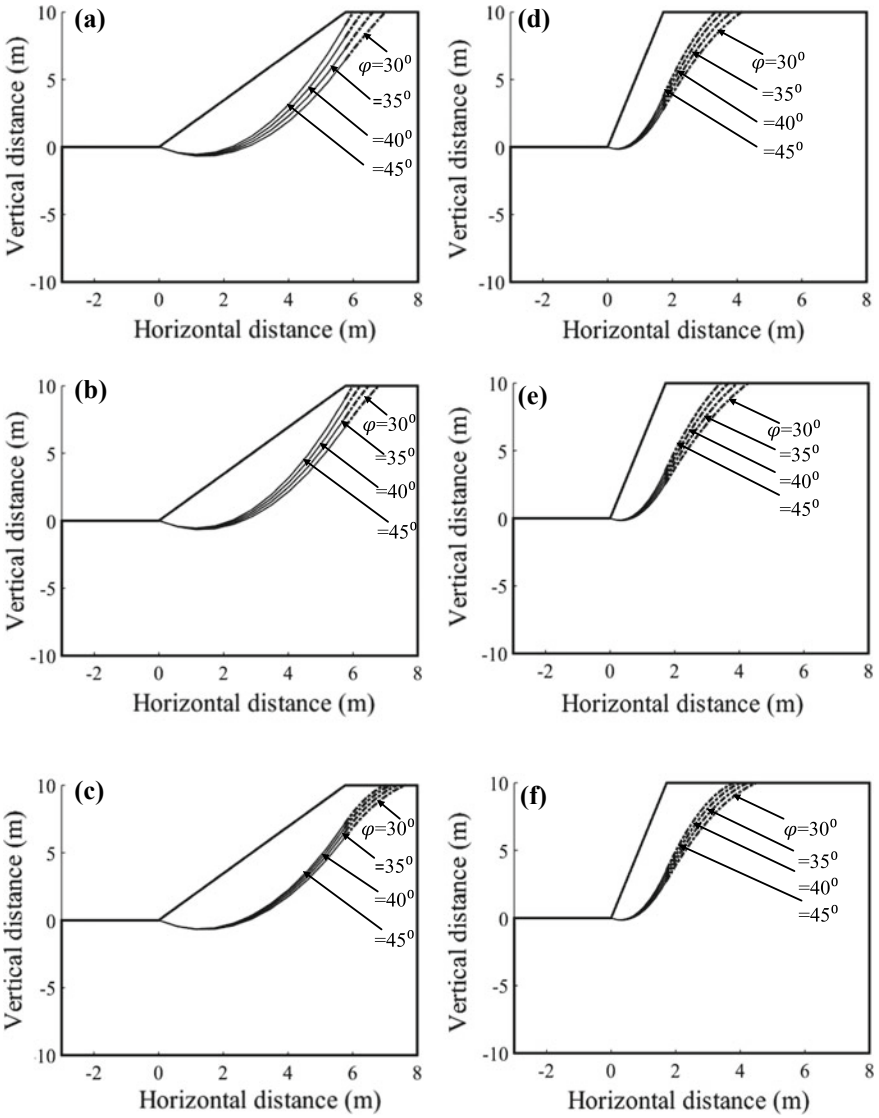

Fig. 4 Form of the critical slip surfaces for: **a** $\beta = 60°$, $k_h = k_v = 0$; **b** $\beta = 60°$, $k_h = 0.3$, $k_v = 0$; **c** $\beta = 60°$, $k_h = k_v = 0.3$; **d** $\beta = 80°$, $k_h = k_v = 0$; **e** $\beta = 80°$, $k_h = 0.3$, $k_v = 0$; and **f** $\beta = 80°$, $k_h = k_v = 0.3$

6 Conclusions

The present article provides pseudo-static analysis of slope using variational method considering no prior assumption on the shape of rupture surface. Design charts are

Table 2 Comparison of factor of safety values obtained by Newmark [20] and Choudhury et al. [8] with the present solutions considering $k_v = 0$

φ	k_h	$\beta = 20°$			$\beta = 25°$			$\beta = 30°$		
		Newmark [20]	Choudhury et al. [8]	Present study	Newmark [20]	Choudhury et al. [8]	Present study	Newmark [20]	Choudhury et al. [8]	Present study
35°	0.1	1.45	1.31	1.57	1.37	1.25	1.30	–	–	1.11
	0.2	1.15	1.15	1.26	–	–	1.08	–	–	0.93
40°	0.1	1.74	1.35	1.86	1.72	1.34	1.54	1.48	1.19	1.31
	0.2	1.38	1.2	1.50	1.34	1.1	1.27	–	–	1.09
	0.3	1.13	1.04	1.25	–	–	1.08	–	–	0.94
45°	0.1	2.08	1.63	2.20	2.01	1.61	1.81	1.79	1.43	1.53
	0.2	1.64	1.44	1.77	1.62	1.43	1.49	1.52	1.30	1.28
	0.3	1.34	1.28	1.48	1.31	1.21	1.27	–	–	1.10

being provided for the factor of safety for different (i) soil properties (φ), (ii) slope geometry (β) and (iii) seismic forces (k_h and k_v). The factor of safety decreases with increase in k_h and k_v and decrease in soil strength. For both the static and pseudo-static case it is observed that the factor of safety reduces drastically with increase in slope angle. The critical slip surface is being plotted for several cases. The obtained solutions compared quite well with the available solutions. This instills further confidence to employ the calculus of variation for solving other stability problems.

Acknowledgements The corresponding author acknowledges the support of 'Department of Science and Technology (DST), Government of India' under grant number DST/INSPIRE/04/2016/001692.

References

1. Ausilio E, Conte E, Dente G (2000) Seismic stability analysis of reinforced slopes. Soil Dyn Earthq Eng 19(3):159–172
2. Baker R, Shukha R, Operstein V, Frydman S (2006) Stability charts for pseudo-static slope stability analysis. Soil Dyn Earthq Eng 26(9):813–823
3. Baker R (2003) Sufficient conditions for existence of physically significant solutions in limiting equilibrium slope stability analysis. Int J Solids Struct 40:3717–3735
4. Baker R, Garber M (1978) Theoretical analysis of the stability of slopes. Geotechnique 28(4):395–411
5. Bishop AW (1955) The use of the slip circle in the stability analysis of slopes. Geotechnique 5(1):7–17
6. Chen J, Yang Z, Hu R, Zhang H (2016) Study on the seismic active earth pressure by variational limit equilibrium method. Shock Vib 1–11. Hindawi Publishing Corporation
7. Chen ZY, Morgenstern NR (1983) Extensions to the generalized method of slices for stability analysis. Can Geotech J 20(1):104–119
8. Choudhury D, Basu S, Bray J (2007) Behaviour of slopes under static and seismic conditions by limit equilibrium method. J Embankments Dams Slopes 1–10
9. Fellenius W (1936) Calculation of stability of earth dam. In: Transactions. 2nd Congress Large Dams, Washington, DC, vol 4, pp 445–462
10. Goodman RE, Seed HB (1966) Earthquake-induced displacements in sand embankments. J Soil Mech Found Eng ASCE 92:125–146
11. Janbu N (1954) Application of composite slip surface for stability analysis. Proc Eur Conf Stab Earth Slopes Sweden 3:43–49
12. Kopacsy J (1961) Distribution des constraintes a' 1a rupture, forme de 1a surface de G1issement et hauteur Theorique des Talus. In: Proceedings 5th international conference on soil mechanics and foundation engineering, vol II. Paris
13. Kramer SL, Smith MW (1997) Modified Newmark model for seismic displacements of compliant slopes. J Geotech Geoenviron Eng ASCE 123(7):635–644
14. Leshchinsky D, San KC (1994) Pseudostatic seismic stability of slopes: design charts. J Geotech Eng ASCE 120:1514–1532
15. Ling HI, Leshchinsky D, Mohri Y (1997) Soil slopes under combined horizontal and vertical seismic accelerations. Earthquake Eng Struct Dyn 26(12):1231–1241
16. Ling HI, Leshchinsky D (1995) Seismic performance of slopes. Soils Foundation 35:85–94
17. Loukidis D, Bandini P, Salgado R (2003) Stability of seismically loaded slopes using limit analysis. Geotechnique 53(5):463–479

18. Morgenstern NU, Price VE (1965) The analysis of the stability of general slip surfaces. Geotechnique 15(1):79–93
19. Narayan CGP (1975) Variational methods in stability analysis of slopes. PhD dissertation submitted to Indian Institute of Technology, Delhi, India
20. Newmark N (1965) Effects of earthquake on dams and embankments. Geotechnique 15(2):139–160
21. Rathje EM, Bray JD (2000) Nonlinear coupled seismic sliding analysis of earth structures. J Geotech Geoenviron Eng ASCE 126(11):1002–1014
22. Revilla J, Castillo E (1977) The calculus of variations applied to stability of slopes. Geotechnique 27(1):1–11
23. Sarma SK (1973) Stability analysis of embankments and slopes. Geotechnique 23:423–433
24. Sarma SK (1975) Seismic stability of earth dams and embankments. Geotechnique 25:743–761
25. Sarma SK (1999) Seismic bearing capacity of shallow strip footings adjacent to a slope. In: Proceedings of 2nd international conference on earthquake geotechnical engineering, Lisbon, Balkema, pp 309–313
26. Spencer E (1967) A method of analysis of the stability of embankments assuming parallel inter-slice forces. Geotechnique 17(1):11–26
27. Taylor DW (1937) Stability of earth slopes. J Boston Soc Civ Engineers 24(3):197–247
28. Wartman J, Bray JD, Seed RB (2003) Inclined plane studies of the Newmark sliding block procedure. J Geotech Geoenviron Eng ASCE 129(8):673–684

Bearing Capacity of Clayey Soil Reinforced with Geogrid

Prachi Lingwal and Ashok Kumar Gupta

Abstract Foundations constructed on soil deposits, cohesive in nature or having plasticity, result in low load-bearing capacity, and settlement exceeding permissible value. This may cause structural damage and reduction in the durability of structure. Conventionally the weak cohesive soil was either excavated and replaced with layer of stronger granular material or the size of footing was increased, or both the methods were adopted. These methods are uneconomical and time-consuming. Further, stability of cohesive soil is difficult because of low permeability which takes substantial time to consolidate. Therefore, the use of geosynthetic material has emerged. This study shows the results of laboratory investigation on square footing resting on clayey soil of medium plasticity reinforced with Geogrid. A square footing of dimension 75 mm $\times$ 75 mm made of mild steel is used. The important parameters that were examined in this study include the vertical distance between the base of footing and first geogrid layer, the number of geogrid layers, the vertical distance between each geogrid layer and its effect on the ultimate bearing capacity. All the experiments were conducted in a steel tank with transparent acrylic sheet in front. The results of tests performed showed that with the incorporation of geogrid in soil increases the bearing capacity as compared to unreinforced soil. The optimal distance of the top geogrid layer from bottom of footing was found to be 0.35B. There was increase in bearing capacity with increase in geogrid layers, however this effect decreases with increase in layers beyond influence depth. Bearing capacity of the soil reduces with increase in the vertical distance between the geogrids.

Keywords Shallow foundation · Cohesive soil · Geogrid · Bearing capacity · Medium plasticity

P. Lingwal (✉)
Civil Engineering, Delhi Technological University, Delhi, India
e-mail: prachilingwal57@gmail.com

A. K. Gupta
Department of Civil Engineering, Delhi Technological University, Delhi, India
e-mail: akgupta@dtu.ac.in

A. Prashant et al. (eds.), *Advances in Computer Methods and Geomechanics*, Lecture Notes in Civil Engineering 55,
https://doi.org/10.1007/978-981-15-0886-8_14

1 Introduction

Soft soils have low shear strength, and are highly compressible with low permeability, generally having shear strength less than 40 kPa and easily molded by applying light pressure. Construction on soft soils is a great challenge because of inadequate bearing capacity which can cause excessive settlement after construction, and also instability of soil while excavation. Due to settlement, load-carrying system of soil gets changed and if groundwater table at the location of construction is high, water will apply buoyancy force thus influencing the total surcharge on soil. This further leads to structural damage or reduction in the performance of the structure therefore affecting the durability of the structure. This will lead to making the structure fail before serving its intended purpose. The commonly used earlier methods involve removal of top existing cohesive soil and replacing it with adequately thick layer of granular fill to increase the load-carrying capacity or for reduction in settlement of the foundation. Another method adopted was to increase the footing size so that load can be distributed to a larger area and lesser pressure is induced in the soil. Sometimes both the methods were adopted to safeguard the structure. But these methods were not economical and didn't provide sufficient strength as actually required. With the increase in use of geosynthetic material in many engineering works as a reinforcement, has wide applications like mechanically stabilized earth walls, slopes, pavements, earth structure, reinforcing foundation soils, long-lasting road constructions, and stable embankment over soft soil.

From the past work done, it has been recorded that inclusion of reinforcement in the soil enhances the load-carrying capacity of the soil mass. One of the noticeable input in this area was made by Binquet and Lee [1] who suggested a method of finding the bearing capacity ratio (BCR). Thereafter researchers evaluated the potential of providing reinforcement for evaluation of bearing capacity ratio. They focused on finding parameters which would directly influence the BCR. Sakti and Das [8] presented laboratory investigation on model strip footing placed over soft clay bed reinforced with geotextile which was heat-bonded nonwoven polypropylene. Das and Omar [3] examined footing width effect on sand and concluded that BCR was practically constant when the width was equal to or more than 130 mm to 140 mm. Tafreshi and Dawson [11] presented laboratory test results of strip footing supported in unreinforced, and sand reinforced with a geotextile bed subjected to static and repeated loads. It was observed that rate of settlement decreased as number of loading cycles increased and with increase in amplitude of repeated load regardless of reinforcement. Lavasan and Ghazavi [6] presented experimental investigation performed on two closely spaced footings one having square shape and other having circular shape. The results obtained showed increase in the ultimate bearing capacity of the interfering footing by about 25–40% but it also showed increase in settlement of the order of 60–100% and tilt by 45% with one geogrid layer and 75% with two geogrid layers. Farsakha et al. [4] studied behavior of foundation on geosynthetic reinforced sandy soil. Test results showed that with two or more reinforcement layers, settlement can be reduced to about 20%. Results also showed that sand reinforced

with geogrid and geotextile composite behaved superior than sand reinforced with geogrid or geotextile alone. Reinforcement also distribute load more uniformly hence reducing stress concentration. Chen et al. [2] studied the behavior of foundations on clayey soil reinforced with geogrid. The result showed increased bearing capacity and reduction in settlement. Settlement could be reduced by more than 50% after providing three or more reinforcing layers.

2 Objective and Scope of Present Study

After reviewing various literatures, it was observed that many researchers have investigated sandy soil reinforced with a geosynthetic material, but limited information was available on clayey soil reinforced. The main purpose of research was to find the potential of clayey soil reinforced with a geosynthetic material. Therefore, for better understanding series of experiments were performed on clayey soil reinforced with geogrid. The parameters considered in this study include the top vertical distance between the base of footing and first geogrid layer (u), number of geogrid layers to be provided (N), vertical distance between the consecutive geogrid layers (h), and the type of reinforcement to be provided. The main objectives of this study were to inspect the benefits of providing reinforcement in clay, its effect on ultimate bearing capacity and to check the optimum number of reinforcing layers to be provided below the footing.

3 Material Properties and Test Procedure

The clayey soil used in this study for carrying out experimental investigation was collected from Tekanpur Town, near Gwalior City, Madhya Pradesh. The soil was intermediate plastic clay having plasticity index 22. The average undisturbed in situ unit weight of clay was 18.7 kN/m^3 with coefficient of internal friction as 4° having cohesion as 83 kPa. The maximum dry density of clay using standard Proctor test was observed as 16.1 kN/m^3 at optimum moisture content of 17.2%.

The testing tank used for carrying out all the experimental study was of dimensions 750 mm × 475 mm × 350 mm high. Compression testing machine (CTM) was used to give static concentrated load on the test footing resting on clay bed and the settlement was measured with help of dial gauges attached to the testing tank. A 25 mm thick mild steel plate square in shape, having dimension 75 mm × 75 mm was used as a footing. Figure 1 shows the line diagram of the testing tank having footing at the surface of the soil reinforced with geogrid. Clay was properly mixed at optimum moisture content which was found from standard Proctor test and placed in a testing tank and compacted in 3 layers with help of rammer falling freely from a height varying between 25 and 102 mm depending upon reinforcement spacing.

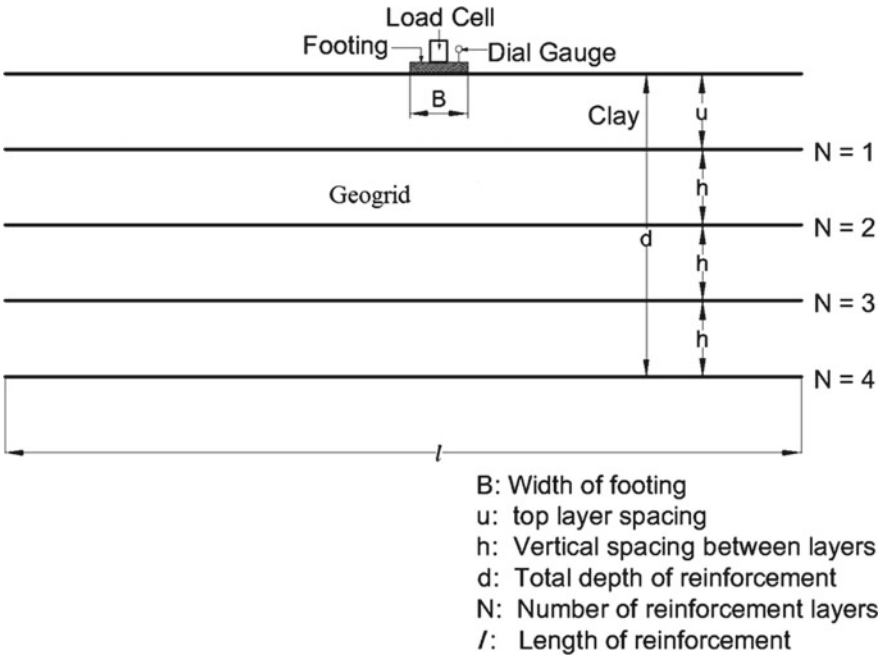

Fig. 1 Geogrid reinforced soil foundation

This was done in various trials for achieving the desired parameters of dry density and moisture content in the tank.

Two types of polypropylene geogrids were used for experimental investigation named here as Geogrid 1 (GG1) and Geogrid 2 (GG2). GG1 is of higher stiffness as compared to GG2. The properties of geogrids are provided by the manufacturer are listed in Table 1.

Table 1 Properties of the geogrid

Particulars		GG1	GG2
Tensile strength (kN/m)	MD*	5.5	3.6
	CD*	7.4	5.1
Tensile modulus (kN/m)	MD*	274	182
	CD*	372	255
Aperture size (mm)		30 × 30	10 × 10

MD* Machine direction
CD* Cross machine direction

4 Testing Procedure

The test was performed for unreinforced condition followed by reinforced condition by keeping square footing at the surface of the soil bed. The load was applied through Compression Testing Machine and the settlement was recorded with the help of dial gauges attached. Figure 1 shows the schematic view of the soil reinforced with geogrid and Table 2 shows the test programs and variables. Bearing capacity ratio (BCR) is defined as the ratio of bearing capacity of reinforced soil to that of unreinforced soil. Bearing capacity is obtained by double tangent method. Two tangents were drawn, one from the start of the curve and another from the end of the curve. The projection of interception on x-axis is the observed bearing capacity.

Table 2 Summary of model test

Test no	Reinforcement configuration	u, mm	u/B	h, mm	h/B	q, kPa	BCR
1	Unreinforced	–	–	–	–	520	–
2	GG1, N = 1	15	0.20	–	–	560	1.08
3	GG1, N = 1	26	0.35	–	–	580	1.12
4	GG1, N = 1	38	0.51	–	–	575	1.11
5	GG1, N = 1	50	0.67	–	–	545	1.05
6	GG1, N = 2	26	0.35	26	0.35	680	1.31
7	GG1, N = 3	26	0.35	26	0.35	730	1.40
8	GG1, N = 4	26	0.35	26	0.35	780	1.50
9	GG1, N = 3	26	0.35	15	0.20	800	1.54
10	GG1, N = 3	26	0.35	26	0.35	730	1.40
11	GG1, N = 3	26	0.35	38	0.51	700	1.35
12	GG1, N = 3	26	0.35	50	0.67	675	1.30
13	GG2, N = 1	15	0.20	–	–	620	1.19
14	GG2, N = 1	26	0.35	–	–	660	1.27
15	GG2, N = 1	38	0.51	–	–	650	1.25
16	GG2, N = 1	50	0.67	–	–	580	1.12
17	GG2, N = 2	26	0.35	26	0.35	740	1.42
18	GG2, N = 3	26	0.35	26	0.35	830	1.60
19	GG2, N = 4	26	0.35	26	0.35	840	1.62
20	GG2, N = 3	26	0.35	15	0.20	860	1.65
21	GG2, N = 3	26	0.35	26	0.35	800	1.54
22	GG2, N = 3	26	0.35	38	0.51	780	1.50
23	GG2, N = 3	26	0.35	50	0.67	690	1.33

BCR Bearing Capacity Ratio; u top layer spacing from footing base; h spacing between layers of footing; B width of footing; q load at peak

5 Comparison and Test Results

All the tests performed are compiled in Table 2. Ultimate BCR is observed at peak load. Bearing Capacity Ratio (BCR) is obtained at peak load.

5.1 Effect of Reinforcement's Top Spacing

Optimum vertical spacing between footing base and first reinforcement layer, u, was investigated using single layer of reinforcement of both type of geogrid, GG1 and GG2, placed below the base of footing. Figures 2 and 3 shows comparative variation

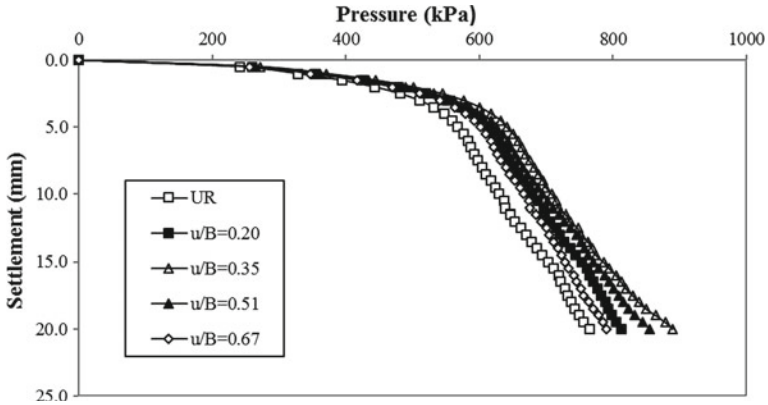

Fig. 2 Pressure–settlement curves with a single layer of GG1 placed at different top layer spacing

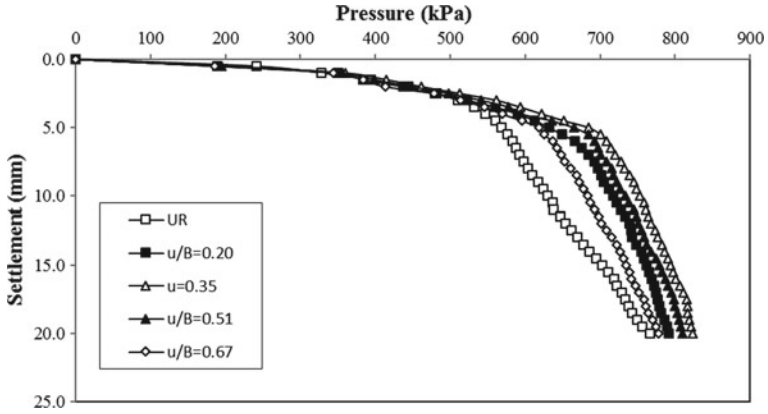

Fig. 3 Pressure–settlement curves with a single layer of GG2 placed at different top layer spacing

of pressure with settlement for GG1 and GG2. The figures show that the distance of vertical spacing increases bearing capacity increases up to maximum value at 26 mm, $u/B = 0.35$, after which there is a downturn in the Bearing Capacity. *u/B is* "top layer spacing ratio" and is defined as the distance of the first reinforcement from the base (u) to the width of the footing (B).

Similar observations were noted by Sakti and Das [8], Chen et al. [2]. Sakti and Das [8] where it was concluded that the incorporation of geotextile in saturated clay improves its bearing capacity. The optimum distance between footing base and first reinforcement is between 0.35 and 0.40B. Chen et al. [2] reported that maximum bearing pressure is found at 0.33B depth when the clay is reinforced with geogrid. For sand reinforced with geocell, Shadmand et al. [9] reported that the ideal vertical distance between the footing base and the first reinforcement layer is at a depth u, of 0.25B to 0.4B.

5.2 *Effect of Number of Reinforcement Layers*

Laboratory tests were performed over clay bed with various layers of reinforcement of two different types geogrid placed at a constant distance of 26 mm in between each layer. Figures 4 and 5 shows variation of pressure with increase in reinforcing layers for both type of geogrid, GG1 and GG2. It is observed that the pressure increases with increase in the number of reinforcements, N varying from 1 to 4. However, the rate of increase in bearing capacity became slight when the influence depth has reached. The increases in bearing capacity were slight after N = 3 form both the geogrid. The influence depth is a depth after which further increase in the number of reinforcing layers will not result much increase in the bearing capacity ratio. From

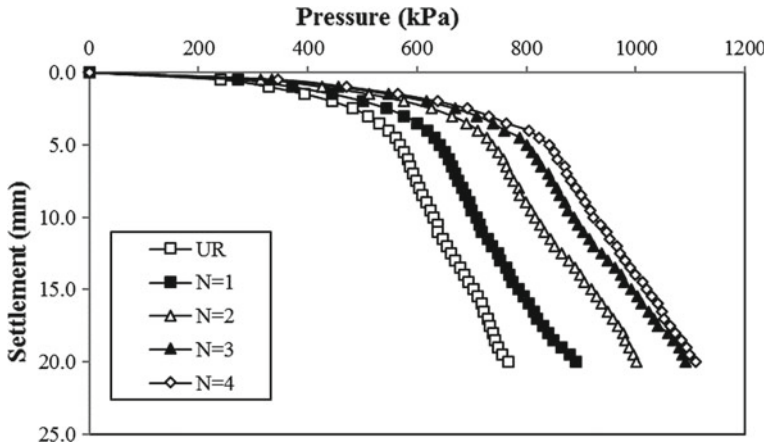

Fig. 4 Pressure–settlement curves with different number of reinforcing layers: GG2 geogrid

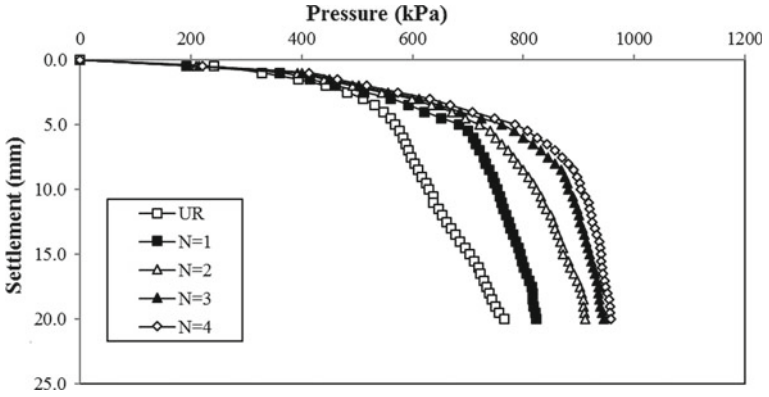

Fig. 5 Pressure–settlement curves with different number of reinforcing layers: GG2 geogrid

the test results, the influence depth is observed to be at a depth of 1.38*B*. Chen et al. [2] reported influence depth as 1.5*B* for a square footing for geogrid reinforcement in clay and 1.25*B* for geotextile reinforcement in clay. Shin et al. [10] observed that influence depth for strip footing over geogrid reinforced clay is 1.8*B*.

5.3 *Effect of Vertical Spacing Between Reinforcements Layers*

Vertical spacing between reinforcement effects was checked using 4 layers of reinforcement for both types of geogrid. The top layer distance of geogrid from the base of the footing was taken as 0.35*B*, i.e., optimum value. The variation in the geogrid layers was from 0.2*B* to 0.67*B*. Figures 6 and 7 shows the variation of pressure with settlement with varying vertical distance between the layers of reinforcement. *h*/*B* is defined as the ratio of vertical distance between the reinforcing layers (*h*) to the width of the footing (*B*). It was noted that ultimate bearing capacity drops with the increase in the vertical distance between layers with maximum value at 0.2*B*. The lesser the distance between reinforcing layers more is the bearing capacity. As suggested by many researchers, vertical spacing effect was driven by other factors also, like spacing between footing and top layer reinforcement distance (*u*), number of reinforcing layers (*N*), and modulus of elasticity of geogrid. The graph also indicates that there is no optimum value of vertical spacing between reinforcing layers. Similar observations were noted by Ingold and Miller [5], on clay reinforced with geogrid. In contrast to this, Yetimoglu et al. [12], performed study on sand reinforced with geogrid below rectangular footing reported that optimum distance between reinforcement having 4 layers is 0.2*B* with top layer spacing as 0.3*B*.

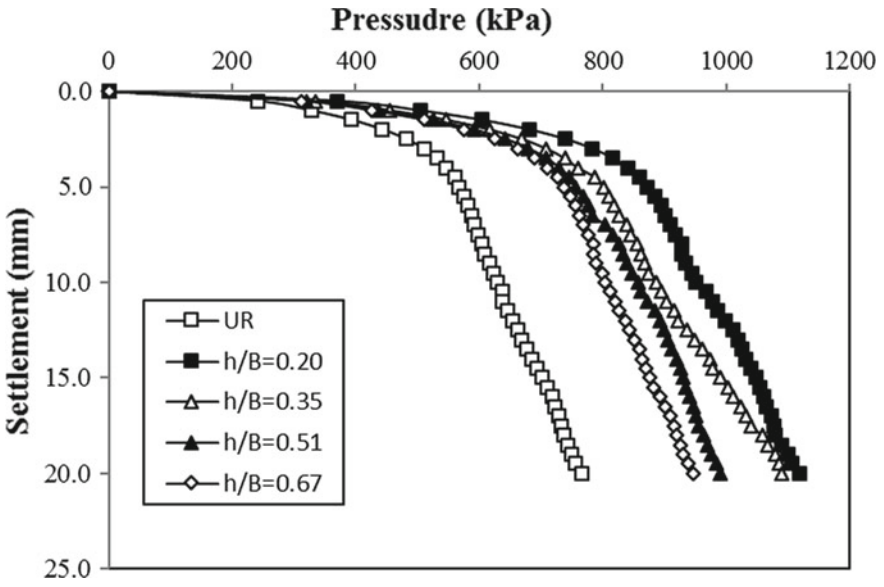

Fig. 6 Pressure–settlement curves with three layers of GG1 placed at different vertical spacing

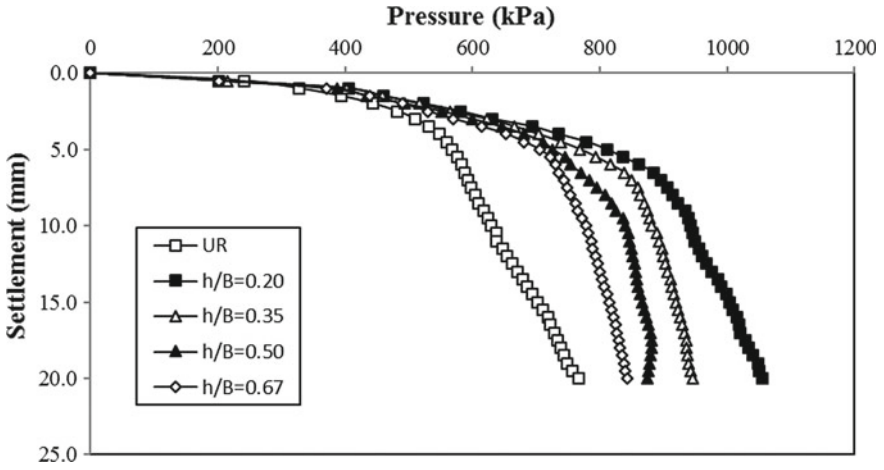

Fig. 7 Pressure–settlement curves with three layers of GG2 placed at different vertical spacing

5.4 Effect of Reinforcement Type and Stiffness

Figure 8 shows a graph plotted between BCR and Reinforcement Type. As seen, geogrid having high stiffness performs superior than that with lower stiffness that is GG1 performed better than GG2. Figure 8 shows that as the stiffness of the geogrid

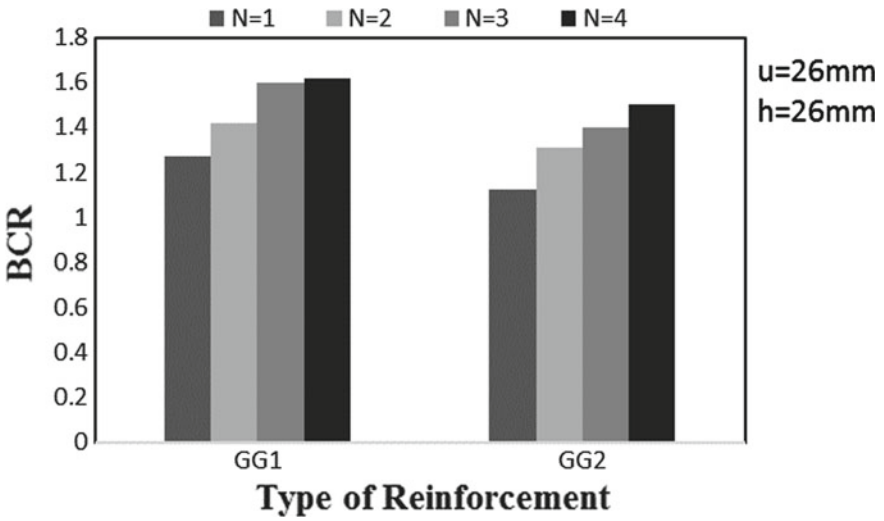

Fig. 8 BCR versus reinforcement type

increases there is an improvement in the bearing capacity ratio. It was also observed that it is also dependent on the settlement of the footing. Similar results were presented by Chen et al. [2] on a square footing resting on a clay bed with four different types of reinforcements. Lee and Manjunath [7] conducted a study on geogrid reinforced sand. Observation was made that geogrid which was having highest stiffness and smallest aperture performed better

6 Conclusions

Based on experimental results, the following conclusions were drawn:

- Optimum spacing of the top Geogrid from the base of the footing was observed around 0.35B on a square footing.
- Bearing capacity of the soil enhances with increase in n reinforcement numbers. The importance of providing additional layer falls with increase in number of layers.
- Bearing capacity drops with increase in vertical spacing between the reinforcement layers.
- Soil reinforced with high stiffness geogrid has high bearing capacity in comparison to the soil reinforced with low stiffness geogrid.

References

1. Binquet J, Lee KL (1975) Bearing capacity tests on reinforced earth slabs. J Geotech Eng Div 101(GT12):1257–1276
2. Chen Q, Farsakh M, Sharma R, Zhang X (2004) Laboratory investigation of behaviour of foundation on geosynthetic reinforced clayey soil. Transp Res Rec J Transp Res Board 28–38
3. Das BM, Omar MT (1994) The effects of foundation width on model tests for the bearing capacity of sand with geogrid reinforcement. Geotech Geol Eng 12:133–141
4. Farsakha M, Chen Q, Sharma R (2013) An experimental evaluation of the behaviour of the footings on Geosynthetic reinforced sand. Jpn Geotech Soc 53:335–348
5. Ingold TS, Miller KS (1982) Analytical and laboratory investigation of reinforced clay. In: Proceedings of 2nd international conference on geotextile, vol 3, pp 587–592
6. Lavasan A, Ghazavi M (2012) Behaviour of closely spaced square and circular footings on reinforced sand. Soil Found 52(1):160–167
7. Lee KM, Manjunath VK (2000) Experimental and numerical studies of geosynthetics-reinforced sand slopes loaded with a footing. Can Geotech J 37:828–842
8. Sakti JP, Das BM (1987) Model tests for strip foundation on clay reinforced with geotextile layers. Transportation Research Record No. 1153, National Research Council, Washington, D.C., pp 40–45
9. Shadmand A, Ghazavi, M Ganjian N (2018) Load-settlement characteristics of large scale square footing on sand reinforced with opening geocell reinforcement. Geotextiles Geomem 46:319–326
10. Shin EC, Das BM, Puri VK, Yen SC, Cook EE (1993) Bearing capacity of strip foundation on geogrid-reinforced clay. Geotech Test J 16(4):534–541
11. Tafreshi M, Dawson AR (2012) Laboratory tests of footing supported on geotextile reinforced sand under repeated loading. In: The 15th world conference on earthquake engineering, vol 25
12. Yetimoglu T, Jonathan TH, Saglamer A (1994) Bearing capacity of rectangular footing on geogrid reinforced sand. J Geotech Eng ASCE 120(12):2083–2099

Effect of Water Absorbing Polymer Amendment on Water Retention Properties of Cohesionless Soil

Abhisekh Saha, Bharat Rattan, S. Sreedeep and Uttam Manna

Abstract Water absorbing polymers (WAP) are chemically cross-linked structures formed with different hydrophilic groups (hydroxyl, amine, and carboxyl) capable of absorbing and storing a huge quantity of water within its three-dimensional network. Due to its high water absorbing capacity, these polymers find applications in improving the water retention behavior of the soil, particularly in arid and semiarid regions. Therefore, it is very important to study the improvement in water retention behavior of soil with different concentration of WAP amendment. The objective of this work is to investigate the effect of different rates (0, 1 g, 2 g, and 4 g/kg of soil) of WAP application on the water retention behavior of a locally available cohesionless soil. For this purpose, water retention characteristics curve (WRCC) of the soil was obtained by monitoring the soil suction and water content variation from saturated state to air-dried condition. The saturated water content and field capacity of the soil was found to be increased by 1.9 times and 2 times with highest amount of WAP addition than the control condition (without WAP). The results indicated that the water retention properties as well as the plant available water content (PAWC) significantly increased with WAP application, which indirectly indicates an increase in plant survival time in water stress conditions.

Keywords WAP · Soil amendment · Drought stress · Cohesionless soil · Suction · Water content · Matric potential sensor

1 Introduction

The problem related to inefficient use of rain and irrigation water by the crops is of great significance in the semiarid and arid regions where water is a limiting factor for plant growth and development [3, 10, 12, 16, 36]. As the rainfall intensity is very

A. Saha (✉) · B. Rattan · S. Sreedeep · U. Manna
Indian Institute of Technology Guwahati, Guwahati, India
e-mail: abhisekh@iitg.ac.in

A. Prashant et al. (eds.), *Advances in Computer Methods and Geomechanics*, Lecture Notes in Civil Engineering 55,
https://doi.org/10.1007/978-981-15-0886-8_15

limited in the semiarid regions, any mismanagement in water use can enhance the drought stress in the plants and crops. India is one of the most drought-prone countries in the world where more than 75% of the cropped area is in the semiarid region [25, 26, 44]. Therefore, appropriate policies are very much necessary to motivate better land management to meet sustainable food security. Cohesionless sandy and silty loams are the most common agricultural soils in the world and they provide proper drainage of water and aeration to the plant roots [37]. On the other hand, low water retention behavior of cohesionless soil can cause migration of nutrients to deeper layer and restricts plant growth. Addition of soil amendment is considered as the best management practice for this type of soils by many previous researchers [5–7, 13, 14, 18, 30]. The potential use of soil amendments is to increase soil-water and nutrient holding capacity over larger period of time especially in regions with water availability [2, 9, 31, 34, 35, 38, 39].

Water absorbing polymers (WAP), sometimes also known as superabsorbent hydrogels (SAH), are chemically cross-linked polymers which have an excellent potential to alleviate the negative effects of soil with low water holding capacity. WAP could be an ideal material to be used as a soil amendment as it absorbs and retains large quantities of water and solute molecules in a swollen state due to presence of different hydrophilic groups such as carboxyl group, amino group, hydroxyl group in the polymeric backbone [8, 15, 23, 24]. The commercially sold SAH in horticulture market has a water-absorbing capacity of 400–1500 g per gram of dry hydrogel [4, 11]. Most of the commercial WAPs are prepared from polymerization of sodium or potassium acrylate salts [17]. Several attempts were also made to synthesize WAP by utilizing cellulose, yeast, starch, chitosan, and other biodegradable waste products to avoid the environmental issues related to pure chemical products. Therefore, it is quite obvious that the water-absorbing capacity of the WAP largely depends on the monomeric composition of the polymer. Despite of various beneficial effects of WAP mentioned in the previous literature, a systematic study of water retention behavior of polymer amended soil is essential through measuring the soil suction and water content variation. Moreover, the appropriate application rate of WAP and its effect on the irrigation frequency need to be studied in detail.

With this perspective, the objective of this study to investigate the effect of different rates (0, 1 g, 2 g, and 4 g/kg of soil) of WAP application on the water retention behavior of a locally available cohesionless soil. The efficacy and suitability of some of the most used suction and water content sensors such as T5 tensiometer, MPS6 (also known as TEROS21) and 5TM for performance evaluation of polymer amended soil was explored. The measured WRCC curve of the bare soil and polymer amended soil indicated a significant increase in the water retention capacity with polymer concentration. The obtained results were also presented in terms of PAWC to obtain amount of water available to the plant roots. The field capacity (FC) and PAWC were increased by 2 times and 1.8 times with highest amount of WAP addition than the control condition (without WAP). Furthermore, the suction variation with time clearly indicates that WAP amendment can prolong plant survival time by an ample number of days during water stress conditions.

2 Materials and Methodology

2.1 Materials

A locally available cohesionless soil from IIT Guwahati campus was selected for this study. The basic geotechnical properties namely specific gravity and particle size distribution were evaluated as per the guidelines provided by the Indian standards [19–22]. The Particle size distribution curve was presented in Fig. 1 while all the basic properties of the used sample were listed in Table 1.

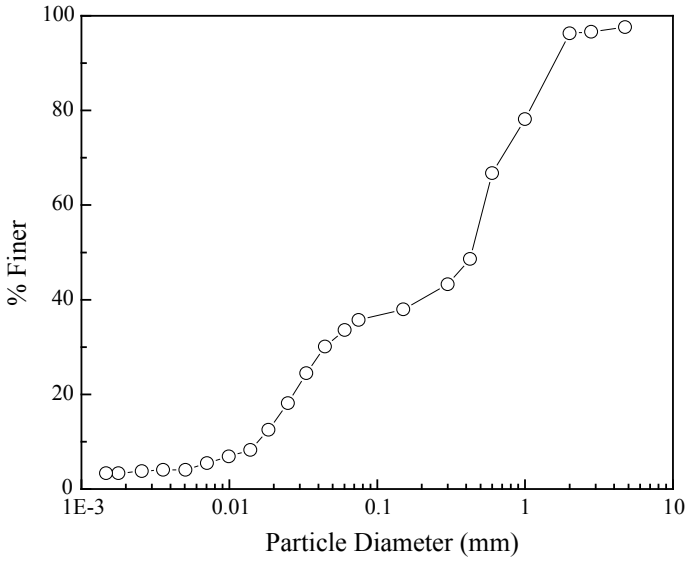

Fig. 1 Particle size distribution curve of the used soil

Table 1 Basic properties of the used soil

Properties	LS
Specific gravity	2.61
Particle size characteristics	
Coarse sand (4.75–2 mm)	11
Medium sand (2–0.425 mm)	38
Fine sand (0.425–0.075 mm)	19
Silt (0.075–0.002 mm)	30
Clay (<0.002 mm)	2
USCS classification	SM

Table 2 Water absorbency of the used polymer

	Distilled water	Tap water	0.9% NaCl solution
Water absorbency (g/g dry WAP)	282	179	74

A commercially available polymer namely Stockosorb, supplied by SargaGreen, Kerala, India was used in this study. It's an acrylic-based polymer with acrylamide cross-linked in the polymeric structure. The water absorbency of the WAP was evaluated in distilled water, tap water, and 0.9% NaCl salt solution and presented in Table 2.

2.2 Experimental Methodology

The MPS6 [32, 33], matric potential sensor was used in this study for measuring matric suction (ψ_m) of soil. The sensor measures the permittivity and water content of the ceramic disk by generating an electromagnetic (EM) field around the disk. The generated EM field is mainly confined to the ceramic disk of the sensor, so that the MPS6 measurement is independent of soil type. The matric suction was determined based on the previously established suction-water content relationship of the porous ceramic. According to the manufacturer calibration, the sensor has an operating range of 9 kPa (near saturation or wet state) to 10^5 kPa (near dry state).

T5 tensiometer, manufactured by UMS GmbH, Munich, Germany has been used to measure ψ_m up to 100 kPa. After inserting the tensiometer in soil, the water present in the tensiometer shaft tries to equilibrate with the water present in the soil-water via

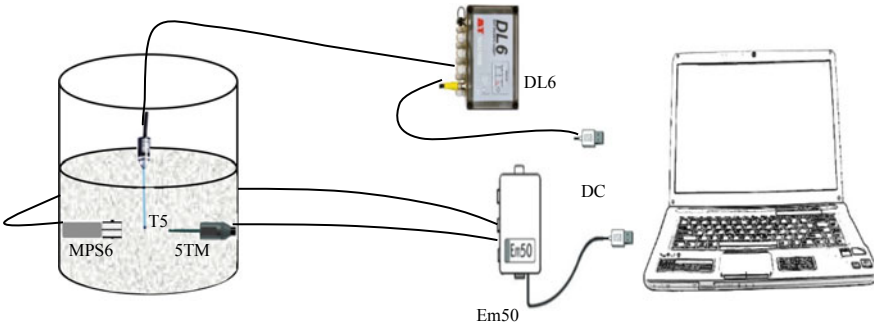

Fig. 2 Methodology adopted for measurement of WRCC of the used samples

the ceramic interface. The continuity of water between the ceramic and soil-water becomes extremely important for accurate measurement of suction. The continuity ensures that the negative pressure developed in soil will be identical with the water tension developed in the shaft. The changes in water tension in the shaft is captured electronically and converted to pressure (T5 User Manual, UMS [41]).

In our study, volumetric water content (θ) was measured using ECH2O 5TM [33]. The θ measurement is based on the dielectric permittivity of the soil which changes with the water content of the soil. The value of dielectric permittivity of water is 80, while for dry soil and air it is around 4 and 1, respectively. This broad range of permittivity helps in measuring the θ of the soil from saturated to dry state condition. The sensor is equipped with an oscillator to generate an electromagnetic field that charges the soil around the sensor. This stored charge is proportional to permittivity and θ, and is measured by the sensor. The dielectric permittivity was converted to θ by soil specific calibration equation developed for each case. For the sake of brevity, the detailed procedure was not discussed here.

The soil sample with different amounts of WAP concentration was mixed with sufficient amount of demineralized water to obtain a high water content sample for ensuring suction close to zero as the initial point. The mixed sample was placed in an airtight chamber for 24 h for maturation and uniform distribution of water content. The wet sample was placed in a PVC container of 10 cm diameter with MPS and 5TM sensors placed in the soil as shown in Fig. 2. Special care was taken to place the ceramic tip of T5, MPS and 5TM at the same level to avoid any influence of spatial variability. The whole setup was subjected to ambient drying till the sample reaches the permanent wilting point (PWP) which is suction corresponding to 1500 kPa.

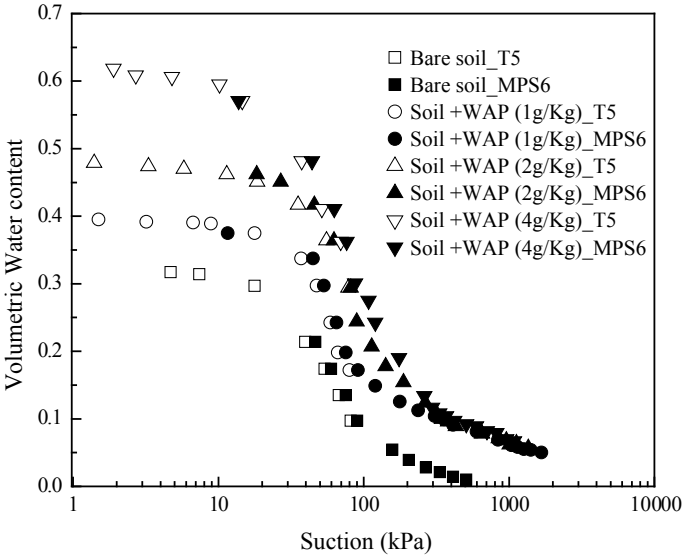

Fig. 3 WRCCs of the used soil with different WAP concentrations

3 Results and Discussions

The obtained WRCCs of the bare soil and with WAP amended soil can be seen in Fig. 3. Performance of the two suction measuring devices T5 and MPS6 were found to be very much effective for measuring suction in polymer amended soil. Both the sensors give identical suction value from near saturated state to the range of T5. Further, the results exhibited that polymer amendment increased the water retention behavior of the soil especially at the low suction range. Presence of WAP in soil alters the soil pore structure (reduction in macro and meso-pores) which affects the water retention at low matric suction [3, 34]. It was reported that the use of hydrophilic polymer can increase the specific surface area of cohesionless soil [12]. It is a well-known fact that, the water retention at low suction predominantly depends on the adsorptive force between the soil surface and water molecule. Hence, an increase in soil specific surface area due to soil amendment can lead to improvement in water retention at low matric suction. Wei and Durian [43] have also reported that the total fraction of water-accessible pore space in soil for a particular packing density decrease exponentially with the increase in polymer concentration As a result, significant changes in the water retention behavior can be seen with increase in WAP concentration.

The measured experimental WRCC data were further fitted to a mathematical equation (Eq. 1) proposed by van Genuchten [42] to obtain the fitting parameters (a_{vg}, n_{vg}, and m_{vg}). These vG models parameters are used as primary input parameters for studies related to the flow of water through porous media [27–29, 40]. In our study, the vG parameters were obtained by using RETC program with m_{vg} parameter constraint by direct relation to n_{vg} parameter as expressed in Eq. [2].

$$\theta_\psi = \theta_r + \frac{(\theta_s - \theta_r)}{\left[\left\{1 + \left(\frac{\psi}{a_{vg}}\right)^{n_{vg}}\right\}^{m_{vg}}\right]} \tag{1}$$

$$m_{vg} = 1 - \frac{1}{n_{vg}} \tag{2}$$

where,

θ_ψ = Volumetric water content at any suction , a_{vg} = parameter related to the air entry value (AEV) of the soil, n_{vg} = function of the rate of water extraction from the soil, m_{vg} = soil parameter that is related to the residual water content of the soil, θ_s = saturated volumetric water content, θ_r = residual volumetric water content, and = soil suction.

The vG fitting curve for the measured WRCC with different polymer amendment can be seen in Fig. 4. The saturated water content of the soil has increased from 0.326 (m^3/m^3) for bare soil to 0.623 (m^3/m^3) for 4 g/kg WAP concentration. This difference is observed due to improvement in the porosity which allows more water to be retained within the soil matrix. The obtained vG parameters with the co-efficient of determination (R^2) value were presented in Table 3. The a_{vg} param-

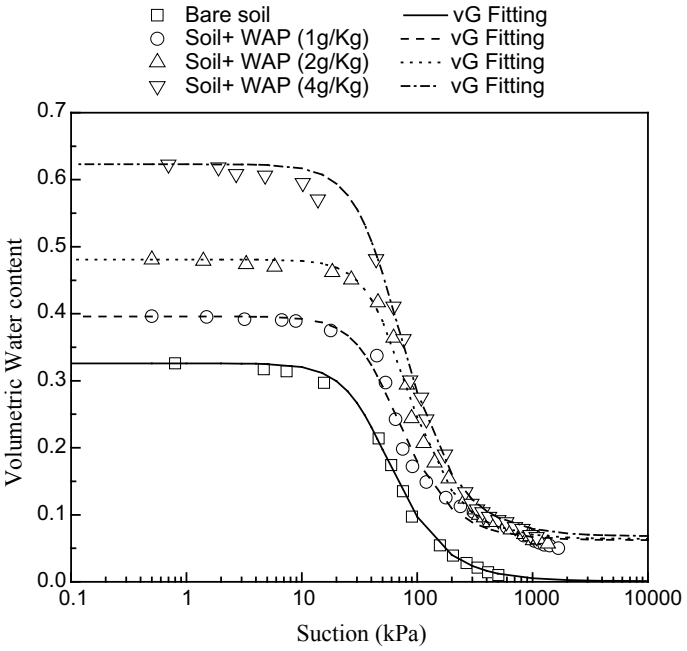

Fig. 4 vG fittings for the measured WRCCs

Table 3 Obtained vG parameters for the used soil with different WAP concentration

vG parameters	Bare soil	Soil + WAP (1 g/kg)	Soil + WAP (2 g/kg)	Soil + WAP (4 g/kg)
θ_s	0.326	0.396	0.481	0.623
θ_r	0.001	0.062	0.064	0.068
a_{vg} (m^{-1})	0.229	0.190	0.153	0.185
n_{vg}	2.374	2.449	2.354	2.344
R^2	0.997	0.991	0.997	0.997

eter which is inversely proportional to AEV of soil is found to be decreasing with the polymer amendment up to a concentration of 2 g/kg WAP.AEV can be defined as the suction value at which air enters the largest pore of the soil matrix. Due to larger pore geometry in cohesionless soils, water is released under lower suction. With the incorporation of WAP, there is a reduction in the diameter of the pore which increased the pressure required for water extraction from that pore.

The volumetric water content at Field capacity (FC) and permanent wilting point (PWP) were evaluated from the WRCC of the used soil with different amounts of WAP. FC of soil is physically defined as the water retained by soil at 33 kPa of suction head whereas PWP is physically defined as the water content at 1500 kPa

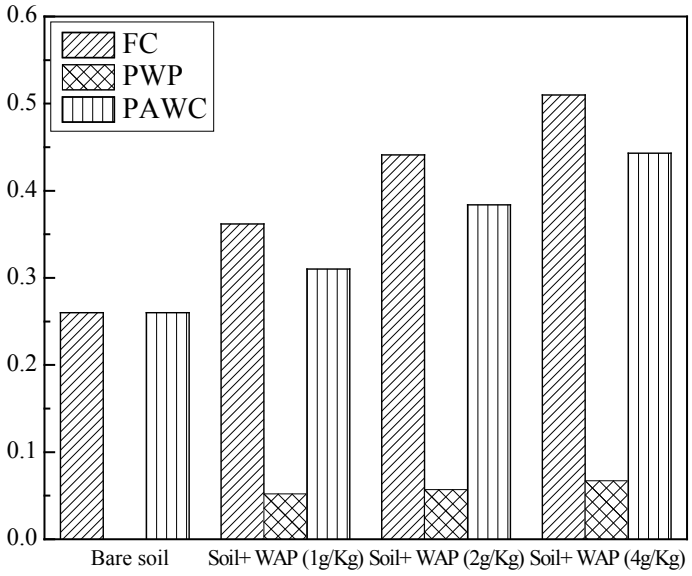

Fig. 5 FC, PWP, and PAWC of bare soil and WAP amended soil

suction head. The difference in FC and the PWP is known as the plant available water content (PAWC). The estimated FC, PWP, and PAWC of bare soil and WAP amended soils were presented in Fig. 5. It can be seen from the figure that the FC of soil has increased from 0.26 to 0.51 m^3/m^3 whereas PAWC has increased from 0.25 to 0.44 m^3/m^3 for 0.4% WAP amendment. These results clearly imply that WAP amendment not only increases the water retention behavior of the soil but also improves the water availability to the plants.

Further, continuous drying curves in terms of soil suction variation with time were also presented in Fig. 6 for four different concentrations of WAP. It can be well understood from the figure that the application of WAP has significantly increased the time to reach the PWP. Generally, the time required to reach PWP denoted as the survival time of the plant in water stress conditions as plant roots were not able to extract water once it reaches the PWP. The bare soil reaches the wilting point within 650 h which is almost 27 days whereas maximum concentration of SAP has extended the survival time to 1750 h, i.e., 73 days. The increase in the survival time can be directly related to the increase in the PAWC. The results give a clear indication that WAP amendment can reduce the irrigation frequency and can contribute to proper management of water in the drought-prone areas.

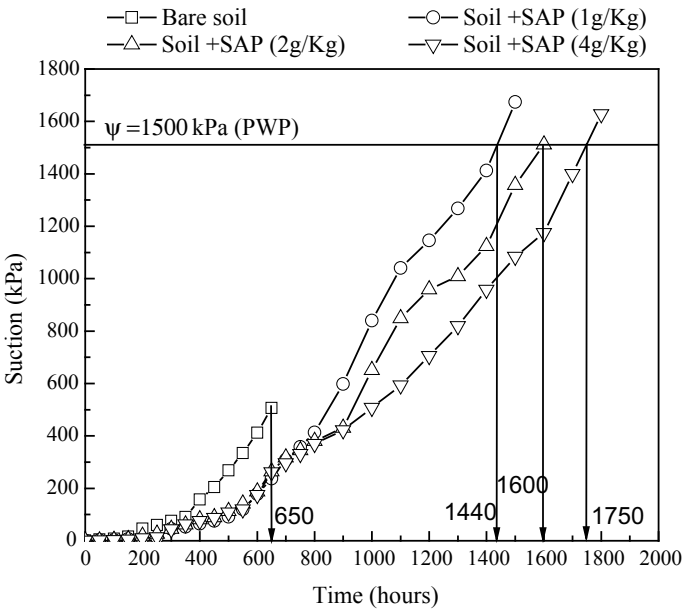

Fig. 6 Suction variation with time for different WAP concentration

4 Conclusions

In this work, a water-absorbing polymer namely stockosorb, was applied at different rates (0, 1 g, 2 g, and 4 g/kg of soil) to locally available cohesionless soil. Water retention curves of the amended soil were measured by continuously monitoring the soil suction and soil-water content with a tensiometer, MPS6 and 5TM, respectively. Performance of the suction measuring sensors were found very effective for long term monitoring the WRCCs of the WAP amendment soils. The WRCCs of the soil with different concentrations of WAP amendment showed a significant increase in the water retention behavior of the soil with increasing polymer concentration. The increase in water retention was found to be more prominent in the lower suction range where suction is primarily governed by pore structure and pore size distribution. The saturated water content, FC and PAWC of the soil with 0.4% WAP amendment was increased by almost two times compared to the bare soil. The results also indicated that WAP amendment can increase the plant survival time in water stress conditions as more water is available for the plants. Therefore, this could be an ideal solution to overcoming the issues such as low water retention behavior of cohesionless soils and excess leaching out of soil nutrients through runoff. Moreover, application of WAP could reduce irrigation frequency in the semiarid and arid regions where efficient use of water resources is the prime concern.

References

1. 5TM Water Content and Temperature Sensors (2017) Operator's manual. METER Group Inc., USA
2. Abedi-Koupai J, Sohrab F, Swarbrick G (2008) Evaluation of hydrogel application on soil water retention characteristics. J Plant Nutr 31(2):317–331
3. Agaba H, Baguma Orikiriza LJ, Osoto Esegu JF, Obua J, Kabasa JD, Hüttermann A (2010) Effects of hydrogel amendment to different soils on plant available water and survival of trees under drought conditions. Clean Soil Air Water 38(4):328–335
4. Akhter J, Mahmood K, Malik KA, Mardan A, Ahmad M, Iqbal MM (2004) Effects of hydrogel amendment on water storage of sandy loam and loam soils and seedling growth of barley, wheat and chickpea. Plant Soil Environ 50(10):463–469
5. Andry H, Yamamoto T, Irie T, Moritani S, Inoue M, Fujiyama H (2009) Water retention, hydraulic conductivity of hydrophilic polymers in sandy soil as affected by temperature and water quality. J Hydrol 373:177–183
6. Arbona V, Iglesias DJ, Jacas J, Primo-Millo E, Talon M, Gómez-Cadenas A (2005) Hydrogel substrate amendment alleviates drought effects on young citrus plants. Plant Soil 270(1):73–82
7. Bai W, Zhang H, Liu B, Wu Y, Song J (2010) Effects of super-absorbent polymers on the physical and chemical properties of soil following different wetting and drying cycles. Soil Use Manag 26:253–260
8. Bao Y, Ma J, Li N (2011) Synthesis and swelling behaviors of sodium carboxymethyl cellulose-g-poly (AA-co-AM-co-AMPS)/MMT superabsorbent hydrogel. Carbohydr Polym 84(1):76–82
9. Bhardwaj AK, McLaughlin RA, Shainberg I, Levy GJ (2009) Hydraulic characteristics of depositional seals as affected by exchangeable cations, clay mineralogy, and polyacrylamide. Soil Sci Soc Am J 73(3):910–918
10. Bhardwaj AK, Shainberg I, Goldstein D, Warrington D, Levy GJ (2007) Water retention and hydraulic conductivity of cross-linked polyacrylamides in sandy soils. Soil Sci Soc Am J 71(2):406–412
11. Bowman DC, Evans RY (1991) Calcium inhibition of polyacrylamide gel hydration is partially reversible by potassium. HortScience 26(8):1063–1065
12. Dorraji SS, Golchin A, Ahmadi A (2010) The effects of hydrophilic polymer and soil salinity on corn growth in sandy and loamy soils. Clean Soil Air Water 38(7):584–591
13. El-Tohamy WA, El-Abagy HM, Ahmed EM, Aggor FS, Hawash SI (2014) Application of super absorbent hydrogel poly (acrylate/acrylic acid) for water conservation in sandy soil. Trans Egypt Soc Chem Eng 40(2):1–8
14. Farrell C, Ang XQ, Rayner JP (2013) Water-retention additives increase plant available water in green roof substrates. Ecol Eng 52:112–118
15. Feng D, Bai B, Ding C, Wang H, Suo Y (2014) Synthesis and swelling behaviors of yeast-g-poly (acrylic acid) superabsorbent co-polymer. Ind Eng Chem Res 53(32):12760–12769
16. Geng SM, Yan DH, Zhang TX, Weng BS, Zhang ZB, Qin TL (2015) Effects of drought stress on agriculture soil. Nat Hazards 75(2):1997–2011
17. Huttermann A, Orikiriza LJB, Agaba H (2009) Application of superabsorbent polymers for improving the ecological chemistry of degraded or polluted lands. Clean Soil Air Water 37 (7):517–526
18. Huttermann A, Zommorodi M, Reise K (1999) Addition of hydrogels to soil for prolonging the survival of pinus halepensis seedlings subjected to drought. Soil Tillage Res 50:295–304
19. IS 2720, Part II (1973) Methods of test for soils: determination of water content. Indian Standards Institute, New Delhi, India
20. IS 2720, Part III (1973) Methods of test for soils: determination of specific gravity. Indian Standards Institute, New Delhi, India
21. IS 2720, Part IV (1985) Methods of test for soils: grain size analysis. Indian Standards Institute, New Delhi, India

22. IS 2720, Part V (1985) Methods of test for soils: determination of liquid limit and plastic limit. Indian Standards Institute, New Delhi, India
23. Ismail H, Irani M, Ahmad Z (2013) Starch-based hydrogels: present status and applications. Int J Polym Mater 62(7):411–420
24. Kabiri K, Omidian H, Zohuriaan-Mehr MJ, Doroudiani S (2011) Superabsorbent hydrogel composites and nanocomposites: a review. Polym Compos 32(2):277–289
25. Kala CP (2017) Environmental and socioeconomic impacts of drought in India: lessons for drought management. Sci Educ 5(2):43–48
26. Kalhapure A, Kumar R, Singh VP, Pandey DS (2016) Hydrogels: a boon for increasing agricultural productivity in water-stressed environment. Curr Sci 111(11):1773
27. Likos WJ, Yao J (2014) Effects of constraints on van Genuchten parameters for modeling soil-water characteristic curves. J Geotech Geoenviron Eng 140(12):06014013
28. Lu N, Likos WJ (2004) Unsaturated soil mechanics. Wiley, New York
29. Mbonimpa M, Aubertin M, Maqsoud A, Bussière B (2006) Predictive model for the water retention curve of deformable clayey soils. J. Geotechn Geoenviron Eng 132(9):1121–1132
30. Mohawesh O, Durner W (2017) Effect of bentonite, hydrogel and biochar amendments on soil hydraulic properties from saturation to oven dryness. Pedosphere
31. Montesano FF, Parente A, Santamaria P, Sannino A, Serio F (2015) Biodegradable superabsorbent hydrogel increases water retention properties of growing media and plant growth. Agric Agric Sci Proc 4:451–458
32. MPS-6 Dielectric Water Potential Sensor (2015) Operator's manual. Decagon Devices, USA
33. MPS-6 Dielectric Water Potential Sensor (2015) Operator's manual. METER Group, Inc., USA
34. Narjary B, Aggarwal P, Singh A, Chakraborty D, Singh R (2012) Water availability in different soils in relation to hydrogel application. Geoderma 187:94–101
35. Nnadi F, Brave C (2011) Environmentally friendly superabsorbent polymers for water conservation in agricultural lands. J Soil Sci Environ Manag 2(7):206–211
36. Orikiriza LJB, Agaba H, Tweheyo M, Eilu G, Kabasa JD, Hüttermann A (2009) Amending soils with hydrogels increases the biomass of nine tree species under nonwater stress conditions. Clean Soil Air Water 37(8):615–620
37. Richards D, Lane M, Beardsell DV (1986) The influence of particle-size distribution in pinebark: sand: brown coal potting mixes on water supply, aeration and plant growth. Sci Hortic 29(1–2):1–14
38. Sepaskhah AR, Shahabizad V (2010) Effects of water quality and PAM application rate on the control of soil erosion, water infiltration and runoff for different soil textures measured in a rainfall simulator. Biosyst Eng 106(4):513–520
39. Shi Y, Li J, Shao J, Deng S, Wang R, Li N, Zheng X (2010) Effects of Stockosorb and Luquasorb polymers on salt and drought tolerance of populus popularis. Sci Hort 124(2):268–273
40. Sivakumar Babu GL, Peter J, Mukesh MD, Gartung E (2005) Significance of soil suction and soil water characteristic curve parameters. Geotech Test J 28(1):102–107
41. UMS GmbH (Umwelt-Monitoring-Systeme) 2001 T5 user manual. Munich, Germany
42. van Genuchten MT (1980) A closed form equation for predicting the hydraulic conductivity of unsaturated soils. Soil Sci Soc Am J 44:892–898
43. Wei Y, Durian DJ (2013) Effect of hydrogel particle additives on water-accessible pore structure of sandy soils: a custom pressure plate apparatus and capillary bundle model. Phys Rev E 87(5):053013
44. Zhang X, Obringer R, Wei C, Chen N, Niyogi D (2017) Droughts in India from 1981 to 2013 and implications to wheat production. Sci Rep 7:44552

Effect of Geosynthetic Stiffness on the Behaviour of Encased Stone Columns Installed in Lithomargic Clay

M. P. Vibhoosha, Anjana Bhasi and Sitaram Nayak

Abstract Columnar systems have been extensively used to support structures on problematic ground conditions. Encased stone columns are very effective for flexible structures such as embankments and storage tanks where a relatively large settlement is permissible. Lithomargic clay is extensively found along the Konkan belt in peninsular India and serves as the foundation for most of the structures. Construction activities in lithomargic clays are challenging due to the fact that there occurs drastic reduction in strength under saturated conditions. In this paper, the effectiveness of encased stone column in lithomargic clay has been studied and a 3D column model was developed to examine the effect of geosynthetic stiffness on the column-load-carrying capacity.

Keywords Lithomargic clay · 3D column · Stone column · Geosynthetic stiffness

1 Introduction

The rapid urbanisation and industrial development lead to the scarcity of suitable construction sites. The advancement in Geotechnical Engineering imparts the evolution of ground improvement techniques for the modification of weak foundation according to designer's choice. Among the various ground modification methods, stone column technique got worldwide popularity. The ease of construction, cost-effectiveness and efficiency makes it the best choice for difficult foundation conditions. The technique has been used since the 1950s for improving both cohesive soils and silty sands [2].

Stone columns are vertical columns of compacted stones constructed in weaker soil at suitable intervals [1]. With the application of external load, stone column

M. P. Vibhoosha (✉) · S. Nayak
National Institute of Technology Karnataka, Surathkal, Karnataka, India
e-mail: vibhoosha@gmail.com

A. Bhasi
National Institute of Technology Calicut, Kozhikode, India

A. Prashant et al. (eds.), *Advances in Computer Methods and Geomechanics*, Lecture Notes in Civil Engineering 55,
https://doi.org/10.1007/978-981-15-0886-8_16

bulges and gets lateral support from the adjacent soil in the form of passive pressure which results in soil-stone column composite. The passive pressure increment in the soft soil leads to consolidation and subsequent relaxation of stresses until it reaches equilibrium. This ground improvement technique has been successfully applied for foundation of structures like liquid storage tanks, earthen embankments, raft foundations, etc. where a relatively large settlement can be tolerated by the structure.

In order to improve the performance of stone columns, it is essential that the tendency of the columns to bulge should be resisted. The squeezing of soft clay into the voids of the aggregates is also prevented effectively. In such situations, stone columns are provided by an additional confinement for better performance. The concept of encasing the stone column by wrapping with geotextile was proposed by Van Impe and De Beer [15]. Confinement by geosynthetic materials has many advantages like increased stiffness of column, preventing the loss of stones into the surrounding soft clay, preserving the drainage and frictional properties of the stone aggregates, etc.

Many researchers have investigated the effect of geosynthetic encased stone columns in soft ground. Raithel et al. [13] carried out the performance analyses of encased stone columns by both numerical and analytical models. Small scale laboratory tests were carried out by Malarvizhi and Ilamparuthi [8] in both untreated and encased stone column-supported bed. Murugesan and Rajagopal [10, 11] investigated the improvement in load capacity of stone columns by encasement through finite element-based parametric studies as well as laboratory model tests. The encased stone columns showed higher load carrying capacity and underwent less compression compared to ordinary stone columns. The failure of encased stone columns was either due to excessive settlement or due to bursting of geosynthetic. Zhang and Lo [17] have reported that the use of geosynthetic encasement would enhance the effectiveness of stone columns by reducing the settlements.

Huang et al. [5] conducted numerical studies to study the time-dependant behaviour of geosynthetic-reinforced column-supported embankments. 3D coupled mechanical and hydraulic modelling was done using FLAC3D. The foundation soil, the embankment fill, and the deep mixed columns were modelled as linearly elastic–perfectly plastic materials with Mohr–Coulomb failure criteria and the geotextile reinforcement was modelled by the geogrid elements in the FLAC3D software. Lo et al. [7] also carried out time-dependent coupled FE analyses on encased stone column-supported embankment. By encasing the columns, considerable reduction in settlement was observed. Castro [4] conducted 2D and 3D finite element analyses to check the performance of groups of encased stone columns beneath a rigid footing. Based on the numerical analyses he concluded that, if the area replacement ratio (area of the columns over area of the footing), and the ratio of encasement stiffness to column diameter are kept constant, the column arrangement (both number of columns and column position) has a small influence on the settlement reduction achieved with the treatment.

Lithomargic clay is extensively found along the Konkan belt in Peninsular India. It is whitish, pinkish or yellowish silty soil. Though it is very strong in dry conditions, the drastic reduction in strength under saturated condition makes construction over this soil difficult. Foundation problems, landslides and slope failures are quite common in this type of soils [14]. Numerous research studies provide information that soil reinforcement, stabilisation using lime, cement, fly ash, waste products and chemicals are effective in lithomargic clay improvement [6, 9, 14].

In this paper the effectiveness of encased stone columns in lithomargic clay was examined by the developed 3D column model. Also the influence of encasement stiffness on the behaviour of stone columns under embankment loading was evaluated.

2 Numerical Analyses

All the analyses were performed using a commercial finite element programme ABAQUS (SIMULIA 2016). This programme has the capability to carry out coupled analysis based on the generalised consolidation theory of [3]. 3D column modelling was used since it considerably reduces the computational time required to perform the calculations while allowing the investigation of the influence of various components on the performance of the system.

2.1 Case Study Considered

A typical embankment construction problem was taken from the literature [16]. An embankment of 6 m height rests on 10 m deep lithomargic clay [12] reinforced with 0.8 m diameter stone columns. A 1 m thick drainage blanket was provided over the top of the clay layer. Stone columns were arranged in square grid pattern with 2.4 m centre to centre spacing. The groundwater table was at 1 m below ground surface as shown in Fig. 1a.

2.2 Numerical Model

A cylindrical unit cell approach was considered for developing the models. Stone column and its tributary area forms a unit cell. The diameter of the unit cell depends on the pattern of stone column arrangement. For square grid arrangement the area of unit cell is as same as that of an equivalent square, and for triangular pattern, same as that of a hexagon. If ‘s’ is the centre to centre spacing between columns, the diameter of unit cell for square grid is 1.13s and 1.05s for triangular pattern. Square portion with an area equal to that of the unit cell was considered and the shaded portion as

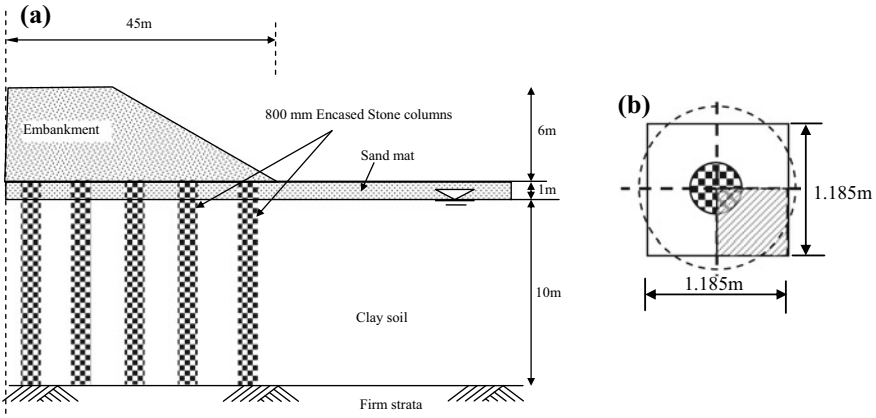

Fig. 1 **a** Cross section of embankment over encased stone columns, **b** 3D column region representation

shown in Fig. 1b was used for 3D column model. The developed model is shown in Fig. 2.

Different constitutive models were used to model various soils and geosynthetic encasement. The various parameters used for modelling is summarised in Table 1. Linear elastic membrane elements were used for geogrid modelling. The thickness of the geogrid was 15 mm and the tensile stiffness was calculated by using the equation,

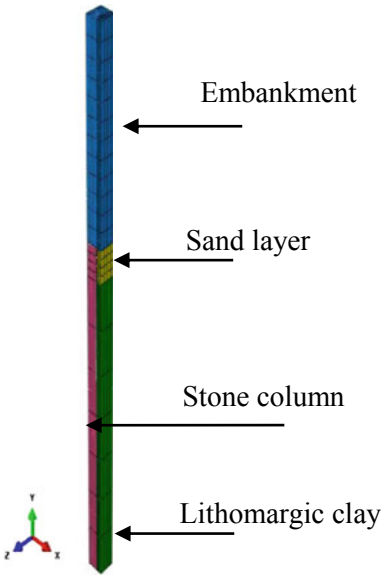

Fig. 2 3D column model

Table 1 Parameters used for numerical modelling [12, 16]

Property	Lithomargic clay	Stone column	Sand/Fill
Model used	Modified cam clay	Mohr–Coulomb	Mohr–Coulomb
Unit weight (kN/m^3)	18.6	19	19
Young's modulus (kPa)	–	40000	15000
Poisson's ratio, υ	0.35	0.3	0.3
Cohesion, c' (kPa)	–	5	3
Friction angle, Φ (degree)	–	40	28
Dilation angle, φ (degree)	–	10	4
Critical state stress ratio, M	1.0	–	–
Logarithmic hardening constant for plasticity, λ	0.2	–	–
Logarithmic bulk modulus for elastic material behaviour, K	0.02	–	–
Initial yield surface size, a_o, (kPa)	50	–	–
Initial void ratio, e_o	1	–	–
Permeability, k (m/s)	4.05×10^{-7}	1.2×10^{-2}	1.2×10^{-2}

J = Et, where E is the Young's modulus and 't' is the thickness. Modified cam clay model was used for lithomargic clay and linear elastic perfectly plastic model with Mohr–Coulomb failure criteria was assumed for sand. The various parameters used for modified cam clay model can be identified based on isotropic compression test oedometer test. Empirical equations based on the index properties were also available. The initial yield surface size was selected based on the consistency of the soft soil.

Vertical sides were horizontally fixed and the base was fully fixed to prevent rigid body motion. Phreatic level was set at the top surface of the clay to generate hydrostatic pore water pressure. Free drainage was modelled by giving zero pore pressure boundary condition at the clay layer top. In finite element meshing, 20-node stress–pore pressure elements with reduced integration (C3D20RP) were used to represent the lithomargic clay layer and the stone column, and 20-node stress only elements (C3D20R) were used for the embankment fill. The geosynthetic reinforcement was modelled using the membrane elements M3D8R. The membrane elements are surface elements that offer strength in the plane of the element but have no bending stiffness, and are known to be particularly useful in modelling the geosynthetic encasement as they offer resistance against out-of-plane bulging.

After establishing the initial geostatic stress and pore pressure distribution with appropriate boundary conditions, the stone columns and the geosynthetic reinforcement were installed by activating corresponding elements. Embankment construction was then simulated in three equal stages with 2 m fill placement. The loading was simulated by adding layers of elements. Each embankment layer was constructed in 15 days followed by consolidation time of 10 days. The analysis was continued till 6 m construction was completed.

2.3 Parametric Studies

The improvement of lithomargic clay reinforced with encased stone columns was evaluated by different parameters. Three different cases were considered in numerical analyses.

(a) Lithomargic clay without any improvement technique
(b) Ordinary stone columns (OSC)
(c) Geosynthetic encased stone columns (GESC).

Initially the embankment loading was applied on lithomargic clay alone and the settlement response with time was evaluated. In the second case the stone columns were installed by replacing an equal amount of native soil and the embankment construction was simulated. In the third stage suitable geogrid material was wrapped along the stone column length and the performance was analysed. The stiffness of the encased material was varied and its effect on settlement, excess pore pressure profile and the bulging behaviour of stone columns were studied.

3 Results and Discussion

3.1 Settlement-Time Response

The improvement of lithomargic clay by stone columns was studied by the settlement-time curves. The surface settlement due to the embankment loading was found out at various time intervals. The response was plotted in Fig. 3. It was observed that the soil without any ground modification settles more and the settlement value decreased with the introduction of columnar structures in the native soil.

The influence of encasement stiffness on the performance of stone columns was studied by varying the tensile stiffness to a wide range of values by keeping all other parameters constant. The tensile stiffness of geogrid is the ratio of tensile force per unit width to the strain in the geogrid, which is $J = Et$, where J is the tensile stiffness, E is the elastic modulus and the t is the thickness of geogrid. The stiffness has varied from 400 to 3000 kN/m.

The settlement time curves depict that the stone column effectively reduces the settlement due to the embankment loading. Thus the load-bearing capacity of unimproved ground can be effectively increased by the stone columns installed at suitable intervals. Stone columns derive lateral resistance from the surrounding soil against the dilation of stones under loading. The incorporation of geosynthetic encasement in stone columns further reduces the settlement. With the increase in stiffness value, the confining stress increases which results in improved load-carrying capacity.

From Table 2, it was clear that the stone columns reduce the settlement by 49% as that of the unimproved ground. When it was encased with a geogrid material of

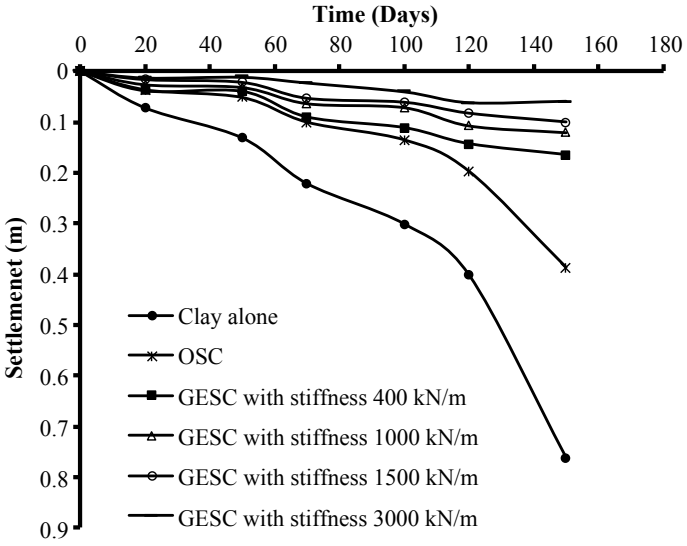

Fig. 3 Settlement-time curves for various cases

Table 2 Surface settlement values due to the embankment loading at different ground conditions

Ground condition	Max. settlement (m)
Lithomargic clay without ground improvement	0.762
OSC	0.387
GESC with stiffness 400 kN/m	0.165
GESC with stiffness 1000 kN/m	0.120
GESC with stiffness 1500 kN/m	0.100
GESC with stiffness 3000 kN/m	0.059

stiffness value 400 kN/m, the settlement reduction was 78% and with stiffness values of 3000 kN/m the reduction was 92%.

3.2 Bulging Characteristics

The lateral bulging profile was plotted along the length of the stone column as shown in Fig. 4. The maximum bulging in the case of ordinary stone column was observed near to the surface. The encased stone columns did not undergo much bulging compared to OSC. The reduction in bulging of stone column leads to lesser surface settlements. In the case of GESCs, the bulging has been controlled by the encasement and the settlement of the stone column was mainly due to the elongation of the

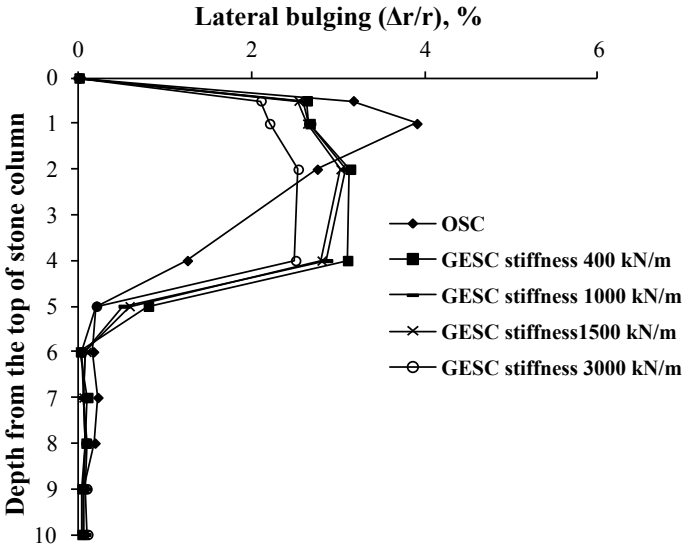

Fig. 4 Lateral bulging of stone column at various encasement stiffness values

geosynthetic encasement. With increase in encasement stiffness the lateral bulging decreased significantly, which implies applied surface load is transmitted deeper into the column. As the geogrid stiffness increases, the lateral bulging decreases due to the increased lateral confinement. The lateral bulging at various depths is presented in terms of the increase in radius (Δr) at different depths normalised with original radius of the stone column (r).

3.3 Excess Pore Water Pressure

Consolidation analyses were carried out to measure the excess pore water pressure along the depth of lithomargic clay. During the consolidation process, the stress concentration ratio increases because more stress is transferred from the surrounding soil to the column, thus some excess pore water pressure dissipates at a faster rate. The embankment load transferred to the stone column was more in the case of GESC due to the higher confining stress. Though the encasement contributes to load-carrying capacity, it also functions as a separator and filter between surrounding soil and stone column. The encasement acts as drainage for the dissipation of excess pore water pressure. The excess pore water pressure profile along the depth of clay layer during consolidation is shown in Fig. 5. It was found that with the increase in stiffness the excess pore water pressure dissipation was faster which gave lesser magnitude of excess pore water pressure at a particular point. This can be explained as, when the stiffness of encasement material increases more load can be transferred from

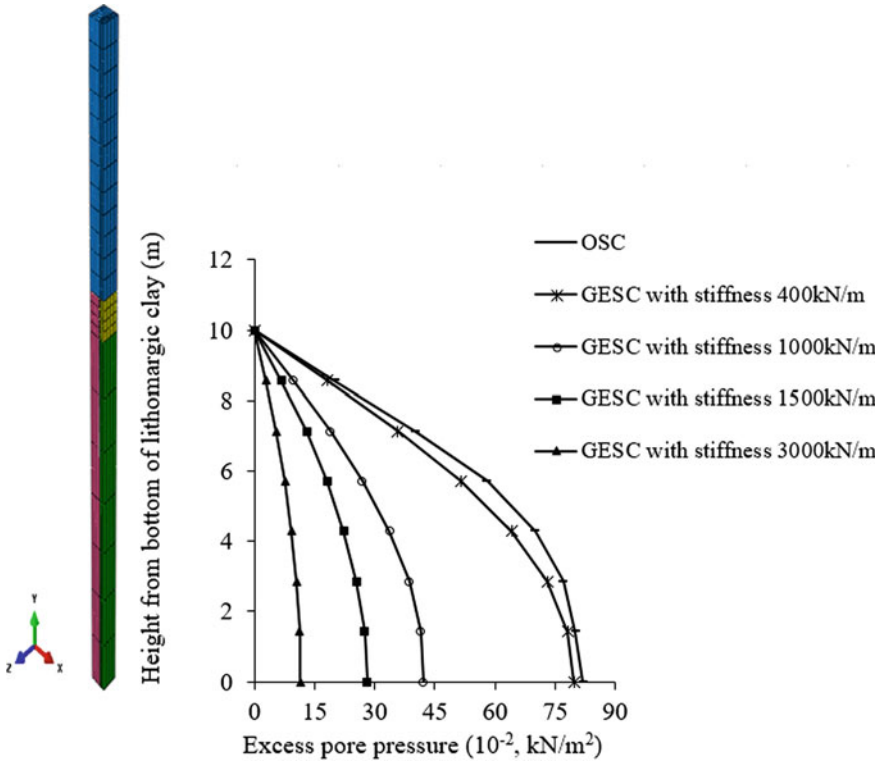

Fig. 5 Excess pore water pressure profile along the clay depth

surrounding soil to the stone column which causes faster dissipation of excess pore water pressure results in reduced time of consolidation.

4 Conclusions

In this paper, the effectiveness of stone columns in lithomargic clay was studied. The following points can be made from numerical results:

1. Inclusion of columnar structures in soft soil reduces the surface settlements due to the embankment loading.
2. Consolidation analyses showed that stone columns improve the load-carrying capacity of lithomargic clay thus reducing the surface settlement due to the embankment loading.

3. The performance of stone columns can be significantly improved by encasing them with geosynthetic materials. With encasement, the confining stress developed will be more and the severe lateral bulging at the ground surface which is observed in the case of ordinary stone column has significantly reduced.
4. Compared to untreated soil, a settlement reduction of 49% was obtained with ordinary stone columns. When it was encased with a geogrid material of stiffness 400 kN/m, the settlement reduction was 78% and with stiffness 3000 kN/m the reduction was 92%.
5. The tensile stiffness of the geosynthetic material plays an important role in the load-carrying capacity of stone column. The stiffer the encasement higher the load-carrying capacity and faster the excess pore water pressure dissipation.

References

1. Ambily AP, Gandhi SR (2007) behaviour of stone columns based on experimental and FEM analysis. J Geotech Geoenviron Eng 133(4):405–415
2. Barksdale RD, Bachus RC (1983) Design and construction of stone columns. Federal highway administration: RD-83/026
3. Biot MA (1941) General theory of three-dimensional consolidation. J Appl Phys 12(2):155–164
4. Castro J (2017) Groups of encased stone columns: influence of column length and arrangement. Geotext Geomembr 45(2):68–80
5. Huang J, Han J, Oztoprak S (2009) Coupled mechanical and hydraulic modelling of geosynthetic-reinforced column-supported embankments. J Geotech Geoenviron Eng 135(80):1011–1021
6. Jayamohan J, Shivashankar R (2012) Some studies on prestressed reinforced granular beds overlying weak soil. ISRN Civil Eng. https://doi.org/10.5402/2012/436327
7. Lo SR, Zhang R, Mak J (2010) Geosynthetic-encased stone columns in soft clay: a numerical study. Geotext Geomembr 28(3):292–302
8. Malarvizhi SN, Ilamparuthi K (2004) Load versus settlement of claybed stabilized with stone and reinforced stone columns. In: Proceedings of the 3rd Asian regional conference on geosynthetics, GEOASIA, Seoul, Korea, pp 322–329
9. Majjagi G, Hiremath SG (2013) Experimental investigation of stone column in shedi soil. Int J Eng Res Tech 2(10):1669–1673
10. Murugesan S, Rajagopal K (2007) Model tests on geosynthetic-encased stone columns. Geosynth Int 14(6):346–354
11. Murugesan S, Rajagopal K (2010) Studies on the behavior of single and group of geosynthetic encased granular columns. Geotech Geoenviron Eng 136(1):129–139
12. Nayak S, Babu MRD, Shivashankar R, James N (2014) Performance of granular column in dispersive soils. ICE Proc 167:72–82
13. Raithel M, Kempfert HG, Kirchner A (2002) Geotextile-encased columns (GEC) for foundation of a dike on very soft soils. In: Proceedings 7th ICG international conference on geosynthetics, Nice, France, pp 1025–1028
14. Ravi Shankar AU, Suresha SN (2006) Strength behaviour of geogrid reinforced shedi soil sub grade and aggregate system. Road Mater Pavement Des 7(3):313–330
15. Van Impe WY, De Beer E (1985) Improvement of settlement behaviour of soft layers by means of stone columns. In: Proceedings of 8th international conference on SMFE, Helsinki, pp 309–312

16. Yoo C, Kim SB (2009) Numerical modeling of geosynthetic-encased stone column-reinforced ground. Geosynth Int 16(3):116–126
17. Zhang R, Lo SR (2008) Analysis of geosynthetic reinforced stone columns in soft clay. In: Proceedings of the 4th Asian regional conference on geosynthetics, Shanghai, China, pp 735–740

Numerical Investigation of the Vertical Response of Bucket Foundations Supporting Offshore Wind Turbines in Sand

Tanmoy Kr. Deb and Baleshwar Singh

Abstract The vertical response of bucket foundations embedded in medium dense and very dense sands was investigated employing finite element method. The effect of bucket length on the vertical load capacity was studied by considering three different foundation geometries, namely, surface circular foundation, bucket foundation and embedded solid foundation. The effect of soil plug on the end-bearing capacity was explored by comparing the vertical load behaviour of bucket and embedded solid foundations, while assuming zero skirt. The vertical capacities of all the considered geometries are noted to be higher in very dense sand, and the maximum vertical capacity is obtained in the case of embedded solid foundation. For bucket foundations, the ultimate vertical bearing capacity is noted to increase in near-linear manner with increasing skirt length. Due to the presence of soil plug inside the bucket foundation, the percentage reduction in end-bearing capacity compared to that of embedded solid foundation is found to be about 21–22% in medium dense sand and 18–19% in very dense sand. Plastic strain contour diagrams indicate surface flow failure mechanism for surface circular foundation, which then changes to confined deep flow failure mechanism with increasing skirt length. Based on the results of the numerical analyses, design expressions are obtained to estimate the vertical bearing capacity of bucket foundations embedded in sand.

Keywords Bucket foundation · Finite element analysis · Sand · Vertical bearing capacity

1 Introduction

In recent times, monopod bucket foundation has gained importance for wind turbine structures located at shallow water depths up to about 40 m. The bucket foundation is of cylindrical shape with a large diameter up to 20 m and has an open-ended base and a closed top cap. The foundation is installed into the seabed in two stages. The

T. Kr. Deb (✉) · B. Singh
Indian Institute of Technology Guwahati, Guwahati, India
e-mail: tanmoy.deb@iitg.ac.in

A. Prashant et al. (eds.), *Advances in Computer Methods and Geomechanics*, Lecture Notes in Civil Engineering 55,
https://doi.org/10.1007/978-981-15-0886-8_17

first stage involves lowering the open end into the bed, which initiates self-weight penetration. Remaining penetration is continued by generating a negative pressure or suction inside the foundation by pumping water out from the top, until the underside of the foundation lid comes in direct contact with the seabed surface.

The response of bucket foundations under compressive vertical loading in sandy soil has been investigated experimentally by means of laboratory and field tests, and by means of numerical methods. Houlsby and Byrne [7] highlighted the possibilities of a novel form of foundation for offshore wind turbines, and discussed the loadings on the suction caisson foundation system which were different from those previously encountered by the offshore oil and gas industry. Later, Byrne and Houlsby [3] reported the results of experimental investigations into the vertical loading response of suction caisson foundations. The experiments involved cyclic loading about different mean loads, including cycling into tension and monotonic loading at different rates. The relationship between the cyclic loading and monotonic loading was explored. Villalobos [10] conducted laboratory experiments on scaled skirted foundations having aspect ratio between 0.26 and 2.0 in two dry sandy soils of different relative densities under pure vertical load, in order to investigate the behaviour during different stages of loading until failure, and compared the experimental results with theoretical results. Eid [5] investigated the behaviour of vertically loaded skirted foundation in dry sand using numerical simulation and laboratory experiments, and presented correlations to determine the minimum bearing capacity and the maximum settlement of the skirted foundation from the corresponding magnitudes of the surface foundation. Barari et al. [2] conducted model tests on bucket foundations as well as three-dimensional finite element analyses on bucket foundations and equivalent embedded solid foundations to examine the uniaxial vertical capacity. On the basis of the tests and analyses, new expressions for the depth factor of shallow foundations were validated for embedment ratios up to unity. Park et al. [9] performed a series of two-dimensional axisymmetric finite element analyses to study the unique load transfer characteristics of bucket foundations in sands, using the Mohr–Coulomb model following a non-associated flow rule. Based on the numerical results, predictive equations for shaft resistance and a combined shape and depth factor for the base capacity were proposed. Haddad et al. [6] conducted experiments on small scale surface and bucket foundations in loose saturated sand to determine their difference in load-settlement behaviour under uniaxial vertical loading. An expression for depth factor was proposed to approximate the bearing capacity of bucket foundation in terms of the surface footing and embedment ratio.

In most of the previous studies, the bucket foundation was analyzed numerically as a skirted strip foundation using two-dimensional finite element analyses or as a cylindrical foundation using three-dimensional finite element analyses [8]. The purpose of the present study is to investigate the response of bucket foundation with three different aspect ratios, under vertical compressive loading in medium dense and very dense sandy seabeds using three-dimensional finite element analyses. In addition, two different types of foundations, namely surface circular foundation and embedded solid foundation were considered to investigate the effect of skirt length on ultimate vertical capacity, and that of entrapped soil plug on the end-bearing capacity

of bucket foundation. On the basis of comparison of ultimate vertical capacities of bucket and surface circular foundations, the variation of depth factor with aspect ratio has been investigated. Furthermore, an expression has been presented to predict the settlement of bucket under vertical load arising from wind turbine superstructure.

2 Finite Element Modelling

The finite element modelling of surface circular, bucket and embedded solid foundations in the soil domain was carried out using finite element software [1]. The geometric details of the three foundation types considered in the study are presented in Table 1. All the three foundation types have the same diameter (D) of 12 m and varying skirt length or embedded length (L).

Considering the geometric and loading symmetry, only a half model of the foundation and semi-cylindrical soil domain was modelled. The soil domain boundary was chosen large enough so as to avoid boundary effects on the vertical response of the foundation. Under vertical loading, the extent of soil domain dimensions were determined by carrying out domain analyses of bucket foundation (D = 12 m & L= 12 m). Initially, based on trials, the lateral extent of the soil domain has been determined to be 9 times the diameter of the foundation (9D). Thereafter, the lateral extent was kept unchanged and analyses were carried out for several vertical extents of the domain ranging between 3 times (3L) to 10 times the length of the foundation (10L). The results showed that the percentage reduction in vertical capacity remained insignificant (<1% approx.) beyond the domain depth of 6L. Therefore, keeping the computational cost and accuracy of numerical simulation into consideration, the soil domain diameter of 9D and depth of 8L have been selected to simulate the vertical bearing capacity of bucket foundation (D = 12 m & L= 12 m). The same domain dimensions have been kept unchanged for the analyses of the other bucket foundations, with the same diameter (D = 12 m) and smaller lengths (L = 6 and 9 m). Similar domain dimensions have been adopted to simulate the vertical bearing capacities of surface circular foundations and embedded solid foundations. The foundation

Table 1 Geometric details of foundations under vertical loading

Foundation type	Geometry	Aspect ratio (L/D)
	D = 12 m	
Surface circular foundation	L = 0 m	0
Bucket foundation	L = 6 m	0.5
	L = 9 m	0.75
	L = 12 m	1.0
Embedded solid foundation	L = 6 m	0.5
	L = 9 m	0.75
	L = 12 m	1.0

and the soil domain were discretized with first-order, 8-node linear brick elements with reduced integration scheme ($C3D8R$). The soil domain was refined with smaller size of elements in the vicinity of the foundation periphery and the size of the elements was gradually increased radially towards the boundary. Figure 1 shows the discretized soil domain and the foundation types considered in the study. At the base of the soil domain, the applied boundary conditions restrained displacements in the three directions (X, Y and Z). In both the symmetric plane and curved periphery of the soil domain, normal displacements were restrained.

The non-linearity of the sandy soil constituting the seabed was modelled using Mohr–Coulomb elastoplastic material model obeying non-associative flow rule. The modulus of elasticity of the soil mass was defined as $E_{\text{soil}} = \kappa.p_{\text{a}}(p/p_{\text{a}})^{\lambda}$, where p is the mean principal stress, p_{a} is the atmospheric pressure, and κ and λ are empirical parameters. The parameters (κ and λ) can be determined from conventional laboratory drained triaxial shear tests performed for the determination of the shear strength

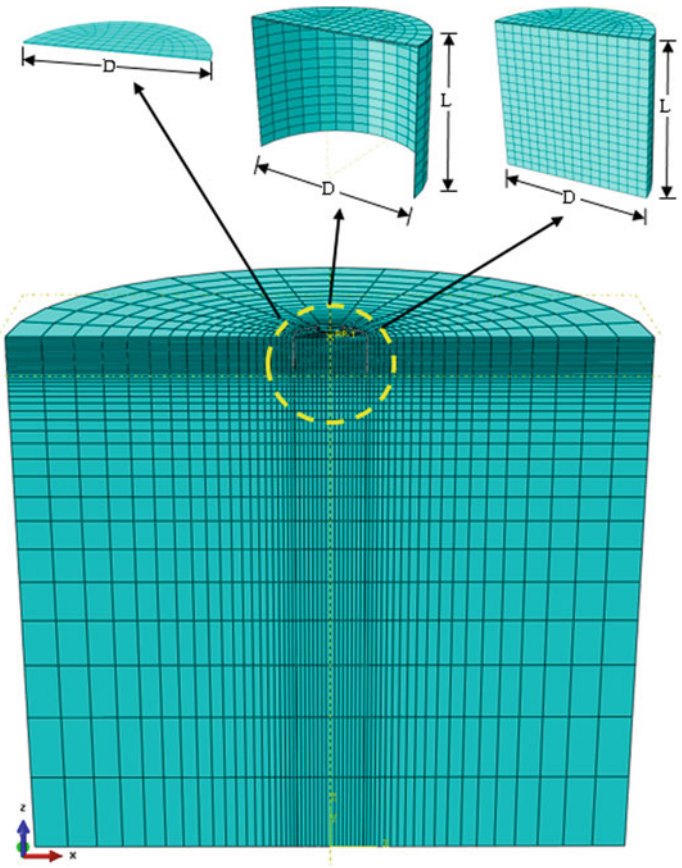

Fig. 1 Discretized soil domain and three foundation types

parameters. The test results are plotted in terms of several minor principal stresses or confining pressures (σ_3) versus logarithm of E_{soil}, where, (E_{soil}) is the slope of the tangent line drawn from the origin in deviator stress versus axial strain plot. A straight line is fitted to the data points. The values of the non-linear soil strength parameters, κ and λ, are respectively the intercept and the slope of this straight line. In this study, the values of the empirical parameters were taken from EAU [4]. The acceptability of the soil parameters for modelling of non-linearity in numerical analysis has been confirmed by validating against the moment-rotation response of the field test carried out on bucket foundation in dense sand in 2002, in Frederikshavn, Denmark. Thereafter, the soil parameters have been utilized for subsequent parametric studies and are listed in Table 2. For the cohesionless sandy soils, a very small value of cohesion was considered in order to avoid convergence issues.

The foundations were considered to be made up of steel. The modulus of elasticity and Poisson's ratio were specified as 2.1 GPa and 0.15, respectively. The unit weight of the foundations was taken similar to that of the surrounding soil mass in order to avoid the effect of self-weight on the vertical response. The numerical analysis was carried out in three stages. In the first step, the geostatic load was applied to achieve initial stress state across the soil domain. In the second step, contacts between the respective foundation and soil surfaces were established using master–slave contact pair algorithm. The interface friction angle between master and slave surfaces was considered as two-thirds of the internal friction angle (ϕ'). In the third step, displacement-controlled vertical load was applied at the top centre of respective foundation.

Table 2 Parameters of the sandy soils

Soil parameter	Medium dense sand	Very dense sand
Effective unit weight (γ'_{Soil}), kN/m^3	9.0	11.0
Oedometric stiffness modulus, κ	400	600
Oedometric stiffness modulus, λ	0.60	0.55
Poisson's ratio, μ	0.25	0.25
Internal friction angle, ϕ'	35°	40°
Dilation angle, δ'	5°	10°
Cohesion (c'), kN/m^2	0.1	0.1

3 Analysis of Results

Generally, under the application of vertical load, failure state of a foundation is assumed to have been reached when there is a continuous increase in the settlement under a nearly constant load. However, in certain cases, the vertical load is noted to increase incrementally despite excessive settlement. In such cases, the ultimate vertical capacity can be defined corresponding to a settlement magnitude which can lead to collapse of the supported structure. In the present study, the ultimate vertical capacity of the foundation is defined as applied load at the top centre, that causes a settlement equal to 10% of the diameter.

3.1 Load-Settlement Response Under Vertical Loading

The variation of vertical load capacity-settlement plots of surface circular, bucket and embedded solid foundations in medium dense sand (MDS) and very dense sand (VDS) are shown in Figs. 2 and 3, respectively. The ultimate vertical capacity values are presented in Table 3. The surface circular foundation is noted to yield the least ultimate capacity, and the maximum ultimate capacity is obtained for the embedded solid foundation.

For the three foundation types, the settlement is noted to increase with applied vertical load in a non-linear manner. In medium dense sand, the ultimate vertical capacity of the surface circular foundation is noted to be 117.07 MN. For the same diameter bucket foundation, the ultimate vertical capacity ($V_{\text{Ultimate, Bucket}}$) enhances to 126.98, 128.61 and 134.36 MN for increasing skirt length of 6, 9 and 12 m, respectively. Similarly, for the embedded solid foundation, the ultimate vertical capacity

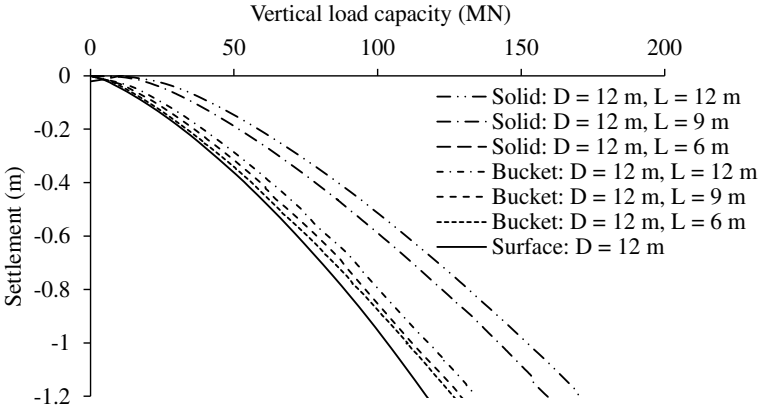

Fig. 2 Vertical load capacity versus settlement response of surface, bucket and embedded solid foundations in medium dense sand

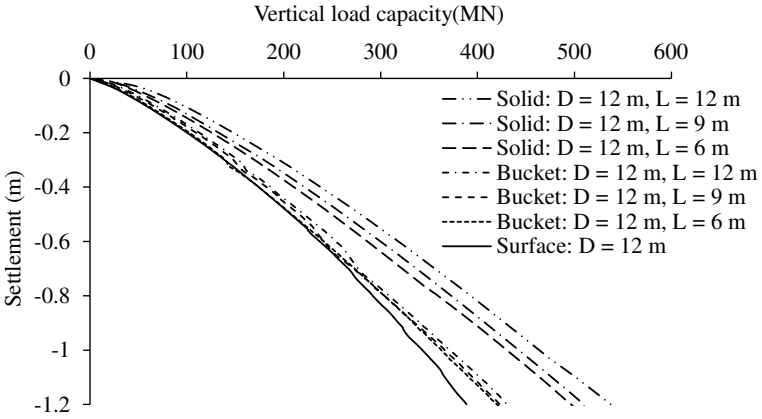

Fig. 3 Vertical load capacity versus settlement response of surface, bucket and embedded solid foundations in very dense sand

Table 3 Ultimate vertical capacity of surface circular, bucket and embedded solid foundations

Type of soil	Type of foundation	Aspect ratio (L/D)	Ultimate vertical capacity (MN)
Medium dense sand	Surface	0	117.07
	Bucket	0.5	126.98
		0.75	128.61
		1	134.36
	Solid	0.5	151.08
		0.75	159.39
		1	170.59
Very dense sand	Surface	0	388.58
	Bucket	0.5	421.73
		0.75	422.59
		1	431.35
	Solid	0.5	498.07
		0.75	510.07
		1	538.68

($V_{\text{Ultimate, Embedded solid}}$) is found to increase to 151.08, 159.39 and 170.59 MN for increasing embedment length of 6, 9 and 12 m, respectively. As compared to medium dense sand, the three foundation types yield higher vertical capacity in very dense sand and the trends remain similar.

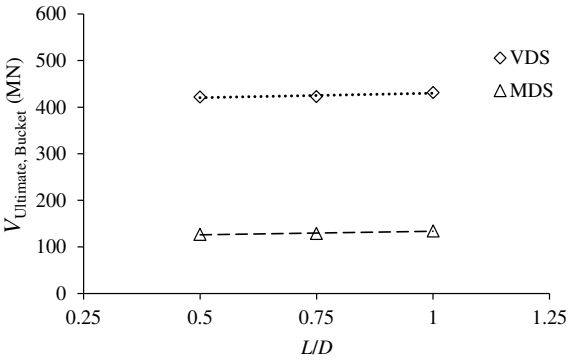

Fig. 4 Variation of ultimate vertical capacity of bucket foundation with aspect ratio

3.2 Effect of Aspect Ratio on Ultimate Vertical Capacity

Figure 4 shows the variation of ultimate vertical capacity with aspect ratio in both sand types for the bucket foundation. In medium dense sand, the ultimate vertical capacity is noted to increase from 126.98 to 134.36 MN in almost a linear manner (an increase of 5.8%) as the aspect ratio of the bucket foundation is increased from 0.5 to 1. Similar marginal variation is noted in very dense sand, with substantially greater magnitude of ultimate capacity more than approximately 3.2 times as in medium dense sand.

3.3 Failure Mechanisms of the Foundation Types

Under the application of vertical load, the foundation settles giving rise to plastic strain. The plastic strains generated at failure are shown in Fig. 5 for the surface circular foundation, and in Fig. 6 for the bucket and embedded solid foundations.

In the case of surface circular foundation in both medium dense sand and very dense sand, a distinct elastic zone of downward moving soil wedge is observed under the foundation, a characteristic of surface flow failure mechanism. Plastic strains are generated from the edges of the foundation and they extend radially outwards and vertically downwards.

In the case of bucket foundation, the surrounding soil mass along the exterior interface of the skirt is noted to yield plastically throughout the embedment length, as shown in Fig. 6a. Along the interior interface near the base, the soil mass also yields generating plastic strain, which then propagates gradually to a certain depth below the foundation. No plastic deformation of the soil plug is noted, which indicates that the plug displaces as a rigid body and acts as an integral part of the bucket foundation. In the case of embedded solid foundation as shown in Fig. 6b, formation of an elastic wedge at the base and generation of plastic strain along the vertical interface have

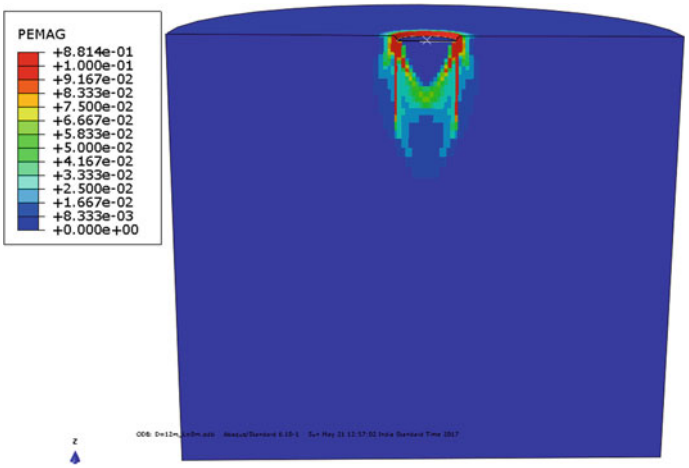

Fig. 5 Plastic deformation at failure in medium dense sand supporting surface circular foundation

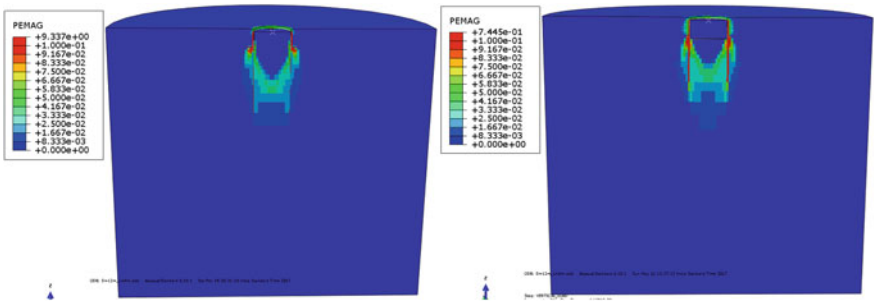

Fig. 6 Plastic deformation at failure in medium dense sand supporting: **a** bucket foundation; and **b** embedded solid foundation

been noted. A comparison of the plastic strain diagrams indicates confined deep flow failure mechanism for both the bucket foundation and embedded solid foundation.

3.4 Effect of Soil Plug on Ultimate Vertical Capacity

The effect of soil plug on the ultimate vertical bearing capacity was investigated by carrying out further numerical simulations considering zero shaft resistance ($Q_s = 0$) on the exterior vertical surface of both bucket and embedded solid foundations. As a result of which, the vertical bearing capacity is due to the end-bearing resistance only. The end-bearing capacities obtained from numerical analyses are presented in

Table 4 Variation in end-bearing capacity of bucket foundation

Soil type	Type of foundation	Aspect ratio (L/D)	End-bearing capacity (MN) for $Q_s = 0$	Reduction in end-bearing capacity (MN)	Reduction in end-bearing capacity (%)
Medium dense sand	Bucket	0.5	114.48	33.07	22.41
		0.75	121.32	33.40	21.59
		1	124.46	35.78	22.33
	Solid	0.5	147.55	–	–
		0.75	154.72	–	–
		1	160.24	–	–
Very dense sand	Bucket	0.5	387.58	88.58	18.60
		0.75	391.95	94.51	19.43
		1	396.72	92.11	18.84
	Solid	0.5	476.16	–	–
		0.75	486.46	–	–
		1	488.83	–	–

Table 4. The effect of soil plug on the vertical bearing capacity is the difference in the end-bearing capacities of the bucket and embedded solid foundations.

Even though the plastic strain diagrams indicate that the soil mass acts as a rigid body and behaves as an integral part of the bucket foundation, the results in the table indicate that while transferring the end-bearing load, the base of the soil plug acts as a cushion as compared to the embedded solid foundation. The reduction in the end-bearing capacity of the bucket foundation from that of the embedded solid foundation with the same aspect ratio ranges between 21 and 22% in medium dense sand and 18–19% in very dense sand.

3.5 Comparison of Ultimate Vertical Capacities of Surface and Bucket Foundations

The ultimate vertical capacities presented in Table 4 have been utilized to determine the vertical capacity depth factor (D_{vc}), which is defined as the ratio of the ultimate vertical bearing capacity of bucket foundation to that of surface circular foundation. The variations of depth factor with aspect ratio in medium dense and very dense sands are illustrated in Figs. 7 and 8, respectively.

In both the sand types, the depth factor is noted to increase marginally with aspect ratio in a non-linear manner. The best-fit curves for the data points can be represented by a general expression (Eq. 1). The values of the coefficients for this equation are presented in Table 5, which can be used to estimate the ultimate vertical capacity of

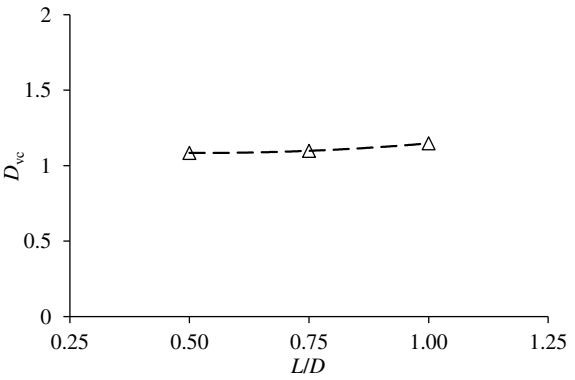

Fig. 7 Variation of vertical capacity depth factor with aspect ratio in medium dense sand

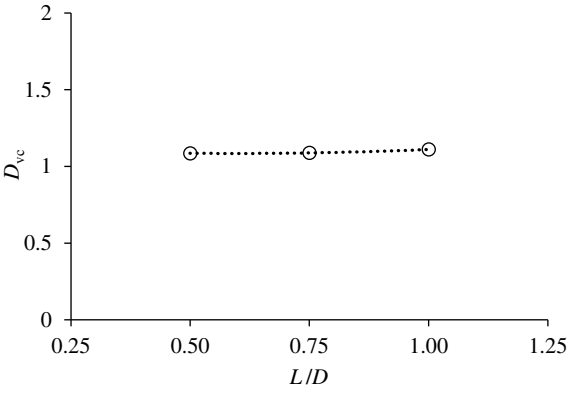

Fig. 8 Variation of vertical capacity depth factor with aspect ratio in very dense sand

Table 5 Values of coefficients for estimation of vertical capacity depth factor

Coefficient	Soil type	
	Medium dense sand	Very dense sand
a	0.2816	0.1625
b	−0.2962	−0.1942
c	1.1624	1.1418

bucket foundation from that of surface foundation.

$$D_{vc} = \frac{V_{\text{Ultimate,Bucket}}}{V_{\text{Ultimate,Surface}}} = a\left(\frac{L}{D}\right)^2 + b\left(\frac{L}{D}\right) + c \tag{1}$$

3.6 Settlement Under Superstructure Load

Under the application of superstructure load of the wind turbine system, the bucket foundation settles downwards. Considering a practical range of superstructure load ranging between 5 and 15 MN, the settlement values for the various bucket foundation geometries are presented in Table 6. For the 12 m diameter bucket foundation, under a superstructure load of 5 MN, the settlement values are found to be 15.5, 14.6 and 13.9 mm for skirt lengths of 6, 9 and 12 m, respectively, in medium dense sand. As expected, the settlement values are observed to increase with higher superstructure loads. Similar variations are noted in very dense sand, though the settlement values are lower.

$$W = L\left[a + b\left(\frac{V}{\gamma' DL^2}\right) + c\left(\frac{V}{\gamma' DL^2}\right)^2\right] \tag{2}$$

The settlement values of Table 6 can be plotted in normalized form against normalized superstructure load (V), and the plots for 5 MN superstructure load are presented in Figs. 9 and 10, respectively for medium dense sand and very dense sand. From the plots, the data points have been utilized to fit curves and a general expression is

Table 6 Settlement of bucket foundation under varying superstructure load

Soil type	Bucket geometry	Settlement under superstructure load (mm)		
		V = 5 MN	V = 10 MN	V = 15 MN
Medium dense sand	D = 12 m, L = 6 m	15.5	31	46.5
	D = 12 m, L = 9 m	14.6	29.2	43.8
	D = 12 m, L = 12 m	13.9	27.7	41.6
Very dense sand	D = 12 m, L = 6 m	5.0	10.1	16.3
	D = 12 m, L = 9 m	4.6	9.1	13.7
	D = 12 m, L = 12 m	4.6	9.1	13.7

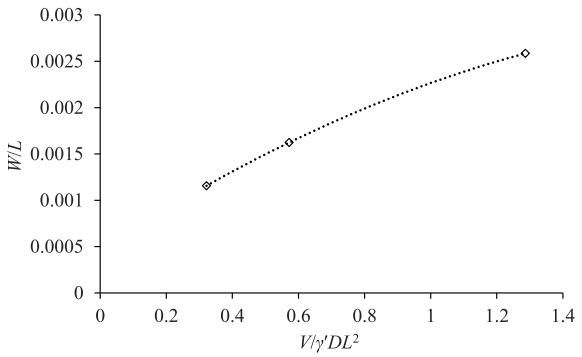

Fig. 9 Normalized settlement versus normalized superstructure load of bucket foundation in medium dense sand

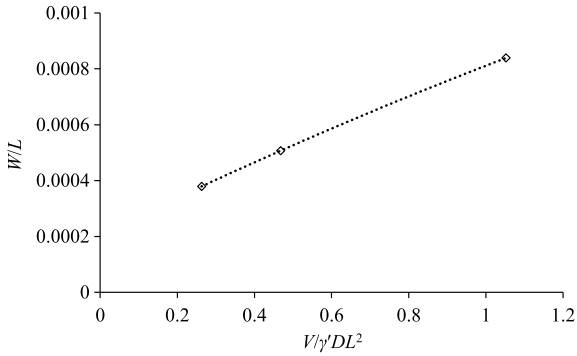

Fig. 10 Normalized settlement versus normalized superstructure load of bucket foundation in very dense sand

Table 7 Values of coefficients for determination of settlement under varying superstructure load

Soil type	Coefficient	Settlement under self-weight (m)		
		$V = 5$ MN	$V = 10$ MN	$V = 15$ MN
Medium dense sand	*a*	−0.0005	−0.0003	−0.0002
	b	0.0023	0.0023	0.0023
	c	0.0005	0.0009	0.0014
Very dense sand	*a*	−7E–05	−3E–05	2E–05
	b	0.0007	0.0007	0.0006
	c	0.0002	0.0004	0.0007

presented in the form of Eq. (2). The coefficients of the equation are presented in Table 7 for the three different superstructure loads for bucket foundations embedded in medium dense sand and very dense sand. The above equation can be utilized to determine the settlement of bucket foundation of 12 m diameter and aspect ratio between 0.5 and 1, under the superstructure load ranging between 5 and 15 MN.

4 Conclusions

Based on the three-dimensional finite element analyses of bucket foundation under vertical compressive loading, the following conclusions have been made:

- The ultimate vertical capacity of embedded solid foundation is found to be maximum followed by bucket and surface foundations. The ultimate capacities of the three foundation types are found to be higher in very dense sand compared to medium dense sand.
- The downward settlement of bucket foundation on account of self-weight is noted to increase with skirt length. The settlement values are lower in very dense sand as compared to medium dense sand.

- For both the sand types, the ultimate vertical capacity of bucket foundation is noted to increase with aspect ratio in a near-linear manner.
- The plastic strain diagrams at failure indicate formation of an elastic wedge under the three foundation types. Surface flow failure mechanism is noted in the case of surface foundation and confined deep flow mechanism is observed for bucket and embedded solid foundations.
- The soil plug entrapped inside the bucket foundation is noted to move downwards along with the foundation and acts as an integral part of the foundation. The soil plug has a cushioning effect while transferring superstructure load to the soil underneath. The soil plug reduces the ultimate vertical capacity by 21–22% in medium dense sand and by 18–19% in very dense sand.
- Predictive expressions have been proposed to estimate the ultimate vertical bearing capacity of monopod bucket foundations.

References

1. Abaqus Version 6.10, Dassault Systemes Simulia Corp. Providence RI USA (2010)
2. Barari A, Ibsen LB, Taghavi Ghalesari A, Larsen KA (2016) Embedment effects on vertical bearing capacity of offshore bucket foundations on cohesionless soil. Int J Geomech 17(4):04016110
3. Byrne BW, Houlsby GT (2002) Experimental investigations of response of suction caissons to transient vertical loading. J Geotech Geoenviron Eng 128(11):926–939
4. EAU (2004) Recommendations of the committee for waterfront structures: harbours and waterways. Ernst & Sohn
5. Eid HT (2012) Bearing capacity and settlement of skirted shallow foundations on sand. Int J Geomech 13(5):645–652
6. Haddad A, Amin, R, Barari A (2018) Effect of embedment on the vertical capacity of bucket foundation in loose saturated sand: physical modeling. Mar Georesour Geotechnol 1–9
7. Houlsby GT, Byrne BW (2000) Suction caisson foundations for offshore wind turbines and anemometer masts. Wind Eng 24(4):249–255
8. Mehravar M, Harireche O, Faramarzi A (2016) Evaluation of undrained failure envelopes of caisson foundations under combined loading. Appl Ocean Res 59(1):129–137
9. Park JS, Park D, Yoo JK (2016) Vertical bearing capacity of bucket foundations in sand. Ocean Eng 121(1):453–461
10. Villalobos F (2007) Bearing capacity of skirted foundations in sand. In: VI Congreso Chileno de Geotecnia, 28–30 Nov 2014, Valparaiso, 1–14

Elasto-Plastic 3D FE Analysis of the Seismic Behavior in Culvert Longitudinal Direction of Three-Hinge Type of Precast Arch Culverts

Y. Miyazaki, Y. Sawamura, K. Kishida and M. Kimura

Abstract The Great East Japan earthquake (11 March 2011) caused loss of serviceability on many three-hinge type of precast arch culverts, which indicated the importance of clarification of its damage mechanism. However, there is no effective seismic evaluation method available in the current design criteria of the precast arch culverts for the observed damages correlated with the inertial force to the longitudinal direction. On the other hand, our research group has conducted the series of dynamic centrifuge tests on the precast arch culverts to observe the seismic behavior in culvert longitudinal direction. As aresult, the seismic behavior in the longitudinal direction of the precast arch culverts is controlled by their longitudinal, structural connectivity and confining stress of the culverts from the embankment. In short, in a numerical analysis, the longitudinal seismic behavior of the precast arch culverts should be governed by these effects due to longitudinal, structural connection and overburden of culverts. Therefore, in the present study, 3D elasto-plastic finite element analyses for three-hinge type of precast arch culvert were conducted to develop a new evaluation method for the longitudinal, seismic performance of the precast arch culverts. In these analyses, the structural connection is modeled by nonlinear spring element and the slip and separation between the culvert and the soil is modeled by joint element. From the analysis results, the patterns of the deformation of the culverts and the embankment and axial force behavior of the structural connections due to the various embankment shape can be evaluated.

Y. Miyazaki (✉) · Y. Sawamura · M. Kimura
Department of Civil and Earth Resources Engineering, Kyoto University, Kyoto, Japan
e-mail: miyazaki.yusuke.73x@st.kyoto-u.ac.jp

Y. Sawamura
e-mail: sawamura.yasuo.6c@kyoto-u.ac.jp

M. Kimura
e-mail: kimura.makoto.8r@kyoto-u.ac.jp

K. Kishida
Department of Urban Management, Kyoto University, Kyoto, Japan
e-mail: kishida.kiyoshi.3r@kyoto-u.ac.jp

A. Prashant et al. (eds.), *Advances in Computer Methods and Geomechanics*, Lecture Notes in Civil Engineering 55,
https://doi.org/10.1007/978-981-15-0886-8_18

Keywords Elasto-plastic 3D FE analysis · Seismic behavior in culvert longitudinal direction · Three-hinge type of precast arch culverts

1 Introduction

Three-hinge type of precast arch culvert (Fig. 1) is one of the precast style culverts which enables labor-saving and high-quality control construction by using precast concrete members. As shown in Fig. 1, this hinged arch culvert is a statically determinate structure due to the three-hinge structures at arch crown and arch foots, respectively. On the other hand, the hinged arch culvert is likely to collapse due to the deviation of hinge, which has emphasized the interest of the seismic stability of the hinge structure; e.g., Sawamura et al. [1] aimed to clarify the damage morphology and the ultimate state of the three-hinged arch culvert through the large table shaking tests on 1/5 model of three-hinged arch culvert. As a result, the deviation in the hinge is unlikely to occur in advance of the failure of the arch members even after a strong earthquake has occurred which has caused more than 7% shear strain of the ground in the three-hinged arch culvert.

On the other hand, the Great East Japan earthquake (11 March 2011) caused critical damages to 9 old types of three-hinged arch culverts (refer to Fig. 1) with the loss of their serviceability. Figure 2 shows the schematic figure of one of the damaged culverts described by Abe and Nakamura [2]. The figure was described based on the observation from the inside of the culvert. The damages to the culverts such as the continuous tip of the arch crown and the water leakages between the arch members seem to be correlated with the inertial force in culvert longitudinal direction. Especially, the old type of the three-hinged arch culvert is weak in the longitudinal structural connectivity without the concrete beam, which seems to cause the larger longitudinal displacements of the arch members.

Although the damage related with culvert longitudinal earthquake was reported, there is no consideration of the longitudinal seismic performance in the design manual of the hinged arch culverts and few related academic researches. Accordingly, the clarification of the damage mechanism and the development of the evaluation method for the seismic behavior in the culvert longitudinal direction are required.

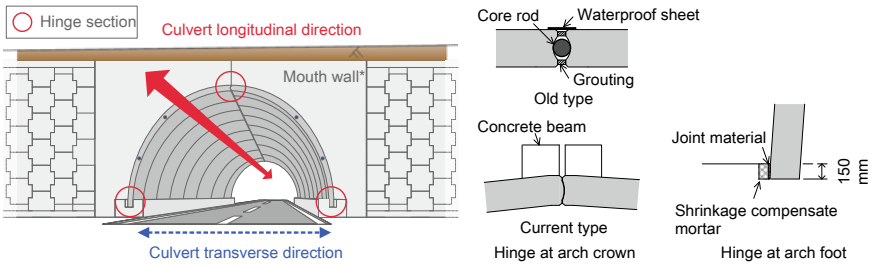

Fig. 1 Structural outline of three-hinge type of precast arch culverts

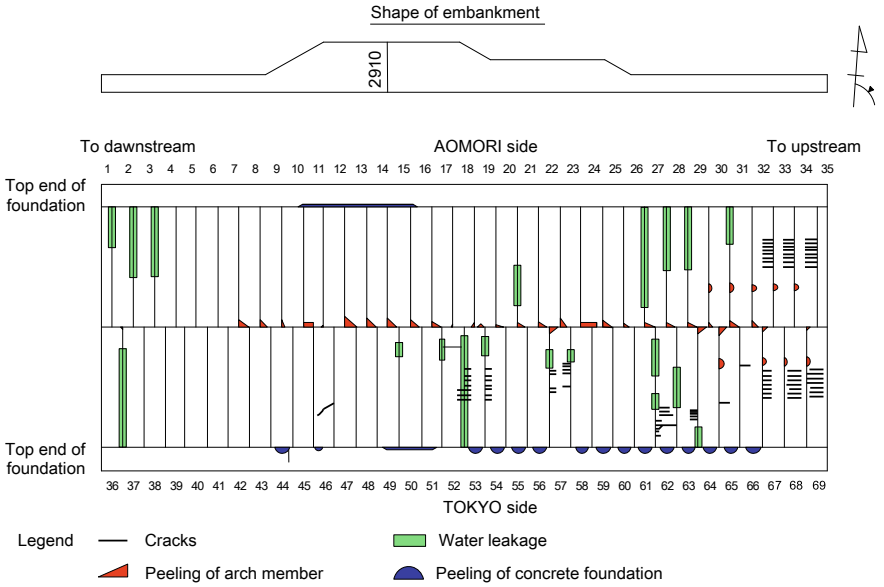

Fig. 2 The schematic drawing of three-hinge type of precast arch culverts after the Great East Japan earthquake reported by Abe and Nakamura [2]

Therefore, our research group has respectively investigated the influence of the structural connectivity of and the embankment patterns of the culverts on the longitudinal seismic behavior. As the experimental results, the structural connectivity dominants the displacements of the culverts; separating the culverts allows the independent movement of each of the culverts, which causes the aperture of the culverts after the earthquake [3]. The embankment patterns strictly control the response acceleration of the culverts; less overburden of the culverts gives less integration of the seismic behavior between the culverts and the embankment [4].

The present study aims to develop a new evaluation method of the seismic performance in the precast arch culverts considering the knowledge based on the above dynamic centrifuge tests. In advance of the development, the 3D elasto-plastic finite element analysis manipulated by DBLEAVES [5] was conducted for the longitudinal seismic behavior of the three-hinged arch culverts. In this paper, how the input wave of culvert longitudinal direction would affect the damage to the culverts with consideration of the longitudinal structural connectivity and the embankment shape is discussed.

2 Outline of Numerical Analysis

2.1 FEM Modeling for Seismic Behavior in Culvert Longitudinal Direction

Figure 3 shows the deformation mode of the culvert with embankment due to culvert longitudinal direction about the observed deformation in the dynamic centrifuge test [3] and the FEM modeling. From Fig. 3a, the longitudinal seismic behavior of the culverts can be explained with rigid rotation and sliding of the culvert with embankment deformation. Therefore, in this FEM analysis, the rigid rotation of the culverts was controlled with nonlinear spring element arranged at the structural connection of culverts and the separation and slip were controlled with joint element arranged at the interface of culvert and soil as shown in the figures (The detail of the arrangements of the spring element and the joint element will be described later in Fig. 6). The embankment deformation was modeled by an elasto-plastic constitutive model.

2.2 FEM Mesh and Analysis Case

Figures 4 and 5 show the analysis meshes. This analysis study focused on the 20 m length of the three-hinged arch culverts on the ground foundation of 5.0 m thickness. The precast arch culverts generally are used as an underpass of road embankment, so that the distance of the culverts was decided to satisfy the available distance for two-lane road of the embankment crown. As shown in the figures, Case-1 was the 1.0 m overburden of the culverts and Case-2 was the 5.0 m overburden of the culverts. The dimension of the analytical mesh was decided by the effect of the culverts on the longitudinal wall displacement and with the consideration of the calculation cost.

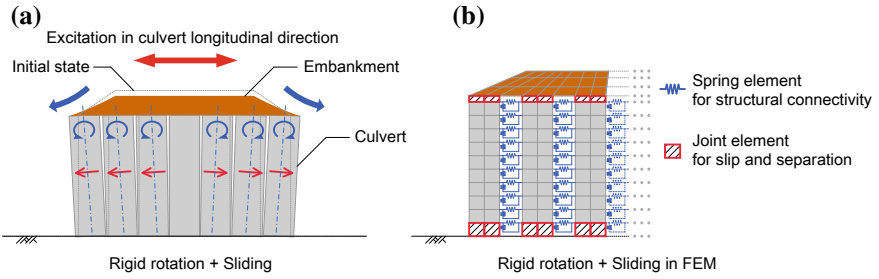

Fig. 3 Deformation mode of culverts due to seismic wave in culvert longitudinal direction. **a** Observed deformation mode in the experiment [3] and **b** expression in finite element method

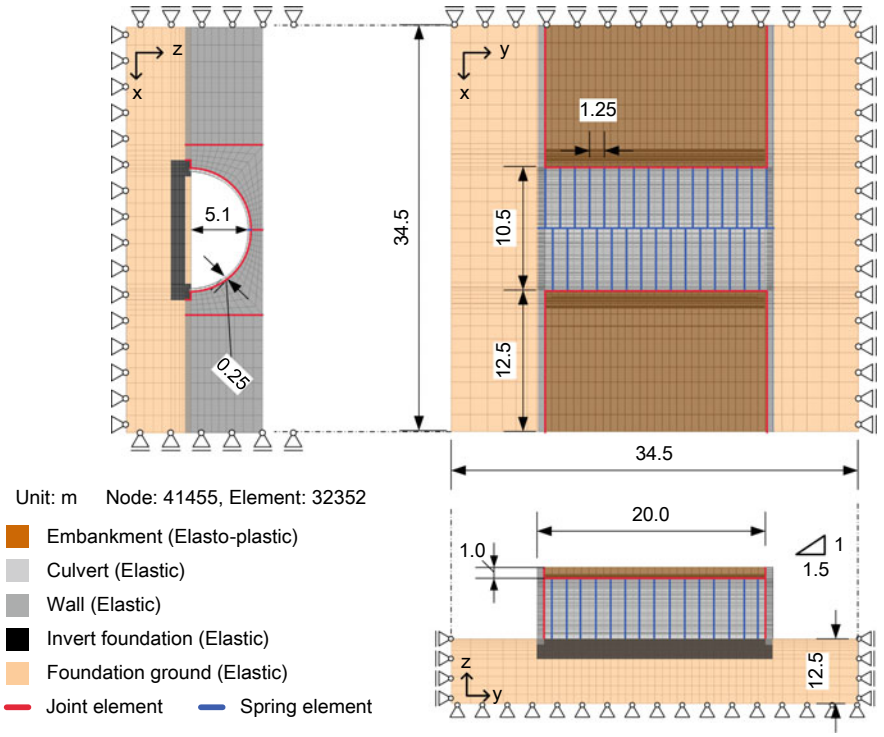

Fig. 4 Analysis mesh in Case-1

2.3 Mechanical Properties of Soil

The mechanical properties of soil were based on Edosaki sand. Foundation ground was modeled by an elastic model whose stiffness equals to 30 in N value of SPT and embankment was modeled by Cyclic mobility model [6]. This constitutive model was developed for simple modeling without change of parameters of stress-induced anisotropic in soil due to soil density, over consolidation ratio, soil structure given by natural accumulating process and various stress histories. These profiles were decided by isotropic consolidation test and triaxial compression test for Edosaki sand [1]. Table 1 shows the parameters of embankment. The initial stress of foundation ground was decided by the self-weight analysis and that of embankment was assumed as K_0 state.

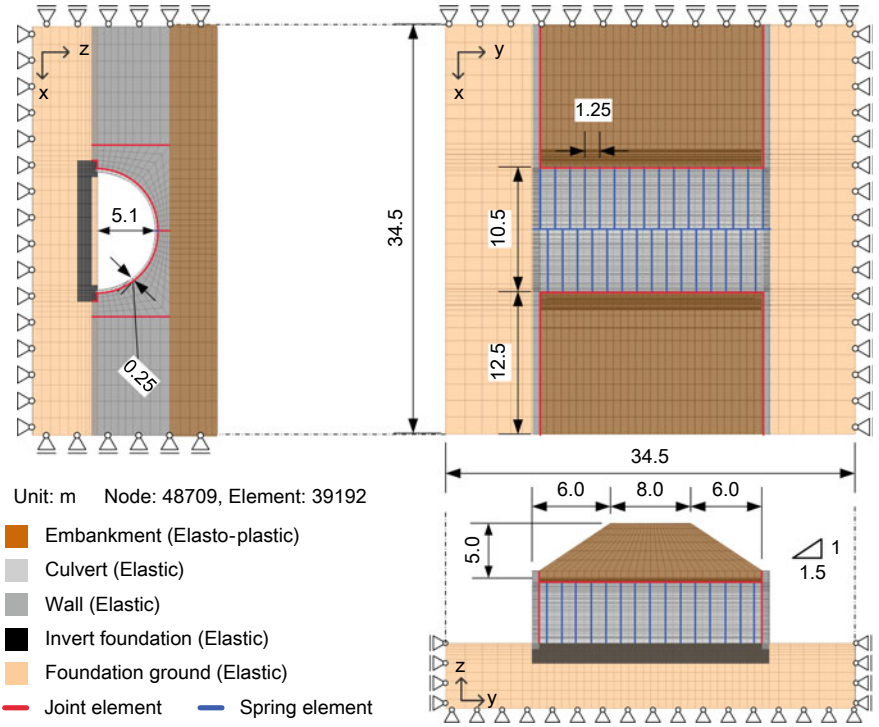

Fig. 5 Analysis mesh in Case-2

Table 1 Soil properties for embankment

Principal stress ratio at critical state $R_{CS} = (\sigma 1/\sigma 3)_{CS(\text{comp.})}$	4.0
Compression index λ	0.08194
Swelling index κ	0.01014
$N = e_{NC}$ at $p = 98\,\text{kPa}$ & $q = 0\,\text{kPa}$	1.06
Poisson s ratio v_e	0.276
Degradation parameter of over consolidation state m	0.02
Degradation parameter of structure a	0.65
Evolution parameter of anisotropy b_r	0.4
Wet unit weight (kN/m^3) γ_t	17.738
Initial degree of structure R^*_0	0.1491–0.1584
Initial anisotropy ζ_0	0.5

Table 2 Properties of concrete

Young's modulus E_a	[kN/m^2]	3.10×10^7
Unit weight γ	[kN/m^3]	24.5
Poisson's ratio v	–	0.20
Damping ratio h	–	0.02

2.4 *Interface of Arch Members*

Figure 6 shows the modeling of soil–structure and structure–structure interface about arch elements and Table 2 shows the material properties of the culvert. From the figures, joint element was arranged on the interface between arch culvert and soil for modeling slip and separation. In longitudinal structural connection of the arch members, nonlinear spring element was arranged. The hinge of the arch crown was modeled with nonlinear spring elements between elements of arch crowns and the hinge of the arch foot was modeled with joint element between elements of the arch foot and foundation.

In this analysis, to express the aperture and water leakage reported in the Great East Japan earthquake, the arch members were modeled in the separated condition without the structural connection. Therefore, the spring constant was controlled to equal zero of tensile stiffness at contactless and enough larger stiffness than concrete at contact. The hinge at the arch crown was modeled by zero of rotating stiffness and the hinges at arch foots were modeled by joint element as shown in the figures. The parameters for the joint element was decided by the direct shear test for mortar and Toyoura sand [1].

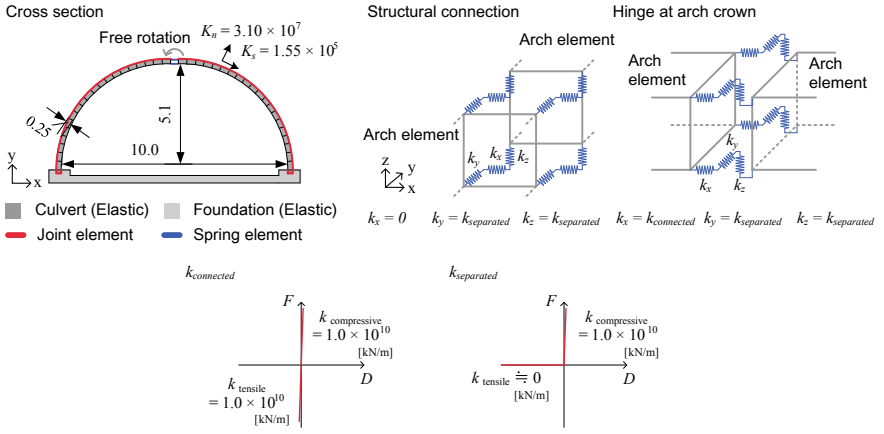

Fig. 6 Soil–structure interface and structure–structure interface of arch element

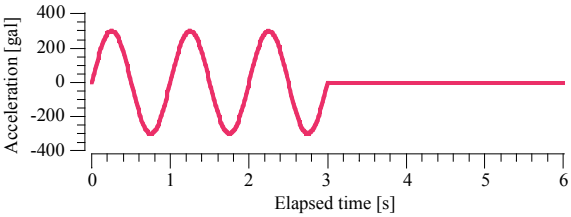

Fig. 7 Input wave is sin wave with 1 Hz, 3 cycles, and 300 gal magnitude

2.5 Model of Mouth Wall

As shown in Fig. 1, the mouth wall of the three-hinged arch culvert is constructed as a perpendicular wall of embankment generally with reinforced earth wall. In the past experiments [4], the unity of embankment and mouth wall modeled as reinforced earth wall was not spoiled during the repeated input of the longitudinal earthquake.

Therefore, in this analysis, considering the unity of embankment and mouth wall, the mouth wall was modeled as an elastic, concrete without reinforcing member. The joint element was arranged at the interface between soil and wall and the shear stiffness was set in enough larger stiffness to express the integral deformation of embankment with mouth wall.

2.6 Input Wave

For the input wave, a sin wave with 1 Hz, 3 cycles, and 300 gal of magnitude (Fig. 7) was used to observe the simple seismic behavior. The wave was input at the bottom of the ground foundation in culvert longitudinal direction. The time interval of calculation was 0.001 s and the time integration was based on a Newmark-β method ($\beta = 1/4$, $\gamma = 1/2$). The proportional stiffness damping model was chosen for the damping.

3 Dynamic Analysis Results

3.1 Seismic Behavior in Culvert Longitudinal Direction

Figure 8 shows the time history of response acceleration in Y direction at the arch crown. From the figures, in Case-1 and Case-2, some vibration appeared in the response acceleration at Pos 1. As mentioned later, the shift of the arch member Pos 1 was occurring. This arch member had unstable behavior due to repeated collision, which caused the vibration of the response acceleration at Pos 1. Here, simply the magnitude of the response acceleration is compared in Case-1 and Case-2.

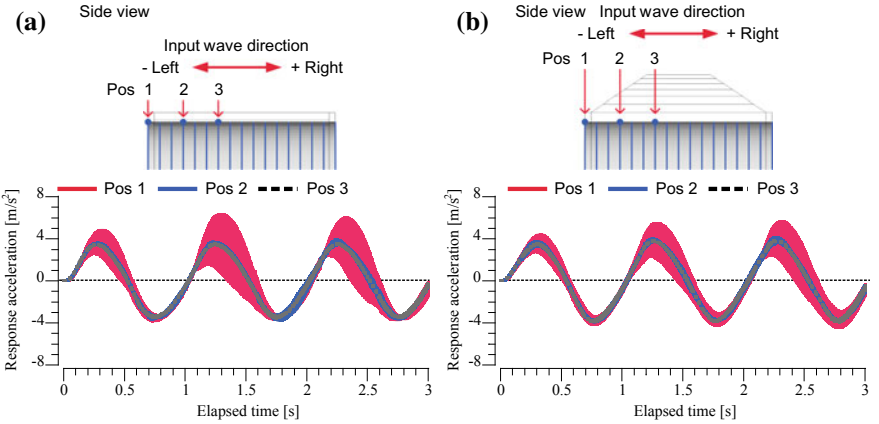

Fig. 8 Time history of response acceleration at the arch crown in *Y* direction: **a** Case-1 and **b** Case-2

The figures, in both Case-1 and Case-2, showed the amplified magnitude at Pos 1 located at the mouth of culvert. Especially in Case-1 which has smaller overburden, the difference of magnitude due to the position was clear. Hence, maximum response accelerations at half of all arch members were plotted in Fig. 9. From the figure, in both Case-1 and Case-2 the maximum response acceleration got increased at the closer position to the mouth of culvert. Additionally, in Case-1, the amplification of acceleration at the arch members near the mouth of culvert got larger compared with Case-2. This is because the smaller overburden of culvert at mouth of culvert gave the smaller confining stress acting on culverts from surrounding ground. As a result, the response acceleration of arch members at mouth of culvert seems to get amplified. This tendency of response acceleration was observed in the dynamic centrifuge tests considering patterns of overburden [4].

This amplified response acceleration of arch members influenced on the aperture of culverts and the unique embankment deformation. Figures 10 and 11, respectively, show the culverts and the embankment after excitation. From the figure of the deformed embankment, compared with Case-2, Case-1 showed the different

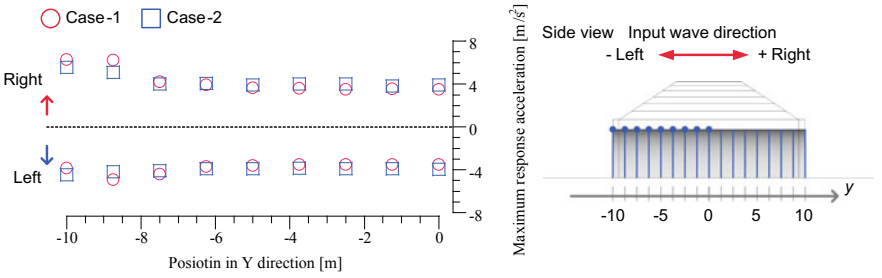

Fig. 9 Maximum response acceleration in *Y* direction at the arch crown of each arch members

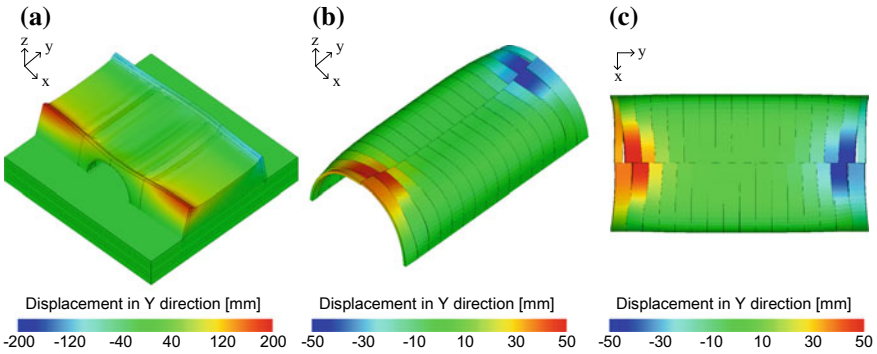

Fig. 10 Heat map of displacement in Case-1 after excitation: **a** displacements in *Y* direction of the culvert with embankment and **b** displacements in *Y* direction of culvert from oblique view and **c** from top view. The displacement output is enlarged by 10 times as the original one

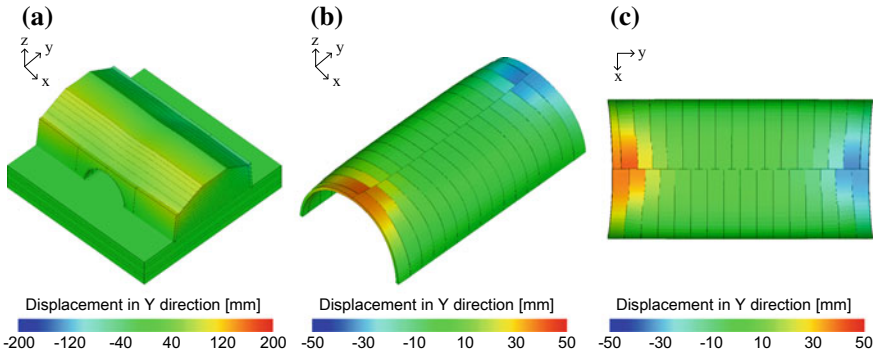

Fig. 11 Heat map of displacement in Case-2 after excitation: **a** displacements in *Y* direction of the culvert with embankment and **b** displacements in *Y* direction of the culvert from oblique view and **c** from top view. The displacement output is enlarged by 10 times as the original one

displacement-mode between area of culvert and are of no culvert. The settlement of the embankment was larger on the culverts and the horizontal displacement of mouth of culvert was smaller near the culverts. About the figure of culvert deformation, in Case-1, there were shifts in vertical direction and aperture of the arch member near the mouth of culvert. In Case-2, there was no observed clear aperture like Case 1 although the shift of the arch member at the mouth of culvert was observed.

From the above results, displacements of arch members are likely to occur in the location under small overburden where confining stress from embankment is weak. Thereby, the aperture of culverts and the water leakage due to the aperture will occur in the arch members with small overburden.

3.2 Stress Condition of Three-Hinged Arch Culvert

In the Great East Japan earthquake, the characteristic damages to the culverts such as the continuous tips of the arch crowns and the bending cracks occurred (Fig. 2). Therefore, about Case-1 and Case-2, the response displacements and stress conditions during excitation were summarized in Figs. 12, 13. In the figure, the output was shown at $t = 2.0$ s when clear embankment deformation began to occur.

From the figures, in Case-1, the displacement in Y direction occurred mainly in the mouth of the culvert. However, in Case-1, the displacements occurred from the mouth of the culvert to the center of culvert. Here, τ_{xy} is the stress to cause the shear deformation in culvert longitudinal direction. When focusing on the arch crown, τ_{xy} seems to be correlated with the displacements in Y direction in both cases. In Case-1, stress concentration occurred on the arch crowns near the mouth of culvert. On the other hand, in Case-2, the stress concentration on the arch crowns continuously occurred along the depth direction. Moreover, the magnitude of the stress was larger in Case-2 than that in Case-1.

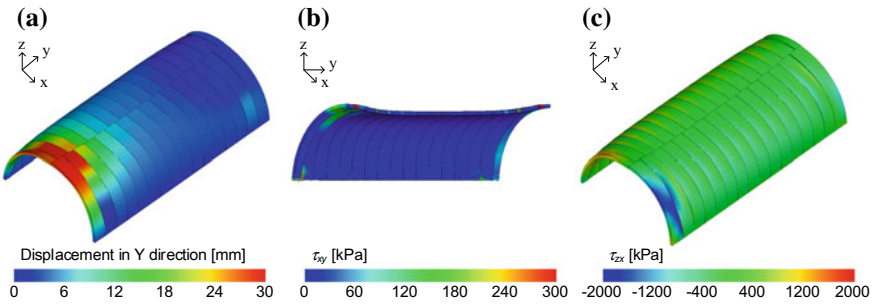

Fig. 12 Heat map of Case-1 at $t = 2.0$ s: **a** displacements in Y direction of the culvert, **b** τ_{xy} on arch crown of cross section and **c** τ_{zx} on culvert from oblique view

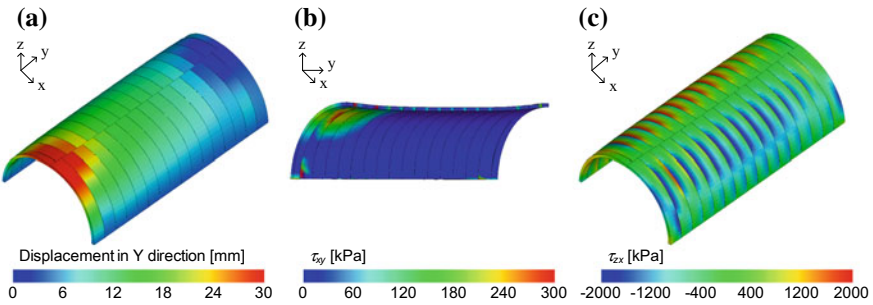

Fig. 13 Heat map of Case-2 at $t = 2.0$ s: **a** displacements in Y direction of the culvert, **b** τ_{xy} on arch crown of cross section and **c** τ_{zx} on culvert from oblique view

Here, τ_{zx} is the stress to cause the shear deformation in culvert transverse direction. Although τ_{xy} was concentrated on the arch shoulders in both cases, the area of stress concentration was different. The stress concentration occurred on the arch members near the mouth of the culvert in Case-1 but on most of the arch members in Case-2. This is because the embankment deformation due to culvert longitudinal earthquake observed in Figs. 10, 11 caused the shear stress of the culvert cross section. Especially in Case-2, the larger shear stress along the excitation direction on each of arch members, which caused the displacement of the arch members. The difference between them are of the shear stress concentration appeared as confining stress of culverts from embankment due to the difference of overburden in Case-1 and Case-2.

Abe and Nakamura [2] assumed the damage mechanism of the arch members observed in the Great East Japan earthquake as shown in Fig. 14. According to the figure, torsion of the arch members occurred due to earthquake and the arch members were knocked against each other, which caused the regular damages to the arch members. Compared with the analysis results, the earthquake in culvert longitudinal direction reproduced the continuous concentration of shear stress on the arch crowns described in Fig. 13b, which seems to correspond to the damage mechanism of the regular tips of the arch crown.

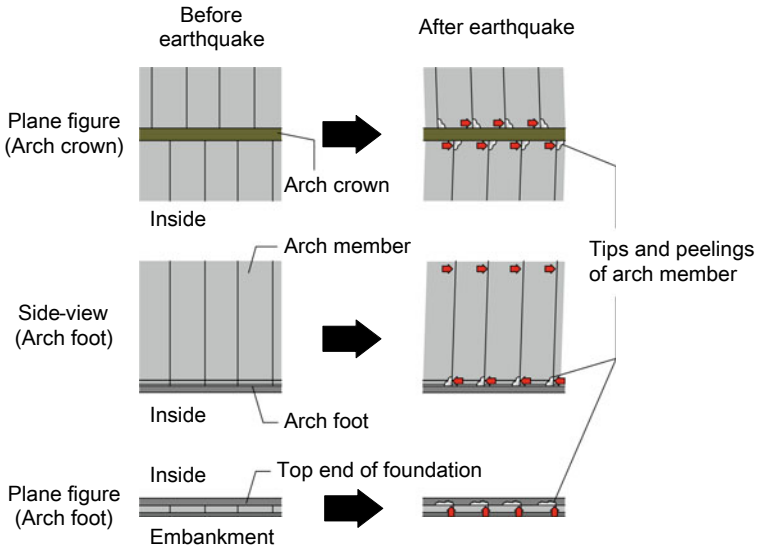

Fig. 14 Mechanism of damage to arch members the Great East Japan earthquake assumed by Abe and Nakamura [2]

4 Conclusions

In the present analyses, the seismic behavior in culvert longitudinal direction of the three-hinged arch culverts without the longitudinal structural connection were conducted by using nonlinear spring element through FEM. The input wave was sin wave with 1 Hz, 3 waves, and 300 gal magnitude. The obtained results are shown below.

(1) The difference of overburden appears as a difference of confining stress acting on culverts. Three-hinged arch culverts with small overburden are likely to suffer the damage related to the displacements of the arch members such as aperture of arch members. On the other hand, the culverts with large overburden are likely to suffer the damages to the arch members themselves due to the increase of shear stress dependent on overburden thickness.
(2) The seismic wave in culvert longitudinal direction causes the concentration of the longitudinal shear stress on the arch crown in the separated culverts. The embankment deformation due to the longitudinal seismic wave increases the shear stress of arch cross section on arch shoulder. As a result, each of stress concentration will cause damage to the arch crown and arch shoulder.

Acknowledgements This work was supported by the Research Foundation on Disaster Prevention of Express Highway by Nexco-Affiliated Companies.

References

1. Sawamura Y, Ishihara H, Kishida K, Kimura M (2016) Experimental study on damage morphology and critical state of three-hinge precast arch culvert through shaking table tests. Procedia Eng Adv Transp Geotech III 143:522–529
2. Abe T, Nakamura M (2014) The use of and the caution in the application of the culvert constructed by large pre-cast element in the expressway construction. Found Eng Equip 42(4):8–11 (in Japanese)
3. Miyazaki Y, Sawamura Y, Kishida K, Kimura M et al (2017) Evaluation of dynamic behavior of embankment with precast arch culverts considering connecting condition of culverts in culvert longitudinal direction. Jpn Geotech Soc Spec Publ 5(2):95–100
4. Miyazaki Y, Sawamura Y, Kishida K, Kimura M et al (2018) Dynamic behavior of three-hinge type precast arch culverts installed in embankment with asymmetrical overburden in culvert longitudinal direction. In: Proceedings of the 9th international conference on physical modelling in geotechnics, pp 915–920, London, United Kingdom, 2018-7
5. Ye B, Ye G, Zhang F, Yashima A (2007) Experiment and numerical simulation of repeated liquefaction-consolidation of sand. Soils Found 47(3):547–558
6. Zhang F, Ye B, Noda T, Nakano M, Nakai K (2007) Explanation of cyclic mobility of soils: approach by stress-induced anisotropy. Soils Found 47(4):547–558

Optimal Foundation Solution for Rail Embankment Resting on Deep Soft Clay Deposits

Jayasai Krishna Gunnu, Tanmay Gupta and Madan Kumar Annam

Abstract Development of transportation infrastructure in coastal areas is one of the major growing facilities in India nowadays. The soil deposits in coastal areas are usually formed over decades with slow deposition rates. Fluctuations in the water table on account of tidal variations make soil weak and create challenges for the practicing geotechnical engineers. Based on the type of transportation infrastructure and soil characteristics, several problems are required to be addresses including but not limited to bearing, settlement, slope stability, and liquefaction. The current study deals with the foundation challenges associated with deep deposits of Marine clay for railway embankment construction at Western Coast Port in India. The geotechnical challenges in terms of bearing capacity, settlements, and overall stability demand suitable ground improvement techniques to support the embankment and moving train loads. Ground improvement technique using vibro stone columns is proposed as optimal foundation solution to meet the performance requirements of the project. Installation of vibro stone columns in soft Marine clay is a challenging task, especially in design, performance, and construction point of view. This paper demonstrates extensive soil investigation works followed by efficient design of vibro stone columns. Several quality control measures before, during, and after ground improvement works are presented to demonstrate the efficiency of treated ground.

Keywords Railway embankment · Soft Marine clay · Soil investigation · Ground improvement · Vibro stone columns · Quality control

J. K. Gunnu (✉) · T. Gupta · M. K. Annam
Keller Ground Engineering India Pvt Ltd., Chennai, India
e-mail: jayasaikrishna@kellerindia.com

T. Gupta
e-mail: tanmay@kellerindia.com

M. K. Annam
e-mail: madankumar@kellerindia.com

A. Prashant et al. (eds.), *Advances in Computer Methods and Geomechanics*, Lecture Notes in Civil Engineering 55,
https://doi.org/10.1007/978-981-15-0886-8_20

1 Introduction

Railway length in India stands at about 114,756 km [7] which is the fifth longest in the World. Despite having such vast network of railway connectivity in India, there is still need for development of railway tracks. One such promising and demanding area of improvement is connectivity of port facilities to support the import-export potential of India. This study details the application of ground improvement using vibro stone columns to deep deposits of soft Marine clay to address the associated geotechnical concerns.

1.1 Motivation

Foundation solution for structures resting on soft clay has always been an area of extreme caution and interest for practicing geotechnical engineers. This paper presents a case study for port facility located on Western Coast of India in the state of Gujarat. The soil at this location is Marine clay formed by deposition over several decades. The Marine clay present is vulnerable to geotechnical concerns including but not limited to Bearing, Settlement, and Slope Stability. The railway connectivity proposed over Marine clay has varying height of embankment to account for railway grades, port level, and high tide level. The embankment and moving train loads shall be accounted to design suitable and adequate foundation system on this Marine clay deposit. The proposed railway embankment is designed using ground improvement with vibro stone columns. The applicability of ground improvement using vibro stone columns in soft Marine clays with low undrained shear strength has been addressed in this study. There have been previous instances of application of ground improvement to support railway tracks [1, 13, 15]. However, this study focusses on railway embankments constructed over vibro stone columns in deep deposits of soft Marine clay.

1.2 Objective

The objective of this study is to propose competent and optimal foundation solution for railway embankment over soft Marine clay. These optimal foundation solutions provide effective measures for addressing foundation problems in cost-effective and time-efficient manner. The project-specific technical criteria and serviceability shall be considered to arrive at suitable optimal foundation system. This paper addresses the applicability of ground improvement using vibro stone columns with proper design and execution control for soft Marine clays. This text details the extensive soil investigation conducted, design objectives, quality control, and post-performance tests. The results from post-performance tests are utilized to conclude and comment

on the efficiency of properly designed and controlled methodology for application of ground improvement in soft Marine clay.

2 Optimal Foundation Solution

The conventional foundation solutions in soil include, bored cast in situ piles, precast driven piles, complete soil replacement in case of shallow depths [6], and accelerating consolidation through band drains 6. In case of deep deposits of soft clay and large surface area of structure, the conventional solution becomes expensive, both in terms of value and time. In order to support such structures on soft clay, optimal foundation using ground improvement by deep vibro techniques is proposed as one of the preferred techniques for addressing geotechnical concerns. Optimal foundations using deep vibro techniques like vibro stone columns [7, 12] and vibro compaction [3] have been successfully used to support tank farms and infrastructure facilities.

2.1 Concept of Vibro Stone Columns

Ground improvement using vibro stone columns is a technique for improving soil such as pure silts/clays or mixed deposits of silts/clays/sands. Ground improvement using vibro stone column technique introduces coarse-grained material as load-bearing elements consisting of stone aggregate as a backfill medium. Thus, by introducing crushed stone aggregates, unimproved soil mass gets improved in terms of bearing, settlement reduction, and drainage [5, 11]. The conceptual sketch of vibro stone columns is presented in Fig. 1.

Vibro stone columns are elements of greater permeability as compared to Marine clay and are effectively stiffer as well. Vibro stone column when installed at design spacing and depth creates a radial drainage path in the soil media and converts the

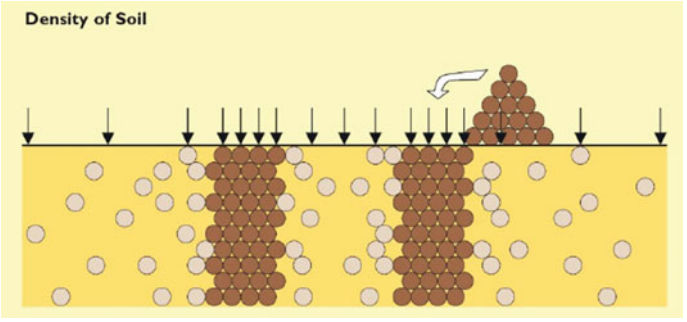

Fig. 1 Basic concept of vibro stone column

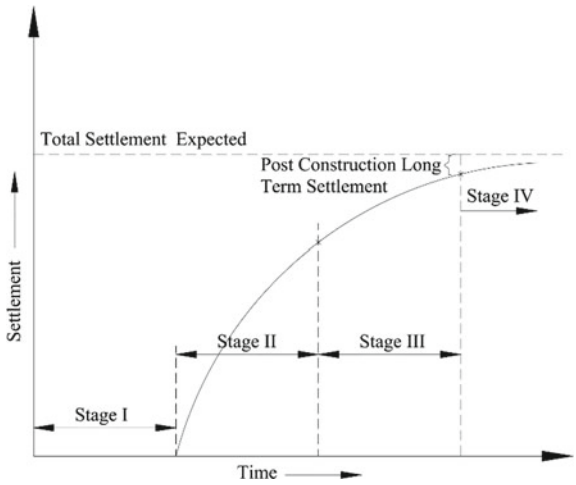

Fig. 2 Settlement concept for clay soil on vibro stone columns

vertical consolidation to radial consolidation. Furthermore, the inclusion of stiffer elements at design spacing provides reinforcement effect to soil continuum which results in increase in bearing capacity of clay soil. The vibro stone columns when used in clay deposits accelerate the rate of settlement. The design may also cater to settlement during constructional stage and the settlement remaining after constructional stage settlement shall be less than the allowable post-construction settlement. A typical settlement progression plot is presented in Fig. 2 showing how the settlements occur in clay continuum after installation of vibro stone columns. Stage I presents installation stage of vibro stone columns where negligible settlements are expected. Stage II is controlled construction of embankment to ensure minimum lateral movement of soil. Stage III is hold period arrived considering radial consolidation equation [2]. Stage IV is operation stage for railway track which shall be as per technical specifications of the project.

3 Case Study: Western Coast Port in India

Railway connectivity is proposed in coastal plains of Western coast to support the inland transportation leading to ports. The existing railway track is being extended to have the freight carriageway till the point of loading and unloading for ships. The proposed stretch covers almost 3700 m of rail line which is resting on soft Marine clay. The proposed area for ground improvement starts from single lead line and branches out to four number of loop lines. Each of these loop lines connects to port facilities of different Berths. Due to presence of natural deep deposits of soft Marine clay, ground improvement using vibro stone columns was proposed to support the railway embankments of varying height as per the design gradient of tracks. The overall layout of the proposed rail line is presented in Fig. 3.

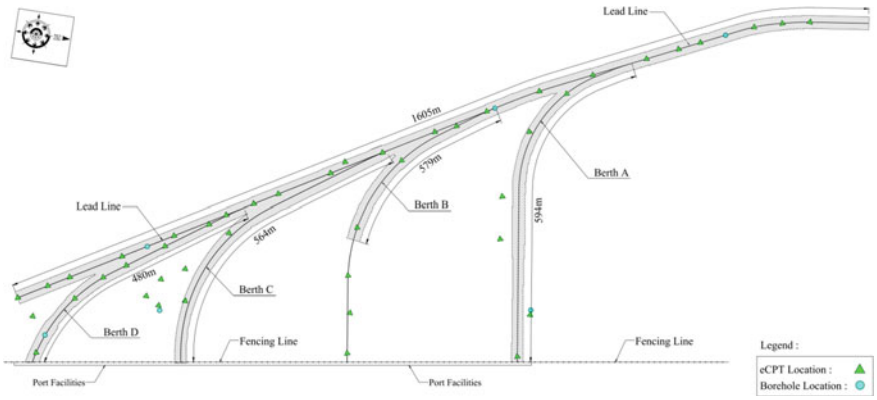

Fig. 3 Layout of proposed rail connectivity

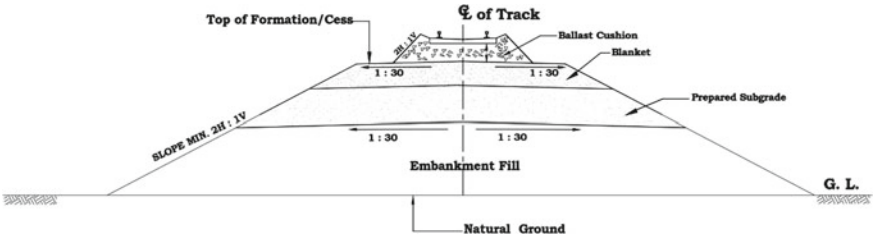

Fig. 4 Details of rail embankment according to GE—14 [4]

3.1 Embankment and Track Details

The project consists of the construction of railway embankment of varying thickness which connects the existing railway line to the port facilities. The project track takes off from mainline which is about –1600 m in length. This lead line branches out in four different loop lines as shown in Fig. 3. The height of railway embankment of the proposed stretch varies from 0.7 to 2.5 m above existing ground level. The rail embankment and track are proposed to carry 32 Ton axle load wagon and are designed according to provisions laid out in GE—14 [4]. The schematic sketch proposed rail embankment is presented in Fig. 4.

3.2 Subsoil Condition

The proposed area of treatment was stretched along—m of length. Extensive soil investigation works were conducted to capture the soil variation and consistency in the lateral extent. The soil investigation includes boreholes for sample collection,

eCPTs for soil behavior and consistency, pore pressure dissipation tests for in situ permeability, and laboratory tests to determine gradation, consolidation, and strength parameters.

To capture the vertical soil profile, boreholes were explored to a maximum depth of 40 m and eCPTs were conducted up to refusal or 30 m, whichever is earlier. Figure 3 shows the layout of soil investigation spread across the rail track length. In general, the soil below existing ground level (EGL) consists of very soft to soft clayey soil in top 18 m. This layer is underlain by firm to stiff clay till 25 m depth followed by dense sand. Average eCPT plots of the soil along the loop lines and lead lines are presented in Fig. 5. Figure 6 presents plot of pore pressure dissipation with time. The pore pressure dissipation tests were performed to record time taken for dissipation of 50% of excess pore water pressure. The results from eCPT and pore pressure dissipation tests were analyzed based on Robertson [16]. Groundwater table was observed at EGL during time of investigation.

3.3 Design of Optimal Foundation

Based on the review of the available soil information and the loading conditions of the proposed railway tracks, following are the major geotechnical concerns to be addressed in the ground improvement design:

- Limit post-construction long term settlements to tolerable limits
- Slope stability
- Enhance Bearing capacity.

Design for Vibro stone columns was done using Priebe's methodology for vibro replacement, Priebe [14]. Figure 7 represents the loading scenarios during construction and operational stages. The range of loading intensity was determined from these load combinations. The loading was arrived as varying from 60 to 85 kPa.

Soil being cohesive in nature is expected to have the majority of settlements as consolidation settlement. The design of vibro stone columns is targeted to achieve 70–80% of consolidation settlement during construction of railway embankment and tracks. Consolidation equations proposed by Balaam and Booker [2] are used to determine the holding period after construction of embankment to allow for soil consolidation.

- Long term post-construction permissible settlements
  - At edge: <150 mm
  - Differential settlement: 1 in 500

Vibro stone column parameters:

- Unit weight of column material: 22 kN/m^3
- Submerged unit weight: 12 kN/m^3

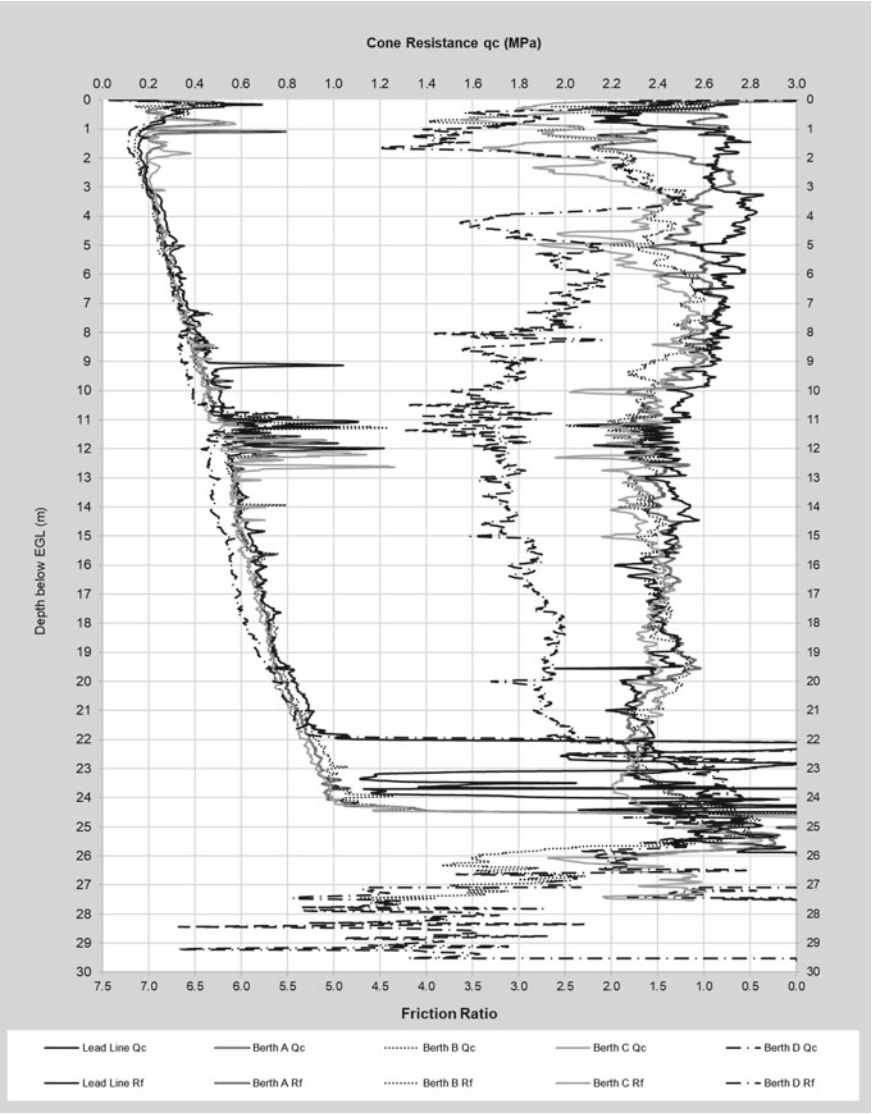

Fig. 5 Average eCPT plots for loop lines and mainline

- Angle of internal friction: 42°
- Modulus of compressibility: 1,20,000 kPa

Proposed treatment scheme:

- Area replacement ratio: 15%.

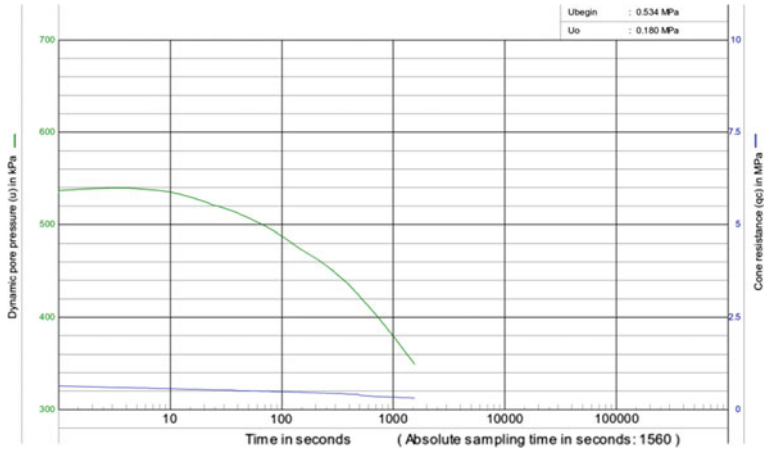

Fig. 6 Pore pressure dissipation plot

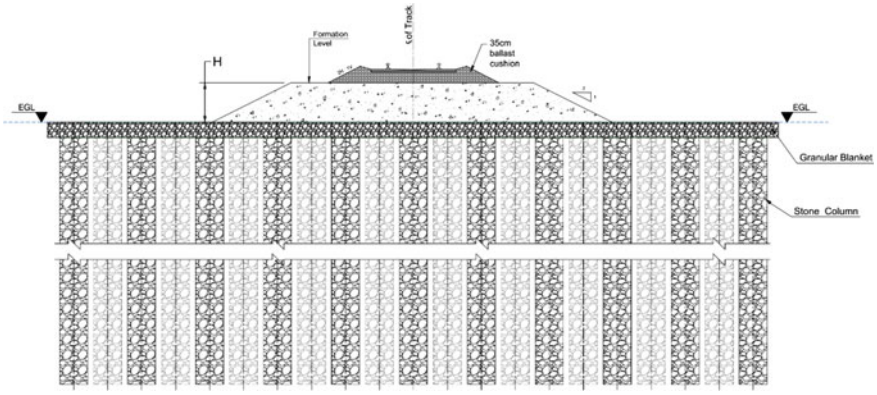

Fig. 7 Conceptual sketch of ground improvement scheme for proposed track

The conceptual sketch of railway embankment founded on vibro stone columns is presented in Fig. 6.

3.4 Quality Assurance and Control

The design of the optimal foundation for any given structure is dependent on the quality procedures adopted during the execution works. The quality assurance and control procedure was strictly followed for this project starting from soil investigation works till completion of load tests and laying of granular blanket above cut off level of vibro stone columns. High-quality control procedures before start of works

were implemented including calibration of piezometric cone, sample collection using thin-walled sampler, and proper packing of samples collected from field.

Quality of vibro stone column works plays a key role in performance of solution provided. Based on soil investigation works, suitable ground improvement solution was provided. The design of vibro stone columns was then successfully verified by conducting initial single and initial group column load tests before start of main works. During execution of main works, state of the art practice using computerized real time output was incorporated. The output is visible to the operator on a digital screen which shows compaction effort being applied at a particular depth. The depth of probe is continuously visible on this screen enabling operator to construct the columns as per the design specifications. These characteristics of installation procedure have indigenous advantage over trivial rammed columns in terms of productivity as well as compaction efficiency.

The quality of stone aggregate was verified as per IS 383 [9] and GE—14 [4]. Post-construction quality check is being verified based on routine load test on every 625 m^2 of treatment area. Typical M4 record from routine installation works is presented in Fig. 8. The plot on left shows depth on horizontal axis and time on vertical axis. The plot on right side shows power amperages on horizontal axis and time on vertical axis. This simultaneous representation of depth and power required for consumption plays a vital role to achieve target compaction and consumption of stone columns.

3.5 Post-performance Tests

As a post-construction performance check, 113 nos. of routine load tests were conducted at regular intervals along the improved stretch. The tests were conducted as per IS 15284 [10, 8] and summary of representative results are presented in Fig. 9. The general trend of load test is presented in Table 1. It is observed that the settlement at design load is confined between 3.6 and 8.6 mm.

4 Observations and Conclusions

The study presented in this paper demonstrates the applicability and performance of ground improvement using vibro stone columns for deep deposits of soft Marine clay. The paper covers various aspects of geotechnical investigation, quality procedures, and post-performance checks.

From soil investigation works, it is observed that the soil is essentially intermediate to high plastic silty clay having cone resistance in the range of 0.2–0.8 MPa in top 18 m. Optimal design of vibro stone columns was proposed to accelerate the consolidation process and to provide reinforcement effect for structural loads. Based on the extensive soil investigation works, ample holding time was proposed after

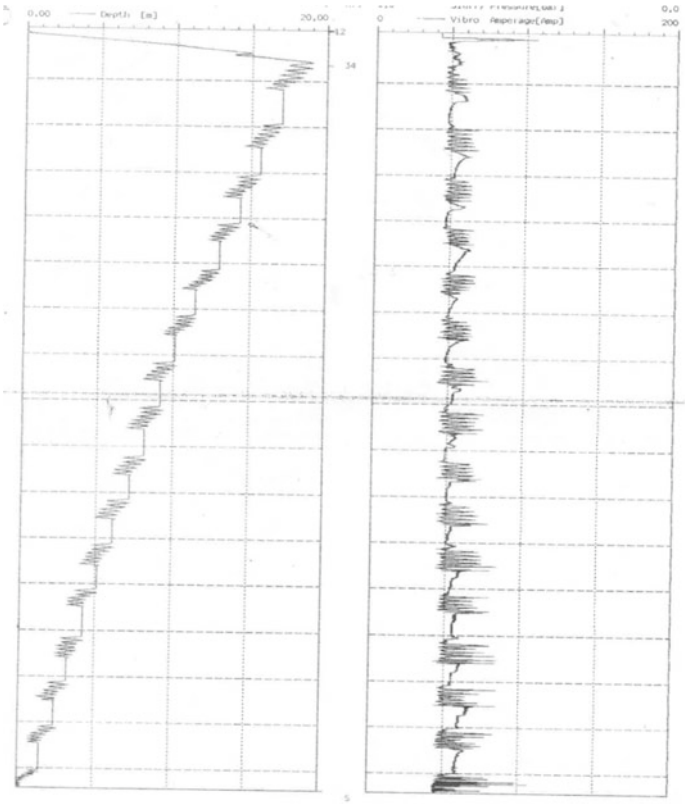

Fig. 8 Typical M4 graph record

construction of embankment to ensure consolidation of the Marine clay deposit. The technical performance criteria were targeted for design of optimal foundation system.

Ground improvement using vibro stone columns was proposed as an effective solution for railway connectivity. Vibro stone columns were targeted to address the settlement and bearing issues related to soil. Quality assurance has been discussed as one of the important monitoring parameters to ensure desired performance of vibro stone columns. Results from ample number of load tests demonstrate that the treated ground can carry the design load within the serviceability limit.

Based on the extensive soil investigation works and design procedures available, an optimal foundation system was proposed for railway embankment. The post-performance tests were conducted to adjudge the efficacy of employed treatment schemes and procedures. Following successful completion of load tests, it is opined that the vibro stone columns are suitable to improve deep deposits of soft Marine clay in case of similar infrastructure projects.

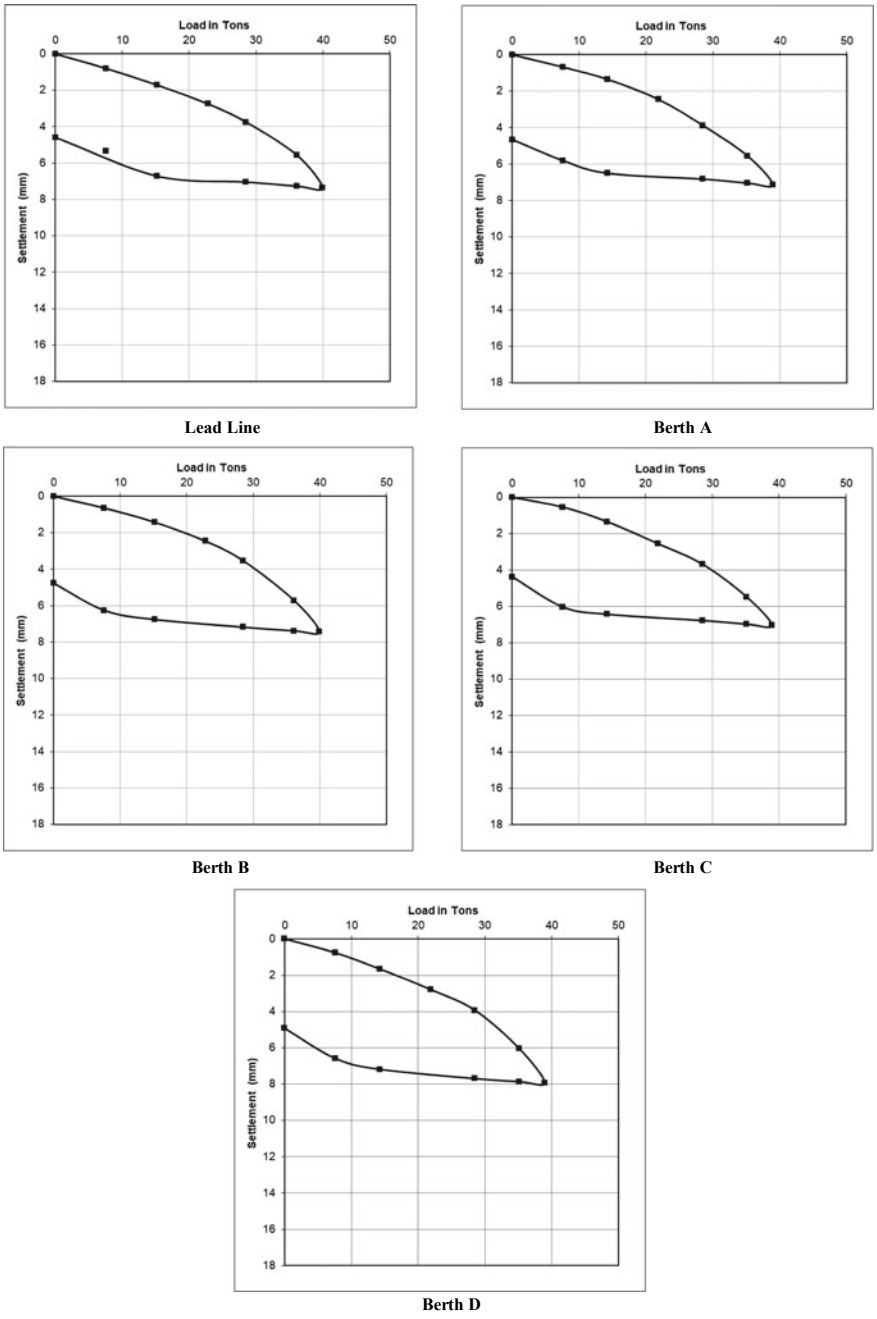

Fig. 9 Typical load versus settlement behavior plots

Reference

1. Arulrajah A, Abdullah A, Bo MW, Bouazza A (2009) Ground improvement techniques for railway embankments. Proc Inst Civ Eng - Gr Improv 162(1):3–14
2. Balaam NP, Booker JR (1981) Analysis of rigid rafts supported on granular piles. Int J Numer Anal Meth Geomech 5(1):379–403
3. Belani T, Shailendra N, Deepak Raj (2013) Study of extent of soil improvement by employing vibro-compaction technique. Int Conf Case Hist Geotech Eng
4. GE 14 (2009) Guidelines and specifications for design of formation for heavy axle load. Government of India Ministry of Railways
5. Gupta T, Sridhar V, Annam M K (2017) Optimal foundation solution for storage terminal in Mangalore. In: Indian Geotechnical Conference, pp 14–17
6. Han J (2015) Principles and practices of ground improvement. Wiley
7. Indian Railways (2017) Facts and figures 2016-17. Ministry of Railways
8. IS, 15284 (2003) Part 2: Design and construction for ground improvement Part 2: Preconsolidation using vertical drains – guidelines, Indian Standard
9. IS, 383 (2016) Coarse and Fine Aggregate for Concrete - Specifications, Indian Standard
10. IS, 15284 (2003) Part 1: Design and construction for ground improvement Part 1: Stone columns – guidelines, Indian Standard
11. Kirsch K, Fabian K (2015) Ground improvement by deep vibratory methods. CRC Press, Taylor and Francis Group
12. Krishna AM, Annam MK, Baruah UK (2018) Stone columns/granular piles for improving liquefiable sites: case studies. Geotech Eng J SEAGS & AGSSEA 49(1):136–142
13. Kumar S, Kumar A, Dahare M (2018) Ground improvement techniques for railway embankments. In: International conference on emanations in modern engineering science & management
14. Priebe HJ (1995) The design of vibro replacement. Ground Eng J 28(10):31–37
15. Raju VR (2003) Ground improvement techniques for railway embankments. Railtech Conference
16. Robertson PK, Cabal KL (2012) Guide to cone penetration testing, pp 1–134

Protection of Buried Pipelines Using Geosynthetics Under Different Loading Conditions—A Review

Margi M. Dave and C. H. Solanki

Abstract The role of buried pipelines is becoming significant day by day in recent urban and industrial development. They act as lifelines of modern infrastructure as they carry essential materials. Damage of buried pipes due to loads acting on them, may result in severe hazards in terms of loss of materials, environmental pollution and sometimes loss of lives too. Hence protection of buried pipelines is extremely important. The paper reviews the effects of geosynthetic reinforcement for buried pipes subjected to different loading conditions. The literature is categorized into six types of loads which may act on pipe namely; static load, repeated load, permanent ground deformation, accidental damage, uplift pressure, and explosion. The paper describes the mechanism of mitigation provided by different geosynthetics. The researches show that the introduction of geosynthetic reinforcement effectively reduces stress, strain, deflection, and vibration in pipes. This paper also reflects the performance of different reinforcement configurations around the pipe. The available experimental and numerical investigations indicate the potentials for the use of geosynthetics to minimize the effects of static as well as dynamic loads on buried pipes.

Keywords Geosynthetics · Reinforcements · Buried pipe · Stress · Strain

1 Introduction

Pipelines are the integral components of development systems of a nation and strongly influence the economy of a country. For efficient land space utilization, buried pipes are more important from infrastructure point of view. The buried pipelines have to deal with several loads acting on them due to surrounding soil, surcharge, vehicular traffic, accidental damages, and earthquake including internal fluid pressure too. Generally, for the better performance of pipeline system, three major factors are given concern namely; design, placement and backfilling (NYSDOT Geotechnical Design Manual). Apart from these, "protection" of buried pipelines is another

M. M. Dave (✉) · C. H. Solanki
Sardar Vallabhbhai National Institute of Technology (SVNIT), Surat, Gujarat, India
e-mail: margidave007@gmail.com

A. Prashant et al. (eds.), *Advances in Computer Methods and Geomechanics*, Lecture Notes in Civil Engineering 55,
https://doi.org/10.1007/978-981-15-0886-8_21

important area that should be taken into account for better serviceability. Geosynthetics have been proved as successful construction material and it is being applied in many civil engineering applications. Its pronounced cost effectiveness, handling techniques, and eco-friendly behavior have replaced the conventional practices [27]. Hence researchers applied this innovative approach of geosynthetic reinforcement to mitigate the adverse effects of various loads acting on buried pipes.

1.1 Buried Pipes

Underground conduits or buried pipelines are generally used to transport water, sewage, fuels, etc. Nowadays telephone and electrical conduits are also becoming essential part of urban development system. Buried pipes are designed to serve two functions: hydraulic and structural. Based on material, pipes are classified into two categories; flexible and rigid [19]. A flexible pipe is defined as one that will deflect at least 2% without structural distress. Rigid pipes show signs of distress before being deflected by 2% [19]. Flexible pipe materials may be steel, ductile iron, Poly Vinyl Chloride (PVC), High Density Polyethylene (HDPE), Fibre Reinforced Polymer (FRP), etc. Rigid pipe includes reinforced concrete cylinder, prestressed concrete cylinder, cast iron pipe, etc.

1.2 Overview of Geosynthetics

The word "Geosynthetics" is composed of two terms: "geo," involving earth/soil and "synthetics," means man-made. Hence geosynthetics are the polymeric man-made products, which are used to improve the ground. Their major functions are reinforcement, separation, filtration, drainage, and protection. The most common geosynthetic products, especially in the context of protection of buried pipelines include: geotextile, geogrid, geonet, geocell, and geofoam. Geotextiles are the permeable textile products. Geogrids are planer, mesh like structure made up of rib (tensile-resistance elements) intersecting at right angle. Geonets have higher rib thickness, intersecting at various angles. Geocells are three dimensional, permeable polymeric products having honeycomb like structure. Geofoams are lightweight and compressible materials, available in slab or block form.

1.3 Existing Pipeline Scenario in India

According to Open Government Data (OGD) Platform of India, the total length of Natural Gas Pipeline is 17,752.697 km as on March 31, 2017; in which major

contribution is from Gas Authority of India Ltd. (GAIL), which owns and operates 11,400 km of natural gas pipeline. Indian Oil Corporation Ltd. (IOCL) operates 13,391 km of pipeline network carrying crude oil, petroleum product, and gas. Besides these there is a much larger network of water and sewage pipeline in India.

1.4 Incidents of Pipeline Damages

On April 29, 2017; there was damage in GAIL operating pipeline due to civil construction operation. As a consequence, a fire broke out on a stretch of road between Garvebhavipalya and Bandepalya off National highway 44 in Karnataka. On June 17, 2017; a rupture occurred in IOCL oil pipeline, 12 feet below ground near Jamnagar, Gujarat. Due to which a farm was flooded with oil. In foreign countries also, several incidents of pipeline disasters are happening. National Transportation Safety Board (NTSB) of United States investigates the transportation accidents. The board has reported numerous case studies of pipeline accidents. Some images of pipeline damages are shown (Figs. 1 and 2).

Fig. 1 Full bore rupture due to lateral ground movement (Image courtesy of Lee EM)

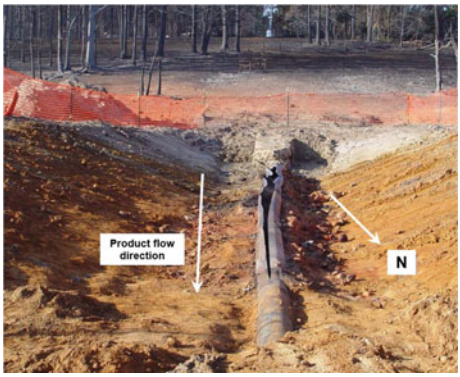

Fig. 2 Mechanical damage of pipeline (Image courtesy of Metropolitan Engineering, Consulting & Environmental Services)

2 Behavior of Buried Pipe Protected with Geosynthetics

Soil-pipe interaction is a complex process to understand as it is a function of pipe properties as well as surrounding soil properties. The stiffness of both the elements plays an important role, that decides the overall performance of buried pipe. Insertion of geosynthetic material adds difficulty in analysis, as geosynthtic properties also affects the behavior of buried pipe system. In order to attenuate the hazard on the buried pipe, selection of proper geosynthetic material is a challenging task. This section discusses about the experimental as well as numerical investigations carried out by several researchers. The section also describes the mechanism of load transfer and stress reduction concept for buried pipe using different geosynthetic materials.

2.1 Static Loading

Static loads act on the buried pipe due to footing, temporary structures, pavements, or embankment, below which they are laid. The load from the backfill material, is also an important factor that affects the stresses generated in pipe. Many researchers experimentally and numerically investigated the behavior of buried pipe, subjected to static load, under geosynthetic-reinforced cohesionless backfill condition [1–4, 8, 12, 13, 23–26].

2.1.1 Investigations Using Geogrid

Rajkumar and Ilamparuthi [25] studied the response of buried PVC pipes in loose and dense sand backfill; along with geogrid reinforcement. The presence of geogrid reinforcement indicated a significant reduction in crown deflection. Corey et al. [3] conducted full-scale plate load test on High Density Polyethylene (HDPE) pipe buried in geogrid reinforced sand trench. The reduction of 11% in soil surface settlement, 26% in pipe deflection, 10% in crown stress, 25% in pipe longitudinal strain were obtained. Ahmed et al. [2] measured radial earth pressure on buried pipeline using tactile sensor technology. Strip surface loading was applied to pipe buried in geogrid reinforced sandy-gravel backfill. A significant reduction in radial stress was found due to geogrid reinforcement as compared to unreinforced case. Pires and Palmeira [24] used three different types of geogrid (having different values of tensile stiffness and aperture size) with three different reinforcement patterns (Fig. 3). The influence of geogrid type and reinforcement pattern on vertical stress (at pipe crown and at spring line), horizontal stress (at spring line), strain (at pipe crown), and pipe settlement was evaluated. As stated earlier the entire performance of pipe-soil-geosynthetic system depends on the properties of individual elements. With regards to the performance of different types of geogrid, not only stiffness but the aperture size of geogrid also plays a vital role. The geogrid having sufficient stiffness as well

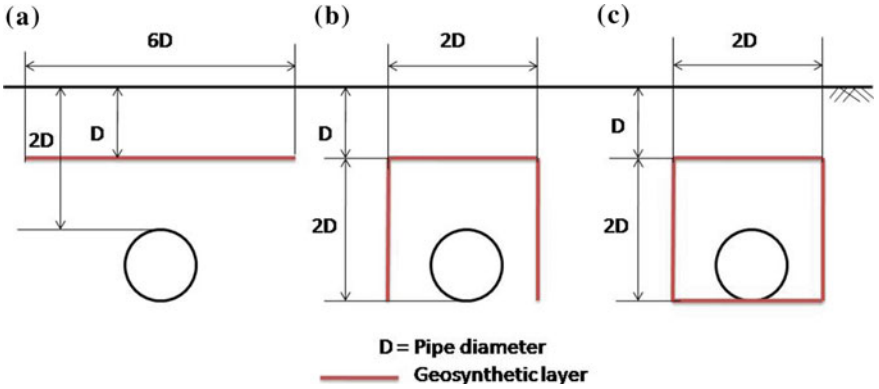

Fig. 3 Reinforcement patterns tested by Pires ACG and Palmeira EM (2017). **a** Horizontal layer. **b** Inverted U arrangement. **c** Enveloped arrangement

as having the aperture size nearly equals to the maximum soil particle diameter, gives good results in terms of stress reduction. The inverted U and envelope system provide confinement to the pipe in lateral direction and thus reduces horizontal stress on pipes; whereas envelope system reduces stress at pipe invert too.

2.1.2 Investigation Using Geofoam

For conduit installation using "Imperfect Ditch Method," EPS geofoams can be used as backfill material. Geofoams are lightweight and compressible materials. Due to their light unit weight, lesser dead load is transferred to the conduit and thus overstressing or rupture of the pipe can be mitigated. On the application of load, it compresses more than that of adjacent soil. Hence shear stresses are mobilized in upward direction, and hence vertical stress on the conduit is reduced (Fig. 4). Kim et al. [12] used EPS geofoams for the reduction of earth pressure on buried pipe. Model tests as well as full-scale tests were conducted with single and double layers of EPS geofoms. Geofoams can also be used for the construction of lightweight embankment above the culvert (Fig. 5).

2.1.3 Investigation Using Geocell

Hedge and Sitharam [8] used geocell, to protect the sand backfilled PVC pipe, from static wheel load. Investigation reflected more than 50% decrease in crown stress and more than 40% decrease in crown strain. The reason behind this is the ability of geocell to distribute the load in lateral direction, up to certain depth and thus it reduces pressure on the pipe.

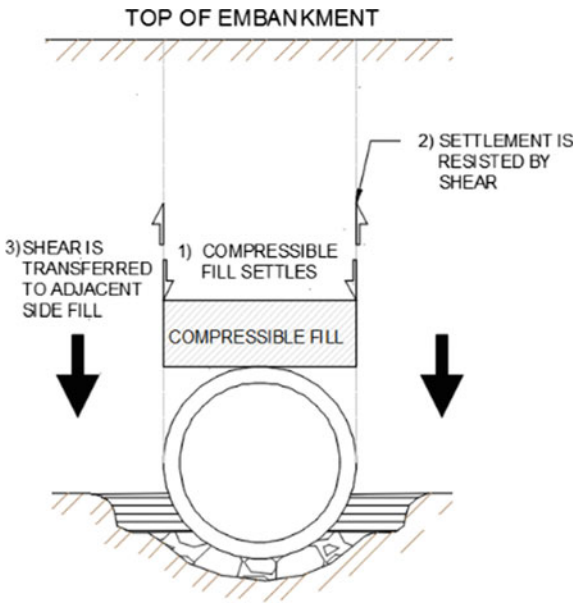

Fig. 4 Stress reduction on the conduit due to arching action (Image courtesy of [28])

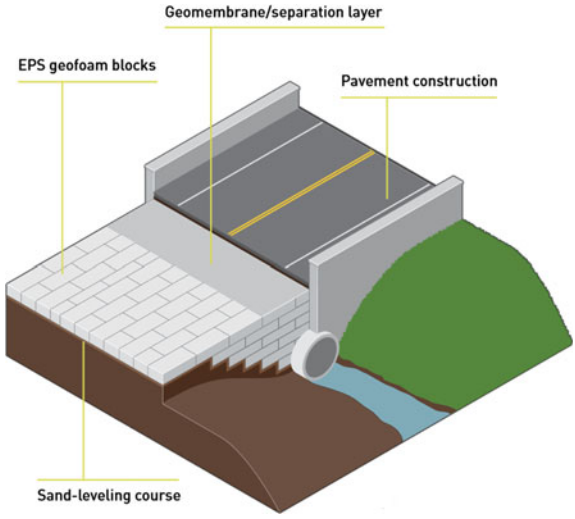

Fig. 5 Schematic drawing of EPS geofoam fill above a culvert (Image courtesy of The EPS Industry Alliance)

2.1.4 Investigation Using Geotextile

Kou et al. [13] found out the effects of width of geotextile on pressure distribution around the pipe by applying footing pressure on the surface of sandy backfill. As the width of reinforcement was increased, the pressure (at crown and spring line) and

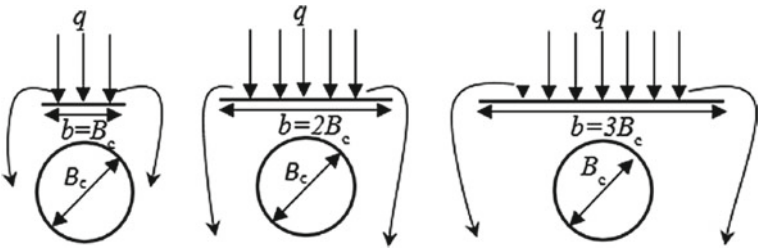

Fig. 6 Pressure distribution around pipe covered with varying width of geotextile (Image courtesy of [13])

deflection were found to be decreased. This is because, the mobilization of geotextile strength caused distribution of footing pressure over larger area (Fig. 6).

2.2 Dynamic Loading

Tafreshi and Khalaj [29], Tavakoli Mehrjardi et al. [30], Fattah and Redha [6], Khalaj et al. [11], Fattah et al. [5] investigated behavior of pipe buried in sand, subjected to repeated loading due to vehicular traffic. Tafreshi and Khalaj [29] examined two parameters, i.e., Radial deformation of pipe and soil surface settlement. The layers of geogrid reinforcement were applied at different relative density of sand and at different embedment depth of pipe. The result indicated that with the introduction of geogrid reinforcement vertical diameter change and soil surface settlement can be decreased up to 56% and 65%, respectively. Tavakoli Mehrjardi et al. [30] used geocell reinforcement and got attenuation of 68% in soil surface settlement and 33% in diametric strain. Khalaj et al. [11] checked the effects of geogrid, EPS geofoam and combination of both on the PVC pipe buried in sand. With the provision of geosynthetic barrier under repeated load, the curvature reversal of the pipe can be reduced.

2.3 Permanent Ground Deformation (PGD)

Permanent Ground Deformation can damage the pipelines. The reason behind deformation may be consolidation settlement, improper compaction, land slide, tectonic faulting, etc. Jiang et al. [10], Lingwall and Bartlett [14], Lingwall [15] used Expanded Polystyrene (EPS) geofoams to mitigate the effects of PGD on buried pipes. Jiang et al. [10] numerically analyzed pipelines wrapped with geofoam. Figure 7 describes the mitigation principle of a pipeline wrapped with EPS geofoam during fault movement. As a compressible material, geofoam deforms more than soil and pipeline and thus protects the pipes through buffer action. For protecting

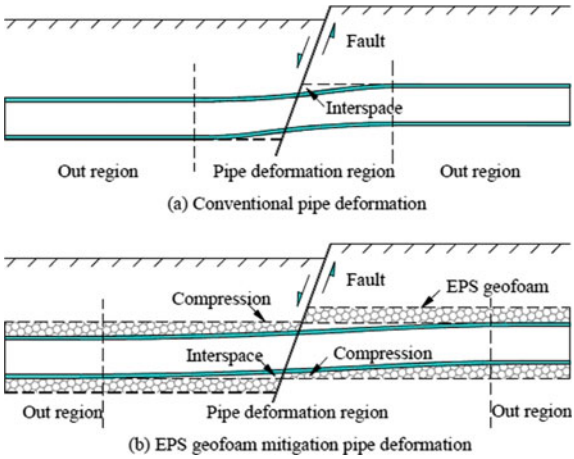

Fig. 7 Mechanism of pipeline mitigation (Image courtesy of Jiang et al. [10])

the pipe from earthquake effects, EPS geofoam can be implemented above a pipe in a trench [15]. The traditional backfill materials such as clay can be replaced with geofoam to prevent pipe damage. Geofoam, being a less stiff material, allows the vertical movement of the pipe and thus reduces bending stresses in pipe. Lingwall [15] carried out full-scale uplift test (Fig. 8). The peak uplift force for the EPS cover system was (1/4)th of the force in case of clayey backfill. The displacement found for the EPS cover system was 2.7 times greater than that of the clayey backfill system. Fig. 9 shows the placement of geofoam block as a lightweight cover atop a 0.6-m diameter steel pipeline crossing the Wasatch fault zone in Salt Lake City, Utah.

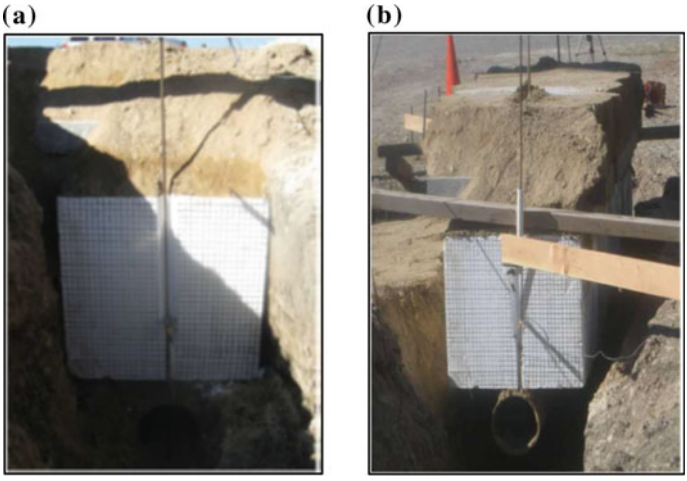

Fig. 8 Uplift test, **a** prior to test, **b** uplifted geofoam (Image courtesy of [15])

Fig. 9 Placement of geofoam block (Image courtesy of [16])

2.4 Accidental Damage

Palmeira and Andrade [22] considered the damage of pipe due to penetration of rigid object into the ground. Laboratory model tests were carried out in which a 20 mm thick plate was penetrated (at various angles) in soil mass to simulate excavation kind of operation. For protecting the pipe, two types of geosynthetic materials (1) geotextile and (2) geogrid, with their three different reinforcement arrangements (Fig. 3) were tested. A reduced stress-strain profile was obtained in case of reinforced soil mass as compared to unreinforced one. The Envelop system gives the best result as it provides complete confinement to pipes. Between geotextile and geogrid; geotextile works better compared to geogrid. The reason behind this is the ability of geotextile to retain the soil particles. But in actual field the damage to the buried pipe due to excavating tool depends on other conditions like pipeline positions, energy applied for digging, etc. Hence for better understanding of accidental damages and its mitigation measures, prototype testing with multivariable analysis should be carried out.

2.5 Uplift Pressure

The rise in groundwater table may cause pipe buckling and floatation. As a result, large horizontal and vertical displacement of pipes may occur. Palmeira and Bernal [23] examined three different types of geogrid and their five different anchorage arrangement (Fig. 10); to protect pipes against uplift pressure. Experiments were conducted in loose homogeneous sandy soil. The reason behind choosing loose soil mass is to simulate critical condition, i.e., uplift pressure under low geostatic stress. Pull out tests were conducted to find out the uplift force. The effect of anchorage length and anchorage pattern on uplift force was studied. For uplift resistance tests, the arrangement covering upper part of pipe and extending in lateral direction as shown in Fig. 10a performed the best. The type of geogrid, which allowed the least passage of soil particles through its aperture was found to be most efficient.

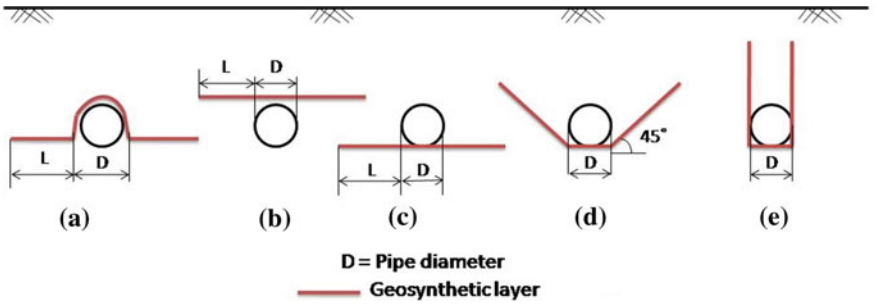

Fig. 10 Reinforcement patterns tested by Palmeira EM and Bernal DF [23]

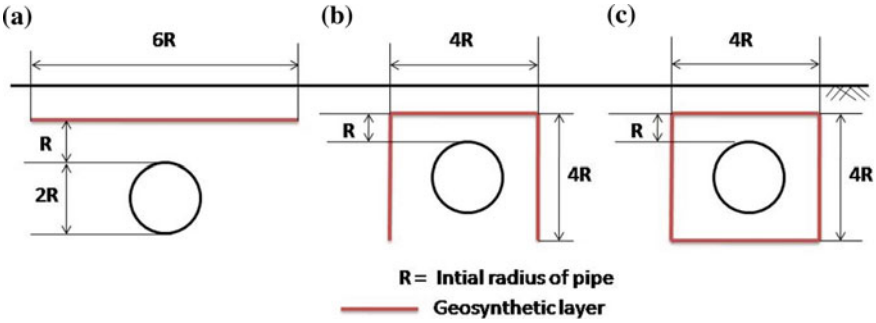

Fig. 11 Reinforcement configurations tested by Tupa and Palmeira [31]. **a** Horizontal reinforcement. **b** Inverted U reinforcement. **c** Envelope

2.6 Explosion

Tupa and Palmeira [31] modeled a situation of pressurized buried pipe. The experiment aimed to study the collapse of pipe inside a tank filled with sand, in both reinforced and unreinforced condition. Two failure mechanisms were considered: (1) expansion of cylindrical cavity in soil mass and (2) collapse due to leakage in the pipe through cracks. Cavity expansion tests were carried out. As a reinforcing materials aluminum sheet, geogrid and three different types of geotextile were tested. Three different reinforcement configurations were examined (Fig. 11). The least permeable geosynthetic and the stronger confining arrangement gives the best performance against the pipe bursting.

3 Conclusion

The experimental and numerical results obtained by the researchers show that the provision of geosynthetic reinforcement effectively attenuates the adverse effects of different kind of loads on pipe. The value of soil surface settlement, pipe deflection,

pipe vibration, pipe strain, vertical, and lateral stresses on pipe, decreases in reinforced soil mass as compared to unreinforced one. Moreover, the bearing capacity of the soil mass increases due to geosynthetic reinforcement; which proves the potential for application of geosynthetics for protecting buried pipes.

Following concluding remarks can be made after analyzing the above investigations.

- With increase in embedment depth of pipe, the susceptibility of pipe damages is reduced. Hence large embedment depth may prove as a better protective measure for pipes. But every time deep embedment is not possible. Hence geosynthetic reinforcement can be used to protect the pipes, buried at shallower depth.
- Geogrid mainly provides protection to the buried pipe due to its membrane effect and stress redistribution action.
- Geocell has the ability to transfer the loads in lateral direction.
- Geofoam induces lesser load on the buried pipe due to their light unit weight. Moreover, their compressible characteristics leads to positive arching action on the application of external load. Hence, they can be used to prevent overstressing of pipe and its deformation.
- Geofoam can be effectively used to mitigate the effects of horizontal as well as vertical ground deformations.
- All the researchers who performed numerical simulation for the validation of experimental data show good agreement.
- Some of the authors performed only laboratory model tests which are not sufficient to understand the actual behavior of the buried pipe system at the field. The prototype testing should be carried out to understand actual behavior at the site.
- Centrifuge testing should be encouraged for parametric experimental study.
- Many of the experiments conducted by the researchers involve single type of pipe material, pipe diameter, pipe backfill material. More variations may provide us the better understanding for different situations.
- The study of a pipe buried in cohesive backfill along with geosynthetic reinforcement is also an unseen area of research, which should be explored out.

Appendix

Details of investigation of pipe buried in geosynthetic-reinforced cohesionless backfill

Author	Type of loading	Type of investigation	Software used for numerical simulation	Type of pipe (Pipe material)	Geosynthetics used
Rajkumar and Ilamparuthi Kim et al. [25]	Static load	Experimental and numerical	PLAXIS 3D	Flexible (PVC)	Geogrid
Kim et al. [12]		Experimental	–	Flexible (Steel)	EPS geofoam
Corey et al. [3]		Experimental	–	Flexible (HDPE)	Geogrid
Ahmed et al. [2]		Experimental and numerical	Finite discrete element (FE-DE) framework	Rigid (Thick walled PVC)	Geogrid
Hedge and Sitharam [8]		Experimental and numerical	FLAC 3D	Flexible (PVC)	Geocell
Raveendran and Thomas[26]		Experimental and numerical	PLAXIS 3D	Flexible (PVC)	Geonet
Pires and Palmeira [24]		Experimental	–	Flexible (Steel)	Geogrid
Abbas [1]		Numerical	PLAXIS 3D	Flexible (PVC)	Geogrid
Kou et al. [13]		Experimental	–	Flexible (uPVC)	Geotextile
Tafreshi and Khalaj [29]	Repeated load	Experimental	–	Flexible (HDPE)	Geogrid
Tavakoli Mehrjardi et al. [30]		Experimental and numerical	FLAC 3D	Flexible (uPVC)	Geocell (with rubber soil mixture)
Fattah and Redha [6]		Experimental	–	Flexible (PVC)	Geocell
Khalaj et al. [11]		Experimental	–	Flexible (PVC)	Geogrid, EPS geofoam

(continued)

(continued)

Author	Type of loading	Type of investigation	Software used for numerical simulation	Type of pipe (Pipe material)	Geosynthetics used
Fattah et al. [5]		Experimental and numerical	PLAXIS 3D	Flexible (PVC)	Geocell
Jiang et al. [10]	Permanent ground deformation	Numerical	ANSYS	Flexible (Steel)	EPS geofoam
Lingwall [15]		Experimental and numerical	FLAC	Flexible (Steel)	EPS geofoam
Palmeira and Andrade [22]	Accidental damage	Experimental	–	Flexible (Steel)	Geotextile, geogrid
Palmeira and Bernal [23]	Uplift pressure	Experimental	–	Flexible (Steel)	Geogrid
Tupa and Palmeira [31]	Explosion	Experimental	–	Rigid (Thick walled PVC)	Geotextile, geogrid

References

1. Abbas BJ (2017) Parametric studies of reducing applied stress on buried PVC pipes using finite element. Muthanna J Eng Technol (MJET) 5(2):21–29
2. Ahmed MR, Tran VDH, Meguid MA (2015) On the role of geogrid reinforcement in reducing earth pressure on buried pipes: experimental and numerical investigations. Soils Found 55(3):588–599
3. Corey R, Han J, Khatri DK, Parsons RL (2014) Laboratory study on geosynthetic protection of buried steel-reinforced HDPE pipes from static loading. J Geotech Geoenvironmental Eng 140(6):04014019
4. Fattah MY, Al-Kalali HHM, Zbar BS (2016) Three-dimensional finite element simulation of the buried pipe problem in geogrid reinforced soil. J Eng 22(5):60–73
5. Fattah MY, Hassan WH, Rasheed SE (2018) Behavior of flexible buried pipes under geocell reinforced subbase subjected to repeated loading. Int J Geotech Earthq Eng (IJGEE) 9(1):22–41
6. Fattah MY, Redha WBM (2016) Effect of geocell reinforcement in the mitigation of traffic loads transmitted to the flexible buried pipes. Glob J Eng Sci Res Manag 3(7):118–128
7. Gas Authority of India Ltd. (GAIL). https://gailebank.gail.co.in
8. Hegde AM, Sitharam TG (2015) Experimental and numerical studies on protection of buried pipelines and underground utilities using geocells. Geotext Geomembr 43(5):372–381
9. Indian Oil Corporation of India (IOCL). https://www.iocl.com
10. Jiang F, Wang X, Gu A (2008) Damage mitigation for buried pipeline using EPS geofoam under permanent ground deformation. In: International conference on Information management, innovation management and industrial engineering. ICIII'08, vol 3, pp 23–26. IEEE
11. Khalaj O, Azizian M, Tafreshi SM, Mašek B (2017) Laboratory investigation of buried pipes using geogrid and EPS geofoam block. In: IOP conference series: earth and environmental science (vol 95, no. 2, p 022002). IOP Publishing

12. Kim H, Choi B, Kim J (2010) Reduction of earth pressure on buried pipes by EPS geofoam inclusions. Geotech Test J 33(4):304–313
13. Kou Y, Shukla SK, Mohyeddin A (2018) Experimental investigation for pressure distribution on flexible conduit covered with sandy soil reinforced with geotextile reinforcement of varying widths. Tunn Undergr Space Technol 80:151–163
14. Lingwall B, Bartlett S (2014) Full-scale testing of an EPS geofoam cover system to protect pipelines at locations of lateral soil displacement. Pipelines 2014:605–615
15. Lingwall BN (2011) Development of an expanded polystyrene geofoam cover system for pipelines at fault crossings. The University of Utah
16. Lingwall B, Bartlett SF (2007) Conceptual design and modeling: EPS geofoam cover system for buried pipelines. Prepared for Questar Gas Corporation, Salt Lake City, Utah
17. List of pipeline accidents. https://en.wikipedia.org/wiki/List_of_pipeline_accidents
18. Metropolitan Engineering, Consulting & Environmental services
19. Moser AP (2001) Buried pipe design. McGraw-Hill, New York
20. NYSDOT Geotechnical Design Manual, Chapter 21: Geotechnical Design Aspects of Pipe Design and Installation. 2018
21. Open Government Data (OGD) Platform of India. https://community.data.gov.in
22. Palmeira EM, Andrade HKPA (2010) Protection of buried pipes against accidental damage using geosynthetics. Geosynth Int 17(4):228–241
23. Palmeira EM, Bernal DF (2015) Uplift resistance of buried pipes anchored with geosynthetics. Geosynth Int 22(2):149–160
24. Pires ACG, Palmeira EM (2017) Geosynthetic protection for buried pipes subjected to surface surcharge loads. Int J Geosynth Ground Eng 3(4):30
25. Rajkumar R, Ilamparuthi K (2008) Experimental study on the behaviour of buried flexible plastic pipe. Electron J Geotech Eng 13:1–10
26. Raveendran G, Thomas N (2017) Geonet as a soil reinforcement system for the protection of buried pipelines. Int Res J Eng Technol (IRJET) 4(4):1894–1897
27. Shukla S (2002) Geosynthetics and their applications. Thomas Telford Publishing, Thomas Telford Ltd
28. Singh S (2016) Pressure reduction on wide culverts with EPS geofoam backfill
29. Tafreshi SM, Khalaj O (2008) Laboratory tests of small-diameter HDPE pipes buried in reinforced sand under repeated-load. Geotext Geomembr 26(2):145–163
30. Tavakoli Mehrjardi G, MoghaddasTafreshi SN, Dawson A (2015) Numerical analysis on Buried pipes protected by combination of geocell reinforcement and rubber-soil mixture. Int J Civ Eng 13(2):90–104
31. Tupa N, Palmeira EM (2007) Geosynthetic reinforcement for the reduction of the effects of explosions of internally pressurised buried pipes. Geotext Geomembr 25(2):109–127

Experimental and Numerical Study on Compacted Sand Bentonite-Tire Fiber Composite for Landfill Application

Krishanu Mukherjee and Anil Kumar Mishra

Abstract The primary aim of the present study is to investigate effect of tire fiber on the shrinkage, hydraulic conductivity and shear strength of sand-bentonite (SB) mixture. The secondary aim is stability analysis of the liner slope with the help of modified fiber soil composite instead of orthodox liner material. A series of consolidated undrained triaxial (CU) and oedometer tests were conducted on sand-bentonite mixture mixed in a proportion of 90:10 and added with tire fibers in a proportion of 0, 5, and 10%. Results indicated that by increasing the tire fiber content the hydraulic conductivity of the mixture increases. From the shrinkage study, volumetric shrinkage (VS) was reduced as the tire fiber content increased. Surface crack and shrinkage crack developed in the mixture after desiccation and expressed in terms of crack intensity factor (CIF) as well as crack density factor (CDF) and both reduced with the addition of tire fiber. Triaxial test results suggested that shear strength parameter and initial tangent modulus enhanced with the percentage of tire fiber increased. Negative excess pore water pressure decreased with increase in tire fiber content. MSW landfill liner model was developed and numerical study had been conducted to investigate the stability as well as the total displacement of landfill liner slope. The analysis suggested that factor of safety increased and total displacement reduced due to the reinforcement effect on liner material (i.e., SB tire fiber composite).

Keywords Landfill · Sand-bentonite mixture · Slope stability · Shear strength · Desiccation cracking

1 Introduction

Due to rapid urbanization and industrialization, the production of municipal solid waste (MSW) has been growing significantly in recent years and causing a major environmental issue in many developing countries. The generation of MSW has

K. Mukherjee (✉) · A. K. Mishra
Indian Institute of Technology, Guwahati, India
e-mail: m.krishanu@iitg.ac.in

A. Prashant et al. (eds.), *Advances in Computer Methods and Geomechanics*, Lecture Notes in Civil Engineering 55,
https://doi.org/10.1007/978-981-15-0886-8_22

been forecasted to rise up to 2.2 billion tons by 2025 [1]. Landfilling is an appropriate and recommended system for the discarding of MSW in several countries across the world [2]. Normally, a compacted blend of sand and bentonite is extensively used as a hydraulic barrier material at landfills. Desiccation induced moisture differences on the compacted sand-bentonite mixture with a low stress can disturb the reduction in plastic deformability [3] and developed shrinkage cracks [4]. Landfill deformations were regulated by settlement [5] in a landfill because of external and self-loading, which may produce tensile cracks, depending on stress levels and materials reliability. Graham et al. [6] performed consolidated undrained (CU) test and reported an effective cohesion and internal frictional angle of saturated compacted sand-bentonite mixture of 40 kPa and 14°, respectively. Previous study suggests that the landfill liner material generally possess a very low value of shear strength [6–8].

Most of the waste tires are discarded illegally, stored, or crammed in a landfill and can cause fire and health risk. Due to its low price and readily accessibility, waste tire fiber has been selected to improve the performance [9–13] and reduce the shrinkage [14] of the hydraulic barrier at the landfill site.

From the earlier studies, it was observed that most of the study had been limited to the influence of several types of the waste tire (i.e., shreds, granulates, and chips) on the geotechnical behavior of sand and sandy-clay. However, no studies have been executed to explore the impact of tire fiber on sand-bentonite mixture mixed in a proportion of 90:10, which are generally, used a landfill material [15]. Compacted sand-bentonite mixture can be threatened for material inconsistency, low shear strength, and excessive settlement because of tensile cracks executed by the environmental factors. According to this fact, consolidated undrained (CU), oedometer, volumetric shrinkage, desiccation cracking, and slope stability analysis have been performed on sand-bentonite mixture reinforced with tire fiber for designing the compacted layers for the application of landfill. MSW (i.e., Municipal solid waste) with Reinforced SB mixture has been used to investigate the stability analysis and experimental results were used for numerical study (i.e., finite element approach) to investigate the stability as well as total displacement of landfill slope.

2 Materials and Methodology

2.1 Material

Sand-bentonite blend added in a ratio of 90:10 (SB10) by their dry weight, and reinforced with 5, and 10% of tire fiber has been implemented for this investigation. Tire fiber dosage has been integrated into the sand-bentonite mixture was preferred based on the source of the research study carried out by other researchers [11, 12].

2.1.1 Properties of Bentonite, Sand, and Tire

Locally available bentonite and sand were used for this present study. The details characteristic of sand and bentonite used in this study were reported by Mukherjee and Mishra [16].

Waste tire fiber is passing through 4.75 mm and retained on 2 mm and it has been considered for the current study. The water absorption capacity of the tire fiber was found out to be 3.78%. The specific gravity of the tire fiber was measured to be 1.14.

2.1.2 Determination of Hydraulic Conductivity

The hydraulic conductivity of a 6 cm diameter and 1.5 mm thickness sample reinforced with tire fiber was determined from consolidation test, which was conducted according to ASTM D2435. The specimens had been prepared by adding deionized (DI) water to get its initial water content to its OMC and specimens were compacted to their individual MDD inside the oedometer ring. Hydraulic conductivity (k) was determined using Terzaghi's theory of consolidation [17] at different consolidation pressure as,

$$k = c_v.m_v.\gamma_w \tag{1}$$

where, γ_{w} is the unit weight of the DI water.

2.2 Consolidated Undrained Triaxial Compression Tests (CU)

To study the impact of fiber on the performance of sand-bentonite, CU test was conducted on compacted sand-bentonite with fiber and compacted sand-bentonite without fiber according to ASTM D4767 [18]. Completely saturated specimen with a minimum measured Skempton's pore water pressure parameter B-value of 0.94 was followed throughout the test. Back pressure up to 480 kPa was applied ensuring to obtain the B-value. Each sample took an average of 21 days to complete the saturation process. An effective confining pressure ranging from 50 to 150 kPa was isotropically applied to consolidate the specimen. Details of the test procedure, i.e., consolidation stage, shearing stage, and strain rate were described by Mukherjee and Mishra [19].

2.3 Determination of Volumetric Shrinkage and Desiccation Cracking of Sand Bentonite—Fiber Composite

Unreinforced and reinforced soil sample had been prepared with a 7.1 cm diameter (i.e., 39.59 cm^2) and 3.01 cm in height. Each specimen had been prepared for their respective MDD and OMC conditions under a room condition of 25 °C (±2 °C). The volumetric shrinkage had been defined as the change in volume (ΔV) to the total volume of the soil sample (v) %, stated by

$$\text{Volumetric shrinkage strain} = \frac{\Delta V}{V} \times 100\% \tag{2}$$

Surface crack and specimen shrinkage were taken by a digital camera (J710F, focal length-3.70 mm) from 30 cm fixed height from the specimen. The analysis of the image had been done by ImageJ 1.51j8 (*Java* 1.8.0-112, 64-*bit*) and essential technique of "ImageJ" was defined by Burger and Burge [20]. All the areas of compacted specimen (i.e., after desiccation), initial specimen area (I_a), reduced specimen (R_s), cracked area (A_c), shrinkage area (S_a), and combined crack area (Cca) were calculated to get cracked intensity factor (CIF) and cracked density factor (CDF) for analyzing the desiccation crack developed in the soil. CIF and CDF had been defined as:

$$\text{CIF} = \frac{A_c \textit{ in square Pixel}}{R_s \textit{ in square Pixel}} \times 100\% \tag{3}$$

$$\text{CDF} = \frac{C_{ca}(\text{i.e. } A_c + S_a) \textit{ in square Pixel}}{I_a \textit{ in square Pixel}} \times 100\% \tag{4}$$

2.4 MSW Slope Stability Analysis by Numerical Techniques

Slope stability of MSW has been performed by using finite element method (PHASE, Rocscience 2017) which can give information of total displacement too.

2.4.1 Problem Define and Performing Procedure

Landfill liner model exhibited in Fig. 1; where, red soil and SB mixes had considered as natural and liner material for the existing model. 11 kN/m^3 unit weight of MSW was taken as suggested by Zekkos et al. (2005) and it acted from 8 m height; therefore load intensity had considered as 88 kN/m^2 and acted as uniformly on the liner. Mohr-Coulomb failure criteria had been considered for this analysis and 3732 number of elements 7657 number of nodes as well as 500 iterations had been selected for this

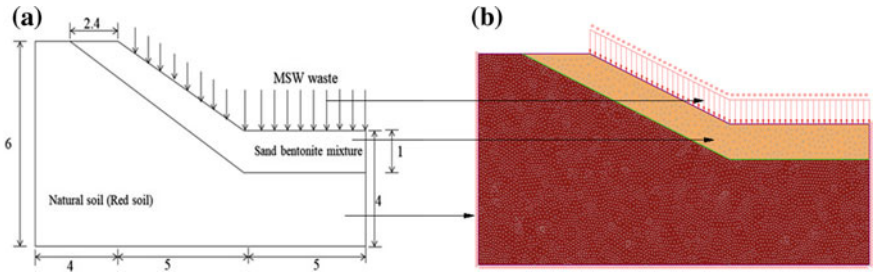

Fig. 1 **a** Schematic diagram of MSW landfill slope model; **b** finite element mesh of MSW slope model

model. The MSW landfill model analyzed with unreinforced as well as reinforced sand-bentonite mixture (i.e., consider for base material) and this scenario can be further explained to case (1), case (2) and case (3) for 0% tire fiber, 5% tire fiber as well as 10% tire fiber to represent the reinforcement effect on the base material. Higher stiffness subgrade soil (i.e., red soil) existed below from the liner material for all landfill models as well as the water table factor did not encounter for this model. Dry density (Υ_d), undrained cohesion (c_u) and internal frictional resistance (φ_u) of subgrade soil were 17.1 kN/m^3, 48 kN/m^2 and 33°, respectively.

PHASE (FEM base, Rocscience [21] has been currently introduced for slope stability analysis in the area of geotechnical engineering [22]. The safety factor (F) has expressed as the factor for the strength parameters require to be reduced to bring the slope to a failure point. This technique is well-known as the shear strength reduction method, which is considered as that point where the solutions fail to meet within a specified number of iterations. The stress distribution failed, which suggested that Mohr–Coulomb failure criterion and the global equilibrium are not satisfied. A sudden rise of displacements associated with the failure of slopes [23].

$$c'_f = \frac{c'}{f} \tag{4}$$

$$\tan \phi'_f = \frac{\tan \phi'}{F} \tag{5}$$

3 Result and Discussion

3.1 *Hydraulic Conductivity* (K) *of Sand Bentonite-Tire Fiber Composite*

k of the soil is the most essential satisfying parameters which must have to be satisfied in order to be used as landfill material. Hauser et al. [24] have suggested that the landfill liner and cover material should have a *k* value lower than 10^{-7} cm/s and 10^{-5} cm/s, respectively. The interactions between the *k* and void ratio as shown in Fig. 2 specified a sharp rise in the *k* with the presence of tire fiber into the soil-fiber matrix. A comparison for the *k* of all the mixtures at a void ratio of 0.48 presented that the hydraulic conductivity increased from 2.7×10^{-8} cm/s to 1.70×10^{-7} (6.29 times) and 7.72×10^{-7} (28.59 times) due to the addition of 5 and 10% tire fiber signifying a noticeable effect of tire fiber on hydraulic conductivity at higher percentage of tire fiber. This behavior may be described in terms of presence of more flow channels for mixture with higher tire fiber contents, which is responsible for a higher value of hydraulic conductivity [25]. However, under the void ratio of 0.4–0.45, hydraulic conductivity of the fiber soil composite were found to 7.21×10^{-9}, 3.79×10^{-8}, and 6.61×10^{-8} cm/s with the inclusion of 5 and 10% tire fiber and blend strongly satisfied the criteria.

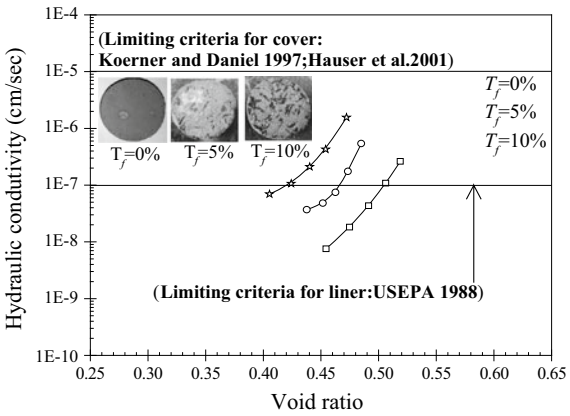

Fig. 2 Hydraulic conductivity and void ratio relationships of fiber soil composite

3.2 *Influence of Tire Fiber on Mechanical Behavior of Sand Bentonite Blend*

The soil should also be physically stable in order to be used as a landfill material and should have the acceptable shear strength to avoid sliding on the slope. The stress-strain response and pore water pressure response of the composites were described below at the confining pressure of 150 kPa.

3.2.1 Effect of Tire Fiber on Stress-Strain and Excess Pore Water Pressure (EPP)

The stress-strain behavior of SB10 composite presented in Fig. 3a. The plots showed that the fiber reinforced specimen showed a peak with large strength improvement for all range of confining pressure. For example, under a confining pressure of 150 kPa, the deviatoric stress of SB10 was improved from 490 kPa to 559 kPa (1.14 times) and 741 kPa (1.51) with the presence of 5 and 10% tire fiber, respectively. As the tire fiber around the soil grains held tight against the shearing, the composite exhibited some extra stress, due to adequate bonding between tire fiber and adjacent soil particle [26]. This behavior was affected the initial tangent modulus (E_i). E_i is strongly affected with increase in confining pressures. For example, E_i was found to be increased from 10.59 to 16.62, and 19.42 MPa under a confining pressure of 150 kPa. A similar kind of trend was followed by other confining pressure also.

The impact of tire fiber on EPP exhibited in Fig. 3b. From the figure, it was noticed that negative EPWP was reduced with tire fiber content. For example, under confining pressure of 150 kPa, negative pore water pressure was found to decrease from 123–89 and 74 kPa due to addition of 5 and 10% tire fiber. This pattern specifies that the tire fiber deformed [27] and stretched during shear, and fiber did not allow the soil

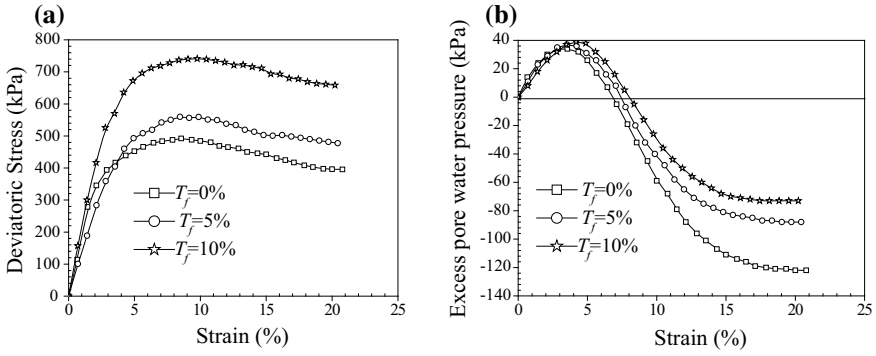

Fig. 3 Stress-strain response of SB10 composite; **a** deviatoric stress-strain behavior of fiber–SB mixes under confining pressure of 150 kPa; **b** excess pore water pressure response of fiber–SB mixes under confining pressure of 150 kPa

particles to move over each other as the negative pore water pressure was reduced, indicating that chances of catastrophic failure of landfill material wereas reduced [25]. On the other hand, it was also observed that positive EPWP was improved from 31 to 36 and 39 kPa, showing that elastic resistance of the blend was improving with tire fiber content.

3.2.2 Impact of Tire Fiber on Failure Pattern and Shear Strength Parameter

The shear strength parameters were obtained from the modified Mohr-Coulomb failure envelop as illustrated in Fig. 4a showed that the effective internal frictional angle of SB10 composite was increased from 27.3° to 28.4° and 31.0° in the presence of 5 and 10% tire fiber content, respectively. Similarly, cohesion component (effective) of SB10 composite was improved from 28.4 to 38.8 and 49.1 kPa due to the combined effect of tire fiber and confining pressure. The above outcomes could be further described over failure pattern, which was presented in Fig. 4b–d under a confining pressure of 150 kPa. From the figure, it was noticed that a mild shear failure noticed (Fig. 4b) for unreinforced soil during shearing. However, reinforced specimen (i.e., f_{tc}= 5%) showed a mixed mode (Fig. 5c) and exhibited a slight shear failure with horizontally bulging. With the increase in fiber content (i.e., f_{tc} = 10%), specimen exhibited barrel failure (Fig. 5d), signifying that the resistance of the composite was improving against volume expansion.

3.3 *Effect of Tire Fiber on VS, CDF, and CIF*

Volumetric shrinkage (VS) was evaluated for the unreinforced as well as reinforced specimen and it was found to decrease with tire fiber content. For example, volumetric

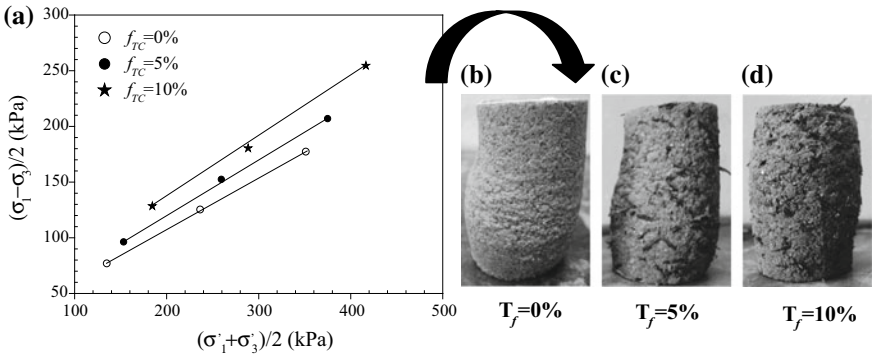

Fig. 4 Modified Mohr-Coulomb failure envelop for SBmix tire fiber composite

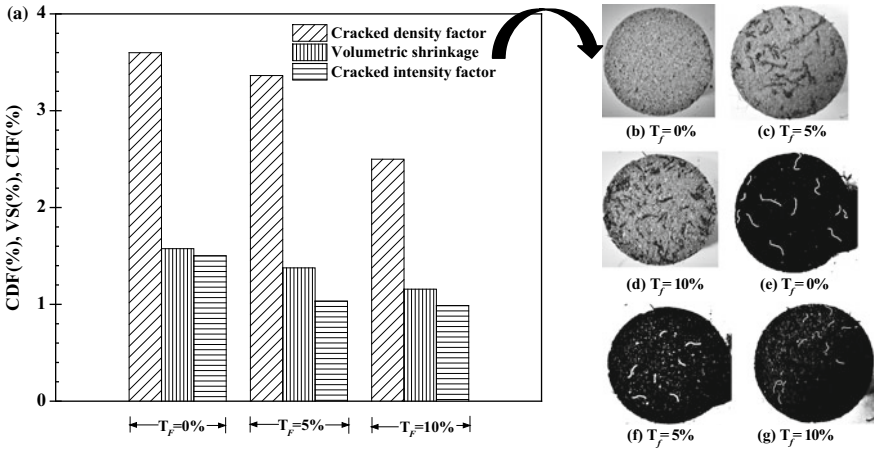

Fig. 5 VS, CDF and CIF of fiber reinforced composite

shrinkage was reduced from 1.58% to 1.38% and 1.16% with 5% and 10% tire fiber, respectively and exhibited in Fig. 5b–d. This mechanism could be defined that effective internal frictional angle was enhanced between the fiber and adjacent soil particle, which provided more resistance from the soil–fiber interaction against the shrinkage strain. The CDF of fiber reinforced specimen showed in Fig. 5a and all the CDF (i.e., total crack) was calculated by image analysis; however, output result was presented in the form of the binary image (i.e., Fig. 5e–g).

From the figure, it was observed that the CDF was continuously reduced with addition of tire fiber. For example, CDF was decreased from 3.6%, to 3.36% and 2.5%, with inclusion of 5 and 10% tire fiber, respectively. Similar trend was also followed by CIF also. With the inclusion of tire fiber CIF of the specimen was decreased from 1.5 to 1.03 and 0.98%, indicating that crack area of the compacted specimen was reduced by the inclusion of tire fiber. Hence, VS, CDF, and CIF were strongly controlled as the fiber content increased, indicating that fiber additive would minimize the shrinkage crack, surface crack as well as volumetric shrinkage strain of hydraulic barrier when desiccation occurred.

3.4 Numerical Analysis

Benson and Othman (1993) reported that shear strength of MSW waste was high in comparison to landfill liner material [8]. Based on SBmix fiber soil composite result, slope stability analysis has been performed and discussed below. For the present study, MSW slope had been divided into two soil layer and stability analysis have been performed by different soil combinations.

3.4.1 Validation of Model

Figure 6 exhibited a three layered slope [28], which had been considered to validate the methodology implemented in using the PHASE programs. Shear strength properties of soil showed in Fig. 6a as well. Three-layer finite element mesh has been presented in Fig. 6a. The critical strength reduction factor (SRF) values found were 1.42 and it much closed to 1.44 as reported by Low [28] under 3000 mesh elements. However, SRF values significantly altered with mesh elements. SRF values obtained were 1.44, 1.5 and 1.49 under 3400, 3800, and 4000 mesh elements, respectively. Thereafter, SRF value did not change with change in mesh elements and SRF value converged with 4000 mesh elements. Hence, 4000 mesh elements have been chosen throughout the analysis. Total displacement contours presented in Fig. 6b and it was almost restricted up to second layer (i.e., Soil B). This was occurred due to third layer (i.e., soil C) had high shear strength properties.

3.5 Stability Analysis of the Liner

The natural soil (i.e., red soil) was fixed and their above soil layer (i.e., liner material) changed with different soil properties and their SRF responses have been noted. Result of the stability analysis has been exhibited in Fig. 7. It was noticed that SRF values of slope was increased with increase in shear strength of base material. Under same slope geometry, SRF values of the slope were found to 1.11, which indicated the MSW slope was highly susceptible for instability. However, SRF values was continuously increased from 1.11 to 1.47 and 1.74 with the inclusion of 5% and 10% tire fiber, respectively, indicating that slope was highly stable with in same slope geometry and it was exhibited in Fig. 7. Base failure of the slope (i.e., throughout entire slope geometry) was observed by distribution of maximum shear strain contour in the case of unreinforced slope (i.e., case 1). However, this pattern was restricted with in the toe for base material reinforced with 5% tire fiber (i.e., case 2); thereafter slope failure was observed in base material reinforced with 10% tire fiber (i.e., case 3). Hence it may be concluded that stability of the liner and possible failure were improved and restricted by the improvement of shear strength of the base material. It

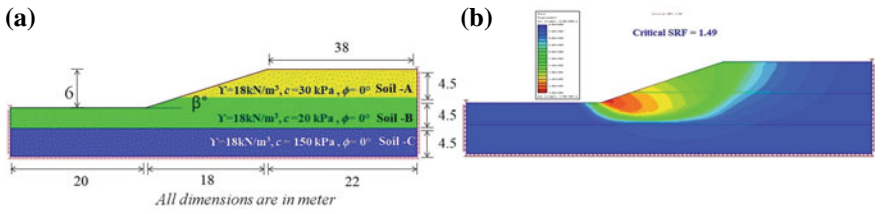

Fig. 6 **a** Finite element mesh for three layered slope model for validations problem [28]; **b** total displacement of three layered slope [28]

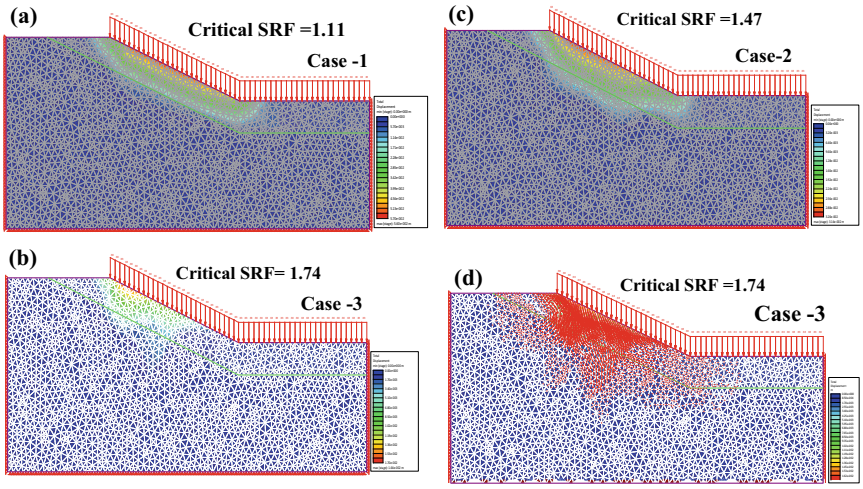

Fig. 7 FOS and total displacement contours MSW slope; **a** base material without tire fiber; **b** base material with 5% tire fiber; **c** base material with 10% tire fiber; **d** total displacement contours with deformation vectors and deformed boundaries for base material with 10% tire fiber

was also observed that deformed vector was moved to downward (i.e., natural soil), indicating failure would start from natural soil in comparison to sand-bentonite fiber soil composite (i.e., reinforced liner material).

3.5.1 Total Displacement of the Liner

Differential settlement of compacted clay liners, caused by compaction over weak ground or over soft spots in an underlying drainage (or leak detection) layer, may result in release of leachate into the surrounding soil/groundwater system [5]. Therefore, total displacement of the MSW slope has been studied and exhibited in Fig. 7. From the figure, it was clear that total displacement (red contour) of the slope was decreased with increase in shear strength in base material. Form the figure; it was observed that total displacement was found to decrease with increase in shear strength of the base material. For case (1), it was noticed that displacement was extended up to base of the slope, but in the second case (i.e., case 2), total displacement concentrated in the middle of the slope (i.e., red contour). However, it was clear that total displacement was continuously reduced and exhibited in red contour, signifying that settlement of slope was also reduced due to reinforcement effect on the base material. Hence, it was suggested that SB10 with 10% tire fiber able to improve the stability and restricted the total displacement of the liner slope.

4 Conclusion

The addition of tire fiber had a significant impact on hydraulic, mechanical as well as stability behavior of landfill liner material (i.e., sand-bentonite mixture). The following findings were drawn from this current study

1. Hydraulic conductivity of the SB10 composite was found to increase with the inclusion of tire fiber but hydraulic conductivity satisfied the design criteria, when their corresponding void ratio would consider from 0.40 to 0.45.
2. Volumetric shrinkage was reduced by tire fiber content. Surface crack and shrinkage crack developed in the mixture after desiccation and expressed in terms of crack intensity factor (CIF) as well as crack density factor (CDF). In contrast, CIF as well as CDF both reduced as the content of tire fiber increased.
3. Effective strength parameter and initial tangent modulus were very poor for unreinforced specimen; however, shear strength and moduli of fiber reinforced soil was found to increase with tire fiber as well as confining pressure.
4. From the numerical model study, it was observed that MSW slope was strongly unstable under the "case 1" condition. Stability considerably improved under the condition of case 2 as well as case 3 (3rd combination). It was also found that the effective strength parameter was the controlling parameter to enhancement the factor of safety of the landfill liner as well as it also reduces the total settlement of the liner.

References

1. Hoornweg D, Bhada-Tata P (2012) What a waste: a global review of solid waste management. World Bank, Urban Development and Local Government Unit, Washington, DC
2. Qian X, Koerner RM, Gray DH (2002) Geotechnical aspects of landfill design and construction. Prentice Hall, New Jersey
3. Morris PH, Graham J, Williams DJ (1992) Cracking in drying soils. Can Geotech J 29(2):263–277
4. Miller CJ, Rifai S (2004) Fiber reinforcement for waste containment soil liners. J Environ Eng 130(8):891–895
5. Maher MH, Ho YC (1994) Mechanical properties of kaolinite/fiber soil composite. J Geotech Eng 120(8):1381–1393
6. Graham J, Saadat F, Gray MN, Dixon DA, Zhang QY (1989) Strength and volume change behaviour of a sand–bentonite mixture. Can Geotech J 26(2):292–305
7. Wan AWL, Graham J, Gray MN (1990) Influence of soil structure on the stress-strain behavior of sand-bentonite mixtures. Geotech Test J 13(3):179–187
8. Jones DRV, Dixon N (2005) Landfill lining stability and integrity: the role of waste settlement. Geotext Geomembr 23(1):27–53
9. Cokca E, Yilmaz Z (2004) Use of rubber and bentonite added fly ash as a liner material. Waste Manag 24(2):153–164
10. Özkul ZH, Baykal G (2007) Shear behaviour of compacted rubber fiber-clay composite in drained and undrained loading. J Geotech Geoenviron Eng 133(7):767–781
11. Ho M, Chan C, Bakar I (2010) One dimensional compressibility characteristics of clay stabilised with cement–rubber chips. Int J Sustain Constr Eng Technol 1(2):91–104

12. Yadav JS, Tiwari SK (2017) Effect of waste rubber fibres on the geotechnical properties of clay stabilized with cement. Appl Clay Sci 149:97–110
13. Mukherjee K, Mishra AK (2017) Performance enhancement of sand–bentonite mixture due to addition of fiber and geosynthetic clay liner. Int J Geotech Eng 11(2):107–113
14. Soltani-Jigheh H, Asadzadeh M, Marefat V (2014) Effects of tire chips on shrinkage and cracking characteristics of cohesive soils. Turk J Eng Environ Sci 37(3):259–271
15. Kumar S, Yong WL (2002) Effect of bentonite on compacted clay landfill barriers. Soil and Sediment Contam 11(1):71–89
16. Mukherjee K, Mishra AK (2019) Evaluation of hydraulic and strength characteristics of sand-bentonite mixtures with added tire fiber for landfill application. J Environ Eng 145(6). https://doi.org/10.1061/(asce)ee.1943-7870.0001537
17. Terzaghi K (1943) Theoretical soil mechanics. Wiley, New York
18. ASTM D4767 (2000) Standard test methods for consolidated undrained triaxial compression test for cohesive soils. West Conshohocken, PA
19. Mukherjee K, Mishra AK (2019) Hydraulic and mechanical characteristics of compacted sand–bentonite: tyre chips mix for its landfill application. Environ Dev Sustain A Multi Approach Theory Pract Sustain Dev 21(3):1411–1428. https://doi.org/10.1007/s10668-018-0094-2
20. Burger W, Burge MJ (2016) Digital image processing: an algorithmic introduction using Java. Springer, London
21. Rocscience (2016b) Phase2 V9.0-2D finite element analysis program. Rocscience, Inc, Toronto
22. Chatterjee D, Murali Krishna A (2018) Stability analysis of two-layered non-homogeneous slopes. Int J Geotech Eng. https://doi.org/10.1080/19386362.2018.1465686
23. Griffiths DV, Lane P (1999) Slope stability analysis by finite elements. Geotechnique 49(3):387–403
24. Hauser VL, Weand BL, Gill MD (2001) Natural covers for landfills and buried waste. J Environ Eng 127(9):768–775
25. Mukherjee K, Mishra AK (2017) The impact of scrapped tyre chips on the mechanical properties of liner materials. Environ Proc 4(1):219–233
26. Mukherjee K, Mishra AK (2019) Undrained performance of sustainable compacted sand-bentonite–glass fiber composite for landfill application. J Cleaner Prod 244. https://doi.org/10.1016/j.jclepro.2019.118662
27. Kaneko T, Orense RP, Hyodo M, Yoshimoto N (2012) Seismic response characteristics of saturated sand deposits mixed with tire chips. J Geotech Geoenviron Eng 139(4):633–643
28. Low B (1989) Stability analysis of embankment on soft ground. J Geotech Eng ASCE 115(2):211–227

Interference Behavior of Four Adjacent Footings on Geosynthetic Reinforced Sand

Sachin S. Saraf and Sunil S. Pusadkar

Abstract Bearing capacity, the supporting power of soil plays an important role in design of shallow foundation. The general scenario is to design the footing as an isolated footing. The interference and spacing effects are generally ignored while designing the footings. In recent years, several heavy axisymmetric structures are coming up very close to each other. Also uses of geosynthetic materials are mostly preferred as soil reinforcement for improving the performance of shallow foundation. The effect of interference of adjacent footing may change the behavior from serviceability point of view and therefore, a need is felt to investigate the effect of interference between closely spaced footings on reinforced soil. In the present study, the bearing capacity of four square adjacent footings on geosynthetic reinforced sand and the effect of different parameters contributing to their performance were studied using model plate load tests. The parameters included were footings placement pattern, depth of footings, type of reinforcement, and number of reinforcement layers. In each case, different center to center distance between footings were applied for the purposes of comparison among all of the results. To evaluate these effects, laboratory model plate load tests were conducted at 55% relative density of sand. It was observed that the footing placement pattern, depth of footings, type of reinforcement, and number of reinforcement layers play a significant role in bearing capacity. The bearing capacity of interfering footing increases as the spacing between footing decreases. Load responses of four footings are similar to those of the single footing at distances greater than three times the footing width.

Keywords Bearing capacity · Four adjacent footings · Reinforced sand · Footing interferences

S. S. Saraf (✉)
P. R. Pote College of Engineering and Management, Amravati, India
e-mail: sachinsaraf2014@gmail.com

S. S. Pusadkar
Goverment College of Engineering, Jalgaon, India

A. Prashant et al. (eds.), *Advances in Computer Methods and Geomechanics*, Lecture Notes in Civil Engineering 55,
https://doi.org/10.1007/978-981-15-0886-8_23

1 Introduction

The structural loads are transmitted to the foundation soil safely without failure in shear or in excessive settlement. The foundations are basically designed keeping in view both criterions. In recent years, several heavy axisymmetric structures are coming up very close to each other. The geosynthetic material is mostly used as soil reinforcement for improving the performance of shallow foundation. The effect of interference of adjacent footing influences the behavior from serviceability point of view and therefore, a need is felt to investigate the effect of interference between closely spaced footings on reinforced soil.

The performance of reinforced soil foundation (RSF) as well as the effect of different parameters on bearing capacity of isolated footing had been experimentally studied by many researchers viz., Patra et al. [25], Basudhar et al. [3], Chen et al. [5], Abu-Farsakh et al. [1, 2], Sharma et al. [28], Vinod et al. [30], Latha and Somwanshi [18, 19], Demir et al. [7], Chakraborty and Kumar [4].

The bearing capacity of two interfering footings on unreinforced sand had been studied by Kumar and Ghosh [17], Kumar and Bhoi [16], Mabrouki et al. [21], Kouzer and Kumar [14], Ghosh and Sharma [11], Ghosh and Kumar [12], Nainegali and Basudhar [23], Srinivasana and Ghosh [29], Nainegali et al. [24] while on reinforced sand by, Ghazavi and Lavasan [8], Ghosh and Kumar [10], Pusadkar and Saraf [26, 27], Ghazavi and Lavasan [9], Pusadkar and Saraf [26, 27], Naderi and Hataf [22]. The result of these research works shows a significant improvement in bearing capacity and settlement after providing continuous geogrid reinforcement. The improvement in the ultimate bearing capacity of adjacent footings had been also observed as the distance between footing decreases.

The literature only shows work on the interfering effects of multiple footings on unreinforced sand by Graham et al. [13], Lee and Eun [20], Kumar and Bhattacharya [15], Daud [6]. It shows that, no study had been carried on interferences behavior of four adjacent square footings on geosynthetic reinforced sand. In order to assess the behavior of four adjacent square footings on reinforced sand, model plate load tests in the laboratory were performed and results were compared for development of knowledge base in this regard.

2 Objective and Scope

The study was intended to investigate the interference behavior of four adjacent square footings on reinforced sand. The parameters affecting the behavior such as footings placement pattern, depth of footings (D), type of reinforcement and number of reinforcement layers (N) were studied. The center to center distance between footings (S) was also varied. The footings were placed in series and square block pattern as shown in Fig. 1a, b, respectively. The depth of footings were varied as

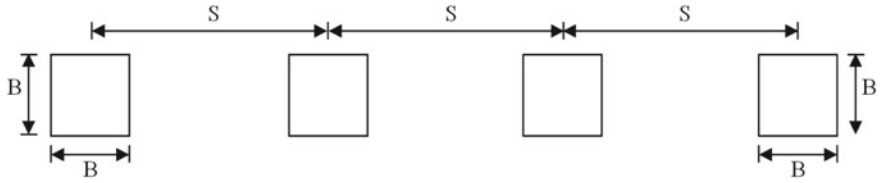

(a) Series pattern

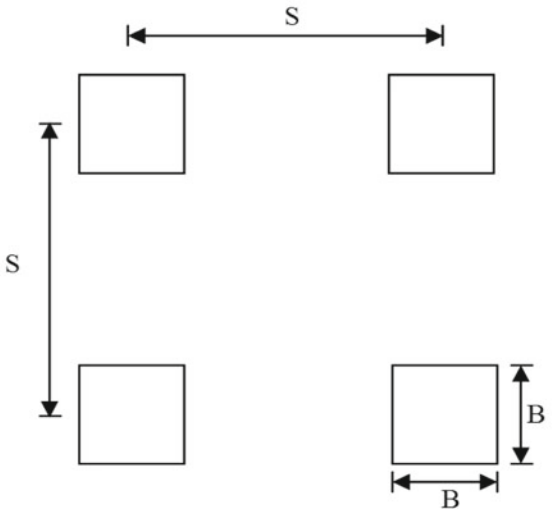

(b) Square block pattern

Fig. 1 Footing placement pattern

the ratio of $D/B = 0$, 1 and 2. The geogrid and geotextile were used as reinforcing material. The numbers of reinforcement layers were l, 2, and 3.

To accomplish the objectives, series of model tests were conducted in laboratory at 55% relative density of sand for all conditions of footing. For reinforced sand $u/B = 0.3$, $h/B = 0.3$, $Lx/B = 3$, and $N = 3$ reinforcement configuration were used. Where u is depth of first reinforcement layer, h is spacing of reinforcement, Lx is the length of reinforcement on either side beyond center of footings and B is width of footing. Figure 2 shows typical layout of multi-layered geosynthetic reinforced sand bed adopted in the model tests for $D/B = 0$ and $N = 3$.

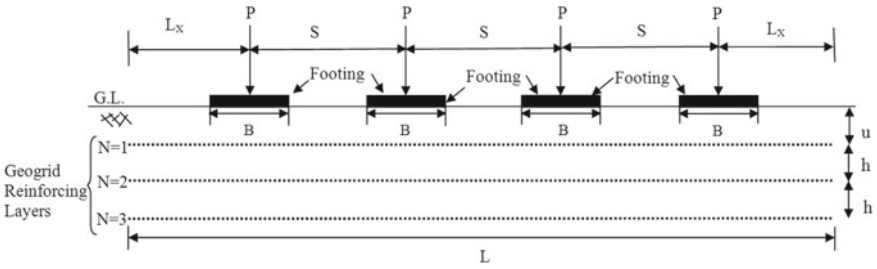

Fig. 2 Typical layout of the geogrid reinforced sand bed for D/B = 0 and $N = 3$

3 Materials and Experimental Program

3.1 Materials

For the model load tests, cohesion-less dry sand (Kanhan Sand) from Nagpur district of Maharashtra state, passing through 2 mm IS sieve and retaining on 1 mm IS sieve was used as the foundation material. The properties of sand used are shown in Table 1.

Commercially available continuous biaxial geogrid and geotextile in three layers were used for reinforcing the sand bed. The properties of the geogrid and geotextile as provided by the manufacturer are as given in Table 2.

Table 1 Properties of sand used

Properties	Values
Specific gravity	2.53
Bulk unit weight (kN/m^3)	15.21
Maximum unit weight (kN/m^3)	16.26
Minimum unit weight (kN/m^3)	14.20
Angle of internal friction	34°
Coefficient of uniformity C_u	2.8
Coefficient of curvature C_c	1.37
Effective size D_{10}	0.50

Table 2 Properties of geogrid and geotextile

Description	Geogrid	Geotextile
Type	Biaxial	Non Woven
Material	Polypropylene	Polypropylene
Thickness (mm)	1.1	1.3
Aperture size (mm)	25 × 25	0
Mass per unit area (g/m^2)	300	160
Tensile Strength (kN/m)	30	16.1

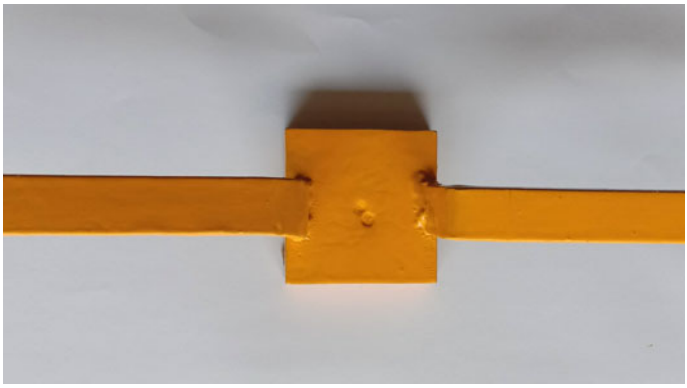

Fig. 3 Model footing

Four model square footings were fabricated from cast iron material. The sizes of each footing were 10 cm × 10 cm. Every footing has a little groove at the center to facilitate the application of load. The base of the model footings was roughened by fixing a thin layer of sand to it with epoxy glue. The footings were provided with the two flanges on two sides of footings to measure the settlement of footing under the action of load with the help of dial gauges as shown in Fig. 3.

3.2 Test Setup

The test setup used for the model tests consists of a test tank, loading frame, hydraulic jack, pumping unit, proving ring, and dial gauges. The test tank of size 2500 mm (length) × 1500 mm (width) × 900 mm (height) was fabricated using steel plates of 6 mm thick. The sand beds were prepared in a test tank. The tank was made rigid by providing the angle sections at different levels, to avoid volume change of tank while preparing test bed as well as during the load test. A loading frame consists of two vertical ISMB 200 girders bolted with ISMB 200 horizontal reaction beam for applying the load to the model footing. The load was applied using controlled hydraulic jack bolted on reaction frame. For transferring the symmetrical loads to four footings, load transfer beam of size 950 mm × 50 mm × 50 mm having arrangement to change the spacing between footings was fabricated and connected to hydraulic jack. Load on each footing was measured with the help of proving ring placed between footing and load transfer beam. Dial gauges were placed on flanges of each footing to measure the settlement. A schematic diagram of test setup used is as shown in Fig. 4.

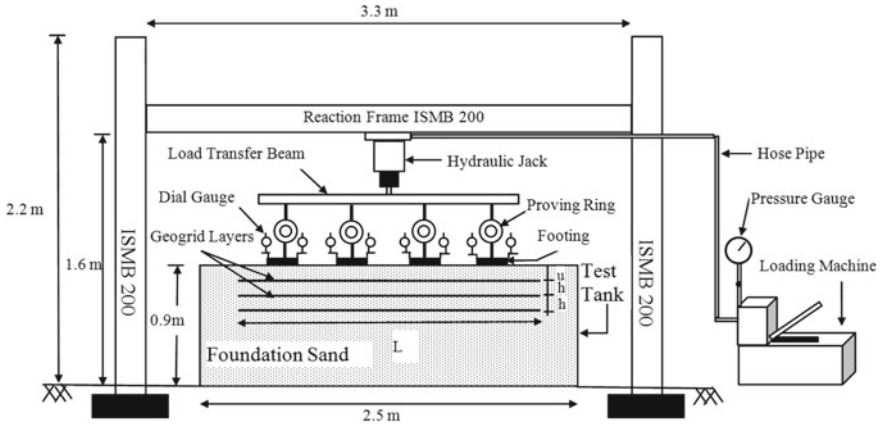

Fig. 4 Schematic diagram of test setup

3.3 Testing Procedure

The test tank was filled with the cohesion-less dry sand passing 2 mm and retaining on 1 mm IS sieve. The rainfall technique was used for the preparation of test bed in a tank. To retain relative density of 55% and average unit weight 15.21 kN/m^3 of the foundation bed the height of fall was kept as 25 cm. The height of sand fall to achieve the desired relative density was determined by performing a series of trials with different heights of fall. The sand deposited to the desired location of the bottom layer geogrid from bottom of footing, the top surface of the sand was leveled and the bottom geogrid was placed. Again, the sand was filled over this geogrid reinforcement layer in the tank up to the desired location of the next layer and similarly the multi-layered geosynthetic reinforced sand bed ($u/B = 0.3$, $h/B = 0.3$, $Lx/B = 3$ and $N = 3$) adopted in the model tests as shown in Fig. 2 were prepared. The prepared top surface of sand was leveled and four square adjacent footings, each 10 cm $\times$ 10 cm size at different spacing are then placed on the prepared reinforced sand bed. Figure 5 shows the actual photograph of the experimental setup used for load tests.

The load was applied to the footings in increments by the controlled hydraulic jack. The load applied was recorded from the reading of proving rings installed between the jack and the test footings. Each load increment was maintained constant until the footing settlement was stabilized. All the four footings were simultaneously loaded. The vertical displacement of each test footing was measured by taking the average of displacement from two dial gauges on diagonal of the plate. The load increments were applied to form the complete load deformation plots up to failure.

Fig. 5 Actual experimental setup used

3.4 Testing Program

Initially one model plate load test was conducted each on isolated surface square footing resting on unreinforced and reinforced sand bed. After that model plate load tests were carried out in four different series (i.e. A to D) on four adjacent square footings resting on geosynthetic reinforced and unreinforced sand bed. Table 3 summarizes each of these series with the parameters used.

4 Result and Discussions

The load settlement curve was plotted for each footing and an average curve was obtained for each set. The typical load settlement curves for isolated and four square footings in series at different spacing for reinforced sand are as shown in Fig. 6. The

Table 3 Summery of laboratory model tests

Test series	Details of parameters used in tests				
	Footing placement pattern	D/B	Type of reinforcement	Number of reinforcing layers	S/B
A	Series and block	0	Geogrid	3	1,2 and 3
B	Series	0,1 and 2	Geogrid	3	1,2 and 3
C	Series	0	Geogrid and Geotextile	3	1,2 and 3
D	Series	0	Geogrid	0,1,2 and 3	1,2 and 3

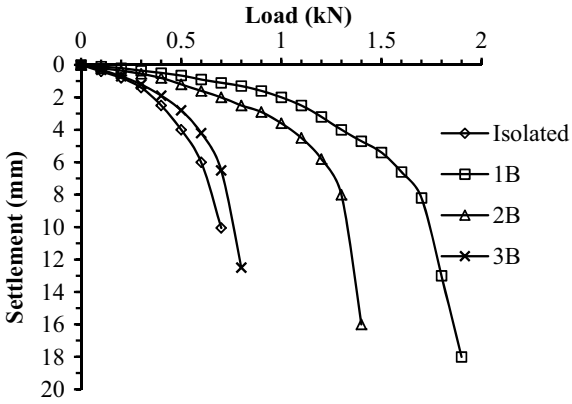

Fig. 6 Typical load settlement curves for isolated and four square footings in series at different spacing for reinforced sand

curves, in general, show a linear variation in the initial portion and become non-linear thereafter. The ultimate failure load was decided from load settlement curve using tangential method.

The performance improvement in terms of the variation in the ultimate bearing capacity due to the provision of geosynthetic reinforcement is quantified through a non-dimensional parameter, the bearing capacity ratio (*B.C.R.*), which is defined as Eq. (1).

$$B.C.R = \left(\frac{q_{u\,\text{int(reinforced)}}}{q_{u\,\text{int(unreinforced)}}} \right) \tag{1}$$

The performance improvement in terms of the variation in the ultimate bearing capacity due to the influence of center to center distance between four footings is quantified through a non-dimensional parameter, the interferences factor (I_f), which is defined as Eq. (2).

$$I_f = \left(\frac{q_{u\,\text{int(reinforced)}}}{q_{u\,\text{iso(reinforced)}}} \right) \tag{2}$$

where $q_{u\ \text{int (reinforced)}}$ is the bearing capacity of an interfering footing on the reinforced sand, $q_{u\ \text{int (unreinforced)}}$ is the bearing capacity of the same footing on unreinforced sand and $q_{u\ \text{iso (reinforced)}}$ is the bearing capacity of the isolated footing on reinforced sand.

4.1 Effect of Footing Placement Pattern

The model plate load tests were performed by placing the four square adjacent footings in series and square block patterns as discussed. For each pattern, different

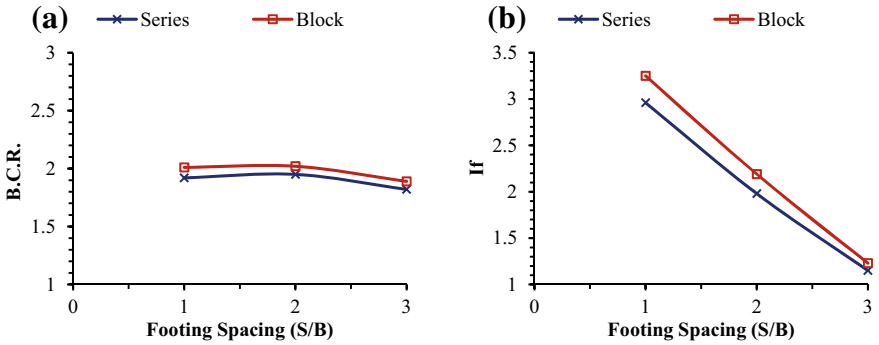

Fig. 7 Variation of B.C.R. and I_f with center to center distance between footings- Test series A

center to center distance between footings were applied ($S/B = 1$, 2 and 3). Footings were placed at surface ($D/B = 0$) on geogrid reinforced sand bed. For reinforcing the sand bed $u/B = 0.3$, $h/B = 0.3$, $Lx/B = 3$, and $N = 3$ reinforcement configuration were used. Figure 7a, b shows the variation of bearing capacity ratio and interferences factor with center to center distance between footings, respectively, for test series (A) as mention in Table 2. It was observed that, in case of square block pattern the U.B.C. increases. For both series and square block pattern, the bearing capacity of interfering footing increases as the center to center distance between four footings decreases. The observed B.C.R. is almost constant for different center to center distances between footings.

4.2 Effect of Depth of Footing (D/B)

The effect of embedment depth on the *U.B.C.* of four adjacent square footings on reinforced sand was investigated by conducting different sets of model tests. One without embedment depth ($D/B = 0$), and two with embedment depth ($D/B = 1$ and $D/B = 2$). In each set, different center to center distance between footings were applied ($S/B = 1$, 2 and 3). Footings were placed in series on geogrid reinforced sand bed. For reinforcing the sand bed $u/B = 0.3$, $h/B = 0.3$, $Lx/B = 3$, and $N = 3$ reinforcement configuration were used. Figure 8a, b shows the variation of *B.C.R.* and interferences factor with center to center distance between footings, respectively, for test series (B) as mention in Table 2. The increase in U.B.C. was observed with the increase in depth of embedment. The interferences factor increases as the center to center distance between four footings decreases and observed to be slightly more for surfaces footing as compared to $D/B = 1$ and $D/B = 2$.

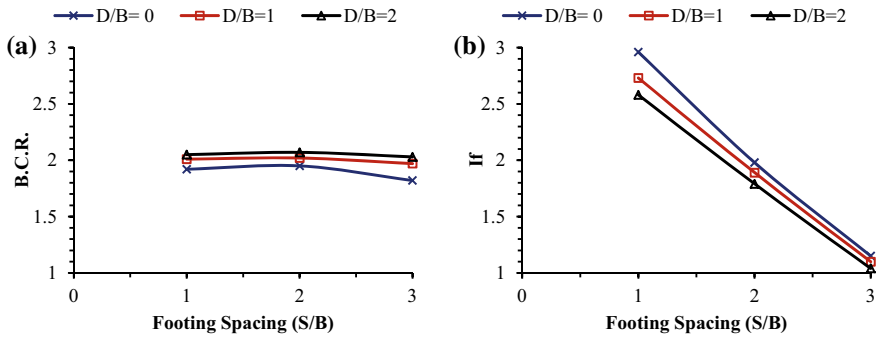

Fig. 8 Variation of B.C.R. and I_f with center to center distance between footings—Test series B

4.3 Effect of Type of Reinforcement

Two different type of geosynthetics reinforcement namely geogrid and geotextile was used in model tests to study the effect of reinforcement type. For each reinforcement type, different center to center distance between footings were used ($S/B = 1$, 2 and 3). Four square adjacent footings were placed in series at the surface ($D/B = 0$) on reinforced sand bed. For reinforcing the sand bed $u/B = 0.3$, $h/B = 0.3$, $Lx/B = 3$, and $N = 3$ reinforcement configuration were used. Figure 9a, b shows the variation of bearing capacity ratio and interferences factor with center to center distance between footings, respectively, for test series (C) as mention in Table 2. It was observed that, the increase in *U.B.C.* due to the provision of geogrid reinforcement is more than the geotextile reinforcement. This better performance of geogrid material as compare to geotextile is due to the characteristic of respective material. The property, tensile strength of geogrid material is more than the geotextile. The bearing capacity of interfering footing increases as the center to center distance between four footings decreases for both geogrid and geotextile reinforcement.

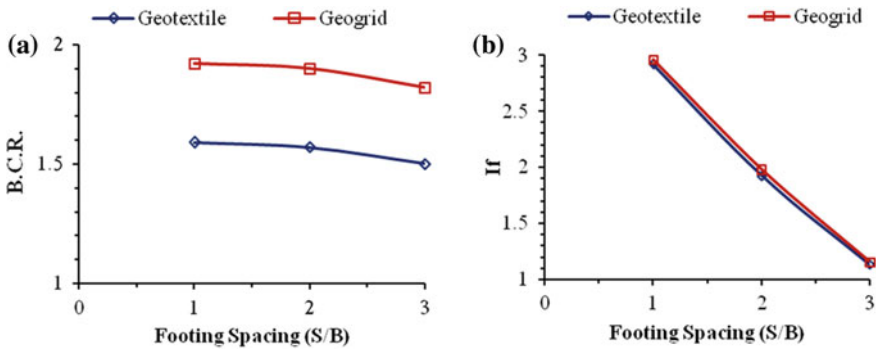

Fig. 9 Variation of B.C.R. and I_f with center to center distance between footings—Test series C

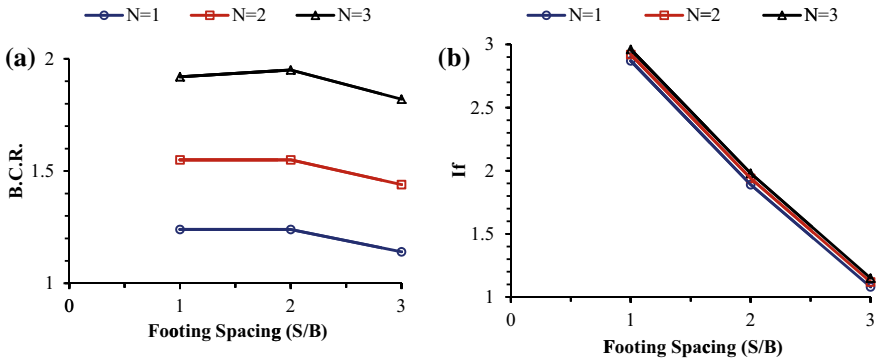

Fig. 10 Variation of B.C.R. and I_f with center to center distance between footings—Test series D

4.4 Effect of Number of Reinforcement Layers (N)

The reinforcement layers, in the foundation were reinforced with 0, l, 2, and 3 layers of geogrid reinforcement. For each case, different center to center distance between footings were applied ($S/B = 1$, 2 and 3). The model plate load tests were performed by placing the four square adjacent footings in series at surface on geogrid reinforced sand bed. For reinforcing the sand bed $u/B = 0.3$, $h/B = 0.3$, and $Lx/B = 3$ reinforcement configuration were used. Figure 10a, b shows the variation of *B.C.R.* and interferences factor with center to center distance between footings, respectively, for test series (*D*) as mention in Table 2. The performance improvement in terms of increase in *U.B.C.* due to the provision of geogrid reinforcement and existence of interfering footing increases with increase in number of reinforcement layers. The bearing capacity of interfering footing increases as the center to center distance between four footings decreases.

5 Conclusions

Based on the test results, the following conclusions were drawn:

- The footing placement pattern plays a considerable effect on the behavior of four adjacent footings on reinforced sand foundation.
- The ultimate bearing capacity found to be more when the footings are placed in block pattern as compared with series pattern.
- Better performance of geogrid reinforcement as compared to geotextile reinforcement was observed and attributed to the tensile strength of geogrid material.
- The depth of footing embedment significantly influences the bearing capacity.
- The bearing capacity of interfering footing on unreinforced and reinforced sand increases as spacing decreases.

- There is no effect of interferences, when the footings are placed at a distance more than three times the width of footing.

References

1. Abu-Farsakh M, Chen Q, Sharma R, Zhang X (2008) Large-scale model footing tests on geogrid reinforced marginal embankment soil. Geotech Test J ASTM 31(5):413–423
2. Abu-Farsakh M, Chen Q, Sharma R (2013) An experimental evaluation of the behavior of footings on geosynthetic-reinforced sand. Soils Found 53(2):335–348
3. Basudhar PK, Saha S, Deb L (2007) Circular footings resting on geotextile-reinforced sand bed. Geotext Geomembr 25(6):377–384
4. Chakraborty M, Kumar J (2014) Bearing capacity of circular foundations reinforced with geogrid sheets. Soils Found 54(4):820–832
5. Chen Q, Abu-Farsakh M, Sharma R, Zhang X (2007) Laboratory investigation of behavior of foundations on geosynthetic-reinforced clayey soil. Transp Res Record: J Transp Res Board 2004:28–38
6. Daud KA (2012) Interference of shallow multiple strip footings on sand. Iraqi J Mech Mater Eng 12(3):492–507
7. Demir A, Laman M, Yildiz A, Ornek M (2013) Large scale field tests on geogrid-reinforced granular fill underlain by clay soil. Geotext Geomembr 38:1–15
8. Ghazavi M, Lavasan AA (2008) Interference effect of shallow foundation constructed on sand reinforced with geosynthetics. Geotext Geomembr Sci Direct 26:404–415
9. Ghazavi M, Lavasan AA (2012) Behaviour of closely spaced square and circular footings on reinforced sand. Soils Found 52(1):160–167
10. Ghosh P, Kumar J (2009) Interference effect of two nearby strip footing on reinforced sand. Contemp Eng Sci 2(12):577–592
11. Ghosh P, Sharma A (2010) Interference effect of two nearby strip footings on layered soil: theory of elasticity approach. Acta Geotech 5(3):189–198
12. Ghosh P, Kumar S (2011) Interference effect of two nearby strip surface footings on cohesionless layered soil. Int J Geotech Eng 5(1):87–94
13. Graham J, Raymon GP, Suppiah A (1984) Bearing capacity of three closely spaced footings on sand. J Geotech 34(2):173–182
14. Kouzer KM, Kumar J (2010) Ultimate bearing capacity of a footing considering the interference of an existing footing on sand. Geotech Geol Eng 28(4):457–470
15. Kumar J, Bhattacharya P (2010) Bearing capacity of interfering multiple strip footings by using lower bound finite elements limit analysis. Comput Geotech 37:731–736
16. Kumar J, Bhoi MK (2008) Interference of two closely spaced strip footings on sand using model tests. J Geotech Geoenviron Eng ASCE 134(4):595–604
17. Kumar J, Ghosh P (2007) Ultimate bearing capacity of two interfering rough strip footings. Int J Geomech ASCE 7(1):53–62
18. Latha GM, Somwanshi A (2009) Bearing capacity of square footings on geosynthetics reinforced sand. Geotext Geomembr 27(4):281–294
19. Latha MG, Somwanshi A (2009) Effect of reinforcement form on the bearing capacity of square footings on sand. Geotext Geomembr 27(6):409–422
20. Lee J, Eun J (2009) Estimation of bearing capacity for multiple footings in sand. Comput Geotech 36:1000–1008
21. Mabrouki A, Benmeddou D, Frank R, Mellas M (2010) Numerical study of the bearing capacity for two interfering strip footings on sand. Comput Geotech 37:431–439
22. Naderi E, Hataf N (2014) Model testing and numerical investigation of interference effect of closely spaced ring and circular footings on reinforced sand. J Geotext Geomembr 42:191–200

23. Nainegali L, Basudhar P (2011) Interference of two closely spaced footings: a finite element modeling. In: Geo-Frontiers, pp 3726–3735
24. Nainegali L, Basudhar P, Ghosh P (2013) Interference of two asymmetric closely spaced strip footings resting on non-homogeneous and linearly elastic soil bed. Int J Geomech ASCE 13(6):840–851
25. Patra CR, Das BM, Atalar C (2005) Bearing capacity of embedded strip foundation on geogrid-reinforced sand. Geotext Geomembr 23:454–462
26. Pusadkar SS, Saraf SS (2012) Interference of adjoining circular footings on reinforced sand. In: Proceeding of the Indian Geotechnical Conference, 13–15 Dec 2012, vol 1. Advances in Geotechnical Engineering at IIT New Delhi India, pp 373–375
27. Pusadkar SS, Saraf SS (2012) Interference of adjoining rectangular footings on reinforced sand. Int J Civil Eng Technol (IJCIET) 3(2):447–454
28. Sharma R, Chen Q, Abu-Farsakh M, Yoon S (2009) Analytical modeling of reinforced soil foundation. Geotext Geomembr 27(1):63–72
29. Srinivasana V, Ghosh P (2013) Experimental investigation on interaction problem of two nearby circular footings on layered cohesionless soil. Geomech Geoeng 8(2):97–106
30. Vinod P, Bhaskar AB, Sreehari S (2009) Behavior of a square model footing on loose sand reinforced with braided coir rope. Geotext Geomembr 27(6):464–474

Numerical Modeling of Massive Timber Piles Supporting Double-Span Stone Arch Bridge Damaged in 2011 Great East Japan Earthquake

Y. Sawamura, Benjamin Markley Lewis and M. Kimura

Abstract Tokiwa Bridge is a double-span stone arch bridge constructed in 1877 in Tokyo designated as a national cultural artifact. Tokiwa Bridge is supported by a timber pile foundation consisting of hundreds of tapered pinewood piles installed in the clayey layer. This feature of the foundation is different from that of stone arch bridges in other areas where the spread foundation is set directly on the rock. Tokiwa Bridge was damaged in the 2011 Great East Japan Earthquake and is currently undergoing seismic retrofit designed to improve its seismic performance while preserving the original timber pile foundation of the bridge. The authors are providing technical support for this project by evaluating the seismic performance of Tokiwa Bridge before and after the ongoing retrofit construction. Although the seismic performance of Tokiwa Bridge should be evaluated through dynamic analysis targeting the whole bridge system, it is difficult to model all the piles due to the limitation of numerical capacity and its complexity. In this study, therefore, a reasonable model was developed for the piled foundation that would not consider piles individually and treat timber piles as an area of hypothetical ground improvement, since the pile arrangement is irregular and the piles are of inconsistent size, shape, and condition. By comparing the results of these results to an analysis considering individual timber piles under pushover analysis conditions the applicability of the numerical model was confirmed.

Keywords Timber piles · Numerical modeling · Hypothetical ground improvement

Y. Sawamura (✉) · M. Kimura
Kyoto University, Kyoto, Japan
e-mail: sawamura.yasuo.6c@kyoto-u.ac.jp

B. M. Lewis
Obayashi Corporation, Tokyo, Japan

A. Prashant et al. (eds.), *Advances in Computer Methods and Geomechanics*, Lecture Notes in Civil Engineering 55,
https://doi.org/10.1007/978-981-15-0886-8_24

1 Introduction

Tokiwa Bridge (Fig. 1) is a stone arch bridge originally constructed in 1877 located in the Chiyoda Ward of Tokyo. It was originally a timber bridge crossing the outer moat to Edo Castle and was reconstructed as a stone arch bridge using recycled stone blocks from the Edo Castle walls. Tokiwa Bridge is registered as a national historic site in recognition of its embodiment of the period of its construction, when Japan was experiencing rapid westernization after ending the *Sakoku* "Closed Country" policy. Tokiwa Bridge represents this history by its characteristic integration of traditional Japanese architecture and contemporary western design elements. However, Tokiwa Bridge suffered damage in the 2011 Great East Japan Earthquake. Afterward, it was immediately disassembled and is currently undergoing retrofit construction at the time of this publication.

On March 11th, 2011, eastern Japan was struck by a magnitude 9.0 megathrust earthquake originating off the eastern coast of Tohoku and the resulting tsunami. At the observatory of the Japan Meteorological Agency, located close to Tokiwa Bridge, shaking with a seismic intensity of 5 upper on the Japanese intensity scale was recorded for about 10 s, and shaking with a seismic intensity of 4 or more was recorded for more than 130 s. Tokiwa Bridge sustained damage during the earthquake and a damage survey was performed after observation of protrusion of voussoirs (stone blocks that form the arch) and deformation of arches (Fig. 2). The survey revealed that the difference of horizontal resistances of foundation on the right and left banks caused the heavy damage at right arch. Since masonry arches rely on compression of voussoirs for structural stability, the bridge was judged to be at risk of total collapse. Due to concerns of a possible total collapse and the danger

Fig. 1 Tokiwa Bridge (before 2011 Great East Japan earthquake)

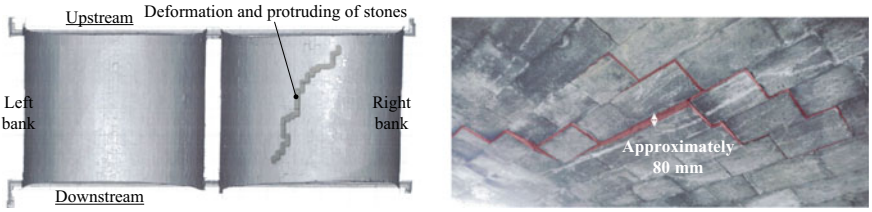

(a) Back face of arch blocks (b) Protruding of stones at right arch of bridge

Fig. 2 Damage to Tokiwa Bridge due to 2011 Great East Japan earthquake

posed to the waterway under the bridge, which sees traffic from sightseeing boats, immediate action was deemed necessary and the bridge was disassembled.

Since Tokiwa Bridge is a national heritage site, the original components are to be reused to restore the structure as much as possible. Hence, approximately 85% of the original bridge materials are to be reused in the retrofitted structure, including the original timber piles. To improve the resistance of the foundation, the retrofit construction plan involves installing additional new timber piles. However, it is difficult to model all the piles due to the limitation of numerical capacity and its complexity.

In this study, 3-dimensional finite element analyses were carried out using "DBLEAVES" developed by Ye et al. [4], and a new reasonable model which treats the piled foundation as a region of hypothetical ground improvement without considering individual piles is proposed. First, soil parameters for the subloading t_{ij} constitutive model were developed based on numerical simulation of CU triaxial tests. Then, the parameters were confirmed using FEM analysis of horizontal and vertical timber pile loading tests performed at the Tokiwa Bridge site. Using these confirmed parameters, a model was developed for the central bridge pier which treated timber piles as an area of hypothetical ground improvement. By comparing the results of these results to an analysis considering individual timber piles under pushover analysis conditions the applicability of the numerical model was confirmed.

2 Structural Features of Tokiwa Bridge

Figure 3 shows a section view of Tokiwa Bridge with the subsurface strata. The foundation material at each support primarily consists of the "Tc layer", a soft high-plasticity silty clay. At each bridge support, the Tc clay layer is heavily overconsolidated due to the bridge static load and is intersected by the "Ts layer", a medium-dense sand layer that was found at varying depths and layer thicknesses throughout the site. Underlying the Tc layer across the whole site is the Tg layer, a very dense gravel layer that is a supple bearing stratum and the Tns, a mudstone layer underlying the site.

Tokiwa Bridge was constructed on a foundation similar to modern piled foundations but with a few crucial differences. The foundation is comprised of, from

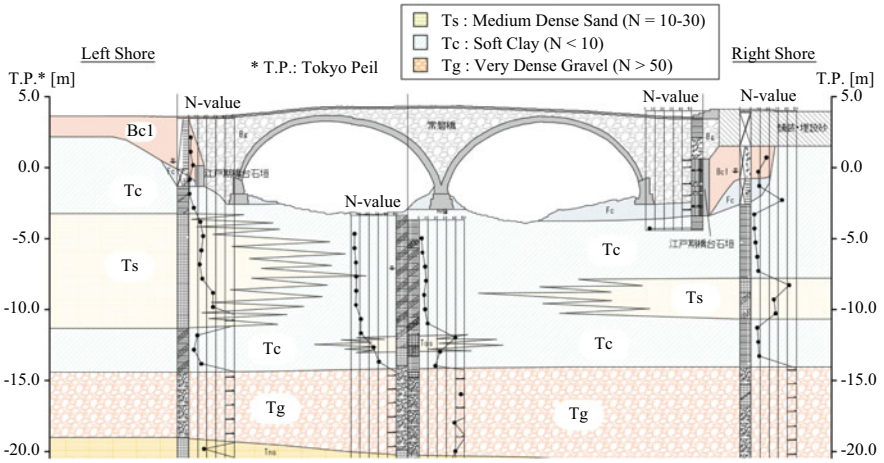

Fig. 3 Subsurface stratigraphy at Tokiwa Bridge site

top to bottom, a *Neishi* (stone plinth), *Sutedodai* (wooden panels), *Dogi* (smaller wooden panels placed atop piles), and timber pile foundation, with timber stakes placed intermittently around the foundation to hold it in place laterally (Fig. 4). The *Neishi* is a large granite stone plinth that forms the base upon which the other stone blocks are arranged. Beneath the *Neishi* are the *Sutedodai* and *Dogi*, which are long timber slabs arranged in a crossed pattern to form a footing-like base for the *Neishi*. Underneath this assembly is a timber pile foundation consisting of hundreds of tapered pinewood piles. The foundation is similar to modern deep foundations, with the *Neishi* and *Sutedodai* behaving as a footing and the *Dogi* analogous to a

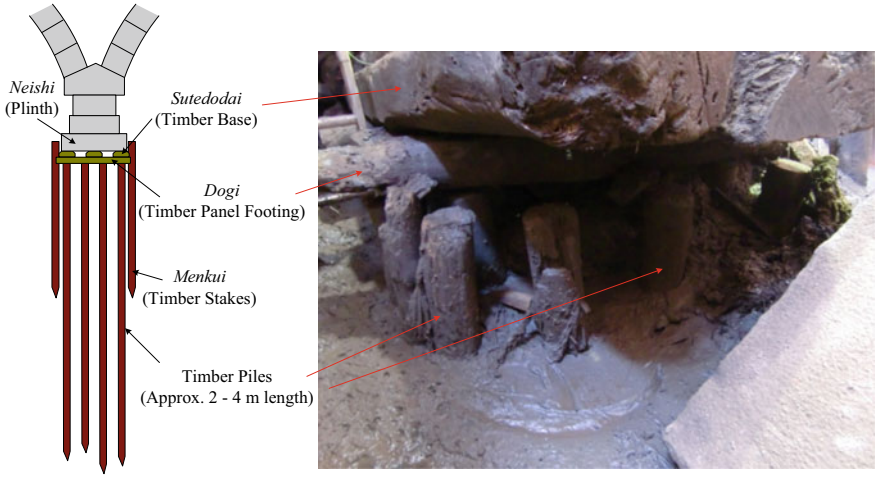

Fig. 4 Foundation components of Tokiwa Bridge

pile cap. However, there are crucial differences between the Tokiwa Bridge foundation and modern foundations—most notably, there is no embedment of timber piles into the *Dogi*, only depressions formed by deformation of the *Dogi* over time by the immense static load of the bridge structure. Additionally, the timber piles are arranged in a largely random pattern in contrast to the orderly distribution of modern pile foundations.

3 Constitutive Model of Soil and Parameter Setting

3.1 Subloading t_{ij} *Model*

In the analyses presented in this paper, soil elements were modeled using the subloading t_{ij} constitutive model developed by Nakai and Hinokio [3]. The model is derived in the same manner as the Cam Clay model with one crucial difference—the stress components t_S and t_N replace the q and p components used in the Cam Clay model. The t_{ij} stress components are derived based on the spatially mobilized plane (SMP; [2]), the orientation of which is defined by the three principal stresses, instead of the octahedral stress space, which is defined by only mean and deviatoric stress components. By this difference, the subloading t_{ij} model is able to account for the influence of the intermediate principal stress, as well as anisotropy induced by the stress conditions. Furthermore, through the introduction of the concept of subloading [1], where the stiffness of overconsolidated soil is increased by a factor related to its difference in void ratio from the normally consolidated soil of the same stress state, the effect of densification can be accounted for. Applicable to both sand and clay, the subloading t_{ij} model can be defined by only seven parameters. α is subloading parameter that increases the stiffness of overconsolidated soils. Higher values also "sharpen" the transition from the overconsolidated region to the normally consolidated region. β is stress-dilatancy parameter which determines the shape of yield surface. When β is equal to 1, the yield surface is the same as the original Cam Clay model.

3.2 Triaxial Testing of Site Soils and Parameter Selection

In order to determine subloading t_{ij} model parameters for the Tc clay layer, samples were taken at a depth of 2 m and isotropically consolidated undrained (ICU) triaxial tests were performed at effective confining pressures of 200 and 400 kPa. The average B-value for the tests was 0.99 for the 200 kPa test and 0.96 for the 400 kPa test. After isotropic consolidation to an effective confining pressure of 200 or 400 kPa, the samples were sheared at a strain rate of 0.045%/min and the effective confining pressure and deviatoric stress was measured. Because it had a more favorable B-value, analysis of the 200 kPa sample was used to parametrically determine the

Table 1 Subloading t_{ij} parameters

Subloading t_{ij} parameter	Tc	Ts
Principal stress ratio at critical state R_{cs}	6.5	3.2
Poisson's ratio ν	0.20	0.20
Compression index λ	0.60	0.07
Swelling index κ	0.02	0.0045
$N = e_{NC}$ at $p = 98$ kPa and $q = 0$ kPa	2.96	1.10
Density parameter a (ANN)	850	60
Parameter for stress-dilatancy relation β	1.5	1.5
Over consolidation ratio (OCR)	2.0	–
Relative density D_r (%)	–	80

subloading t_{ij} model parameters for the Tc layer listed in Table 1 by a simple 1 element analysis with a constant confining pressure and forced axial strain loading. The principal stress ratio at critical state, which can be derived from measured values during the triaxial shear test, was measured at 12.0. However, this value was too high and caused numerical instability, so it was lowered to 6.5 in order to ensure stable calculations heading forward. Figure 5 shows the measured results for the triaxial shear tests and comparison with the analytical values. The stress ratio versus axial strain curves achieved acceptable agreement between the measured and analytical values. The deviation is partially due to the unreasonably high measured value of principal stress ratio at a critical state, 12.0, which had to be lowered to protect the analyses from numerical instability. Additional the deviation is caused by limitations of the analytical model, which cannot account for certain soil characteristics such as structuring.

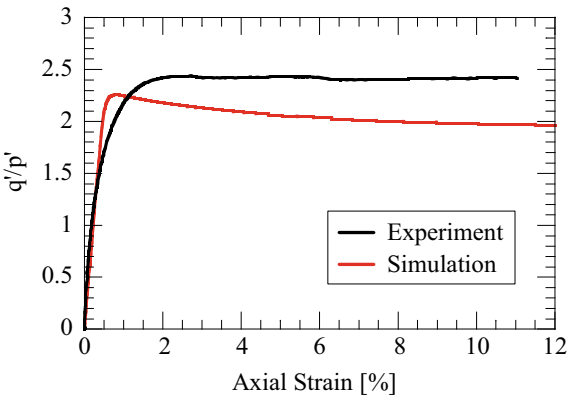

Fig. 5 Triaxial test result and comparison with analysis

3.3 *Confirmation of Soil Parameters Through Lateral and Vertical Pile Load Test Analyses*

At the Tokiwa Bridge site, lateral and vertical pile load tests were commissioned in order to observe the behavior of the piles when loaded and provide valuable information for future analyses of the pile foundation. Numerical simulations of these pile load tests were performed using soil parameters determined from triaxial tests of the Tc layer, as described earlier, in order to evaluate the applicability of the employed model to actual measured field tests.

The timber pile was modeled in the lateral pile load test using hybrid column elements [5] as depicted in Fig. 6, where 90% of the pile bending stiffness is allocated to an axial beam element and the remaining 10% is distributed to four solid elements surrounding the beam. Hybrid column elements have the benefit of using a beam element to describe the flexural behavior of the pile, while also accounting for the area of the pile through the solid elements. The finite element mesh and analysis conditions for the lateral pile load test are depicted in Fig. 7. During the on-site

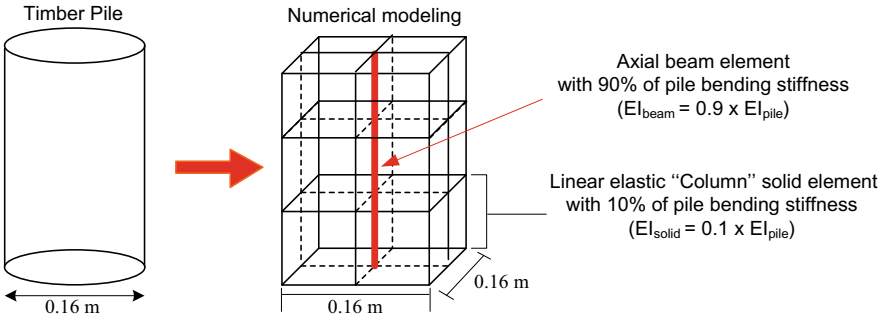

Fig. 6 Diagram of hybrid column elements (After [5])

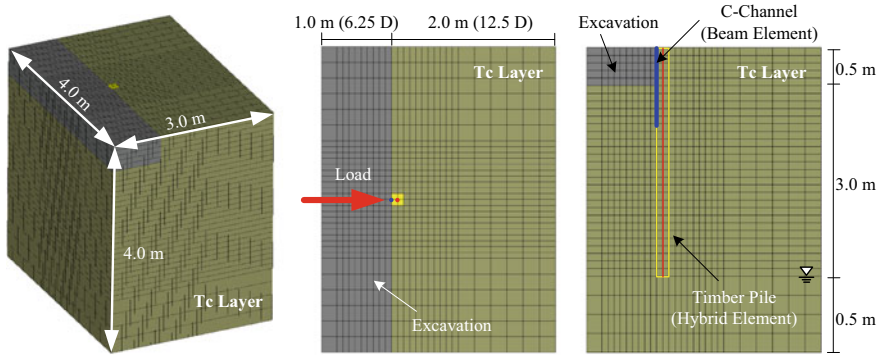

Fig. 7 Analysis outline for lateral pile load test

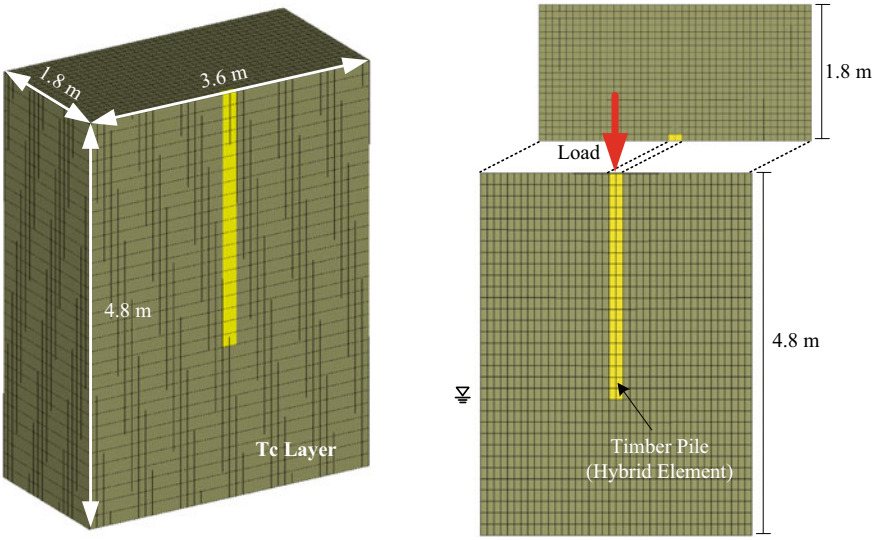

Fig. 8 Vertical pile load test analysis outline

lateral pile load test, a steel C-channel was inserted between the load jack and the timber pile to a depth of 1 m in order to prevent damage to the timber pile from direct contact with the loading jack. This C-channel was considered in the analysis, and modeled as a beam element on the loaded face of the timber pile. The loaded face of the timber pile was also excavated to allow for placement of the load jack; this excavation was modeled using elastic elements with a stiffness of zero. Elastic properties for the timber pile were determined from compression tests of recovered timber pile materials ($E = 5.42 \times 10^6$ kN/m^2, $\nu = 0.33$, $\rho = 0.60$ g/cm^3). In the vertical pile load test, the pile and soil were both modeled as depicted in Fig. 8 using only linear elastic solid elements.

The measured and analytical load–displacement relationships for the lateral and vertical pile load tests are depicted in Figs. 9 and 10, respectively. The lateral pile load test showed some deviations between the measured and analytical values, particularly for post-yielding behavior. One likely limitation is the linear elastic model for the timber pile, which does not allow for decreases in bending stiffness. Additionally, the C-channel used in the field test potentially impacted the quality of the original pile load test, because the steel C-channel has a much greater bending stiffness than the timber pile. However, in consideration of these limitations the results are in good agreement. The vertical pile test load–displacement curves show close agreement between the measured and analytical values despite facing limitations similar to those of the lateral pile load test, namely the unknown length of timber pile. In consideration of these factors, the pile load test analyses can be considered to be acceptable evidence that the parameters determined from the triaxial shear test analyses are suitable for the site conditions.

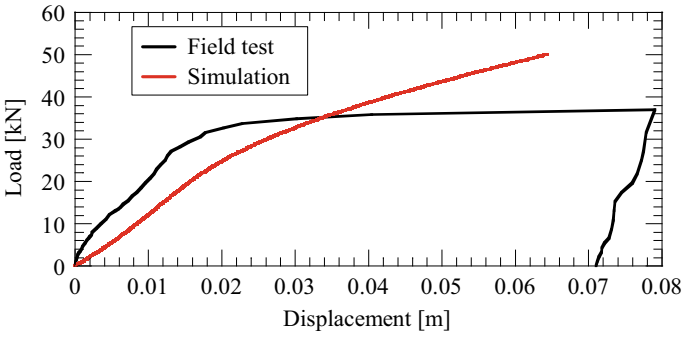

Fig. 9 Load-displacement curve for lateral pile load test and comparison with analytical result

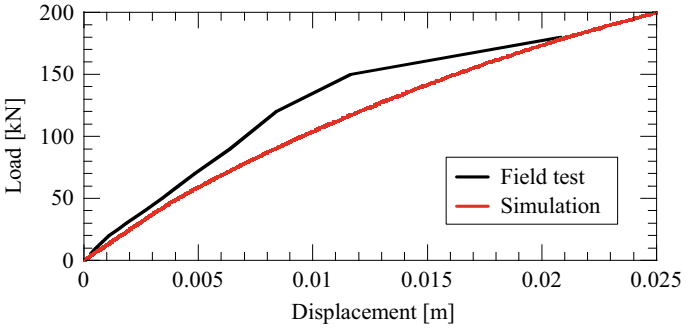

Fig. 10 Load-displacement curve for vertical pile load test and comparison with analytical result

4 Modeling of Massive Timber Piles as an Area of Hypothetical Ground Improvement

4.1 Pushover Analysis Modeling Timber Piles as Hybrid Elements

Due to the irregular distribution and small size of the timber piles supporting Tokiwa Bridge, a model was developed to treat the timber pile foundation as a hypothetical area of ground improvement. In other words, a model was developed that considers the effects of timber piles by changing soil parameters without including timber piles in the analytical mesh. The results were validated through comparison with a mesh considering every timber pile individually in pushover analyses.

Firstly, the influence of the location of timber piles affecting the lateral resistance of the central bridge pier is investigated. Figure 11 shows the actual distribution of timber piles at the central bridge support of Tokiwa Bridge, with their location in the FEM mesh used for pushover analysis overlain. In order to include the location

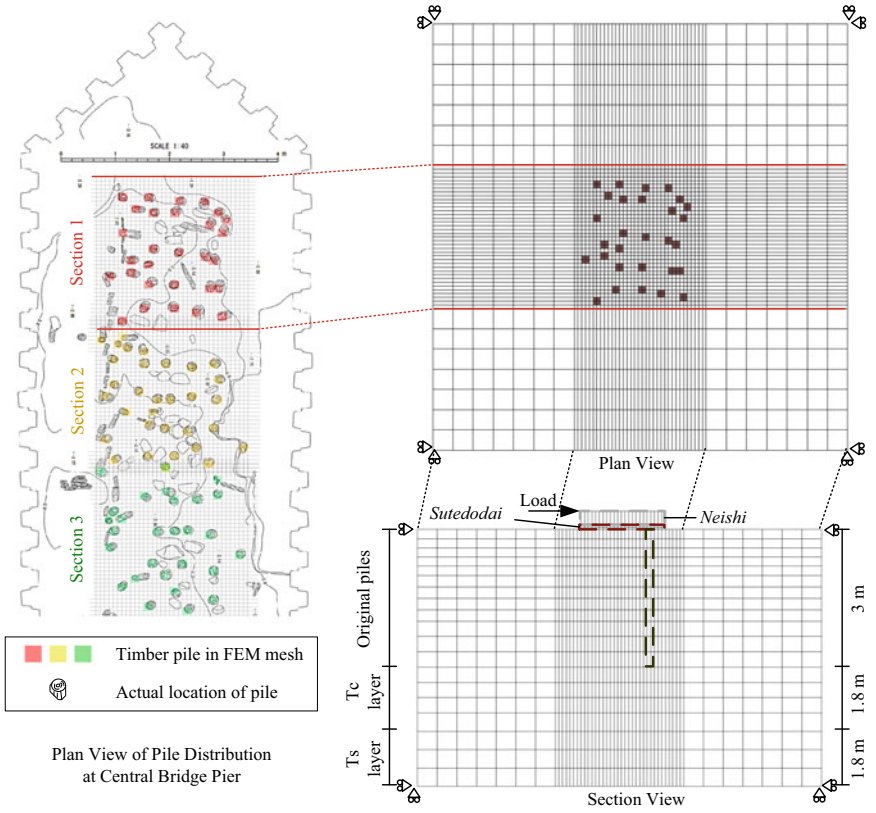

Fig. 11 Analysis outline of pushover analyses considering timber piles

of every timber pile with less than 4 cm of error in their location, a very fine mesh of 8 cm by 8 cm was used. The central bridge pier was separated into six sections, separated by colors in the plan view in Fig. 11. Piles were assumed to be 3.0 m long, the approximate average length of piles at the central bridge pier. All piles were modeled as hybrid column elements, and the load was applied as a distributed load at the top edge of the *Neishi* in conjunction with an assumed superstructure vertical load of 588 kPa. Input parameters for *Neishi* used the general physical properties of granite ($E = 1.00 \times 10^7$ kN/m^2, $\nu = 0.33$, $\rho = 2.60$ g/cm^3). The load–displacement relationship for all three sections is depicted in Fig. 12. As a result, it was confirmed that the load–displacement relationship of the pile head agreed in all the groups despite the sections.

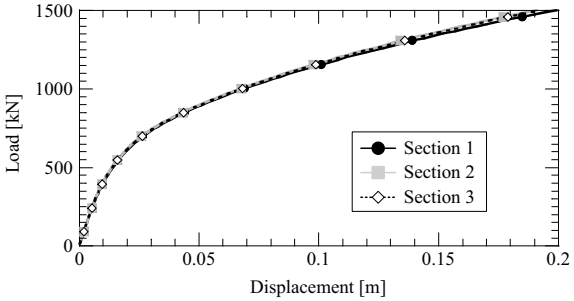

Fig. 12 Load-displacement curve comparison across sections

4.2 *Pushover Analysis Modeling Timber Piles as Ground Improvement*

A model was developed to treat the piled foundation as a hypothetical area of ground improvement parametrically through comparison with the analytical results from Sect. 4.1. The process was conducted for two cases: (1) only considering piles that were present at the central bridge pier from the original construction of Tokiwa Bridge and (2) considering new piles installed in 2016 as part of the retrofit construction. The length of the new piles was assumed to be 4.8 m such that they would reach the Ts sand layer underlying the Tc clay (Fig. 13). The load-displacement results of the pushover analyses for both patterns are depicted in Fig. 14 in comparison with the parametrically determined soil parameters modeling the timber pile foundation as hypothetical ground improvement. In these analyses of hypothetical ground improvement, the parameters (λ and κ) of the part of Tc layer where timber piles installed were changed. For analyses only considering the original timber piles, the results are

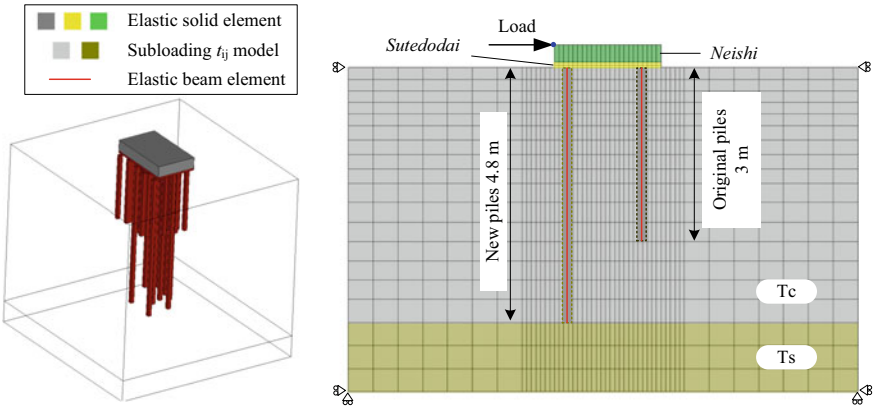

Fig. 13 Diagram of pushover analyses considering new piles

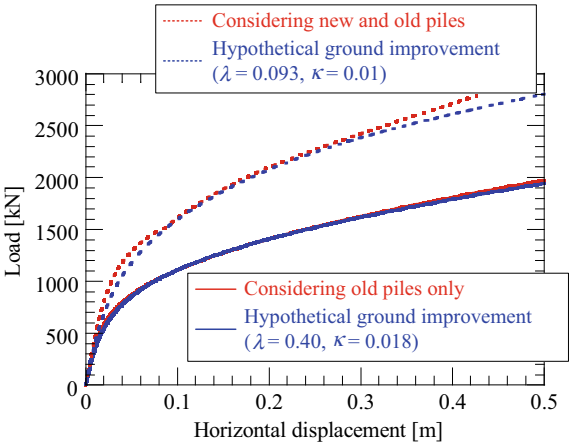

Fig. 14 Pushover analysis results considering timber piles and comparison with hypothetical ground improvement

almost indistinguishable. Because the relative stiffness of the pile is low and the pile length is short, the pile group effect for the timber pile foundation is strong, causing the piled foundation to behave rather similarly to a "block" of soil. In contrast to this, the load-displacement curves for the analyses considering newly inserted piles show a slight discrepancy, likely due to the longer length of the new piles, thereby reducing the pile group effect and making the behavior slightly different from a block of soil.

Figure 15 shows the distribution of shear stresses and lateral stresses in the foundation for the analysis considering piles and the hypothetical ground improvement analysis. Both the shear stress distribution and lateral stress distribution are closely replicated even without considering timber piles, providing evidence to support the applicability of this model for the site conditions. It is likely that these results are only acceptable because the pile group effect for this particular case is strong, and such results would not be replicable for piles that are longer, spaced at wider intervals, or of greater stiffness.

5 Conclusions

The following conclusions can be drawn from the results of the analyses presented in this paper:

1. The employed analytical model was able to accurately represent the mechanical behavior of the timber piles and surrounding clay foundation at the central bridge pier, as demonstrated by analysis of pile load tests conducted on site.
2. The behavior of the timber pile foundation of the central bridge pier under static pushover loading was accurately replicated using a model that treats the piled foundation as a region of hypothetical ground improvement without considering individual piles.

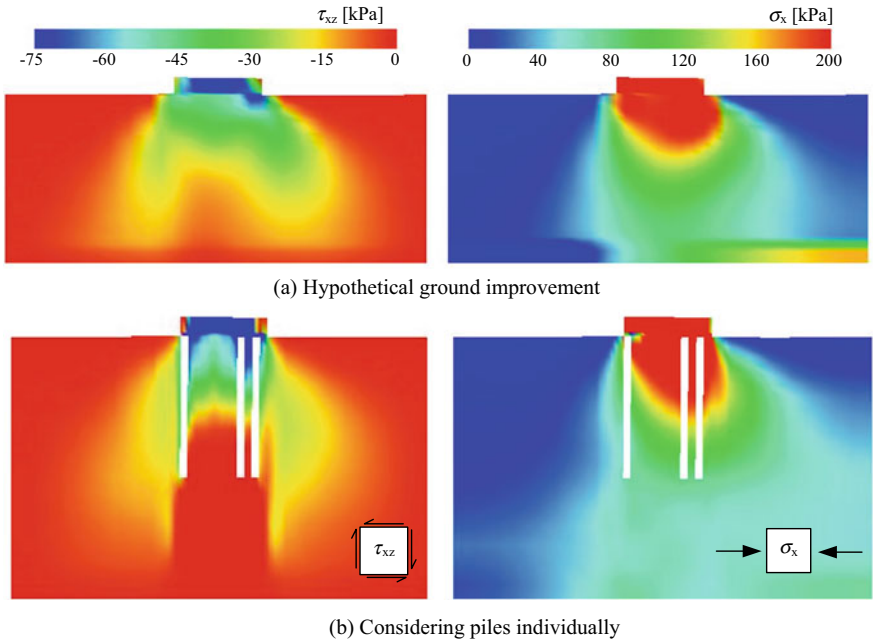

Fig. 15 Shear stress and lateral stress distribution considering timber piles and comparison with hypothetical ground improvement

Acknowledgements We wish to thank Mr. Yuto Nishimura of Japan Cultural Heritage Consultancy for his advice on the retrofit design.

References

1. Hashiguchi K (1980) Constitutive equations of elastoplastic materials with elastic-plastic transition. J Appl Mech 102(2):226–272
2. Matsuoka H, Nakai T (1974) Stress-deformation and strength characteristics of soil under three different principal stresses. Proc Jpn Soc Civil Eng 232:59–70
3. Nakai T, Hinokio M (2004) A simple elastoplastic model for normally and over consolidated soils with unified material parameters. Soils Found 44(2):53–70
4. Ye B, Ye GL, Zhang F, Yashima A (2007) Experiment and numerical simulation of repeated liquefaction-consolidation of sand. Soils Found 47(3):547–558
5. Zhang F, Kimura M, Nakai T, Hoshikawa T (2000) Mechanical behavior of pile foundations subjected to cyclic lateral loading up to the ultimate state. Soils Found 40(5):1–17

Behavioural Study on Geomaterial Undergoing Chemo-Mechanical Degradation

P. Viswanath and Arghya Das

Abstract The behaviour of any granular media primarily depends on the packing of grains. Any process that alters the packing of the granular assembly has a direct influence on its strength properties. Dissolution is one such processes, which induces a change in the grain size and thereby the index properties of the granular material change. In the present study, the response of carbonate sand to chemo-mechanical loading is experimentally analysed using a modified oedometer test setup capable of measuring both vertical and lateral stresses. Two sets of coupled chemo-mechanical experiments are performed to explore the variation of the rate of dissolution. In the first set, the corrosive fluid used for degradation is kept stagnant thereby varying the reaction rate. In the second set, the fluid is in flowing condition, maintaining the degradation rate almost constant. Our aim is to observe the variation in the lateral earth pressure coefficient with the two types of dissolution processes. Here the degree of dissolution is quantified by a chemical state variable defined in terms of mass loss with reference to the initial mass. The results show a rapid initial decay in the lateral earth pressure coefficient followed by an increasing or stable trend, depending on the type of test either stagnant or flowing.

Keywords Chemo-mechanics · Dissolution · 1D compression · Carbonate sand · Constitutive model

1 Introduction

Geomaterials undergo weathering induced degradation depending on the mineralogy and corrosiveness of the surrounding environment. Such degradation affects the textural properties, size and voids of the granular geomaterials. In nature weathering degradation is in the form coupled chemo-mechanical since it is often accompanied by mechanical forces. Among the various minerals, carbonate is the most vulnerable to chemical degradation. Various case studies show that carbonate-rich areas undergo

P. Viswanath (✉) · A. Das
Department of Civil Engineering, Indian Institute of Technology Kanpur, Kanpur, India
e-mail: viswan@iitk.ac.in

A. Prashant et al. (eds.), *Advances in Computer Methods and Geomechanics*, Lecture Notes in Civil Engineering 55,
https://doi.org/10.1007/978-981-15-0886-8_25

severe weathering and affect the surrounding habitats [1, 6, 10]. The mechanism of calcarenite rock degradation was extensively studied by Ciantia and Hueckel [5]. In the study, a microscale development of microcracks and a mesoscale development of pore fluid due to dissolution were coupled to get a complete constitutive model. A few researchers tried to examine the dissolution effect in granular materials by mixing natural geomaterial with an easily degradable mineral [9].

The experimental observation of chemical degradation demonstrates a drastic shift in the lateral earth pressure coefficient, which is an important aspect of various geotechnical design problems. Jaky's formula is widely used for the determination of at-rest earth pressure coefficient. Though this is popularly adopted, other relations involving Poisson's ratio is also used. These theories are convenient when the basic properties of soil like grain size distribution do not vary. Thus, the formulations need to be modified depending on the microstructural evolution of the material. The imperative properties related to earth pressure coefficient (k_0) for a granular material is the compressibility, density, and internal frictional angle. The variation of these three in a sand sample was studied by Guo [7]. Variation of k_0 with void ratio during triaxial consolidation experiment was explored by Chu and Gan [4]. The variation of k_0 with void ratio was observed to be more profound in the loose sample when compared to the medium dense samples. The fluctuation of earth pressure coefficient with dissolution was studied by Shin and Santamarina [9] through sets of 1D compression experiments on a mixture of sand and salt. During the experiment, water was passed to dissolve the salts. The study showed a deviation of lateral earth pressure coefficient from at-rest condition to active condition during dissolution. On the contrary, in cemented granular material (carbonate rock) the earth pressure coefficient was found increasing with dissolution and void ratio increases [3].

In the present study, the response of a reactive granular geomaterial under coupled chemo-mechanical degradation is experimentally explored. For the same, the detailed experimental setup is discussed. Also, chemical exposure is varied to observe its impact. Later a discussion is presented on the mechanism behind the specific nature of the stress-strain response and possible modelling scheme to capture such a response.

2 Material and Test Setup

Calcite granules are used as reactive material for the present study. Preliminary geotechnical investigation confirms that the granules are of sub-angular shape and uniform grain size distribution in the range of 1 mm to 3 mm diameter. Other properties of the material are listed in Table 1. On the other hand, a mild acetic acid solution is used as a pore fluid for chemical degradation experiments. Calcite granules which are predominantly of $CaCO_3$ reacts with acetic acid and grain size reduces. The chemical reaction is given in Eqs. 1–3. During reaction $Ca(CH_3COO)_2$ produced as the by-product, which, mixes with the pore fluid and then the carbon dioxide expels out from the sample. The reaction rate depends on the acid concentration and pore fluid flow as discussed later.

Table 1 Basic properties of carbonate sand

Property	Value
Specific gravity, G	2.67
Max. void ratio, e_{max}	0.818
Min. void ratio, e_{min}	0.722
d_{30} (mm)	2.08
d_{50} (mm)	2.84

$$CaCO_3 + 2CH_3COOH \rightarrow Ca(CH_3COO)_2 + H_2O + CO_2 \quad (1)$$

$$CH_3COOH \rightarrow CH_3COO^- + H^+ \quad (2)$$

$$H_2O \rightarrow H^+ + OH^- \quad (3)$$

The chemical dissolution experiment is carried out within an oedometric setup under a constant load. In other words, 1D compression tests are performed in parallel to dissolution. A flexible wall soft-ring oedometer is used for this study. Such setup enables us to measure the lateral stress along with vertical deformation [8].

Figure 1 illustrates the cross section and dimension of the used oedometer setup. As can be seen, the base of the mould contains three openings to allow acid injection. In addition, the base is corrugated to allow homogeneous acid flow throughout the sample. The oedometer ring is made up of stainless steel and attached with three

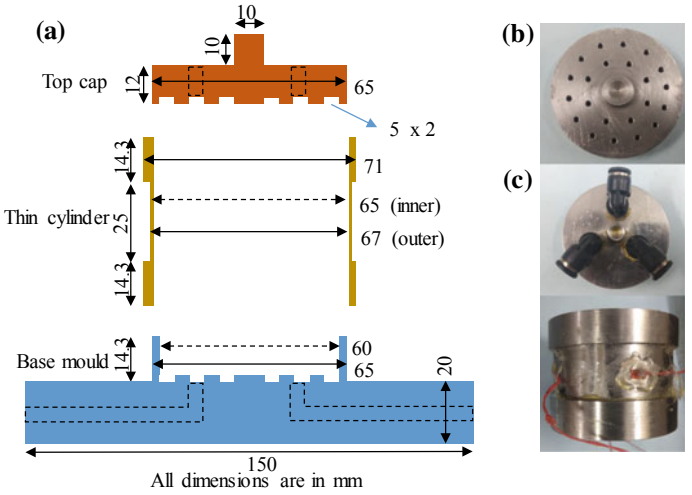

Fig. 1 Different parts of the soft oedometer setup. **a** Dimensions of each part, **b** Top cap used for stagnant tests with perforations. **c** Top cap for the flowing test and **d** The thin cylinder fitted with strain gauges

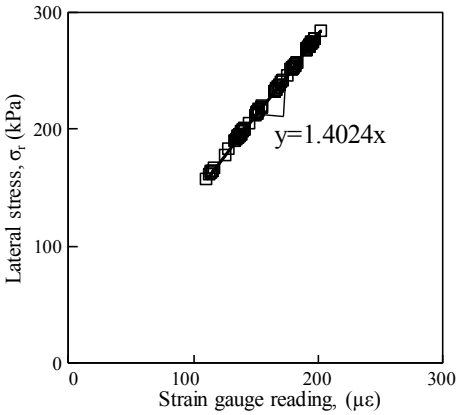

Fig. 2 Calibration of strain gauge used in the thin ring

strain gauges (Fig. 1d), in order to measure the radial deformation during chemo-mechanical loading. The middle portion of the ring is thinner than the conventional oedometer ring in order to allow slight radial expansion or contraction so that the lateral stress can be measured.

Assuming the expansion or contraction of the ring is within the elastic limit of the ring material (stainless steel), during the deformation of the reactive granules, hoop strain formed in the thin cylinder can be written as,

$$\varepsilon_h = \frac{p_i d}{2tE}, \tag{4}$$

where ε_h is the hoop strain in the thin ring; p_i is the uniform internal pressure acting inside the cylinder; E is the modulus of the used stainless steel; d is the internal diameter and t is the thickness of the ring. To estimate the lateral stress (σ_r) or internal pressure based on the hoop strain measured via strain gauges, the soft oedometer ring is calibrated. Figure 2 represents the calibration scheme.

Two sets of tests are performed in this study, namely the stagnant and flowing test. In the case of stagnant test, a fixed volume of acid solution with predetermined pH is injected from the bottom of the oedometer mould. On the other hand, in the flowing test, a constant rate of the acid solution flow is maintained from the bottom of the sample by creating a suction at the top of the sample through a thick loading plate. Important to note here that two different types of loading plates are used (Fig. 1b) for expelling the carbon dioxide in these two test scenarios. In the second case, the plate is connected to the suction channels of a peristaltic pump. A schematic diagram of the setup for the case of flowing test is given in Fig. 3.

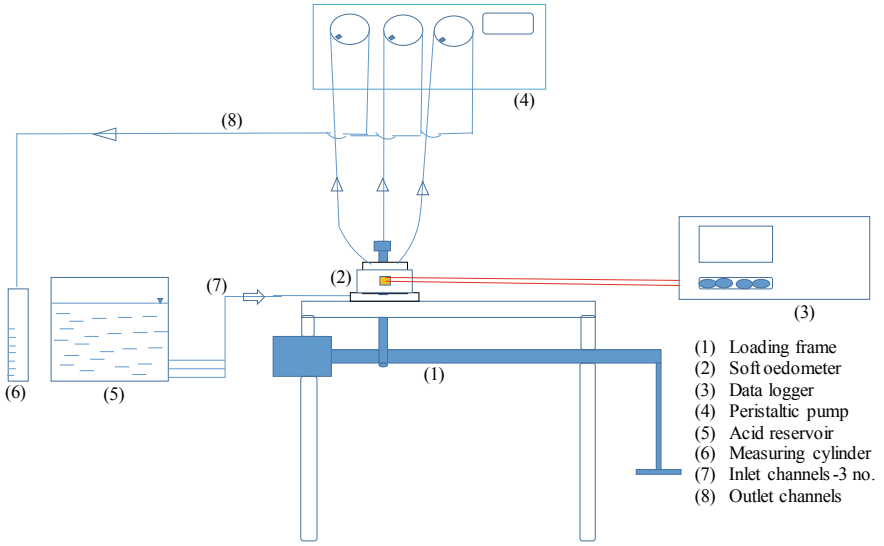

Fig. 3 The schematic diagram showing the whole setup used for the coupled chemo-mechanical experiments

3 Experimental Program

The sample for both flowing and stagnant tests are prepared at an initial relative density of 50% using air pluviation method. After that, a seating load of 10 kPa is applied through the loading plate by using the oedometer loading frame. The sample is saturated and then loaded stepwise to attain a maximum vertical (axial) stress, σ_a, of 580 kPa. This load is maintained throughout the experiment. After loading stage is over, a small-time gap is provided before the injection of the acid solution to check the stability in the strain gauge readings.

3.1 Stagnant Test

Acetic acid of a premeditated volume is injected from the bottom of the mould. The volume of the acid solution required is calculated in such a manner that the initial pH of 2.8 is attained when mixed with the pore water present during saturation. The vertical displacement and the strain gauge values were recorded with respect to time. Once the axial displacement becomes negligible, the experiment is stopped as it indicates the completion of the chemical degradation. Since only an initial injection of acid is given the reaction rate reduces with time. On the completion of the experiment, the sample is removed and weighed to determine the dissolved mass of calcite.

3.2 Flowing Test

In the flowing test, the oedometer mould is connected to a peristaltic pump for a continuous flow. Initially, water is allowed to pass through for a long time, so that no air bubble appears in the transparent channel of the peristaltic pump. This ensures saturation of the sample. After saturation and attaining stability in the strain gauge readings, the acid solution is allowed to pass through the sample. The initial pH is kept at 2.8. The acid solution reacts with the calcite granules and the formed by-products are collected in a measuring jar. Later at different intervals, samples are collected from the measuring jar. These samples are then used for measuring the calcium dissolution with the help of calcium ion probe. Once the amount of calcium is known in parts per million, the mass of calcium carbonate dissolved from the sample can be calculated by considering the dilution during ion measurement and molecular weight of calcium carbonate. Thus, the amount of mass dissolved is estimated, and the degree of dissolution at different intervals is quantified. Along with the calcium ion measurement, pH of the outflow is monitored. Also, the volume of outlet fluid is measured to monitor the flow pattern, and its variation as the reaction continues. The flow is continued for sufficient time so that axial strain of more than 10% is attained. Once the test is over, the sample is taken out and dried for measuring the undissolved mass. This is considered as a crosscheck for the calcium ion measurement. The average response of three tests maintaining identical initial conditions are presented here.

4 Results

In order to quantify the amount of dissolution, a chemical state variable namely mass reduction factor, X_d, is introduced. It is defined as the ratio of mass dissolved (m_d) upon the original mass of the sample (m_o) used for the test as shown in Eq. 5.

$$X_d = \frac{m_d}{m_o} \tag{5}$$

In the flowing test, X_d is determined at regular intervals from the measured ion concentration. On the other hand, in the stagnant test, the amount of pore fluid is limited and thus representative homogeneous samples cannot be taken out in between the test for calcium ion estimation. However, the total mass reduction is obtained by weighing the sample at the end of the test.

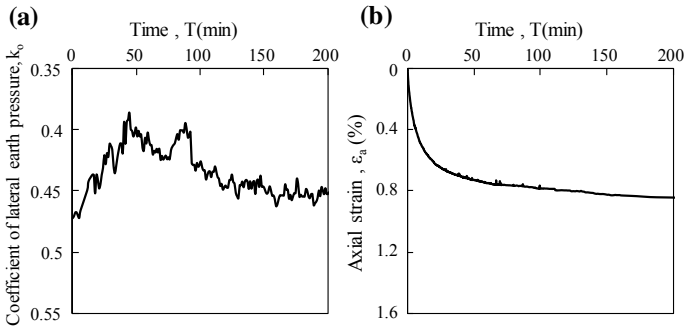

Fig. 4 Test results of stagnant test. **a** Variation of lateral earth pressure with time. **b** Variation of axial strain with time

4.1 Stagnant Test

Figure 4a shows the variation of the lateral earth pressure coefficient (σ_r/σ_a) with time. Here the lateral stress rapidly reduced just after the injection of the acidic solution. A reduction of around 70 kPa in the lateral stress from the initial is recorded. With time the acid concentration reduces, and hence the reaction rate reduces. A similar trend is confirmed by the axial deformation shown in Fig. 4b. The axial deformation rate is negligible after around 150 min. It can be noticed from Fig. 4b that once the axial deformation is almost insignificant, the lateral earth pressure coefficient regains the original value. The initial reduction of the lateral earth pressure coefficient can be due to two factors, (1) the change in particle size and consequent detachment of the assembly from the oedometer ring; (2) a change in the mobilized friction which reduces the lateral pressure coefficient (k) from at-rest to active state as illustrated by Shin and Santamarina [9].

4.2 Flowing Test

In Fig. 5 the mean variation of earth pressure coefficient (with error bars) for three tests having identical boundary conditions is plotted. Within 2% of axial strain, a reduction of 25% lateral earth pressure coefficient is recorded (Fig. 5a). In Fig. 5b the variation of lateral earth pressure coefficient with mass reduction factor is shown. Both the plots indicate an initial rapid reduction in the lateral earth pressure followed by steady growth. In comparison to the observations obtained in the stagnant test, as long as the reaction continues the lateral earth pressure coefficient does not regain its original value. Starting from an initial $k = 0.47$, it reduces to a 0.35 (± 0.025). At different stages of the tests, the outlet pH and discharge flow rate are recorded. Table 2 indicates that irrespective of increasing calcite dissolution the outlet pH is maintained around 5.53 (± 0.02), and the average flow rate attains a steady rate of

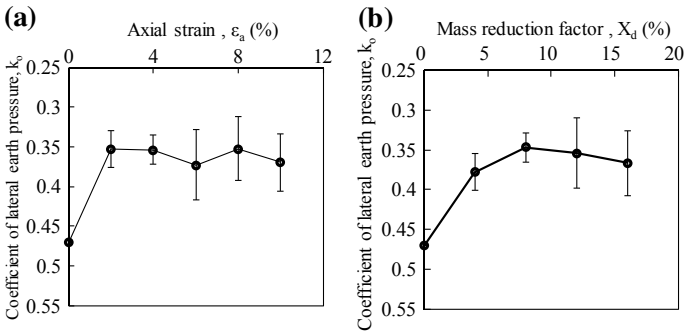

Fig. 5 Experimental results of three flowing tests. **a** Variation of lateral earth pressure coefficient with axial strain. **b** Variation of lateral earth pressure coefficient with mass reduction factor

Table 2 Flow variations during the test 1

X_d (%)	Inlet pH	Outlet pH	Flow rate (ml/min)
0	6.88	6.88	44.8
4.1	2.8	5.51	29.7
10.9	2.8	5.51	22.1
15.45	2.8	5.55	22.7
18.44	2.8	5.56	21.3

22 ml/min (± 1.0). The reduction in the flow rate occurs primarily because of the mixing of the expelling CO_2 with the acidic solution.

5 A Discussion on Conceptual Modelling

Majority of mechanical models focus on cemented granular material or bonded geomaterial to resemble rock structure [2, 3, 5]. Regarding the introduction of chemical degradation, the material hardening variable (p_k) is enhanced as a function of the chemical state variable (e.g., X_d). Castellanza and Nova [3] derived the general expression of axial strain increment for a specific kinematic constraint like oedometer condition,

$$d\varepsilon_a = \left\{ \frac{\partial g}{\partial \sigma_a} - \frac{2C_{zzxx}}{H\left(C_{yyxx} + C_{xxxx}\right)} \frac{\partial g}{\partial \sigma_r} \right\} \frac{b}{H} dX_d, \tag{6}$$

where H is the hardening modulus; C_{ijkl} is the elastic compliance matrix; and $b = (\partial f/\partial p_k)(\partial p_k/\partial X_d)$. f and g represent the yield function and plastic potential, respectively. However, for realistic material parameters Eq. 6 expression only

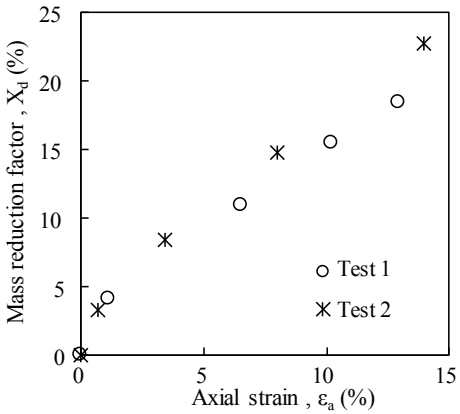

Fig. 6 Variation of axial strain due to dissolution in oedometric compression

captures the dissolution in cemented granular rock since $d\varepsilon_a$ linearly increases with dX_d.

It appears from the present experimental simulations, there exists a time lag in between the several responses (Fig. 6). For instance, in all the cases the reduction in radial stress is a faster process. In other words, particle dissolution and subsequent reduction in contact between the particle and the soft-ring is a rapid process as compared to the settlement of the vertical plate (up to 1% axial strain). This feature indicates particle rearrangement and consequent settlement as a relatively slow process as compared to void evolution due to particle degradation.

Therefore, an alternative relation would be in the form of non-linear relation like

$$\varepsilon_a = AX_d^2 + BX_d, \tag{7}$$

Also, the radial stress has to reduce during the initial chemical loading. It indicates that the sample undergoes radial contraction while it is axially compressed. Any conventional constitutive model unable to simulate such scenario, since axial compression always raises the radial stress. A few possible strategies would be:

(1) Consideration of chemical void ratio which may not be captured properly through the axial deformation or volumetric strain measured. During dissolution, the material may rearrange loosely. Thus, only a part of the evolved void is reflected through the axial deformation.
(2) With dissolution, the sample becomes softer as compared to that of the initial packing. Therefore, the stiffness of the material must be considered as a function dissolution [11].

6 Conclusions

In the present study deformation response of reactive granular materials has been studied under coupled chemo-mechanical degradation. Two sets of dissolution experiments are conducted under constant axial stress: (1) in stagnant acidic solution and (2) in flowing acidic solution. In both the experiments it has been observed that the radial stress dropped rapidly at the initial phase of dissolution without much axial deformation. Later radial stress further increases in the case of stagnant condition, while it becomes steady in the case of flowing condition. From the test results, it appears that the volumetric strain does not reflect the entire porosity evolution caused by the chemical dissolution. In addition, the time scale involves in the granular rearrangement followed by the axial deformation is different from that of chemical degradation and void evolution. Conventional models that account for the chemical degradation are unable to capture such behaviour. Thus, the model should include chemical void evolution and stiffness degradation.

References

1. Andriani GF, Walsh N (2007) Rocky coast geomorphology and erosional processes: a case study along the Murgia coastline South of Bari, Apulia—SE Italy. Geomorphology 87(3):224–238. https://doi.org/10.1016/j.geomorph.2006.03.033
2. Buscarnera G, Das A (2016) Chemo-mechanics of cemented granular solids subjected to precipitation and dissolution of mineral species. Int J Numer Anal Methods Geomech 40(9):1295–1320. https://doi.org/10.1002/nag.2486
3. Castellanza R, Nova R (2004) J Geotech Geoenvironmental Eng. J Geotech Geoenvironmental Eng 130(7):728–739. https://doi.org/10.1061/(ASCE)1090-0241(2004)130:7(728)
4. Chu J, Gan CL (2004) Effect of void ratio on K_0 of loose sand. Géotechnique 54(4):285–288. https://doi.org/10.1680/geot.2004.54.4.285
5. Ciantia MO, Hueckel T (2013) Weathering of submerged stressed calcarenites: chemo-mechanical coupling mechanisms. Géotechnique 63(9):768–785. https://doi.org/10.1680/geot.SIP13.P.024
6. Davis KJ, Nealson KH, Lüttge A (2007) Calcite and dolomite dissolution rates in the context of microbe-mineral surface interactions. Geobiology 5(2):191–205. https://doi.org/10.1111/j.1472-4669.2007.00112.x
7. Guo P (2010) Effect of density and compressibility on K_0 of cohesionless soils. Acta Geotech 5(4):225–238. https://doi.org/10.1007/s11440-010-0125-0
8. Kolymbas D, Bauep E (1993) Soft Oedometer - a new testing device and its application for the calibration of hypoplastic constitutive laws. Geotech Test J 16(2):263–270
9. Shin H, Santamarina JC (2009) Mineral dissolution and the evolution of k_0. J Geotech. Geoenvironmental Eng 135(8):1141–1147. https://doi.org/10.1061/(ASCE)GT.1943-5606.0000053
10. Subhas AV, Adkins JF, Rollins NE, Naviaux J, Erez J, Berelson WM (2017) Catalysis and chemical mechanisms of calcite dissolution in seawater. Proc Natl Acad Sci 114(31):8175–8180. https://doi.org/10.1073/pnas.1703604114
11. Viswanath P, Das A (2017) Effects of particle dissolution on the constitutive response of granular materials. Poromechanics VI, American Society of Civil Engineers, pp 732–739

Influence of Nonhomogeneous Viscosity on the Dynamics of Debris Flow: A Numerical Study

Gaurav Bhutani, Mousumi Mukherjee and Dikshita Nath

Abstract Debris flow is a geological phenomenon occurring in nature under the action of gravitational forces over a sloping surface and exists in different forms, e.g. landslides, rockfalls, debris avalanches or mudslides. The significance of studying debris flow lies in the effective estimation of flow-height, front velocities, impact pressures and amount of material deposition at the runout zone, which are essential for designing barriers, rock fence or rock sheds as protective measures against such mass movements. A numerical framework can be adopted to solve the field equations associated with the debris flow phenomenon in conjunction with a suitable material model mimicking the constitutive behaviour of the flowing mass. The front velocity and debris runout length are better predicted when the momentum balance equation takes into account the flow resistance due to turbulence, which inherently results in a nonhomogeneous distribution of the flow viscosity. Moreover, due to the heterogeneous nature of the debris mixture there appears to be no plausible reason for the mechanical model to assume a homogeneous rheological parameter. The influence of nonhomogeneous viscosity on the dynamics of debris flow has been explored in this work, through Newtonian, single-phase, multi-material, laminar-flow simulations. An efficient adaptive-mesh hybrid finite-element/control volume (FE/CV) framework—Fluidity, which enables full Eulerian-based large deformation analysis has been utilised for this purpose. Based on the results obtained, it is noticed that the viscous nature of the lower layer primarily dictates the final flow pattern of the debris.

G. Bhutani · M. Mukherjee (✉)
Assistant Professor, School of Engineering, Indian Institute of Technology Mandi, Mandi 175005, India
e-mail: mousumi@iitmandi.ac.in; mousumi.ju06@gmail.com

G. Bhutani
e-mail: gaurav@iitmandi.ac.in

D. Nath
Graduate Research Scholar, School of Engineering, Indian Institute of Technology Mandi, Mandi 175005, India
e-mail: dikshita.iitmandi@gmail.com

A. Prashant et al. (eds.), *Advances in Computer Methods and Geomechanics*, Lecture Notes in Civil Engineering 55,
https://doi.org/10.1007/978-981-15-0886-8_26

Keywords Debris flow · Newtonian fluid · Nonhomogeneous viscosity · 2D-FEM · Multi-material model

1 Introduction

Debris flow is a generic term used to describe the geological phenomenon of complex flows, e.g. landslides, rockfalls, debris avalanches or mudslides, which occur under the action of gravitational forces over a sloping surface. In order to evaluate potential hazard associated with such mass movements and design various mitigation measures, it is imperative to study the debris flow dynamics for effective estimation of flow-height, front velocities, impact force and amount of material deposition at the runout zone. Depth-averaged Savage–Hutter (SH) equations [7], originally developed for modelling shallow flow of granular materials, are widely used for simulation of debris flows; however, such formulation fails to predict the impact pressure distribution along the flow depth which is important for designing defence structures [7]. A generalised formulation that resolves the depth-wise distribution of dynamic parameters, through the solution of field equations, must, therefore, be adopted. In addition, the coupled partial differential equations, which are obtained after the application of a suitable material model mimicking the constitutive behaviour of the flowing mass, should be solved numerically using an efficient numerical method, e.g. an adaptive-mesh finite-element method (FEM).

Along with polydisperse solids, debris flows also contain water and exhibit a flow behaviour somewhere between the mass movements of solid material and water flow. Due to a limited understanding of the mechanics of such complex flows, the solid–fluid mixture is often idealised as a single-phase homogeneous fluid [3]. Existing literature suggests that the rheological properties assumed for the flowing mass have a significant impact on the prediction of front velocities and other flow characteristics in a numerical simulation [6]. Further, comparison of such numerical simulations against field debris flow measurements has revealed an under-prediction of front velocities associated with the laminar-flow assumption (with homogeneous distribution of rheological properties). The front velocity and debris runout length is better predicted when the flow model takes into account the resistance due to turbulence [4], which inherently results in a nonhomogeneous distribution of the flow viscosity (with the use of turbulent-viscosity models). Moreover, due to the heterogeneous nature of the debris mixture there appears to be no plausible reason for the mechanical model to assume a homogeneous rheological parameter. The present numerical study aims to explore the influence of the nonhomogeneity of viscosity along the flow depth on the dynamics of debris flow.

In the present work, the simulations were performed using a hybrid finite-element/control volume (FE/CV) framework, which enables full Eulerian-based large deformation analysis, through the solution of field equations. This generalised open-source framework, known as Fluidity, is highly-parallelised and allows for the use of adaptive-mesh refinement (AMR) which makes it extremely tractable

and a preferred choice when modelling field-scale/industrial-scale problems [1, 2]. A single-phase Newtonian-type laminar fluid model was selected to represent the rheological behaviour of the flowing mass with a nonhomogeneous viscosity over the flow depth. The most simple flow model—Newtonian laminar flow—was chosen in the present work to demonstrate the effect of nonhomogeneity of the viscosity field on flow behaviour. The nonhomogeneity was introduced through linear and exponential functions for modelling the viscosity parameter. Evolution of front velocity and impact force for the nonhomogeneous distribution of viscosity was evaluated and compared with the homogeneous cases.

2 Computational Framework

Debris flow in the present work was modelled as a *single-phase multi-material* continuum. The continuum mechanics equations for the conservation of mass and momentum were, therefore, solved in this work. For an incompressible flow, they are given as:

$$u_{i,i} = 0 \tag{1}$$

and

$$\rho \dot{u}_i = \sigma_{ij,j} + \rho b_i, \tag{2}$$

where u_i is the velocity field, ρ is the density field, σ_{ij} is the Cauchy stress tensor field and b_i is the body force per unit mass. It should be noted that the Einstein notation has been used in this text.

Since the present model is single phase, only one momentum equation was solved. The two materials—debris and air—were modelled through the volume fraction scalar fields—α_a and α_d, where subscripts a and d represent air and debris, respectively. The evolution of the debris volume fraction was predicted through the following advection equation:

$$\partial_t \alpha_d + u_i \alpha_{d,i} = 0 \tag{3}$$

and the air volume fraction, α_a, was calculated as $1 - \alpha_d$. Densities of the materials were weighted using the volume fractions to obtain the overall phase density ρ, which is used in the above momentum equation (Eq. (2)). The flow was considered incompressible, as seen from Eq. (1), which is a realistic assumption considering the low Mach number values in this problem.

For a linear (Newtonian) fluid, the Cauchy stress tensor can be modelled using the following constitutive law (after the application of the Stokes' hypothesis):

$$\sigma_{ij} = -p\delta_{ij} + 2\mu \left(D_{ij} - \frac{1}{3} D_{kk} \delta_{ij} \right), \tag{4}$$

where p is the thermodynamic pressure, μ is the dynamic viscosity and D_{ij} is the rate of deformation tensor given as $(u_{i,j} + u_{j,i})/2$. Substituting Eq. (4) in Eq. (2) (and using Eq. (1)) results in the following equation:

$$\rho(\partial_t u_i + u_j u_{i,j}) = -p_{,i} + \mu u_{i,jj} + \mu_{,j}(u_{i,j} + u_{j,i}) + \rho b_i, \tag{5}$$

which is the incompressible form of the Navier–Stokes (NS) equation for a nonhomogeneous viscosity field. The above NS equation was solved using the Fluidity framework.

3 Problem Description

The two-dimensional computational domain selected in this work, with the dimensions 3.22 m long and 2 m high, is shown in Fig. 1. An initial rectangular debris heap of 1.2×0.6 m was selected and allowed to avalanche down the incline after $t = 0$ s. The problem dimensions are inspired from the dam-break experiment of [8] which has been incorporated as an example in the Fluidity Manual [1]. For the present debris flow dynamics study, the domain was inclined at an angle of 45° with the horizontal. The debris heap collapses and flows down the incline under the action of gravity and hits the right wall.

The boundary conditions (BC) chosen for the solution of the mass and momentum balance equations are shown in Table 1. A no-slip BC was chosen for the flow velocity at the walls and incline, whereas free BC was chosen for the top boundary, which makes it an outlet. Dirichlet pressure BC was selected for the pressure at the top boundary. All boundaries were considered 'closed' for the materials and hence a no flux BC for the debris volume fraction was selected. Both materials were at rest initially, with the volume fraction chosen to mimic the heap that is shown in Fig. 1.

All simulations were continued for a 10 s period (also called the *simulation time*) which was arrived-at through adaptive time-stepping with a bound on the maximum Courant number. The Crank–Nicholson time discretisation scheme was selected for the volume fraction and velocity equations. A nonlinear relaxation factor of 0.5 was used in linearising the momentum equation. The discontinuous Galerkin (DG) finite-element method was used to discretise the velocity field whereas a control volume method was used in discretising the pressure. The above choice of elements, which results in the $P_0 P_{1CV}$ velocity–pressure pair, was motivated from the famous LBB stability criterion. The volume fraction advection equation was solved in a non-conservative form and face value limiting was applied to ensure boundedness. See [2] for more details on the discretsation methods.

The densities of the two materials, i.e. air and debris, were set to $\rho_a = 1.0\,\mathrm{kgm}^{-3}$ and $\rho_d = 1500\,\mathrm{kgm}^{-3}$. The viscosity field, which is common for the two materials, was chosen in different ways which resulted in seven different simulation cases,

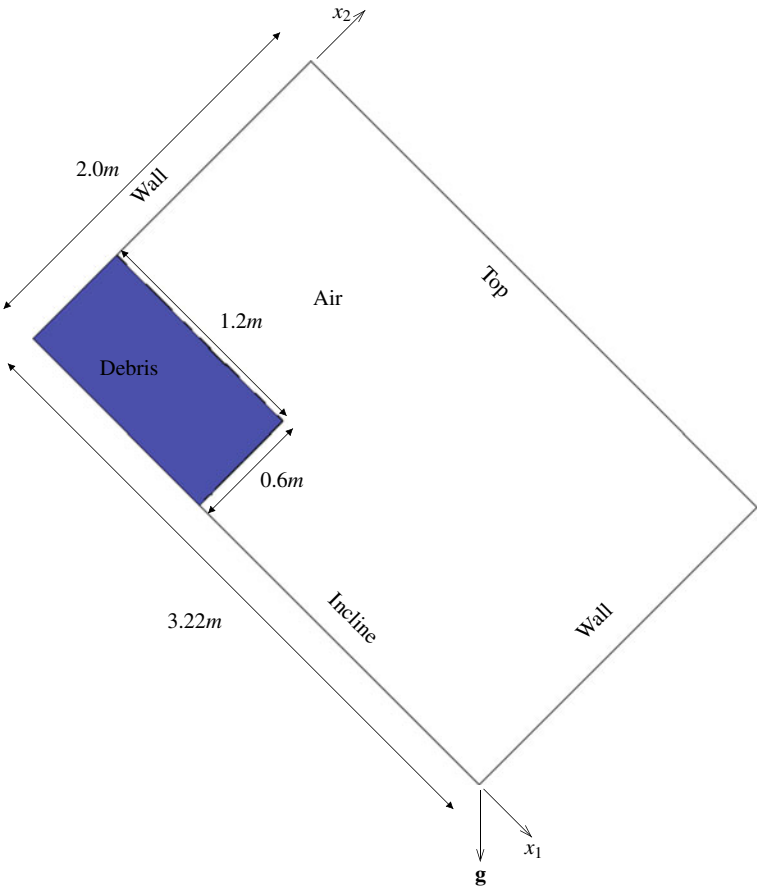

Fig. 1 Two-dimensional domain used for modelling the debris flow problem in this work. The domain is inclined at an angle of 45° with horizontal

Table 1 Boundary conditions for the flow fields; n_i here denotes the unit normal to boundary

Flow field	Incline	Walls	Top
Velocity	$u_i = 0$	$u_i = 0$	$u_{i,j} n_j = 0$
Pressure	$p_{,i} n_i = 0$	$p_{,i} n_i = 0$	$p = 0$
Debris volume fraction	no flux	no flux	no flux

which are described in Table 2. The choice of bounds for the debris viscosity was motivated from [4, 5]. Results were computed and analysed for these seven cases and are discussed in the next section.

Table 2 Simulation cases

Case number	Description
1	Inviscid
2	$\mu = 80\,\text{Pa} \cdot \text{s}$
3	$\mu = 800\,\text{Pa} \cdot \text{s}$
4	Linear change of viscosity between $x_2 = 0\,\text{m}$ and $0.2\,\text{m}$ from $80 - 800\,\text{Pa} \cdot \text{s}$, $\mu = 800\,\text{Pa} \cdot \text{s}$ beyond that
5	Exponential change of viscosity between $x_20 = 0\,\text{m}$ and $0.2\,\text{m}$ from $80 - 800\,\text{Pa} \cdot \text{s}$, $\mu = 800\,\text{Pa} \cdot \text{s}$ beyond that
6	Linear change of viscosity between $x_2 = 0\,\text{m}$ and $0.2\,\text{m}$ from $800 - 80\,\text{Pa} \cdot \text{s}$, $\mu = 800\,\text{Pa} \cdot \text{s}$ beyond that
7	Exponential change of viscosity between $x_20 = 0\,\text{m}$ and $0.2\,\text{m}$ from $800 - 80\,\text{Pa} \cdot \text{s}$, $\mu = 80\,\text{Pa} \cdot \text{s}$ beyond that

4 Results and Discussions

Adaptive-mesh refinement was applied to ensure the effectiveness of all computational simulations in the present work. Prior to executing adaptive-mesh simulations, a comparison was carried out between a fine fixed-mesh simulation and an adaptive-mesh simulation. Case 4 was chosen to carry out the above comparison, the results of which are presented in Fig. 2. A good match in the debris flow front position can be seen from Fig. 2a and b.

The above adaptive-mesh simulation was six-times quicker than the corresponding fixed-mesh simulation. A 5 s simulation required 9 min on an adaptive mesh in comparison to 56 min on the fixed mesh. This can be attributed to the reduced number of nodes—380–5400 in the adaptive mesh in contrast to 19100 in the fine fixed mesh. Meshes were adapted to the debris volume fraction in the present work, however,

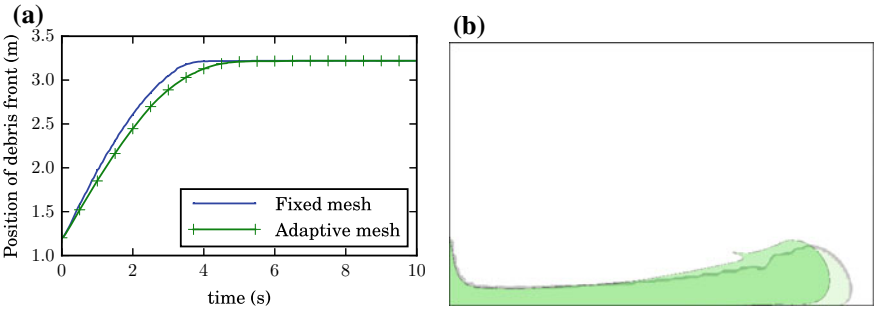

Fig. 2 Comparison of fixed-mesh and adaptive-mesh simulation results for Case 4 ($\mu = 80 - 800\,\text{Pa} \cdot \text{s}$ linear). **a** Debris front position for the two meshes are displayed. **b** Debris volume fraction at $t = 3\,\text{s}$, adaptive-mesh simulation debris front lags behind

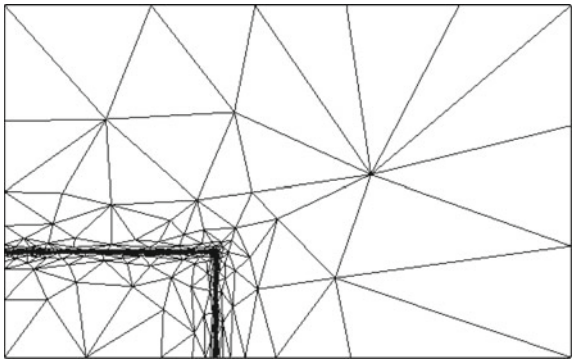

Fig. 3 Initial mesh (i.e. at $t = 0$ s) that was used in all simulations

it is possible to choose more than one field for adaptation, if required. All simulations were executed on an Intel Core i7-7700K 4.2 GHz quadcore processor with 32 GB RAM. The initial adaptive mesh, which resolves the initial material volume fractions quite well, is presented in Fig. 3. The fully unstructured highly-anisotropic nature of the mesh can be seen clearly. In AMR, adaptivity is only carried out after a few timesteps to minimise the computation time spent on adaptivity. In the present computation the mesh metric was also advected using the flow velocity to preempt new node positions which further added to the numerical efficiency. Therefore, all simulations in this work were run on adaptive meshes.

Incomplete resolution of the viscosity field in the 0.2 m thick *lower layer* due to coarse meshes resulting from AMR may result in computational inaccuracies. To verify this hypothesis, an adaptive-mesh simulation was designed with mesh resolution in the x_2-direction kept fixed in the zone of nonhomogeneous viscosity and the resulting computation was compared with a fully adaptive-mesh one. Figure 4 shows the agreement between the two simulation results for Case 4. Maximum mesh length in x_2-direction in the lower layer was restricted to 0.01 m in the high-resolution mesh, which ensured a total of 20 nodes in the lower layer in the x_2-direction. The low resolution simulation refers to the case where no constraint to the maximum mesh size was applied, which resulted in a mesh containing as few as four nodes in the lower band. (*Low resolution*) Adaptive mesh without any constraint on maximum mesh length was therefore chosen to model nonhomogeneous viscosity throughout this work.

Figure 5 depicts the evolution of debris volume fraction with time for Case 2 along with the corresponding adaptive meshes. It can be observed that the flow reaches the barrier around $t = 1$ s and starts spreading post that time. A few trapped air bubbles can be seen in (b) which rise due to buoyancy, as seen from (c) and (d). It must be noted that the direction of gravity is 45° SE in the present plots. Figure 6 presents a snapshot of debris volume fraction for all the cases at $t = 10$ s. Amongst the three uniform viscosity cases, the flow with the lowest viscosity (Case 1) hits the barrier first. Although no significant difference can be noticed in the flow profiles of the linear and the corresponding exponential cases, the viscous nature of the lower layer

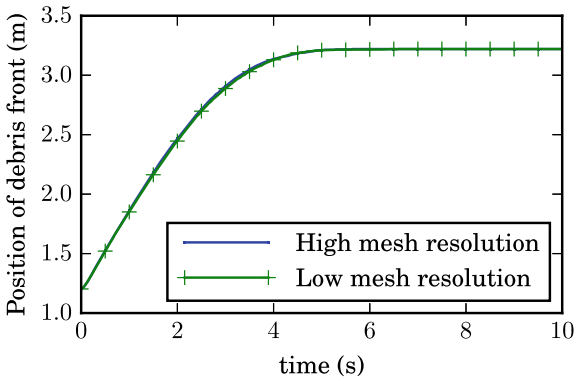

Fig. 4 Debris front position plots comparing the effect of resolving the region containing linear variation of viscosity in Case 4

primarily dictates the final flow pattern, as seen in the contrasting heap pictures of Cases 4 and 6.

Viscosity effects are further explored in Fig. 7 where the position of the debris front has been plotted against the time scale. Debris front for Cases 4 and 5, which represent an increasing viscosity in the x_2-direction, behave very differently when compared to Cases 6 and 7, which correspond to a decreasing viscosity in the positive x_2-direction. The nature of nonhomogeneity, induced through different viscosity distributions, can be associated, qualitatively, to the type of debris flow. For example, Case 6/7 may represent a flowing debris of porous granular particles (like sand) which allow the surface water to seep in and produce a thin cohesive layer of sand at the bottom. The top portion of the debris, in this case, is modelled as a low-viscosity fluid due to the free-flowing dry grains. Case 4/5 is more suited to model debris of fine clayey sediments which soak the water flux at top resulting in flow with decreasing viscosity down into the debris.

The x_1-velocity of the debris front is plotted in Fig. 8, which is the slope of Fig. 7. It shows the maximum front velocity for Case 1 and the least for Case 3. In case of inviscid flow, the flowing mass gains velocity with time and hits the barrier with the peak velocity. The sharp drop in its velocity profile indicates the collision between the debris and the barrier. Increase in the viscosity leads to higher amount of viscous drag which retards the flow leading to the overall decrease in the flow velocity. Interestingly, none of the cases with viscous flows attain a velocity peak at the collision point, but at some time before the impact. It is hypothesised that the entrapped air between the debris front and the barrier imparts extra resistance to the moving mass, which results in early peak in the velocity profile. In case of highly viscous flow (Case 3), the overall flow velocity itself remains very low which gives ample time for the free movement of the entrapped air resulting in a gradual decay in the velocity magnitude. It is important to note that the constraint imposed by the use of a common viscosity field for debris and air might have induced extra damping in the system. As a result, the peak velocity is attained before the collision point for all the cases with viscous flow. The debris momentum finally gets translated into the impact force exerted by the flowing debris on a rigid barrier which has been

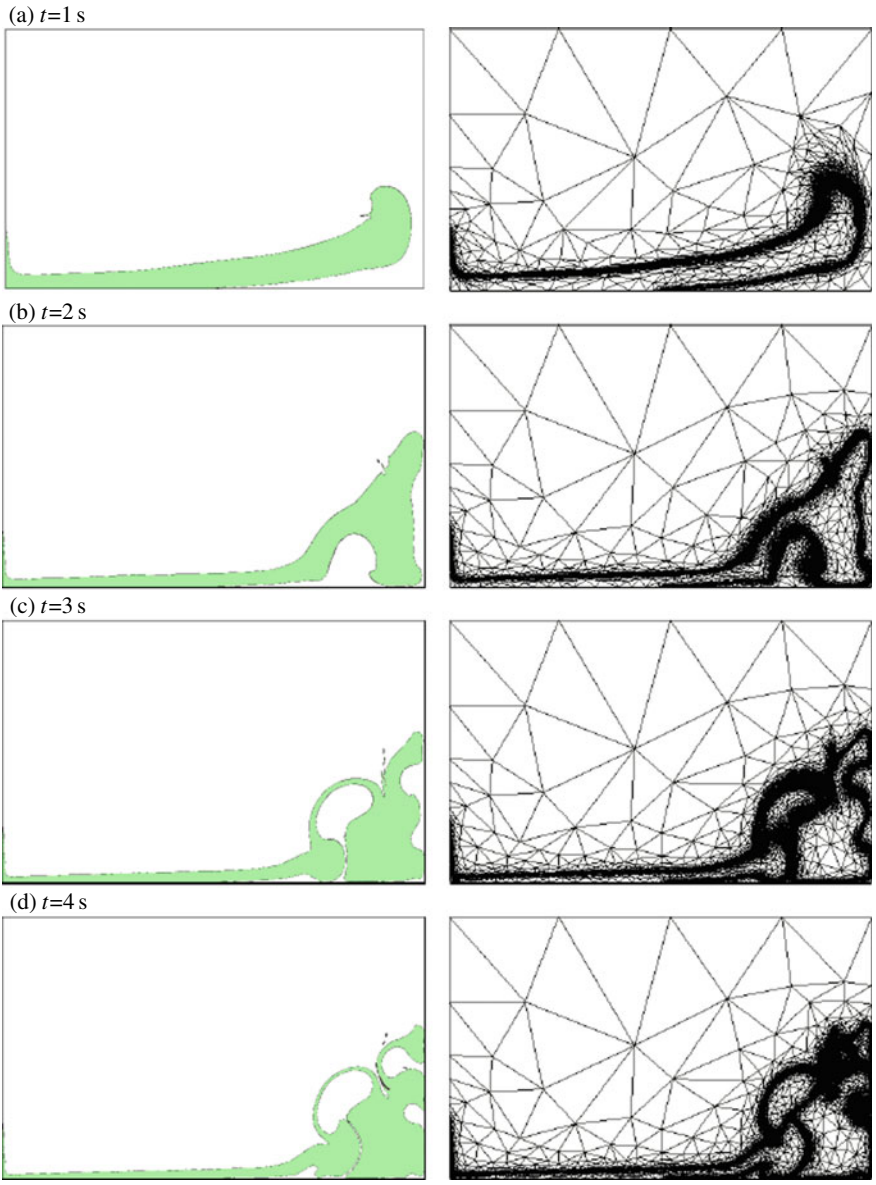

Fig. 5 Debris volume fraction evolution with time for Case 2 (constant $\mu = 80\,\mathrm{Pa}\cdot\mathrm{s}$). Corresponding adapted meshes are shown in the second column

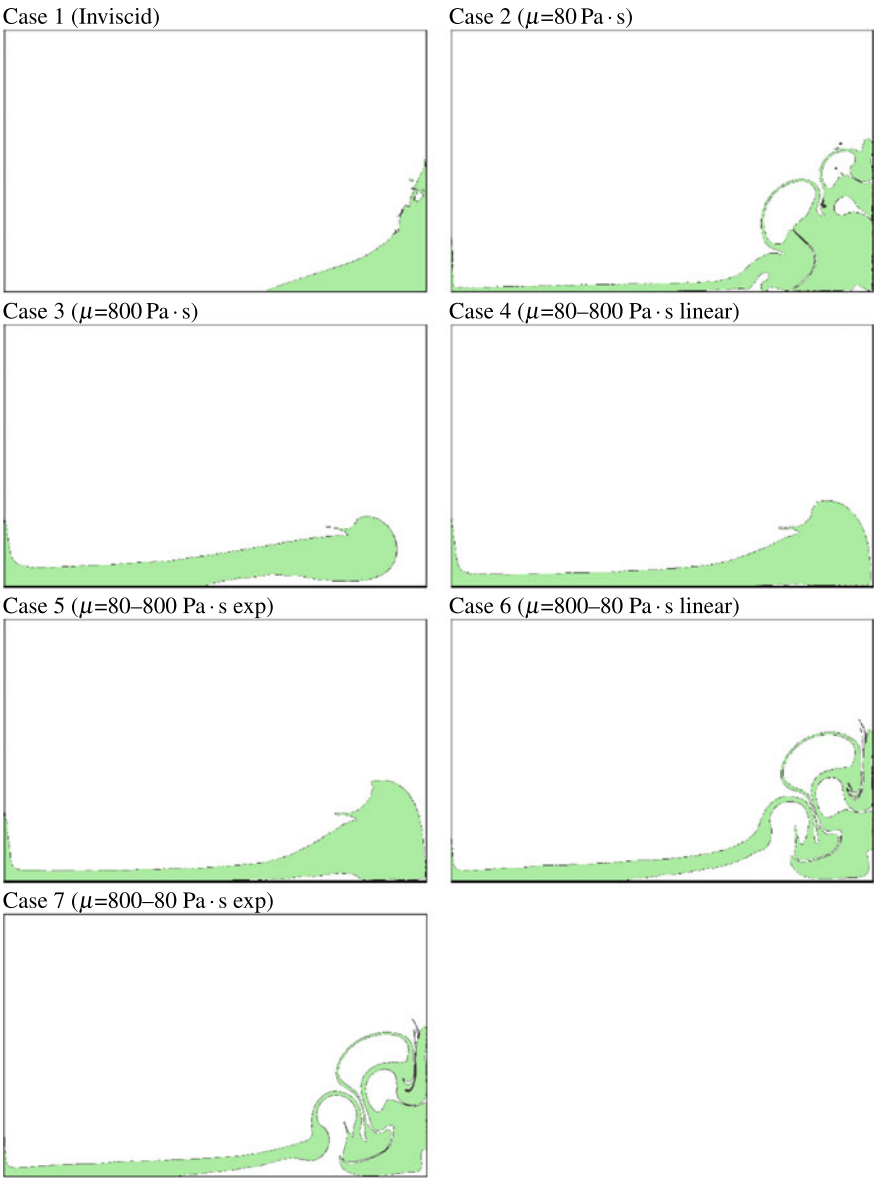

Fig. 6 Debris volume fraction at t = 10 s for the seven different cases

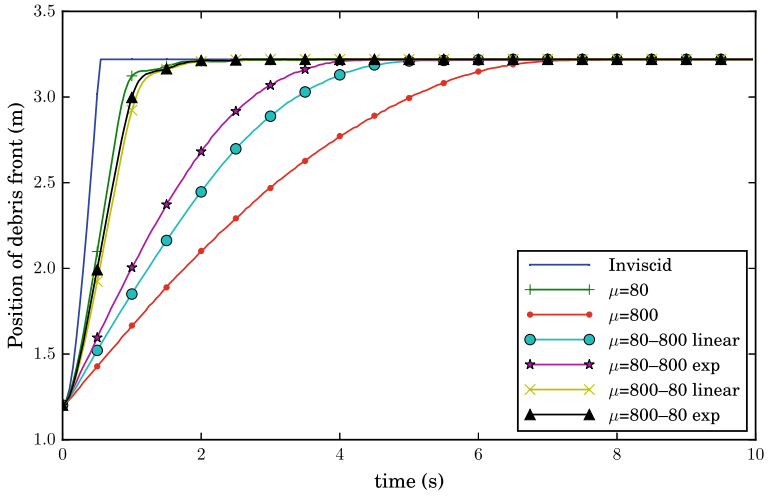

Fig. 7 Debris front position for the seven different cases. Cases are in the order of legend reference

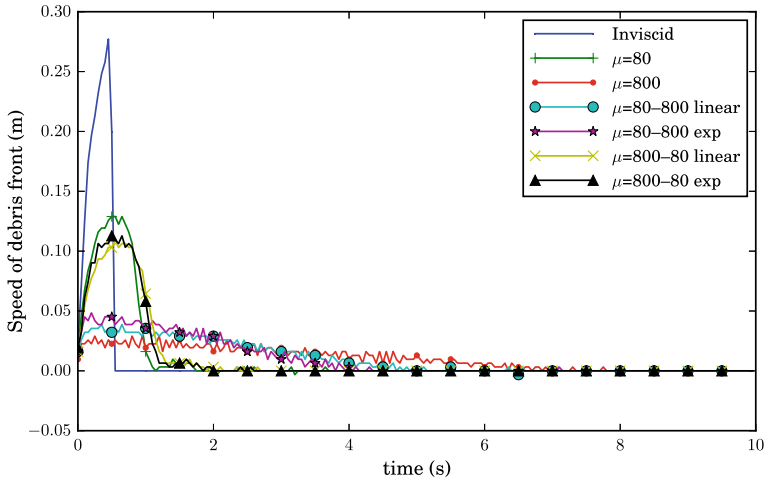

Fig. 8 Debris front x_1-velocity for the seven different cases

discussed further in Fig. 9. Owing to the lower flow velocity, the generated impact force is smaller for the highly viscous flows. In the case of inviscid flow, the sloshing phenomena results in a fluctuation in the impact force, which eventually attains a constant value corresponding to the hydrostatic pressure distribution.

Fluidity code is parallelised and adaptive-mesh refinement can be applied in conjunction with this coarse-grain parallelism to result in a highly-efficient solver. Load balancing is carried out using the Zoltan library. Fluidity code can be scaled to 1000+ cores using its distributed-memory parallelised approach. Parallelisation however

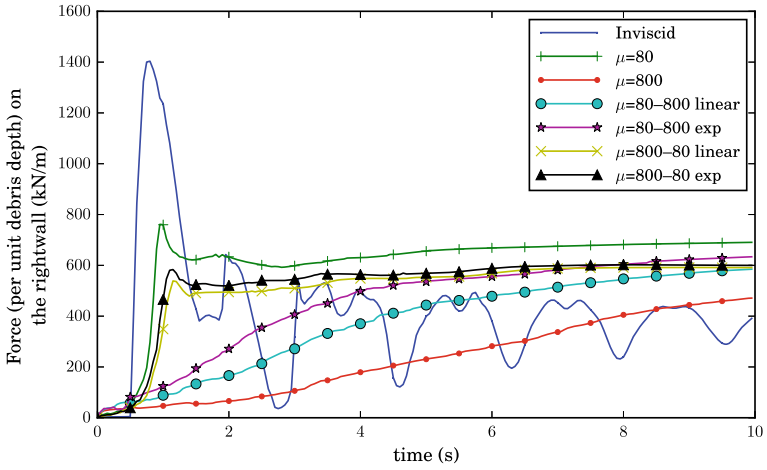

Fig. 9 Force on the right wall

only becomes effective when the number of nodes per thread is large (>5000). Since the present computational domain was lab-scale, there was no need to use parallelisation. However, this feature becomes most essential when computing the dynamics of field-scale debris flow events. Fluidity provides tractability to the potential computational modelling of debris flow dynamics on real mountain topography.

5 Conclusions

The influence of nonhomogeneous viscosity on the dynamics of debris flow was explored using 2D multi-material laminar-flow simulations. Eulerian-based large deformation analysis was carried out in the open-source software—Fluidity, which uses hybrid finite-element/control volume discretisation methods to solve the mass and momentum conservation equations. The flowing mass was idealised to behave like a single-phase Newtonian fluid with viscosity varying along the depth of the debris flow. Front velocity and exerted impact force on a rigid barrier were evaluated for the nonhomogeneous viscosity case and compared with the homogeneous one. It was noticed that the viscous nature of the lower layer primarily dictates the final flow pattern of the debris.

Numerical analyses presented in this paper help conclude the effectiveness of the adaptive-mesh refinement feature of Fluidity for modelling debris flow dynamics. Adaptive-mesh simulations were many times faster than the corresponding fixed-mesh simulations with similar accuracies. Although 2D simulations were presented in this paper, Fluidity code implementation is generalised for up to three spatial dimensions. Therefore, fully-3D multimaterial simulations can be performed, if required.

Since the aim of this work was to present the effect of the nonhomogeneity of viscosity in predicting the debris flow fields, two dimensions ensured simplification.

There have been previous studies that have modelled the nonhomogeneity of viscosity through the inclusion of a turbulent-flow model, however, that results in an expensive solution method linked to resolving the scales of turbulence. The present work can be interpreted as an approach that 'models' the nonhomogeneity of viscosity instead of 'resolving' it, which is similar to the simple zero-equation gradient-diffusion turbulence models. In the present work, debris flow has been 'modelled' as a fluid whose'viscosity' results from cohesion of particles in the debris. DEM simulations along with small-scale experiments are required to understand the physics of the debris flows and model the dependence of viscosity on debris parameters to quantify the nonhomogeneity function. Another way to map the nonhomogeneity with debris flow regimes is through lab-scale experimental validation, which will be presented in the future work by the authors.

References

1. AMCG (2015) Fluidity manual v4.1.12. Imperial College London
2. Bhutani G, Brito-Parada PR, Cilliers JJ (2016) Polydispersed flow modelling using population balances in an adaptive mesh finite element framework. Comput Chem Eng 87:208–225
3. Imran J, Parker G, Locat J, Lee H (2001) 1D numerical model of muddy subaqueous and subaerial debris flows. Comput Geotech 127(11):959–967
4. Koch T (1998) Testing various constitutive equations for debris flow modelling. In: Hydrology, water resources and ecology in headwaters (Proceedings of the headwater'98 conference held at Meran/Merano, Italy), vol 248, pp 249–257
5. Lee K, Jeong S (2018) Large deformation FE analysis of a debris flow with entrainment of the soil layer. Comput Geotech 96:258–268
6. Naef D, Rickenmann D, Rutschmann P, McArdell B (2006) Comparison of flow resistance relations for debris flows using a one-dimensional finite element simulation model. Nat Hazards Earth Syst Sci 6:155–165
7. Savage S, Hutter K (1989) The motion of a finite mass of granular material down a rough incline. J Fluid Mech 199:177–215
8. Zhou Z, De Kat J, Buchner B (1999) A nonlinear 3-D approach to simulate green water dynamics on deck. In: Proceedings of the seventh international conference on numerical ship hydrodynamics, Nantes, France, pp 1–15

Design of Water Retaining Embankment Using Geosynthetics for Hydraulic Conditions

Shubham Soni and Amit Prashant

Abstract Sand is often used in chimney and blanket drain to control the seepage inside the water retaining embankment. On many sites it is not economical to find a sufficient quantity of good quality sand. The objective of the present study is to minimize use of sand in design of water-retaining embankment by using geosynthetics material to control the seepage. Accordingly, two alternative designs of water retaining embankment with internal drainage system have been proposed. These designs are 'water retaining embankment with vertical drainage composite' and 'water retaining embankment with horizontal drainage composite'. The functions of geosynthetics in both the designs are filtration and drainage, and the geosynthetics material used are geotextile, drainage composite (geonet sandwiched by geotextile) and perforated pipe. The performance of geosynthetics for drainage and filtration in various structures like earth dam, retaining wall, highway drains and landfills provides confidence to use geosynthetics effectively in place of sand in water retaining embankment. A detailed methodology is set to determine the drainage and filtration requirement of geosynthetics material in each component of proposed alternative designs. The specifications required for geosynthetics material in each component of the proposed alternative design are also given. Depending upon the requirement any one of the alternatives can be used in place of the conventional system.

Keywords Seepage · Internal drainage · Drainage composite · Filtration · Drainage

S. Soni (✉)
Urban Development and Administration Department, Bhopal, India
e-mail: shubham.soni@mtech2015.iitgn.ac.in

A. Prashant
Indian Institute of Technology Gandhinagar, Gandhinagar, India
e-mail: ap@iitgn.ac.in

A. Prashant et al. (eds.), *Advances in Computer Methods and Geomechanics*, Lecture Notes in Civil Engineering 55,
https://doi.org/10.1007/978-981-15-0886-8_27

1 Introduction

Water retaining embankment includes structure like small tailing dam, dykes and low height earth dam. It consists of the upstream and downstream slope, internal drainage system and erosion control system. The height of embankment is generally in the range of 3–10 m. In order to control the seepage inside the water retaining embankment, conventionally it is provided with internal drainage system which generally consists of chimney and blanket drain. These drains are composed of materials which have a high permeability (to drain the seeping water) and their particle size is such that piping doesn't occur (particle retention). The functions of these drains are filtration and drainage. Sand is the ideal material, which fulfils the requirement of chimney and blanket drain. However, sand is not often available at every site and transportation of such a huge quantity of sand from other sites potentially increases the cost of the project. Hence, it is required to find some alternative to usage of sand in the internal drainage system of water retaining embankment.

In this study alternative to sand is taken as geosynthetics, which is being used in various structures in past. The functions performed by geosynthetics in such structure will be filtration and drainage which are similar to the function of sand in chimney drain and blanket drain in water retaining embankments. The application of geosynthetics material in earthen embankment was first reported in Valcross dam constructed in 1970 by Faure et al. [1], in which non-woven geotextile was used as a filter for rock toe. The use of geosynthetics as a filtering geotextile for vertical chimney drain, filter geotextile for sloping drain in Chateauvieux dam and use of horizontal layers of drainage composite for seepage control in Roquebrune-sur-Argens dam was described by Degoutte et al. [2]. The use of drainage composite in internal drainage system for 18 m height of earth dam is mentioned by Volkmer and Dias [3] and application of geosynthetics in this project reduced the total cost by 75% in comparison to the earth dam with conventional drainage system. The performance of geosynthetics highway drain at 91 field sites in seventeen states of USA was studied by Koerner et al. [4] and reported that out of 91 sites at 63 sites geocomposite drains performed satisfactorily. Chang et al. [5] examined the performance of drainage composite to relieve the uplift pressure below the raft foundation by a case study in Taiwan. McKean and Inoye [6] reported satisfactory performance of drainage composite to drain groundwater in vertical trench and behind retaining wall at three sites in Oregan and Northen California. In all the above structures geosynthetics product replaced the function performed by granular drainage and filtration materials.

Considering the performance and functions of geosynthetics in the structures reported in literature, two alternative designs for water retaining embankment have been proposed in the present study. The proposed designs incorporate the application of geosynthetics to control the seepage of water. In these designs geosynthetics are provided in such a way that the downstream side of the water retaining embankment should be dry. These designs are 'water retaining embankment with vertical drainage composite' and 'water retaining embankment with horizontal drainage composite'.

The water retaining embankment with vertical drainage composite consists of vertical drainage composite, drainage trench, horizontal drainage system and horizontal drainage composite. Water retaining embankment with horizontal drainage composite consists of horizontal layers of drainage composite and downslope drainage system. In both the designs, function of geosynthetics is focused on proper implementation of drainage and filtration requirements for seepage control in water retaining embankment. The drainage composite to be used should have sufficient drainage capacity to drain seepage water and filtration properties such that clogging and piping will not occur in water retaining embankment.

The drainage composite used in both the designs can be thick non-woven geotextile or geonet sandwiched between geotextile. Palmeira and Gardoni [7, 8] and Pak and Zahmatkesh [9] studied the effect of normal pressure on transmissivity of non-woven geotextile and reported that the increase in normal pressure caused decrease in transmissivity of non-woven geotextile in 2–3 orders of magnitude. In case of drainage composite normal pressure causes the intrusion of geotextile into the geonet which leads to decrease in transmissivity. Hwu et al. [10] investigated this phenomenon by conducting experiments. The experimental results showed that the intrusion of geotextile depends upon the initial modulus of geotextile and the reduction in drainage capacity is found to be 39–88% from original values due to short-term intrusion of geotextile into the drainage core. It is seen from the above study that the transmissivity of geotextile decreases exponentially with an increase in normal pressure and there can be more chances of clogging compared to drainage composite with geonet. It is therefore recommended to generally use geonet sandwiched between geotextile as a drainage composite for internal drainage system of water retaining embankment. The thickness of geonet to be used in drainage composite should not be less than 5 mm, to minimize the effect of geotextile intrusion on transmissivity of drainage composite. The requirements of geosynthetics for filtration and drainage in each component of proposed alternative design are different. The details of design requirements and material parameters for the proposed alternative designs have been worked out based on the state of the art and described in this paper.

2 Water Retaining Embankment with Vertical Drainage Composite

A schematic of water retaining embankment with vertical drainage composite is shown in Fig. 1. In this design, the drainage composite is installed vertically at the centre of the water-retaining embankment and connected to the drainage trench. The seepage water is trapped by the vertical drainage composite and transferred to the drainage trench. A horizontal drainage system consisting of pipe having initial portion perforated is connected to the drainage trench. This pipe collects water from drainage trench and drains out from the water-retaining embankment. Drainage composite

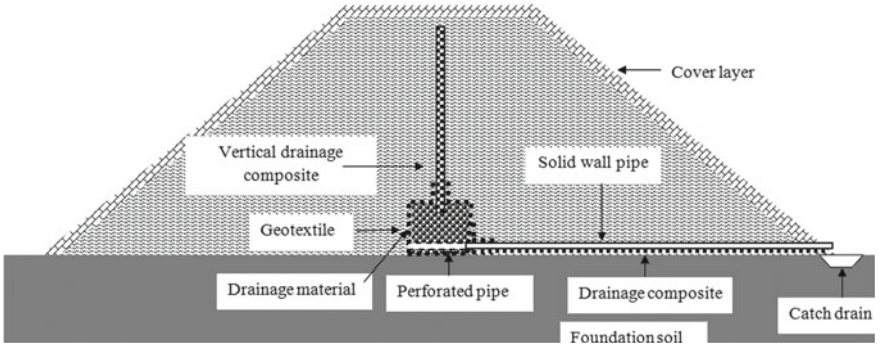

Fig. 1 Water retaining embankment with vertical drainage composite

is installed in downstream side of the water retaining embankment to control the seepage coming from foundation soil.

2.1 Vertical Drainage Composite

The vertical drainage composite is designed for filtration and drainage. In the vertical drainage composite, the function of geotextile is to allow water seepage through it (permeability) and at the same time retain the soil particles on its upstream side (soil retention), i.e. filtration function. The permeability requirement of geotextile is determined in terms of permittivity. The total quantity of seepage (q) per metre length is calculated from seepage analysis and the required permittivity of geotextile is found by Eq. 1.

$$\Psi_{\text{req}} = \frac{q}{H * A} \tag{1}$$

where, Ψ_{req} is required permittivity of geotextile, q is discharge per unit length, H is the height of vertical drainage composite and A is area of geotextile.

The allowable permittivity value of geotextile is determined by using Eq. 2. The allowable permittivity (Ψ_{req}) of geotextile should be greater than the required permittivity of geotextile.

$$\Psi_{\text{alw}} = \frac{\Psi_{\text{ult}}}{RF_{\text{SCB}} * RF_{\text{CR}} * RF_{\text{IN}} * RF_{\text{CC}} * RF_{\text{BC}}} \tag{2}$$

where, Ψ_{alw} is allowable permittivity of geotextile, Ψ_{ult} is permittivity of geotextile determined in the laboratory, RF_{SCB} is the reduction factor for soil clogging, RF_{CR} is the reduction factor for creep, RF_{IN} is the reduction factor for adjacent material intruding in geotextile, RF_{BC} is the reduction factor for biological clogging RF_{CC}

Table 1 Various reduction factors for permittivity and transmissivity (Koerner 2005)

Application	RF_{SCB}	RF_{CR}	RF_{IN}	RF_{CC}	RF_{BC}
Permittivity	2.0–4.0	2.0–3.0	1.0–1.2	1.2–1.5	1.2–1.5
Transmissivity	3.0–4.0	1.4–2.0	1.5–2.0	1.1–1.5	1.0–1.5

is the reduction factor for chemical clogging. These factors are required for long-term performance of geotextile. The values for reduction factors should be taken in designing are given in Table 1. The permeability of geotextile is determined by multiplication of allowable permittivity with the thickness of geotextile at specified pressure. Degoutte and Fry [11] mentioned that permeability of geotextile should be 100 times greater than the permeability of fill soil for filtration function. This factor is required to consider the effect of reduction in flow area on the downstream face of geotextile due to contact with geonet, change in thickness of geotextile due to confinement pressure of soil and increase in permeability requirement of geotextile due to formation of high permeability filter cake on the upstream side of it.

For soil retention, the fabric structure of geotextile is such that the upstream soil particles will not pass through it. The fabric structure of geotextile is defined by apparent opening size. Here, the required apparent opening size (O_{95}) for geotextile is found by retention criteria flow chart developed by Luettich et al. [12]. Geotextile used in water retaining embankment should satisfy the minimum filtration properties as given in AASHTO [13] and IRC SP 59 [14]. Geotextile used for filtration should not clog during its design life. Caroll [15] studied the hydraulic properties of geotextiles required for filter design and the corresponding laboratory test methods to determine those. Caroll [15] found that the long-term clogging potential of geotextile cannot be defined by apparent opening size and permeability of geotextile. There is no direct method for determining clogging of geotextile. Some of the laboratory tests are available which can give an idea about clogging of candidate geotextile. These tests and typical values for non-clogging are Gradient ratio test (GR < 3), Long-term flow test (LTF) and Hydraulic conductivity ratio test HCR (0.3–0.7). Any one of the above tests can be used for determining long-term filtration behaviour of candidate geotextile.

The drainage requirement of vertical drainage composite is given in terms of the transmissivity. The transmissivity of drainage composite is determined by multiplication of in-plane permeability and thickness of drainage medium. The required in-plane drainage capacity (transmissivity) for drainage composite per unit length can be determined by using Eq. 4.

$$\theta = \frac{q}{i} \tag{3}$$

$$\theta_{req} = 10 * \theta \tag{4}$$

where, θ_{req} is the required transmissivity of drainage composite, q is discharge per unit width and i is hydraulic gradient for drainage composite.

The transmissivity of drainage medium found in the laboratory may not represent the actual field conditions. Hence, transmissivity of drainage medium should be decreased to consider the effect of confining pressure, the intrusion of geotextile in geonet, clogging due to upstream soil particle and bending of drainage composite due to the settlement of soil. The allowable transmissivity of drainage medium is calculated by Eq. 5. The allowable transmissivity of drainage composite provided in water retaining embankment is greater than the required transmissivity. The required transmissivity of drainage composite increases 10 times to consider the effect of improper compaction of fill soil, improper installation of drainage composite and long-term flow capacity.

$$\theta_{alw} = \frac{\theta_{ult}}{RF_{SCB} * RF_{CR} * RF_{IN} * RF_{CC} * RF_{BC}} = \tag{5}$$

where, θ_{alw} is allowable transmissivity, θ_{ult} is transmissivity of drainage medium determined in laboratory, reduction factors are the same as used in Eq. 2 and their values are given in Table 1.

The other factors that affect the performance of drainage composite are survivability and durability. For that the geotextile used for filtration should have sufficient strength to resist damage caused by installation and post-installation stresses due to stretching, puncturing, tearing and abrasion. To account for these issues the geotextile used should have minimum strength as given AASHTO M 288 [13] and IRC SP 59 [14]. The compressive strength of drainage composite should be greater than the overburden pressure acting on it from surrounding soil, to avoid the breakage of drainage core (geonet) in the long term. Geotextile is manufactured by polymer like polyester, polypropylene and polyethylene. It has low resistance against UV light, oxidation but it is a minor concern for geosynthetics in these alternate designs because geosynthetics is buried inside the soil.

2.2 Drainage Trench

To provide a smooth transition for seeping water, a drainage trench is excavated along the centre line of the water retaining embankment which collects the seepage water from vertical drainage composite and drains out from the embankment. A typical section of the drainage trench is shown in Fig. 2. The size of the drainage trench depends upon the quantity of seepage water. The minimum size of trench in mechanical stabilized earth (MSE) wall drainage system is recommended as $0.6 * 0.6$ m^2 [16] and it has the same function as drainage trench in water retaining embankment with vertical drainage composite. The minimum size of drainage trench in this case is taken as $0.75 * 0.75$ m^2 and it can be increased depending upon the seepage flow. The shape of trench is taken as rectangular because construction of rectangular trench is easy. Drainage trench is filled with a high permeability material which is wrapped by geotextile. The material filled in the drainage trench should not clog the perforation

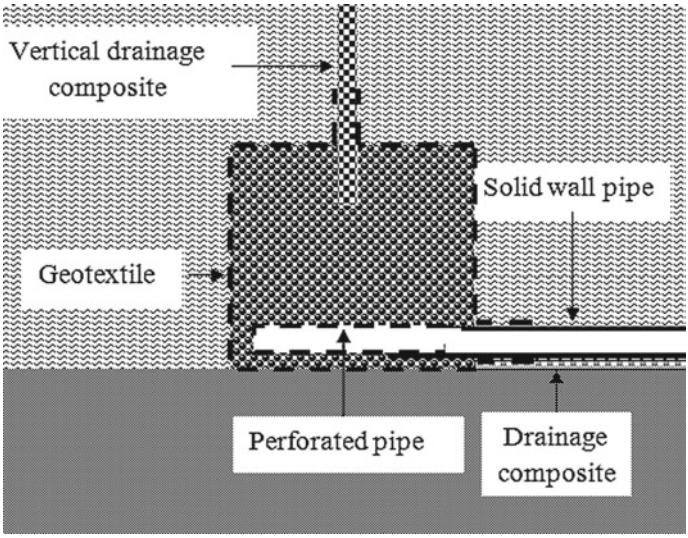

Fig. 2 A typical section of the drainage trench

of the pipe. The material filled in the drainage trench should be well graded crushed stone, broken rock or gravel. The material filled in the trench is durable and weather resistant, and hence material like limestone, sandstone or shale cannot be used. The size of the material to be used can vary from 10 to 75 mm [17] and it should not have sharp edges. The function of geotextile around the trench is to avoid clogging of material in trench by surrounding soil. The design of geotextile for filtration in drainage trench is the same as the design of geotextile in vertical drainage composite. Here, the geotextile is directly placed on the aggregate, hence strength requirement like burst strength, puncture strength and tensile strength is evaluated carefully. The required burst strength, tensile strength and puncture strength of geotextile for trench are evaluated by the theory developed by Giroud [18]. The strength of geotextile provided in drainage trench should not be less than the minimum strength requirement of geotextile as given in AASHTO M 288 [13] and IRC SP 59 [14].

2.3 Horizontal Drainage System

The horizontal drainage system consists of the arrangement of lateral pipes which is connected to the drainage trench. These pipes are solid wall pipe of PVC or HDPE. The initial part of pipe which is inside the trench is perforated and another part is solid wall pipe. Perforated pipes collect water from trench and pass it to solid wall pipe to drain outside the water retaining embankment. Drain pipe is designed to have long service life, adequate flow capacity and sufficient strength to resist all loading conditions and foundation settlement. Pipe should have sufficient strength to take

load coming on it, i.e. load from construction equipment and load due to soil above the pipe (overburden). The pipe used should have material grade PE80 or PE100, and it should have minimum pipe stiffness 200 kPa. The minimum cover of 0.5 m is required on the pipe while doing compaction of the fill soil. The size and spacing of pipe depends upon the quantity of seepage and the strength requirement. The drain pipe is designed for gravity flow and the maximum depth of flow in the pipe is taken as 50% of its diameter (half full flow). Pipe in water retaining embankment is installed at a 2% gradient to allow gravity flow. The design discharge for pipe is taken as discharge per unit length calculated from seepage analysis multiplied by the spacing of pipe. The required diameter of drain pipe is found by Eq. 6, which is based on Mannings equation with pipe flowing half full. The diameter of pipe provided in the water retaining embankment is three times the diameter of pipe required. The minimum diameter of the pipe to be used in water retaining embankment is 50 mm and the maximum diameter of the pipe to be provided should not be greater than 100 mm for avoiding the chances of wall bucking due to external soil pressure. The maximum spacing at which pipe is provided in water retaining embankment is limited to 3 m.

$$D = 2 * \left(\frac{Q_p * n}{\sqrt{s}} \right)^{3/8} \tag{6}$$

where, Q_p is the design discharge for pipe, D is the required diameter of pipe, n is the Mannings roughness coefficient, s is the slope at which the pipe is installed.

Water in the pipe enters from the perforation provided on the surface of the pipe. The required area of perforation on the pipe is calculated by applying the concept of flow through orifice. Here the perforation in pipe is assumed as an orifice and the perforated area on the pipe is expressed as the total open area per metre length of pipe. The required total area of perforation on surface of pipe is found by Eq. 7.

$$a_{\text{req}} = \frac{Q_{\text{p}}}{C_{\text{d}} * \sqrt{2 * g * h}} \tag{7}$$

where, Q_{p} is the design discharge for pipe, a is the total area of perforation require, C_{d} is the coefficient of discharge (0.6), h is the maximum height of water above pipe.

For calculating the area of perforation, head of water (h) is taken as the height between pipe and top of the trench. This is the maximum head available for pipe and at this condition, water should enter the pipe without accumulating in drainage trench. The area of perforation provided in drainage trench is found by multiplication of perforation area per unit length of pipe to the length of pipe in drainage trench. The perforation can be circular or rectangular slot. The effective perforation area for circular perforation is taken as 30% of total perforation area and in the case of rectangular perforation it is 60% as mentioned in Technical Manual 'Plastic Pipe Used in Embankment Dam' [19]. This reduction is due to blockage of perforation due to aggregate in drainage trench. The effective area of perforation provided is 10 times greater than the area of perforation required. The minimum length of perforated

pipe provided in drainage trench is 0.5 m. The perforation size of the pipe is such that the surrounding material should not enter into the pipe. The size of perforation depends upon the gradation of surrounding material (drainage aggregate) and found by filter criteria, by following the criteria developed by US Army corps (2004) and Bureau of reclamation (2007) which is given in Technical Manual. 'Plastic Pipe Used in Embankment Dam' FEMA [19].

2.4 Horizontal Drainage Composite

Drainage composite is installed in the downstream side of the water retaining embankment to collect the seepage coming from the foundation soil. The type of composite to be used and its filtration and drainage requirement is determined in a similar way as for the vertical drainage composite. In this case, the filtration requirement of drainage composite is determined for both fill and foundation soil. The design discharge is taken as seepage of water coming from the foundation soil. The discharge coming from foundation soil is calculated by the procedure given in IS 9429 [20]. Here drainage composite can be continuous or at some horizontal spacing depending upon quantity of seepage from foundation soil. The spacing of drainage composite is found by Eq. 8. If drainage composite is provided at some horizontal spacing then the minimum 50% coverage ratio for drainage composite is maintained and the clear spacing provided between two drainage composite should not be greater than 2 m. The arrangement of horizontal drainage composite in downstream side of water retaining embankment is shown in Fig. 3. Seepage from foundation soil can

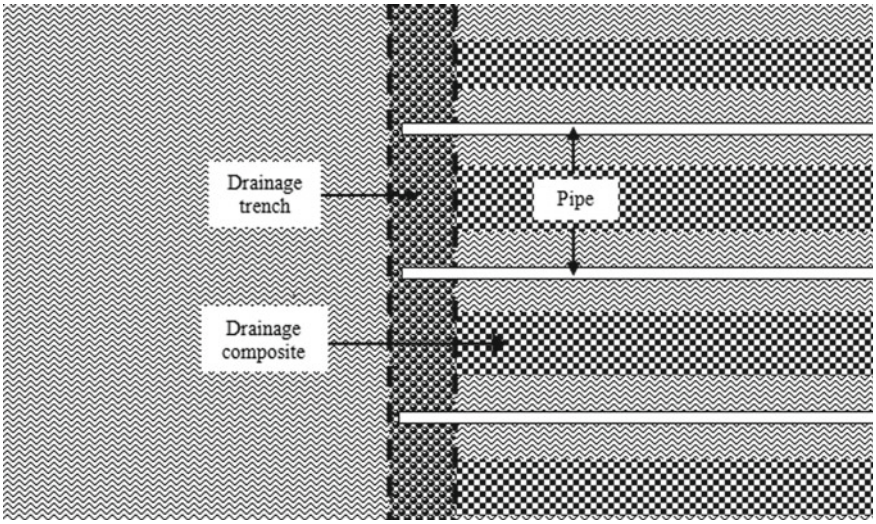

Fig. 3 Arrangement of perforated pipe and drainage composite

also come into the trench besides going directly to the drainage composite. The size of trench has to be kept such that water should not accumulate. For that, drainage capacity of trench and area of perforation provided on pipe is checked for total seepage coming from upstream side and foundation soil.

$$S_{\mathrm{H}} = \frac{\theta_{\mathrm{alw}} * B}{\theta_{\mathrm{req}}} \tag{8}$$

where, S_{H} is the horizontal spacing of drainage composite sheet, θ_{alw} is the allowable transmissivity of drainage composite, B is the width of drainage composite sheet and θ_{req} is the required transmissivity of drainage composite for seepage from foundation soil.

3 Water Retaining Embankment with Horizontal Drainage Composite

A Schematic of water retaining embankment having different layers of drainage composite and downslope drainage system is shown in Fig. 4. In this design, the water retaining embankment consists of drainage composite which is installed horizontally at different levels, as used in Roquebrune-sur-Argens [2] dam. The top drainage composite is extended up to the height of filled water. The drainage composite collects seepage water from different levels in water retaining embankment and drains out from it. Seepage water flows in the horizontal drainage composites and reaches the downstream surface of the water retaining embankment. If this water directly flows on the downstream face of water retaining embankment it will cause erosion of the downstream slope. To control these, a downslope drainage system is provided on the

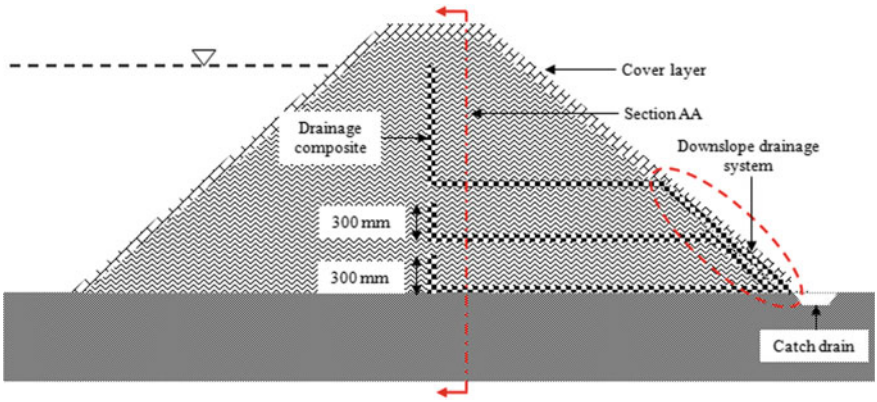

Fig. 4 Water retaining embankment with horizontal drainage composite

downstream surface by extending the drainage composite up to the toe drain and it will act as drainage layer for cover material.

3.1 Horizontal Drainage Composite

Here the drainage composite is installed in horizontal layers and placement of drainage composite in the water retaining embankment is such that in all possible conditions the phreatic line should not cut the downstream slope. The drainage requirement for drainage composite is determined by performing seepage analysis and the design for filtration is done the same way as in the case of vertical drainage composite. Only the filtration requirement of bottom drainage composite is checked for both fill and foundation soil. A minimum three layers of drainage composite should be provided up to one-third height of the water retaining embankment. The vertical spacing of drainage composite depends upon the height of the water-retaining embankment, quantity of seepage through the water retaining embankment and transmissivity of drainage composite. The maximum vertical spacing for 3–10 m height water retaining embankment is 0.5–1.5 m. The minimum vertical spacing between two drainage composites will be 0.3 m for compaction of fill soil on drainage composite. If the quantity of seepage flow through the water retaining embankment is high then more number of layers can be provided at closer spacing inside the water retaining embankment. The horizontal spacing of drainage composite depends on its transmissivity. The bottom drainage must be continuous and upper layers can be provided in staggered fashion at some horizontal spacing with minimum 50% coverage. The horizontal spacing of drainage composite has to be found by Eq. 8 after determining the required transmissivity. The clear spacing between two drainage composites should not be greater than 2 m. The arrangement of various layers of horizontal drainage composite is shown in Fig. 5.

To determine the required transmissivity of drainage composite, water retaining embankment can be modelled in FEM software for seepage analysis with different layers of drainage composite. FEM software like FINE -GEO5, Geo- Slope and Plaxis can be used for seepage analysis. For 2D seepage analysis, the vertical spacing of drainage composite is decided first according to above-mentioned criteria. The input parameters required are permeability and void ratio of the soil, transverse and longitudinal permeability of drainage composite. First the geometry of water retaining embankment is created and then the interface is provided at the location of drainage composite and drainage composite must have a slope of 2% towards downstream side. After that the interface is converted to partial permeable contacts of given thickness and longitudinal and transverse permeability. Here, thickness of drainage composite in seepage analysis is taken as 5–10 mm because it is the generally available thickness of drainage composite. The transverse permeability in seepage analysis should be generally taken as permeability of geotextile (permittivity $*$ thickness). The required longitudinal permeability of drainage composite is found by performing seepage analysis. The thickness of partial permeable contact provided

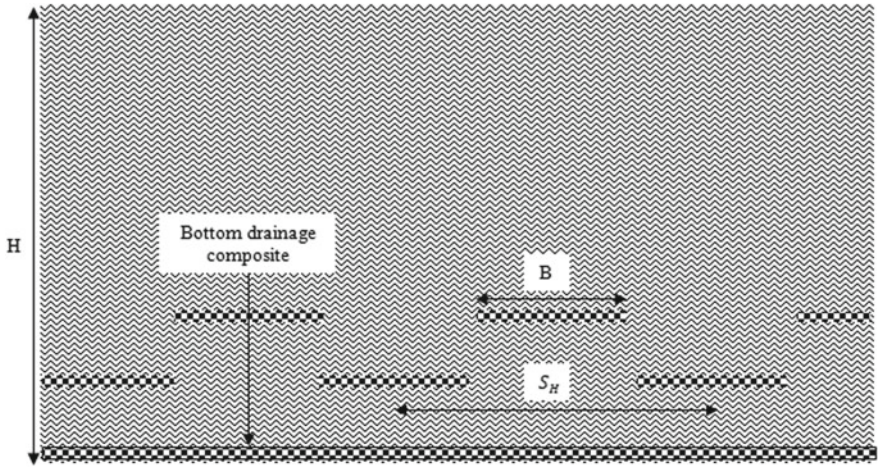

Fig. 5 Arrangement of drainage composite in water retaining embankment along section AA

in seepage analysis is used for calculation of transmissivity requirement and it is not necessary to provide the same thickness of drainage composite in the water retaining embankment.

After seepage analysis, it is checked that the phreatic line is not cutting downstream slope of water retaining embankment and most of the downstream side of water retaining embankment is dry. If the above condition is not met, the seepage analysis is again performed by changing the longitudinal permeability of drainage composite or by providing more layer of drainage composite. This cycle is repeated until the phreatic line is found to be well within the embankment body. Corresponding to the above condition, the longitudinal permeability of drainage composite is noted. From the longitudinal permeability, the required transmissivity of drainage composite is calculated using the Eq. 10. After determining the required transmissivity the other requirement of drainage composite should be checked, in the same way as it is proposed to be done for the vertical drainage composite.

$$\theta = k_l * t_c \tag{9}$$

$$\theta_{\text{req}} = 10 * \theta \tag{10}$$

In this design, the drainage composite is installed in horizontal layers and it will provide some reinforcement action to the slope due to its nominal tensile strength. However, contribution of this should not be considered in stability analysis of downstream slope.

4 Summary

Two alternative designs are proposed, 'water retaining embankment with vertical drainage composite' and 'water retaining embankment with horizontal drainage composite'. The geosynthetics materials used in the proposed designs are drainage composite, geotextile and perforated pipe. At the site where the required quantity and quality of aggregate is not available, then it is preferable to use water retaining embankment with horizontal drainage composite. In other cases where the quantity of seepage is high and the number of drainage composite layers required to control seepage in water retaining embankment is more, one can use the water retaining embankment with vertical drainage composite as an alternative design. Hence any of the above proposed alternative designs can be used depending on site conditions.

References

1. Faure YH et al (1999) Analysis of geotextile filter behaviour after 21 years in Valcros dam. Geotext Geomembr 17(5):353–370
2. Degoutte Gérard (1987) Practical examples of geotextile used in small earth dams. Geotext Geomembr 5(4):239–250
3. Vogt Volkmer M, Gerheim Souza Dias T (2012) Design and construction aspects of a geocomposite drainage system in a dam. In: 2nd Pan-American geosynthetics conference: geoamericas
4. Koerner GR, Koerner RM, Wilson-Fahmy RF (1996) Field performance of geosynthetic highway drainage systems. In: Recent developments in geotextile filters and prefabricated drainage geocomposites. ASTM International
5. Chang DT-T, Wu JY, Nieh YC (1996) Use of geosynthetics in the uplift pressure relief system for a raft foundation. In: Recent developments in geotextile filters and prefabricated drainage geocomposites. ASTM International
6. McKean Jim, Inouye Ken (2001) Field evaluation of the long-term performance of geocomposite sheet drains. Geotext Geomembr 19(4):213–234
7. Palmeira EM, Gardoni MG (2000) The influence of partial clogging and pressure on the behaviour of geotextiles in drainage systems. Geosynth Int 7(4-6):403–431
8. Palmeira Ennio M, Gardoni Maria G (2002) Drainage and filtration properties of non-woven geotextiles under confinement using different experimental techniques. Geotext Geomembr 20(2):97–115
9. Pak Ali, Zahmatkesh Zahra (2011) Experimental study of geotextile's drainage and filteration propertis under different hydraulic gradients and confining pressures. Int J Civ Eng 9(2):98–102
10. Hwu B, Koerner RM, Sprague CJ (1990) Geotextile intrusion into geonets. In: Proceedings of the international conference on geotextiles, The Hague
11. Degoutte G, Fry JJ (2002) Geotextiles in dams, feedback. In: Technical symposium on geotextiles and geomembranes in dams, held on behalf of CFG and FCOLD, 29 p
12. Luettich SM, Giroud JP, Bachus RC (1992) Geotextile filter design guide. Geotext Geomembr 11(4-6):355–370
13. AASHTO (2006) Standard specifications for geotextiles—M 288, Standard specifications for transportation materials and methods of sampling and testing, 26th edn. American Association of State Transportation and Highway Officials, Washington, DC
14. IRC (2002) Guidelines for use of geotextiles in road pavements and associated works. SP—59, India Roads Congress, New Delhi, India

15. Carroll RC (1987) Hydraulic properties of geotextiles. In: Geotextile testing and the design engineer. ASTM International
16. Berg RR, Christopher BR, Samtani NC (2009) Design of mechanically stabilized earth walls and reinforced soil slopes–volume I. No. FHWA-NHI-10-024
17. Sinha R (2005) Geo environmental design practice in fly ash disposal & utilization. Allied Publishers
18. Giroud J-P (1981) Designing with geotextiles. Mater Struct 14(4):257–272
19. Technical manual (2007) Plastic pipe used in embankment dam FEMA
20. IS: 9429, Drainage system for Earth and Rockfill Dam

A Numerical Study on the Effect of Initial Void Ratio and Areal Extent of Heterogeneity on Instability Onset in Granular Media

Debayan Bhattacharya and Amit Prashant

Abstract The present study numerically explores the coupled biaxial undrained instability analysis of Hostun RF sand with varying initial void ratio (e_0) for a given confining pressure (σ'_c). A transient analysis of 100 mm × 100 mm sand specimen has been carried out with the implementation of a generalized 3D nonassociative elastoplastic material model. Finite element analysis has been performed in ABAQUS v6.14 and the constitutive model has been incorporated by scripting a user-defined material model subroutine (UMAT). The standard custom for instability analysis involves introduction of some form of heterogeneity within the material domain (perturbation) and probing its response against the prescribed boundary conditions. Mesh sensitivity of instability onset has been explored in the current context numerically while material imperfection has been introduced in terms of e_0. The coupled analysis allowed local fluid motion within the material continuum, while the undrained boundary condition was imposed globally. Instability onset gets delayed as e_0 is decreased (relatively denser specimens) for a given σ'_c with distinct signatures of dilative and contractive zones existing adjacent to each other (for specimens with e_0 < critical void ratio (e_c)) for a particular perturbation magnitude. Influence of spatial extent of heterogeneity for a given perturbation intensity and σ'_c also showed some effect in lowering down the instability onset strain to some degree and ceased to display significant impact on further increase in the areal extent of material imperfection.

Keywords Sand · Instability · Strain localization · Plane strain · Transient analysis · Perturbation

D. Bhattacharya · A. Prashant (✉)
Indian Institute of Technology Gandhinagar, Gandhinagar, India
e-mail: ap@iitgn.ac.in

D. Bhattacharya
e-mail: debayan.bhattacharya@iitgn.ac.in

A. Prashant et al. (eds.), *Advances in Computer Methods and Geomechanics*, Lecture Notes in Civil Engineering 55,
https://doi.org/10.1007/978-981-15-0886-8_28

1 Introduction

A soil specimen analysed in the laboratory is inherently heterogeneous in nature although the measurements are accomplished considering it as a single element. However, it is these inherent material imperfections that lead to the specimen exhibiting non-uniform deformation modes suddenly from a state of uniform homogeneous material response and leading to instability in granular materials. This state is coined as bifurcation of the material behaviour and the localized plastic strain accumulation associated with it is an omnipresent feature of granular media undergoing non-uniform deformations. Experimental findings report that plastic instabilities are often encountered in the form of localized zones of extensive shearing (deformation bands), bulging of the specimen or buckling of surfaces and volume instability [8–11, 17–20, 24]. The emergence of these plastic instabilities suddenly from the uniform stress–strain state depends on the material properties, type of loading, boundary and drainage conditions [27, 28]. These deformation bands essentially form the weak planes and are found to exist in various geologic materials (e.g. soil, rock, concrete, etc.) in the form of fault gouges, shear bands etc. [6]. In addition to this, fluid flow within the fully saturated porous media not only affects the strength of these materials, but also influences the movement of fluids entrapped (e.g. gases, hydrocarbons, etc.) within it [3]. Strain localization is one such ubiquitous feature in geomaterials and acts as a precursor to failure that may result in sudden collapse of earthen embankments, etc., particularly in an undrained situation (rapid drawdown case) by virtue of which, investigation regarding its onset is of main concern in contemporary geomechanics research.

The experimental findings and the theoretical predictions related to dense sand specimens exhibiting persistent shear bands under drained conditions (allowing global volume change) are in good agreement with each other and have been explored extensively in the past by several researchers [10, 11, 17]. On the contrary, instability studies related to soil specimens under (globally) undrained conditions reported contrasting account of observations [9, 11, 18, 19, 21, 22]. Nucleation of shear bands in conjugate arrays has been reported to initiate in sand specimens during initial stages of loading while performing an undrained test, which later manifests itself into a distinct zone of extensive strain accumulation. These localized zones are dilative in nature accompanied by contractive zones adjacent to them which reveal local fluid movement within the material continuum although global isochoric condition (constant volume—globally undrained) was imposed on the sand specimen [15, 16]. This signature exhibited by granular media gives the motivation to carry out a coupled undrained instability analysis in sands by incorporating transient diffusion process for the fluid flow in the present study.

Numerical investigation (FEM analysis) of the strain localization phenomenon in granular media has received much attention in past few decades in the form of several noteworthy contributions by Borja and Regueiro [7]; Fleck and Hutchinson [12]; Bažant and Jirásek [4] etc. owing to its various ‘pathological’ issues. A significant amount of effort has been devoted so as to model the strain-softening behaviour and

shear banding phenomenon acceptably well within the realms of continuum mechanics. Nevertheless, the onset of instability in pressure-dependent elastoplastic solids and the post-localization material response are two different features and should be dealt with separately. The present study deals with numerical investigation of instability onset in granular media by introducing some form of perturbation(weak element) in the material domain and checking its response against the prescribed boundary conditions. This calls for a standard mesh convergence study with material imperfection (for a particular perturbation intensity) and also aims at matching the theoretically predicted instability onset strain as reported by Mukherjee et al. [23] on Hostun RF sand. A theoretical study has been carried out by Mukherjee et al. [23] within the bifurcation analysis framework on Hostun RF sand with varying densities, confining pressure and boundary conditions—flexible as well as rigid to estimate the onset of instability in granular media. The emergence of two possible modes of instability in the form of localized zones of strain accumulation and 'liquefaction-type solid-fluid' instability has been reported in their study under rigid and flexible boundary conditions. The present study deals with undrained biaxial shearing of Hostun RF sand at a particular confining pressure and perturbation magnitude but with varying initial void ratio (e_0) so as to explore its effect on the instability onset strain.

2 Plane Strain Problem Formulation—Geometry and Material Model

Figure 1 illustrates the schematic representation of a biaxially loaded saturated sand specimen of 100 mm × 100 mm size. No shear stress has been considered in any of the boundaries. Plane strain biaxial shearing of the sand specimen (deformation rate = 0.1 mm/min) was accomplished under a globally undrained condition while

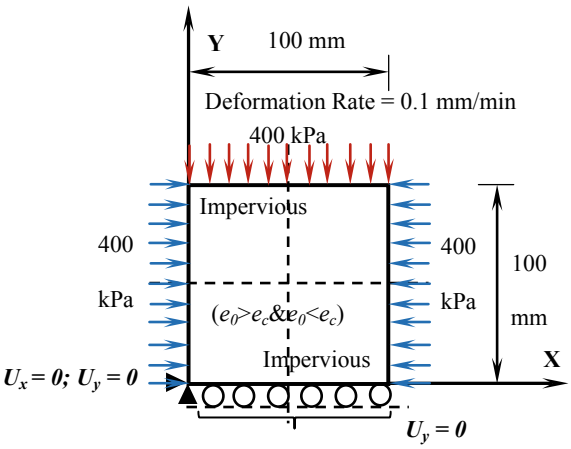

Fig. 1 Schematic illustration of biaxial plane strain problem showing geometry and boundary conditions

local fluid movement within the porous granular media was allowed. Both vertical and horizontal movement were constrained at the leftmost bottom corner node of the sand specimen while rest of the bottom nodes allowed horizontal movement (roller support) only. The top as well as the bottom surfaces portray rigid boundary conditions with equal deformation at all nodes and the lateral boundaries on the other hand are flexible in nature.

Numerical investigation has been performed on Hostun RF sand specimens with different e_0 varying from 0.6 (dense sand specimens, $e_0 < e_c$) to 0.8 (loose specimens, $e_0 > e_c$) at a confining pressure of 400 kPa. Coupled equilibrium equations for the soil skeleton along with the continuity equation for fluid (water) flow have been considered in the present context. In order to incorporate a generalized 3D nonassociative elastoplastic constitutive relationship [29], a user-defined material model subroutine (UMAT) has been implemented within the numerical framework of ABAQUS v6.14. The material model has been formulated in the realms of Critical State theory [25] and it incorporates both shear as well as volumetric hardening [13]. It considers the widely used Mohr–Coulomb failure criteria and assimilates the stiffness and strength dependence on state parameter (ψ) with critical state theory. A hyperbolic relationship dictates the evolution of plastic stiffness while the flow rule has been drawn upon similar lines of Cam-Clay model within bounding-surface plasticity framework. The elastic response is considered to be linear while the yield surface (f) and the plastic potential function (g) governing the inelastic material behaviour are defined as,

$$f(\sigma', \varepsilon_q^p, \varepsilon_v^p) = \sqrt{3J_2} + \eta_y \frac{I_1'}{3} = 0;\ g(\boldsymbol{\sigma'}) = \sqrt{3J_2} + M_c \frac{I_1'}{3} \ln \frac{3P_r'}{I_1'} = 0 \quad (1)$$

In Eq. (1), ε_q^p and ε_v^p represent the shear and the volumetric plastic strains, respectively; I_1' and J_2 denote first invariant of the stress tensor and second invariant of the deviatoric stress tensor, respectively. M_c is the slope of critical state line in shear stress and $-I_1'/3$ plane; P_r' is the intercept of g on $-I_1'/3$ axis and η_y is the shear stress ratio (i.e. ratio of deviatoric stress q and mean effective stress p'), which is a state variable of the material model. Evolution of η_y is governed by ε_q^p which itself is dependent on another state variable (ψ) that incorporates the effect of p' and density of the specimen. Material parameters considered for the constitutive model have been adopted from Gajo and Wood [13] and Wood [29].

The porous media has been modelled with the aid of an Eulerian mesh i.e. the finite element (FEM) mesh of the soil skeleton is affixed to the fluid mesh. In order to carry out the undrained (globally undrained, locally drained) transient analysis, continuum stress/displacement (*C*) 8-noded plane strain (*PE 8*) quadrilateral, biquadratic displacement, bilinear pore pressure (*P*) elements (*CPE8P*) [1] have been utilized in the present study. The backward Euler approximation approach has been adopted in the current context to integrate the coupled variational forms of the continuity equation ensuring fluid flow within the specimen and equilibrium equations of the porous medium. These coupled equations have been solved at the nodal points by

employing full Newton-Raphson iteration scheme with the implementation of an unsymmetrical solver.

3 Mesh Sensitivity and Perturbation Intensity Dependence of Instability Onset

In a related study, Bhattacharya et al. [5], examined the instability onset during undrained (locally drained, globally undrained) biaxial shearing of Hostun RF sand specimens for a particular perturbation magnitude and confining pressure and reported that instability onset within a numerical framework is a mesh dependent phenomenon. The global force (F) displacement (δ) response (specimens with σ'_c = 400 kPa and e_0 = 0.65) for a small heterogeneity (0.01% of e_0) induced in the middle element of the specimen was found to be uniform for less number of elements (N = 9 or 16). However, finer mesh discretization resulted in drop in the F-δ response for 225 elements with axial strain at instability onset (ε^b_{ao}) reducing down to 3.3%. Interestingly, with further refinement of mesh, ε^b_{ao} reduced down to 1.77% and 1.37% for 400 and 625, elements, respectively, although it still followed the same homogeneous material response (F-δ) curve before instability onset (drop in F-δ response). The present discussion limits itself to investigation of instability onset in granular media only and does not delve into the post-localization material response. In this post-instability region, several governing factors (e.g. length scale, deformation rate and characteristic time scale) play a pivotal role in the mechanical response of granular media [14]. Although, a small perturbation was introduced in the material domain, ε^b_{ao} became almost asymptotic (Fig. 2) to the theoretically predicted (ε_{th}) value reported by Mukherjee et al. [23] at a finer mesh only and this is achieved at the cost of significant amount of computing time since the time increment (Δt) is proportional to the square of the element size $(\Delta l)^2$ during a transient analysis. Despite the fact transient diffusion process involved in the coupled analysis introduces an inherent length scale in the numerical simulations, they are not adequate enough to examine the post-instability material response [2] of the sand specimens.

Perturbation (weak element) intensity (P) significantly influences ε^b_{ao} and in order to explore this effect, material heterogeneity has been induced in the middle element (in terms of e_0) of the sand specimens i.e. by locally weakening the element. All the simulations exploring this effect have been probed with 400 elements (with σ'_c = 400 kPa and e_0 = 0.65) which was sufficient enough for the current analysis under consideration. The computational time for carrying out a transient undrained biaxial shearing of Hostun RF sand with the aid of Intel ® Core-TM i7-processor (4 Cores); 3.6 GHz clock speed was estimated to be around 15 ~ 16 h for 400 elements which heightened to 19 ~ 20 h for 625 elements—thus finer mesh discretization was avoided. Previous studies by Borja and Regueiro [7], Shuttle and Smith [26] report introduction of perturbation in terms of reduction of the value of material model (nonassociative Drucker-Prager type) parameter by 1% or by reducing the undrained

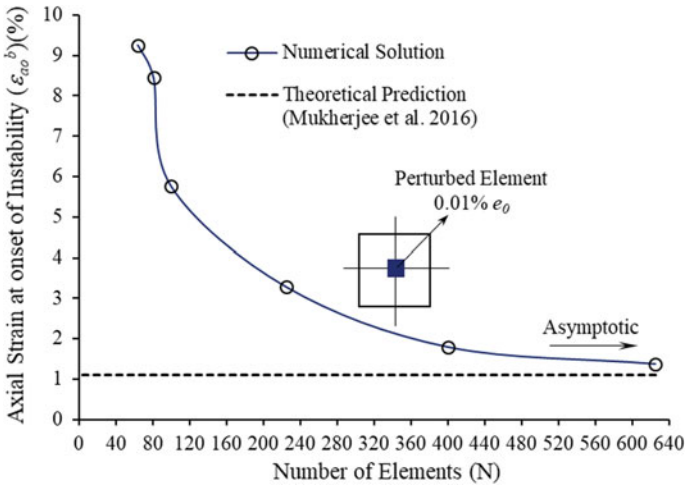

Fig. 2 Axial Strain at onset of instability (ε^b_{ao}) (%) versus number of elements (N) with perturbation intensity 0.01% e_0 (0.65) at middle element

cohesion (c_u) value to 20 kPa in the 'trigger element' as compared to 70 kPa for other elements throughout the specimen—but these were chosen intuitively and lacked a systematic study of perturbation intensity effect on instability onset strain. For $P =$ 0.1% and 2.5% ε^b_{ao} was estimated to be $\approx$ 1.78% and 1.6%, respectively (Fig. 3). Increased value of P to 10% of e_0 resulted in decrease of ε^b_{ao} to nearly ε_{th}. However, with $P = 25\%$ and 50% (very weak zone encountered within the soil mass), ε^b_{ao} was

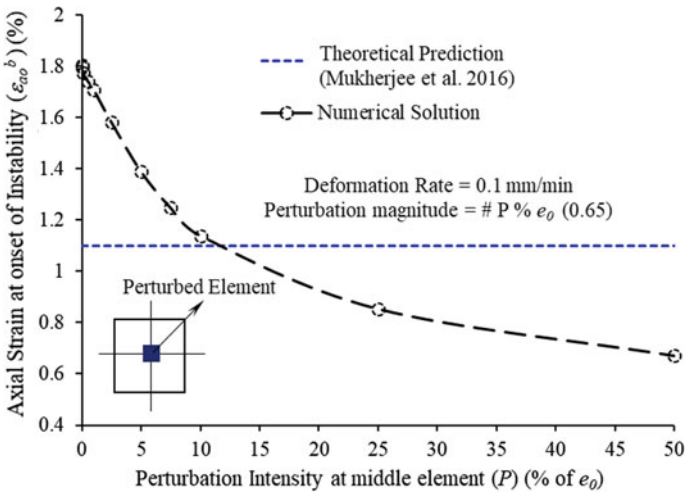

Fig. 3 Axial strain at onset of instability (ε^b_{ao}) (%) versus perturbation intensity (P # %of $e_0 =$ 0.65)

found to be well below ε_{th}. This points out a reasonable estimate of what should be the perturbation intensity so as to explore instability onset within any numerical framework.

Imperfection has been introduced within the material domain in terms of initial void ratio (e_0) in the current context in all the simulations, although it is acknowledged that the perturbation intensity effect may be somewhat different if the material heterogeneity is incorporated in terms of a state variable of the constitutive model and characterization of instability becomes material model-dependent phenomenon in that case.

4 Effect of Initial Void Ratio (e_0) on Instability Onset

The material state of the soil specimen (e.g. void ratio) is one of the key factors that can trigger instability (either localization or 'solid-fluid' type instability) onset in granular materials. The present study aims to examine this effect of the initial void ratio (e_0) on instability onset strain as well. For this purpose, undrained biaxial shearing has been carried out on all the sand specimens (e_0 varying from 0.6 to 0.8) at a confining pressure of 400 kPa with a perturbation intensity $P = 1\%$ of e_0 at the middle element. Figure 4a illustrates the F-δ response of various sand specimens with varying initial void ratios. For a dense specimen, with $e_0 = 0.6$ ($e_0 < e_c$), the drop in F-δ response i.e. instability onset was observed to be at $\varepsilon_{ao}^b \sim 4.75\%$ although the specimen exhibited strain hardening behaviour till this point of loading. On increasinge_0 to 0.65 ($e_0 < e_c$) (medium dense specimen), the sand sample still displayed a strain hardening behaviour although ε_{ao}^b reduced down significantly to ~ 1.71% and localized dilative zones were noticed along with contractive zones adjacent to it at this stage. For $e_0 = 0.7$ and 0.75 ($e_0 < e_c$, in both the cases), ε_{ao}^b was estimated to be ~ 0.9% and 0.74%, respectively. It can be noticed from Fig. 4a that the Hostun RF sand specimen with $e_0 = 0.75$ did not exhibit any strain hardening behaviour and this value of e_0 was very close to the critical void ratio (at $\sigma'_c = 400$ kPa), $e_c = 0.789$. When e_0 was further increased to 0.8 (loose specimen, $e_0 > e_c$), instability onset was estimated to occur at a much lower axial strain level ~ 0.5%. No drop in F-δresponse was observed in this case and the specimen was devoid of any distinct localized zones of extensive shearing. Strain softening behaviour could be noticed from F-δ plot for this sand specimen and the theoretical study byMukherjee et al. [23] also suggested that undrained strain softening behaviour is associated with 'liquefaction-type solid-fluid' instability modes in granular media. Thus, in this case, 'solid-fluid' type instability could have been triggered due to high initial void ratio (loose sand specimens) and generation of significant amount of excess pore water pressure during undrained shearing(locally drained, globally undrained). Figure 4b represents the variation in axial strain at instability onset, ε_{ao}^b with e_0. Lower initial void ratio of Hostun RF sand specimens (dense specimens) resulted in delayed (at the same confining pressure) onset of instability indicating a decisive

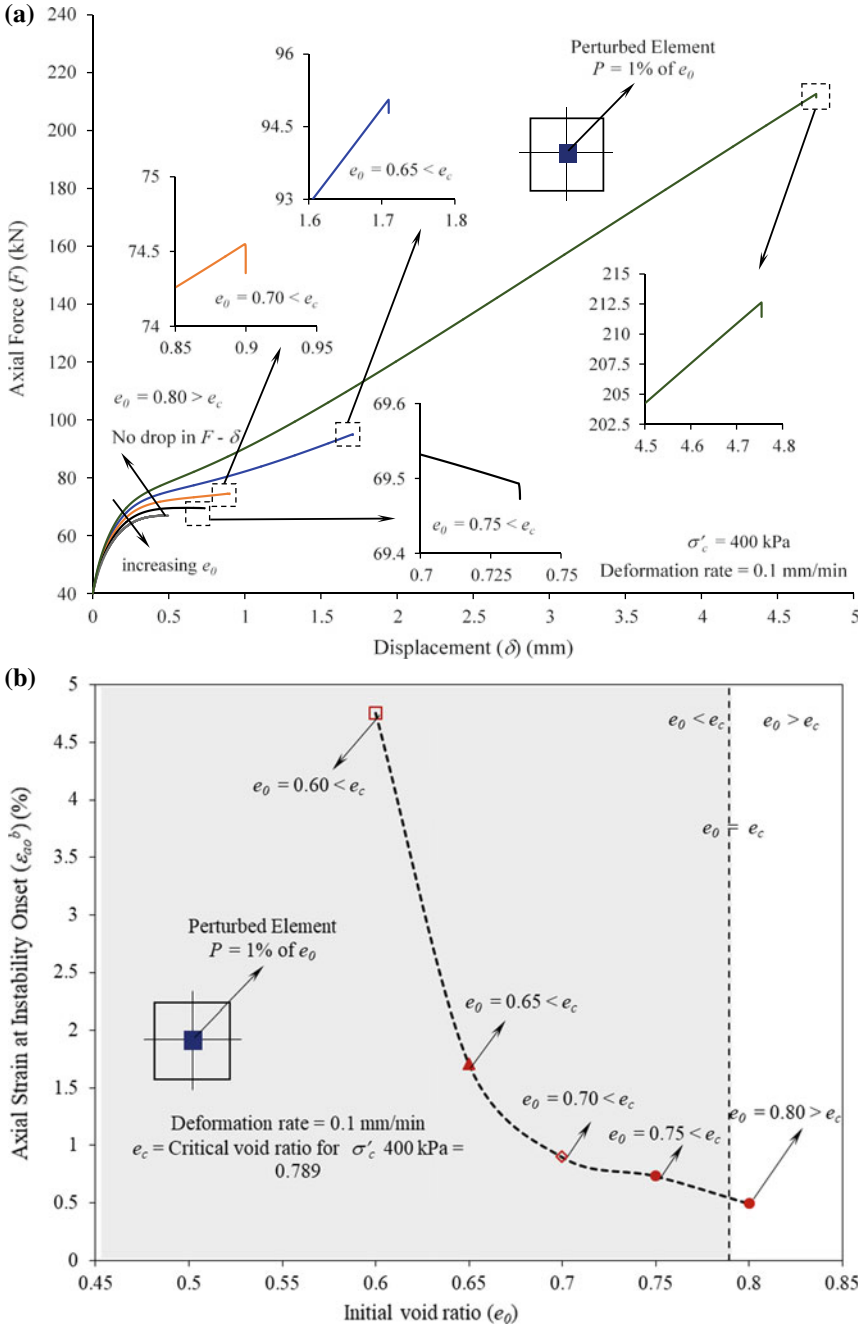

Fig. 4 **a** Force (F)—displacement (δ) plot for Hostun RF sand specimens with varying initial void ratio (e_0) (0.6–0.8). **b** Axial strain at onset of instability (ε_{ao}^{b}) (%) versus e_0

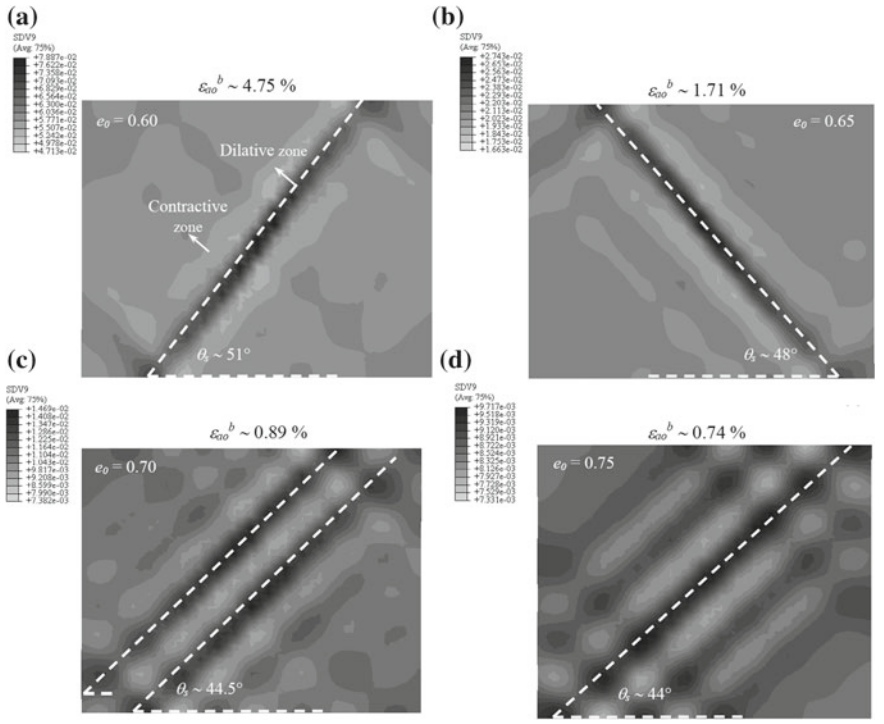

Fig. 5 Shear strain (SDV9) (ε_q) profiles at onset of instability for different Hostun RF sand specimens with varying initial void ratio e_0 (at $\sigma'_c = 400$ kPa) **a** 0.6 **b** 0.65 **c** 0.7 **d** 0.75

phase transformation occurring in the specimens when e_0 is gradually changed from 0.8 (loose) to 0.6 (dense specimen).

Figure 5 depicts the shear strain contours (ε_q) of Hostun RF sand specimens with varying e_0 at the onset of instability (ε^b_{ao}). For a dense specimen ($e_0 = 0.6$), a distinct zone of localized strain accumulation could be identified (Fig. 5a) with the shear band inclination angle (θ_s) being ~ 51°. A straight line was fit across all the points with excessive shear strain along the height of the specimen for estimating θ_s. On the other hand, in case of a medium dense sand specimen ($e_0 = 0.65$), the orientation of the shear band angle got reversed which is evident from Fig. 5b and θ_s was estimated ~ 48°. With further increase in e_0 to 0.7 and 0.75 (relatively looser specimen), θ_s was evaluated to be ~ 44.5° and 44° (Fig. 5c and d), respectively, and a single distinct zone of shearing could not be identified. In all of these cases contractive zones were found to exist adjacent to the localized dilative zone(s) indicating local fluid motion within the sand specimens although global undrained conditions were imposed on the boundaries. Interestingly, it is to be noted that with an increase in the initial void ratio (as it moves towards becoming a looser specimen), the estimated shear band angle in an undrained biaxial shearing became flatter i.e. the instability mode slowly moved towards a 'solid-fluid' type from a localized one.

5 Patch Area (A) Effect on Instability Onset for a Particular Perturbation Intensity

The effect of areal extent of material heterogeneity for a fixed perturbation magnitude on instability onset has also been examined in the present article. Coupled undrained numerical simulations for this particular case have been performed on sand specimens with 400 elements (nearly converged mesh) and $e_0 = 0.65$ at a confining pressure of 400 kPa and with an induced perturbation intensity of 1% of e_0. Spatial extent of a single element of the sand specimen under consideration has been denoted as the patch area A.

Effect of patch area (A) on instability onset has been explored by varying the number of elements in which the perturbation was introduced and this has been illustrated in Fig. 6. Undrained biaxial shearing of Hostun RF sand revealed that instability onset strain (ε_{ao}^{b}) lowered down from ~ 1.7% for 1A to ~ 1.5% for 9A. However, a further increase in patch area to 16A and 25A did not show any variation in ε_{ao}^{b}. Thus, increase in spatial extent of patch area lowered down ε_{ao}^{b} to some extent, however it ceased to exhibit any influence when the material heterogeneity (fixed perturbation intensity) was induced over a larger area.

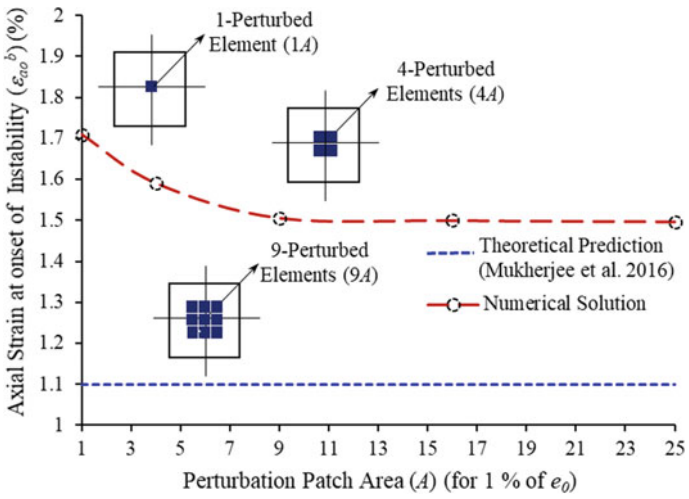

Fig. 6 Axial strain at instability onset (ε_{ao}^{b}) versus Patch Area (A) ($P = 1\%$ of e_0; 0.65)

6 Conclusions

Numerical investigation of instability onset in granular media has been explored in the current study by inducing material heterogeneity in Hostun RF sand specimens under biaxial loading. The F-δ response was uniform for a lesser number of elements (N = 9 or 16) even when a small perturbation (0.01% of e_0; 0.65) was introduced in the middle element. However, with mesh refinement the material behaviour deviated from its uniform F-δ response and ε_{ao}^{b} was estimated ~ 1.8% for 400 elements. Thus, instability onset in granular media (drop in F-δ) was found to be a mesh-dependent phenomenon within a numerical framework. Perturbation intensity (Pin terms of % of e_0) also had significant impact in lowering down ε_{ao}^{b} to nearly theoretically predicted value for $P = 10\%$ of e_0. Undrained biaxial shearing of Hostun RF sand specimens revealed that decrease in e_0 resulted in delayed instability onset. The emergence of localized mode of instability could be well apprehended for denser specimens ($e_0 < e_c$) whereas, initiation of strain-softening behaviour was captured for the loose specimen ($e_0 > e_c$) in which 'liquefaction-type solid-fluid' instability mode becomes the triggering mechanism. These localized dilative zones were accompanied with contractive zones adjacent to them indicating local fluid movement within the sand specimen although global undrained condition was imposed on the boundaries. Increase in spatial extent of material heterogeneity (for a fixed perturbation magnitude) leads to an early onset of instability in Hostun RF sand specimens to a certain degree and it did not exhibit any considerable effect on further increasing the areal expanse of material imperfection.

References

1. ABAQUS Inc. (2014) ABAQUS Analysis User's Manual, Version 6.14. Providence, RI, Simulia
2. Andrade JE, Borja RI (2007) Modeling deformation banding in dense and loose fluid-saturated sands. Finite Elem Anal Des 43(5):361–383
3. Aydin A (2000) Fractures, faults, and hydrocarbon entrapment, migration and flow. Mar Pet Geol 17(7):797–814
4. Bažant ZP, Jirásek M (2002) Nonlocal integral formulations of plasticity and damage: survey of progress. J Eng Mech 128(11):1119–1149
5. Bhattacharya D, Mukherjee M, Prashant A (2019) Perturbation intensity and mesh convergence in coupled undrained instability analysis in sands under biaxial loading. Int J Geomech (In Review)
6. Bésuelle P (2001) Compacting and dilating shear bands in porous rock: theoretical and experimental conditions. J Geophys Res: Solid Earth 106(B7):13435–13442
7. Borja RI, Regueiro RA (2001) Strain localization in frictional materials exhibiting displacement jumps. Comput Methods Appl Mech Eng 190(20–21):2555–2580
8. Daouadji A, Darve F, Al Gali H, Hicher PY, Laouafa F, Lignon S, Nicot F, Nova R, Pinheiro M, Prunier F, Sibille L (2011) Diffuse failure in geomaterials: Experiments, theory and modelling. Int J Numer Anal Meth Geomech 35(16):1731–1773
9. Desrues J, Georgopoulos IO (2006) An investigation of diffuse failure modes in undrained triaxial tests on loose sand. Soils Found 46(5):585–594

10. Finno RJ, Harris WW, Mooney MA, Viggiani G (1996) Strain localization and undrained steady state of sand. J Geotech Eng 122(6):462–473
11. Finno RJ, Harris WW, Mooney MA, Viggiani G (1997) Shear bands in plane strain compression of loose sand. Ge′otechnique 47(1):149–165
12. Fleck NA, Hutchinson JW (2001) A reformulation of strain gradient plasticity. J Mech Phys Solids 49(10):2245–2271
13. Gajo A, Muir Wood D (1999) A kinematic hardening constitutive model for sands: the multiaxial formulation. Int J Numer Anal Meth Geomech 23(9):925–965
14. Garagash DI (2005) Diffuse versus localized instability in compacting geomaterials under undrained conditions. In: Geomechanics: testing, modeling, and simulation, pp 444–462
15. Guo P (2013) Undrained shear band in water saturated granular media: a critical revisiting with numerical examples. Int J Numer Anal Meth Geomech 37(4):353–373
16. Guo P, Stolle DFE (2013) Coupled analysis of bifurcation and shear band in saturated soils. Soils Found 53(4):525–539
17. Han C, Drescher A (1993) Shear bands in biaxial tests on dry coarse sand. Soils Found 33(1):118–132
18. Han C, Vardoulakis IG (1991) Plane-strain compression experiments on water-saturated fine-grained sand. Ge′otechnique 41(1):49–78
19. Khoa HDV, Georgopoulos IO, Darve F, Laouafa F (2006) Diffuse failure in geomaterials: experiments and modelling. Comput Geotech 33(1):1–14
20. Lade PV, Pradel D (1990) Instability and plastic flow of soils. I: experimental observations. J Eng Mech 116(11):2532–2550
21. Mokni M, Desrues J (1999) Strain localization measurements in undrained plane-strain biaxial tests on Hostun RF sand. Mech Cohesive-Frict Mater 4(4):419–441
22. Mooney MA, Viggiani G, Finno RJ (1997) Undrained shear band deformation in granular media. J Eng Mech 123(6):577–585
23. Mukherjee M, Gupta A, Prashant A (2016) Instability analysis of sand under undrained biaxial loading with rigid and flexible boundary. Int J Geomech 17(1):04016042
24. Nicot F, Darve F (2011) Diffuse and localized failure modes: two competing mechanisms. Int J Numer Anal Meth Geomech 35(5):586–601
25. Schofield A, Wroth P (1968) Critical state soil mechanics. McGraw-Hill, London
26. Shuttle DA, Smith IM (1988) Numerical simulation of shear band formation in soils. Int J Numer Anal Methods Geomech 12(6):611–626
27. Vardoulakis I (1981) Bifurcation analysis of the plane rectilinear deformation on dry sand samples. Int J Solids Struct 17(11):1085–1101
28. Vardoulakis I (1985) Stability and bifurcation of undrained, plane rectilinear deformations on water-saturated granular soils. Int J Numer Anal Meth Geomech 9(5):399–414
29. Wood DM (2004) Geotechnical Modelling. CRC Press

A Comparative Study on Various Codes and Current Practices for Design of Caissons

Mohit Kumar and Kaustav Chatterjee

Abstract Caissons are among the less frequently used but among the most important type of foundations as they support lifeline structures like bridges. In the present study, different codes of practice adopted in different countries and the progress made by various researchers has been reviewed. One of the important parts of design of caissons is the determination of scour depth, which is given by different methods for different types of strata. In alluvium, Lacey's theory is a well-accepted theory which is adopted globally. However, for other types of soil, different codes recommend different methods of analysis, which has been reviewed in the current study. The computation of lateral stability of caissons was previously based on Terzaghi's (1943) analysis for a free, rigid bulkhead. Pender (1947) (see [8]) analyzed the situation by considering soil around the pier to behave as linear springs with their stiffness increasing with depth. Banerjee and Gangopadhyay (1960) derived equations for lateral stability of well foundations using Pender's plastic flow concepts along with Terzaghi's rigid bulkhead stress distribution and subgrade modulus concepts. In this study, caisson has been designed for a given set of site conditions using recommendations of different codes and comparisons have been drawn between recommendations of different codes. Upon review of all the codal practices and methodologies available for design of caissons, it was concluded that there is significant scope for improvement and amendment in the codes to keep up with the advancement in technology with time.

Keywords Caissons · Lifeline structure · Scour depth · Plastic flow

M. Kumar (✉) · K. Chatterjee
Indian Institute of Technology Roorkee, Roorkee, India
e-mail: mhtkmr123@gmail.com

A. Prashant et al. (eds.), *Advances in Computer Methods and Geomechanics*, Lecture Notes in Civil Engineering 55,
https://doi.org/10.1007/978-981-15-0886-8_29

1 Introduction

Caissons are massive monolithic foundations which are capable of resisting high magnitudes of weight, uplift, and even lateral loads. Their large stiffness enables them to safely withstand lateral loads while the mass helps in resisting uplift forces. For this reason, they are natural choice as foundations under bridge piers.

1.1 General

Different forces that can be considered while deciding the load combinations on a caisson under a bridge are dead loads of superstructure and self weight, live loads, wind forces, forces due to water current, forces due to tractive effort of vehicles or by braking of vehicles, centrifugal forces in case the caisson is located on a curve, buoyancy, earth pressure, temperature and seismic forces. (see [8]). All these loads could be expressed in terms of a net vertical load, a lateral load, and a moment acting at the top of the caisson. Various stresses developed in the caissons under the actions of these loads have been shown in Fig. 1.

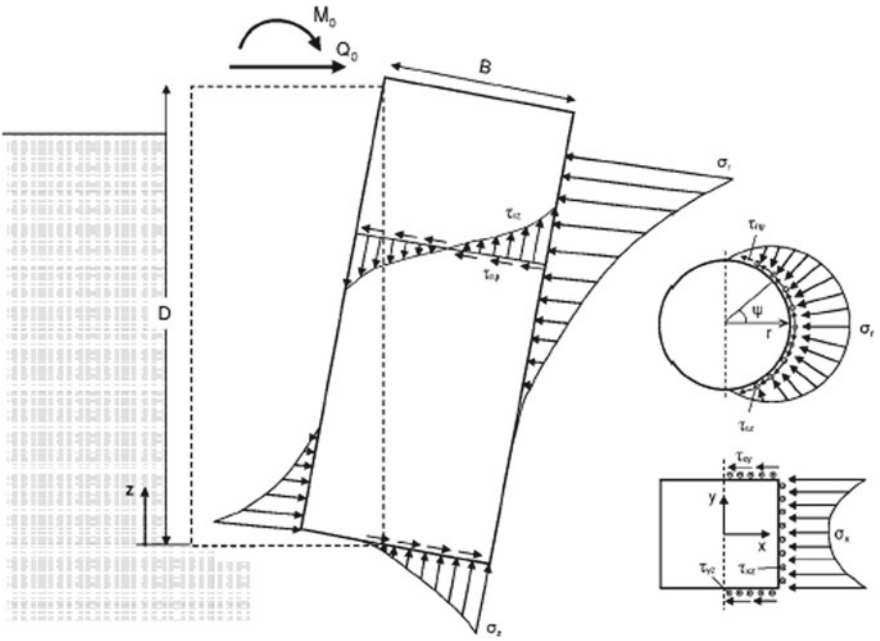

Fig. 1 Stresses at caisson-soil interface for circular and square plan shape [4]

σ_r is the lateral soil pressure and σ_z is the base pressure acting on the caisson. τ_{rz} and $\tau_{r\psi}$ are the bending shear stress inside the caisson and surface traction along the periphery of the caisson, respectively.

1.2 Review of Literature

Terzaghi was the pioneer in the research of lateral stability of caissons. The method proposed by Terzaghi (1943) for the analysis of a free, rigid bulkhead was used earlier. Thereafter, in 1947, Pender proposed a method of analysis in which the soil surrounding the pier was assumed to behave like linear springs. The stiffness of these springs was assumed to increase with depth. A decade later in 1960, Banerjee and Gangopadhyay made use of the above two analyses to derive equations for lateral stability of wells. The authors coupled Terzaghi's rigid bulkhead stress distribution and subgrade modulus concepts with Pender's plastic flow concepts. Thereafter a number of researchers performed a series of model tests based on which Indian Road Congress (IRC) in 1972, gave recommendations for formulas to estimate soil resistance below maximum scour level for caissons in cohesionless soil. In USA, National Highway Institute (NHI) in collaboration with Federal Highway Administration (FHWA)gave life to Construction Method and LRFD (Load and Resistance Factor Design) Design of Drilled Shafts in 2007. Joint Research Centre (JRC) published a scientific and technical report in 2007 which incorporated different Eurocodes including Eurocode 7 (Geotechnical design) required for design and construction of bridges.

2 Theories

For design of caissons, depth and embedment depth, diameter and thickness of caisson are required. While all other parameters are guided by external loading alone, depth of caisson is also guided by the magnitude of maximum scour depth. In this study, we assume the caissons to be circular in plan.

2.1 Maximum Scour Depth

2.1.1 Indian Standards

In most general terms, scour is the eroding away of bed material of streams due to flowing water. IS:3955 [7] recommends use of Lacey's formula given by Eq. (1) for calculation of scour depth below HFL for natural streams in alluvial beds.

$$d = 0.473\left(\frac{Q}{f}\right)^{\frac{1}{3}} \tag{1}$$

where,

d = Normal depth of scour in m
Q = Design discharge in cumecs
f = Lacey's silt factor = $1.76\sqrt{m}$
m = Mean size of particle in mm.

IS:3955 [7] further recommends due allowances to be made in scour depth if waterway is contracted from regime. IRC specifications (1966) and IS:3955 [7] then suggested increase in maximum depth of scour by a factor between 1.27 and 2.75 depending upon the section.

2.1.2 American Standards

Hydraulic Engineering Circular No. 18 (HEC-18) is adopted by FHWA for evaluating scour at bridges. HEC-18 breaks down total scour into three parts, namely, long-term degradation of riverbeds, contraction scour at bridge and local scour at piers and abutments. Contraction scour is said to occur when flow area of a stream is reduced during floods because of increased velocity and bed shear stress. Local scour at piers occurs due to formation of vortices near base of piers or any other obstruction. The expressions for contraction and local scour are given in Eq. 2 and Eq. 3, respectively, whereas long-term degradation is obtained from past records and computer programs.

$$\frac{y_2}{y_1} = \left(\frac{Q_2}{Q_1}\right)^{\frac{6}{7}}\left(\frac{W_1}{W_2}\right)^{k_1} \tag{2}$$

where

y_1, y_2 = Average depth in the u/s main channel and contracted section, respectively, (m)
Q_1, Q_2 = Flow in the upstream channel and contracted channel, respectively, (m^3/s)
W_1, W_2 = Bottom width of the upstream main channel and contracted section less pier width, respectively, (m)
k_1 = Exponent determined on the basis of shear velocity and fall velocity.

Average contraction scour depth $y_{s1} = y_2 - y_0$, where y_0 is the existing depth in contracted section before scour, (m). HEC-18 pier scour equation gives local pier scour y_{s2} as

$$\frac{y_{s2}}{y_1} = 2K_1K_2K_3\left(\frac{a}{y_1}\right)^{0.65}F_{r_1}^{0.43} \tag{3}$$

where

y_{s2} = Pier scour depth, (m)
y_1 = Flow depth directly upstream of the pier, (m)
K_1 = Correction factor for pier nose shape from Fig. 7.3 and Table 7.1 in HEC-18
K_2 = Correction factor for angle of attack of flow from Table 7.2 or Eq. 7.4 in HEC-18
K_3 = Correction factor for bed condition from Table 7.3 in HEC-18
a = Pier width, (m)
F_{r1} = Froude Number directly upstream of the pier.

2.1.3 British Standards

Eurocode EN 1991-1-6 [3] divides total scour depth as combination of general scour depth and local scour depth as shown in Fig. 2. General scour is defined as the scour river flow independent of any obstacle. It is the overall depression in riverbed through the stretch of river at any section due to river flow velocity. It depends only on the flood magnitudes. Local scour depth is the scour due to water vortices next to an obstruction. The Eurocode, however, does not provide any expression for the determination of these scour depths. However, the definition of different scour depths in both American Standards and British Standards is same. In Fig. 2, regions 3, 4, and 5 represent general, local and total scour depth, respectively.

2.2 Load Combinations

In different regions, different loads take different precedence.

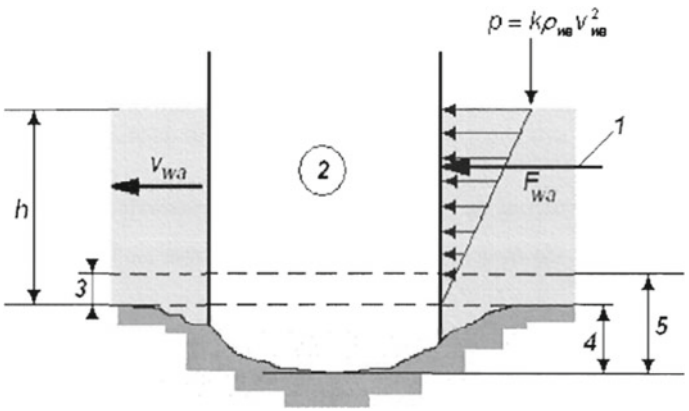

Fig. 2 Pressure, forces, and scour due to water currents [EN 1991-1-6 [3]]

2.2.1 Indian Standards

IRC:45 [6] recommends the use of the most severe of the following load combinations:

$$1.1D$$
$$1.1D + B + 1.4(W_c + E_p + W \text{ or } S)$$
$$1.1D + 1.6L$$
$$1.1D + B + 1.4(L + W_c + E_p)$$
$$1.1D + B + 1.25(L + W_c + E_p + W \text{ or } S)$$

where

D = Dead load
L = Live load including braking effect
B = Buoyancy effect
W_c = Water current force
E_p= Earth pressure force
W = Wind force and
S = Seismic force.

2.2.2 American Standards

See Table 1.

2.3 Stresses and Moments

2.3.1 Indian Standards

IRC:45 [6] recommends that the design should first be checked for

- The point of rotation of caisson lies at the base. This could be achieved by making sure that frictional force at the base does not allow movement of well.
- The soil on the sides remains elastic. This can be ensured by keeping slope of the pressure parabola at the top below the passive pressure line.
- Maximum compressive pressure at the base is less than allowable bearing pressure and minimum pressure is not tensile.

The bending moment is computed at a height of 0.2 times the depth of caisson above the base of caisson. This moment is then compared with the moment of resistance factored by 0.7. Total moment of resistance consists of resisting moment at the base, resisting moment due to passive soil resistance at sides and resisting moment due to frictional resistance at sides.

Table 1 Different load combinations recommended by NHI [1]

Load combination limit state	PL	LL	WA	WS	WL	FR	TCS	TG	SE	Use one of these at a time			
										EQ	IC	CT	CV
Strength I	γ_p	1.75	1.0	–	–	1.0	0.5/1.2	γ_{TG}	γ_{SE}	–	–	–	–
Strength II	γ_p	1.35	1.0	–	–	1.0	0.5/1.2	γ_{TG}	γ_{SE}	–	–	–	–
Strength III	γ_p	–	1.0	1.4	–	1.0	0.5/1.2	γ_{TG}	γ_{SE}	–	–	–	–
Strength IV	γ_p	–	1.0	–	–	1.0	0.5/1.2	–	–	–	–	–	–
Strength V	γ_p	1.35	1.0	0.4	1.0	1.0	0.5/1.2	γ_{TG}	γ_{SE}	–	–	–	–
Extreme event I	γ_p	γ_{EQ}	1.0	–	–	1.0	–	–	–	1.0	–	–	–
Extreme event II	γ_p	0.5	1.0	–	–	1.0	–	–	–	–	1.0	1.0	1.0
Service I	1.0	1.0	1.0	0.3	1.0	1.0	1.0/1.2	γ_{TG}	γ_{SE}	–	–	–	–
Service II	1.0	1.3	1.0	–	–	1.0	1.0/1.2	–	–	–	–	–	–
Service III	1.0	0.8	1.0	–	–	1.0	1.0/1.2	γ_{TG}	γ_{SE}	–	–	–	–
Service IV	1.0	–	1.0	0.7	–	1.0	1.0/1.2	–	1.0	–	–	–	–
Fatigue	–	0.75	–	–	–	–	–	–	–	–	–	–	–

PL: Permanent Load, WL: Wind on Live Load, EQ: Earthquake
LL: Live Load, FR: Friction IC: Ice Load
WA: Water Load and Stream Pressure, TG: Temperature Gradient, CT: Vehicular Collision Force
WS: Wind Load on Structure, SE: Settlement, CV: Vessel Collision Force
TCS: Uniorm Temperature, Creep and Shrinkage
γ_P: Load factor for permanent loads
γ_{TG}: Load factor for temperature gradient
γ_{SE}: Load factor for settlement

2.3.2 American Standards

The LRFD design requirement recommended by NHI was suggested by AASHTO can be expressed in most general terms as "for all limit states, the summation of factored load effects should not affect the factored resistance." NHI, similar to Indian Standards, recommends different load factors for different loads. However, it also recommends different resistance factors as shown in Table 2 for resistance developed in different parts as opposed to single value (0.7) recommended by IRC:45 [6]. The calculation of moments and stresses is done using nonlinear analysis with computer programs. Broms' model is used to model the lateral load response in cohesionless soil as is used in Indian Standards. So, the magnitude of stresses and maximum moments should be similar in both cases.

2.3.3 British Standards

Eurocode EN: 1990 [2] terms different loads as "actions" and classifies it into three categories namely:

Table 2 Resistance factor φ for different resistance components recommended by NHI for FHWA

Limit state	Component of resistance	Geomaterial	Resistance factor, φ
Strength I through Strength V Geotechnical axial resistance	Side resistance in compression/uplift	Cohesionless soil	0.55
	Base resistance	Cohesionless soil	0.5
Service I	All cases	All geomaterials	1.0
Extreme event I and Extreme event II	Axial geotechnical uplift resistance	All geomaterials	0.8
	Geotechnical lateral resistance	All geomaterials	0.8

- Permanent actions (G) which are likely to act throughout a given reference period for which change in magnitude is negligible.
- Variable actions (Q) for which variation in magnitude with time are neither negligible nor monotonic.
- Accidental actions (A) which are usually of short duration but significant magnitude.

Critical load combinations are then selected using different factors ψ and sub-factors γ in combination with characteristic and representative values of different actions.

3 Design Data and Calculations

See Table 3.

The bridge abutments consist of vertical walls with wing walls, width = 37.2 m; with three sets of piers consisting of three columns 0.38 m in diameter.

Table 3 Design data for scour calculation

Property	Magnitude	Property	Magnitude
U/S channel width (m)	98.2	U/S channel depth (m)	2.62
Discharge (m^3/s)	773	Bed material size, D_{50} (mm)	0.31
Fall velocity (m/s)	0.10	Original depth at bridge (m)	2.16
Width of pier, a (m)	1.22	Length of pier, L (m)	18

3.1 Scour Calculation

3.1.1 Indian Standards

Using Eq. (1), for m = 0.31 mm and Q = 773 cumecs
Normal scour depth using Lacey's formula, d = 4.37 m
Maximum scour depth = 1.27d = 5.55 m
Minimum depth of caisson below HFL = 1.33 × 5.55 m = 7.4 m.

3.1.2 American Standards

$k_1 = 0.69$ based on the magnitudes of shear velocity and fall velocity calculated from the data
Using Eq. (2), $y_2 = 5.24$ m, $y_0 = 2.16$ m
Contraction scour, $y_{s1} = y_2 - y_0 = 3.08$ m
Velocity in u/s reach, $v_1 = Q/W_1 y_1 = 3$ m/s; $F_{r1} = v_1/(gy_1)^{1/2} = 0.592$
From Table 7.1, 7.2 and 7.3 of HEC-18, [5] $K_1 = K_2 = 1.0$ and $K_3 = 1.1$
Using Eq. (3), pier scour depth, $y_{s2} = 2.8$ m
Also, y_{s2} should not exceed 2.4a for $F_{r1} < 0.8$ which is found to be OK.
Total scour depth, $y_s = y_{s1} + y_{s2} = 3.08\,\text{m} + 2.8\,\text{m} = 5.88$ m.

3.1.3 British Standards

The Eurocode does not mention any specific formula for scour calculation but defines the total scour in exactly the same manner as the American Standards. So, the value for total scour depth calculated using HEC-18 recommendations has been taken for British Standards also,i.e., Total scour depth = 5.88 m (Table 4).

Table 4 Design data for stress and moment calculation

Property	Magnitude	Property	Magnitude
Net downward load on caisson	1400 t	Horizontal force at scour level	200 t
Moment at scour level	4150 t − m	Saturated unit weight of sand	2 t/m^3
Angle of shearing resistance of subsoil	35°	Angle of wall friction	20°
Allowable bearing pressure	55 t/m^2		

3.2 Stress and Moment Calculation

Assuming the external diameter of caisson as 8.5 m and internal diameter as 5.5 m and depth of caisson below scour level as 15 m.

3.2.1 Indian Standard

Maximum base pressure = 28.39 t/m^2 < Allowable bearing pressure (55 t/m^2)
Minimum base pressure = 15.27 t/m^2 > 0 t/m^2,
Resisting moment at base, $M_b = 4416.2\,t - m$
Moment of resistance due to passive soil resistance, $M_s = 20035.35\,t - m$
Moment of resistance due to frictional resistance, $M_f = 4745.99\,t - m$
Factored moment of resistance, $M_r = 0.7(M_b + M_s + M_f) = 20438.3\,t - m >$ Moment at scour level (4150 t − m)
Maximum bending moment = M + 2Qx/3 = 4849.46 t − m.

3.2.2 American Standards

As mentioned in Sect. 2.3.2, the magnitudes of stresses and moments should be similar to that obtained by Indian Standards as both the codes have adopted same model for lateral response of caisson.

From Table 2, the resistance factors for base and side resistance are 0.5 and 0.55, respectively.

$M_r = 0.5M_b + 0.55(M_s + M_f) = 15837.84\,t - m >$ Moment at scour level$(4150\,t - m)$

3.2.3 British Standards

There is no mention of use of caissons as foundation system for bridge piers or abutments in Eurocode. Instead, Eurocodes recommend the use of spread footing as bridge foundation.

4 Results and Discussions

Review of the three codes of practices yielded some interesting results. IS:3955 [7] suggested single value of scour depth using Lacey's formula whereas HEC-18 and EN:1991-1-6 [3] both suggest two different components of scour depths. Naturally,

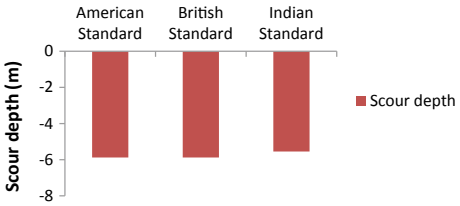

Fig. 3 Scour depth as obtained from American standards, British standards, and Indian standards

the value of maximum scour depth from Indian Standards considerations comes out to be lower than the other two codes as shown in Fig. 3.

Furthermore, it was seen that the load combinations varied a lot for codes of practice in different countries. Due to variation in resistance factor in American Standards for different reactions, the moment of resistance also varied drastically as compared to Indian standards. This variation was as large as 29%.

5 Conclusions

Based on the current study, following conclusions can be drawn:

1. American Standard code is more conservative than Indian Standard code as it yields higher value of scour depth and lower magnitude of moment of resistance.
2. Moment of resistance calculated from Indian Standards was found to be 29% higher than that from American Standards while the depth of scour calculated from American Standards was found to be 5.95% higher than that from Indian Standards.
3. Eurocode does not mention use of caissons as foundation system under bridge piers. Instead use of spread footings has been recommended.
4. American Standard recommends use of nonlinear analysis for stress and moment calculation as opposed to the linear elastic analysis recommended in Indian Standard. Consideration of linear elastic behavior is not realistic for high strain levels. The use of nonlinear analysis by American Standards requires high computational effort which could not be solved manually.

References

1. Brown DA, Turner JP, Castelli RJ (2010) Drilled shafts: construction procedures and LRFD design methods, NHI course no. 132014, Geotechnical engineering circular no. 10, New York
2. EN:1990 (2002) Eurocode—basis of structural design, European Committee for Standardization, Brussels
3. EN:1991-1-6 (2005) Eurocode 1—actions on structures Part 1–6: general actions—actions during execution, European Committee for Standardization, Brussels

4. Gerolymos N, Gazetas G (2006) Winkler model for lateral response of rigid caisson foundations in linear soil. Soil Dyn Earthq Eng 26(5):347–361
5. HEC-18 (2012) Evaluating scour at bridges, Federal Highway Administration, Virginia
6. IRC:45 (1972) Recommendations for estimating the resistance of soil below the maximum scour level in the design of well foundation of bridges, Indian Road Congress, New Delhi
7. IS:3955 (1967) Indian standard code of practice of design and construction of well foundation, Bureau of Indian Standard, New Delhi
8. Ranjan G, Rao ASR (2014) Basic and applied soil mechanics, 2nd edn. New Age International Publishers, New Delhi

New Prediction Models for Compressive Strength of GGBS-Based Geopolymer Clays Using Swarm Assisted Optimization

T. Vamsi Nagaraju and Ch. Durga Prasad

Abstract This paper discusses experimental data on unconfined compressive strength (UCS) of an expansive soil chemically altered with GGBS-based geopolymer with varying amounts of GGBS content. Ground granulated blast furnace slag (GGBS) was added to the expansive soil up to 25% in increments of 5%. Scanning Electron Microscopy (SEM) analysis was undertaken to know the microstructural development in the GGBS-based geopolymer clay blends. The unconfined compressive strength (UCS) of the GGBS-based geopolymer clay blends increased with increasing additive content. This paper also presents the viability of particle swarm optimization (PSO) technique in predicting 28 days UCS of alkali-activated blended expansive clays. With availability of limited experimental data accurate estimation is possible with PSO. In multilinear model UCS equation, the coefficients are adjusted by PSO has been developed for the prediction of UCS for geotechnical designs is the key factor presented in this paper.

Keywords Alkali-activation · Expansive clay · GGBS · PSO · Unconfined compressive strength

1 Introduction

The problems posed by expansive soils, such as volume increase or swelling in monsoons and volume reduction or shrinkage in summers, have been recorded all over the world. Due to alternate swelling and shrinkage, lightly loaded civil engineering structures such as residential buildings, pavements and canal linings founded in them experience severe distress. This results in heavy financial loss all over the world [4].

T. V. Nagaraju (✉)
Department of Civil Engineering, S. R. K. R Engineering College, Bhimavaram, India
e-mail: varshit.varma@gmail.com

Ch. D. Prasad
Department of Electrical Engineering, S. R. K. R. Engineering College, Bhimavaram, India

A. Prashant et al. (eds.), *Advances in Computer Methods and Geomechanics*, Lecture Notes in Civil Engineering 55,
https://doi.org/10.1007/978-981-15-0886-8_30

Many innovative foundation techniques have been suggested for counteracting the detrimental problems posed by expansive soils. Chemical alteration is one of the successful methods among them; in this method, different chemicals such as lime, cement, calcium chloride, and fly ash are added to expansive clays to reduce their swelling properties. Lime is quite effective in reducing plasticity and volume change behaviour of expansive clays. Further, lime treatment of expansive clays also increases their shear strength [3, 8, 9, 11]; Phanikumar and Nagaraju, 2018). Cement as an additive to expansive clay also reduces their plasticity and swelling and increases their shear strength [3, 8, 9]. However, the production process of traditional stabilizers such as ordinary Portland cement (OPC) and lime was energy-intensive and emit a large quantity of CO_2. Geopolymer is cementitious materials with three-dimensional networks of alumina silicate molecules formed by the dissolution of materials containing reactive alumina and silica, with its high strength, low cost, low energy consumption, and CO_2 emission during synthesis, offers a promising alternative to OPC.

In recent years many researchers have been contributed for various approaches to predict the geotechnical parameters using linear regression analysis (LRA), artificial neural networks (ANN) and support vector machine (SVM), since then the number of published studies using various optimization techniques has increased tremendously [10, 13].

The particle swarm optimization (PSO) is one among them, it is a stochastic optimization technique was developed and this was pioneered by Dr. Eberhart and Dr. Kennedy [7] for the optimization of nonlinear functions. PSO has predominantly applied to continuous-discrete heterogeneous strongly nonlinear numerical optimization and it thus used almost everywhere in the world in different disciplines [1, 5]. Geotechnical engineers could make use of ANN, LRA, and SVM in soils, and today, a large number of literature are available on aforementioned optimization techniques. However, literature on PSO are very limited in geotechnical application compared to other fields of civil engineering (Ismail and Jeng 2012). At present scenario PSO technique having wider global applicability because of its comprehensible performance as well as simplicity of its operation.

This paper presents experimental data on unconfined compressive strength of the alkali-activated expansive clays and their microstructural development. This paper also explores the prediction of 28 days unconfined compressive strength of the blends using linear particle optimization. The models consider relative proportions in the alkali-activated blended mix (soil and GGBS), molarity (M), alkali-activated solution, Na/Al and Si/Al as the input variables.

2 Experimental Investigation

2.1 Materials

The materials used in the experimental investigation were (i) an expansive clay, (ii) ground granulated blast furnace slag (GGBS), and (iii) alkali-activated solution, which is a mixture of sodium silicate gel (Na_2SiO_3) and sodium hydroxide pallets (NaOH) of 7 M concentration. The ratio of Na_2SiO_3/NaOH was chosen as 2.5. Based on the LL of 81.5% and PI of 57% of the expansive soil, the soil can be classified as CH according to the USCS classification system. Tables 1 and 2 show the engineering properties of expansive clay, and chemical composition of expansive soil and GGBS, respectively. Figures 1a and b show SEM micrographs of expansive soil and GGBS, respectively.

Table 1 Engineering properties of expansive soil

Property	Free swell index (%)	Optimum moisture content (%)	Maximum dry density (kN/m^3)	Unconfined compressive strength (kPa)	Swell potential (%)	Swelling pressure (kPa)
Value	145	18	16.8	193	7.05	88

Table 2 Chemical composition of expansive soil and GGBS

Chemical composition	SiO_2	Al_2O_3	Fe_2O_3	CaO	MgO	SO_3	Na_2O	LOI
Soil	58	19	7.8	3.28	2.63	–	5.2	0.23
GGBS	40	13.5	1.8	39.2	3.6	0.2	–	0

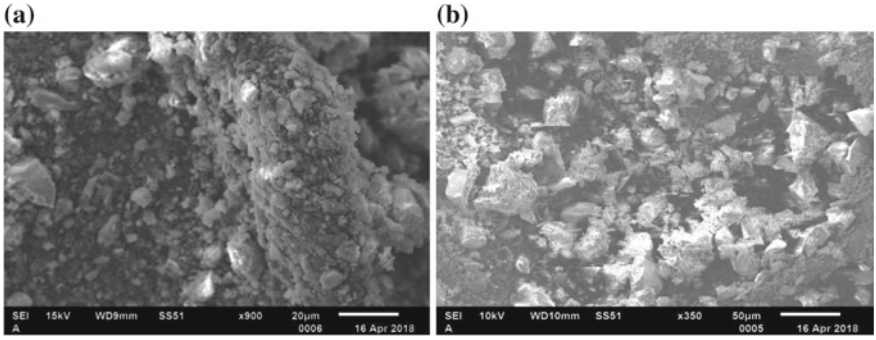

Fig. 1 SEM micrographs of, **a** expansive clay, **b** ground granulated blast furnace slag

2.2 Tests Performed

Alkali-activated GGBS-soil blends were prepared to vary the GGBS content as 0, 5, 10, 15, 20 and 25% by dry weight of the soil for determining unconfined compressive strength. The SEM images were used to assess the morphology of the alkali-activated blends.

3 Results and Discussion

Figure 2 shows the stress–strain behaviour of alkali-activated GGBS-soil blends for the curing periods of 28 days. The stress–strain data show that, for a given % strain, the stress increased with increasing GGBS content. This behaviour was found to be true for all the variation of alkali-activator contents. (vide Fig. 3). As the GGBS content in the blends increases, effective geopolymerization happens in the blends, and the blends become harder. As a result, the vertical compressive stress required to be applied on the cylindrical blend specimens increases for a

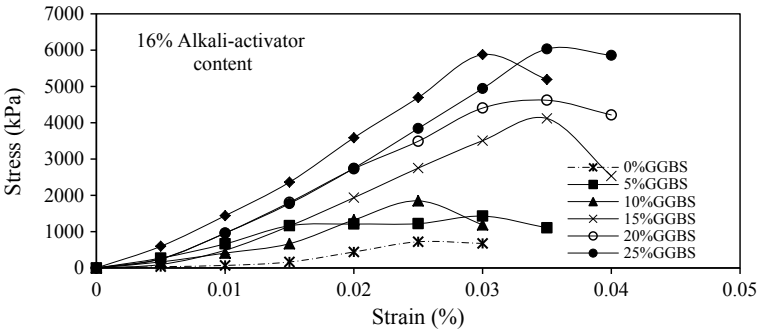

Fig. 2 Stress strain curves

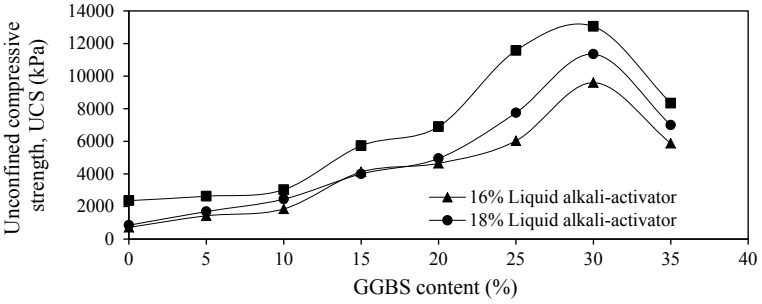

Fig. 3 Variation of unconfined compressive strength (kPa)

given % strain. Hence, the peak stress also increases with GGBS content. With increasing molar concentration of NaOH and liquid alkali-activator content, more significant geopolymerization occurs in the blends as stronger geopolymer products (aluminosilicate gel and calciumsilicate hydrate gel) develop in them. This is true for all GGBS contents.

3.1 SEM Characterization

For observing the chemical reaction and the development of the geopolymer matrix with the varying GGBS content in the soil-GGBS geopolymer blends, SEM analysis was adopted.

Figure 4a, b, c and d illustrates the influence of GGBS content on the microstructural development of the blends. As observed in Fig. 4d, surface of the blends represents the micro flaws or cracks, this may cause poor bonds. However, this situation

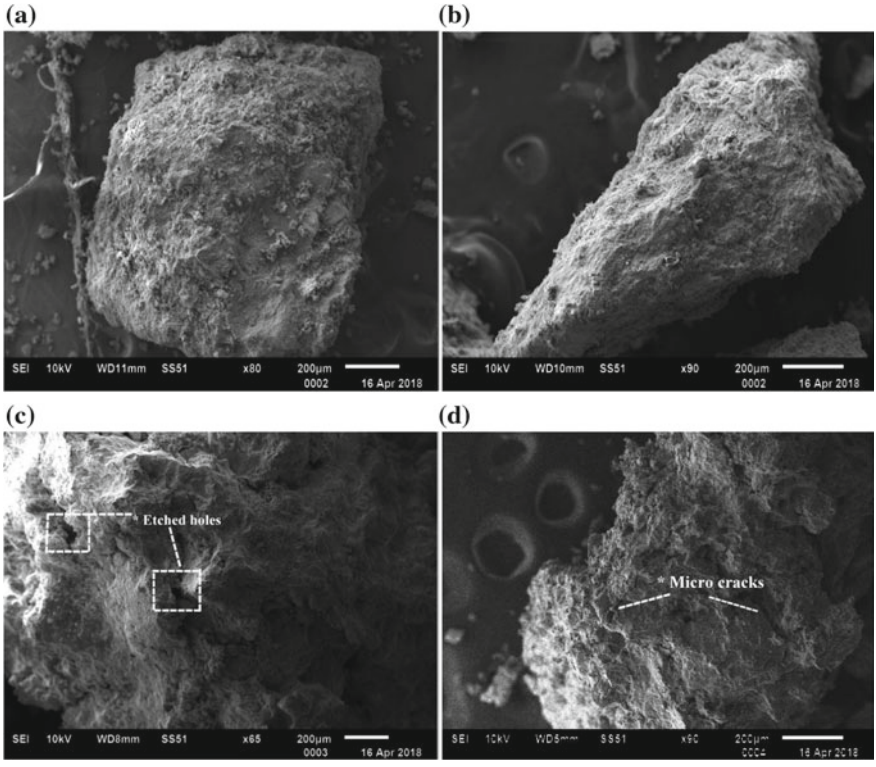

Fig. 4 SEM micrographs of alkali-activated soil blends, **a** 10% GGBS content, **b** 15% GGBS content, **c** 20% GGBS content and **d** 25% GGBS content

is not surprising in view of the heterogeneous nature of geopolymerization products and the method of combining the various phases (presence of glassy phase) of this composite material into a single whole, so, these micro-cracks were not effective on the strength of samples [14].

On the other hand, etched holes are observed at the higher GGBS contents (20 and 25%) (Vide Fig. 4c and d). The etched holes indicate the leaching of silica and alumina oxides from GGBS by alkaline dissolution. The leached silica and alumina ions react with Ca^{+2} and Na^{+2} ions and result in formation of geopolymerization products (sodium aluminosilicate hydrate, Na-C-S-H) coexisting with calciumsilicate hydrate (C-S-H) and/or calcium alumino hydrate (C-A-S-H). The similar formation of C-S-H and/or C-A-S-H with in the geopolymer matrix was previously reported by Itthikorn et al. [6].

3.2 Particle Swarm Optimization Algorithm (PSO)

Estimation of unconfined compressive strength (UCS) is obtained by a well known Metaheuristic optimization algorithm called particle swarm optimization (PSO). This optimization technique may produce high-quality solutions within shorter calculation time and it is not possible in numerical optimization techniques. On the other hand, stable convergence characteristics can be achieved with PSO algorithm than other stochastic methods such as genetic algorithm. In PSO, the process of searching can be introduced by a group of particles (in general birds) that looking for food in a particular region (constraint-based optimization) with random manner. The position of each particle can be treated as a solution to given problem. Initially these positions (solutions) are randomly generated. These current positions (current solution) of a particle may not consist food hence the bird will move to the next position (best solution) by update its velocity. To get closer to the location of the food (considered as best solution), all of the birds follow the nearest bird that is closer to the food place. Each particle/bird is having two vectors x_i, v_i represents the position and velocity of the particle at every iteration. All of the particles regulate their route for the next iteration based on their experience and other particle experiences at the present iteration. Let x_i^k denotes the particle position vector in search of space of solutions and the new position for each particle is taken place randomly as

$$x_i^{k+1} = x_i^k + v_i^{k+1} \tag{1}$$

where v_i^{k+1} is the velocity vector of particle that drives the process towards optimization. The position of every individual bird is p_i^k and the velocity is v_i^k. The best position of each particle is p_{best} and the overall optimized position is g_{best}. Then the velocity of each organism in the swarm is updated as

$$V_i^{k+1} = \omega V_i^k + c_1 r_1 (p_{\text{best}_i} - x_i^k) + c_2 r_2 \left(g_{\text{best}_i} - x_i^k\right) \tag{2}$$

In Eq. (2), c_1 and c_2 are acceleration constants, r_1 and r_2 are random numbers varies between 0 and 1 and ω is the inertia weight factor. PSO technique has two type parameters known as common parameters and control parameters.

3.3 Application of PSO for Unconfined Compressive Strength (UCS) Estimation

In this paper, PSO is used to estimate unconfined compressive strength (UCS) using the test data. The test data contain samples of information of relative proportions in the alkali-activated blended mix (soil and GGBS), molarity (M), alkali-activated solution, Na/Al and Si/Al. While estimation, the above six parameters are considered as input variables on which compression index value depends. The six variables are denoted with X_1, X_2, X_3, X_4, X_5 and X_6 letters. X_1 denotes soil proportion in the blends, X_2 denotes GGBS content in the blend, X_3 denotes molarities of NaOH solution, X_4 denotes the amount of alkali solution, X_5 denotes the Na/Al ratio value and X_6 denotes the Si/Al ratio value. From samples of test data, the UCS value changes proportionally with variables from X_1 to X_6. Hence a linear equation is formulated which involving all available six variables as shown in Eq. (3)

$$C_{c(\text{est})} = W_1.X_1 + W_2.X_2 + W_3.X_3 + W_4.X_4 + W_5.X_5 + W_6.X_6 \tag{3}$$

where W_1, W_2, W_3, W_4, W_5, and W_6 are weighted coefficients need to be estimated property to calculate final output variable UCS. The above Eq. (3) is further modified to include 'n' number of input parameters with same proportionality is given by

$$UCS_{(\text{est})} = \sum_{i=1}^{n} W_i.X_i \tag{4}$$

For estimation of weighted coefficients, ANN and Fuzzy type intelligent models were used. However, these techniques required large data to train and test the results. With minimum data availability, application of aforementioned techniques gives large errors. Hence, PSO is used in this paper for estimation of UCS with the help of minimum data availability and obtained better results. For this purpose, PSO algorithm is started with initial random solution set of (W_1, W_2, W_3, W_4, W_5 and

W_6) and the estimated UCS is calculating using Eq. (4). For the entire data samples, UCS is estimated and an error is evaluated from actual data of UCS. For evaluation of error, the following formula is used.

$$E(k) = \sum_{i=1}^{N} \left(UCS_{(\text{act})}(i,k) - UCS_{(\text{est})}(i,k) \right)^2 \tag{5}$$

In Eq. (5), k represents the iteration number. N is total number of data samples, $UCS_{(act)}$ is actual value of unconfined compressive strength and $UCS_{(est)}$ estimated value of unconfined compressive index. The error calculated from both estimated and actual values of UCS for an iteration 'k' is represented by E. From calculated error values, the objective function (J) is formed as shown in Eq. (6)

$$J = \min(E) \tag{6}$$

The above objective function depends on six variables as aforementioned. Limits of these variables depend on the user requirement and/or data set availability. On the other hand, the weights are obtained by PSO for accurate estimation of compression index that is included as PSO variables, which are included in the problem as PSO constraints. For this problem, initially the limits are fixed in between −1000 and 1000. Later after verification of few trails by random variations of PSO control and common parameters limits are adjusted to get more suitable weights.

3.4 PSO Assessment Results for Estimation

As PSO is operated with constant inertia weight strategy, several investigations are carried out on test data with varying inertia weights to obtain the best linear equation to predict UCS. Estimation and the final unconfined compressive strength estimation equation obtained at inertia weight 0.75, by PSO are given by Eq. (7) and a plot as shown in Fig. 5.

$$UCS_{(\text{est})} = -151.637X_1 + 190.274X_2 + 0.107X_3 + 206.068X_4 + 10000X_5 + 755.56X_6 \tag{7}$$

Figure 5 shows the overall comparison of actual measured UCS and predicted UCS by PSO for given test data (from Appendix 1). From Fig. 5, it is clearly observed that the predicted values are very close to actual UCS for most of the data samples.

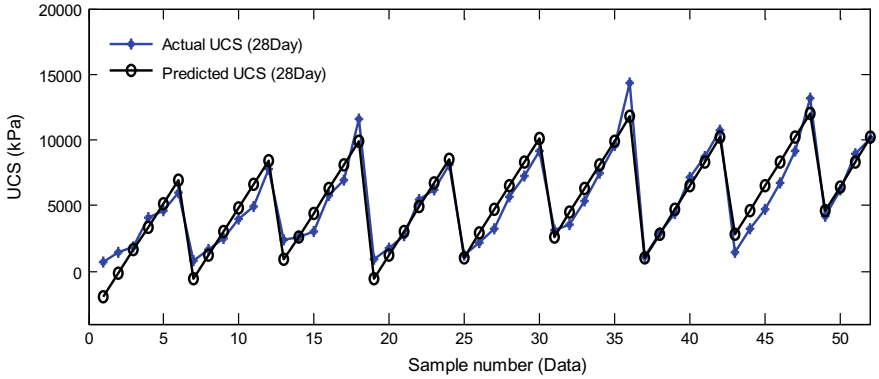

Fig. 5 Verification of simulated results against experimental data

Fig. 6 Correlations of the actual and predicted UCS of geopolymer blends

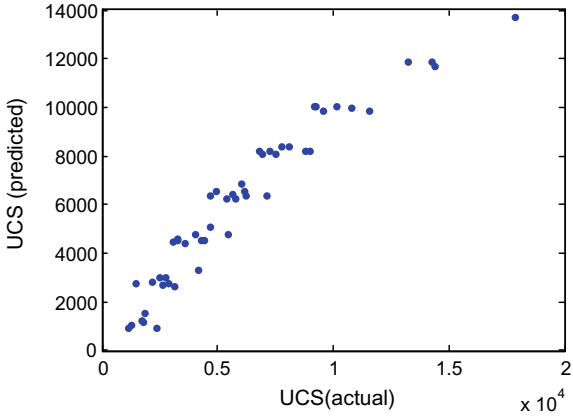

In Fig. 6, the variation of actual and predicted UCS plot is given; it is clearly evident that the importance of the multilinear regression model using PSO for predicting UCS.

4 Conclusions

The following conclusions can be drawn from the foregoing study:

1. Unconfined compressive strength (UCS) of blends increased with increasing additive content.

2. With the aid of the SEM micrographs, the formation of the geopolymer products in the blends was qualitatively confirmed. The enhancement in the mechanical properties of the alkali-activated blends was most likely provided by the growth of geopolymerization products (aluminosilicate gel).
3. The unconfined compressive strength (UCS) is one of the vital properties of expansive clays that are essential for geotechnical designs. Moreover, especially in alkali-activated blends, many factors were influencing the strength characteristics such as molarity of NaOH solution, Na/Al and Si/Al. One aim will be to give the engineer an integrated tool helping him in designing an efficient way by without any time consuming, cumbersome and unwieldiness testing.
4. Regarding UCS prediction, six important parameters (relative proportions of soil and GGBS, molarities of NaOH solution, alkali-activator content, Na/Al and Si/Al) were identified considering that the linear equation resulted from swarm assisted multiple linear regression. PSO is a simple and potential algorithm for adjusting number of particles within a limited data set. The accuracy and performance of the algorithm performed on various inertia weights, and obtained trail results indicated that 0.75 inertia weight gives the best convergent plot. Furthermore, PSO was the best method to cope for prediction models with limited data sets, mostly in geotechnical discipline.
5. Geopolymer stabilization enhances soil engineering properties, and its application in order to reduce the environmental footprint in the sustainable city of the future.

Appendix 1

Details of experimental variables and test results.

Clay	GGBS	M	Alkali solution (%)	Na/Al	Si/Al	28 days UCS (kPa)	Clay	GGBS	M	Alkali solution (%)	Na/Al	Si/Al	28 days UCS (kPa)
100	0	7	32	0.4675	2.5723	720	85	15	10	36	0.7182	2.5638	5642
95	5	7	32	0.4744	2.5695	1430	80	20	10	36	0.7292	2.5609	7246
90	10	7	32	0.4815	2.5667	1850	75	25	10	36	0.7406	2.5578	9210
85	15	7	32	0.4888	2.5638	4120	100	0	10	40	0.7633	2.5723	3120
80	20	7	32	0.4963	2.5609	4650	95	5	10	40	0.7745	2.5695	3564
75	25	7	32	0.5040	2.5578	6030	90	10	10	40	0.7861	2.5667	5347
100	0	7	36	0.5260	2.5723	851	85	15	10	40	0.7980	2.5638	7520
95	5	7	36	0.5337	2.5695	1690	80	20	10	40	0.8102	2.5609	9540
90	10	7	36	0.5417	2.5667	2450	75	25	10	40	0.8229	2.5578	14380
85	15	7	36	0.5499	2.5638	4000	100	0	14	32	0.7672	2.5723	1125
80	20	7	36	0.5583	2.5609	4950	95	5	14	32	0.7785	2.5695	2890
75	25	7	36	0.5670	2.5578	7750	90	10	14	32	0.7901	2.5667	4375
100	0	7	40	0.5844	2.5723	2360	85	15	14	32	0.8021	2.5638	7120
95	5	7	40	0.5930	2.5695	2630	80	20	14	32	0.8144	2.5609	8750
90	10	7	40	0.6018	2.5667	3030	75	25	14	32	0.8271	2.5578	10800
85	15	7	40	0.6110	2.5638	5730	100	0	14	36	0.8631	2.5723	1450
80	20	7	40	0.6203	2.5609	6900	95	5	14	36	0.8758	2.5695	3248
75	25	7	40	0.6300	2.5578	11570	90	10	14	36	0.8889	2.5667	4680
100	0	10	32	0.6107	2.5723	934	85	15	14	36	0.9023	2.5638	6784
95	5	10	32	0.6196	2.5695	1740	80	20	14	36	0.9162	2.5609	9150
90	10	10	32	0.6289	2.5667	2734	75	25	14	36	0.9305	2.5578	13230

(continued)

(continued)

Clay	GGBS	M	Alkali solution (%)	Na/Al	Si/Al	28 days UCS (kPa)	Clay	GGBS	M	Alkali solution (%)	Na/Al	Si/Al	28 days UCS (kPa)
85	15	10	32	0.6384	2.5638	5430	100	0	14	40	0.9591	2.5723	4245
80	20	10	32	0.6482	2.5609	6160	95	5	14	40	0.9731	2.5695	6213
75	25	10	32	0.6583	2.5578	8055	90	10	14	40	0.9876	2.5667	8946
100	0	10	36	0.6870	2.5723	1256	85	15	14	40	1.0026	2.5638	10158
95	5	10	36	0.6971	2.5695	2185	80	20	14	40	1.0180	2.5609	14220
90	10	10	36	0.7075	2.5667	3240	75	25	14	40	1.0339	2.5578	17850

References

1. AlRashidi MR, El-Hawary ME (2006) A survey of particle swarm optimization applications in electric power systems. IEEE Trans Evol Comput. https://doi.org/10.1109/TEVC.2006.880326
2. Botao L, Cerato Amy B (2012) Prediction of expansive soil swelling based on four micro-scale properties. Bull Eng Geol Environ 71:71–78
3. Chen FH (1988) Foundations on expansive soils. Elsevier Scientific Publishing Co., Amsterdam
4. Gourley CS, Newill D, Schreiner HD (1993) Expansive soils: TRL's research strategy. In: Proceedings, 1st international symposium on engineering characteristics of arid soils, London
5. Hajihassani M, Armaghani DJ, Kalatehjari R (2017) Applications of particle swarm optimization in geotechnical engineering: a comprehensive review. Geotech Geol Eng. https://doi.org/10.1007/s10706-017-0356-z
6. Itthikorn P, Suksun H, Tanakorn P, Arul A, Shui-Long S (2016) Marginal lateritic soil stabilized with calcium carbide residue and fly ash geopolymers as a sustainable pavement base material. J Mater Civ Eng ASCE 29(2):04016195
7. Kennedy J, Eberhart R (1995) Particle Swarm Optimization. In: IEEE, 0-7803-2768-3/95, pp 1942–1948
8. Phanikumar BR, Nagaraju TV (2018) Engineering behaviour of expansive clays blended with cement and GGBS. Ground Improv. https://doi.org/10.1680/jgrim.17.00054
9. Phanikumar BR, Nagaraju TV (2018) Swell compressibility characteristics of expansive clay lumps and powders blended with GGBS—a comparison. Indian Geotech J, ISSN 2277–3347:1–9
10. Ruhul Amin Mozumder and Aminul Islam Laskar (2015) Prediction of unconfined compressive strength of geopolymer stabilized clayey soil using artificial neural network. Comput Geotech 69:291–300
11. Ramesh HNG, Sivapullaiah PV (2010) Role of moulding water content in lime stabilization of soil. Ground Improv 64(1):15–19
12. Ranganatham BV, Sathyanarayana B (1965) A rational method of predicting swelling potential for compacted expansive clays, In: Proceedings of the 6th international conference on S.M. and F.E., Canada, vol 1, pp 92–96
13. Sarat KD, Pijush S, Akshaya Kumar S, Sitharam TG (2010) Prediction of swelling pressure of soil using artificial intelligence techniques. Environ Earth Sci 16:393–403
14. Shaymaa A, Nima F, Afshin A, Bujang KM (2017) Collapsibility potential of gypseous soil stabilized with fly ash geopolymer; characterization and assessment. Constr Build Mater 137:390–409

Factors Influencing Transient Response of Shallow Strip Footing on Granular Soil Subjected to Vertical Pulse Load

Suvendu Kumar Sasmal and Rabi Narayan Behera

Abstract The structures located near seashore and industrial areas, basically apart from static loads are subjected to dynamic loads in the form of natural wind, storm loads, and machine vibrations. Uncertainty in the time of occurrence is something that makes these dynamic loads dangerous. Normally before the arrival of dynamic load, the foundation remains in a stable (steady) state, the state which is distorted with a sudden change in loading, putting the foundation in a trauma state. In an attempt to observe the transient response, the present study uses a numerical technique based on Finite Element Method (FEM) to model a footing-soil interface system following the concept of Beam on Nonlinear Winkler Foundation (BNWF) to minutely observe the transient response of a strip footing, i.e., the settlement due to first load cycle. Significant amount of influencing parameters including four intensities of static load, three depths of embedment of footing, three intensities of cyclic load, and three different relative densities of sand have been considered to find out the settlement of the footing. The results obtained from the numerical model, created and analyzed by numerical programming tool *OpenSees* suggest that the transient settlement is significantly affected by soil, footing, and loading characteristics with the allowable static load being the most dominant factor. An empirical expression is also developed to estimate the settlement of strip footing due to first load cycle.

Keywords Strip footing · Cyclic load · Finite Element Method · Beam on Nonlinear Winkler Foundation · Settlement

S. K. Sasmal · R. N. Behera (✉)
Department of Civil Engineering, National Institute of Technology Rourkela, Rourkela 769008, India
e-mail: rnbehera82@gmail.com

S. K. Sasmal
e-mail: suvendukumarsasmal@gmail.com

A. Prashant et al. (eds.), *Advances in Computer Methods and Geomechanics*, Lecture Notes in Civil Engineering 55,
https://doi.org/10.1007/978-981-15-0886-8_31

1 Introduction

The response of anything to a load that varies with time consists of two distinct parts; the transient response and the steady-state response. The transient response is the response of an object to sudden fluctuation in the state of that object. In the case of shallow foundations, these sudden changes of state generally take place when dynamic loads in the form of vibratory shocks from machines and earthquake-induced ground motions strike the foundation. Pulse load considered in the present study is in most cases generated from a rhythmically vibrating machine on the foundation or more specifically the load suffered by the railroad foundation. The analysis of the transient response of foundation is necessary keeping in view the fact that the behavior of footing directly affects any superstructure supported by it. When a pulse load is applied on the foundation, the first load cycle is something that distorts the state of the foundation which is previously loaded with only static load. As a response to the first load cycle, the foundation suddenly displaces from its original position and with the continuation of loading, the foundation attains the steady stage. Hence, the response of the footing to first load cycle, referred hereafter as the transient response is important in determining the magnitude of damage that the foundation will suffer.

The settlement of plane strain footing under the influence of cyclic load was observed by Raymond and Komos [15]. Their study indicated the importance of soil and loading parameters in determining the settlement of footing. Similar methodology was carried out by Das et al. [5] to study the response of a square footing. Sawicki et al. [17] studied the settlement of circular footing under the influence of cyclic load. Apart from different experimental techniques, the dynamic response of shallow foundation has been studied by using numerical model like Beam on Nonlinear Winkler Foundation (BNWF) model by various researchers like Allotey and Naggar [1], Harden et al. [8], Allotey and Naggar [2], Raychowdhury and Hutchinson [14].

The field of soil dynamics has always been dominated by steady-state response. However, a key concept of physics is that before the steady-state, a system behaves haphazardly in a response to external loads for a very small duration. In an attempt to prove the significance of transient response, in the present study, a shallow strip footing is taken as a physical system and its transient response to vertical pulse load is observed. Influencing parameters like allowable static load depending on the factor of safety (FS), embedment ratio (D_f/B), Intensity of pulse load $q_{d(\max)}$ and relative density of soil (D_r %) are considered to observe the settlement of footing due to first pulse load. A statistical model equation is also developed based on nonlinear regression to analyze the significance of the input parameters.

2 Finite Element Model

A strip footing having dimension 0.5 m × 0.1 m × 0.03 m (Length × Width × Thickness) is divided into one hundred discrete elastic beam-column elements. The nonlinear springs used in the present BNWF model are for capturing the response of the footing-soil interface to applied external static and cyclic load. The footing consists of 100 elements and 101 nodes. The footing nodes are joined with the help of one-dimensional elastic beam-column. Each footing node is connected to soil node with the help of springs modeled as zero-length elements. The zero-length elements are one-dimensional nonlinear inelastic springs that are independent of each other and are modeled using QzSimple2, PySimple2, and TzSimple2 material models, and these spring elements simulate the vertical load displacement behavior, horizontal passive load displacement behavior against the side of the footing and horizontal shear sliding behavior at the base of the footing, respectively. The schematic diagram of the BNWF model is given by Fig. 1. Each footing node has three degrees of freedom (Two translations and one rotation). The soil nodes are fixed. The footing rests on free field soil and the springs capture the soil-footing interface response. The model is created using OpenSees [11].

The springs are distributed across the length of the footing according to Harden et al. [8]. The nonlinear properties are assigned to the springs as per Raychowdhury [13]. The stiffness of any spring is a function of soil strength parameters. Depending on the Shear modulus (G) and the Poisson's ratio (υ) of the soil, the stiffness of each spring is calculated as per Gazetas [7]. Procedures mentioned in Gazetas [7] are considered to include the effect of embedment, in case of embedded foundation. In all governing expressions, the shear modulus is calculated as $G = E/2(1 + \upsilon)$. To capture the passive resistance and the sliding resistance of footing, horizontal springs are provided in addition to vertical springs. The passive capacity is determined according to Rankine's method. The sliding resistance (t_{ult}) is calculated as

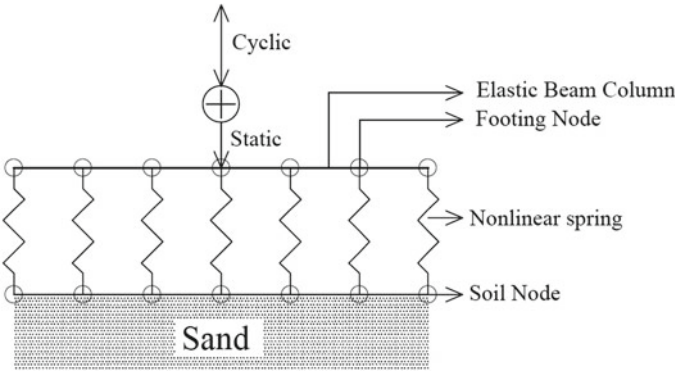

Fig. 1 Schematic diagram of the BNWF model and loading conditions

Table 1 Soil parameters used in the numerical model

Relative density (D_r, %)	Angle of internal friction (ϕ, degree)	Unit weight of soil (γ, kN/m^3)	Modulus of elasticity (E, MPa)	Poisson's ratio (υ)
35	34	13.34	20	0.3
51	37.5	13.97	36	0.32
69	40.8	14.36	55	0.35

$$t_{\text{ult}} = W \tan \delta \tag{1}$$

where W = weight on footing, δ = the soil-concrete interfacial friction angle = 0.66 $\times$ ϕ, ϕ = angle of internal friction of soil.

Three different embedment ratios (D_f/B) of footing are considered, i.e., 0, 0.5 and 1 along with three different intensities ($q_{d(\max)}/q_u$) of pulse load, i.e., 5, 10 and 13%. The intensity of pulse load is generally taken as some percentage of static failure load depending on the ultimate bearing capacity for corresponding soil and embedment condition. The different types of soil used in the present study and their strength defining parameters are provided in Table 1. The soil parameters like relative density(D_r), angle of internal friction (ϕ) and unit weight (γ) for dense and medium dense sand are taken as per Patra et al. [12]. The parameters for loose sand are taken as per Sahu et al. [16]. The modulus of elasticity (E) and Poisson's ratio (υ) are taken as per EPRI [6], considering the range of relative densities given in Das [4].

3 Results and Discussions

First, the present numerical model is validated for loose sand conditions with the results obtained from Plaxis 3D (Brinkgreve et al. [3]).

In the present BNWF model, the behavior is controlled by the nonlinear springs. Nonlinear smooth backbone curves are used to define the springs rather than multi-linear material model. The Plaxis 3D model is created using Mohr–Coulomb constitutive model for the same soil and footing condition. The load-settlement curve obtained is then compared with that obtained from FEM analysis and the comparison seems to be reasonably good. The load-settlement curve in the static condition is given by Fig. 2. From Fig. 2. it can be inferred that the present model predicts the foundation response with reasonable accuracy. For the same soil condition and footing dimensions, theoretical ultimate bearing capacity as per Meyerhof [9] is found to be 22 kPa verifying the ultimate bearing capacity obtained from the present model.

Figures 3, 4 and 5 represent the response of footing for particular values of $q_{d(\max)}/q_{u,}$ i.e., 5, 10, and 13%, respectively, whereas all other parameters are varied within their specified ranges. It is observed that for a particular intensity of cyclic load, the total settlement after the striking of the cyclic load is dominated by the

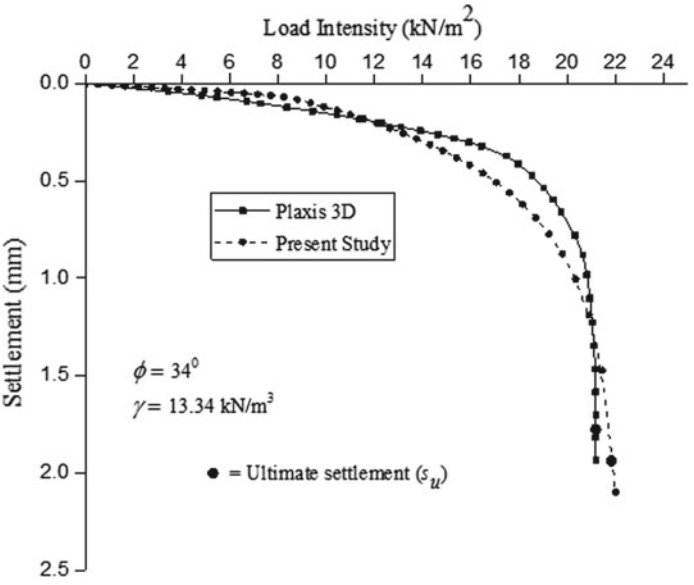

Fig. 2 Load-settlement curve for loose sand in static condition

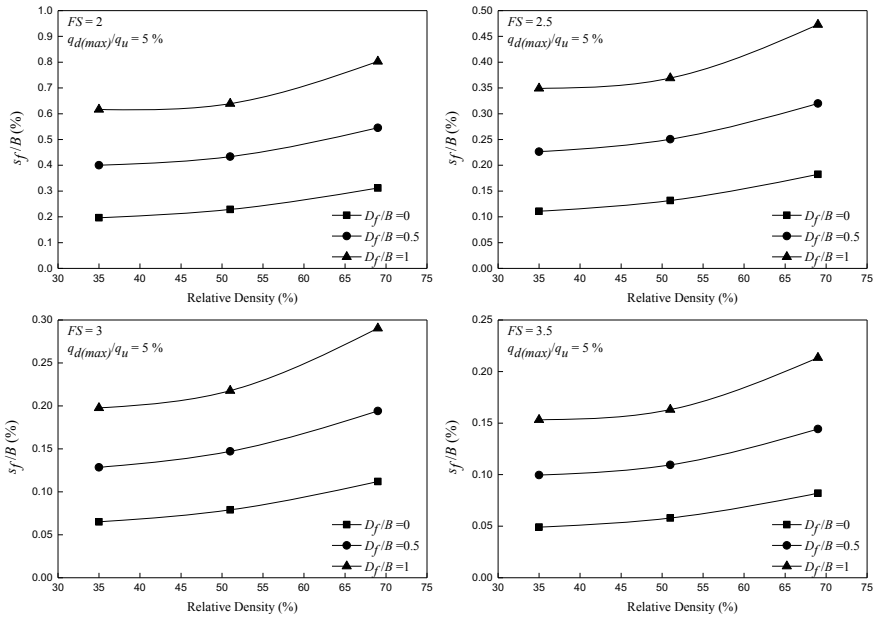

Fig. 3 Settlement of strip footing due to first load cycle ($q_{d(\max)}/q_u = 5\%$)

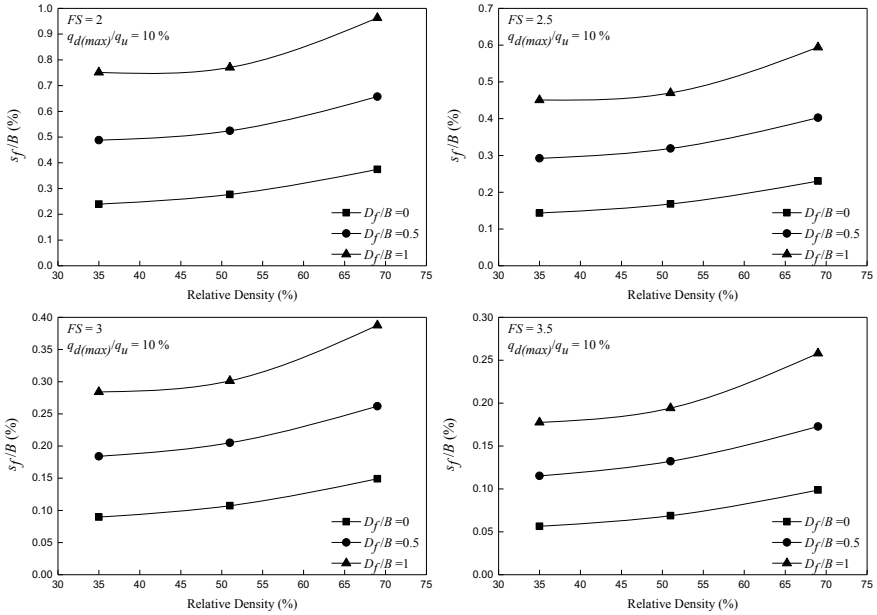

Fig. 4 Settlement of strip footing due to first load cycle ($q_{d(\max)}/q_u = 10\%$)

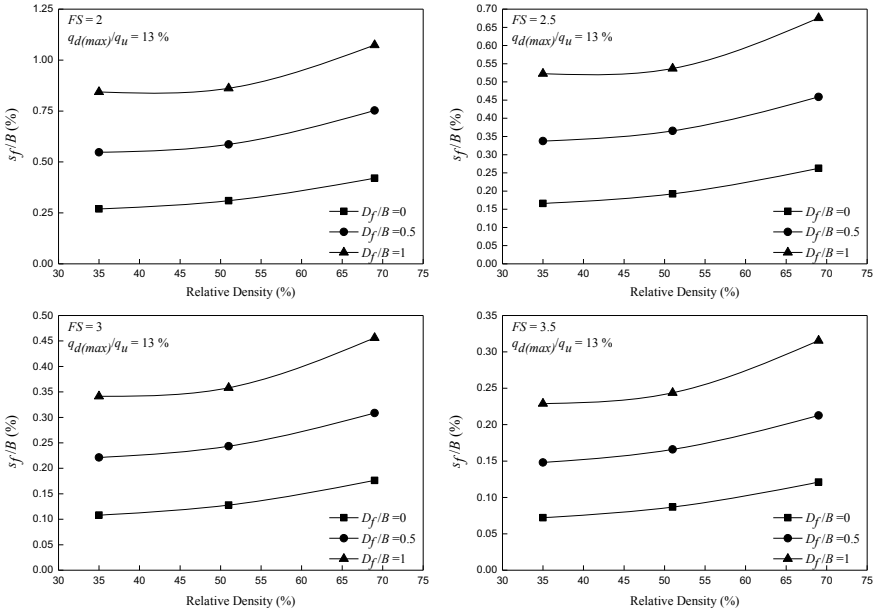

Fig. 5 Settlement of strip footing due to first load cycle ($q_{d(\max)}/q_u = 13\%$)

allowable static load on the foundation. It is also observed that keeping all the influencing parameters constant, as the intensity of cyclic load increases the settlement of footing also increases. The intensity of cyclic load is a function of ultimate bearing capacity (q_u) which in turn is directly related to the relative density of soil (D_r) and the embedment ratio (D_f/B). An increase in both the parameters results in a higher value of q_u, leading to an increase in $q_{d(\max)}$ which is attributed to larger settlement of footing as observed from Figs. 3, 4, and 5. As the settlement is a combined response of footing due to the allowable static load and the cyclic load, as *FS* decreases the corresponding settlement of footing increases thanks to larger amount of static load.

3.1 Development of Empirical Equation for Nondimensional Settlement

To develop an empirical expression for finding the normalized settlement due to the first load cycle, i.e., s_f/s_u (%), 108 number of data set containing inputs and corresponding output are considered, the statistical values of which are shown in Table 2. The term s_f indicates the settlement due to allowable static load + first load cycle, i.e., called as transient settlement whereas (s_u) is the ultimate settlement of footing in static condition. The study indicates that a significant portion of the total settlement of footing occurs due to the first load cycle. Up to 14% of ultimate static settlement (s_u) takes place at this stage.

A statistical model is developed incorporating four input parameters to find out the settlement due to the first cycle of loading. The model equation is developed using Nonlinear regression analysis program NLREG [10]. The equation is assumed in the following form;

$$s_f/s_u(\%) = a \times FS + b \times \exp\left(D_f/B\right) + c \times \left(q_{d(\max)}/q_u(\%)\right) + d \times (D_r(\%))^e \quad (2)$$

The numerical values of the parameters are mentioned in Table 3. The R^2 obtained from the regression analysis is 0.91. Without affecting the accuracy of the model, the numerical values of the coefficients are approximated as shown in Column3 of Table 3. The final equation can be expressed as Eq. (3).

Table 2 Statistical values of input and output parameters

Parameter	Maximum value	Minimum value	Average value	Standard deviation
FS	3.5	2	2.8	0.6
D_f/B	1	0	0.5	0.4
$q_{d(\max)}/q_u$ (%)	13	5	9	3
D_r (%)	69	35	52	14
s_f/s_u (%)	14.02	1.82	5.93	3.17

Table 3 Numeric values of coefficients obtained from regression analysis

Coefficients (1)	Numeric value (Regression) (2)	Approximated value (3)
a	−5.13	−5
b	−0.28	−0.3
c	0.26	0.3
d	21.58	21
e	−0.045	−0.05

$$s_f/s_u(\%) = -5 \times FS - 0.3 \times \exp\left(D_f/B\right) + 0.3 \times \left(q_{d(\max)}/q_u(\%)\right) + 21 \times (D_r(\%))^{-0.05} \quad (3)$$

Comparison between the observed output and predicted output (using Eq. (3)) is shown in Fig. 6. It can be concluded that the developed empirical expression can estimate the transient settlement of footing with reasonable accuracy having R^2 equal to 0.91, with majority of data lying inside ± 10% deviation lines.

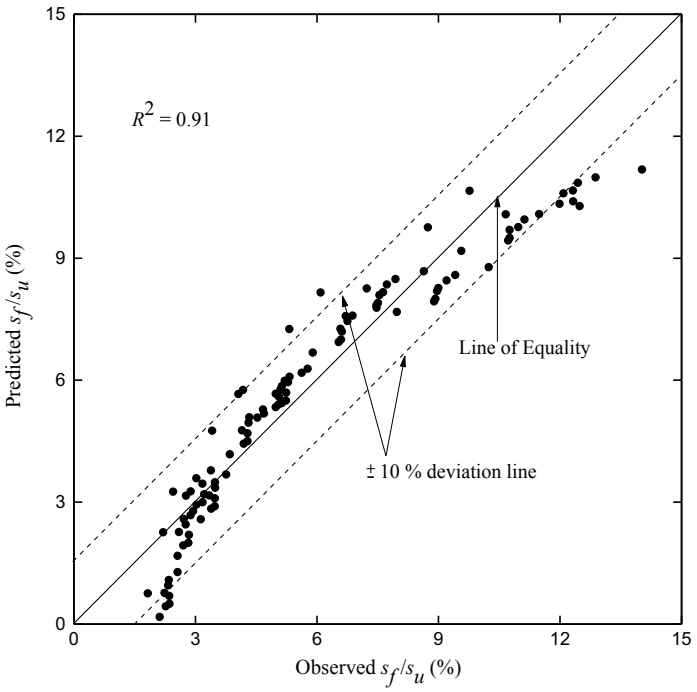

Fig. 6 Comparison between observed s_f/s_u (%) and predicted s_f/s_u (%)

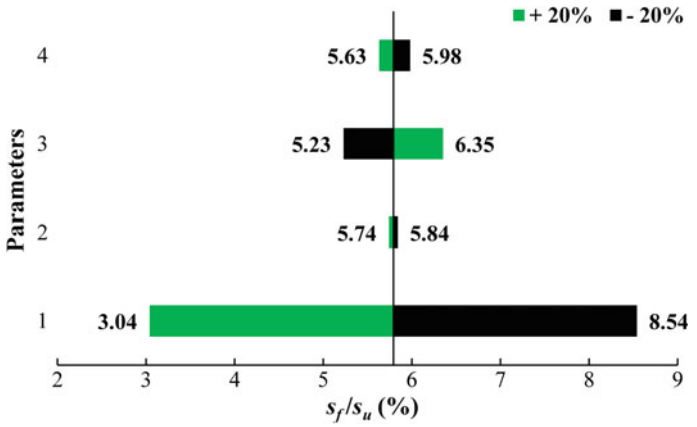

Fig. 7 Tornado plot showing variation of normalized settlement

3.1.1 Sensitivity Analysis

The sensitivity of input parameters toward determining the output is studied with the help of a tornado plot as shown in Fig. 7.

First, the output is determined for mean values of input parameters. Then the mean values of the input parameters are perturbed, one at a time by ± 20%, keeping all other parameters untouched, to observe the variation of the output. In Fig. 7. Parameters 1, 2, 3, 4 represent *FS*, D_f/B, $q_{d(\max)}/q_u$ (%), and D_r (%), respectively. It is observed that apart from $q_{d(\max)}/q_u$ (%), for all other input parameters, a positive perturbation results in decrease in (s_f/s_u) % and vice versa. Hence, it can be inferred that among all the input variables only $q_{d(\max)}/q_u$ (%) directly affects the output. *FS*, D_f/B, *and* D_r (%) inversely affect the (s_f/s_u) %. Depending on the range of variation of the output, as observed from Fig. 7, *FS* is the most influencing parameter followed by $q_{d(\max)}/q_u$ (%), D_r (%) and D_f/B.

4 Conclusions

Based on the numerical and statistical analyses carried out in the present study to estimate the transient settlement of shallow strip footing due to the initiation of dynamic loading in the form of a vertical pulse, the following major inferences are drawn;

- The transient settlement (s_f) due to the first load cycle can be up to 14% of the settlement of the footing under static failure load (s_u).
- With the decrease in *FS* and increase in D_r (%), $q_{d(\max)}/q_u$ (%), D_f/B, the transient settlement (s_f) of the footing increases. However, the normalized settlement (s_f/s_u) % decreases with increase in *FS,* D_r (%), D_f/B and decrease in $q_{d(\max)}/q_u$ (%).

- An empirical equation in the form of Eq. (3) is developed to predict the normalized settlement (s_f/s_u) % of the footing with reasonable accuracy.
- *FS* is the most significant parameter controlling transient response followed by $q_{d(\max)}/q_u$ (%), D_r (%) and D_f/B.

References

1. Allotey N, El Naggar MH (2003) Analytical moment–rotation curves for rigid foundations based on a Winkler model. Soil Dyn Earthq Eng 23(5):367–381
2. Allotey N, El Naggar MH (2008) Generalized dynamic Winkler model for nonlinear soil–structure interaction analysis. Can Geotech J 45(4):560–573
3. Brinkgreve RBJ, Engin E, Swolfs WM (2013) PLAXIS 3D 2013 user manual. Plaxis bv, Delft
4. Das BM (2016) Principle of foundation engineering. 8th edn. Cengage Learning
5. Das BM, Yen SC, Singh G (1995) Settlement of shallow foundation on sand due to cyclic loading. In: The international conference on recent advances in geotechnical earthquake engineering and soil dynamics 8:385–388
6. EPRI (1990) Manual on estimating soil properties for foundation design. Electric Power Research Institute, Palo Alto, California
7. Gazetas G (1991) Formulas and charts for impedances of surface and embedded foundations. J Geotech Eng 117(9):1363–1381
8. Harden C, Hutchinson T, Martin GR, Kutter BL (2005) Numerical modeling of the nonlinear cyclic response of shallow foundations. Report no 2005/04 Pacific Earthquake Engineering Research Center (PEER) Berkeley California
9. Meyerhof GG (1963) Some recent research on the bearing capacity of foundations. Can Geotech J 1(1):16–26
10. NLREG: Non-linear regression computer program, Version 6.6
11. OpenSees [Computer Program]. Open system for earthquake engineering simulation, Pacific Earthquake Engineering Research Center (PEER), University of California, Berkeley. http://OpenSees.berkeley.edu
12. Patra CR, Behara RN, Sivakugan N, Das BM (2012) Ultimate bearing capacity of shallow strip foundation under eccentrically inclined load, Part I. Int J Geotech Eng 6(3):343–352
13. Raychowdhury P (2008) Nonlinear Winkler-based shallow foundation model for performance assessment of seismically loaded structures. Ph. D Dissertation. University of California, San Diego
14. Raychowdhury P, Hutchinson TC (2010) Sensitivity of shallow foundation response to model input parameters. J Geotech Geoenvironmental Eng ASCE 136(3):538–541
15. Raymond GP, Komos FE (1978) Repeated load testing of a model plane strain footing. Can Geotech J 15(2):190–201
16. Sahu R, Patra CR, Das BM, Sivakugan N (2016) Bearing capacity of shallow strip foundation on geogrid-reinforced sand subjected to inclined load. Int J Geotech Eng 10(2):183–189
17. Sawicki A, Swidzinski W, Zadroga B (1998) Settlement of shallow foundation due to cyclic vertical force. Soils Found 38(1):35–43

Analysis of Heave Behaviour of Expansive Soil Provided with Granular Pile Anchors Using Plaxis

S. Sangeetha and P. Hari Krishna

Abstract The majority of the lightly loaded structures built on expansive soils exhibits swelling behaviour with varying moisture content. To nullify this effect, numerous remedial techniques are evolved. Granular Pile Anchor Foundation (GPAF) is one among the innovative short tensile pile technique that can be promisingly suggested as a foundation method in expansive soil. GPAF traces its origin from the discrete granular pile, which is widely used in soft clays and loose sand. Problems for the foundation in expansive soil are uplift. Hence, the granular piles are provided with anchor rod centrally, which anchors the footing to the anchor plate placed at the bottom. In the year 2006, a research was carried out to study the heave control behaviour of granular pile anchor for footing resting on expansive soil. Outcomes of the research proved the efficacy of GPA over concrete piles. In present work, numerical simulation of the previous field study was made to analyse the heave control phenomena of granular pile anchor using Plaxis 2D, an analysis software based on the finite element method. Performance of Granular Pile Anchor in numerical analysis agrees with that of field test outcomes. Heave control phenomena of Granular Pile Anchor is better than that of concrete piles. This is mainly due to the thorough interlocking of rough-surfaced granular pile material at the interface which is absent in case of concrete pile. Heave of footings is decreasing with increase in length and diameter of the piles used to anchor the footings. The heave values obtained using Plaxis are greater than that from field experiments. This may be due to the empirical assumption of material properties used in the input.

Keywords Expansive soil · Swelling · Granular pile anchor · Numerical simulation · Plaxis 2D

S. Sangeetha (✉)
VNR Vignana Jyothi Institute of Engineering and Technology, National Institute of Technology, Warangal, India
e-mail: sangeetha_s@vnrvjiet.in

P. Hari Krishna (✉)
National Institute of Technology, Warangal, India
e-mail: phari@nitw.ac.in

A. Prashant et al. (eds.), *Advances in Computer Methods and Geomechanics*, Lecture Notes in Civil Engineering 55,
https://doi.org/10.1007/978-981-15-0886-8_32

1 Introduction

With ever increasing population and over-exploitation of suitable strata for construction, it is a high time to engineer unsuitable strata to a suitable one, so as to accommodate the foundation with adequate stability. Expansive soil is one among the challenging soil in Geotechnical Engineering. This soil covers about 20% of total land area in India. The damages caused by the swell shrink behaviour of expansive soil estimate about several billions of dollars across the globe. In order to pacify the volumetric changes in expansive soil towards alternate wetting and drying conditions, numerous methods are being evolved by scientists continuously throughout the sphere.

Granular pile anchor is one among the promising heave mitigating techniques in expansive soils, which is highly advantageous compared to the other methods. Several types of research have been carried out since the inception of this novel method on expansive soils by various laboratory investigations to study the heave behaviour and pullout capacity. In order to understand the in situ behaviour of granular anchor piles provided to footings resting on expansive soil towards heave control, a detailed field study was carried out at NIT, Warangal in the year 2006.

In the era of Computational Geotechnics, analysis of any evolving technology may be simplified in terms of time and labour. However, reliability of the method depends on its agreement with the proven facts. Finite element method is a powerful analytical technique that can be used effectively to analyse the soil-pile system in expansive soils. In the present work, numerical heave studies were made using PLAXIS 2D and the results were compared with those of field studies. Also, concrete piles of similar dimension were modelled and compared with those granular piles. The axisymmetric stress condition was used and the vertical ground heave was used to simulate swell behaviour of expansive soil. It is found that granular pile anchors perform better than the concrete pile towards heave control, which agrees with the experimental analysis. The rate of heave reduction increases with increase in dimensions of the piles.

2 Literature Review

The granular anchor pile can be defined as an improved granular pile, which is reinforced with a suitable anchor rod protruding above the pile head whose lower end is fixed with an anchor plate embedded in a predrilled borehole, which is followed by compaction of granular material with an internally operating hammer provided with a central hole for the passage of anchor rod through it. Hence, the granular anchor pile system is installed into the ground by anchoring the foundation to the base anchor plate using an anchor rod. Due to this anchorage action, the resistance to pullout loads gets generated all long the pile-soil interface and will counteract the pullout loads that are acting on these foundation systems. The amount of pullout

resistance generated along the pile-soil interface depends on the frictional angle at this interface [8].

Phani kumar has confirmed that the capacity of granular pile anchors in resisting the uplift loads increased with an increase in their length and relative density of the pile material. All his observations are based on laboratory investigations only, which may not reflect the actual field conditions.

Based on the experimental study performed by Subba Rao and Venkatesh [29] on the behaviour of pile embedded in saturated clay, the average unit skin friction increases linearly with shear strength of soil mass. For both smooth and rough piles, the value of skin friction tends to become constant at higher stress levels. In case of rough piles in clay, the failure is observed to take place away from the pile and within the soil rather than along the pile-soil interface as is generally assumed, to compute the shaft resistance. The extent of such failure would essentially depend on the pile roughness and embedment length.

Tsubakihara and Kishida [30] have also stated that, for rough piles, the shear failure occurs within the clay specimen instead of interface sliding. Hence, they concluded that the maximum resistance of friction is upper bounded by the shear strength of clay. Mochtar and Edil (1988) found that the surface of the smooth piles was clear and free from any trace of clay, whereas for the granular pile, it was clearly covered by the clay. This clearly implies that the failure plane was at the pile-clay interface for the smooth piles and out in the clay for the rough piles.

Saad et al. (2014) performed numerical analysis of GPAF system installed on expansive soil under hypothetical field conditions. The results were compared with that of laboratory experiment and a mathematical model was developed using SPSS (17.0) for statistical analysis based on the results of finite element analysis.

2.1 Previous Work

Previously, in order to study the performance of granular anchor piles to control heave of footings resting on expansive soil, a site was chosen near the northern boundary of NIT-Warangal campus by Hari Krishna [8] where the soil profile consists of about 2.0–2.2 m thick black cotton soil followed by murrum up to a depth of 6 m. Hard disintegrated rock follows murrum up to about 12–15 m underlined by fissured and fractured rock to depth of about 18–20 m. The ground is found to heave during the rainy season. During summer, map-type cracks were observed all over the site, indicating the potential for high expansiveness of the soil. Before designing a method for heave control, a study was conducted to understand characteristics and behaviour of soil at the proposed location of site. Heave behaviour of footings provided with different tension piles embedded in expansive soil was studied under laboratory and field conditions.

2.2 Heave Stake Test

In order to determine the percentage free swell in situ Hari et al. (2006) performed the ground heave stake test using precast concrete pedestal inserted at different depths from the surface up to the depth of 2 m as shown in Fig. 1. Over seasons, the heave was measured using the levelling instrument.

The whole area is subjected to alternate wetting and drying condition. The heave measurements were continued till maximum heave is recorded. The uplift movement of the pedestal was found to decrease with increase of depth. The percentage one-dimensional unrestrained or free swell of these soil layers is calculated, which is expressed as a ratio S (%) = (Δh/h) $\times$ 100 and the values are listed in Table 1.

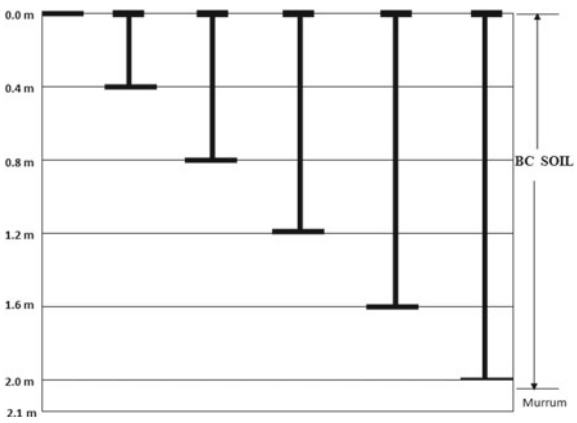

Fig. 1 Cross-Sectional view of field setup for studying the in situ heave measurements at different depths

Table 1 Ultimate heave and free swell values of stakes installed at different depths

Depth of heave stake (m)	Ultimate heave (mm)	Free swell (%)
Surface	108	5.1
0.4	65	3.8
0.8	45	3.5
1.2	27	3.0
1.6	10	2.0
2.0	2	2.0

3 Methodology

Field setup of footings provided with different tension piles installed in expansive soil was analysed using Plaxis. Cross-sectional view of treated and untreated footings under the site condition as shown in Fig. 2. was considered for modelling. In the field, the pits were filled with water for a period of about 90 days to observe their heave movements and the maximum heaves were observed during that period. Axis symmetric model was used to model the field setup as it is suitable and simple for single pile behaviour.

3.1 Input Data

Corresponding to the field setup as shown in Fig. 2, the geometry of the model was extended to 2.1 m in the vertical direction to represent the depth of expansive soil in field. The size of the footing used in the field was 1.5 m. The width of the model was considered to be three times the width of the footing. Being axisymmetric, the size of the footing was taken as 0.75 m. Hence, the geometry was made up to 2.25 m horizontally, which was three times axisymmetric footing size (3×0.75). The geometry of the soil cluster was partitioned in such way to show excavation up to the depth of 0.6 m and width 0.75 m that can be deactivated in the proceeding calculation phase. At the left bottom of the excavation line, the geometry of Granular pile anchor was made with axisymmetric configuration i.e. quarter pile. However, initially the cluster was assigned with expansive soil property so as simulate initial field condition and was later with granular pile material in construction stages (Table 2).

Expansive Soil cluster and granular pile material were modelled using Mohr–coulomb model, which is a nonlinear model. The material type was considered to be drained for granular material and undrained for expansive soil in case of untreated footing and drained for treated footing as the granular material provides passage for draining and the properties of the material are given in Table 3. The concrete pile was modelled as nonporous linear elastic material. Footing and anchor plates of

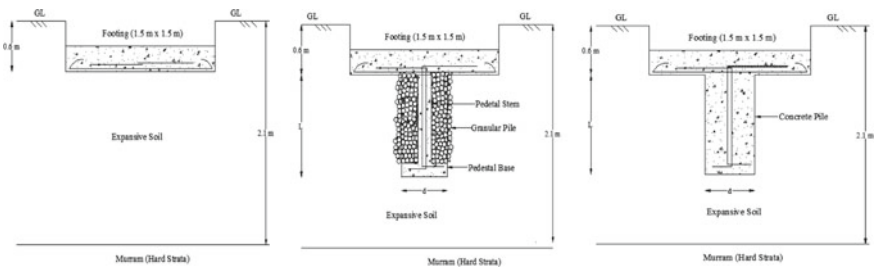

(a) Untreated Footing **(b) With Granular pile** **(c) Concrete Pile**

Fig. 2 Vertical displacements of footing

Table 2 Properties of the material used

Soil	Expansive soil	Granular pile	Concrete
Model	Mohr–coulomb	Mohr–coulomb	Linear Elastic
Type	Drained	Drained	Nonporous
γ_{unsat} (kN/m^3)	16	24	24
γ_{sat} (kN/m^3)	17	25	24
$E_{ref,}$ Modulus of elasticity (kPa)	5000	50000	1.94×10^7
Poisson's ratio	0.35	0.3	0.15
Cohesive strength (C_u in kPa)	135	0.0001	–
Angle of internal Friction	0	43°	0
Dilatancy angle	0	13°	–
Permeability K_x(m/day)	0.0001	1	–
Permeability K_y(m/day)	0.0001	1	–
R_{inter} (between concrete and expansive clay)	0.8	1	1

Table 3 Properties of the Structural Element

Plates	Footing	Anchor plate	Anchor rod
Material	M15 concrete	Mild steel	Mild steel
EI kNm^2/m	1620	133.33	–
EA kN/m	1.94×10^6	4×10^6	3.6×10^6
Poisson's ratio	0.15	0.33	–

GPA were modelled as plate element and anchor rod was specified as node-to-node anchor.

3.2 Boundary Condition

The standard fixity condition was assigned to the model. (i.e.) Horizontal displacements are considered to be zero at the left and the right boundaries. Also, both horizontal and vertical displacements were taken as zero at the bottom. This assumption agreed with the behaviour in nature where the surrounding soil of large horizontal extent functions as horizontal fixities [13]. After assigning all the necessary inputs to the model, the automated mesh was generated in Plaxis as shown in Fig. 3. Coarse mesh generated was made of 157 elements, 1323 nodes and 1884 stress points.

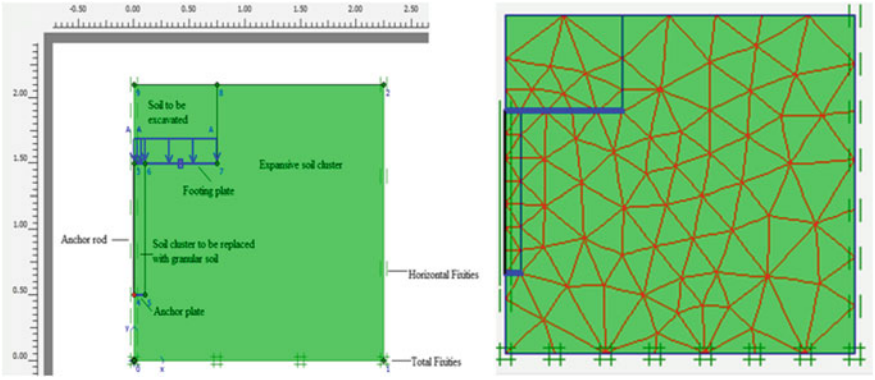

Fig. 3 2D Axis symmetric Input model with description and generated mesh

3.3 Initial Condition

While assigning the initial conditions the water table is assumed to be at the base of model as no water table was found up to the depth of 6 m at the site [8]. Then initial stresses were calculated by assuming coefficient earth pressure at rest, $K_0 = 1$, where $K_0 = 1\text{-}\sin\varphi$ as given by Jacky's formula.

3.4 Calculation Phases

In PLAXIS, there is a provision to assign construction in stages. The present analysis was performed in three stages. Of these first two phases were plastic and the third phase was consolidation as in Fig. 4.

In the first phase, similar to the field study, expansive soil model was excavated to a depth of 0.6 m and to a width of 0.75 m in the axisymmetric model from the left boundary (half of the Footing size, 1.5 m) by deactivating the corresponding soil

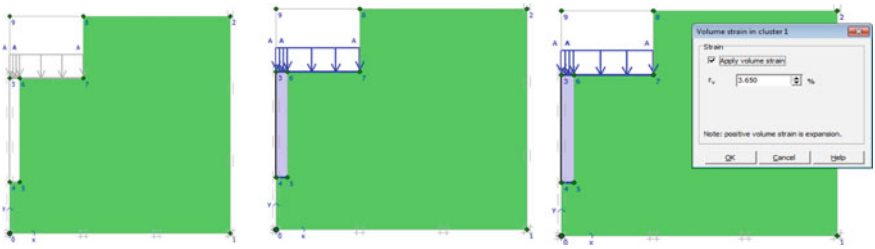

(a) Excavation phase **(b) Construction phase** **(c) Swelling phase**

Fig. 4 Calculation phases defined in PLAXIS analysis

cluster. Then the borehole was made for GPA installation, again by deactivating the respective soil cluster. In the second phase of construction, anchor plate, anchor rod, granular anchor material, footing plate and uniformly distributed load corresponding to the self-weight of the footing (2.4 kN/m^2) were activated by defining the parameter through parameter tab.

To account for the time effect, the third phase was performed as a consolidation phase with a time interval of 90 days, which was according saturation period in the field experiment conducted. Also, ultimate heave was witnessed within that period in the field. Hence, in order to simulate heave condition, a volumetric strain of 3.65% was applied to the expansive soil cluster in the model input window. This value was according to the average percentage of free swell at the depth 0.6 m which was obtained from the field prediction of ground heave by Heave stake test after Hari Krishna as given in Table 1. The volumetric strain acts as heave in the vertical direction as the later displacements were arrested by the boundary conditions in the given model.

For the purpose of comparison, concrete piles of equivalent dimension as of GPA were modelled. To understand the relative performance of tension piles in controlling heave of footings resting on expansive soils, footings of different dimensions (1, 1.5, 2.0 m) without piles were also modelled and ultimate heaves were obtained for each case.

4 Results and Discussions

Even though uniform vertical heave was assigned to the model, the vertical displacement was found to decrease with depth due to overburden as given in Fig. 5a, b and c. The ultimate vertical displacement of the footing element is depicted in Fig. 6.

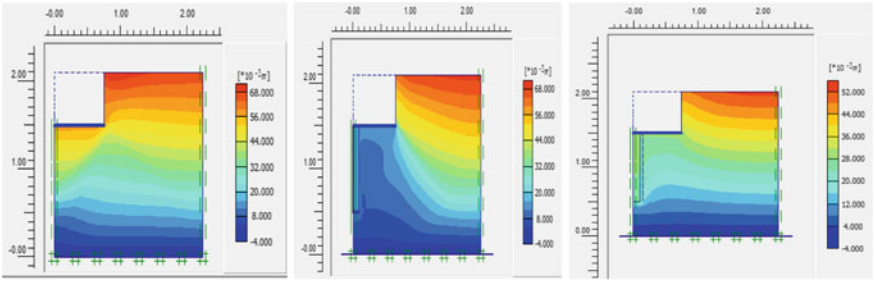

(a) Untreated Footing **(b) With Granular pile** **(c) Concrete Pile**

Fig. 5 Vertical displacements of footing

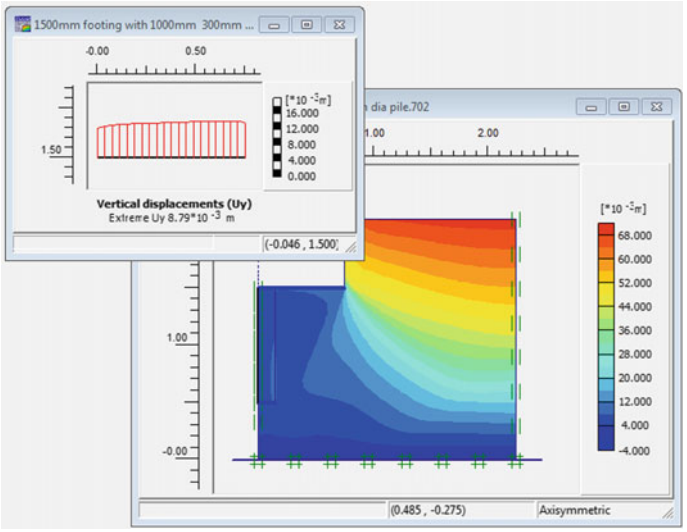

Fig. 6 Out put window showing the vertical displacement of GPA (L = 1 m and D = 300 mm)

4.1 Swell Potential and Percentage of Heave Reduction

The results from the numerical analysis on the heave behaviour of footings supported by different dimensions of granular pile anchor are given in Table 4. As can be seen from this table, the results of these footings under-treated and untreated conditions were analysed using swell potential and percentage reduction in heave. Hari Krishna [8] used swell potential as the ratio of change in thickness of soil (i.e., heave of footing plate to the original soil thickness).

Hence,

$$\text{Swell potential}\,(\%) = (\Delta H/H) \times 100$$

Table 4 Swell potential and percentage reduction in heave of footings with GPA of different dimension on expansive soil (Footing size = 1.5 m)

S. No.	Pile dimension (m)		Heave (mm)	Swell potential (%)	Percentage reduction in heave (%)
	Length	Diameter			
1	Without any pile		58.26	3.9	–
2	0.5	0.2	20.11	1.3	65
3	1	0.1	20.92	1.4	64
4	1	0.2	14.38	1.0	75
5	1	0.3	8.79	0.6	85
6	1.5	0.2	3.12	0.2	95

Table 5 Swell potential and percentage reduction in heave of footings with concrete piles of different dimensions on expansive soil

S. No.	Pile dimension (m)		Heave (mm)	Swell potential (%)	Percentage reduction in heave (%)
	Length	Diameter			
1	Without any pile		58.26	3.9	–
2	0.5	0.2	38.88	2.4	33
3	1	0.1	35.73	2.3	39
4	1	0.2	29.28	1.8	50
5	1	0.3	25.9	1.2	56
6	1.5	0.2	24.63	1.0	58

where ΔH is the change in thickness of soil and H is the original soil thickness.

The percentage reduction in heave due to the treatment condition, i.e. difference between heave values of treated (h′) and untreated conditions (h) to the heave of untreated condition (h), expressed as a percentage.

$$\text{Percentage reduction in heave} = \left\{\left(h - h'\right)/h\right\} \times 100$$

From the table, it can be seen that swell potential decreases with increase in length and diameter of the pile. Percentage reduction in heave increases with increase in dimension of the pile. For granular pile anchor of length 1 m and diameter 200 mm 75% of heave reduction was accounted. About 95% of heave reduction can be witnessed upon providing granular pile anchor throughout the length of the expansive soil. Similarly, the swell potential and the percentage of heave reduction for footings provided with concrete piles of different dimensions are listed in Table 5. In case of concrete pile, only 58% of heave reduction can be seen on providing concrete pile throughout the length of the expansive soil. Decrement of swell potential on increment of dimensions of concrete pile was not that pronounced as in case of GPA. For concrete pile of length 0.5 m and 200 mm diameter, the percentage of heave reduction is about 33%. By providing concrete pile of same diameter and of 1.5 m length throughout the expansive soil layer, heave reduction was increased to just 58%. The efficiency of granular pile anchor in reducing swell potential was about 5 times greater than that of concrete pile when provided throughout the depth of the expansive soil.

4.2 Comparison of Numerical Analysis and Field Study

The heave values of untreated and treated footings obtained from numerical analysis using Plaxis were given in Table 6. The tabulated values were compared against results of field analysis discussed in literature. It was found that in numerical study,

Table 6 Heavevalues for Footings provided with/without tension piles

S. No.	Footing size (m)	Pile type	Pile dimension		Heave in mm	
			Pile length (m)	Diameter (m)	Numerical analysis εv = 3.65%	Field study
1	1	No pile	N/A	N/A	57.46	51
2	1.5	No pile	N/A	N/A	58.26	60
3	2	No pile	N/A	N/A	60.68	76
4	1.5	CP	0.5	0.2	38.88	36
6	1.5	CP	1	0.1	35.73	34
5	1.5	CP	1	0.2	29.28	27
7	1.5	CP	1	0.3	25.9	18
8	1.5	CP	1.5	0.2	24.63	15
9	1.5	GPA	0.5	0.2	20.11	15
11	1.5	GPA	1	0.1	20.92	17
10	1.5	GPA	1	0.2	14.38	9
12	1.5	GPA	1	0.3	8.79	4
13	1.5	GPA	1.5	0.2	3.18	5

heave of the footing was found to increase by 1.4% when footing size was increased by 50%. Also heave was increased by 5.6% when the footing size was doubled. However, in case of field study heave was increased by 18% upon 50% footing size increment and around 49% heave increment was accounted for doubling the footing size. Heave increment upon increase in size of the footing was not pronounced in the field study. This may be due to the fact that heave was modelled as volumetric strain. However, in the field heave increases due to removal of overburden and increase of exposed swell surface.

Heave got decreased with increasing dimensions of the pile (Ala Nasir et al. 2014). The reduction trend followed is on par with the aforesaid field study. For the same surface area, heave reduction is more with the length increment than that of the diameter. This may be attributed to the increased length of interlocking surface. The phenomenon is in line with the findings of Phanikumar [19], Phanikumar et al. [20], Rao et al. [26], Phanikumar et al. [12, 14, 21]. The values of heave obtained from the numerical analysis were on average 1.33 times greater than that of field tests. This can be accounted for the variation of material properties used in FEM analysis for soil clusters, which were basically derived using empirical relation. Also, the exact weather condition prevailed during the field test could not be simulated in the numerical model.

In the case of concrete piles, due to the reduction of strength at the interface, the heave mitigating effect is comparatively less. For the piles provided throughout the length of the expansive soil, the percentage of heave reduction for concrete pile is

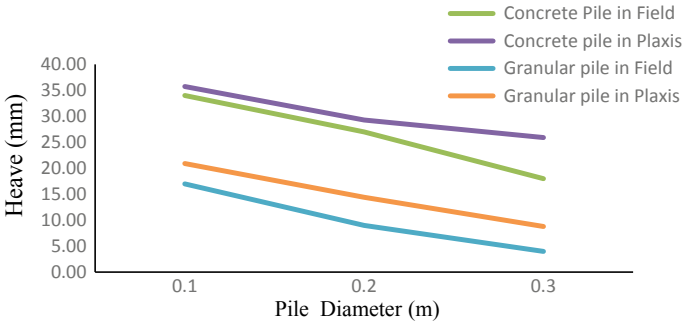

Fig. 7 Comparison between numerical and field analysis on heave behaviour of piles of different diameter

Fig. 8 Comparison between numerical and field analysis on heave behaviour of piles of different length

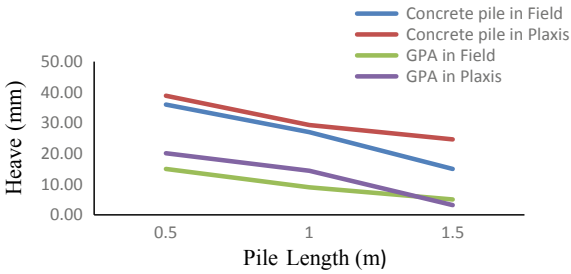

58% whereas for GPA it is about 95%. A comparison between results of field test and numerical analysis for piles of different lengths and diameters is shown in Figs. 7 and 8.

5 Conclusions

Performance of Granular Pile Anchor in numerical analysis agrees with that of field test outcomes.

1. Heave control phenomena of Granular Pile Anchor is better than that of concrete piles. This is mainly due to the thorough interlocking of rough-surfaced granular pile material at the interface which is absent in case of concrete pile.
2. Swell potential of footings provided with tensile pile decreases with increase in length and diameter of the pile.
3. Heave of footings is decreasing with increase in length and diameter of the piles used to anchor the footings. And out of the two parameters increase in length of the pile is resulting in more percentage of heave reduction than diameter for the same pile surface.

The heave values obtained using Plaxis are greater than that from field experiments. This may be due to the empirical assumption of material properties used in the input. Also densification of the surrounding medium by ramming of pile material and increase in size of GPA after installation could not be accounted in the numerical analysis. Based on its agreement with field study, analysis may be extended for piles of different lengths and diameter on soils of different swelling behaviour and a mathematical model can be developed which could be used in the design of granular pile anchor for expansive soils.

References

1. Ambily AP, Gandhi SR (2007) Behavior of stone columns based on experimental and FEM analysis. J Geotech Geoenvironmental Eng
2. Al-Omari RR, Oraibi WK (2000) Cyclic behaviour of reinforced expansive clay. J Soils Found, Jpn Geotech Soc 40(2):1–8
3. Bhandari RK, Humad SM, Prakash C (1987) Two New Types of Foundation for Light Structures on Expansive Soils. In: Proceedings of the 6th international conference on expansive soils, New Delhi, India, pp 295–300
4. Bowles JE (1988) A text book on "Foundation analysis and design", 4th edn. Mc. Graw–Hill Book Co., New Delhi
5. Chen FH (1988) A text book on "Foundations on expansive soils". Elsevier Pub. Co., Amsterdam
6. Ranjan G, Kumar P (2000) Behavior of granular piles under compressive and tensile loads. Geotech Eng J 31(3)
7. Hari Krishna P, Murthy VR, Narasimhulu J (2005) Anchored granular micropiles as ground anchors, IGC
8. Hari Krishna P (2006) A study on the use of granular anchor piles to control heave of footings resting on expansive soils, Ph.D. thesis. NIT Warangal
9. Hari Krishna P, Murthy VR (2002) In-Situ heave measurements of concrete and anchored granular micropiled footings. In: Proceedings of IGC-2002. Allahabad, India, pp 377–380
10. Hughes JM, Withers NJ (1974) Reinforcing of soft cohesive soils with stone columns, ground engineering, London, 17(3):42–49
11. Ibrahim SF, Aljorany AN, Aladly AI (2014) Heave behavior of granular pile anchor-foundation (GPA-foundation) system in expansive soil. J Civil Eng Urban 4(3):213–222
12. Ismail MA, Shahin M (2011). Finite element analysis of granular pile anchors as a foundation option for reactive soils. In: International conference on advances in geotechnical engineering. Perth, Australia
13. Kaufmann KL, Nielsen BN, Augustesen AH (2010) Finite element investigations on the interaction between a pile and swelling clay. In: Aalborg: Department of Civil Engineering, Aalborg University. (DCE Technical Reports; No. 104)
14. Krishna PH, Murty VR, Vakula J (2013) A filed study on reduction of flooring panels resting on expansive soils using granular anchor piles and cushions. Int J Eng Sci (IJES) 2(3):111–115
15. Mitchell JK, Huber TR (1985) Performance of a stone column foundation. J Geotech Engrg 111–2:205–223
16. Mohammed Zein YEA, Mohammed MG, Sharief AMEI (1991) Finite element analysis of short piles in expansive soils. J Comput Geotech Elsevier, 231 –243
17. Murthy Srinivasa BR, Nagaraj TS (1987) Prediction of heave in swelling soils. In: 6th international conference on expansive soils
18. O'Neill MW, Poormoayed N (1980) Methodology for foundation on expansive clays. J Geotec Eng, Proc ASCE 106(GT12)

19. Phanikumar BR (1997) A study of swelling characteristics of and granular pile-anchor foundation system in expansive soils. Ph.D thesis, JNTU, Hyderabad, India
20. Phani Kumar BR, Sharma RS, Rao AS, Madhav MR (2004) Granular pile anchor foundation (GPAF) system for improving the engineering behavior of expansive clay beds. Geotech Test J 27(3):279–287
21. Phanikumar BR, Rao AS, Suresh K (2008) Field behavior of granular pile anchors in expansive soils. Ground Improv J Proceeding Inst Civ Eng (ICE) 4:199–206
22. Plaxis 2D version 8 Manual
23. Poulos HG, Davis EH (1980) Pile foundation analysis and design. Wiley, New York
24. Kumar P, Ranjan G, Saran S (2003) GAP system for resistance of uplift forces. In: Proceedings of IGC-2003, pp 597–602
25. Ranjan G (1989) Ground treated with granular piles and its response under load. Indian Geotech J 19(1):1–86
26. Rao AS, Phanikumar BR, Babu RD, Suresh K (2007) Pullout behavior of granular pile anchors in expansive clay beds In-situ. J Geotech Geoenvironmental Eng, ASCE 133(5):531–538, Via Iraqi Virtual Science Library (IVSL)
27. Snethen DR et al (1979) An evaluation of methodology for prediction and minimization of detrimental volume change of expansive soils in highway subgrades, Research report, vol 1, Prepared for federal highway administration
28. Sridharan A, Rao VG (1987) Mechanism controlling swelling of clays, IISC Bangalore
29. Subba Rao KS, Venkatesh KH (2003) Laboratory investigations on the bearing capacity of buried piles in clay. In: Proceedings of IGC-2003, Roorkee, pp 125–128
30. TsubakiharaY, Kishida H (1993) Frictional behaviour between NC clay and steel by two direct shear type apparatuses. Soils Found, Jpn Soc Soil Mech Found Eng 33(2):1–13

Comparison of Theoretical and Laboratory Permeability for Coarse-Grained Soil

Satyajit Roy, R. K. Bharti, Mahabir Dixit and R. Chitra

Abstract The permeability of soil is an essential parameter in estimating the quantity of seepage under foundation of hydraulic structures, which in turn affect the stability of structures. Empirical correlations such as Hazen, Kozeny–Carman, Breyer, Slitcher, Terzaghi, USBR, Alyamani and Sen are function of grain sizes, porosity/void ratio, coefficient of uniformity (C_u), coefficient of curvature (C_c) and viscosity of pore fluids. These correlations are quite effective for preliminary assessment of permeability during prefeasibility stage. However, at the designing stage, actual measurement of permeability is very important for structural integrity. The measurement of permeability is carried out by in situ tests for assessment of foundation of hydraulic structures and also for investigation of canals in cutting. The assessment of permeability of borrow area soils for construction of embankment is determined by laboratory methods. Depending upon the size of the soil particles, gradation, interaction among the soil particles, etc. constant head and falling head laboratory tests are more popular for coarse-grained and fine-grained soil, respectively. In the present study, attempt has been made to correlate permeability values evaluated through these correlations and also through constant head laboratory test. The samples were packed in permeability mould at 95% relative density. For comparison, four different types of soils from different sources have been selected. The values of laboratory permeability and theoretical permeability obtained through correlations are compared and have been discussed in the present paper. The results are also compared with Odong Odong (J Am Sci 3(3), 2007, [1]) and same indicate close resemblance in terms of applicability of correlation for assessment of permeability of different types of sands.

Keywords Coefficient of uniformity · Coefficient of curvature · Coefficient of permeability · Constant head method · Relative density

S. Roy (✉) · R. K. Bharti · M. Dixit · R. Chitra
Central Soil and Materials Research Station, New Delhi 110016, India
e-mail: satyajitcsmrs@gmail.com

A. Prashant et al. (eds.), *Advances in Computer Methods and Geomechanics*, Lecture Notes in Civil Engineering 55,
https://doi.org/10.1007/978-981-15-0886-8_33

1 Introduction

The permeability is useful in the solution of many engineering problems such as (i) dewatering and drainage of excavations, backfills and subgrades, (ii) determining yield of water-bearing strata, (iii) estimating seepage through the body of earth dams, (iv) determination of yield of water-bearing strata, and (iv) calculation of losses from canal.

Permeability is a direct function of average grain size distribution of granular porous media [2]. The interrelationship is quite effective for preliminary investigation especially at prefeasibility stage. However, proper investigation of soil is required during the designing stage, it is important to know the actual response of soil towards permeability for structural integrity by laboratory methods. Several researchers made an effort to calculate the coefficient of permeability and develop several indirect empirical formulae as laboratory testing sometimes takes considerable time in arriving at meaningful conclusion. Empirical correlations are function of grain sizes, porosity/void ratio, C_u, C_c and viscosity of pore fluids. The actual measurement of permeability is quite complex due to anisotropic nature of material. Depending upon the size of the soil particles, gradation, interaction among the soil particles, etc. constant head and falling head laboratory tests are used for coarse-grained and fine-grained soil, respectively. The samples of coarse-grained soil are packed at those relative densities which can be achieved in the field whereas fine-grained soil is packed at closer to maximum dry density. The approximate permeability during planning stage is also estimated by empirical formulae, which have been developed over different basin on the basis of grain size distribution characteristics.

There are various empirical correlations available in the literature such as Hazen, Kozeny–Carman, Breyer, Slitcher, Terzaghi, USBR, Alyamani and Sen. Several investigators have studied these relationships and modified these formulae based on experimental work. The applicability of these formulae depends on the type of soil and compactness of the soil for which coefficient of permeability is required to be estimated. As per Vukovic and Soro [3], the applications of different empirical formulae to the same porous medium material can yield different values of coefficient of permeability. The objective of this paper is to study the applicability and reliability of some of the commonly used empirical formulae and to compare the coefficient of permeability values of unconsolidated soil materials from these formulas for sandy soil of different gradations with laboratory permeability values determined through constant head tests at 95% of maximum relative density.

1.1 Established Empirical Formulae

Vukovic and Soro [3] summarized several empirical methods from former studies and presented a general formula:

$$k = \frac{g}{\gamma} \cdot C \cdot f(n) \cdot {d_e}^2 \tag{1}$$

where k = coefficient of permeability, g = acceleration due to gravity, v = kinematic viscosity, C = sorting coefficient, $f(n)$ = porosity function, and d_e = effective grain diameter. The kinematic viscosity (γ) is related to dynamic viscosity (μ), fluid (water) density (ρ) as follows:

$$v = \frac{\mu}{\rho} \tag{2}$$

The values of C (n) and de are dependent on the different methods used in the grain size analysis. According to Vukovic and Soro [3], porosity (n) may be derived from the empirical relationship with the coefficient of grain uniformity (C_u) as follows:

$$n = 0.255\left(1 + 0.83^{C_u}\right) \tag{3}$$

where C_u is the coefficient of grain uniformity and is given by

$$\left(C_u = \frac{d_{60}}{d_{10}}\right) \tag{4}$$

Here, d_{60} and d_{10} in the formula represent the grain diameter in (mm) for which 60% and 10% of the sample, respectively, are finer than d_{60} and d_{10}.

Former studies presented the following formulae which took the general form and presented in Eq. (1) but with varying C, $f(n)$ and devalues and their domains of applicability.

(a) **Hazen Formula** [4]: It was widely used for the estimation of coefficient of permeability of uniformly graded soils ranges from fine sand to gravel of diameter 0.1–3 mm, respectively, and uniformity coefficient less than 5. This formula only depends on the effective size of grains as

$$k = \frac{g}{v} \times 6 \times 10^{-4}[1 + 10(n - 0.26)]d_{10}^2$$

(b) **Kozeny–Carman Equation** [5]: The KC equation is not appropriate for soil with effective size above 3 mm or clayey soil [6]. The KC equation is widely used and accepted for coefficient of permeability estimation because it depends on both the effective grain size and porosity (number of pores) of the porous media as given below.

$$k = \frac{g}{v} \times 8.3 \times 10^{-3}\left[\frac{n^3}{(1-n)^2}\right]d_{10}^2$$

(c) **Breyer** [7]: This method does not consider porosity and therefore, porosity function takes on value 1. Breyer formula is often considered most useful for

materials with heterogeneous distributions and poorly sorted grains with uniformity coefficient between 1 and 20, and effective grain size between 0.06 and 0.6 mm.

$$k = \frac{g}{\nu} \times 6.0 \times 10^{-4} \times \log\left[\frac{500}{C_u}\right] d_{10}^2$$

(d) **Slitcher** [8]: This formula is most applicable for grain size between 0.01 and 5 mm.

$$k = \frac{g}{\nu} \times 1.0 \times 10^{-2} \times n^{3.287} d_{10}^2$$

(e) **Terzaghi** [9]:

$$k = \frac{g}{\nu} \times C_t \times \left(\frac{n - 0.13}{\sqrt[3]{1-n}}\right)^2 \times d_{10}^2$$

where C_t = sorting coefficient. In this study, the average value of C_t is used. Terzaghi formula is most applicable for coarse-grain sand [10].

(f) **USBR**:

$$k = \frac{g}{\nu} \times 4.8 \times 10^{-4} \times d_{20}^{0.3} \times d_{10}^2$$

U.S. Bureau of Reclamation (USBR) formula calculates coefficient of permeability from the d_{20}, and does not depend on porosity; hence, porosity function is unity. The formula is most suitable for medium-grain sand with uniformity coefficient less than 5 [10].

(g) **Alyamani and Sen** [11]:

$$k = 1300[I_o + 0.025(d_{50} - d_{10})]^2$$

where k is the coefficient of permeability (m/day), I_o is the intercept (in mm) of the line formed by d_{50} and d_{10} with the grain size axis, d_{10} is the effective grain diameter (mm), and d_{50} is the median grain diameter (mm). The method considers both sediment grain sizes d_{10} and d_{50} and the sorting characteristics. This formula, therefore, is exceptionally different from those that take the general form of Eq. (1) above.

2 Materials and Methods

In order to compare results obtained from these correlations with laboratory test results, four sandy soil samples were selected from different sources for comparing the permeability values. The photographs of samples selected are presented in Fig. 1. Mechanical analysis of soil samples were carried out as per IS 2720 (Part 4) [12]. Since the samples are sandy and cohesionless in nature, constant head method for determination of permeability of soil as per IS 2720 (Part 17)—[13] was selected. The particle size distributions of all four samples are presented in Table 1 and Fig. 2, respectively. The grain size distribution indicates that sample 1 and sample 4 have predominance of medium sand. Sample 2 has predominance of fine sand whereas sample 3 has fine to medium sand in equal proportions. The effective size 'd_{10}' value of these samples varies from 0.019 to 0.40. C_u for three samples is less than 5, whereas for sample no. 3, it is 28.95. The different grain sizes of the sands are presented in Table 2.

The maximum and minimum density and required density at 95% of relative density for all selected samples are presented in Table 3. Samples were packed in permeability mould in three layers at 95% of relative density.

The relative density of the soil samples was determined according to IS 2720 (Part 14) 1986 [14]. Figure 3 presents the Relative Density apparatus.

The density index (relative density, I_d) expressed, as a percentage was calculated as follows:

$$I_d = \left[\frac{\gamma_{max}(\gamma_d - \gamma_{min})}{\gamma_d(\gamma_{max} - \gamma_{min})}\right] \times 100$$

Here, in calculating required density γ_d, relative density (I_d) was considered as 95%. The minimum density, maximum density, and required density γ_d calculated for different sand are calculated and shown in Table 3. For 95% relative density, the γ_d vary from 1.56 to 1.74 g/cc.

The laboratory permeability was determined by constant head method as described in IS 2720 (Part 17)—1986. The schematic diagram of constant head method is presented in Fig. 4.

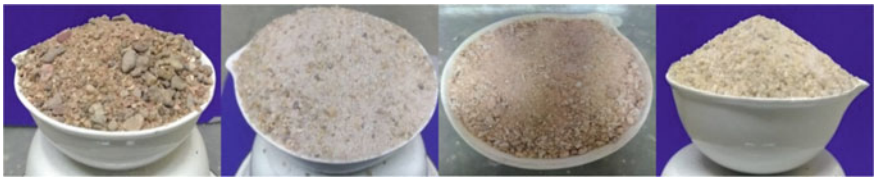

Sample No. 1 (Sindh River Sand (MP)) | Sample No. 2 (Yamuna River sand) | Sample No. 3 (Rajasthan Crushed Stone) | Sample No. 4 (Ennore Standard Sand)

Fig. 1 Pictures of types of sand selected

Table 1 Particle size distribution

Sample	Mechanical analysis						Soil type (IS: 1498)	Remarks
	0.002 mm and less	0.002–0.075 mm	0.075–0.425 mm	0.425–2.0 mm	2.0–4.75 mm	4.75 mm and above		
	Clay	Silt	Fine sand	Medium sand	Coarse sand	Gravel		
1	0.0	1.0	10.7	74.5	11.9	1.9	SP	Medium sand
2	0.0	7.4	75.8	7.9	7.7	1.2	SP-SM	Fine sand
3	0.9	17.9	35.5	37.2	8.5	0.0	SM	(Fine to medium sand) however in theoretical permeability calculation this has been taken as fine sand and silt is in more than 50%
4	0.0	1.7	26.5	70.7	1.1	0.0	SP	Medium sand

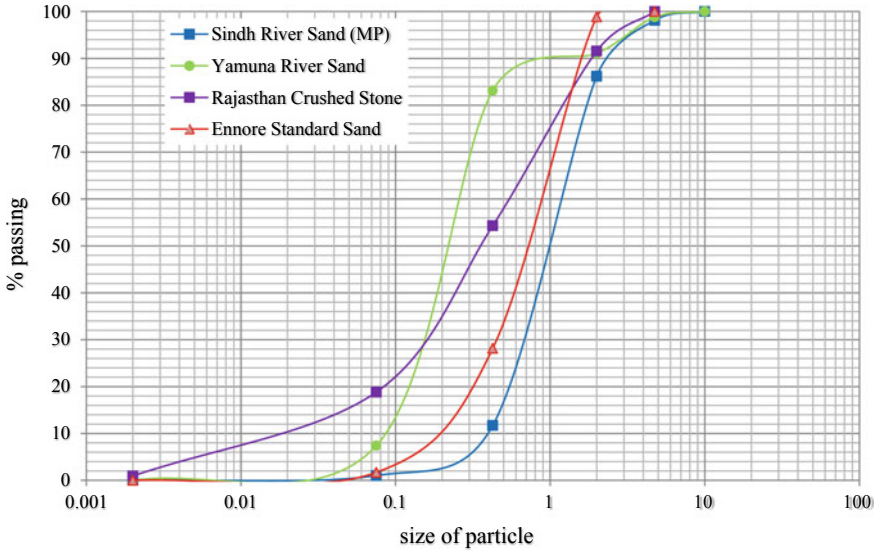

Fig. 2 Grain size distribution curve

Table 2 Different grain sizes of samples

Parameters	Sindh River sand (MP)	Yamuna River sand	Rajasthan crushed stone	Ennore standard sand
d_{10}	0.40	0.09	0.019	0.19
d_{20}	0.55	0.13	0.085	0.32
d_{30}	0.69	0.17	0.16	0.47
d_{50}	1.00	0.22	0.35	0.72
d_{60}	1.30	0.26	0.55	0.90
C_u	3.25	2.89	28.95	4.74
C_c	0.92	1.23	2.45	1.29

Table 3 Calculated values of minimum, maximum and required density

Type of Soil	Sindh River sand (MP)	Yamuna River sand	Rajasthan crushed stone	Ennore standard sand
Min density γ_{min} (g/cc)	1.444	1.371	1.318	1.509
Max density γ_{max} (g/cc)	1.757	1.573	1.661	1.736
required density @ 95% of relative density (g/cc) γ_d	1.74	1.56	1.64	1.72

Fig. 3 Relative density apparatus

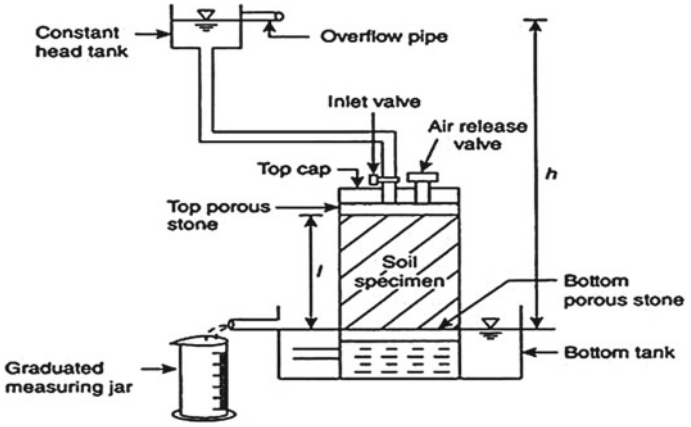

Fig. 4 Schematic diagram of constant head method

The test is performed by measuring (i) quantity of water (Q) flowing through soil specimen per second, (ii) length of soil specimen (L), and (iii) head of water (h).

If Q is the total quantity of flow in a time interval 't', from Darcy's law,

$$q = \frac{Q}{t} = kiA$$
$$k = \frac{Q}{t}\frac{1}{iA} = \frac{Q}{t}\frac{L}{h}\frac{1}{A}$$

Here,

A = Area of the specimen, 1005 cm^2

Table 4 Result of constant head permeability test

Sl. No.	Type of sand	Time in second	Discharge (ml)	Coefficient of Permeability 'k' (cm/s)	Avg. value of coefficient of permeability 'k' (cm/s)
1	Sindh River sand (MP)	300	620	2.09×10^{-04}	2.03×10^{-04}
2		300	590	1.99×10^{-04}	
3		300	590	1.99×10^{-04}	
4	Yamuna River sand	300	370	1.25×10^{-04}	1.25×10^{-04}
5		300	370	1.25×10^{-04}	
6		300	370	1.25×10^{-04}	
7	Rajasthan crushed stone	300	180	6.02×10^{-05}	4.98×10^{-05}
8		300	140	4.63×10^{-05}	
9		300	130	4.40×10^{-05}	
10	Ennore standard sand	300	1120	3.77×10^{-04}	3.60×10^{-04}
11		300	1100	3.72×10^{-04}	
12		300	980	3.30×10^{-04}	

$L = 12.70$ cm
$H = 125.00$ cm
$Q =$ flow through soil specimen cm^3
$t =$ time in s
$k =$ cm/s.

The result of constant head permeability tests is presented in Table 4.

The coefficient of permeability calculated from grain size analysis using empirical formulae is presented in Table 5.

3 Result and Discussions

The comparison of results of permeability values obtained through existing correlations and laboratory permeability values as presented in Tables 4 and 5, respectively. The basic reason for this divergence is due to applicability of these formulae under restrictive conditions. These formulae are applicable for unconsolidated soil; however, in present case, these values have been compared with sandy soil samples compacted at 95% relative density. Further, depending upon gradations of different type of sand applicability of these formulae are questionable as explained below.

The Hazen and USBR methods are applicable in soil where $C_u < 5$. However for Rajasthan Crushed Stone, the C_u value is 28.7, therefore, this formula is not applicable. Terzaghi and USBR empirical correlations are applicable for coarse sand and medium sand, respectively.

Table 5 Coefficient of permeability based on empirical equations

Type of sand	Hazen 'k' (cm/s)	Kozeny–Carman 'k' (cm/s)	Breyer 'k' (cm/s)	Slitcher 'k' (cm/s)	Terzaghi 'k' (cm/s)	USBR 'k' (cm/s)	Alyamani and Sen 'k' (cm/s)
Sindh River sand (MP)	2.19×10^{-01}	9.43×10^{-02}	2.05×10^{-01}	7.32×10^{-02}	NA	1.49×10^{-02}	1.49×10^{-01}
Yamuna River sand	1.16×10^{-02}	5.17×10^{-03}	1.06×10^{-02}	4.03×10^{-03}	NA	NA	6.02×10^{-03}
Rajasthan crushed stone	NA	5.21×10^{-05}	2.66×10^{-04}	4.05×10^{-05}	NA	NA	2.26×10^{-04}
Ennore standard sand	4.23×10^{-02}	1.57×10^{-02}	4.28×10^{-02}	1.23×10^{-02}	NA	4.29×10^{-03}	4.01×10^{-02}

The coefficient of permeability by USBR and Slitcher methods are lower values as compared to other methods as presented in Table 5. These values support conclusions drawn by Vukovic and Soro [3], Cheng and Chen [10]. Breyer method is most useful for analyzing heterogeneous sample with well-graded grain [15]. It is the best estimator for sample no. 3. However, for less heterogeneous sample, i.e., sample no. 1, 2, and 4, this method underestimates the values. Hazen method is less accurate than Kozeny–Carman because Hazen is based on d_{10} particle size only whereas Kozeny–Carman is based on particle size distribution as well as particle shape [6]. Therefore, the estimations by Kozeny–Carman for sample no. (1, 2 and 4) are more accurate than Hazen, and possibly the best estimation in the study. Alyamani and Sen Methods is very sensitive to the shape of the grading curve and more accurate for well-graded sample. It is found that in case of sample no. 3 laboratory value is more than the empirical value (Breyer equation), where $C_u = 28.95$. In rest all the cases, laboratory values are far less than the theoretical values.

From empirical equations,

$$k_{(\text{Sindh River Sand (MP)})} > k_{(\text{Ennore Standard Sand})} > k_{(\text{Yamuna River sand})} > k_{(\text{Rajasthan Crushed Stone})}.$$

From Laboratory values

$$k_{(\text{Ennore Standard Sand})} > k_{(\text{Sindh River Sand (MP)})} > k_{(\text{Yamuna River sand})} > k_{(\text{Rajasthan Crushed Stone})}.$$

In both the cases permeability values are more for medium-grained sand, and lower for sand having significant amount of silts. Silt helps in filling the voids in between sands, thus reducing permeability value.

Based on the above study the most suitable assessment of coefficient of permeability is as follows: Sample 1 (Kozeny–Carman formula) = 9.43×10^{-02} cm/s, Sample 2 (Kozeny–Carman formula) = 5.17×10^{-03} cm/s, Sample 3 (Breyer formula) = 2.66×10^{-04} cm/s, with value of constant head parameter acceptable, and Sample 4 (Kozeny–Carman formula) = 1.57×10^{-02} cm/s.

The results are also compared with Odong [1] and same indicate close resemblance in terms of applicability of correlation.

4 Conclusions

Based on results and discussions, the following conclusions can be drawn:

(a) Empirical equations used for estimating the coefficient of permeability of soils may lead to underestimation or overestimation unless the appropriate method is used. Depending upon on size of the particles, gradation curve, etc.
(b) Laboratory permeability values are very low as compared to empirical values in most of the samples barring sample no. 3. This may be probably a high relative density used in laboratory tests whereas these correlations have been developed unconsolidated soils.
(c) Kozeny–Carman's followed by Hazen formulae good for estimation of coefficient of permeability of homogeneous (soils having excess of one fraction as compared to others) soils having coefficient of uniformity less than 5. These are applicable for wide range of soils. However, the Breyer formula suitable for heterogeneous soils.
(d) Slitcher, Terzaghi, and USBR formulae grossly underestimated the coefficient of permeability in comparison to other evaluated formulae.
(e) Based on above result and analysis, the most appropriate formulae for estimation of coefficient of permeability are as follows:

    Sample 1 (Kozeny–Carman formula) = 9.43×10^{-02} cm/s, Sample 2 (Kozeny–Carman formula) = 5.17×10^{-03} cm/s, Sample 3 (Breyer formula) = 2.66×10^{-04} cm/s, with value of constant head parameter acceptable, and Sample 4 (Kozeny–Carman formula) = 1.57×10^{-02} cm/s.
(f) From the calculated values of coefficient of permeability, in case of empirical equations,

$$k_{(\text{Sindh River Sand (MP)})} > k_{(\text{Ennore Standard Sand})} > k_{(\text{Yamuna River sand})} > k_{(\text{Rajasthan Crushed Stone})}.$$

From Laboratory values

$$k_{(\text{Ennore Standard Sand})} > k_{(\text{Sindh River Sand (MP)})} > k_{(\text{Yamuna River sand})} > k_{(\text{Rajasthan Crushed Stone})}.$$

In both cases, it is found that as the silt content increases coefficient of permeability decreases for a particular coarse-grained soil irrespective of their grading.

References

1. Odong J (2007) Evaluation of empirical formulae for determination of hydraulic conductivity based on grain-size analysis. J Am Sci 3(3)
2. Freeze RA, Cherry JA (1979) Groundwater. Prentice Hall Inc., Englewood Cliffs, New Jersey
3. Vukovic M, Soro A (1992) Determination of hydraulic conductivity of porous media from grain-size composition. Water Resources Publications, Littleton, Colorado
4. Hazen A (1995) Some physical properties of sands and gravels, with special reference to their use in filtration, 1892. Massachusetts State Board of Health, Boston, pp 539–556
5. Kozeny J (1927) Über KapillareLeitung Des Wassers in Boden, Sitzungsber. Akad Wiss Wien Math Naturwiss Kl 2a(136):271–306
6. Carrier WD (2003) Goodbye Hazen: hello. Kozeny-Carman. J Geotech Geoenviron Eng, 1054
7. Breyer W (1964) ZurBestimmung der Wasserdurchlässigkeit von Kiesen und Sanden aus der Kornverteilungskurve, Wasserwirtschaft und technik
8. Slichter CS (1905) Field measurements of the rate of movement of underground waters. U S Geological Survey. Water-supply and irrigation paper 1905, Washington, Government Printing Office 122, iii p.
9. Terzaghi K, Peck RB (1964) Soil mechanics in engineering practice. Wiley, New York
10. Cheng C, Chen X (2007) Evaluation of methods for determination of hydraulic properties in an aquifer-aquitard system hydrologically connected to river. Hydrogeol J 15:669–678
11. Alyamani MS, Sen Z (1993) Determination of hydraulic conductivity from complete grain-size distribution curves. Groundwater 31(4):551–555
12. IS 2720-4 (1985) Methods of test for soils, part 4: grain size analysis
13. IS 2720-Part-17 (1986) Methods of test for soils, part 17: laboratory determination of permeability
14. IS 2720-14 (1983) Methods of test for soils, part 14: determination of density index (relative density) of cohesion less soil
15. Pinder GF, Celia MA (2006) Subsurface hydrology. John Wiley & Sons Inc., Hoboken, New Jersey.

Seismic Wave Propagation in Layered Liquefiable Soils

Praveen M. Huded and Suresh R. Dash

Abstract Many past earthquakes with the magnitude close to 7.0 (M_w) or more have shown liquefaction phenomenon. Often liquefiable deposits occur in layers. Seismic waves travelling from bedrock are modified by the presence of layered soil, where seismic impedance contrast is seen as the reason. Recent studies have shown that the presence of a liquefiable soil layer can significantly reduce inertial load on the superstructure, i.e. liquefaction of soil layer prevents the transmission of seismic waves (mainly shear waves) acting as shield protecting the above layers (base isolation effect). However, many studies are limited to only two-layered soil, where a liquefiable soil layer is present above a non-liquefiable soil layer. However, in the field, there could be situations with multiple soil layers and a liquefiable layer could be present as a sandwiched layer between non-liquefiable layers. The seismic site response study considering the effect of layering in the soil deposits for liquefiable sites is least considered while carrying out foundation design. In the present study, two soil profiles (a sandwiched liquefiable layer and a sandwiched non-liquefiable layer) were studied by varying the thickness of each soil layer. The soil profiles were subjected to a typical ground motionfrom 1995 Kobe earthquake. The effect of layered liquefiable deposits on the seismic response of the ground is studied. The results, such as attenuation of acceleration, displacement and the spectral acceleration, were studied in detail and presented in this paper.

Keywords Seismic response study · Site amplification · Attenuation · Layered liquefiable soil

P. M. Huded (✉)
Research Scholar, Civil Engineering, Indian Institute of Technology Bhubaneswar, Bhubaneswar, India
e-mail: ph01@iitbbs.ac.in

S. R. Dash
Assistant Professor, Civil Engineering, Indian Institute of Technology Bhubaneswar, Bhubaneswar, India
e-mail: srdash@iitbbs.ac.in

A. Prashant et al. (eds.), *Advances in Computer Methods and Geomechanics*, Lecture Notes in Civil Engineering 55,
https://doi.org/10.1007/978-981-15-0886-8_34

1 Introduction

Liquefaction during earthquakes is quite established in the engineering practice as observed in many past earthquakes having magnitude close to 7.0 or more, for example, 1964 Alaska earthquake, 1964 Niigata earthquake, 1991 Luzon earthquake, 1995 Kobe earthquake, 2001 Bhuj earthquake, 2011 Christchurch earthquake, 2011 Tohoku Earthquake, etc. The liquefaction during an earthquake may cause severe ground deformation and modify the seismic waves that are propagating through the ground. To address these two effects at a particular site, site response study or free field study is normally carried out. Building codes such as the Uniform Building Code (UBC) 1997 and International Building Code (IBC) mandates the requirement of the ground response study of sites underlain by liquefiable soil. It has been widely noticed by many researchers that once soil layers liquefies at depth reduces the inertial load on the super structure by acting as a natural seismic isolation layer [1, 2], i.e. liquefied subsoil acts as a protecting layer to the superstructure. Hadjian et al. [3] conducted an afield study of an instrumented site in Taiwan, which was underlain by liquefiable soil. They have observed severe ground softening and reduction in soil stiffness during both forced vibration and during the tests where the site was subjected to past recorded earthquake motions. It was also observed that the ground softening increased the fundamental time period of the site when the acceleration of the applied load increased from $0.01g$ to $0.13g$. Trifunac and Todorovskaa [4] and Trifunac et al. [5] studied the effects of 1994 Northridge earthquake and observed the reduction of acceleration amplitude on soft soils and shifting of the peak value in the response spectra towards the longer period.

Kokusho [6] referring to Kanai's [7] work inferred that during the Niigata earthquake of 1964, buildings constructed on deposits where liquefaction occurred suffered only settlement and tilting with no major structural damage (e.g. Apartment buildings in Kawagishi-cho, Photos from Nippou News Company [8]. Similar observations were also made by Adalier [9] about the Wildlife site records and by Lai et al. [10] after 1993 Kushiro Oki earthquake. Seismic recording in Kobe port Island (man-made island where the top 16 m depth of soil was completely liquefied) during the 1995 Kobe earthquake clearly indicated the attenuation of horizontal acceleration [11]. Matsui and Oda [12] reported that during the 1995 Kobe earthquake, a viaduct highway route passing through coastal liquefied island suffered minor damage to the superstructure, whereas another similar structure on a highway on non-liquefied ground suffered major damage to its RC columns. Also, Kokusho and Motoyama [13] calculated the seismic energy flow using recordings of the downhole records of 1995 Kobe earthquake and observed that a significant level of energy dissipation had occurred in the liquefiable soil and concluded that liquefied soil act as energy absorbers. Reports from the reconnaissance survey in Turkey after Kocaeli earthquake of 1999 also showed significant damage to structures in non-liquefied areas as compared to the buildings in the liquefied area. The buildings in liquefied ground, however, settled or tilted without any major structural damage [14]. Youd and

Carter [2] studied the influence of soil softening on-ground response by analysing the recording from five instrumented sites. The effects were analysed by comparing the recorded motions and the response spectrum and concluded that if the soil softening occurs early then it would affect the short period spectral acceleration, whereas, if it occurs at the later stage, it will have minimal effect on the short period spectral acceleration but may amplify the long-period waves. In 2011 Tohoku earthquake, many buildings with shallow foundations suffered damages in terms of severing settlement and tilting in the liquefaction affected areas as reported by Tokimatsu et al. [15]. Bouckovalas et al. [1] analysed the recordings of the two instrumented sites namely Port Island seismic array during 1995 Kobe earthquake and Wildlife liquefaction array during 1987 Superstition Hills earthquake. They observed that amplification had occurred in the latter case and attenuation in the first case. Based on the analytical and numerical work they recommended that thickness of the liquefied soil layer and the seismic excitation period plays an important role in amplification or seismic isolation effect. Also in many instances, liquefaction has caused large tilting of substructure leading to failure of superstructure [e.g. Showa bridge failure, Niigata family court and apartment building in Kawagishi-choin 1964 Niigata Earthquake, many structures damaged in Luzon earthquake (1990) and Tohoku earthquake (2011)].

Hence, the beneficial or detrimental effect to the performance of a structure in the presence of liquefiable soil layer underneath is still an area of active research. Also, as per major available literature, the numerical investigations have been confined to only two-layer soils having a liquefiable layer on top of a non-liquefiable base. In the present study, it has been tried to find out the ground response for a layered soil with two configurations, i.e. (a) liquefiable soil layer in between non-liquefiable layer and (b) non-liquefiable soil layer in between liquefiable soil layer.

2 Numerical Modelling

Two soil profiles shown in Fig. 1 are considered in the present study for site response analysis. The total depth of both the soil profiles was 30 m and the water level was at the ground level (at 0 m). Depth of the sandwiched liquefiable and non-liquefiable layer was varied. For two models, four different configurations (Model 1, 2, 3, and 4) have been chosen. These configurations for both soil profiles are shown in Table 1.

2.1 Soil Model

The numerical model for this study has been developed in PLAXIS 3D® software. There are different material models available in PLAXIS to simulate the mechanical behaviour of the soil from "simple linear elastic" model to advanced models such as "hardening soil model", "hardening soil model with small strain", etc. In the present

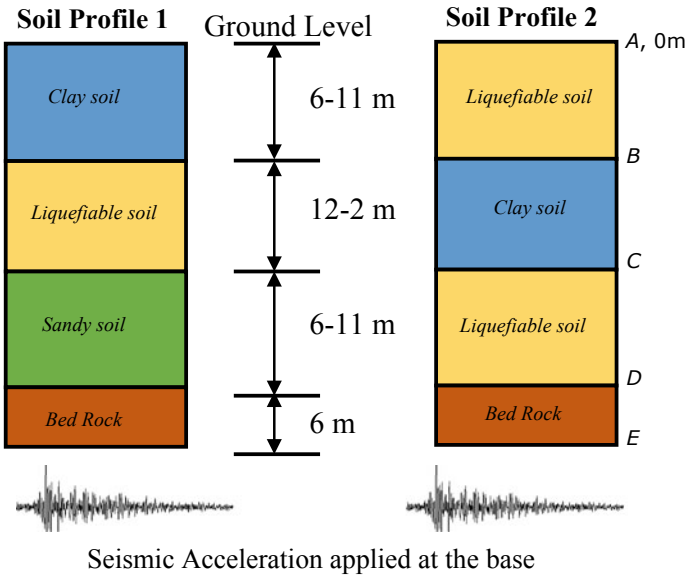

Fig. 1 Two sandwiched soil profiles considered in the present study

Table 1 Dimension of the soil profiles used in the present study

Soil profile 1	Soil profile 2	Model 1 (m)	Model 2 (m)	Model 3 (m)	Model 4 (m)
Clay	Liquefiable soil	11	10	8	6
Liquefiable soil	Clay	2	4	8	12
Sand	Liquefiable soil	11	10	8	6
Bed rock	Bed rock	6	6	6	6

study, hardening soil model was used for the clay layer deposit and hardening soil model with small strain type material model for Sandy soil deposit. UBC-3D PLM model [16] was used for the liquefiable soil deposit. The parameters of each material model used in the study are explained below and the material properties are listed in Tables 2, 3 and 4.

2.2 Loading

In the present study, the ground motion data of the 1995 Kobe Earthquake (M_w 6.9) has been used (http://peer.berkeley.edu/peer_ground_motion_database). The time

Table 2 Soil parameters used in the present study for non-liquefiable soil

Parameter	Symbol	Unit	Clay layer	Sandy layer
Material model			HS small	HS model
Drainage type			Undrained (B)	Undrained (A)
Soil unit weight, saturated	γ_{sat}	kN/m^3	20	20
Soil unit weight, unsaturated	γ_{unsat}	kN/m^3	16	20
Secant stiffness in standard	E_{50}^{ref}	MPa	20	30
Tangent stiffness for oedometer loading	E_{oed}^{ref}	MPa	25	36
Unloading/reloading stiffness	E_{ur}^{ref}	MPa	80	110.8
Stress level dependency power	m		1.0	0.5
Dilatancy angle	ψ	°	0	0
Angle of friction	φ	°	–	28
Cohesion	C'	kPa	10	5
Shear strain at $G_s = 0.7\ G_o$	$\gamma_{0.7}$	MPa	0.00012	–
Shear modulus at very small strain	G_o^{ref}	MPa	180	–
Poisson's ratio	ν_{ur}		0.2	0.2
Reference pre-consolidation	P_{ref}	kPa	100	100
K_o for normally consolidated soil	K_o		1.0	0.5305

history data of the earthquake along with its Fourier spectrum with 0.45 g peak ground acceleration (PGA) is shown in Fig. 2. The loading was applied to the model at the bedrock level.

2.3 Boundary Conditions

Sensitivity studies have been conducted on the chosen soil model to fix the geometric boundary and element size. PLAXIS offers three types of boundary conditions for dynamic analysis namely, viscous, free field and compliant base. In the present study for x_{min} and x_{max} free field boundary condition was used and for z_{min} complaint base was used.

3 Site Response Results for Liquefiable Soil Layer Sandwiched Between Non-liquefying Soil Layers

The soil profile 1 consists of liquefiable soil layer sandwiched between two non-liquefiable soil layers. Different models with varying thickness of soil layer are

Table 3 Soil parameters used in the present study for liquefiable soil

Parameter	Symbol	Unit	Liquefiable soil
Material model			UBC3D-PLM
Drainage type			Undrained (A)
Soil unit weight, saturated	γ_{sat}	kN/m^3	20
Soil unit weight, unsaturated	γ_{unsat}	kN/m^3	18
Elastic bulk modulus	${k^*}_B{}^e$	–	877
Elastic shear modulus	${k^*}_G{}^e$	–	1100
Elastic plastic modulus	${k^*}_G{}^p$	–	310
Elastic bulk modulus index	*me*	–	0.5
Elastic shear modulus index	*ne*	–	0.5
Plastic shear modulus index	*np*	–	0.4
Constant volume friction angle	φ_{cv}	°	33°
Peak friction angle	φ_p	°	33.8°
Cohesion	*c*	kPa	0
Tension cutoff	σt	–	0
Atmospheric pressure	P_{ref}	kPa	100
SPT value	$N_{1,60}$	–	8.0
Post liquefaction factor	f_{Epost}	–	0.6
Failure ratio	R_{f}	–	0.9

Table 4 Material properties for bed rock formation

Parameter	Symbol	Unit	Value
Material model	–	–	Linear elastic
Drainage type	–	–	Drained
Soil unit weight, saturated	γ_{sat}	kN/m^3	22
Soil unit weight, unsaturated	γ_{unsat}	kN/m^3	22
Elastic modulus	*E*	kN/m^2	8,011,000
Poisson's ratio	ν_{ur}	–	0.2

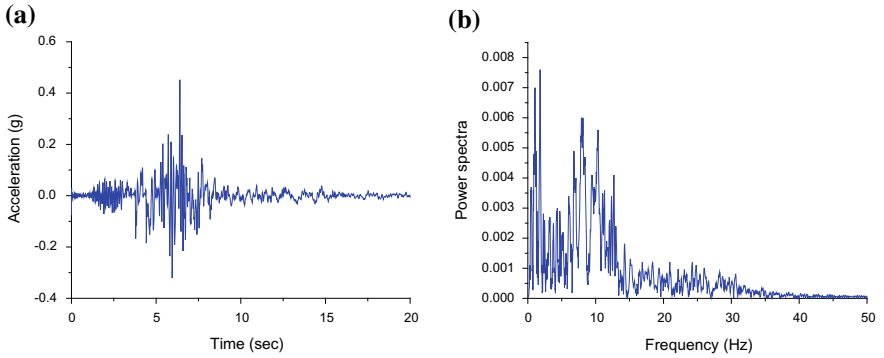

Fig. 2 **a** Acceleration time history of 1995 Kobe earthquake, **b** Fourier spectrum of 1995 Kobe earthquake

subjected to Kobe earthquake of 1995. The results that have been drawn from the analysis are described as follows.

3.1 Acceleration Time History, Excess Pore Pressure Development and Displacement at the Surface

Figure 3a shows the acceleration time history graph for model 1 at surface and the input ground motion. It is clear from the figure that both the accelerations are in phase till the time period of 4.5 s. Once the excess pore pressure reaches 118 kN/m^2, r_u (where r_u is pore water pressure ratio) is found to be greater than 0.9 and beyond 5 s, the liquefiable soil (2 m depth in the second layer) is completely liquefied which resulted in the attenuation of ground acceleration. However, it can be inferred that till the liquefaction occurs, the amplitude of acceleration reaching the surface was more (i.e. amplified till 4 s). As the depth of liquefiable soil layer increases, the attenuation effect also increases, i.e. the amplitude of the acceleration reaching the surface is very low. However, it is to be noted that after the full liquefaction of the middle liquefiable soil layer, the increase in the depth of the liquefiable layer from 8 m to 12 m has not caused any major change in the attenuation of the acceleration, i.e. the effect of 8 m liquefied and 12 m liquefied soil is approximately same after 5 s (after full liquefaction). Figure 3b shows the variation of excess pore pressure development with respect to time for all the models at the centre of the liquefiable soil layer. Much variation has been observed from 4 to 6.5 s, i.e. during the time from start of the liquefaction to just before the full liquefaction.

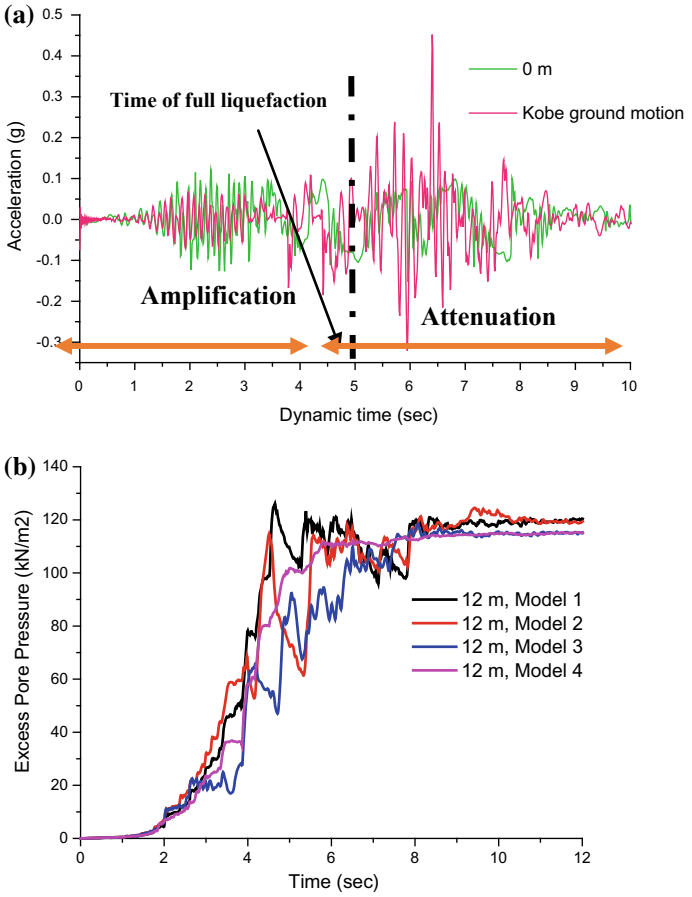

Fig. 3 **a** Acceleration time history for model 1 at surface level (i.e. at 0 m) and the input motion, **b** excess pore pressure versus time for all models

4 Site Response Results for Non-liquefying Soil Layer Sandwiched Between Liquefiable Soil Layers

The soil profile 2 consists of non-liquefiable soil sandwiched between two liquefiable soil layers, Different models such as Model 1, 2, 3 and 4 with varying thickness of soil layers are subjected to Kobe earthquake of 1995. The results such as acceleration and displacement time history, Psuedo spectral acceleration and development of excess pore pressure are discussed below for the soil profile 2.

4.1 Acceleration Time History, Excess Pore Pressure Development and Displacement History at the Surface

Figure 4a shows the plot of acceleration versus time at the surface (i.e. 0 m depth) along with the input ground motion for Model 1. It can be inferred from the figure that the acceleration has been de amplified after 4 s. Before 4 s, accelerations at the ground surface were higher than the input ground motion. The bottom liquefiable soil

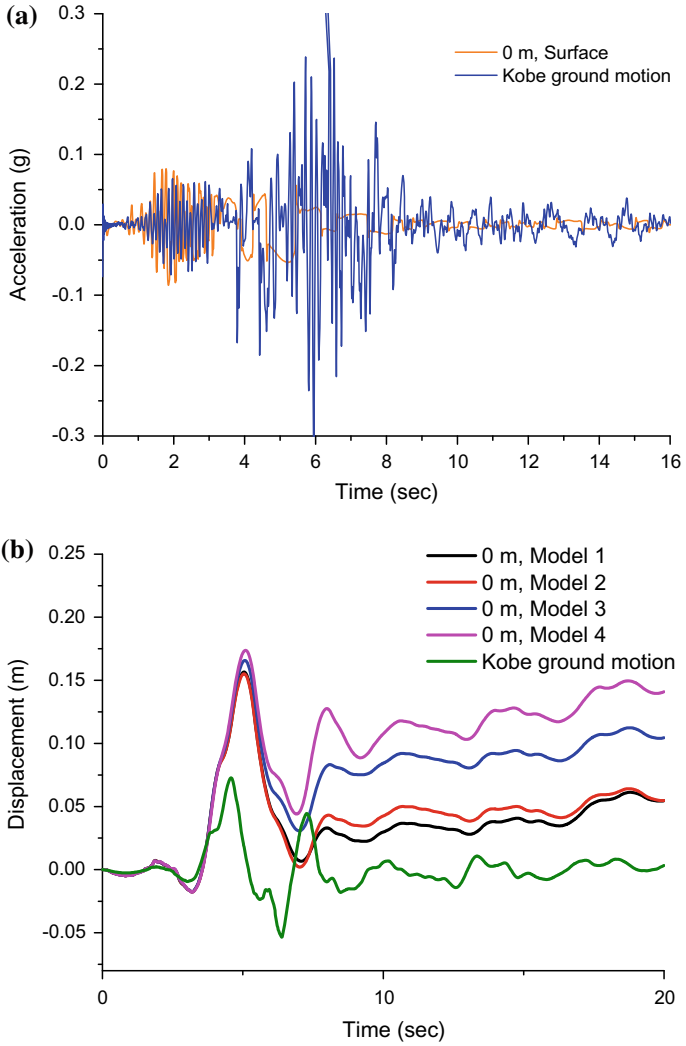

Fig. 4 **a** Acceleration versus time at the surface and the input ground motion for model 1, **b** displacement versus time plot for all models

layer started liquefying around 6 s and complete liquefaction occurred at 8 s. This delay in liquefaction of top and bottom liquefiable layers can be attributed to the fact that the liquefaction occur top-down and here the top layer liquefied first and then the bottom layer. Study also inferred that effect of increase in depth of non-liquefied soil layer is negligible because once the soil liquefies completely; irrespective of the thickness of non-liquefiable soil layer the acceleration amplitudes were attenuated.

Figure 4b shows the displacement variation in all models. It is clear from the figure that increase in the thickness of the non-liquefied soil results in higher displacement as the depth of the soil undergoing liquefaction reduces. Hence, the attenuation reduces from models 1 to 4 which resulted in higher displacement.

5 Amplification of Frequencies in Soil Profile 1 and 2

Figure 5a, b shows the amplification of various frequencies for soil profiles 1 and 2, respectively. In case of soil profile 1 where there is a liquefiable soil layer in between two non-liquefiable soil layers, it was found that the amplification factor decreased with increase in the thickness of the liquefiable soil layer (Fig. 5a). Even in case of soil profile 2, the amplification factor reduces with increase in the thickness of the non-liquefiable soil layer. In case of soil profile 1, low frequencies were amplified where as in soil profile 2, the frequencies amplified varied from 1 to 12 Hz. It can be inferred that both non-liquefiable soil layer as well as liquefiable soil layer showing reduced amplification factor.

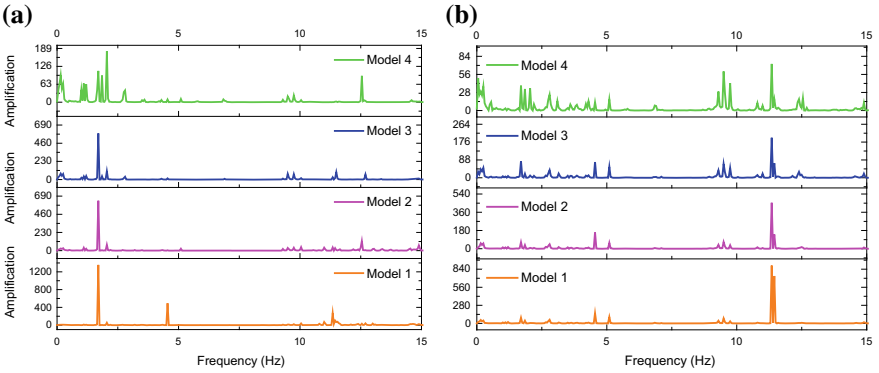

Fig. 5 Amplification of frequencies for **a** soil profile 1, **b** soil profile 2

6 Conclusion

The present study investigates seismic wave propagation in a layered liquefiable soil deposit. Two soil profiles were considered in the study with varying soil thickness and are subjected to typical ground motion of 1995 Kobe earthquake. The results such as acceleration time history, pore water pressure development displacement time history, amplification effects were discussed.

Soil profile 1 consists of two non-liquefiable soil layers and a liquefiable soil layer sandwiched between them. It was observed that after the onset of full liquefaction of liquefiable soil, the acceleration amplitudes observed at the ground level were attenuated. This effect was found to be increasing with increase in the thickness of the liquefied soil. Soil profile 2 consists of two liquefiable soil layer and a non-liquefiable soil layer sandwiched between them. Even in this case the acceleration amplitudes were attenuated because of full liquefaction of liquefiable soil layers. However, when the thickness of the sandwiched non-liquefiable soil layer increased, the attenuation of acceleration amplitude was less as compared to the models where the thickness of non-liquefiable soil layer is less. It was found that the variation in the thickness of the non-liquefiable soil layer effect displacement time history. It can be inferred from the study that if a subsoil layer liquefies then it will attenuate the acceleration amplitude reaching the surface; this can be advantageous in designing the structures with shallow foundations because of resulting lesser inertial forces. However, it is evident from the literature that liquefaction of subsoil may result in excessive settlement and tilting without any major damage to the superstructure.

Acknowledgements The first author would like to thank Ministry of Human Resources Department (MHRD), Government of India for providing financial assistance during the research work.

References

1. Bouckovalas GD, Tsiapas YZ, Theocharis AI, Chaloulos YK (2016) Ground response at liquefied sites: seismic isolation or amplification? Soil Dyn Earthq Eng 91:329–339
2. Youd TL, Carter BL (2004) Influence of soil softening and liquefaction on spectral acceleration. J Geotech Geoenvironmental Eng 131(7):811–825
3. Hadjian AH, Anderson D, Tseng WS, Tsai NC, Chang CY (1991) The learning from the large scale Lotung soil-structure interaction experiments. In: Proceedings of the 2nd International Confernce on Recent Advances in Geotechnical Earthquake Engineering and Soil Dynamics, University of Missouri at Rolla, Rolla, Mo. 3, pp 2047–2070
4. Trifunac MD, Todorovska MI (1996) Nonlinear soil response—1994 Northridge, California, earthquake. J Geotech Eng 122(9):725–735
5. Trifunac MD, Hao TY, Todorovska MI (1999) On recurrence of site specific response. Soil Dyn Earthq Eng 18(8):569–592
6. Kokusho T (2014) Seismic base-isolation mechanism in liquefied sand in terms of energy. Soil Dyn Earthq Eng 63:92–97
7. Kanai KA (1966) short note on the seismological features of the Niigata earthquake. Soils Founds VI(2):8–13

8. Photographs in Records of Niigata Earthquake (1964) Niigata Nippou News Company (in Japanese)
9. Adalier K, Zeghal M, Elgamal AW (1997) Liquefaction mechanism and counter measures. Seismic behaviour of ground and geotechnical structures. In: Proceedings of discussion special technical session on earthquake geotechnical engineering during 14. International conference on soil mechanics and foundation engineering, Hamburg, Germany, 6–12 Sept 1997, pp 155–162
10. Lai S, Morita T, Kameoka T, Matsunaga Y, Abiko K (1995) Response of a dense sand deposit during 1993 Kushiro-Oki earthquake. Soils Found 35(1):115–131
11. Sato K, Kokusho T, Matsumoto M, Yamada E (1996) Nonlinear seismic response and soil property during strong motion. Soils Found, 41–52
12. Matsui T, Oda K (1996) Foundation damage of structures. Soils Found 36:189–200
13. Kokusho T, Motoyama R (2002) Energy dissipation in surface layer due to vertically propagating SH wave. J Geotech Geoenvironmental Eng 128(4):309–318
14. Yoshida N, Tokimatsu K, Yasuda S, Kokusho T, Okimura T (2001) Geotechnical aspects of damage in Adapazari city during 1999 Kocaeli, Turkey earthquake. Soils Found 41(4):25–45
15. Tokimatsu K, Tamura S, Suzuki H, Katsumata K (2012) Building damage associated with geotechnical problems in the 2011 Tohoku Pacific earthquake. Soils Found 52(5):956–974
16. Petalas A, Galavi V (2013) PLAXIS liquefaction model UBC3D-PLM. Technical report, PLAXIS
17. http://peer.berkeley.edu/peer_ground_motion_database, accessed on 22 Aug 2018

Effect of Soil Spatial Variability on Lateral Response of Well Foundation Embedded in Linear Elastic Soil

Ramyasri Rachamadugu, Sanshrit Singhai and Gyan Vikash

Abstract This paper presents, the effect of soil spatial variability on response of laterally loaded well foundation embedded in linear elastic soil medium. The spatial variation of elastic modulus of soil along embedment depth of the foundation is modeled using random field theory. Elastic modulus of soil is considered to be random variable that follows Log-Normal probability distribution. Monte Carlo simulation technique is used to generate various random realization of spatial variability of elastic modulus of soil. Random realization is done for different values of coefficient of variation of elastic modulus with different spatial correlation distance. A finite element model is developed for laterally loaded well foundation embedded in linear soil. The finite element model is then coupled with the random field of elastic modulus of soil to analyze effect of soil spatial variability on the response of well foundation under different values of lateral load. The results obtained from this study indicate that spatial variation of soil elastic properties has small effect on lateral response of well foundation irrespective of magnitude of lateral load.

Keywords Spatial variability · Random soil · Lateral load · Well foundation

1 Introduction

Well foundation is commonly used in India for road and railway bridges constructed over a river. This foundation is used when no firm bed is available for large depth below the ground surface and the topsoil is liable to scour [5–8]. Although it is commonly used in practice, only a few analytical models are available to analyze a well foundation under different loading conditions [3, 4, 10]. Apart from this, the studies available on lateral response of well foundation are deterministic which considers surrounding soil medium as a single homogeneous layer idealized with mean value of soil's mechanical properties. However, in reality, natural soils are heterogeneous and random in their physical and mechanical properties because of their mode of

R. Rachamadugu · S. Singhai · G. Vikash (✉)
Shiv Nadar University, Gautam Buddha Nagar, Uttar Pradesh, India
e-mail: gyan.vikash@snu.edu.in

A. Prashant et al. (eds.), *Advances in Computer Methods and Geomechanics*, Lecture Notes in Civil Engineering 55,
https://doi.org/10.1007/978-981-15-0886-8_35

formation. The mechanical properties of soil vary significantly from one location to other. The variation of mechanical properties of soil in spatial domain may lead uncertainty in response estimation of geotechnical structure. In the past, several random field generator algorithms have been developed. These are moving average methods, Discrete Fourier transforms method, Covariance matrix decomposition, Fast Fourier transform method, Turning band method, and Local subaverage subdivision method [1]. Among these available algorithms, Fenton and Griffiths [2] found Local subaverage subdivision method more suitable to generate random field for spatially varying soil domain. In the present study, random field theory developed by Fenton and Griffiths [2] is used to model the random variability of soil properties in spatial domain along embedment depth of the foundation. A finite element model is developed for laterally loaded soil-well foundation system. The present finite element model models the well foundation by Euler–Bernoulli beam element and surrounding soil by Winkler springs proposed by Varun et al. [10]. Random field theory and the finite element model are then coupled to study the effect of soil spatial variability on the response of laterally loaded soil-well foundation system. The elastic modulus of soil is considered herein as random variable using Log-Normal probability distribution. Different values of correlation distance and coefficient of variation are considered to represent varying degrees of randomness of elastic modulus of soil in spatial domain. Monte Carlo simulation is performed to obtain multiple realizations of the random variable. Subsequently these realizations are fed into the finite element model developed herein to compute the response of soil-well foundation system under lateral loading condition.

2 Problem Definition and Analysis Methodology

2.1 Problem Definition

Well foundation is a type of deep foundation which is hollow from inside. The hollow portion of well foundation is generally filled with sandy soil. The circumferential portion of well foundation, which is known as well steining, is generally made of reinforced concrete with minimum M25 concrete [8]. Top and bottom parts of well foundation are filled with plane concrete. Well foundation is commonly used in India for road and railway bridges over a river with alluvial deposit. For most of the railway bridges in India over Ganga River, external diameter of well foundation varies from 9 to 18 m and depth of the foundation varies from 30 to 70 m [8]. Thickness of well steining is generally taken from 3 to 5 m.

The studied problem is shown in Fig. 1. A well foundation with depth 65 m, external diameter 12 m, and internal diameter 9 m is considered in this study. Hollow portion of the well foundation is filled with sandy soil whereof modulus of elasticity is

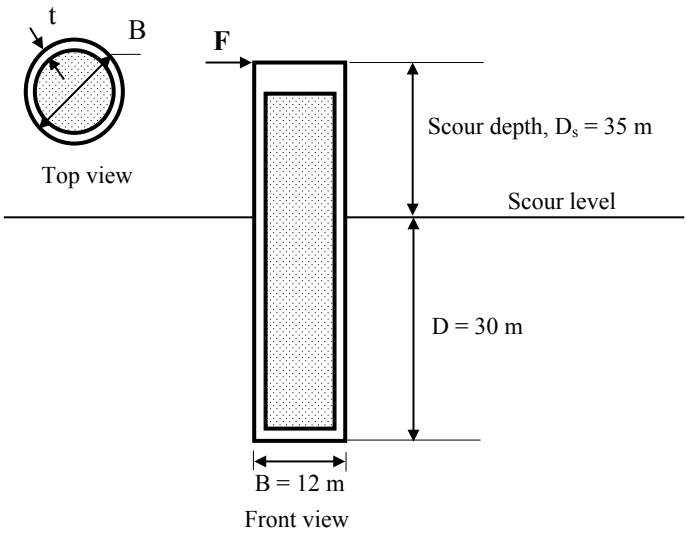

Fig. 1 Schematic diagram of the well foundation considered in the present study

50 MPa. Scour depth is considered 35 m and embedment depth is considered 30 m. Mean value of Modulus of elasticity of embedment soil, which supports the well foundation, is considered 50 MPa. It is considered that the well foundation is made of M30 reinforced concrete, which has modulus of elasticity 27 GPa. It is according to the relation given in IS 456: 2000. In order to understand lateral response of well foundation considered herein, lateral loads of different magnitudes are applied at the top of well foundation. In the present problem, scour depth acts like eccentric distance for the lateral load. Present analysis has been done for lateral load of 15 KN, 1000 KN, and 5000 KN, respectively.

2.2 Winkler Model for Analysis of Well Foundation

In the present study, well foundation is modeled by Euler–Bernoulli beam element. Modeling the well foundation by Euler–Bernoulli beam element allows consideration of flexibility of the foundation in the analysis. Modulus of elasticity of well foundation filled with sandy soil is obtained 8 GPa. It is determined by considering well-filled soil system as composite system. Four-spring model is implemented to model the surrounding soils as shown in Fig. 2. This model has potential to represent complex resistance mechanisms developed at the soil-foundation interface [3]. Varun et al. [10] reported that the contribution of base rotation spring $K_{b\theta}$ decreases significantly with *D/B* ratio, and it becomes almost negligible for *D/B* is greater than 0.75. As *D/B* ratio of the well foundation considered in the present study is 2.5, therefore $K_{b\theta}$ is neglected

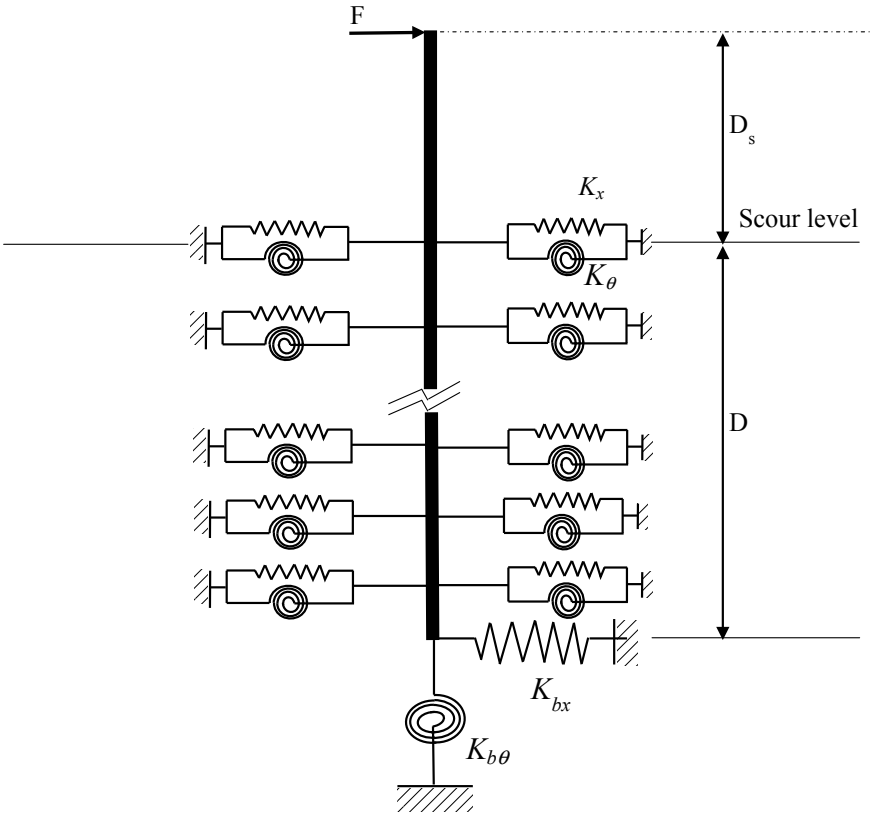

Fig. 2 Modeling of soil-well foundation system by four-spring Winkler model

in this study. Expression derived for lateral spring K_x, rotational spring K_θ, and base lateral spring K_{bx} by Varun et al. [10] is considered herein to determine the value of other three springs. The expressions for K_x, K_θ, and K_{bx} as a function of embedment depth D, Diameter B, and modulus of elasticity E of soil, considered herein are as follows:

$$\frac{K_x}{E} = 1.828\left(\frac{D}{B}\right)^{-0.15} \tag{1}$$

$$\frac{K_{bx}}{EB} = 0.669 + 0.129\left(\frac{D}{B}\right) \tag{2}$$

$$\frac{K_\theta}{EB^2} = 1.106 + 0.227\left(\frac{D}{B}\right) \tag{3}$$

Opensees, a finite element based numerical code, is used in the present study to analyze the soil-well foundation system. Well foundation in discretized into a number of beam elements with different element sizes to perform sensitivity analysis. Sensitivity analysis yields size of 0.25 m beam element as optimum element size for the present analysis.

2.3 Modeling Soil Spatial Variability

The random field model proposed by Fenton and Griffiths [2] is used to model spatial variability of soil mechanical properties. Fenton and Griffiths [2] developed the random field model following local average subdivision approach. As the soil-well foundation system is modeled as one-dimensional problem, therefore randomly varying soil mechanical properties are generated along the embedment depth of the well foundation. The spatial variation of soil properties is represented by the mean value, coefficient of variation and correlation distance. Correlation distance θ is the parameter which is used to measure spatial variability of in situ soil. In reality, large amount of data is required to quantify accurately correlation distance. However, it is observed that θ varies within the range of 10–40 m in horizontal direction and 0.5–3 m in vertical direction [9]. The variation in θlargely depends on composition of the soil, stress history, and depositional mechanism. The present study considers elastic modulus E as random variable. It is considered that E follows Log-Normal distribution which is characterized by parameters μ_E, standard deviation σ_E and spatial correlation distance θ. A Log Normally distributed random field if defined as

$$E(z) = \exp\{\mu_{\ln E}(z) + \sigma_{\ln E}(z).G(z)\} \tag{4}$$

where z is the spatial location at which E is to be determined. G is defined as multiplication of lower triangle of correlation matrix obtained by LU decomposition with a randomly generated number having zero mean and unit variance.

The value of $\mu_{\ln E}$ and $\sigma_{\ln E}$ can be determined as

$$\sigma^2_{\ln E} = \ln\left(1 + \frac{\sigma_E^2}{\mu_E^2}\right) = \ln\left(1 + \mathrm{COV}_E^2\right) \tag{5}$$

$$\mu_{\ln E} = \ln \mu_E - \frac{1}{2}\sigma^2_{\ln E} \tag{6}$$

Further, distance-dependent spatial correlation coefficient is defined as

$$\rho_E = \exp\left(-\frac{2\tau}{\theta}\right) \tag{7}$$

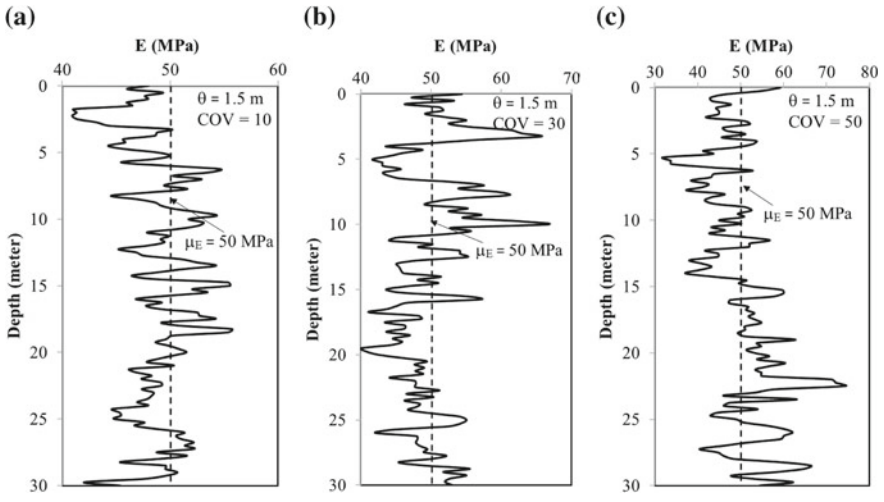

Fig. 3 Typical plot showing one realization of random field, **a** COV = 10%, $\theta = 1.5$ m; **b** COV = 30%, $\theta = 1.5$ m; **c** COV = 50%, $\theta = 1.5$ m

where τ is the absolute distance between the two points. Cholesky decomposition is used to obtain a correlation matrix. Monte Carlo simulation method is used to generate several realizations of 1D Log-Normal random field of E. In the present study, 200 random realizations have been done for $\mu_E = 50$ kPa with different values of COV (10, 30, and 50%) and correlation distance (1.5, 5.0, 15, and 50 m).

Figure 3 shows a typical plot showing one realization of Monte Carlo simulation for $\theta = 1.5$ m and COV = 10%, 30%, and 50%, respectively. It can be observed from this figure that for COV = 10%, 30% and 50%, range of E lies between 42–55 MPa, 40–65 MPa, and 30–70 MPa, respectively.

It can be therefore inferred from Fig. 3 that for given correlation length θ variation in E increases with increase in COV.

3 Results and Discussion

Table 1 shows different combinations of θ and COV for which analysis has been done. Case A consists of minimum randomness in elastic modulus E and Case L allows maximum randomness in E values. Influence of randomness of E is analyzed by comparing the response obtained from random values of E with that of mean value of E. Figure 4 shows the variation of lateral displacement of foundation, soil reaction, bending moment and shear force along the depth of the foundation for 15 KN lateral load for mean value of E and random values of E obtained for case L. Case L consists of combination of highest value of θ and COV. Thus it will yield highest spatial variability in E among other cases. From Fig. 4 it can be observed

Table 1 Different cases considered for present analysis

Cases	Correlation length (θ)	Coefficient of variance (COV %)
A	1.5	10
B	1.5	30
C	1.5	50
D	5	10
E	5	30
F	5	50
G	15	10
H	15	30
I	15	50
J	50	10
K	50	30
L	50	50

that for mean value of *E*, lateral displacement, maximum value of soil reaction, bending moment and shear force are obtained to be 21 mm, 7.86 KN, 526.78 KN m and 55.38 KN, respectively. The influence of randomness in *E* is evident in soil reaction along the depth as shown in Fig. 4b. However, insignificant variation in soil reaction, bending and shear force is observed for spatially random values of *E* as depicted in Fig. 4. Figure 5 shows variation in responses to different cases. It indicates variability in values with the help of a box plot and range of variations with minimum and maximum values. Variability in values is noticed for soil reaction, bending moment, and shear force for case L but there is not much variability in displacement response. The range of soil reaction values varies from 8.14 to 3.36 KN, bending moment varies from 527.24 to 525 KN m, shear force varies from 58.86 to 38.77 KN and magnitude of displacement ranges from 21 to 26 mm. The effect of load magnitude and randomness of E on the displacement of foundation have been analyzed with lateral loads 1000 and 5000 kN (Fig. 6). Variability in values increased with increase in magnitude of lateral load but still values are close to that obtained with mean *E*. Range of values for 1000 kN is 1.185–1.78 m and for 5000 KN, it is 7.13–8.9 m. It is to be noted that lateral displacement of foundation calculated with mean value of *E* is 1.43 m and 7.87 m for 1000 and 5000 KN, respectively. This indicates that the values of lateral displacement obtained for spatially random *E* are close to that obtained with mean value of *E*. Therefore, it can be inferred that the soil spatial variability has insignificant effect on lateral response of well foundation in linear elastic soil medium.

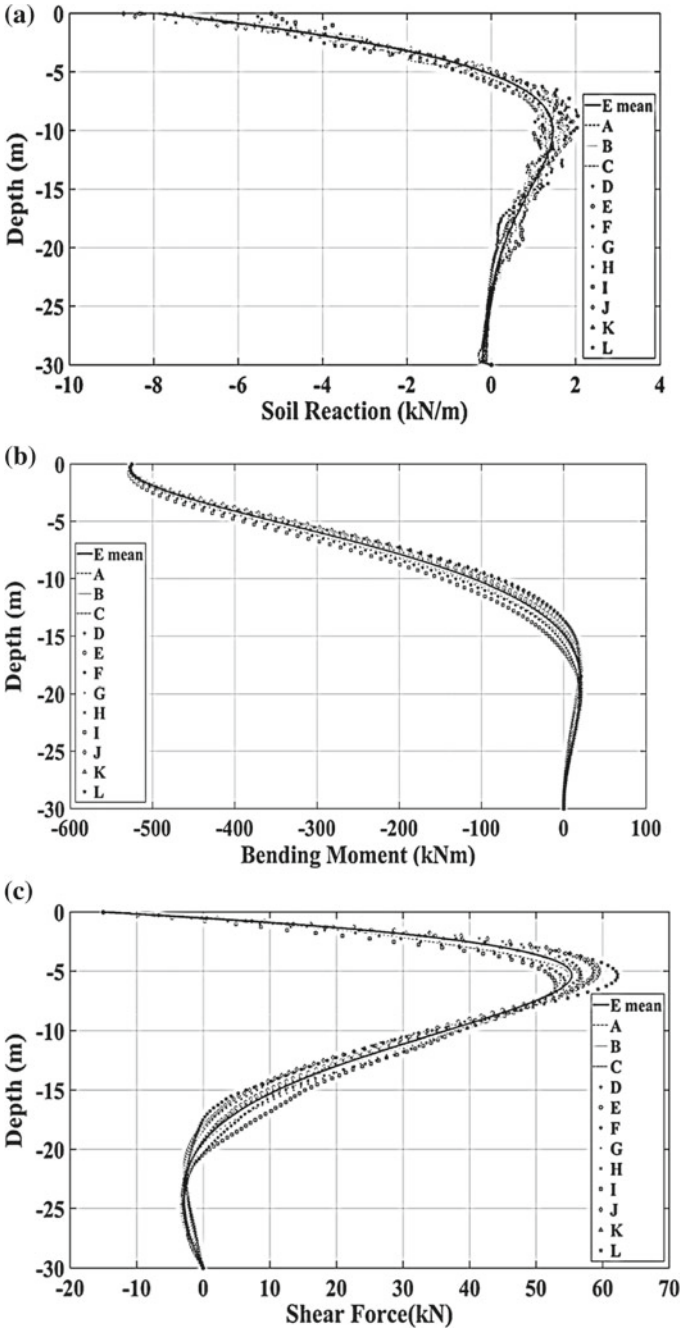

Fig. 4 Response of well foundation for mean value of *E* and random values of *E* for 15 KN lateral load **a** soil reaction, **b** bending moment, **c** shear force

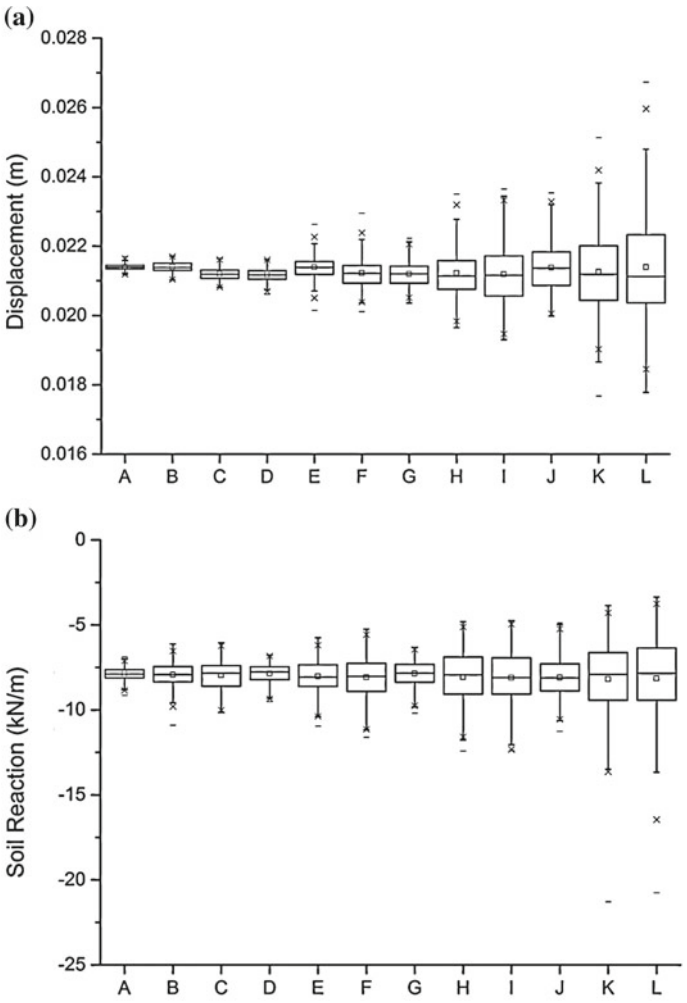

Fig. 5 Variation in **a** displacement, **b** soil reaction, **c** bending moment, **d** shear force over the cases A to L

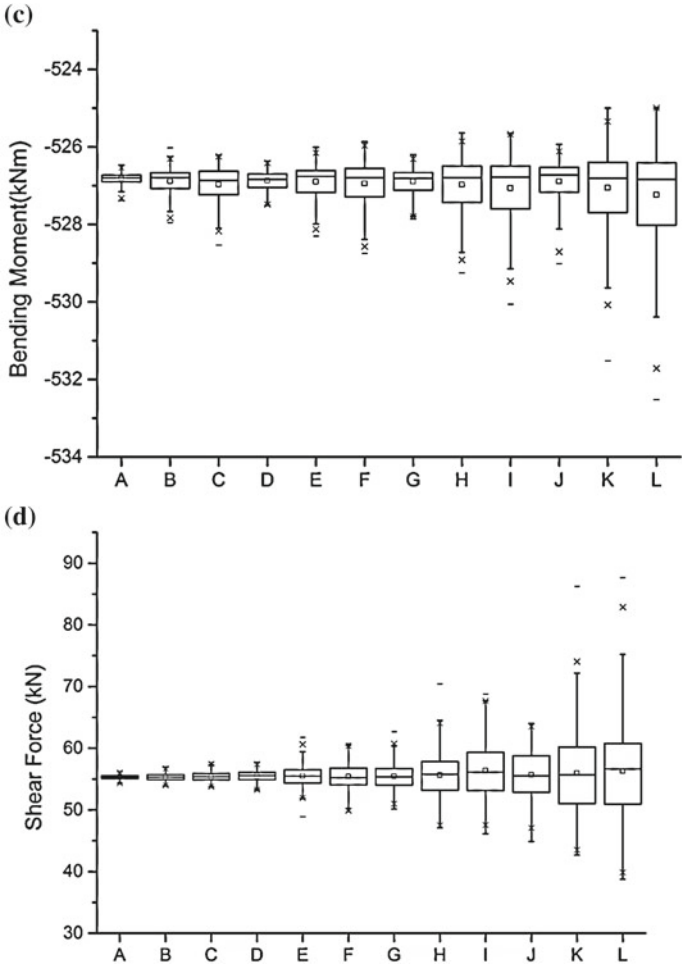

Fig. 5 (continued)

4 Conclusions

In the present paper, the effect of spatial variability of soil mechanical properties on lateral response of well foundation embedded in linear elastic soil medium was studied. The spatial random variability of soil elastic modulus was obtained by using random field theory. Elastic modulus of soil was considered to follow Log-Normal distribution. Monte Carlo simulation technique was used to get multiple realizations of spatially varying elastic modulus for different values of COV with varying spatial correlation length. A finite element model was developed to model soil-well foundation system. Randomly spatially varying elastic modulus of soil, obtained from Monte Carlo simulation, was given as input in the finite element model. The results

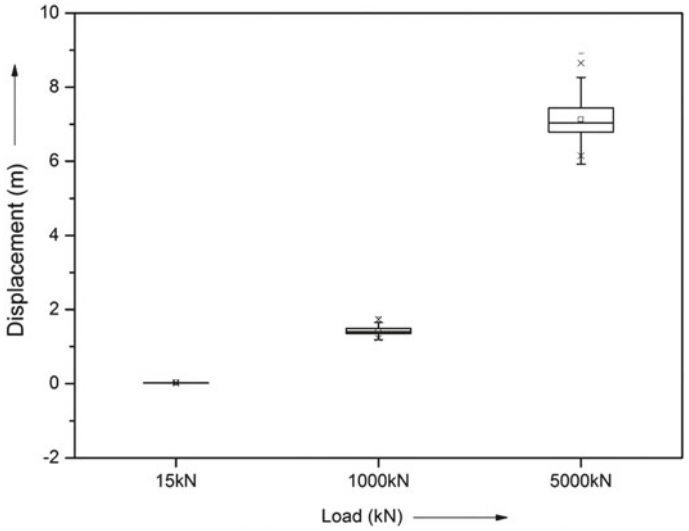

Fig. 6 Variation in lateral displacement for different values of lateral load

obtained in the present study indicate that the spatial variability of elastic modulus of soil has small effect on lateral response of well foundation irrespective of the magnitude of lateral loads.

References

1. Fenton GA (1994) Error evaluation of three random field generators. J Eng Mech ASCE 120(12):2478–2497. https://doi.org/10.1061/(ASCE)0733-9399(1994)120:12(2478)
2. Fenton GA, Griffiths DV (2002) Probabilistic foundation settlement on a spatially random soil. J Geotech Geoenvironmental Eng 128(5):381–390
3. Gerolymos N, Gazetas G (2006) Winkler model for lateral response of rigid caisson foundations in linear soil. Soil Dyn Earthq Eng 26(5):347–361
4. Gerolymos N, Gazetas G (2006) Static and dynamic response of massive caisson foundations with soil and interface nonlinearities-validation and results. Soil Dyn Earthq Eng 26(5):377–394
5. Jain SK (2016) Earthquake safety in India: achievements, challenges and opportunities. Bull Earthq Eng 14(5):1337–1436. https://doi.org/10.1007/s10518-016-9870-2
6. Mondal G, Prashant A, Jain SK (2012) Significance of interface nonlinearity on seismic response of well-pier system in cohesionless soil. Earthq Spectra 28(3):1117–1145. https://doi.org/10.1193/1.4000074
7. Mondal G, Prashant A, Jain SK (2012) Simplified seismic analysis of soil Well-Pier system for bridges. Soil Dyn Earthq Eng 32(1):42–55. https://doi.org/10.1016/j.soildyn.2011.08.002
8. Ponnuswamy S (2008) Bridge engineering, 2nd edn. McGraw Hill Professional
9. Suchomel R, Masin D (2009) Comparison of different probabilistic methods for predicting stability of a slope in spatially variable c-ϕ soil. Comput Geotech 37:132–140
10. Varun, Assimaki D, Gazetas G (2009) A simplified model for lateral response of large diameter caisson foundations—linear elastic formulation. Soil Dyn Earthq Eng 29:268–291

A Comparative Study on the Design of Flexible Faced and Rigid Faced Geosynthetic Reinforced Soil Walls

Kirupairaja Thanushan, Kolli Mohan Krishna and Amit Prashant

Abstract In practice, Geosynthetic reinforced soil (GRS) walls are constructed using different types of fascia with different levels of rigidity. It is believed that fascia does not have any role on the load transfer behavior. It was observed that only RTRI (Railway Technical Research Institute) guidelines of Japan utilizes stability effects provided by the fascia while considering it as rigid and proposes entirely different design approaches compared to the design guidelines in other countries. RTRI guidelines also consider fascia as a load-carrying member in rigid faced GRS walls. This study is focused on the comparative study of design approaches involved in the design of flexible faced GRS walls (BS 8006) and rigid faced GRS walls (RTRI). Some of the key aspects like physical phenomena involved in both design approaches have been explained with a real-life example of design of bridge approach which is located near Bhagur in Nashik, India. An approximate material cost comparison study is also made which showed 30–40% cost reduction with rigid faced systems. Some of the construction and stability advantages of rigid faced GRS walls have been highlighted in this study.

Keywords Design · GRS walls · BS 8006 · RTRI · Flexible fascia · Rigid fascia

1 Introduction

Geosynthetic reinforced soil walls (GRS walls) are widely used in the construction of retaining walls and abutments due to their low cost, reliability, durability, ease in construction and ability to tolerate large deformation without structural failure

K. Thanushan (✉)
University of Jaffna, Kilinochchi, Sri Lanka
e-mail: thanushnov17@gmail.com

K. M. Krishna · A. Prashant
Indian Institute of Technology Gandhinagar, Gandhinagar, India
e-mail: mohan.kolli@iitgn.ac.in

A. Prashant
e-mail: ap@iitgn.ac.in

A. Prashant et al. (eds.), *Advances in Computer Methods and Geomechanics*, Lecture Notes in Civil Engineering 55,
https://doi.org/10.1007/978-981-15-0886-8_36

compared to conventional concrete retaining wall. Those benefits made reinforced earth walls play an important role in the development of infrastructure around the world. Geosynthetic reinforced soil walls typically consist of four components: (1) Reinforcement, (2) Reinforced fill (soil), (3) Fascia and associated connections, and (4) Drainage. The mutual interaction of these components influences the overall mechanical response of the wall. Stiffness of each component impacts the overall behavior and is majorly governed by the reinforcement stiffness, length, and spacing for a given fill [6] a part from fill. In these GRS walls, fascia is not generally considered as structural component instead considered for covering the reinforced fill from erosion and local failures.

In practice, different types of fascia are used to construct GRS walls which have different types of rigidities. Recent studies showed that fascia can play a considerable role in behavior of walls. Tatsuoka [13] reported that full height rigid fascia stabilizes active zone, which is the result of high tensile force of reinforcement produced at fascia creating a high confining pressure within the active zone as reaction. It was also reported that different from the conventional reinforcing method, short planar reinforcement with rigid facing structure is more economical one. Liu et al. [8] also reported that rigidity of fascia forms an additional confining pressure that directly applies back to the reinforced zone. All these studies also reported that there is reduction in the lateral deformations of reinforced zone with increase in global stiffness of fascia and also full earth pressure/maximum reinforcement tension mobilization at rigid facings. It was observed that load can transfer to toe of facing (globally) which resulted in decrease of strains in reinforcement [3]. Allen et al. [1] based on the measurement from the field monitoring developed a new working stress method for internal stability analysis called as "K-stiffness" method which considers stability effects of fascia as one the influence factor. This factor is the result of resistance provided by the stiffness of facing and restraint at toe which reduced the reinforcement forces.

Guidelines like FHWA (No. FHWA-RD-89-043) and BS 8006 do not suggest anything about the design of fascia and its stabilizing effects on reinforced zone, as they depend on the design of flexible faced wall, they suggest to provide sufficient connection strength. EBGEO guidelines have suggested design of fascia for a part or full earth pressure mobilized on facing but does not consider the stabilizing effects of fascia rigidity on reinforced fill. RTRI guidelines (Design standards for railway structures) are the only design guidelines consider stabilizing effects of full rigid fascia. The key steps of rigid faced GRS wall design as per RTRI guidelines include (a) Use shorter reinforcement, (b) Double wedge method of stability analysis with failure plane evolution from toe only, and (c) Design of fascia for full earth pressure by analyzing it as beam connected to springs.

In this study flexible GRS wall design as per BS 8006 and rigid faced wall design as per RTRI guidelines has been carried out to evaluate the consistency in load transfer mechanisms, stability, and economical aspects. In this study, a real case of

highway bridge approach which exists in India was considered for the design as per both guidelines. For the comparison, the wall is designed at three different sections along the alignment while loading conditions were kept constant for both designs.

2 Description of Data for Design

The bridge approach to be constructed near Bhagur in Nashik, India has been considered for this study which has a length of 135 m and width of 24 m with maximum height of 8.8 m and minimum height of 1.9 m as shown in Fig. 1. The soil investigation report showed that morrum soil layer exists till 3 m below the ground level and basalt rock is below morrum and groundwater was not observed up to 13 m depth of investigation. The reinforced soil, backfill soil and foundation soil properties are listed in Table 1.

TechGrid polyester Geogrids U-40, U-60, U-80, U-100, U-120, and U-150 are considered for the design with interaction coefficient of 0.9 for pullout and 0.8 for internal sliding. Wall was divided into three sections according to the height of the wall such as 8.8, 7.3, and 5 m as shown in Fig. 1 and each section is designed as per

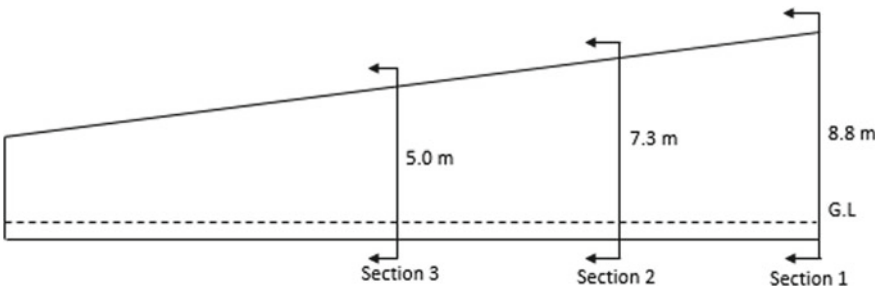

Fig. 1 Side view of the bridge approach

Table 1 Soil properties

Material properties	Friction angle (°)	Unit weight of the soil (kN/m^3)	Cohesion (kPa)
Reinforced fill	30	18	0
Back fill	30	18	0
Foundation fill	32	20	0

both codes with dead load of 15.4 kPa, live load of 24 kPa and strip vertical load due to crash barrier of 12 kN/m.

3 Design of Flexible Faced GRS Wall as per BS 8006

The British standard follows limit state principles which are ultimate limit state and serviceability limit state. Accordingly, the design wall is carried out as per three load combinations where stability of reinforced wall is analyzed to check against external stability and internal stability. The analysis of internal stability is essentially checking against tension failure and ensuring no pullout by providing sufficient anchorage length into the stable soil behind potential failure surface. Failure mode of forward sliding, overturning, internal sliding failure, and bearing failure were considered in external stability. Settlement of foundation and deformation in wall are considered in serviceability limit state with load combination C which consider the dead load only with partial load factor of one and does not include the live load. Tie back method is generally used for walls with extensible reinforcement and coherent method is used for walls with inextensible reinforcement. In this study only tie back wedge method is used which involves linear failure wedge.

The strengths of reinforcement used in BS 8006 are listed in Table 2. As this study is to compare both flexible and rigid fascia designs, 0.3 m spacing is fixed which is suggested as vertical spacing by RTRI. The MSEW software is used to design the reinforced wall as per BS 8006. The final designs of the three sections as per BS 8006 are shown in Table 3 and Fig. 2.

Table 2 Long-term design strength of reinforcement as per BS 8006

Property	U-40	U-60	U-80	U-100	U-120	U-150
Short term strength (kN/m)	40	60	80	100	120	150
Long-term strength (kN/m)	19.2	28.9	38.5	48.1	57.7	72.2

Table 3 Design details of three sections

Section	Height of wall, H (m)	Length of geogrid, L (m)	Reinforcement strength (kN/m)
1	8.8	9.4	150
2	7.3	8	120
3	5	6	100

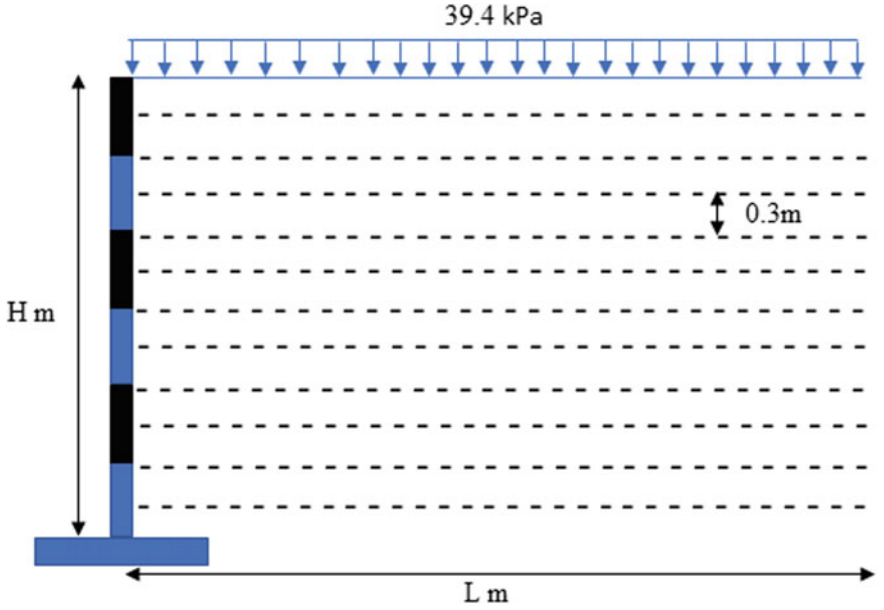

Fig. 2 Designed flexible wall section

4 Design of Rigid Faced GRS Wall as per RTRI (Japanese Code)

Design standards for Railway Structures of Japan (of RTRI) consider the stability effects provided by the rigid fascia and accordingly developed their design method for the GRS walls. This code follows performance-based design with limit state design procedure. The performance-based design suggests three required performance such as safety performance, serviceability performance, and restorability performance. Rupture of reinforcement, pull out of reinforcement, and stability of supporting ground, wall external stability, and wall internal stability are checked under the safety performance. The appearance is evaluated in serviceability performance. Wall residual displacement and wall damage are accounted in restorability performance.

RTRI, which considers different kinds of reduction factors compared to BS 8006 such as alkaline reduction factors, mechanical reduction factors, creep reduction factors, material reduction factors, instant load reduction factors, and trainload reduction factors results in different long-term strength as shown in Table 4.

As per the design, reinforcement should be placed at the spacing of 0.3 m and the reinforcement has to be placed up to the line drawn from the toe of wall at the angle equal to the internal friction angle of the backfill for every 1.5 m height. The same is shown in Fig. 4. Wall internal stability has two failure modes which are overturning and sliding failure of fascia with reinforcement connected to it and anchored in stable zone. The wall external stability accounts the overall slip circle

failure. The reinforcement tension failure is checked by force developed in spring when fascia is modeled as beam column with reinforcement as springs and loaded with a rest earth pressure. So, the fascia should be a full height rigid fascia. The facing of reinforced wall is modeled in SAP 2000 as continuous beam supported by a series of spring which is represented reinforcement layer and beam subjected to earth pressure as external force as shown in Fig. 3. From the bending moments and shear force developed, fascia having height of 8.8 m is designed with thickness of 0.3 m at the top, 0.4 m at bottom with concrete grade M-30. Bending moment and deflection have been found to be safe. The stiffness of springs is to be taken as strength of reinforcement at 5% strain over 1.5 m length of reinforcement. A code developed in MATLAB is used to check walls internal stability for double wedge method and Geo 5 is used to check global stability. The final design as per RTRI is given in Table 5 and Fig. 4. The line drawn at angle of friction angle in Fig. 4 should not be confused with failure wedge as it represents the maximum line till which reinforcement has to be extended.

Table 4 Long-term design Strength of reinforcement as per RTRI

Property	U-40	U-60	U-80	U-100	U-120	U-150
Short term strength (kN/m)	40	60	80	100	120	150
Long-term strength (kN/m)	16	24	32	40	48	60

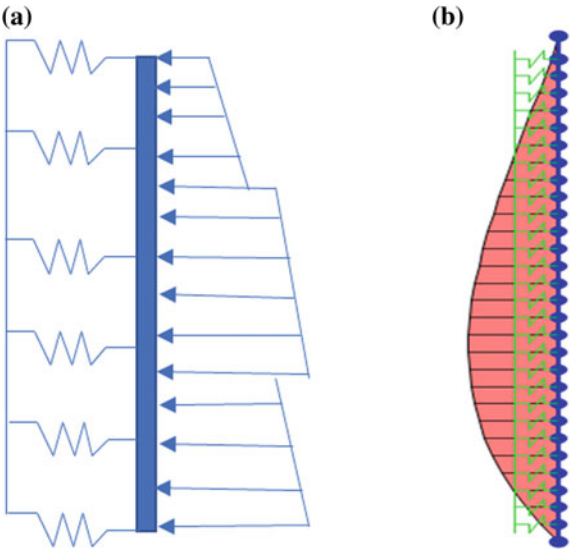

Fig. 3 (**a**) 1-D model and (**b**) bending moment diagram of the fascia as per RTRI

Table 5 details of final three design section as per RTRI

Section	Height of wall (m)	Length of geogrid (m)	Strength of geogrid (kN/m)	Normal layers	Extended layers
1	8.8	4	150	23	5
2	7.3	3.5	120	19	4
3	5	3	100	13	3

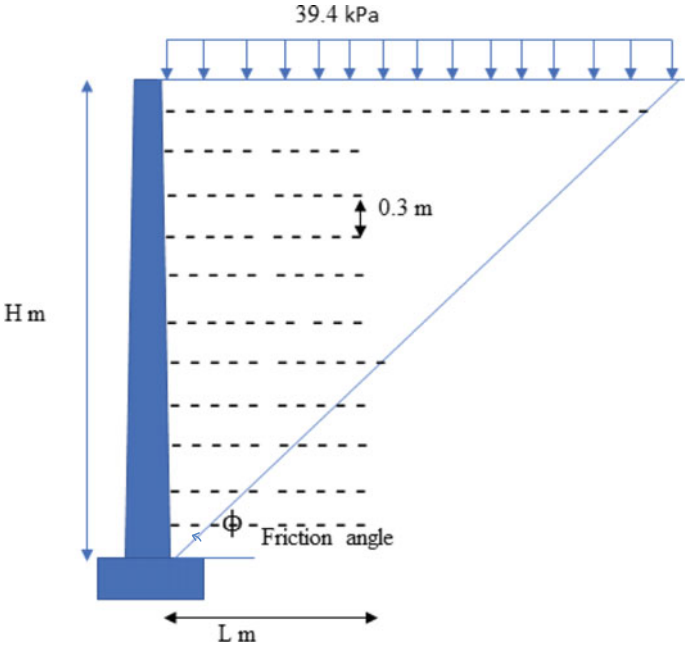

Fig. 4 Designed section as per RTRI

5 Comparison of Design

5.1 Configuration

In general, 0.7H is the minimum reinforcement length as per BS 8006, while, 0.6 m is the restriction for maximum vertical spacing. Maximum of 1.5 m and 0.35H is to be used as minimum reinforcement length in rigid faced wall with constant vertical spacing of 0.3 m as per RTRI. The final design of bridge approach walls resulted in reinforcement length equal to H and 0.4H, respectively, for flexible and rigid wall. There is considerable difference in the length of reinforcement, i.e., base width of

wall among two design codes. This is due to the considerations of difference in the load resistance mechanisms of two systems followed by the two codes. Flexible walls as per BS code involves whole internal load to be resisted by the reinforcement itself. While in the rigid faced wall system, the weight component of fascia is going to come into picture. The earth pressures are resisted by base resistance of fascia and tensile force of reinforcement behind failure wedge. In a way this is a hybrid system, where load is distributed among the fascia and reinforcement. This can be thought of a gravity wall (fascia) tied into the retained soil by reinforcement. The whole load should be taken by reinforcement in flexible wall while fascia and reinforcement share the load in rigid fascia wall, so that small length of reinforcement is good as per RTRI.

Further, both BS 8006 and RTRI code are silent about the minimum vertical spacing of reinforcement which should be specified for the full mobilization of the force in the reinforcement. BS 8006 specified the maximum vertical spacing as 0.6 m while RTRI code fixed the vertical spacing as 0.3 m that cannot be changed.

5.2 Earth Pressure Force

Rankine and coulomb wedge method can be used to find out the earth pressure acting on the reinforced fill made of extensible reinforcement by assuming the active condition throughout the wall for both ultimate and serviceability limit states in BS 8006. Coherent gravity method is used for inextensible reinforcement used reinforced wall with the assumption of active earth pressure that is acting on the bottom of the wall and at rest earth pressure at the depth 6.0 m and constant beyond 6.0 m depth. Using those two methods mentioned above, the lateral force is calculated in flexible wall. Several failure planes have to be investigated as the failure planes in flexible fascia system can evolve from any level of fascia.

Two-wedge stability analysis is the fundamental approach of rigid wall to compute the earth's pressure that acting on the wall facing. As fascia is rigid, failure planes can only start from the toe of the wall. In two-wedge method, for various failure plane angles and reinforcement load mobilized in the cut portion (minimum of pullout and breaking force) the minimum factor of safety against sliding and overturning is calculated by equilibrium. Since the minimum of long-term design strength and pullout resistance is taken as force on the Geogrid, the maximum earth pressure does not necessarily provide the minimum factor of safety. The wedge destabilizing force is resisted by the force mobilized in the anchored reinforcement and the weight of fascia. It was assumed that the reinforcement which was cut the failure plane only will resist the force, but not all the reinforcements. The equilibrium equations of two-wedge method have been solved using MATLAB to get directly factor of safety values. The schematic free body diagram of two-wedge method is shown in Fig. 5.

Fig. 5 Two-wedge method

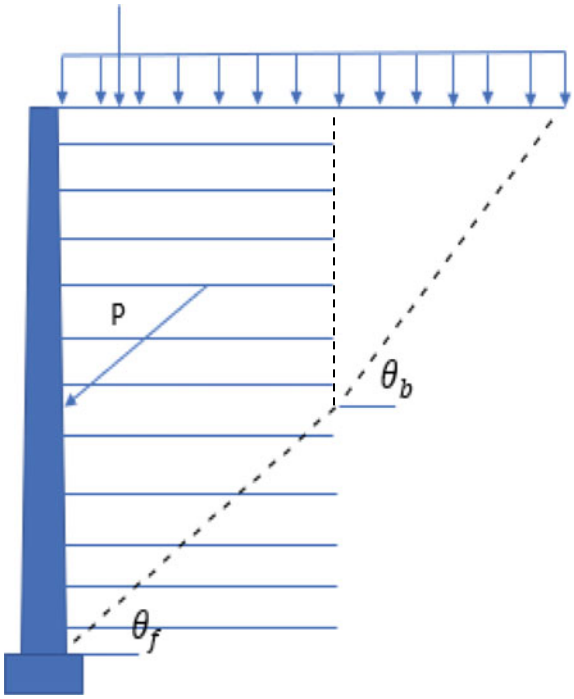

5.3 Fascia

The BS codes commonly suggest the flexible fascia of discrete panel, full height panel, wrap-around facing and segmental block facing even though they vary in their stiffness relatively Flexible fascia is only intended to prevent local failure, accommodates settlement and gives esthetic appearance. Tatsuoka et al. [13] classified different fascia systems as facing system that can provide local stiffness like wraparound fascia, overall axial rigidity like block panel fascia, overall bending–shear rigidity like full height panel fascia and overall bending-shear-gravity rigidity like full height rigid fascia. According to RTRI full height rigid (FHR) wall is constructed by casting concrete on the wrapped face of Geogrid reinforcement, so that the facing and reinforcement layer is firmly connected to each other by fresh concrete. Rigid fascia gives confining effect to the reinforced mass and further improves the performance of system [11]. This effect is completely utilized in RTRI code by taking gravity effect of fascia in the limit equilibrium design. Flexible facing lacks to exhibit the high resistance against to loads like Full height rigid (FHR).

5.4 Cost

The cost of material required per meter length of wall is estimated in both codes to find out the economical different of flexible and rigid fascia. The material costs (not included construction costs) for flexible wall designed as per BS 8006 are 62,000, 45,000 and 25,000 Indian rupees for Sects. 1, 2 and 3, respectively, while the rigid fascia is costing 34,500, 26,500, and 17,000 as per RTRI for Sects. 1, 2, and 3, respectively. Sections 1, 2, and 3 have material cost reduction of 40%, 35%, and 32%, respectively, if rigid fascia is constructed rather than constructing flexible. Since the flexible wall requires higher length of geogrid and backfill than rigid wall, so that reinforcement quantity and reinforced fill quantity vary very much in both designs so that the cost also varies in both designs. Rigid fascia saves more money and becomes a more economical design. The rates of material used for the cost calculations are shown in Tables 6 and 7.

Table 6 Cost of the flexible facing reinforced zone in Indian rupees per meter run

Description	Unit	Rate	Quantity in BS 8006			Cost		
			S1	S2	S3	S1	S2	S3
GSB below leveling pad	m^3	943	0.15	0.15	0.15	142	142	142
Leveling pad	m^3	2000	0.12	0.12	0.12	240	240	240
Fascia	m^3	1200	8.8	7.3	5.0	10,560	8760	6000
Selected filling in RF zone	m^3	300	83	58.4	30	24,816	17,520	9000
Geogrid	m^2	100	264	184	96	26,320	18,400	9600
Total cost						62,000	45,000	25,000

Table 7 Cost of the rigid facing reinforced zone in Indian rupees per meter run

Description	Unit	Rate	Quantity in RTRI			Cost		
			S1	S2	S3	S1	S2	S3
GSB below leveling pad	m^3	943	0.15	0.15	0.15	142	142	142
Leveling pad	m^3	2000	0.12	0.12	0.12	240	240	240
Fascia	m^3	4000	3.1	3.0	1.8	12,320	10,240	7000
Selected filling in RF zone	m^3	300	35	26	15	10,260	7665	4500
Geogrid	m^2	100	112	81	48	11,200	8050	4800
Total cost						34,500	26,500	17,000

5.5 Safety

Since factor safety against every condition in both designs is found as safe as per both codes, both code designs are considered as safe design. As per past studies, flexible fascia is being failed even in static condition but having a rigid fascia let the wall to be safe even in seismic conditions [12]. Since RTRI codes following rigid fascia showed no failure in the past, it appeases to be more stable than flexible fascia.

5.6 Construction Issues

The staged cast-in situ fascia construction method is used for rigid faced wall construction as per RTRI. The staged construction method of FHR faced walls is constructed using Cast-in situ concrete fascia with reinforcement layers firmly connected to fascia by means of fresh concrete after the wraparound reinforced zone is constructed. The main advantage of staged cast-in-situ fascia construction method is that the major deformations of wall had happened when the wraparound wall is constructed itself and when rigid fascia is casted; it enhances stability and further deformations will be negligible. These types of constructions were very helpful when there are stringent limitations of settlement/lateral deflections like in high-speed rail embankment.

The main constructional difficulty in FHR facing is to maintain a strong connection between fascia and reinforcement. It requires steel reinforcement rods inserted into reinforced zone extended from fascia for high compatible connection to provide confining effect. So, utmost care is required for connections in FHR fascia construction.

Flexible fascia like wraparound fascia is easy to construct and need not to wait for full deformations to get happen like in FHR fascia. It can easily accommodate to vertical settlements. These types of constructions were practiced when there are no stringent limitations of settlement/lateral deflections.

6 Conclusions

Design of rigid and flexible fascia has been compared to highlight their difference by taking a real scenario into consideration. BS 8006 and RTRI have completely different design concepts such limit state design procedure and performance based with limit state design procedure, respectively. The rigid and flexible fascia have unique method of design process. The major difference was the rigid fascia is considered as load-carrying element along with reinforcement while flexible is not considered. The rigid fascia was completely considered as load-carrying element in RTRI while in BS 8006 there is not much concern about fascia since it is not used for carrying loads. The

material cost of rigid fascia wall is less than cost of flexible fascia. The rigid fascia wall gives cost reduction of about 30–40% according to the design considered in this study.

References

1. Allen TM, Bathurst RJ, Holtz RD, Walters D, Lee WF (2003) A new working stress method for prediction of reinforcement loads in geosynthetic walls. Can Geotech J 40(5):976–994
2. Bathurst RJ (1998) NCMA segmental retaining wall seismic design procedure: supplement to design manual for segmental retaining walls. National Concrete Masonry Association, Herdon, VA
3. Bathurst RJ, Vlachopoulos N, Walters DL, Burgess PG, Allen TM (2006) The influence of facing stiffness on the performance of two geosynthetic reinforced soil retaining walls. Can Geotech J 43(12):1225–1237
4. Christopher BR, Gill S, Giroud JP, Juran I, Mitchell JK, Schlosser F, Dunnicliff J (1990) Reinforced soil structures. Volume I, design and construction guidelines (No. FHWA-RD-89-043). Federal Highway Administration, United States
5. EBGEO (2011) Recommendations for design and analysis of earth structures using geosynthetic reinforcements–EBGEO
6. Holtz RD, Lee WF (2002) Internal stability analyses of geosynthetic reinforced retaining walls (No. WA-RD 532.1). Washington State Department of Transportation, Olympia, Washington
7. Koseki J, Bathurst RJ, Guler E, Kuwano J, Maugeri M (2006) Seismic stability of reinforced soil walls. In: Proceedings of the 8th international conference on geosynthetics, vol 1, pp 51–77
8. Liu CN, Yang KH, Nguyen MD (2014) Behavior of geogrid–reinforced sand and effect of reinforcement anchorage in large-scale plane strain compression. Geotext Geomembr 42(5):479–493
9. RTRI (2012) Design standards for railway structures and commentary, earth retaining structures-selected part for GRS structures
10. Standard B. BS8006-1 (2010) Code of practice for strengthened/reinforced soils and other fills. ISBN 978(0), 580
11. Tatsuoka F (1989) Earth retaining wall with short geotextile and a rigid facing. In: Proceedings of the 12th ICSMFE, vol 2, pp 1311–1314
12. Tatsuoka F, Tateyama M, Koseki J, Yonezawa T (2014) Geosynthetic-reinforced soil structures for railways in Japan. Transp Infrastruct Geotechnol 1(1):3–53
13. Tatsuoka F (1992) Permanent geosynthetic-reinforced soil retaining walls used for railway embankments in Japan. In: Proceedings of the international symposium on geosynthetic-reinforced soil retaining walls, Balkema

Screening of Train-Induced Vibration with Open Trench—A Numerical Study

Majumder Mainak and Ghosh Priyanka

Abstract The present study aims to explore the effectiveness of open trench (*OT*) as a vibration barrier in reducing the ground-borne vibration induced by the moving trains. A numerical investigation has been performed using 2D finite element analysis coupled with infinite elements. The moving train is simulated as a sequence of pulse loads vibrating at different excitation frequencies. The performance of *OT* in screening the train-induced vibration is evaluated with respect to amplitude reduction ratio (*ARR*) defined later. The effect of train speed and optimum geometric parameters of *OT* on the screening effectiveness has been explored in detail.

Keywords Amplitude reduction ratio · Open trench · Screening efficiency · Train-induced vibration · Vibration screening

1 Introduction

The emergence of railway track in the built-up areas of developing countries like India leads to one of the major causes of unwanted vibration developed in the ground. In India, the modern development of infrastructures causes an expansion of the railway track all over country especially in the urban areas. However, the train-induced vibration due to high-speed trains and rapid transit systems in the metropolitan cities is still a gray area of research. Therefore, a careful assessment of train-induced vibration is required before construction of a new railway track in the urban areas. The vibration caused by the passage of trains may cause unwanted shaking in the adjacent residential, industrial buildings, hospitals, etc. Such unwanted vibration due to the passage of trains transmits through the track structures including rails, sleepers, ballast, and subgrade, and propagates as the stress waves through the soil medium [19]. Therefore, eliminating or at least minimizing such undesirable train-induced vibration is important from the comfort point of view. There are several ways of reducing such vibration, which can be classified into three major categories such as vibration

M. Mainak · G. Priyanka (✉)
Indian Institute of Technology Kanpur, Kanpur, India
e-mail: priyog@iitk.ac.in

A. Prashant et al. (eds.), *Advances in Computer Methods and Geomechanics*, Lecture Notes in Civil Engineering 55,
https://doi.org/10.1007/978-981-15-0886-8_37

screening at the source, receiver, and wave propagation path. Vibration screening at the source includes various types of technique implemented in the railway structures such as floating slabs [15], rail grinding, use of several pads [16], vehicle primary suspension system, ballast mats or resilient wheels [11] etc. whereas the mitigation of vibration at the receiver includes different measures taken at the receiving point to reduce building or other receiver response (passive isolation). On the contrary, the screening of vibration at the wave propagation path includes a barrier or trench installed across the path of the propagating waves, which may include hollow as well as infilled trench with different geometries. The trench across the wave propagation path provides an active vibration screening when it is installed in the vicinity of the source [19].

The problem of screening the vibration induced by different sources has received major attraction from the researchers since 1960. Previous studies [2, 3, 5, 7, 13, 19] related to different stationary (non-movable) vibratory sources are mostly dominated by single frequency. Hence, the screening efficiency can be achieved by simply adjusting the dimension of the trench. On the contrary, the same effect of vibration screening cannot be achieved for moving train excitations since the train-induced vibration usually involves a wide range of frequencies. In the literature, fewer studies are available on the screening efficiency of trench to reduce the train-induced vibration. Yang and Hung [18] and Hung et al. [9] have employed 2.5D finite/infinite element scheme to investigate the screening performance of *OT*, infilled trench and wave impedance blocks (WIB) under the train-induced ground vibration. Different train speeds and excitation frequencies have been considered in their studies. Adam and Von Estorff [1] have investigated the direct modeling of a structure (building) as a receiver to screen the pulse train loads using open and soil-bentonite fill trenches. Unlike most of the previous formulations, this model completely considers the soil structure interaction effect and directly determines the effect of trench on the structural response. Andersen and Nielsen [4] have developed coupled finite element–boundary element (FE-BE) model in the frequency domain to investigate the reduction of ground-borne vibration due to vertical and horizontal excitation on the railway track by considering both open and rubber chip infilled trenches. A coupled FE-BE model of the track and the subsoil is employed adopting a formulation in the moving frame of reference following the vehicle. Itoh et al. [10] have also numerically investigated the screening efficiency of wave barriers to reduce the train-induced ground vibration. The numerical investigations of Itoh et al. [10] have been carried out using *ABAQUS* along with the infinite elements to simulate the nonreflecting boundary conditions. It has been concluded that both geometry (depth and width) and materials of the barriers (Aluminum, Acryl, and EPS geofoam) have a significant influence on the vibration screening efficiency. Di Mino et al. [8] have studied the effect of *OT* on the train-induced vibration in terms of the reduction of vertical and horizontal displacements and velocities. 2D FE simulation has been performed and several open trench configurations have been analyzed varying the main geometric features such as width and depth of the trench, distance from the rail, thickness of the soil layer over the rigid bedrock, type of the ground, and thickness of the soil layer. Connolly et al. [6] have modeled bogie, wheel, rail, sleepers and track interaction using Hertzian

nonlinear contact analysis in *ABAQUS*/Explicit 6.14 (Dassault Systems 2014) with a 3D domain. The developed model utilizes a modified spherical absorbing boundary condition for enhancing the performance of the model, and a staggered integration scheme is adopted to couple the track and the train models.

Among all the previous studies related to the application of trench in reducing the train-induced vibration, the screening efficiency of *OT* is considered to be the best. However, a comprehensive design of *OT* in reducing the train-induced vibration has not drawn much attention from the researchers. Hence, a two-dimensional *FE* analysis using *ABAQUS*/Explicit 6.14 (Dassault systems 2014) has been performed in this paper to predict the efficiency of *OT* to screen the train-induced vibration effectively. Different geometric parameters of *OT* along with the speed of the train are considered in the parametric study.

2 Problem Definition and Basic Assumptions

The pictorial view of the problem in hand is depicted in Fig. 1. A moving train with speed, V travels on the railway track resting on the embankment-soil system. To mitigate the train-induced vibration, an open trench of width, w and depth, d is placed on one side of the embankment at a distance, l from the toe of the embankment (Fig. 2). The subgrade soil is assumed to be homogeneous, isotropic, and linearly

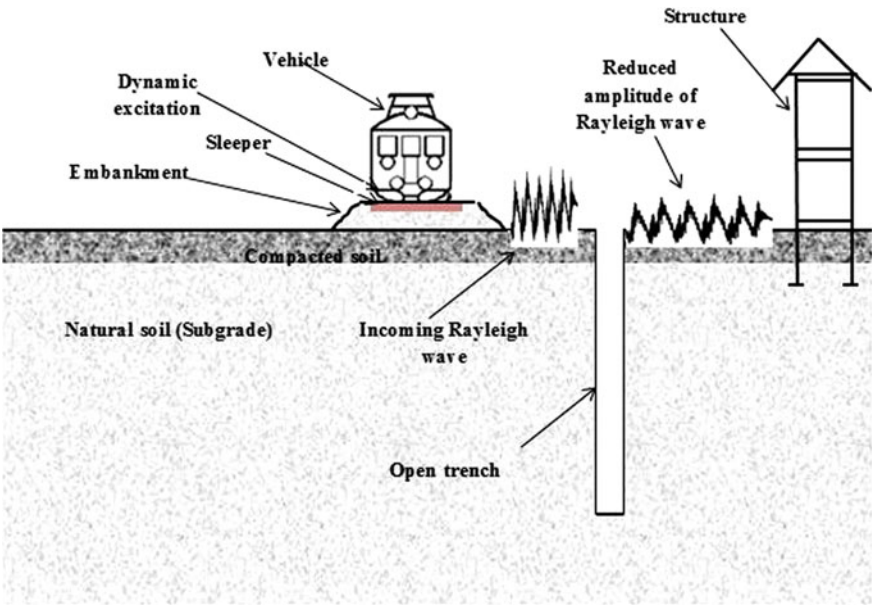

Fig. 1 Pictorial view of the influence domain

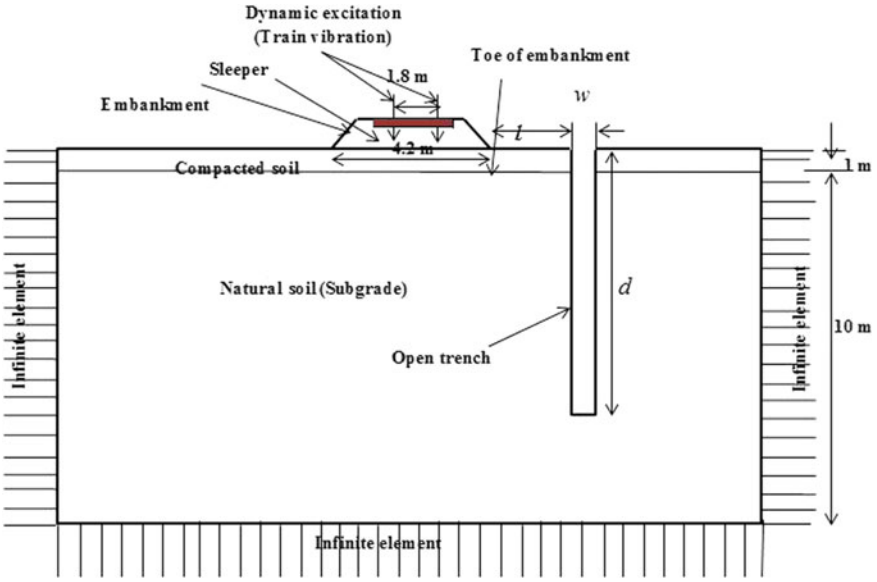

Fig. 2 Schematic diagram of influence domain and geometric parameters of trench

elastic under the wave propagation. The whole influence domain is considered to be divided into three parts such as the railway track superstructure consisting of sleepers and ballast, the substructures consisting of compacted soil and natural subgrade soil (near field), and the remaining soil deposit (far-field). The objective of the present study is to determine the active vibration screening efficiency of *OT* in terms of amplitude reduction ratio (*ARR*) by measuring the average value of the amplitude reduction factor (*ARF*) over a specific region (three times the Rayleigh wavelength, λ_R) along the ground surface, where *ARF* and *ARR* can be defined as

$$ARF = \frac{\text{absolute maximum value of the vertical velocity at a point in presence of trench}}{\text{absolute maximum value of the vertical velocity at a point without trench}} \quad (1)$$

$$ARR = \frac{1}{c}\int_0^c ARF \cdot (y) \cdot \mathrm{d}y \quad (2)$$

where c is the span of the specific region; assumed as $3\lambda_R$.

3 Model Development

3.1 Material Properties

The properties of the soil are considered according to the geotechnical investigation reported by Zakeri et al. [20]. As reported by Zakeri et al. [20], the soil deposit includes top 1 m depth of compacted soil and thereafter homogenous soil up to 10 m as shown in Fig. 2. The elastic and dynamic properties of the soil deposit are reported in Table 1. The properties of sleeper and ballast in the embankment are also reported in Table 1.

3.2 Loading Pattern

In the present analysis, the moving trainload has been modeled as a series of moving step loads as shown in Fig. 3. It is worth mentioning that the pattern of loading corresponds to the passage of freight train at a velocity of 60 km/h with a boogie axle distance of 9 m [8]. The time history of each load consists of four consecutive impulses; each impulse has a time duration of 0.02 s and amplitude of 1000 kN as shown in Fig. 3. Two concentrated loads act over the rails at a spacing of 2.4 m. The loading pattern for different train speeds (critical, supercritical, and subcritical) has been calculated as per the formula proposed by Popp and Schiehlen [14].

Table 1 Material properties of finite simulation [20]

Material	Elastic modulus (E in kPa)	Poisson's ratio (ν)	Density (ρ in kg/m^3)	Shear wave velocity (V_S in m/s)	Rayleigh wave velocity (V_R in m/s)
Sleeper	2×10^7	0.2	2500	1826	1664.5
Ballast	3.89×10^5	0.3	2200	260.8	241.9
Compacted fill	9.075×10^4	0.3	1800	138.7	128.6
Subgrade soil	25.36×10^5	0.35	1600	76.6	71.6

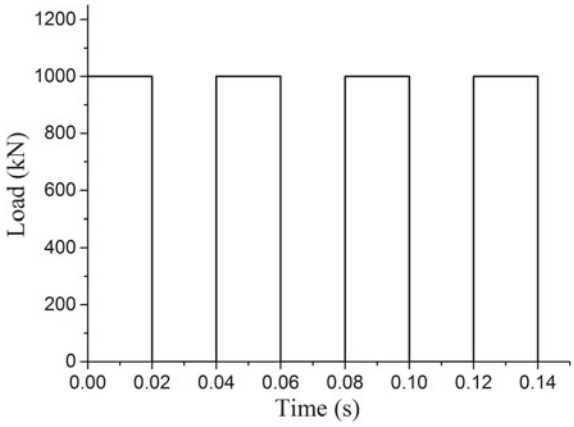

Fig. 3 Pattern of train loading

3.3 Finite Element Modeling

A dynamic, explicit time domain, finite element model has been developed using *ABAQUS*. The whole influence domain has been discretized using quadratic four-noded element CPE4R (four-noded bilinear plane strain quadrilateral, reduced integration and hourglass control). The far-field of the domain has been discretized using infinite elements CINPE4 (four-noded linear plane strain one-way infinite quadrilateral). The contacts between the sleeper and the ballast, and the ballast and the soil have been assumed as hard contact. Based on the average vertical displacement at the side boundary a sensitivity analysis has been carried out to determine the optimum half-domain size along the horizontal direction (Fig. 4). It can be observed that the effect of domain size on the average vertical displacement at the boundary becomes insignificant beyond 17.1 m. The average element size (0.42 m) is chosen based on the criteria of wave propagation as proposed by Kramer [12]. However, to capture the wave propagation more accurately, finer mesh is considered near the source and the trench, where the average element size is considered as 0.32 m and 0.24 m, respectively. In Fig. 5 the discretized model with applied boundary conditions is shown. The time increment for the analysis is determined based on the fastest propagation velocity of the wave and the element size [17]. The total dynamic excitation time is considered as 10 s. The energy dissipation mechanism for the soil is simulated with the Rayleigh damping. The mass and stiffness coefficients for the Rayleigh damping are determined as $\alpha = 1.2$ and $\beta = 0.0004$, which provide the damping ratio (ξ) of 5%. In the present analysis, the Rayleigh wavelength (λ_R) is found to be 2.04 m with a train speed of 60 km/h.

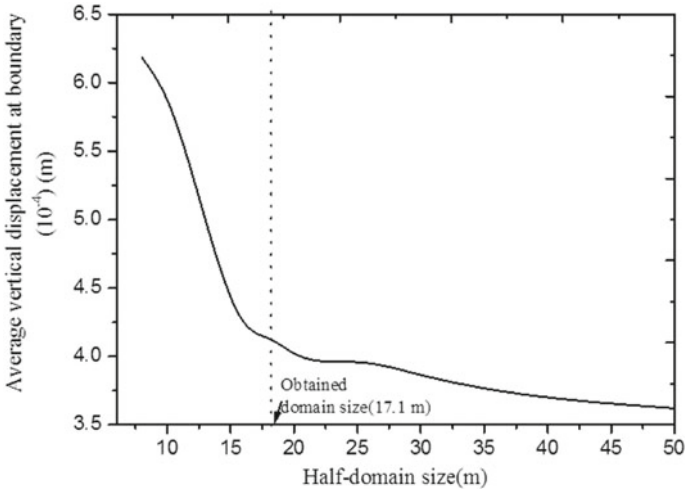

Fig. 4 Domain size sensitivity analysis considering half-domain

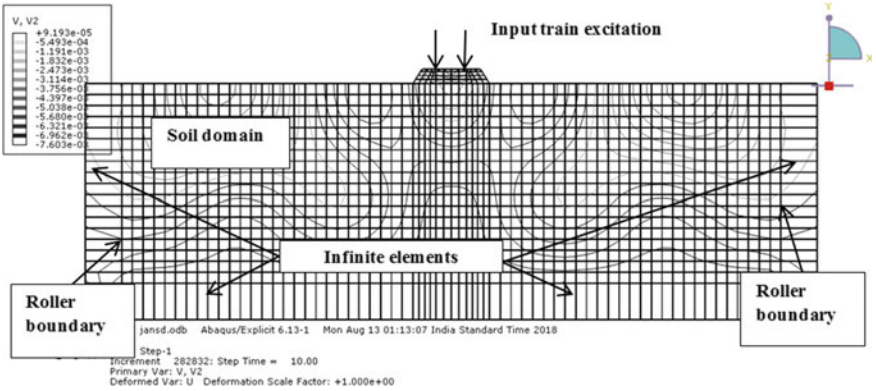

Fig. 5 Discretized domain with finite/infinite element

4 Results and Discussion

4.1 Finite Element Model Verification

In order to verify the present FE model, the results are compared with the values reported by Beskos et al. [5] and Di Mino et al. [8]. For the verification purpose, an open trench having λ_R depth and $0.1\lambda_R$ width ($\lambda_R = 2.8$ m) is considered in an elastic half-space at a distance of 10.04 m from the axis of the rigid foundation (width 0.7 m), which is subjected to a harmonic load of frequency 50 Hz. In Fig. 6, the comparison is presented in terms of the attenuation ratio (A_r) at various normalized

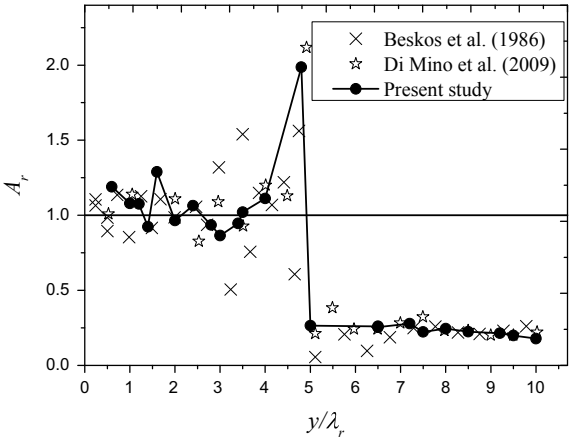

Fig. 6 Verification of present model with the existing studies for open trench [5, 8]

distances, y/λ_R, where y is the horizontal distance of the generic point from the axis of the source. The present results show a good agreement with the values reported in the literature and hence, authenticate the correctness of the present model. The present model has been also validated with the investigation of Zakeri et al. [20] since the geotechnical properties considered in both the studies are found to be same. In Fig. 7, the velocity-time history captured at the center of the embankment for the present study is compared with that of Zakeri et al. [20]. It is worth mentioning that the analysis of Zakeri et al. [20] is based on the train-induced vibration for the same loading pattern [8]. The present FE model is found to predict a reasonably good match with that of Zakeri et al. [20] with a maximum difference of 6%.

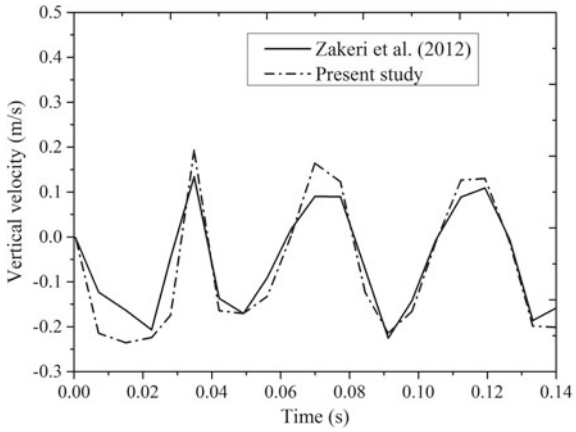

Fig. 7 Validation of present model with the model of Zakeri et al. [20]

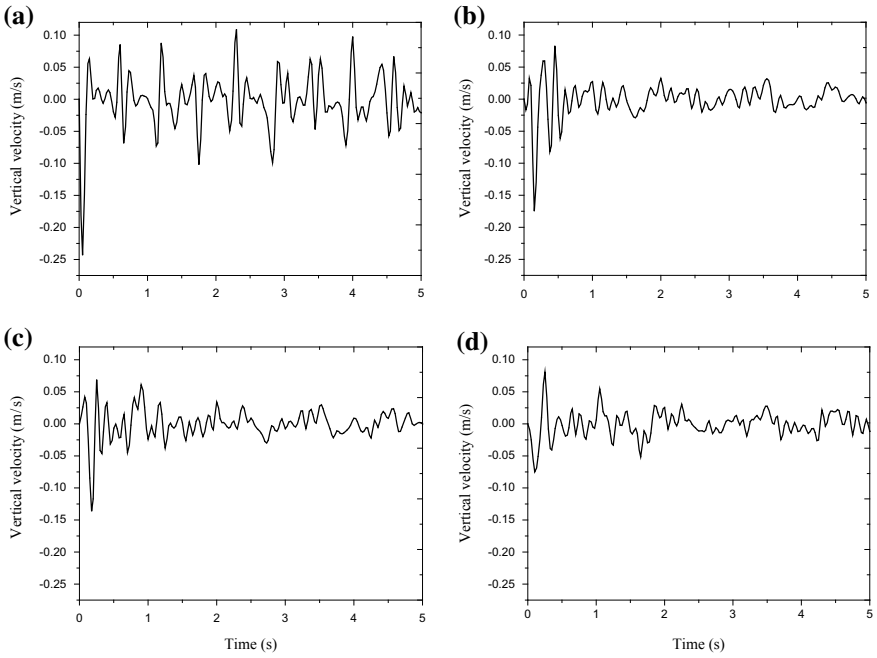

Fig. 8 Free field response at **a** 0.5 m, **b** 1.0 m, **c** 1.5 m, **d** 3.0 m from the toe of the embankment

4.2 Free Field Response

Figure 8 shows the dynamic response along the ground surface at various distances from the toe of the embankment (0.5, 1, 1.5, 3.9 m) for the train traveling at a velocity of 60 km/h. The value of the absolute maximum vertical velocity at different pickup locations is found to be in the range of 0.0678–0.1182 m/s, which may cause some serviceability issues.

4.3 Screening Efficiency of OT

To evaluate the screening efficiency of *OT*, different geometric parameters are considered to obtain the most efficient design of open trench. The *ARR* values are calculated as mentioned earlier to check the influence of different geometric parameters of *OT*. A nomenclature ($L_iW_jD_kV_m$) is defined to identify the problem and associated details, where

L_i: L represents the location factor of the trench (l/λ_R), where i stands for different magnitudes of $L = \{0.8, 1.0, 1.25. 1.5, 2.0, 2.5, 3.0\}$.
W_j: W represents the width factor of the trench (w/λ_R), where j is equal to 0.25.

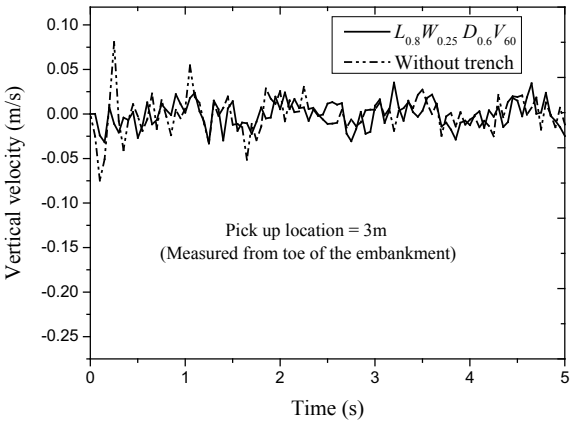

Fig. 9 Variation of vertical velocity with time at $L = 0.8$

D_k: D represents the depth factor of the trench (d/λ_R), where k stands for different magnitudes of $D = \{0.6, 0.8, 1.0, 1.2, 1.5, 1.8\}$.
V_m: V represents the train speed in km/h, where m stands for different magnitudes of $V = \{60, 137.8, 220.6, 257.8, 275.76, 328.3\}$.

Woods [19] has proposed that the width of *OT* does not play a crucial role in the screening efficiency and hence, it is kept fixed ($W = 0.25$) throughout the analysis.

4.3.1 Effect of Trench Location

To determine the optimum value of L, the magnitude of L is varied keeping other parameters constant ($D = 0.6$, $V = 60$ km/h). Figure 8 shows the variation of vertical velocity with time for $L = 0.8$ at a distance of 3 m from the toe of the embankment. The variation of vertical velocity for without trench condition is also depicted in Fig. 9. It can be seen that the peak absolute vertical velocity decreases by 56.43% after the installation of *OT*. The variation of *ARR* with L for $D = 0.6$, $V = 60$ km/h is shown in Fig. 10. It can be noted that the *ARR* value increases from 0.354 to 0.371 with the increase in L from 0.8 to 1.5. However, beyond $L = 1.25$, the variation in *ARR* is in the range of 4–6%, which is considered to be nominal. Hence, $L = 1.25$ is recommended for obtaining an effective screening efficiency of *OT*.

4.3.2 Effect of Trench Depth

To determine the optimum value of D, the magnitude of D is varied keeping other parameters constant ($L = 1.25$, $V = 60$ km/h). Figure 11 shows the variation of vertical velocity with time for $D = 1.8$ at a distance of 3 m from the toe of the embankment. The variation of vertical velocity for without trench condition is also depicted in Fig. 10. It can be seen that the peak absolute vertical velocity decreases

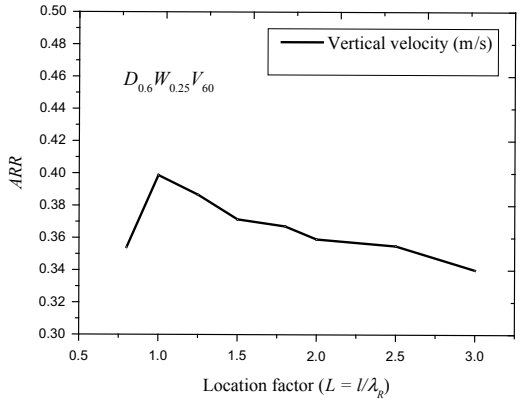

Fig. 10 Variation of *ARR* with *L*

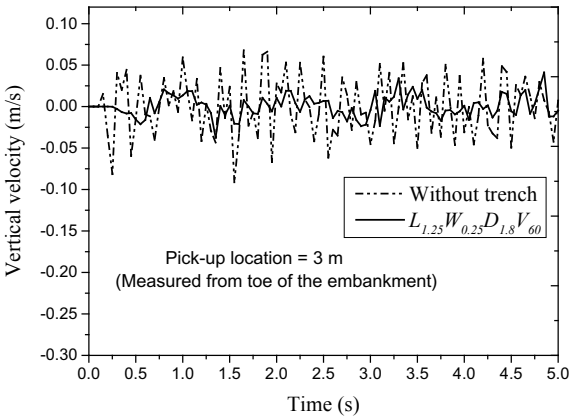

Fig. 11 Variation of vertical velocity with time at $D = 1.8$

by 80.92% after the installation of *OT*. The variation of *ARR* with *D* for $L = 1.25$, $V = 60$ km/h is shown in Fig. 12. It can be observed that the *ARR* value decreases from 0.387 to 0.252 with the increase in *D* from 0.6 to 1.8. However, from practical point of view, $D = 1.0$ is chosen as the optimum *D* value in the present study.

4.3.3 Effect of Train Speed

In the present study, the effect of train speed has been explored considering the Mach number (M_2). Mach number (M_2) can be defined as V/V_s, where V and V_s are the train speed (m/s) and shear wave velocity in the soil (m/s), respectively. $M_2 = 1.0$ corresponds to the critical speed, whereas $M_2 < 1.0$ and $M_2 > 1.0$ denote the subcritical and the supercritical speed region, respectively. Figure 13 shows the variation of *ARR* with different Mach numbers. It can be noticed that *OT* is more effective in the supercritical speed region than the subcritical one. However, the

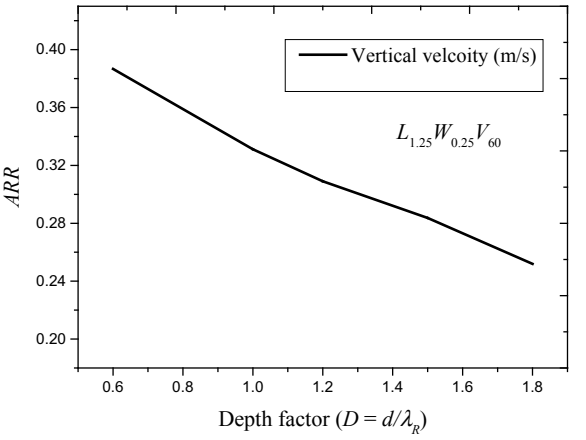

Fig. 12 Variation of *ARR* with *D*

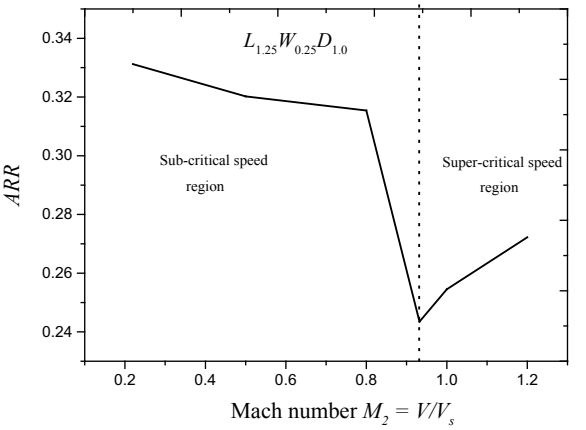

Fig. 13 Variation of *ARR* with Mach number

development of actual shape of Mach cones cannot be observed in the 2D dynamic analysis as the longitudinal direction is not considered in the analysis.

5 Conclusions

The present finite element analysis explores the usefulness of *OT* to screen the train-induced vibration. The effect of different geometric parameters of *OT* and train speed on the screening efficiency has been explored. Based on the present investigation, the following conclusions can be made

- Train-induced vibration amplitude may cause a detrimental effect on the surrounding sensitive structures. The present study shows that the vibration level may be severe for the vertical velocity amplitude ranging from 0.1182 to 0.5843 m/s.
- A significant reduction in *ARR* can be achieved using *OT*. The maximum screening efficiency reaches up to 80% using *OT*.
- To determine the optimum design parameters of *OT*, the values of *L* and *D* are found to be 1.25 and 1.0, respectively. Trench depth and location from the source are the two key parameters in the design of *OT* to reduce the train-induced vibration.
- *OT* performs better in the supercritical speed range, hence, for reducing the vibration induced by high-speed train, *OT* seems to be more effective.

References

1. Adam M, Von Estorff O (2005) Reduction of train-induced building vibrations by using open and filled trenches. Comput Struct 83:11–24
2. Ahmad S, Al-Hussaini T (1991) Simplified design for vibration screening by open and in-filled trenches. J Geotech Eng Div ASCE 117(1):67–88
3. Alzawi A, El Naggar MH (2009) Vibration scattering sing geofoam material as vibration wave barriers. In: Proceedings of the geo-Halifax, 62nd Canadian geotechnical conference, Halifax, NB, Canada
4. Andersen L, Nielsen SRK (2005) Reduction of ground vibration by means of barriers or soil improvement along a railway track. Soil Dyn Earthq Eng 25:701–716
5. Beskos DE, Dasgupta B, Vardoulakis IG (1986) Vibration isolation using open and in-filled trenches. Part 1: 2D homogeneous soil. Comput Mech 1:43–63
6. Connolly D, Giannopulos A, Forde M (2013) Numerical modeling of ground borne vibrations from high speed rail lines on embankments. Soil Dyn Earthq 46:13–19
7. Dasgupta B, Beskos DE, Vardoulakis IG (1986) 2D vibration isolation using open trenches. In: Shaw RP (ed) Innovative numerical methods in engineering. Springer, Berlin
8. Di Mino G, Giunta M, Di Liberto CM (2009) Assessing the open trenches in screening railway ground vibrations by means of artificial neural network. Adv Acoust Vib 2009(i):1–12
9. Hung HH, Yang YB, Chang DW (2004) Wave barriers for reduction of train-induced vibrations in soils. J Geotech Geoenvironmental Eng ASCE 130:1283–1291
10. Itoh K, Zeng X, Koda M, Murata O, Kusakabe O (2005) Centrifuge simulation of wave propagation due to vertical vibration on shallow foundations and vibration attenuation countermeasures. J Vib Control 11:781–800
11. Kouroussis G, Verlinden O, Conti C (2011) Efficiency of resilient wheels on the alleviation pf railway ground vibrations. Proc Inst Mech Eng Part F J Rail Rapid Transit 226(4):381–396
12. Kramer SL (1996) Geotechnical earthquake engineering. Prentice-Hall International series in Civil Engineering and Engineering Mechanics, Prentice-Hall, New Jersey
13. Majumder M, Ghosh P (2015) Intermittent geofoam in-filled trench for vibration screening considering soil non-linearity. KSCE J Civil Eng 00:1–11
14. Popp K, Schiehlen W (2003) System dynamics and long-term behavior of railway vehicles, track and subgrade. Lecture Notes in Applied and Computational Mechanics, vol 6. Springer, Berlin
15. Tayabji S, Bilow D (2001) Concrete slab track state of the practice. Transp Res Rec J Transp Res Board 1742:87–96
16. Thompson D (2009) Railway noise and vibration. Mechanisms, modeling and means of control. Elsevier Ltd.

17. Valliappan HS, Murti V (1984) Finite element constraints in the analysis of wave propagation problems. UNICIV Rep. NO. R-218, School of Civil Engineering, University of New South Wales, New South Wales, Australia
18. Yang YB, Hung HH (2001) A 2.5D finite/infinite element approach for modeling visco-elastic body subjected to moving loads. Int J Numer Methods Eng 51:1317–1336
19. Woods RD (1968) Screening of surface waves in soil. J Soil Mech Found Eng ASCE 94(4):951–979
20. Zakeri JA, Esmaeili M, Fathali M (2011) Effects of vibration in desert area caused by moving trains. J Modern Transp 20(1):16–23

Experimental Comparative Study on Strength Parameters of Concrete Assimilating Glass Fibers of Fine Aggregate, Cement with Rubber and GGBS

Arjun Sil, Naveen Kumar Vanapalli, Anisha Kumari, Pratyasha Gogoi and Debasish Mojumder

Abstract The utilization of fibers and waste materials from industry in concrete is making a remarkable change in properties of concrete. For the present study a comparison of effectiveness in strength properties when rubber, GGBS and silica fumes are used as a substitute for fine aggregate and cement respectively and alkali-resistant glass fibers are added in concrete. The effect of addition or replacement of fibers and materials on strength parameters are studied. Fine aggregate is replaced with crumb rubber and cement is also replaced with GGBS in addition to Silica fumes, as required target strength is not attained when fine aggregate is replaced with rubber. A maximum of 30% of replacement of rubber is done, depending upon the results, it is known that replacement of rubber should be restricted and low w/c ratios should be adopted. Simultaneously, in another mix glass fibers are added to plain concrete in varying percentages, maximum of 1.5%. It is observed that the use of glass fibers in concrete mixes increases tensile strength without affecting its compressive strength, thus making it beneficial to use glass fibers as there is significant increase in strength. Depending upon the percentage of replacement and addition six trial, mixes are adopted. The strength comparison is done between the six trial mixes with nominal mix of grade M25 and are presented here.

Keywords Crumb rubber · GGBS · Silica fumes · Fibres · Strength parameters

1 Introduction

Cement is one of the key ingredients in the development of shelter and other infrastructural facilities. Disposal of waste materials like crumb rubber, silica fumes, and GGBS is hazardous to environment. So, these can be used as compensates in concrete structures. In the current situation, the use of conventional waste materials such as crumb rubber, GGBS and silica fume as a substitute in concrete presents

A. Sil · N. K. Vanapalli (✉) · A. Kumari · P. Gogoi · D. Mojumder
Department of Civil Engineering, NIT Silchar, Silchar, Assam, India
e-mail: vanapallinaveen57@gmail.com

A. Prashant et al. (eds.), *Advances in Computer Methods and Geomechanics*, Lecture Notes in Civil Engineering 55,
https://doi.org/10.1007/978-981-15-0886-8_38

a feasible solution with multiple benefits for the imperishable development of the concrete industry. Therefore, a great potential exists to reduce the concrete industries contributions, to greenhouse gases through reduction in cement consumption.

The present experimental work was carried out on the concrete by addition of alkali-resistant glass fibers and partial substitution of cement with ground granulated blast furnace slag and silica fumes and fine aggregate with crumb rubber. The main ingredients used in concrete mix are Portland cement, glass fibers, Ground granulated blast slag, Silica fumes, fine aggregate (sand), crump rubber, coarse aggregate (Fig. 1).

Various kinds of fibers namely steel, glass, plastic, asbestos, acrylic, nylon, etc., are available in the market. These are used to fiber reinforce plain concrete to enhance its strength and mechanical properties. However not all materials contribute in the same manner and extent toward strengthening conventional concrete. Experimental studies on various kinds of fibers have shown that glass fibers are most advantageous among those mentioned. The main advantage of glass is its light weight and high surface area and good fire-resisting properties.

A new and recent addition to the family of fibers is the alkali-resistant glass fibers that exhibit high tensile strength, high stiffness, high chemical resistance and appreciable durability to fiber reinforced concrete by entrapping air within them, blocks of glass fiber makes good thermal insulation. For the present study, glass fibers are used to understand the benefit of using them (Fig. 2).

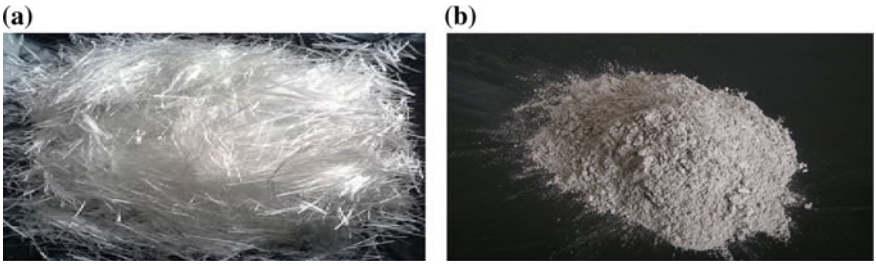

Fig. 1 **a** Glass fibers (Google image). **b** GGBS (Google image)

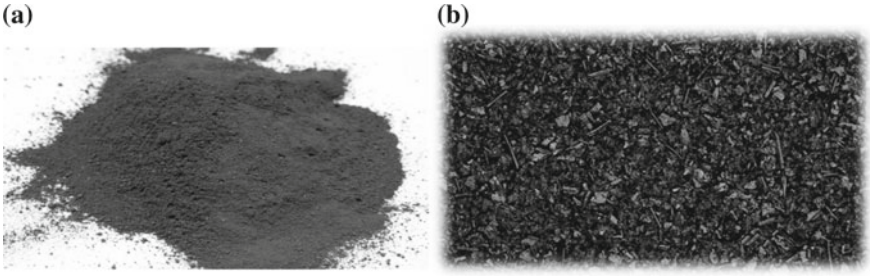

Fig. 2 **a** Silica fume (Google image). **b** Crumb rubber (Google image)

Silica fume is a by-product from industries which produce ferrosilicon. Silica fume is very fine and highly reactive admixture. As silica fume is a highly reactive pozzolanic material it is used in very small amounts, it also creates in homogeneity and non-uniformity in pore structure.

Crumb rubber is reusable rubber processed from automobile and truck scrap tires [1]. During the recycling process tier chord are removed, leaving tier rubber with a granular consistency. The particle size of rubber is reduced by processing them into granulator mill.

Thomas et al. [2] conducted experimental and analytical studies on durable properties of concrete when natural fine aggregate is replaced with crumb rubber from 0 to 20% in multiples of 2.5%. It is observed that there is less depth of chloride penetration, loss of weight and strength in the rubberized concrete in the experimental results and analytical analysis, from this it is known that rubberized concrete is efficient in aggressive environmental conditions having possibilities of acid attack but will have loss in strength.

Shariq et al. [3] conducted experiments on concrete mixes of two grades when ground granulated blast slag is substituted in the concrete mix to understand the effect of replacement in properties of the mixes. Three mixes for each grade with replacement of cement in 20, 40, and 60% with GGBS is done. The mixes with 40% replacements showed that there is a significant increase in compressive strength at 56 and 180 days.

Fibers are used in the form of dispersion in the matrix which has given positive response to researchers. Curing is necessary to keep concrete hydrated and maintain moisture content and ultimately gain strength. Improper and inadequate curing may result in shrinkage cracks and map cracking. It affects the gain of strength in concrete and reduces durability.

Wroblewski et al. [4] conducted durability studies on externally bonded fiber reinforced polymers to concrete beam specimens. Flax and glass are used as fibers. To understand the bond strength and tensile properties analytical study is done. It is observed that the specimens with glass FRP has taken 20% more load that the specimens with Flax FRP.

Dawood and Mezal [5] worked to develop gypsum plaster by adding 1% of admixture and reinforcing bar chips with various percentages of 0.5, 1, 1.25 and 1.5 and found that 1% fiber gives the optimum strength.

Glass fiber is light in weight and has high surface area. Glass fibers are easily available and cost effective. Moreover, when glass reinforced fiber concrete is used it is found to impart tensile and flexural strength to the concrete without affecting the compressive strength.

2 Methodology

For the present study compressive strength, flexural strength and split tensile strength of concrete for M25 grade of nominal mix is compared with the strengths of the mixes of which cement is replaced with GGBS and fine aggregate is replaced with crump rubber [6]. As per the literature replacement of rubber with fine aggregate does not attain the target strength, so silica fumes are added in extra to the trial mixes to attain the target strength. 30% of fine aggregate is replaced with rubber [7, 8]. A maximum of 30% of silica fumes are added to the mix. For glass fiber reinforced concrete, alkali-resistant glass fibers were added at the rate of 0, 0.5, 1, and 1.5% while preparing the concrete mix [9]. These fibers are uniformly dispersed in the matrix and enhance the mechanical properties of concrete. Depending upon the results of first two trial mixes, as the target strength is not attained, 30% of cement is replaced with GGBS in the last trial mix. A water cement ratio of 0.43 is used depending upon previous studies.

As per the literature substitution of crumb rubber increase the acid attack resistance but reduces the strength of concrete to overcome this loss of strength other industrial materials are used to attain the target strength. GGBS is one of the alternative materials for replacement of pozzolonic material but according to literature blast furnace slag gains strength with time, so for initial gain in strength, silica fumes are used which has higher surface area and high content of amorphous silica which reacts fast when compared to other ordinary pozzalonic materials to help the mix to attain at least half of the target strength by 28 days.

The glass fibers used are of 12 mm in length 14 microns in diameter and are having modulus of elasticity 72 GPa, specific gravity 2.68 with aspect ratio of 857.1. 36 specimens (cube, cylinder and prism 9 each of standard sizes) are casted for all the trial mixes [10–15]. Alkali-resistant glass fibers are used to improve resistance to the alkaline environment in Portland cement based mixes (Table 1).

Table 1 Trial mixes

Mix	Crumb rubber (%)	Silica fumes (%)	GGBS (%)	Fibers (%)
Mix 1	30	10	–	–
Mix 2	30	20	–	–
Mix 3	30	30	30	–
Mix 4	–	–	–	0.5
Mix 5	–	–	–	1
Mix 6	–	–	–	1.5

3 Results and Discussions

The specimens are tested for 7 and 28 days. There is a lot of deviation in the target strength. The replacement of 30% of rubber for fine aggregate reduced the compressive strength of the specimens in a large scale. The maximum loss of strength is 62%. The test results of the specimens are tabulated and graphs are plotted. Mix 3 has showed a reduction in loss of strength of the specimens due to the replacement of cement with 30% of GGBS. It can be predicted that there could be reduction in loss of the strength when cement is replaced with GGBS and gains the target strength with time. The increase in addition of silica fumes to the mix can reduce the loss of strength of the specimens and attaining strength at the early age (Table 2; Figs. 3 and 4).

3.1 Effect of Glass Fibers

Glass fibers were added to concrete at the rate of 0.5, 1, and 1.5% by weight of fine aggregates. The results are tabulated and graphs are plotted. From the experimental analysis it may be observed that addition of glass fibers imparts compressive strength, flexure strength and tensile strength to normal concrete. However, it has also been

Table 2 Test results for first three mixes

S. No.	Mix	Compressive strength (MPa)		Tensile strength (MPa)		Flexure strength (MPa)	
		7 D	28 D	7 D	28 D	7 D	28 D
1.	Nominal mix	14.99	24.8	2.91	3.34	6.66	7.24
2.	Mix 1	8.50	9.57	1.20	1.91	9.66	10.29
3.	Mix 2	6.385	10.83	1.53	2.26	10.66	12.67
4.	Mix 3	8.903	13.12	1.79	2.64	9.8	11.67

Fig. 3 Failure of specimen in compression and flexure under load applied using universal testing machine

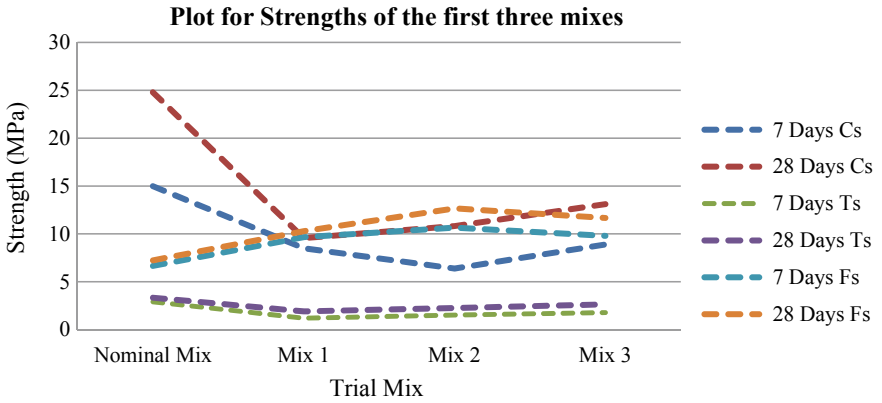

Fig. 4 Plot for various strengths (Ts-tensile, Cs-compressive and Fs-flexure) of the first three mixes as per the age (days) of the concrete

Table 3 Test results for last three mixes

S. No	Mix	Compressive strength (MPa)		Tensile strength (MPa)		Flexure strength (MPa)	
		7 Days	28 Days	7 Days	28 Days	7 Days	28 Days
1.	Nominal mix	14.99	24.8	2.91	3.34	6.66	7.24
2.	Mix 4	17.86	26.77	3.61	4.04	9.66	10.29
3.	Mix 5	22.53	34.21	3.83	4.66	10.66	12.67
4.	Mix 6	20.96	30.36	3.88	4.89	9.8	11.67

observed that after a certain limit of 1% addition of glass fiber, the strength no longer increases. This indicates that it is safe and beneficial to add glass fibers up to a limit of 1% in order to obtain higher strength than that of conventional concrete. But addition of up to 1.5% glass fibers showed increase in tensile strength while tested for split tensile strength (Table 3; Fig. 5).

4 Discussion and Conclusion

According to the results obtained it is observed that due to the replacement of rubber there is great reduction in the strength of concrete. But there is a reduction in loss of strength when cement is replaced with GGBS and addition of silica fumes. It can be suggested from the study that the addition of silica fumes should not be done more than 30% of the fine aggregate as the loss in strength is more for 30% itself so if more percentage of replacement than 30 is done there is a chance of further more loss in strength. It is also observed that addition of glass fibers in concrete mix will

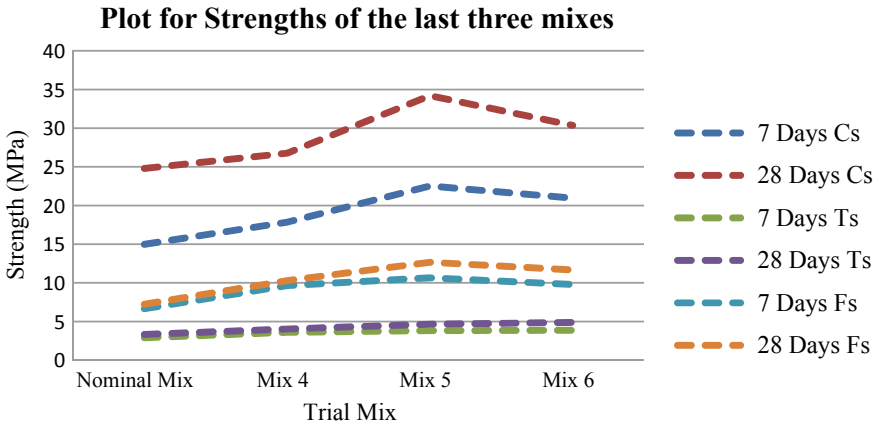

Fig. 5 Plot for various strengths (Ts-tensile, Cs-compressive and Fs-Flexure) of the last three mixes as per the age (days) of the concrete

increase the strength and durable properties of concrete. Initial percentage, i.e., 0.5% addition of glass fiber in concrete has not shown significant increase in strength but 1% addition has shown relevant increase in strength while addition of fibers beyond 1%, i.e., mix with 1.5% fibers has shown reduction in strength when compared with 1% mixes. But tensile strength, for the mix with 1.5% fibers showed good result than 1% mix. However, it is observed that there has been a gradual increase in compressive strength as compared to the nominal mix.

As per the results the crumb rubber reduces the strength of concrete which is also observed in the literature. The main purpose of usage of crumb rubber is for the development of ductile behavior and chloride resistivity of the concrete, the ineffectiveness in attaining required strength is becoming a barrier for regular replacement in concrete. For overcoming this inability cement should be replaced with materials which gain strength. Silica fumes have the capacity to increase the strength of the concrete as it has higher bonding strength and gains strength in short time. Shariq et al. [3] work proved that GGBS attains strength with time so for the present study cement is replaced with GGBS and Silica fumes to attain at least half strength within 28 days as silica fumes has high surface area. The purpose of silica fumes addition for gain in initial strength is successful and the target strength will be reached with time by replacement of GGBS which is not possible by ordinary cement.

The addition of glass fibers is done to increase the bond strength and has given the expected results which are similar to Dawood and Mezal [5] work and shows significant increase in compressive, tensile, and flexure strength. The reduction in strength for 1.5% of glass fiber is due to the high aspect ratio, i.e., length-to-diameter ratio and the significant effect of density is also a reason for reduction of strength after 1% increase in glass fibers. So as per the study 1% of alkali-resistant glass fibers is optimum for addition in concrete to improve its properties.

Acknowledgements This work is mainly carried out receiving the financial support from the DST-SERB, GOI under sanction no. ECR/2016/001329.

References

1. Scrap Tires: Deflating a Growing Problem (1988) Compressed air magazine
2. Thomas BS, Gupta RC, Vinu JP (2016) Recycling of waste tire rubber as aggregate in concrete: durability-related performance. J Clean Prod 112(1):504–513
3. Shariq M, Prasad J, Masood A (2010) Effect of GGBFS on time dependent compressive strength of concrete. J Constr Build Mater 24(8):1469–1478
4. Wroblewskia L, Hristozova D, Sadeghianb P (2016) Durability of bond between concrete beams and FRP composites made of flax and glass fibers. J Constr Build Mater 126(15):800–811
5. Dawood ET, Mezal AM (2014) The properties of fiber reinforced gypsum plaster. J Sci Res Rep 3(10):1339–1347
6. Concrete and Aggregate (1988) Annual book of ASTM standards, vol 04.02, ASTM, Philadelphia, PA
7. Guidelines for Using Recycled Tire Carcasses in Highway Maintenance (1987) Office of Transportation Laboratory, California Department of Transportation, Sacramento, California
8. Payne AR, Scott JR (1960) The properties, testing and design of rubber as an engineering material. Inter-science Publishers, New York, N.Y.
9. Popovics S (1987) A hypothesis concerning the effects of macro-porosity on mechanical properties of concrete. In: Proceedings of the SEM/RELIM international conference on fracture of concrete and rock. Springer, New York, pp 170–174
10. Grade Ordinary Portland Cement (1989) IS 8112—Bureau of Indian Standard, New Delhi
11. Code for Concrete Mix Proportioning (2009) IS 10262—Bureau of Indian Standard, New Delhi
12. Plain and Reinforced Concrete Code or Practice (Fourth Revision) (2000) IS 456—Bureau of Indian Standard, New Delhi
13. Specification for Coarse and Fine Aggregate from Natural Sources for Concrete (Second Revision) (1970) IS 383—Bureau of Indian Standard, New Delhi
14. Indian Standard Concrete Admixture Specification (1999) IS 9103—Bureau of Indian Standard, New Delhi
15. Methods of Tests for Strength of Concrete (1959) IS 516—Bureau of Indian Standard, New Delhi

Study on River Bed Material and Numerical Analysis of Stabilized Road Embankment on Soft Soil

Champakali Das and Ambarish Ghosh

Abstract The experimental study has been carried out to evaluate the effectiveness of stabilization of the river Brahmaputra bed materials with varying percentages of Portland cement. Numerical modeling has been done to study the suitability of the stabilized river bed material with respect to strength and settlement. The Brahmaputra River Bed materials were stabilized with Portland cement with varying percentages (2, 4, and 6%) cured for 7, 14, 28, 45, and 90 days. The samples were cured in a humidity control chamber at temperature 30 ± 1 °C and humidity 95 ± 1%. The mechanical behavior of this potential new material was assessed by a series of tests, including unconsolidated undrained triaxial tests on samples with different percentages of cement. It is revealed from the results that the stabilized bed materials are suitable for use in subgrade of the embankment of the low volume roads as per relevant standards. To investigate the performance of an embankment constructed using the proposed material, a numerical analysis was undertaken using the software Plaxis with the properties obtained for an embankment fill material (i.e., cement stabilized and unstabilized soil). The highway embankment has been consisting of four layers, the bottom two layers represent natural soft subgrade and the top two layers represent the embankment fill with stabilized river bed materials. In the present paper filling material has been considered as an elasto-plastic material. Plastic behavior of the filling material has been defined by Mohr–Coulomb plasticity model and the input parameter for numerical analysis has been obtained from laboratory experiments.

Keywords Embankment · Plaxis · Modulus of elasticity · Stabilized soil

C. Das (✉) · A. Ghosh
Indian Institute of Engineering Science and Technology, Shibpur, India
e-mail: champakali.rs2013@civil.iiests.ac.in

A. Ghosh
e-mail: ambarish@civil.iiests.ac.in

A. Prashant et al. (eds.), *Advances in Computer Methods and Geomechanics*, Lecture Notes in Civil Engineering 55,
https://doi.org/10.1007/978-981-15-0886-8_39

1 Introduction

With the development of the economy in India, many highway projects were commenced, particularly the construction of embankments. In addition, good quality soil must be transported from considerable distances, affecting the cost of the projects. However, there are enormous quantities of eroded sand or silt is deposited in river, which may be used in road construction to retain the profile of the river bed, Wang and Miao [1]. The basic reasons for choosing the river bed materials are (i) over spreading of the river bank (ii) continuous erosion of the bed in the upstream region (iii) deposition of soil particles causes reducing the depth of the river in the downstream region, Das and Ghosh [2]. Numerous investigators have developed different kinds of lightweight soil as filling material, including geo-foam, air-foam and waste tyres, in an attempt to reduce costs, enhance project performance and benefit the environment, Oh et al. [7]. It is very essential that the sub grade soil is suitable for road construction and an economical embankment is one which is performing for more than one decade, Das and Ghosh [2]. Nowadays different types of stabilized soil used in soil sub grade, for this the strength of the sub-grade increases. Bearing in mind the advantages of using river bed material as embankment fill, it has been investigated the possibility of mixing river bed materials with Portland cement in different percentages. The mechanical behavior of this potential new material was assessed by a series of tests. Numerical analysis by using software Plaxis was also to be conducted to analyze the feasibility of the new material having applied as embankment filling.

2 Experimental Programme

This section presents the material used in this study, experimental methodology of the work and the graphical representation following with the experimented results of engineering properties.

2.1 Materials

The following materials given in Table 1 have been used in the present investigation:

a. River bed materials: The river bed materials used in the experimental program was collected in a loose and dry state from 8 No. Spur site (8S, under Jorhat district, Assam, 26° 49′ 33.74″N, and 94° 08′ 59.28″E). And Soft soil has been procured from Batanagar, Budge Budge, West Bengal, India. The Bed materials collected from the river Brahmaputra is designated as B-sand.
b. Cement: In this paper Portland cement has been used as stabilized agent and it is basically available in the local market. For stabilization of the river bed materials

Table 1 Engineering properties of the bed materials and soft soil

Engineering properties	B-sand	Soft soil	Engineering properties	B-sand	Soft soil
Specific gravity test	2.72	2.57	Plasticity index, PI (%)	NA	22.0
Grain size analysis			Liquid limit (W_L) (%)		40.0
Sand size, 4.75–0.075 mm (%)	98.55	2.70	Plastic limit (W_p) (%)	NA	18.0
Silt size, 0.075–0.002 mm (%)	1.45	63.30	Modified proctor test		
Clay size, <0.002 mm (%)	0.00	34.00	Optimum moisture content (%)	18.51	16.0
D_{10} (mm)	0.17	0.075	Maximum dry density (gm/cc)	1.58	1.80
D_{30} (mm)	0.20	0.20	CBR (%)		
D_{60} (mm)	0.24	0.50	Soaked CBR	17.00	7.00
Uniformity coefficient (C_u)	1.41	6.66	Unsoaked CBR	19.00	4.50
Coefficient of curvature (C_c)	0.98	1.06	Triaxial test (UU)		
Group symbol	SM	MC	Cohesion (C) (kPa)	1.32	77.12
Group name	Silty sand	Clayey silt	Angel of Internal Friction ($\varphi°$)	33°	9°

Portland cement used with specific percentages (0, 2, 4, and 6%) with the bed materials according to the weight. Followings are the reactions that take place in the soil–cement stabilization:

$$C_3S + H_2O \rightarrow C_3S_2HX + Ca(OH)_2 \quad (1)$$

$$Ca(OH)_2 \rightarrow Ca^{++} + 2(OH)^- \quad (2)$$

$$Ca^{++} + 2(OH)^- + SiO_2 \rightarrow CS \quad (3)$$

$$Ca^{++} + 2(OH)^- + Al_2O_3 \rightarrow CAH \quad (4)$$

2.2 Methodology

For identifying the engineering properties all the test has been conducted in the Geotechnical engineering laboratory, IIEST, Shibpur according to the ASTM standards. To find out the engineering properties of the materials, following test has to be done: Grain Size Analysis (ASTM D422-63(2007)), Liquid and Plastic Limits (ASTM D4318-05)), Specific Gravity (ASTM D854-06), Modified Proctor test (ASTM D1557), California Bearing Ratio Test (ASTM D1883-07), Unconsolidated Undrained Triaxial Compression Test (ASTM D2850-03(2007)).

2.3 Engineering Properties

Characterization of collected river bed materials has been tabulated with graph. From the test results it has been observed that The River Brahmaputra bed material is under Silty Sand category, the group name is SM as per ASTM code. The bed material is fine in nature and non-plastic. Grain size distribution of river bed material and soft soil has been shown in Fig. 1.

- Modified Proctor Test:

The graphical representation of maximum dry density (MDD) with the corresponding optimum moisture content (OMC) of stabilized B-Sand with cement, unstabilized B-Sand and soft soil from modified Proctor test has been shown in Fig. 2. From the results given in Table 2 it has been shown that maximum dry density increased with increasing Cement Content (CC). Maximum dry density increased due to the

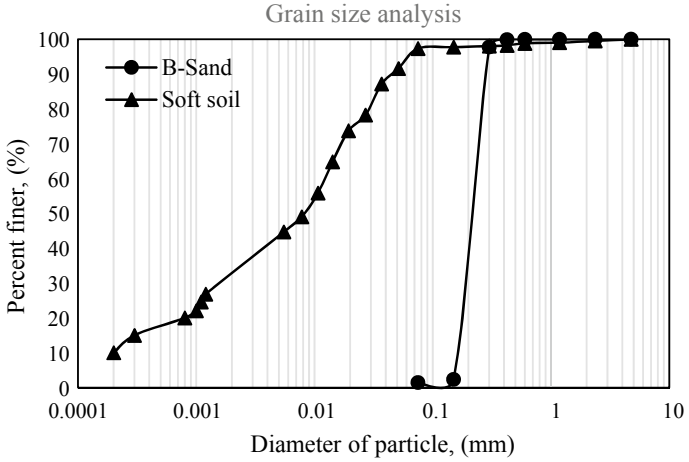

Fig. 1 Grain size analysis of soft soil and the bed materials from the river Brahmaputra

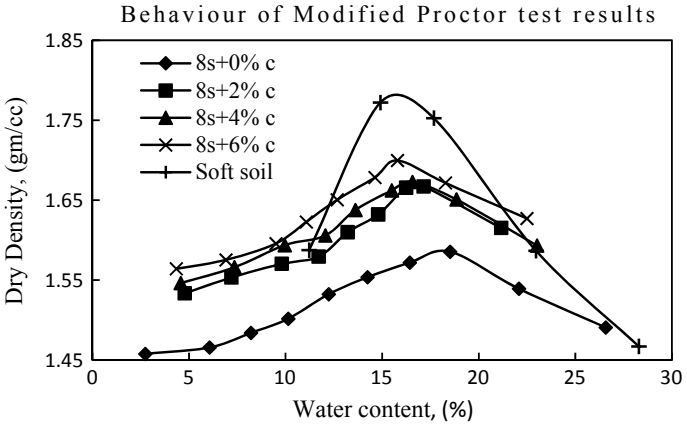

Fig. 2 Behaviour of Modified Proctor of the materials

Table 2 Modified Proctor test results of the stabilized and unstabilized materials

	OMC (%)				MDD (gm/cc)			
Soft soil	16.0				1.78			
CC (%)	0	2	4	6	0	2	4	6
8S	18.5	17.0	16.6	15.8	1.58	1.66	1.68	1.70

water present in the compacted B-sand for two reasons: The first reason is voids of sand particles is filled by finer particles of cement and second is due to water, it compressed by minimizing the voids. The energy dissipated on to the soil matrix and voids reduces to increase the density.

- California Bearing Ratio (CBR):

Unstabilized B-sand satisfied the CBR value for used in subgrade and sub base material as per ASTM D1883-07. But B-sand is not suitable in the slope of the embankment due to its cohesion less characteristics. To increase the cohesion in the matrix, stabilization plays an important role. Figure 3 represented the graphical behavior of soaked and unsoaked CBR of cement stabilized and unstabilized B-sand. From the results given in Table 3, it has been shown that the value of soaked CBR is higher than the unsoaked CBR in cement stabilized B-sand. But for unstabilized B-sand, unsoaked CBR is higher than the soaked CBR. This difference in the behavior of CBR values for unstabilized to stabilized B-sand with cement has been shown because of the water cement reaction. When the finer material cement is mixed with water in a specific percent, its molecules form bond with each other with the help of water and increase the strength and generates an amount of heat. It is well known that, immediately after mixing cement with water, the hydration process takes place. CSH is the compound resulting from hydration and it gives strength.

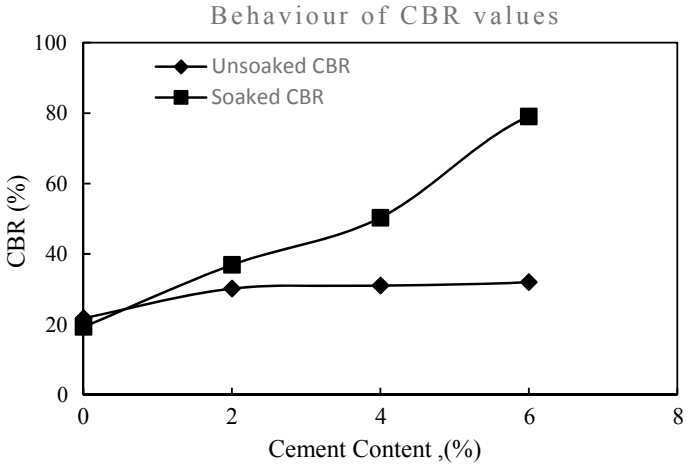

Fig. 3 Variation of CBR values with varying cement content

Table 3 Unsoaked and Soaked CBR of cement stabilized and unstabilized B-sand

CC	Unsoaked CBR, %				Soaked CBR, %			
	0%	2%	4%	6%	0%	2%	4%	6%
8S	22	30	31	32	19	37	50	79

CC cement content, *8S* = 8 No. Spur site

- Unconsolidated Undrained Triaxial Test:

The shear strength parameters of the proposed material obtained from unconsolidated undrained triaxial test results. The size of the test specimen is 38 mm in diameter and height is 76 mm and the sample is cylindrical in shape. Stabilized samples were prepared with different percentages of cement (2.0, 4.0, and 6.0%). Once the sample is compacted with modified Proctor energy, with the help of sample extractor it has to be removed and placed in desiccator to control the moisture for 24 h. After 24 h the samples were packed with cellophane paper so that moisture content will not be changed and placed in the humidity control chamber with temperature 30 ± 1 °C and humidity 95 ± 1%, Ghosh [3], Ghosh and Subbarao [4] for specific curing days of 7, 14, 28, 45, and 90 days. The cylindrical sample were removed from humidity chamber after the specific curing periods and placed in the triaxial test machine for unconsolidated undrained triaxial (UU) test under different confining pressure (100, 200, and 400 kPa) with strain rate 1.50%. Unconsolidated undrained (UU) triaxial test results of stabilized B-sand with cement of 8 no. spur site (8S) are given in Table 4 and from the results it has been shown that the cohesion (C) increases with increased curing period. The graphical representation of stress strain behavior has shown in Fig. 4.

Table 4 Shear strength properties of stabilized river bed materials

Days	7D	14D	21D	45D	90D
	$8S + 2.0\% CC$				
$\sigma_3 = 100$	313.01	323.79	378.62	404.74	447.60
$\sigma_3 = 200$	422.73	438.21	530.49	558.54	617.32
$\sigma_3 = 400$	580.22	688.62	745.28	787.89	803.91
C, kPa	120.00	137.00	146.00	154.00	192.00
	$8S + 4.0\% CC$				
$\sigma_3 = 100$	351.21	392.30	439.20	473.92	528.29
$\sigma_3 = 200$	484.58	550.52	669.16	727.02	798.46
$\sigma_3 = 400$	604.97	754.41	819.03	905.40	954.79
C, kPa	126.00	181.00	186.00	188.00	218.00
	$8S + 6.0\% CC$				
$\sigma_3 = 100$	359.66	430.29	446.09	707.22	809.47
$\sigma_3 = 400$	509.76	630.53	690.44	843.55	916.71
$\sigma_3 = 400$	741.85	799.87	835.75	1251.12	1326.22
C, kPa	129.00	140.00	187.00	231.00	251.00

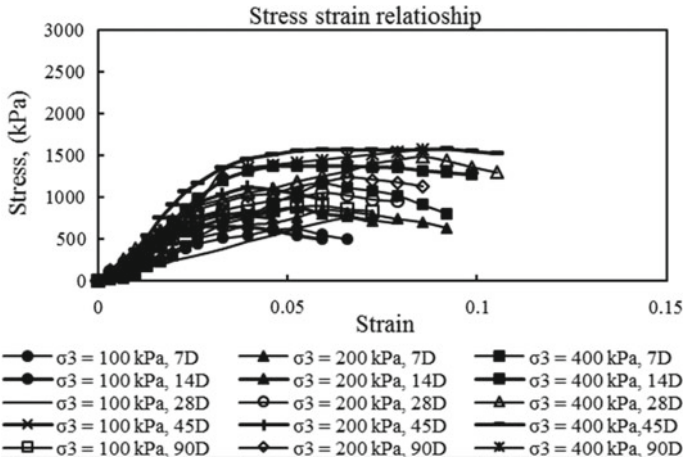

Fig. 4 Graphical representations of stress strain behaviour of cement stabilized bed materials from the river Brahmaputra

From the above results and observation 8s + 2% CC is found to be suitable for used as embankment fill material as it is economical.

3 Numerical Study

The highway embankment rested on soft soil profile shown in Fig. 5 has been evaluated for the numerical study of stabilized river bed material. As the model is symmetric with respect to center line, half of the embankment has been modeled. The framework of the numerical model was adopted from the Plaxis manual; the only difference was the properties of the filling material, Plaxis Reference Manual [5], Plaxis BV, Delft, The Netherlands; The Embankment composed of stabilized B-sand (SM). The soft soil under embankment is a compressible soil, low plasticity clay (CL), that has a cohesion of $C = 77.0$ kPa and an angle of friction $\phi = 9°$. The undrained soil conditions were assumed to be valid for the clay (i.e., soft soil) and drained for embankment fill. The modulus of elasticity (E) was determined from the secant modulus of the unconsolidated undrained triaxial test results. From the experimental results, 8S + 2% CC has been selected as embankment fill as it has the suitable CBR value in minimum cement content. The material properties of the soil used for the numerical analysis test are given in Table 5 together with model parameters. This study investigates displacement and factor of safety of embankment fill with and without cement stabilized B-sand. As examined the cases carefully, it is seen that the investigation is focused on the effect of the stabilization of the bed materials and placement to embankment under traffic loading.

The cross section of the road embankment has been shown in Fig. 5. The embankment is 7.50 m wide and 3.75 m high with slopes of 1V:2H and the depth of soft soil is 6.25 m below the embankment. The problem is symmetric, so only one half is modeled. The upper two layers represented the stabilized B-sand whereas the last two layers represented the soft soil. The standard boundary was used to define the

Table 5 Soil properties used in the model

Parameter	Name	Unit	B-sand	Stabilized B-sand (8S + 2% C)	Soft soil
Material model	Model	–	MC	MC	MC
Material behavior	Type	–	drained	drained	Undrained
Soil unit weight above phreatic level	γ_{dry}	gm/cc	1.58	1.66	1.80
Soil unit weight below phreatic level	γ_{sat}	gm/cc	1.88	1.96	2.10
Horizontal permeability	kx	m/day	1.00	0.50	1×10^{-6}
Vertical permeability	ky	m/day	1.00	0.50	1×10^{-6}
Young's modulus	E	kN/m^2	4800	21,000	3833
Poisson's ratio	υ	–	0.30	0.33	0.31
Cohesion	C	kN/m^2	1.32	120	77
Friction angle	ϕ		33	30	9
Dilatancy angle	ψ		0	0	0

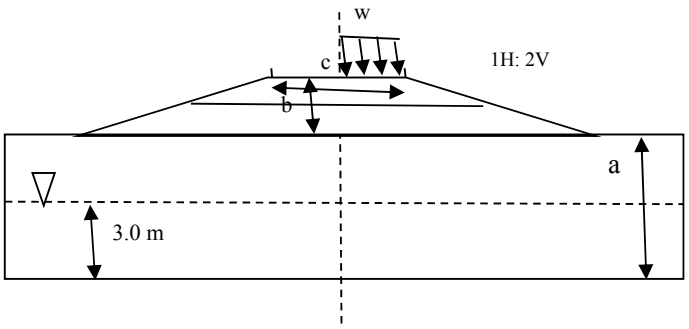

a = 6.25 m; c = 7.5 m; b = 3.75 m, w = 24 kPa traffic load
a: Height of the soft soil, b: Height of the filled sub grade and
c: Top width of the sub grade

Fig. 5 Layers in highway embankment used in the study (model is not in scale)

boundary conditions (i.e., the base boundary was fixed in the x and y directions, and the side boundaries were fixed only in *x* direction). Depth of the water table is 3.0 m from the bottom. The model mesh is shown in Fig. 6. The embankment was constructed in two stages of 1.875 m each; the construction time was 5 days. After the construction, a traffic loading of 24 kPa was added with a loading time of 15 years, the typical duration of highway projects.

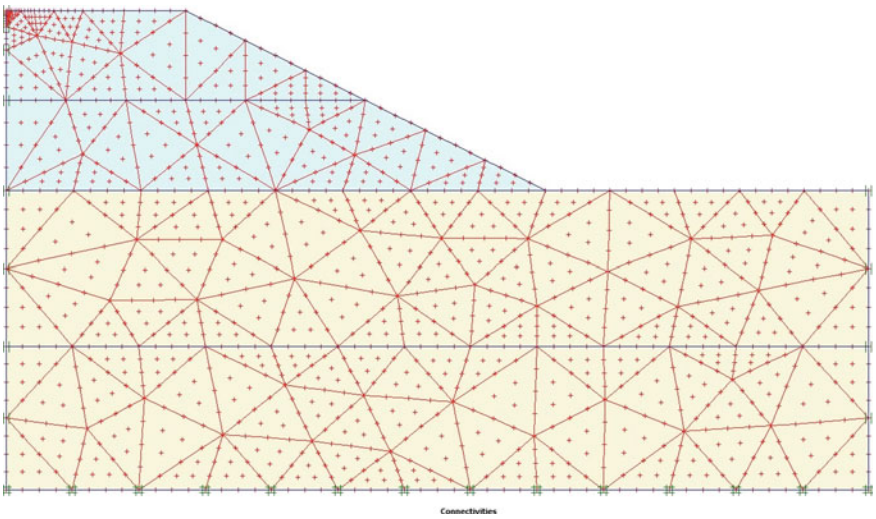

Fig. 6 Discretized model of the embankment along with the soft soil layer

3.1 Development of FE Model Using Plaxis

The numerical study of highway embankment stabilized with Portland cement under traffic load has been done by Plaxis. Finite element method was used for the numerical analysis. Since the behavior of embankment can be defined as a two-dimensional analysis, geometry of embankment as plane strain mode has been used for the finite element modeling. It is known that the plane strain is used for the geometries with a (more or less) uniform cross section and corresponding stress-state and loading scheme over a certain length perpendicular to the cross section. The soil profile has been modeled using 15 nodded triangular elements. The boundary conditions are defined by the standard fixities for static loading and standard absorbent boundaries for loading. As shown material model Mohr–Coulomb failure criteria is used for non-linear behavior of the layers that are soft soil, embankment fill. The Mohr–Coulomb model has a fixed yield surface and the yield surface is not affected by plastic straining.

- Mohr–Coulomb model

Mohr–Coulomb (MC) soil model is commonly used in geotechnical analysis for embankment fill materials. Plasticity is associated with the development of irreversible strains. MC model involves five input parameters. Elastic parameters being modulus of elasticity E and Poisson's ratio v. Plastic parameters being cohesion c, friction angle ϕ and angle of dilatancy ψ. This model represents a 'first order' approximation of material behavior. Beside the five model parameters, initial material conditions also play a significant role in most deformation problems. The embankment construction consists of two phases, each taking 5 days. After the first construction phase a consolidation period of 30 days is introduced to allow the excess pore pressures to dissipate. After the second construction phase another consolidation period is introduced from which the final settlements may be determined. Hence, a total of four calculation phases have to be defined.

4 Results and Discussion

The numerical analysis of the cement stabilized embankment fill has been shown in Figs. 6 and 7a, b. Traffic surcharge 24 kPa used as per BS 8006-2010 and the results are given in Table 6. The experimental study and the numerical analysis have shown the suitability of a mixture of cement, the Brahmaputra River Bed materials as a construction material for highway embankments over soft soil. The proposed material can also be used to reduce the cumulative settlement. Figure 7a, b presents the settlement profile after embankment construction for both the unstabilized bed material and cement stabilized bed material. Settlement is an important parameter in embankment projects. It has been clearly shown that the maximum settlement for the cement stabilized embankment is approximately 2.73 cm compared with 3.70 cm

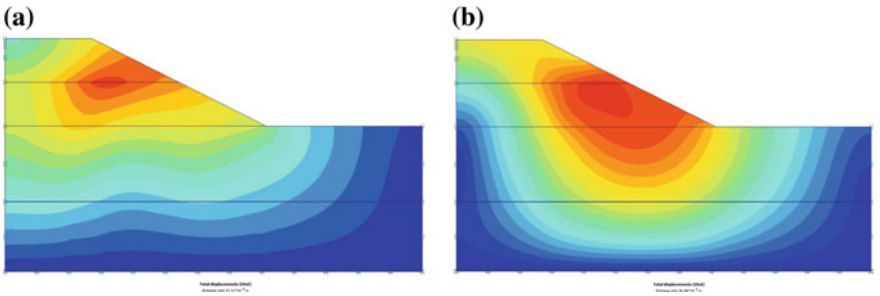

Fig. 7 Total settlement due to traffic loading **a** embankment fill with cement stabilization, M1 **b** embankment fill without stabilization, M2

Table 6 Values of horizontal and vertical displacements with factor of safety and settlement

Model	Factor of safety	Settlement (cm)	Horizontal displacement (cm)	Vertical displacement (cm)
Embankment fill with stabilization (M_1)	7.59	2.73	2.50	1.70
Embankment fill without stabilization (M_2)	1.71	3.70	3.63	2.43

for the unstabilized embankment. And the factor of safety for the cement stabilized embankment is 7.59 whereas for unstabilized embankment it is 1.71.

4.1 Validation of Results

To validate the test results showing in Table 6, following procedure has been taken. For the two-dimensional Embankment Loading Using Osterberg's Method, the increase in vertical stress (σ_z) may be expressed as follows, Das [6].

$$\Delta\sigma_z = \frac{q_o}{\pi}\left[\left(\frac{B_1 + B_2}{B_2}\right)(\alpha_1 + \alpha_2) - \frac{B_1}{B_2}(\alpha_2)\right] \tag{5}$$

For settlement calculation of the Embankment initial consolidation settlement has been considered. And necessary data's has been assumed for the calculation of settlement and factor safety (Fig. 8).

From the calculation using the above Eq. (5), the settlement of the embankment with stabilization is 3.91 cm and without stabilization is 4.58 cm. Whereas from the

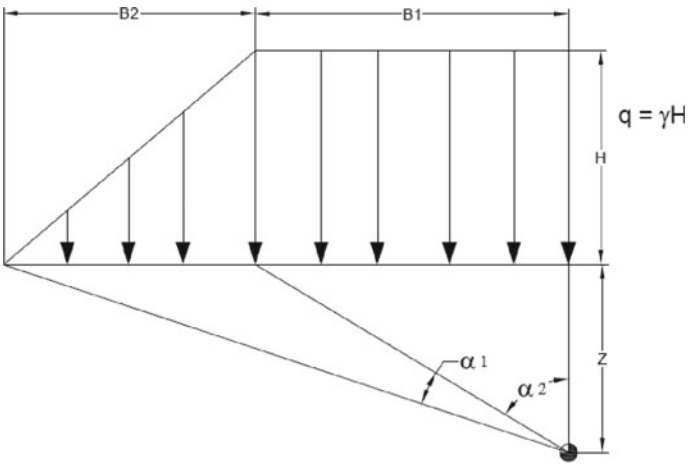

Fig. 8 Embankment loading using Osterberg's Method, Das [6]

numerical analysis the settlement of the embankment with stabilization is 2.73 cm and without stabilization is 3.70 cm. Further validation of the results, physical model test of the embankment is required and this has been incorporated in the next plan of work.

Factor of safety of the embankment has been calculated with method of slices method for both the cases (a) with stabilization of cement and (b) without stabilization of cement of the embankment. And from the calculation it has found that, the factor of safety of the embankment without stabilization is 2.23 and with stabilization is 8.11. It can conclude that the settlement and factor of safety are greater than the numerical analysis and this difference may acceptable as the difference is very negligible.

5 Conclusions

A numerical study has been done for analyzing highway embankment with Portland cement stabilized fill material under traffic loading. In this present study laboratory investigation and a numerical based study has been carried out to evaluate effectiveness of stabilization of the river bed material to use in low volume roads by using Plaxis 2D. Overall, good agreement with settlements has been demonstrated using the Mohr–Coulomb model for different layers.

1. From the above test results, it can be concluded that for the site conditions, in comparison with unstabilized soil, maximum dry density (MDD) increases with increasing amount of cement and consecutively optimum moisture content (OMC) decreases. Similar trends have been observed in California Bearing Ratio (CBR) test, i.e., bearing capacity of the unstabilized bed material increases with

increasing amount of cement and as the percentage of cement has been increased, the cohesive property has been also induced within the soil mass.
2. From the numerical analysis of the embankment fill it has found that after stabilization with cement the settlement decreases and Factor of safety of the slope increases. It is due to the cement present in the embankment fill. As decreasing horizontal displacements of embankment has important role in stability of embankment.
3. From this experimental and numerical study, it can conclude that river Brahmaputra bed material is suitable for filling materials of embankment. To increase the cohesion for slope stability Portland cement in a small percentage is suitable and the cohesion parameter increased with increment of time.

Acknowledgements I acknowledge my gratefulness to Department of Science and Technology, Ministry of Science and Technology, Govt. of India for financial support vide Reference No. SR/WOS-A/ET-21/2017 (G) and (C) under Kiran Division for women in Science "Women Scientist Scheme–A".

References

1. Wang F, Miao L (2009) A proposed lightweight fill for embankments using cement-treated Yangzi River sand and expanded polystyrene (EPS) beads. Bull Eng Geol Environ 68:517–524. https://doi.org/10.1007/s10064-009-0228-8
2. Das C, Ghosh A (2017) Shear strength behaviour and regression analysis of cement stabilized river bed material for use in subgrade. In: Indian geotechnical conference 2017 GeoNEst, 14–16 Dec 2017, IIT Guwahati, India
3. Ghosh A (2010) Compaction characteristics and bearing ratio of pond ash stabilized with lime and phosphogypsum. J Mater Civil Eng ASCE 344. https://doi.org/10.1061/(asce)mt.1943-5533.0000028
4. Ghosh A, Subbarao C (2011) Deformation modulus of fly ash modified with lime and gypsum. Geotech Geol Eng 30:299–311. https://doi.org/10.1007/s10706-011-9468-z
5. Plaxis Reference Manual (2006) Plaxis BV. Delft, The Netherlands
6. Das BM (2006) Principles of geotechnical engineering. Brooks/Cole Pub Co. 589 p.
7. Oh SW, Lee JK, Kwon YC (2002) Bearing Capacity of Light Weight Soil using Recycled Styrofoam Beads. Proceedings of The Twelfth (2002) International Offshore and Polar Engineering Conference, Kitakyushu, Japan, 26–31 May 2002. Copyright © 2002 by the International Society of Offshore and Polar Engineers, ISBN 1-880653-58-3 (Set); ISSN 1098-6189 (Set)
8. American Society for Testing and Materials (ASTM) (2007) Standard Test Method for Particle-Size Analysis of Soils. Designation D422-63(2007), Philadelphia
9. American Society for Testing and Materials (ASTM) (2005) Standard Test Methods for Liquid Limit, Plastic Limit, and Plasticity Index of Soils. Designation D4318-05, Philadelphia
10. American Society for Testing and Materials (ASTM) (2006) Standard test methods for specific gravity of soil solids by water pycnometer. Designation D854-06, Philadelphia
11. American Society for Testing and Materials (ASTM) (2007) Standard test methods for laboratory compaction characteristics of soil using modified effort (2674 kJ/m^3). Designation D1557-07, Philadelphia
12. American Society for Testing and Materials (ASTM) (2007) Standard test method for California bearing ratio of laboratory-compacted soils. Designation D1883-07, Philadelphia

13. American Society for Testing and Materials (ASTM) (2007) Standard test methods for unconsolidated undrained triaxial compression test on cohesive soils. Designation D2850-03(2007), Philadelphia
14. BS 8006-2010: Code of practice for strengthened/reinforced soils and other fills

Adsorption and Hydraulic Conductivity Studies on Bentonites in the Presence of Zinc

Saswati Ray, Anil Kumar Mishra and Ajay S. Kalamdhad

Abstract Clay liners are commonly used in landfills to avoid the contaminant migration from the waste to the groundwater and the surrounding environment. Bentonite contains montmorillonite mineral that offers favourable properties such as low hydraulic conductivity, high adsorption capacity, high cation exchange capacity and capacity to retard the percolation of pollutant through sorption. However, properties of bentonite can be affected due to the presence of various heavy metals in the leachate. The present investigation was conducted to examine the change in hydraulic conductivity and sorption capacity of bentonites in the presence of zinc (Zn^{2+}). Two different bentonites with different swelling, chemical and mineralogical composition were exposed to a series of consolidation test and batch study to examine the hydraulic conductivity and metal adsorption capacity for the geoenvironmental application. Langmuir and Freundlich models were used in order to understand the adsorption mechanism. Tests were performed at a various concentration of Zn^{2+} ranges from 100 to 1000 mg/L at room temperature and pH 5. The results indicate that with the increase in metal concentration hydraulic conductivity increases. Bentonite with a higher swelling capacity shows higher removal percentage and sorption capacity in comparison to bentonite of lower swelling capacity. The isotherm study predicts that equilibrium data obtained from the study fitted well with the Langmuir model. The study will assist the designer and engineer for opting bentonite type in the various geoenvironmental application.

Keywords Bentonite · Clay liner · Hydraulic conductivity · Sorption · Isotherm

1 Introduction

High exposure of zinc can cause a potential threat to the ecosystem and can impose an adverse consequence on the human being. Zinc can be highly toxic to the health of adults and children if the quantity exceeds the allowable limit. Major sources of

S. Ray (✉) · A. K. Mishra · A. S. Kalamdhad
Indian Institute of Technology Guwahati, Assam, India
e-mail: r.saswati@iitg.ac.in

A. Prashant et al. (eds.), *Advances in Computer Methods and Geomechanics*, Lecture Notes in Civil Engineering 55,
https://doi.org/10.1007/978-981-15-0886-8_40

zinc exposure to the human being and surrounding environment are sewage water, industrial wastewater containing zinc, households, tap water system, mining and smelting. This exposure can cause several severe health issues like infertility, stomach cramp, vomiting, nausea and cholesterol balance can even weaken the function of the immune system [27]. In order to decrease the processing costs, several researchers have focused on the practice of low-cost adsorbent. Clay minerals are cost-effective, easily available, and a good alternative for conventional treatment of the landfill leachate as an adsorbent [22]. Many investigations have been carried out by researchers to determine the sorption behaviour of the various types of pollutants such as lead, copper, cadmium and nickel by using clay minerals [5, 15]. Removal of toxic contaminants from aqueous solution was also carried out by using different clay minerals such as palygorskite clays and raw kaolinite [20, 25]. Leachate comprises toxic pollutants, which can pollute the surrounding environment and groundwater. Clay liner is used in the landfill in order to stop contamination by leachate so that it cannot further percolate. Due to low hydraulic conductivity, high specific surface area, contaminant adsorption capability and high swelling capacity bentonite are generally used as a barrier material in the landfill [9]. The compressibility of liner material is one of the utmost vital properties that help in computing the settlement analysis of the liner material [16]. Bentonite being a highly compressible material is easily gets compressed due to the presence of overburden pressure imposed by the waste piled in the garbage dumpsite. When the surcharge load is given to a saturated clay, the process of consolidation begins because of compression, which consequences in settlement of the liner material, and the extent is analysed after the thorough dissipation of the generated pore-water pressure [26]. In the past, many investigations have been carried out by several researchers concerning the change in the behaviour of bentonite in the presence of numerous toxic chemicals. Lo et al. [14] studied the migration of cadmium lead and zinc in Ottawa sand and bentonite-soil admixture and concluded that the hydraulic conductivity of bentonite-soil admixture increases noticeably when it is infused with the metal solution. Ouhadi et al. [19] investigated the interaction of the metal ion with bentonite at several pH ranges and concluded that at lower pH and higher metal concentration, there is a microstructural variation in bentonite and rheological performance of bentonite is controlled by the osmotic phenomenon. Nakano et al. [17] examined hydraulic conductivity behaviour and lead retention mechanisms on three locally available Japanese bentonites and one US bentonite to estimate the mechanisms and concluded that carbonate plays the important role at low lead concentration and precipitate as $PbCO_3$. They also showed that due to higher swelling capacity and montmorillonite content, hydraulic conductivity of the U.S. bentonite is lower as compared to Japanese bentonite. Liu and Zhou [13] investigated the sorption of nickel and copper on Na-bentonite in a single and binary system and concluded that Cu^{2+} exhibited greater sorption percentage than Ni^{2+} at the similar pH. Freitas et al. [10] examined the binary sorption of copper and silver on to the bentonite and the concluded that copper exhibited a higher sorption capacity as compared to silver.

For the practicality as a barrier material in the landfill, adsorption and hydraulic conductivity are important parameters of bentonite. Therefore, it is very necessary

to know the alteration in the behaviour of bentonite in the presence of heavy metal in order to predict the fate of heavy metal. The objective of the present study is to examine the influence of bentonites in the presence of different concentration of zinc (Zn^{2+}). Since bentonites with different mineralogical and chemical composition may act differently in the presence of heavy-metal pollutant, it is very necessary to study the behaviour of different bentonites in the presence of the heavy-metal pollutant. In the present investigation, two different bentonites having different chemical and mineralogical properties were evaluated for hydraulic conductivity and adsorption in the presence of various concentration of Zn^{2+}. The result of the study will help engineers in the design of liner systems. The heavy metal selected in the present study was Zn^{2+} as it is very dangerous and menacing for the human being and environment.

2 Materials and Methods

Bentonites used for the study were obtained from Barmer District of Rajasthan, India. The chemical, physical and elemental compositions of the bentonites are listed in Tables 1 and 2.

The free swelling test for the bentonite was performed as per ASTM D 5890 (2001). Atterberg's limits were performed according to ASTM D 4318 [2]. The specific surface area (SSA) of the bentonite was analysed by the method described by Cerato and Lutenegger [7]. The method defined by Chapman [8] and Pratt [21] was used to analyse the cation exchange capacity (CEC) of the bentonite. ASTM D698 [4] was followed to determine the maximum dry density (MDD) and the optimum moisture content (OMC) of the bentonite. The powder X-ray diffraction analysis was carried out on the bentonites to determine the montmorillonite content.

Table 1 Properties of bentonites

Properties	Bentonite-1	Bentonite-2
CEC (meq/100 gm)	40.2	36.2
Specific Surface Area (SSA) (m^2/g)	396.3	340.4
Free Swelling (mL/2g)	32.5	20.0
pH	8.9	9.2
Montmorillonite content (%)	72	64
Liquid limit (%)	480.0	305.0
Plastic limit (%)	40.0	39.0
Specific gravity	2.73	2.7
Optimum moisture content (OMC) (%)	33	33.5
Maximum dry density (MDD) (g/cm^3)	1.31	1.30

Table 2 Elemental composition of bentonites expressed as weight percent of the major element

Major and minor element oxides	Bentonite-1	Bentonite-2
SiO_2	48.79	50.70
Al_2O_3	18.17	19.09
Fe_2O_3	16.16	16.29
MnO	0.454	0.313
MgO	0.94	1.06
CaO	1.20	1.10
Na_2O	4.67	3.59
K_2O	1.45	1.52
TiO_2	2.00	2.13
P_2O_5	0.18	0.21

By X-ray fluorescence (XRF) by Gauhati University SAIF, Guwahati, India elemental composition of the bentonites was determined. A major amount in the leachate contributes to heavy metal. Zinc is chosen for the study since it is one of the main pollutants present in landfill leachate and can cause severe effects on surroundings and human health.

2.1 Determination of Hydraulic Conductivity

Consolidation tests were conducted to determine the hydraulic conductivities as per ASTM D 2435 [1]. Bentonites were mixed with water at their respective optimum moisture content and kept in the moisture-controlled desiccator for 24 h to achieve the moisture equilibrium. The moisture-equilibrated samples were then statically compacted in oedometer rings of a diameter of 60 mm to a thickness of 15 mm to its MDD. The whole assembly was then placed in the consolidation cell and positioned in the loading frame. The specimens were swamped in the DI water or to the respective zinc concentration (100 and 1000 mg/L) under the nominal pressure of 4.9 kPa and permitted to swell. The samples were consolidated by increasing the pressure slowly by an increment ratio of 1 (i.e., increased by 4.9, 9.8, 19.6 kPa at each step) to a maximum pressure of 784.8 kPa once the swelling was analysed. Then the change in the thickness of the soil sample was measured for each pressure increment from the dial gauge readings. The change in the void ratio corresponding to the increase in the overburden pressure was calculated as

$$\Delta e = \frac{\Delta H(1 + e_0)}{H} \tag{1}$$

where ΔH is the change in the thickness of sample due to the increase in pressure; H is the initial thickness of the sample; e_0 is the initial void ratio.

From the consolidation test result, a time-settlement curve was obtained at each pressure increment. The coefficient of consolidation (c_v) was obtained using Taylor's square root time ($\sqrt{T}$) method [23]. The coefficient of volume change was calculated as

$$m_v = -\frac{\Delta e}{\Delta\sigma(1+e_0)} \tag{2}$$

where $\Delta\sigma$ is the change in pressure and Δe is the change in void ratio. Coefficient of consolidation (c_v) was determined by the square root of time fitting method given by Taylor [23] (IS 2720 part XV).

The hydraulic conductivity (k) was calculated by fitting Terzaghi's theory of consolidation [24] for various pressure increments using the c_v and m_v as

$$k = c_v m_v \gamma_w \tag{3}$$

2.2 Batch Study

According to ASTM [3], a series of batch test was performed to investigate the sorption of zinc on bentonite clay. A stock solution of zinc was prepared by dissolving the desired amount of zinc nitrate [$Zn(NO_3)_2{\cdot}3H_2O$] in deionized water (DI water). Batch adsorption tests were conducted in conical flask including 100 ml of aqueous solutions having initial zinc concentration of 100, 250, 500, 750 and 1000 mg/L and 5 g of the bentonite-soil as an adsorbent at the temperature of 28 ± 2 °C and pH of 5. The value of pH was adjusted by using diluted NaOH and HNO_3 solution. The flask containing the solution was shaken at 150 rpm in a shaker for 24 h. The solution was then centrifuged for 15 min at 3000 rpm. The supernatant was separated by filtration by using Whatman 42 filter paper. The concentration was analysed by using atomic absorption spectrophotometer (AAS) (Varian Spectra 55B).

The amount of Zn^{2+} adsorbed was calculated using the following equation:

$$q_e = \frac{(C_0 - C_e)V}{m} \tag{4}$$

where q_e(mg/g) is the amount of Zn^{2+} adsorbed on the bentonites, C_0(mg/L) is the initial concentration of Zn^{2+}, C_e(mg/L) is the concentration of Zn^{2+} in equilibrium solution, $V(L)$ is the volume of Zn^{2+} solution, and m(g) is the mass of the adsorbent. The tests were done in triplicates.

2.3 Adsorption Isotherm

The acquired experimental data are generally well fitted with the Langmuir and Freundlich models. Langmuir model explains the monolayer coverage at higher concentrations, whereas Freundlich models describe the adsorption process at low coverage. Adsorption isotherm models of bentonites for Zn^{2+} were described mathematically in terms of Langmuir and Freundlich models [11, 12].

The equation for the Langmuir isotherm model can be denoted by

$$q_e = \frac{bq_{\max}C_e}{1 + bC_e} \tag{5}$$

where $q_{\max}$ is the maximum capacity of contaminant retained per unit mass of the bentonite clay and b is a constant for Langmuir isotherm model.

The equation for the Freundlich isotherm model can be denoted by

$$q_e = K_f C_e^{1/n} \tag{6}$$

where K_f and n are constants for the Freundlich isotherm model.

3 Results and Discussion

3.1 Hydraulic Conductivity

The plot in Fig. 1 shows the relationship between hydraulic conductivity and void ratio of both the bentonites in the presence of DI water and 100 and 1000 mg/L of Zn^{2+}. Figure 1 represents that with the rise in Zn^{2+} concentration from 0 to 100 mg/L the hydraulic conductivity of both the bentonite increased slightly, though, the hydraulic conductivity increased considerably with the rise in concentration from 100 to 1000 mg/L. This is because with the increase in Zn^{2+} concentration, clay particles come nearer to each other and thickness of diffuse double layer gets reduced, causing a rise in the hydraulic conductivity value for bentonites [18]. Due to the increase in the concentration of Zn^{2+} from 0 to 100 mg/L, the hydraulic conductivity of Bentonite-2 was increased from 3.0×10^{-10} to 3.3×10^{-10} cm/s (39.91% increase). With a further rise in concentration to 1000 mg/L, the hydraulic conductivity value increased to 3.9×10^{-10} cm/s. Similarly, for Bentonite-1 the hydraulic conductivity increased by 14.28% for 1000 mg/L of Zn^{2+} concentration respectively.

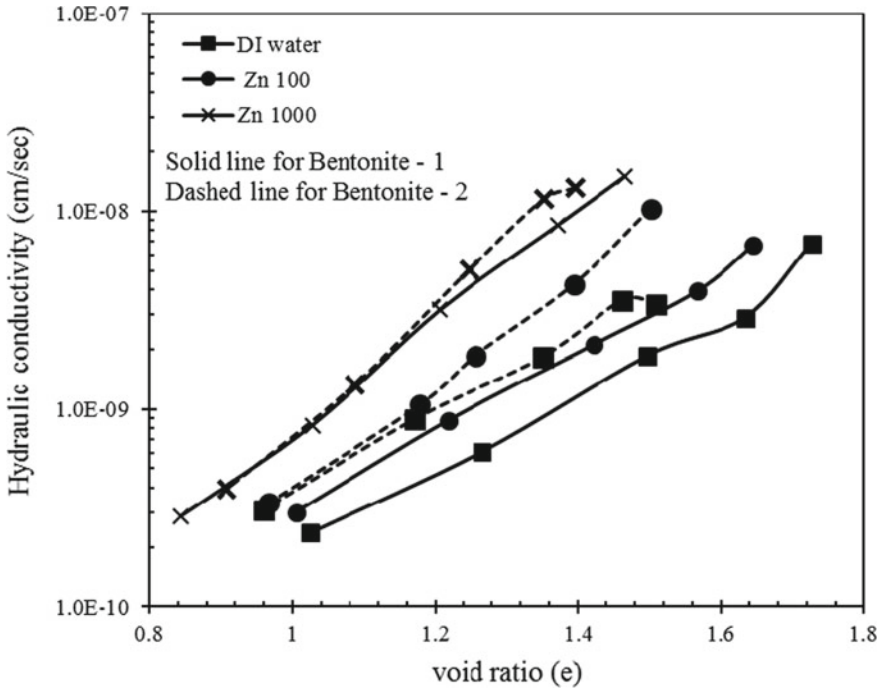

Fig. 1 Hydraulic conductivity versus void ratio with the Zn^{+2} solution of different concentration for the bentonites

3.2 Batch Study

Figure 2 shows the plot between the amounts of zinc adsorbed on both the bentonites for different initial Zn^{2+} concentrations ranging from 100 to 1000 mg/L. It shows that the adsorption capacity increased with the increase in Zn^{2+} concentration. Figure 2 also shows that at lower concentration ranged from 100 to 500 mg/L, the quantity of Zn^{2+} adsorbed on both the bentonites were nearly equal. It may be due to the availability of the considerable number of sorption sites present on the bentonites. Montmorillonite is majorly present in bentonite, which is a clay substantial of the aluminium phyllosilicate. The higher adsorption capacity of bentonite can be clarified by vital attributes of smectite mineral of montmorillonite. The fundamental normal for montmorillonite is to assimilate the water atoms between its layers which cause huge swelling of bentonite. Montmorillonite likewise has the capacity to adsorb metal ions on the outside and inward surfaces. Adsorption happens by cation exchange in the inside surfaces and it additionally happens by the arrangement of Si–O and Al–O groups on the outer surfaces. Since the quantity of layer charges in the inward surfaces is higher than the quantity of edge charges on the outer surfaces, the cation

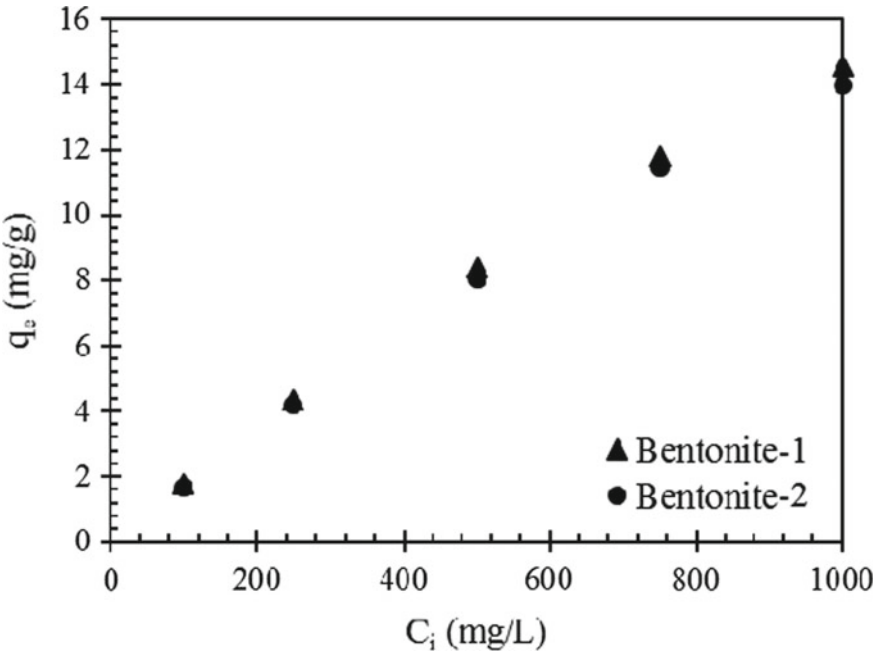

Fig. 2 Effect of initial concentration of Zn^{2+} on bentonites

exchange is for the most part seen in the inner surfaces contrasted and the adsorption on the outside surfaces. In the interior surfaces, the gem structure of montmorillonite comprises two tetrahedral and octahedral layers. The focal tetravalent silicon (Si^{4+}) can be displaced by trivalent aluminium particles (Al^{3+}) in the tetrahedral layers, and the trivalent aluminium particles (Al^{3+}) can be displaced by divalent cations (normally Mg^{2+} and Fe^{2+}) in the octahedral layers. Thus, the layers turn out to be negatively charged. The negatively charged layers are regularly balanced by the hydrated cations in the inside surfaces. The cations are reinforced with electrostatic forces of attraction to these interior surfaces; thus they can be displaced with different cations. Cations can be reinforced into the crystal lattice when the span of the cation is like the pore sizes in the structure of montmorillonite, and accordingly, they diminish the negatively charged layer [6]. Bentonite-1 showed 4.25% higher adsorption capacity as compared to Bentonite-2 at 1000 mg/L of initial Zn^{2+}. The difference may be due to the difference in cations associated at exchangeable sites and mineralogical composition.

Figure 3 shows the plot between removal percentage and initial zinc concentration. It illustrates that, with the increase in zinc concentration, removal percentage decreased. At 100 mg/L the higher percentage removal was obtained due to the availability of more number of sorption sites for both the bentonite. With the increase in

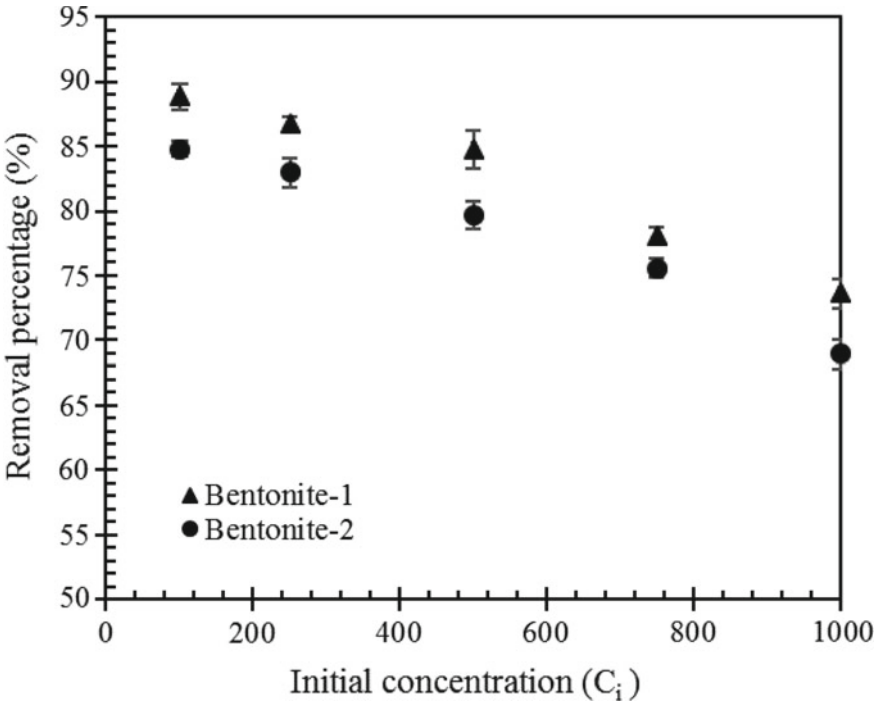

Fig. 3 Percentage removal of the Zn^{2+} at various initial concentrations

concentration to 1000 mg/L, the removal percentage was 73.63% and 68.94% for Bentonite-1 and Bentonite-2 respectively.

3.3 Isotherm Study

Figures 4 and 5 and experimental data revealed that both the bentonites fitted well to Langmuir and Freundlich isotherms models. However, the Langmuir model fitted better than the Freundlich model. The values obtained from both the isotherm models are listed in Table 3. The table illustrates that the regression coefficients (R^2) values of Langmuir model ($R^2 > 0.99$) are slightly higher than Freundlich model ($R^2 > 0.98$) which indicates that adsorption takes place in monolayer coverage on the bentonite surface.

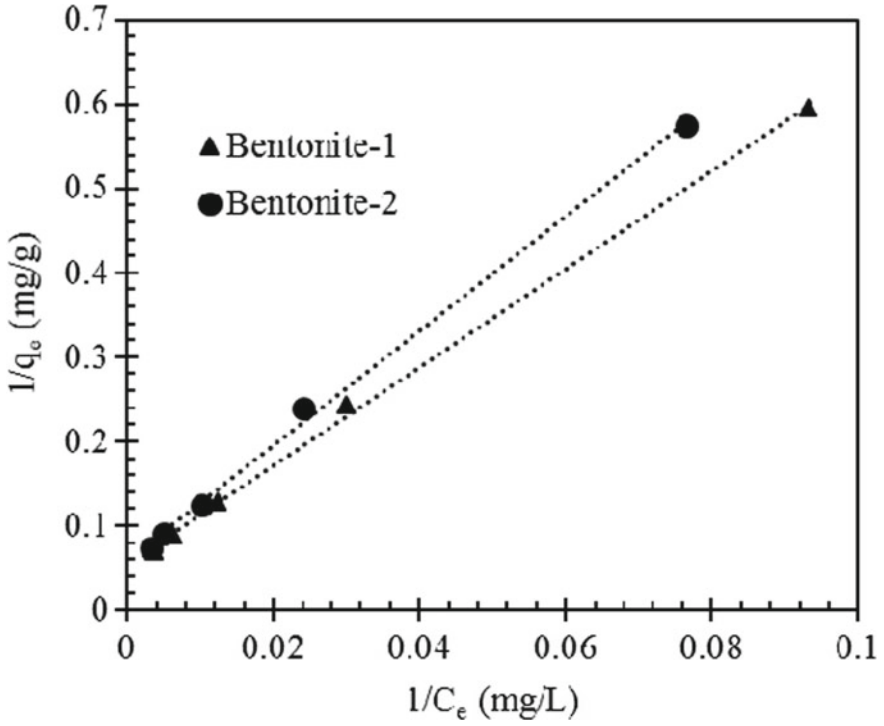

Fig. 4 Linearized Langmuir for Zn^{2+} removal by bentonites

4 Conclusions

This investigation was conducted to study the effect of zinc on the behaviour of bentonites having different chemical and mineralogical compositions. Bentonites were studied for their change in the adsorption characteristics and hydraulic conductivity due to the presence of various concentrations of zinc. The results showed that with the increase in zinc concentration, hydraulic conductivity value of both the bentonite increased. The adsorption study shows that with the increase in zinc concentration adsorption capacity increased. Bentonite-1 shows 4.25% higher adsorption capacity than Bentonite-2 at 1000 mg/L of the initial concentration of Zn^{2+}. Bentonite-1 with a higher cation exchange capacity, specific surface area and swelling capacity shows 6.38% higher removal percentage in comparison to Bentonite-2 at 1000 mg/L of Zn^{2+} concentration. Isotherm study shows that experimental data fitted well with Langmuir isotherm.

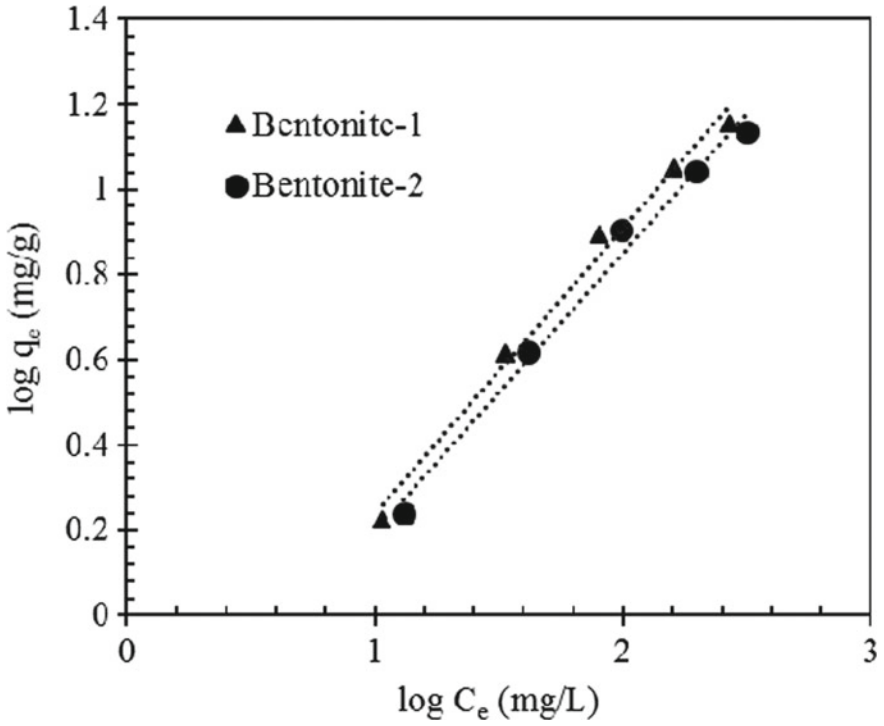

Fig. 5 Freundlich isotherm for Zn^{2+} removal by bentonites

Table 3 Parameters of sorption isotherms models for Zn^{2+}

Isotherm models	Parameters	Bentonite-1	Bentonite-2
Langmuir Isotherm	q_{max} (mg/g)	18.21	14.94
	b	0.017	0.015
	R^2	0.99	0.99
Freundlich isotherm	k_f	0.64	0.63
	$1/n$	0.67	0.65
	R^2	0.98	0.98

References

1. ASTM (1996) Standard test method for one-dimensional consolidation properties of soils. D 2435. American Society for Testing and Materials Philadelphia
2. ASTM (2000) Standard test methods for liquid limit, plastic limit, and plasticity index of soils. D 4318. American Society for Testing and Materials Philadelphia
3. ASTM (2008) Standard test methods for 24-h batch type measurement of contaminant sorption by soils and sediments. D4646-03. American Society for Testing and Materials West Conshohocken

4. ASTM (2012) Standard test methods for laboratory compaction characteristics of soil using standard effort. D 698, American Society for Testing and Materials Philadelphia
5. Barbier F, Duc G, Petit-Ramel M (2000) Adsorption of lead and cadmium ions from aqueous solution to the montmorillonite/water interface. Colloids Surf A 166:153–159
6. Baylan N, Meriçboyu AE (2016) Adsorption of lead and copper on bentonite and grape seed activated carbon in single-and binary-ion systems. Sep Sci Technol 51(14):2360–2368
7. Cerato AB, Lutenegger AJ (2002) Determination of surface area of fine-grained soils by the ethylene glycol monoethyl ether (EGME) method. Geotech Test J 25:1–7
8. Chapman HD (1965) Cation exchange capacity, Methods of soil analysis, part 2, chemical and microbiological properties, 2nd edn. Soil Science Society of America, Madison, Wisconsin, USA, pp 891–895
9. Dutta J, Mishra AK (2016) Influence of the presence of heavy metals on the behaviour of bentonites. Environ Earth Sci 75(11):1–10
10. Freitas ED, Carmo ACR, Neto AA, Vieira MGA (2017) Binary adsorption of silver and copper on Verde-lodo bentonite: kinetic and equilibrium study. Appl Clay Sci 137:69–76
11. Freundlich H (1906) Over the adsorption in solution. J Phys Chem 57:385–470
12. Langmuir I (1918) The adsorption of gases on plane surface of glass, mica and platinum. J Am Chem Soc 40:1361–1368
13. Liu ZR, Zhou SQ (2010) Adsorption of copper and nickel on Na-bentonite. Process Saf Environ Prot 88(1):62–66
14. Lo I, Luk A, Yang X (2004) Migration of heavy metals in saturated sand and bentonite/soil admixture. J Environ Eng 130(8):906–909. https://doi.org/10.1061/(ASCE)0733-9372(2004)130:8(906)
15. Mellah A, Chegrouche S (1997) The removal of zinc from aqueous solutions by natural bentonite. Water Res 31(3):621–629
16. Mishra AK, Ohtsubo M, Li LY, Higashi T (2010) Influence of the bentonite on the consolidation behaviour of soil bentonite mixtures. Carbonates Evaporites 25(1):43–49
17. Nakano A, Li LY, Ohtsubo M, Mishra AK (2008) Lead retention mechanisms and hydraulic conductivity studies of various bentonites for geoenvironment applications. Environ Technol 29:505–514
18. Ouhadi VR, Sedighi M (2003) Variation of experimental results of oedometer testing due to the changes of pore fluid. Deformation characteristics of geomaterials. A.A. Balkema, Rotterdam, Netherlands, pp 299–304
19. Ouhadi VR, Yong RN, Sedighi M (2006) Influence of heavy metal contaminants at variable pH regimes on rheological behaviour of bentonite. Appl Clay Sci 32:217–231
20. Potgieter JH, Potgieter-Vermaak SS, Kalibantonga PD (2006) Heavy metals removal from solution by palygorskite clay. Miner Eng 19(5):463–470
21. Pratt PF (1965) Sodium, methods of soil analysis, Part 2 chemical and microbiological properties, 2nd edn. Soil Science Society of America, Madison, Wisconsin, USA, pp 1031–1034
22. Sanchez AG, Ayuso EA, Blas O (1999) Sorption of heavy metals from industrial waste water by low-cost mineral silicates. Clay Miner 34(3):469–469
23. Taylor DW (1948) Fundamentals of soil mechanics. Wiley, New York
24. Terzaghi K (1943) Theoretical soil mechanics. Wiley, New York
25. Yavuz Ö, Altunkaynak Y, Güzel F (2003) Removal of copper, nickel, cobalt and manganese from aqueous solution by kaolinite. Water Res 37(4):948–952
26. Yong RN, Warkentin BP (1975) Soil properties and behaviour. Elsevier, New York
27. Zhang X, Yang L, Li Y, Li H, Wang W, Ye B (2012) Impacts of lead/zinc mining and smelting on the environment and human health in China. Environ Monit Assess 184(4):2261–2273

Development of Soft Soil Improvement Scheme for Lateral Stability of Railway Bridge Abutment

Md. Jahangir Alam, Mahmudul Islam and Muhammad Saiful Islam

Abstract This paper describes the development of a design scheme of soft ground improvement using Sand Compaction Pile (SCP) around the abutment of Railway Bridge. Subsoil at studied bridge abutment location was thick soft clay underlain by medium dense to dense sand layers. It was found that lateral movement of pile supported abutment was 100 mm without subsoil improvement. To control excessive lateral deformation of abutment, soft clay later need to be improved. SCP was considered as the ground treatment scheme. 3D finite-element simulation was conducted to optimize replacement ratio and extent of ground treatment. 3D finite element parametric study shows that lateral displacement of the abutment is within allowable limit when the subsoil is improved using SCP. It was also concluded that SCOP treatment needed to be extended 5 m towards the river side, 5 m surrounding the pile cap and 10 m in land side for optimum effect of ground improvement.

Keywords Soft ground improvement · Abutment lateral stability · Sand compaction pile

1 Introduction

Design of pile supported bridge abutment in soft clay is challenging. If subsoil is not improved, some problems are raised; for example, lateral capacity of pile is so low that number of pile increases, due to negative skin friction vertical capacity of pile also decreases and differential settlement between abutment and approach embankment would create serviceability problem of railway track.

The studied railway bridge abutment is located on 9 m thick soft clay layer underlain by sand layer. As per design, abutments are supported on pile foundation where embankment is on soft clay/silt. The construction sequence was such that, the abutments are constructed before approach embankment construction. This construction

Md. J. Alam · M. Islam (✉) · M. S. Islam
Bangladesh University of Engineering & Technology, Dhaka, Bangladesh
e-mail: mahmudul.ie@gmail.com

A. Prashant et al. (eds.), *Advances in Computer Methods and Geomechanics*, Lecture Notes in Civil Engineering 55,
https://doi.org/10.1007/978-981-15-0886-8_41

sequence led to problems such as squeezing out of soft soils underneath the abutment during construction of approach embankment, which may cause instability of the abutment losing its serviceability. This lateral soil movement induces severe damage to infrastructure. Many researchers have contributed to the study of the lateral movement of piled bridge abutments that undergo lateral soil movement in soft ground [5–7, 14–16] etc. De Beer and Wallays [4] noted, if piles are placed in such soil, stresses and deflection will develop on the piles due to the lateral earth pressure from the soft ground. Damages to abutments caused by lateral soil movement are still being reported [2, 10, 13, 18]. Therefore, lateral stability of abutment on soft clayey soil is an important factor for designers to consider while designing ground improvement scheme.

Ground improvement scheme using Sand Compaction Pile (SCP) is one of the many solutions available currently. Traditional ground improvement under approach embankment using SCP typically consist varying or uniform length of SCP distributed along the length of the bridge approach embankment. But, in the studied case here, installation of piles and abutment construction were completed before subsoil improvement, which led to modification of ground improvement scheme. This paper presents the development of a ground improvement scheme under such condition.

Predictions of lateral movements using the finite-element method are demonstrated by Siriwardane et al. [17]. To illustrate the studied problem, 5 m high embankment on field subsoil condition was modeled in FEM software, PLAXIS 3D. Without subsoil improvement, excessive lateral displacement of abutment was noticed. To control this excessive displacement within an allowable limit, various extent of SCP improved ground and different replacement ratio were studied.

2 Ground Improvement

2.1 Subsoil Condition at Site

At studied bridge approach location, subsoil is 9 m thick soft clay underlain by medium dense to dense sand layers. Due to the soft clay layer, following problems were identified:

a. Lateral instability of abutment,
b. Long-term settlement of embankment at bridge approaches
c. Differential settlement between abutment and approach embankment
d. Negative skin friction at piles under abutment

As per design, embankment at the investigated site is 5 m high, abutments are supported on group of piles. Longitudinal sections of the embankment near the bridge approach is as shown in Fig. 1, which is a schematic longitudinal section, showing

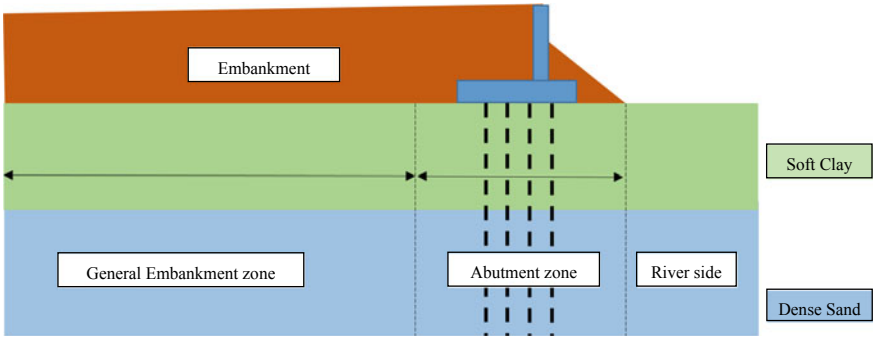

Fig. 1 Longitudinal section of bridge approach

different zones represented to describe extent of ground improvement, and subsoil condition at site.

2.2 Sand Compaction Pile Design

Barksdale and Bachus [1] and Juran and Guermazi [11] showed granular piles are most effective in clayey soils with undrained shear strength in the range of 7–50 kPa. In this studied approach embankment, susboisl consist 9 m thick soft clay. According to Castro et al. [3], Han and Ye [9] and Greenwood [8] granular piles can be used in cohesive soils in order to improve bearing capacity, accelerate the consolidation process hence, reduction in post consolidation settlement and total settlements by quick dissipation of excess pore pressure. Therefore, to mitigate identified problems listed above, SCP was preferred. Based on the available SCP installation method in Bangladesh, 300 mm diameter of SCP and triangular distribution pattern is selected as shown in Fig. 2. Spacing of SCP and respective area replacement ratio is selected from the lateral deflection versus replacement ratio curve as shown in Fig. 7. Starting with spacing 600 mm up to 1500 mm was considered initially, then considering lateral stability and cost optimization, 800 mm (respective area replacement ratio 0.13) spacing is selected. Extent of ground improvement was selected from the results of FE analyses. All the FE analyses are discussed in following sections.

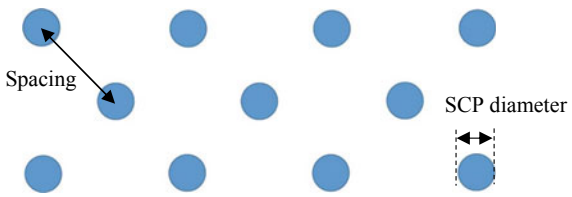

Fig. 2 Triangular patterned SCP

2.3 Design Criteria

Failure modes considered for ground improvement under bridge abutment founded on group piles, includes lateral stability of the abutment, slip failure of the abutment during embankment construction, cost optimization and project time constraints. Lateral stability of the abutment is the focus of this study. Therefore, other failure modes are not discussed in this paper although they were checked as well.

Hambly showed global behavior of pile supported abutment on soft soil can be thought of as resisting a circular motion of the embankment and ground as shown in Fig. 3. Probable failure mode and lateral displacement of bridge abutment on soft soil was assumed to be this way initially which was later compared to the analyses results. Ground improvement had to be designed to mitigate abutment lateral displacement as shown.

Allowable lateral displacement of abutment varies depending on the required serviceability. Moulton [12] regarded lateral movement of abutment that exceeds 2 in. (50 mm) as intolerable. Lateral movement criteria for bridge abutments expressed in terms of movement magnitude in Korea, where lateral movement magnitude of abutment less than 15 mm is considered tolerable. According to Japanese specifications for highway bridges Part II (Steel Bridge) or Part III (Concrete Bridge), 2012 the allowable lateral displacement at the top of abutment wall is 15 mm. According to BNBC-2017, maximum permissible lateral displacement of pile top is 5 mm, and according to NAVFAC DM 7.2 (2) the maximum allowable deflection of pile is often 6 mm. In this study, maximum allowable lateral deflection of abutment wall top was kept within 8 mm, so that pile top lateral displacement is less than that to satisfy limits mentioned above.

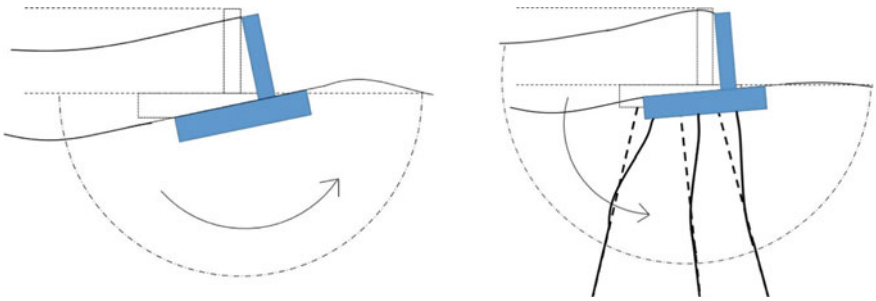

Fig. 3 Failure mode of bridge abutment (with and without piles) on soft soil

3 PLAXIS 3D Model

3.1 Geometry

FE analyses are conducted on bridge approach with pile supported abutment under working load. Dimension of the embankment is modeled as per design of embankment. Subsoil is modeled according to the respective bore hole log of the site. Figures 4 and 5 shows the components of the model.

From the results of the FE analysis of untreated ground, extent of SCP improved ground in has been varied to develop an optimum ground improvement scheme.

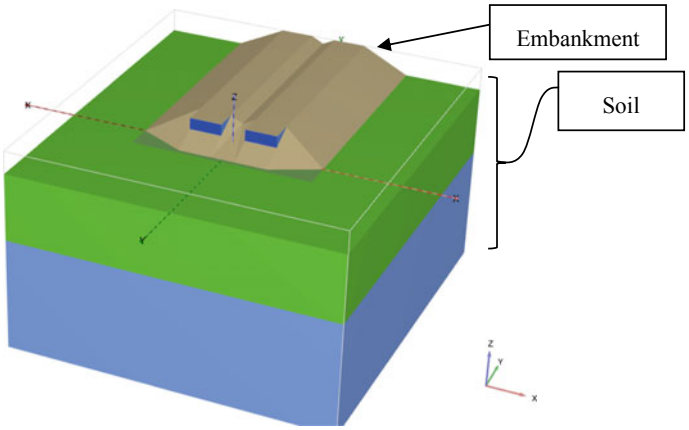

Fig. 4 FE Plaxis 3D model

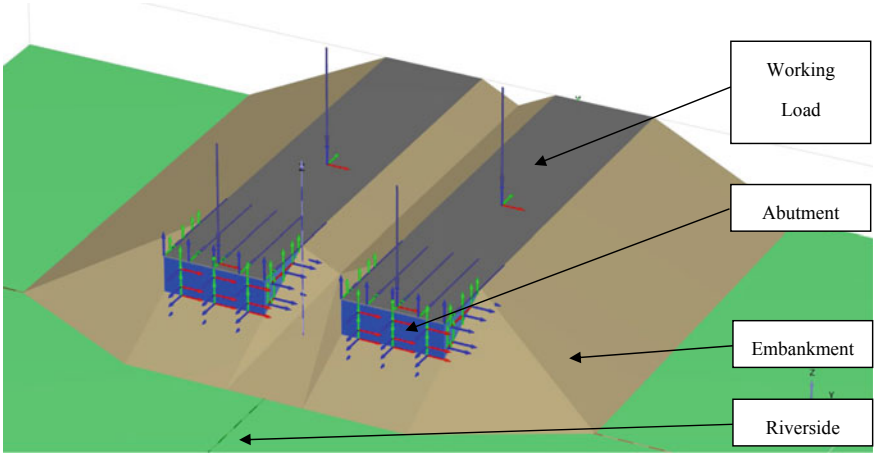

Fig. 5 Close-up view of model: showing embankment, abutment, loading

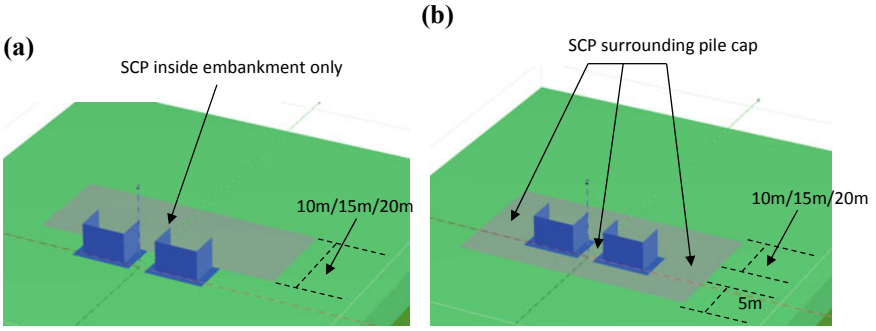

Fig. 6 SCP improved ground extent; **a** 10 m/15 m/20 m inside the embankment only, **b** 10 m/15 m/20 m inside the embankment + 5 m towards river side + surrounding the pile cap (excluding area under the pile cap)

Ground improvement extent inside the embankment from pile cap varied from 10, 15 and 20 m as shown in Fig. 6a. Then ground improvement extent inside the embankment (10/15/20 m) as well as 5 m towards the river side was checked as shown in Fig. 6b.

3.2 Materials

Material properties are based on the field bore hole log. Laboratory data from geotechnical investigation report has been used to determine some of the properties. Some assumptions such as material properties (e.g., dilatancy angle = 0°), ground water level at ground surface, are made to be on the conservative side. The material parameters used in model, are presented in Table 1.

4 Results and Discussions

4.1 Replacement Ratio

To select the spacing of the sand piles, 3D FE analysis was conducted varying replacement ratio. For these initial analyses, ground improvement extent was throughout the length of the embankment and towards riverside, and under the pile cap as well. Results indicated that deflection of the abutment top varies from 2 mm to 10 mm for different replacement ratios as shown in Fig. 7. From the curve, it was evident that lateral displacement of abutment can be controlled within limit, even with low replacement ratio if only ground improvement is applied under the abutment and pile

Table 1 Material properties used for analysis

Parameter	Name (Unit)	Embankment	Soft clay	Dense sand	Sand pile
Plaxis model		Mohr-Coulomb	Mohr-Coulomb	Mohr-Coulomb	Mohr-Coulomb
Unit weight (unsaturated)	γ_{unsat} (kN/m^3)	18	16	18	18
Unit weight (saturated)	γ_{sat} (kN/m^3)	20	18	20	20
Drained elastic modulus	E′ (KN/m^2)	20,000	12,000	20,000	18,000
Poisson's ratio	v′ (nu)	0.30	0.35	0.30	0.33
Effective cohesion	c′ or s_u (kPa)	30	10	1	1
Effective friction angle	φ′ (degree)	35	0	35	30
Dilatancy angle	ψ′ (degree)	0	0	0	0

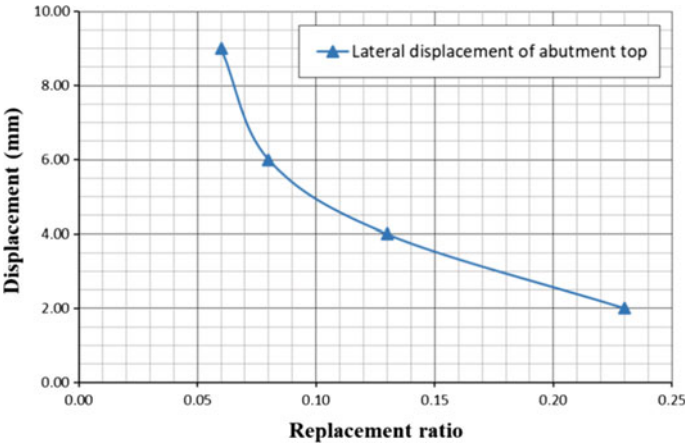

Fig. 7 Effect of replacement ratio on lateral displacement of abutment top

cap along with the surrounding areas and along the embankment length. But as mentioned earlier, piles and abutment had been constructed already, ground improvement was not possible below the abutment; therefore, extent of improved ground needed to be modified keeping the soil underneath the abutment unimproved.

4.2 *Lateral Displacement of Abutment*

Without ground improvement, lateral displacement of abutment is excessive. But from this analysis of untreated ground condition, the extent of maximum affected area is identified as shown in Fig. 8.

After identifying the extent of ground improvement required, extent of SCP improved ground was varied to find the best optimized solution for lateral stability of abutment. Ground improvement extent only inside the embankment is studied for 10, 15 and 20 m extension inside the embankment. Also, ground improvement was extended 5 m towards the river side and analyzed. Lateral displacement of abutment top versus different ground improvement extent is plotted and shown in Fig. 9.

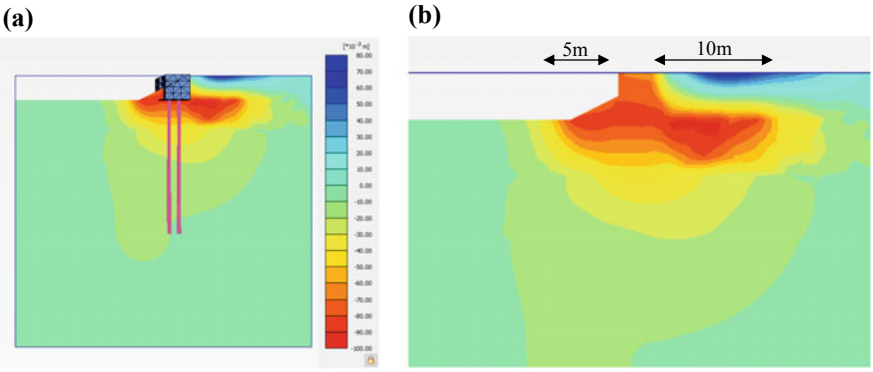

Fig. 8 Displacement of pile supported abutment on unimproved ground **a** showing structures **b** extent of maximum affected area

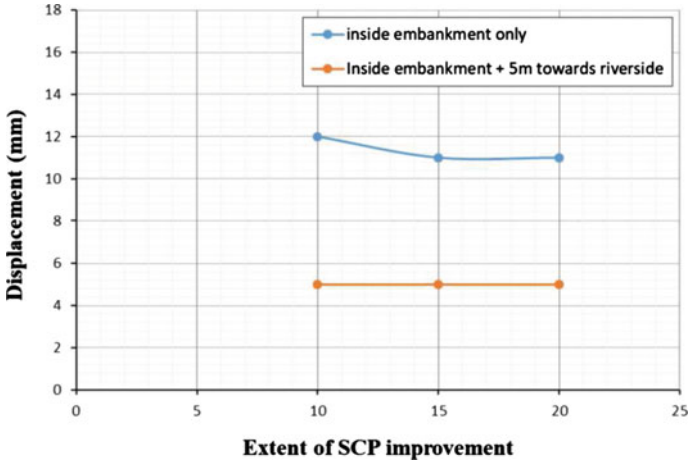

Fig. 9 Lateral displacement of abutment top versus different extent of ground improvement

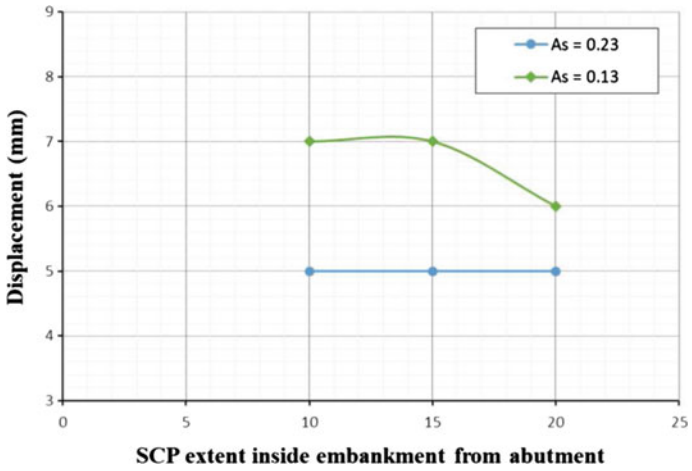

Fig. 10 Lateral displacement of abutment top versus SCP extent (different A_s)

It is clear that lateral stability of abutment increases with the extension of ground improvement inside the embankment when there is no ground improvement towards riverside. But when ground improvement was extended 5 m towards the river, it increased lateral stability of the abutment significantly, regardless the extension of improvement inside the embankment.

Further, ground improvement extent in both sides (towards riverside & inside the embankment) of abutment was studied for 600 and 800 mm spacing of SCP, respective area replacement ratios (a_s) are 0.23 and 0.13. Lateral displacement of abutment top vs a_s is plotted as shown in Fig. 10. It is clear that, if $a_s = 0.23$, extent of ground improvement inside the embankment can be minimized to 10 m only. But if $a_s = 0.13$, similar lateral stability can be obtained but improvement must be extended more than 20 m or so.

All the analyses performed for this study are listed below.

- option *a*: 10 m inside the embankment only
- option *b*: 15 m inside the embankment only
- option *c*: 20 m inside the embankment only
- option *d*: 10 m inside the embankment + 5 m towards riverside
- option *e*: 15 m inside the embankment + 5 m towards riverside
- option *f*: 20 m inside the embankment + 5 m towards riverside

Results of the analyses are compiled and shown in Table 2; where "Inside embankment only" refers to analyses of models as shown in Fig. 6a and "Inside embankment + towards river + surrounding pile cap" refers to analyses of models as shown Fig. 6b.

From the results, it is found that ground improvement extent option *d*, option *e*, option *f* shown in Table 2, with $a_s = 0.23$ (spacing 600 mm) provides the best lateral stability.

Table 2 Lateral displacement of abutment top for various options of ground improvement

		SCP distribution on bridge approach								
		Inside embankment only			Inside embankment + towards river + surrounding pile cap					
	Without SCP	a. 10 m inside embankment	b. 15 m inside embankment	c. 20 m inside embankment	d. 10 m inside + 5 m outside		e. 15 m inside + 5 m outside		f. 20 m inside + 5 m outside	
A_s	–	0.23	0.23	0.23	0.23	0.13	0.23	0.13	0.23	0.13
Displacement (mm)	90	12	11	11	5	7	5	7	5	6

**all the displacements are towards river side

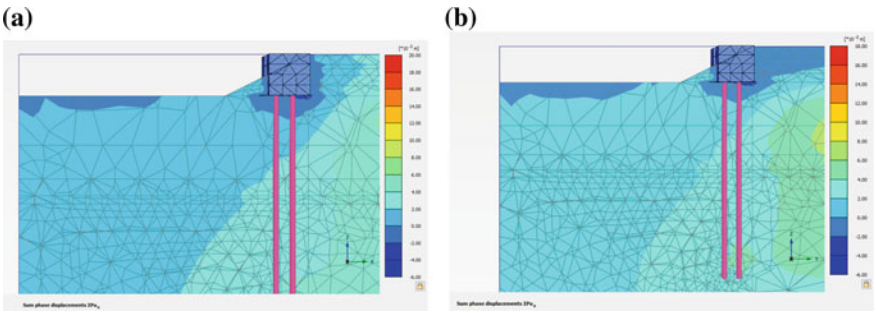

Fig. 11 Lateral displacement of abutment using $a_s = 0.23$ and improvement extent **a** option *d* **b** option *f*

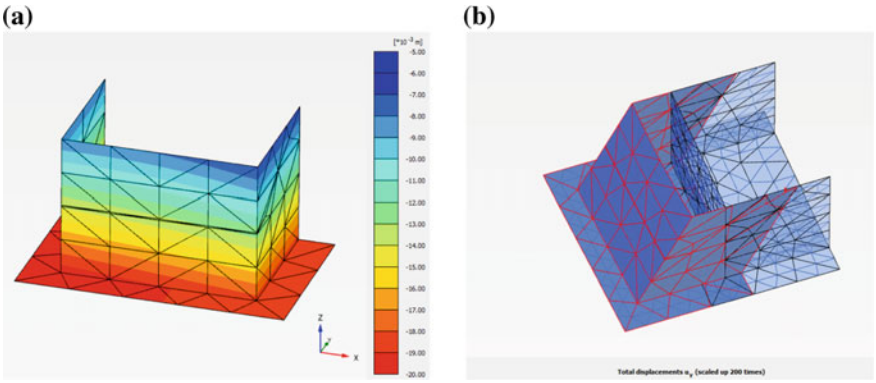

Fig. 12 Lateral displacement of abutment **a** using option *d* with $a_s = 0.23$ **b** deformed shape

Figure 11 shows results of option *d* and option *f*. These two options provide the similar results. But from an economic consideration, option *d* seemed to be more suitable. Figure 12 shows lateral displacement of abutment. Figure 12b verifies failure mode suggested by Hambly.

5 Conclusions

The development of an alternative ground improvement scheme under railway embankment bridge approach considering constraints in design has been discussed in this paper. The following conclusions can be drawn from the results of the analyses.

- Lateral displacement of abutment decreases with the increase of area replacement ratio of Sand Compaction Pile;

- Lateral displacement of abutment can be controlled using very low area replacement ratios (0.06) if SCP is done under and around abutment.
- For an embankment of 5 m height, SCP improvement extent at least 10 m inside the embankment and 5 m towards the river side from abutment and surrounding the pile cap found to be satisfactory for lateral stability.
- Generation of excess pore pressure and dissipation could have been modeled if effective stress coupled models were used to simulated soft clay.

Further studies and field instrumentations are needed for validation of the developed method. It is usually not required to model the full foundation but a representative section is sufficient. By doing so, the validity of numerical models can be significantly improved.

References

1. Barksdale RD, Bachus RC (1983) Design and construction of stone columns, federal highway administration, RD-83/026
2. Bozozuk M (1978) Bridge foundation move. Transp Res Rec 678:17–21
3. Castro J, Cimentada A, Costa A, Canizal J, Sagaseta C (2013) Consolidation and deformation around stone columns: comparison of theoretical and laboratory results. Comput Geotech 49:326–337
4. De Beer EE, Wallays M (1972) Forces induced in piles by unsymmetrical surcharges on the soil around the piles. In: Proceedings of 5th ICSMFE, pp 325–332
5. Duncan JM, Chang CY (1970) Nonlinear analysis of stress and strain in soils. J Soil Mech Foundation Eng 96:1629–1653
6. Ellis EA, Springman SM (2001) Modeling of soil-structure for a piled bridge abutment in plane strain FEM analysis. Comput Geotech 28(2):79–98
7. Folkes DJ, Crooks JHA (1985) Effective stress paths and yielding in soft clays below embankments. Can Geotech J 22:357–374
8. Greenwod DA (1970) Mechanical improvement of soils below ground surfaces, ground engineering conference, institution of civil engineers, London, pp 11–22
9. Han J, Ye SL (2001) Simplified method for consolidation rate of stone column reinforced foundation. J. Geotech Geoenv Eng ASCE 127(7):597–603
10. Hong WP, Kwon OH, Han JG, Cho SH (1994) A study on lateral movement of bridge abutment on soft ground. J Korean Geotech Soc 10(4):53–65 (in Korean)
11. Juran I, Guermazi A (1988) Settlement response of soft soils reinforced by compacted sand columns. J Geotech Geoenv Eng ASCE 114(8):903–943
12. Moulton LK (1986) Tolerable movement criteria for highway bridges. Final Report No. FHWA-TS-85–228, Federal Highway Administration, Washington, DC (1986) 86 pp
13. NAVFAC (1982) Soil mechanics design manual 7.1. Department of the Navy, Naval Facilities Engineering Command, Alexandria, VA
14. Reese LC, Cox WR, Koop FD (1975) Field testing and analysis of laterally loaded piles in stiff clay. In: Proceedings of 7th Offshore Technology Conference, pp 671–690
15. Smith IM, Hobbs R (1974) Finite element analysis of centrifuged and built-up slopes. Geotechnique 24:531–559
16. Stewart DP, Jewell RJ, Randolph MF (1994) Design of piled bridge abutments on soft clay for loading from lateral soil movements. Geotechnique 44(2):277–296

17. Siriwardane HJ, Moulton LK, Chen RJ (1984) Prediction of lateral movement of bridge abutments on piles. In Transportation Research Record 998: Testing and Modeling Soils and Soil Stabilizers, Transportation Research Board, National Research Council, Washington, DC, pp 14–24
18. Wahls HE (1990) Design and construction of bridge approaches. National Cooperative Highway Research Program Synthesis of Highway Practice 159. Transportation Research Board. Washington, DC

Effect of Interaction of Nearby Footings on Settlement of Foundation Under Building

Md. Jahangir Alam, Muhammad Saiful Islam, Mahmudul Islam and Md. Nazam Uddin

Abstract When the settlement of footing under building is calculated, it is common practice to estimate settlement of individual footing without considering the impact of neighboring footings. This common type of practice is unrealistic. This paper presents the impact of neighboring footing on elastic settlement of sand. In order to compare, settlement behavior of footings under building and isolated location, Finite Element Models have been generated by using PLAXIS 3D. The variation of settlement at different location especially at center, mid-edge and corner of building are presented. Settlement of individual footings under building is 1.5–5 times the settlement of individual footing at isolated location. Therefore, this issue should not be ignored during designing individual footings of a building. Settlements of individual footings under a building vary with the distance from center of the building. Maximum settlement was found at center of building. Footing Interaction Parameter (B/L), applied footing pressure and building size were found to be the most influential parameters.

Keywords Footing interaction · Footing · Elastic settlement · Plaxis 3D · Finite element model

1 Introduction

Professional Civil Engineers usually calculate settlement of individual footings without considering overlapping of pressure bulb of neighboring footings. The increase in number of neighboring footings, location, spacing, and contact pressure of footings has significant influences on settlement of footings under building. The increase in settlement of footing under building may reach up to 4–5 times the settlement

Md. J. Alam · M. S. Islam (✉) · M. Islam
Department of Civil Engineering, Bangladesh University of Engineering and Technology, Dhaka 1000, Bangladesh
e-mail: saifulislamce@gmail.com

Md. N. Uddin
Department of Civil Engineering, European University of Bangladesh, Dhaka, Bangladesh

A. Prashant et al. (eds.), *Advances in Computer Methods and Geomechanics*, Lecture Notes in Civil Engineering 55,
https://doi.org/10.1007/978-981-15-0886-8_42

of individual footing at isolated location [1]. Most geotechnical problems are very sensitive to foundation geometry (length, diameter, and spacing), flexural stiffness, etc. [2].

Settlement of an individual footing is highly influenced by number of neighboring footings and spacing of footings. A parametric study was conducted using 3D finite element elasto-plastic analysis. Studied parameters are modulus of elasticity, size of square footing, spacing of footings, building length and footing contact pressure. The variation of settlement at different location especially at center, mid-edge, and corner of building are compared with the settlement of single footing at isolated location where there is no neighboring footings within the pressure bulb of the footing. This paper presents the parametric study results. The result of the analysis suggested that the effect of neighboring footing on single footing settlement is significant. A new terminology named as Footing Interaction Parameter (B/L) which is the ratio of footing size (B) and spacing (L). Study reveals that most influential parameters are Footing Interaction Parameter, applied pressure and building size.

2 Finite Element Model

Plaxis 3D software was used for FE Analysis of the parametric study. 100–300 kPa pressure is applied to footings. Figure 1 shows a typical pattern of columns and footings where 9 footings are arranged in 3 × 3 matrix. The soil profile consists of 30 m sand layer under which hard stratum is assumed to simplify the analysis. The ground water level considered at ground surface. Footing bottom level is 2 m beneath the ground surface. Properties of idealized sand layer are given in Table 1. Variations of parameters are shown in Table 2. Figure 2 shows the deformed mesh of the FE model of footings and soil.

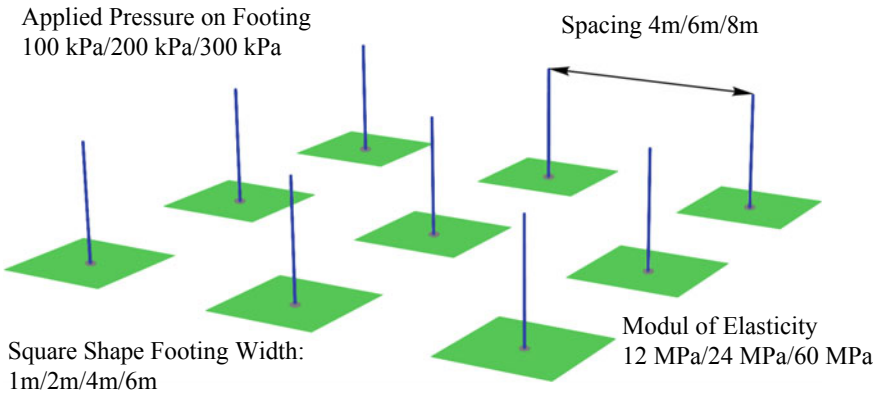

Fig. 1 3 × 3 matrix pattern footing arrangement

Table 1 Engineering properties of subsoil

Properties of Sand	Value
Constitutive model	Mohr-Coulomb
Saturated unit weight, γ_{sat}	18 kN/m^3
Initial void ratio, e_o	0.800
Modulus of elasticity, E	12–60 MPa
Poisson's ratio, υ	0.3
Cohesion, c	5 kN/m^2
Drained angle of friction, ϕ	35°

Table 2 Variation of parameters

Properties	Value
Modulus of elasticity	12 MPa, 24 MPa; 60 MPa
Square footing width	1 m, 2 m, 4 m, 6 m.
Footing arrangement pattern	1 × 1 matrix; 3 × 3 matrix; 5 × 5 matrix; 7 × 7 matrix.
Applied pressure on footings	100 kPa, 200 kPa, 300 kPa

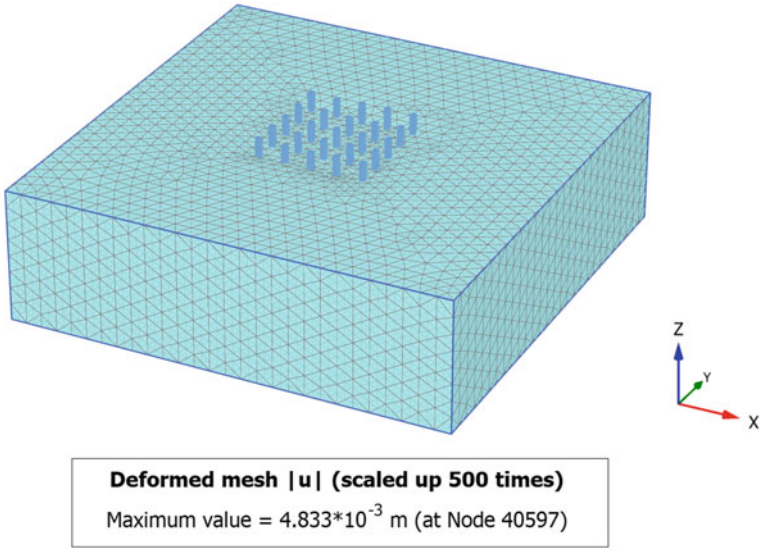

Fig. 2 Generated deformed mesh of FEM model in Plaxis 3D

3 Data Interpretation of Settlement Analysis

Settlement profile of 5 × 5 matrix footings is shown in Fig. 3 for 300 kPa contact pressure, Elastic Modulus 24 MPa and 6 m c/c footing spacing. Figure 3 shows that

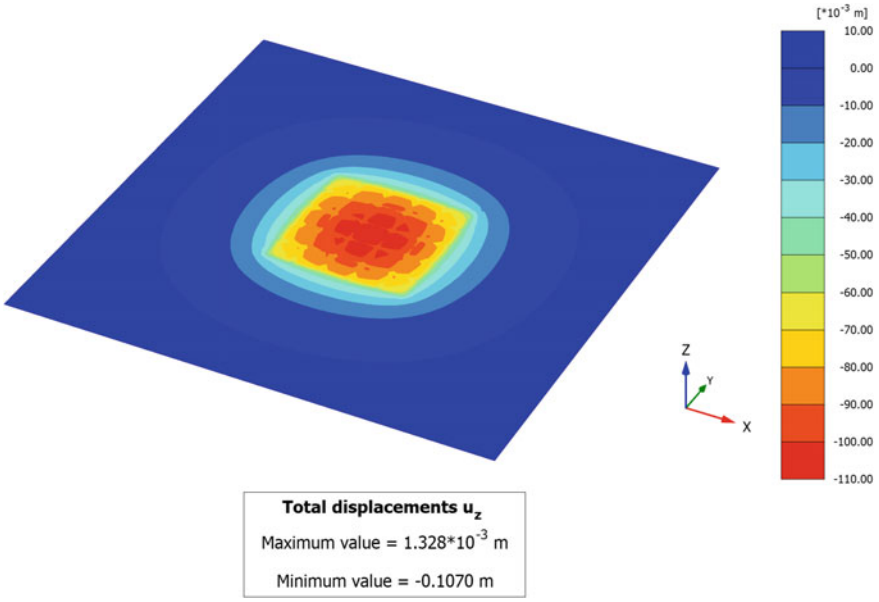

Fig. 3 General settlement profile for uniform contact pressure 300 kPa, 4 m × 4 m footing size, E = 24 MPa and 5 × 5 matrix of footings

higher settlement occurs at center footing and with the increase of distance from center footing, settlement of footings decreases.

3.1 Effect of Modulus of Elasticity and Building Size

It is obvious that settlement decreases with the increase of modulus of elasticity of soil. Since our objective is to find the ratio of settlement of an individual footing under building to that of an isolated individual footing (S_{center}/S_{ind}), S_{center}/S_{ind} is plotted against E in Fig. 4 for different building sizes. Here, the analyses were done using spacing 6 m, Poison's ratio 0.3 and footing size 4 mx4 m. S_{ind} denotes settlement of individual footing at isolated location and S_{center} is settlement of footing at center of the building. From this figure it is found that S_{center}/S_{ind} is sensitive to building sizes and insensitive to modulus of elasticity. S_{center}/S_{ind} increases with the increase of building size. When building size increases, depth of combined pressure bulb of all footings increases. This is the reason of increasing S_{center}/S_{ind} with building size. This fact is clearly visible in Figs. 5 and 6.

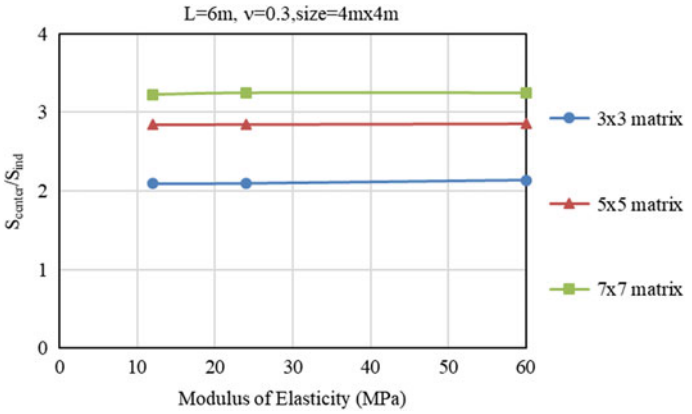

Fig. 4 Comparison of settlement variation with respect to modulus of elasticity of soil

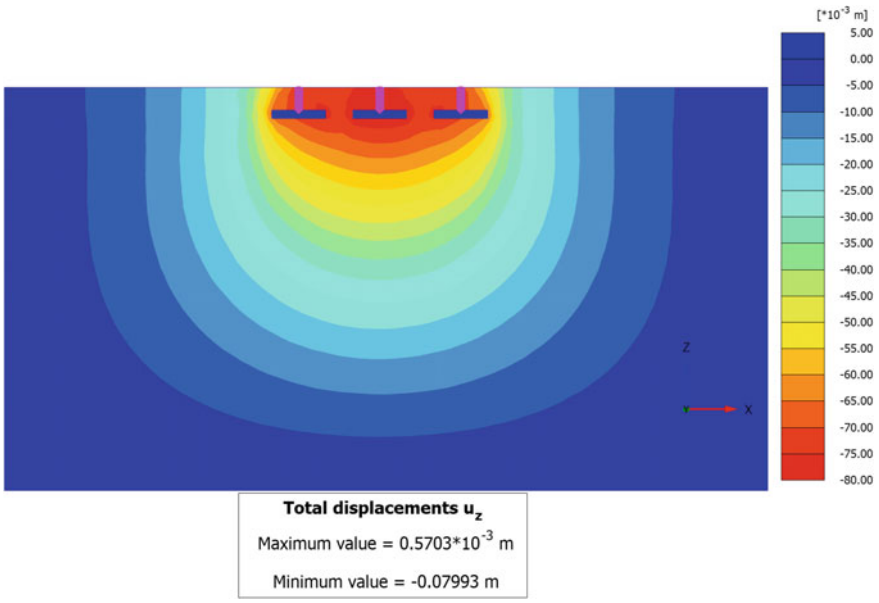

Fig. 5 Pressure bulb of 3 × 3 matrix of footings for 4 mx4 m footing size, 6 m spacing, E = 24 MPa and 300 kPa contact pressure

3.2 Effect of Footing Interaction Parameter

Ratio of footing width (B) to footing spacing (L) is defined as Footing Interaction Parameter (B/L). For spacing 6 m, poison's ratio 0.3 and E = 24 MPa, S_{center}/S_{ind} is plotted against B/L in Fig. 7 for different building sizes. It is clearly observed

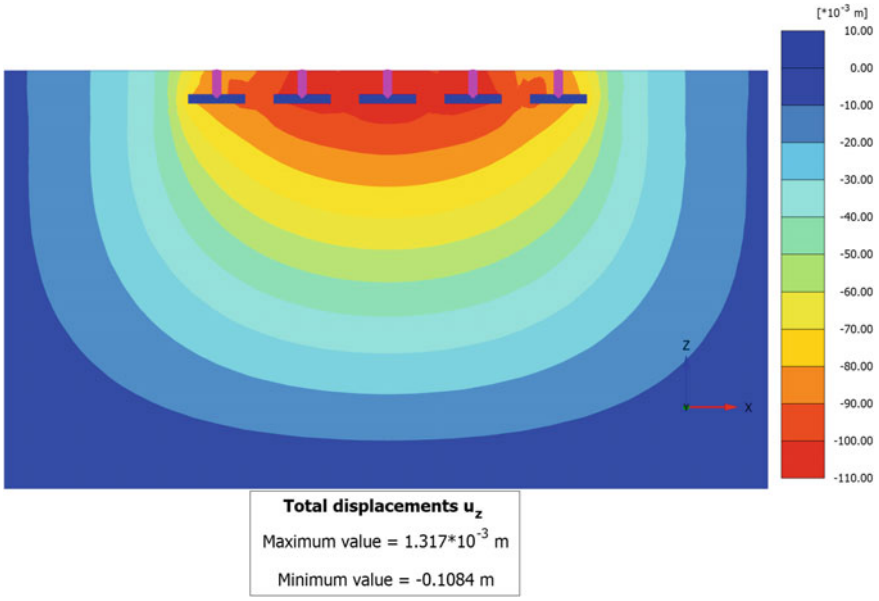

Fig. 6 Pressure bulb of 5 × 5 matrix of footings for 4 m × 4 m footing size, 6 m spacing, E = 24 MPa and 300 kPa contact pressure

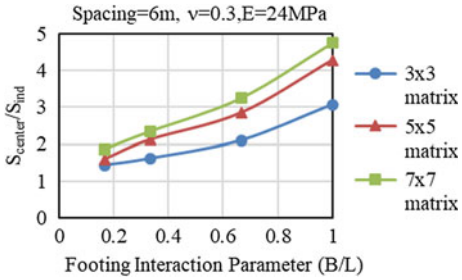

Fig. 7 Comparison of settlement variation with respect to Footing Interaction Parameter (B/L) and building size

that S_{center}/S_{ind} increases with the increase of B/L. Value of B/L 1.0 means total area is covered by individual footings which is something similar to a large flexible mat. Pressure bulbs of individual footings can no longer exist in this situation. With the increase of B/L, overlapping of individual pressure bulbs increases which is the reason of increasing S_{center}/S_{ind}.

For 3 × 3 matrix pattern footing arrangement, poison's ratio 0.3, E = 24 MPa, S_{center}/S_{ind} is plotted against B/L in Fig. 8 for different spacing of footings. With the decrease of spacing, overlapping of individual pressure bulbs increases which increases the S_{center}/S_{ind}. Also, effect of B/L is significant.

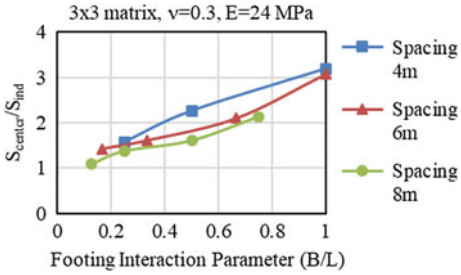

Fig. 8 Comparison of settlement variation with respect to footing interaction parameter and spacing

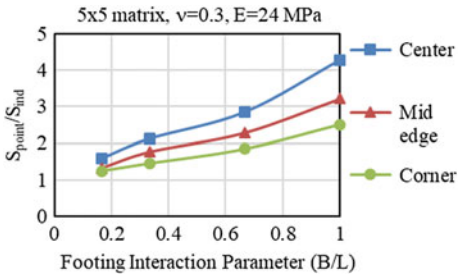

Fig. 9 Comparison of settlement variation at center, mid edge and corner for E 24000 kN/m^2

For 5 × 5 matrix, modulus of elasticity, E = 24 MPa, poison's ratio 0.3 S_{point}/S_{ind} is plotted against B/L in Fig. 9 for center, edge and corner footings. It is seen that settlement of all footings under a building is highly influenced by Footing Interaction Parameter.

3.3 Effect of Distance from Center of Building

Maximum settlement is found at center of the building. Settlement of footings at corner is minimum. Settlement of footing decreases with the increase of distance from center of building. S_{point}/S_{center} is plotted against distance from center of the

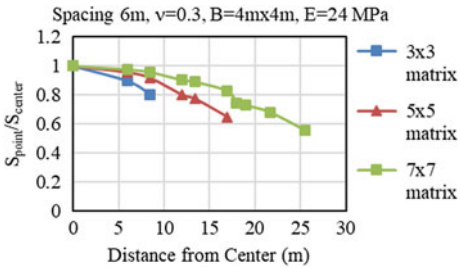

Fig. 10 Comparison of settlement variation with respect to footing distance from center

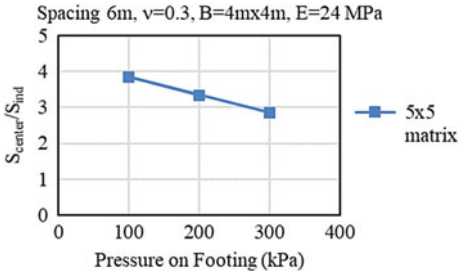

Fig. 11 Comparison of settlement variation with respect to applied pressure on footing

building in Fig. 10. For footing spacing 6 m, poison's ratio 0.3, footing size 4 m × 4 m and E = 24 MPa, these analyses were done.

3.4 Effect of Pressure on Footing

For increased pressure, settlement increases. However, S_{center}/S_{ind} decreases with the increase of applied pressure on footing. Figure 11 shows variation of S_{center}/S_{ind} with pressure for footing spacing 6 m, poison's ratio 0.3, modulus of elasticity, E = 24 MPa.

4 Validation of Results

A number of theories are available for the calculation of settlement of a single footing. However, only limited information is available to determining the influence of neighboring footings on a footing under building. So it is recommended to conduct further investigation with varieties of soil parameters and spacing. A comparison with Marawan Shahein, 2013 analyzed result is shown in below (Table 3).

5 Conclusions

The following conclusions may be drawn from the results of this parametric study:

- Settlement of individual footings under building is 1.5–5 times the settlement of individual footing at isolated location. Therefore, this issue should not be ignored during designing individual footings of a building.
- Settlement individual footings under a building vary with the distance from center of the building. Maximum settlement was found at center of building.
- S_{center}/S_{ind} is highly sensitive with Footing Interaction Parameter (B/L) and Building size. S_{center}/S_{ind} increases with the increase of B/L and building size.

Table 3 A comparison with Marawan Shahein 2013 and present study

Properties	Marawan Shahein, 2013	Present study
Comparison point	Center footing	Center footing
Soil profile and properties	Drained friction angle almost 35° and Deformation modulus E = 20–75 MPa	Drained friction angle 35° and Deformation Modulus E = 24 MPa
Total dimension of building	21 m × 27 m	24 m × 24 m
Size of footings	1.3 m × 1.3 m to 3.4 m × 3.4 m	4 m × 4 m size
Spacing of footings	3–5.75 m	6 m
Applied stress on footing	57–132 kPa	100 kPa. Details are given in Fig. 11
Comparison of settlement	Settlement of individual footings under building is 4 times the settlement of individual footing at isolated location	Settlement of individual footings under building is 3.9 times the settlement of individual footing at isolated location

- For increased pressure, settlement increases. However, S_{center}/S_{ind} decreases with the increase of applied pressure on footing.
- S_{center}/S_{ind} is not sensitive with Modulus of Elasticity. However, settlement increases with the decrease of Modulus of Elasticity.

References

1. Shahein M, Hefdhallah A (2013) Effect of neighboring footings on single footing settlement. In: Mossouri: Seventh international conference on case histories in Geotechnical engineering symposium in honor of Clyde baker, At Chicago, Illinoi, USA
2. Madhira M, Abhishek SV, Rajyalakshmi K (2015) Modelling ground–foundation interactions. Hyderabad, India: International Conference on Innovations in Structural Engineering, At Osmania University, December

Evaluation of Ground Motion Scaling Techniques

Jayaprakash Vemuri and Subramaniam Kolluru

Abstract Nonlinear Time History Analysis (NTHA) is a rigorous technique requiring the analyst to assemble a suite of ground motions to perform structural analyses. In current practice and literature, there are several techniques available to select and scale records: however, there is little or no consensus among researchers or designers regarding the accuracy of these techniques towards acceptability in structural design. The selection criteria for ground motions are unclear: parameters such as earthquake magnitude, epicentre distance, soil type, geotectonic setup and, the ratio of peak ground acceleration to velocity (A/V) have been used to develop ground motion suites. There is ambiguity in the current ground motion modification procedures as well: three techniques, namely, amplitude scaling, spectral matching and normalisation of records to the expected peak ground acceleration (PGA) are employed variously by researchers. Some codes allow the use of only one record while others permit three to seven records. In this study, the effect of selection and scaling of records on the structural response is examined using a single degree of freedom (SDOF) model of an unreinforced masonry wall. The structural response parameter is wall displacement. Data from major Himalayan earthquakes is used to develop a suite of records. Statistics of the storey displacement indicate that the amplitude scaling of records to match the PGA leads to inaccurate estimates of displacements. Amplitude scaling of records at the structure's fundamental period and spectral matching of records in a defined period range lead to better estimates of actual storey displacements. The use of one or three records for analyses leads to an incorrect estimation of seismic demand.

Keywords Nonlinear time history analysis · Ground motion · Amplitude scaling · Spectrum matching · Fundamental period

J. Vemuri (✉)
Department of Civil Engineering, Mahindra Ecole Centrale, Hyderabad, India
e-mail: jayaprakash.vemuri@mechyd.ac.in

S. Kolluru
Department of Civil Engineering, IIT Hyderabad, Hyderabad, India

A. Prashant et al. (eds.), *Advances in Computer Methods and Geomechanics*, Lecture Notes in Civil Engineering 55,
https://doi.org/10.1007/978-981-15-0886-8_43

1 Introduction

Unreinforced masonry (URM) structures comprise a large percentage of buildings in the Himalayan region. URM buildings have been severely damaged in recent Himalayan earthquakes [1] and consequently, a seismic risk assessment of the non-engineered brick masonry construction in this region is necessary [2]. For a proper seismic assessment of URM structures, nonlinear time history analysis (NTHA) is essential. However, due to the lack of historical records in the region of interest, designers are often forced to use modified records from other regions [3]. This paper quantifies the impact of ground motion modification techniques, using the case study of Sikkim which was struck by a major earthquake in 2011.

Earthquake ground motions consist of three components: two horizontal components and one vertical component. A set of these three components comprises one 'record'. An ideal ground motion record ought to consider the design earthquake magnitude and fault mechanisms, epicentral distance, transmission path properties and site effects. For example, the ASCE/ SEI 7-05 [4] and ASCE 41-06 [5] emphasise that records should have magnitudes, event distances and source mechanisms that are consistent with the maximum expected earthquake. Since an earthquake signal is a realisation of a stochastic process, it is difficult to define and obtain an 'ideal' ground motion record. It is indeed a challenge for the structural engineer/designer to identify and select a set of records, which are reasonably expected to affect the building site. There are two common techniques to select ground motions:

(a) From a Database of Real Records

Here, the earthquake record is selected from a database of historical ground motions and the magnitude (M) and distance (R) are chosen to be representative of the design earthquake. If seismic disaggregation data for the region is available, ground motions can also be chosen using (M, R) scenarios that dominate the seismic hazard at the site. It is advisable to keep the magnitude window narrow: Stewart et al. [6] suggest a magnitude half-bin width of $\pm 0.25 M_w$ while Bommer and Acevedo [7] recommend a width of $\pm 0.20 M_w$. The soil profile at the site is also used as an additional selection criterion. Lee et al. [8] used soil categories S_1 (rock), S_2 (stiff soil) and S_3 (soft soil).

(b) From a Database of Modified Records

In regions where a rich database of historical records is unavailable, NTHA may be carried out using modified records, either by generating synthetic records [9] or by altering natural records. Synthetic records are used in the complete absence of historical records from regions having a similar geotectonic setup. However, synthetic ground motions have a drawback: they exhibit smooth spectra while natural records do not show such ideal spectra. The alternate method involves modifying natural records either in the time domain (amplitude scaling) or in the frequency domain (spectral matching). Time domain scaling typically preserves the seismological features of the records [10]–the complete acceleration record is multiplied by a constant number. Typically, ground motions are scaled linearly to match either

a target peak ground acceleration (PGA) or a target spectral acceleration value at a single period [11, 12]. In the spectral matching technique, the response spectra of the ground motions are matched to a target spectrum. The advantages and drawbacks of the method are discussed in Sect. 2.

2 Problems with Current Ground Motion Scaling Techniques

There is no consensus on the scaling factor to be used in amplitude scaling. The civil works engineering and construction bulletin, EC1110-2-6000 [13] states that there is no limit on the scaling factor. However, Kalkan and Chopra [14] state the need to have limits on the scaling factor to accurately model the desired earthquake. If the target response spectrum is obtained from PSHA, the ground motion variability will already be integrated into the target spectrum and hence, using amplitude scaling would lead to double counting of this aleatory variability [15]. Further, the average response spectra from scaled records can have a different shape from the design spectrum in certain period ranges and may amplify higher mode response [16]. Finally, as the period of a structure increases as damage progresses, matching ground motion spectrum at a single period may not be appropriate.

In light of the above pitfalls in the amplitude scaling technique, researchers and seismic codes suggest the use of 'spectral matching' technique. Here, the response spectra of the ground motions are matched to a target spectra using spectral matching techniques that modify the frequency content and/or the phasing of the record [17]. The target response spectrum may be a uniform hazard response spectrum or a response spectrum for scenario events computed from a ground motion prediction relationship. This method has been adopted by leading seismic standards [18, 19]. However, the spectral matching technique may sometimes drastically alter the physical characteristics of the ground motion record. Further, the suggested upper bound on the spectrum period range is different in various seismic codes: this bound must be based on the expected structural damage.

Researchers (and seismic codes) also differ in their opinion on the number of earthquake records to use in the analysis. ASCE 4-98 [20] allowed the use of a single accelerogram for dynamic analyses. Both EC8 and ASCE 41-06 allow nonlinear dynamic analyses with the use of at least three records. However, Dhakal et al. [21] state that the use of only three randomly chosen ground motions gives significantly low confidence in the predicted seismic demand. Five records are allowed for nonlinear dynamic analysis, both by EC1110-2-6000: Selection of Design Earthquakes and Associated Ground Motions [13] and the UFC 3-310-04: Seismic Design of Buildings [22]. For calculation of demands on structural components, UFC guidelines state that when seven or more records are used, the arithmetic mean response of the structure can be used for design and when less than seven records are used, the maximal response of the structure should be considered for design. Recent research

[23], on the basis of observed variability, suggests that seven ground motions are inadequate for a multi-storey structure which is influenced by higher modes. Indeed, different ground motions may have different phasing characteristics, i.e., sequence of pulses, which are key to nonlinear structural response but these may have identical response spectra.

Ideally, the number of records to be used should be based on the observed dispersion in the structural response. A reduction in the variability of inelastic response may imply that fewer records may be needed to predict the response. In structures having irregularity in plan and elevation, it may also depend on the structural behaviour.

3 Ground Motion Scaling for Sikkim Earthquake, 2011

The state of Sikkim is mostly hilly in terrain, with the northern, eastern and western borders of the state comprising of the Himalayan Mountains. The southern part has the lower Himalayas. On 18th September 2011, at 18:10 IST, an earthquake with a magnitude of 6.9 occurred on the Sikkim–Nepal border region. The epicentre was 27°41′N and 88°12′E, situated at 68 km northwest of Gangtok, the capital city of Sikkim. Due to the convergence of the Indian and the Eurasian plate, earthquakes in this region are mostly inter-plate in origin. However, recent literature suggests that this earthquake had a complex origin and could be intra-plate in nature. Overall, the Sikkim earthquake caused considerable damage to reinforced concrete and masonry structures. As per IS1893: 2002, Sikkim lies in seismic zone 4. The response spectrum for zone 4 (5% damping) is shown in Fig. 1. For this design spectra, the zone factor, Z is 0.24 (so Z/2 = 0.12), Importance Factor, I is 1, and the response reduction factor, R is 1. As only a small number of ground motions are available from

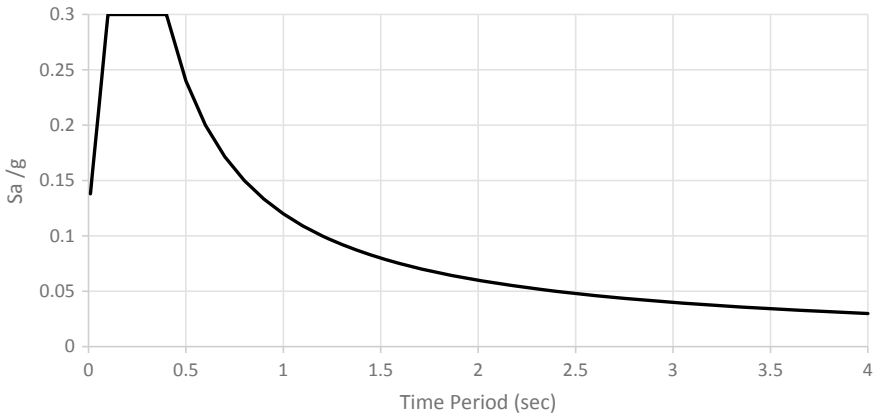

Fig. 1 5% damped response spectra for Sikkim (Zone-4)

Sikkim, a suite of ground motions from are developed using data acquired from COSMOS (Consortium of Organizations for Strong Motion Observation Systems) [24] for two major Himalayan earthquakes: the 1991, Uttarkashi and the 1999 Chamoli earthquake. These records were chosen as Uttarakhand and Sikkim have similar geotectonic setup (Disaster Mitigation and Management Centre Uttarakhand, [25]. Figure 2 shows the response spectra of some ground motions from these earthquakes. Figure 3 illustrates amplitude scaling, i.e. PGA matching and T_1 matching, of two records to the 15% damped design spectrum (the damping factor for 15% damping is 0.7 as per IS1893:2016) (Fig. 1).

Nonlinear Time History Analyses (NTHA) are performed on a Single Degree of Freedom (SDOF) unreinforced masonry (URM) wall. Figure 4a shows the SDOF model of a masonry wall. The Unreinforced Masonry (URM) Wall has a mass of 10,000 kg, height of 1000 mm, length of 4240 mm and thickness of 240 mm [26]. The dimensions and the aspect ratio of the wall correspond to a parapet/boundary wall. The compressive strength of soft mortar and a stiff brick are 1 and 12 MPa,

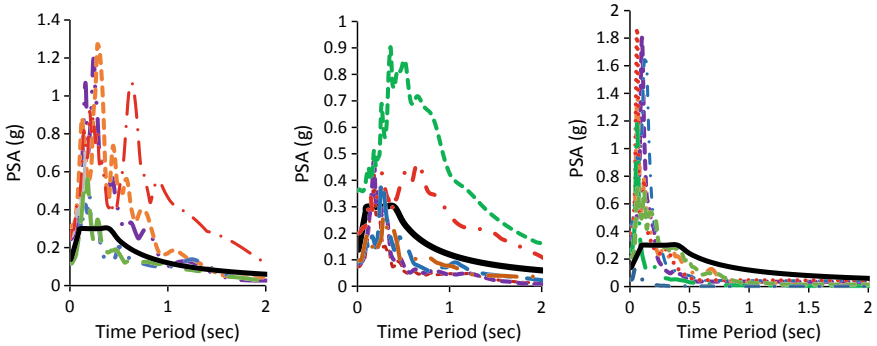

Fig. 2 Response Spectra (1991 Uttarkashi Earthquake, 1999 Chamoli Earthquake, 2011 Sikkim Earthquake)

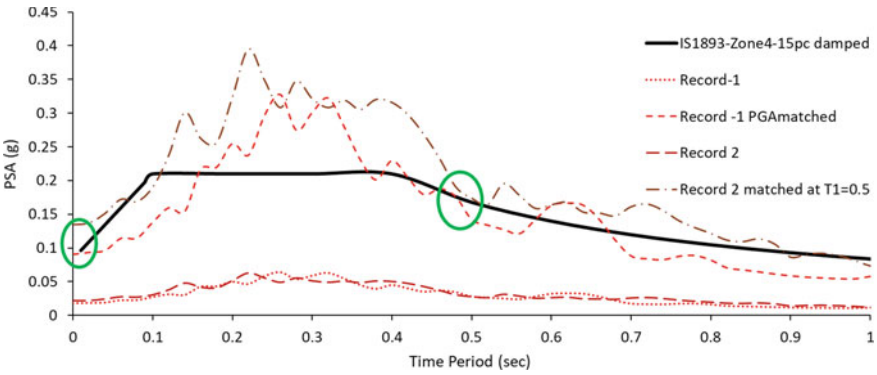

Fig. 3 Scaling of records to PGA and natural period, T_1 (15% damped spectrum)

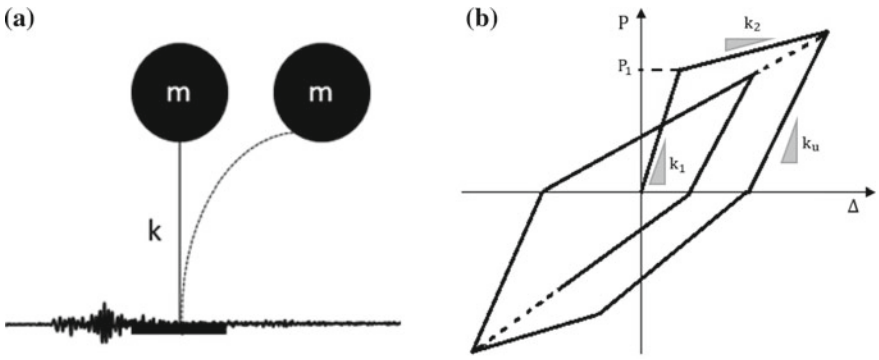

Fig. 4 **a** SDOF model of the URM Wall. **b** Modified-Takeda Model

respectively. The Young's Modulus is 7000 MPa and 12,000 MPa, respectively. The damping ratio, ζ is 15% and the natural frequency is 2 Hz. The hysteretic behaviour of the masonry wall is simulated using the Modified-Takeda model, seen in Fig. 4b. The characteristic values of the model were calibrated by Chow and Vera [26] as: $\mathrm{SR} = \frac{P_1}{mg} = 0.232,\ \alpha = \frac{k_2}{k_1} = 0.168, k_u = k_1\left(\frac{d_y}{d_{max}}\right)^q$ with $q = 0.4$

4 Results from Nonlinear Time History Analyses

Tables 1 and 2 show the results from the nonlinear time history analyses performed using records from the 1991 Uttarakashi and the 1999 Chamoli earthquakes. The results indicate that the maximum and average value of displacement, computed using records of the Uttarakashi earthquake, were 40.69 mm and 6.99 mm, respectively. The standard deviation of the displacement is 8.59 mm. Similarly, the maximum and average value of displacement computed using records of the Chamoli earthquake was observed to be 55.54 mm and 6.67 mm, respectively. The standard deviation of the displacement is 11.56 mm. The average of the displacements of the wall for ground motions from the Uttarakashi earthquake and Chamoli earthquakes are comparable.

Table 3 shows the displacement values obtained from a relatively small sample of seven real ground motions from Sikkim. Some direct observations may be ascertained from these tables: the results from the seven real ground motions of Sikkim, compare poorly with the larger population (*true value*) set obtained from the 1991 and 1999 earthquakes. Similarly, PGA matching which anchors the records at a single point on the response spectrum produces results which do not match favourably with the true solution. In contrast, when the sample set is scaled by matching at the natural period, T_1, results of mean displacement values are closer to the true value. Similarly, spectral matching in the period range of 0.2 T_1 to 2 T_1 results in displacement values with the least standard deviation. It is evident that the choice of one or three records

Table 1 NTHA Results: 26 records from the 1991 Uttarkashi Earthquake

S. no.	EQ record	Distance (km)	Soil type	PGA (g)	U_{max} (mm)
1	Almora-L	158	A	0.018	1.38
2	Almora-T	158	A	0.021	1.47
3	Barkot-L	53	A	0.082	6.47
4	Barkot-T	53	A	0.095	4.71
5	Bhatwari-L	53	A	0.247	20.01
6	Bhatwari-T	53	A	0.253	40.69
7	Ghansiali-L	42	A	0.117	7.34
8	Ghansiali-T	42	A	0.118	7.06
9	Karnprayag-L	73	A	0.062	3.66
10	Karnprayag-T	73	A	0.079	4.59
11	Kosani-L	152	A	0.029	0.99
12	Kosani-T	152	A	0.032	1.48
13	Koteshwar-L	64	A	0.101	5.76
14	Koteshwar-T	64	A	0.067	3.64
15	Koti-L	98	A	0.042	1.93
16	Koti- T	98	A	0.021	3.79
17	Purola-L	67	A	0.075	4.67
18	Purola-T	67	A	0.094	3.75
19	Rudraprayag-L	60	A	0.053	2.40
20	Rudraprayag-.T	60	A	0.052	3.32
21	Srinagar-L	62	A	0.067	1.78
22	Srinagar-T	62	A	0.05	1.99
23	Tehri-L	53	A	0.073	4.26
24	Tehri-T	53	A	0.062	4.78
25	Uttarakashi-L	31	A	0.242	14.95
26	Uttarakashi-T	31	A	0.31	24.75

can lead to incorrect estimations of displacement. A larger set of real records can produce results which are closer to the true solution.

However, response spectrum scaling has its pitfalls. Figure 5 shows the modification in the frequency content due to spectral matching, in the various components of the ground motions from the 2011 Sikkim earthquake. It is observed that there is a clear increase in the matched mean period as compared to the original mean period. While spectral matching techniques are more accurate than other techniques, the method needs to be implemented with caution, since, in some cases, the use of modified ground motions having vastly different frequency content (as compared to the original ground motions) may impact the results obtained from nonlinear time history analyses.

Table 2 NTHA Results: 22 records from the 1999 Chamoli Earthquake

S. no.	EQ record	Distance (km)	Soil Type	PGA(g)	U_{max}(mm)
1	Almora-L	106	A	0.027	3.02
2	Almora-T	106	A	0.028	2.49
3	Barkot-L	118	A	0.023	0.68
4	Barkot-T	118	A	0.017	0.98
5	Chinaylisaur-L	103	A	0.045	4.09
6	Chinaylisaur-T	103	A	0.052	5.58
7	Ghansiali-L	73	A	0.083	3.12
8	Ghansiali-T	73	A	0.073	3.23
9	Gopeshwar-L	14	A	0.197	19.25
10	Gopeshwar-T	14	A	0.356	55.54
11	Joshimath-L	17	A	0.064	3.08
12	Joshimath-T	17	A	0.071	4.57
13	Lansch-L	102	A	0.006	0.30
14	Lansdowne-T	102	A	0.005	0.23
15	Roorkee-L	162	C	0.047	4.64
16	Roorkee-T	162	C	0.056	3.68
17	Tehri-L	88	A	0.054	6.84
18	Tehri-T	88	A	0.062	6.25
19	Ukhimath-L	29	A	0.097	5.73
20	Ukhimath-T	29	A	0.091	5.01
21	Uttarakashi-L	94	A	0.064	3.91
22	Uttarakashi-T	94	A	0.053	4.52

5 Discussion

The results from nonlinear time history analyses using various scaling techniques, give rise to several key observations. The objective of any scaling procedure is to obtain ground motions corresponding to the seismic hazard of the region (defined by the response spectrum). The PGA scaling and T_1 scaling techniques, pinch the ground motions to a 0 period and T_1 period on the response spectrum. In both these methods, a single-scale factor is used on the complete time series. The spectrum matching procedure tries to amplify the GMs to fit within 5% of the spectrum. Several scale factors are used on the GM which may alter the frequency content and other parameters. Currently, designers and researchers only aim to get a good spectrum match. However, in a new refined procedure, meeting several goals would be an iterative procedure to find the best scaling parameters. Further research is required to develop improved techniques to minimise the modification to the non-stationary characteristics of accelerograms.

Table 3 NTHA Results: 7 (larger) horizontal components, 2011 Sikkim Earthquake

S. no.	Displacement, U_{max} (mm)					
	EQ record	PGA(g)	Real Accelerogram	PGA Matched	T1 matched	Spectrum Matched (0.2T to 1.5T)
1	Gezing	0.451	2.65	0.568	5.65	5.76
2	Mangan	0.388	3.24	0.806	8.05	7.07
3	Gangtok	0.294	4.44	1.622	6.92	6.14
4	Chungthang	0.360	2.13	0.566	7.68	7.08
5	Singtam	0.216	6.78	2.81	6.17	6.59
6	Melli	0.266	1.53	0.580	7.74	7.93
7	Siliguri	0.052	0.10	0.181	6.65	5.98
Average			2.98	1.08	6.98	6.65
Maximum			6.78	3.22	8.05	7.93
Standard Deviation			2.15	1.04	0.89	0.76

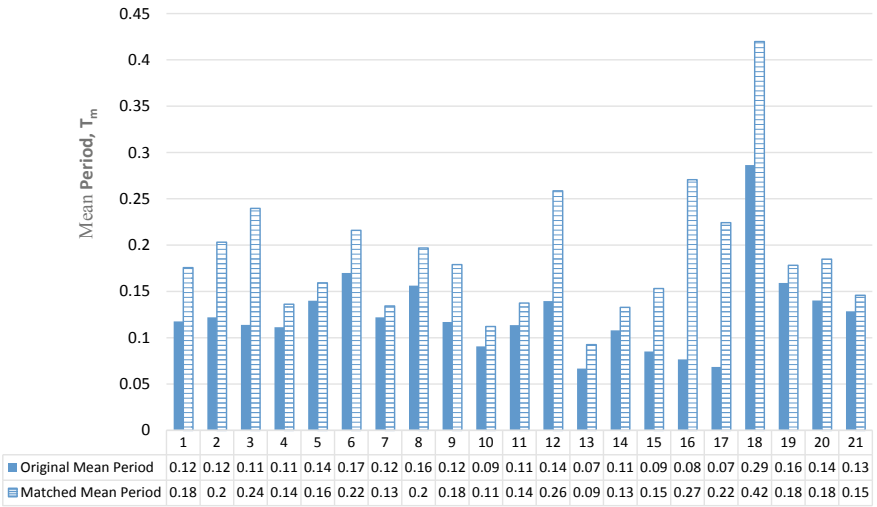

Fig. 5 Shift in mean period of ground motions (2011 Sikkim) due to Spectrum Matching

6 Conclusions

In this paper, several ground motion scaling techniques were examined. Nonlinear time history analyses were performed on a single degree of freedom model of an unreinforced masonry wall. In PGA matching, the mean of the observed displacement did not match with the true solution. There is high dispersion in the results. In

matching at the fundamental period, T_1, it was observed that the displacement values obtained from modified Sikkim records were close to the 'true' solution obtained from the larger population of records from Uttarakhand. Additionally, the observed dispersion was low. In Spectral Matching, the modified records from Sikkim, produced results that were close to the 'true' solution. However, it is noted that the results depend on the tolerance level and the period range selected for matching. The observed dispersion was low. However, it was observed spectral matching caused significant modifications to the frequency content, peak acceleration, peak velocity and Arias Intensity. Another key finding from this study is that the spectrum matching technique used for scaling must be refined, and should be based on the observed changes to several parameters of scaled ground motions. It is concluded that the use of fewer than three records may lead to an incorrect estimate of structural response.

References

1. Vemuri J, Ehteshamuddin S, Kolluru SV (2018) Evaluation of seismic displacement demand for unreinforced masonry shear walls. Cogent Eng 1480189
2. Vemuri JP, Kolluru S (2017) Seismic analysis of unreinforced masonry walls. Integr Disaster Risk Manag J 6(2):102–115
3. Vemuri J, Kolluru S, Chopra S (2018) Surface level synthetic ground motions for M7. 6 2001 Gujarat Earthquake. Geosciences 8(12):429
4. American Society of Civil Engineers (2006) Minimum design loads for buildings and other structures, ASCE/SEI-7-05. Reston, VA
5. American Society of Civil Engineers (2007) Seismic rehabilitation of existing buildings, ASCE/SEI 41-06. Reston, Va
6. Stewart JP, Chiou SJ, Bray JD, Graves RW, Somerville PG, Abrahamson NA (2001) Ground motion evaluation procedures for performance-based design. PEER Report 2001/09, Pacific Earthquake Engineering Research Center, University of California, Berkeley
7. Bommer JJ, Acevedo AB (2004) The use of real earthquake accelerograms as input to dynamic analysis. J Earthquake Eng 8(Special Issue 1): 43–91
8. Lee LH, Lee HH, Han SW (2000) Method of selecting design earthquake ground motions for tall buildings. Struct Design Tall Buildings 9(3):201–213
9. Vemuri J, Ehteshamuddin S, Kolluru S (2018) Numerical simulation of soft brick unreinforced masonry walls subjected to lateral loads. Cogent Eng 5(1):140189
10. Koboevic S, Guilini-Charrette K, Castonguay PX, Tremblay R (2011) Selection and scaling of NBCC 2005 compatible simulated ground motions for nonlinear seismic analysis of low-rise steel building structures. Can J Civ Eng 38(12):1391–1403
11. Shome N, Cornell C (1998) Normalization and scaling accelerograms for nonlinear structural analysis. In: Proceedings of the 6th U.S. national conference on earthquake engineering, Earthquake Engineering Research Institute, Seattle
12. Shome N, Cornell CA, Bazzurro P, Caraballo JE (1998) Earthquakes, records, and nonlinear responses. Earthquake Spectra 14(3):467–500
13. US Army Corps of Engineers (2009) Selection of design earthquakes and associated ground motions, ECB (EM) 1110-2-6000. Department of the Army, USA
14. Kalkan E, Chopra AK (2010) Practical Guidelines to Select and Scale Earthquake Records for Nonlinear Analysis of Structures. USGS Open-File Report 2010, 113 p
15. Abrahamson N (2014) Comments on near fault ground motions. COSMOS Annual Meeting, Nov. 14, 2014, Burlingame, California

16. Mazzoni S, Hachem M, Sinclair M (2012) An improved approach for ground motion suite selection and modification for use in response history analysis. In: 15th world conference on earthquake engineering, Lisboa, Portugal
17. Hancock J, Watson-Lamprey J, Abrahamson NA, Bommer JJ, Markatis A, McCoy E, Mendis R (2006) An improved method of matching response spectra of recorded earthquake ground motions using wavelets. J Earthquake Eng 10. Special Issue 1:67–89
18. CEN. Eurocode 8: Design of Structures for Earthquake Resistance—Part 1: General Rules, Seismic Actions and Rules for Buildings. EN 1998–1: 2003 E. Comité Européen de Normalisation, Brussels, 2003
19. American Society of Civil Engineers (2010) "Minimum Design Loads for Buildings and Other Structures", ASCE-7-10. Reston, VA
20. ASCE 4-98, 2000. Seismic Analysis of Safety-Related Nuclear Structures and Commentary. ASCE, Reston, Virginia
21. Dhakal RP, Singh S, Mander JB (2007) Effectiveness of earthquake selection and scaling method in New Zealand, Bulletin of the NZSEE
22. Department of Defense, USA (2004) Seismic Design for Buildings, UFC 3-310-04, BiblioGov, 128 pp
23. Heo Y, Kunnath SK, Abrahamson N (2011) Amplitude-scaled versus spectrum-matched ground motions for seismic performance assessment. J Struct Eng 137(3):278–288
24. Consortium of Organizations for Strong-Motion Observation Systems (COSMOS). www.cosmos-eq.org. Last accessed July 2015
25. Disaster Mitigation and Management Centre (2012): Sikkim Earthquake of 18th September, 2011. http://dmmc.uk.gov.in/files/Sikkim_Report.pdf, Department of Disaster Management, Government of Uttarakhand, Dehradun, Uttarakhand, India
26. Vera CO, Chouw N (2008) Comparison of record scaling methods proposed by standards currently applied in different countries. In: Proceedings of the 14th world conference on earthquake engineering, Beijing, China

Comparative Analysis and Behavior of Cantilever Retaining Wall with and Without Relief Shelves

Mandira Faldesai and P. Savoikar

Abstract Retaining walls are an essential part of almost all infrastructure projects, to support vertical backfills. There are various ways of constructing a retaining wall. Retaining wall with relief shelves is one of the subset of cantilever retaining walls. A retaining wall with pressure relief shelves decreases the active lateral earth pressure and increases the overall stability of the retaining wall. As a result of reduced earth pressure, the thickness of stem also gets reduced which results in to an economic design. The present study aims at comprehending the performance of such walls and to discover the effectiveness of these walls to reduce earth pressure. The influence of factors like the location of the shelf and stiffness of shelf, shelf width, etc., on the behavior of the retaining wall is also studied. This work presents a thorough comparative analysis of RCC cantilever retaining walls with (i) no shelves. (ii) single shelf. (iii) two shelves. (iv) three shelves (v) four shelves, with finding out the best location for providing shelves.

Keywords Cantilever retaining walls · Relief shelf · Lateral pressure · Overall stability

1 Introduction

Lateral earth pressure on retaining walls is the major factor which influences the sectional dimensions of the wall. If the height of soil retained is large, the retaining walls are required to resist larger lateral earth pressure and in such cases the reinforced soil walls are found to be a possible solution. But for construction of such walls, a well graded granular material is preferable due to its higher shear resistance and good soil reinforcement interaction hence availability of a suitable backfill material is the main criteria. Thus, to tackle such issues the lateral thrust on the wall should be

M. Faldesai · P. Savoikar (✉)
Department of Civil Engineering, Goa Engineering College, Goa 403 401, India
e-mail: psavoikar@gmail.com

M. Faldesai
e-mail: mandira115@gmail.com

A. Prashant et al. (eds.), *Advances in Computer Methods and Geomechanics*, Lecture Notes in Civil Engineering 55,
https://doi.org/10.1007/978-981-15-0886-8_44

reduced, which would apparently reduce the sectional dimensions of the wall and cost of the project. There are many ways to reduce the lateral earth pressure such as use of Geo-inclusion, light weight backfill, etc. Providing a relief shelves connected to the stem of the cantilever retaining wall can reduce the earth pressure and are considered to be the special case of retaining walls [1]. The relief shelves are provided on the retained side of the retaining wall. These shelves break the total retained height in to smaller heights of stem which results in reduction of soil pressure on the stem. As a result of this, the thickness of stem reduces which results into an economical design there is less use of reinforcement in the wall cross section [1]. Relieving shelves are horizontal slabs incorporated in the stems of R. C. cantilever retaining walls, with the objective of providing partial relief of the active earth pressure acting on the stem. Number of such shelves is constructed at regular spacing along the height of the wall. Kurian [2] explains the contribution of the relieving shelf to the stability of the retaining wall and to the reduction of the stem thickness due to the reduction in earth pressure, besides examining the scope of overall economy from a cost- benefit angle.

Jumikis [3] presented the effect of provision of relief shelves on the earth pressure and noted that extending them beyond the rupture surface in the backfill can significantly reduce the lateral earth pressure and increase the stability of retaining wall. Klein [4] reported a distribution for the earth pressure above and under the shelf which was observed to be in line with the results obtained by [5]. It was concluded that solution of [4] was in good agreement with the results of the FEM and while Jumikis's solution (1964) was not. Chaudhuri [6] reported that wall with relief shelf can retain larger height of sand just prior to the emerging overturning compared to wall without relief shelf. Yakovlev [5] concluded that for the same embedded depths of a shelf, the dimensions of the sliding zone increases with increasing platform width. Phatak [7] presented experimental study on flexible cantilever wall with relief shelf to show extensive reduction in earth pressure. Phatak [7] corrected an error in Raychaudhuri's solution. Bowles [8] recommended such walls as a likely solution for high retaining walls, while alerting that the soil must be satisfactorily compacted up to relief shelf. Raychaudhuri [9] studied the influence of the relief shelf by deducting the weight of the soil above the shelf from the failure wedge; though the change in the center of gravity for the wedge was not considered. Bell [10] in his Ground Engineer's book, assumed that there is a transition zone under the shelf and after this zone the earth returns to its original distribution; i.e., to the distribution of the cantilever retaining wall.

Padhye and Ullagaddi [11] reported that active earth pressure and lever arm are considerably reduced due to provision of shelf and there by achieves a considerable reduction in the moment about the base. Liu and Lin [12] recommended a mathematical model to calculate the earth pressure for different shelf widths. It was recommended that the distribution of the earth pressure starts at zero under the shelf and increases linearly with depth. For short shelves, an additional rupture surface starting from the end of the shelf and running parallel to the global rupture line was recommended. It was reported that the FEM has limitations and that the other methods are in good agreement with each other. Liu et al. [13] reported that when the

depth of relief shelf exceeds a certain value, active earth pressure on the upper wall was not reduced significantly. The width of relief shelf has a strong influence on earth pressure near the surface of relief shelf, but not much effect was found on the overall distribution of earth pressure on upper wall. Liu et al. [14] conducted model study of pile-supported cantilever retaining wall with single relief shelf and demonstrated that the earth pressure is zero below the relief shelf. Cantilever retaining walls with relief shelves is one of the special case of retaining walls [1]. Providing relief shelves on the soil retained side, decreases the total active earth pressure on the wall, which results in reducing the thickness of the wall resulting in to an economic design due to use of less reinforcement on wall horizontal cross section on the level of contraction joints [1]. Hany [1] studied the influence of number of shelves on the earth pressure acting on the wall. The shelves work on decreasing the maximum bending moment and the top movement of the wall significantly. It was reported that the provision of a single shelf at the height of 0.3 H results in reduction of bending moments by about 30% as compared to a retaining wall without shelves. The shelf width is recommended to be extended after the rupture surface with thickness ratio ($t_s/b = 0.10$).

2 Influence of Shelves on Active Earth Pressure Distribution

Figure 1 shows the effect of providing relieving shelf on distribution of earth pressure behind the retaining wall.

In the present study, the analysis of cantilever retaining wall with pressure relief shelves is done to optimize the number and the best location of shelves.

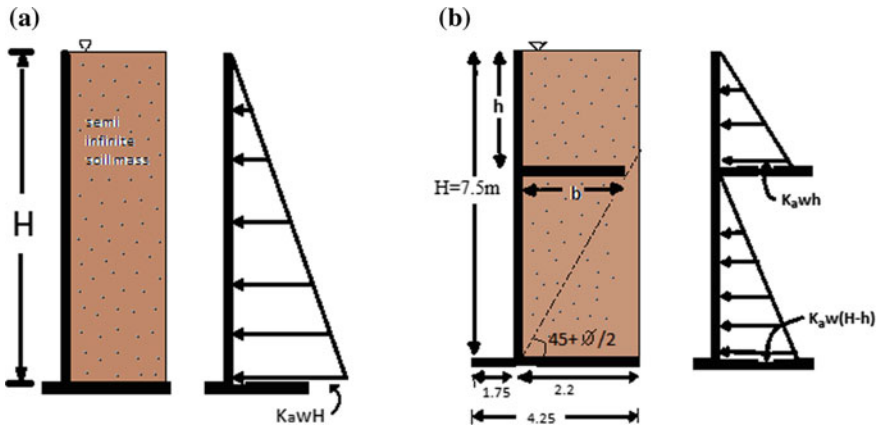

Fig. 1 Pressure distribution on stem **a** without shelf **b** with shelf

Fig. 2 Ambaji–Fatorda, Goa Landslide site

Table 1 Geotechnical properties of the soil at the site

Site	Grain size analysis			Spec. gravity	Dry density kN/m^3	Liquid limit %	Plastic limit %	PI
	Gravel content (%)	Sand content (%)	Silt and clay content (%)					
Ambaji	28.06	65.61	6.33	2.66	15.3	41	21	20

3 Methodology

A retaining wall relief shelf is designed for a slope at Ambaji–Fatorda, Margao Goa. The site is located South Goa Collectorate building at Margao Goa. The site had a steep slope covered with medium to dense vegetation. Landslide had occurred due to flowing down of debris during rains (Fig. 2).

Parametric studies were carried out. Height of slope is 13.8 m and inclination of slope is 71.60°. Geotechnical investigation for the site is given in Table 1.

4 Analysis of Cases

Analysis of cantilever retaining wall with and without relief shelf is done on the slope at Ambajim Margao site. STAAD Pro V8i software was used for analysis. The following analytical models are analyzed and designed for cantilever retaining wall with: (1) Case 1: no shelves (CWNS), (2) Case 2: with one shelf (CWOS), (3) Case 3: with two shelves (CWTS) and (4) Case 4: with three shelves (CWThS). (5) Case 5: with four shelves (CWFS). Each model is designed using same data for the study. Assumed and calculated data are given in Table 2.

Table 2 Assumed data for all models

Sr. No.	Description	Details
1	Height of retaining wall, H	13.8 m
2	Unit weight of soil, γ	17.2 kN/m^3
3	Cohesion of backfill soil, c	8 kN/m^2
4	Safe bearing capacity of soil, q_s	200 kN/m^2
5	Internal friction angle of soil, ϕ	28.3°
6	Coeff. of friction bet concrete and soil, μ	0.5
7	Inclination of slope	71.60°
8	Grade of concrete	M35
9	Grade of steel	Fe415
10	Depth of foundation	1.5 m
11	Coefficient of active earth pressure	0.356
12	Thickness of base slab	1.3 m
13	Width of base slab	7.5 m
14	Toe projection	2 m
15	Thickness of stem at the base	1.5 m
16	Thickness at the top	0.5 m
17	Height of stem	14 m
18	Heel projection	4 m

4.1 Analysis of CWNS

The analysis of the cantilever retaining wall with no shelf (CWNS) is shown in Fig. 3a and its pressure distribution is shown in Fig. 3b. The bending moment diagram (BMD)

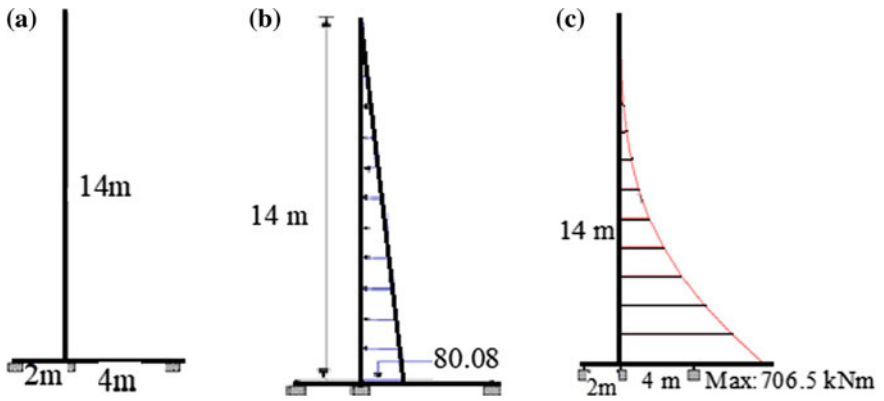

Fig. 3 **a** Analysis of retaining wall without shelf, **b** Lateral pressure distribution diagram, **c** BMD from STAAD Pro Software

Table 3 Bending moment details for CWNS

BM at the base of the stem at 14 m	Area of BMD
760.5 kN-m	2661.175 kNm^2

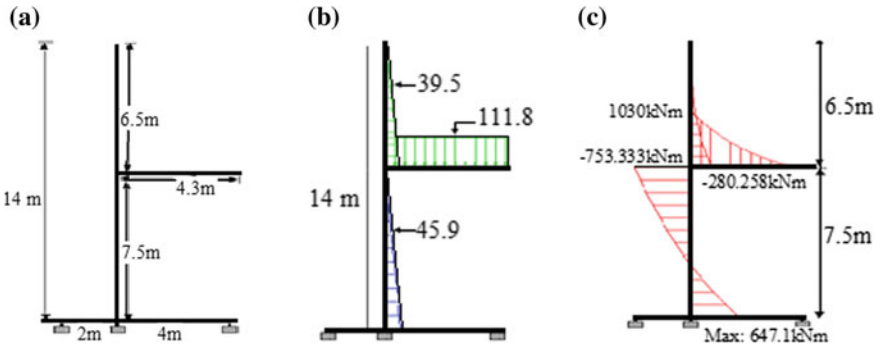

Fig. 4 **a** Analysis of retaining wall with one shelf, **b** Pressure distribution diagram, **c** BMD from STAAD Pro Software

for the stem obtained from STAAD Pro software is shown in Fig. 3c. The results are given in Table 3.

4.2 Analysis of CWOS

The analysis of cantilever retaining wall with single shelf for a retained height of 14 m is worked out. Position of shelf is varied from H/28 to 27H/28, measured from top of the stem. Lateral soil pressure is calculated for the various cases and from which area of BMD is estimated. The model of cantilever retaining wall with one shelf is shown in Fig. 4a and its pressure distribution is shown in Fig. 4b. BMD of CWOS from STAAD Pro is shown in Fig. 4c. The values achieved from the analysis are given below in Table 4.

BMD for different possible shelf height is obtained and the area of BMD is calculated from which the least value is selected as the optimum height for shelf. For cantilever with one shelf the optimum position for shelf is found to be 13H/28 i.e. 6.5 m height from the top of the stem.

4.3 Analysis of CWTS

The analysis of cantilever wall with two shelves is done for various locations of shelf. The choice of position of top shelf is of range H/28 to 26H/28 and that of bottom shelf is from 2H/28 to 27H/28 considered from top of stem and area of BMD is computed.

Table 4 BMD areas for various shelf positions for CWOS

Location of shelf from top of stem	Area of BMD (kNm^2)
H/28	2936.53
2H/28	3254.7
3H/28	2695.2
4H/28	2508.1
5H/28	1262.815
6H/28	−1164.2
7H/28	−1028.175
8H/28	−863.63
9H/28	−802.5
10H/28	3259.5
11H/28	3304.56
12H/28	3755.5
13H/28	**1276.5**
14H/28	1707.517
15H/28	1753.65
16H/28	1896.3
17H/28	2759.3
18H/28	1942.6
19H/28	1802.54
20H/28	2168.54
21H/28	2463.25
22H/28	2683.78
23H/28	2546.36
24H/28	2741.12
25H/28	2896.35
26H/28	3689.56
27H/28	3726.14

The model of cantilever retaining wall with two shelves is shown in Fig. 5a and its pressure distribution is shown in Fig. 5b. The BMD of the cantilever wall with two shelves from STAAD Pro is shown in Fig. 5c. The values gained from the analysis for the most a precise position of shelves is given in Table 5.

4.4 Analysis of CWThS

The analysis of CWThS for height of 14 m is done for different location of shelf. The series of position of upper shelf is H/28 to 25H/28 and that of middle shelf is from

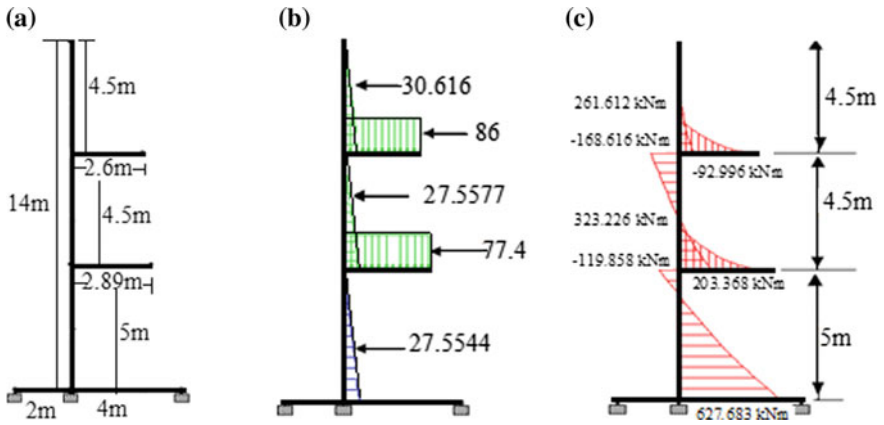

Fig. 5 **a** Analysis of retaining wall with two shelves, **b** Pressure distribution diagram, **c** BMD from STAAD Pro Software

Table 5 BMD details for CWTS

Depiction	Location of shelves from top of stem, 1st shelf at 5H/15 and 2nd shelf at 10H/15
BM at joint 5 due to soil weight above 1st shelf	261.612 kN-m
BM at joint 5	−92.996 kN-m
BM just below point 5	−168.616 kN-m
BM at point 3 just above 2nd shelf	323.226 kN-m
BM at point 3	203.368 kN-m
BM just below point 3	−119.858 kN-m
BM at point 1	627.683 kN-m
Area of BMD	963.38 kNm^2

2H/28 to 26H/28 and for lower shelf is from 3H/28 to 27H/28 measured from top of stem and its area of BMD is computed. The model of cantilever retaining wall with three shelves is shown in Fig. 6a. Pressure distribution of the stem of CWSS is shown in Fig. 6b. BMD of CWTS from STAAD Pro is shown in Fig. 6c. The values attained from the analysis for the most a precise position of shelves is given in Table 6.

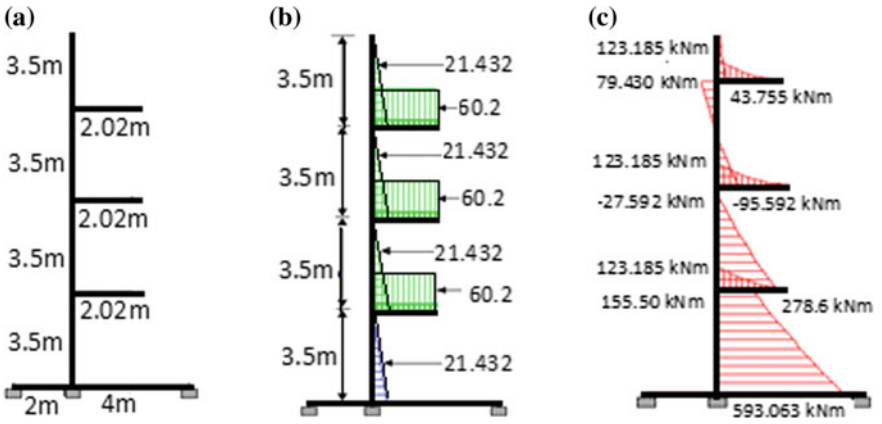

Fig. 6 **a** Analysis of retaining wall with three shelves, **b** Pressure distribution diagram, **c** BMD from STAAD Pro Software

Table 6 BMD details for CWThS

Depiction	Location of shelves from top of stem, 1st shelf at 7H/28; 2nd shelf at 14H/28; 3rd shelf at 21H/28
BM at point 7 due to soil weight above 1st shelf	123.185 kN-m
BM at point 7	43.755 kN-m
BM just below point 7	79.430 kN-m
BM at point 5 just above 2nd shelf	123.185 kN-m
BM at point 5	−95.592 kN-m
BM just below point 5	−27.592 kN-m
BM at point 3 due to soil wt above 3rd shelf	123.185 kN-m
BM at point 3	278.6 kN-m
BM just below point 3	155.509 kN-m
BM at point1	593.063 kN-m
Area of BMD	724.917 k-Nm^2

4.5 Analysis of CWFS

The analysis of CWFS for height of 14 m is done for different location of shelf. The series of position of upper shelf is H/28 to 24H/28 and that of second shelf from top is from 2H/28 to 25H/28 and for third shelf is from 3H/28 to 26H/28 and forth shelf that is the lower shelf is from 4 h/28 to 27 h/28 measured from top of stem and its

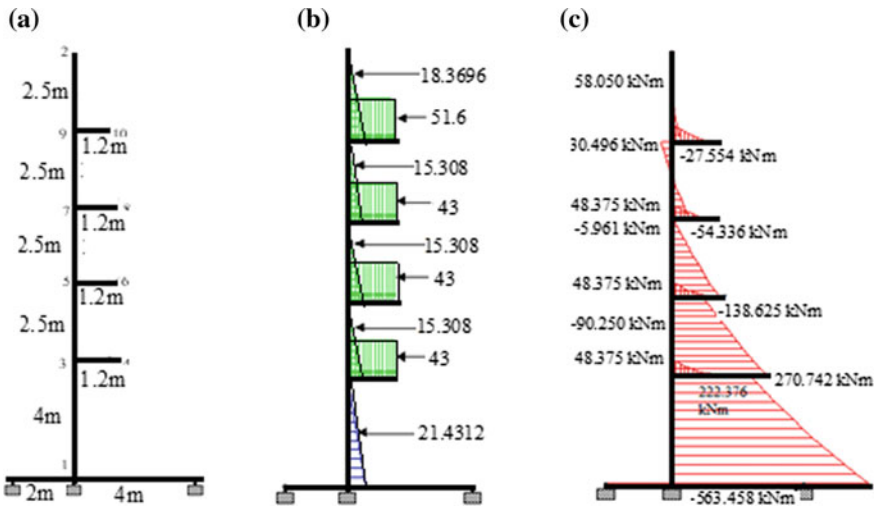

Fig. 7 **a** Analysis of retaining wall with three shelves, **b** Pressure distribution diagram, **c** BMD from STAAD Pro Software

area of BMD is computed. The model of cantilever retaining wall with three shelves is shown in Fig. 7a. Pressure distribution of the stem of CWSS is shown in Fig. 7b. BMD of CWTS from STAAD Pro is shown in Fig. 7c. The values attained from the analysis for the most a precise position of shelves is given in Table 7.

5 Results

From the analysis of CWNS, CWOS, CWTS, CWThS, and CWFS for different shelf positions the results are found (Table 8).

6 Lateral Displacement of Retaining Walls

Lateral displacement of the wall away from backfill is studied and shown in Fig. 8. It can be seen that provision of relief shelves to the wall has marginally reduced the maximum lateral displacement of the wall from 30.4 mm (wall without relief shelf) to 23 mm (walls with relief shelf). Provision of shelf reduces the total thrust on the wall and hence weight of wall increases which reduces the maximum displacement.

Table 7 BMD details for CWFS

Depiction	Location of shelves from top of stem, 1st shelf at 6H/28; 2nd shelf at 11H/28; 3rd shelf at 16H/28; 4th shelf at 21H/28
BM at point 9 due to soil weight above 1st shelf BM at point 9 BM just below point 9 BM at point 7 due to soil wt above 2nd shelf	58.050 kN-m −27.554 kN-m 30.496 kN-m 48.375 kN-m
BM at point 7	−54.336 kN-m
BM just below point 7	−5.961 kN-m
BM at point 5 just above 3rd shelf	48.375 kN-m
BM at point 5	−138.625 kN-m
BM just below point 5	−90.250 kN-m
BM at point 3 due to soil wt above 4th shelf	48.375 kN-m
BM at point 3	270.742 kN-m
BM just below point 3	222.376 kN-m
BM at point 1	−563.458 kN-m
Area of BMD	615.375 k Nm^2

Table 8 Comparison between different cantilever walls

Quantities	Model 1: CWNS	Model 2: CWOS	Model 3: CWTS	Model 4: CWThS	Model 5: CWFS
BMD Area (kN-m^2)	2661.175	1276.5	963.38	724.286	615.375
Economic shelf location	–	13H/28	8H/28-upper 18H/28-lower	7H/28-upper 14H/28-middle 21H/28-lower	6H/28-1st 11H/28-2nd 16H/28-3rd 21H/28-4th
Reduction in thrust in %	–	14.91	17.46	22.01	25.90
Steel in tonnes	17.01	14.34	12.54	12.32	12.01
Comparison of steel with Model 1	–	15.81%	26.27%	27.57	29.39%

7 Influence of Thickness and Length of Shelves

The shelf inflexibility "stiffness" is affected by the shelf width and its thickness. For stability, shelf should be extended beyond rupture surface. It is observed that shelves reduce the lateral earth pressure and thereby the maximum moment acting on the wall. It is also observed that the maximum bending moment and deflection of the

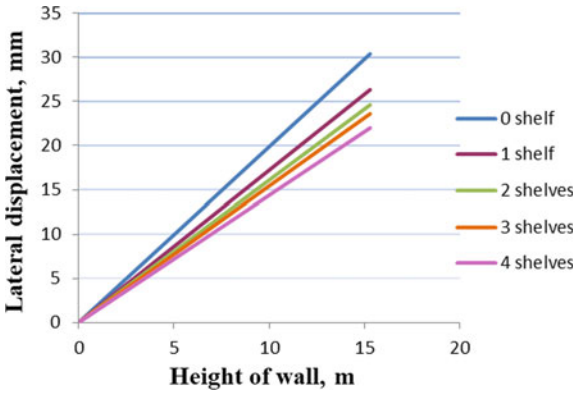

Fig. 8 Lateral displacement of retaining wall with relief shelves

top of the stem is also influenced by the position of the shelves. One of the important criterions to be considered while providing relief shelf on the cantilever wall is the deflection of relief shelves. A comparison of deflection outlines of relief shelves with differing width and thickness are produced below in Fig. 9a, b. In the first case length of shelf (measured perpendicular to the stem wall) of retaining wall is varied from 0.5 to 1.5 m and deflection is noted. Retaining wall with one shelf with the best shelf positions i.e. 13H/28 is used for this case. The influence of shelf length on BMD and deflection is studied by keeping thickness of shelf constant, equal to 0.3 m. In the next case, the shelf length is kept constant equal to 1.2 m and shelf thickness is varied from 0.2 m to 0.5 m, keeping shelf position at 13H/28 from the top of the stem.

It is seen from Fig. 9a, that maximum deflection of relief shelves increases with the length of the shelf. As the length of the shelf increases, the deflection also increases. This reduces the total thrust on the wall due to the increased weight of the wall. There exists a sure value beyond which the length of the relief shelf cannot be increased as greater length results in large deflection which leads to excessive backfill settlement which in turn affects the durability of the neighboring structures. This study would limit maximum length of relief shelves to 1.2 m. As greater length of shelves lead

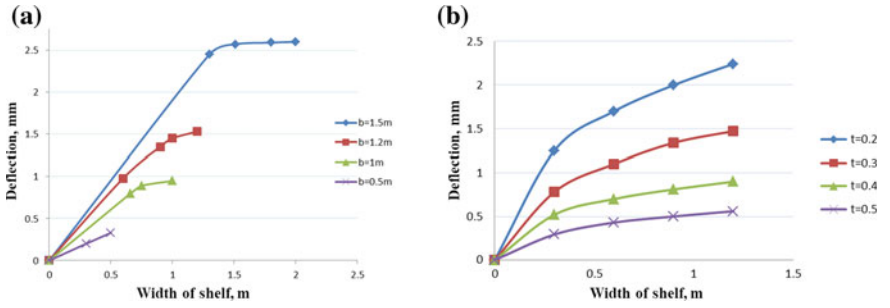

Fig. 9 Deflection profile of relief shelves **a** with different widths **b** with different thickness

Table 9 Maximum deflection (mm) of relief shelves for various retaining walls

Relief shelf	RS0.5	RS1	RS1.2	RS1.5
RS1	1.56	2.17	2.85	3.85
RS2	1.17	1.5	2.32	2.83
RS3	0.95	1.43	1.71	2.71
RS4	0.33	0.95	1.63	2.60

to extreme deflection due to its own weight, this can increase further due to creep. Amongst all the cases of retaining wall with relief shelf, the shelf with length of 1.2 m delivers highest benefit, not leading to unnecessary deflection of shelves. From Fig. 9b, it is observed that defection of shelves is reduced with increase in thickness of the shelf. The lesser thickness shelf tends to deflect more than the larger one. This deflection tends to make the shelf rest on the beneath soil which results in increase of the vertical stresses on the soil, thus leading to increase the lateral earth pressure on the wall below the shelf. In this case the prominent thickness amongst all the cases of retaining wall with relief shelf is shelf of thickness 0.3 m. From Fig. 9a, b, it is credited to the fact that relief shelves perform similar to cantilever beams having uniform distributed loading. As the deflection of cantilever beam with uniform distributed loading is relative to the forth power of length of cantilever beam and inversely proportional to moment if inertia (Table 9).

7.1 Deflection of Relief Shelves

Deflection of shelves from top to bottom are observed and compared. Deflection at different shelf position are noted and given in Table 10. RS1, RS2, RS3 and RS4 represent the relief shelves from upper to lower retaining wall. RS0.5, RS1, RS1.2 and RS1.5 represent the width of relief shelf.

It can be seen that the deflection of relief shelves from top to bottom of wall decreases and is found to be minimum for the lowest shelf, for all retaining walls with relief shelves. However, it was observed that the deflection of relief shelves significantly increases when length of the shelf is 1.5 m. Hence, the maximum length of relief shelf is to be restricted to 1.2 m.

8 Conclusions

The study involves thorough analysis using STAAD Pro software to assess the efficiency of providing relief shelves to the retaining walls.

It is seen that retaining walls with shelves are efficient in comparison to cantilever retaining wall with without shelves. Based on the present study, it can be concluded that

1. In the case of cantilever retaining wall with single shelf, the optimized location is at 13H/28 from top of the stem, while for retaining wall with two shelves, the optimized location of shelves is 9H/28 and 18H/28 where H is the height of stem, measured from top of the wall.
2. In the case of retaining wall with three shelves, the optimized position of shelves are 7H/28, 17H/28, and 21H/28 respectively, measured from top of the wall.
3. In the case of retaining wall with four shelves, the optimized position of shelves are 6H/28, 11H/28, 16H/28, and 21H/28 respectively, measured from top of the wall.
4. Provision of two shelves is economical proposition than single shelf, while three shelves are further economical than two shelves.
5. Maximum deflection of relief shelves are increased with the width of the relief shelf and decreased with increase in thickness of the shelf.
6. It can be concluded that providing four shelves at economic locations i.e. 6H/28(upper), 11H/28, 16H/28, and 21H/28 of shelf thickness 0.3 m and shelf width 1.2 m will give the greatest serviceability and efficiency making the wall much safer in bearing capacity failure mode.

References

1. Hany F (2015) Effectiveness of using shelves with cantilever retaining walls
2. Kurian NP (2007) Design of foundation systems, principles and practice, 3rd edn. Narosa Publishing House, Delhi
3. Jumikis AR (1964) Mechanics of soils. D Van Nostrand Co., Inc, Princeton
4. Klein GK (1964) Calculation of retaining ralls". VysshayaShkola, Mosco [in Russian]
5. Yakovlev PI (1974) Experimental investigation of earth pressure on walls with two platforms in the case of breaking loads relieving on the backfill. Odessa Institute of Naval Engineers, Translated from Osnovaniya, FundamentyMekhanikaGruntov 3:7–9
6. Chaudhuri PR, Garg AK, Rao MVB, Sharma RN, Satija PD (1973) Design of retaining wall with relieving shelves. IRC J. 35(2):289–325
7. Phatak DR and Patil V (1975) Effect of relief shelves on earth pressure, Institute of Engineers (India) Journal-C1, 55:156–159
8. Bowles JE (1996) Foundation analysis and design, 5th edn. McGraw-Hill, Singapore
9. Raychaudhuri P (1973) Design of retaining walls with relieving shelves", Paper No. 295, IRC J, 35(2):289 – 325
10. Bell FG (1987) Ground engineer's reference book. Butterworths, London
11. Padhye RD, Ullagaddi PB (2011) Analysis of retaining wall with pressure relief shelf by Coulomb's method. In: Proceedings of Indian Geotechnical Conference IGC-2011, Kochi, pp 671–673
12. Liu and Lin SF (2008) Earth pressure calculation for retaining structure with relieving platform, Port Eng. Tech, 182(4)

13. Liu G, Hu R, Pan X, Liu Y (2011) Model tests on earth pressure of upper part wall of sheet pile wall with relieving platform. Rock Soil Mech 32(2):103–110
14. Liu G, Hu R, Pan X and Liu Y (2013) Model tests on mechanical behaviors of sheet pile wall with relieving platform. Chin J Geotech Eng 35(1):94–99

Comparative Study of Expansive and Non-expansive Soils Stabilized with Lime and Rice Husk Ash (RHA)

Kaling Taki and Paramita Bhattacharya

Abstract The study focusses on comparative analysis of mechanical properties of Bentonite (expansive soil) and Kaolinite (non-expansive soil) treated with Lime and Rice Husk Ash (RHA). Unconfined Compressive Strength (UCS) tests were carried out for different curing periods of 0, 3, 7, 21 and 28 days. X-ray Diffraction and Scanning Electron Microscope tests were carried out to study the mineralogical and microstructural properties of the soil. Beyond optimum content the strength was found to decrease for all cases. In case of Lime the reduction in strength may be due to formation of the silica gel or excess Lime content beyond the optimum content may act as a lubricating agent between two-soil particle and reducing the shear resistance. In case of RHA the reduction in strength may be due to the formation of coarse particles which results in lower densities and more void formation. It was observed that UCS of Lime treatment is approximately 3 times higher than that of RHA treatment. In case of non-expansive soil, it was 3.5 times higher in Lime than RHA treatment.

Keywords Lime · Rice husk ash (RHA) · Free swell index (FSI) · Bentonite · Kaolinite

1 Introduction

Soil stabilization is the method by which the strength and durability of the soil can be improved. This process is of two types: mechanical stabilization and chemical stabilization. In mechanical stabilization, the mechanical property of the soil is improved by changing the orientation of the soil particles by means of vibration, compaction, etc. On the other hand, the chemical property of the soil is improved by bringing

K. Taki (✉)
Civil Engineering, Indian Institute of Technology Gandhinagar, Gandhinagar, India
e-mail: kaling.taki@iitgn.ac.in

P. Bhattacharya
Civil Engineering, Indian Institute of Technology Kharagpur, Kharagpur, India
e-mail: paramita@civil.iitkgp.ernet.in

A. Prashant et al. (eds.), *Advances in Computer Methods and Geomechanics*, Lecture Notes in Civil Engineering 55,
https://doi.org/10.1007/978-981-15-0886-8_45

about physiochemical changes in the soil particles by addition of certain chemical admixtures in chemical stabilization. The admixture changes the microstructural and mineralogical properties of the soil. Generally, industrial or agricultural by-products are widely used as admixtures. Lime (CaO), is an industrial by-product formed after the burning of Limestone ($CaCO_3$) and is widely used as basic construction material. In earlier days, its application in the field of geotechnical engineering was not known because of inadequate knowledge about the subject [1]. But in modern times its applicability increases in the areas of highways, foundation base, slope protection, embankments, etc. Rice Husk Ash (RHA) is a kind of agricultural waste material, which obtained from incineration of the rice husk at a controlled temperature of 75–80 °C. RHA is enriched by amorphous silica. The objectives of the present study are to improve the strength of highly plastic clayey soil, which can be used as the foundation or construction material by using aforementioned additives, and make a comparative study on these two additives to find out which additives imparts higher compressive strength in the soils. Unconfined compressive test (UCS) test has been carried out as a measure of strength gain in the soil by using with both the additives for varied curing periods, i.e. 0, 3, 7, 21 and 28 days.

Bell [2] showed that the addition of small percentage of Lime by weight of the soil can help in the stabilization of the clay soil. Based on strength test Bell [2] reported that 4% Lime content was the optimum Lime content for Montomorillonite rich soils, 4–6% Lime content for Kaolinite and 4% for quartz respectively. Nalbantoglu [3] found that Lime was very effective in increasing the unconfined compressive strength of treated soils. The formation of new cementation compounds also provided for a long-term strength development of stabilized soils. Bashaa et al. [4] used residual granite soil, the additives used were RHA and cement. There was reduction in plasticity of cement/RHA stabilized soils. Brooks [5] used the expansive soil as a construction material by using rice husk ash (RHA) and fly ash, which are agricultural and industrial by-products, respectively. Brooks [5] reported that stress strain behaviour of unconfined compressive strength showed that failure stress and strain increased by 160% and 50% respectively when the fly ash content was increased from 0 to 25%.

Dash and Hussain [6] used commercially available Bentonite as expansive soil (ES) and a non-expansive residual soil (RS). A laboratory reagent grade quick Lime (CaO) was used as the stabilizing agent. Dash and Hussain [6] reported that the Lime content gives the maximum strength of 9% for expansive soil and 5% for residual soil. Yadu et al. [7] found that addition of FA and RHA in black cotton soil reduces its plasticity index (PI) of the soils. Al-Mukhtar et al. [8] used Lime to stabilize clay samples. As a consequence, the plasticity index and swelling pressure are reduced, while unconfined compressive stress and permeability are increased. Fattah et al. [9] used Rice Husk Ash (RHA) for soil stabilization and found that unconfined compressive strength was increased for RHA between 6 and 8%.

The main objective of the present work is to perform a comparative study to find out the difference in strength achieved when two different soil expansive and non-expansive, are treated with Lime and RHA, separately. This article mainly focusses

on to understand the effect of addition of RHA alone and to compare the quantitative difference in the strength achieved in comparison to active stabilizing additive Lime.

2 Experimental Program

2.1 Material Properties

For the study two types of soils have been incorporated, an expansive soil (ES): Bentonite, the soil is classified as a clay with high compressibility (CH) type and a non-expansive soil (NES): Kaolinite, the soil is classified as clay with low compressibility (CL) type. The properties for the two types of soils have been given in Table 1.

The X-ray diffraction test has been conducted on both the soils and Montomorillonite, Quartz (SiO_2) and Aluminium oxide are found as dominant mineral in Bentonite and Magnetite, Quartz (SiO_2) are found as dominant mineral in Kaolinite as shown in Fig. 2. XRD revealed that the amount of Quartz present in the Kaolinite (9000 cps) is more than that present in Bentonite (1700 cps). The additive used in laboratory experiments are laboratory Lime (M = 56.08 g/mol, which contain $\geq$ 90% CaO and loss on ignition at 800 °C is $\leq$ 10%) and Rice husk Ash (RHA) passing through 75 μm IS sieve, RHA contains more than 85% of SiO_2. The chemical composition and geotechnical properties of RHA have been presented in Table 2.

Table 1 Basic properties of test materials

Sl. no	Soil properties	Description-1	Description-2
1	Soil type	Expansive soil (ES)	Non-expansive soil (NES)
2	Soil name	Bentonite	Kaolinite
3	Colour	Brown	White
4	Specific gravity (G)	2.62	2.57
5	pH	7.93	7.33
6	Liquid limit (LL)	410%	72%
7	Plastic limit (PL)	50%	25.84%
8	Soil classification	CH	MH
9	Optimum moisture content	34.5%	28%
10	Max. Dry density	12.5 kN/m^3	13.5 kN/m^3

Table 2 Chemical composition of Rice Husk Ash (RHA)

Sl. no	Composition		Geotechnical properties	
	Components	Percentages (%)	Properties	Description
1	SiO_2	86.0	Liquid Limit	Non-plastic
2	Al_2O_3	2.6	Plastic Limit	Non-plastic
3	Fe_2O_3	1.8	Specific gravity	2.04
4	CaO	3.6	Maximum dry density	6.97%
5	MgO	0.27	Optimum moisture content	45.5%
6	Loss in ignition	4.2		

2.2 Testing Procedure

The experiments have been conducted on the clayey soil samples were to determine physical and chemical properties. The liquid limit and plastic limits were determined as per IS: 2720 (part 5)-1985 [10]. The pH for both the soils provided in Table 1 has been found out as per IS: 2720 (part 26)-1987 [11]. The plasticity index is accounted as the numerical difference between liquid limit and plastic limit. Free swell index test (FSI) was conducted as per IS: 2720 (part 40)-1977 [12] for expansive soil by using both the additives and the values are tabulated in Tables 3 and 4. From the values we can see that the free swell is effectively controlled by addition of Lime than that of RHA.

Table 3 Free swell index (FSI) values for Bentonite and Lime

Sl. no	Soil	FSI (%)
1	ES + 0% Lime	971.4
2	ES + 3% Lime	128.6
3	ES + 6% Lime	114.3
4	ES + 9% Lime	100.0
5	ES + 12% Lime	85.7
6	ES + 15% Lime	71.4

Table 4 Free swell index (FSI) values for Bentonite and RHA

Sl. no	Soil	FSI (%)
1	ES + 0% RHA	971.4
2	ES + 3% RHA	828.6
3	ES + 6% RHA	685.7
4	ES + 9% RHA	657.1
5	ES + 12% RHA	542.9
6	ES + 15%RHA	500.0

To compute the optimum moisture content (OMC) and maximum dry density both the soil was mixed with varying percentages of moisture and cured for 3 days in desiccator to ensure uniform moisture distribution, since it is fine grained. The soil was static compacted for OMC using Mini compacter, a cylindrical mould of 38.1 mm diameter and 100 mm in height. The mini compacter used in the study was proposed by Sivapullaiah and Sridharan [13]. The compacter is used specially for fine grained soils. For Unconfined compressive strength (UCS) test, the dimension of sample was 38 mm diameter and 76 mm length, the sample were prepared at their maximum dry density of 12.5 and 13.5 kN/m^3 and optimum moisture contents of 34.5 and 28% for Bentonite and Kaolinite respectively.

The soil samples prepared at their optimum moisture contents was treated with Lime and RHA separately in 0, 3, 6, 9, 12 and 15% of the weight of the soils and cured for different periods (say 0, 3, 7, 21 and 28 days) for UCStest. In addition to optimum moisture content an additional water of 32% by weight of the Lime was added during sample preparation time to compensate for the hydration reaction of Lime [14]. The prepared soil samples were covered with plastic sheet and kept inside the desiccator till the desired period of curing was reached under 100% relative humidity. The samples for the UCS test were prepared by static compaction using Mini compacter. The test was conducted as per IS: 2720 (part 10)-1973 under a constant strain rate of 1.25 mm/min [15]. The samples which achieved higher unconfined compressive strength were considered for XRD and SEM test to know their mineralogical and microstructural changes in the matrix of the soil because of the additives. Soil samples for SEM and XRD were collected from the UCS tested samples, dried and sieve through 75 μm IS sieve and cured for 28 days. The powered sample was mounted on the specimen holder and coated with a thin layer of gold to provide surface conductivity. The coated specimen was placed in scanning electron microscope operating at 15 kV, and the photomicrographs were obtained. Also X-ray diffraction tests were done to know the mineralogical compositions. The diffractometer system was XPERT-PRO and measurement program was XCELERATOR, no monochromator was used and the anode material used was copper (Cu). The general voltage used was 40 kV and tube current was 30 mA. For mineral identification X' Pert High Score and match software was used.

3 Results and Discussion

3.1 Strength Property

The samples were prepared for unconfined compressive strength test and cured for different time periods (immediately, 3, 7, 21 and 28 days) with varying percentages, say, 0, 3, 6, 9, 12 and 15%, of both the additives by weight. The load at which the soil fails is referred as the strength of the soils. Typical strength (i.e. unconfined compressive strength at failure) with variation of Lime and RHA amended soils is

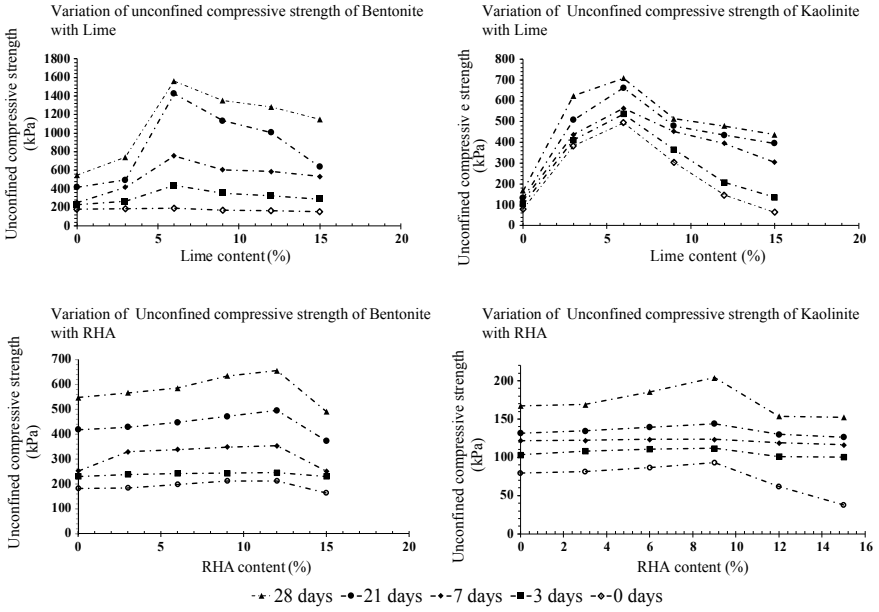

Fig. 1 Unconfined compressive strength of Bentonite and Kaolinite with different amount of Lime and RHA for different curing period

presented in Fig. 1. Initially when Lime is added in very small quantity the increase in strength is practically negligible. Even though the sample is cured for long period of time with small quantity of Lime the effect is not appreciable. When the Lime is added into the soils up to some quantity, say, approximately or above 3%, it is capable to alter the diffused double layer of the soils to which it is added. Therefore, the strength is remarkably less in initial stages of Lime addition (less than 3%), as cementation is too weak to provide some amount of appreciable strength. As the quantity of Lime is increased up to certain amount, say approximately 3% or above, the pozzolanic reaction starts to reach its peak, and produce cementitious compounds which results in the higher strength of the soil. It can be seen from the stress versus strain curve in Fig. 1 by conducting unconfined compressive strength test that addition of 6% Lime is the optimum value for both expansive (Bentonite) and non-expansive (Kaolinite) soils. The strength of both the soils after 28 days has increased to approximately 1600 and 700 kPa for Bentonite and Kaolinite, respectively, where the strength of untreated Bentonite and Kaolinite soils were found to be equal to approximately 181.6 kPa and 79.12 kPa, respectively. However, it was found that the increase in Lime content beyond the optimum value in both expansive and non-expansive soils results in reduction of strength. Such reduction of strength is caused due to lubricating action of Lime as it is neither frictional nor cohesive material [2]. Kumar et al. [16] attributed that the reduction in strength is occurred due to the platy shape of the Lime particles which is in unreacted state. As the Lime content is increased the pH

value is also increased, as a consequence this high alkaline environment leads to the formation of calcium silicate hydrate (CSH) gel. CSH is composed of solid product which is produced from hydration reactions between Lime and water. This water which is normally adsorbed on the surface of hydrates (i.e. CSH) resulting from hydration is called as Gel water. The volume of the gel water is found to be more than 28% of the volume of gel [17]. So as Lime content is increased, the soil matrix tends to become very much porous due to the formation of excessive gel material.

Normally addition of Lime in to the soil causes reduction of elasticity, swelling and increment of work ability and compressive strength. These improved soil properties are resulted from three basic chemical reactions [18]: (i) cation exchange, flocculation and agglomeration, (ii) cementation (resulting from Pozzolanic reaction), and (iii) carbonation. The cation exchange process leads to agglomeration of the clay particles into coarser particles. The cementation reaction results the formation of calcium silicate and calcium aluminate or calcium-aluminate—silicates which are normally characterized by achieving high strength.

Figure 1 also represents the UCS curves for the soils treated with RHA in different percentages by weight of soil. It was found that RHA slightly increases the strength of the soil due to lack of its cementation property. From the UCS curve it can be seen that after 28 days the optimum RHA content was found to be 12% for Bentonite and 9% for Kaolinite. The increase in strength after 28 days is approximately 660 and 206 kPa for Bentonite and Kaolinite, respectively, while the strength of untreated Bentonite and Kaolinite is found to be equal to 181.6 kPa and 79.12 kPa, respectively. The improvement of strength is prominent in case of Lime compared to RHA. Beyond optimum content of RHA the strength of both soils was found to be decreased. This may be attributed due to decrease in the maximum dry unit weight which is caused by the replacement of soil by RHA [19, 20]. When RHA is added to both the soils, it may coat the soil particles resulting in the formation of large particles having larger voids and less density [21]. It can be observed in Fig. 1 that the optimum Lime content for both the soils (ES and NES) is found to be equal to 6% whereas the optimum RHA content is found to be equal to 12% and 9% for Bentonite (ES) and Kaolinite (NES), respectively. The amount of RHA required in case of expansive soil is more than non-expansive soil because when water is added to Bentonite soil, it expands due to its expansive nature. The expansion of Bentonite causes the formation of voids within it. When RHA is added initially it starts filling the voids created by the soil. On the contrary Kaolinite is non-expansive such trend of expansion of soil was not observed. It was also found that the unconfined compressive strength of Lime-treated Bentonite soil is approximately 3 times higher than that of RHA-treated Bentonite whereas for Lime-treated Kaolinite soil, unconfined compressive strength is approximately 3.5 times higher than that of RHA-treated Kaolinite soil. Since Lime is providing higher strength compared to RHA the microstructure and mineralogical properties of the Lime-treated soil after 28 days of curing were studied.

3.2 Microstructure and Mineralogical Properties

The microstructure and mineralogical properties of Lime-treated soils are studied by X-Ray diffraction (XRD) and scanning electron microscope (SEM) tests (Fig. 3). The sample for XRD and SEM tests were prepared by taking small amount of dried and powdered (passing through IS 75 μm sieve) each specimen from the UCS tested sample. Typical X-Ray diffractograms for 6% Lime-treated expansive and non-expansive soils allowed to cure for zero day and 28 days has been shown in Fig. 2. After the analysis it has been found out that many new compounds are formed in Lime-treated soils. Among these newly formed compounds the major cementitious compound are gyrolite ($2Ca_2SiO_4 \cdot 6H_2O$), Calcium silicate hydrate (CSH) ($5Ca_2SiO_4 \cdot 6H_2O$) and calcium aluminium silicate hydroxide hydrate (CASHH) ($Ca_5Si_5Al(OH)O_{17} \cdot 5H_2O$) which impart strength in the soils. The formation of these compounds is occurred due to reaction between Lime and soil [2, 6], Diamond and Kinter 1966a & b). Quartz is also present in the cementitious compounds as well as in the untreated soils. Moreover, visible reduction in the quartz peak is also occurred from untreated soil to treated soil, which indicates that quartz reacted with Lime and form silica gel. It can also be noted in SEM micrographs (Fig. 3) that cemented crystalline structure has been formed in both the soils due to addition of 6% Lime. This cemented crystalline structure enables the soils to carry higher load. However, the crystalline structure is very well developed in Bentonite compared to that in the Kaolinite where the patches of reaction products can be seen. This resulted higher strength in Bentonite compared to Kaolinite after 28 days of curing.

The crystalline structure was very well developed in Bentonite compared to that in Kaolinite soil because, it can be observed from the XRD the quantity of quartz is relatively higher in Kaolinite than that of Bentonite soil. Which in turn retarded the bonding between the surface lime and clay particles, because of this the partial crystallization of CASH takes place, which further not entirely converted to the crystallized compounds such as CSH and CAH leading to not fully developed crystalline structure [22].

4 Conclusions

From the study it was found that both the admixtures Lime and RHA can improve the strength of soil but in different extend, the optimum Lime content was found to be 6% for both Bentonite and Kaolinite, in case of RHA it was about 12% and 9% RHA for Bentonite and Kaolinite respectively. It was found that the unconfined compressive strength of Lime-treated Bentonite soil was approximately 3 times higher than that of RHA-treated Bentonite soil. Also, the unconfined compressive strength of Lime-treated Kaolinite clay is 3.5 times higher than that of RHA-treated Kaolinite. Beyond certain limit, excessive additions of Lime lead to the drastic reduction in the strength characteristic of soil. 12% RHA consumption in case of Bentonite and 9% RHA

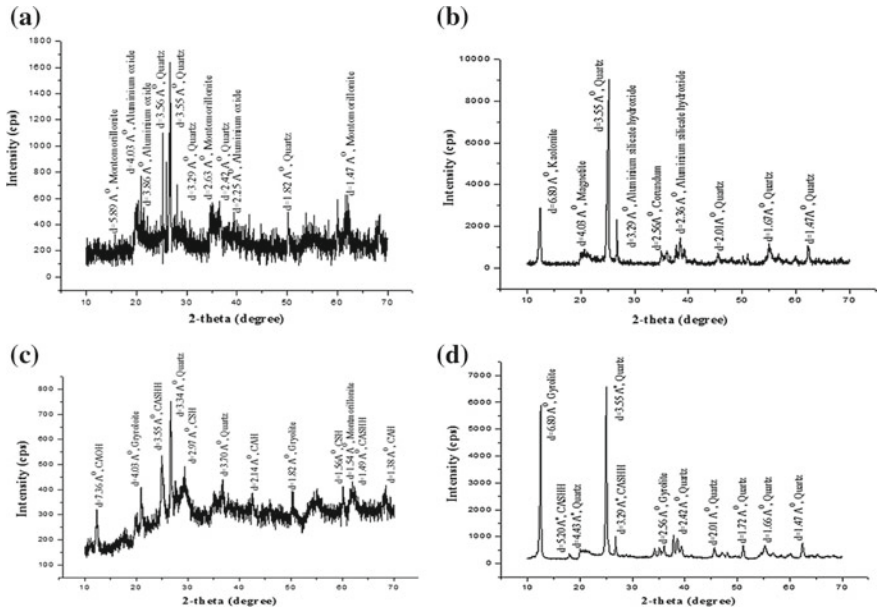

Fig. 2 X-ray diffraction results **a** Bentonite at 0 days curing period **b** Bentonite at 28 days curing period **c** Kaolinite at 0 days curing period and **d** Kaolinite at 28 days curing period

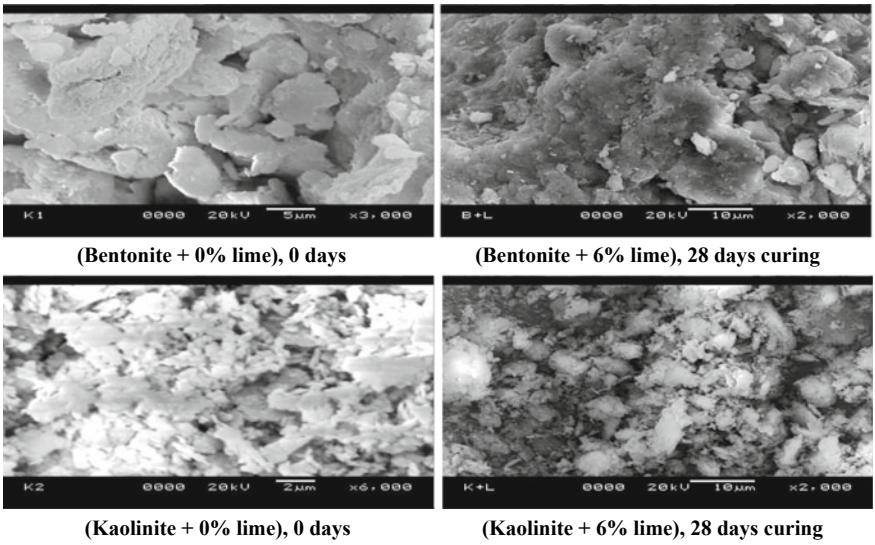

(Bentonite + 0% lime), 0 days **(Bentonite + 6% lime), 28 days curing**

(Kaolinite + 0% lime), 0 days **(Kaolinite + 6% lime), 28 days curing**

Fig. 3 SEM results of Bentonite and Kaolinite at 0 days and 28 days of curing period

consumption in case of Kaolinite, it is occurred because due to expansive nature of Bentonite. The performance of the Lime was found to be very effective to achieve strength compared to that of Rice Husk Ash (RHA).

The applicability of the present research work throws light on the potential of Lime application compared to RHAas an effective way to modify soils by improving both workability and load-bearing characteristics, while increasing stability and impermeability. Also, Lime can be used to dry wet soils at construction sites, reducing downtime and providing an improved working surface. The application of Lime will result in long-term strength gain, developed through a pozzolanic reaction and can continue for a very long period of time, even many years.

Acknowledgements Financial Support from IIT Kharagpur is gratefully acknowledged. Any opinions, findings, and conclusions or recommendations expressed in this material are those of authors and do not necessarily reflect the views of IIT Kharagpur.

References

1. Herrin M, Mitchell H (1961) Lime-soil mixtures. Bulletin No. 304, Highway Research Board, Washington, DC, 99–138
2. Bell FG (1996) Lime stabilization of clay minerals and soils. J Eng Geol 42(1996):223–237
3. Nalbantoglu, Z (2006) Taylor & Francis Group, London, UK
4. Basha EA, Hashim R, Mahmud HB, Muntohar AS (2004) Stabilization of residual soil with rice husk ash and cement. J Construct Build Mater 19(2005):448–453
5. Brooks RM (2009) Soil Stabilization with Fly Ash and Rice Husk Ash. Journal of Research and Reviews in applied Science 1:209–217
6. Dash SK, Hussain M (2012) Lime Stabilization of Soils: Reappraisal. ASCE Journal of Materials in Civil Engineering 24(6):707–714
7. Yadu L, Tripathi RK, Singh D (2011) Comparison of fly ash and rice husk ash stabilized black cotton soil. Int J Earth Sci Eng 4(6):42–45
8. Al-Mukhtar M, Khattab S, Alcover JF (2012) Microstructure and geotechnical properties of lime–treated expansive clayey soil. J Eng Geol 17(27):139–140
9. Fattah MY, Rahil FH, Al-Soudany KYH (2013) Improvement of clayey soil using rice husk ash. J Civil Eng Urbanism 3(1):12–18
10. IS: 2720 (Part 5)-1985. "Determination of liquid and plastic limit (second revision)"
11. IS: 2720 (Part 26)-1987. Determination of pH value (second revision)
12. IS: 2720 (Part 40)-1977. Determination of free swell index of soils
13. Sivapullaiah PV, Sridharan A (2005) Mini compaction test apparatus for fine. J Geotech Test 28(3):240–246
14. Greaves HM (1996) An introduction to lime stabilization. Proc. Symp. on Lime Stabilization, Thomas Telford, London, pp 5–12
15. IS: 2720 (Part 10)-1973. Determination of Unconfined compressive strength (first revision)
16. Kumar A, Walia BS, Abjaj A (2007) Influence of fly ash, lime, and polyester fibres on compaction and strength properties of expansive soil. J Mater Civil Eng 19(3):242–248
17. Neville AM, Brooks JJ (2004) Concrete technology. 4th Indian reprint, Pearson Education, Delhi
18. Fang HY (1991) Foundation Engineering Handbook, 2nd ed., Van Nostrand Reinhold Publishing Company

19. Ola SA (1975) Stabilization of Nigeria lateritic soils with cement, bitumen and lime. In: Proceedings of 6th regional conference Africa on Soil mechanics and foundation engineering, Durban, South Africa
20. Osinubi KJ, Katte VY (1997) Effect of elapsed time after mixing on grain size and plasticity characteristic, I: soil-lime mixe. NSE Technical Transactions 32(4):65–76
21. Osula DOA (1991) lime modification of problem laterite. J Eng Geol 30:141–149
22. Saeed KA, Kassim KA, Yunus NZ, Nur H (2013) Characterization of hydrated lime-stabilized brown kaolin clay. Int J Eng Res Technol 2(11):3722–3727

Energy Dissipation Response of Unsaturated Cohesive Soil Under Dynamic Loading Conditions

Saloni Pandya and Ajanta Sachan

Abstract Partially saturated soils are commonly encountered in various geotechnical engineering projects across the world. Existence of matric suction in the three-phase system of unsaturated soil governs its strength and volumetric response. Environmental changes cause alterations in the geometric arrangement of unsaturated soil due to seasonal variation in the matric suction of soil leading to change in mechanical response of unsaturated soils. Cyclic high/low amplitude loading on soils such as seismic loading, machine vibrations, wave loading, traffic loading, blast loading, etc., can instigate the loss in strength and stability of soils. Energy dissipation during cyclic loading can provide information regarding internal deformation characteristics of soils. Current study evaluates the influence of initial static loading, matric suction, dry density and water content on the energy dissipation characteristics of unsaturated cohesive soil. Series of strain-controlled cyclic triaxial tests were conducted on cohesive soil from Ahmedabad (India) under unsaturated conditions (as-compacted) at varying initial static axial strain (S), dry density and water content. In-contact filter paper method was used to evaluate matric suction of Ahmedabad soil. Application of different axial strain (S) significantly affected the cumulative energy dissipation (ΔW_T) of unsaturated cohesive soil. Matric suction of soil exhibited significant impact on the energy dissipation characteristics of Ahmedabad cohesive soil. Dry density of unsaturated Ahmedabad cohesive soil was observed to play an important role in the energy dissipation characteristics. Substantial energy dissipation along with larger stiffness degradation indicated soil under unsaturated conditions to be metastable and prone to severe damages during dynamic loading conditions.

Keywords Unsaturated · Matric suction · Cyclic triaxial testing · Energy dissipation

S. Pandya (✉) · A. Sachan
Civil Engineering, Indian Institute of Technology Gandhinagar, Ahmedabad, India
e-mail: pandya_saloni@phd2012.iitgn.ac.in

A. Prashant et al. (eds.), *Advances in Computer Methods and Geomechanics*, Lecture Notes in Civil Engineering 55,
https://doi.org/10.1007/978-981-15-0886-8_46

1 Introduction

Unsaturated soils present in the vadoze zone layer above natural hydraulic datum comprises of three-phase system (soil matrix, water, and air) with degree of saturation (S_r) < 100%. Hyper arid, arid and semi-arid regions cover around 33% of the Earth's continental surface. In such regions, the annual evaporation rates are found to be significantly higher than annual precipitation rate leading to availability of water table at greater depths. In these regions (Hyper arid, arid, and semi-arid), most of the geotechnical and subsurface construction takes place in unsaturated zone. Most of the construction practices such as foundations of buildings, pavements, foundation of retaining walls etc. on natural ground even in the humid climatic conditions are carried out in vadose zone owing to the overall ease of construction. Apart from the natural availability of soils in unsaturated state, compacted soils are also found under partially saturated conditions. Such compacted soils are part of large portion of structures for instance pavements, airfields, embankments, tunnels, earthen dams, natural slope linings retaining walls, and landfill covers. Multiphase interactions (air, water and soil matrix) in unsaturated state of soil separate the mechanical response of unsaturated soil from that of saturated soil. Under unsaturated conditions, soil possesses negative pore water pressure with reference to the ground water table (Natural Hydraulic datum). Negative pore pressure indicates mathematically the difference between pore air and pore water pressures ($u_a - u_w$) originated due to surface tension and capillarity, which is invariably described as matric suction. Presence of negative pore water pressure (matric suction) in the unsaturated soils terminates the implementation of principles of conventional soil mechanics to unsaturated soils [1]. Strength and volumetric response of unsaturated soil is extensively governed by matric suction of the soil. Several researchers [1–5] have reported unsaturated strength of the soil as a function of matric suction ($u_a - u_w$). Apparent cohesion developed in the unsaturated state of soil due to occurrence of matric suction, would dominate the stiffness and strength of unsaturated soil [1].

Soils (saturated or unsaturated) in natural environment are vulnerable to various types of cyclic/dynamic loading, i.e., seismic loading, wave loading, machine vibrations, traffic loading, blast loading, etc. Dynamic loading on soils may cause loss in strength and instability within the soil mass, which requires the estimation of degradation and energy dissipation characteristics of soils under such loading conditions. Degradation in the cyclic strength of soil is governed by internal soil structure. Seasonal alterations in the soil fabric take place due to transient changes in the matric suction of the soil [6, 7]. The strength degradation and energy dissipation characteristics of soil during dynamic loading are imperative for solving various problems involving soil-structure interaction and other geotechnical issues. Dynamic responses of saturated soils were examined by several researchers [8–17]. However, energy dissipation behavior of soil in as-compacted (unsaturated) condition with increment in number of loading cycles remains unexamined. The current research is an extension of research presented in Pandya and Sachan [6, 7] which focuses on the evaluation of energy dissipation characteristics of Ahmedabad cohesive soil

during dynamic loading conditions. The study incorporates the influence of initial static loading, as-compacted dry density and water content and as-compacted matric suction on energy dissipation characteristics of Ahmedabad cohesive soil.

2 Material Properties and Specimen Preparation

The unsaturated cohesive soil sample was collected from 0.5 m depth (to avoid any organic matter present on the surface) from Chandkheda, Ahmedabad (Gujarat, India). In situ bulk density and water content of Ahmedabad soil was 2.0 gm/cc and 22% respectively. The specific gravity, liquid limit (Cassagrande's apparatus), plastic limit and shrinkage limit tests were performed on collected soil sample and the corresponding values obtained are 2.7%, 51%, 20%, and 14% respectively. Grain size distribution curve of Ahmedabad soil indicated that soil to be a combination soil containing mixture of 1% gravel, 15% sand, 52% silt and 32% clay. The XRD (X-ray Diffraction) analysis of soil revealed the mineralogical composition of Ahmedabad soil to be 86% Quartz, 12% Montmorillonite and 2% Kaolinite. The soil has been classified as CH, the cohesive soil with high plasticity and compressibility. Compressibility parameters (C_c and C_r), Shear Strength parameters (c and ϕ) and undrained cohesion (c_u) were determined under in situ conditions using Oedometer test, unconsolidated undrained (UU) triaxial test and unconfined compression (UC) test, respectively. Compressibility parameters (C_c and C_r) were obtained by loading and unloading the soil specimens at different vertical pressures (5, 10, 20, 50, 100, 200, 400, 800 kPa) by evaluating slope of loading and unloading curves respectively. Poisson's ratio (υ) of Ahmedabad soil was obtained using unconfined compression (UC) setup facilitated with lateral strain measurements. Compressibility, shear strength properties and Poisson's ratio of Ahmedabad soil at in situ density and water content have been specified in Pandya and Sachan [6]. Moist tamping method was selected as the specimen preparation technique for all the filter paper and dynamic triaxial tests. Procedure of moist tamping method is mentioned in detail in Pandya and Sachan [6].

3 Experimental Program

3.1 In-Contact Filter Paper Tests

In the current study, matric suction ($u_a - u_w$) of cohesive soil was assessed using filter paper method at varying dry density and water content. The in-contact filter paper technique encloses large range of suction (10 kPa to 100 MPa). This method has been testified to be the most simple and accurate technique for suction measurements [6]. Incorporating this technique the matric suction of CH soil was measured as per ASTM

code (ASTM D5298 − 10, 2013). In this procedure, ashless filter paper Whatman 42 was used. In the current research series of filter paper tests were carried out at varying dry density and water content. In this technique, 55 mm diameter filter paper of was intercalated between two 60 mm diameter filter papers (top and bottom) to disallow the contamination of central filter paper. The piled up filter papers were then cautiously positioned between two similar soil cakes (h-25 mm and d-75 mm) prepared using moist tamping method. Both the soil cakes were prepared at equal dry density and water content. Whatman 42 filter papers (top, central and bottom) were dried overnight (at least 16 h) in oven at 105°± 5 °C. In order to prevent contamination and moisture loss, all the soil specimens and filter papers were handled using handgolves and tweezers. The entire soil specimen comprising of piled up filter papers between soil cakes were then enclosed employing an insulation tape (electric tape) from all the sides to maintain proper contact between soil specimens and filter paper and an air tight atmosphere. Sealed specimen was carefully placed in a glass container, which was again sealed employing an electric tape to preserve air tight atmosphere and to ensure moisture equilibration. For 7 days of equilibration process, biological incubator (Scigenics Biotech—ORBITEK) with humidity and temperature control system was used to keep the glass container comprising of the specimens at 20 °C ± 0.1 °C. The soil specimen was moved out of the incubator after 7 days of equilibration and central filter paper (d-55 mm) was immediately (in an interval of 5 s) was placed in a small metal container. The wet weight of the filter paper in the metal container was determined to nearest 0.0001 g and then was placed in oven for 24 h drying process. The lid of the metal container was kept 1/4th open during the drying process. Lid of the container was closed for 15 min before evaluating the dry weight (after 24 h) to allow temperature equilibration. The metal container was taken out of oven and placed for 20 s on heat sink (aluminum plate) to achieve minimal fluctuation of temperature during dry weight determination. Mass of dried filter paper was evaluated and water content was assessed. Matric suction of the soil at obtained water content of filter paper was found from the ASTM calibration chart for Whatman 42 ashless filter paper [18]. The obtained matric suction values of unsaturated CH soil specimens (S1–S11) at varying dry density and water content are represented in Table 1. Sequential procedure for performing filter paper test has been elaborated in Fig. 1.

3.2 Cyclic Triaxial Tests

Multiple series of cyclic triaxial tests under strain-controlled conditions were conducted on Ahmedabad soil under unsaturated (as-compacted) conditions. Reconstituted cylindrical soil specimens of 100 mm height and 50 mm diameter were obtained by using moist tamping sample preparation technique. All the tests were conducted by applying initial static axial strain (S) followed by strain-controlled cyclic loading (C) for given S/C ratio. Cyclic loading (C) of 0.2 mm axial strain amplitude was applied on soil specimen at 0.5 Hz loading frequency up to 50 cycles under 100 kPa

Table 1 Matric suction of the Ahmedabad cohesive soil at different dry densities and water content [6]

Specimen number	Dry density (gm/cc)	As-compacted water content (%)	$u_a - u_w$ (kPa)
S1	1.46 gm/cc (84% of MDD)	9.5 (7% dry of OMC)	7781
S2		13.5 (3% dry of OMC)	5442
S3		16.5 (OMC)	4101
S4		19.5 (3% wet of OMC)	618
S5		23.5 (7% wet of OMC)	124
S6	1.64 gm/cc 94% of MDD	9.5 (7% dry of OMC)	6685
S7		13.5 (3% dry of OMC)	2710
S8		16.5 (OMC)	2204
S9	1.74 gm/cc 100% of MDD	9.5 (7% dry of OMC)	6027
S10		13.5 (3% dry of OMC)	2439
S11		16.5 (OMC)	2438

[a]MDD—Maximum Dry Density, OMC—Optimum Moisture content

confining pressure (CP) for all the tests. First series of tests was focused on the effect of varying initial static strain on dynamic behavior of unsaturated Ahmedabad soil, which was carried out by applying initial static loading (S) to the specimen succeeded by application of cyclic loading (C) at chosen S/C ratio (static/cyclic) varying from 1 to 10. Second series was conducted to obtain the dominance of matric suction on dynamic response of as-compacted soil at varying water content and dry density for S/C of 10.

Study on shear modulus reduction with increase in number of loading also carried out for second series by analyzing the cyclic degradation index (δ) of Ahmedabad cohesive soil for each cycle of loading. Both the test series were conducted at 0.2% cyclic axial strain amplitude (C) and 0.5 Hz frequency. All the specimens were statically compressed/strained to a specific percentage and then were loaded cyclically [6]. The static loading was changed to acquire varying S/C ratio. The cyclic loading at a particular S/C ratio would simulate a with the condition of a railway/highway embankment, where the embankment dead load on soil would simulate initial static loading (S) and moving vehicles would simulate cyclic loading (C). Produced static load on the specimen due to the application of initial static axial strain (S) during cyclic triaxial was equivalent to that developed during monotonic triaxial test on the similar specimen under same boundary conditions. Monotonic triaxial tests were performed on same unsaturated cohesive soil specimens under in situ conditions at 100 kPa of confining pressure to obtain the static loading (S values), which were further used to perform the cyclic triaxial tests at different S/C ratio (Fig. 3b, c respectively).

Dynamic parameters (Shear modulus & Damping ratio) of soil were evaluated for 0, 1, 2, 3, 4, 10, 20, 30, 40 loading cycles. Dynamic Young's modulus (E_{dyn}), Shear Modulus (G) and Damping ratio were determined using similar procedure as mentioned in Pandya and Sachan [6]. Poisson's ratio of the cohesive soil under in situ conditions was assessed by conducting unconfined compression tests outfitted with lateral dial gauges to obtain horizontal strain measurements. Results showed the

Fig. 1 Step-wise sequential procedure of In-contact filter paper method for matric suction determination

Poisson's ratio (υ) of as-compacted Ahmedabad cohesive soil specimen to be 0.35. Cyclic softening of Ahmedabad soil was assessed by evaluating stiffness degradation of cohesive soil with increase in number of loading cycles by calculating cyclic degradation index (δ).

Cyclic degradation index for Ahmedabad soil has been presented in Pandya and Sachan [6] for varying dry densities and water content.

Energy Criterion can be employed to evaluate dynamic instability in the soil. Dissipated energy from the soil specimen furnishes information about the internal structure of the soil specimen. Cumulative dissipated energy (ΔW_T) for a unit volume of soil can be assessed employing the formulation given by Voznesensky and Nordal [19] and Okur and Ansal [20], as described in Eq. 1.

$$\Delta W_T = \sum_{i=1}^{n-1} 0.5(\sigma_{i+1} - \sigma_i)(\varepsilon_{i+1} - \varepsilon_i) \quad (1)$$

Energy dissipated (W) has been evaluated for 1, 2, 3, 4, 5, 10, 20, 30 and 40 loading cycles. Furthermore, cumulative energy dissipation (ΔW_T) has been assessed for entire test in all four series of cyclic triaxial tests.

4 Results and Discussion

4.1 Effect of Initial Static Loading on Energy Dissipation Response of Unsaturated Cohesive Soil

Amount of dissipated energy exhibits the total amount of energy dissipated owing to application of cyclic loading on the soil. In the present study, dissipated energy (W) was evaluated for each loading cycle for all cyclic triaxial tests conducted at varying S/C ratio. The Cumulative Energy dissipated (ΔW_T) at the end of each test in the first series of testing has been depicted in Fig. 2. It was observed that the dissipated cumulative energy increased up to S/C ratio of 7.5 and then suddenly decreased for S/C ratio of 10. The result was found to be analogous to the damping response of unsaturated Ahmedabad cohesive soil at varying S/C ratio [6]. This indicated that application of initial static axial strain of 2% densified the soil specimen enough to cause the least energy dissipation as compared to the application of lower initial static axial strain values. Pandya and Sachan [6] reported that the static axial strain application of 2% (S/C = 10) provided the improved and standardized hysteresis

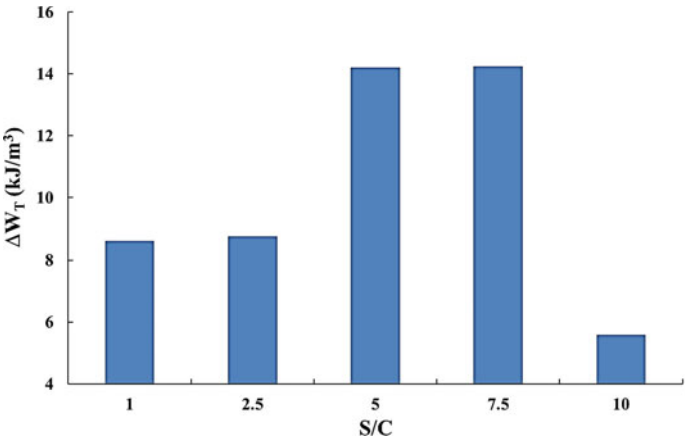

Fig. 2 Variation of cumulative energy dissipated (ΔW_T) at the end of each cycle of loading with Static/Cyclic (S/C) applied during cyclic triaxial testing

response of the soil specimen as the stiffness degradation response of soil in loading and unloading phase of the curve was found to be similar. However, at lower S/C ratio the stiffness degradation was found to be negligible in the unloading phase of the curve. Least cumulative energy dissipation for S/C = 10 proved that the induced load on the specimen subjected to initial static axial strain of 2% might led to the weakening of the additional interparticle compressive force in the unsaturated soil due to the overall compression or densification of the soil specimen due to static load. This would allow the plastic deformations in the unloading portion which were restricted earlier by strong interparticle compressive force owing to the existence of matric suction ($u_a - u_w$) in the unsaturated state of cohesive soil. This lead to similar stiffness degradation behavior in the loading and the unloading phase of the curve. Resistance to deformation or load handling capacity of the soil at higher S/C ratio = 10 was observed to increase, which led to lower dissipation of energy.

4.2 Influence of Dry Density and Water Content on Energy Dissipation Response of Unsaturated Cohesive Soil

In the second portion of the study, a series of cyclic triaxial tests was conducted on Ahmedabad cohesive soil at varying dry density and water content, as shown in Table 1. The dynamic behavior of Ahmedabad soil has been investigated in Pandya and Sachan 2017 a & b. The current study has been focused on the energy dissipation response of Ahmedabad cohesive soil at varying dry density and water content. It was observed that the dissipated energy at the end of each loading cycle decreased for a particular dry density with increase in as-compacted water content of the specimen. Figure 3 depicts the energy dissipation response of the specimens S1–S6 prepared at 1.46 gm/cc dry density and varying water content ranging from 9.5 to 23.5%. The dissipation of energy was found to be least for specimen S6 (w = 23.5%) and

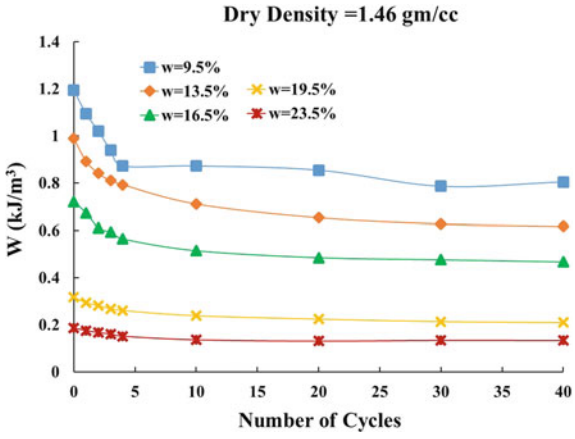

Fig. 3 Influence of as-compacted water content on the energy dissipation (W) response of Ahmedabad cohesive soil

maximum for specimen S1 (w = 9.5%). Analogous response was observed for dry density 1.64 and 1.74 gm/cc, as represented in Table 2. With the increase in water content of the soil specimen, the portion of the bulk water inside the soil skeleton increased, which would lead to the disappearance of the meniscus water due to vanishing of the air-water interface. This might cause disappearance of the interparticle resistive force between two particles. This resulted in lower endurance capacity to the induced load, eventually leading to the lower stiffness of the soil specimen and lesser stiffness degradation [6] of the Ahmedabad soil specimen prepared at higher water content; hence resulted into lower dissipated energy. Moreover, the dissipated energy was observed to decrease for a particular water content with increase in the as-compacted dry density of soil specimen.

Figure 4 describes the energy dissipation response of Ahmedabad soil at similar water content of 9.5% and varying dry density (1.46 gm/cc, 1.64 gm/cc, and 1.74 gm/cc). Least dissipated energy at the end of each cycle was observed for specimen prepared at highest dry density. Analogous response was obtained for all the water contents, as shown in Table 2. Increment in the denser configuration (with increase in the dry density) of particles regardless of water content of the specimen improved the load enduring potential of the soil mass significantly [6]. Variation of dissipated energy with respect to dry density was observed to be analogous to that for damping response of cohesive soil. Both dissipated energy and damping ratio were found to be higher for the specimen prepared at lower dry density exhibiting occurrence of higher internal deformations within the soil mass under dynamic loading conditions as compared to the specimens prepared with denser packing at higher dry density.

4.3 Effect of Matric Suction on Energy Dissipation Response of Unsaturated Cohesive Soil

Matric suction of the soil can be understood as the unit attractive force of soil for water in unsaturated state. It arises due to surface tension, cohesive and adhesive forces. Existence of matric suction governs the engineering behavior of soil in unsaturated state [7]. It was observed from the present study that the cumulative energy dissipated (ΔW_T) at the end of each test decreased with the decrease in matric suction of Ahmedabad cohesive soil. As depicted in the Fig. 5, maximum energy dissipation was observed for maximum matric suction of specimen S1 and minimum was observed for specimen S11. The response was analogous to the response of damping ratio with matric suction [6]. Energy dissipation in the soil specimen would occur due to material degradation. Dynamic instability of any soil would be concentrated on the amount of energy dissipated during dynamic loading conditions. The instability during the dynamic loading inside the soil skeleton could occur due to progressive failure of structural bonds, which could result in the material strength degradation resulting in the formation of multiple and severe localized deformations inside the soil mass [19]. Thus, it could be depicted from the present study that the specimen

Table 2 Energy dissipation response of Ahmedabad cohesive soil with varying dry density, water content and number of loading cycles. (a) ρ_d = 1.46 gm/cc, (b) ρ_d = 1.64 gm/cc and (c) ρ_d = 1.74 gm/cc

(a) ρ_d = 1.46 gm/cc

w = 9.5%		w = 13.5%		w = 16.5%		w = 19.5%		w = 23.5%	
No. of cycles	W (kJ/m^3)	No. of cycles	W (kJ/m^3)	No. of cycles	W (kJ/m^3)	No. of cycles	W (kJ/m^3)	No. of cycles	W (kJ/m^3)
0	1.19	0	0.99	0	0.72	0	0.32	0	0.19
1	1.09	1	0.89	1	0.67	1	0.29	1	0.18
2	1.02	2	0.84	2	0.61	2	0.28	2	0.17
3	0.94	3	0.81	3	0.59	3	0.27	3	0.16
4	0.87	4	0.79	4	0.56	4	0.26	4	0.15
10	0.87	10	0.71	10	0.51	10	0.24	10	0.14
20	0.85	20	0.65	20	0.48	20	0.22	20	0.13
30	0.79	30	0.63	30	0.48	30	0.21	30	0.13
40	0.80	40	0.62	40	0.47	40	0.21	40	0.13

(b) ρ_d = 1.64 gm/cc

w = 9.5%		w = 13.5%		w = 16.5%	
No. of cycles	W (kJ/m^3)	No. of cycles	W (kJ/m^3)	No. of cycles	W (kJ/m^3)
0	0.75	0	0.31	0	0.28
1	0.70	1	0.33	1	0.32
2	0.64	2	0.29	2	0.29
3	0.62	3	0.27	3	0.29
4	0.58	4	0.26	4	0.27
10	0.51	10	0.24	10	0.25

(continued)

Table 2 (continued)

(b) ρ_d = 1.64 gm/cc					
w = 9.5%		w = 13.5%		w = 16.5%	
No. of cycles	W (kJ/m^3)	No. of cycles	W (kJ/m^3)	No. of cycles	W (kJ/m^3)
20	0.46	20	0.22	20	0.23
30	0.44	30	0.21	30	0.22
40	0.44	40	0.21	40	0.22
(a) ρ_d = 1.74 gm/cc					
w = 9.5%		w = 13.5%		w = 16.5%	
No. of cycles	W (kJ/m^3)	No. of cycles	W (kJ/m^3)	No. of cycles	W (kJ/m^3)
0	0.74	0	0.42	0	0.34
1	0.69	1	0.43	1	0.35
2	0.60	2	0.43	2	0.32
3	0.56	3	0.42	3	0.31
4	0.52	4	0.41	4	0.30
10	0.46	10	0.36	10	0.26
20	0.41	20	0.33	20	0.24
30	0.39	30	0.31	30	0.23
40	0.38	40	0.30	40	0.22

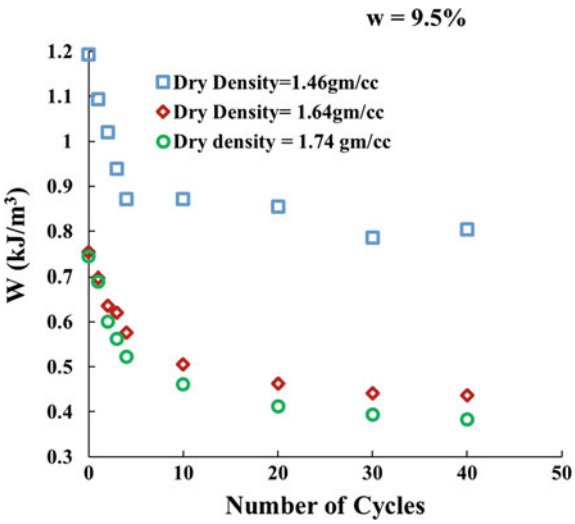

Fig. 4 Effect of dry density on energy dissipation response of Ahmedabad cohesive soil

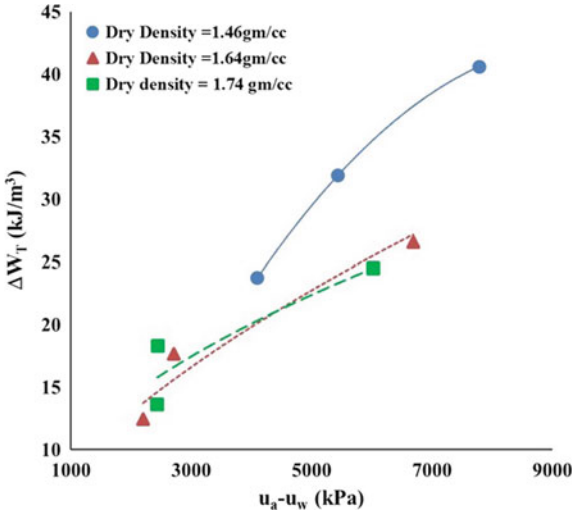

Fig. 5 Variation of cumulative energy dissipated (ΔW_T) at the end of each test with as-compacted matric suction ($u_a - u_w$) of Ahmedabad cohesive soil

possessing highest matric suction was found to be highly unstable during dynamic loading conditions. Dynamic instability in the unsaturated Ahmedabad soil specimen reduced with the decrease in matric suction of cohesive soil. Therefore, in spite of possessing highest matric suction, higher stiffness and larger cyclic strength the specimen S1 was observed to be more unstable as compared to specimen S6 possessing lower matric suction, smaller stiffness and lesser cyclic strength. Thus, irrespective of dry density and water content, the soil specimen with larger as-compacted matric suction would dissipate higher energy, and hence would be highly unstable during dynamic loading conditions. The cyclic degradation response and collapse potential

of Ahmedabad cohesive soil was obtained and discussed in Pandya and Sachan [7]. From energy dissipation response, stiffness degradation and collapse behavior of soil, it could be concluded that the specimen possessing higher matric suction possess a metastable internal soil structure. Hence, the soil specimen under such conditions would show brittle and fragile behavior resulting into collapse of the soil fabric with dynamic loading causing dynamic instability. Thus, soil specimen with higher matric suction would be dynamically unstable, volatile to excessive deformation and hence would be unsafe.

5 Conclusions

The current study represents the energy dissipation response of unsaturated cohesive soil with application of various S/C ratios for varying as-compacted dry density, water content, and matric suction of soil. Following conclusions have been drawn from the present analysis.

(a) Progressive degradation of dissipated energy with the increase in number of loading cycles was observed during the application of strain-controlled cyclic loading on unsaturated cohesive soil.
(b) Increment in applied initial static axial strain (S) led to the initial increase in the energy dissipation during cyclic loading. However at the S/C ratio of 10, the induced static load on the unsaturated soil specimen was found to cause weakening of the additional interparticle resistive force or capillary force leading to lower amount of energy dissipation for $S = 2\%$.
(c) With the increment in as-compacted water content and dry density of unsaturated cohesive soil specimen, the dissipated energy was found to degrade.
(d) Energy dissipation during dynamic loading was found to be higher for specimens with lower dry density and lower water content, in spite of possessing greater stiffness at higher matric suction. This response was found to be analogous to the collapse and stiffness degradation characteristics of the soil indicating brittle behavior of soil at lower dry density and lower saturation. The unsaturated cohesive soil specimens with higher matric suction were found to be capable of higher load enduring capacity but underwent higher energy dissipation owing to meta-stable soil structure.

References

1. Fredlund DG, Rahardjo H (1993) Soil mechanics for unsaturated soils. Wiley
2. Fredlund DG, Morgenstern NR, Widger RA (1978) The shear strength of unsaturated soils. Can Geotech J 15(3):313–321
3. Fredlund DG, Vanapalli SK (2002) Shear strength of unsaturated soils. Methods Soil Anal Part 4:329–361

4. Rahardjo H, Lim TT, Chang MF, Fredlund DG (1995) Shear-strength characteristics of a residual soil. Can Geotech J 32(1):60–77
5. Vanapalli SK, Pufahl DE, Fredlund DG (1999) Interpretation of the shear strength of unsaturated soils in undrained loading conditions. In: Proceedings of 52nd Canadian geotechnical conference, Regina, Sask, pp 25–27
6. Pandya S, Sachan A (2017) Effect of matric suction and initial static loading on dynamic behaviour of unsaturated cohesive soil. Int J Geotech Eng Taylor & Francis 12(5):438–448
7. Pandya S, Sachan A (2017) Variation of collapse potential and stiffness degradation with matric suction of compacted unsaturated cohesive soil. Int J Geotech Eng Taylor & Francis, online available, 07 Nov 2017
8. Boulanger RW, Arulnathan R, Jr LF H, Torres RA, Driller, MW (1998) Dynamic properties of Sherman Island peat. J Geotech Geoenviron Eng 124(1):12–20
9. Cavallaro A, Presti DCL, Maugeri M (2001) The degradation behaviour of Fabriano soil during cyclic loading. Italian Geotech J 35(2):108–117
10. Delfosse-Ribay E, Djeran-Maigre I, Cabrillac R, Gouvenot D (2004) Shear modulus and damping ratio of grouted sand. Soil Dynam Earthquake Eng 24(6):461–471
11. Jiang, M, Cai Z, Cao P, Liu D (2010) Effect of cyclic loading frequency on dynamic properties of marine clay. In: Soil dynamics and earthquake engineering, pp 240–245
12. Khan Z, El Naggar MH, Cascante G (2011) Frequency dependent dynamic properties from resonant column and cyclic triaxial tests. J Franklin Inst 348(7):1363–1376
13. Moses GG, Rao SN (2003) Degradation in cemented marine clay subjected to cyclic compressive loading. Mar Georesour Geotechnol 21(1):37–62
14. Sitharam TG, Govindaraju L, Sridharan A (2004) Dynamic properties and liquefaction potential of soils. Curr Sci 87(10):1370–1387
15. Soralump S, Prasomsri J (2015) Cyclic pore water pressure generation and stiffness degradation in compacted clays. J Geotech Geoenviron Eng 142(1): 04015060-1-.04015060-13
16. Vucetic M, Dobry R (1988) Degradation of marine clays under cyclic loading. J Geotech Eng 114(2):133–149
17. Zhou J, Gong X (2001) Strain degradation of saturated clay under cyclic loading. Can Geotech J 38(1):208–212
18. ASTM D5298-10 (2013). Standard test method for measurement of soil potential (suction) using filter paper. D5298-10, West Conshohocken, Pennsylvania, USA
19. Voznesensky EA, Nordal S (1999) Dynamic instability of clays: an energy approach. Soil Dynam Earthquake Eng 18(2):125–133
20. Okur V, Ansal A (2011) Evaluation of cyclic behavior of fine-grained soils using the energy method. J Earthquake Eng 15(4):601–619

Bearing Capacity of Shallow Circular and Strip Foundation Resting on Two Layered Clays

Prateek Kumar and Manash Chakraborty

Abstract By using the lower and upper bound limit analysis in conjunction with finite elements and nonlinear optimization undrained bearing capacity of rough circular and strip foundation resting on two layered clayey soil is computed. The circular and the strip foundation are analyzed by assuming the axisymmetric and the plane strain condition, respectively. The clay is assumed to follow Mohr–Coulomb yield criteria and an associated flow rule. Results are provided for different (i) *t/b* ratio and (ii) c_{u1}/c_{u2} ratio; where, t = top layer thickness, b = diameter/width of the foundation, and c_{u1} and c_{u2} refers to the undrained cohesion of the top and bottom layers, respectively. The results indicate that there is an optimum *t/b* ratio beyond which the bearing capacity remains the same. The magnitude of the optimum *t/b* ratio depends on c_{u1}/c_{u2} ratio and the type of the foundation. For the same c_{u1}/c_{u2} ratio, the optimum *t/b* ratio for the circular foundation is less in comparison to the strip foundation. The obtained numerical solutions are in good agreement with the previously available literatures. Failure patterns and nodal velocity contour are provided for a few cases.

Keywords Bearing capacity · Circular foundation · Limit analysis · Layered clay · Strip foundation

1 Introduction

The bearing capacity of shallow foundation is generally estimated by considering soil as a homogeneous medium. However, the natural soil deposits are generally stratified. One of the earliest work to estimate the bearing capacity of two-layered clay deposit was carried out by Reddy and Srinivasan [1] by using limit equilibrium method and assuming circular failure mechanism. Based on the experimental results, Brown and Meyerhof [2] proposed empirical equations to calculate the bearing capacity of two layered clay for circular and strip foundation. Chen [3] addressed the layered problem by employing the upper bound limit analysis and adopting the

P. Kumar · M. Chakraborty (✉)
Indian Institute of Technology (Banaras Hindu University), Varanasi 221005, India
e-mail: manashchakra.civ@itbhu.ac.in

A. Prashant et al. (eds.), *Advances in Computer Methods and Geomechanics*, Lecture Notes in Civil Engineering 55,
https://doi.org/10.1007/978-981-15-0886-8_47

circular failure mechanism. Meyerhof and Hanna [4] proposed the semi-empirical formulae for estimating the bearing capacity of strip and circular foundation resting over strong layer overlaying weak deposit and weak layer over strong deposits. A punching shear failure mechanism was suggested for the case of strong layer overlying weak deposits. For the case of weak layer overlaying strong deposits, the failure was assumed by squeezing of the top weak layer. By using slip surface method, Georgiadis and Michalopoulos [5] presented bearing capacity of strip foundation for any combination of cohesive and cohesionless soil. Merifield et al. [6] bracketed the bearing capacity of strip foundation resting on two layered clayey soil by using linear approximation of Tresca yield criterion. Michalowski [7] presented the upper bound solution for strip foundation placed on two-layered clay subjected to both horizontal and vertical loads. Kuo et al. [8] predicted the bearing capacity of strip foundation on multilayer clayey soil by adopting ANN-based model. Benmebarek et al. [9] and later. Ahmadi et al. [10] used explicit finite difference code FLAC estimate the bearing capacity of strip foundation placed on two-layered clay soil.

From the available literature, it is evident that most of the studies on layered clays have been carried out for strip foundations and the available rigorous solutions for the strip foundations are based on linearization of the yield criterion. However, there are very few literatures available for determining the bearing capacity of circular foundations. In the present study, an attempt is made to estimate the rigorous bearing capacity of strip and circular foundation resting on two-layered clays by using the lower and upper bound limit analysis in conjunction with finite elements and nonlinear optimization. The advantage of finite-element limit analysis is that it does not require any assumption regarding the size and shape of the failure surface and the failure mechanism. The bearing capacity for strip and circular foundation are presented for different ratios of t/b and c_{u1}/c_{u2}. The obtained solutions are further compared with the available data from the literature.

2 Problem Domain, Boundary Conditions, and Statement of the Problem

A rough circular footing of diameter b (for strip footing, b equals to width of the footing) is rested over two layered clays; where, the undrained cohesive strength of the top (of thickness t) and the bottom layers are c_{u1} and c_{u2} respectively. The bearing capacity of strip and circular foundation are calculated by assuming the problem to be of plane strain case and axisymmetric case, respectively. In the present analysis, full domain is being adopted for the plane strain case. However, due to its symmetricity and two-dimensional nature of the axisymmetric problem, only half of the domain is considered in the analysis. The boundary conditions of the plane strain and the axisymmetric case are depicted in Fig. 1.

The length and the depth of the domain are chosen to be sufficiently large so that the failure zone is confined well within the domain; the magnitude of L and D for strip

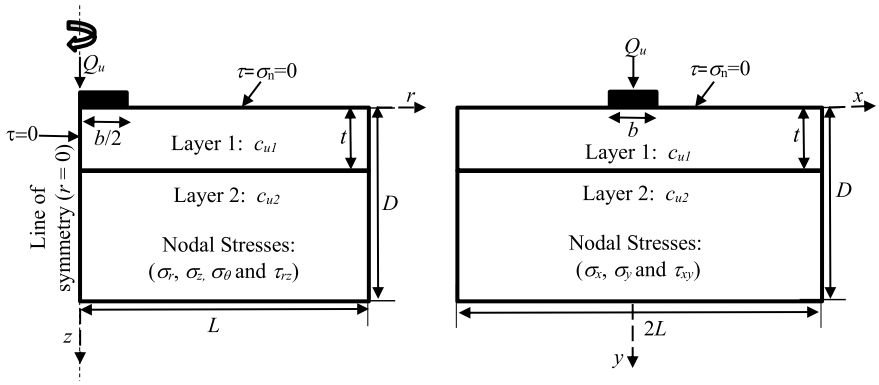

Fig. 1 Problem Domain and boundary conditions for **a** circular foundation, and **b** strip foundation

and circular footing are considered to be 7.5 b. Both the clay layers are assumed to be perfectly plastic and governed by the Mohr–Coulomb yield criterion and associated flow rule. It is intended to calculate the bearing capacity of the foundation for different ratios of t/b and c_{u1}/c_{u2}.

3 Methodology

The numerical limit theorems are applied here for obtaining the limiting solutions. In order to obtain the lower bound solution a statically admissible stress field is required to construct in the domain. On the contrary, a kinematically admissible velocity field is required to perform the upper bound analysis. The detailed methodology of obtaining the limiting solutions for plane strain problems using linear/nonlinear optimization can be referred in the work of Sloan [11], Sloan and Kleeman [12], Makrodimopoulos and Martin [13, 14], Chakraborty and Kumar [15]. The basis of obtaining both the extremities for axisymmetric problems can be viewed in the article of Kumar and Khatri [16], Kumar and Chakraborty [17].

In the present article, the lower and upper bound limit analysis has been performed using Optum G2 [18] along with adaptive mesh refinement based on plastic shear dissipation. Mesh refinement based on shear dissipation is considered most efficient and reliable for limit analysis. The clay in both the layer is assumed to isotropic, undrained and completely saturated. It can be noted that for undrained and completely saturated case (i.e., $\phi = 0°$) Mohr–Coulomb yield criterion eventually becomes the Tresca criterion.

4 Results

4.1 Numerical Solutions

The bearing capacity (q_u) for strip and circular footing is obtained by lower (LB) and upper bound (UB) limit analysis. The difference between the LB and UB solutions remains negligible in most of the cases. The actual collapse load is supposed to be within these two extreme values. The solutions are presented as the non-dimensional form of the bearing capacity, namely, q_u/c_{u2}. Figures 2 and 3 depict the variation of q_u/c_{u2} with t/b corresponding to different values of c_{u1}/c_{u2} ratio. The bearing capacities are presented as the average of the LB and UB solutions.

Figure 2 represents the bearing capacity for the case where the footings are placed over stiff clay overlying soft clay (Case A) and Fig. 3 represents the bearing capacity for the footings placed over soft clay overlying stiff clay (Case B). It is observed that the bearing capacity depends upon (i) t/b ratio, (ii) c_{u1}/c_{u2} ratio and (iii) the type of foundation. In this analysis, the ratio of c_{u1}/c_{u2} was varied between 0.1 and 10. This range is sufficient to cover almost all practical cases. From the results of Meyerhof and Hanna [4] and Merifield et al. [6] it can be inferred that when (i) $t/b < 0.125$, the top layer does not have appreciable influence on q_u and (ii) $t/b > 2$, the bearing capacity of circular/strip footing depends only on the top layer. Hence, the range of t/b, correspond to a certain c_{u1}/c_{u2} ratio, is kept between 0.125 and 3.

For Case A, the magnitude of the bearing capacity increases with increase in t/b and c_{u1}/c_{u2} ratio. Figure 2 shows that for a specific c_{u1}/c_{u2} ratio, the increment of the bearing capacity takes place up to a certain value of t/b; beyond this particular value of t/b there is no further improvement in strength prediction. For Case B, the graph shows completely opposite trend. The value of q_u/c_{u2} decreases with increase in t/b.

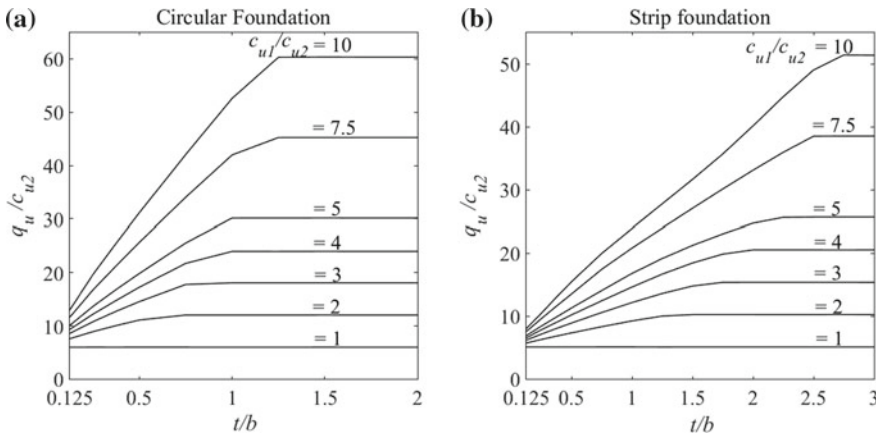

Fig. 2 Variation of non-dimensional bearing capacity (q_u/c_{u2}) for stiff layer overlaying soft layer ($c_{u1}/c_{u2} > 1$) for **a** circular foundation, and **b** strip foundation

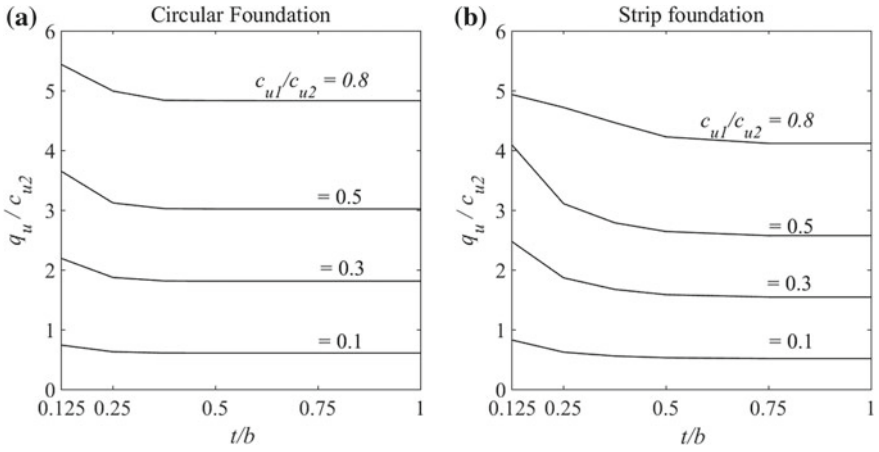

Fig. 3 Variation of non-dimensional bearing capacity (q_u/c_{u2}) for soft layer overlaying stiff layer ($c_{u1}/c_{u2} < 1$) for **a** circular foundation, and **b** strip foundation

The rate of decrement is significantly higher for smaller *t/b*. After a certain value of *t/b*, the graph attains a constant value. In this text, the particular value of *t/b* beyond which there is no appreciable change of bearing capacity is denoted as t_{opt}/b (i.e., optimum *t/b*). This can be interpreted as that the bearing capacity is solely governed by the strength characteristics of the top layer (c_{u1}) when *t/b* is greater than t_{opt}/b. The magnitude of t_{opt}/b depends on c_{u1}/c_{u2} ratio and the type of the foundation.

Figure 4 presents the variation of t_{opt}/b with different values of c_{u1}/c_{u2} ratio. It is observed that as long as c_{u1}/c_{u2} is smaller than 1, the magnitude of t_{opt}/b remains to be constant. On the contrary, for Case A, t_{opt}/b increases continuously with increase in c_{u1}/c_{u2}; however, the rate of increment reduces with higher c_{u1}/c_{u2} value.

Figure 2 also suggests that for a specific *t/b* and c_{u1}/c_{u2} ratio, the bearing capacity of circular foundation is greater than that of its strip counterpart. The difference between the bearing capacity increases with increase in c_{u1}/c_{u2}. It is quite evident

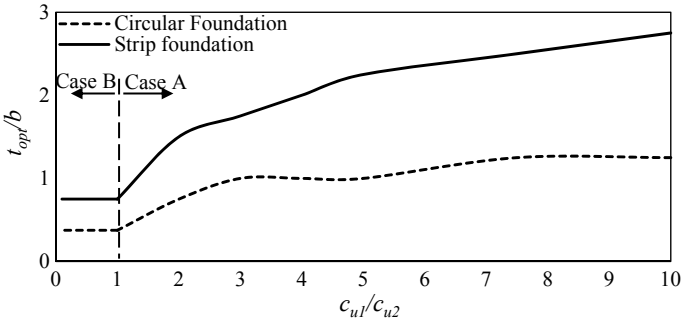

Fig. 4 Variation of t_{opt}/b with c_{u1}/c_{u2} for the circular and strip foundation

from Fig. 4 that for the same c_{u1}/c_{u2}, the t_{opt}/b value for circular foundation is quite smaller as compared to that of strip foundation.

4.2 Failure Patterns

Lower bound solutions are used to obtain the failure patterns for several cases. For the strip footing, the state of stress at any point is being specified by (i) σ_x, σ_y and τ_{xy} for the strip footing, and, (ii) σ_r, σ_z, τ_{rz} and σ_θ for the circular footing. After obtaining the stresses at each node, the ratio of *a/d* is calculated; where, *a* represent the radius of Mohr circle defining the state of stress at the node and *d* represents the radius of Mohr circle touching the failure envelope. On the basis of *a/d* ratio the failure patterns are drawn. As *a/d* approaches 1, plastic shear failure of the soil will take place and if $a/d < 1$ the state of soil will be in a non-plastic state. The detailed procedure of calculating *a* and *d* for circular footing can be seen in the work of Kumar and Chakraborty [19].

Figures 5 and 6 depict the failure pattern for strip and circular foundation corresponding to Case A and Case B, respectively. The figures were drawn for different *t/b* ratio corresponding to a specific c_{u1}/c_{u2} ratio. The dark patch in the figures indicates the failure zone. For the sake of clarity half of the failure domain beneath the strip foundation is shown in the present article. From Fig. 5, it is observed that the horizontal and the vertical extent of the failure zone gets further extended with the increase of *t/b* value. The extension of the plastic zone continues up to t_{opt}/b; beyond that the failure zone decreases and remains confined only to the top layer. The failure pattern also suggests that for the same type of strata, strip footing yields larger failure zone than the circular footing. Comparing Figs. 5 and 6, it can be concluded that the expansion of the failure zone for Case A is far higher than that of Case B. This is observed for both the strip as well as circular footing. From the failure pattern a non-plastic triangular wedge is observed below the foundation. The size of the wedge reduces with the increase of *t/b* ratio. A second non-plastic wedge is also observed adjacent to the strip footing, as mentioned by Merifield et al. [6]. This adjacent wedge increases in size with the increase in *t/b* ratio.

4.3 Nodal Velocities

Velocity contours are plotted from the results of upper bound analysis. The nodal velocity diagrams illustrate the magnitudes and the directions of the soil movement at various points within the considered domain. Figures 7 and 8 present nodal velocity pattern for strip and circular foundation corresponding to two different c_{u1}/c_{u2} ratios, namely, 3 and 0.5. It can be clearly observed that the velocities of the soil particles along the ground surface and adjacent to the footing edge are significantly higher as compared to the velocities of the soil particles just beneath the footing edge. The

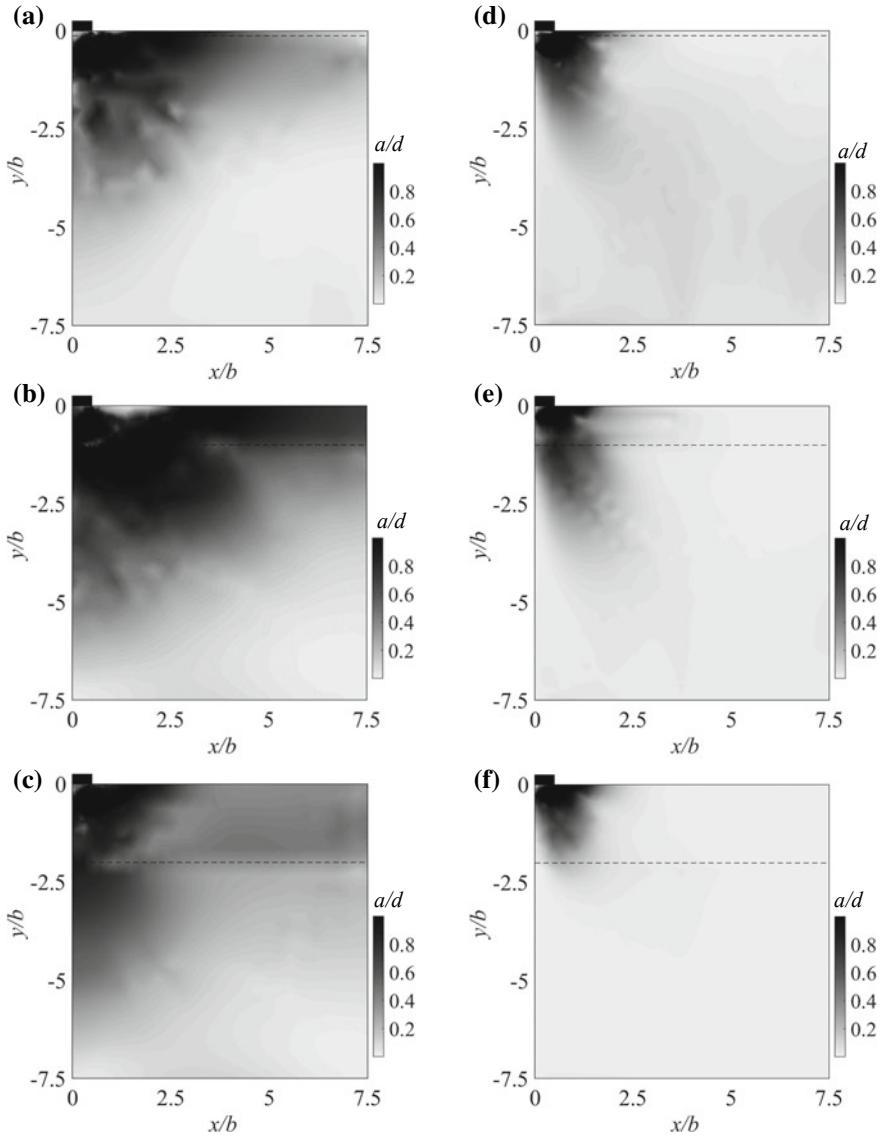

Fig. 5 For $c_{u1}/c_{u2}= 2$, the failure patterns for a strip foundation with *t/b* equals to **a** 0.125, **b** 1, and **c** 2 and for a circular foundation with *t/b* equals to **d** 0.125, **e** 1, and **f** 2

formation of the triangular rigid wedge beneath the footing replicates the similar outcome as observed in the failure contour drawn by using the lower bound stress field solution. The velocity discontinuities are found to be prominent near the footing edge. The zone of influence which indicates the soil portion where the velocities are significantly higher than the rest of the domain depends highly on c_{u1}/c_{u2}, *t/b*, and,

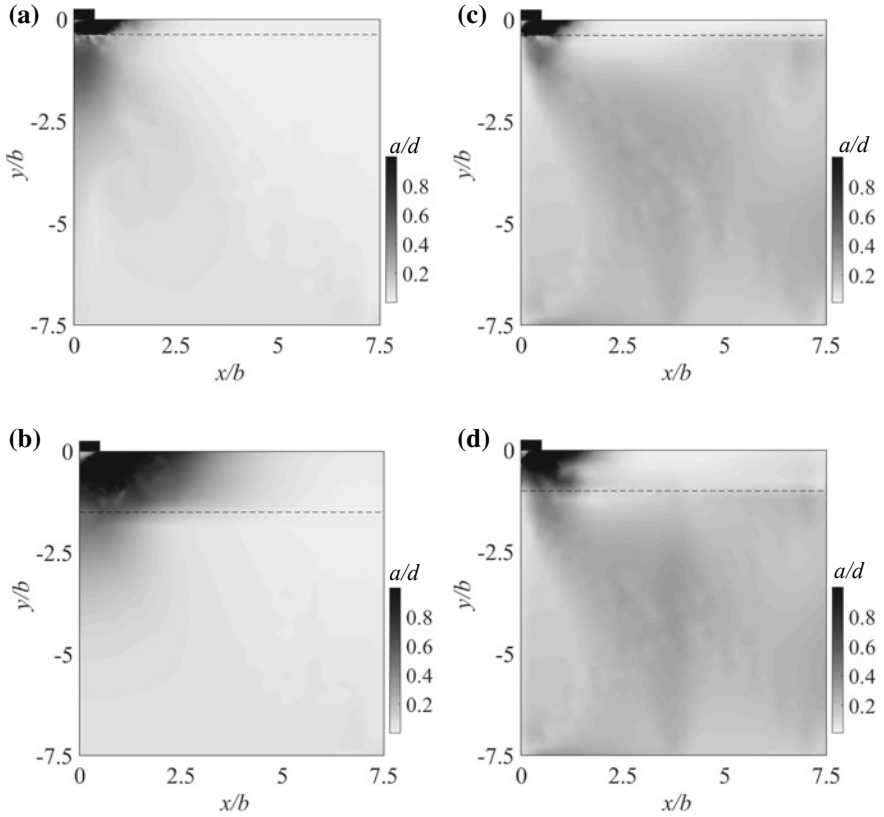

Fig. 6 For c_{u1}/c_{u2}= 0.5, the failure patterns for a strip foundation with *t/b* equals to **a** 0.375, and **b** 1.5, and for a circular foundation with *t/b* equals to **c** 0.375, and **d** 1

the type of foundation. It is clearly observed that compare to the strip foundation the extent of the zone of influence is lesser for the case of circular foundation.

5 Comparison of Results

Table 1 presents the comparison of the obtained limiting solutions for the strip footings with the available solutions in the literature. The present solutions are validated on the basis of bearing capacity factor, N_c^*, where $N_c^* = q_u/c_{u1}$. The comparisons are provided for Case A as well as Case B. The LB and the UB solutions remain closer to each other. The comparisons show that the UB and LB solutions obtained from the present analysis lie between the limiting values presented by Merifield et al. [6]. The LB and UB solutions obtained by Merifield et al. [6] were within a 12% bracket of the average collapse load whereas the current solutions lie within a 2% bracket

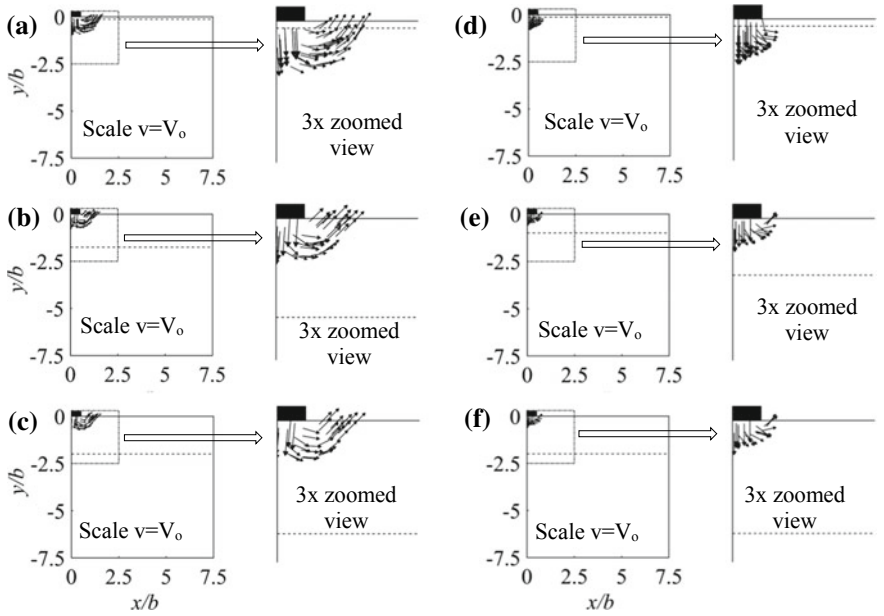

Fig. 7 For $c_{u1}/c_{u2} = 3$, the nodal velocity contours for a strip foundation with *t/b* equals to **a** 0.125, **b** 1.75, and **c** 2 and for a circular foundation with *t/b* equals to **d** 0.125, **e** 1, and **f** 2

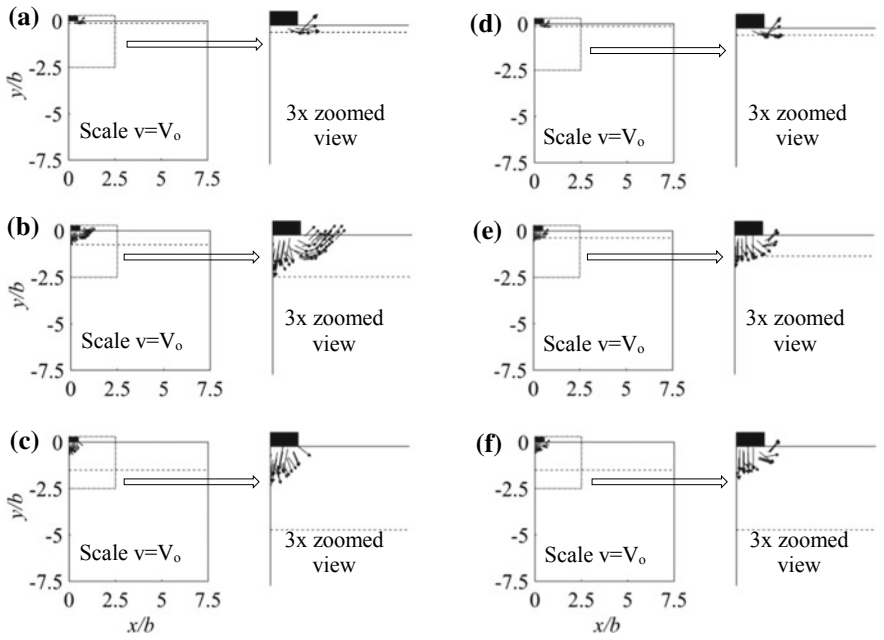

Fig. 8 For $c_{u1}/c_{u2} = 0.5$, the nodal velocity contours for a strip foundation with *t/b* equals to **a** 0.125, **b** 0.75, and **c** 1.5 and for a circular foundation with *t/b* equals to **d** 0.125, **e** 0.375, and **f** 1.5

Table 1 Value of bearing capacity factor ($N_c^{*)}$ for strip foundation

	t/b	c_{u1}/c_{u2}	Present solution		Merifield et al. [6]		Michalowski [7]	Ahmadi et al. [10]	Meyerhof and Hanna [4]
			LB[a]	UB[a]	LB[a]	UB[a]	UB[a]		
Stiff clay layer overlaying clay soft layer (Case A)	0.125	5	1.37	1.41	1.3	1.55	1.52	–	1.23
		4	1.62	1.68	1.56	1.82	1.77	–	1.49
		3	2.06	2.10	1.97	2.27	2.17	–	1.93
		2	2.86	2.91	2.73	3.09	2.93	–	2.80
	1	5	3.34	3.39	3.10	3.54	3.77	3.28	2.61
		4	3.64	3.69	3.46	3.83	3.99	3.56	2.94
		3	4.04	4.10	3.89	4.24	4.30	3.91	3.46
		2	4.61	4.78	4.44	4.82	4.74	4.53	4.46
	2	5	4.91	4.98	4.61	5.32	–	5.00	4.20
		4	5.10	5.18	4.81	5.32	–	5.13	4.60
		3	5.10	5.18	4.61	5.27	–	5.09	5.14
		2	5.10	5.18	4.61	5.27	–	5.10	5.14
Soft clay layer overlaying stiff clay layer (Case B)	0.125	1[b]	5.09	5.18	4.94	5.32	5.14	–	5.14
		0.8	6.12	6.21	5.87	6.36	6.22	–	6.12
		0.5	8.02	8.31	7.78	8.55	9.39	–	9.08
	0.5	1[b]	5.09	5.18	4.94	5.32	5.14	5.15	5.14
		0.8	5.23	5.33	4.98	5.49	5.31	5.29	5.46
		0.5	5.23	5.33	4.98	5.49	5.31	5.31	6.43
	1	1[b]	5.10	5.18	4.94	5.32	5.14	–	5.14
		0.8	5.11	5.18	4.94	5.30	5.14	–	5.14
		0.5	5.11	5.18	4.94	5.30	–	–	5.14

Note (a) LB and UB indicates lower bound and upper bound, respectively
(b) $c_{u1}/c_{u2} = 1$ refers to the homogenous soil

of the average solution. The reason of this improvement can be attributed to the fact that unlike the liner optimization employed by Merifield et al. [6], the present analysis is performed by second order conic optimization. The present solutions are also compared with the semi-analytical solutions of Meyerhof and Hanna [4], numerical solutions of Michalowski [7] and Ahmadi et al. [10]. The present solutions compare quite well with the available solutions. Table 2 shows the comparison for the circular footings with the available semi-analytical solutions of Meyerhof and Hanna [4]. The obtained limiting solutions are higher than the values provided by Meyerhof and Hanna [4] for Case A. However, for Case B, the bearing capacity factor presented by Meyerhof and Hanna [4] are on the higher side. This trend is being observed for both the strip and circular footing. The difference between the present and the semi-analytical solutions are noticeable as long as $t/b < t_{opt}/b$. The present solutions are also verified with the results of experimental model test performed by Meyerhof and Hanna [4] and are displayed in Table 3. The average value of LB and UB solution agrees quite well with the experimental observations.

The optimum *t/b* ratio for both circular and strip foundation obtained from the solution of Meyerhof and Hanna [4] are higher as compared to the optimum *t/b* ratio of the present solution.

6 Conclusion

In this article, the bearing capacity for strip and circular footing resting on two layered clay medium has been estimated by using numerical limit theorems in conjunction with finite elements and second order cone optimization. The strength predictions were carried out by varying the (i) undrained shear strength of the two layers (represented as non-dimensional form, namely, c_{u1}/c_{u2}) and (ii) top layer thickness (represented as *t/b* ratio). The design charts are provided by averaging out the lower and upper bound solutions. There always remains a certain top layer thickness (t_{opt}) beyond which there is no impact of the bottom layer strength value. The value of t_{opt}/b varies with the type of foundation and c_{u1}/c_{u2} ratio. The failure contours and the nodal velocity patterns further present clearly the extent of the failure zone and the magnitude and the direction of the movement of the soil particles in the zone of influence. The results from the analysis were found to match reasonably well with the available analytical, numerical, and experimental solutions from the literature.

Acknowledgements The corresponding author acknowledges the support of "Department of Science and Technology (DST), Government of India" under grant number DST/INSPIRE/04/2016/001692.

Table 2 Value of bearing capacity factor (N_c^*) for circular foundation

Stiff clay overlaying clay soft (Case A)					Soft clay overlaying stiff clay (Case B)				
t/b	c_{u1}/c_{u2}	Present solution		Meyerhof and Hanna [4]	*t/b*	c_{u1}/c_{u2}	Present solution		Meyerhof and Hanna [4]
		LB[a]	UB[a]				LB[a]	UB[a]	
0.125	5	2.01	2.05	1.63	0.125	1[b]	5.99	6.07	6.17
	4	2.35	2.41	1.96		0.8	6.74	6.84	7.35
	3	2.86	2.91	2.49		0.5	7.20	7.37	10.89
	2	3.80	3.84	3.56		0.3	7.20	7.37	–
0.5	5	3.95	4.00	2.82	0.25	1[b]	6.00	6.07	6.17
	4	4.33	4.39	3.20		0.8	6.19	6.28	7.04
	3	4.83	4.90	3.80		0.5	6.19	6.28	9.64
	2	5.54	5.60	4.98		0.3	6.19	6.28	–
1	5	6.00	6.07	4.40	0.5	1[b]	6.00	6.07	6.17
	4	6.00	6.07	4.85		0.8	6.01	6.07	6.55
	3	6.00	6.07	5.55		0.5	6.00	6.07	7.71
	2	6.00	6.07	6.17		0.3	6.00	6.07	–

Note (a) LB and UB indicates lower bound and upper bound respectively
(b) $c_{u1}/c_{u2} = 1$ refers to the homogenous soil

Table 3 Comparison with experimental result for $c_{u1}/c_{u2}= 3.5$

Strip foundation			Circular foundation		
t/b	q_u/c_{u1}		*t/b*	q_u/c_{u1}	
	Model test*	Present solution		Model test*	Present solution
0.50	2.47	2.70	0.50	3.55	4.57
1.00	3.41	3.87	0.69	3.80	5.43
1.50	4.04	4.83	1.00	4.91	6.00
2.00	4.74	5.18	1.40	6.06	6.00

Note (a) The present solutions are obtained by averaging the lower bound and upper bound solution (b) Model test results of Meyerhof and Hanna [4]

References

1. Reddy AS, Srinivasan RJ (1967) Bearing capacity of footings on layered clays. J. Soil Mech. Found. Div., ASCE 93, SM2, 83-99
2. Brown JD, Meyerhof GG (1969) An experimental study of ultimate bearing capacity of layered clay foundations. In: Proceedings of 7th international conference on soil mechanics and foundation engineering, Sociedad Mexicana de Mecanica de Suelos, Mexico City, 45–51
3. Chen WF (1975) Limit analysis and soil plasticity. Elsevier, Amsterdam
4. Meyerhof GG, Hanna AM (1978) Ultimate bearing capacity of foundations on layered soils under inclined load. Can Geotech J 15:565–572
5. Georgiadis M, Michalopoulos AP (1985) Bearing capacity of gravity bases on layered soil. J. Geotech. Eng. 111:712–729
6. Merifield R, Sloan SW, Yu HS (1999) Rigorous solutions for the bearing capacity of two-layered clay soils. Geotechnique 49:471–490
7. Michalowski R (2002) Collapse loads over two-layer clay foundation soils. Soils Found 42:1–7
8. Kuo YL, Jaksa M, Lyamin A, Kaggwa WS (2008) ANN-based model for predicting the bearing capacity of strip footing on multi-layered cohesive soil. Computers and Geotechnics. 36. https://doi.org/10.1016/j.compgeo.2008.07.002
9. Benmebarek S, Benmoussa S, Belounar L, Benmebarek N (2012) Bearing capacity of shallow foundation on two clay layers by numerical approach. Geotech Geol Eng 30. https://doi.org/10.1007/s10706-012-9513-6
10. Ahmadi MM, Kouchaki BM (2016) New and simple equations for ultimate bearing capacity of strip footings on two-layered clays: numerical study. Int J Geomech 16(4):06015014
11. Sloan SW (1988) Lower bound limit analysis using finite elements and linear programming. Int. J. Numer. Anal. Methods Geomech. 12:61–77
12. Sloan SW, Kleeman PW (1995) Upper bound limit analysis using discontinuous velocity fields. Comp. Methods Applied Mech. Eng. 127(1):293–314
13. Makrodimopoulos A, Martin CM (2006) Lower bound limit analysis of cohesive frictional materials using second-order cone programming. Int J Numer Meth Eng 66:604–634
14. Makrodimopoulos A, Martin CM (2007) Upper bound limit analysis using simplex strain elements and second-order cone programming. Int J Numer Anal Meth Geomech 31:835–865
15. Chakraborty M, Kumar J (2014) Lower bound axisymmetric formulation for geomechanics problems using nonlinear optimization. Int J Geomech 15:06014024
16. Kumar J, Khatri VN (2011) Bearing capacity factors of circular foundations for a general c-φ soil using lower bound finite elements limit analysis. Int J Numer Anal Methods Geomech 35(3):393–405
17. Kumar J, Chakraborty M (2014) Upper-bound axisymmetric limit analysis using the Mohr-Coulomb yield criterion, finite elements, and linear optimization. J Eng Mech 140(12):06014012

18. Optum G2, Version: 2018.06.08 (academic license) Optum Computational Engineering, Copenhagen, Denmark
19. Kumar J, Chakraborty M (2015) Bearing capacity of a circular foundation on layered sand–clay media. Soils and Found. 55(5):1058–1068

Condition Assessment and Failure Probability of Existing Bridges in the Cachar District, Assam

Joydeep Das and Arjun Sil

Abstract This paper deals with the description of the probabilistic methodology to evaluate the failure probability of the bridges in the Cachar district (Assam, India) based on the present condition data. Condition assessment of the bridge decks is done by the help of visual inspection following as per National Bridge Inventory (NBI) Survey procedure adopting the condition rating of bridges is evaluated and categorized. The aging and maturity of the bridge are the important factor, the work thinking adopted is from initial age of construction to till date and estimation of the adequate probabilistic distribution with respect to the data available of the study area selected, and then the parameters of probability distribution and its contents come to act in finding of the probability failure percentage. The paper also establishes the facts about the bridge deck failure percentage in 20 years (in time) and the condition of the bridge deck in 10% probability failure state; with respect to years and the outcome it shows that the condition of the rural bridges (being in higher condition rating) are in unsatisfactory state than the highway bridges and also shows the difference in condition of the concrete and pre-stressed bridges in the district. The concept of the study would provide a rational decision-making idea about the condition of the in-service bridges and probability of failure of the deck component available, which however will ensure the maintenance service and its proper cost utilization.

Keywords Condition assessment method · Condition rating · Weibull distribution · Probability of failure

J. Das (✉) · A. Sil
Department of Civil Engineering, National Institute of Technology Silchar, Silchar, Assam, India
e-mail: jdas7248@gmail.com

A. Sil
e-mail: silarjun@gmail.com

A. Prashant et al. (eds.), *Advances in Computer Methods and Geomechanics*, Lecture Notes in Civil Engineering 55,
https://doi.org/10.1007/978-981-15-0886-8_48

1 Introduction

Bridges are vital infrastructure for the continuous development of nations. Generally, bridge failures are somewhat rare, it happens only when some unexpected circumstances like natural and man-made hazards such as earthquake, flood and fire occur. However, it is the aging of in-service bridges which make the bridge weaker and there are also other reasons such as increase traffic, materials used during construction, loading pattern, increase in population vehicles, etc. The bridges present in the location are mostly short span, but of different types. By using probabilistic analysis and condition assessment of the bridge (deck), the quality of the bridge condition can be found and are listed in the condition-rating table. In recent years, lot of studies are done in this domain and concentrated basically on the condition states or condition rating of the bridges span-wise rather than NBI condition rating. The approach based on Weibull distribution (WD) was used to find condition states of bridges and damage outlines in numerous studies [1–3]. Numerous studies took the Markovian approach to find conversions of probabilities from the data (which has condition states and parameters) [4, 5] work was accompanied to forecast damage in deck using condition states [6, 7]. Sobjano et al. (2010) in their work they have used Weibull distribution to find condition rating of bridges in decent condition over a restricted period of time and finding the damage pattern in the highway (interstates and non-interstates) bridges of the state of Florida. The bridge safety models grounded on the aspects of probability and reliability are developed by several researchers completely and partially Hajializadeh et al. [8] implemented the safety assessment model on the railway bridges (short span) to find the analytic train speeds with respect to probability of failure. Suo and Stewart [9] worked on the spatial time-dependent reliability study which was amalgamated with visual inspection in order to forecast the likelihood of RC corrosion-instigating cracking. Nasrollahi and Washer [10] estimated inspection intervals for bridges of the Oregon (United States) by using 20 years' period of condition rating historical data and by the help of statistical analysis and WD approach predicted time-in-condition rating and probability of failure. Another influential technique to combine a probabilistic model with less volume of information data from quantity to improve the surviving model is Bayesian updating. This has been implemented by different structural researchers in the field of different domain such as finding the characteristics load effect of bridge [11]; finding the effects of corrosion in RC structure [12]; updating fatigue reliability of steel structures and degradation estimation of RC structures [13]; etc. Probabilistic analysis can deliver a useful calculation tool since it provides a balanced standard for the contrast of the efficiency of decisions taken under improbability. As seen in above studies, all the works are done in foreign countries (like Florida, Oregon, etc.). Such work practices are rarely done in Indian bridges and the bridges around the states, because of which the main obstacle came to be seen is the problem of data collection, that is, to find maximum bridges and where it is situated and visit each of the bridges for the purpose of condition assessment (visual inspection) process and then processing the found data. Therefore, the concept of the study in this paper will give a glance

details about the condition of the in-service bridges and failure probability of the deck component available in the district Cachar, state of Assam (India) which will ensure the maintenance service and its proper cost utilization.

2 Condition Assessment Method

The analysis of the condition of any structural members or structure with respect to age, construction techniques, materials used and design error of the structure examined/assessed after the structure is in service. This method is used in any qualitative analysis of structure to find its damage and reliability properties [10, 14] have used the method in their own research. The method concerns about corrosion or damage found when the inspection is done. So, in this paper the use of condition assessment method is valid and this method is applied to predict the damage level and categorizing the damage. As in this paper, visual inspection method is taken for the purpose of finding distress in bridge deck available in the bridges around the district. Under the visual inspection method, we find different distress such as Air pockets, Honeycombing, Polishing, Pop outs, Potholing, Scaling, Spalling and Cracking.

3 Condition Rating

The definition of Condition rating (CR) is the present or current status of in-service condition, established bridge as compared to the actual built condition (as per NBI coding guide), and meaning is that the difference between the bridge in the present condition to the condition when it was built (initial/starting). Table 1 show that the damage level of the bridge and its characteristics. It also states the condition in which it is now present, which helps to categorise the bridge as per rating. Table 2 describes the bridges available in the highway and rural sectors of the Cachar district and its location along with condition rating. [Note: RCC and PSC type of bridge (and its deck) is considered, Steel Bridge has been excluded because of limited data].

4 Methodology and Analysis

4.1 Stochastic Model

With the help of stochastic model estimation of probability distribution of possible outcomes can be found or evaluated. The model helps to find the best-suitable distribution which leads to a study of goodness-of-fit test. Quite a few goodness-of-fit

Table 1 NBIS guidelines for bridge deck condition rating (CR)

Code	Descriptions
N	**Not applicable**—No clear or significant deficiencies which upset the condition of the deck
9	**Excellent condition**—No clear or notable insufficiencies are present which would distress the deck condition state
8	**Very good condition**—No significant crushing, notable rotting or splitting
7	**Good condition**—Minor cracking or splitting with no loss of capacity. Considerable damage of curbs, sidewalks, parapets or railing (need repair). Non-structural hairline cracks with no breakdown. Unaffected load capacity of deck structure
6	**Satisfactory condition** – Some minor corrosion can be seen in structural components. Some cracking or splitting with no loss of capacity. Hairline structural cracks maybe there. Extensive deterioration of curbs, sidewalks, parapets or railing
5	**Fair condition**—All key structural elements are in sound condition; however, it may have some minor loss of section, cracking, spalling or scour. Numerous (30-40%) area of deck checked, split or crushed. Many planks are loose and reinforcing steel visible. Some deck (< 10%) are in need of additional repairment
4	**Poor condition**—Advanced segment loss, deterioration or corrosion, spalling or scour. Majority of deck area are crushed or damaged. Reckonable cracks in the structure or large spall areas are seen. Reinforcing steel visible with reckonable section loss. Effect on structural load capacities of deck. Over 10% of the deck areas are in need of replacement or repairment
3	**Serious condition**—This rating is applied if severe or serious symbols of distress in the structure are visible. Holes in the deck, loss of section, deterioration of segments, spalling or scour have extremely affected primary components of structure. Possibility of Local failures. Introduction of Cracks due to fatigue in steel or cracks due to shear in concrete may be visible
2	**Critical condition**—Advanced weakening of primary components of structure. Cracks due to fatigue in steel may be visible or cracks due to shear in concrete may be present or may substructure support may have been removed by scour. Unless closely observed it may be obligatory to close the bridge till useful action is taken
1	**"IMMINENT" failure condition**—Main deterioration or segment loss present in critical components of structure or apparent vertical or horizontal motion affecting stability of the structure. Bridge is closed to traffic but helpful action may put back in light service
0	**Failed condition**—Out of service—outside of remedial action

tests which can be approached, here in the present study, the Anderson-Darling test was found suitable for the determination of distribution for the available data.

4.2 Anderson Darling Statistics

The Anderson-Darling statistic [15]; (Stephen 1974) measures how good the data monitors a particular distribution. It is the modified version of Kolmogorov Smirnov

Table 2 Name and Condition Rating (CR) of the Bridge in National Highway Sector [NH-37 (BADARPUR- ZIRIBAM) and NH-54 (SILCHAR-LAILAPUR)] and also the rural bridges around the district

Name of the bridge in the national highway	Condition rating of the bridge deck	Name of the bridge in the rural areas	Condition rating of the bridge deck
BANSK AND I BRIDGE	6	NARAYANPUR BRIDGE	8
ZULUKI BRIDGE	6	BHAGA BAZAR BRIDGE	8
WALZUR BRIDGE	5	VEIROBI BRIDGE	8
ALIPUR BRIDGE 1	6	LAKHIPUR-SONAI RD BRIDGE	7
CHIRI BRIDGE	6	SILCHR MED RD.	8
DHOLAI 2 BRIDGE	5	POLOI GARDEN 1	7
ANURPUI BRIDGE	7	TILANAGAR BRIDGE	8
RANGAKHI 1 BRIDGE	6	BIDYARATANPUR BRIDGE	6
LAISPUII BRIDGE	5	HADMA BRIDGE	7
DHOLAI 1 BRIDGE	5	JAMIRKHAL BRIDGE	7
BADRI BRIDGE	7	KHULICHORA BRIDGE	5
SUSAGAR MUKAM BRIDGE	5	AMJURGHAT BRIDGE	8
HUNANKUR BRIDGE	6	HAWAITHANG BRIDGE	8
KALAKHAL BRIDGE	7	JHULANPUR BRIDGE	6
FULERTHAL BRIDGE	7	CHANNIGHAT BRIDGE	6
ALIPUR BRIDGE 2	8	POLOI GARDEN 2	8
JIRI BRIDGE	7	ARADHANPUR BRIDGE 1	8
KHULICHERRA BRIDGE	5	DHOLAI 3 BRIDGE	6
PANCHERRA BRIDGE	5	ARADHANPUR BRIDGE 2	7

test which does not deal with critical value of specific distribution. For a specific set of data and distribution, the smaller the statistic value, the better is the distribution fitting the data. AD statistics allows more sensitivity towards the test which is a merit quality but it also has demerit quality which is that it calculates each distribution critical values.

The Anderson-Darling test statistic is

$$AD^2 = -N - R \tag{1}$$

where

$$R = \sum i = 1N(2i - 1)N[lnF(Y_i) + ln(1 - F(Y_{N+1-i}))] \tag{2}$$

F is the cumulative distribution function of the specified distribution. Yi are the order data.

4.3 Weibull Distribution

In according to investigate failure probability time, the Weibull distribution gives the most springiness for the analysis (Table 3). As here in the research work, random variables are time in condition, and the failure as per a given condition rating (CR) is such that that the bridge deck components is not in that CR any longer. The formulation definition of the [16] Weibull probability-density function (PDF) is

$$f(t) = \frac{\beta(t-\delta)^{\beta-1}}{\theta^{\beta}} \exp -\left(\frac{(t-\delta)}{\theta}\right) \tag{3}$$

where, t = variable that demonstrates time during bridge deck has a particular CR; β = shape parameter; θ = scale parameter; δ = location parameter.

4.4 Explanation of the Parameters

The shape parameter β defines in what way the available data is distributed. When $0 < \beta < 1$, the Weibull distribution defines a deteriorating failure rate representing the failures at early-age that reduce with interval (time). When β equals to 1, this means the rate of failure is constant; i.e., failure does not dependent with time. When values β are greater than 1 defines a failure of wearing-out where the rate of failure rises with time. The ranges of the shape parameter β found in the Weibull distribution for all the condition rating are between 5 and 23, which are quite larger and rare (Table 4). The factor which makes the values larger is the number of samples which are very less and there is difference between the values; if the number sample is more and the difference between the samples are less than the shape factor values would be less (shown in Table 4). The parameter of location (δ), occasionally called the guarantee time which denotes a time period in which there is no occurrence of failures at the foundation of the service life of a deck component. But for bridges, when the service

Table 3 Anderson-Darling values for RCC and PSC bridges deck component

Condition Rating	Normal for (RCC) concrete	Normal for pre-stressed concrete	Exponential for (RCC) concrete	Exponential for pre-stressed concrete	Weibull for (RCC) concrete	Weibull for pre-stressed concrete	Lognormal for (RCC) concrete	Lognormal for pre-stressed concrete
5	2.51	2.93	3.66	3.77	2.50	2.91	2.52	2.93
6	3.76	3.68	4.03	4.18	3.71	3.65	3.73	3.69
7	3.07	2.69	3.84	3.64	3.07	2.65	3.06	2.68
8	2.45	4.86	3.76	4.86	2.43	4.85	2.44	4.86

Table 4 Characteristics of Weibull distribution for RCC and PSC bridges deck component in Cachar

Parameter	CR 5 for RCC	CR 5 for PSC	CR6 for RCC	CR 6 for PSC	CR 7 for RCC	CR 7 for PSC	CR 8 for RCC	CR8 for PSC
Shape Parameter β	10.56	10.74	5.90	23.14	12.90	9.32	15.20	3.87
Scale Parameter θ	28.58	22.01	25.87	23.24	23.10	18.96	19.66	11.12
Mean	27.2	21	24	22.67	22.25	18	19	10
Variance	12.6736	5.01	27.9841	1.53	4.2436	4.36	2.49	9
SD	3.56	2.24	5.29	1.24	2.06	2.09	1.58	3
P value	>0.250	>0.250	>0.250	>0.250	>0.250	>0.250	>0.250	>0.250
Number of samples	5	4	5	6	5	5	6	4

life starts, failures are possible, Weibull distribution is used in which it is assumed that δ equal to 0. The location parameter is taken as zero, because of no historical or past data found.

Table 4, shows the parameters considered for condition ratings of 5–8 for the concrete bridges and for pre-stressed concrete bridges. The table contain the confidence intervals value which is 95% for the β and θ parameters, and also for the P-values. The scale defines the position of the Weibull curve in relation to the threshold, which is analogous to the way the mean describes a normal curve position.

The analysis section is then led by the help of MINITAB'17 & MATLAB, where the data (maturity of bridge) is given as input for different condition rating for concrete bridges and pre-stressed concrete bridges. The maximum-likelihood method was used to compute the Weibull distribution parameters.

The input then results in the determination of the PDFs and CDFs of the bridges, which helps to calculate and analyse with the parameter found. The expected mean value is found for both the concrete bridge deck and pre-stressed concrete bridge deck in Table 4. The method is based on the format of reliability, and we know about the basic relation between the reliability andprobability of failure equation:

$$\text{Reliability} = 1-(\text{Probability of failure}) \tag{4}$$

This above Eq. 4 helps to find the probability of failure in time which will be seen later described below. Now the expected mean value of concrete is highest for condition rating 5 equal to 27.2 and lowest for condition rating 8 equal to 19, this means the average maturity of CR 5 is more than CR 8. Again, for pre-stressed concrete bridge deck, CR 6 has more than CR 5. The PDFs of condition ratings of

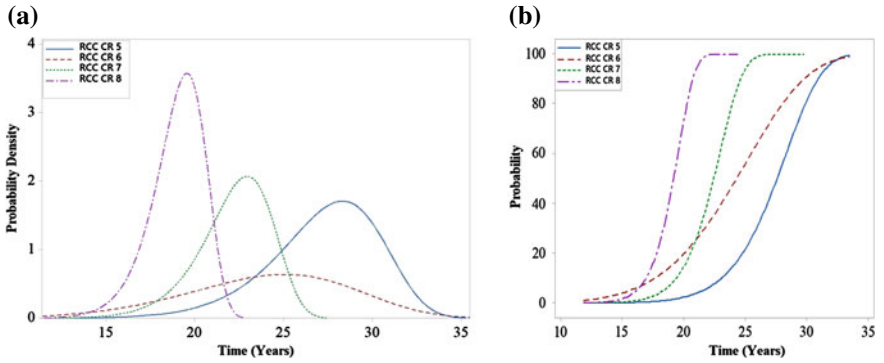

Fig. 1 **a** Probability density function (PDF) and 1**b** Cumulative density function (CDF) for concrete bridges in Cachar district

5–8 for concrete category is shown in Fig. 1a and the PDFs of pre-stressed concrete type of bridge deck component is shown in Fig. 2a. These figures show the graphical view of the data presented in Table 4, it explains the overall behaviour of each type of bridge studied. Figure 1a, b gives the PDF and CDF of the concrete bridge deck and Fig. 2a, b gives the PDF and CDF of the pre-stressed concrete bridge deck. Figures 3 and 4 gives the probability failure % for time interval of 20 years (20 years is taken just as an assumption of mean value as for all type of bridges the major failure starts after 15 years, so 20 is taken as standard value of maturity). Table 6 gives the important values of probability of failure (%) for threshold 10% for all the condition rating and for all type of bridge deck available. Figures 1b and 2b show the resulting failure probability earlier than a specific time for a particular CR (condition ratings) fluctuating from one condition rating to another (higher to lower). As the following section shows, these diagrams helps the management section of bridge inspection very strongly by predicting the probable condition rating of a bridge with respect

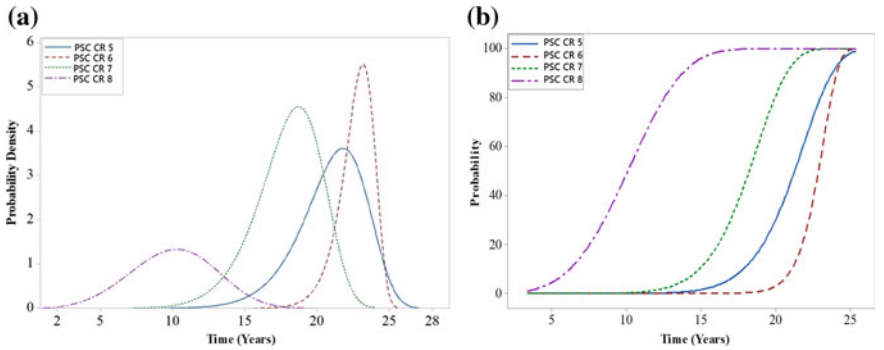

Fig. 2 **a** Probability density function (PDF) and 2**b** Cumulative density function (CDF) for pre-stressed concrete bridges in Cachar district

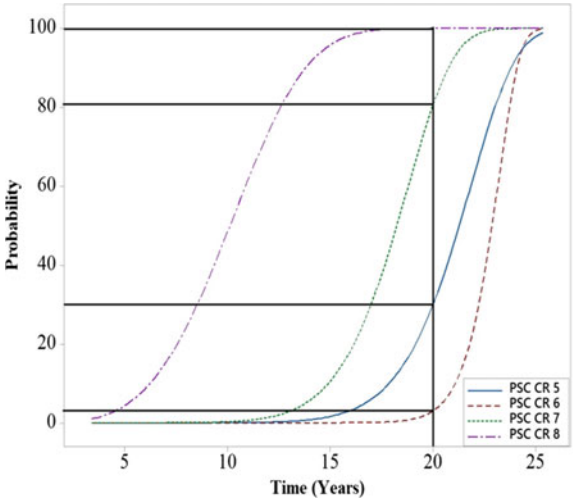

Fig. 3 Probability of failure in time (20 years) for concrete deck components

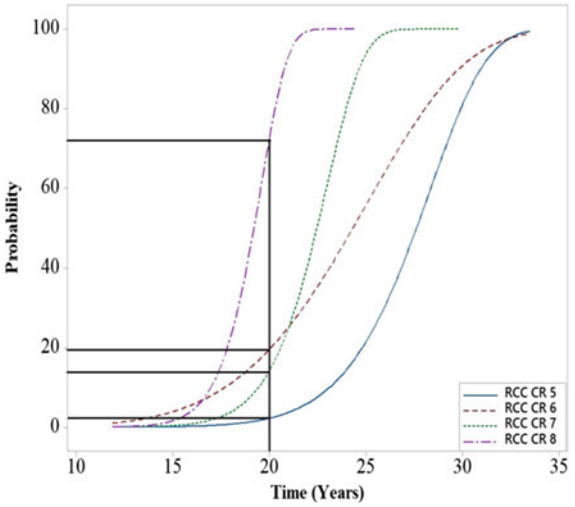

Fig. 4 Probability of failure in time (20 years) for pre-stressed concrete deck components

to time. This CDF graph also shows that it is very probable that the CR (condition rating) of bridge deck components present in the district changes before 35 years. As a matter of fact, if we see the substantial size of sample of bridges present and used in the present study shows the scale parameters in the table are significantly less than 35 years. Therefore, cumulatively the bridges of the locality have maturity of less than 35 years. The PDF and CDF provide the idea to know about the failure probability per cent of the different condition rating of the type of bridges available in the district.

Table 5 Probability of failure (%) in 20 years' time for RCC bridge deck and PSC bridge deck

Type of deck	Condition rating 5	Condition rating 6	Condition rating 7	Condition rating 8
RCC bridge deck	3% = (100 − 3) = 97%	20% = (100 − 20) = 80%	19% = (100 − 19) = 81%	76% = (100 − 76) = 24%
PSC bridge deck	30% = (100 − 30) = 70%	4% = (100 − 4) = 96%	82% = (100 − 82) = 18%	98% = (100 − 98) = 2%

4.5 Probability of Failure of Deck Components in the Cachar District

Figures 3 and 4 signify the concrete and pre-stressed bridge deck component, probability failure in 20 years' time interval. From Table 5, the condition rating 5 (concrete) has 97%, that is, in general if the bridge is not repaired it will change the condition to lower or failed condition, these bridges are in both the rural areas and also in highway zone still the repairing is less done. The condition rating 8 (concrete) has value 24% failure, that is, it has chances of failure if it is not maintained in proper manner, and showing the difference in probability of failure between higher and lower CR. Now, Table 5 also shows the percentage of probability of failure in pre-stressed concrete deck component of bridge. It shows that CR 5 has 70%, CR 6 has 96%, and CR 8 has 2%, it results that the maintenance of CR 6 bridges should be given more importance as because of probability of failure (to go in lower condition rating) is more as compared to CR 5 and CR 8.

Let us assume the threshold value for probability of failure 10% for the concrete and pre-stressed bridge deck component in the area as presented Table 6. The table indicates the different condition rating with its probability of failure (%), since we

Table 6 Probability of failure (threshold 10%) for deck components of different condition rating

Probability of failure (%)	Time in condition rating (years)							
	CR 5 for RCC	CR 5 for PSC	CR 6 for RCC	CR 6 for PSC	CR 7 for RCC	CR 7 for PSC	CR 8 for RCC	CR 8 for PSC
1	18.49	14.34	11.87	19.04	16.19	11.57	14.53	3.39
2	19.75	15.30	13.35	19.63	17.09	12.48	15.21	4.06
3	20.54	15.90	14.34	19.98	17.64	13.04	15.63	4.51
4	21.11	16.34	15.05	20.23	18.04	13.45	15.93	4.87
5	21.57	16.69	15.63	20.43	18.37	13.79	16.17	5.16
6	21.96	16.98	16.15	20.60	18.64	14.07	16.37	5.42
7	22.29	17.24	16.59	20.74	18.86	14.31	16.55	5.65
8	22.59	17.46	16.98	20.87	19.07	14.52	16.70	5.85
9	22.85	17.66	17.34	20.98	19.25	14.72	16.83	6.04
10	23.10	17.85	17.67	21.08	19.41	14.89	16.96	6.22

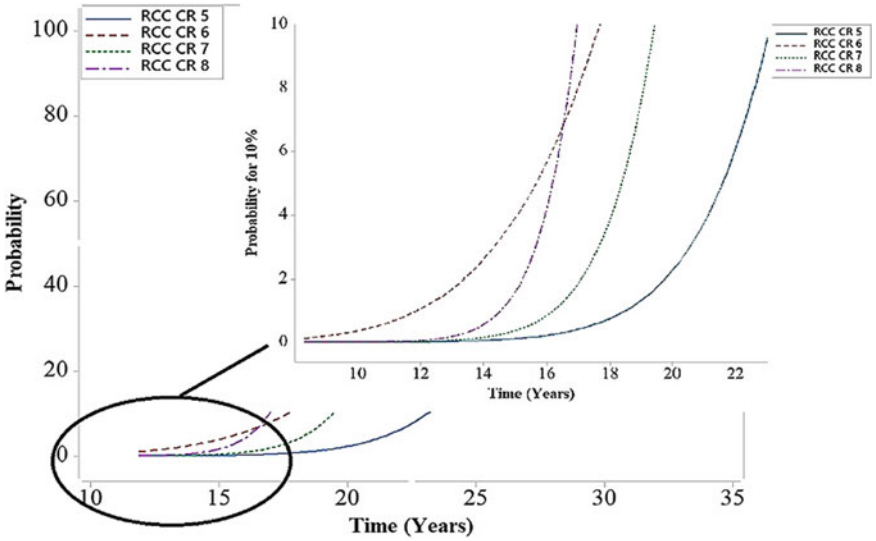

Fig. 5 Time in condition rating for 10% failure probability in concrete deck component

know the condition rating of the bridges and also by knowing their respective maturity and age, using the proposed model we can determine the failure probability of the bridge. Now, for example if we have a bridge with 20 years of maturity and it is in CR 5 it means that the bridge is in the verge of 3% probability of failure. Or if we have a bridge with CR 7 and age 22 years it has exceeded 10% probability threshold and it is in the failing condition and in need of immediate rehabilitation. Figure 5 and 6 which shows the photographic enlargement of the 10% probability of failure portion for concrete and pre-stressed concrete bridge deck respectively. As we can see that in Table 5 for concrete bridges the probability of failure for given threshold (10%), CR 5 has 23.10 equivalent to 24 years or less and CR 8 has 16.96 equivalent to 17 years or less both of them being in different condition rating (lower and higher) shows that CR 5 are more in NH region and CR 8 are in rural region, this says that the inspection in national highway and rural roads are done in improper manner. The observation shows that the CR 8(concrete) and CR 8 (pre-stressed concrete) with respect to its age it has quickly approached towards the damage condition. It should have maintained its quality and stayed in the better position. We generally know that CR 8 (higher condition rating) probability of failure should be lower than CR 5 (lower condition rating), but here it shows different values with more in support to lower CR. Thus, it leads to other factor which can cause such problems in material used in the construction, traffic load, loading pattern, improper maintenance, etc. these threats should be kept in mind. So, the factor of threats is same here and proper management of maintenance service is very necessary.

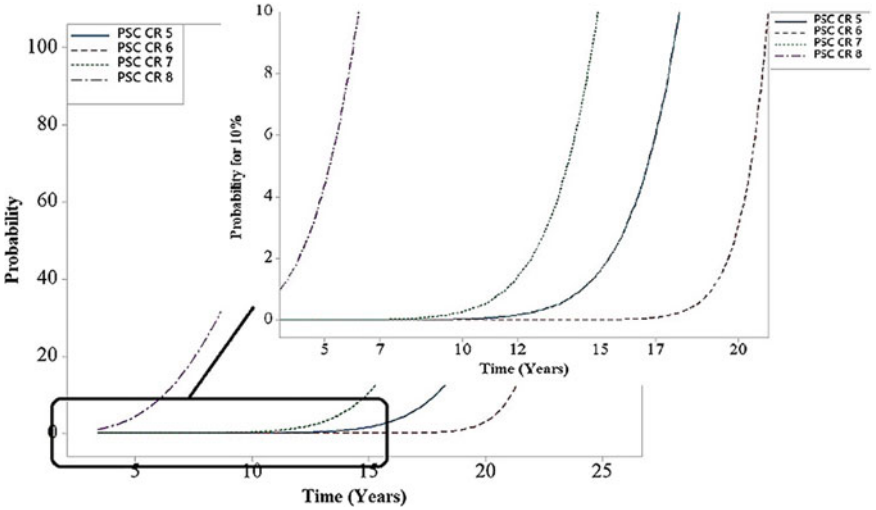

Fig. 6 Time in condition rating for 10% failure probability in pre-stressed concrete deck

5 Summary and Conclusions

In summary, the location (Cachar district) has different types of bridges (concrete, steel and pre-stressed concrete) available. The district has national highways road connecting bridges and rural areas where other bridges are located, both are important in transportation network. But the population of concrete and pre-stressed concrete are more in number compared to steel bridges, so steel bridge is excluded during the methodology work. The condition assessments of the bridges are done as per NBIS and are categorized in the form of condition rating. We have found the area has bridges between condition rating 5 and 8 (fair condition to very good condition). Now, data collection helps us to know about the maturity of the bridge and gives statistical idea about the length and population of the bridge. This leads to the next step, that is, the stochastic model is introduced, and the AD test used to evaluate the predictable distributions to find the goodness of fit test for proper description of the TICR in probabilistic technique. The test provides the Weibull distribution to be the best suitable distribution, which helps to estimate the parameters for the available data of the bridges in different condition rating and used to find the PDF and CDF of the deck component of concrete and pre-stressed concrete bridge, which gives the idea about the probability of failure. The observation shows that the CR 5 for concrete and CR 6 pre-stressed concrete with respect to its age has quickly approach towards the damage condition. It should have maintained its quality and stayed in the better position. Even the RCC bridge deck of CR 8 are having more failure percent probability and should be repaired for the better transportation facility. The probability of failure section shows that the bridges in the rural area are improperly maintained and as there are higher condition rating bridges still it shows more failure

in upcoming years. These model and methodology helps to give the idea about the bridges present in the location and can be useful in balanced decision making in the maintenance and rehabilitation program of the bridges in the district.

Acknowledgements This work was mainly carried out receiving the financial support from the DST-SERB, GOI under sanction no.ECR/2016/001329.

References

1. Agrawal AK, Kawaguchi A, Chen Z (2010) Deterioration rates of typical bridge elements in New York. J Bridge Eng 10.1061/ (ASCE) BE.1943–5592.0000123, 419–429
2. Kobayashi K, Kaito K, Lethanh N (2010) Deterioration forecasting model with multistage Weibull hazard functions. J Infrastruct Syst 10.1061/ (ASCE) IS.1943-555X.0000033, pp 282–291
3. Mishalani RG, Madanat SM (2002) Computation of infrastructure transition probabilities using stochastic duration models. J Infrastruct Syst 10.1061/(ASCE) 1076-0342(2002)8:4(139), 139–148
4. Madanat S, Ibrahim WHW (1995) Poisson regression models of infrastructure transition probabilities. J Transp Eng 10.1061/ (ASCE) 0733-947X (1995)121:3(267), pp 267–272
5. Masovic S, Hajdin R (2014) Modelling of bridge elements deterioration for Serbian bridge inventory. Structure and Infrastructure Eng. 10(8), 976–987
6. Mauch M, Madanat S (2001) Semi parametric hazard rate models of Reinforced Concrete Bridge deck deterioration. J Infrastruct Syst 10.1061/ (ASCE) 1076-0342 (2001)7:2(49), 49–57
7. Tabatabai H, Tabatabai M, Lee CW (2011) Reliability of bridge decks in Wisconsin". J Bridge Eng. https://doi.org/10.1061/(ASCE)BE.1943-5592.0000133
8. Hajializadeh D, OBrien EJ, Stewart MG (2014) The sensitivity of bridge safety to spatial correlation of load and resistance", Engineering Structures (2014) 71 99–111
9. Suo Q, Stewart MG (2009) Corrosion cracking prediction updating of deteriorating RC structures using inspection information. Reliab Eng Syst Safety 94(8):1340–1348
10. Nasrollahi M, Washer G (2014) Estimating inspection intervals for bridges based on statistical analysis of national bridge inventory data. 10.1061/ (ASCE) BE. 1943–5592. 0000710
11. Enright B, Leahy C, O'Brien EJ (2014) A Bayesian approach for estimating characteristics bridge traffic load effects. Civil engineering research in Ireland, Belfast, UK
12. Ma Y, Zhang J, Wang L, Liu Y (2013) Probabilistic prediction with Bayesian updating for strength degradation of RC bridge beams. Struct Saf 44:102–109
13. Zhang R, Mahadevan S (2000) Model uncertainty and Bayesian updating in reliability-based inspection. Struct Saf 22:145–160
14. Sobanjo J, Mtenga P, Rambo-Roddenberry (2010) Reliability based modelling of bridge deterioration hazards. J Bridge Eng 10.1061/ (ASCE) BE. 1943– 5592.0000074, 671–683
15. Anderson TW, Darling DA (1954) A test of goodness of fit. J Am Stat Assoc 49(268):765–769
16. Dodson B (2006) The Weibull analysis handbook. ASQ Quality Press, Milwaukee, WI
17. Federal Highway Administration (FHWA). (1988) Revisions to the national bridge inspection standards (NBIS). Tech. Advisory 5140.21, Washington, DC. Rep. No. FHWA-PD-96–001, Washington, DC

A Comparative Deterministic and Probabilistic Stability Analysis of Rock-Fill Tailing Dam

Tanmoy Das and A. Hegde

Abstract This paper presents a comparative study between simple deterministic stability analysis and probabilistic analysis, considering the case of an existing rock-fill tailing dam of 51 m height located in Rajasthan, India. A detailed seismic stability analysis was carried out considering the pseudostatic approach. All the analyses were carried out in CAD-based 2-D limit equilibrium program SLIDE 2D. In order to integrate the soil heterogeneity, stochastic Monte Carlo Simulation (MCS) technique was used. A minimal random number generator developed by Park and Miller (Association for Computing Machinery 31(10):1193–1201, 1988) was used in the analysis. The factor of safety values were calculated using Spencer's method by considering circular failure surfaces. The cohesive strength (c), the angle of friction (φ) and the acceleration (α_h) due to earthquakes were considered as the random variable in the study. For the critical geometry of the slope, the observed factor of safety values in case of upstream slope (1.67) and downstream slope (1.15) were found to be higher than the values specified in the IS 7894 (Code of practice for the stability analysis of the earth dams. Indian Standard, New Delhi, 1975) (reaffirmed in 1997) and ANCOLD (Guidelines on tailings dam design, construction and operation. Australian National Committee on Large Dam, 1999). The seismic deformation analysis was also carried for the downstream slope using the Newmark displacement method. Permanent displacement of the slope was found within the tolerable limits. Further, the results revealed that the spatial variability of the soil significantly influences the factor of safety values. Hence, the present study recommends the probabilistic stability analysis over the deterministic stability analysis for the rock-fill tailing dams.

Keywords Tailing dam · Monte Carlo simulation · Random number generator · Newmark displacement method · Inherent spatial variability

T. Das (✉) · A. Hegde
Department of Civil & Environmental Engineering, Indian Institute of Technology Patna, Patna, India
e-mail: tanmoy.mtce17@iitp.ac.in

A. Hegde
e-mail: ahegde@iitp.ac.in

A. Prashant et al. (eds.), *Advances in Computer Methods and Geomechanics*, Lecture Notes in Civil Engineering 55,
https://doi.org/10.1007/978-981-15-0886-8_49

1 Introduction

Indian mining industries are contributing immensely to the economic growth of the country. About 3100 mines are spread all over India. Out of which, the major portion is used for extraction of nonmetal products and the rest of are metal and fuel products. Demand for minerals has increased tremendously from the past few decades due to infrastructure development and automotive production. As a result, the waste disposal problem has also arisen heavily in the country. Indian Bureau of mines [10] defines tailings as valueless mineral remaining at the "tail" end of the mineral extraction operation. For the retention of tailings slurry, the tailing dams are constructed using mill tailings, mine waste or rock. This tailing slurry has a high potential energy that causes dam break risk. Tailings dam failure leads to loss of life, economic losses and has social as well as environmental impact. According to statistics, the tailing disaster is one of the major disasters in the world after the earthquake, cholera, floods, and bomb blast [25]. Approximately, 147 cases of tailing dam failures were reported at present, out of these 26 cases from Europe and 57 cases from USA [18]. Hence, to ensure the safety of the tailing dam has become the topmost priority of the scientists and engineers. The traditional deterministic analysis methods may not ensure the complete safety of the tailing dams. Soil inherent spatial variability is a major factor that influences the overall stability of the dam. Unfortunately, the conventional methods do not consider the effect of spatial variability in the analysis. Apart from inherent randomness, several features like measurement errors, approximations, assumptions, model parameter uncertainties, absence of geological details make the analysis more uncertain. The reliability-based methods explicitly consider the uncertainties involved in stability analyses [5].

In general, the factor of safety is defined as the ratio between the shear strength of the soil and shear stress required for equilibrium. In deterministic approach, the factor of safety value greater than 1 represents the stable slope. Whereas, in probabilistic approach, mean value and variance of strength parameters are taken into consideration while addressing the uncertainty. In the reliability-based analysis, the factor of safety is expressed in terms of its mean value and variance [8]. In addition to a range of safety factor, probabilistic approach calculates the probability of failure (POF) and reliability index (β) for a particular slope.

One of the well-known robust and conceptually simple tools for analyzing the reliability of slope considering spatial variability is Monte Carlo Simulation (MCS) [6, 27, 28]. Monte Carlo Simulation (MCS) is a numerical process of repeatedly calculating a mathematical or empirical operator in which the variables within the operator are random or contain uncertainty with prescribed probability distribution [2]. The critical slip surface varies spatially and needs to be located for each random sample generated during MCS. A common approach is to locate the critical slip surface from the deterministic analysis and calculate the POF corresponding to that surface [22]. However, the critical surface with the minimum factor of safety may not be the surface with maximum probability of failure [7]. Under the probabilistic framework, POF of any slope is determined on the basis of the slip surface which

is greater than the failure probability of any individual potential slip surface present on that particular slope. Many of the previous studies have focused on various slope failure modes caused by stratification. However, the inherent spatial variability of soil properties in soil layer is rarely considered in the analysis [13].

This paper presents a comparative study between simple deterministic stability analysis and probabilistic analysis. The cross section of the tailing dam reported by Sitharam and Hegde [21] was considered, which belongs to Rampura-Agucha mines in Rajasthan, India. In addition, the seismic deformation analysis was also carried out using the Newmark displacement method.

2 Methodology

All the analyses were carried out using the limit equilibrium method based SLIDE 7.0 software. It is a 2D slope stability analysis package with CAD-based graphical interface. SLIDE provides a numerous number of slope stability methods for analysis. Out of these, Spencer's method was chosen for both deterministic as well as probabilistic analysis. Spencer [24] method satisfies both force equilibrium as well as moment equilibrium equations and is applicable to failure surfaces of any shape. This method is also known for its accuracy in calculating the factor of safety [22]. The probabilistic analysis is carried out on the global minimum slip surface located by the regular (deterministic) slope stability analysis. The safety factor was re-computed for 1000 number of samples for the global minimum slip surface, by virtue of a different set of input variables that are randomly generated. MCS is a stochastic technique for using random or pseudo-random numbers to sample from a given input probability distribution. This method is generally used to model the probability of different outcomes in a process that cannot easily be predicted due to the intervention of random variables and uncertainty. MCS method is widely used in geotechnical engineering, especially for slope stability related problem where uncertainty in geotechnical properties plays a major role. Using MCS, the system probability of failure (POF) can be calculated using Eq. 1 as suggested by Li et al. [15] and Jiang et al. [13].

$$P_f = \frac{1}{N_t} \sum_{k=1}^{N_t} I\,(\mathrm{FS}_{\min} < 1) \tag{1}$$

where P_f = probability of failure; N_t = total number of samples generated; $\mathrm{FS}_{\min}$ = minimum factor of safety among the factor of safety values of a large but finite number of potential slip surfaces for a given set of random samples. For a given random sample, $I\ (\mathrm{FS}_{\min} < 1)$ is considered as 1 when $\mathrm{FS}_{\min} < 1$ occurs, otherwise it is equal to zero. POF is nothing but the number of analyses with safety factor less than one, divided by the total number of samples. It is calculated for the most critical failure surface with a minimum factor of safety [19].

Table 1 Soil properties used in the analysis [22]

Material	Property	Distribution	Mean	Min	Max	Standard deviation
Mine muck	(a) Cohesion, c (kPa)	Normal	2	0	4	1
	(b) Friction angle, φ (°)	Normal	39	30	48	3
Mine tailings	(c) Cohesion, c (kPa)	Normal	1	0	2	1
	(d) Friction angle, φ (°)	Normal	35	26	44	3
–	Horizontal seismic coefficient, α_h	Exponential	0.06	0	0.12	–

MCS uses uniformly distributed random numbers with a large number of iterations. The cohesion (c), friction angle (φ), and horizontal seismic coefficient (α_h) were considered as random variables. For cohesion and the friction angle, normal distribution was assumed. The horizontal seismic coefficient was assumed to follow the exponential distribution. Usually, the normal distribution is assumed for the soil parameters [26]. If the occurrences of an event constitute a Poisson process, then the recurrence time would be described by the exponential distribution [2]. Also, if the waiting time before a given event occurs is unknown, it is often appropriate to consider the exponential distribution of the random variables. Hence, it is suitable to use exponential distribution in case of earthquake acceleration coefficient. Table 1 lists out the different random variable considered in the analysis and their properties as reported by Sitharam and Hegde [22].

To simulate a true random analysis, a new seed value was generated after each run, based on the current time on the user system. This means that the analysis results will be different each time after re-running the analysis [19]. A minimal random number generator developed by Park and Miller [17], which can produce an almost bottomless sequence of distinct random numbers (approximately 2 ^ 31) was used in the analysis. It is a type of linear congruential generator (LCG) that operates in the multiplicative group of integers modulo m.

Since the tailing dam was constructed using waste rocks, the possibility of pore water pressure generation is negligible. The upstream face of the dam was covered with impervious clay liner, thus the steady seepage situation also does not occur. Furthermore, in this case, the drawdown situation does not occur [21]. Hence, only the factor of safety against end of construction with and without earthquake condition was analyzed in this study. The minimum threshold values of factor of safety were selected as per IS 7894 [12] (reaffirmed in 1997) and ANCOLD [1].

The tailing dam is located in the earthquake zone-II as per seismic zonal divisions in India (IS 1893: 1984). The value of the horizontal seismic coefficient was considered as 0.06, as per the guidelines of IS: 1893 [11]. The minimum specified

Table 2 Minimum desired values of factor of safety for different loading conditions as per IS 7894 [12] (reaffirmed in 1997)

Case no.	Loading condition of the dam	Slope most likely to be critical	Minimum desired factor of safety
I.	Construction condition with or without partial pool	Upstream and downstream	1
II.	Reservoir partial pool	Upstream	1.3
III.	Sudden drawdown:		
	(a) Maximum head water to minimum with tail water at maximum	Upstream	1.3
	(b) Maximum tail water to minimum with reservoir full	Downstream	1.3
IV.	Steady seepage with reservoir full	Downstream	1.5
V.	Steady seepage with sustained rainfall	Downstream	1.3
VI.	Earthquake condition:		
	(a) Steady seepage	Downstream	1
	(b) Reservoir full	Upstream	1

values of factor of safety as per IS 7894 [12] (reaffirmed in 1997), also conforming to ANCOLD [1] are summarized in Table 2.

Furthermore, seismic displacement analysis was also performed on the downstream slope using the Newmark displacement method. The purpose of the Newmark [16] method is to estimate the slope deformation for those cases where the pseudo-static factor of safety is less than 1 [4]. The acceleration time history of the past earthquake of the particular region was taken into consideration for the displacement analysis. The obtained displacement value was checked with a maximum value of displacement, suggested by several researchers.

3 Results and Discussions

The results of both deterministic and probabilistic analysis are presented in this section. Sitharam and Hegde [21] reported the deterministic stability analysis of the 51 m high tailing dam of the Rampura-Agucha mine. In the present study, the similar dam section was considered. Initially, the deterministic analysis was performed similar to Sitharam and Hegde [21]. The deterministic analysis was also used for the validation. The cross-section and the material properties similar Sitharam and Hegde [21] were used in the deterministic analysis. Figures 1 and 2 shows the results of the

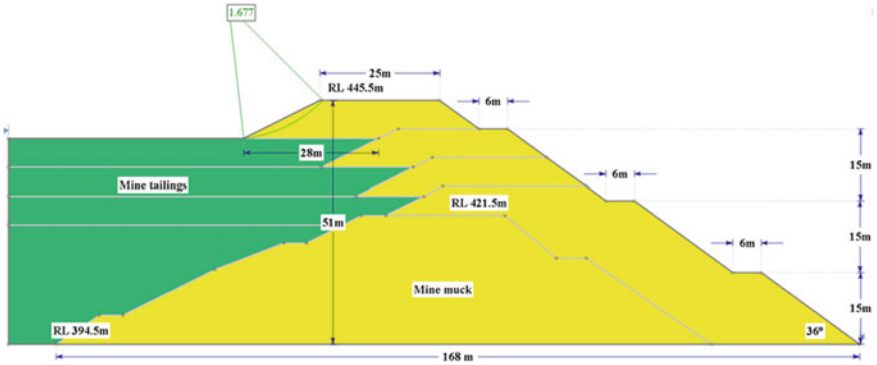

Fig. 1 Deterministic analysis results of upstream slope

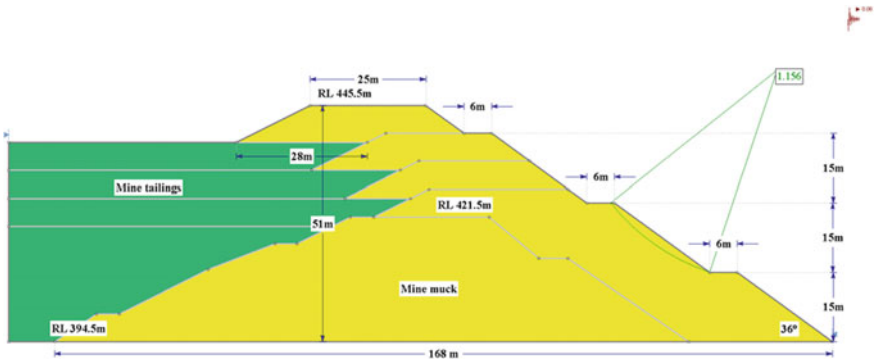

Fig. 2 Deterministic analysis results of downstream slope

deterministic analysis performed on the upstream and downstream slope respectively. The global minimum factor of safety of 1.67 and 1.15 was observed for upstream and downstream slopes respectively. The calculated FS values were higher than the threshold value suggested by IS 7894 [12] (reaffirmed in 1997). These values were found to be in good agreement with the values reported by Sitharam and Hegde [21]. Once the validation was completed, the same cross section was used for the probabilistic analysis.

The probabilistic analysis results for upstream and downstream slopes are shown in Figs. 3 and 4 respectively. Each analysis was re-run for 100 times to study the effect of re-running the analysis, using different random numbers generated from different seed values with respect to time. These results are summarized in Table 3. It was observed that the mean factor safety obtained from the probabilistic analysis is more than that of deterministic analysis. The upstream slope is fully safe with 0% POF. Whereas, the downstream slope had the POF value in the range of 5–9% with a reliability index of 1.3–1.6%. According to Sjoberg [23], the probability of

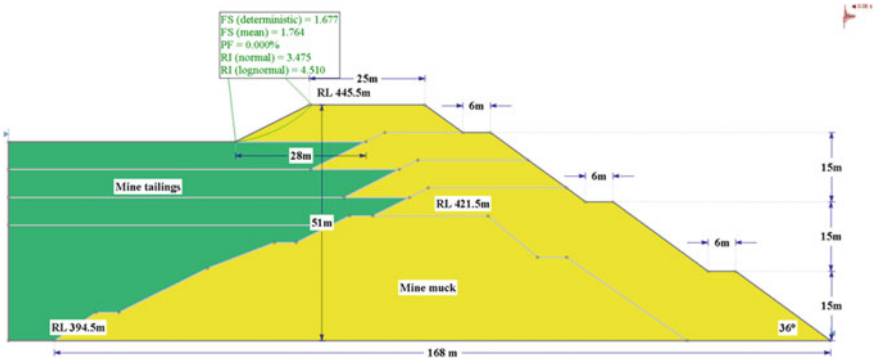

Fig. 3 Probabilistic analysis results of upstream slope

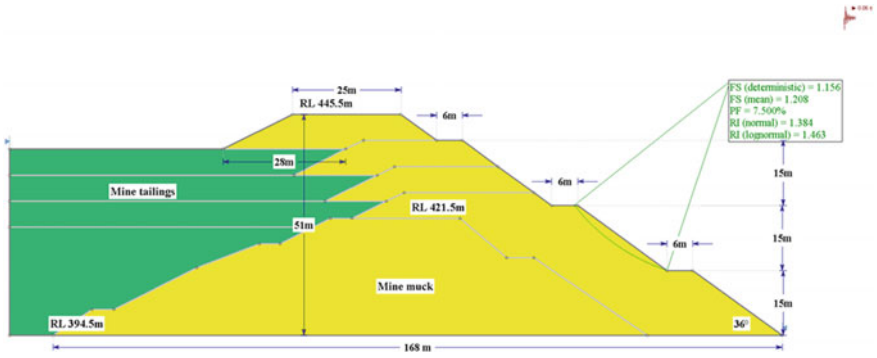

Fig. 4 Probabilistic analysis result of downstream slope

Table 3 Probabilistic analysis results for upstream and downstream slope

Slope type	Deterministic FOS	Mean FOS	POF (%)	Reliability index
Upstream slope	1.677	1.7–1.8	0	3.2–3.6
Downstream slope	1.156	1.19–1.22	5–9	1.3–1.6

failure less than 10% is considered as a safe condition. Hence the embankment was considered safe for height 51 m.

The histogram was plotted for factor safety for both upstream and downstream slope analysis as shown in Fig. 5a, b. The safety factor values less than 1 were highlighted. The POF can be graphically illustrated with the help of the histogram. Here, the POF is equal to the area of the histogram having the factor of safety less than 1, divided by the total area of the histogram.

The factor of safety values were found to be fitted nicely with gamma distribution as compared to other distributions. The gamma distribution is a two-parameter family of continuous probability distribution and exponential distribution. In this study, two

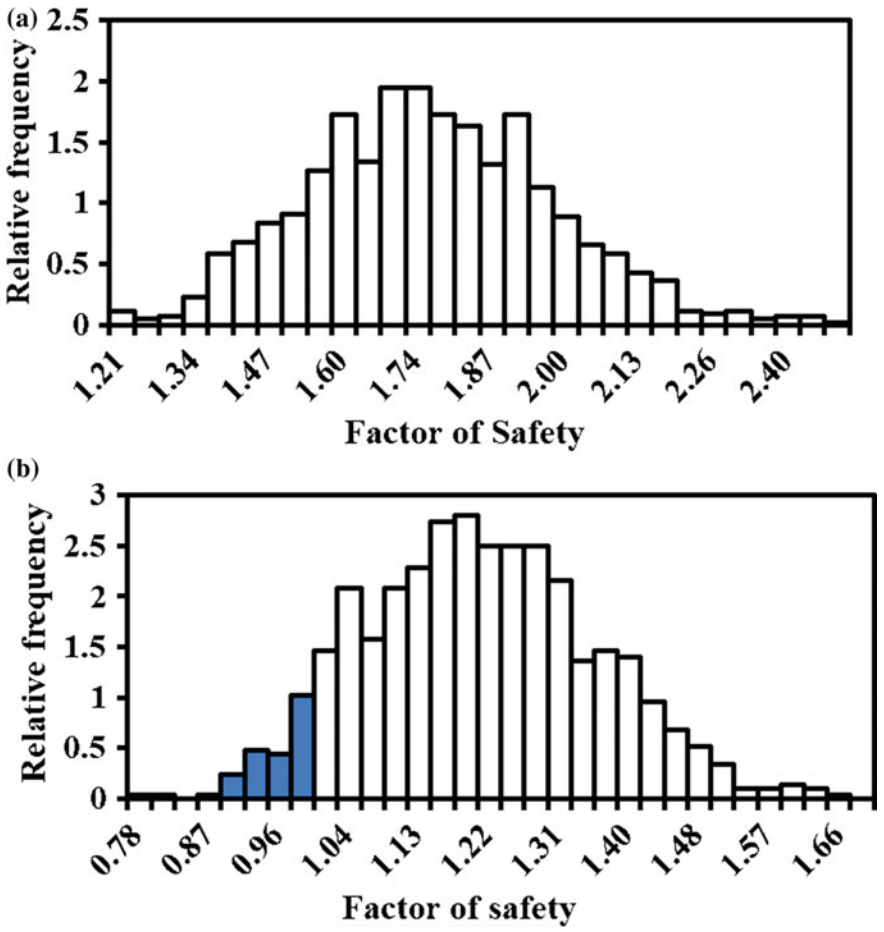

Fig. 5 **a**, **b** Histogram plot of factor of safety values: **a** upstream slope; **b** downstream slope

different distributions in the form of normal and exponential were considered in the case of input parameters. However, the outputs are following gamma distribution.

To analyze the dependency of factor of safety on the soil parameters, scatter plots has been plotted for the downstream slope between the factor of safety and two major soil properties namely, cohesion and friction angle as shown in Fig. 6a, b. The plot between the factor of safety and friction angle shows a strong correlation, as all the points on the plot are converging towards the regression line. The correlation coefficient was found to be 0.8; which is close to 1. On the other hand, less dependency of safety factor on the cohesion was observed with a correlation coefficient of magnitude 0.3. It indicates that the friction angle has a strong influence on the factor of safety values and probability of failure too.

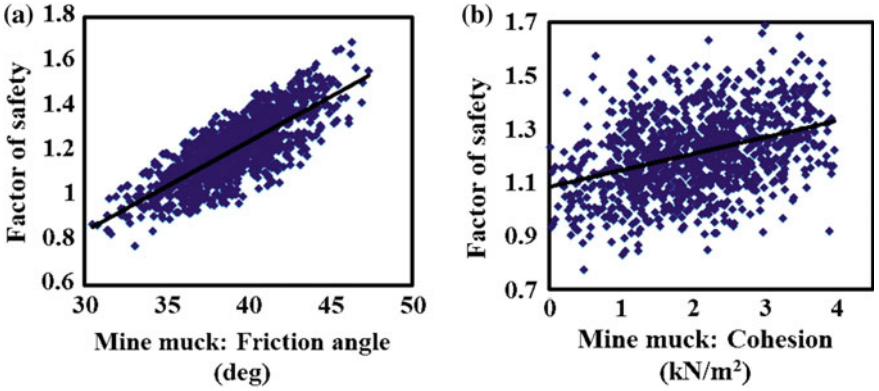

Fig. 6 **a**, **b** Scatter plots: **a** factor safety versus friction angle; **b** factor safety versus cohesion

According to ANCOLD [1], if the factor of safety is lower than 1.3 or 1.5, deformations should be estimated using the simplified deformation analysis. In that context, Newmark displacement analysis was performed for downstream slope. Generally, this method is used to calculate the post-earthquake displacement of a rigid sliding mass, first suggested by Newmark [16]. The analysis assumes one directional displacement of the sliding rigid soil block on a plane surface [5]. The acceleration time history data of the 2006 Alwar earthquake (shown in Fig. 7) was used in the analysis. Alwar is located in the northeastern part of Rajasthan.

The analysis was performed on the downstream slope of the tailing dam. Figure 8 shows the results of the displacement analysis. The obtained displacement was found to be within the tolerable limit suggested by various researchers [3, 9, 14, 20]. Hence, the dynamic stability of the tailing dam was fully satisfied.

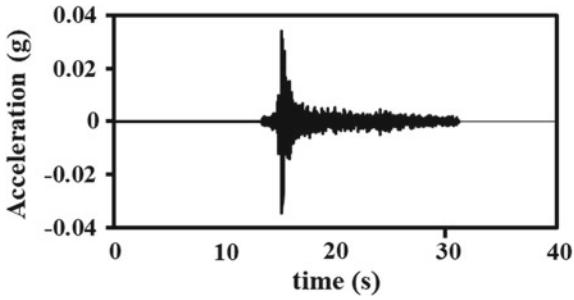

Fig. 7 Time history curve of Alwar Earthquake (2006)

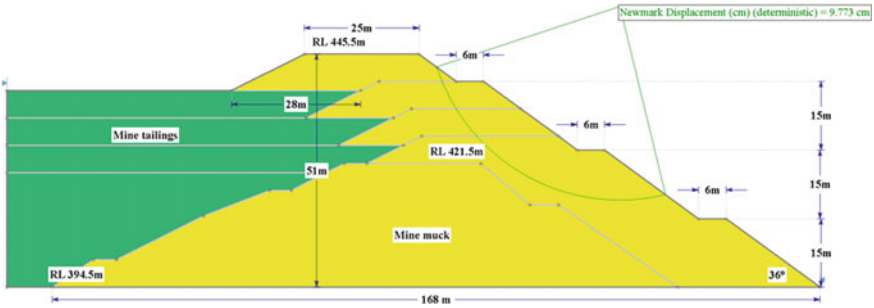

Fig. 8 Seismic displacement analysis of downstream slope using Newmark method

4 Conclusions

The comprehensive slope stability analyses of a rock-fill tailing dam were performed in the present study. The results of the deterministic and probabilistic analysis were compared. In the probabilistic analysis, soil properties like cohesion, friction angle and horizontal seismic coefficient were considered as random variables. The factor of safety values of upstream and downstream slopes were found to be higher than the specified values recommended by IS 7894 [12] (reaffirmed in 1997) and ANCOLD [1]. The mean factor safety obtained from the probabilistic analysis was found to be higher than that of deterministic analysis. Friction angle found to be the predominated factor that highly influences the factor of safety. Further, the probability of failure value was less than 10% for both upstream and downstream slopes. The seismic displacement analysis suggested that slope displacements were within the tolerable limits. In overall, the existing tailing dam was found to be stable against all possible modes of failure. As Duncan et al. [5] stated, knowing the values of both factors of safety and probability of failure is more useful than knowing either one alone. Considering the safety of downstream public, it is always recommended to perform the probabilistic stability analysis along with the deterministic analysis.

References

1. ANCOLD (1999) Guidelines on tailings dam design, construction and operation. Australian National Committee on Large Dam
2. Ang Alfredo HS, Tang WH (2007) Probability concepts in engineering. Wiley, New Jersey
3. Bray JD, Rathje EM, Augello AJ, Merry SM (1998) Simplified seismic design procedure for geosynthetic-lined solid waste landfills. Geosynthetics Int 5(1–2):203–235
4. Day RW (2002) Geotechnical earthquake engineering handbook. McGraw-Hill, New York
5. Duncan JM, Wright SG, Brandon TL (2005) Soil strength and slope stability. Wiley, New Jersey
6. Hammersley JM, Handscomb DC (1964) Monte Carlo methods. Wiley, New York
7. Hassan AM, Wolff TF (1999) Search algorithm for minimum reliability index of earth slopes. J Geotech Eng Div 125:301–308

8. Husein Malkawi AI, Hassan W, Abdulla F (2000) Uncertainty and reliability analysis applied to slope stability. Struct Saf 22:161–187
9. Hynes-Griffrin ME, Franklin AG (1984) Rationalizing the seismic coefficient method. Final Report, Miscellaneous Paper GL-84-13. Waterways Experiment Station, U.S. Army Corps of Engineers, Vicksburg
10. Indian Bureau of mines technical bulletin no. 30. Tailing dam design. Nagpur (1995)
11. IS: 1893(I) (2002) Criteria for earthquake resistant design of the structures. Indian Standard, New Delhi
12. IS: 7894 (1975) Code of practice for the stability analysis of the earth dams. Indian Standard, New Delhi
13. Jiang SH, Li DQ, Cao ZJ, Zhou CB, Phoon KK (2015) Efficient system reliability analysis of slope stability in spatially variable soils using monte carlo simulation. J Geotech Geoenviron Eng 141(2):1–13
14. Kavazanjian EJ, Matasovic N, Hadj-Hamou T, Sabatini PJ (1997) Geotechnical engineering circular#3, Design guidance: geotechnical earthquake engineering for highways, vol 1, design principles. Federal Highway Administration, U.S. Dept. of Transportation, Washington
15. Li L, Wang Y, Cao Z, Chu X (2013) Risk de-aggregation and system reliability analysis of slope stability using representative slip surfaces. Comput Geotech 53:95–105
16. Newmark NM (1965) Effects of earthquakes on dams and embankments. Geotechnique 15:139–160
17. Park SK, Miller KW (1988) Random numbers generators: good ones are hard to find. Assoc Comput Mach 31(10):1193–1201
18. Rico M, Benito G, Salgueiro AR, Díez-Herrero A, Pereira HG (2008) Reported tailings dam failures. J Hazard Mater 152:846–852
19. Rocscience Inc (2018) slide version 7.0. Tutorials do slide 7.0. https://www.rocscience.com/help/slide2/pdf_files/tutorials/Tutorial_08_Probabilistic_Analysis.pdf
20. Seed HB (1979) Considerations in the earthquake-resistant design of earth and rockfill dams. Geotechnique 29(3):215–263
21. Sitharam TG, Hegde A (2017a) Stability analysis of rock-fill tailing dam: an Indian case study. Int J Geotech Eng 11(4):332–342
22. Sitharam TG, Hegde A (2017b) Probabilistic seismic slope stability analyses of rock fill tailing dams: a case study. In: Proceedings of the 19th International Conference on Soil Mechanics and Geotechnical Engineering, Technical Committee 210. Seoul, pp 2439–2442
23. Sjoberg J (1999) Analysis of large scale rock slopes. Doctoral Thesis, Lulea University of Technology. Division of Rock Mechanics, Sweden
24. Spencer EE (1967) A method of the analysis of the stability of embankments assuming parallel inter-slice forces. Geotechnique 17:11–26
25. Tian WQ, Xue JG (2006) Tailings pond safety technology and management. Coal Industry Press, Beijing
26. Tobutt DC, Richards EA (1979) The reliability of earth slopes. Int J Numer Anal Meth Geomech 3:323–354
27. Wang Y (2013) MCS-based probabilistic design of embedded sheet pile walls. Georisk 7(3):151–162
28. Wang Y, Cao ZJ, Au SK (2011) Practical reliability analysis of slope stability by advanced monte carlo simulations in a spreadsheet. Can Geotech J 48(1):162–172

Subgrade Stabilization Using Non-biodegradable Waste Material

Asif Farooq and Fayaz A. Mir

Abstract Non-biodegradable waste materials pose a major environmental threat. The need for their safe discarding has increased. Incorporation of non-biodegradable waste materials in various engineering applications such as in highways and runways, etc., has been among main agendas of geotechnical engineers. In this paper, the results of testing to evaluate the effect of using non-biodegradable waste rubber powder in soft soils as an additive is reported. The soil behavior has been characterized by CBR as the intention is to use the in situ soil after the inclusion of the waste rubber material in road sub-grades so that the necessity of transporting good soil from borrow pits is eliminated. This will result in economic and environmental benefits. With the inclusion of non-biodegradable waste material, numbers of CBR tests were performed on soil samples. Non-biodegradable waste rubber powder is added to soil in different percentages as 0.5, 1, 1.5, 2, 2.5, 3, 3.5, 4, 5, 6, 7, 8, and 10% of dry weight of soil. The testing process was carried to check the consequences of using non-biodegradable waste material on CBR values of soil subgrade. The results showed that the use of non-biodegradable waste materials for soil stabilization improved the CBR properties of soil. The optimum value of rubber powder that can be added to soil is found out to be 7% of dry weight of soil. Further increase of rubber power after 7% resulted in a decrease in the CBR value.

Keywords Non-biodegradable waste material · Rubber powder · Subgrade stabilization · California bearing ratio · Soft soil stabilization

A. Farooq (✉) · F. A. Mir
Department of Civil Engineering, National Institute of Technology, Srinagar, India
e-mail: asif.nit16@gmail.com

F. A. Mir
e-mail: fayazamir@yahoo.co.in

A. Prashant et al. (eds.), *Advances in Computer Methods and Geomechanics*, Lecture Notes in Civil Engineering 55,
https://doi.org/10.1007/978-981-15-0886-8_50

1 Introduction

A large stockpile of industry and municipality generated wastes such as rubber waste, glass waste, plastic waste, fly ash, etc., are a result of rapid urbanization and industrialization. For the developing countries like India, the disposal of the waste in an environment-friendly way has been a big problem and challenge. India alone produces a great stockpile of waste tires. In USA stockpile of wastes crap tires is 275 million and increasing. These waste tires are disposed of either by burning or by landfilling, causing dangerous environmental, and health-related issues which can only be reduced by encouraging recycling process. Numerous efforts are being carried on for its use in pavements, as lining material so as to act as waterproofing layer, source of reducing vibrations in railway tracks. Further waste rubber tires are found to be having a fine scope of being used as aggregate in certain types of concretes. Bulks of experimentation programs are being carried by engineers to find the proper methods of incorporation of waste materials in soil so as to improve its properties.

Due to lower specific gravity of rubber particle, the overall unit weight of soil-rubber mix gets reduced upon the incorporation of waste tire material in sandy soil. Researches also suggest increase in shear strength of soil resulting due to better intermeshing of soil and tire particles. The rubber waste tires in the form of fibers can be used for clay reinforcement due to its high resilience, high durability, and lesser compressibility properties. The research related to stabilization of clayey soil using waste rubber materials like, fibers, crumbs, and powdered rubber is very scarce.

1.1 Background

Various properties of soil are influences by the incorporation of different types of waste tires. Research shows soil properties like OMC and MDD of clayey soil decreases with the increasing the percentage of waste rubber and its credit was given to lesser specific gravity of rubber [1, 2]. However few researchers observed a 2–3% increase in OMC value while increasing the rubber percentage. One of the causes of increased OMC of rubber-clay mixture can be that the extra water is needed for greasing of rubber particles [3].

In case of clayey soil, UC strength have been noticed to decrease due to use of waste tire material in it. The reasons given by the investigations include low secant modulus of rubber particle and low fusing of rubber and clay particles [1, 4]. Few studies suggested an improvement of UC strength of soil upon waste tire inclusion up to maximum value of 2% [5, 6]. Some of the researchers have studied the freeze-thaw effect of soil modified with rubber, it was observed by them that soil-rubber mixture possessed higher freezing-thawing durability [5].

An experiment to study the effect of shredded rubber tires as reinforcing the material in soft clay stabilized using cement was carried out. Results obtained demonstrated that the used of shredded rubber tires increased the ductility properties of

mix but at the same time it decreased its stiffness [2] carried some tests and their results showed that increase in the CBR values of clay due to the inclusion of rubber particles. The maximum value of rubber particles up to which CBR value increased was reported as 5%. Recent experiments were carried to study the influence of different types of rubber wastes namely fibers, granulate and shreds on various properties of soil. The investigation focused on the use of waste tires in powdered form for stabilization of soft subgrade soil is not done yet. Therefore a detailed experimental investigation is necessary to study the influence of rubber tires in powdered form on soft subgrade soil.

2 Sample Preparation and Material Properties

2.1 Sample Preparation

Collect 5 kg of soil sample. Pass the sample through sieve of 19 mm. Add the required percentage of rubber powder (passing 75 μ) to the sample and mix it while dry. Add optimum moisture content to the soil-rubber mixture. Mix the water and soil-rubber mixture properly. Place the filter paper on spacer disk, which is finally to be placed above the base plate at bottom of CBR mould. Cleaning and oiling of CBR mould is done. Soil is filled in CBR mould in three layers and each layer is compacted using 2.6 kg hammer with 56 blows per layer. After final layer collar is taken off and excess soil is removed. Baseplate is removed and mould is inverted. Surcharge of 2.5 kg is kept on top of soil and mould along with soil and surcharge is placed machine used for testing. Contact between plunger and soil is created using seating load of 4 kg. Application is load is such that the rate of penetration is 1.25 mm/min.

2.2 Material Properties

2.2.1 Soil

The soil used in the work is a silt of high compressibility, highly fibrous and organic in nature obtained from campus of Central University of Ganderbal, J&K, India with a specific gravity of 2.32. The particle size distribution curve is shown in Fig. 1 and Image 1. Various soil properties found using laboratory testing programs done as per Indian Standards are given in Table 1 as below.

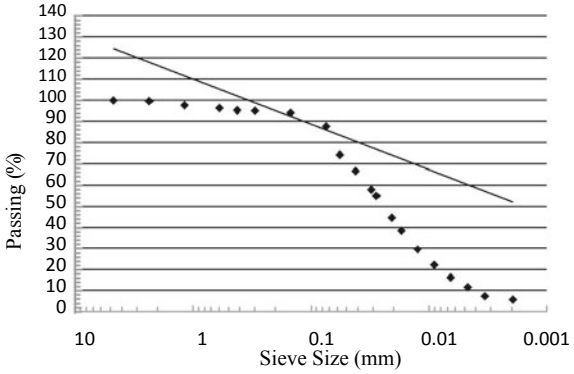

Fig. 1 Particle size distribution characteristics

Image 1 Insitu state of soil (*Source* self clicked image of Insitu site condition)

2.2.2 Rubber Powder

Rubber powder was formed by rigorous crushing and grinding of rubber tires. The gradation analysis was carried and the rubber powder passing 75 μ was used as reinforcement to the soil (Image 2 and Table 2).

3 Results and Discussion

The influence of rubber powder (obtained from waste tires) on geotechnical properties of soil is studied by performing series of CBR tests (both soaked and unsoaked). To

Table 1 Geotechnical properties of soil

Property	Value	Property	Value
Insitu moisture content (%)	135.77	Plasticity index (%)	25.28
Insitu bulk density (g/cc)	1.3	Plasticity index of A-line (%)	27.74
Insitu dry density (g/cc)	0.55	Activity	4.26
Degree of saturation	0.97	Flow index (%)	11.36
Sand (%)	12.37	Toughness index (%)	2.22
Clay (%)	5.93	Shrinkage limit	24.98
Silt (%)	81.7	Shrinkage ratio	0.04
Soil classification	OH	Volumetric shrinkage	7.96
D60	0.035	Linear shrinkage	2.52
D30	0.015	Specific gravity at 27 °C	2.32
D10	0.003	Cohesion (kpa)	2.77
Uniformity coeff.	10.93	Angle of internal friction (°)	5.50
Coeff. of curvature	2.0	qu (Insitu) (kPa)	4.2
Liquid limit (%)	58	qu (Remoulded) (kPa)	7.7
Plastic limit (%)	32.72	Sensitivity	0.58
Average organic content (%)	23		
OMC (%)	40	CBR (unsoaked) (%)	2.01
Dry density (g/cc)	1.51	CBR (soaked) (%)	1.86

investigate the effect waste tire powder is added from 0.5 to 10% in increments and the percentage increase in CBR reading in noted (Table 3).

From the results obtained after conducting a series of CBR tests in Soaked condition it is noted that the curves obtained (Fig. 2) show typical increase in CBR values upon the incremental increase in rubber powder up to 7%, the increase in CBR value is credited to the fact that the waste tire rubber powder acts as a filler material, therefore by increasing the rubber percentage, the voids are filled and the CBR increase. After 7% further addition of rubber powder resulted in the considerable decrease in CBR value. The decrease in CBR strength after 7% is attributed to weak adhesion between waste rubber particles and soil. However, rubber being of higher compressibility as compared to soil resulting in lesser resistance to penetration can also be the reason for the decrease in CBR value after 7% of waste rubber powder in the soil. The value of CBR (soaked) at an optimum amount of rubber powder, i.e., 7%

Image 2 Fine rubber powder used as additive (*Source* as provided by powder supplier)

Table 2 Characteristics of rubber powder (as provided by the manufacturer)

Properties	Value
Density (kg/m^3)	0.83
Size (m)	100% passing 75 μ
Elongation (%)	420

Table 3 CBR results (soaked) while increasing the quantity of rubber powder as an additive

Rubber powder (%)	CBR value (soaked) (%)
0	1.86
0.5	2.03
1	2.08
1.5	2.48
2	2.82
2.5	2.96
3	3.19
3.5	3.48
4	3.72
5	3.79
6	3.85
7	3.96
8	1.59
10	1.41

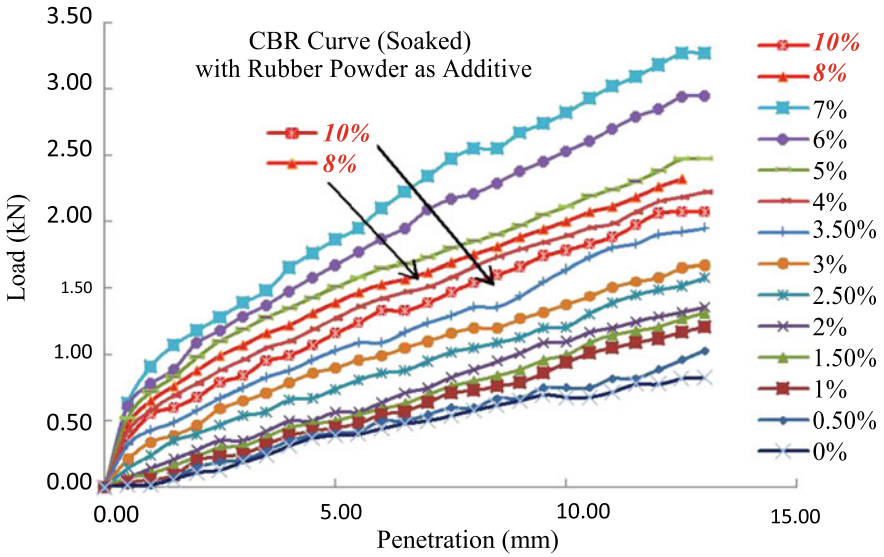

Fig. 2 CBR value (soaked) with increasing percentage of rubber powder as additive

is found to be 3.96%, after which there is a considerable decrease in CBR values (Table 4).

As observed from the results (Fig. 3), the behavior curves of CBR unsoaked tests show a considerable increase in CBR values upon the incremental increase in rubber powder up to 7%, after which further addition in rubber powder results in a decrease

Table 4 CBR value (unsoaked) with increasing percentage of rubber powder as an additive

Rubber powder (%)	CBR value (unsoaked) (%)
0	2.01
0.5	2.48
1	2.97
1.5	3.17
2	3.52
2.5	3.62
3	3.72
3.5	3.96
4	4.25
5	4.42
6	4.51
7	4.72
8	2.39
10	2.12

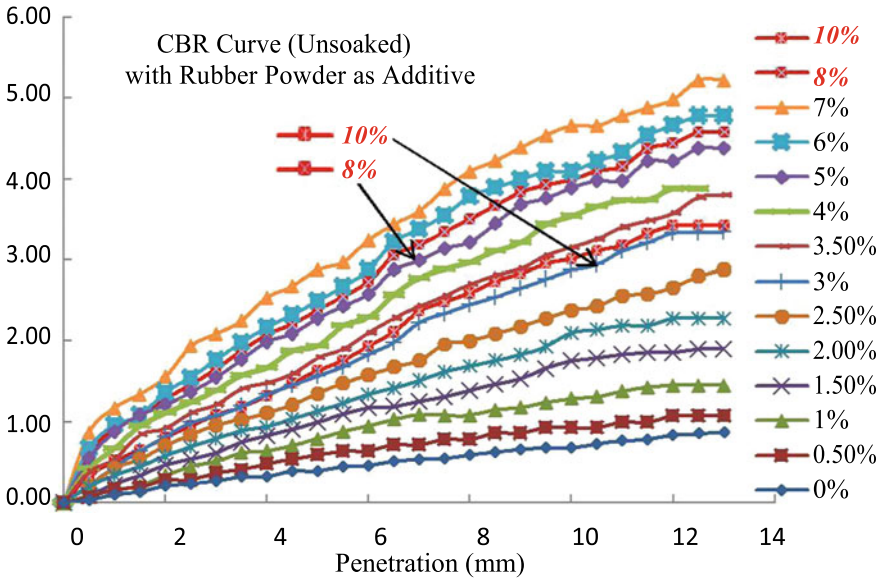

Fig. 3 CBR value (unsoaked) with increasing percentage of rubber powder as additive

Table 5 Percentage increase in CBR value with increasing percentage of rubber powder as an additive

Rubber powder (%)	Percentage CBR (soaked)	Value percentage CBR value (unsoaked)
0.5	9.13	19.08
1	17.33	32.44
1.5	26.48	44.32
2	40.11	61.04
2.5	48.81	73
3	61.44	81.67
3.5	68.12	93.56
4	75	104.32
5	84.33	119.32
6	89.10	136.20
7	91.31	141.32
8	84.22	128.44
10	72.08	117.87

in CBR. At the optimum value of rubber powder, i.e., 7%, the CBR value is found to be 4.72%, which is more than what was found for the soaked test.

From Table 5, it can be observed that the percentage increase in CBR value is higher in the unsoaked test as compared to soaked test, this is attributed to the fact

that shear strength of dry soil is higher as compared to wet soil. Further, after the optimum value is reached CBR values decrease both in soaked and unsoaked tests. It can be concluded that the rubber powder as a stabilizer has higher efficiency in dry subgrade as compared to wet, even though it reasonably increases subgrade strength in submerged condition as well.

The results obtained are valid only for the soil used in the research.

4 Conclusion

Various conclusions can be obtained from above experimental results:

1. Inclusion of non-biodegradable waste material, i.e., rubber powder in soil increased the strength of Subgrade soil.
2. The CBR values increases with increase in rubber powder content in soil with optimum value at 7%.
3. Overall cost of pavement is reduced due to increase in CBR value resulting in decrease of thickness of pavement.
4. Apart from improving the engineering properties of soil, use of non-biodegradable waste material, i.e.; waste rubber as reinforcement help in reducing some part of the environmental waste.

References

1. Cabalar et al. (2015) Behaviour of clayey soil with waste aluminium pieces. Elsevier
2. Yadav JS, Tiwari SK (2017) A study on the potential utilization of crumb rubber in cement treated soft clay. J Build Eng
3. Yong YIN, Xiao-jun YU (2009) Research on applying glass fiber cement soil to strengthen soft soil subgrade. GeoHunan International Conference
4. Al Tabba et al. (2000) Soil mixing of stratified contaminated grounds. Elsevier
5. Kalkan et al. (2013) Preparation of scrap tire rubber fibre-silica fume mixture for modification of clayey soil. Elsevier
6. Yadav JS, Tiwari SK (2011) Effect of waste rubber fibers on the geotechnical properties of clay stabilized with cement. Elsevier
7. Yadav JS, Tiwari SK (2016) Geotechnical properties of Dune sand-Waste Tires Composite. ICEMS
8. Tiwari B, Ajmera B, Moubayed S (2012) Soil modification with shredded rubber tires. GeoCongress
9. IS 2720: Part 2: 1973 Methods of test for soils: Part 2 Determination of water content
10. IS 2720: Part 3: Sec 1: 1980 Methods of test for soils: Part 3 Determination of specific gravity Section 1 fine-grained soils
11. IS 2720: Part III: Sec 2: 1980 Test for Soils—Part III: Determination of Specific Gravity—Section 2: Fine, Medium and Coarse-Grained Soils
12. IS 2720: Part 4: 1985 Methods of Test for Soils—Part 4: Grain Size Analysis
13. IS 2720: Part 5: 1985 Method of Test for Soils—Part 5: Determination of Liquid and Plastic Limit

14. IS 2720: Part 6: 1972 Methods of test for soils: Part 6 Determination of shrinkage factors
15. IS 2720: Part VII: 1980 Methods of Test for Soils—Part VII: Determination of Water Content-Dry Density Relation Using Light Compaction
16. IS 2720: Part 10: 1991 Methods of test for soils: Part 10 Determination of unconfined compressive strength
17. IS 2720: Part 16: 1987 Methods of Test for Soil—Part 16: Laboratory Determination of CBR
18. Murthy VNS (2007) Advanced foundation engineering, 1st edn. CBS Publications
19. Purshotam R (2016) Ground improvement techniques, 2nd edn. Laxmi Publications

Seismic Response of Structure Isolated with Quintuple Friction Pendulum Bearing Under Directivity Focusing Earthquakes

Ankit Sodha, Sandeep Vasanwala and Devesh Soni

Abstract Quintuple Friction Pendulum (QTFP) isolator having five effective pendula with nine stage sliding regimes operation is an extended technology of Triple Friction Pendulum (TFP) isolator. Because of its multiple sliding surfaces, Quintuple Friction Pendulum system shows highly adaptive behavior instead of being passive system. The paper describes nonlinear mathematical model and seismic response of a structure isolated with Quintuple friction pendulum bearing. Different configurations depending on displacement capacities, effective time period and effective damping are considered for a design of QTFP bearing. The seismic demand parameters like top floor absolute acceleration, base shear and isolator displacement have been studied. Further, to study a seismic behavior of QTFP bearing under a Directivity Focusing Earthquakes, total nine records including far-field, near-fault ground motion with directivity effect and fling step effect are considered. Depending on the directivity effect and rupture pattern, for a given earthquake event, the near-fault ground motions are highly variable from far-field ground motions. It is found that, due to backward and forward momentum conveyed by the directivity pulse, near-fault directivity effect imposes higher demand compare to fling step having forward momentum only.

Keywords Seismic isolation · Quintuple friction pendulum system · Near-fault with forward directivity · Fling step

A. Sodha (✉) · S. Vasanwala
Applied Mechanics Department, Sardar Vallabhbhai National Institute of Technology, Surat 395007, Gujarat, India
e-mail: aankitsodha@gmail.com

D. Soni
Department of Civil Engineering, Sardar Vallabhbhai Patel Institute of Technology, Vasad 388 306, Gujarat, India

A. Prashant et al. (eds.), *Advances in Computer Methods and Geomechanics*, Lecture Notes in Civil Engineering 55,
https://doi.org/10.1007/978-981-15-0886-8_51

1 Introduction

One of the most effective passive vibration control technology is Base isolation. It survives structure from seismic impact by decoupling the structure from its foundation. The main research work related to base isolation is focused on friction type of bearing mainly due to effectiveness for a wide range of frequency input. Based on concept of sliding friction, Initially Resilient-friction base isolator [1] and friction pendulum [2] are developed. To increase the displacement capacity and to reduce heat due to friction, multiple friction pendulum systems were developed [3]. Further, Double Concave Friction Pendulum (DCFP) bearing with two concave surfaces and Triple Friction Pendulum (TFP) bearings with four sliding surfaces have been developed [4–7].

Very recently developed Quintuple Friction Pendulum (QTFP) bearing consisting of six spherical sliding surfaces [8] is an extension of the Triple Friction Pendulum (TFP) bearings [4–7]. Ground motions having effects tend to increase the long-period portion of the acceleration response spectrum, effects tend to increase the long-period portion of the acceleration response spectrum [9]. To dissipate this input energy with few large displacement excursions, ground motions may generate high demands that force the structures.

The prime objective of the paper is to explore seismic behavior, along with adaptive one, of a newly developed QTFP system under wide range of excitation including multi hazard level excitation and near-fault excitation with directivity focusing and fling step. Six different QTFP configurations are designed to achieve specified effective period, damping and displacement capacity. Further, to study effect of directivity focusing and fling step, a set of nine records along with three far-fields, three near-faults with directivity effect and three fling step effects are also considered. The seismic demand parameters studied are base shear, top floor absolute acceleration and isolator displacement.

2 Ground Motions

Based on the directivity effect and rupture pattern, the far-field earthquake ground motions are different from near-fault ground motions. Near-fault ground motions are divided into two displacement patterns, one is forward directivity in which direction of slip on fault is aligned with site and the rupture propagates forward toward the site. Ground motions with this type of path generate large-amplitude, short duration and long-period pulses due to its specified radiation patterns. Here rupture propagates with velocity near to shear wave velocity. Another event namely fling step generates due to permanent ground displacement linked with rupture mechanism. It ends in a higher velocity pulse ensuing in a high unidirectional step in displacement history. In a site subjected forward directivity, the displacement, velocity and ground acceleration can be very excessive even in occasion of moderate earthquakes. Total nine records

Table 1 Earthquake records comprising of far-field, near-fault ground motion with directivity effect and fling step effect

Earthquake	Magnitude	Station	PGA (g)	Fling disp. (cm)
Far-field ground motions				
1999 Chamoli	6.4	Chamoli	0.359	–
1940 Imperial Valley	6.95	El Centro	0.313	–
1994 Northridge	6.7	Canoga Park	0.477	–
Near-fault ground motions with forward directivity				
1994 Northridge	6.7	Rinaldi	0.890	–
1994 Northridge	6.7	Newhall	0.720	–
1979 Imperial Valley	6.4	EL Centro Array 7	0.460	–
Near-fault ground motions with fling step				
1999 Chi Chi	7.6	TCU129_NS	0.610	67.54
1999 Chi Chi	7.6	TCU052_NS	0.440	697.12
1999 Chi Chi	7.6	TCU068_EW	0.500	601.84

consist of three far-fields, three near-faults with directivity effect and three fling step effects are used as presented in Table 1 [10].

3 Properties of the Isolation System

The QTFP systems designed to achieve effective damping ratio of 20% with effective time period of 6 s, respectively, for displacement capacity of 1.5 m for the purpose of studying QTFP system having different values of effective damping, time period and displacement capacity. The effective period, T_{eff} and damping ratio, ξ_{eff}, are given by,

$$T_{\text{eff}} = 2\pi\sqrt{\frac{W}{K_{\text{eff}}g}} \tag{1}$$

$$\xi_{\text{eff}} = \frac{E_{\text{loop}}}{2\pi K_{\text{eff}} D^2} \tag{2}$$

for the QTFP, the K_{eff} and E_{loop} are derived from the geometry of force-deformation curve as shown in Fig. 1b as given by,

$$K_{\text{eff}} = \frac{\begin{array}{l} K_1 D_y + K_2\left(u^I - D_y\right) + K_3\left(u^{II} - u^I\right) + K_4\left(u^{III} - u^{II}\right)\ldots \\ \ldots\ldots\ldots + K_5\left(u^{IV} - u^{III}\right) + K_6\left(D - u^{IV}\right) \end{array}}{D} W \tag{3}$$

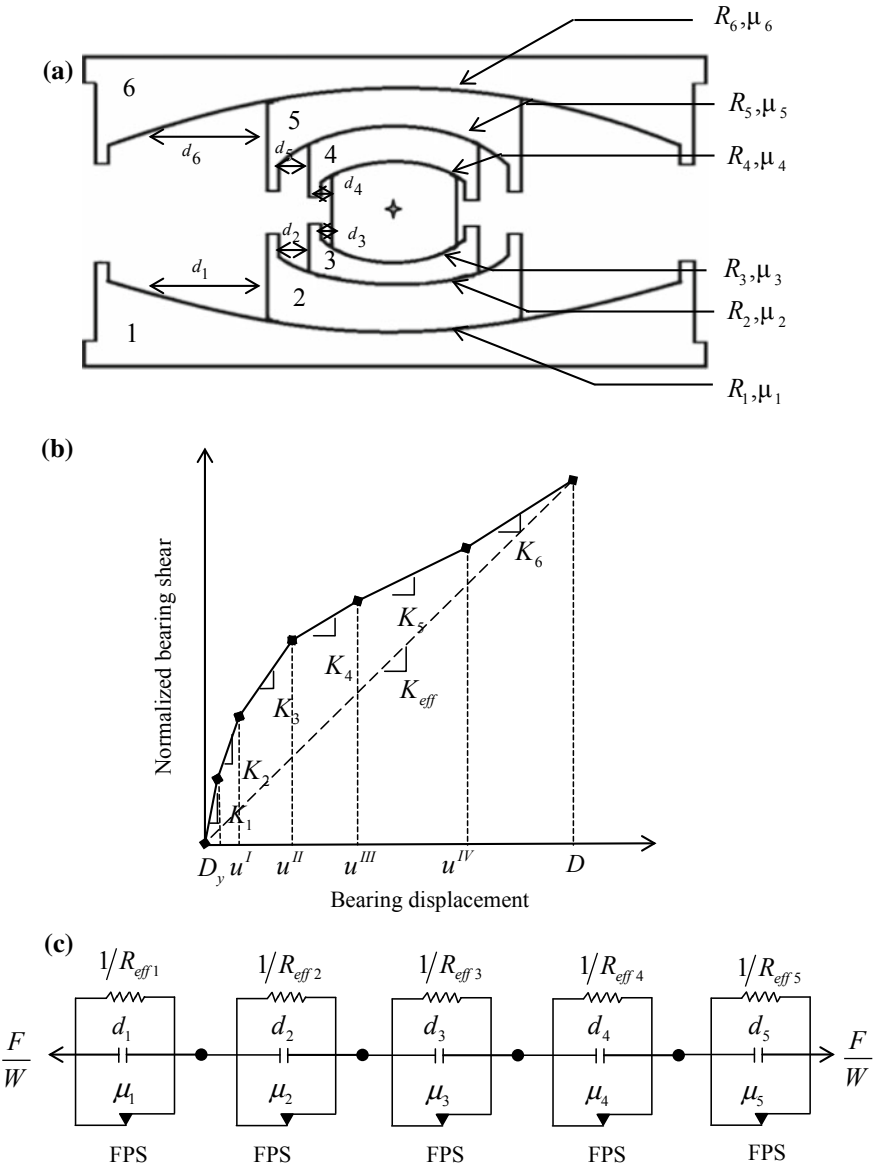

Fig. 1 **a** Schematic diagram of QTFPS, **b** hysteretic force-displacement relationship of QTFPS, **c** series model of QTFPS

$$\begin{aligned} E_{\text{loop}} &= 4D_y^2(K_1 - K_2)W + 4\left(u^I\right)^2(K_2 - K_3)W \\ &+ 4\left(u^{II}\right)^2(K_3 - K_4)W + 4\left(u^{III}\right)^2(K_4 - K_5)W \\ &+ 4\left(u^{IV}\right)^2(K_5 - K_6)W + 4u^{IV}D(K_6 - K_5)W \\ &+ 4D_yD(K_2 - K_1)W + 4u^{II}D(K_4 - K_3)W \\ &+ 4u^{III}D(K_5 - K_4)W + 4u^{I}D(K_3 - K_2)W \end{aligned} \tag{4}$$

where

$$K_1 = \frac{1}{R_{\text{eff3}}};\ K_2 = \frac{1}{R_{\text{eff3}} + R_{\text{eff4}}};\ K_3 = \frac{1}{R_{\text{eff3}} + R_{\text{eff5}}};$$
$$K_4 = \frac{1}{R_{\text{eff2}} + R_{\text{eff5}}};\ K_5 = \frac{1}{R_{\text{eff2}} + R_{\text{eff6}}};\ K_6 = \frac{1}{R_{\text{eff1}} + R_{\text{eff6}}} \tag{5}$$

$$u^I = (\mu_5 - \mu_3)R_{\text{eff3}} + (\mu_5 - \mu_4)R_{\text{eff4}} \tag{6}$$

$$u^{II} = u^I + (\mu_2 - \mu_5)(R_{\text{eff3}} + R_{\text{eff5}}) \tag{7}$$

$$u^{III} = u^{II} + (\mu_6 - \mu_2)(R_{\text{eff2}} + R_{\text{eff5}}) \tag{8}$$

$$u^{IV} = u^{III} + (\mu_1 - \mu_6)(R_{\text{eff2}} + R_{\text{eff6}}) \tag{9}$$

Here, D_y is the isolator displacement at which motion on the sliding surface initiates. The D_y is takes as 0.025 cm in this study [11].

4 Numerical Study

In this study, a five-storey shear building with diagonal mass matrix is considered. The mass, stiffness and modal damping ratio of the each floor is kept constant in each mode of vibration for simplicity in analysis. The time period of superstructure can be kept fixed at the base by selecting such a value of stiffness. The characterization of base isolated system done by the parameters like, the ratio of base mass to the superstructure floor mass, m_b/m, damping ratio of the superstructure, ξ_s and the fundamental time period of the superstructure, T_s. The numerical values are kept constant as $T_s = 0.5$ s, $\xi_s = 0.02$, $m_b/m = 1$ and $m_{si}/m = 0.0005$ in this study. To achieve desirable fundamental period of 0.5 s, the storey stiffness, $K = 115{,}740$ kN/m and floor mass, $m = 59{,}378$ kg have been taken and along with bay width 3.0 m and storey height 5.0 and 3.0 m. To study seismic response, all three response quantities, i.e., isolator displacement, u_b, base shear normalized by total weight of the building, F_b/W, and top floor absolute acceleration, $A(g)$ are considered.

Table 2 Peak values of top floor absolute acceleration, $A(g)$, displacement, u_b, and base shear, F_b/W

	$A(g)$	u_b	F_b/W
Far-field earthquake			
1940 Imperial Valley (Elcx)	0.081	103.370	0.024
1999 Chamoli (chamoli)	0.059	117.370	0.022
1994 Northridge (Cnpx)	0.150	336.400	0.039
Near-fault earthquake			
1979 Imperial Valley (EQ21)	0.162	771.740	0.091
1994 Northridge (EQ31)	0.199	428.700	0.065
1994 Northridge (EQ51)	0.206	594.030	0.078
Fling step earthquake			
1999 Chi Chi (TCU052_NS)	0.964	1085.800	0.460
1999 Chi Chi (TCU068_EW)	0.685	1530.400	0.193
1999 Chi Chi (TCU129_NS)	0.230	258.160	0.050

5 Behavior of QTFP Under Directivity Focusing Earthquakes

For the purpose of studying seismic behavior under Directivity Focusing Earthquakes, total nine records comprising of far-field, near-fault ground motion with directivity effect and fling step effect are considered and shown in Table 2. The hysteretic behavior of the QTFP under the far-field ground motion and near-fault ground motion with directivity effect and fling step is shown in Fig. 2. In case of far-field ground motion, initially, the inner sliding surfaces 3 and 4 with lower value of coefficient of friction get activated as lateral force acting on isolator is comparatively low. Further increase in lateral force, the isolator deforms into sliding regime IV, with rigid bi-linear behavior of force-deformation. For near-fault earthquake due to inherent velocity pulse the lateral force is so large that motion occurs on surfaces 1 and 6 then motion reaches up to sliding regime IX.

The response under all three types of ground motions are shown in Fig. 3 and tabulated in Table 2. Near-fault directivity effect having a forward and back ward momentum conveyed by the directivity pulse, while fling step having only forward momentum. It imposes higher demand at near-fault directivity compare to fling step. For the large velocity pulse and fling displacement of near-fault ground motion, the demand parameters increases compared to far-field motion.

6 Conclusions

The behavior of QTFP system using nonlinear time history analysis with directivity focusing earthquakes are presented in this paper. The MDOF system is analyzed for nine records consist of three far-fields, near-fault ground motion with three directivity

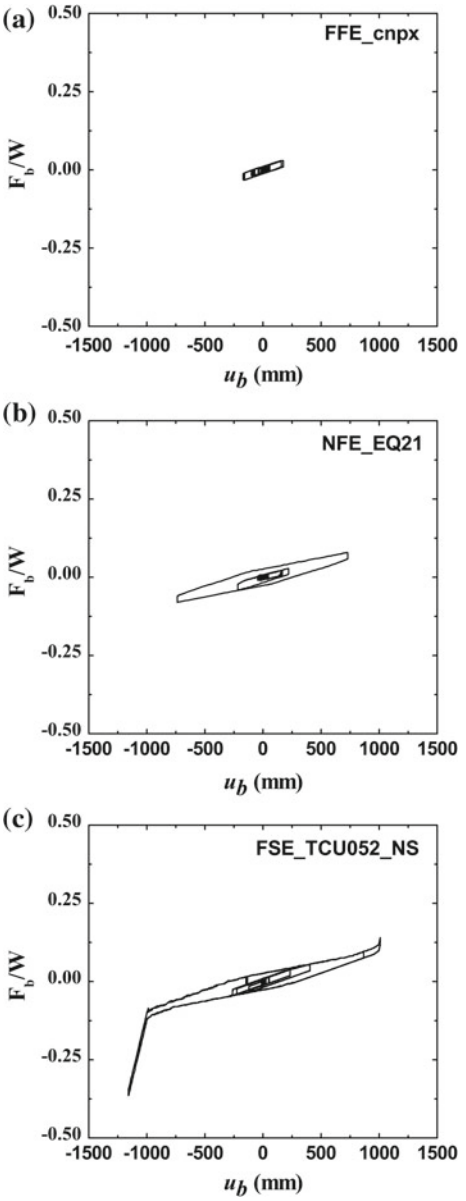

Fig. 2 Hysteretic behavior of all the elements of QTFP under **a** 1994 Northridge, **b** 1979 Imperial Valley, and **c** 1999 Chi–Chi earthquakes

effects and three fling step effect to achieve a wide range variation in frequency and intensities to understand the behavior comprehensively. For this study, following conclusions can be derived:

1. At the low input of ground motions (far-field ground motions), The QTFP bearing stiffens. By increasing the input it gets softe and again stiffens at higher input

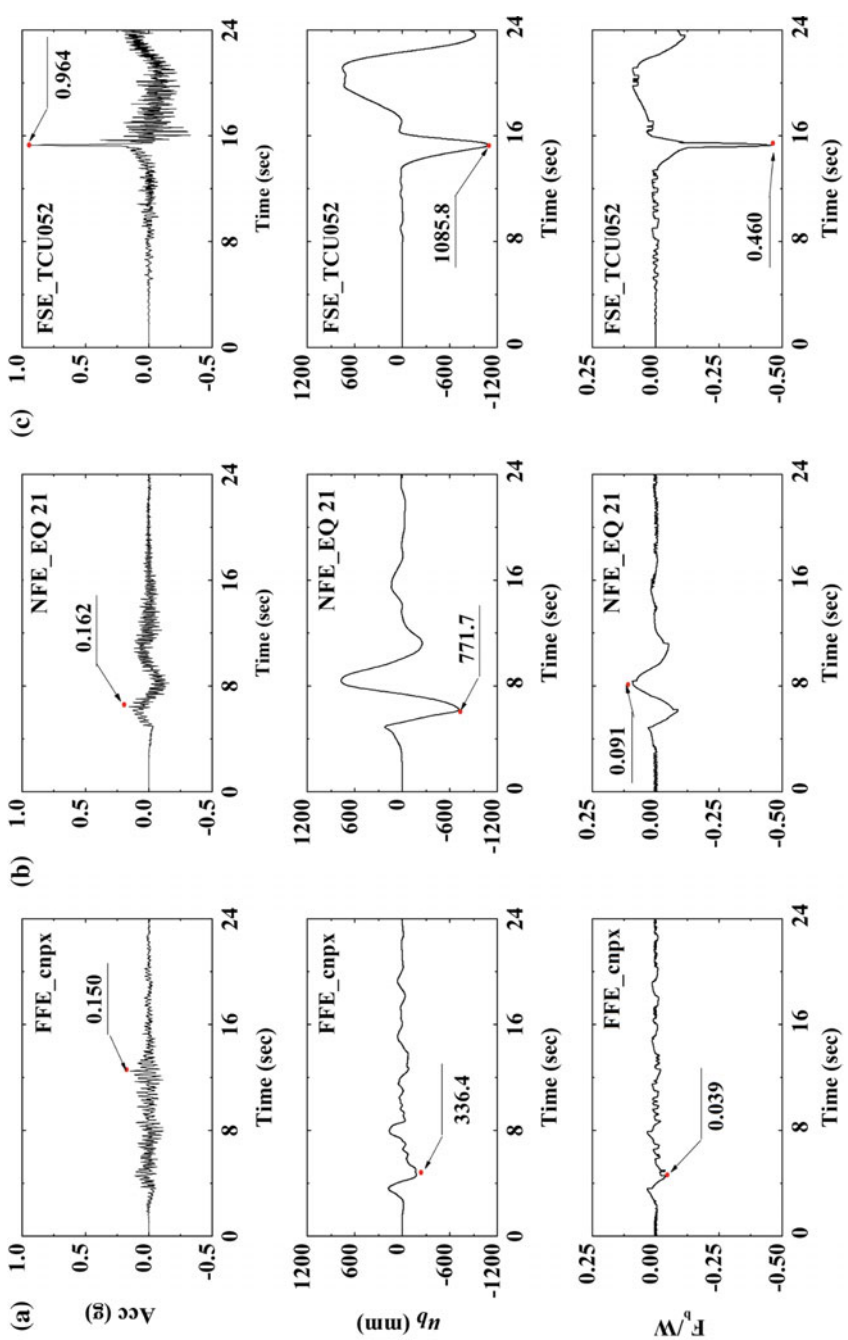

Fig. 3 Response of QTFP under **a** 1994 Northridge, **b** 1979 Imperial Valley, and **c** 1999 Chi–Chi earthquakes

of ground motions (near-fault ground motions). Thus, it shows highly adaptive behavior under different hazard level of earthquake.
2. The demand parameters increases significantly for near-fault ground motion compared to far-field motion despite lower value of peak ground acceleration of near-fault ground motion.
3. Compare to fling step having forward momentum only, near-fault directivity effect imposes higher demand due to forward and back ward momentum conveyed by the directivity pulse.

References

1. Mostaghel N, Tanbakuchi J (1983) Response of sliding structures to earthquake support motion. Earthquake Eng Struct Dynam 11(6):729–748
2. Gueraud R, Noel-Leroux JP, Livolant M, Michalopoulos AP (1985) Seismic isolation using sliding-elastomer bearing pads. Nucl Eng Des 84(3):363–377
3. Mostaghel N, Khodaverdian M (1987) Dynamics of resilient-friction base isolator (R-FBI). Earthquake Eng Struct Dynam 15(3):379–390
4. Tsai CS, Lin YC, Su HC (2010) Characterization and modeling of multiple friction pendulum isolation system with numerous sliding interfaces. Earthquake Eng Struct Dynam 39(13):1463–1491
5. Fenz DM, Constantinou MC (2006) Behaviour of the double concave friction pendulum bearing. Earthquake Eng Struct Dynam 35(11):1403–1424
6. Fenz DM, Constantinou MC (2008) Modeling triple friction pendulum bearings for response-history analysis. Earthquake Spectra 24(4):1011–1028
7. Becker TC, Mahin SA (2013) Approximating peak responses in seismically isolated buildings using generalized modal analysis. Earthquake Eng Struct Dynam 42(12):1807–1825
8. Lee D, Constantinou MC (2015) Quintuple friction pendulum isolator-behavior, modeling and validation. In: Technical Report MCEER-15-0007, Multidisciplinary Center for Earthquake Engineering Research. University at Buffalo, Buffalo, NY
9. Galesorkhi R, Gouchon J (2000) Near-source effects and correlation to recent recorded data. In: Proceedings, 6th U.S. National Conference on Earthquake Engineering, Seattle, Wash
10. Kalkan E, Kunnath SK (2006) Effects of fling step and forward directivity on seismic response of buildings. Earthquake Spectra 22(2):367–390
11. Constantinou M, Mokha A, Reinhorn A (1990) Teflon bearings in base isolation II: modeling. J Struct Eng 116(2):455–474

Element-Free Galerkin Method for Reinforced Timoshenko Beam on Elastic Foundation

Vivek Varshney, Sarvesh Chandra and Stephane Bordas

Abstract The aim of this paper is to present an efficient and reliable computational technique for the analysis of soil structure interaction problems. In this paper a reinforced Timoshenko beam resting on an elastic foundation subjected to distributed load and point load have been analysed by means of Element-Free Galerkin method (EFGM). This is one of the efficient mesh-free methods which needs only nodal data and does not need any nodal connectivity, which provides an advantage over the FEM. Its shape function is constructed by Moving least square approximation. Galerkin weak form is used to develop the discretized system of equations. EFGM poses difficulties in enforcing essential boundary conditions. To overcome this difficulty Lagrange Multiplier is used. The results presented in this paper are checked for validity, convergence and accuracy of numerical solutions and compared with the exact analytical solutions. The granular fill, soft soil, and geosynthetic reinforcements are considered as linear elastic materials. The geosynthetic reinforcements are modeled as cable elements fully bonded with the surrounding soil, thus neglecting any slip between the reinforcement and the soil.

Keywords Timoshenko beam · Winkler springs · Element-free galerkin method · Geosynthetic shear stiffness · Tension modulus

V. Varshney (✉) · S. Chandra
Civil Engineering Department, IIT Kanpur, Kanpur 208 016, India
e-mail: vivek27varshney@gmail.com

S. Chandra
e-mail: sarv@iitk.ac.in

S. Bordas
Civil Engineering Department, University of Glasgow, Glasgow G12 8QQ, Scotland
e-mail: bordas@civil.gla.ac.uk

A. Prashant et al. (eds.), *Advances in Computer Methods and Geomechanics*, Lecture Notes in Civil Engineering 55,
https://doi.org/10.1007/978-981-15-0886-8_52

1 Introduction

The problems of the beam resting on an elastic foundation are extensively studied by geotechnical, pavement, railway, mechanical, and aeronautical engineers. In geotechnical applications combined footing and strip footings are analysed and designed using this approach.

The analysis of interaction between foundations and supporting soil medium has been developed using three approaches given below:

1. Interaction between elastic bodies.
2. Interaction between an elastic medium and a rigid body.
3. Interaction between elastic bodies and structural elements.

Third situation is a special case of the general interaction problem which deals with the analysis of interaction between structural elements and idealized linearly deformable elastic media. These types of problems are taken into consideration in soil mechanics and foundation engineering where the solutions are applied to the analysis and design of structural foundations and flexible pavement systems. For the analysis of the soil-foundation interaction problem it is generally assumed that soil is homogenous, isotropic, and linearly elastic material and occupying a half space region. Linear elastic behavior of the supporting soil medium is presented by simplest mechanical model by Winkler (1867). Winkler foundation is termed as a system of closely spaced unconnected linear spring elements with spring constant k (modulus of subgrade reaction).

Bernoulli–Euler-beam theory [13] and Timoshenko beam theory [10] is generally used for modeling of beam elements. It has been assumed that plane cross sections remains plane and normal to the longitudinal axis after bending in Euler beam theory. This means that transverse shear strain is zero. This theory is well applicable for thin beams but for the analysis of thick beams one needs to go for Timoshenko beam theory in which transverse shear strain is taken in consideration. There are many practical situations in the field where reinforced granular beds are placed on top of a weak layer to reduce the load transfer on the weak soil and the settlement.

The reinforced granular fill can be simulated by a Timoshenko beam and the weak soil layer may be idealized as an elastic foundation of Winkler type [4, 11, 14].

Yin [15, 16] proposed a model for the interaction analysis of a reinforced structure and soil which is based on Timoshenko beam theory. The idealization of the problem is shown in Fig. 1. A closed form solutions for a finite beam subjected to uniform loading and an infinite beam subjected to a point load resting on elastic foundations was obtained. The aim of this paper is to present a numerical method which can be used as a substitute for complex mathematical formulations. Element-Free Galerkin Method (EFGM) is used for the analysis of this problem (Fig. 2).

The results obtained by this method are compared with the results obtained by Yin [15, 16] using closed form solutions.

Finite element method (FEM) is used widely as a computational tool to analyze all sorts of engineering problems related to solids and structures in past decades.

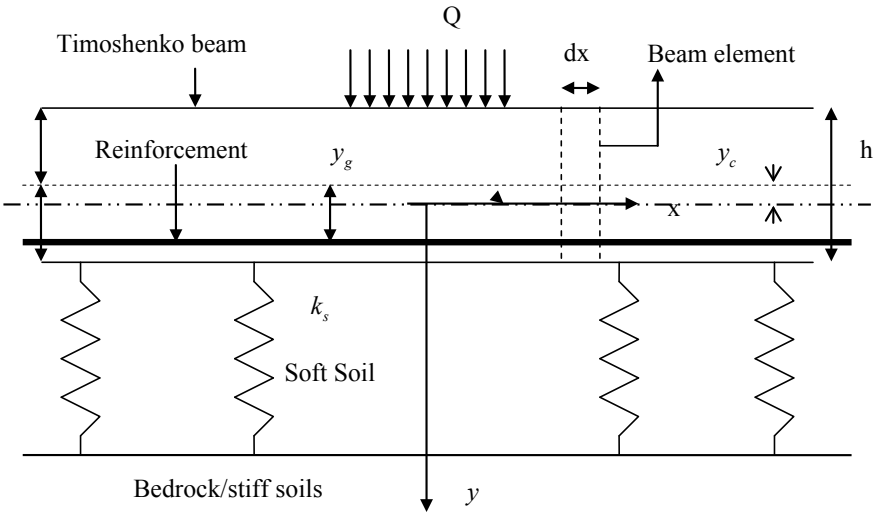

Fig. 1 1-D model of reinforced Timoshenko beam on Winkler foundation

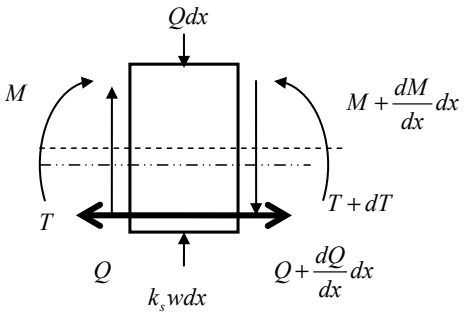

Fig. 2 Free body diagram of beam element

The main difficulties associated with FEM are choosing the type of elements with predefined connectivity and developing the mesh of adequate size. It is generally observed that the FEM is not well suited to problems having large deformations of materials.

In this paper the concept of mesh free method has been applied to a geotechnical engineering problem. The spatial domain of the problem is defined by a set of arbitrarily distributed nodes instead of elements. It is to be noted that in this method there is no mesh and hence connectivity is eliminated. It means one can add or remove nodes depending upon the stress concentration in the domain. There are several mesh free methods reported in literature and the method used in this paper is Element Free Galerkin Method (EFGM) [3, 6, 8, 12] which is a very versatile method.

EFGM was proposed by Belytschko et al. [1, 2] and the method needs no mesh for field variables but needs background mesh for integration purpose. In this method, Moving Least Square (MLS) approximation [7–9] is used for constructing shape functions of the trial and test functions. MLS is an effective technique for approximating a function using a set of scattered data. Galerkin weak form is used to develop the discretized system of equations. This method has difficulty in imposing essential boundary conditions exactly because the shape functions created by MLS approximations do not satisfy the Kronecker delta property. Hence to overcome this difficulty a special treatment is needed in terms of Lagrange Multipliers approach.

It has been seen that shear locking phenomenon commonly occurs in the analysis of Timoshenko beams if the length and thickness ratio of the beam is greater than 50. To eliminate shear locking Kanok-Nukulchai et al. [5] has given a method which uses a shape function for the rotation that is one order lower than that for the deflection. This is easily implemented within the EFGM since MLS shape functions are not tied to an element nodal structure, as in the FEM. Using high–order basis function and larger MLS weight function supports may alleviate, but not totally suppress, shear locking effects.

In this paper the results of the beam are presented for a case where no shear locking takes place but the methodology adopted is general and can handle cases where the shear locking is also present.

1.1 Method of Analysis

1.1.1 Moving Least Squares Approximation

Moving least square method has been used for construction of EFG shape functions for approximation of test and trial functions. Let $w(x)$ and $\psi(x)$ be the deflection and rotation variables for Timoshenko beam defined in the domain Ω. This beam is expressed by a line defined by its neutral axis in a 1D domain Ω. The beam is discretized into a set of nodes which are properly distributed along the neutral axis. This set of nodes is called as field nodes such that each node has a corresponding nodal variable in terms of deflection $w(x)$ and rotation $\psi(x)$. The local approximations of $w(x)$ and $\psi(x)$ at point x_q are written as

$$w^h(x, x_q) = \sum_{j=1}^{m+1} P_j(x) a_j(x_q) = P^T(x) a(x_q) \tag{1}$$

$$\psi^h(x, x_q) = \sum_{j=1}^{m} p_j(x) b_j(x_q) = p^T(x) b(x_q) \tag{2}$$

where m is the number of terms in the basis, $P(x)$ and $p(x)$ are the complete polynomial. $a_j(x)$ is the coefficient which are functions of the spatial coordinates x which

contains non constant coefficients. A quadratic basis in one dimension is provided by $m = 1$.

$$P^T(x) = [1\ x\ x^2] \text{ and } p^T(x) = [1\ x]$$

The unknown parameters $a_j(x)$ and $b_j(x)$ at any given point are determined by minimizing the difference between the local approximations at that point and the nodal parameters.

$$J = \sum_{i=1}^{n} \left[W(x - x_i) \left\{ P^T(x_i) a(x) - w_i \right\}^2 + W(x - x_i) \left\{ p^T(x_i) b(x) - \psi_i \right\}^2 \right] \quad (3)$$

where n is the number of points in the neighborhood of x for which the weight functions $W(x - x_i) \neq 0$. w_i and ψ_i are the nodal parameters at $x = x_i$. This neighborhood of x is called the domain of influence of x.

By differentiating J in Eq. (3) with respect to $a(x)$ and $b(x)$ followed by putting $\frac{\partial J}{\partial a} = 0$ and $\frac{\partial J}{\partial b} = 0$ gives following equations:

$$A_w(x)a(x) = B_w(x)U \text{ and } A_\psi(x)b(x) = B_\psi(x)\varphi$$

So

$$a(x) = A_w^{-1}(x)B_w(x)U \quad (4)$$

$$b(x) = A_\psi^{-1}(x)B_\psi(x)\varphi \quad (5)$$

Again,

$$A_w(x) = \sum_{i=1}^{n} W_i(x)P^T(x_i)P(x_i), \text{ where } W_i(x) = W(x - x_i) \quad (6)$$

$$B_w(x) = [W_1(x)P(x_1),\ W_2(x)P(x_2),\ W_3(x)P(x_3), \ldots\ldots\ldots\ldots\ldots\ldots\ldots.., W_n(x)P(x_n)] \quad (7)$$

$$A_\psi(x) = \sum_{i=1}^{n} W_i(x)p^T(x_i)p(x_i),\ W_i(x) = W(x - x_i) \quad (8)$$

$$B_\psi(x) = [W_1(x)p(x_1),\ W_2(x)p(x_2),\ W_3(x)p(x_3), \ldots\ldots\ldots\ldots\ldots\ldots\ldots.., W_n(x)p(x_n)] \quad (9)$$

$$U^T = [w_1, w_2, w_3, \ldots\ldots\ldots\ldots\ldots\ldots\ldots\ldots\ldots, w_n]$$
$$\varphi^T = [\psi_1, \psi_2, \psi_3, \ldots\ldots\ldots\ldots\ldots\ldots\ldots\ldots\ldots, \psi_n]$$
$$D = \{U,\ \varphi\}^T$$

we have

$$w^h(x) = \sum_{i=1}^{n}\sum_{j=1}^{m} P_j(x)(A_w^{-1}(x)B_w(x))_{ji} w_i = \sum_{i}^{n} \phi_{iw}(x) w_i \tag{10}$$

and

$$\psi^h(x) = \sum_{i=1}^{n}\sum_{j=1}^{m} p_j(x)(A_\psi^{-1}(x)B_\psi(x))_{ji} \psi_i = \sum_{i}^{n} \phi_{i\psi}(x) \psi_i \tag{11}$$

So the shape functions are written as

$$\phi_{iw} = \sum_{j=1}^{m} P_j(x)(A_w^{-1}(x)B_w(x))_{ji} \tag{12}$$

$$\phi_{i\psi} = \sum_{j=1}^{m} p_j(x)(A_\psi^{-1}(x)B_\psi(x))_{ji} \tag{13}$$

The partial derivatives of ϕ_{iw} and $\phi_{i\psi}$ can be obtained as

$$\phi_{iw,x} = \sum_{j=1}^{m} \left\{ P_{j,x}(A_w^{-1}B_w)_{ji} + P_j(A_{w,x}^{-1}B_w + A_w^{-1}B_{w,x})_{ji} \right\} \tag{14}$$

$$\phi_{i\psi,x} = \sum_{j=1}^{m} \left\{ p_{j,x}(A_\psi^{-1}B_\psi)_{ji} + p_j(A_{\psi,x}^{-1}B_\psi + A_\psi^{-1}B_{\psi,x})_{ji} \right\} \tag{15}$$

where $A_x^{-1} = -A^{-1}A_x$, A^{-1}.

2 Selection of Weight Function

Selection of the weight functions plays an important role in the performance of EFG method. These should be constructed such that these are positive and a unique solution $a(x)$ is guaranteed. These are monotonic decreasing functions with respect to distance from x to x_i which implies that the magnitudes decrease as the distance from x to x_i increases. It is obvious that weight function should be continuous and positive in its support. Different types of weight functions are used in EFGM. In this work quartic spline weight function has been used. The function is expressed as:

$$W_i(d) = \begin{cases} 1 - 6\left(\frac{d}{dm_i}\right)^2 + 8\left(\frac{d}{dm_i}\right)^3 - 3\left(\frac{d}{dm_i}\right)^4 & 0 \le d/dm_i \le 1 \\ 0 & d/dm_i > 1 \end{cases}$$

where dm_i is the size of the domain of influence of the ith node, the weight function can be written as a function of the normalized radius r which can be expressed as

$$r = d_i/dm_i \quad \text{where} \quad d_i = \|x - x_i\| \quad \text{and} \quad dm_i = d_{\max} c_i$$

Again $d_{\max}$ is a scaling parameter which is taken 2.0–4.0 for static analysis.c_i is a characteristic length that relates to the nodal spacing near the point at x_q.

3 EFG Formulation with Lagrange Multipliers for Timoshenko Beam

The equilibrium equations of the reinforced Timoshenko beam on an elastic foundation are given as

$$M = EI\frac{d\psi}{dx}, \quad V = GAk\left(\frac{dw}{dx} + \psi\right), \quad V - \frac{dM}{dx} = 0, \quad -\frac{dV}{dx} + k_s w = q \tag{16}$$

The governing equations in terms of the deflection w and rotation ψ become

$$-\frac{d}{dx}\left[GAk\left(\frac{dw}{dx} + \psi\right)\right] + k_s w = q \tag{17}$$

$$-\frac{d}{dx}\left(EI\frac{d\psi}{dx}\right) + GAk\left(\frac{dw}{dx} + \psi\right) = 0 \tag{18}$$

where w and ψ are termed as settlement and rotation which are two independent variables in Timoshenko beam. V and M are the shear force and moment due to reinforcement. G is the shear modulus, EI is the flexural rigidity, k_s is the coefficient of subgrade reaction in kN/m^3, q is the arbitrary pressure on the beam, A is cross-sectional area of the beam and k is the shear correction coefficient. k is taken into account for the difference in the constant state of shear stress in this theory and the parabolic variation of the shear stress predicted by elasticity theory through the beam thickness. If the aspect ratio of the beam is less than 20 then $\psi \neq -\left(\frac{dw}{dx}\right)$ which means that transverse shear strain is not zero. The shear forces and bending moments at the ends of the beam is expressed as in domain $\Omega = (0, L)$

$$V(0) = 0, \quad V(L) = 0, \quad M(0) = 0, \quad M(L) = 0 \tag{19}$$

It is also given that the essential boundary conditions are not prescribed then no need to apply Lagrange Multipliers.

The total potential energy functional of this beam is given as

$$\prod(w,\psi)=\int_{\Omega}\left[\frac{EI}{2}\left(\frac{d\psi}{dx}\right)^2+GAk\left(\frac{dw}{dx}+\psi\right)^2+\frac{1}{2}k_s w^2-wq\right]d\Omega+\int_{\Gamma_w}\lambda_w(w-\bar{w})d\Gamma_w$$
$$+\int_{\Gamma_\psi}\lambda_\psi(\psi-\bar{\psi})d\Gamma_\psi \tag{20}$$

The first term represents the elastic strain energy due to bending, the second term represents the elastic energy due to the transverse shear deformation, the third term is the strain energy stored in the elastic foundation, and the last term represents the work done by the distributed load. It is to be noted that in the first case both the ends of the beam are free implying that shear force and bending moment at both the ends are zero. Hence there is no potential energy function due to the shear force and bending moment at the ends. Using the principle of minimum total potential energy, the weak form is obtained as

$$\left.\begin{aligned}\int_{\Omega}\left[GAk\left(\psi+\frac{dw}{dx}\right)\frac{d\delta w}{dx}+k_s w\delta w-q\delta w\right]d\Omega=0\\ \int_{\Omega}\left[EI\frac{d\psi}{dx}\frac{d\delta\psi}{dx}+GAk\left(\psi+\frac{dw}{dx}\right)\delta\psi\right]d\Omega=0\end{aligned}\right\} \tag{21}$$

where δw and $\delta\psi$ are test functions such that w_1 V and ψ_1 M have the unit of work. The trial functions w and ψ do not satisfy the essential boundary conditions, so that these are imposed by Lagrange multipliers.λ is the vector of Lagrange multiplies introduced here to apply essential boundary conditions, on Γ. The Lagrange multiplier λ is expressed by

$$\lambda_w(x)=\sum_{I=1}^{n_\lambda}N_{Iw}(s)\lambda_I,\quad x\in\Gamma_w \tag{22}$$

$$\lambda_\psi(x)=\sum_{I=1}^{n_\lambda}N_{I\psi}(s)\lambda_I,\quad x\in\Gamma_\psi \tag{23}$$

where $N_I(s)$ a Lagrange interpolant and s is the arc length along the boundary. The governing discrete equations are obtained as

$$\begin{pmatrix}K & GG\\ GG & 0\end{pmatrix}\begin{Bmatrix}D\\ \lambda\end{Bmatrix}=\begin{Bmatrix}f\\ q\end{Bmatrix} \tag{24}$$

$$K=\begin{pmatrix}K_{ij}^{11} & K_{ij}^{12}\\ K_{ij}^{21} & K_{ij}^{22}\end{pmatrix} \tag{25}$$

$$K_{ij}^{11}=\int_{\Omega}\left(GAk\frac{dw_i}{dx}\frac{dw_j}{dx}+k_s w_i\psi_j\right)d\Omega \tag{26}$$

$$K_{ij}^{12} = \int_{\Omega} \left(GAk \frac{dw_i}{dx} \psi_j \right) d\Omega = K_{ji}^{21} \tag{27}$$

$$K_{ij}^{22} = \int_{\Omega} \left(EI \frac{d\psi_i}{dx} \frac{d\psi_j}{dx} + GAkw_i \psi_j \right) d\Omega \tag{28}$$

$$GG_{ik} = -\begin{bmatrix} \phi_{iw}(x_k) & 0 \\ 0 & \phi_{i\psi}(x_k) \end{bmatrix} \tag{29}$$

$$f = \int_{\Omega} \phi_{iw} q d\Omega \tag{30}$$

$$Q_k = -\int_{\Gamma_w} N_k \bar{w} d\Gamma \tag{31}$$

4 Results and Discussions

Two problems are analyzed and the results are presented below.

Example 1 Yin [15, 16] obtained a closed form solution for a finite reinforced Timoshenko beam on an elastic foundation under vertical pressure loading. In this paper the mesh free analysis for the same problem is presented. The results give the validity of mesh free method for this problem (Fig. 3).

Yin [15, 16] obtained a closed form solution for a finite reinforced Timoshenko beam on an elastic foundation under vertical uniform loading. In this paper the mesh free analysis for the same problem is presented. The results give the validity of mesh free method for this problem.

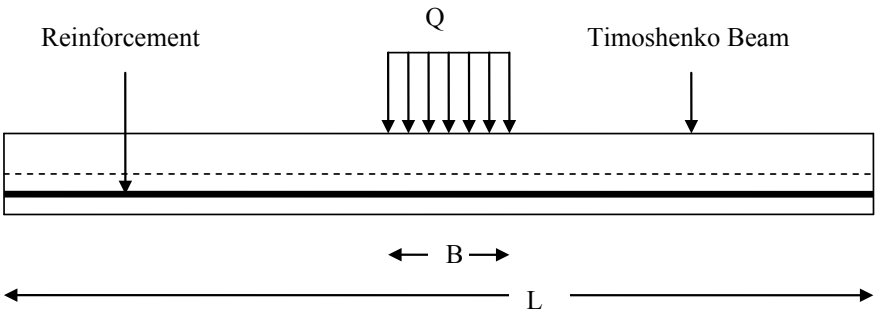

Fig. 3 Reinforced Timoshenko finite beam on elastic foundation

In this problem uniform loading applied is 1000 KN/m for length of $B = 0.1$ m vertically downward.

The length of the Timoshenko beam is taken 3 m, width is taken as unity and h is the thickness of the beam, taken as 0.64 m. yg is distance of the geosynthetic layer from the center line, taken as 0.24 m and yc is the distance of the neutral axis from the center line, taken as 0.146 m.

Tension stiffness, $E_g = 50000$ KN/m
Young's modulus of the beam, $E = 50000$ KN/m^2
Coefficient of subgrade reaction, ks $= 26666.7$ KN/m^3
Poisson's ratio, $\upsilon = 0.30$
Uniform loading, $P = 1000$ KN/m
Geosynthetic shear stiffness, $C = 26797.4$ KN/m

Element-Free Galerkin method has been used to analyze this problem. Four-point gauss quadrature is used to integrate stiffness matrix and force vector f. A convergence study is carried out to minimize the numerical error by varying the number of nodes. It has been observed that results are converging for 1041 nodes. The numerical results obtained by this method are compared with the close form solution of Yin [15, 16]. The maximum settlement at $x = 1.5$ m is 0.003109 m which having an error of 1.7%. As far as rotation is concerned at both the ends of the beam which is 0.00224, the error observed is 0.5%. The numerical result for reinforced tension is obtained at the center of the beam is 37.574 kN/m having error of 4.3%. All the results are presented in Figs. 4, 5, and 6.

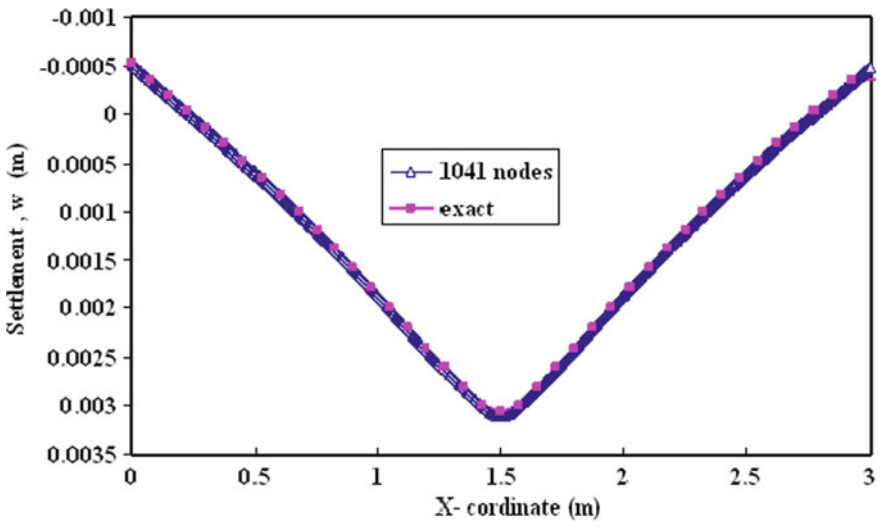

Fig. 4 Settlement along the length of beam and comparison with exact solution of Yin [15, 16]

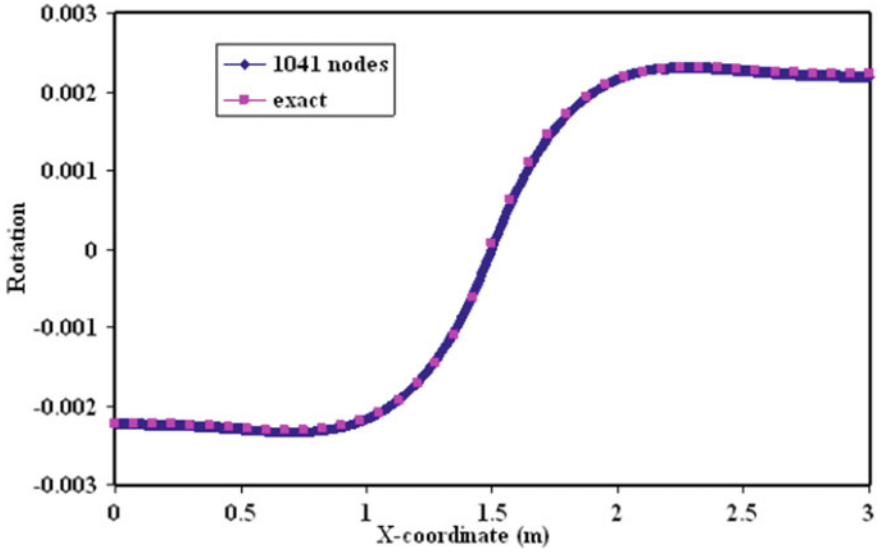

Fig. 5 Settlement along the length of beam and comparison with exact solution of Yin [15, 16]

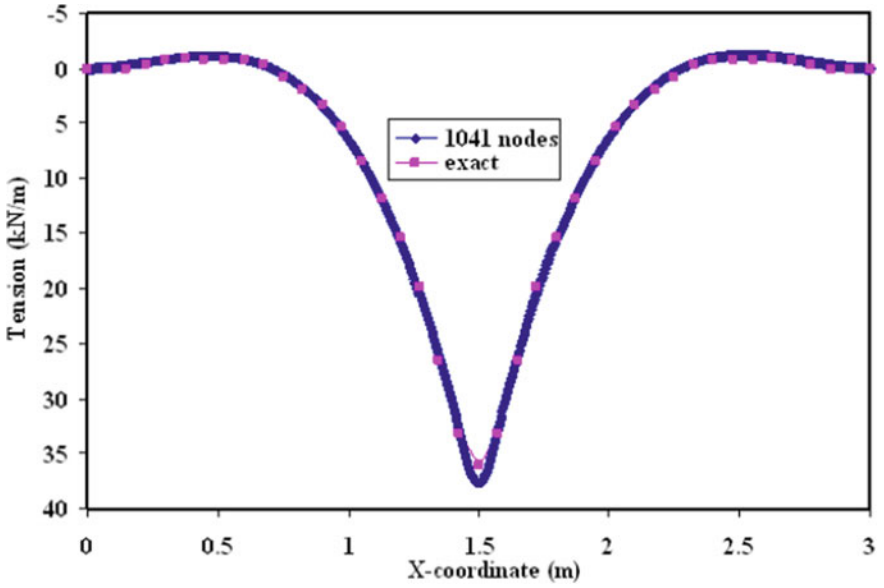

Fig. 6 Variation of reinforced tension along the length of beam

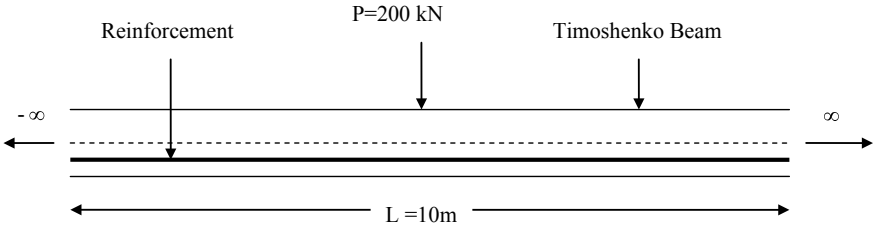

Fig. 7 Reinforced Timoshenko infinite beam on elastic foundation with point load

Example 2 In this problem, an infinite Timoshenko beam of length $L = 10$ m and unit width is placed on elastic foundation. A concentrated load $P = 1000$ kN is applied at the center of the beam. Geosynthetic sheet of thickness 0.02 m is provided horizontally 0.21 m from the central line of the beam, shown in dotted line. Thickness of the beam is taken as 0.62 m (Fig. 7).

Required data

E = Young's modulus of the beam = 1045 kN/m^2
k_s = coefficient of subgrade reaction = 263 kN/m^3
υ = Poisson's ratio = 0.49
P = 200 kN

The numerical results are obtained by EFG method [17] and compared with the exact solution of Yin [14, 15]. The results are presented in Figs. 8, 9, and 10. In Fig. 8 settlement at $x = 0$ is calculated as 0.2415 m having an error of 3.8% with the analytical solution. Numerical results are comparable with the exact solution throughout the length of the beam. For Rotation of the beam result obtained by EFG method is -0.1428 at $x = 4.4$ m which is shown in Fig. 9. Figure 10 is drawn for showing variation of the Tension of geosynthetic along the length of the beam. Tension T is obtained as 51.4946 KN/m at $x = 5$ having an error of 7.2%. All the results are presented in Figs. 8, 9 and 10.

5 Conclusions

In this paper Element-Free Galerkin Method (EFGM) is used for the analysis of a Timoshenko beam resting on an elastic foundation. Timoshenko beam is used to simulate the effect of shear for the modeling of compacted granular soil which is reinforced by means of geosynthetic. The soft soil is modeled by Winkler medium. Yin [15, 16] derived governing ordinary differential equations for Timoshenko beam (reinforced granular soil) on soft soil and its closed form solution was obtained. EFGM is tried as a numerical method to obtain the solution and the results are compared with the closed form solution. It is generally experienced that in linear analysis meshing is time consuming work in Finite Element method (FEM). To avoid

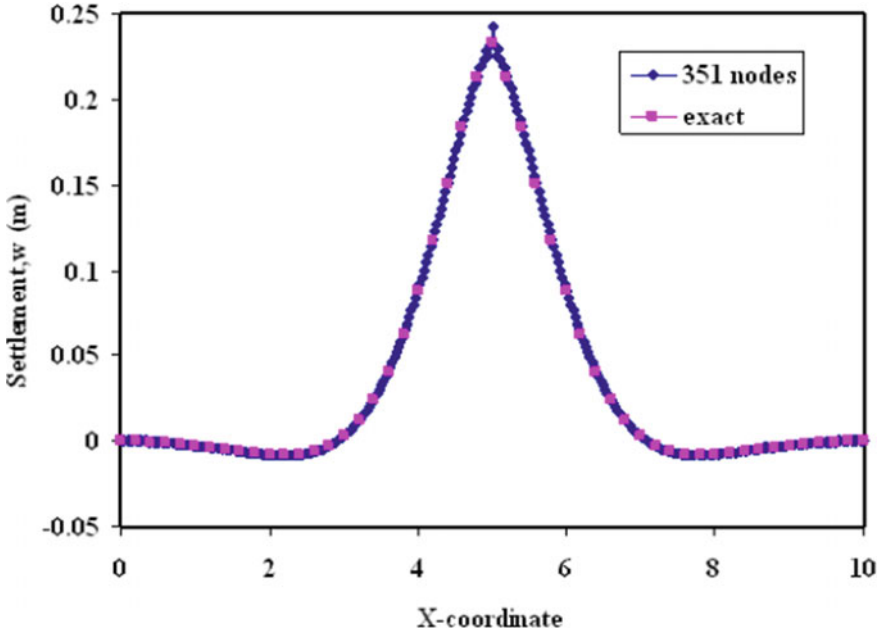

Fig. 8 Settlement along the length of beam

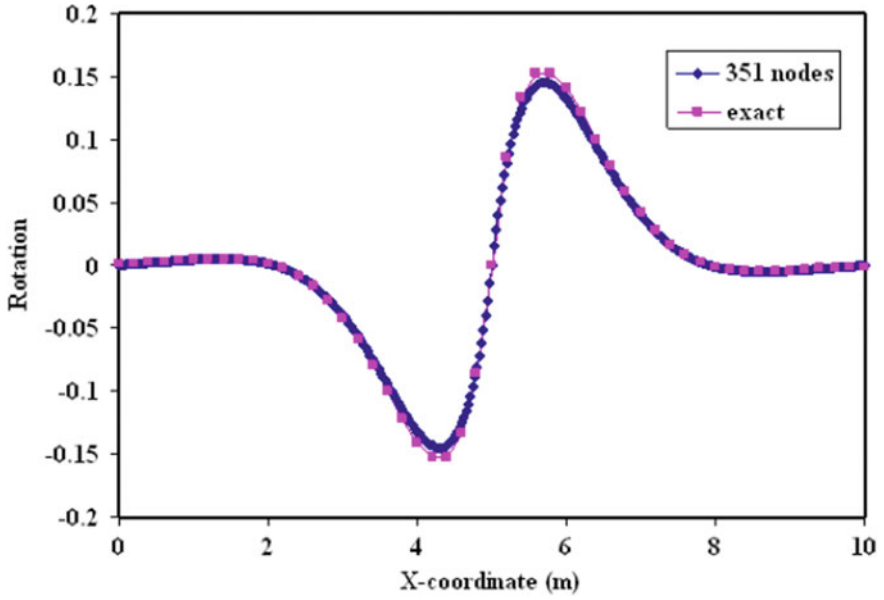

Fig. 9 Rotation along the length of beam

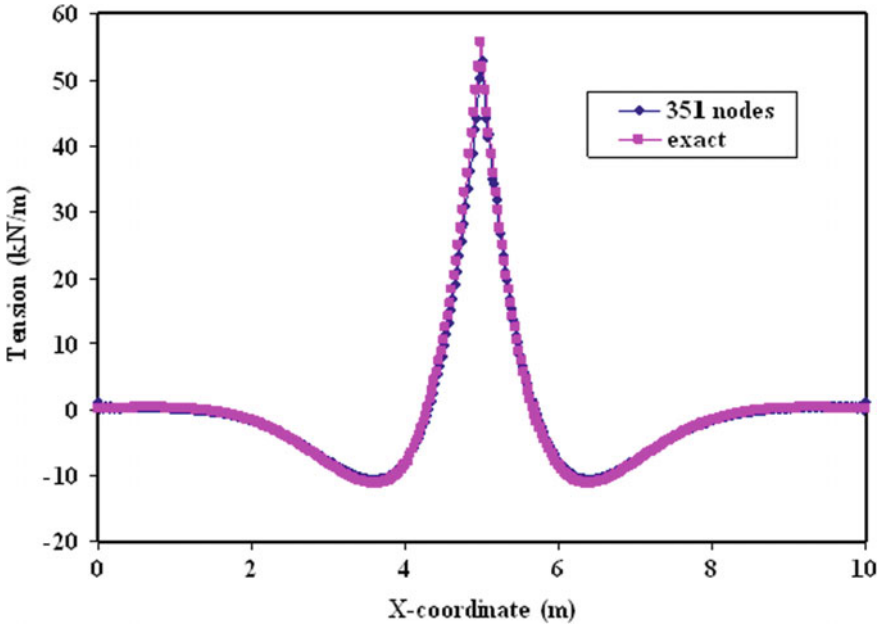

Fig. 10 Variation of reinforced tension along the length of beam

this EFG is used which does not require mesh nodes and elements and hence there is no need of connectivity. Two numerical examples are presented in this paper which shows good agreement with closed form solution. It has been observed that results converge very fast and accurately to exact solution with less number of nodes as compared to FEM. This paper consists of EFGM application in one dimension beam only and proper shape functions have been constructed for field variables to avoid shear locking. Mesh-free method can be used for complex soil structure interaction problems.

References

1. Belytschko T, Lu YY, Gu L (1994) Element-free Galerkin methods. Int J Numer Meth Eng 37:229–256
2. Dolbow J, Belytschko T (1998) An introduction to programming the Meshless element-free Galerkin method. Arch Comput Mech 5(3):207–241
3. Elouatouati A, Johnson DA (1999) A new approach for numerical modal analysis using the Element-Free method. Int J Numer Methods Eng 46:1–27
4. Hetenyi M (1946) Beams on elastic foundations. The University of Michigan Press, Ann Arbor, Michigan
5. Kanok- Nukulchai W, Barry W, Saran-Yasoontorn K, Bouillard PH (2001) On elimination of shear locking in the element-free Galerkin method. Int J Numer Meth Eng 52:705–725

6. Krongauz Y, Belytschko T (1998) Enforcement of essential boundary conditions in meshless approximation using finite elements. Comput Methods Appl Mech Eng 131:133–145
7. Lancaster P, Salkauskas K (1981) Surfaces generated by moving least squares methods. Math Comput 37:141–158
8. Liu GR (2003) Mesh free methods: moving beyond the finite element method. CRC Press, Boca Raton
9. Nguyen VP, Rabczuk T, Bordas S, Duflot M (2008) Meshfree methods: review and key computer implementation aspects. Math Comput Simul
10. Reddy JN (2005) An Introduction to the finite element method, 3rd edn. Tata McGraw-Hill, New Delhi
11. Selvadurai APS (1979) Elastic analysis of soil-foundation interaction: development of geotechnical engineering, vol 17. Elsevier Scientific, Amsterdam
12. Sunitha NV (2007) Fuzzy finite element and meshless methods for soil structure interaction problems. M. S. Thesis, IIT Madras, Chennai
13. Wang CM (1995) Timoshenko beam-bending solution in terms of Euler-Bernoulli solutions. J Eng Mech Div ASCE 121(6):763–765
14. Yankelevsky DZ, Eisenberger M (1986) Analysis of a beam column on elastic foundation. Comput Struct 23(3):351–356
15. Yin JH (2000a) Comparative modelling study on reinforced beam on elastic foundation. J Geotech Geo Environ Eng Div ASCE 126(3):265–271
16. Yin JH (2000b) Closed-form solution for reinforced Timoshenko beam on elastic foundation. J Eng Mech Div ASCE 26(8):868–874
17. Zuohui P (2000) Treatment of point loads in element free Galerkin method (EFGM). Commun Numer Methods Eng 16:335–341

Dynamic Lattice Element Modelling of Cemented Geomaterials

Zarghaam Haider Rizvi, Syed Husain Mustafa, Amir Shorian Sattari, Shahbaz Ahmad, Peter Furtner and Frank Wuttke

Abstract Cemented geomaterial due to inherent porosity and composition difference has many stress localization spots. These spots when they exceed the material limit locally form centres for crack nucleation and propagation. A vast pool of numerical and analytical methods is available, but these methods fail to solve the problem of wave motion at the granular level. The problem offers a daunting task in static or pseudo-dynamic loading but becomes highly challenging in a dynamic loading scenario. Here, in this paper, we present the lattice element method from the family of discrete element method to solve the problem of mechanical waves in rock mass or cemented granular material under dynamic excitation. The method offers a robust solution to the problem of crack initiation and propagation in a dynamic loading scenario. The lattice element method is capable of handling the nucleation, propagation, coalescence and branching of the cracks with relative ease. The method could be extended to impact loading and multiphysics scenarios in a straight-forward manner.

Keywords Lattice element method · Dynamic loading · Granular physics · Computational fracture mechanics

Z. H. Rizvi (✉) · A. S. Sattari · F. Wuttke
Geomechanics and Geotechnics, Kiel University, Kiel, Germany
e-mail: zarghaam.rizvi@ifg.uni-kiel.de

S. H. Mustafa
Department of Computer Engineering, Aligarh Muslim University, Aligarh, India

S. Ahmad
Zachry Department of Civil & Environmental Engineering, Texas A&M University, College Station, USA

P. Furtner
Vienna Consulting Engineers, Vienna, Austria

A. Prashant et al. (eds.), *Advances in Computer Methods and Geomechanics*, Lecture Notes in Civil Engineering 55,
https://doi.org/10.1007/978-981-15-0886-8_53

1 Introduction

For the natural or artificial cemented granular media, such as rock, soil and concrete, the location and distribution of the grains and bonds dramatically affects the dynamic characteristics. Microstructural contact laws based on Hertz contact model and multibody dynamics relying on Newton's' law for accelerating bodies offer a solid foundation for development and optimization of new knowledge for both mathematical and numerical solution of such a complex problem. The first attempt to numerically model the granular media with multibody interaction with circular particle and computation of macroscopic deformation was shown by Cundall and Strack [1]. Zhang and Evans [2] provided a rich review of different model setup schemes for the Discrete Element Method (DEM) and the limitation of such a model. The DEM models offer an implacable solution for large deformation problems but are limited in its ability for modelling of the microscopic intergranular interaction and nucleation, propagation, fingering, coalescence and branching of the cracks in cemented granular media. A more challenging scenario arises in case of cemented granular media developing cracks subjected to a dynamic load. Modelling of such a system considering the mesoscale geometry, which primarily influences the wave motion and cracks propagation behaviour is a daunting task. The extended finite element method (XFEM) that allow for arbitrary cohesive crack propagation and the embedded strong discontinuity finite element method (ED-FEM) both treat with the cracks in a mesh independent approach due to their enrichment. The computation costly tracking algorithms are often used with these methods, mainly to solve the problematic crack phenomena in dynamics, such as bifurcating, also shown in Nikolić et al. [3]. The phase field models for the granular system requires mammoth computational resource and many fitting parameters are included in an ad hoc manner. Therefore, Lattice element method, derived from condense physics matter which offers an accurate and computationally efficient solution is considered here.

The Lattice Element Method (LEM), was first introduced by Hrennikoff [4] and later by Kawai [5], in which they developed the truss framework to discretize the elastic continua. The lattice model is defined as an assembly of discrete cohesive link elements for the representation of a structural solid. This simplification of continua is not a rudimentary assumption for modelling of complex solids or structures and the approach results to a lighter computational cost. Moreover, efficient representation of some aspects, which are not easily tackled with simplicity and successful description of the localized failure and cracking mechanisms are the most critical features that led to the rapid development of lattice models shown in Nikolić et al. [6]. Failure and cracking mechanisms can be simulated straightforwardly usually by detecting if any lattice element, which represents the cohesive force between the particles, has reached a specific failure criterion. These failure criteria could be based on Linear Elastic Fracture Mechanics (LEFM) shown in Wuttke et al. [7], Rizvi et al. [8–10] or the classical failure models Khan et al. [11]. Once the critical failure value is reached, a cohesive fracture is initiated, leading to the gradual separation of the crack surfaces across the cohesive zone. This simple assumption helps in bypassing

the issue of the singularity of the stress at the crack tip, which is present in linear elastic fracture mechanics. Additionally, with lattice models, it is possible to simulate multiple cracks without worrying about numerous crack interactions.

Despite being applied mostly to quasi-static loading conditions, the lattice elements can also be used for simulation of impact problems as well as shown in Nikolić et al. [3]. The broad applicability of this model is ranging from the quasi-static uniaxial loading and shearing of geomaterials to the dynamic fragmentation due to explosion, impact and collision of solids. The model is suitable for impact simulations in which cracks occur as a result of large movements of the rigid Voronoi particles. However, the applicability of these models is limited to a very regular type of grain sizes. Karavelić et al. [12] Here, we present a lattice element model for a full grain size range capable of capturing wave motion in plain and cracked cemented granular matter at a meagre computational cost.

2 Mesh Generation and Mathematical Formulation

To generate the granular assembly, a random set of points are generated in a Euclidean plane and the nearest neighbour points are computed using the Voronoi tessellation algorithm (Fig. 1). For a set of random points $P = \{p_1, \ldots, p_n\} \subset \mathbb{R}^2$, where $2 < n < \infty$ and $x_i \neq x_j$ for $i \neq j, i, j \epsilon I_n$. The region by Eq. (1) is the Voronoi polygon for the node p_i.

$$V(p_i) = \left\{x \| x - x_i \| \leq \left\| x - x_j \right\| \text{for } j \neq i,\ j \in I_n \right\} \tag{1}$$

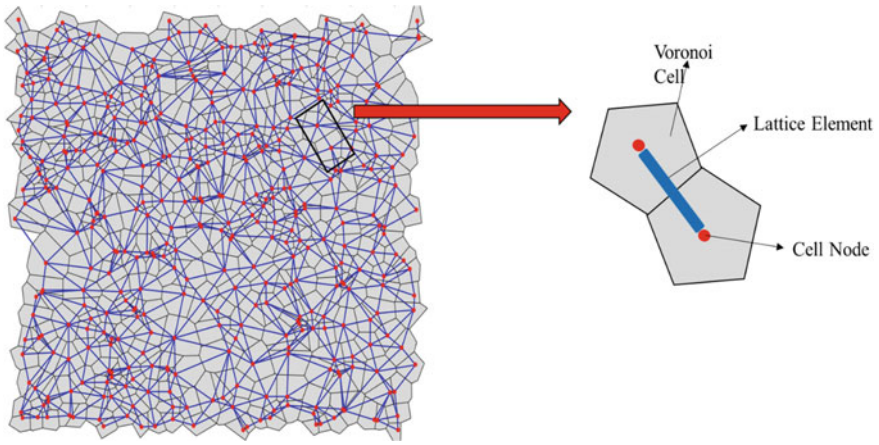

Fig. 1 Cell nodes, Voronoi cells and Lattice elements. Voronoi Algorithm is used to find the nearest neighbours and Delaunay triangulation to connect the neighbouring nodes to form the lattice elements

The set of all the polygons thus generated for the nodes p_i are the PoissionVoronoi diagram. The dual tessellation of the Voronoi diagram is generated to form the connections among the neighboring Voronoi cells. This triangulation scheme is called the Delaunay triangulation. Mathematically, *V(P)* be the Voronoi diagram generated by a set of n distinct points $P = \{p_1, \ldots, p_n\} \subset \mathbb{R}^2$, $3 \leq n < \infty$ that satisfies the non-collinearity assumption (D_1); $Q = \{q_1, \ldots, q_{nv}\}$ be the set of Voronoi vertices in V; and $\{x_{i1}, \ldots, x_{ik1}\}$ be the location vectors of the generator points whose Voronoi polygons share a vertex q_i [13].

$$T_i = \left\{ x | x = \sum_{j=1}^{k_i} \lambda_j x_{ij}, \text{ where } \sum_{j=1}^{k_i} \lambda_j = 1, \lambda_j \geq 0, j \in I_{k_i} \right\} \tag{2}$$

$$D = \{T_1, \ldots, T_{nv}\} \tag{3}$$

Equation (3) represents the *Delaunay triangulation* of the represented points.

The material properties are assigned to the Voronoi cells and then transferred to the elements thus generated by the Delaunay triangulation scheme shown in Rizvi et al. [13] and Shrestha et al. [14]. Material damping is not considered here.

For the dynamic simulation, the equation of motion for each element is solved with Newmark beta method. For a forced undamped system, the equation of motion is given as

$$M\ddot{u} + Ku = F(t) \tag{4}$$

where $\boldsymbol{M}$ and $\boldsymbol{K}$ are the mass and the stiffness matrices terms and *F(t)* is the applied time dependent force.

2.1 Mass Matrix Generation

The mass matrix or the consistent mass matrix (CMM) is generated either by lumping the mass at the nodes or by following the variation mass lumping (VMM) scheme. The VMM scheme is also implemented in the finite element method for dynamic simulations.

The element mass M^e is computed using the following equation:

$$M_e = \int \rho \left[N_v^e \right]^T N_v d\Omega \tag{5}$$

If the shape function are identical, that is, $N_v^e = N^e$, the mass matrix is called the consistent mass matrix (CMM) or M_c^e.

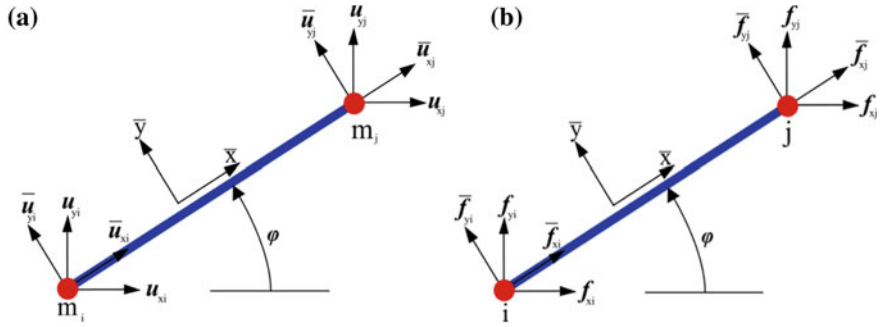

Fig. 2 **a** Bar element with diagonally lumped mass moving in 2D. **b** The transformation of node displacement and force components from the local system $\bar{u}_x, \bar{u}_y$ to the global system u_x, u_y

$$M_c^e = \int_0^l \rho A [N^e]^T N^e dx = \frac{1}{4}\rho l A \int_{-1}^{1} \begin{bmatrix} 1-\xi \\ 1+\xi \end{bmatrix} \begin{bmatrix} 1-\xi & 1+\xi \end{bmatrix} d\xi \tag{6}$$

where ρ is the density assigned to the Voronoi cells and A and l are the area and the length of the lattice elements.

The elemental mass matrix is symmetric, physical symmetric, and complies with the condition of conservation and positivity. To obtain the global mass matrix, a congruent transformation is applied. In contrast to the stiffness matrix, translational masses never vanish. All the translational masses are retained in the local mass matrix. The global transform is achieved through the following equation:

$$\bar{M}_c^e = \left[T^e\right]^T \left[M_c^e\right] \left[T^e\right]$$

$$M_c^e = \frac{1}{6} m^e \begin{bmatrix} 2 & 1 & 0 & 0 \\ 1 & 2 & 0 & 0 \\ 0 & 0 & 2 & 1 \\ 0 & 0 & 1 & 2 \end{bmatrix}$$

2.2 *Element Stiffness Matrix*

The force displacement component of a truss element is given by the spring relation

$$\{F\} = [K]\{U\} \tag{9}$$

The vectors $\{F\}$ and $\{U\}$ are the member joint force and member joint displacement, respectively shown in Fig. 2. The member stiffness matrix or the local stiffness

matrix is $[K]$. For a truss element it is given by

$$[K] = \frac{EA}{L}\begin{bmatrix} 1\,0 & -1\,0 \\ 0\,0 & 0\,\,0 \\ -1\,0 & 1\,0 \\ 0\,\,0 & 0\,0 \end{bmatrix} \tag{10}$$

After applying the congruent transformation, the member stiffness matrix in global coordinates are given as

$$\left[K^e\right] = \left[T^e\right]^T [K]\left[T^e\right] \tag{11}$$

$$K^e = \frac{E^e A^e}{L^e}\begin{bmatrix} l^2 & lm & -l^2 & -lm \\ lm & -m^2 & -lm & -m^2 \\ -l^2 & -lm & l^2 & lm \\ -lm & -m^2 & lm & m^2 \end{bmatrix} \tag{12}$$

where $l = \cos\varphi^e$, $m = \sin\varphi^e$ and φ^e is the orientation angle as shown in Fig. 2.

The equation of motion for the linear system of equations is solved with the Newmark beta method due to its unconditional stability. The displacement and the velocity terms for the next time are calculated as follows:

$$u_t = u_{t-\Delta t} + \Delta t\dot{u}_{t-\Delta t} + \left(\frac{1}{2} - \beta\right)\Delta t^2\ddot{u}_{t-\Delta t} + \beta\Delta t^2\ddot{u}_t \tag{13}$$

$$\dot{u}_t = \dot{u}_{t-\Delta t} + (1-\gamma)\Delta t\dot{u}_{t-\Delta t} + \gamma\Delta t\ddot{u}_t \tag{14}$$

We follow the average acceleration approach with $\beta = 1/4$ and $\gamma = 1/2$.

The Newmark beta method solves the algebraic form of the equation of motion (EOM) of undamped forced vibration at the end time interval $t + \Delta t$.

$$F_{t+\Delta t} = \boldsymbol{M}\ddot{u}_{t+\Delta t} + \boldsymbol{K}u_{t+\Delta t} \tag{15}$$

The stiffness and the mass matrices are computed in the following fashion to reduce in the form of Eq. (9)

$$\hat{\boldsymbol{K}} = \boldsymbol{K} + a_0\boldsymbol{M} \tag{16}$$

where $\hat{K}$ is the *effective stiffness matrix* and $a_0 = \frac{6}{\gamma\Delta t^2}$.

Similarly, the effective load vector at time $t + \Delta t$ is calculated as in (17).

$$\hat{F}_{t+\Delta t} = F_{t+\Delta t} + M(a_0 u_t + a_2\dot{u}_t + a_3\ddot{u}_t) \tag{17}$$

Here, $a_2 = \frac{1}{\gamma\Delta t}$ and $a_3 = \frac{1}{2\gamma}$.

The above simplification leads to the algebraic form

$$\left\{\widehat{F}_{t+\Delta t}\right\} = \left[\hat{K}\right]\{U_{t+\Delta t}\} \tag{18}$$

From the above equation, displacement of each node is calculated for every time step.

The natural frequency of the system is calculated as given below

$$\omega^2[M]\phi = [K]\phi \tag{19}$$

$$\omega^2 = \mathrm{eig}\left([M]^{-1}[K]\right) \tag{20}$$

3 Results and Discussion

Three different systems are generated with the defined boundary conditions, as shown in Fig. 3a–c. A granular assembly is generated with the Voronoi tessellation and Delaunay triangulation, as explained in Sect. 2. For the first scenario (Fig. 3a), 550 cell points have been used. The other two simulations are performed with 6400 points. MATLAB programming environment is used for computation. As reported earlier in literature Nikolic et al. [3, 6], Rizvi et al. [8] the mesh dependence response of the method is not significant and will be dealt in detail in future works.

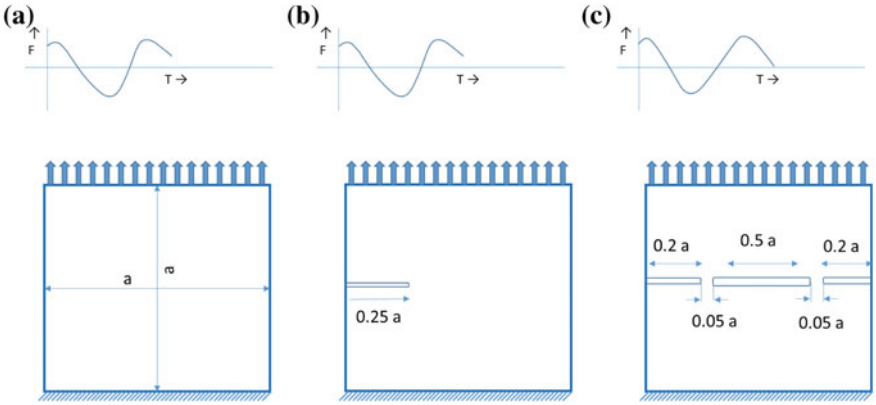

Fig. 3 The schematic diagrams of the boundary conditions for the simulations. **a** A cemented square plate with side $a = 1$ cm. **b** A square cemented granular plate with a single crack of 0.25 a length. **c** Two granular systems connected with two bridges of 0.05 a length each. A harmonic force is applied at the top and the bottom is held fixed

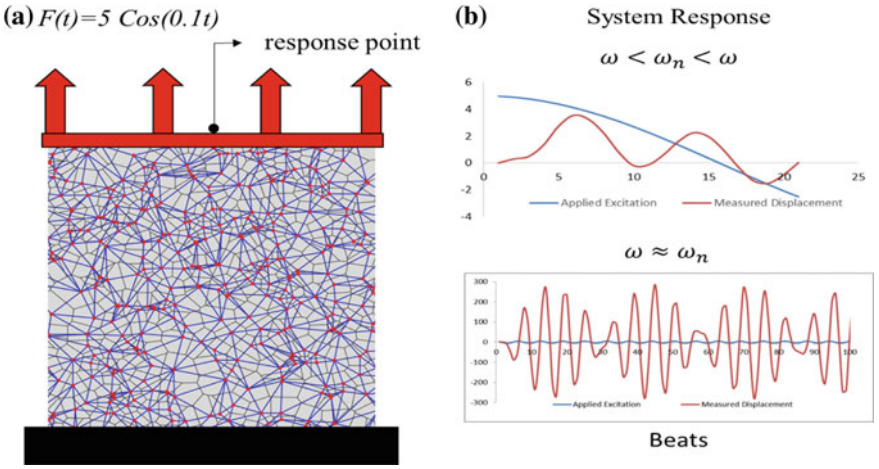

Fig. 4 **a** Assembly of the granular system and the applied loading with the boundary condition. **b** Response of system at excitation frequency away from the resonance frequency (top) and (bottom) near to the resonance frequency ω_n. Beat formation is recognisable at frequencies close to the excitation frequency

The above-generated system is subjected to a time-harmonic excitation, as shown in the Fig. 3a. The response of the system is measured at the top. The bottom nodes are fixed, and the excitation is applied to the top nodes.

The natural frequency of the system is calculated from Eq. (20). The system is excited to a frequency far from the resonant frequency. Figure 4b shows the response of the system. The excitation force is shown with a blue line, and the computed response at the top is plotted in red. As the excitation frequency is brought closer to the natural frequency of the system, beats are observed (Fig. 4b). This confirms the validity of the method.

Figure 5 shows the movement of mechanical waves in a cemented granular system. A time depended force, as shown in Fig. 3 is applied at the top surface, and the displacement of the nodes are plotted. This indicates the formation of high and low displacement zones. The phenomenon of wave movement is puffed rice grains has been investigated, and the creation of a band has been reported in Guillard et al. [15]. A similar pattern is observed here too (Fig. 5). After the first cycle at time $t = 25$, the system does not return to its original position. A residual negative strain in the system remains. A further investigation with voids and different density particles will be reported elsewhere.

Figure 6 shows the response of a cracked cemented granular assembly subject to the same cosine loading (Fig. 3b). The presence of a crack modifies the wave path, and the existing crack behaves as a stress concentrator. A similar result is reported with existing cracks in a homogeneous plate with the Boundary Element Method (BEM) shown in Rizvi et al. [16]. However, it is impossible to capture the intra and intergranular response with BEM. The simulation in Fig. 6 shows the modification in

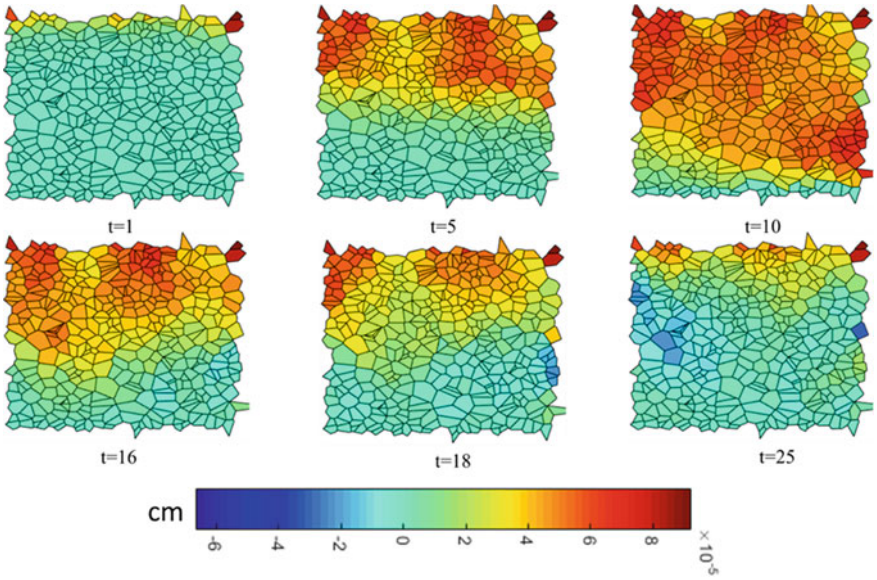

Fig. 5 Propagation of waves in the cemented granular media. The figure shows the response of a cosine excited wave of the system. The red colour shows the maximum amplitude and the blue the minimum

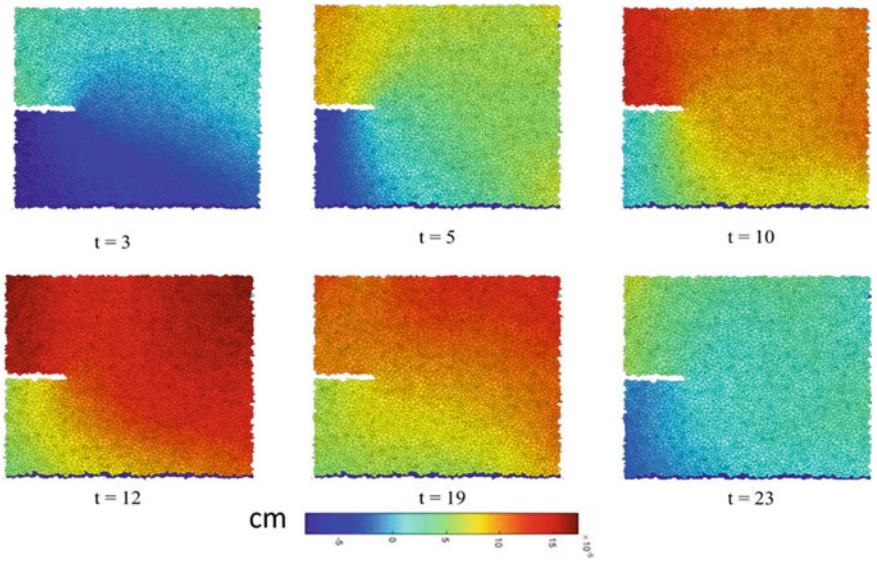

Fig. 6 Propagation of waves in the cemented granular media. The figure shows the response of a cosine excited wave of the system. The excitation is applied at top and bottom is held fixed. The red colour shows the maximum amplitude and the blue the minimum

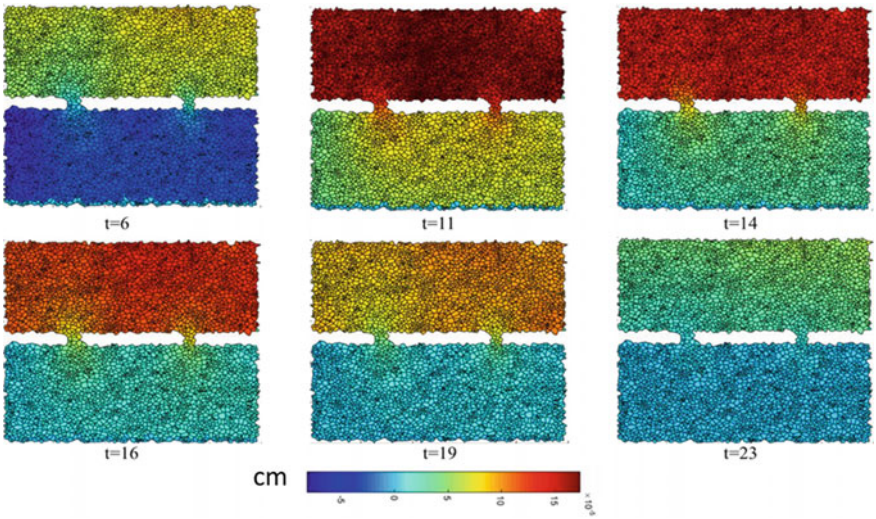

Fig. 7 Mechanical wave propagation in two granular cemented blocks with two contact points. The excitation is applied at top of the top block and bottom is held fixed. The dynamic lattice element method is capable of capturing this complex response with ease

the near and far field of the existing crack. The method combined with conventional lattice element methods is capable of modelling crack initiation and propagation. These results will be reported elsewhere.

Figure 7 shows two cemented granular blocks connected with two granular pillars. The top surface of the top block is excited with the harmonic force, as explained in Fig. 3c. The bottom surface of the base block is held fixed. The waves started at the top block travels through the granular pillars to the lower block. The movement of mechanical waves in such a non-trivial system is captured with relative ease.

4 Conclusion

The dynamic lattice element method is reported here for cemented granular medium, and the following conclusions are drawn from this study.

1. Lattice element method coupled with average acceleration Newmark beta method is capable of solving the mechanical wave movement with relative ease and at a low computational cost.
2. The pre-existing cracks modify the near and far field displacement and act as stress concentrators and distributors.
3. Wave motion in cemented granular media with existing cracks are modelled easily, which offers computational and mathematical challenges in other numerical and analytical methods.

Acknowledgements Z. H. R, F. W and P. F want to acknowledge the *Marie Curie* project *ExchangeRisk* (Grant No. 691213) for financial support. A. S. S acknowledge the Grant GeoMInt (03G0866B). Z. H. R acknowledges and thanks *Vienna Consulting Engineers ZT GmbH* for hosting the research work. ZHR and SHM prepared and communicated the manuscript.

References

1. Cundall PA, Strack ODL (1979) A discrete numerical model for granular assemblies. Géotechnique 29(1):47–65
2. Zhang L, Evans TM (2018) Boundary effects in discrete element method modeling of undrained cyclic triaxial and simple shear element tests. Granular Matter 20:60
3. Nikolić M, Do XN, Ibrahimbegovic A, Nikolić Z (2018) Crack propagation in dynamics by embedded strong discontinuity approach: enhanced solid versus discrete lattice model. Comput Methods Appl Mech Eng 340:480–499
4. Hrennikoff A (1941) Solution of problems of elasticity by the framework method. ASME J Appl Mech 8:A619–A715
5. Kawai T (1978) New discrete models and their application to seismic response analysis of structures. Nucl Eng Des 48(1):207–229
6. Nikolić M, Karavelić E, Ibrahimbegovic A, Miščević P (2018) Lattice element models and their peculiarities. Arch Comput Methods Eng 25(3):753–784
7. Wuttke F, Sattari AS, Rizvi ZH, Motra HB (2017) Advanced meso-scale modelling to study the effective thermo-mechanical parameter in solid geomaterial. In: Advances in laboratory testing and modelling of soils and shales (ATMSS). Springer Series in Geomechanics and Geoengineering. https://doi.org/10.1007/978-3-319-52773-4_9
8. Rizvi ZH, Nikolic M, Wuttke F (2019a) Lattice element method for simulations of failure in bio-cemented sands. Granular Matter 21:18. doi:https://link.springer.com/article/10.1007/s10035-019-0878-6
9. Rizvi ZH, Shrestha D, Sattari AS, Wuttke F (2018a) Numerical modelling of effective thermal conductivity for modified geomaterial using Lattice Element Method. Heat Mass Transf 54(2):483–499. doi:https://link.springer.com/article/10.1007%2Fs00231-017-2140-2
10. Rizvi ZH, Wuttke F, Sattari AS (2018b) Dynamic analysis by lattice element method simulation. In: Proceedings of China-Europe conference on geotechnical engineering, pp 405–409. doi:https://doi.org/10.1007/978-3-319-97112-4_91
11. Khan MA, Rizvi ZH, Panda S (2018) Effect of material and geometrical parameters on peeling rip-off failure—numerical study. Mater Today Proc. 5(9):19400–19409. https://www.sciencedirect.com/science/article/pii/S2214785318314238
12. Karavelić E, Nikolic M, Ibrahimbegovic A, Kurtović A (2019) Concrete meso-scale model with full set of 3D failure modes with random distribution of aggregate and cement phase. Part I: formulation and numerical implementation. Comput Methods Appl Mech Eng 344:1051–1072. doi:https://doi.org/10.1016/j.cma.2017.09.013
13. Rizvi ZH, Sembdner K, Suman A, Giri Prasad MJ, Wuttke F (2019b) Experimental and numerical investigation of thermo-mechanical properties for nano-geo composite. Int J Thermophys 40:54
14. Shrestha D, Rizvi ZH, Wuttke F (2019) Effective thermal conductivity of unsaturated granular geocomposite using Lattice Element Method. Heat Mass Transf 55(6):1671–1683. doi:https://link.springer.com/article/10.1007/s00231-018-02544-3
15. Guillard F, Golshan P, Shen L, Valdes JR, Einav I (2015) Dynamic patterns of compaction in brittle porous media. Nat Phys 11(10):835–838
16. Rizvi ZH, Khan MA, Sembdner K, Husain SF (2018c) Numerical modelling of crack wave interaction with BEM. Mater Today Proc 5(14):28253–28261. https://www.sciencedirect.com/science/article/pii/S2214785318323587

Effect of Stabilization on Characteristics of Subgrade Soil: A Review

Pritam Sinha and Kannan K. R. Iyer

Abstract Scarcity of suitable subgrade soil for developing infrastructure facilities has led to need for improving the properties of available soil. The soil can be improved by stabilization with pozzolonic materials (viz., cement, lime, fly ash, etc.) or by reinforcing the soil with inclusions such as geosynthetics material. The present work reviews the effect of soil stabilization (viz., influence of stabilizer content, curing period, thickness of stabilization) on soil subgrade characteristics like compressive strength, modulus of subgrade reaction, California bearing ratio, elastic modulus, settlement, swelling and shrinkage, optimum moisture content, maximum dry density and consistency limits. The review of earlier studies reveals that lime is more popular for cohesive soil stabilization with optimum lime content reported as 4–5%. Other additives such as cement, fly ash and chemical stabilizers have also been used in addition to lime for soil stabilization. The unconfined compressive strength and modulus of elasticity of soil is significantly improved due to addition of stabilizer and proper curing time. The improvement in compressive strength is higher for soft soil as compared to stiff soil. The modulus of subgrade reaction increases with increase in thickness of stabilized soil. Further, significant increase in California bearing ratio is observed for stabilized soils as compared to unstabilized soils. Soil stabilization reduces plasticity index and maximum dry density of soil, while optimum moisture content increases. This paper present the synthesis of effect of stabilization on different soil characteristics and highlights the recent developments in utilization of industrial residue and sustainable materials for soil stabilization.

Keywords Stabilization · Subgrade soil · Soil characteristics · Sustainable materials

P. Sinha · K. K. R. Iyer (✉)
Department of Civil Engineering, Institute of Infrastructure Technology Research and Management, Near Khokhra Circle, Maninagar (East), Ahmedabad 380026, India
e-mail: kannaniyer@iitram.ac.in

A. Prashant et al. (eds.), *Advances in Computer Methods and Geomechanics*, Lecture Notes in Civil Engineering 55,
https://doi.org/10.1007/978-981-15-0886-8_54

1 Introduction

In recent years, soil stabilization has gained wide acceptance due to scarcity of suitable soil for various infrastructure projects and the significant improvement in soil properties achieved by soil stabilization. The main objective of soil stabilization is to improve the strength of the soil and reduce probable settlement [31] especially for soft soils, expansive soils as well as for soils with high plasticity and moisture content. The different materials used for soil stabilization are lime, cement, fly ash, other chemical stabilizers or their combination (DPSMS Report [5]). Lime is used for low strength cohesive soil [28, 30] and cement is preferred for cohesionless soil [28]. Chemical stabilization is suitable for clay and silt which loses strength with increase in water content. By stabilization, the strength and durability properties of soil can be improved and undesirable soil response such as change in strength and volume change behavior due to change in water content can be minimized.

Lime is one of the most widely used chemical stabilizers [30]. It reduces plasticity and improves the shear strength of cohesive soil. In recent years, utilization of fly ash for soil stabilization is increasing. Fly ash basically is an industrial waste with pozzolonic reactive property and is economically viable for soil stabilization. Fly ash stabilization reduces the void ratio of soil but increases the optimum moisture content for soil compaction process; leads to increase in liquid limit values but reduction in plasticity index. Fly ash stabilized soil exhibit lower values of secondary compression coefficient which leads to reduction in secondary consolidation of soil [30]. Based on the property of burned coal, its residue viz., fly ash can be classified as class C and class F. Class C fly ash has pozzolonic and self-cementing properties, whereas class F fly ash is pozzolonic in nature, but requires an activator such as lime or cement for pozzolonic reaction.

When a stabilizer is blended with soil, four stages of changes are observed. The first two stages can be considered as soil modification and the last two stages are considered as soil stabilization [20]. Firstly cation exchange takes place with soil. For lime stabilization, excess Ca^{++} ions (having less affinity to water) due to addition of lime replaces the monovalent cations such as Na^{+} present in soil, hence the susceptibility of soil to water content variation reduces. Secondly development of flocculation and agglomeration of soil particles takes place. For lime stabilization, C–S–H (Calcium Silicate Hydrate) get formed due to the reaction of soil with lime, which causes fibrous formation in soil and the micro-pores of soil gets filled with these fibrous structures, which have cementing properties. This phenomenon is mainly responsible for the increase in subgrade modulus (K) and elastic modulus (E) of soil. Thirdly pozzolonic reaction takes place depending on the available calcium and soil mineralogy, which is a long-term process for gaining strength similar to concrete, and the improvement due to this pozzolonic reaction remains for years. Fourth stage is attributed to the autogenous healing process, which helps to regain strength after thaw weakening type of phenomena due to ingress of water in soil. Two factors which influence the soil stabilization process in addition to type of stabilizer are the mix design and the curing period. For obtaining the proper mix

design, the host soil samples are usually mixed with a stabilizer at intended proportion and cured for different time duration. These samples are evaluated for strength, water susceptibility, resistance to freeze and thaw (if required) and then compared with the desired properties of stabilized soil. After the mix design is finalized, the stabilization will follow four stages—soil preparation, stabilizer spreading, mixing of stabilizer and compaction. During preparation of soil, bulking effect needs to be minimized by mixing at wet of optimum moisture content. Next stage is spreading which is done by distributing the dry stabilizer at the site or slurried distribution to avoid air pollution. It is usually distributed in terms of weight per square area for the considered thickness of layer. Further, the mixing process is done in one stage for low plasticity soil and preferably two stages for high plasticity soil. Generally, it is recommended that 1–3% more lime is desired for high plasticity soil and mixing is done by a teethed drum. The compaction is done (to improve strength and durability of the soil) just after mixing to ensure sufficient water in soil during the compaction process. It is usually done by steel drum roller for soil strata less than 200 mm and for thickness of layer between 200 and 300 mm, it is first rolled by sheep foot roller followed by compaction with steel drum roller [8]. To maintain enough water the soil needs curing which is done by either spraying water on the surface of soil or by spraying bitumen on treated surface of soil.

Curing period is one of the most important parameter which affects the extent of soil stabilization as it affects the rate of gain of soil strength directly. Addition of lime in soil causes exothermic reaction which causes loss of moisture content which is good for soil stabilization; however for completion of the stabilization process, adequate moisture content is required. Hence, curing is important step for proper stabilization process of soil. It has been noted from various earlier studies [3, 10, 32] that soil-stabilizer mixture when exposed to different curing periods, results in different properties of soil. The present work reviews the effect of soil stabilization on different soil parameters such as maximum dry density and optimum moisture content during compaction process. The study also reviews the effect of soil stabilization on soil characteristics such as plasticity, strength and stiffness properties of soil, permeability and volume change behavior of soil. Tables 1, 2 and 3 as well as Figs. 1, 2, 3, 4, and 5 presents the details of different studies on response of stabilized soil. The paper also highlights the recent developments related to utilization of industrial waste and sustainable materials for soil stabilization.

2 Effect of Soil Stabilization on Different Soil Parameters/Characteristics

2.1 Moisture Content and Dry Density

Dry density and corresponding moisture content is important for stability of the soil. High moisture content in soil will cause higher pore water pressure in fine-grained

Table 1 Strength and related properties of stabilized soil

Researchers	Properties	Stabilizers	Conclusions
Little et al. [20]	CBR, UCS and resilient modulus	Lime (3–5%)	By addition of lime in soil, CBR, UCS and resilient modulus values increase by 2.5 times, 2.4 times and 10 times, respectively
Beeghly [3]	Compressive strength	Lime and LFA	As compared to lime, fly ash is 50% cheaper. Strength gain for 4% quick lime with 8% fly ash is approximately 1/5 times that using 6% lime alone
Makusa [22]	E_s	Lime (2.5%), fly ash (16%)	For stabilized soil, lime has more influence on E_s as compared to fly ash. For 16% fly ash content, the value of E_s after 56 days of curing was observed to be same as that after 28 days of curing, however it was noted to double after 180 days of curing. The delay is attributed to slow reactivity of fly ash in absence of any activator. For lime-stabilized soil (2.5% lime), E_s increases by 2–2.5 times after 56 days of curing as compared with 28 days curing period, mainly due to pozzolonic reaction of lime, which forms a cemented micro-structure within soil mass

(continued)

Table 1 (continued)

Researchers	Properties	Stabilizers	Conclusions
Puppala et al. [27]	Resilient modulus and plasticity	Cement	For stabilization of expansive soil as well as sulphate rich soil, sulphate resistance cement has been reported to show better results as compared to other stabilizers in context of reduction in plasticity index and increase in resilient modulus of soil
Pillappa [25]	Resilient modulus	Cement (8%)	Increase in resilient modulus (soil + cement) at optimum moisture content (OMC) is approximately 8 times, for dry side of OMC it is 2 times and for wet side of OMC it is 7 times against their initial values (without cement) at corresponding moisture content
Saing and Djainal [31]	E_s, K_s and settlement	Lime (10%)	K_s and E_s increases by 4 and 3 times respectively and settlement decreases by 3.5 times approximately

soil under loading [18], and soil would undergo higher settlement and experience changes in effective stress during dissipation of the pore water pressure. Addition of lime in soil causes exothermic reaction and results in loss in moisture content of soil [28]. Water in soil which stays within the diffused double layer around soil particles is minimized due to this loss of moisture content, which reduces the thickness of diffused double layer and the soil particles attraction increases, thus providing more resistance of the soil against deformation. When water enters the stabilized soil mass during wetting process, the water is not able to affect the stabilized soil structure significantly as the cations present in stabilized soil have less affinity to cation exchange process during the ingress of water [20, 23]. By chemical stabilization, maximum dry density (MDD) in soil is achieved at higher value of optimum moisture content (OMC) as compared to the unstabilized soil [3]. Lime-fly ash (LFA) stabilizer also

Table 2 Cracking, compaction and volume change properties of stabilized soil

Researchers	Properties	Stabilizers	Conclusions
George [7]	Cracking characteristics of soil	Lime-fly ash, cement and GGBFS	Lime-fly ash stabilized soil performed very well to control the shrinkage cracking as compared to admixtures such as cement and GGBFS (moderate cracking was observed as early as 3 days and continued up to 28 days), mainly due to persistent dry and hot weather conditions. Hence curing is important aspect in controlling the cracking of stabilized soil
Beeghly [3]	OMC, MDD	Lime (4%), fly ash (8%)	Silty soil treated with 4% lime and 8% fly ash, exhibits reduction in MDD by 6% and increase in OMC by 5% as compared to MDD and OMC for unstabilized soil
Quigley [28]	Plasticity index	Lime	Increase in plasticity index at less amount lime (1%) but increase in lime content decreases plasticity index
Jones et al. [14]	Shrinkage cracking of soil	Cement	Shrinkage cracking in cementitious stabilized soil subgrade is less than unstabilized base material; however it is important to control the shrinkage cracking by controlling the moisture content and adequate curing of the stabilized soil layer

(continued)

Table 2 (continued)

Researchers	Properties	Stabilizers	Conclusions
Jha and Sivapullaiah [13]	void ratio, volume change	Lime (2%)	Soil with 6% sand, 31% silt and 63% clay treated with 2% lime and 28 days of curing, exhibited reduction of percentage swell from 4.5 to 0.5%. 40–45% reduction in volumetric strain for 2% of lime at 28 days of curing as compared to zero days curing at same lime content
Pancar and Akpinar [24]	Settlement	Lime (12%), geosynthetics	CBR increases by 5 times and settlement decreases by 5.6 times

Table 3 Elastic properties, stiffness and other parameters for stabilized soil

Researchers	Properties	Stabilizers	Conclusions
Reinhold [29]	E_s and Poisson's number	Cement	In this study four types of soils are taken according to percentage composition clay and sand in mixture and three soil:cement ratio. All the samples were cured for 28 days uniformly. It is seen from this study that E_s is directly proportional to cement content and inversely to clay content and m (Poisson's number) is directly proportional to clay content
Suddath [32]	Compressive strength, modulus of rupture and flexural modulus	Lime (4%)	Compressive strength, modulus of rupture and flexural modulus increases approximately 2, 1.7 and 3 times respectively and linear increase with curing period from 2 to 56 days is observed

(continued)

Table 3 (continued)

Researchers	Properties	Stabilizers	Conclusions
Ismaiel [10]	Tensile strength and UCS	Lime and fly ash	Based on study of three soils (tertiary clay, organic silt and weathered soil), it is concluded that for tertiary clay at 2.5% lime and 8% fly ash, UCS and tensile strength increases approximately 3.5 and 3.25 times respectively for 180 days curing with respect to 7 days curing
			For organic silt at 2% lime and 12% fly ash, UCS and tensile strength increases approximately 3 and 4 times respectively for 180 days curing with respect to 7 days curing
	CBR and UCS		Soil with same admixture content shows nearly 1.2 to 1.5, 1.5 to 2 times and 2 to 2.5 times higher strength (UCS) at 28 days, 56 days and 180 days of curing, respectively as compared to strength at 7 days curing. CBR value at 180 days of curing is 2–2.5 times that at 7 days of curing
	Plasticity index		Reduction in plasticity index (improvement in plasticity property of soil) is different for different soils. Reduction is higher for Tertiary clay and organic silt as compared to weathered soil, mainly due to higher percentage of fines in Tertiary clay followed by organic silt and weathered soil
	Permeability		Permeability increases by up to 90–95 times for clays with 16% fly ash, 180 days curing; 60–65 times for organic silt with 20% fly ash, 28 days curing and 2600 times for weathered soil with 35% fly ash, 7 days curing

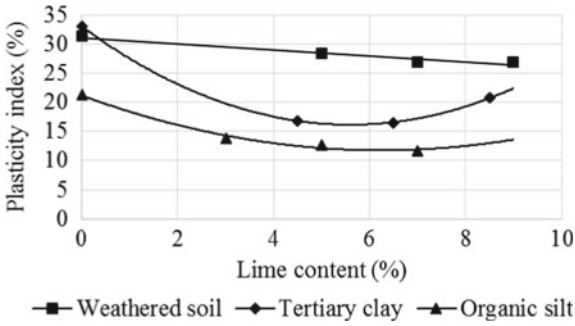

Fig. 1 Variation of plasticity index with lime content (for three soils reported by [10])

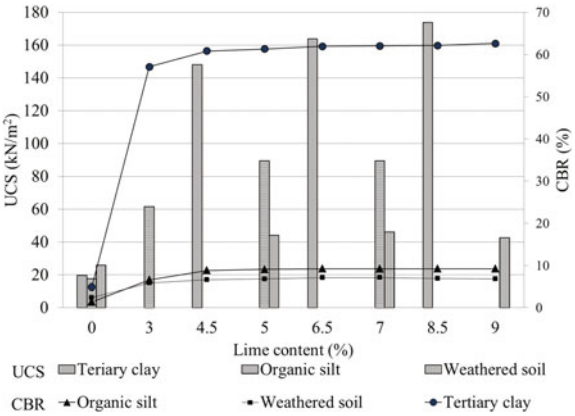

Fig. 2 Comparison of unconfined compression strength and CBR values for different lime content (for three soils reported by [10])

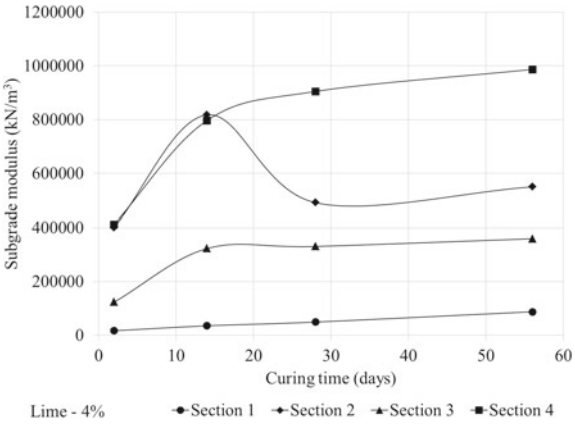

Fig. 3 Variation of subgrade modulus with curing time for soil reported by Suddah et al. [32]

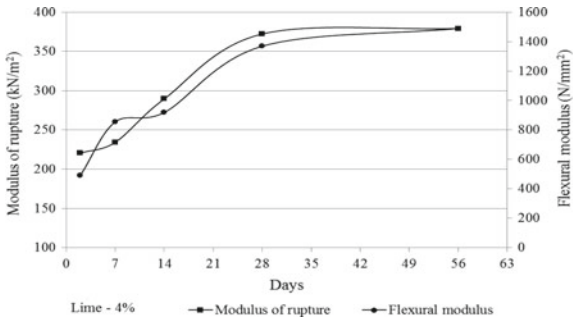

Fig. 4 Variation of modulus of rupture and flexural modulus with curing time for soil reported by Suddah et al. [32]

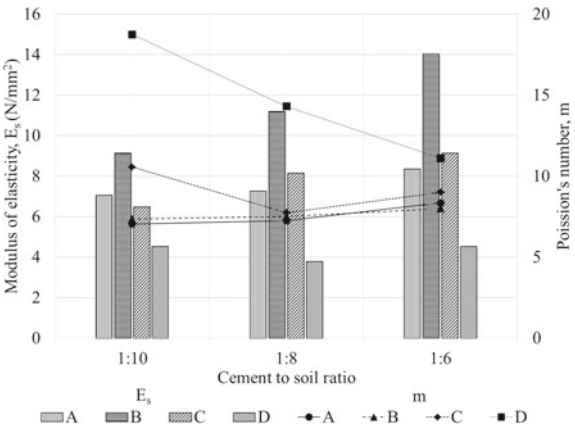

Fig. 5 Variation of modulus of elasticity (E_s) and Poisson's number (m) with cement to soil ratio and soil type (for four soils A, B, C and D reported by [29])

causes compaction MDD at high moisture content as compared to unstabilized soil ([3], refer Table 2). Hydraulic binder (e.g. cement or blend of lime, cement and industrial residue such GGBFS/fly ash) decreases the MDD and increase OMC because of formation of floccules by pozzolonic reaction of cementitious stabilizer, these floccules will offer resistance to compaction effort hence resulting in lower values of MDD [8]. The increase in OMC for stabilized soil can be attributed to higher consumption of water during the exothermic reaction of pozzolonic stabilizer within soil mass.

2.2 Soil Plasticity

Plasticity is the property of soil to undergo irreversible deformation without cracking. It is quantified by plasticity index which is the difference between liquid limit and plastic limit of soil. Plasticity of soil affects the volume change response of the soil such as swelling and shrinkage (one of the most challenging geotechnical aspect). Due to shrinkage of soil during drying, it experiences cracking due to differential

tensile stresses caused during the shrinkage process. During the wetting process, water will penetrate through the cracks thus accelerating the soil weakening process and soil loses its strength. Soils with active minerals may also experience swelling during wetting cycles. Hence it is important that plasticity of soil is under control. Table 2 presents details of studies which suggest that soil stabilization reduces soil plasticity. The reduction in soil plasticity can be attributed to cementing nature of lime due to the pozzolonic reaction. Studies indicate that influence of soil stabilization varies for different soils ([10], refer Table 3 and Fig. 1). Further, for expansive and sulphate rich soils, sulphate resistance cement is more effective in reducing plasticity index and increasing the soil stiffness [27] as summarized in Table 1.

2.3 Soil Strength

Strength of soil mixture depends on various factors such as parent soil properties, soil water content during stabilization, environmental parameters such as humidity and temperature, type of admixture, admixture content, curing period and the mixing process. Strength of soil can be assessed for stabilized soil by either unconfined compression strength (UCS) test, shear strength tests or indirectly by California bearing ratio (CBR) test. Studies have reported that fine-grained soil exhibit higher strength after stabilization [29], mainly due to higher surface area of clay particles for interaction with cations in presence of water during the pozzolonic reaction. The exposure conditions of stabilized soil also affect its strength and durability properties. Submerged condition will result in higher brittleness of stabilized soil, whereas excessive dry environment will obstruct the complete stabilization process due to lack of water for complete pozzolonic reaction, and result in lower strength. Freezing or extremely hot conditions are not ideal for soil stabilization process. Admixture content also affects the strength gain process in stabilized soil. It has been reported that the unconfined compression strength values of stabilized soil increases up to 4.5–6% lime content, however further increase in lime content would either result in no gain in strength or some reduction in strength [20]. For lime/fly ash combination, the optimum admixture content could be in the range of 2–2.5% lime and 16–30% fly ash depending upon soil properties [10]. The influence of soil stabilization on increase in CBR and UCS values and reduction in settlement of soil is significant as presented in Tables 3 and 2, respectively [10, 24]. Figure 2 depicts the comparison of UCS and CBR values based on the information reported by Ismaiel [10] for three soils. For these soils (tertiary clay, organic silt and weathered soil) it was highlighted that the extent of improvement in unconfined compression strength (UCS) and California Bearing Ratio (CBR) values is different for different soils stabilized with lime. The comparison shows that for higher UCS values, CBR values are also higher as expected. Further, improvement for tertiary clay (with higher percentage of clay fraction) is significantly higher than other two soils.

2.4 Soil Stiffness

The stiffness of soil governs its stress-strain behavior, which depends on the modulus of elasticity (E_s) and Poisson's ratio (μ). The improvement in stiffness of stabilized soil indicates its ability to resist higher load and undergo lower settlement under the loading. Researchers have suggested that modulus of elasticity (E_s) gives idea of the stress-strain response of the soil, whereas Poisson's number ($m = 1/\mu$) indicates the compressibility of the stabilized soil [29]. The pseudo elastic nature of soil can be expressed by modulus of subgrade reaction, K_s [18]. It is not a fundamental or intrinsic property of soil but it depends on foundation dimensions, stiffness; type, magnitude and location of loading; type and degree of compaction or stabilization of soil [33]. It has been noted by earlier studies that increase in K_s optimizes foundation design due to higher allowable foundation pressure and reduced settlement [18]. Details of studies on stiffness properties of soil such as E_s, m and K_s are presented in Tables 1 and 3. The influence of curing time on subgrade modulus, modulus of rupture and flexural modulus are depicted in Figs. 3 and 4, which is plotted based on the information given by Suddah et al. [32]. It can be observed that all these properties increases with increase in curing time. Another study highlighted the influence of cement to soil ratio on modulus of elasticity (E_s) and Poisson's number, m [29]. Figure 5 depicts that with increase in cement content, E_s increases and m reduces.

2.5 Permeability of Soil

Permeability (k) is the property of soil to permit water or air flow through its pore network. The process of flow of water based on its permeability is called seepage. Seepage is one of the major geotechnical engineering problems especially in embankments, water containment facilities, dams, canal slopes, etc. Seepage can lead to various problems such as internal erosion due to suffusion [9], piping failure caused by seepage and subsequently leading to subsidence or catastrophe failure of hydraulic structure such as earthen dams [6]. Inadequate dissipation of pore pressure under cyclic loading can lead to liquefaction of saturated silty soil or fine sand due to inadequate permeability under cyclic loading conditions.

Studies by Ismaiel [10] have shown that the permeability of the soil can be increased by the chemical stabilization (refer Table 3). Due stabilization of soil the dispersed soil structure get modified into flocculated structure by the floccules of C–S–H and C–A–H, which are formed during flocculation-agglomeration process of stabilization [21]. The increase in permeability can be attributed to shift of particle size distribution by addition of coarser fly ash particles and cementation of particles resulting in formation of flocculated structure. The study also suggested 28 days curing period as optimum for soil stabilization.

2.6 Volume Change and Cracking Characteristics of Soil

Volume change in expansive soil is one of the biggest challenges in civil engineering [25] which can be evaluated by free swell index, swelling pressure and compression index. The volume change behavior of soil depends on the mineralogy, water content, fabric and pore-structure of soil. The activity of soil minerals, susceptibility of soil to water content changes and volume change due to changes in soil fabric- and pore-structure can be reduced by addition of admixtures [23]. These admixtures can be lime, fly ash, other additives or their combination. When fly ash and free lime are mixed with soil, the C–S–H and C–A–H gels get formed due to the cation exchange phenomena [15]. This pozzolonic reaction influences the volume change and strength properties. Kate [15] through his study observed that bentonite clay exhibits 80–85% reduction in free swell index (FSI) with 3% lime and soil with 50% bentonite and 50% kaolinite stabilized with 3% lime shows reduction of 70–75% in FSI. Table 2 presents some studies showing the effectiveness of soil stabilization in reducing the volume change and cracking response of soil.

3 Recent Developments in Utilization of Sustainable Materials for Soil Stabilization

Utilization of lime and cement leads to reduction in natural resources such as limestone. The manufacturing of cement requires about 5.6 kJ of energy (per ton of cement), 1.5 tons of raw quarry material and produces about 0.9 ton of CO_2 [11]. In recent years, industrial residues such as micro silica or silica fume, sludge ash, ground granulated blast furnace slag (GGBFS), ash from rice husk and palm oil fuel, organic stabilizer, etc. have been used for sustainable soil stabilization.

Bagherpour and Choobbasti [2] have studied the influence of micro-silica with lime/cement for stabilization of fine-grained soils. It has been concluded that micro silica enhances the formation of calcium silicate hydrates instead of calcium aluminate hydrates, resulting in higher rate of pozzolonic reaction and higher unconfined compression strength. The addition of micro silica increases plasticity index and hence workability of micro silica-cement stabilized soils, but for micro silica-lime-stabilized soil, effect on plasticity index is not significant. Another recent study reported that optimum percentage of micro-silica-lime stabilizer is 4% micro silica and 7% lime [1]. In another study, Lin et al. [19] have reported the application of sludge ash for improving properties of soft soil. It have been observed that plasticity index, swelling potential were both reduced. The study reported that sludge ash performs better than fly ash for reducing the swelling potential of soil. Optimum sludge ash content of 8% was recommended in the study.

GGBFS has been noted to have slower initial setting time as compared to cement and usually requires addition of lime for activation. Studies have reported that GGBFS can be used to mitigate the effects of sulphates [34] and results in improvement in

strength properties [16, 35]. The application of palm oil fuel ash (POFA) for stabilization of clayey soil has been reported by Pourakbar et al. [26]. In the study it was noted that use of POFA alone resulted in slight increase in unconfined compression strength (UCS) values of soil, however POFA with cement resulted in significant increase in UCS values of stabilized soil. The addition of POFA also resulted in reduction in optimum moisture content and increase in maximum dry density of stabilized soil as compared to unstabilized soil. Studies by Behak [4] on soil stabilization of sandy soil with rice husk and lime stabilizer revealed that rice husk ash has low reactivity; however their addition with lime results in cementitious products that bond the soil grains, resulting in strength gain. However, the strength gain is less as compared to other stabilizers. Some studies have demonstrated the application of lignin-based stabilizer (organic stabilizer) for soil stabilization [17]. The lignin based stabilizer used in combination of fly ash resulted in about 100–300% increase in unconfined compression strength values. The specimens also exhibited significant improvement in moisture resistance (resistance to reduction in strength due to wetting).

A recent detailed review of utilization of sustainable materials for soil stabilization suggested possible utilization of variety of sustainable materials such as cement kiln dust, red mud and textile waste in addition to above discussed sustainable materials [12]. The above studies suggest that the utilization of sustainable materials for soil stabilization has resulted in encouraging outcome. Considering the need to reduce the use of natural resources and with focus of environmental friendly and sustainable solutions for soil stabilization, these materials are expected to gain popularity in near future.

4 Conclusion

The present paper reviews the state of the art related to soil stabilization and attempts to present the effect of stabilization on different properties of subgrade soil. The concluding remarks from the study are listed below:

1. Lime improves plasticity (reduces plasticity index up to 5% lime) and strength properties of cohesive soil, but has less effect on compaction characteristics (maximum dry density and optimum moisture content). It is also noted that usage of hydraulic binder improves the compaction characteristics of soil.
2. For stabilization of expansive as well as sulphate rich soil, sulphate resistance cement has been reported to shows better results as compared to other stabilizers in context of reduction in plasticity index and increase in stiffness of soil.
3. Inferences from earlier studies suggest that for the optimum proportion of stabilizers, it is recommended to utilize the combination of lime, fly ash and cement for soil stabilization.
4. Soil stabilization studies at different curing period up to 180 days have shown that the strength of stabilized soil increases with increase in curing period. For

fly ash stabilized soil, the long-term strength is significantly higher as compared to short term strength.

5. It has been noted that different soils exhibit different improvement in CBR and unconfined compression strength values for same amount of stabilizer. The soil with finer particle size distribution shows better improvement in CBR and UCS values as compared to soil with coarser particle size distribution.
6. Stabilization effect (in term of gain in strength and reduction in plasticity) in fine-grained soil is much more evident as compared to coarse-grained soils.
7. Stabilization is usually preferred over replacement of soil, if it is relatively economical, environment friendly and feasible at the construction site. It is recommended that further research be focussed on utilizing industrial waste such as fly ash, cement kiln dust, micro silica, red mud, etc. for soil stabilization in place of lime, cement and other chemical stabilizers.

References

1. Alrubaye AJ, Hasan M, Fattah MY (2017) Stabilization of soft kaolin clay with silica fume and lime. Int J Geotech Eng 11(1):90–96
2. Bagherpour I, Choobbasti AJ (2003) Stabilization of fine-grained soils by adding microsilica and lime or microsilica and cement. Electron J Geotech Eng 8:1–10
3. Beeghly JH (2003) Recent experiences with lime—fly ash stabilization of pavement subgrade soils, base and recycled asphalt. In: International Ash Utilization Symposium, Center for Applied Energy Research, University of Kentucky, Paper#46
4. Behak L (2017) Soil stabilization with rice husk ash, Chapter 3. Rice-Technology and Production. Intech Publishers. http://dx.doi.org/10.5772/66311
5. DPSMS Report, Design Procedures for Soil Modification or Stabilization (2008) Report of Office of Geotechnical Engineering. Indianapolis, Indiana, USA
6. Fell R, Wan CF, Cyganiewicz J, Foster M (2003) Time for development of internal erosion and piping in embankment dams. J Geotech Geoenviron Eng ASCE 129(4):307–314
7. George KP (2001) Soil stabilization field trial. Report for US Department of Transporation, Federal Highway Administration and The Portland Cement Association, USA
8. Holt C (2010) Chemical stabilization of inherently weak subgrade soils for road construction—applicability in Canada. In: Conference of the Transportation Association of Canada Halifax, Nova Scotia
9. Indraratna B, Nguyen V, Rujikiatkamjorn C (2011) Assessing the potential of internal erosion and suffusion of granular soil. J Geotech Geoenviron Eng ASCE 137(5):550–554
10. Ismaiel HAH (2006) Treatment and improvement of the geotechnical properties of different soft fine-grained soils using chemical stabilization. Institute of Geology, Martin Luther Halle-Wittenberg University, Germany
11. Jafer HM, Atherton W, Ruddock FM (2015) Soft soil stabilization using high calcium waste material fly ash. In: 12th International Post-Graduate Research Conference, Manchester-Salford, UK
12. Jayanthi PNV, Singh DN (2016) Utilization of sustainable materials for soil stabilization: state-of-the-art. Adv Civil Eng Mater 5(1):46–79
13. Jha AK, Sivapullaiah PV (2015) Mechanism of improvement in the strength and volume change behaviour. Eng Geol 198(2015):53–64
14. Jones D, Rahim A, Saadeh S, Harvey JT (2011) Guidelines for the stabilization of subgrade soils in California. Report submitted to California Department of Transportation, USA

15. Kate JM(2005) Strength and volume change behavior of expansive soils treated with fly ash. Innovations in Grouting and Soil Improvement Innovations in Grouting and Soil Improvement, ASCE
16. Kavek A, Bilgen G (2016) Reuse of ground granulated blast furnace slag (GGBFS) in lime stabilized embankment materials. IACSIT Int J Eng Technol 8(1):11–14
17. Kim S, Gopalakrishnan K, Ceylan H (2012) Moisture susceptibility of subgrade soils stabilized by lignin-based renewable energy coproduct. J Transp Eng ASCE 138(11):1283–1290
18. Larkela A, Mengelt M, Stapelfeldt T (2013) Determination of distribution of modulus of subgrade reaction. In: 18th International Conference on Soil Mechanics and Geotechnical Engineering, Paris, France
19. Lin DF, Lin KL, Luo HL (2007) A comparison between sludge ash and fly ash on the improvement in soft soil. Air Waste Manage Assoc 57:59–64
20. Little DN, Scullion T, Kota PBVS, Bhuiyan J (1995) Identification of the structural benefits of base and subgrade stabilization. Texas Department of Transportation, FHWA/TX-94/1287-2
21. Little DN, Males EH, Prusinski JR, Stewart B (2000) Cementitious stabilization, A2J01: Committee on Cementitious Stabilization
22. Makusa GP (2004) A review of geotechnical behavior of stabilized soils. Department of Civil, Environmental and Natural Resources Engineering, Division of Mining and Geotechnical Engineering, Luleå University of Technology, Luleå, Sweden
23. Mitchell JK, Soga K (1993) Fundamental of soil behavior, 2nd edn. Wiley, New York, USA
24. Pancar EB, Akpinar MV (2016) Comparison of effects of using geosynthetics and lime stabilization to increase bearing capacity of unpaved road subgrade. Hindawi Publishing Corporation, Advances in Materials Science and Engineering
25. Pillappa GS (2005) Field and experimental studies to assess the performance of stabilized expansive clay. The University of Texas at Arlington
26. Pourakbar S, Asadi A, Haut BBK, Hamed M (2015) Stabilization of clayey soil using ultrafine palm oil fuel ash (POFA) and cement. Transp Geotech 3:24–35
27. Puppala A, Griffin JA, Hoyos LR, Chomtid S (2004) Studies on sulfate-resistant cement stabilization methods to address sulfate-induced soil heave. J Geotech Geoenviron Eng ASCE 130(4). doi:https://doi.org/10.1061/(asce)1090-0241(2004)130:4(391)
28. Quigley P (2006) Modification/stabilization of low strength cohesive soils under foundations and floor slabs. Geotechnical Society of Ireland
29. Reinhold F (1955) Elastic behavior of soil-cement mixtures. Bulletin, Issue No. 108, Highway Research Board, Washington D.C., pp 128–137
30. Saied A, Amin C, Hamid N (2012) A review on the lime and fly ash application in soil stabilization. Int J Biol Ecol Environ Sci (IJBEES) 3:2277–4394
31. Saing Z and Djainal H (2018) Effect of lime stabilization on vertical deformation of Laterite Halmahera soil. In: IOP Conf. Series: Earth and Environmental Science
32. Suddath LP (1975) Load-deflection behavior of lime stabilized layers. Army Construction Engineering Research Laboratory, Illinois
33. Terzaghi K (1955) Evaluation of coefficient of subgrade reaction. Geotechnique 5(4):297–326
34. Wild S, Kunuthia JM, Robinson RB, Humphreys I (1995) Effects of ground granulated blast furnace slag (GGBS) on the strength and swelling properties of lime-stabilized kaolinite in the presence of sulphates. Clay Minerals 31:423–433
35. Yadu L, Tripathi RK (2013) Effects of granulated blast furnace slag in the engineering behaviour of stabilized soft soil. Procedia Eng 51:125–131

Effect of Anisotropy on Stress-Strain and Pore Pressure Response of Normally and Heavily Over Consolidated Nagpur Expansive Soil

Naman Kantesaria and Ajanta Sachan

Abstract Expansive soil is a residual cohesive soil, mostly present in the arid and semi-arid regions of the world. Stress induced anisotropy is an important aspect to be considered for the analysis and design of several geotechnical structures on expansive soils. Though, its effect is yet to be explored. Hence, the aim of the current study is to evaluate the effect of stress induced anisotropy on the shear behavior of normally and heavily over consolidated Nagpur expansive soil. Nagpur expansive soil is classified as CH (clay with high plasticity) type of soil with high amount of clay content (60%) and high value of differential free swell index (DFSI, 123%). Experimental research has been performed on Nagpur soil by conducting a series of anisotropically ($K_c = 0.70, 0.85, 1$) consolidated undrained (CU) triaxial compression tests at an over consolidation ratio (OCR) of 1 and 10. Change in void ratio during anisotropic consolidation phase was found to be a function of both, the mean effective stress and deviatoric stress. As Nagpur expansive soil was subjected to pre-shear stress during consolidation phase, its shear behavior showed distinctive response that was different from isotropic condition because of induced stress anisotropy. Normalized undrained shear strength was reduced for anisotropically consolidated specimen in comparison to isotropically consolidated specimen for both the OCR 1 and 10. Excess pore water pressure behavior and the A and β_{max} parameters were also significantly influenced by the induced stress anisotropy for both the normally and heavily over consolidated states.

Keywords Anisotropy · Stress-strain · Pore pressure · Expansive soil · K_0 consolidation

N. Kantesaria (✉) · A. Sachan
Civil Engineering, Indian Institute of Technology Gandhinagar, Palaj, India
e-mail: naman.kantesaria@iitgn.ac.in

A. Sachan
e-mail: ajanta@iitgn.ac.in

A. Prashant et al. (eds.), *Advances in Computer Methods and Geomechanics*, Lecture Notes in Civil Engineering 55,
https://doi.org/10.1007/978-981-15-0886-8_55

1 Introduction

The shear behavior of clayey soil is dependent on the many parameters including stress history, inherent and induced anisotropy, microfabric arrangement, initial water content, drainage condition, strain rate and stress path followed during consolidation. Most of the natural soils have inherent anisotropy due to their fabric orientation or material characteristics through the process of deposition. When such a soil is re-consolidated under some pre-shear deviatoric stress, the different anisotropy is generated and it is known as induced anisotropy. The shear behavior of such kind of soils is distinctly different than that of isotropically consolidated soils. During most of the geotechnical investigation, the failure criterions were chosen based on considering the soil in the isotropic state. However, this is not always true. Naturally deposited soils are usually consolidated in K_0 condition. Where, K_0 is the ratio of effective minor to major principal stresses at rest conditions (under no lateral strain condition). However, this condition of stresses altered in some cases such as embankment construction, pit excavation for foundations, tunnel construction and other geotechnical structures [4, 5, 16]. During such processes, the active stress conditions changed from the initial K_0 condition to some other stress ratio (K_c) condition. Due to this loading or unloading, the re-consolidation of soil took place when all the generated excess pore water pressure dissipated [5]. It would lead to generation of stress induced anisotropy effect along with stress history effect within the clayey soil mass. Thus, the microstructure of clayey soil would change and the shear behavior of such soils could be largely dependent on the arrangement of microfabric after consolidation [2, 3, 11, 14–17]. The aim of current research is to evaluate the shear behavior of expansive soil influenced by the effects of induced anisotropy and stress history.

The response of clayey soil under the effect of K_0 consolidation was studied by several authors under normally consolidated (NC) and over consolidated states (OC) [1–3, 8, 10, 12]. Most of the researchers observed the effect of anisotropic consolidation under K_0 condition. These researchers [5, 6, 16] mainly focused on the comparison of mechanical behavior of isotropically and K_0 consolidated clayey soil. It was reported that the anisotropic shear strength was lower than that of isotropic shear strength. Only few of them discussed about the possible microfabric changes during this process. Some researchers also discussed about the volume change behavior during anisotropic consolidation and tried to understand its dependency on stress state system [6, 7, 16]. It was reported that the water content of soil, after consolidation was not the unique function of deviatoric stress. Mayne [13] compared the available data of researchers and concluded that the undrained anisotropic shear strength was approximately ranged in between 75 and 100% of isotropic strength in compression loading.

Despite of significant effect of induced anisotropy and stress history, there is not much work available for the very high plasticity natural clay such as Nagpur expansive soil under those combined effect. Hence, a series of undrained triaxial compression tests was carried out under the effect of various anisotropic consolidation

conditions ($K_c = 0.70, 0.85, 1$) and stress history (OCR = 1, 10). The results were evaluated based on the responses of volumetric strain, stress-strain, excess pore water pressure and effective stress path. The significant influence of induced anisotropy and stress history on shear behavior of Nagpur expansive soil was observed.

2 Experimental Program

2.1 Material Properties and Specimen Preparation

Soil used for the present study was collected from the Left Bank Canal of Gosikhurd dam, Nagpur (Maharashtra, India). The disturbed representative sample was obtained from the field and reconstituted in the laboratory at in situ density and water content. The grain size distribution (GSD) of Nagpur soil exhibited presence of high amount of fines content (94%) as shown in Fig. 1. The soil had 6% sand, 34% silt, 60% clay, which was classified as CH (Clay of high plasticity) type of soil according to Indian standard (IS) soil classification. Differential free swell index (DFSI) value of Nagpur soil was 123%, indicating high degree of expansiveness (IS: 2911 Part III [9]). Basic geotechnical properties of Nagpur expansive soil including specific gravity, Atterberg limits, GSD, compaction parameters, shear strength parameters and DFSI are presented in Table 1. Moist tamping method was adopted to prepare 50 mm diameter and 100 mm height specimen of expansive soil at its in situ dry density and water content of 1.34 g/cm^3 and 34% respectively. The oven dried soil was passed from 4.75 mm sieve and mixed uniformly with required amount of water. This mixture was kept in plastic bag and stored for 24 h in the desiccator to ensure uniform water distribution and to allow swelling of soil particles prior to specimen preparation. Specimen was prepared in five layers of different thickness, in which, the layer

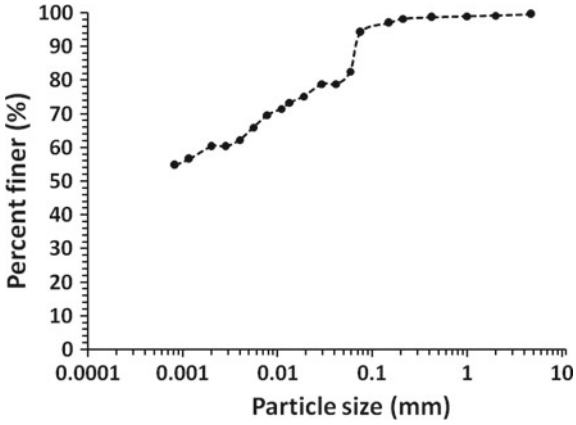

Fig. 1 Grain size distribution (GSD) curve of Nagpur expansive soil

Table 1 Geotechnical properties of Nagpur expansive soil

Specif-ic gravity G_s	Sand (%)	Silt (%)	Clay (%)	Liquid limit, w_L (%)	Plastic limit, w_P (%)	Shrink-age limit, w_S (%)	Plastic-ity index, I_p (%)	DFSI (%)	MDD, $\wp_d$ (g/cm^3)	OMC (%)
2.74	6	34	60	77	28.5	10.5	48.5	123	1.40	32

thickness was increased from bottom to top as 10, 15, 20, 25, 30 mm respectively, in order to avoid over compaction of bottom layers and under compaction of top layers.

2.2 Testing Procedure

The effect of stress anisotropy on the shear behavior of normally (OCR = 1) and heavily overconsolidated (OCR = 10) Nagpur expansive soil was investigated by performing a series of consolidated undrained (CU) triaxial compression tests. The prepared soil specimen was mounted on the loading frame of Automated *K* stress path Triaxial System. The filter paper strips were attached with the specimen to provide radial drainage to speed up the saturation and consolidation process. Saturation procedure was conducted in two steps; water flushing and forced saturation. Water flushing was done for the time duration of 24 h by pushing the water inside the specimen till the volume of water equal to 1.5 times the volume of specimen flushed through it. This process was done under 50 kPa of cell pressure while maintaining the back pressure of 30 kPa. The saturation ramp (1 kPa increase/1 min) was then applied in increments of 40 kPa for both cell pressure and back pressure, while maintaining the effective confining pressure as 20 kPa. The saturation of specimen was achieved at back pressure of 310 kPa by ensuring the value of Skempton's pore pressure parameter B ($=\Delta u/\Delta\sigma_c$) [18] greater than 0.95. The specimens were then consolidated one-dimensionally ($K_0 = 0.70$), anisotropically ($K_c = 0.85$) and isotropically ($K_c = 1$) for both the normally and heavily over consolidated state. The ratio of effective minor principle stress to the effective major principle stress is defined as stress anisotropy (K_c) value and mentioned in Eq. 1.

$$K_c = \left(\frac{\sigma_3'}{\sigma_1'}\right) = \left(\frac{\sigma_r'}{\sigma_a'}\right) \tag{1}$$

where $\sigma_1' = \sigma_a'$ and $\sigma_3' = \sigma_r'$ are effective major and minor principal stresses or effective axial and radial stresses respectively. The over consolidation ratio (OCR) can be defined as the ratio of pre-consolidation stress to current consolidation stress and expresses in Eq. 2.

$$\text{OCR} = \left(\frac{\sigma_{1(\text{OC})}'}{\sigma_1'}\right) \tag{2}$$

The concept of modified Mohr Coulomb in q–p' space as per MIT definition is mentioned in Eqs. 3 and 4. The relation between p' and q and K_c is mentioned in Eq. 5.

$$p' = \left(\frac{\sigma_1' + \sigma_3'}{2}\right) \tag{3}$$

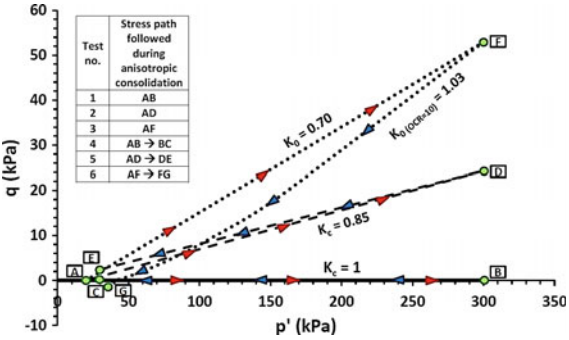

Fig. 2 Effective stress path of Nagpur expansive soil during anisotropic consolidation

$$q' = \left(\frac{\sigma_1' - \sigma_3'}{2}\right) \tag{4}$$

$$\frac{q'}{p'} = \left(\frac{\sigma_1' - \sigma_3'}{\sigma_1' + \sigma_3'}\right) = \left(\frac{1 - K_c}{1 + K_c}\right) \tag{5}$$

where p' is mean effective stress and q is shear stress. Stress anisotropy was induced in the specimens by applying pre-shear stress in the direction of compression loading till the mean effective stress (p') of 300 kPa for all the values of anisotropy. This pre-shear stress was applied through constant stress path ramp loading during consolidation phase of testing. OCR = 10 specimens were generated by reducing the effective axial stress (σ_a') to 1/10th of NC specimen while maintaining anisotropy values constant for $K_c = 0.85$ and 1. For K_0 consolidated specimen, the anisotropy value during unloading is obtained as $K_{0(OC)} = 1.03$ to maintain the condition of zero lateral strain. The stress paths followed during consolidation for isotropic, anisotropic and K_0 consolidation are (AB, BC), (AD, DE) and (AF, FG) respectively, as shown in Fig. 2. The undrained shearing was then applied at B, D and F points for OCR = 1 and at C, E and G for OCR = 10. Shear deformation of specimens was conducted by applying compression loading at the constant strain rate of 0.05%/min under undrained conditions till the failure reached.

2.2.1 K_0 Consolidation Stress Path ($K_0 = 0.70$)

During K_0 consolidation, the deformation of soil specimen occurred only in one direction. In the current research, K_0 value for Nagpur soil was determined experimentally by performing K_0 stress path test. In K_0 stress path consolidation, the lateral strain (ε_r) was maintained as zero by keeping volumetric strain (ε_v) equal to axial strain (ε_a), $\varepsilon_v = \varepsilon_a$. The cell pressure was set to be increased by the rate of 1 kPa per 10 min, while keeping the back pressure constant, till the mean effective stress (p') reached to the value of 300 kPa. This rate was chosen to ensure no excess pore water pressure development within the specimen. The volumetric strain was calculated

from the water volume coming out from the specimen. To maintain the condition of $\varepsilon_r = 0$ and $\varepsilon_v = \varepsilon_a$, the axial load was calculated and adjusted by GDS automated software. After target pressures were achieved, the specimen was kept under the same stresses for further 24 h to ensure proper consolidation. Approximately 72 h were required to complete the consolidation process. The experimentally determined $K_{0(\mathrm{NC})}$ value was 0.70 for NC state. To obtain the overconsolidated specimen, the cell pressure was then reduced by the same rate while maintaining the K_0 condition. The stress path followed in unloading was non-linear and different than that of loading. The K_0 value for OCR 10 was obtained as $K_{0(\mathrm{OCR})}$ (=1.03). Additional time of 70 h was required for unloading process.

2.2.2 Anisotropic Consolidation Stress Path ($K_c = 0.85, 1$)

Stress path module of automated K stress path triaxial system was used to consolidate the soil specimen anisotropically. By fixing the target mean effective stress ($p' =$ 300 kPa) and stress anisotropy value ($K_c = 0.85{,}1$), the q value was calculated by using Eq. (4). The calculated values of q and p' were set as an input in the stress path module, while keeping the back pressure constant. The rate of increase of cell pressure was chosen as 1 kPa per 10 min, which was same as in the case of K_0 consolidation. Overconsolidated specimens were obtained by reducing the cell pressure at the same rate while maintaining the same K_c value. For $K_c = 1$, the axial pressure was kept same as cell pressure ($\sigma_1' = \sigma_3'$) to maintain the isotropic condition while keeping the cell pressure increment at same rate (1 kPa/10 min). Time required to complete the stage was found to be equivalent to K_0 condition.

3 Results and Discussion

The shear behavior of clayey soil is very much dependent on the micro-structural arrangement of clay matrix and experienced stress system in the past. The micro-structural orientation of platy clay particles changes with the change in active stress system. Orientation of clay fabric changes from flocculated (face-to-edge and edge-to-edge) to dispersed (face-to-face), as the degree of anisotropy increases [15]. The platy clay particles try to settle as their longer axis parallel with horizontal direction to achieve most stable condition. The similar phenomenon usually observed in the natural sedimentation process of clayey soil as the stress system while sedimentation is anisotropic in nature, especially K_0. Along with anisotropy, the stress history effect generated due to load removal also affects the shear behavior of soil. Hence, the current aim of the study was to evaluate the changes in shear behavior of expansive soil due to anisotropy for normally and heavily over consolidated state by performing a series of consolidated undrained triaxial compression tests. Different degrees of anisotropy were induced inside the soil specimen by consolidating the soil specimen under different stress systems.

3.1 Volume Change Behavior During Consolidation

The various parameters at the end of consolidation are listed in the Table 2. Change in void ratio (Δe) during consolidation is calculated using volumetric strain (ε_v) data and plotted against mean effective stress (p') on semi-log plot, as shown in Fig. 3a. The total volumetric strain (ε_v) during anisotropic consolidation can be expressed as summation of volumetric strain due to mean effective stress (ε_{vm}) and volumetric strain due to deviatoric stress (ε_{vd}) using Eq. 6.

$$\varepsilon_v = \varepsilon_{vm} + \varepsilon_{vd} \tag{6}$$

At $K_c = 1$, $\varepsilon_{vd} = 0$ and therefore, $\varepsilon_v = \varepsilon_{vm}$. The effect of deviatoric stress on the volume change behavior during anisotropic consolidation could be evaluated by the volumetric strain ratio of ε_{vd} to ε_{vm} ($\varepsilon_{vd}/\varepsilon_{vm}$). From the values mentioned in the Table 2, it was observed that the volumetric strain and volumetric strain ratio was higher for the specimen consolidated anisotropically than that of isotropically under the same mean effective stress (p') of 300 kPa. This extra volumetric strain was generated because of applied additional deviatoric stress at lower K_c values for the same mean effective stress. During anisotropic consolidation, it was observed the

Table 2 Consolidation behavior of Nagpur expansive soil at NC and OC state

Test no.	OCR	K_c	Final void ratio, e_f	Volumetric strain, ε_v (%)	p' (kPa)	q (kPa)	σ'_{vc} (kPa)	$\varepsilon_{vd}/\varepsilon_{vm}$ (%)
1	1	1	0.8331	10.9	300	0	300	0
2		0.85	0.8009	11.6	300	24.32	324.3	15.5
3		0.7	0.7925	12.2	300	52.94	352.9	19.5
4	10	1	0.8664	8.5	30	0	30	0
5		0.85	0.8413	9.8	30.06	2.43	32.4	14.4
6		1.03	0.8239	10.6	35.74	−0.45	35.2	24.4

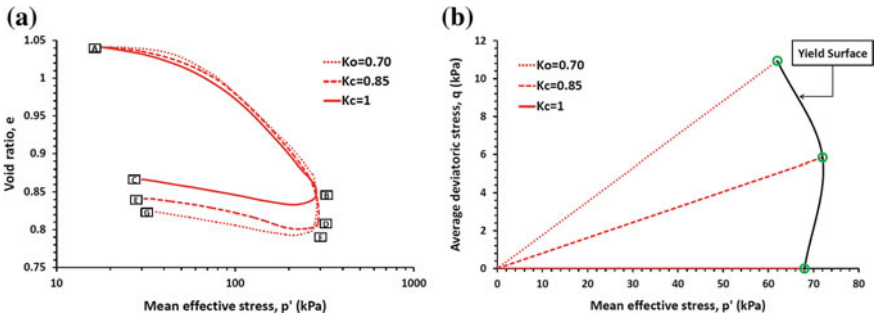

Fig. 3 Consolidation response of Nagpur expansive soil **a** e versus log(p') curve, **b** yield surface

volumetric strain was not only dependent on mean effective stress but also dependent on deviatoric stress. The void ratio was increased a little due to soil's elasto-plastic nature during the process of stress release to create OCR 10. The compression index (C_c) and swelling index (C_s) was found to be 0.251 and 0.045 respectively, from the relationship of e versus log(p'). Their values remained constant for all the values of K_c. The yield stress obtained from e versus log(p') was plotted on the q–p' space to obtained the yield surface, as shown in Fig. 3b. The yield surface signified the limiting mean effective stress value till the stress history effect generated during specimen preparation governing the mechanical behavior of soil. When the active stress system crossed the yield surface, the influence of initial yield surface vanished and the soil shear behavior was governed by further loading stresses.

3.2 Normalized Stress-Strain and Pore Water Pressure Response

The normalization of stress-strain and pore pressure response was conducted to eliminate the effect of confining pressure and compare the results of isotropically and anisotropically consolidated specimens at OCR 1 and 10. The stress-strain and excess pore water pressure response were normalized by dividing them with pre-shear effective vertical stress (σ'_{vc}), as mentioned in Table 2. The various parameters related to shear behavior of Nagpur expansive soil is mentioned in Table 3. The shear behavior response is shown in Fig. 4a, b. The normalized undrained shear strength $(\sigma_{dn})_f$ was found to be lower for anisotropically ($K_c < 1$) consolidated specimen than that of isotropically ($K_c = 1$) consolidated specimen for both OCR 1 and 10. The $(\sigma_{dn})_f$ of the NC (OCR = 1) specimen consolidated at $K_0 = 0.70$ and $K_c = 0.85$ was 72.2% and 84.6% of the strength obtained by specimen consolidated at $K_c = 1$ respectively. The results were observed to be consistent with the findings of Mayne [13]. This variation was reduced for OCR 10 specimens and found to be 87.4% and 93.6% for $K_{0(\mathrm{OC})} = 1.03$ and $K_c = 0.85$ respectively. Some portion of total deviatoric stress was already taken up by the soil specimen during process of anisotropic consolidation ($K_c < 1$). Hence, the deviatoric stress generated during undrained shearing was less for lower K_c values specimens than that of specimen for which, $K_c = 1$. The reduction in the normalized undrained shear strength $(\sigma_{dn})_f$ with anisotropy value (K_c) was found to be linear in nature for OCR 1 specimens and the relationship is expressed in Eq. 7.

$$(\sigma_{dn})_f = (0.5063 * K_c) + 0.0415 \tag{7}$$

Due to the stress history effect, the stress-strain response and normalized undrained shear strength of OC soil was observed to be much higher than that of NC soil.

Table 3 Shear behavior of Nagpur expansive soil at NC and OC state

Test no.	OCR	K_c	$(\sigma_d)_f$ (kPa)	$(u_w)_f$ (kPa)	$(\sigma_{dn})_f$ (kPa)	$(u_{wn})_f$ (kPa)	$(\varepsilon_a)_f$ (%)	A_f	$(\beta_{\max})_f$ degree
1	1	1	165.2	149.3	0.551	0.498	7.92	0.904	19.5
2		0.85	151.2	139.8	0.466	0.431	8.54	1.423	19.7
3		0.7	140.6	124.9	0.398	0.354	6.11	3.996	19.8
4	10	1	133.5	−34.6	4.452	−1.153	5.72	−0.259	26.9
5		0.85	135.1	−32.7	4.166	−1.008	4.08	−0.26	27.9
6		1.03	137.3	−9.9	3.891	−0.28	2.54	−0.071	30.9

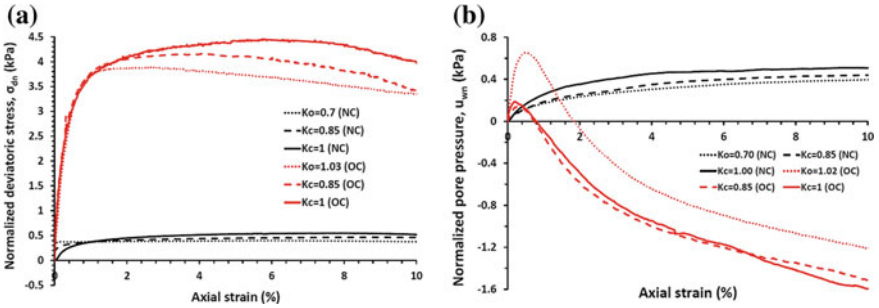

Fig. 4 Shear behavior of Nagpur expansive soil **a** normalized stress-strain, **b** normalized excess pore pressure

The generation of positive pore water pressure for NC soil indicated the contractive behavior, whereas initially positive and then negative response of OC soil represented dilative response. This could be attributed due to the effect of stress history applied on the specimen, which resulted in the void ratio alteration. The generated void ratio at the end of stress relaxation could be considered as less for that particular confining pressure. Hence, the particles tried to move away during shearing and observed response was dilative for OCR 10 specimens. The magnitude of positive pore water pressure and associated contractive nature of NC specimen was increased from $K_0 = 0.70$ to $K_c = 1$. The void ratio at the end of consolidation was higher for $K_c = 1$ specimen than that of $K_c < 1$ specimen. The void ratio at the end of consolidation was higher for $K_c = 1$ specimen than that of $K_c < 1$ specimen. Hence, the possible contraction and rearrangement of soil particles was higher for $K_c = 1$ specimen during undrained shearing. The same phenomena could be applicable for OC specimens except $K_{0(\mathrm{OC})} = 1.03$ specimen. The higher initial contractive response was observed in K_0 overconsolidated specimen due to the applied negative deviatoric stress (σ_d) before shearing. The failure strain was observed to reduce and stiffness to increase with the reduction in anisotropy (K_c) value. This reduction was more prominent for OC specimens because failure strain value reduced from 5.72% to 2.54% as consolidation changes from isotropic to 1-D respectively. This nature was attributed due to the formation of more dispersed microstructure as the consolidation stresses changed to anisotropic [3, 14, 17]. The failure of dispersed microfabric was detected to occur at early strain as compared to other possible structures because of its low particle rearrangement [15]. The possible changes in microstructure from specimen preparation to completion of consolidation stage were explained in Fig. 5. The sample was prepared on the wet side of optimum and that indicated the prior presence of more dispersed microstructure of clay particles. When it was further consolidated anisotropically, more and more clay particles oriented in face-to-face arrangement (dispersed microstructure). The similar behavior was observed for both normally (NC) and over consolidated (OC) specimens.

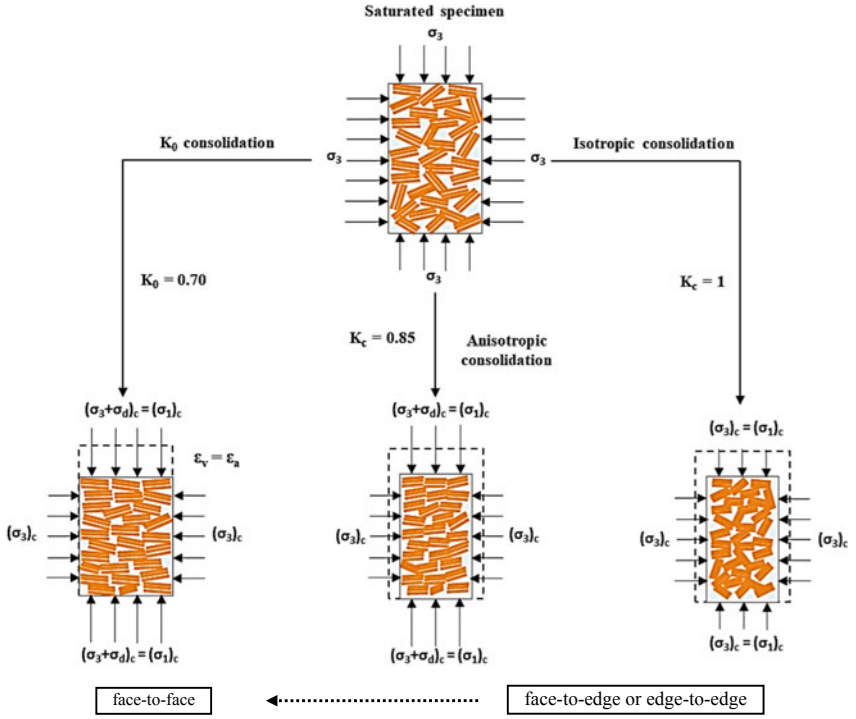

Fig. 5 Schematic representation of possible microstructure changes during consolidation

3.3 Effective Stress Path Behavior

The MIT model of q versus p' diagram is used to obtain the effective stress path of Nagpur expansive soil, as shown in Fig. 6b. The curves for NC specimens indicated

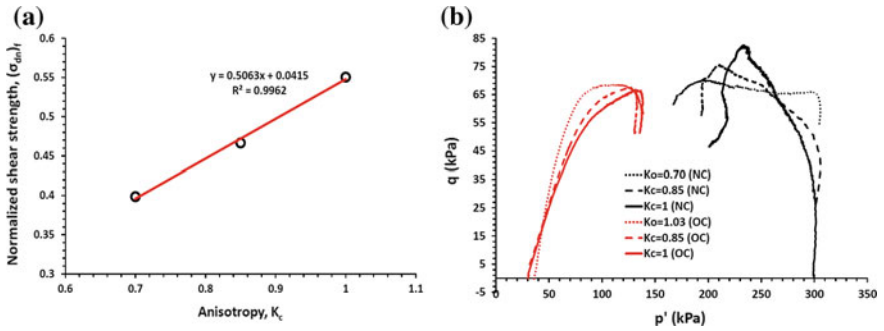

Fig. 6 Shear response of Nagpur expansive soil **a** normalized shear strength versus anisotropy, **b** effective stress path including anisotropy effect

the movement of ESPs towards the origin exhibiting contractive nature for all the K_c values 0.70, 0.85 and 1. On the other side, the curves of OC specimen showed dilative response as ESPs moved away from the origin. The effective stress path for NC specimens were observed to be flatter from $K_c = 1$ to $K_0 = 0.70$. It indicated that the deviatoric stress remained almost constant or varying very less with the increase in axial strain, which could be due to the generation of majorly plastic deformation during shearing as the soil specimen already took some elastic shear deformation during anisotropic consolidation phase. In the case of OC specimens, not much variation in peak deviatoric stress was observed but the initial stiffness of anisotropically consolidated specimen was found to be higher than that of isotropically consolidated specimens. The sharp reduction in the shear stress (q) was observed after achieving peak shear stress ($q_{\max}$) for all the specimens. It could be attributed due to the failure of specimen by local concentration of strains leading to the formation of shear bands.

3.4 *Evolution of 'A' and 'β_{max}' Parameters*

The evolution of excess pore water pressure with deviatoric stress is expressed by Skempton's pore pressure parameter A, which is defined in Eq. 8 [18].

$$A = \frac{\Delta u}{\Delta(\sigma_1 - \sigma_3)} \tag{8}$$

The A parameter evolution with axial strain during shearing is shown in Fig. 7a. Positive and negative values of A parameter were observed for NC and OC state respectively. In NC specimens, A parameter value at failure (A_f) was increased from 0.904 for $K_c = 1$ to 3.996 for $K_0 = 0.70$. In OC specimens, A parameter changed from -0.26 for $K_c = 1$ to -0.071 for $K_{0(\mathrm{OC})} = 1.02$. With the same changes in deviatoric stress, the more pore water pressure was generated for anisotropically consolidated

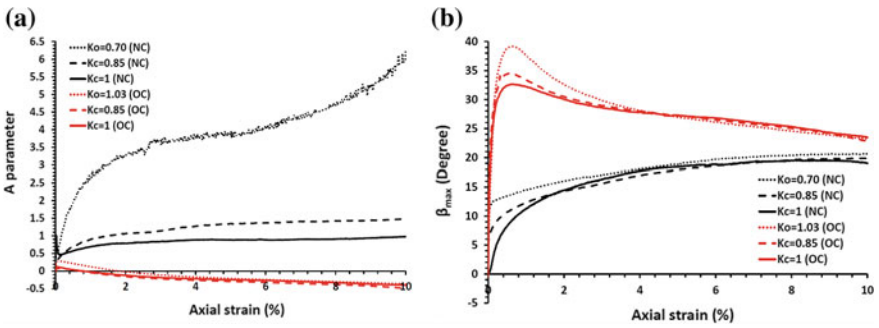

Fig. 7 Undrained shear behavior of Nagpur expansive soil **a** A parameter, **b** $\beta_{\max}$ evolution

specimen than that of isotropically consolidated specimen. The continuously increasing response of $K_0 = 0.70$ specimen was observed due to the continuously increasing pore pressure with almost constant deviatoric stress during shearing.

The effect of anisotropy and stress history on maximum angle of obliquity (β_{max}) is shown in Fig. 7b by plotting the curve between β_{max} and axial strain. This can be defined as another failure criterion which exhibited the effect of effective normal stresses in addition to effective shear stresses. It is the slope of the mid-point of Mohr circle. The mathematical definition of β_{max} in q–p' space is given in Eq. 9.

$$\beta_{\max} = \tan^{-1}\left(\frac{\sigma_1' - \sigma_3'}{\sigma_1' + \sigma_3'}\right) = \tan^{-1}\left(\frac{q'}{p'}\right) \tag{9}$$

The response for NC specimens indicated gradual increase in β_{max} value with axial strain without showing any distinct peak; whereas the OC specimens shown distinct peak for all the K_c values. The reason could be the phase transformation (PT) of soil from contractive to dilative during shearing process of OC specimens. At peak deviatoric stress, the values of β_{max} was almost constant for all K_c values in NC state and increase of 3° was observed as consolidation changes from isotropic to anisotropic in OC state.

4 Conclusions

The current study examined the effect of stress history and anisotropy on shear behavior of Nagpur expansive soil. The experiments were conducted under the undrained triaxial compression loading conditions and results were analyzed in terms of consolidation volumetric strains, normalized stress-strain, excess pore water pressure response, effective stress path and evolution of A and β_{max} parameters. Key observations are summarized as follows:

- The volumetric strain of specimen (ε_v) during anisotropic consolidation was observed to be higher than that of isotropic consolidation at given mean effective stress (p') due to additional volumetric strain generated from deviatoric stress. Hence, the change in void ratio during consolidation was found to be a function of mean effective stress and deviatoric stress.
- Normalized undrained shear strength was reduced significantly for anisotropically consolidated specimens at both NC and OC state. The reduction in strength was found to be linear with anisotropy value (K_c) for NC soil. The reduction in failure strain and increase in stiffness was observed for anisotropically consolidated NC and OC specimens due to possible formation of more dispersed microstructure.
- The generation of positive pore water pressure for NC soil indicated the contractive behavior, whereas initially positive and then negative response of OC soil represented dilative response at failure for all the specimens with different K_c values. Due to the smaller final void ratio after anisotropic consolidation, the generation of

positive pore water pressure and contractive response was observed to be smaller as compared to isotropically consolidated specimens under NC state.
- The Skempton's pore pressure parameter at failure (A_f) was observed to increase with the decrease in K_c value. This indicated that with the same changes in deviatoric stress, the more pore water pressure was generated for anisotropically consolidated specimen than that of isotropically consolidated specimen at NC and OC state.

Acknowledgements Financial Support from IIT Gandhinagar is gratefully acknowledged. Any opinions, findings, and conclusions or recommendations expressed in this material are those of authors and do not necessarily reflect the views of IIT Gandhinagar.

References

1. Abdulhadi NO, Germaine JT, Whittle AJ (2012) Stress-dependent behavior of saturated clay. Can Geotech J 49(8):907–916
2. Amorosi A, Rampello S (2007) An experimental investigation into the mechanical behaviour of a structured stiff clay. Géotechnique 57(2):153–166
3. Anandarajah A, Kuganenthira N, Zhao D (1996) Variation of fabric anisotropy of kaolinite in triaxial loading. J Geotech Eng 122(8):633–640
4. Bozzano F, Bretschneider A, Martino S, Prestininzi A (2014) Time variations of the K0 coefficient in overconsolidated clays due to morphological evolution of slopes. Eng Geol 169:69–79
5. Cai Y, Hao B, Gu C, Wang J, Pan L (2018) Effect of anisotropic consolidation stress paths on the undrained shear behavior of reconstituted Wenzhou clay. Eng Geol 242:23–33
6. Donaghe RT, Townsend FC (1978) Effects of anisotropic versus isotropic consolidation in consolidated-undrained triaxial compression tests of cohesive soils. Geotech Test J 1(4):173–189
7. Gao YB (2013) Compression and extension yield of an anisotropically consolidated soil. Soils Found 53(3):431–442
8. Henkel DJ, Sowa VA (1964) The influence of stress history on stress paths in undrained triaxial tests on clay. In: Laboratory shear testing of soils. ASTM International
9. IS: 2911 (PART-III) (1980) Indian Standard code of practice for design and construction of under-reamed piles. BIS
10. Kamei T (2003) Effects of stress paths on undrained shear characteristics of anisotropically consolidated cohesive soil. J Jpn Soc Eng Geol 44(2):119–122
11. Kurukulasuriya LC, Oda M, Kazama H (1999) Anisotropy of undrained shear strength of an over-consolidated soil by triaxial and plane strain tests. Soils Found 39(1):21–29
12. Ladd CC (1965) Stress-strain behaviour of anisotropically consolidated clays during undrained shear. In: Proceedings of the 6th international conference on soil mechanics and foundation engineering, Montréal, vol 1, pp 282–286
13. Mayne PW (1985) Stress anisotropy effects on clay strength. J Geotech Eng 111(3):356–366
14. Mitchell JK, Soga K (2005) Fundamentals of soil behavior, vol 3. Wiley, New York
15. Sachan A, Penumadu D (2007) Effect of microfabric on shear behavior of kaolin clay. J Geotech Geoenviron Eng 133(3):306–318

16. Shi J, Qian S, Zeng LL, Bian X (2015) Influence of anisotropic consolidation stress paths on compression behaviour of reconstituted Wenzhou clay. Géotechnique Lett 5(4):275–280
17. Sivakumar V, Doran IG, Graham J (2002) Particle orientation and its influence on the mechanical behaviour of isotropically consolidated reconstituted clay. Eng Geol 66(3–4):197–209
18. Skempton AW (1954) The pore-pressure coefficients A and B. Geotechnique 4(4):143–147

Study of Effect of Stiffening and Rigidity of Bearing Stratum-On Tip Load for Single and Group of Granular Piles

Vaibhaw Garg and Jitendra Kumar Sharma

Abstract In the modern time due to population explosion and growing demands with constrains of limited land resources, engineers are forced to use those areas for construction, which have soft soils or even other worst soil conditions. Application of granular piles is one among the various existing solution to the problem. The present paper investigates the comparison of variation in the percentage tip load of the partially stiffened granular pile. The granular pile is partially stiffened means some portion of granular pile at the top is replaced by a better engineering material. The effect of stiffening is studied in two forms namely relative length of stiffening, i.e., the percentage length of stiffening considered from top of the granular pile and the relative stiffness of the material of top portion of granular pile. The analysis is carried out for both categories of granular piles viz. floating and end-bearing. This paper reveals the study of variation in percentage base load, showing the effect of relative length, normalized spacing between the partially stiffened granular piles, stiffening parameters, rigidity of bearing stratum, etc., on a single and group of two, three and four axially loaded, symmetrically placed, partially stiffened granular piles each loaded with equal load is studied. It was found that the pile percentage tip load increases with the increase in stiffening parameters as well as with the rigidity of the bearing stratum in all cases. The stiffening effect incorporated at the top of the granular piles is more effective in transferring the loads, in case of relative stiffening range of granular pile. It also acts as an effective remedial measure for the problem of bulging of the granular piles.

Keywords Ground improvement · Granular pile · Relative length of stiffening · Relative stiffness · Bearing stratum

V. Garg (✉) · J. K. Sharma
Civil Engineering Department, University Department, Rajasthan Technical University, Kota 324010, Rajasthan, India
e-mail: vgarg@rtu.ac.in

J. K. Sharma
e-mail: jksrtu@gmail.com

A. Prashant et al. (eds.), *Advances in Computer Methods and Geomechanics*, Lecture Notes in Civil Engineering 55,
https://doi.org/10.1007/978-981-15-0886-8_56

Abbreviations

GP	Granular pile
L	Length of granular pile
'n'	Total number of elements of GP
$d = (2a)$	Diameter of granular pile
P	Axial load on each granular pile of granular pile group
P_b	Load on the base of the GP
L/d	Relative length of granular pile
E_{gp}	Deformation modulus of un-stiffened portion of granular pile
E_b	Deformation modulus of bearing stratum
E_b/E_s	Relative stiffness of bearing stratum on which the piles are resting
E_{gpst}	Deformation modulus of stiffened portion of granular pile
E_s	Deformation modulus of soil
ν_s	Poisson's ratio of soil
K_{gp}	Relative stiffness of granular pile $= (E_{gp}/E_s)$
p_b	Granular pile base pressure
s	Spacing between center to center of the granular piles
s/d	Normalized spacing, between granular piles
ρ	Normalized displacement of GP along its length
L_s	Length of the pile stiffened from the top of the pile
$\eta = L_s/L$	Relative length of stiffening from top of GP
χ	Relative stiffness factor (ratio of K_{gp} of stiffened top portion of GP to K_{gp} of the un-stiffened portion of GP) ($\chi > 1$, for stiffening)
$(P_b/P) \times 100$	Percentage load transferred to the base of a GP in a group of GPs

1 Introduction

Civil engineers normally face the challenges in providing an economical, viable solution for foundations in the areas consisting of soft soils. This paper analyses the comparison of percentage tip load transferred to the base of a group of floating [$E_b/E_s \rightarrow 1$] and end bearing [$E_b/E_s \rightarrow \infty$] partially stiffened granular piles. The analysis is based on the elastic continuum approach. Pile displacement matrix is developed by incorporating the relative stiffness factor and relative length of stiffening from top of GP. Soil displacement matrix is generated by integrating, Mindlin's [10, 11] equations. The mirror image technique of solution developed by Mattes and Poulos [9] for end-bearing piles is used for obtaining the solution.

Major assumptions made during analysis

[A] Stress-strain behavior is assumed to be linear.
[B] The base of stone column/granular pile is assumed to be smooth across which the load is uniformly distributed [8].

[C] The installation effects in the in situ soil due to the installation of granular piles are ignored and as also consolidation with time.
[D] Soil is assumed to be homogeneous, isotropic and behave linearly.
[E] No slip or yield condition at the pile—soil interface.

Poulos and Mattes [13] were pioneers in presenting the solution for foundation in soft soils by studying settlement analysis of group of compressible piles. Keykhosropur et al. [7] developed a 3D numerical approach to study the effect of varying the encasement length of different columns of a group of GECs on the overall group behavior. Ghazavi and Afshar [3] experimentally studied the comparison of the effectiveness of vertical encapsulating of stone columns in the same conditions for various stone column diameters. Results obtained shows that the stone column bearing capacity increases by using vertical reinforcing material. Chen et al. [1] studied the reaction of geosynthetic-encased stone columns (GECs) in soft soils under embankment loading using finite element methods. The study revealed that the failure of the GECs is caused by the bending of the columns rather than shear. Zhang and Zhao [14] presented the, analytical solutions based on the unit-cell concept to predict deformation behaviors of geo-textile-encased stone columns at any depth below the top plane of the columns. Grover et al. [4] studied the effect of stiffening on a single granular pile for both types of piles viz. floating and end bearing. The analysis of settlement for single pile with raft has been done. The effects of encasement stiffness and strength on the response of individual geo-textile encased granular columns embedded in soft soil through model tests was studied by Hong et al. [6]. Gupta and Sharma [5] carried out the analysis of a non homogeneous granular pile with non linear deformation modulus. Settlement analysis based on parabolic behavior is done. Garg and Sharma [2] analyze analytically settlement of single and group of two partially stiffened floating granular piles, by partially stiffening the GPs from top.

2 Problem Definition and Method of Analysis

A group of two, three and four GPs symmetrically placed bearing on a relatively stiff layer each of length 'L', diameter, 'd' = ($2a$) and subjected to an axial load 'P' (Fig. 1a–c). The GPs are each partially stiffened over a length, L_s. The relative stiffness of GP is defined as, $K_{gp} = E_{gp}/E_s$, i.e., the ratio of deformation modulus of granular pile to that of the in situ soil. The relative stiffness of the bearing stratum is defined as, $K_b = E_b/E_s$, where E_b is the modulus of deformation of the bearing stratum. Parameters, 'χ' (=E_{gpst}/E_{gp}), where 'E_{gpst}' and 'E_{gp}' are the deformation moduli of the stiffened and un-stiffened portions respectively of a granular pile and η (=L_s/L) the relative stiffness factor and relative length of stiffening from top of GP are incorporated to define the partial stiffening. Mirror image technique is used [12] for the analysis of the end-bearing GP.

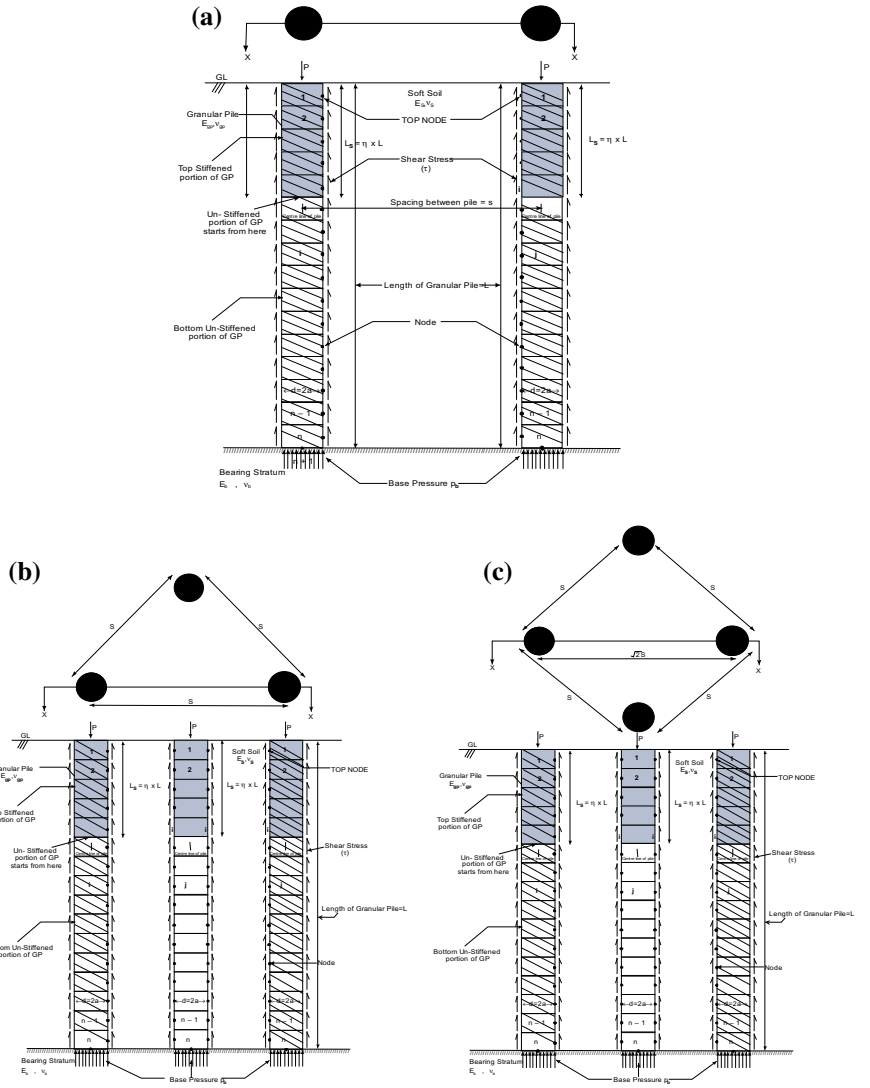

Fig. 1 **a** Plan and sectional elevation at X–X of a group of two placed partially stiffened end-bearing GPs, **b** plan and sectional elevation at X–X of a group of three placed partially stiffened end-bearing, GPs **c** plan and sectional elevation at X–X of a group of four placed partially stiffened end-bearing GPs

For a group of two floating granular piles

$$\{\rho^s\} = \left\{\frac{S^s}{d}\right\} = [[{}_1IF^s] + [{}_2IF^s]]\left\{\frac{\tau}{E_s}\right\} \tag{1}$$

where $\{S^s\}$ and $\{\rho^s\}$, are soil displacement and normalized soil displacement vectors of size, $(n+1)$ respectively. $\{\tau\}$, is a column vector of size, $(n+1)$, for GP-soil interface shear stresses including the normal stress at base, $\left[\left[{}_1IF^S\right]+\left[{}_2IF^S\right]\right]$, is a square matrix for soil displacement influence coefficients of size, $(n+1)$, for a floating granular pile in which, $\left[{}_1IF^S\right]$ and $\left[{}_2IF^S\right]$ are matrices of influence due to shear and base stresses on own and adjacent GP respectively Garg and Sharma [2].

For evaluating the soil displacements in case of end-bearing GP group, mirror image technique is used as suggested by Poulos and Davis [12].

For group of four granular piles resting on stiff bearing stratum, the soil displacement equations are

$$\{\rho^s\}=\left\{\frac{S^s}{d}\right\}=\begin{bmatrix}[{}_1IF^{sp}]+[{}_2IF^{sp}]+[{}_3IF^{sp}]+[{}_4IF^{sp}] \\ -\kappa\left[{}_1IF^{spim}\right]-\kappa\left[{}_2IF^{spim}\right]-\kappa\left[{}_3IF^{spim}\right]-\kappa\left[{}_4IF^{spim}\right]\end{bmatrix} \times\left\{\frac{\tau}{E_s}\right\} \tag{2}$$

where $[{}_1IF^{sp}]$, $[{}_2IF^{sp}]$, $[{}_3IF^{sp}]$ and $[{}_4IF^{sp}]$ are square matrices of size $(n+1)$ each due to influence of elemental shear stresses of own (first), second (for spacing s), third (for spacing s) and fourth GP (for spacing $\sqrt{2}$s), while $\left[{}_1IF^{spim}\right]$, $\left[{}_2IF^{spim}\right]$ $\left[{}_2IF^{spim}\right]$ and $\left[{}_2IF^{spim}\right]$ are soil displacement influence coefficients due to shear stresses on imaginary elements on four GPs as just described and κ is a non-dimensional parameter used for incorporating the rigidity of bearing stratum.

For a group of four granular piles resting on stiff bearing stratum the interface shear stresses are

$$\left\{\frac{\tau}{E_s}\right\}=\begin{bmatrix}[{}_1IF^{sp}]+2\times[{}_2IF^{sp}]+[{}_4IF^{sp}] \\ -\kappa\left[{}_1IF^{spim}\right]-2\times\kappa\left[{}_2IF^{spim}\right]-\kappa\left[{}_4IF^{spim}\right]-[\Delta]\end{bmatrix}^{-1}\{Y\} \tag{3}$$

where

$$\{Y\}=\frac{P\left(1-\upsilon_b^2\right)}{(E_b/E_s)d^2E_s}\{1\}+\frac{P}{\left(\pi d^2/4\right)E_s}[\Delta_1]\{1\}$$

$$[\Delta]=-\frac{4(L/d)}{n}[\Delta_1][\Delta_2]-\frac{\pi(L/d)\left(1-\nu_b^2\right)}{n(E_b/E_s)}[1]$$

Again $[\Delta_1]$ is defined as below, i.e., a matrix of size $(n\times n)$

$$[\Delta_1] = \frac{(L/d)}{nK_{gp}} \begin{bmatrix} \frac{0.5}{\chi} & \frac{1}{\chi} & \frac{1}{\chi} & 1 & - & - & - & - & 1 \\ 0 & \frac{0.5}{\chi} & \frac{1}{\chi} & 1 & - & - & - & - & 1 \\ 0 & 0 & \frac{0.5}{\chi} & 1 & - & - & - & - & 1 \\ 0 & 0 & 0 & 0.5 & - & - & - & - & 1 \\ . & . & . & . & . & . & . & . & . \\ 0.5 & 1 & 1 & 1 & 1 & 1 & 1 & 1 & 1 \\ 0 & 0.5 & 1 & 1 & 1 & 1 & 1 & 1 & 1 \\ . & . & . & . & . & . & . & . & . \\ 0 & 0 & 0 & 0 & 0 & 0 & 0 & 0 & 0.5 \end{bmatrix} \quad \begin{bmatrix} \text{Here } K_{gp} \text{ will be} \\ \text{replaced by } \chi\ K_{gp} \\ \text{for top elements} \\ \text{of GP to take into} \\ \text{consideration of} \\ \text{effect of} \\ \text{stiffening upto} \\ \text{a depth } \frac{\eta L}{d} \text{ as shown} \end{bmatrix}$$

and $[\Delta_2]$ is lower triangular matrix of size 'n' in which the diagonal and off diagonal terms are 0.5 and 1.0 respectively.

For the estimation of κ (a non-dimensional parameter, used in mirror image technique for incorporating the effect of rigidity of bearing stratum, $\kappa = 0$ for floating GP and its value is approaching to 1 for very rigid bearing stratum), an iterative technique suggested by [9] is used. From the equilibrium equation, the base pressure, p_b, can be obtained as

$$p_b = \frac{P}{\pi d^2/4} - \frac{4(L/d)}{n} \sum_{j=1}^{j=n} \tau_j \tag{4}$$

where τ_j, is the shear stress on jth element and 'n' is total number of elements of GP. With an initial chosen values of, κ, Eqs. (3) and (4) are solved to estimate the 'n' unknown shear stresses, τ, and base pressure, p_b. Having obtained the solution for chosen values of, κ, a closer estimate of the correct values of, κ, is obtained by considering the compatibility between displacements of soil and bearing stratum at the pile tip. The soil displacement at the pile tip is

$$\begin{aligned} \rho_b^s = \frac{S_b^s}{d} &= \begin{Bmatrix} \left\{ {}_1IF_j^{sb} \right\} + 2\left\{ {}_2IF_j^{sb} \right\} + \left\{ {}_4IF_j^{sb} \right\} - \kappa \left\{ {}_1IF_j^{sbim} \right\} - 2x\kappa \left\{ {}_2IF_j^{sbim} \right\} \\ -\kappa \left\{ {}_4IF_j^{sbim} \right\} \end{Bmatrix} \left\{ \frac{\tau}{E_s} \right\} \\ &= \frac{\sum_{j=1}^{j=n} \left({}_1IF_j^{sb} + 2{}_2IF_j^{sb} + {}_4IF_j^{sb} - \kappa {}_1IF_j^{sbim} - 2\kappa {}_2IF_j^{sbim} - \kappa \left\{ {}_4IF_j^{sbim} \right\} \right) \tau_j}{E_s} \end{aligned} \tag{5}$$

${}_1IF_j^{sb}$ and ${}_1IF_j^{sbim}$, ${}_2IF_j^{sb}$ and ${}_2IF_j^{sbim}$ and ${}_4IF_j^{sb}$ and ${}_4IF_j^{sbim}$ are respectively the displacement influence coefficients for the tip due to shear stresses on real and imaginary elements 'j' of own and adjacent GP and fourth GP at spacing $\sqrt{2}$ s. However due to symmetry ${}_1IF_j^{sb} = {}_1IF_j^{sbim}$ and ${}_2IF_j^{sb} = {}_2IF_j^{sbim}$. Equating the soil displacement at the pile tip to the displacement of the base due to base stress, p_b, the new values of non-dimensional parameter, κ, is obtained as

$$\kappa = 1 - \frac{\pi\left(1 - \nu_b^2\right) p_b}{4(E_b/E_s)\sum_{j=1}^{j=n} \tau_j \left({}_1IF_j^{sb} + 2{}_2IF_j^{sb} + {}_2IF_j^{sb}\right)} \tag{6}$$

Above Eq. (6) is solved iteratively using the new values of, κ, and the process repeated until the required convergence is obtained for the values of, κ. Here required convergence means that the percentage difference between the new values of, κ, and last calculated values of, κ, is 0.01%.

Percentage tip load is defined as $= P_b/P \times 100$

where P_b is the load transferred to the base of a GP in group of floating and end-bearing GPs and P is the load on a GP in group of GPs.

Similar analysis is also carried out for group of other arrangements of GPs.

3 Results and Discussion

Validation of results for percentage tip load is done with work of Gupta and Sharma [5] and Garg and Sharma [2] and Madhav et al. [8] (Table 1).

Parameters affecting the response are (i) relative length, i.e., length to diameter ratio of the GP, (L/d), (ii) the relative stiffness of GP, $K_{gp} = (E_{gp}/E_s)$, (iii) the relative stiffness of the bearing stratum, $K_b = E_b/E_s$, in case of the end-bearing GP (iv) normalized spacing, s/d (v) Relative length of stiffening from top of GP, η ($=L_s/L$) and (vi) Relative stiffness factor, $\chi = E_{gpst}/E_{gp}$. Effect of Poisson's ratios of the soft soil, ν_s and of the bearing stratum, ν_b is found to be insignificant.

Table 1 Validation of results for percentage tip load (for un-stiffened GP)

Parameters	Madhav et al. [8]	Gupta and Sharma [5]	Garg and Sharma [2]	Present study
Single floating pile $L/d = 10$, $K_{gp} = 50$, $\nu_s = 0.5$	–	4.86	–	4.85
Floating two pile group $L/d = 10$, $K_{gp} = 50$, $s/d = 2$, $\nu_s = 0.5$	–	–	9.46	9.46
Single end-bearing pile $L/d = 10$, $K_{gp} = 100$, $E_b/E_s = 100$, $\nu_s = 0.5$, $\nu_b = 0.5$	65.5	–	–	65.49

Figure 2 shows the variation of percentage tip load for a GP in a group of GP with relative stiffness of bearing stratum, E_b/E_s. As seen from the graph that for relative stiffness of bearing stratum, $E_b/E_s \rightarrow 1$ which is representative of the floating condition of piles very low values of percentage tip load on a GP in a group of GPs is observed. While in case of higher values of relative stiffness of bearing stratum, $E_b/\mathrm{E_s}$ representing the end-bearing condition of piles, a higher value of percentage tip load on a GP in a group of GPs is observed. It can be seen that at $E_b/E_s = 1$ with relative stiffness of GP, $K_{gp} = 50$, relative length, $L/d = 10$, normalized spacing, $s/d = 2$, relative length of stiffening from top of GP, $\eta = 0.2$ and relative stiffness factor, $\chi = 2$ the percentage tip load on a GP in a group of GPs values are 4.9, 9.5, 14.5, and 18.5 respectively for single GP and a GP in a group of two, three and four GPs. The value of percentage tip load on a GP in a group of GPs at relative stiffness of GP, $K_{gp} = 100$ and rest parameters as it is as just described are 6, 11, 16, and 20 respectively for single GP and a GP in a group of two, three and four GPs revealing a percentage increase of 83, 166 and 233 with respect to single pile. Hence it was found that as relative stiffness of GP, K_{gp} increases the percentage tip load on a GP in a group of GPs increases, due to better load transferring properties. Also revealing that as the number of piles increases in a group, the percentage tip load on a GP in a group of GPs increases due to more influence of stresses in group. For end-bearing conditions with relative stiffness of bearing stratum, $E_b/E_s = 100$, relative stiffness of GP, $K_{gp} = 50$, relative length, $L/d = 10$, normalized spacing, $s/d = 2$, relative length of stiffening from top of GP, $\eta = 0.2$ and relative stiffness factor, $\chi = 2$ the percentage tip load on a GP in a group of GPs values are 50, 62, 73 and 78 respectively for single GP and a GP in a group of two, three and four GPs. With relative stiffness of GP, $K_{gp} = 100$ and other parameters as same the values of percentage tip load on a GP in a group of GPs are 65, 76, 83 and 86 respectively for single GP and a GP in a group of two, three and four GPs. Hence it is found that the percentage increase is comparatively less in case of end-bearing piles, although increasing trend is maintained.

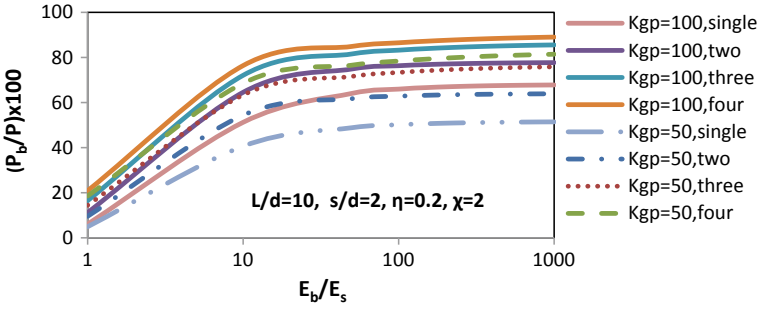

Fig. 2 Variation of percentage tip load $(P_b/P) \times 100$ on a GP in a group of GPs with relative stiffness of bearing stratum, E_b/E_s—effect of relative stiffness of GP, K_{gp} and number of piles in the group ($L/d = 10$, $s/d = 2$, $\eta = 0.2$, $\chi = 2$)

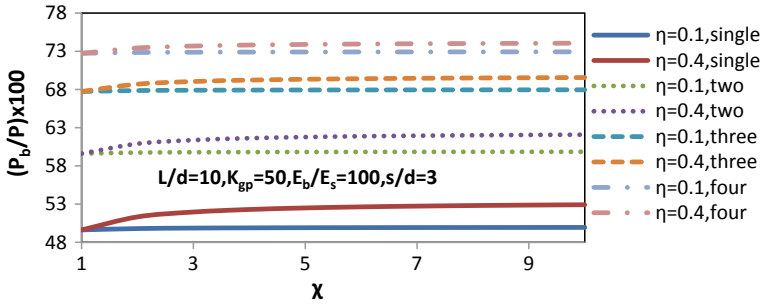

Fig. 3 Variation of percentage tip load $(P_b/P) \times 100$ on a GP in a group of end-bearing GPs with relative stiffness factor, χ—effect of relative length of stiffening from top of GP, η and number of piles in the group ($L/d = 10$, $K_{gp} = 50$, $E_b/E_s = 100$, $s/d = 3$)

The variation of percentage tip load on a GP in a group of GPs with relative stiffness factor, χ, relative length of stiffening from top of GP, η, for relative stiffness of bearing stratum, $E_b/E_s = 100$, relative stiffness of GP, $K_{gp} = 50$, relative length, $L/d = 10$, normalized spacing, $s/d = 3$, is depicted in Fig. 3. It reveals that the percentage tip load on a GP in a group of GPs for end-bearing conditions having relative stiffness factor, relative length of stiffening from top of GP, $\eta = 0.1$ are 49.6, 59.6, 67.7 and 72.7 respectively for single GP and a GP in a group of two, three, and four GPs at $\chi = 1$. At $\chi = 2$ these value of percentage tip load on a GP in a group of GPs are 49.8, 59.7, 67.9 and 72.8, indicating a marginal increase in the percentage tip load with relative stiffness factor. The same values at $\eta = 0.4$ are 49.6, 59.6, 67.7 and 72.7 at $\chi = 1$ while at $\chi = 2$ these values are 51.33, 60.89, 68.69 and 73.42, i.e., a higher value at higher relative length of stiffening from top of GP. It may be also noted from the graph that relative stiffness factor works mainly in the range 1–3. The difference in values of percentage tip load with $\eta = 0.1$ and 0.4 shows that difference is also reducing with increase in number of GPs in the group.

Figure 4 represents the variation of percentage tip load of a GP in single and group of two, three, and four GPs with relative stiffness of bearing stratum, E_b/E_s, with effect of relative length, L/d. It can be seen that at $E_b/E_s = 1$ with relative length, $L/d = 10$ relative stiffness of GP, $K_{gp} = 100$, normalized spacing, $s/d = 2$, relative length of stiffening from top of GP, $\eta = 0.3$ and relative stiffness factor, $\chi = 2$ the percentage tip load on a GP in a group of GPs values are 6, 11, 16 and 20 respectively for single GP and a GP in a group of two, three and four GPs. The value of percentage tip load on a GP in a group of GPs at relative length, $L/d = 20$, relative stiffness of bearing stratum, $E_b/E_s = 1$, relative length, $L/d = 10$ relative stiffness of GP, $K_{gp} = 100$, normalized spacing, $s/d = 2$, relative length of stiffening from top of GP, $\eta = 0.3$ and relative stiffness factor, $\chi = 2$ are 2, 5, 8, and 11 respectively for single GP and a GP in a group of two, three and four GPs. Hence it was found that as relative length, L/d increases the percentage tip load on a GP in a group of GPs decreases, due to more length of pile, so more shear stresses developed; hence load transferred to the tip of the GP decreases.

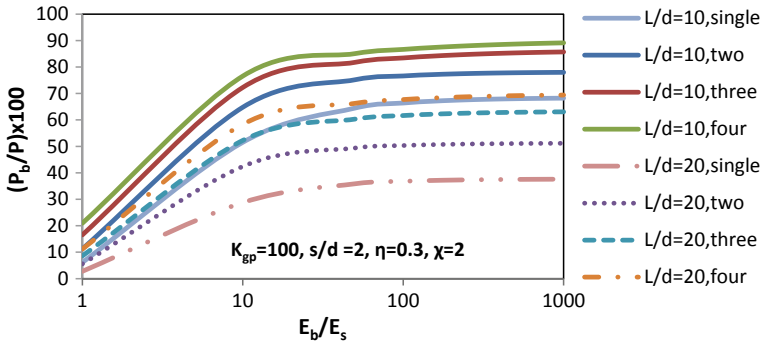

Fig. 4 Variation of percentage tip load $(P_b/P) \times 100$ on a GP in a group of GPs with relative stiffness of bearing stratum, E_b/E_s—effect of relative length, L/d, and number of piles in the group ($K_{gp} = 100$, $s/d = 2$, $\eta = 0.3$, $\chi = 2$)

From Fig. 4 if end-bearing conditions are focused say with relative stiffness of bearing stratum, $E_b/E_s = 100$, relative stiffness of GP, $K_{gp} = 50$, relative length, $L/d = 10$, normalized spacing, $s/d = 2$, relative length of stiffening from top of GP, $\eta = 0.3$ and relative stiffness factor, $\chi = 2$ the percentage tip load on a GP in a group of GPs values are 66, 76, 83, and 86 respectively for single GP and a GP in a group of two, three and four GPs. With relative length, $L/d = 20$ with same set of parameters as just described the values of percentage tip load on a GP in a group of GPs are 36, 50, 61, and 67 respectively for single GP and a GP in a group of two, three, and four GPs. The values of percentage tip load on a GP in a group of GPs decreases with increase in relative length, as the bearing stratum is moving away in case of higher values of L/d, so load transferring characteristics declines.

Figure 5 shows the variation of percentage tip load on a GP in a group of GPs with relative stiffness factor, χ having effect of relative length of stiffening from top of GP, η for floating GPs at relative stiffness of GP, $K_{gp} = 50$, relative length, $L/d = 10$, normalized spacing, $s/d = 3$. It may be noted from the graph that for relative

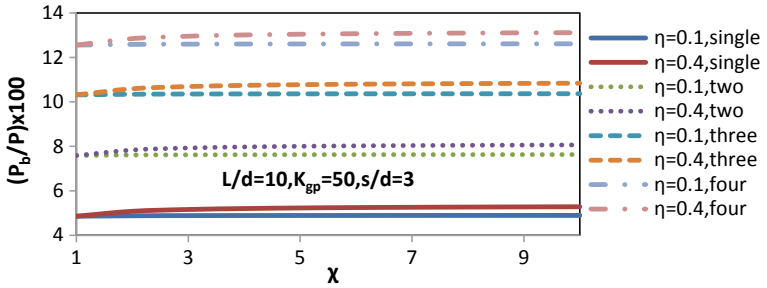

Fig. 5 Variation of percentage tip load $(P_b/P) \times 100$ on a GP in a group of floating GPs with relative stiffness factor, χ—effect of relative length of stiffening from top of GP, η and number of piles in the group ($L/d = 10$, $K_{gp} = 50$, $s/d = 3$)

length of stiffening from top of GP, $\eta = 0.1$ and relative stiffness factor, $\chi = 1$ the percentage tip load on a GP in a group of GPs values are 4.85, 7.58, 10.31 and 12.55 respectively for single GP and a GP in a group of two, three and four GPs. The value of percentage tip load on a GP in a group of GPs at relative length of stiffening from top of GP, $\eta = 0.4$, at $\chi = 3$ considering other parameters to be same, are 5.15, 7.92, 10.69, and 12.95 respectively for single GP and a GP in a group of two, three and four GPs. It may be noted from the graph that stiffening parameters are very less sensitive to the percentage tip load and relative stiffness factor is mainly sensitive in the range 1–3.

It can be seen from Fig. 6 that at relative stiffness of bearing stratum, $E_b/E_s = 1$ with relative stiffness of GP, $K_{gp} = 100$, relative length, $L/d = 10$, normalized spacing, $s/d = 2$, relative length of stiffening from top of GP, $\eta = 0.3$ and relative stiffness factor, $\chi = 2$ the percentage tip load on a GP in a group of GPs values are 11, 16, and 20 respectively for a GP in a group of two, three and four GPs. The value of percentage tip load on a GP in a group of GPs at normalized spacing, $s/d = 3$, relative stiffness of bearing stratum, $E_b/E_s = 1$, relative stiffness of GP, $K_{gp} = 100$, relative length, $L/d = 10$, relative length of stiffening from top of GP, $\eta = 0.3$ and relative stiffness factor, $\chi = 2$ are 9, 12 and 14 respectively for a GP in a group of two, three and four GPs. Hence it was found that as normalized spacing, s/d increases the percentage tip load on a GP in a group of GPs decreases, due to reduced influence of one pile over another in the group.

Figure 6 also reveals the same trends as obtained for floating pile groups for end-bearing piles with relative stiffness of bearing stratum, $E_b/E_s = 100$, relative stiffness of GP, $K_{gp} = 100$, relative length, $L/d = 10$, normalized spacing, $s/d = 2$, relative length of stiffening from top of GP, $\eta = 0.3$ and relative stiffness factor, $\chi = 2$ the percentage tip load on a GP in a group of GPs values are 76, 83, and 86 respectively for a GP in a group of two, three and four GPs. With normalized spacing, $s/d = 3$, relative stiffness of bearing stratum, $E_b/E_s = 100$, relative stiffness of GP, $K_{gp} =$

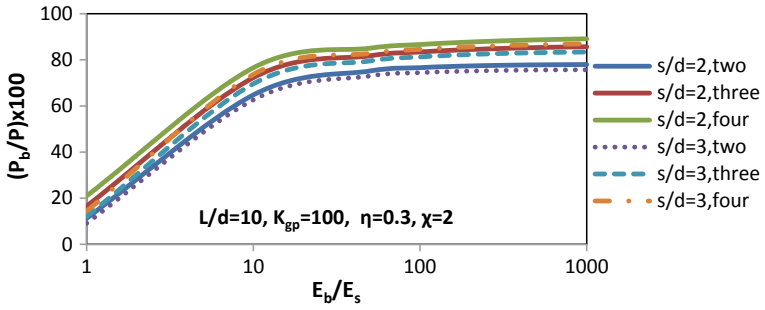

Fig. 6 Variation of percentage tip load $(P_b/P) \times 100$ on a GP in a group of GPs with relative stiffness of bearing stratum, E_b/E_s—effect of normalized spacing, s/d, and number of piles in the group ($L/d = 10$, $K_{gp} = 100$, $\eta = 0.3$, $\chi = 2$)

100, relative length, $L/d = 10$, relative length of stiffening from top of GP, $\eta = 0.3$ and relative stiffness factor, $\chi = 2$ the values of percentage tip load on a GP in a group of GPs are 74, 81 and 84 respectively for a GP in a group of two, three, and four GPs.

4 Conclusions

The study of percentage tip load on a GP in a group of GPs variation with introduction of two new parameters viz. relative stiffness factor, χ and relative length of stiffening from top of GP, η is done. New pile displacement matrix is developed and percentage tip load on a GP in a group of GPs is analysed using elastic continuum approach.

The percentage tip load on a GP in a group of GPs is found to increase marginally with relative stiffness factor, χ and relative length of stiffening from top of GP, η, and is also found to increase with increase in the number of GPs in the group.

With increase in relative length from 10 to 20 the percentage tip load on a GP in a group of GPs in case of end-bearing piles at, relative stiffness of bearing stratum $E_b/E_s = 50$ with relative stiffness of GP, $K_{gp} = 100$, normalized spacing, $s/d = 2$, relative length of stiffening from top of GP, $\eta = 0.3$ and relative stiffness factor, $\chi = 2$ the percentage tip load on a GP in a group of GPs values decreases from 64, 75, 81 and 85 respectively for single GP and a GP in a group of two, three and four GPs to 35,49,60 and 66 at, $L/d = 20$, thus causing a percentage reduction of, 45, 34, 26, and 22 respectively for single GP and a GP in a group of two, three and four GPs. In case of floating piles this reduction is of the order of 50% in all groups of partially stiffened GPs at relative stiffness of bearing stratum $E_b/E_s = 1$ with relative stiffness of GP, $K_{gp} = 100$, normalized spacing, $s/d = 2$, relative length of stiffening from top of GP, $\eta = 0.3$ and relative stiffness factor, $\chi = 2$, for L/d varying from 10 to 20.

The values of percentage tip load on a GP in a group of GPs in case of end-bearing and floating group of GPs decreases with increase in normalized spacing, s/d, because as the normalized spacing increases the effect of one pile over the other decreases in the group. For end-bearing GPs with relative stiffness of bearing stratum $E_b/E_s = 50$ with relative stiffness of GP, $K_{gp} = 100$, relative length, $L/d = 10$, relative length of stiffening from top of GP, $\eta = 0.3$ and relative stiffness factor, $\chi = 2$ the percentage tip load on a GP in a group of GPs values decreases from 75, 81 and 85 respectively at normalized spacing, $s/d = 2$, for a GP in a group of two, three and four GPs to 72,79 and 82 for normalized spacing, $s/d = 3$. Hence observing a percentage decrease of 4, 2 and 3 respectively for a GP in a group of two, three and four GPs.

For floating group of GPs the percent reduction is of the order of 18, 25 and 30 respectively for a GP in a group of two, three and four GPs at relative stiffness of bearing stratum $E_b/E_s = 1$ with relative stiffness of GP, $K_{gp} = 100$, relative length, $L/d = 10$, relative length of stiffening from top of GP, $\eta = 0.3$ and relative stiffness factor, $\chi = 2$, when the normalized spacing, s/d increases from 2 to 3.

As the relative stiffness of GP, K_{gp} increases from 50 to 100 the value of percentage tip load on a GP in a group of GPs for end-bearing group of GPs with relative stiffness

of bearing stratum, $E_b/E_s = 50$, relative length, $L/d = 10$, relative length of stiffening from top of GP, $\eta = 0.2$ and relative stiffness factor, $\chi = 2$, normalized spacing, $s/d = 2$, the percentage tip load on a GP in a group of GPs values increases from 48, 61, 71, and 76 respectively, for single GP and for a GP in a group of two, three and four GPs to 64,74, 81, and 84, thereby causing a percentage increase of 33, 21, 14, and 10 for respectively, for single GP and for a GP in a group of two, three and four GPs.

In case of floating group of piles, as the relative stiffness of GP, K_{gp} increases from 50 to 100 the value of percentage tip load on a GP in a group of GPs with relative stiffness of bearing stratum, $E_b/E_s = 1$, relative length, $L/d = 10$, relative length of stiffening from top of GP, $\eta = 0.2$ and relative stiffness factor, $\chi = 2$, normalized spacing, $s/d = 2$, the percentage tip load on a GP in a group of GPs values increases from 4, 9, 14, and 18 respectively, for single GP and for a GP in a group of two, three and four GPs to 6,11, 16, and 20, thereby causing a percentage increase of 50, 22, 14 and 11 for respectively, for single GP and for a GP in a group of two, three and four GPs.

It was found that increase in value of relative stiffness of bearing stratum, E_b/E_s, is mainly affecting the percentage tip load on a GP in a group of GPs values in the range of 1–50.

References

1. Chen JF, Li LY, Xue JF, Feng SZ (2015) Failure mechanism of geosynthetic encased stone columns in soft soils under embankment. Geotext Geomembr 43(5):424–431
2. Garg V, Sharma JK (2018) Analysis and settlement of partially stiffened single and group of two floating granular piles. Indian Geotech J 1–13. doi:https://doi.org/10.1007/s40098-018-0321-7
3. Ghazavi M, Afshar JN (2013) Bearing capacity of geosynthetic encased stone columns. Geotext Geomembr 38:26–36
4. Grover KS, Sharma JK, Madhav MR (2015) Settlement analysis of single granular pile with stiffened top. Int J Sci Eng Res 6(6):61–75
5. Gupta P, Sharma JK (2017) Settlement analysis of non-homogeneous single granular pile. Indian Geotech J 48:1–10
6. Hong YS, Wu CS, Yu YS (2016) Model tests on geotextile-encased granular columns under 1-g and undrained conditions. Geotext Geomembr 44(1):13–27
7. Keykhosropur L, Soroush A, Imam R (2012) 3D numerical analyses of geosynthetic encased stone columns. Geotext Geomembr 35:61–68
8. Madhav MR, Sharma JK, Chandra S (2006) Analysis and settlement of a non-homogeneous granular pile. Indian Geotech J 36(3):249–271
9. Mattes NS, Poulos HG (1969) Settlement of single compressible pile. J Soil Mech Found Div ASCE 95(SM1):189–207
10. Mindlin RD (1936) Force at a point in the interior of a semi infinite solid. Physics 7:195–202
11. Mindlin RD (1937) Stress system in a circular disk under radial forces. In: Presented at the joint meeting of applied mechanics and Hydraulic division of the ASME held at Cornell University, N.Y, pp A115–A118
12. Poulos HG, Davis EH (1980) Pile foundation analysis and design. Wiley, Australia

13. Poulos HG, Mattes NS (1971) Settlement and load distribution analysis of pile groups. Aust Geomech J G2(1):11–20
14. Zhang L, Zhao M (2015) Deformation analysis of geo-textile encased stone columns. Int J Geomech 15(3):1–10

Evaluation of Macroscopic Soil Model Parameters Using the Discrete Element Method

Mandeep Singh Basson, Roberto Cudmani and G. V. Ramana

Abstract The engineering properties of the granular materials are controlled by the physical characteristics of the particles, the fabric, the granular matrix and the state of the material. For these discontinuous materials, numerical modeling using continuum-based methods are not able to capture the complex microscale interactions that control the macro scale behavior into detail. On the other hand, with appropriate contact algorithms, provision for complex grain shapes/gradations and modeling of mechanical behavior using real size discrete particles, the Discrete Element Method has been used by researchers to simulate the behavior of granular materials at the microscale. The objective of this study is to highlight the applicability of the DEM over a range of laboratory tests, including the determination of maximum and minimum void ratio, geometric compression tests, and drained triaxial compression tests. The comparison of experimental and numerical results demonstrates the ability of the DEM to realistically model macroscopic soil behavior based on only a few parameters in the micro scale. We conclude that back-calculation of the parameters in the microscale based on few conventional laboratory tests along with the application of the DEM to simulate complex stress- and strain-paths, that cannot be easily realized in experiments, can be a procedure for the development, validation and calibration of the advanced constitutive models required for solving real geotechnical boundary problems numerically.

Keywords Discrete element method · Granular materials · Hypoplastic law · Triaxial test · Minimum void ratio · Maximum void ratio

M. S. Basson (✉)
University of California at Davis, Davis, USA
e-mail: mbasson@ucdavis.edu

R. Cudmani
Technical University of Munich, Munich, Germany

G. V. Ramana
Indian Institute of Technology Delhi, Delhi, India

A. Prashant et al. (eds.), *Advances in Computer Methods and Geomechanics*, Lecture Notes in Civil Engineering 55,
https://doi.org/10.1007/978-981-15-0886-8_57

1 Introduction

To understand boundary value problems for various practical geotechnical problems, understanding the behavior of soil under generalized loading conditions becomes paramount. The classical methodology of solving such problems is to formulate an analytical solution which becomes complex and cumbersome with an increase in difficulty. Numerical methods, with appropriate constitutive models, facilitate computation of a solution but require proper development, calibration, and refinement [6]. Capturing the various aspects of the behavior of soils gives rise to a large number of constitutive law, which is often too sophisticated to be used in practical problems. At the cost of simplicity, these constitutive laws define rigid mathematically derived parameters which are difficult to obtain through comprehensive experimental testing of soils [19]. As an alternative to classical elasto-plastic theory, the hypoplastic model was developed to describe the mechanical behavior of granular materials. The cornerstone of hypoplastic law is its simplicity and definition of parameters which can be derived experimentally, through routine laboratory test and its inherit nonlinearity which facilitates the localization of deformation. It is a rate type constitutive law which relates the strain rate to the stress rate and stems from rational mechanics in which a single equation can capture the different essential features of the behavior of granular materials [2, 13].

Pioneering attempts of physicist to simulate fracture with discrete models gave birth to Lattice methods. In parallel to these, methods, where each node corresponds to a single particle/aggregate, were developed called the Discrete Element Method Cundall and Strack [5]. Later, DEM became a prominent tool in micromechanics research with the introduction of interparticle shear and particle rotations [8]. As the mechanical behavior of granular materials depends upon the fabric/configuration characteristics and the properties of constituting soil particles, modeling of each grain particle in DEM directly simulates the microstructure of granular materials, and can be used to study different micro-level events such as initiation, formation, and growth of shear zones [10, 12, 14]. With DEM codes being widely available and implemented in parallel computing, cloud computing, and high-performance computing, the computation times have become significantly low.

The objective of this paper is to act as a bridge between the laboratory experiments, continuum and discontinuum mechanics. An attempt was made by Lin and Wu [11] to compare the DEM and hypoplasticity for 2D simulations with considerable success. Firstly, a brief theory of hypoplasticity and discrete element method is presented. Secondly, by simulating three-dimensional quasi-static drained triaxial tests, the contact law parameters are calibrated with results of experimental triaxial tests conducted on Karlsruhe sand. These calibrated contact parameters are then used in DEM simulations of routine geotechnical laboratory tests (gravity deposition, vibration table, compression) in order to find the critical parameters for hypoplastic constitutive law. Thirdly, using a MATLAB code, triaxial tests using hypoplastic parameters obtained using DEM simulations and from the literature are simulated. Finally, a comparison is presented of experimental results, DEM simulation results

for triaxial tests, triaxial test simulated using hypoplastic parameters obtained from DEM simulations and triaxial test simulated using hypoplastic parameters obtained from the literature.

2 Theories (or Experiments, or Methodology)

2.1 Hypoplasticity

Non-linear tensor function establishes the core component of Hypoplasticity, instead of decomposition of deformation into elastic and plastic parts. With no distinction between elastic and plastic deformation, a single unique equation can be used for both loading and unloading. The equation is given in Herleand Gudehus [7] and used in this paper which relates stress rate tensor (T) with the stretching rate D, the Cauchy skeleton stress T_s and the void ratio e with a tensor function h given as:

$$\dot{T}_s = h(T_s, D, e) \tag{1}$$

In compression, the tensorial equation reduces to two scalar equations given as

$$\dot{T}_{s1} = f_s \frac{(T_{s1} + 2T_{s2})^2}{T_{s1}^2 + 2T_{s2}^2} \Bigg[D_1 + a^2 \frac{T_{s1} D_1 + 2T_{s2} D_2}{(T_{s1} + 2T_{s2})^2} T_{s1} + f_d \frac{a}{3} \frac{5T_{s1} - 2T_{s2}}{T_{s1} + 2T_{s2}} \sqrt{D_1^2 + 2D_2^2} \Bigg] \tag{2}$$

$$\dot{T}_{s2} = f_s \frac{(T_{s1} + 2T_{s2})^2}{T_{s1}^2 + 2T_{s2}^2} \Bigg[D_2 + a^2 \frac{T_{s1} D_1 + 2T_{s2} D_2}{(T_{s1} + 2T_{s2})^2} T_{s2} + f_d \frac{a}{3} \frac{4T_{s2} - T_{s1}}{T_{s1} + 2T_{s2}} \sqrt{D_1^2 + 2D_2^2} \Bigg] \tag{3}$$

The barotropic factor f_b takes into consideration the increase of stiffness with an increase of the mean stress and is given as

$$f_s = \frac{h_s}{n} \left(\frac{e_i}{e} \right)^{\beta} \frac{1 + e_i}{e_i} \left(\frac{3p_s}{h_s} \right)^{1-n} \left[3 + a^2 - a\sqrt{3} \left(\frac{e_{i0} - e_{d0}}{e_{c0} - e_{d0}} \right)^{\alpha} \right]^{-1} \tag{4}$$

Finally, f_d is the pressure dependent relative void ratio and is computed as:

$$f_d = \left(\frac{e - e_d}{e_c - e_d} \right)^{\alpha} \tag{5}$$

In total eight parameters are required to define a hypoplastic model which are, e_{i0}, e_{c0}, e_{d0}, h_s, n, a, α and β. A detailed description of a, α and β, can be found in [7].

2.2 Discrete Element Method

YADE, a three-dimensional discrete element software developed by the University of Grenoble, is used in this study [17]. It implements the soft particle approach to model the contact deformation and computes the force-displacement while tracking the positions, velocities, and accelerations of individual particles. These forces are divided into normal and tangential components which control the normal deformation, sliding, and rotation at contacts. With the total forces, the particles are pushed into new positions, and their accelerations are computed by integrating Newton's equations of motion [10]. To complement the simplicity of hypoplastic law, a simple linear elastic normal contact with linear rotational moment law is proposed to simulate the response of spherical particles. The normal and tangential forces are proportional to the normal stiffness and tangential stiffness as (Fig. 1):

$$\overrightarrow{F_n} = k_n U \vec{N} \tag{6}$$

$$\Delta \overrightarrow{F_s} = k_s \Delta \overrightarrow{X_s} \tag{7}$$

where U is the depth of penetration and ΔX is the tangential displacement vector. The stiffness parameters k_n and k_s are computed using the stiffness of the grain contact E_c and radii of the particles R_a and R_b respectively.

$$k_n = E_c \frac{2\,R_a R_b}{R_a + R_b} \text{ and } k_s = v_c E_c \frac{2\,R_a R_b}{R_a + R_b} \tag{8}$$

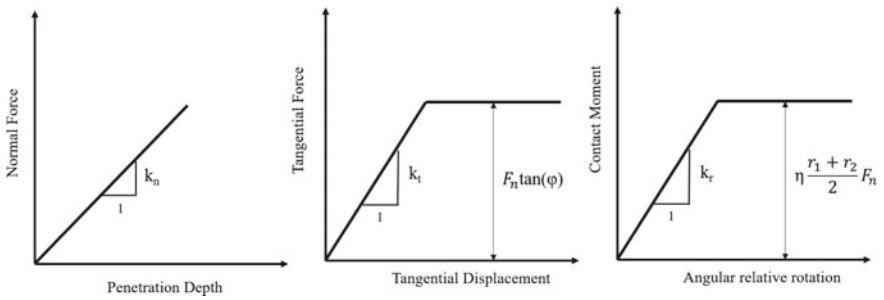

Fig. 1 The response of the contact law and the grain size distribution of Karlsruhe sand

The frictional sliding is mobilized when the Mohr-Coulomb law is satisfied;

$$\overrightarrow{F_s} \leq \overrightarrow{F_n} \tan(\mu) \tag{9}$$

where, μ is the inter particle friction angle. To increase the rolling resistance of pure spheres, simple linear rotational moment law is introduced. Due to the normal forces, the rotation of the particles is arrested, resisting the rotation as

$$\Delta M = k_r \Delta \vec{\omega} \tag{10}$$

Iwashita and Oda [8] related the rotational stiffness k_r to the tangential stiffness k_s as

$$k_r = \beta k_s R_a R_b \tag{11}$$

A dimensionless rotation coefficient is introduced to control the moment of rotation (similar to Mohr–Coulomb sliding),

$$\overrightarrow{\mathrm{M}} \leq \eta \frac{R_a + R_b}{2} \overrightarrow{F_n} \tag{12}$$

As compared to other discrete models incorporating contact moments, YADE is designed primarily for 3D simulations where rolling resistance is an independent parameter; rotations are described using quaternions and grain shape coefficient is not included [18]. In a total of five micromechanical parameters are required for discrete simulations E_c, μ, ν_c, η, β; along with ρ (density of particles) and damping.

2.3 Calibration of Contact Parameters

The most important part of any simulation is the calibration of the underlying law with experimental/physical results. The contact parameters were calibrated using the corresponding triaxial test experimentally conducted on Karlsruhe sand by Kolymbas and Wu [9]. Each component of the contact law affects the macroscopic response of the material depicted in the stress-strain and volume change curves as shown in Fig. 2 [3, 16]. In numerical simulations, a cloud of 10,000 particles was created in a cuboidal space of 0.25 cm × 0.25 cm × 0.75 cm space (aspect ratio of 3) with periodic boundaries. The particles were created based on the upscaled grain size distribution of Karlsruhe sand to decrease the time of simulation. The whole simulation process was divided into two main parts. In the first part, the cloud of the particle was isotropically compressed to the required confining stress under gravity-free conditions. If the required void ratio ($e = 0.53$) was not reached during isotropic compression, the friction angle was reduced in order to assist the tighter rearrangement of particles. Once the confining stress was reached isotropically and the unbalanced forces

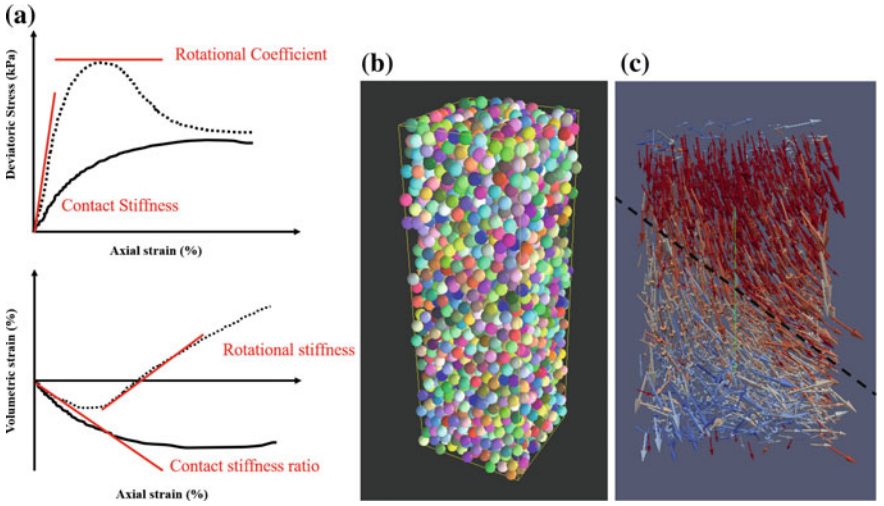

Fig. 2 **a** Effect of contact parameters on the typical response of soil in the triaxial test; **b** numerical sample for the triaxial test in YADE; **c** velocity vectors at the final stage of shearing showing the slip plane

reached low enough values, the friction angle was changed to the desired value, and the shearing in the form of axial strain application (a quasi-static condition with the loading of 1 mm/s) was started. Damping coefficient is kept at a low value of 0.1 in order to exclude the effect of damping on simulation results, yet large enough to dissipate the unbalanced energies and lower the time of simulation. Deviator stresses and corresponding volume change with axial strain were plotted at the constant interval during the simulation.

2.4 Limiting Void Ratios at Zero Pressure

The limiting void ratio e_i, e_d and e_c decrease exponentially with increase in p_s following Eq. 13. The parameters h_s and n control the pressure dependence of grain assembly. h_s, which has the units of stress, is called the reference pressure and controls the slope of the void ratio confining pressure curve. Exponent n controls the nonlinearity of the void ratio with confining pressure curve, which shows the increase in incremental stiffness with increasing confining stress. At zero p_s, the limiting void ratio reaches a maximum value (e_{i0}, e_{d0}, and e_{c0}) and each of them is determined using DEM in subsequent sections (Fig. 3).

$$\frac{e_i}{e_{i0}} = \frac{e_c}{e_{c0}} = \frac{e_d}{e_{d0}} = \exp\left[-\left(\frac{3p_s}{h_s}\right)^n\right] \tag{13}$$

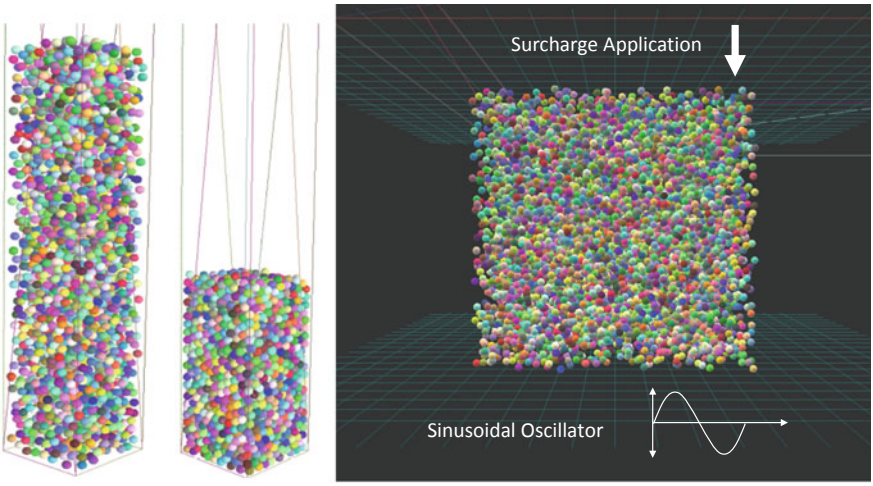

Fig. 3 Numerical simulation of a gravity deposition test (left), boundary conditions and sample for minimum void ratio test (right)

2.4.1 Maximum Void Ratio at Zero Pressure (e_{i0})

e_{i0} is the loosest void ratio for a grain skeleton which is reached when a cloud of particles is isotropically compressed in a gravity-free space. As pure isotropic compression is difficult in the laboratory, it is almost impossible to determine the value of e_{i0} experimentally. DEM, on the other hand, provides control over the strain rate and gravitational forces in the system. Isotropic compression has been used extensively for numerical sample preparations, especially for subsequent triaxial testing. To compute e_{i0} for Karlsruhe sand, isotropic compression was simulated in a periodic cube of size 0.1 m. The contact parameters used were the same as calibrated in Sect. 2.3. By observing the force chains and void ratio with confining stress curve, 5 kPa was used as a limit to report e_{i0} values. Using the same compression curve, the values of h_s and n were computed using the methodology given by Herle and Gudehus [7].

2.4.2 Critical Void Ratio at Zero Pressure (e_{c0})

In a laboratory test for determination of maximum void ratio ($e_{\max}$), sand is poured into a cylinder with vanishing height. As large deformations are developed during the steady state at zero pressure, a state close to critical state is reached. Furthermore, a comparison of e_{c0} and $e_{\max}$ reveals good correspondence [7]. Assuming $e_{c0} = e_{\max}$, gravity deposition simulations were carried out similar to the methodology proposed by Abbireddy and Clayton [1]. A cuboidal space of size 0.15 m $\times$ 0.15 m $\times$ 0.45 m was filled with a randomly distributed cloud of particles with no overlap and very

high initial porosity. Gravity was switched on, and the particles were free to settle in the cuboid. Once the unbalanced forces reach a stable value of 0.01, the void ratio of the settled particles was computed. Many researchers have studied the effect of the wall on the void ratio [15], and due to these boundary effects, the void ratios were computed at a distance of $2.5d_{50}$ from the edges and $5d_{50}$ from the bottom.

2.4.3 Minimum Void Ratio at Zero Pressure (e_{d0})

When a packing of particles is subjected to tapping or vibrations, the packing experiences densification which depends on the conditions of the vibrations applied and this forms the basis for determination of minimum void ratio in the laboratory (e_{min}). Moreover, when cyclic shearing with small amplitude is performed after static compression, e_{d0} is reached asymptotically. A comparison of e_{d0} and e_{min} shows that the values are usually close to each other. Therefore, e_{d0} is equal to e_{min} is assumed in this study [7]. Chang et al. [4] followed the standard ASTM D4253 to simulate densification using DEM. Similar to their methodology, densification simulations with vertical vibrations were conducted to compute the e_{d0} values. To simplify the simulations, a cloud of particles were created in a cubical container of size 0.2 m. These particles were allowed to settle under gravity in a stable loose packing. The top plate of the container was pressed with a surcharge of 14 kPa. The bottom plate was vibrated as a sinusoidal oscillator whose amplitude was taken as 0.2 times the maximum particle size with the frequency of 60 Hz. e_{d0} was reported when a stable void ratio was reached asymptotically, which did not change with the time of simulation.

3 Results and Discussion

3.1 Calibration of Contact Parameters

Figure 4 shows the comparison of numerical and experimental results for triaxial tests for dense Karlsruhe sand ($e = 0.53$) at different confining pressure. Both experimental curves, global axial normal stress with axial strain and volumetric strain with axial strain, were reproduced very well. The calculated friction angle from simulations is 41.4° which correlates well with the experimental value of 43.7°. Similarly, the dilatancy angle from simulations is 31.2° and is in satisfactory agreement with the experimental result of 28.5°. The calibrated micromechanical parameters obtained were: $E_c = 85$ GPa, $\nu = 0.2$, $\rho = 2660$ kg/m^3, $\mu = 3°$, $\beta = 0.15$, $\eta = 0.5$. For $E_c =$ 85 GPa, approximate k_n value is computed close to 0.85 GPa, which is in the range of values found in the literature. These calibrated contact parameters were used in the simulations in the subsequent simulations to compute the value of hypoplastic law parameters using simple experimental simulations.

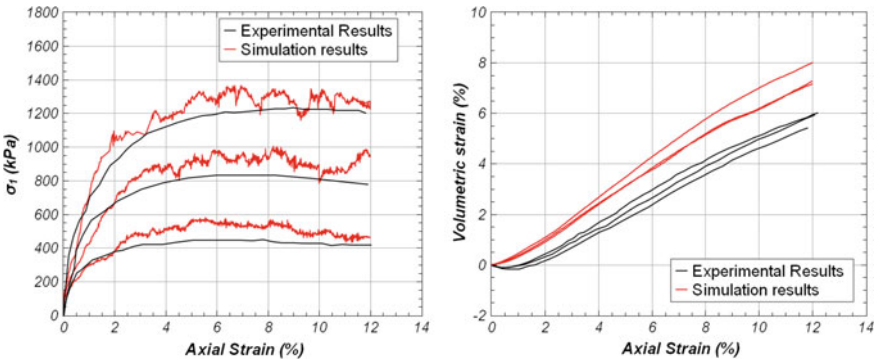

Fig. 4 Comparison of results from numerical and experiment results of the triaxial test on Karlsruhe Sand

3.2 Limiting Void Ratios at Zero Pressure

Figure 5 shows the variation of void ratio with confining stress during isotropic compression from a cloud of particles in a gravity-free space. The solid black lines show the result of isotropic compression as obtained from YADE and dotted red lines shows the fit theoretical curve. Also, Fig. 5 shows the variation of void ratio with time for vertical vibrations simulation. The initial straight part is the gravity deposition process and after the particles are settled the particles are vibrated. Parameters obtained from DEM simulations and the corresponding values as given in [7] are summarized in Table 1. Even through the angularity of particles is simulated by using a rotational resistance at the contact, due to inherit sphericity of the particles, the limiting void ratios are lower in value for simulated results. In order for rotational resistance to come into the picture, the simulation has to be done in a quasi-static regime which is not the case with gravity deposition. Also, the value of h_s is lower for

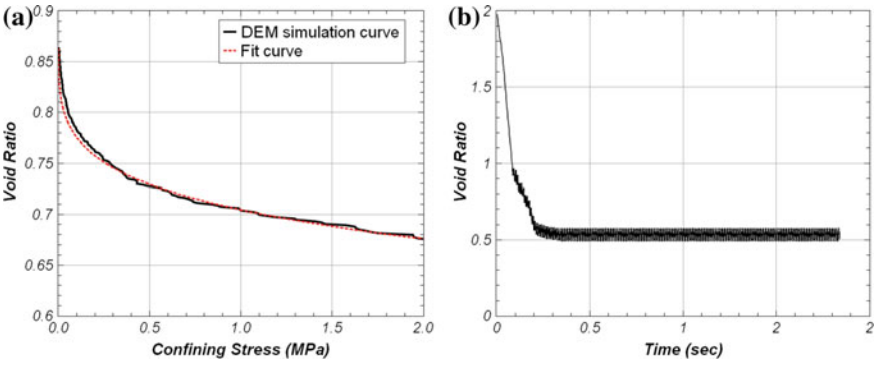

Fig. 5 **a** Variation of void ratio with confining stress during isotropic compression; **b** variation of void ratio with a time of simulation for vertical vibration test

Table 1 Summary of hypoplastic parameters as obtained from DEM simulations and literature

Parameter	DEM simulation	[7]
e_{i0}	0.86	1.00
e_{c0}	0.74	0.84
e_{d0}	0.54	0.53
h_s	1450 MPa	5800 MPa
n	0.26	0.28
α	0.15	0.13
β	1.0	1.1

simulation results than literature values. The value of 1450 MPa is close to the value of Hochstetten sand, Hostun RF sand, and Lausitz sand, which are predominately subrounded in shape.

3.3 Triaxial Test Simulations

A MATLAB code was created to simulate the triaxial test using eight parameters of hypoplastic law. Using Eqs. 2 and 3, the code computes the corresponding stress-strain and volume change for every time step Fig. 6 shows the comparison of stress-strain and volume change behavior of Karlsruhe sand as obtained from experiments, DEM simulations, simulations using hypoplastic law with parameters obtained from literature and simulations using hypoplastic law with parameters obtained from DEM simulations. Only the results from hypoplastic simulations using parameters from the literature show a distinct peak state. The results from hypoplastic simulations with parameters from DEM simulations are on the lower side, yet follow the experimental results in parallel. In all the cases the DEM simulation results and simulations using hypoplastic law with parameters obtained from the literature are more dilative in comparison to other results. It is interesting to note that although the limiting void ratios from DEM simulations are lower than the values from literature, they do not change the triaxial test simulation results considerably. This is because the computation of parameters f_d (Eq. 4) and f_b (Eq. 5), the limiting void ratios are taken in the form of a ratio, which remains fairly constant over the range of stress. For example, the value of the ratio $(e_{i0} - e_{d0})/(e_{c0} - e_{d0})$ for parameters in column 2 of Table 1 comes out to be 1.6, and for column 3 of Table 1 it comes out to a similar value of 1.52. The trend of similar ratio value is continued throughout the stress range. The major difference in the response of the two hypoplastic simulations comes from the different values of h_s and, a higher h_s value makes the overall response more dilative with a distinct peak.

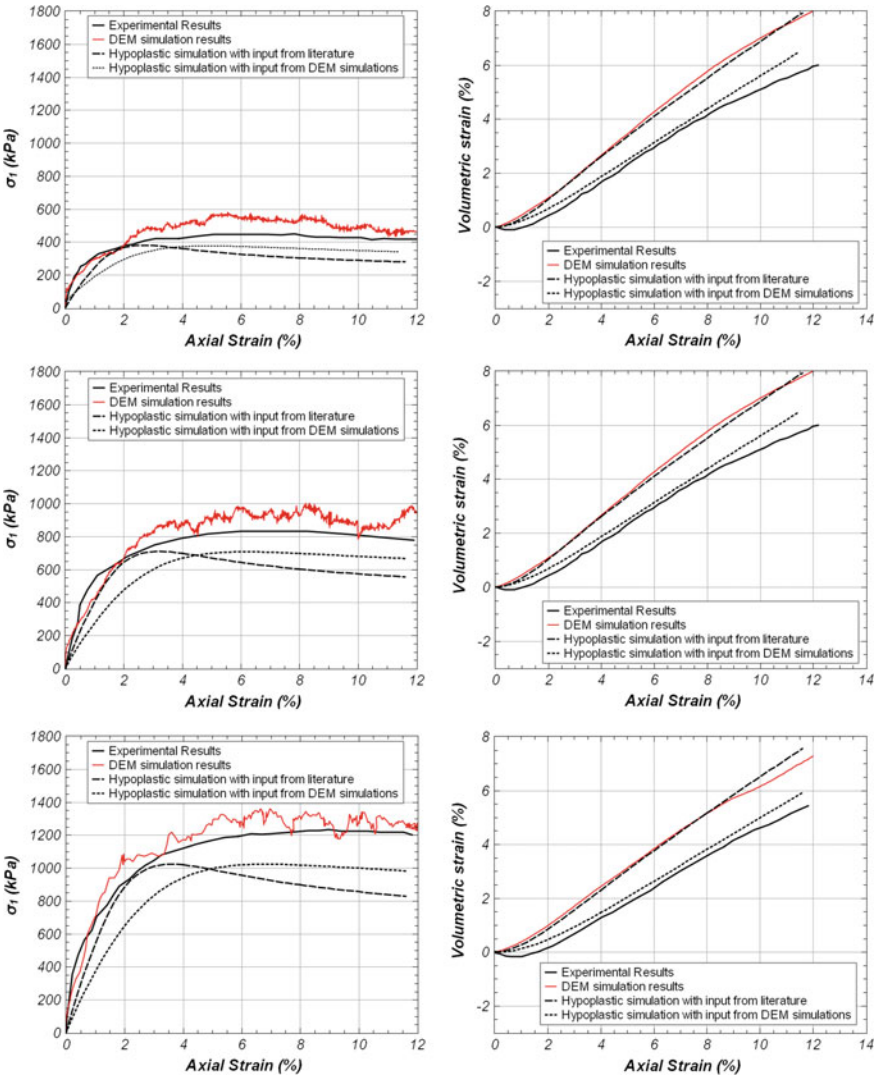

Fig. 6 Comparison of triaxial test results at confining pressure of 100 kPa (top), 200 kPa (middle) and 300 kPa (bottom)

4 Conclusions

This paper illustrates the versatility of the Discrete Element Method in the simulation of conventional geotechnical tests, in order to understand the underlying mechanics behind the behavior of granular materials. An attempt has been made to understand the behavior of sands in macro-, micro- and continuum scale, under generalized loading conditions. The main conclusions are

1. Numerical simulations of a quasi-static triaxial test using DEM show good correspondence with the experimental results on Karlsruhe Sand. To complement the simplicity of hypoplastic law, a simple linear elastic normal contact with linear, rotational moment law is proposed to simulate the response of particles over upscaled grain sized distribution of Karlsruhe sand. At failure, a clear slip plane is observed for a sample with an aspect ratio of 3 (Fig. 2).
2. Limiting void ratios for the hypoplastic law parameters were computed using various DEM simulations (e_{i0} using isotropic compression, e_{c0} using gravity deposition, e_{d0} using vertical vibrations) and compared to the values reported in the literature. Although rotational law was used to simulate the angularity of the particles, limiting void ratios for DEM simulations were lower than the ones reported in the literature.
3. MATLAB code was created to simulate the triaxial test using hypoplastic constitutive law. The results of experimental triaxial tests on Karlsruhe Sand were fairly well produced by triaxial test simulation using hypoplastic law with parameters obtained from the literature, as well as, DEM simulations of simple geotechnical tests. As the limiting void ratios are computed as ratios in Eqs. 4 and 5, the effect of the difference between experimental and simulated limiting void ratio on the results of triaxial test simulations using hypoplasticity appears to be inconsequential. The difference could be attributed to the value of peak friction angle, critical friction angle, and parameter (h_s). A parametric study is required to understand the effect of different parameters on the result of triaxial simulations with hypoplastic.

With this paper, we take one step forward in the formulation of a unified theory which can help us understand the behavior of soils using experiments, micro-scale dis-continuum DEM simulations and continuum-based constitutive laws.

References

1. Abbireddy COR, Clayton CRI (2010) Varying initial void ratios for DEM simulations. Géotechnique 60(6):497–502
2. Bauer E (1996) Calibration of a comprehensive hypoplastic model for granular materials. Soils Found 36(1):13–26
3. Belheine N, Plassiard JP, Donzé FV, Darve F, Seridi A (2009) Numerical simulation of drained triaxial test using 3D discrete element modelling. Comput Geotech 36(1–2):320–331
4. Chang CS, Deng Y, Yang Z (2017) Modeling of minimum void ratio for granular soil with effect of particle size distribution. J Eng Mech 143(9):04017060
5. Cundall PA, Strack ODL (1979) A discrete numerical model for granular assemblies. Géotechnique 29(1):47–65
6. Dakoulas BP, Sun Y (1993) Fine ottawa sand: experimental behavior and theoretical predictions. J of Geotech Eng 118(12):1906–1923
7. Herle I, Gudehus G (1999) Determination of parameters of a hypoplastic constitutive model from properties of grain assemblies. Mech Cohesive-Frict Mater 4(5):461–486
8. Iwashita K, Oda M (1998) Rolling resistance at contacts in simulation of shear band development by DEM. J Eng Mech 124(3):285

9. Kolymbas D, Wu W (1990) Recent results of triaxial tests with granular materials. Powder Technol 60(2):99–119
10. Kozicki J, Tejchman J, Mühlhaus HB (2014) Discrete simulations of a triaxial compression test for sand by DEM. Int J Numer Anal Methods Geomech 38(18):1923–1952
11. Lin J, Wu W (2013) Comparison of DEM simulation and hypoplastic model. In: Proceedings of American Society of Civil Engineers fifth biot conference on poromechanics, pp 1815–1819, Vienna, Austria
12. Lu Y, Frost D (2010) Three-dimensional DEM modeling of triaxial compression of sands. In: Proceedings of American Society of Civil Engineers GeoShanghai international conference 2010, pp 220–226, Shanghai, China in Soil Behavior and Geo-Micromechanics
13. Niemunis A, Herle I (1997) Hypoplastic model for cohesionless soils with elastic strain range. Mech Cohesive-Frict Mater 2(4):279–299
14. O'Sullivan C (2011) Particle-based discrete element modeling: geomechanics perspective. Int J Geomech 11(6):449–464
15. Reboul N, Vincens E, Cambou B (2008) A statistical analysis of void size distribution in a simulated narrowly graded packing of spheres. Granul Matter 10(6):457–468
16. Salot, C, Gottel P, Villard P. (2009) Influence of relative density on granular materials behavior: DEM simulations of triaxial tests. Granul Matter 11(4):221–236
17. Šmilauer V, Chareyre B (2015) DEM Formulation. Yade Documentation 2nd ed
18. Widuliński Ł, Kozicki J, Tejchman J (2009) Numerical simulations of triaxial test with sand using DEM. Arch Hydro Eng Environ Mech 56(3):149–171
19. Wu W, Bauer E (1994) A simple hypoplastic constitutive model for sand. Int J Numer Anal Methods Geomech 18(12):833–862

Experimental Studies on Polyester Geo-Fabric Strengthened Masonry Elements

K. S. Sreekeshava, A. S. Arunkumar and B. V. Ravishankar

Abstract The masonry elements exhibit high compression and weak tensile strength properties. The tensile strength of masonry elements can be improved by providing necessary reinforcements. The behavior of masonry in addition to any relevant materials needs significant studies. The present work focuses on enhancing the performance of masonry wallets by providing reinforcement with polyester Geo-fabric. The present experimental investigation shows comparison between conventional masonry elements and masonry elements strengthened with polyester Geo-fabrics. Polyester geo-fabrics are Geo-synthetic materials used in many infrastructure works for enhancement of tensile properties of structural members. The various masonry elements considered for experimental investigations are prisms, triplets and wallets. The fabrics were placed at interfaces of bed joints in prisms and triplets, in wallets the strengthening was done by applying double-sided configuration by considering one-third distances on each face perpendicular to bed joint. Performances of polyester geo-fabrics reinforced specimens are compared with conventional specimens in terms of strength and failure mechanisms.

Keywords Masonry · Polyester · Wallets · Interfaces · Infrastructure · Performance

1 Introduction

Masonry is a composite material and their behaviors under lateral loads are highly unpredictable because of its versatile nature. Reinforced frame with masonry in-fills is widely used across the world. The in-fills help to increase the lateral stiffness of the

K. S. Sreekeshava (✉)
Jyothy Institute of Technology Bengaluru, Affiliated to Visvesvaraya Technological University, Belagavi, Karnataka, India
e-mail: sreekeshava.ks@jyothyit.ac.in

A. S. Arunkumar · B. V. Ravishankar
BMS College of Engineering Bengaluru, Affiliated to Visvesvaraya Technological University, Belagavi, Karnataka, India

A. Prashant et al. (eds.), *Advances in Computer Methods and Geomechanics*, Lecture Notes in Civil Engineering 55,
https://doi.org/10.1007/978-981-15-0886-8_58

structures but because of its poor interfacial behavior between reinforced concrete frame and masonry infill causes vulnerable effect under lateral loads.

In the recent past, the fiber-reinforced polymer [FRP] composites with laminates are used to strengthen the wallets; it shows better improvements in stiffness and strength over un-strengthened wallets [1, 2]. The drawbacks faced in durability aspects and complexity in handling while applying on wet surfaces remains unanswered. The poor performance of unreinforced masonry walls due to insufficient shear and flexural capacity. In recent studies, Geo-fabrics are widely used as a composite material for several civil engineering infrastructural activities. More recently Geo-fabrics has been used as bed reinforcements in masonry structures for different configurations and the study has proven that effectiveness of Geo-fabrics under lateral loads in terms of strength and durability.

To improve the performance of unreinforced masonry walls especially under lateral loads much more studies are needed. Some effective studies have been done like fabric reinforced cementitious matrix [FRCM] shows better behavior in all structural aspects [3, 4]. The basic characterization of reinforced masonry wallets has been effectively studied under compression and diagonal compression. More recently masonry panels strengthened with FRP and FRCM showed good efficiency of retrofitting and increments of bearing capacity compared with normal conventional unreinforced masonry wallets [5, 6].

The glass fiber-reinforced polymer [GFRP] and Geo-grid bed joint reinforcements showed better performance under seismic loads in terms of energy dissipation and in-plane flexural strength provided with various types of bed joints [7].

2 Experimental Program

2.1 Basic Material Testing

Ordinary Portland cement of 53 grade confirming to IS 12269:1987 was used for mortar without any admixtures. The manufactured confining to IS: 383-1970. First class well-burnt clay bricks were used in the brick masonry infill panels. The water absorption measured as per IS 3495 (1992). The ability of brick to absorb water is measured by the initial rate of absorption test conducted as per ASTM C 67 (2009) and the flexure test was performed by single point loading as per IS 3495 (part-III-1976). The various mechanical properties are listed in Table 1.

Bi-axial polyester Geo-fabrics was used to enhance the various properties of concrete and masonry elements. The Polyester geo-fabrics are tested under 25 kN Digital UTM machine as shown in Fig. 1. The results are tabulated in Table 2.

2.2 Experimental Studies on Polyester Geo-Fabric Reinforced Mortar and Concrete

The compression, flexure and split tensile test concrete specimens were cast by using a mix proportion of 1:1.5:3 with water–cement (W/C) ratio of 0.5. The polyester placing in concrete specimens depends on the failure pattern of conventional specimens plastic hinge formation spots and the tests were conducted as per IS 516 (1959). The 28 days cube strength; flexural strength and split tensile strength of concrete specimens were found to be 41.8 Mpa, 3.5 Mpa, and 3.8 Mpa respectively.

The flexural strength of mortar was conducted as per ASTM D 7264/D 7264 M-07. In this method, three-point loading is followed to find the flexural strength of composite material. The cement mortar 1:6 is used along with Geo-fabrics to prepare the test specimens. The specimens are prepared with 1:6 mortar and thickness of specimen is 14 mm. The gauge length of the specimen is 90 and 2 mm Geo-fabrics are laminated with 6 mm thick mortar on both sides. The test is carried under digital 25 kN composite test UTM. The average flexural strength of Polyester Geo-fabric mortar laminate is 4.20 Mpa and Young's modulus is 2109.21 Mpa. The testing specimens are shown in Fig. 2.

Table 1 Basic properties of bricks

Dimension (mm)	Weight density (kN/m^3)	Water absorption (%)	Initial rate of absorption ($g/cm^2/min$)	Modulus of rupture (Mpa)	Compressive strength (Mpa)
210 × 100 × 70	14.63	13.64	0.15	1.185	3.9

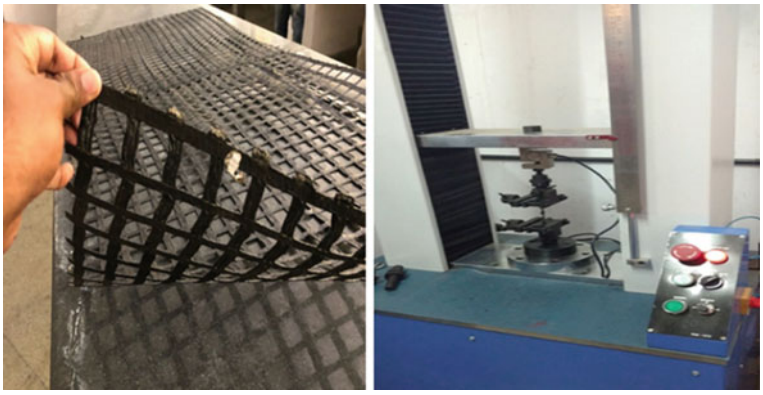

(A) Polyester Geo-fabric (B) Testing arrangement

Fig. 1 Polyester geo-fabric and testing arrangement in UTM

Table 2 Basic properties of polyester geo-fabric

Geo-fabric	Ultimate load (N)	Ultimate tensile strength (N/mm^2)	Breaking load (N)	Breaking stress (N/mm^2)	Young's modulus (N/mm^2)
Polyester	915	132.083	870	119.4	1.15×10^6

Fig. 2 Reinforced concrete test specimens

Fig. 3 Compression test on masonry prism

2.3 Experimental Studies on Masonry Elements

2.3.1 Compressive Strength of Prisms

The compressive strength test was performed according to IS 1905-1987 [8]. Five brick stack bonded prisms shown in Fig. 3 were used by uni-axial compression tests to obtain basic compressive strength with and without Geo-fabric reinforced masonry prisms. The specimens were cured under wet gunny bags for a period of 28 days and tested in wet conditions. Stack bonded masonry prisms of size 210 × 100 × 435 mm were prepared using clay brick with 1:6 cement mortar. The polyester Geo-fabrics are sandwiched between mortar bed joint of thickness 12 mm in each bed joints

Table 3 Compressive strength of polyester Masonry Prisms

Material	Dimension (mm)	Load (kN)	Compressive load (N/mm^2)	Correction factor	Corrected compressive stress N/mm^2	Efficiency (%)
Conventional prism	210 × 100 × 435	55.4	2.63	0.968	2.55	32
Prism with polyester	210 × 100 × 435	65.1	3.10	0.968	3.00	38

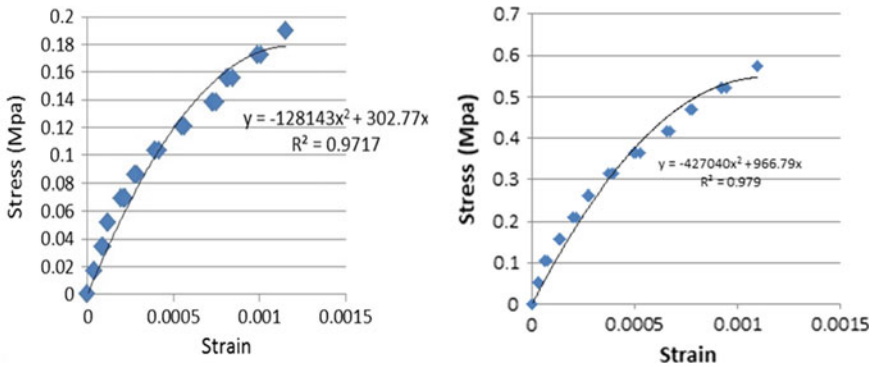

(A) Without Polyester Geo-fabric (B) With Polyester Geo-fabric

Fig. 4 Stress-strain curve for masonry prisms

of masonry prism specimens. The compressive strength of the prisms is tabulated in Table 3. Stress-strain graph was plotted for load versus deformation of prisms represented in Fig. 4.

Elastic modulus obtained from plotting curves for peak stress and peak strain of all specimens. The common failure patterns observed were the vertical cracking failure, mortar tended to spread outward of vertical plane and pulled the bricks along with it, bricks which were weak on tensile forces failed by splitting apart and bond failure. The test results shows elastic modulus for without polyester Geo-fabric is 303 Mpa and with polyester, Geo-fabric is 967 Mpa.

2.3.2 Bond Strength of Masonry Triplets

The shear characteristics of the brick masonry and the interaction parameters of brick/mortar joint were determined with and without polyester masonry triplets; by triplet prism test [9]. The polyester Geo-fabrics were placed in between the 1:6 cement mortar bed joint of the specimens. The shear strength was assessed from the triplet test shown in Fig. 4. The vertical shear load (P_v) was applied at the uniform rate until shear failure occurred. The average bond stress (τ_b) evaluated as

Table 4 Bond strength of masonry triplets

Specimen	Specimen dimension (mm)	Breaking load (N)	Bond strength (Mpa)
Conventional masonry triplet	250 × 220 × 110	9935	0.199
Polyester geo-fabric triplet	250 × 220 × 110	11956	0.245

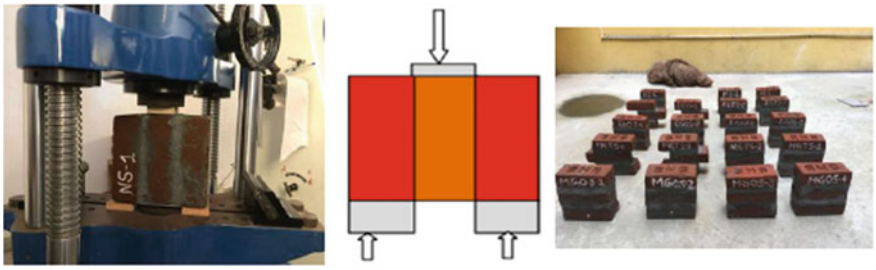

Fig. 5 Masonry triplets

$$\tau_{b=\frac{P_v}{2A}} \tag{1}$$

where

P_v Vertical Compressive load in N
A Cross-sectional area of Triplet prism in mm^2

The breaking load and bond strength of with and without polyester Geo-fabric triplets are reported in Table 4 and testing arrangement shown in Fig. 5.

2.3.3 Load-Bearing Capacity of Masonry Wallets

The load-bearing capacity of masonry with and without polyester wallets was determined by considering three numbers of 0.7 × 0.7 × 0.23 m wallet dimensions. The test is carried under the 2000 ton loading frame. The unreinforced masonry walled shown in Fig. 6. In wallets, the strengthening was done by applying double-sided configuration by considering one-third distances on each face shown in Fig. 7. The load is applied gradually with the help of hydraulic jack and stress against strain to get modulus of elasticity was assessed by plotting stress/strain values represented in Fig. 8. The modulus of Elasticity for without polyester masonry wallets is 1976 Mpa and with Polyester Geo-fabric masonry wallet is 2353 Mpa respectively (Fig. 9). The test specimens and test is carried in accordance with European Standards [10].

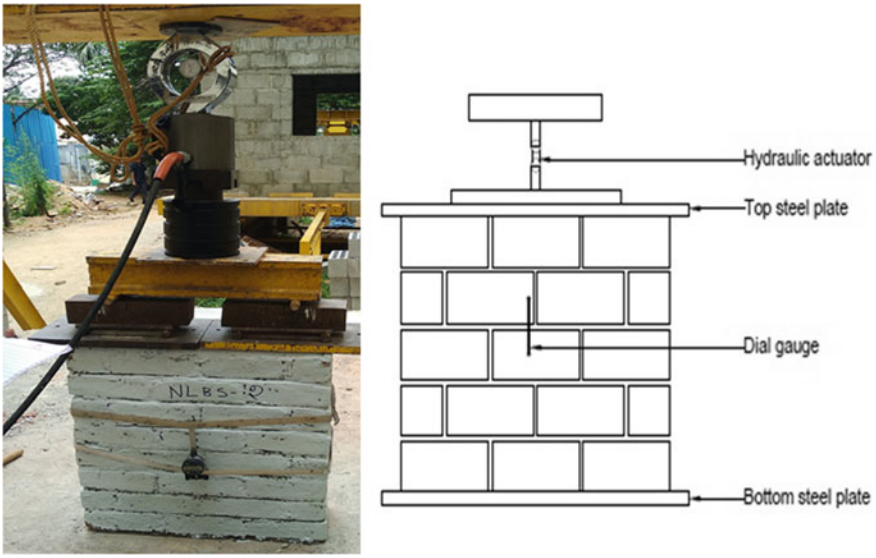

Fig. 6 Masonry wallets

Fig. 7 Polyester reinforced masonry wallets

2.3.4 Diagonal Compression of Masonry Wallets

Diagonal compression test was performed with and without polyester double-sided configured masonry specimens (700 × 700 × 230 mm) in order to obtain the diagonal tensile (Shear) strength of the wallets. All panels were built in the following techniques and were positioned in the testing machine with a diagonal axis in the vertical direction. The compressive load has been applied along the direction of diagonal axis shown in Fig. 10.

According to ASTM standards (ASTM 519:2010), the test setup is composed of steel loading shoes which were fixed in opposite corners of a diagonal of masonry

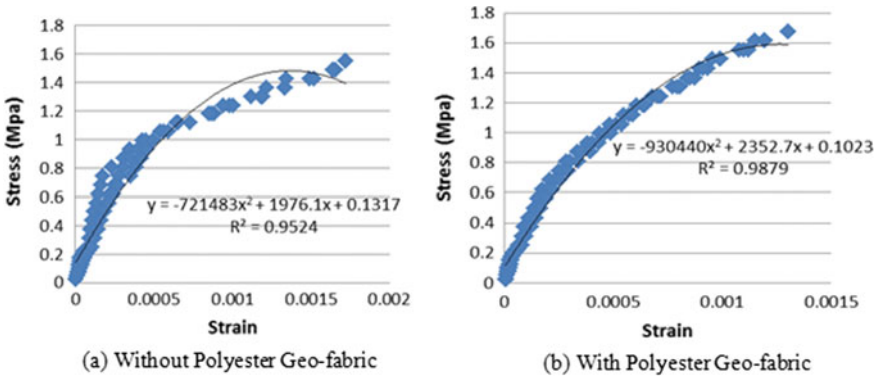

Fig. 8 Stress-strain curve for masonry wallets

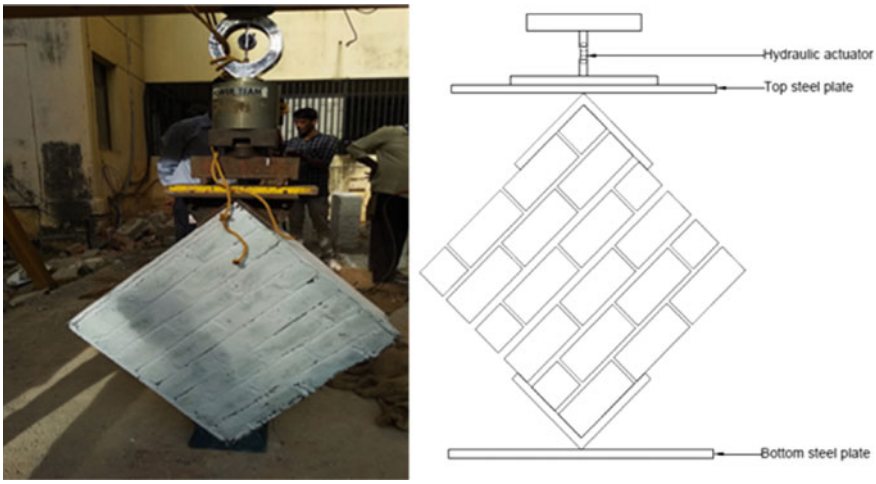

Fig. 9 Diagonal compression test of wallets

specimens [11, 12]. The shear stress (τ) assured by Eq. (2).

$$\tau = \frac{(0.707P)}{A_n} \tag{2}$$

where P is Axial load applied with jack and A_n is the net area of Specimen.

The average values of maximum load and shear stress are tabulated in Table 5. The shear stress-induced without a polyester wallet is 1.61 Mpa while with polyester wallet is 2.08 Mpa.

Fig. 10 Specimens after test

Table 5 Shear stress of masonry wallets

Specimen	Specimen dimension (mm)	Axial load (kN)	Shear stress (τ) (Mpa)
Masonry wallet without polyester geo-fabric	700 × 700 × 230	260	1.61
Masonry wallet with polyester geo-fabric	700 × 700 × 230	323.42	2.08

3 Conclusion

The results presented in this paper show that the material characteristics of the polyester Geo-fabric played a major role in improving the strength properties of the masonry elements. The elastic modulus of Polyester Geo-fabric stack bonded prism shows 3 times higher the value of unreinforced masonry prism. This shows stiffness of reinforced prisms is higher compared to conventional prisms. The compressive strength and bond strength shows significant increment (85% increases) for polyester geo-fabric material compared with normal unreinforced masonry elements. However, the use of polyester Geo-fabrics perpendicular to bed joints also shown considerable increment in load carrying capacity compared with unreinforced specimens. This shows significant improvement (78% increases) in shear carrying capacity under diagonal compression.

It is evidenced from experimental investigations that the structural performance and strength of unreinforced masonry elements subjected to different load conditions

can be enhanced by using polyester Geo-fabric material. Based on the experimental result, using polyester Geo-fabric as bed joint reinforcement is recommended over normal masonry bed joint. Polyester Geo-fabric is recyclable material, corrosion resistant, and very cheap. Therefore, it has advantageous and could be more economical to use as reinforcement in masonry elements.

Acknowledgements Authors would like to acknowledge Strata India Pvt. Ltd for providing Polyester Geo-fabric material for the strengthening of Masonry In-fills.

References

1. Tumialan JG, Galati N, Nanni A (2003) Fiber-reinforced polymer strengthening of unreinforced masonry walls subjected to out-of-plane loads. ACI Struct J 100(3):312–329
2. Silva PF, Yu P, Nanni A (2008) Monte Carlo simulation for validating the in-plane shear capacity of URM walls strengthened with GFRP grid reinforced polyuria. J Compost Constr 12(4):405–415
3. Sagar SL, Singhal V, Rai DC, Gudur P (2016) Diagonal shear and out of plane flexural strength of fabric reinforced cementitious matrix-strengthened masonry wallets. J Compost Constr. https://doi.org/10.1061/(ASCE)CC.1943-5614.0000796
4. Sagar SL, Singhal V, Rai DC (2017) In-plane and out of the plane performance of Masonry infill strengthened with fabric reinforced cementitious matrix. In: 13th Canadian masonry symposium. Dalhousie University
5. Mazzotti C, Ferracuti B, Incerti A (2016) Diagonal compression tests on masonry panels strengthened by FRP and FRCM. In: Proceeding structural analysis of historical constructions-anamnesis, diagnosis-Van Balen, Taylor & Francis Group, London, ISBN 978-1-138-02951-4
6. Basil M, Marcari G, Vestroni F (2016) Nonlinear analysis of masonry panels strengthened with textile reinforced mortar. Eng Struct 113:245–258 (Elsevier)
7. Sadak H, Lissel S (2013) Seismic performance of masonry walls with GFRP and geogrid bed joint reinforcement. Constr Build Mater 41(2013):977–989
8. BIS (Bureau of Indian Standards) (1987) Indian standard code of practice for structural use of unreinforced masonry, IS 1905, New Delhi, India
9. Bureau of Indian Standards (BIS) (2002) Indian standard criteria for earthquake resistant design of a structure, part-1: general provisions and buildings. IS 1893, 5th Rev., New Delhi, India
10. European Standard BS EN 1052-1:1999: Methods of testing for masonry part-1 determination of compressive strength
11. Milosevic R, Bento AS, Lopes M (2012) Shear tests on rubble stone masonry panels- diagonal compression tests. In: Proceeding 15 WCEE LISBOA
12. ASTM (2010) Standard test methods for diagonal tension (shear) in masonry assemblages. ASTM E519/E519M, West Conshohocken, PA

Influence of Cementing Solution Concentration on Calcite Precipitation Pattern in Biocementation

Deepak Mori, Poonam Jyoti, Tejinder Thakur, Shyam K. Masakapalli and K. V. Uday

Abstract Enhancing the strength characteristics of soil by mechanical, chemical, biological or a combination of these approaches needs thorough investigation. One of the most sustainable biological methods to improve the engineering property of soil is Microbial-Induced Calcite Precipitation (MICP). MICP is the process in which the urease-producing bacteria in the presence of cementing solution deposits calcite in the soil voids thereby enhancing the in situ soil shear strength mainly by binding the particles together. For efficient bio-cementation, not only the amount of calcium carbonate but also its precipitation pattern is one of the major influencing factors. Earlier studies have depicted the pattern of calcium carbonate deposition for soil saturated with bacteria and cementing solution; however, the gap exists to understand the efficiency in relation to the percolated flow of bacteria and cementing solution. Keeping this in view, the current study is focused on understanding the precipitation pattern of calcium carbonate induced by *Sporosarcina pasteurii* (NCIM 2477) and cementing solution. This is achieved by sand column experiment with percolation method under different concentrations of cementing solution in unsaturated soil conditions and SEM-EDAX image analysis of the specimen derived from sand columns. Our results suggest that the concentration of cementing solution affects the precipitation pattern. We conclude that the sand columns percolated with S pasteurii cells followed by addition of multiple doses of low concentration of cementing solutions at defined time intervals resulted in the homogeneous pattern of calcite precipitation.

Keywords MICP · Biocementation · Percolation · SEM-EDAX · Cementing solution

D. Mori · T. Thakur · K. V. Uday (✉)
School of Engineering, IIT Mandi, Mandi, Himachal Pradesh, India175005
e-mail: uday@iitmandi.ac.in; uday1112@gmail.com

P. Jyoti · S. K. Masakapalli
School of Basic Sciences, IIT Mandi, Mandi, Himachal Pradesh, India175005

A. Prashant et al. (eds.), *Advances in Computer Methods and Geomechanics*, Lecture Notes in Civil Engineering 55,
https://doi.org/10.1007/978-981-15-0886-8_59

1 Introduction

Most of the researchers consider soil as an inert material but some researchers have given their valuable inputs to improve the engineering properties of soil by various biochemical methods [1]. Depicted that microbial activity can lead to the reduction in permeability with time [2]. Observed that there are 10^{12} microorganisms in one kilogram of soil sample and these microbes can be used to improve the engineering properties of soil. Such methods like biocementation which increases the shear strength of soil by the production of particle binding material, bioclogging where the reduction in permeability of the soil is achieved by pore filling material are few current focus areas of bio-treatment of soils.

One efficient method of bio cementation is MICP (Microbial Induced Calcite Production) which uses urease enzyme producing bacteria to hydrolyse urea. The urea gets hydrolyzed to ammonium and carbonate ions which increases the pH of the system. When any source of calcium (say calcium chloride) is provided to the hydrolysed urea, the calcium ions pair with the carbonate ion and thereby precipitate calcium carbonate. The calcium carbonate crystal gets deposited in voids of the soil particles and acts as a binding material for soil.

$$CO(NH_2)_2 + 2H_2O \xrightarrow{\text{urease}} 2NH^{4+} + CO_3^{2-} \tag{1}$$

$$Ca^{2+} + CO_3^{2-} \rightarrow CaCO_3 \tag{2}$$

Nemati and Voordouw [3] used urease enzyme and it was observed that concentration of urease enzyme from 0.01 to 0.1 g/l urea and calcium chloride concentration of 0.6 M shows optimum production of calcium carbonate. In the practical condition, it is very difficult to maintain the urease production ability of the bacteria in the soil and it is also a difficult task to retain all the bacteria in the soil homogeneously. Wiffin et al. [4] performed a sand column experiment of length 5 m to improve the soil engineering property with *S. pasteurii* and it was observed that calcium carbonate was detected all over the column but the precipitation was not homogeneous [5], proved that a 2 phase injection method, supplying a fixation fluid of high saline content (50 mM $CaCl_2$) immediately after supplying the bacteria is an efficient method to retain the bacteria in the sand column. The bacterial retention can be improved by supplying the bacteria and cementing solution in multiple layers and bacterial retention increase as the number of layers and incubation time increases as stated by Cheng and Cord Ruwisch [6].

In the case of saturating the soil with bacteria and cementing solution, more bacteria retains in the soil as compared to the unsaturated condition, so more is the amount of calcite deposited more is the strength gained. In the case of saturation, the increase in strength is not as much as the amount of calcite generated which makes this process inefficient, [7]. In the case of percolation flow, less calcite content can give rise to more localized strength as fewer amounts, but at the optimum location, calcium carbonate is deposited. Cementing solution concentration also plays an important

role in the strength of the sand column. The strength of the soil sample increases as the concentration of cementing solution is reduced, as observed by Qubany and Soga [8]. Not only the strength but calcium carbonate precipitation pattern also varies as the concentration of cementing reagent changes as shown by Qubany et al. [9].

As the traditional trend of MICP, filling all the voids with bacteria and cementing solution results in the saturation condition in the soil, which gives rise to calcite deposition at voids between the soil particles and surface of the soil grain, Though this process has been reported to increase in shear strength, [10] it may not be an efficient process as calcium carbonate also deposit on the free surface of the sand particle. The deposition of calcium carbonate on the free surface of sand grain is not desirable as the calcite deposited only at the optimum location which is at particle–particle contacts give rise to increase in shear strength to soil and calcium carbonate deposited on the soil grain surface does not play any role in strength improvement. The deposition pattern of calcium carbonate is not well studied in the case of percolation flow when the soil is not able to reach a saturated condition. As observed by [11] premixing method of supplying bacteria and cementing solution is not as efficient as percolation method, pressure injection can also be used for soil bio-treatment, which needs specialized pressure equipment. The current study focuses on the influence of cementing solution concentration (urea-calcium chloride solution) on precipitation pattern of calcium carbonate when the reagents and bacteria are supplied to the sand column by percolation method, taking the advantage of experimentation in sands.

2 Materials and Methodology

2.1 Sand

Indian standard sand grade 3 (D_{10} = 146 μm, D_{30} = 213 μm, D_{60} = 317 μm) was used for the experiment. According to unified soil classification (USCS. ASTM D2487), it is classified as poorly graded sand (SP). Observed specific gravity of sand is 2.6. Scanning electron microscopy (SEM) (Fig. 1a) revealed that the particles are of angular to subangular shape, which was also observed by Uday et al. [12] while performing an experiment on the same type of sand.

2.2 Bacteria

Bacterial strain *Sporosarcina pasteurii* NCIM 2477 (obtained from NCIM, Pune) was selected for biocementation, because of its efficient urea hydrolyzing ability. The cells were maintained in nutrient media (5 g peptone, 2 g yeast extract, 5 g sodium chloride per litre, pH-7). Cells were stored in the deep freezer (−80 °C)

by glycerol stocks (500 μL of overnight grown culture was mixed with 500 μL of 40% glycerol solution) for further experiments. For the biocementation experiment, *S. pasteurii* cells were grown in liquid media containing 20 g yeast extract, 5 g peptone, 10 g ammonium chloride and 0.1 mM nickel chloride per litre, pH-8.5 at 30 °C on an orbital shaker running at 200 rpm for 30 h. The working volume of cell culture media was 250 ml in a one litre bottle (Culture volume to Headspace ratio of 1:3) which ensures sufficient aeration. Cell density was measured at an optical density at 600 nm, OD_{600} using uv/vis spectrophotometer. Initial OD of the bacterial cells was 0.05, the growth conditions allowed the bacteria to multiply to an OD of 1.5 in 30 h. Bacterial cells were allowed to grow in the culture medium to the late exponential phase. Though, the measurement of the colonies could not be measured, however, based on the empirical relation [13] this has been computed to be 1.49×10^8 CFU/ml. Where Y denotes colony density CFU/ml and Z denotes the value of OD_{600}.

$$Y = 8.59 \times 10^7 \cdot Z^{1.3627} \tag{3}$$

2.3 Cementing Solution

The cementing solution was prepared using the culture medium (20 g yeast extract, 5 g peptone, 10 g ammonium chloride per litre, pH-8.5) supplemented with equi-molar solution of urea and calcium chloride di-hydrate in the ratio (1:1). Urea serves as an energy source for the bacteria while calcium chloride acts as the calcium source for calcium carbonate crystal formation, 2.12 g/l of sodium bicarbonate was also added to stabilize the pH. Reactants were homogenized using chemical stirrer.

2.4 Sand Column Parameters

The plastic PVC pipes having a diameter of 50 mm and length 160 mm were used as sand columns. The PVC pipes were greased properly to ease the removal of sand column from the pipe. First, scotch brite pad was placed at the bottom of the pipe and 1 cm thick gravel filter and a filter paper were placed above the pad. The sand was compacted in the pipe at the density of 1.57 g/cc (relative density of 54%) for the height of 10 cm. Gravel, filter paper and scotch brite pad were placed above the sand to maintain the homogenous flow.

2.5 Treatments

Four sets of sand column experiments were performed in which the cementing solution concentration was varied from 0.25, 0.5, 0.75, and 1 M. The input rate of chemical addition adopted was 0.042 mol/L/h as depicted by Qubany and Soga [8]. During the experiments, the flow rate of all the reactants was maintained at 90 ml/h.

First, one pore volume of water was supplied in the column. For calcite crystal formation to begin, bacteria and cementing solution were added. Percolation flow was adopted to supply the reactants and to maintain unsaturated flow conditions. After supplying the first batch of bacteria no incubation was provided. After 48 h only cementing solution was supplied at every 6, 12, 18 and 24 h for 0.25 M, 0.5 M, 0.75 M, and 1 M respectively as suggested by Qubany and Soga [8].

3 Results and Discussion

The SEM image of Standard sand grade 3 shows that the particles are angular and sub-angular in shape (Fig. 1a), as also observed by Uday [12]. The specimens derived from sand column, treated with various concentration of cementing solution with variation in supply duration were analysed in SEM test. For example, the 1 M cementing solution concentration media was supplied only 3 times in three days, but 0.25 M cementing solution media was supplied 4 times a day for 3 days.

In the case of 0.25 M cementing solution as cementing media, more homogeneous calcium carbonate deposition was observed as compared to the higher concentration cementing media. In the current study, when the concentration of cementing media was less, more numbers of nucleation sites are produced as compared to the high molar concentration of media, This may be due to favourable condition for production of new nucleation site as compared to crystal growth which ultimately leads to more uniform and small sized calcite deposition on sand grain (Fig. 1). The calcium carbonate gets deposited at the particle-particle contact point at various locations. The square block at the left side (Fig. 1a) shows the broken bond of calcite, which broke while preparing the sample for SEM analysis.

Calcium carbonate deposition in case of 0.25 M cementing solution concentration is not as uniform as observed by Qubany et al. [9], the reason behind this observation is that the higher degree of super-saturation and homogeneous distribution of bacteria is required for more homogeneous nucleation and thereby depositing more homogeneous calcium carbonate, which is not possible in case of percolation flow.

The two major phenomena governing the calcium carbonate deposition, stock fisher et al. [14] is that the bacteria acts as a nucleation site and pH rise around the bacterial cell due to urea hydrolysis. In the case of percolation flow, both phenomena play the equally important role because the amount of bacteria retained on all the soil particles is not equal and distribution of cementing solution is also not uniform

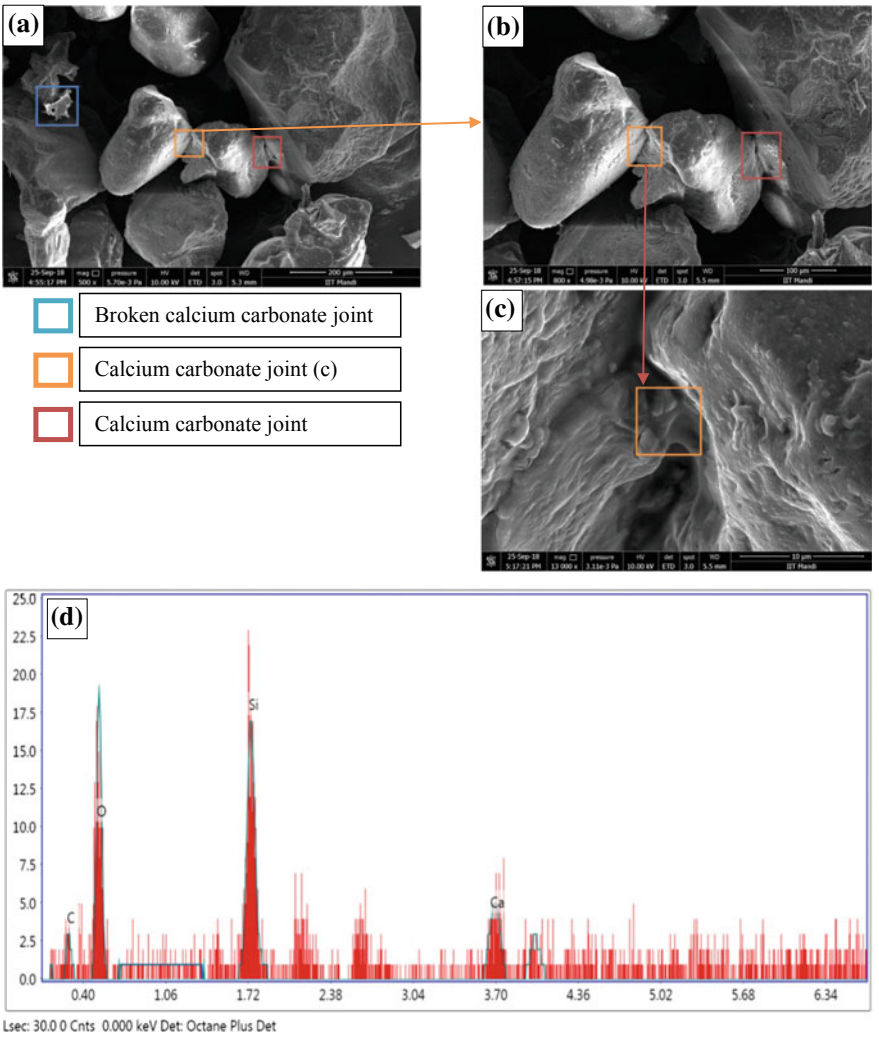

Fig. 1 SEM image for sample supplied with 0.25 M cementing solution at different magnification. **a** 200 μ, **b** 100 μ, **c** 10 μ and **d** EDAX analysis of (**c**) (Table 1)

as it retains more at particle–particle contact points, which gives rise to the more localized increase in pH and non-uniform calcite deposition.

In the case of higher cementing solution concentration as cementing media, it was observed that the calcium carbonate deposition was heavily random (Fig. 2a) as compared to the 0.25 M cementing media. It was also observed that the amount of calcium carbonate deposited at the junction of particles was more in case of high molar cementing solution concentration and a thick layer of calcium carbonate (Fig. 2a) was observed as compared to a thin easily breakable layer in case of low

Table 1 EDAX data of Fig. 1c

Element	Weight (%)	Atomic (%)	Error (%)	(K) ratio
C (K)	6.30	11.46	41.62	0.02
O (K)	39.46	53.88	17.88	0.15
Si (K)	21.86	17.01	13.22	0.20
Ca (K)	32.38	17.65	18.96	0.29

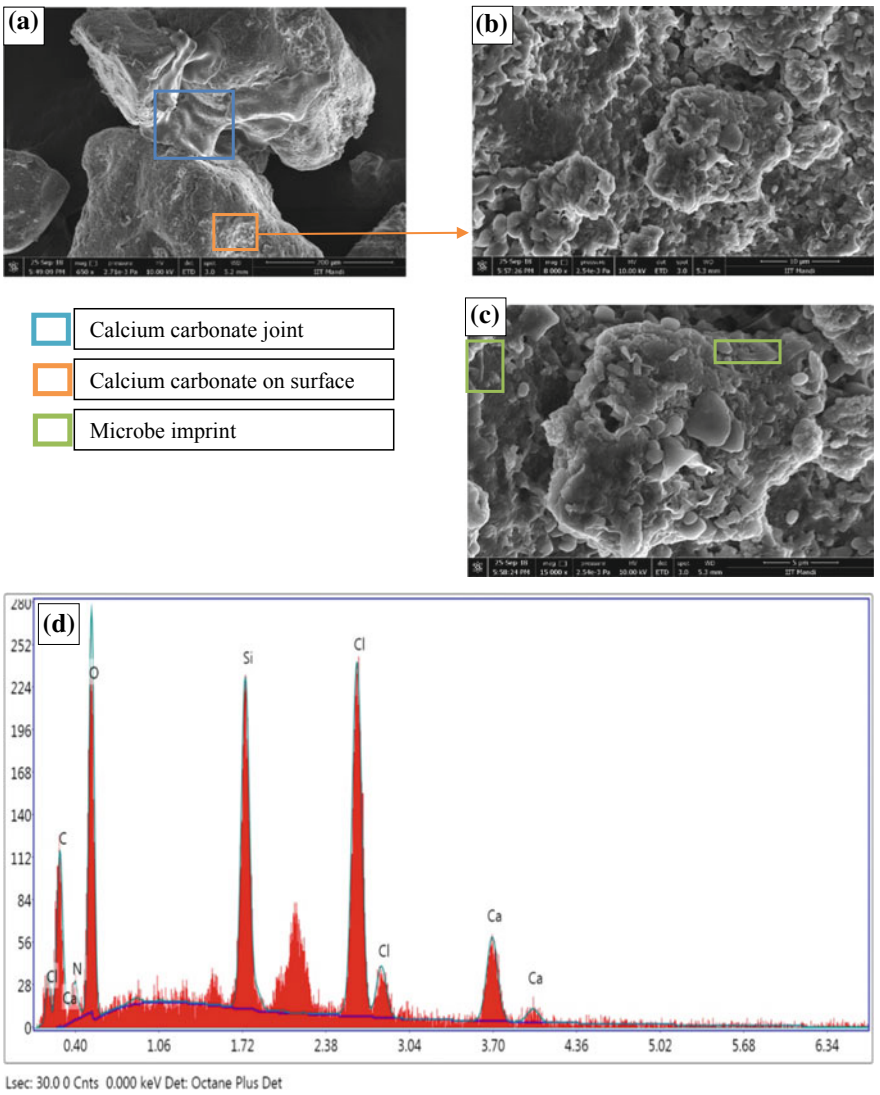

Fig. 2 SEM image for sample supplied with 0.75 M cementing solution at different magnification **a** 200 μ, **b** 10 μ, **c** 5 μ and **d** EDAX analysis of (**b**)

concentration of cementing solution (Fig. 3). The reason for this phenomenon may be that in case of higher concentration cementing solution, localized rise in pH takes place which results in thick calcium carbonate layer as observed by Qubany and Soga [8].

The SEM image at higher magnification shows the bacterial imprint on the calcium carbonate deposited on the sand particle (Fig. 2c) which shows that bacteria acts as a nucleation site. The bacteria are rod-shaped and approximately of length 2 μm. Deposition of calcium carbonate is observed to be of various shapes such as rounded, rhombohedral and platy shape (Fig. 2c). There are chances that the produced calcium carbonate is not only calcite but a mixture of calcite and vaterite which may be the reason for various shapes of calcium carbonate deposition.

Deposition of calcium carbonate takes place both at the particle–particle contact point as well as at the sand grain surface but it was also observed that the calcium carbonate was deposited maximum at the particle-particle interaction point and very less amount of calcium carbonate was deposited at the surface of the sand grain as depicted by Fig. 2a. As the supply of cementing solution and bacteria were performed by the percolation method the solution does not stay more at the surface but gets accumulated at particle-particle contact point because of menisci formation. This menisci formation results in the filling of gaps between the particles and results in the increase in shear strength of the soil.

4 Conclusion

The impact of various cementing solution concentration on the calcium carbonate deposition was observed by the SEM image analysis, supported by EDAX, and it was observed that more homogeneous calcite was deposited in the low concentration cementing solution supplied with more number of injection as compared to higher concentration cementing solution supplied with less number of injection.

The mechanism of bacteria acting as a nucleation site for calcium carbonate deposition was also observed from the images as postulated by Stock Fisher et al. [14]. It may also be concluded from the SEM images that, both the mechanism for calcium carbonate deposition, bacteria acting as the nucleation site and rise in pH for urea hydrolysis by the bacterial cell are the equally important phenomenon in case of percolation flow as both bacteria and urea both gets distributed irrespective to each other.

To increase the efficiency of the method, the percolation method was adopted and it was observed that most of the calcite only gets deposited at the junctions and very less calcium carbonate at the surface. The major advantage of percolation flow is that non-homogeneous calcium carbonate deposition is not harmful until the calcium carbonate is getting deposited at the optimum location and the strength increase in soil is at the required value. However, the development of bonding and its influence on shear strength can be expressed more confidently in the presence of

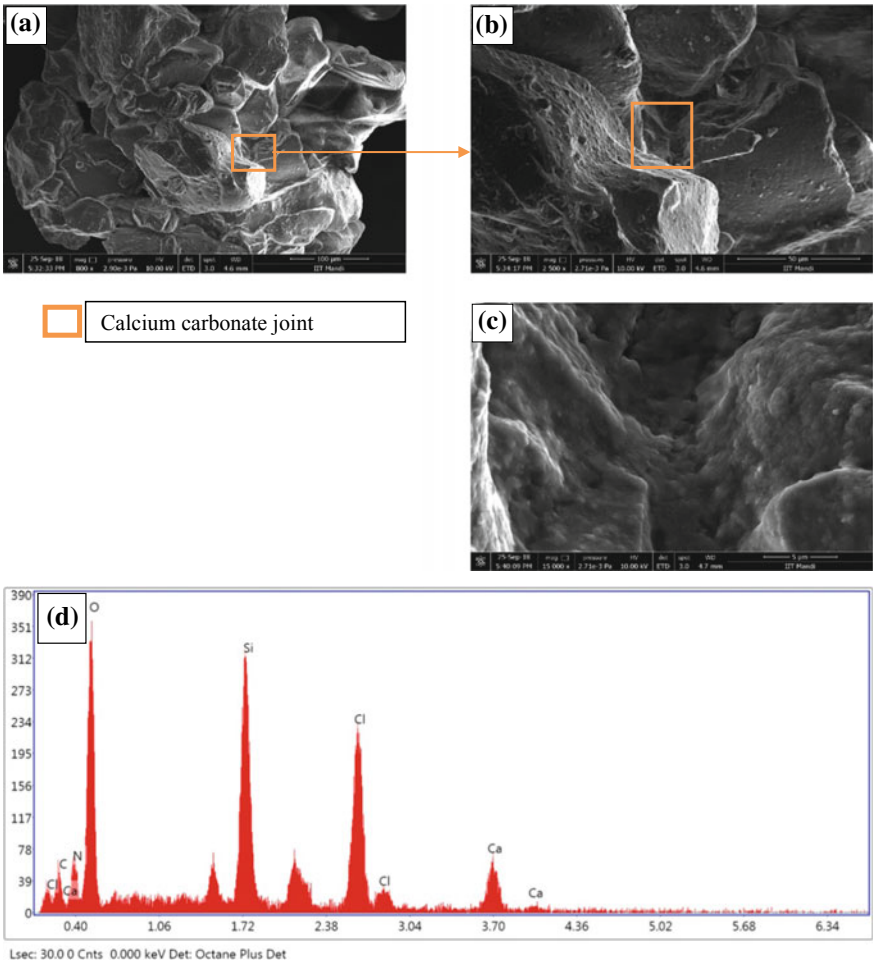

Fig. 3 SEM image for sample supplied with 1 M cementing solution at different magnification. **a** 100 μ, **b** 50 μ, **c** 5 μ and **d** EDAX analysis of (**c**)

support from UCS (Unconfined Compressive Strength), XRF (X-Ray Fluorescence) and XRD (X-Ray Diffraction) data.

References

1. Frankenberger WT, Troeh FR, Dumenil LC (1979) Bacterial effects on hydraulic conductivity of soils. Soil Sci Soc Am J 43:333–338
2. Mitchell JK, Santamarina JC (2005) Biological considerations in geotechnical engineering. J Geotech Geoenvironmental Eng 131(10):1222–1233

3. Nemati M, Voordouw G (2003) Modification of porous media permeability, using calcium carbonate produced enzymatically in situ. Enzyme Microb Technol 33(5):635–642
4. Whiffin VS, Van Paassen LA, Harkes MP (2007) Microbial carbonate precipitation as a soil improvement technique. Geomicrobiol J 24(5):417–423
5. Harkes MP, Van Paassen LA, Booster JL, Whiffin VS, Van Loosdrecht MCM (2010) Fixation and distribution of bacterial activity in sand to induce carbonate precipitation for ground reinforcement. Ecol Eng 36(2):112–117
6. Cheng L, Cord Ruwisch R (2012) In situ soil cementation with ureolytic bacteria by surface percolation. Ecol Eng 42:64–72
7. Cheng L, Shahin MA, Mujah D (2016) Influence of key environmental conditions on microbially induced cementation for soil stabilization. J Geotech Geoenvironmental Eng 143(1):1–13
8. Al Qabany A, Soga K (2013) Effect of chemical treatment used in MICP on engineering properties of cemented soils. Géotechnique 63(4):331–339
9. Al Qabany A, Soga K, Santamarina C (2012) Factors affecting efficiency of microbially induced calcite precipitation. J Geotech Geoenvironmental Eng 138(8):992–1001
10. Cheng L, Cord Ruwisch R, Shahin MA (2013) Cementation of sand soil by microbially induced calcite precipitation at various degrees of saturation. Can Geotech J 50(1):81–90
11. Ismail MA, Joer HA, Randolph MF, Meritt A (2002) Cementation of porous materials using calcite. Geotechnique 52(5):313–324
12. Uday KV, Padmakumar GP, Singh DN (2013) Some studies on morphology of coarse-grained soils. Eng Geol 152(1):48–55
13. Ramachandran SK, Ramakrishnan V, Bang SS (2001) Remediation of Concrete using microorganisms. ACI Mater J-Am Concr Inst 98(1):3–9
14. Stocks Fischer S, Galinat JK, Bang SS (1999) Microbiological precipitation of $CaCO_3$. Soil Biol Biochem 31(11):1563–1571